

Geotechnical Special Publication
No. 232

IACGE 2013

Challenges and Recent Advances
in Geotechnical and Seismic Research
and Practices



Proceedings of the Second International Conference
on Geotechnical and Earthquake Engineering



EDITED BY

Jianping Hu, Jianlin Ma, Jorge Meneses,
Tong Qiu, Xiong (Bill) Yu, and
Xiangwu (David) Zeng



GEOTECHNICAL SPECIAL PUBLICATION NO. 232

IACGE 2013

*CHALLENGES AND RECENT ADVANCES IN
GEOTECHNICAL AND SEISMIC RESEARCH AND
PRACTICES*

PROCEEDINGS OF THE SECOND INTERNATIONAL CONFERENCE ON
GEOTECHNICAL AND EARTHQUAKE ENGINEERING

October 25-27, 2013
Chengdu, China

SPONSORED BY

The International Association of Chinese Geotechnical Engineers
The Chinese Academy of Engineering, Division of Civil, Hydraulic, and
Architecture Engineering
The Geo-Institute of the American Society of Civil Engineers

EDITED BY

Jianping Hu
Jianlin Ma
Jorge Meneses
Tong Qiu
Xiong (Bill) Yu
Xiangwu (David) Zeng



Published by the American Society of Civil Engineers

Library of Congress Cataloging-in-Publication Data

International Conference on Geotechnical and Earthquake Engineering (2nd : 2013 : Chengdu, China)

IACGE 2013 : challenges and recent advances in geotechnical and seismic research and practices : proceedings of the second International Conference on Geotechnical and Earthquake Engineering, October 25-27, 2013, Chengdu, China / sponsored by the International Association of Chinese Geotechnical Engineers, the Chinese Academy of Engineering, Division of Civil, Hydraulic, and Architecture Engineering, the Geo-Institute of the American Society of Civil Engineers ; edited by Jianping Hu, Jianlin Ma, Jorge Meneses, Tong Qiu, Xiong (Bill) Yu, Xiangwu (David) Zeng.

pages cm -- (Geotechnical special publication ; no. 232)

Includes bibliographical references.

ISBN 978-0-7844-1312-8 (pbk.) -- ISBN 978-0-7844-7797-7 (PDF)

I. Geotechnical engineering--Congresses. 2. Earthquake engineering--Congresses. I. Hu, Jianping, 1972- II. International Association of Chinese Geotechnical Engineers. III. Zhongguo gong cheng yuan. Tu mu shui li yu jian zhu gong cheng xue bu. IV. American Society of Civil Engineers. Geo-Institute. V. Title. VI. Title: Challenges and recent advances in geotechnical and seismic research and practices. VII. Title: Proceedings of the second International Conference on Geotechnical and Earthquake Engineering, October 25-27, 2013, Chengdu, China.

TA710.A114728 2013

624.1'51--dc23

2013028467

American Society of Civil Engineers

1801 Alexander Bell Drive

Reston, Virginia, 20191-4400

www.pubs.asce.org

Any statements expressed in these materials are those of the individual authors and do not necessarily represent the views of ASCE, which takes no responsibility for any statement made herein. No reference made in this publication to any specific method, product, process, or service constitutes or implies an endorsement, recommendation, or warranty thereof by ASCE. The materials are for general information only and do not represent a standard of ASCE, nor are they intended as a reference in purchase specifications, contracts, regulations, statutes, or any other legal document. ASCE makes no representation or warranty of any kind, whether express or implied, concerning the accuracy, completeness, suitability, or utility of any information, apparatus, product, or process discussed in this publication, and assumes no liability therefore. This information should not be used without first securing competent advice with respect to its suitability for any general or specific application. Anyone utilizing this information assumes all liability arising from such use, including but not limited to infringement of any patent or patents.

ASCE and American Society of Civil Engineers—Registered in U.S. Patent and Trademark Office.

Photocopies and permissions. Permission to photocopy or reproduce material from ASCE publications can be obtained by sending an e-mail to permissions@asce.org or by locating a title in ASCE's online database (<http://cedb.asce.org>) and using the "Permission to Reuse" link. *Bulk reprints.* Information regarding reprints of 100 or more copies is available at <http://www.asce.org/reprints>.

Copyright © 2013 by the American Society of Civil Engineers.

All Rights Reserved.

ISBN 978-0-7844-1312-8 (print)

ISBN 978-0-7844-7797-7 (PDF)

Manufactured in the United States of America.

Preface

This Geotechnical Special Publication contains selected technical papers of the 2nd International Conference on Geotechnical and Earthquake Engineering organized by the International Association of Chinese Geotechnical Engineers (IACGE) and the Chinese Academy of Engineering, Division of Civil, Hydraulic and Architecture Engineering. The conference covers a broad field of topics in geotechnical and geotechnical earthquake engineering, including soil dynamics and earthquake engineering, foundation engineering and pile testing, excavation and shoring, embankments and retaining walls, tunnels and underground structures, dams and levees, slopes and landslides, expansive soils and loess, geology and rock mechanics, ground improvement techniques, geotechnical numerical modeling and computation, and geotechnical support technologies during construction.

About four hundred abstracts were received in response to the Call for Papers. The abstracts were reviewed by the organizing committee and as a result three hundred and fifty invitations were extended to prepare and submit full-length papers. A total of three hundred and twenty full-length papers were received in response to these invitations and one hundred and seventy papers out of the total were written in English.

The papers written in English were reviewed following the same procedures and technical standards of the ASCE Geotechnical Special Publications. Each paper must have received two positive reviews to be accepted and must have revised to conform to the mandatory revisions of the reviewers. A number of papers went through more than one cycle of review and revision. Standard editorial review forms and checklists were utilized to maintain uniform technical standards of the papers. As a result, one hundred and thirty papers were accepted for the conference and ninety-two papers were selected to be included in this ASCE Geotechnical Special Publications. All the papers selected for the Geotechnical Special Publications are eligible for discussion in the ASCE Journal of Geotechnical and Geoenvironmental Engineering and for ASCE award nominations.

The paper review would not have been possible without the help of a group of lead reviewers, who, on behalf of the Technical Committee, organized and in some cases conducted the review of a group of papers. The editors would like to acknowledge the invaluable contribution of the following lead reviewers:

| | | |
|------------------|-----------------------|----------------|
| Fu, Haiying | Hu, Jianping | Liu, Jinyuan |
| Mok, Chinman | Qiu, Tong | Meneses, Jorge |
| Mao, Jianqiang | Ma, Jianlin | Shang, Julie |
| Wu, Xingxu | Yan, Li | Yan, Liping |
| Yu, Xiong (Bill) | Zeng, Xiangwu (David) | Zhang, Jianhai |
| Zhang, Jianjin | Zhang, Jichun | Zhou, Depei |
| Zhu, Ming | | |

This publication would not have been possible without the dedication and professionalism of the paper reviewers. The names of these highly qualified reviewers are listed in the followings. For any additional reviewers whose names were inadvertently missed, we offer our sincere apologies.

| | | |
|----------------------|--------------------------|-----------------------|
| Andrei, Dragos | Li, Xiang Song | Sui, Wanghua |
| Arnold, Arnold | Li, Yuru | Sura, Joseph |
| Bergado, Dennes | Liang, Qingguo | Tan, Phalkun |
| Cao, Laifa | Liao, Yun | Tang, Xiaochao |
| Chen, Xingnian | Lin, Peiyuan | Tao, Junliang |
| Conkle, Chris | Lin, Sean | Tareq, Tareq |
| Cook, Michael O. | Liu, Chi-Tseng | Torsiello, Michael |
| C-T, Carlos | Liu, Chunyang | Varatharaj, Raj |
| Cui, Zhen-Dong | Liu, Fang | Vincente, Earnest |
| Darson, Ethan | Liu, Hua | Wainaina, Njoroge |
| Deng, Lijun | Liu, Jinyuan | Wang, Chen |
| Dodds, Andy | Liu, Pinghui | Wang, Jay |
| Dong, Xuejiang | Liu, Yaoru | Wang, Ning |
| Ebrahimi, Ali | Liu, Ying | Wang, Zhi-Liang |
| Eitthoef, Alan | Liu, Zhen | Williams, Adam S. |
| Escandon, Richard F. | Lu, Dechun | Wu, Xingxu |
| Fahmy, Ahmed | Lu, Jinchi | Xiao, Ming |
| Fanyu, Fanyu | Lukkarila, Chad | Yan, Li |
| Franke, Kevin | Luo, Xiangqi | Yan, Liping |
| Fu, Haiying | Ma, Jianlin | Yang, Hong |
| Gao, Bo | Maki, Ian | Yao, John |
| Gao, Quan | Mao, Jianqiang | Yi, Fred |
| Gao, Yue | Matasovic, Neven | Ying, Zongze |
| Ge, Louis | Meneses, Jorge | Yu, Xiong (Bill) |
| Guptill, Paul D. | Mohamedelhassan, Eltayeb | Yuan, Jiabei |
| He, Liangcai | Mok, Chinman | Yuan, Lei |
| Hsiao, Evan | Motamed, Ramin | Yuan, Xuanxun |
| Hu, Jianping | Nadeswaran, Vallipuram | Zeng, Xiangwu (David) |
| Hu, Jianying | Nguyen, Thang | Zhang, Jianhai |
| Huang, Jerry | Peiyuan, Peiyuan | Zhang, Jianjin |
| Huo, Yili | Peng, Shuquan | Zhang, Jichun |
| Jaeger, Robert | Pradel, Daniel | Zhang, Min |
| Joshi, Rutuparna | Qin, Jin | Zhang, Ru |
| Kim, Byungmin | Qiu, Tong | Zhang, Xiong |
| Kim, Sangmin | Rugg, Scott | Zhong, Peng |
| Laifa, Laifa | Salifee, Ali | Zhou, Cheng |
| Lam, Carlos | Salloum, Tareq | Zhou, Depei |
| Lee, Joon K | Shafiee, Ali | Zhou, Xiaojun |
| Lemmer, Robert | Shang, Julie | Zhou, Youwei |
| Li, Chunling | Shenthan, T. | Zhu, Fanyu |
| Li, Feng | Sivathasan, Siva | Zhu, Ming |
| Li, Longqi | Su, Bei | |

We are thankful to the Southwest Jiaotong University, HydroChina Chengdu Engineering Corporation, Sichuan University, China Railway Eryuan Engineering Group, China Railway Southwest Research Institute, and Changjiang River Scientific Research Institute for hosting this conference. Thanks are also extended to Robert Schweinfurth, ASCE Geo-Institute Director, for his coordination and enthusiastic support to this conference. The editors also acknowledge the assistance of Ms. Donna Dickert at ASCE Geo-Institute in the final production of this Geotechnical Special Publication.

Finally, we would like to express our sincere appreciation to all the authors for their significant contributions to the success of the conference.

Jianping Hu
Los Angeles Department of Water and Power

Jianlin Ma
Southwest Jiaotong University

Jorge Meneses
GEI Consultants Inc.

Tong Qiu
The Pennsylvania State University

Xiong (Bill) Yu
Case Western Reserve University

Xiangwu (David) Zeng
Case Western Reserve University

June 26, 2013

This page intentionally left blank

Contents

| | |
|--|------------|
| Some Advice on Vertical Draining Channels in Settlement Calculation of Soft-Soil Roadbed with Finite Element Method (Vacuum Preloading) | 1 |
| Zhen-Yu Wand, Ming Lei, and Xing-hua Wang | |
| Theoretical Solution for Dynamic Responses of Saturated Soils | 11 |
| Chuanxiang Xiong, Xiaobing Lu, and Xuhui Zhang | |
| Application of Modified Terzaghi Theory in Deposited Sediment Consolidation | 19 |
| Yanqiu Meng, Peiqing Wang, Fuhai Zhang, and Shuaijie Guo | |
| Rotating Block Method for Seismic Displacement of Slopes of Saturated Clay | 27 |
| X. Zeng and C. He | |
| Attenuation Plateau Characteristics and Fitting Analysis of the Dynamic Compaction Shockwave | 37 |
| Xing Fang, Tianbin Li, Hongmin Ma, and Feng Wang | |
| Developing an Economical and Reliable Test for Measuring the Resilient Modulus and Poisson's Ratio of Subgrade Soils | 45 |
| X. Zeng and R. Hu | |
| Numerical Analysis of Dynamic Response and Influence Factors on PCC Pile Composite Foundation of High Speed Railway | 54 |
| Qiang Fu, Xuanming Ding, Hanlong Liu, and Gangqiang Kong | |
| Analysis on Deformation Mechanism of PCC Pile Composite Foundation under Train Vibration Load | 62 |
| Qiang Fu, Xuanming Ding, Hanlong Liu, and Gangqiang Kong | |
| Study on Formation Mechanism of Liujiawan Landslide Triggered by Wenchuan Earthquake | 70 |
| Yonghong Luo, Yunsheng Wang, Ronghua Fu, and Jie Liu | |
| Study on the Classification of Loess Ground in Tunnel Engineering | 79 |
| Qing-guo Liang, Lili Wang, and De-wu Li | |
| Shear Strength Characteristics of an Artificially Cemented Sand-Gravel Mixture | 88 |
| Younes Amini, Amir Hamidi, and Ebrahim Asghari | |
| Key Factors of Subgrade Influencing Dynamic Wheel/Rail Loads at Railway Transition Zones | 96 |
| Hanbing Hu and Hans Brinkman | |
| Dynamic Characteristics of Subgrade Bed for Ballastless Track | 105 |
| Xianghui Kong, Guanlu Jiang, Dong Xiao, and Anhong Li | |
| Study on Seepage-Induced Debris Flow Initiation under the Rainfall Action for Loose Soil | 112 |
| Chi Li, Wenhui Zhu, and Xiaobing Lu | |

| | |
|--|------------|
| Reasonable Layout of Cross Passages for the Qianjiang River Tunnel Based on Seismic Analysis | 120 |
| Qizhu Jiao, Di Zhang, Shaoming Liao, and Yizhi Xu | |
| Study on Stability and Failure Mode of Bedding Rock Slope Affected by Rock Mass Structural Plane Parameters | 128 |
| S. Huang and B. Song | |
| Numerical Analysis of Failure Mode of Geocell Flexible Retaining Wall | 136 |
| Fei Song, Geng-Ren Cao, Lu-Yu Zhang, and Xiu-Mei Tan | |
| Shear Modeled from Random Particle Movement..... | 146 |
| Paul G. Joseph | |
| A Stability Analysis Method for Arbitrary Slip Block Based on Finite Element Method | 154 |
| Xikang Liu, Jianhai Zhang, and Wenguang Zhao | |
| A Similar Cam-Clay Model for Sand Based on the Generalized Potential Theory..... | 162 |
| Yong Wen, Guanghua Yang, Zhihui Zhong, Xudong Fu, and Yucheng Zhang | |
| Stability Behavior of Lime-Stabilized Gypseous Soil under Long-Term Soaking..... | 170 |
| A. Aldaood, M. Bouasker, and M. Al-Mukhtar | |
| The Study on the Influences of Drainage Way Arrangements on the Law of Seepage Flow in the Slope | 178 |
| Bing Yang, Chong Wang, Fengtao Wan, Tao Yang, and Qiorong Yan | |
| Visualization of Grout Permeation inside Transparent Soil..... | 188 |
| Jinyuan Liu, Yue Gao, and Wanghua Sui | |
| Influence of Curing Time on the Main Mechanical Characteristics of High-Water Content and Quick-Setting Stones | 195 |
| Hui Xie, Changwu Liu, Yu Wang, and Dingyang Ye | |
| Soil Cementation Generated and Enhanced by Electrokinetics | 205 |
| Julie Q. Shang and Ping hui Liu | |
| The Effect of Excavation Disturbance on Rockburst Trigger under Different Horizontal Geostress | 213 |
| Ru Zhang, Gang Wu, Ming-zhong Gao, Jin-bing Wei, and Yan-fei Zhang | |
| Parametric Study on the Effect of Deep Excavation on the Adjacent Metro Station in Suzhou | 223 |
| Shifeng Wei, Shaoming Liao, Yanbing Zhu, Xiang Li, and Yong Tan | |
| A Visco-Elastic Model with Loading History Dependent Modulus and Damping for Seismic Response Analyses of Soils..... | 231 |
| Zhiliang Wang and Fenggang Ma | |
| Investigation of Influencing Factors on Strain Localization inside Sand Specimens Subjected to Triaxial Loading | 241 |
| Ye Lu | |
| Influential Factors on Slope Stability and Landslide Mobility | 247 |
| Deping Guo, Masanori Hamada, and Hongyu Jia | |

| | |
|---|------------|
| Test Research of Dynamic Strength and Deformation on Geogrid-Reinforced Cohesive Soil under Cyclic Loading | 255 |
| Ning Wang, Zhixing Han, Wenmei Su, and Wenxu Li | |
| A Numerical Study on Artificial Fill Embankment with Liquefiable Foundation Using FLAC | 263 |
| Genlong Wang, Hengxing Lan, and Guoqiang Yu | |
| Reference Strain γ_r in Hyperbolic Modeling of Dynamic Shear Modulus of Soils | 271 |
| Zhijia Wang, Gang Fan, Jianwei Han, Weiming Liao, and Jianjing Zhang | |
| Physical and Analytical Modeling of Tire Mat-Reinforced Vegetated Slope | 279 |
| Cheng Zhou, Jiao Liu, Yao-Wen Xing, Hong-Liang Zhu, and Zhi-Gang Rao | |
| Experimental Study on Compression Modulus of Sandy Soil..... | 287 |
| Qi Yang, Wu-ming Leng, Sheng Zhang, and Ru-song Nie | |
| Model Test Study on Force and Deformation Characteristics of Steel Tubular Composite Piles..... | 297 |
| Min Zhang, Jianlin Ma, Weisheng Wu, and Hongbing Xie | |
| The Chemical-Physical Combined Method for Improving Clay Slurry in Land Reclamation | 308 |
| Dong Qing Wu, Wen Yu Xu, and Dan Ping Zhu | |
| Research on New Dam Structure for High Earth Core Rockfill Dam on Thick Overburden..... | 316 |
| Han Xu, Bin Huang, Xibao Rao, Jiajun Pan, and Yun Chen | |
| Shear Strength Characteristics of Fissure Plane in Expansive Soil..... | 324 |
| Hu Bo and Sun Hui | |
| Dynamic Model of Subgrade Using a Coupled Vehicle-Track-Subgrade Method | 334 |
| Xue Ning Ma, Xu Wang, Bo Liang, and Song Hong Yan | |
| Reliability Analysis on Anti-Overturning Stability of Supporting Structure of Excavation Using Monte Carlo Method | 343 |
| Weiming Hu, Jianlin Ma, Xiongzhi Peng, and Leilei Li | |
| Foundation Treatment Methods of Metro Station on Geologically-Sensitive Area..... | 352 |
| Chao Zou, Yi-Min Wang, Wen-Ming Song, and Yin-Lin Tang | |
| Field Comparative Tests for Studying the Vertical Loading Performance of Piles Due to Water Level Periodical Fluctuation in Foundation Soils | 361 |
| Ru-song Nie, Wu-ming Leng, and Qi Yang | |
| Simulation of the Dangerous Area by PFC for the Lvchunba Crag Body | 371 |
| Jun Xu, Anhong Li, Yongxin Wei, Chugen Li, and Yang Liu | |
| Stability Assessments of the Slope Controlled by Deep Seated Concentrating Belts of Unloading Fractures in Dagangshan, China: A Case Study | 380 |
| Mingli Xiao, Hongqiang Xie, Jiangda He, Baiyu Xiang, and Hualin Yang | |
| Shallow Slope Stability Analysis Method for Vegetated Slope | 388 |
| Junyun Zhang | |

| | |
|--|-----|
| Research on the Settlement Behavior of Ram-Compacted Piles with Bearing Base | 396 |
| Hongyun Chen, Jianlin Ma, Guotang Zhao, and Zailiang Xu | |
| Imaging the Graben Structure Based on Microtremor with H/V Spectral Ratio | 406 |
| Qian Zhang, Boming Zhao, Jianda Liu, Hangang Xu, and Zhibing Gao | |
| Measuring Shear and Compression Wave Velocities in Laboratory Triaxial Tests Using Disk-Shaped Composite P/S Piezoelectric Transducer | 414 |
| Muhammad Irfan and Taro Uchimura | |
| Analysis of Elastic Support Beam on Dynamic Load | 422 |
| Yang Liu, Ming-yang Wang, and Chun-ming Song | |
| Field Deformation Study on Enclosure Structure and Environment of Subway Shaft Construction under Complex Conditions | 430 |
| Aijun Yao, Hu Peng, Huanfang Chen, and Fangduan Ning | |
| Effect Analysis of Soft Rock Slope Reinforced by Bolts under Blasting Dynamic Load | 438 |
| Xinkuan Zou, Jichun Zhang, Hongchao Shi, and Zhongda Wang | |
| The Mechanism of Ground Subsidence Induced by EPB Tunneling in Sand and Cobble Stratum | 447 |
| Mingzhong Gao, Ru Zhang, and Man Wang | |
| Study on the Movement of Soil and Rock Mass Resulting from Underground Excavation of Horizontal Rectangle Section | 455 |
| Shi-Fan Qiao, Xi-Bao Zhang, Xiao Sun, and Bao-Chen Liu | |
| Discussion on Superposition Empirical Formula of Ultimate Bearing Capacity Based on the Upper Bound Limit Analysis Theory | 462 |
| Lianheng Zhao, Feng Yang, Fu Huang, and Wuming Len | |
| Back Analysis of Landslide Deposit Basal Failure Plane Residual Shear Strength | 471 |
| N. Matasovic, C. Conkle, A. F. Witthoef, A. Stern, and T. Hadj-Hamou | |
| Study on the Modified Coefficient of Dynamic Penetration Rod Length | 481 |
| Yongzhen Zuo, Zhanlin Cheng, Hongshun Ding, and Jianhui Liao | |
| Study on Hydrodynamic Pressure and Dynamic Response of Pier under Long-Period Earthquakes | 489 |
| Bo Song and Shuai Huang | |
| Seismic Damage Rules and Seismic Risk of Tunnel Portals Based on Fuzzy Comprehensive Evaluation Method | 498 |
| Wan-Jun Zang and Zheng-Zheng Wang | |
| Influence of Overlying Goaf Dip Angle on Stability of Highway Tunnel during Excavation | 507 |
| Ya-peng Fu, Yong Fang, Ge Cui, and Bin Yang | |
| Stability Analysis of Landslide Dam under Rainfall | 515 |
| Pei-Hsun Tsai, Zheng-Yi Feng, Fan-Chieh Yu, and Jian-Han Lin | |
| Experimental Study on Strength and Deformation Characteristics of Gassy Muddy Clay with Thin Silt Interlayers | 523 |
| Yong Wang, Kun Mu, and Yanli Wang | |

| | |
|--|-----|
| Analysis of Surrounding Rock Displacement Induced by Tunnel Excavation in Horizontal Interbedding Rock Mass | 531 |
| Yong Fang, Ya-peng Fu, Bin Yang, Ge Cui, and Xiao-min Wang | |
| A Transversely Isotropic Cosserat Continuum Model and Its Numerical Application | 541 |
| Zhaolong Hu and Hongxiang Tang | |
| 3-D Masing Behavior of a Parallel Iwan Model | 549 |
| Ethan Dawson, Wolfgang Roth, and Bei Su | |
| Soil-Pile-Structure Interaction in Earthquake Engineering | 557 |
| Yingcai Han and Shin-Tower Wang | |
| Application of Soil-Structure Interaction (SSI) in the Analysis of Flexible Retaining Walls | 567 |
| Shin-Tower Wang, Luis Vasquez, and Daqing Xu | |
| Mechanistic Empirical Pavement Design Guide Input Parameters for Unbound Aggregates in Oklahoma | 578 |
| Zahid Hossain, Musharraf Zaman, and Curtis Doiron | |
| Large-Span Rock-Anchored Beam Safety Pre-Warning Method and Its Application in Underground Powerhouse | 586 |
| Chunyu Gao and Jianhui Deng | |
| Consolidation Behavior of Ultra-Soft Slurry and 1-D Consolidation Model Considering Viscosity | 595 |
| Jun Tong, Noriyuki Yasufuku, and Kiyoshi Omine | |
| The Settlement Behavior of Piled Raft Interaction in Undrained Soil | 605 |
| Abbasali Taghavi Ghalesari, Amin Barari, Pedram Fardad Amini, and Lars Bo Ibsen | |
| Pile Foundation Seismic Design Approach for the Padma Bridge, Bangladesh | 613 |
| Suraj De Silva, Chao Li, and GuoXiong Yu | |
| Aseismic Analysis of Circular Deep Grouting for Tunnel Surrounding Rock in Strong Earthquake Zone | 625 |
| Yusheng Shen, Bo Gao, Joshua Li, Yumin Wen, and Kelvin C. P. Wang | |
| Investigation of Liquefaction Potential of Alluvium underneath an Earth Embankment Dam | 635 |
| Jiaer Wu, Lelio Mejia, Erik Newman, and Michael Mooers | |
| Centrifuge Model Tests of Settling Characteristics about Extremely Deep Soft Subgrade Reinforcement by Composite Pile | 647 |
| Chunhui Su, Jianlin Ma, Yanqing Huang, and Zhongbo Hu | |
| On the Compressibility of Cement-Stabilized Zinc-Contaminated Kaolin Clay | 659 |
| Ning-Jun Jiang, Yan-Jun Du, Song-Yu Liu, and Jing-Jing Zhu | |
| The Role of Polypropylene Fibers and Polypropylene Geotextiles in Erosion Control | 669 |
| Muawia Dafalla and Ali Obaid | |
| Lateral Load on a Large Pile Group: A 3D Finite Element Model | 677 |
| Ning Wang, Jinchi Lu, and Ahmed Elgamal | |

| | |
|--|------------|
| Evaluation of Effective Soil Density in Resonant Column Tests | 685 |
| Yanbo Huang and Tong Qiu | |
| Geotechnical Impact of the 2008 Wenchuan Earthquake | 694 |
| Robert C. Lo | |
| A Case History of the Design and Construction of a Corrosion Protection System for a Steel Sheet Pile Wall..... | 704 |
| Ming Zhu, Fan Zhu, Chris Conkle, and John F. Beech | |
| Modeling of Debris Flow Using Distinct Element Method | 713 |
| Sung-Chi Hsu, Chich-Hong Jaing, and Ni-Chi Chen | |
| Shear Stress-Strain Curves Based on the G/G_{max} Logic: A Procedure for Strength Compatibility | 721 |
| James R. Gingery and Ahmed Elgamal | |
| Micro-Structure Behavior of Soft Clay under Consolidation through Radial Flow Using PVDs..... | 730 |
| Manish V. Shah and Arvind V. Shroff | |
| Evaluation of Pile Foundations Subjected to Liquefaction-Induced Lateral Spreading..... | 738 |
| Hua Liu and Endi Zhai | |
| Nonlinear Analysis for the Cooling Effect of Road Subgrade with Varying Spacings of Thermosyphons in Cold Regions | 746 |
| Yahu Tian and Jiankun Liu | |
| Prediction and Application of Equilibrium Water Content of Expansive Soil Subgrade..... | 754 |
| Jianlong Zheng and Rui Zhang | |
| Field Tests on Vibration Response of Ballastless Subgrade under Excitation of High Speed Train in China..... | 762 |
| Jianlin Ma, Yanxin Yang, Fuchun Xue, Liping Yan, Fei Jiang, and Cong Shi | |
| Field Test and Analysis of Piled-Raft Structure of High-Speed Railway Foundation | 770 |
| Duc-phong Pham, Qian Su, Hao Bai, Bao Liu, Hong-lin Sun, and Shang-yong Chen | |
| Experimental Study on Strength Characteristics of Unsaturated Remolded Loess..... | 779 |
| Sun Hui and Hu Bo | |
| Computer Simulations on the Effects of Desaturation on Soil Liquefaction Resistance | 786 |
| Quan Gao, Zhen Liu, and Xiong (Bill) Yu | |
| Reliability-Based Dam Erodibility Assessment | 796 |
| Chin Man Mok, Robert Wright, James Cooley, Eng Sew Aw, and Robert White | |

Author List

- Aldaood, A., 170
Al-Mukhtar, M., 170
Amini, Pedram Fardad, 605
Amini, Younes, 88
Asghari, Ebrahim, 88
Aw, Eng Sew, 796
- Bai, Hao, 770
Barari, Amin, 605
Beech, John F., 704
Bo, Hu, 324, 779
Bouasker, M., 170
Brinkman, Hans, 96
- Cao, Geng-Ren, 136
Chen, Hongyun, 396
Chen, Huanfang, 430
Chen, Ni-Chi, 713
Chen, Shang-yong, 770
Chen, Yun, 316
Cheng, Zhanlin, 481
Conkle, C., 471
Conkle, Chris, 704
Cooley, James, 796
Cui, Ge, 507, 531
- Dafalla, Muawia, 669
Dawson, Ethan, 549
De Silva, Suraj, 613
Deng, Jianhui, 586
Ding, Hongshun, 481
Ding, Xuanming, 54, 62
Doiron, Curtis, 578
Du, Yan-Jun, 659
- Elgamal, Ahmed, 677, 721
- Fan, Gang, 271
Fang, Xing, 37
Fang, Yong, 507, 531
- Feng, Zheng-Yi, 515
Fu, Qiang, 54, 62
Fu, Ronghua, 70
Fu, Xudong, 162
Fu, Ya-peng, 507, 531
- Gao, Bo, 625
Gao, Chunyu, 586
Gao, Mingzhong, 447
Gao, Ming-zhong, 213
Gao, Quan, 786
Gao, Yue, 188
Gao, Zhibing, 406
Ghalesari, Abbasali Taghavi, 605
Gingery, James R., 721
Guo, Deping, 247
Guo, Shuaijie, 19
- Hadj-Hamou, T., 471
Hamada, Masanori, 247
Hamidi, Amir, 88
Han, Jianwei, 271
Han, Yingcai, 557
Han, Zhixing, 255
He, C., 27
He, Jiangda, 380
Hossain, Zahid, 578
Hsu, Sung-Chi, 713
Hu, Hanbing, 96
Hu, R., 45
Hu, Weiming, 343
Hu, Zhaolong, 541
Hu, Zhongbo, 647
Huang, Bin, 316
Huang, Fu, 462
Huang, S., 128
Huang, Shuai, 489
Huang, Yanbo, 685
Huang, Yanqing, 647
Hui, Sun, 324, 779

Ibsen, Lars Bo, 605
Irfan, Muhammad, 414

Jaing, Chich-Hong, 713
Jia, Hongyu, 247
Jiang, Fei, 762
Jiang, Guanlu, 105
Jiang, Ning-Jun, 659
Jiao, Qizhu, 120
Joseph, Paul G., 146

Kong, Gangqiang, 54, 62
Kong, Xianghui, 105

Lan, Hengxing, 263
Lei, Ming, 1
Len, Wuming, 462
Leng, Wu-ming, 287, 361
Li, Anhong, 105, 371
Li, Chao, 613
Li, Chi, 112
Li, Chugen, 371
Li, De-wu, 79
Li, Joshua, 625
Li, Leilei, 343
Li, Tianbin, 37
Li, Wenxu, 255
Li, Xiang, 223
Liang, Bo, 334
Liang, Qing-guo, 79
Liao, Jianhui, 481
Liao, Shaoming, 120, 223
Liao, Weiming, 271
Lin, Jian-Han, 515
Liu, Bao, 770
Liu, Bao-Chen, 455
Liu, Changwu, 195
Liu, Hanlong, 54, 62
Liu, Hua, 738
Liu, Jianda, 406
Liu, Jiankun, 746
Liu, Jiao, 279
Liu, Jie, 70
Liu, Jinyuan, 188

Liu, Ping hui, 205
Liu, Song-Yu, 659
Liu, Xikang, 154
Liu, Yang, 371, 422
Liu, Zhen, 786
Lo, Robert C., 694
Lu, Jinchí, 677
Lu, Xiaobing, 11, 112
Lu, Ye, 241
Luo, Yonghong, 70

Ma, Fenggang, 231
Ma, Hongmin, 37
Ma, Jianlin, 297, 343, 396, 647, 762
Ma, Xue Ning, 334
Matasovic, N., 471
Mejia, Lelio, 635
Meng, Yanqiu, 19
Mok, Chin Man, 796
Moers, Michael, 635
Mu, Kun, 523

Newman, Erik, 635
Nie, Ru-song, 287, 361
Ning, Fangduan, 430

Obaid, Ali, 669
Omine, Kiyoshi, 595

Pan, Jiajun, 316
Peng, Hu, 430
Peng, Xiongzhi, 343
Pham, Duc-phong, 770

Qiao, Shi-Fan, 455
Qiu, Tong, 685

Rao, Xibao, 316
Rao, Zhi-Gang, 279
Roth, Wolfgang, 549

Shah, Manish V., 730
Shang, Julie Q., 205
Shen, Yusheng, 625

Shi, Cong, 762
 Shi, Hongchao, 438
 Shroff, Arvind V., 730
 Song, B., 128
 Song, Bo, 489
 Song, Chun-ming, 422
 Song, Fei, 136
 Song, Wen-Ming, 352
 Stern, A., 471
 Su, Bei, 549
 Su, Chunhui, 647
 Su, Qian, 770
 Su, Wenmei, 255
 Sui, Wanghua, 188
 Sun, Hong-lin, 770
 Sun, Xiao, 455

 Tan, Xiu-Mei, 136
 Tan, Yong, 223
 Tang, Hongxiang, 541
 Tang, Yin-Lin, 352
 Tian, Yahu, 746
 Tong, Jun, 595
 Tsai, Pei-Hsun, 515

 Uchimura, Taro, 414

 Vasquez, Luis, 567

 Wan, Fengtao, 178
 Wand, Zhen-Yu, 1
 Wang, Chong, 178
 Wang, Feng, 37
 Wang, Genlong, 263
 Wang, Kelvin C. P., 625
 Wang, Lili, 79
 Wang, Man, 447
 Wang, Ming-yang, 422
 Wang, Ning, 255, 677
 Wang, Peiqing, 19
 Wang, Shin-Tower, 557, 567
 Wang, Xiao-min, 531
 Wang, Xing-hua, 1
 Wang, Xu, 334

 Wang, Yanli, 523
 Wang, Yi-Min, 352
 Wang, Yong, 523
 Wang, Yu, 195
 Wang, Yunsheng, 70
 Wang, Zheng-Zheng, 498
 Wang, Zhijia, 271
 Wang, Zhiliang, 231
 Wang, Zhongda, 438
 Wei, Jin-bing, 213
 Wei, Shifeng, 223
 Wei, Yongxin, 371
 Wen, Yong, 162
 Wen, Yumin, 625
 White, Robert, 796
 Witthoeft, A. F., 471
 Wright, Robert, 796
 Wu, Dong Qing, 308
 Wu, Gang, 213
 Wu, Jiaer, 635
 Wu, Weisheng, 297

 Xiang, Baiyu, 380
 Xiao, Dong, 105
 Xiao, Mingli, 380
 Xie, Hongbing, 297
 Xie, Hongqiang, 380
 Xie, Hui, 195
 Xing, Yao-Wen, 279
 Xiong, Chuanxiang, 11
 Xu, Daqing, 567
 Xu, Han, 316
 Xu, Hangang, 406
 Xu, Jun, 371
 Xu, Wen Yu, 308
 Xu, Yizhi, 120
 Xu, Zailiang, 396
 Xue, Fuchun, 762

 Yan, Liping, 762
 Yan, Qiorong, 178
 Yan, Song Hong, 334
 Yang, Bin, 507, 531
 Yang, Bing, 178

Yang, Feng, 462
Yang, Guanghua, 162
Yang, Hualin, 380
Yang, Qi, 287, 361
Yang, Tao, 178
Yang, Yanxin, 762
Yao, Aijun, 430
Yasufuku, Noriyuki, 595
Ye, Dingyang, 195
Yu, Fan-Chieh, 515
Yu, Guoqiang, 263
Yu, GuoXiong, 613
Yu, Xiong (Bill), 786

Zaman, Musharraf, 578
Zang, Wan-Jun, 498
Zeng, X., 27, 45
Zhai, Endi, 738
Zhang, Di, 120
Zhang, Fuhai, 19
Zhang, Jianhai, 154
Zhang, Jianjing, 271
Zhang, Jichun, 438
Zhang, Junyun, 388
Zhang, Lu-Yu, 136
Zhang, Min, 297

Zhang, Qian, 406
Zhang, Ru, 213, 447
Zhang, Rui, 754
Zhang, Sheng, 287
Zhang, Xi-Bao, 455
Zhang, Xuhui, 11
Zhang, Yan-fei, 213
Zhang, Yucheng, 162
Zhao, Boming, 406
Zhao, Guotang, 396
Zhao, Lianheng, 462
Zhao, Wenguang, 154
Zheng, Jianlong, 754
Zhong, Zhihui, 162
Zhou, Cheng, 279
Zhu, Dan Ping, 308
Zhu, Fan, 704
Zhu, Hong-Liang, 279
Zhu, Jing-Jing, 659
Zhu, Ming, 704
Zhu, Wenhui, 112
Zhu, Yanbing, 223
Zou, Chao, 352
Zou, Xinkuan, 438
Zuo, Yongzhen, 481

Some Advice on Vertical Draining Channels in Settlement Calculation of Soft-Soil Roadbed with Finite Element Method (Vacuum Preloading)

Zhen-Yu Wand^{1,4}, Ming Lei^{1,3} and Xing-hua Wang^{1,2*}

¹Civil Engineering College, Central South University, Changsha 410075, P.R. China

²Department of Civil and Environment Engineering, College of Engineering, the Penn State University, University Park, PA 16802, USA

³Civil Engineering Department, Changsha College, Changsha 410011, P.R. China

⁴CCCC Tunnel Engineering Co., Ltd., Beijing 100088, China

ABSTRACT: Aiming at some disputation about disposal methods on vertical draining channels in model of numerical analysis of vacuum preloading, some analysis was carried out in the paper. Through a practical key project, two different disposal methods of vertical draining channels were used in the project. The finite element software was used to simulate the consolidation process of soft-soil in site. The results of simulating calculation and results measuring in site were compared. Differences of the two methods were shown clearly in the paper. Applicable instances for the two different disposal methods were pointed out.

INTRODUCTION

Vacuum preloading is an effective method that reinforces soft-soil foundation at present. For expedite consolidation speed of soft-soil foundation, some vertical draining channels with some depth are often set up in the foundation. The vertical draining channel may be sand drain and also it may be plastic draining board. The methods of numerical calculation of vacuum preloading of reinforcing soft-soil foundation have been studied by some researchers at home and abroad (Dong et al. 2008; He et al. 2005; Qin 2003; Wang et al. 2001; Xu et al. 2004; Zhu et al. 2007). But there are some disputes about the methods of numerical calculation. One of the disputes is about treating of vertical draining channel. However it can not reach an agreement that is that the vertical draining channel is thought as a media with high permeability through adjusting its permeability coefficient or that the vertical draining channel is considered as a stable negative pressure boundary condition with some rule in depth. In the paper, settlement and displacement of soft-soil in a key

engineering project were calculated with finite element software on different treatment methods of vertical draining channel but other condition is same. The results of calculation and measuring result in practice were contrastive analyzed.

PROJECT AND GEOLOGY SURVEY

The experimental field (Wang 2010) is on Kunshan City, Jiangsu province, between Hanjing Village Medium Bridge and Xugong River Medium Bridge. It is on the Taihu lacustrine plain. The landform is flatness. There are some man-made fish ponds in the plain. The ground level is about 2.5m. The experimental field area is K0+000~K0+850. The length of line is 850m. Of which K0+000~K0+38.40 and K0+833.95~K0+850 are experimental sections of bridge pile foundation. K0+38.4~K0+833.95 is experimental section of roadbed. The linearis is a right line. Longitudinal gradient is 0‰. Two terminal of the experimental section are two medium bridges. Hanjing Village terminal of experimental section is Hanjing Village Medium Bridge. Xugong River terminal of the experimental section is Xugong River Medium Bridge. There are 4 culvers in the roadbed section.

The foundation of experimental section is Rush Lake Bed, Holocene Series, Quaternary System. Strata distributing from above to below are:

(1) Clay, sallowness, soft ~ hard plastic, layer thickness is 0.76~3.6m;

(2) Sludge silty clay, deep gray, flow plastic. There is a little humus. There is sheet silty sand in part, with some characteristic of high compactibility, low strength, high thixotropic. Layer thickness is 32~16.5m.

(3) Clay, sage green, black gray, soft plastic ~ hard plastic. Layer thickness is 0~7.4m. It is distributed in K0+405 ~ K0+845. The horizon of the clay is stable. It is medium on the low side compressibility soil.

(4) Muddy soil in part hold sheet silty sand or clay, sallowness, soft ~ hard plastic. Layer thickness is 0~5.4m. It is distributed in K0+405 ~ K0+845. The horizon of the clay is stable. It is medium on the low side compressibility soil.

Physical and mechanical index of each soil layer are showed in Table 1.

Table 1. Physical Index and Mechanics Index of Every Soil Layer

| Index Soil layer | W | γ | e | W_L | W_p | Φ_u | C_u | a_v | E_s | C_v | C_h |
|------------------------|------|-------------------|------|-----------|-----------|----------|-------|-------------------|-------|--------------------|--------------------|
| | % | kN/m ³ | | % | % | ° | kPa | MPa ⁻¹ | MPa | cm ² /s | cm ² /s |
| (1) | 32.2 | 19.2 | 0.90 | 32.8~48.2 | 17.1~21.9 | 11.7 | 27.3 | 0.31 | 5.5 | 0.002593 | 0.001452 |
| (2) | 44.9 | 17.7 | 1.24 | 28.6~42.2 | 16.5~24.9 | 7.0 | 8.5 | 0.92 | 2.47 | 0.003167 | 0.005526 |
| (3) | 24.8 | 20.2 | 0.67 | 33.0~38.4 | 14~19.8 | 14.3 | 51.5 | 0.24 | 4.17 | 0.009585 | 0.004820 |
| (4) | 39.8 | 17.9 | 1.02 | 31.6~40.4 | 18.4~22.8 | 19.3 | 9.0 | 0.17 | 5.88 | 0.019030 | 0.018400 |

LAYOUT OF REINFORCEMENT

Through field survey, the foundation soil of researched experimental section is main clay and sludge silty clay. It is more suitable for forming a stable negative pressure boundary condition in reinforcing area. Vacuum preloading method is selected.

The section of K0+276.51 ~ K0+535 is selected as vacuum preloading experimental section. Plastics draining bar is used as vertical draining body. They are arrangement in quincunx.

FINITE ELEMENT CALCULATION

The consolidation of foundation under action of bar loading can be considered as plane strain and plane seepage. It has been proved by Xie (1987). In the paper, because the loading added to the foundation is strip loading, the consolidation will be treated as plane issue.

(1) The treatment of plastic draining bar

At first issue, vertical draining channel is considered as a medium with very high permeability:

While carrying out finite elemental calculation, the distance between two plastic bars will be enlarged. There are 6 sand walls in the foundation. According to the comparing of result of strain consolidation theory with two-way strain and two-way seepage and result of Baolong axis symmetry consolidation theory, under the condition of stable consolidation degree or stable average bore pressure of the soil, some equivalent calculation formula can be obtained as following, equivalent of sand well and sand wall in foundation can be obtained through adjusting their permeability coefficients(Zhao, etc. 1998):

$$\begin{aligned} k_{hq} &= D_h \cdot k_{hj} \\ k_{vq} &= D_v \cdot k_{vj} \end{aligned} \quad (1)$$

where: k_{hq} 、 k_{vq} , level permeability coefficient and vertical permeability coefficient of sand wall separate,

k_{hj} 、 k_{vj} , level permeability coefficient and vertical permeability coefficient of sand well separate,

D_h 、 D_v , adjusting coefficient of level and vertical permeability coefficient separate.

$$D_h = \frac{4(n_p - s_p)^2(1+\nu)L^2}{9n_p^2\mu_a - 12(1+\nu)\beta(n_p - s_p)(s_p - 1)L^2} \quad (2)$$

$$D_v = \frac{2(1+\nu)}{3}$$

where: L , enlarging coefficient of space between sand wells, $L = B/r_e$

B , a half of space between sand walls (4m),

r_e , radius of effective catchment area of sand well,

$$n_p = B/r_{wp} \quad (3)$$

r_{wp} , a half of width of sand wall (1m),

$$s_p = r_{sp}/r_{wp} \quad (4)$$

r_{sp} , a half of width of smearing area of sand wall foundation,

r_{wp} , a half of width of sand wall,

$$\beta = k_{hj}/k_{vj} \quad (5)$$

ν , Poisson's ratio

$$\mu_a = \frac{n^2}{n^2 - s^2} \ln \frac{n}{s} - \frac{3n^2 - s^2}{4n^2} + \frac{k_{hj}}{k_{vj}} \frac{n^2 - s^2}{n^2} \ln s \quad (6)$$

n , hole diameter ratio of sand well, $n = r_e/r_{wa}$,

r_{wa} , radii of sand well,

$$s = r_s/r_{wa} \quad (7)$$

r_s , radii of smearing area,

r_{wa} , radii of sand well.

In practical calculation, the sand wells will be replaced with plastic bars. The equivalent diameter of plastics draining bar can be calculated as following:

$$D_p = \alpha \frac{2(b+\delta)}{\pi} \quad (8)$$

D_p , equivalent diameter of plastics draining bar (cm),

α , conversion coefficient, without experimental data, it may be 0.75~1.00,

b , width of plastics draining bar,

δ , thickness of plastics draining bar.

In the proceeding of reinforcing soft soil foundation with plastic draining bar, some suggested $\alpha=1$.

The diameter of effective draining area of plastics draining bar can be calculated with as following formula:

$$d_e = 1.05S \quad (9)$$

Where: S, distance between two plastics draining bars.

Because well resistance and smearing action of plastics draining bar is very little than that of sand well, let $S=1$.

The second issue, vertical draining channel can be considered as boundary condition of negative pressure:

According to characteristic of vacuum preloading, in numerical analysis of vacuum preloading reinforcing foundation, the pore water pressure of crunode in negative pressure boundary is equal to the value of vacuum degree under the pressurized film (Qin 2003). While carrying out finite element calculation, the pore water pressure of cell crunode of surface boundary covered with pressurized film will be adjusted as stable negative pore water pressure according to practical measured vacuum degree. Through observation pore water pressure under pressurized film varies -20kPa ~ -30kPa. So the pore water pressure of cell crunode is setup as -25kPa (taking an average value). In the where the sand wall is set, the pore water pressure of cell crunode of boundary tangent with the soil along portrait was adjusted as a stable negative pore water pressure according to practical measured vacuum degree, the pore water pressure varies from large to small linearis from surface to low. The pore water pressure on the bottom of sand wall was 0, it is in basic agreement with observed pore water pressure. The permeability coefficient and other parameters of soil in the sand wall are same as that of around soil.

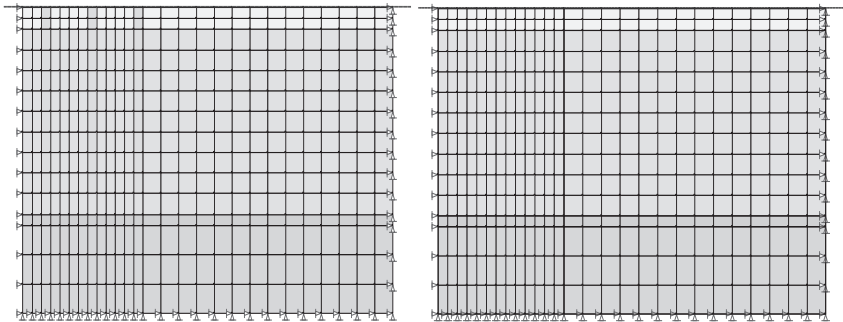
(2) Cell division

Reinforcing area is a simplex structure. Half of the area is taken. The center is symmetric axis. Compression stratum was calculated with layerwise summation method alone depth. It is 28m depth. Width is 40m. For simplifying calculation, the horizontal is presumed is on the level of ground surface. There are 3 sand walls in the foundation cell. Each soil layer is a cell area. Plastics draining bar is an alone sell area. There are 405 cells. Such as is showed as in Fig.1.

(3) Boundary condition

Because roadbed is symmetry, half of the roadbed was considered in calculation. Net flow of water on the center line of roadbed is zero, so left of calculation graph is

set as impervious boundary. There is not horizontal displacement in the roadbed, there is but only vertical settlement. The below calculation range is a sand layer, so the surface is set as a breaking through of water boundary. There is not any horizontal displacement and vertical settlement in the roadbed. Vacuum effect in right of calculating range is very little. Because seepage of water is not evidence, it can be ignore. The right of calculation figure is impervious boundary. There is not any horizontal displacement and vertical settlement in the roadbed. In the range of super face pressurized film, during numerical analysis of reinforcing foundation with vacuum preloading, the pore water pressure of node of negative pressure boundary is equal to the value of vacuum degree under the pressurized film according to the characteristic of vacuum preloading (Qin 2003). The pore water pressure of cell node is set as stable negative pore water pressure. Through observation, the pore water pressure under the film varies between $-20\text{kPa} \sim -30\text{kPa}$, so the pore water pressure of cell node is set as -25kPa (taking an average value). Region of super face excentant roadbed is free displacement boundary.



Treating vertical draining channels as a medium with very high permeability

Treating vertical draining channels as negative pressure boundary

FIG. 1. Element partition and boundary condition.

Note: one red triangle of the boundary condition in picture deputies a tie rod.

(4) Constitutive model

Many literatures (Ali et al. 2005; Gong 1981; Li et al. 2005; Liu et al. 2009; Liu et al. 2006; Qian et al. 1991; Qiu et al. 2007) have indicated that elastic model is best used constitutive model of soil. Also because it is contrasted that which treating method of vacuum preloading is the most near to the actual measured value, in the paper elastic model is only used.

ANALYSIS OF CALCULATING RESULTS

(1) Settlement of surface layer of center point of roadbed

The calculating result (see Fig.2) shows that the calculating result of finite element that the vertical draining channel is considered as a medium (coarse sand) with very high permeability is very close to the actual measured result. The calculating result of finite element that the vertical draining channel is considered as negative pressure boundary is evident larger than actual measured result. The calculating result of finite element in about 10 days that the vertical draining channel is considered as a medium with very high permeability is also larger than actual measured result. It is because during actual construction the vacuum pump was paused in about 10 days, the vacuum degree descend but the calculation condition is was set as ideal condition during the calculation. The curves of calculating result of two treating methods of vertical draining channel are more smoothing, but the curve of actual measured result is undulation. Also it is because that the model parameters are set as ideal condition during the calculation (each soil layer has same parameters), but in different place their soil parameters in the same soil layer are not same in fact.

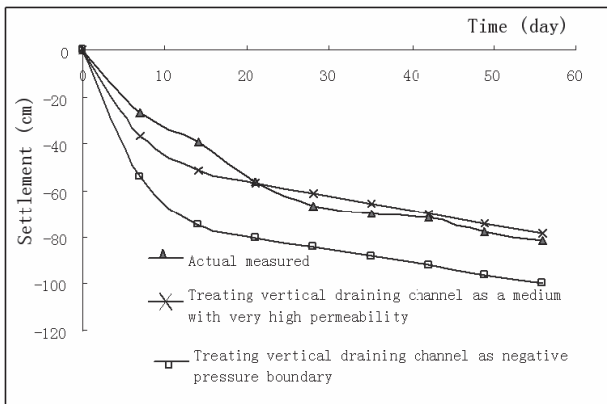


FIG. 2. Comparing between calculating result and actual measured data in surface center of roadbed with time.

(2) Settlement distributing of surface layer along transect of roadbed

Under action of bar loading settlement curve of soft soil roadbed is a basin curve according to the Boussinesq's solution. In the center of roadbed the settlement is the largest and the more little the settlement, the more near both sides of roadbed. But the phenomenon was not evident during vacuum preloading reinforcing soft soil. During actual construction the difference of settlement in the center line and in the edge of roadbed is not large. The distribution of settlement along transect of roadbed is more uniformity. From the Figure 2 we can know that the difference of calculating result of the two treating methods of vertical draining channel is not large. The more near the two calculating results, the more anear the center line of roadbed. After comparing the calculating results and actual measured result, the difference value

between calculating result of vertical draining channel that is considered as negative pressure boundary and actual measured result along transect of roadbed is more stable, but the litter the difference between the calculating result of vertical draining channel that is considered as a medium with very high permeability and actual measured result, the more near the edge of roadbed. It may be that because the plastic draining bar is set as sand wall in the latter calculation is more near actual roadbed. Taking all in all, the calculating result of vertical draining channel is considered as a medium with very high permeability is more perfect than the calculating result of vertical draining channel is considered as negative pressure boundary.

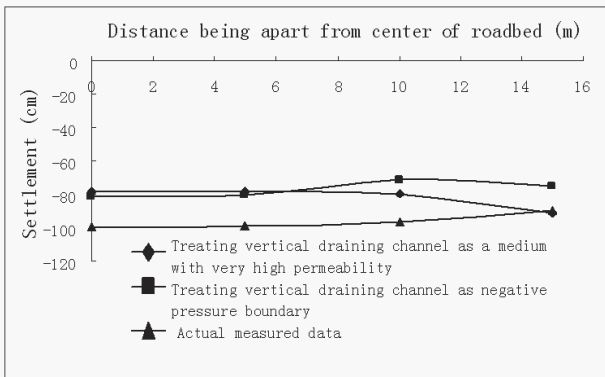


FIG. 3. Comparing between calculating result and actual measured data of surface of roadbed along with transect.

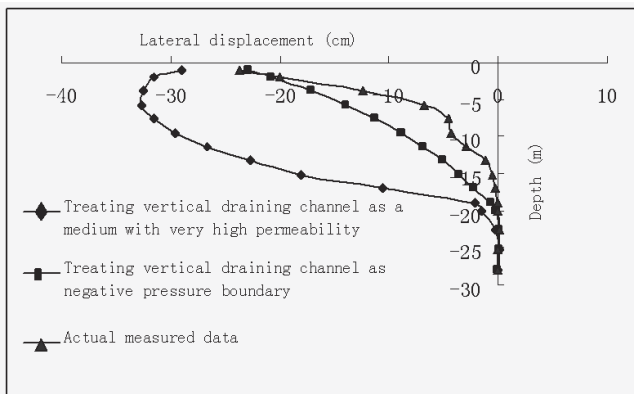


FIG. 4. Comparing between calculating result and actual measured data of lateral displacement of edge of roadbed along depth.

(3) Cross range displacement of roadbed edge

Under action of bing-loading the soil mass of soft soil roadbed edge will take place crossrange extruding displacement. Under action of vacuum loading the soil mass of soft soil roadbed edge will take place diffidence contraction displacement. The contraction displacement is sufficient produced in the calculating result of the two treating methods and actual measured result. The calculating results of the two treating methods on the surface of roadbed are near to the actual measured result. Especially the calculating result of vertical draining channel is considered as negative pressure boundary is almost same as the actual measured result on the surface of roadbed. In the depth range of 5m ~ 20m, the calculating results of the two treating methods are very different with actual measured result. To take all in all, the calculating result of vertical draining channel is considered as negative pressure boundary is more near the actual measured result.

CONCLUSIONS

Through above analysis, during construction of vacuum preloading, while calculating settlement, the calculating precision of settlement, which vertical draining channel is considered as a medium with very high permeability, is far higher than that, which vertical draining channel is considered as negative pressure boundary. For calculating crossrange displacement on the toe of slope of roadbed, the treating method of vertical draining channel is considered as negative pressure boundary is more ideal.

ACKNOWLEDGMENTS

The authors appreciate the support of the Engineering Research Foundation of the China Railway 4th Engineering Group Co., Ltd.

REFERENCES

- Ali, H. M. and Liu, H. (2005). "Laboratory study for effects vacuum preloading on physical and mechanical properties of soft clayey soils." *J. of Southeast University* (English Edition), No.1: 82-87.
- Dong, Z-L, Chen, P-S, Mo, H-H And Zhang, G-Xn (2008). "Comparison of numerical simulation with finite element method for vacuum preloading." *Chinese J. of Rock Mechanics and Engineering*, 27 (11): 2347-2353, in Chinese.
- Gong, X-N (1981). Finite element analysis of consolidation of soft soil foundation, *Master Degree Thesis*, Zhejiang University, in Chinese.
- Guo, H-Wi (2003). "Application of the vacuum preloading method in the subgrade of the light railway of Tianjin." *Geotech. Engineering World*, 6 (10): 31-34, in Chinese.

- He, L-D, Song S-H, Xiong G-P, Tao D-J and Liu, Q. (2005). "Analytical solution to terminal stress and displacement of foundation under vacuum preloading." *J. of Hehai University (Natural Sciences)*, 33 (2):194-197, in Chinese.
- Li, Q-S, Wu, A-X, Huang, J-X, Xi, Y and Zhang, J. (2005). "Infiltrating-concretion in vacuum seepage field." *J. of Central South University (Science and Technology)*, 36 (4): 689-693, in Chinese.
- Liu, H, Qian D-L and Fu, C. (2009). "Finite element analysis of consolidation of soft clay based on ABAQUS." *J. of Hefei University of Technology (Natural Science)*, 32 (8):1229-1232, in Chinese.
- Liu, H-L, Peng, J and Chen Y-H (2006). "Simplified method of ground settlement under vacuum combined surcharge preloading." *Rock and Soil Mechanics*, 27 (5): 745-748, in Chinese.
- Qin, Y-R (2003). Vacuum preloading: experiment and theory, *Ph. D. Degree Thesis*, Zhejiang University, in Chinese.
- Qian, J-H and Yin, Z-Z (1991). *Numerical analysis of soil engineering*, Press of China Railway, Beijing, p25, in Chinese
- Qiu, Q-C, Mo H-H and Dong Z-L (2007). "Analysis of pressure drop of fluid in prefabricated vertical drains in vacuum preloading ground." *J. of South China University of Technology (Natural Science Edition)*, 35 (3):132-135, in Chinese.
- Wang, Y-H, Li, L-J and Li, Y-P (2001). *Base and programmer of finite element*, Press of South China University of Technology, Guangzhou, No. 1, P21, in Chinese.
- Wang, Y-G (2010). Theory and Experiment of Vacuum Combined Surcharge Preloading Method for Foundation Improvement, *Ph.D. Thesis*, Central South University, in Chinese.
- Xie, K-H (1987). Consolidation theory of sand well: numerical analysis and optimizing design, *Ph.D. Thesis*, Zhejiang University, in Chinese.
- Xu, L-X, Chen Y-M, Lu Q-L and Wang H-R (2004). "Three-dimensional Biot consolidation finite element analysis of soft foundation of expressways improved with vacuum preloading method." *J. of Hehai University (Natural Sciences)*, 32 (5): 589-591, in Chinese.
- Zhao, W-B; Chen, Y-G and Gong, Y-P (1998). "A methodology for modeling sand-drain ground in plain strain analysis." *J. of Hydraulic Engineering*, No.6: 54-58, in Chinese.
- Zhu, B, Chen R-X, Chen Y-M and Zhan L-T (2007). "Modeling and experimental study of one-dimensional large strain consolidation of soft soil under multi-layer vacuum preloading." *J. of Zhejiang University (Engineering Science)*, 41 (11): 1927-1936, in Chinese.

Theoretical Solution for Dynamic Responses of Saturated Soils

Xiong Chuanxiang¹, Lu Xiaobing² and Zhang Xuhui²

¹School of Environment and Resources, Fuzhou University, Fujian 350108, China

²Institute of Mechanics, Chinese Academy of Sciences, Beijing 100080, China

ABSTRACT: Dynamic responses of soil foundation are difficult to analyze though it is related to kinds of practices. In this paper dynamic responses of soil foundation under dynamic load were analyzed theoretically. Perturbation method was used to obtain the theoretical solution. Controlling equations were about liquid-solid two-phase media. Flow function and potential function were introduced to decouple the controlling equations. Then perturbation expansion was introduced into the equations of flow function and potential function. The responses characteristics are discussed.

INTRODUCTION

More and more dynamic responses of soil foundations are required to be analyzed in practice. For an example, offshore platforms are applied in more and more complicated ocean environments and geological conditions, so dynamic failure becomes the key problem of platforms (Wang et al. 2006; Lu et al. 2005a; Lu et al. 2005; Lu et al. 2005b; Bye et al. 1995). Load of ocean wave or ice-induced vibration can be transferred to the ocean floor by platform foundations (piles, suction caissons etc.) to cause the dynamic responses of ocean floor such as deformation and even liquefaction (Lu et al. 2004).

Up to now, few theoretical methodologies have been proposed to analyze the dynamic responses of soil foundations subjected to dynamic load (Mamoon and Banerjee 1990; Lu et al. 2006). Structural foundations are most embedded in saturated soils. Thus the methodology must be able to consider the percolation in saturated soils and pore pressure increase and the soil strength decrease. The development of pore pressure and soil strength is crucial for understanding the liquefaction mechanism of the soil foundations.

In this paper the dynamic responses of soil foundation in saturated soils under horizontal dynamic load are investigated by using the perturbation expansion method. The behavior of saturated soils is described by poro-elastic two-phase media. By introducing the potential and flow functions, the solving process is simplified. The development of pore pressure is mainly discussed.

PROBLEM AND CONTROLLING EQUATION

Problem is assumed as a half-infinite plane (Fig. 1). Dynamic load is applied at the left boundary. The upper boundary is free, the bottom is fixed and undrained. The soil layer is saturated. The water and soil grains are incompressible. Change of porosity is small and its gradient can be neglected. All equations are linearized with constant coefficients. Density of each phase is constant. Hooke's law suits for soil skeleton.

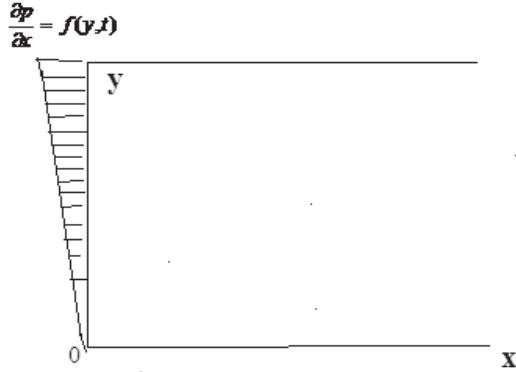


FIG. 1. Sketch of the problem.

MODEL OF THE PROBLEM

Momentum Equations of The Skeleton and the Pore Water

$$\begin{aligned} \frac{\partial \sigma_{ij}}{\partial x_j} - \frac{\partial p}{\partial x_i} - \varepsilon \rho g_i - (1-\varepsilon)\rho_s g_i &= (1-\varepsilon)\rho_s \frac{\partial^2 u_i}{\partial t^2} + \varepsilon \rho \frac{\partial v_i}{\partial t} \\ - \frac{\partial \varepsilon p}{\partial x_i} + p \frac{\partial \varepsilon}{\partial x_i} - \frac{\varepsilon^2 \mu}{K} (v_i - \frac{\partial u_i}{\partial t}) - \varepsilon \rho g_i &= \varepsilon \rho \frac{\partial v_i}{\partial t} \end{aligned} \quad (1)$$

To remove the static effective stresses and pore pressure we shall replace henceforth σ_{ij} by $\sigma_{ij} - (1-\varepsilon)(\rho_s - \rho)g_j \delta_{ij}$ and p by $p + \rho g y$.

Then the above equations become homogeneous

$$\begin{aligned} \frac{\partial \sigma_{ij}}{\partial x_j} - \frac{\partial p}{\partial x_i} &= (1-\varepsilon)\rho_s \frac{\partial^2 u_i}{\partial t^2} + \varepsilon \rho \frac{\partial v_i}{\partial t} \\ - \frac{\partial p}{\partial x_i} - \frac{\varepsilon \mu}{K} (v_i - \frac{\partial u_i}{\partial t}) &= \rho \frac{\partial v_i}{\partial t} \end{aligned} \quad (2)$$

Eliminating p the first equation becomes

$$\frac{\partial \sigma_{ij}}{\partial x_j} + \frac{\varepsilon \mu}{K} (v_i - \frac{\partial u_i}{\partial t}) = (1-\varepsilon)\rho_s \frac{\partial^2 u_i}{\partial t^2} - \rho \frac{\partial v_i}{\partial t} \quad (3)$$

Mass Conservation Equations of Skeleton and Pore Water

$$\begin{aligned}\frac{\partial \varepsilon \rho}{\partial t} + \frac{\partial \varepsilon \rho v_i}{\partial x_i} &= 0 \\ \frac{\partial (1-\varepsilon) \rho_s}{\partial t} + \frac{\partial^2 (1-\varepsilon) \rho_s u_i}{\partial t \partial x_i} &= 0\end{aligned}\quad (4)$$

For constant density, these two equations combine to form

$$\varepsilon \frac{\partial v_i}{\partial x_i} + (1-\varepsilon) \frac{\partial^2 u_i}{\partial t \partial x_i} = 0 \quad (5)$$

Constitutive Equations—Hooke's Law

$$\sigma_{ij} = G \left(\frac{\partial u_i}{\partial x_j} + \frac{\partial u_j}{\partial x_i} \right) + \delta_{ij} \frac{2G\nu}{1-2\nu} \frac{\partial u_k}{\partial x_k} \quad (6)$$

Reduction of Equations

Introduce potential and “flow” functions such that

$$\bar{u} = \text{Grad} \varphi_s + \text{Curl} \bar{\psi}_s \quad \text{with} \quad \text{Div} \bar{\psi}_s = 0 \quad (7)$$

$$\bar{v} = \text{Grad} \varphi + \text{Curl} \bar{\psi} \quad \text{with} \quad \text{Div} \bar{\psi} = 0$$

From the mass conservation relation (5)

$$\varepsilon \nabla^2 \varphi + (1-\varepsilon) \nabla^2 \frac{\partial \varphi_s}{\partial t} = 0 \quad (8)$$

We shall choose

$$\varepsilon \rho + (1-\varepsilon) \frac{\partial \varphi_s}{\partial t} = 0 \quad (9)$$

From the second of equation (2), we have

$$\nabla^2 p = -\rho \nabla^2 \frac{\partial \varphi}{\partial t} - \frac{\varepsilon \mu}{K} \nabla^2 \left(\varphi - \frac{\partial \varphi_s}{\partial t} \right) \quad (10)$$

And

$$\frac{\varepsilon \mu}{K} \nabla^2 \left(\bar{\psi} - \frac{\partial \bar{\psi}_s}{\partial t} \right) = -\rho \nabla^2 \frac{\partial \bar{\psi}}{\partial t} \quad (11)$$

We choose

$$\frac{\varepsilon \mu}{K} \left(\bar{\psi} - \frac{\partial \bar{\psi}_s}{\partial t} \right) = -\rho \frac{\partial \bar{\psi}}{\partial t} \quad (12)$$

Similarly taking the divergence and curl of equation (3) respectively, we have

$$\frac{2G(1-\nu)}{\rho_s(1-2\nu)} \nabla^2 \varphi_s = (1-\varepsilon) \left(1 + \frac{1-\varepsilon}{\varepsilon} \frac{\rho}{\rho_s} \right) \frac{\partial^2 \varphi_s}{\partial t^2} + \frac{\mu}{\rho_s K} \frac{\partial \varphi_s}{\partial t} \quad (13)$$

and

$$\frac{G}{\rho_s} \nabla^2 \bar{\psi}_s = \left(1 - \varepsilon + \frac{\varepsilon \rho}{\rho_s} \right) \frac{\partial^2 \bar{\psi}_s}{\partial t^2} \quad (14)$$

In this problem, $\eta = \omega \rho_s K / \mu$ is a small parameter, we can give the asymptotic expansions by using of multi-scale method:

$$\begin{cases} \varphi_s = \varphi_s^0(x_i, \tau_1, \tau_2) + \sum_{n=1}^{\infty} \eta^n \varphi_s^{(n)}(x_i, \tau_1, \tau_2) \\ \bar{\psi}_s = \bar{\psi}_s^0(x_i, \tau_1, \tau_2) + \bar{\psi}_s^{(n)}(x_i, \tau_1, \tau_2) \end{cases} \quad (15)$$

in which $\tau_1 = \tau$, $\tau_2 = \eta\tau$. Institute these expressions into eq.(13) and (14), we can obtain:

$$\begin{cases} D\nabla^2 \varphi_s^{(1)} = \frac{\partial \varphi_s^{(1)}}{\partial \tau_1} \\ D\nabla^2 \varphi_s^{(n)} = \frac{\partial \varphi_s^{(n)}}{\partial \tau_1} + \frac{\partial \varphi_s^{(n-1)}}{\partial \tau_2} + (1-\varepsilon)\left(1 + \frac{1-\varepsilon}{\varepsilon} \frac{\rho}{\rho_s}\right) \left(\frac{\partial^2 \varphi_s^{(n-1)}}{\partial \tau_1^2} + \frac{\partial^2 \varphi_s^{(n-2)}}{\partial \tau_1 \partial \tau_2} + \frac{\partial^2 \varphi_s^{(n-3)}}{\partial \tau_2^2} \right) \\ \lambda \nabla^2 \bar{\psi}_s^{(0)} = \frac{\partial^2 \bar{\psi}_s^{(0)}}{\partial \tau_1^2} \\ \lambda \nabla^2 \bar{\psi}_s^{(1)} = \frac{\partial^2 \bar{\psi}_s^{(1)}}{\partial \tau_1^2} + \frac{\partial^2 \bar{\psi}_s^{(0)}}{\partial \tau_1 \partial \tau_2} \\ \lambda \nabla^2 \bar{\psi}_s^{(n)} = \frac{\partial^2 \bar{\psi}_s^{(n)}}{\partial \tau_1^2} + \frac{\partial^2 \bar{\psi}_s^{(n-1)}}{\partial \tau_1 \partial \tau_2} + \frac{\partial^2 \bar{\psi}_s^{(n-2)}}{\partial \tau_2^2} \end{cases} \quad (16)$$

$$\text{in which } D = \frac{2GK(1-\nu)}{\mu\omega(1-2\nu)}, \quad \varphi_s^{(0)} = 0, \quad \lambda = \frac{G}{\omega^2[(1-\varepsilon)\rho_s + \varepsilon\rho]}.$$

Institute eq.(15) into eq.(10) and neglecting the high order small parameter, we can obtain:

$$\begin{cases} \frac{1}{\rho} \nabla^2 p^{(0)} = -\varepsilon \nabla^2 \left(\varphi^{(1)} - \frac{\partial \varphi_s^{(1)}}{\partial \tau_1} \right) \\ \frac{1}{\rho} \nabla^2 p^{(1)} = -\nabla^2 \frac{\partial \varphi^{(1)}}{\partial \tau_1} + \varepsilon \nabla^2 \frac{\partial \varphi_s^{(1)}}{\partial \tau_2} \end{cases} \quad (17)$$

Then institute eq. (9) into the above equation:

$$\begin{cases} \frac{1}{\rho} \nabla^2 p^{(0)} = \nabla^2 \frac{\partial \varphi_s^{(1)}}{\partial \tau_1} \\ \frac{1}{\rho} \nabla^2 p^{(1)} = -\frac{1-\varepsilon}{\varepsilon} \nabla^2 \frac{\partial^2 \varphi_s^{(1)}}{\partial \tau_1^2} + \varepsilon \nabla^2 \frac{\partial \varphi_s^{(1)}}{\partial \tau_2} \end{cases} \quad (18)$$

Considering the first one in the above equation, the first one of eq.(16) becomes:

$$D\nabla^2 p^{(0)} = \frac{\partial p^{(0)}}{\partial \tau_1} \quad (19)$$

The boundary and initial conditions for p is as follows:

$$\begin{cases} x = 0; & u_{sx} = aye^{i\omega t} \\ x \rightarrow \infty; & \text{No radiation} \\ y = 0; & \frac{\partial p^{(0)}}{\partial y} = 0 \\ y = L; & p^{(0)} = 0 \\ t = 0; & p^{(0)} = 0 \end{cases} \quad (20)$$

in which L is the depth of the soil layer. Then p can be obtained as follows:

$$p^{(0)} = \sum_{n=0}^{\infty} \frac{2a[(-1)^n \beta_n L - 1]}{\beta_n^2 L \sqrt{\beta_n^2 + \frac{i\omega}{D}}} \cos \beta_n y e^{-\sqrt{\beta_n^2 + \frac{i\omega}{D}} x} e^{i\omega t} \quad (21)$$

in which $\beta_n = \frac{(2n+1)\pi}{2L}$.

By the first of eq.(18), we have

$$\varphi^{(1)} - \frac{\partial \varphi_s^{(1)}}{\partial \tau_1} = - \sum_{n=0}^{\infty} \frac{2a[(-1)^n \beta_n L - 1]}{\rho \omega \beta_n^2 L \sqrt{\beta_n^2 + \frac{i\omega}{D}}} \cos \beta_n y e^{-\sqrt{\beta_n^2 + \frac{i\omega}{D}} x} e^{i\omega t} \quad (22)$$

So

$$\frac{\partial \varphi_s^{(1)}}{\partial \tau_1} = \sum_{n=0}^{\infty} \frac{2a[(-1)^n \beta_n L - 1]}{\rho \beta_n^2 L \sqrt{\beta_n^2 + \frac{i\omega}{D}}} \cos \beta_n y e^{-\sqrt{\beta_n^2 + \frac{i\omega}{D}} x} e^{i\omega t} \quad (23)$$

and

$$\varphi_s^{(1)} = - \sum_{n=0}^{\infty} \frac{2ia[(-1)^n \beta_n L - 1]}{\omega \rho \beta_n^2 L \sqrt{\beta_n^2 + \frac{i\omega}{D}}} \cos \beta_n y e^{-\sqrt{\beta_n^2 + \frac{i\omega}{D}} x} e^{i\omega t} \quad (24)$$

We first seek for the zero order solution

$$\lambda \nabla^2 \bar{\psi}_s^{(0)} = \frac{\partial^2 \bar{\psi}_s^{(0)}}{\partial \tau_1^2} \quad (25)$$

Boundary conditions: $y=0, \frac{\partial \bar{\psi}_s^{(0)}}{\partial x} = 0,$

$$y=L, \frac{\partial^2 \bar{\psi}_s^{(0)}}{\partial x^2} = \frac{\partial^2 \bar{\psi}_s^{(0)}}{\partial y^2}$$

$$x=0, \frac{\partial \bar{\psi}_s^{(0)}}{\partial y} = aye^{i\omega t}$$

$$x=\infty, \frac{\partial \bar{\psi}_s^{(0)}}{\partial x} = 0 \quad (26)$$

$$\psi_s^{(0)} = \sum_0^{\infty} \frac{(-1)^{n+1}}{n} \frac{2aL}{\pi} e^{-\sqrt{\omega^2 - \left(\frac{n\pi}{L}\right)^2} x} \sin \frac{n\pi}{L} y e^{i\omega t} \quad (27)$$

By the fourth of eq.(14), $\bar{\psi}_s^{(1)}$ can be obtained in the following way.

Boundary conditions:

$$x=0, \frac{\partial \bar{\psi}_s^{(1)}}{\partial y} = - \sum_{n=0}^{\infty} a_n \cos \beta_n y \sqrt{\beta_n^2 + \frac{i\omega}{D}} e^{i\omega t} \quad (28)$$

$$x \rightarrow \infty, \bar{\psi}_s^{(1)} \rightarrow 0 \quad (29)$$

$$y=0, \frac{\partial \bar{\psi}_s^{(1)}}{\partial y} = 0 \quad (30)$$

$$y=L, \frac{\partial^2 \bar{\psi}_s^{(1)}}{\partial y^2} - \frac{\partial^2 \bar{\psi}_s^{(1)}}{\partial x^2} = 2 \sum_{n=0}^{\infty} a_n \beta_n \sin \beta_n y \sqrt{\beta_n^2 + \frac{i\omega}{D}} e^{-\sqrt{\beta_n^2 + \frac{i\omega}{D}} x} e^{i\omega \tau} \quad (31)$$

Initial conditions:

$$t=0, \bar{\psi}_s^{(1)} = 0 \quad (32)$$

$\bar{\psi}_s$ can be expressed as:

$$\bar{\psi}_s^{(1)} = e^{i\omega \tau} \left[\sum_{n=0}^{\infty} \sin \gamma_n y \left(d_n e^{-\sqrt{\gamma_n^2 - \omega^2} x} + V_n e^{-\sqrt{\beta_n^2 + i\omega/D} x} \right) + \sum_{i=0}^{\infty} C_n \sin \beta_n y e^{-\sqrt{\beta_n^2 + i\omega/D} x} \right] \quad (33)$$

$$\text{in which } C_n = -\frac{2a_n \beta_n}{2\beta_n^2 + i\omega/D} \sqrt{\beta_n^2 + i\omega/D}$$

$$V_n = \frac{(\omega^2 + i\omega/D) C_n}{\lambda(\beta_n^2 - \gamma_n^2 + i\omega/D + \omega^2)} \frac{8n}{(4n+1)\pi}$$

$$\gamma_n = \frac{n\pi}{L}$$

$$u_n = -\frac{a_n \sqrt{\beta_n^2 + i\omega/D} + \beta_n C_n}{\gamma_n} \frac{8n+4}{(4n+1)\pi}$$

$$d_n = u_n - V_n$$

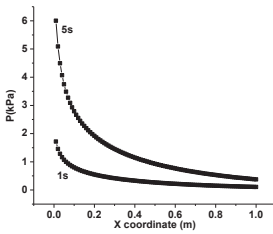
By the second of eq.(18), $p^{(1)}$ can be obtained:

$$p^{(1)} = -\frac{\rho(1-\varepsilon)}{\varepsilon} \sum_{n=0}^{\infty} \frac{2\omega i a \left[(-1)^n \beta_n L - 1 \right]}{\rho \beta_n^2 L \sqrt{\beta_n^2 + \frac{i\omega}{D}}} \cos \beta_n y e^{-\sqrt{\beta_n^2 + \frac{i\omega}{D}} x} e^{i\omega \tau} \quad (34)$$

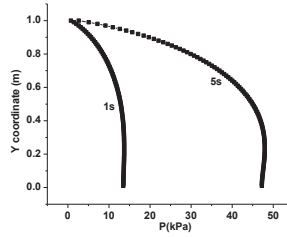
The solution of the problem (eqs.(21), (27),(32) and (34)) is formed by stable terms and decaying terms in x direction, which means that the seepage and deformation decay gradually away from the load side.

Responses of soil layer can be obtained by computation with the above equations. Basic parameters are as follows: depth of soil layer $L=1$, porosity $\varepsilon=0.3$, density of water $\rho_w=1000\text{kg/m}^3$, density of skeleton $\rho_s=2650\text{kg/m}^3$, Poisson ratio $\mu=0.3$, shear modulus $G=10^5\text{Pa}$, viscosity of water $\nu=0.001$, physical permeability 10^{-10}m^2 , coefficient $a=10^5$, frequency $\omega=1.0$.

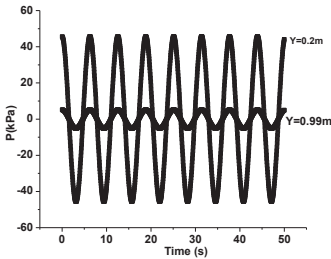
The numerical solutions show that the response of the soil decays gradually in horizontal direction. Pore pressure decreases fast in the range of 20% of the total length in horizontal direction near the load end (Fig.2a). In vertical direction, the pore pressure increases from the top to the bottom. Pore pressure increases fast in the upper part about 50% of the total depth (Fig.2b). At any location, pore pressure fluctuations with time (Fig.2c). It is shown that the numerical results are agreement well with the experimental results (Lu et al. 2007) (Fig.2d).



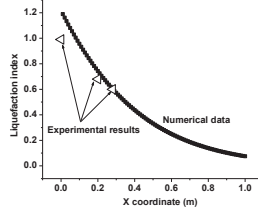
(a) In x direction (y=0.99m)



(b) In y direction (x=0.01m)



Development with time
(x=0.1, y=0.99)



(d) Comparison with experimental results (Fig. 14 in literature [3])

FIG.2. Development of pore pressure.

CONCLUSIONS

Dynamic responses of soil foundation under horizontal distributed dynamic load were analyzed theoretically. A method to obtain the direct analytical solution is presented. Based on liquid-solid media theory, two dimensional two-phase controlling equations are obtained. Flow function and potential function are introduced to decouple the controlling equations, which makes the solving of the equations much simple.

The response is formed by stable part and decaying part, which means that the response becomes to stable gradually. At about 1m from the load end, about equals to the length of the soil layer, the response disappears. So there is a maximum affected zone in the soil layer under dynamic load.

ACKNOWLEDGEMENTS

This work was supported by the National Science Foundation of China (No.11272314 and No.11102209).

REFERENCES

- Wang Y. H., Lu X. B. Wang S. Y. et al. (2006). "The responses of the bucket foundation under horizontal dynamic loading." *Ocean Engrg.*, Vol.33: 964-973.
- Lu X. B., Zhang J. H., Wang S. Y. et al. (2005). "Experimental study of the pore pressure and deformation of suction bucket foundations under horizontal dynamic loading." *Chinese Ocean Engrg.*, Vol. 19(4): 671-680.
- Lu X. B., Wu Y. R., Jiao B. T. et al. (2007). "Centrifugal experimental study of suction bucket foundations under dynamic loading." *ACTA Mech. Sinica*, Vol. 23: 689-698.
- Lu X. B., Liu C., Wang S. Y. et al. (2005). "On the bearing capacity of bucket foundations in saturated sands." *Int. J. Offshore Polar Engrg.*, Vol.15 (4): 300-303.
- Bye A., Erbrich C., Earl K. et al. (1995). "Geotechnical design of bucket foundation." *Proc. Offshore Tech. Conf.*, OTC10994, Houston, USA, OTC7793, 869-883
- Lu X. B., Tan Q. M., Cheng Z. M. et al.(2004). "Liquefaction and displacement of saturated sand under vertical vibration loading." *ACTA Mech. Sinica*, Vol. 20 (1): 96-105.
- Mamoon S. M. and Banerjee P.K. (1990). "Response of piles and pile groups to traveling SH-waves." *Earthquake Eng. Struct. Dynam.*, Vol.19: 597-610.
- Lu J. F., Dong S. J., Wei D. N. (2006). "Dynamic response of a pile embedded in a porous medium subjected to plane SH waves." *Computers and Geotechnics*, Vol.33: 404-418.

NOMENCLATURE

- ρ density of fluid
- ρ_s density of solid
- u_i displacements of solid in three directions
- v_i velocities of fluid in three directions
- ε porosity
- p fluid pressure
- σ_{ij} effective stress
- g gravitational acceleration
- G shear modulus
- ν Poisson ratio
- φ_s Potential functions of solid
- ψ_s flow functions of solid
- φ Potential functions of water
- ψ flow functions of water
- K the physical permeability ($= \rho_w g / (\mu k)$)
- ρ_w the density of the water
- k the Darcy's permeability
- g the gravity acceleration

Application of Modified Terzaghi Theory in Deposited Sediment Consolidation

Meng Yanqiu¹, Wang Peiqing², Zhang Fuhai³ and Guo Shuaijie⁴

¹Instructor, Hydraulic Engineering Institute, Changsha University of Science & Technology, Changsha 410114, China, mengyanqiu@126.com.

²Associate Professor, Department of Water Conservancy and Civil Engineering, Tibet Agricultural and Animal Husbandry College, Linzhi, 860000, Tibet, China, wpq518@163.com.

³Associate Professor, Institute of Geotechnical Engineering, HoHai University, Nanjing, 210098.

⁴Doctoral Candidate, Institute of Geotechnical Engineering, HoHai University, Nanjing, 210098.

ABSTRACT: Deposited sediment shows significant large strain characteristics during weight consolidation with variable consolidation parameters. Non-neglected prediction errors will appear if applied classic Terzaghi theory in large strain consolidation calculation, especially as the settlement amount exceeds 50% which will lead great coordinate errors and can't reflect the nonlinear features. In this paper, a new piece-consolidation model based on modified Terzaghi theory is proposed for deposited sediment consolidation prediction. Of which, large strain consolidation process is divided into a series of small strain consolidation, and each strain step consolidation is predicted by Terzaghi theory with necessary parameters modification. Power functional equation is applied for the constitutive relationship between permeability, compressibility and void ratio. With the assumption that each strain step consolidation coefficient is constant, large strain consolidation process can be determined by all the strain step settlement accumulation. Piece-consolidation model based on Terzaghi theory successfully meets the basic assumptions and reflects the nonlinear features. Moreover, model outputs also show a well agreement to the experimental measured.

INTRODUCTION

High moisture and void ratio deposited sediment is formed by sediment particles sedimentation and consolidation, which also is the main challenge in port and channel dredging area. Deposited sediment weight consolidation shows large strain characteristics and consolidation parameters such as hydraulic conductivity, compressibility as well as consolidation coefficient will keep changing as variables. Classic consolidation theory will not be reasonable if not with some necessary modifications (Guo 2011).

Terzaghi (1923) first developed one-dimensional consolidation theory based on assumptions that the consolidation coefficient is constant, soil is saturated and linear elastic. However, for deposited sediment weight consolidation, the initial void ratio may be over 15.0 which will become problematic in the applicant of Terzaghi theory. Meanwhile, the small strain assumption of Terzaghi theory is only made to get the an-

analytical solution under relatively simple boundary condition (Xie 2003). On some meanings, Terzaghi equation is the simplified form of Gibson equation (Yin 2007), and there is no small strain restriction in application area. Therefore, it is reasonable to apply Terzaghi theory in large strain problems with variable consolidation parameters. With some modification and successive correction methods, it is possible and effective to extend the application of Terzaghi theory into large strain consolidation field.

The objective of this paper is to present a modified Terzaghi theory model (Piece-consolidation model) for large strain consolidation based on power functional constitutive relationship. Deposited sediment weight consolidation can be simplified as one dimensional large strain consolidation and can be simulated by this new developed model, where the prediction can be certified by the laboratory settlement column experiment. Meanwhile, power functional relationship equation parameters for hydraulic conductivity and effective stress are determined by sediment settlement column experiment respectively.

TERZAGHI CONSOLIDATION THEORY

Based on linear elastic soil consolidation constitutive relationship, settlement and excessive pore pressure will be relatively coupled, and the soil consolidation will be completely consistent either with the variables of void ratio or the excessive pore pressure (Wei 1993). And then, classic Terzaghi equation can be expressed with void ratio variables, and the analytical solution in series form is as Eq. 1.

$$e(z, t) = e_{\infty} - \sigma_0' m_v (1 + e_1) + m_v \gamma_w (G_s - 1)(z - H) + \frac{2}{H} \cdot \sum_{n=1}^{\infty} \int_0^H [e_0(z) - m_v \gamma_w (G_s - 1)(z - H) - e_{\infty} + \sigma_0' m_v (1 + e_1)] \cdot \cos \frac{(2n-1)\pi z}{2H} dz \cdot e^{-\frac{(2n-1)^2 C_v \pi^2 t}{4H^2}} \cdot \cos \frac{(2n-1)\pi z}{2H} \quad n = 1 \ 2 \ 3 \dots \quad (1)$$

Strain consolidation ratio is defined as settlement development ratio. By the void ratio distribution, sediment settlement S_t and strain consolidation ratio U_t at time t are

$$S_t = \int_0^H [e_0(z) - e(z, t)] dz; \quad U_t = \frac{S_t}{S_{\infty}} = \frac{\int_0^H [e_0(z) - e(z, t)] dz}{\int_0^H [e_0(z) - e(z, \infty)] dz} \quad (2)$$

Where S_t is the soil interface settlement amount at time t , and S_{∞} is the soil final total settlement amount, z is the vertical coordinate.

MODEL DEVELOPMENT

Soil Constitutive Equation

Hydraulic conductivity and soil compressibility are the two main consolidation parameters (Townsend 1990; Znidarcic 1982; Pane 1981), and both can be considered varying in the consolidation process, so the key to predict large strain consolidation is to determine reasonable consolidation constitutive equation. Effective stress and hy-

hydraulic conductivity trends are shown in Fig. 1. And the current constitutive formulations are summarized as: the power function, the extended power function and the Weibull function. Of which, deposited sediment hydraulic conductivity and effective stress is generally provided as extended power function in void ratio form.

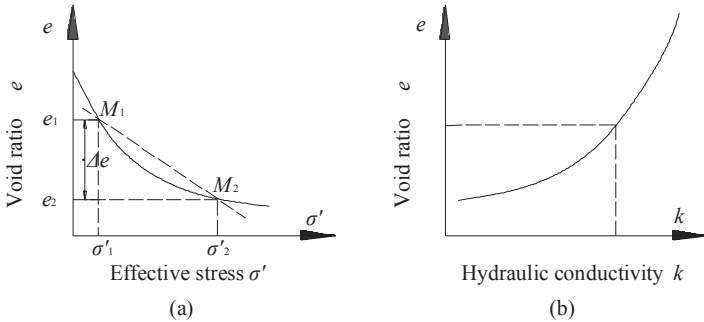


FIG. 1. Consolidation Parameters Trends: (a) Effective Stress (b) Permeability

Fang (1979), Hong (1987) obtained the nonlinear constitutive equation with some hydraulic and consolidation experiments. Patrick (2005) applied a piecewise linear numeric model to express the nonlinear features. Lucas (2000) used power function with volume fraction to research large strain consolidation characteristics. In the study of this paper, extended power functional constitutive relationship Eq. 3 is applied.

$$\sigma' = K_{\sigma} (1+e)^n ; \quad k = K_k (1+e)^m \quad (3)$$

Where K_{σ} is the effective stress coefficient, n is the effective stress index, K_k is the hydraulic conductivity coefficient, and m is the hydraulic conductivity index.

Constitutive Equation Parameter Determination

As mentioned above, four consolidation constitutive parameters as K_{σ} , n , K_k , m , n should be determined by settlement column experiment, so some sediment deposition experiments must be carried out in order to apply extend power constitutive Equation (3) in large strain calculation. Lucas (2000) developed the govern equation for sediment consolidation settlement and volume fraction distribution, and from which all the constitutive parameters can be determined through some calibration tests.

The main experiment device is 1000 mm high PMMA column with 130 mm inner diameter. Sediment settlement is carried out with different initial concentration, and settlement curves are shown in Fig. 2(a), meanwhile, final void ratio distribution curves is shown in Fig. 2(b) by layer sampling operation. According to the sediment settlement curves on double logarithmic coordinates in Fig. 2(a), there is clear linear relationship part. And from the void ratio distribution curves, the effective stress constitutive equation parameters also can be obtained. Finally, constitutive parameters in Eq. 3 can be fitted as $K_{\sigma} = 1.38 \times 10^5 \text{ Pa}$, $n = -3.40$; $K_k = 1.96 \times 10^{-14} \text{ m/s}$, $m = 7.72$.

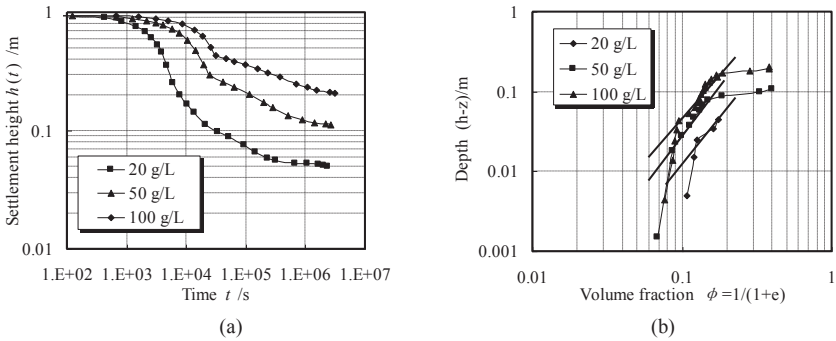


FIG. 2. Settlement column experiment final results: (a) Settlement curves; (b) Void ratio distribution curves

Piece-consolidation Model

In order to enlarge Terzaghi theory application into large strain calculation, a Piece-consolidation Model is developed with some necessary assumptions. The model main ideas are as: large strain process can be divided into a series of small strain step and Terzaghi theory is applied on each small strain step; by accumulating step settlement gradually with changing consolidation parameters, consolidation ratio and settlement curves can be obtained subsequently.

Piece-consolidation model process is as follows:

Firstly, give the allowed constant strain limit ε . By the initial void ratio distribution and consolidation parameters, the first strain step consolidation process can be obtained, and then the second the third step. If having determined the void ratio distribution $e_i(z)$ at the i th strain step, then the practical average void ratio e_{avg} and settlement strain ε_i within time increment Δt_i can be calculated by Eq. 4.

$$e_{avg\ i} = \int_0^H e_i(z) dz / H ; \quad \varepsilon_i = S_i / H_{i-1} = \int_0^H [e_{i-1}(z) - e_i(z)] dz / H_{i-1} \quad (4)$$

Secondly, if the settlement strain ε_i within time increment Δt_i doesn't over the given strain limit ε , then increase the time increment value Δt_i and calculate the next reasonable average void ratio $e_{avg\ i}$ and settlement strain ε_i until $\varepsilon_i \geq \varepsilon$.

Thirdly, if settlement strain ε_i within time increment Δt_i had been over the constant strain limit ε , consolidation parameters must be updated with the new void ratio distribution and accumulate the time increment which are $i=i+1$, $T(i) = T(i-1) + \Delta t_i$. New consolidation parameters, boundary and initial conditions for next step is modified as

$$\begin{aligned} \sigma'(i+1) &= K_\sigma (1 + e_{avg\ i})^n \\ k(i+1) &= K_k (1 + e_{avg\ i})^m \\ m_v(i+1) &= -1 / [n K_\sigma (1 + e_{avg\ i})^n] \\ C_v(i+1) &= -n K_k K_\sigma e_{avg\ i}^{n+m} / \rho_w g \end{aligned} \quad (5)$$

$$\begin{aligned}
 e|_{z=0} &= e_0(z) ; \\
 e|_{z=H} &= e_t ; \\
 de/dz|_{z=0} &= -\gamma_w (G_s - 1) / [nK_\sigma (1 + e_{avg i})^n]
 \end{aligned}
 \tag{6}$$

RESULTS AND DISCUSSIONS

In order to discuss the performances of Piece-consolidation Model in small and large strain conditions, three calculation cases are chosen out which are:

- (I) Small strain consolidation prediction by different strain step.
- (II) Compressibility coefficient a_v and hydraulic conductivity are both as constant, but with variable consolidation coefficient.
- (III) Nonlinear large strain consolidation for deposited sediment which the consolidation parameters keep changing with void ratio.

Model Performance in Small Strain Consolidation

The new developed model must be reasonable for small strain consolidation with no consolidation parameters changing. The first calculation case (I) initial parameters are listed in Table 1 and with pervious top surface and impervious bottom.

Table 1. Soil Layer Condition and Physical Properties

| Initial height H (m) | Initial void ratio e_1 | Compressibility coefficient a_v (kPa^{-1}) | Hydraulic conductivity k (m/s) | Weight loading p (kPa) | Final settlement strain ε (%) |
|---------------------------|-----------------------------|--|-------------------------------------|-----------------------------|--|
| 10.0 | 0.8 | 2.5×10^{-4} | 6.342×10^{-10} | 240 | 4.8 |

During Piece-consolidation Model application in case (I), boundary condition and consolidation coefficient keeps constant as the initial. Settlement curves with different strain step limit (0.1%, 0.3%, 0.5% and 0.8%) are shown in Fig. 3 (a) which indicates that with constant consolidation parameters, Piece-consolidation Model will give a well agreement and completely consistent with classic Terzaghi theory, so the new model can be applied in small strain consolidation.

Model Performance with Variable Consolidation Coefficient

For the case (II) soft soil calculation situation, soil hydraulic conductivity and compressibility coefficient are constant, but consolidation coefficient C_v is variable with void ratio. According to the consolidation calculation results, it is reasonable to discuss the differences between Terzaghi theory and Piece-consolidation Model.

In the comparison example, the saturated soft soil is 10.0 m in depth, initial void ratio $e_1=4$, compressibility coefficient $a_v=2.0 \times 10^{-5} \text{ kPa}^{-1}$, hydraulic conductivity $k=1.0 \times 10^{-8} \text{ m/s}$, and the uniform external surface loading is 100 kPa. The final settlement strain is 47% which belongs to large strain consolidation problem. Piece-

consolidation model outputs with different strain step limits (0.1%, 0.3%, 0.5% and 0.8%) as well as Terzaghi theory calculation results are shown in Fig. 3 (b).

Settlement curves in Fig. 3 (b) shows that there are clear differences between Piece-consolidation Model and Terzaghi theory, consolidation process by Piece-consolidation Model is more quickly than Terzaghi theory, and the final settlement is a little smaller. It also can conclude that Piece-consolidation Model can reflect some large strain consolidation features and reduce the errors induced by the basic assumptions. Consolidation time by Piece-consolidation model for 80% consolidation ratio is merely half of Terzaghi theory, which also has been approbated by many scholars that large strain consolidation process is more quickly than small strain theory (Xie 1998).

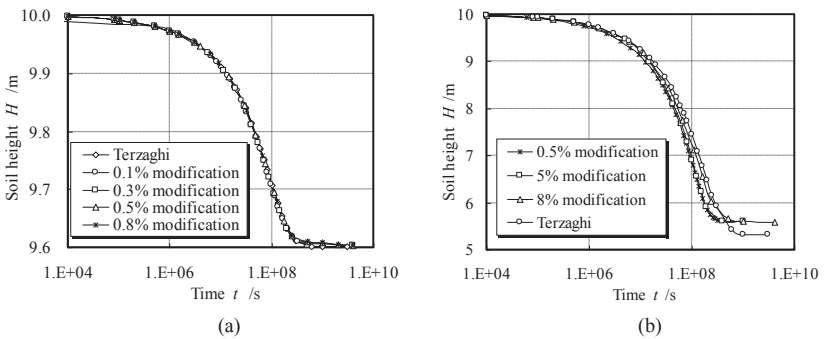


FIG. 3. Settlement prediction curves: (a) Case (I); (b) Case (II).

Model Performance with Double Variables

Double parameter modification applies the extended power functional constitutive Eq. 3 and the deposited sediment initial parameters are listed in Table 2.

Table 2. Consolidated Soil Layer Condition and Soil Physical Properties

| Initial height H (m) | Initial void ratio e_1 | Initial Compressibility coefficient $a_v(1)$ (Pa^{-1}) | Initial Hydraulic conductivity $k(1)$ (m/s) | Initial Consolidation coefficient C_v (m^2/s) | Final strain ε (%) |
|---------------------------|-----------------------------|--|--|--|-----------------------------------|
| 0.43 | 11.45 | 0.14 | 5.6×10^{-6} | 5.0×10^{-8} | 52 |

The final strain related to the initial deposited sediment height in Table 2 is 52%, so it is a typical large strain consolidation case. Piece-consolidation model outputs based on double parameters modification, Terzaghi theory result and the measured settlement curve by settlement column experiment are shown in Fig. 4(a). Void ratio in the top surface is constant as $e_t=11.45$, and the bottom void ratio should be regulated according to the boundary conditions. Settlement strain limits are made as 1%, 5% and 10%, and the void ratio distribution curves with strain limit 1% are shown in Fig. 4(b).

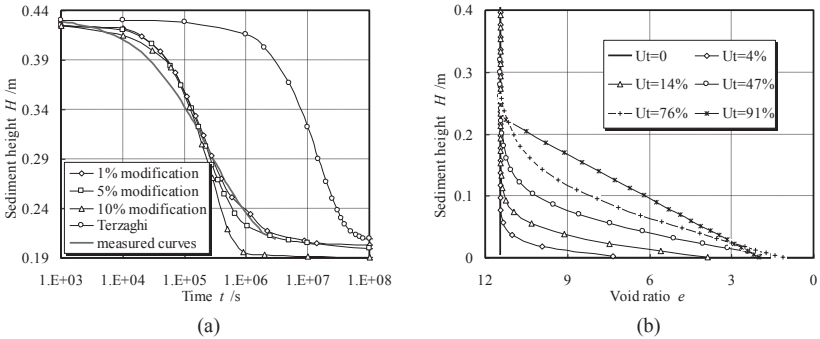


FIG. 4. Piece-consolidation Model Outputs: (a) Settlement Curves with Different Strain Limits; (b) Void Ratio Distribution with 1% Strain Limit

It can be seen from Fig. 4(a) that Piece-consolidation Model can reflect the nonlinear large strain characteristics, and the outputs give a well agreement to the measured one. Additionally, classic Terzaghi theory settlement curve is far behind the outputs by Piece-consolidation Model and the measured one.

Void ratio distribution and development curves in Fig. 4(b) reflect deposited sediment basic characteristics where the void ratio is of nonlinear distribution until to the final consolidation stage. The impermeable bottom condition determine the void ratio development, however, void ratio in the bottom somewhere enlarges in the final consolidation stage which doesn't match to the measured for the bottom condition keeps changing. Moreover, a more reasonable treatment of the bottom boundary condition is one of the most valuable optimization directions to improve the Piece-consolidation model prediction accuracy.

For large strain consolidation, Terzaghi theory main errors are induced by the differences between convective and Euler coordinates. And constant consolidation parameters cannot reflect the large strain and nonlinear characteristics. With the fact that Terzaghi theory analytical solution is accurate for small strain and also the large-strain consolidation can be divided into a series of small strain step, the new consolidation prediction model named Piece-consolidation model successfully meet the requirements of small strain with consolidation parameters modification according to the current void ratio. Finally, deposited sediment large strain consolidation can be obtained through Terzaghi theory and the step strain consolidation settlement accumulation.

CONCLUSIONS

(1) With some necessary modification Terzaghi theory can be applied in deposited sediment large strain consolidation prediction. The new proposed Piece-consolidation model based on modified Terzaghi theory can perfectly meet the requirement of large strain as well as the small strain consolidation calculation.

(2) Continuous power functional constitutive equation is applied to express the nonlinear relationships of effective stress and hydraulic conductivity with void ratio variables. According to the results of three different consolidation cases, it can be con-

cluded that Piece-consolidation model is convergences to small strain consolidation theory, and the double parameters modification outputs also give a well agreement to the measured one.

(3) The key problem in the application of Piece-consolidation model is the treatment of boundary condition. Void ratio boundary keeps changing during consolidation, and non-neglected errors will be induced if not dealt properly. The impermeable boundary reasonable treatment and how to consider the sediment weight effect properly are the two main optimization directions in current study.

ACKNOWLEDGEMENT

The authors appreciate the financial support provided by the programme of “*Pond sediment deposition mechanisms and the treatment technology*” and “*The Doctoral Fund of Education Ministry of People's Republic of China*” (NO. 20100094110002), and also the financial support to the third author has been provided by the “*Fundamental Research Funds for the Central Universities*” (NO. 2009B13514).

REFERENCES

- Fang K.Z. and Gao X.K. (1979). “Evaluation of one-dimensional nonlinear Dredged-fill soil consolidation.” *Yellow River*, (3): 66-78
- Guo S.J., Zhang F.H. and Wang B.T. (2011). “Settlement and Consolidation Mechanism of Cohesive Sedimentation in Estuarine Environment.” *Advanced Materials Research*, v.261-263: 1654-1658.
- Hong Z.S. (1987). “One-dimensional mathematical model for large strain consolidation of dredged-fill soil.” *Journal of HoHai University*, 15(6): 27-36.
- Lucas M.B. (2000). “Consolidation and strength evolution of soft mud layers.” Holland: Technique University Delft.
- Pane V. and Schiffman R.L. (1981). “A comparison between two theories of finite strain consolidation.” *Soils and Foundations*, 21(4): 81-84.
- Patrick J.F., Lee J. and Qiu T. (2005). “Model for large strain consolidation by centrifuge.” *International Journal of Geomechanics*, ASCE, 5(4): 267-275.
- Townsend F.C. and Mevay M.C. (1990). “Large-strain consolidation predictions.” *Journal of Geotechnical Engineering*, 116(2): 166-176.
- Wei R.L. (1993). “Derivation for coefficient of consolidation from settlement observation.” *Chinese Journal of Geotechnical Engineering*, 15(2): 12-19.
- Xie K.H., Zheng H and Leo C.J. (2003). “Analytical solution for 1-D large strain consolidation of saturated soft clay under time-depending loading.” *SHUILI XUEBAO*, (10): 1-10.
- Xie X.Y., Zhu X.R. and Xia J.Z. (1998). “The research on the one-dimensional large-strain coefficient of consolidation for saturated soil.” *Journal of Zhejiang University*, 32(3): 319-324.
- Yin Z.Z. (2007). “*Geotechnical Principles*.” Beijing: China Water Power Press.
- Znidarcic D. and Schiffman R.L. (1982). “On Terzaghi's concept of consolidation.” *Geotechnique*, 32(4): 387-389.

Rotating Block Method for Seismic Displacement of Slopes of Saturated Clay

X. Zeng¹ and C. He²

¹Dept. of Civil Engineering, Case Western Reserve University, Cleveland, Ohio, 44106-7201, USA; PH (216)368-2923; Fax: (216)368-5229; Email: xxz16@case.edu

²Barr & Prevoist Inc., 2800 Corporate Exchange Drive, Suite 240, Columbus, Ohio 43231, USA; Phone: 216-258-4072; Fax: 614-714-0323; Email: springmay_he@hotmail.com

ABSTRACT: A rotating block method is developed to calculate the rotational displacement of slopes of saturated clay under seismic loading. The method is similar to the pseudo-static sliding block method of Newmark and is quite easy to use in design calculations. When the threshold acceleration for rotation is exceeded, the slope will start to rotate until the angular velocity for rotation is reduced to zero. Rotational displacement will be accumulated each time the threshold acceleration is exceeded during ground vibration. The influence of ground motion characteristics on the computed slope deformation is evaluated. Implications for design are discussed.

INTRODUCTION

As a large number of slope failures have occurred during past earthquakes, geotechnical engineers working in seismically active regions have to routinely evaluate the seismic stability of earth slopes. Maximum seismic displacement is one of the most important parameters in design calculations. Over the past several decades, analytical methods have been developed to estimate the displacement of slopes under earthquake loading for specific applications.

Newmark (1965) proposed a practical slope displacement model under earthquake loading, based on the analogy of a sliding block. Using the concept of a yield or threshold acceleration, relative displacement between a rigid block and the ground beneath will be initiated at the instant the ground acceleration exceeds the threshold value until the block and the ground have the same velocity again. Most of the established methods for the prediction of sliding displacement of slopes are based on the sliding block method of Newmark. For example, the procedure proposed by Makdisi and Seek (1978) for calculating permanent seismic slope displacement is based on the Newmark sliding block method but uses average accelerations computed with the shear beam method using the method proposed by Chopra (1966).

However, the critical surface for certain slopes (i.e. homogeneous slopes made of saturated clay) usually has a circular or a log-spiral slope. For such slopes, rotational displacement or coupled rotation and sliding are the most likely damage or “failure” mechanisms. Little research has been conducted on the development of design methods for rotational slope displacement. Similar to stress-deformation analyses of static slope stability performed by using static finite element programs, stress-deformation analyses of seismic slope stability (e.g., Seed et al. 1973; Lee 1974;

Daddazio et al. 1987) are usually carried out using dynamic finite element programs. While these complicated finite element calculations are available, they are not very useful in daily engineering design. Moreover, many of these procedures use complicated constitutive models which are difficult to calibrate and have not been verified by experimental data.

Zeng and Steedman (2000) proposed a rotating block method for the seismic displacement of gravity walls. Based on this approach, a rotating block method is developed to calculate the rotational displacements of slopes under earthquake loading. This paper describes the methodology used in this design method. The influence of significant design parameters is also evaluated.

ROTATING BLOCK METHOD

The heterogeneous nature of soils often makes it impossible to set up an exact stability analysis. As in many other physical sciences, simplifying assumptions, which give solutions of reasonable accuracy, must often be made. The forces acting on a slope under earthquake loading are shown in Fig.1 using a pseudo-static approach. A number of assumptions are adopted in this method:

1. The potential failure mass (also called rotating block) and the remaining part of slope are rigid so that the failure mass is assumed to rotate about a center of rotation (point O). The potential failure surface can be determined use a pseudo-static method that takes into consideration of both static and earthquake loading.

2. It is assumed that the rotating block cannot rotate upslope. This is a conservative assumption since it is unlikely to occur, and if it did occur, it would reduce the angle of rotation.

3. The angle of rotation of the block is small. Therefore, the change in the geometry of the problem and the coordinates of centroid x_c , y_c can be ignored.

4. The slope is made of saturated clay with undrained shear strength c_{ui} , and there is no free water in front of the slope.

5. The potential failure surface is an arc with the center located at O. The exact location of O and the failure surface can be determined by using traditional limit equilibrium approach.

In Fig.1, (a_x) = centroidal acceleration in x direction; (a_y) = centroidal acceleration in y direction; \vec{a}_c = acceleration vector at the centroid of the rotating block; \vec{a}_h = horizontal ground acceleration vector; \vec{a}_v = vertical ground acceleration vector; \vec{r}_c = vector from the rotation center O to the centroid of the rotating block; $\vec{\alpha}$ = angular acceleration vector of rotation; W = total weight of the rotating block in the slope; c_{ui} = undrained shear strength of clay layer i; R = rotating block radius; L_i = arc length of soil layer i; γ_i = unit weight of soil layer i; θ = angle of rotation; x_c = horizontal distance between the rotation center and the combined centroid of the rotating block; and y_c = vertical distance between the rotation center and the combined centroid of the rotating block.

During an earthquake, forces are induced on the block which lead to elastic deformations and can ultimately result in permanent rotation. During a block rotation, a rotational acceleration with regard to the center of rotation O is developed immediately as the threshold for rotation is exceeded, which leads to the accumulation

of permanent rotation relative to the foundation. When the ground acceleration drops below the critical acceleration for rotation, the speed of rotation will be slowed down by the restoring forces and moments. Thus, the rate of increase in the rotation angle is reduced. The rotation will continue until the angular velocity of rotation is dropped to zero. Thus, a permanent rotation is developed. During each cycle of vibration, whenever the threshold acceleration for rotation is exceeded, rotation will be induced, and the rotational angle will be accumulated in the same manner as the sliding displacement in Newmark sliding block method.

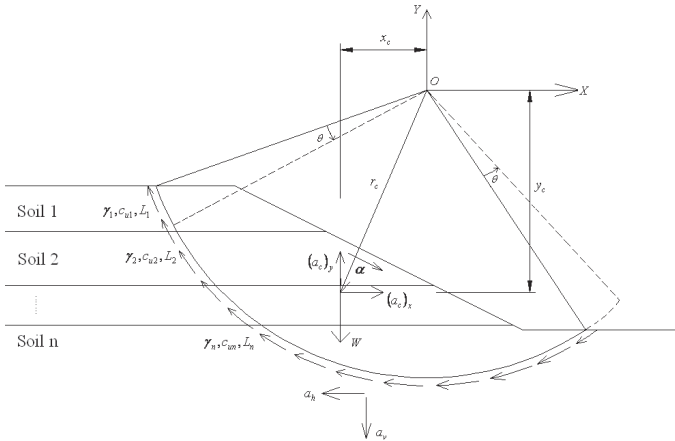


FIG. 1. Forces and accelerations on a block with rotation during base shaking.

DETERMINATION OF THRESHOLD ACCELERATION

Following this method, a rotation of the block will occur when the driving moment exceeds the resisting moment. For the slope shown in Fig.1, using a pseudo-static approach, at the instant when a rotation starts, the rotating moment equals the restoring moment with respect to the center of rotation. Thus

$$k_h W y_c + W x_c = \left(\sum_{i=1}^n c_{ui} L_i \right) R + k_v W x_c \tag{1}$$

in which k_h = horizontal earthquake acceleration coefficient and k_v = vertical earthquake acceleration coefficient. From equation (1), the threshold acceleration coefficient for rotation ($k_r = k_h$ when rotation is initiated) can be deduced:

$$k_r = \frac{\left(\sum_{i=1}^n c_{ui} L_i \right) R + k_v W x_c - W x_c}{W y_c} \tag{2}$$

Thus, the threshold acceleration for rotation $a_r (= k_r g)$ can be obtained.

DETERMINATION OF ROTATIONAL DISPLACEMENT

For the slope shown in Fig. 1, the equation of motion when rotation has started is (with regard to the rotation center O):

$$\sum M_o = -x_c (W/g)(a_c)_y + y_c (W/g)(a_c)_x + I_c \alpha \tag{3}$$

where M_o = moment about the rotation center O; g = gravitational acceleration; and I_c = polar moment of inertia of the rotating block about the centroid. The acceleration at the centroid is the sum of three components:

$$\vec{a}_c = \vec{a}_h + \vec{a}_v + \vec{\alpha} \times \vec{r}_c - \omega^2 \vec{r}_c \quad (4)$$

in which ω = angular velocity of rotation. From Fig. 1, the horizontal and vertical accelerations at the centroid of the rotating block are

$$(a_c)_x = -a_h + \alpha y_c + \omega^2 x_c \quad (5a)$$

and

$$(a_c)_y = -a_v - \alpha x_c + \omega^2 y_c \quad (5b)$$

Substituting (5a) into (5b) and calculating $\sum M_o$ gives:

$$(W/g)a_h y_c + W x_c - \left(\sum_{i=1}^n c_{ui} L_i \right) R - (W/g)a_v x_c = [(W/g)r_c^2 + I_c] \alpha \quad (6)$$

and the angular acceleration for rotation can be expressed as:

$$\alpha = \frac{(W/g)a_h y_c + W x_c - \left(\sum_{i=1}^n c_{ui} L_i \right) R - (W/g)a_v x_c}{I_c + (W/g)r_c^2} \quad (7)$$

or:

$$\alpha = \frac{k_h W y_c + W x_c - \left(\sum_{i=1}^n c_{ui} L_i \right) R - k_v W x_c}{I_c + (W/g)r_c^2} \quad (8)$$

where $k_h = a_h / g$; $k_v = a_v / g$.

The velocity of rotation (or angular velocity) can then be derived by the integration of rotational acceleration:

$$\omega = \int_0^t \alpha dt \quad \text{when } \omega > 0 \quad (9a)$$

$$\omega = 0 \quad \text{when (9a) gives } \omega < 0 \quad (9b)$$

Equation (9b) is the direct result of assumption 2, which presumes that the block cannot rotate back. Then the rotation angle is the integration of the angular velocity of rotation over the period of time being considered:

$$\theta = \int_0^t \omega dt \quad (10)$$

For each cycle of vibration this procedure can be repeated when the threshold acceleration for rotation is exceeded. Therefore, the final rotation angle is obtained as the accumulation of rotation angles during the entire earthquake.

EXAMPLES AND PARAMETRIC STUDY

Following the procedures of the rotating block method for seismic displacement of slopes described above, three examples are given to show how this procedure can be applied.

EXAMPLE 1

A uniform clay ($\phi_u = 0$ condition) slope of height 9.14 meters is shown in Fig. 2a. The shear strength c_u of the clay is 47.8 kN/m². The unit weight of the clay is 17.2 kN/m³. Arc OAB is determined to be the critical failure surface using a limit equilibrium method, with radius ($R=15.5$ meter) and arc angle ($\theta = 104^\circ$). The area of the critical failure surface is 146 square meters. The idealized ground acceleration comprises a half-cycle square wave with a peak of value of 0.5g and duration of 0.5 s (shown in Fig. 2b).

Using Equation (2), the threshold acceleration coefficient for rotation can be determined from

$$k_{tr} = \frac{c_u LR - Wx_c}{Wy_c} = 0.465$$

Thus, the threshold acceleration for rotation is:

$$\alpha_{tr} = 0.465g$$

Since $a_h > a_{tr}$, the rotating block will rotate about the center O .

Between $t = 0 \sim 0.5$ s, the dynamic force on the block will generate a rotation with an angular acceleration of

$$\alpha = \frac{k_h Wy_c + Wx_c - c_u LR}{I_c + (W/g)r_c^2}$$

where

$$I_c = 3632.8kg \cdot m^2 / m; k_h = a_h / g = 0.5; r_c^2 = x_c^2 + y_c^2 = 196m^2.$$

Using the parameters given in this example α is found to be 0.018 rad/s². Therefore,

$$\omega = \omega_{(t=0)} + \alpha t = 0.018t$$

and

$$\theta = \theta_{(t=0)} + \omega_{(t=0)} + 0.5\alpha t^2$$

At $t = 0.5$ s, $\omega = 0.009$ rad/s, and $\theta = 0.0023$ rad = 0.13°. After $t = 0.5$ s, the restoring forces acting on the rotating block will slow the rotation down, giving an angular deceleration:

$$\alpha = \frac{Wx_c - c_u LR}{I_c + (W/g)r_c^2}$$

Using the parameters for this example, α is found to be -0.243 rad/s² and the rotational velocity is then given by

$$\omega = \omega_{(t=0.5)} - 0.243(t - 0.5) = 0.009 - 0.243(t - 0.5)$$

until ω drops to zero when it is assumed in this approach that permanent rotation ceases until the threshold acceleration for rotation is exceeded again. Solving for $\omega = 0$, the outward rotation will stop at $t_1 = 0.537$ s, and the final angle can be calculated:

$$\theta = \theta_{(t=0.5)} + \omega_{(t=0.5)}(t_1 - 0.5) + 0.5\alpha(t_1 - 0.5)^2$$

$$\theta = 0.0024rad = 0.14^\circ$$

as illustrated in Fig. 2.

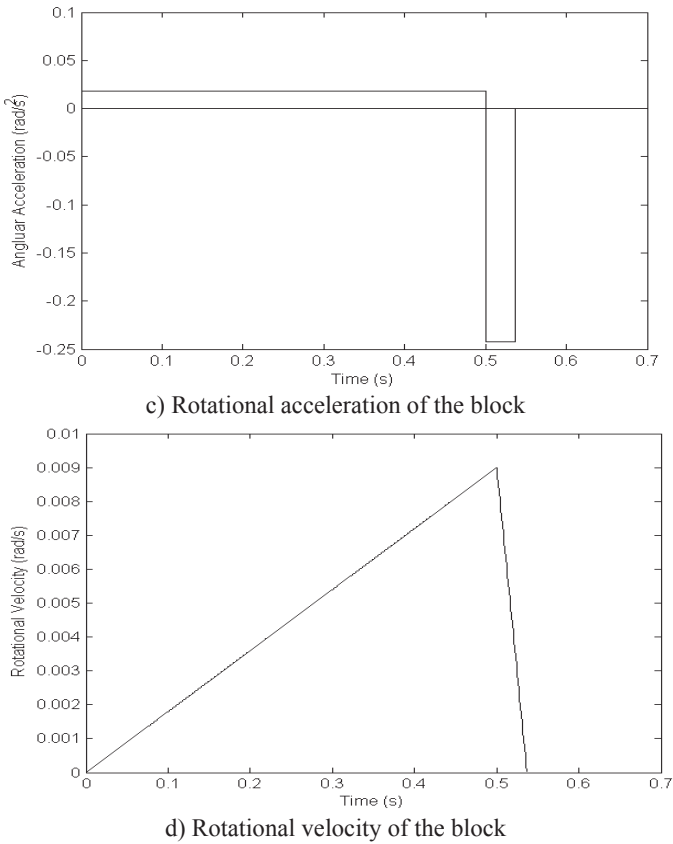
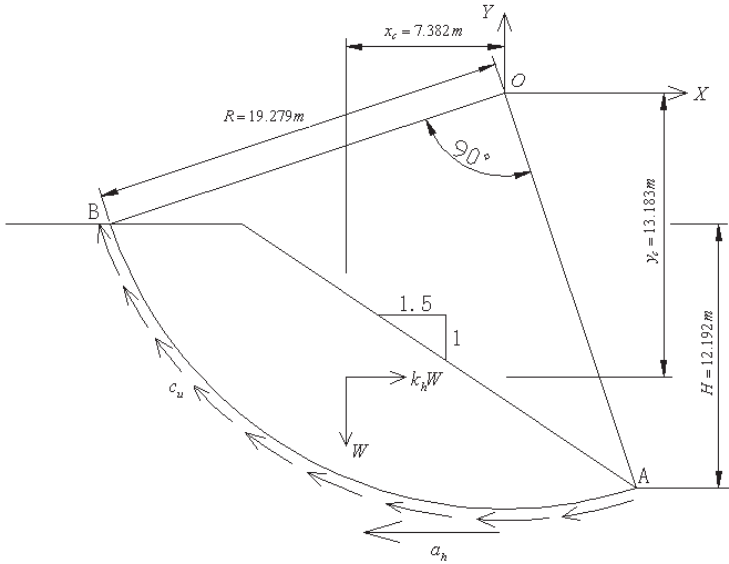


FIG. 2. Example 1 of application of rotating block method.

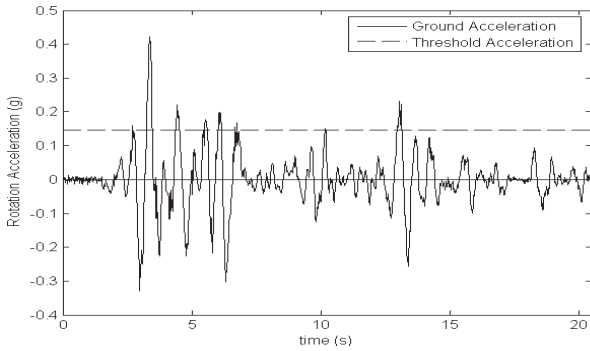
The final rotation angle of the block can be obtained: $\theta = 0.0047 \text{ rad} = 0.2701^\circ$. For the rotating block in this example, 0.2701° of rotation will result in a 90.9 millimeter outward displacement at the toe of the block.

EXAMPLE 3

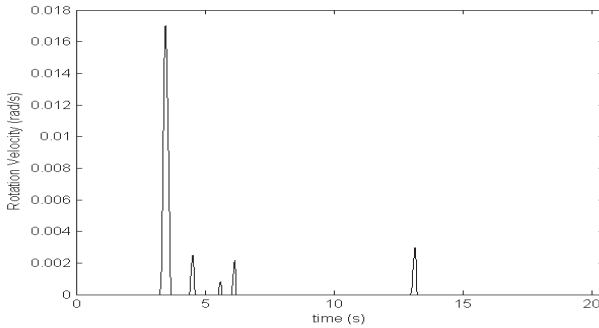
A parametric study is carried out in order to show the effects of ground motion characteristics on the computed displacement. For the clay slope shown in Fig.2a with soil parameters $\gamma = 18.8 \text{ kN/m}^3$ and $c_u = 38.3 \text{ kN/m}^2$, a simple time history which comprised of ten uniform sinusoidal cycles (Fig.4a) of varying amplitude and period is used. From Fig.4b, it is clear that the peak ground acceleration has a significant influence on the final angle of rotation of the slope. The period of ground acceleration is varied and again is seen to have a significant influence on the final angle of rotation of failure mass (see Fig.4c). The angle of rotation is approximately proportional to T^2 , where T is the period of ground acceleration.



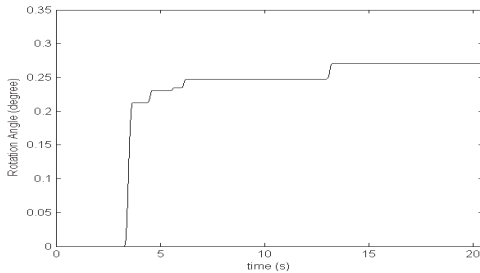
a) An example clay slope



b) Acceleration time history



c) Rotational velocity of the block



d) Rotation angle of the block

FIG. 3. Example 2 of application of rotating block method.

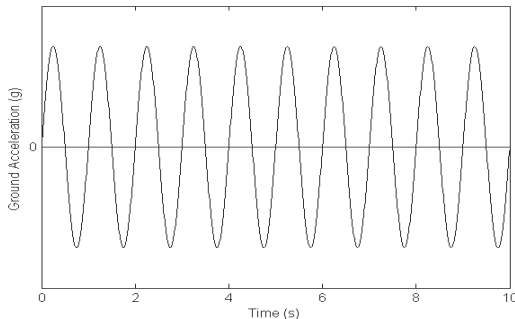
CONCLUSIONS

A pseudo-static type of rotating block method has been developed to calculate the maximum seismic displacement of a slope with a circular failure surface. The model is based on Zeng and Steedman's rotating block method. It is more realistic and practical for homogeneous clay slopes than Newmark sliding block method. Parametric studies show that once the threshold is exceeded, the peak input acceleration has a strong influence on the final rotation angle of the failure mass and the period of ground acceleration has a significant impact on the overall rotation angle. In this method, it was found that the computed rotation is approximately proportional to T^2 , where T is the period of the ground acceleration. The characteristic of the rotating block method is similar to that of the Newmark sliding method.

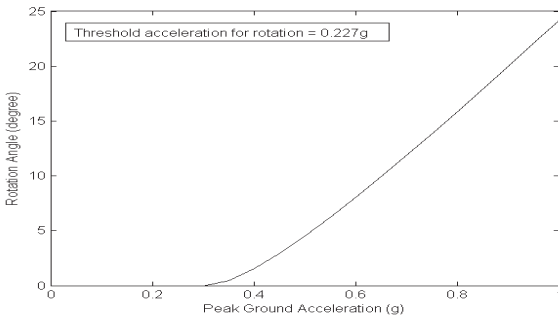
The assumption that the rotation angle is small is purely for the simplicity of calculation. This factor can be easily incorporated into the procedure by updating the location of the slope and its influence on the directions of external forces during each time increment of calculation. The influence of hydrodynamic pressure and excess pore pressure has also been ignored. Again, as with the geometrical effects, the factors can be incorporated to the calculation if needed.

REFERENCES

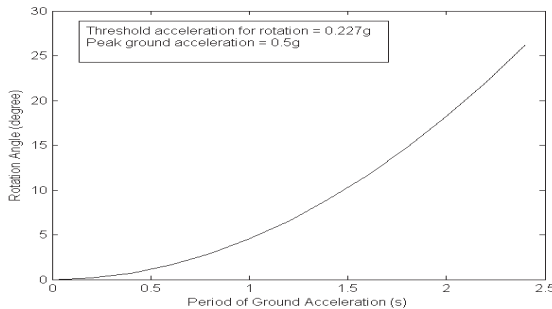
Chopra, A. K. (1966). Earthquake effects on dams, *Ph.D. Dissertation*, University of California, Berkeley.



a) Time history of input motion



b) Influence of peak ground acceleration on rotation angle



c) Influence of ground acceleration period on rotation angle

FIG.4. Influences of peak acceleration and period on rotation angle.

- Daddazio, R. P., Ettouney, M. M., and Sandler, I. S. (1987). "Nonlinear dynamic slope stability analysis." *Journal of Geotechnical Engineering*, ASCE, Vol. 112, No. 4: 285-298.
- Lee, K. L. (1974). Seismic permanent deformations in earth dams, *Report No. UCLA-ENG-7497*, School of Engineering and Applied Science, University of California at Los Angeles.
- Makdisi, F. I. and Seed, H.B. (1978). "Simplified procedure for estimating dam and embankment earthquake-induced deformations." *Journal of the Geotechnical Engineering Division*, ASCE, Vol. 104, N. GT7: 849-867.
- Newmark, K. M. (1965). "Effect of earthquakes on dams and embankments." *Geotechnique*, London, 15 (2): 139- 160.
- Seed, H. B., Lee, K. L., Idriss, I. M., and Makdisi, R. (1973). "Analysis of the slides in the San Fernando dams during the earthquake of Feb. 9, 1971." *Report No. EERC 73-2*, Earthquake Engineering Research Center, University of California, Berkeley, 150 p.
- Zeng, X., and Steedman, R. S. (2000). "Rotating block method for seismic displacement of gravity walls." *Journal of Geotechnical and Geoenvironmental Engineering*, ASCE, Vol. 126, No. 8.

Attenuation Plateau Characteristics and Fitting Analysis of the Dynamic Compaction Shockwave

Fang Xing¹; Li Tianbin²; Ma Hongmin³; and Wang Feng⁴

1 State Key Laboratory of Geohazard Prevention & Geoenvironment Protection, Chengdu University of Technology, Chengdu, China, 610059; Email: fangxing622@yahoo.com.cn

2 State Key Laboratory of Geohazard Prevention & Geoenvironment Protection, Chengdu University of Technology, Chengdu, China, 610059; Email: ltb@cdut.edu.cn

3 Northwest Research Institute of Engineering Investigations and Design, Xi'an, China, 710003; Email: himhm@126.com

4 State Key Laboratory of Geohazard Prevention & Geoenvironment Protection, Chengdu University of Technology, Chengdu, China, 610059; Email: fengbaker@qq.com

ABSTRACT: The attenuation plateau formed during radiation of dynamic compaction shockwave has a severe impact on construction work in loess backfill site and safety of buildings nearby. With essential targets of finding out reasons for attenuation plateau formation and providing basis for safe distance determination, geophysical prospecting was adopted in the test for in-depth investigation on the attenuation plateau characteristics of shockwave so as to provide basic data for attenuation law study of shockwave. Appropriate cut-off frequency was selected according to the test results and energy composition characteristics of elastic wave in semi-infinite soil, the shockwave energy was divided into body wave energy and surface wave energy in order to analyze energy attenuation characteristics of different waves. It is confirmed that main reasons for attenuation plateau formation in the area were proportion and radiation characteristics of body wave energy. On this basis, staircase method was used to fit the radiation attenuation characteristics of dynamic compaction shockwave through subsection regression and compare with traditional fitting methods. The results showed that in close-distance and high-density dynamic compaction work, staircase method can be more accurate to mark out safe distance.

INTRODUCTION

During the dynamic compaction (hereinafter referred to as 'DC') test of 8000kN.m energy level in loess backfill site of large thickness, it is found that vibration radiation

peak of DC decreases very slowly within a certain distance, resulting in the attenuation plateau. Scholars, home and abroad, have a lot of research achievements on improving the efficiency and quality of dynamic compaction (Poran et al. 1992; Dize et al. 1994; Nashed et al., 2006), but, there is few research on how to protect the related areas from the damage of dynamic compaction. Isolation method can maintain security of important construction (Farzad & Kelly 1999; Calio & Marletta 2003; Yang et al. 2005), but it is only adopted in mega projects for the high cost and complex techniques. Meanwhile, the method to mark out safe distance is usually adopted in foundation consolidation, however, traditional analysis method cannot meet the security requirement in close-distance and high-density DC work as a result of the attenuation plateau.

In China, when single-tamping energy is within 1000KN.m, the safe distance should be over 15m; and when it's more than 1000KN.m, the safe distance for instrument workshop or high sensitivity buildings should be actually modified according to measured results of trail tamping (Fang et al., 2001). Mathematical functions are usually used to fill seismic wave attenuation law. Li (Li et al. 2010) points out that the vibration radiation peak of DC is accord with the Exponential Function attenuation law. Tan (Tan et al. 2001) analyzes the vibration spectrum of DC shockwave and finds out attenuation law of each single-frequency components wave is in line with the Negative Exponential Function law. Miller (Miller & Pursey 1955) believes that in geophysical experiment, only the energy radiated by compression wave is effective. But there is another theory says that surface wave can be destructive to ground buildings nearby. This shows that there is no common understanding of the radiation law of tamping shockwave energy.

In this context, we have carried out geophysical prospecting to study the radiation law of DC shockwave in test site. This paper analyzes the proportion and variation of body wave energy and surface wave energy within different frequency bands and confirms that the proportion and variation of surface wave energy are main reasons for attenuation plateau formation. And then, staircase method is used to fit the radiation attenuation law of DC shockwave. Comparing with traditional fitting method, it is shown that in close-distance and high-density DC work, staircase method can be more accurate to mark out safe distance.

DC TEST AND DATA FEATURE

The DC site is a part of the loess ravine region, the layers of which from top to the bottom are as follows:

1. Cultivated soil, Quaternary Holocene slope and Diluvia loess shape soil;
2. Quaternary Late Pleistocene Aeolian loess and Residual paleosol;
3. Quaternary Mid-Pleistocene Aeolian loess and Residual paleosol;
4. The Lower Triassic Wayaobao group Sandstone and interbedded body with sand and shale.

The backfill soil is mainly composed of Quaternary Holocene slope and Diluvial loess shape soil, and the average backfill thickness is more than 20m.

The DC of 8000kN.m energy level with a drop hammer weight of 40t and a falling height of 20m was taken as the test object. Spacing of geophone was 5m, and the total number of geophones was 24 (Fig. 1). As vibration characteristics of the tamping points could not be measured, we took the closest geophone (1#) into account. The test stopped when average settlement of the last two tamping was less than 20cm, and the total tamping times were 14 in the test.

Surface wave energy with low frequency is the main part of DC radiation energy, so geophone with low natural frequency was chosen as the monitoring device (Fig. 2) with natural frequency of 4.5Hz and sensitivity coefficient of 28.2mV/mm/s. Gypsum was chosen as the coupling material between geophone and soil in order to ensure accuracy of the monitoring data in the test.

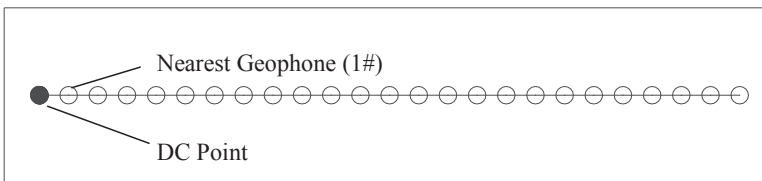


Fig. 1. Layout of Measured Line and Geophone.

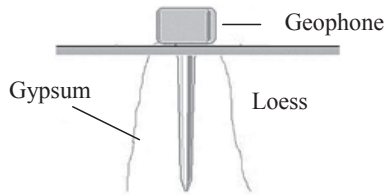


Fig. 2. Layout method of Geophone.

The test takes engineering seismograph as the monitoring host, parameters of which are described as Table 1.

Table 1. Parameters of Engineering Seismograph

| Number of Channels | Sample Interval(ms) | Number of Samples | Trigger Mode |
|--------------------|---------------------|-------------------|------------------|
| 24 | 1 | 8 192 | External trigger |

Vibration characteristics of each tamping were substantially similar. Normally, the

final tamping has the strongest impact owing to the maximum soil compactness. Therefore, we analyzed measured data of the final tamping by:

1. Extracting the vibration peak (hereinafter referred to as 'VP') of amplitude curve of each geophone, which is the magnitude of voltage obtained from geophone;
2. Calculating the vibration energy (hereinafter referred to as 'VE') by integrating spectrogram curve obtained through Time-Frequency conversion from time-history curve.

The attenuation plateau range, which is between 5m and 25m, is identified by dotted line (Fig. 3), in which VP hardly attenuates and similarly VE reduction is very limited. VP curve is described by Linear Coordinate and VE curve by Logarithmic Coordinate, and VE is dimensionless numerical.

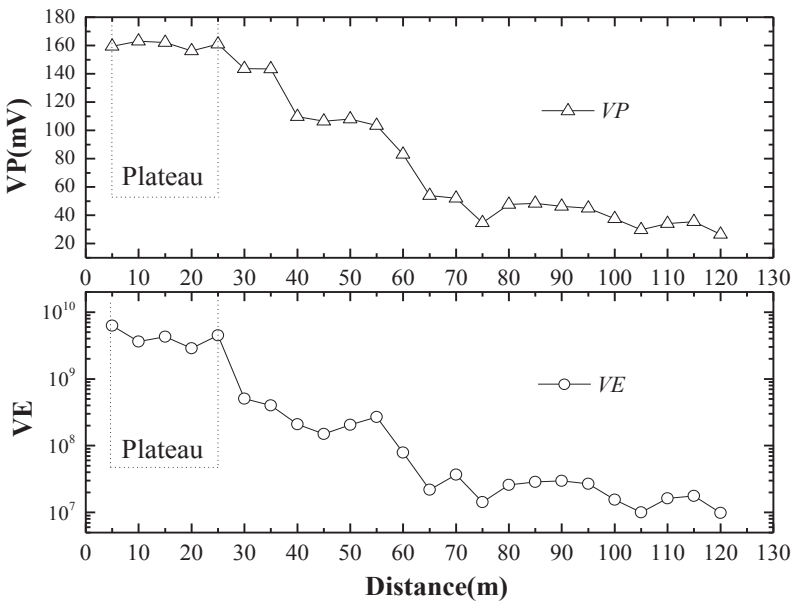


Fig. 3. Attenuation Curve of the VP and VE

ANALYSIS AND DISCUSSION

Reasons for attenuation plateau formation

This paper discusses reasons for attenuation plateau formation from the aspect of energy attenuation of shockwave with different frequency bands.

Formula proposed by Miller used to calculate radiation energy of waves is as follow:

$$W_C = 2.945 \frac{\pi^3 v^2 a^4 P_0^2}{\rho V_c^3}, W_{Sh} = 10.415 \frac{\pi^3 v^2 a^4 P_0^2}{\rho V_c^3}, W_{Su} = 25.21 \frac{\pi^3 v^2 a^4 P_0^2}{\rho V_c^3} \quad (1)$$

Therefore, we obtain:

$$(W_C + W_{Sh}) : W_{Su} \approx 1 : 2 \quad (2)$$

In which, W_C is the compression wave energy, W_{Sh} the shear wave energy and W_{Su} the surface wave energy.

Based on the measured data of 1# geophone (Fig. 1), VE of different waves were calculated by integrating spectrogram curve. The VE and proportion in each frequency band was calculated repeatedly by selecting different cut-off frequency, and then reasonable cut-off frequency to distinguish surface wave and body wave could be determined when the proportion could meet Formula 2.

In our DC test, reasonable cut-off frequency was 8Hz. Fig. 4 and Fig. 5 are double Y axis graphs drawn after signals processing by low-pass filtering and high-pass filtering, in which the vertical dashed line was the right boundary of attenuation plateau and the horizontal dashed line presented the proportion of 50%. Then VE and proportion in different frequency bands had following four characteristics:

1. The VE of surface wave was of fluctuant downtrend while body wave energy stayed stable in the plateau;
2. The VE proportion of surface wave was of fluctuant attenuation while the VE proportion of body wave was of fluctuant ascendant trend in the plateau;
3. The body wave proportion is overall more than surface wave except the nearest geophone (1#).
4. The VE proportion of surface wave continued to reduce with the distance increase, and finally achieved the stable energy proportion of 10%. At the same time, VE of body wave accounted for 90% approximately.

Therefore, from features mentioned above, it could be concluded that the VE of body wave kept the VP of each geophone stable in the plateau. And the impact of body wave is greater than surface wave on ground vibration when the VE was radiating around.

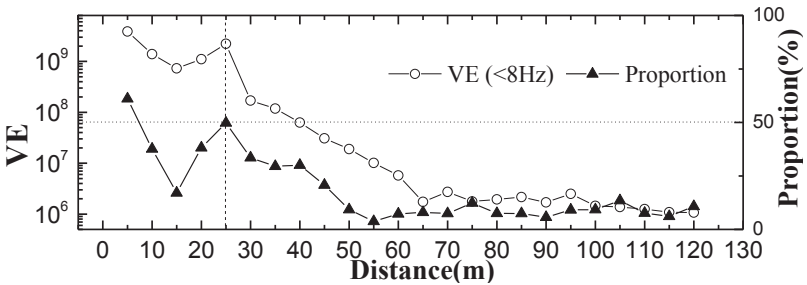


Fig. 4. The VE curve and Proportion curve lower than 8 Hz

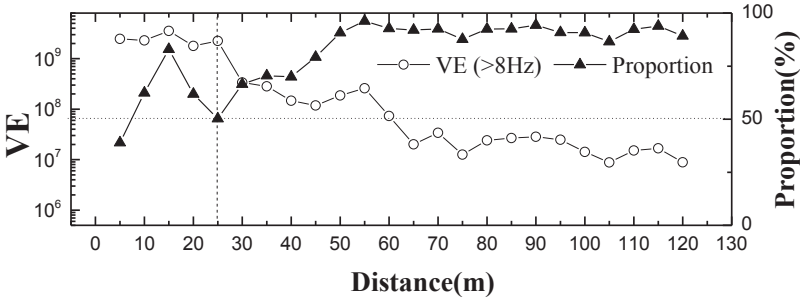


Fig. 5. The VE curve and Proportion curve higher than 8 Hz

Fitting analysis of VP

VP was selected as basic parameter to describe vibration characteristics. Meanwhile, impact of DC vibration can be accurately evaluated through regression analysis.

Owing to the attenuation plateau, traditional method to mark out safe distance would cause large error. Therefore, we introduced the staircase method (Formula 3) to describe radiation law of the tamping vibration:

$$\begin{cases} VP = cons \tan t (a \leq D \leq b) \\ VP = \delta \cdot e^{-\varepsilon \cdot D} (D > b) \end{cases} \quad (3)$$

Where, D was the safe distance of vibration; a and b were the left and right boundary of the plateau; and δ and ε were the undetermined coefficient.

The a equaled to 5 and b equaled to 25 when plateau range was between 5m and 25m in presented test (Fig. 2). The cons tan t, gained by calculating the arithmetic mean value of each vibration peak in the plateau range, equaled to 160.3532. Meanwhile, the undetermined coefficients could be confirmed through regression analysis between 25m and 120m on the attenuation curve of VP (Fig. 2): $\delta = 275.4970$, $\varepsilon = 0.0209$. Substituting the parameters into formula 3:

$$\begin{cases} VP = 160.3532 (5 \leq D \leq 25) \\ VP = 275.4970 \cdot e^{-0.0209D} (D > 25) \end{cases} \quad (4)$$

By contrast, traditional method (Formula 5) was used to fit measured data:

$$VP' = \delta' \cdot e^{-\varepsilon' \cdot R} \quad (5)$$

Fitting range is between 5 m and 120m, and then we could obtain: $\delta' = 205.2736$, $\varepsilon' = 0.0159$. And then:

$$VP' = 205.2736 \cdot e^{-0.0159 \cdot R} \quad (6)$$

Comparative curves were drawn according to Formulae 4 and Formulae 6 by comparing with measured value of VP (Fig.6). The chart indicated that the value

calculated by staircase method was closer to the actual value than by traditional method in plateau range.

Maximum relative error and mean absolute error of the calculated value could be greatly reduced by staircase method in plateau range of 5m and 25m (Table 2).

Table 2. Error Evaluation for Fitting Results

| Method | Maximum relative error (%) | Mean absolute error (mV) |
|--------------------|----------------------------|--------------------------|
| Traditional method | 18.94 | 14.5061 |
| Staircase method | 2.60 ↓ | 2.0136 ↓ |

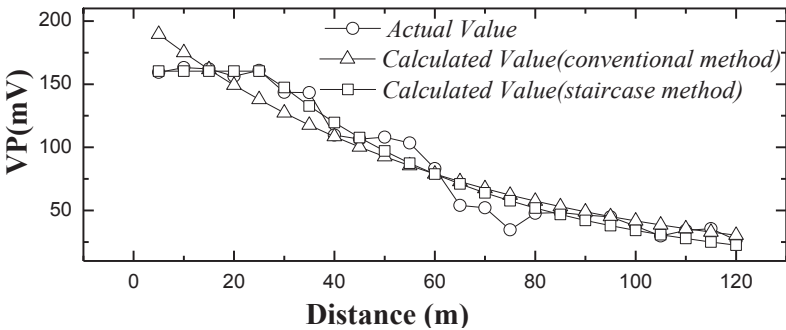


Fig. 6. Comparative curves between actual value and calculated value

For dangerous buildings, the allowable vibration speed was within 0.15 cm/s (GB6722-2011, 2011), the corresponding VP was 42.3mV and the safe distance was 90m. The test site was divided into three parts according to Formula 4:

1. Extreme Risk Area: $5m \leq D \leq 25m$;
2. Risk Area: $25m < D \leq 90m$;
3. Safe Area: $D > 90m$.

CONCLUSIONS

Studies in this paper showed that body wave plays an important role in attenuation plateau formation. From the above studies, conclusions can be drawn as follow:

1. Proportion and radiation features of body wave are confirmed to be the main reasons for attenuation plateau formation. The body wave keeps VE of shockwave stable in attenuation plateau; and during the shockwave radiation, body wave has gradually

become dominant.

2. Compare with traditional method, the staircase method could significantly reduce the Maximum relative error and Mean absolute error, and characterize quantitatively vibration near the DC point.

3. The construction area was divided into three parts: extreme risk area, risk area and safe area so as to ensure the safety in close-distance and high-density DC work.

ACKNOWLEDGMENTS

This research was supported by the Program of National Natural Science Foundation of China(41172279) and the Cultivating programme of excellent innovation team of Chengdu university of technology(HY0084).

REFERENCE

- Poran, Chalm J., Heh, King-Sen, and Rodriguez, Jorge A. (1992). "New technique for quality control of dynamic compaction" J. Geotech Spec Publ, 30, 915-926
- Dise, Karl, Stevens, Michael G., Von Thun, J. Lawrence, (1994). "Dynamic compaction to remediate liquefiable embankment foundation soils" J. Geotech Spec Publ, 45, 1-25
- Nashed, R., Thevanayagam, S.; Martin, G.R. (2006) "Simulation of dynamic compaction processes in saturated silty soils" J. GeoCongr. Geotech. Eng. Info. Technol. Age, 2006, 284
- Farzad N., and Kelly J. M. (1999). "Design of seismic isolated structures: from theory to practice". Hoboken: Wiley, 2011.
- Calio I., and Marletta M. (2003). "Passive control of the seismic rocking response of art objects" J. Engineering Structure, 25, 1009-1018
- Yang YB, Lu LY, and Yau JD (2005). "Chapter 22: structure and equipment isolation: Vibration and shock handbook". Boca Raton: CRC Press Inc, 2005
- Fang L., Jing F. and Liu Y. S. (2001). "Influence of vibration caused by dynamic compaction and safe distances for buildings" J. Journal of southeast university (natural science edition), 31, 29-32.
- Li H. Q., Ni Y.J., and Teng X. L. (2010). "Ground vibration attenuation law caused by the dynamic compaction and the environmental assessment" J. Road Engineering, 5, 56-57.
- Tan H. H., Sun J. Z., and Qi S. W. (2001). Research On the attenuation rule of the dynamic compaction J. Geotechnical Investigation & Surveying, 5, 11-14.
- Miller G. F., and Pursey H. (1955). "On the partition of energy between elastic waves in a semi-infinite Solid" J.: Proceedings of the Royal Society of London Series A: Mathematical and Physical Sciences. 233, 55-69.
- GB6722-2011, 2011: Blast Safety Regulations[S]. Beijing: China Zhijian Publishing House, 2011.

Developing an Economical and Reliable Test for Measuring the Resilient Modulus and Poisson's Ratio of Subgrade Soils

X. Zeng¹ and R. Hu²

¹Dept. of Civil Engineering, Case Western Reserve University, Cleveland, Ohio, 44106-7201, USA; PH (216)368-2923; Fax: (216)368-5229; Email: xxz16@case.edu

²Dept. of Civil Engineering, Case Western Reserve University, Cleveland, Ohio, 44106-7201, USA; PH (216)368-2950; Fax: (216)368-5229; Email: rxh241@gmail.com

ABSTRACT

The resilient modulus and Poisson's ratio of subgrade soils in highway foundation are important parameters in design and quality control process. The currently used techniques include CBR (California Bearing Ratio) test, resilient modulus test, DCP (Dynamic Cone Penetrometer), and FWD (Falling Weight Deflectometer) tests. However, these techniques have certain limitations and sometimes fail to satisfy the requirement and accuracy for design purposes.

In recent years, piezoelectric sensors have been widely used for laboratory measurement of wave velocities in soil and rock specimens. For shear wave velocity determination, bender elements have been applied to the tests. On the other hand, extender elements have been used for the measurement of primary wave velocity.

This new laboratory testing technique is adopted to measure the two important parameters, the resilient modulus and Poisson's ratio of subgrade soils in laboratory tests. The results of using this technique on a soil sample is presented and compared with that obtained from CBR tests. It is concluded that this new technique is simple, accurate and has potential to be widely used in engineering practice.

INTRODUCTION

In the design of highway pavement, resilient modulus and Poisson's ratio of the subgrade materials are two important design parameters. The currently used techniques to measure resilient modulus include CBR (California Bearing Ratio) test, resilient modulus test, DCP (Dynamic Cone Penetrometer) and FWD (Falling Weight Deflectometer) tests. However, these techniques have certain limitations and sometimes fail to satisfy the requirements and accuracy for design purposes, as discussed by Zeng et al. (2003).

The California Bearing Ratio (CBR) test was developed by the California Division of Highways in 1929 as a means of classifying the suitability of a soil for use as a subgrade or base material in highway construction. During World War II, the U.S. Army Corps of Engineers adopted the test for use in airfield construction. The CBR test is currently used in pavement design for both road and airfields. Some state Departments of Transportation use the CBR directly. Others convert the CBR value to either the modulus of subgrade reaction k_s or to the resilient modulus M_R using an

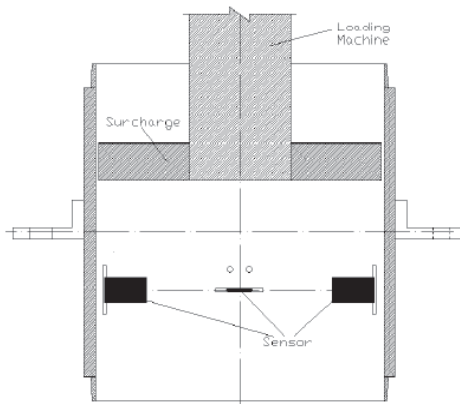
empirical relationship (Bowles, 1992). For example AASHTO converts CBR to M_R using

$$M_R = 10340 \times \text{CBR} \text{ (kPa)} \quad (1)$$

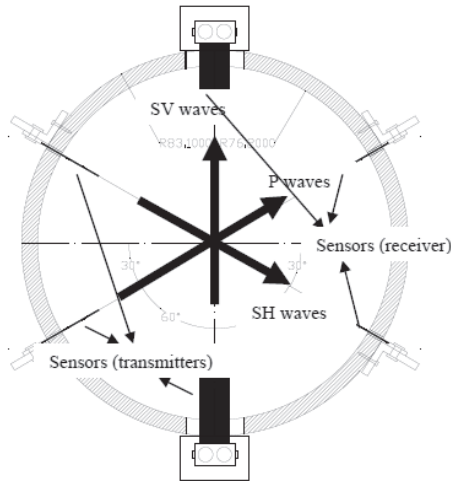
EXPERIMENTAL SETUP

For the new method described in the paper, the device consists of a compaction mold used in the CBR test, with three pairs of piezoelectric sensors fitted in. Three of the sensors on one side are used as wave transmitters and the other three on the opposite side are used as wave receivers. The technology of using piezoelectric sensors to measure wave velocities in soil has been widely used in geotechnical engineering in recent years. The application of the technology is discussed by Leung et al. (2009).

The experimental technique used in this method to measure resilient modulus and Poisson's ratio of compacted soils takes advantage of piezoelectric sensors. These sensors are made of piezo-ceramic materials, in which as an electrical excitation is applied to a transmitter element, it leads to mechanical vibrations, which generates shear (S) waves for a bender element or primary (P) waves for an extender element in a soil. Similarly for a wave receiver, a mechanical vibration of the element induced by waves leads to an electrical output. Therefore, the velocity of S or P waves can be determined by measuring their travel time and the distance between the wave transmitter and receiver. Since the maximum strain generated by a piezoelectric sensor in the surrounding soil is on the order of 10^{-3} % as reported by Dyvik and Madshus (1985), the stress-strain relationship is within the elastic range of soils. This technique has been used by a number of researchers such as Dyvik and Madshus (1985), Thomann and Hryciw (1990), Jovicic et al. (1996), Viggiani and Atkinson (1995), Hryciw and Thomann (1993), Jovicic and Coop (1998), and Zeng and Ni (1998, 1999) to measure the stiffness of sands and clays in the laboratory in recent years. Therefore, it is used to determine the resilient modulus and Poisson's ratio. The test setup is shown in Fig. 1.



a) Cross-sectional view of the compaction mold equipped with piezoelectric sensors



b) Top plan view of the compaction mold with three pairs of piezoelectric sensors
Fig.1 CBR compaction mold equipped with piezoelectric sensors

While measuring the wave velocities by sensors, different ranges of pressure loading applied by CBR machine will be exerted on the samples. Since the diameter of the piston is larger than the tip-to-tip distance of the sensors, we can measure the average wave velocities under different pressures.

SENSORS AND SOIL USED

The soil used for testing was a brown silty clay: this kind of clay is commonly seen in the state of Ohio for highway subgrade construction. The optimum moisture content of the clay is 13.4% and the maximum dry unit weight is 18.85 kN/m^3 . A standard CBR compaction mold which is 152 mm in diameter and 178 mm in height was used. A CBR penetration rate of 1.3mm/min was used for loading.

The bender and extender elements were made of piezoelectric sensors (A220-A4-303YB and A220-A4-303XB) manufactured by Piezo Systems INC. An Agilent 33120A function generator and an Agilent 54621A Oscilloscope were used to generate the waves and capture the waves, respectively. A sine wave pulse was used to trigger the vibration of wave generators.

TEST RESULTS

The results of CBR tests on the clay are shown in Fig.2. From the CBR test, it can be derived: soaked resistance = 375 kPa; standard resistance = 6900 kPa; un-soaked CBR = $614(100)/6900 = 8.9(\%)$; soaked CBR = $375(100)/6900 = 5.43(\%)$; % Reduction = $1.0-5.43/8.9 = 0.39$ or 39%. The estimated resilient modules of soils are: for soaked soil $M_{RS} = 10340 \times 5.43 = 56146.2 \text{ kPa} = 56.15 \text{ MPa}$ and for un-soaked soil: $M_{RU} = 10340 \times 8.9 = 92026 \text{ kPa} = 92.03 \text{ MPa}$.

When using piezoelectric sensors, the bender–extender elements were positioned through the slots cut in the compaction mold for CBR test with the

protrusion length of approximately 25 mm and fixed in position using silicone adhesive sealant. The sensors are fragile and non-waterproof so they were coated with a uniform layer of epoxy resin. Fig.3 shows a sensor with resin coated during the experiment. Typical result of piezoelectric sensor tests is shown in Fig.4.

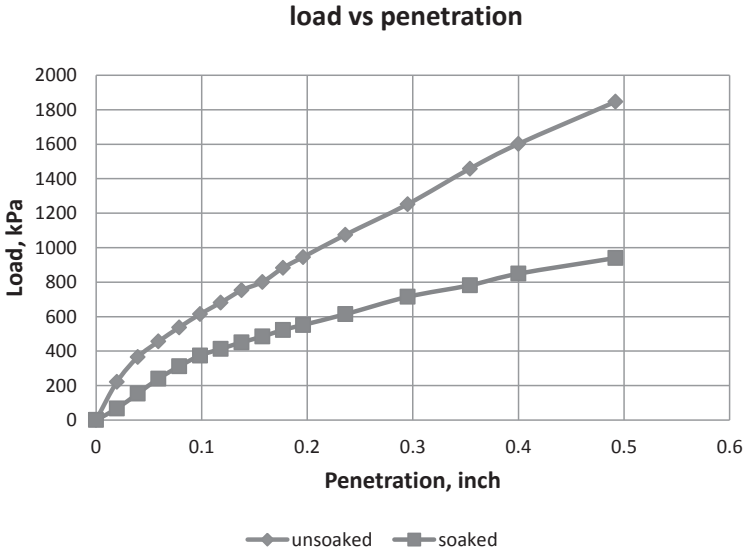


Fig.2 Result of CBR Test - Penetration vs. Piston Load

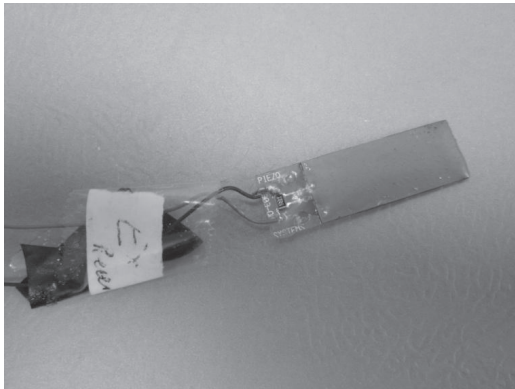


Fig.3 Bender Element with Epoxy Resin Coating

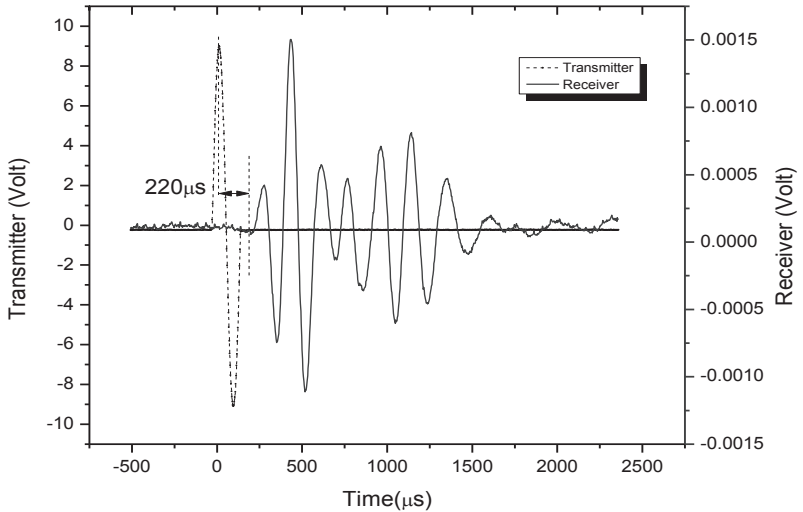


Fig.4 Typical P Wave Signals Recorded on Oscilloscope

The results of wave tests on un-soaked and soaked samples are summarized in Tables 1&2. For S waves, the velocities of both SV and SH waves are measured.

Table 1. Travel Time of SV, SH and P Waves (μs) – Soaked Samples.

| Piston Load, kPa | S vertical | S horizontal | P |
|------------------|------------|--------------|-----|
| 0 | 910 | 740 | 260 |
| 250(0.05 inch) | 870 | 660 | 250 |
| 360(0.1 inch) | 832 | 620 | 241 |
| 550(0.2 inch) | 823 | 614 | 234 |

Table 2. Travel Time of SV, SH and P Waves (μs) – Un-Soaked Samples.

| Piston Load, kPa | S vertical | S horizontal | P |
|------------------|------------|--------------|-----|
| 0 | 880 | 630 | 220 |
| 250(0.05 inch) | 856 | 587 | 210 |
| 360(0.1 inch) | 820 | 555 | 205 |
| 550(0.2 inch) | 818 | 550 | 200 |

Using the measured travel time of waves, the distance between the wave generators and wave receivers, and the mass density of the soil in the compaction mold, the shear modulus, elastic modulus, and Poisson's ratio of the soil can be calculated. Suppose

the distance between the SV wave transmitter and receiver is L_{sv} , the average shear wave velocity is then

$$V_{sv} = L_{sv}/t_{sv} = 10 \text{ cm}/910 \text{ } \mu\text{s} = 109.9 \text{ m/s} \quad (3)$$

The shear modulus in the vertical plane $G_{\max,v}$ would be:

$$G_{\max,v} = \rho_d V_{sv}^2 = 2.06 \times 10^3 \times 109.9^2 = 2.49 \times 10^7 \text{ Pa} \quad (4)$$

Similarly, the shear modulus in the horizontal plane $G_{\max,h}$ is:

$$G_{\max,h} = \rho V_{sh}^2 = 2.06 \times 10^3 \times 135.14^2 = 3.76 \times 10^7 \text{ Pa} \quad (5)$$

For P waves

$$V_p = L_p/t_p = 10 \text{ cm}/260 \text{ } \mu\text{s} = 384.6 \text{ m/s} \quad (6)$$

The constrained modulus of the soil in the horizontal plane would be

$$M = \rho V_p^2 = 2.06 \times 10^3 \times 384.6^2 = 3.05 \times 10^8 \text{ Pa} \quad (7)$$

The Poisson's ratio μ in the vertical plane would be

$$\mu_{v} = [(M/G_{\max,v}-2)/(2 M/G_{\max,v}-2)] = 0.45 \quad (8)$$

The Poisson's ratio μ in the horizontal plane would be

$$\mu_{h} = [(M/G_{\max,h}-2)/(2 M/G_{\max,h}-2)] = 0.43 \quad (9)$$

For a soil near saturation, Poisson's ratio near 0.5 is reasonable. The resilient modulus in the horizontal and vertical planes can be determined as:

$$E_{h} = 2 G_{\max,h} (1 + \mu_{h}) = 2 \times 3.76 \times 10^7 \times (1 + 0.43) = 107.5 \text{ MPa} \quad (10)$$

$$E_{v} = 2 G_{\max,v} (1 + \mu_{v}) = 2 \times 2.49 \times 10^7 \times (1 + 0.45) = 72.2 \text{ MPa} \quad (11)$$

The results are summarized in Table 3.

Table 3. Resilient Modulus (MPa) for Soaked and Un-Soaked Soil Samples.

| Load(kPa) | $E_{h}(\text{soak})$ | $E_{sv}(\text{soak})$ | $E_{h}(\text{unsoak})$ | $E_{sv}(\text{unsoak})$ |
|-----------|----------------------|-----------------------|------------------------|-------------------------|
| 0 | 107.5 | 72.2 | 151.3 | 79.7 |
| 250 | 135.3 | 78.9 | 174.2 | 84.1 |
| 360 | 153.3 | 86.13 | 195 | 91.5 |
| 550 | 156.3 | 88.16 | 198.5 | 92.3 |

The results from the wave tests are shown in Fig.5. Also shown in the figure are the results of resilient modulus measured by CBR tests.

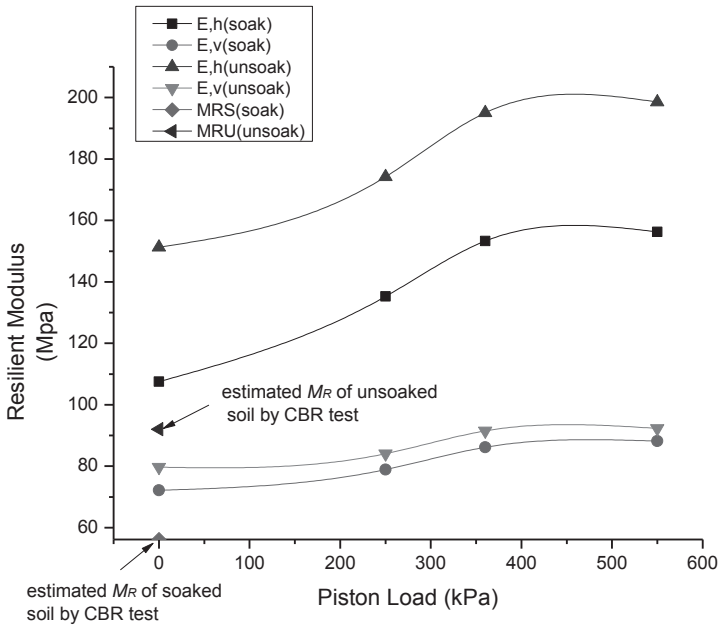


Fig.5 Relationship between measured resilient modulus and vertical pressure

As shown in Fig.5, all the elastic moduli measured increase with vertical pressure, consistent with general principles in soil mechanics. The elastic modulus in the horizontal plane is consistently higher than that in the vertical plane. This situation could happen in heavily compacted clay, indicating the horizontal stress is higher than the vertical stress, or earth pressure coefficient K_0 larger than 1.

For the un-soaked clay samples, the measured elastic modulus in the horizontal plane is higher than that measured by CBR method while the measured elastic modulus in the vertical plane is a little bit lower. The fact that we are getting CBR test result in between the two results using bender elements in different directions can be explained as this: Generally speaking, the resilient modulus estimated by bearing ratio in CBR test can be seen as the combined effects of two directions: the moduli on vertical and horizontal planes. Hence, it is completely reasonable to obtain the combination in the middle of the moduli in two directions.

On the other hand, the test on soaked clay samples shows that the measured elastic moduli on both the horizontal and vertical planes are higher than that were determined by CBR method. This can be explained by the different water contents and consolidation effect, which could have significant influences on the test results. These clay samples were immersed under water for 96 hours and were considered saturated. In the CBR test, after the sample was taken out of water tank, it was immediately put on the CBR compaction machine and being tested. Whereas in bender element tests,

after the bender elements had been pushed into the mold with silicone adhesive sealant, at least 24 hours would be needed for completely air dry. Even though several layers of waterproof wrap were already applied on the sample to avoid water evaporation, it could still cause loss in water content. Besides, when stress was applied to the soil in a relatively long time, consolidation would occur. Excess pore water pressure dissipated and the soil strength increased. This may explain why the CBR test result turns out lower than the elastic modulus on both vertical and horizontal planes measured by piezoelectric sensors.

CONCLUSIONS

While in pavement engineering practice CBR test is still widely used, there are a number of limitations for CBR method. Firstly, the reliability and repeatability of the experimental results are not satisfying. Secondly, each specimen has to be disposed after the test because the samples are getting disturbed or damaged after a loading application. Whenever there is a new testing condition such as a different confining pressure or different water content, a new specimen needs to be prepared. In addition, Poisson's ratio, which is also an important parameter in the design calculation, cannot be measured from the CBR test. At present, Poisson's ratio is estimated rather than measured directly in most soil tests. Last but not the least, from a mechanics perspective, the loading conditions in a CBR test is different compared with those in the field. The pavement thickness is larger than 50 mm, so when the loads from tires transmit to the sub-layer, they are exerted on a wider range of area on the soil due to the stress dispersion, which brings out the fact that it is unreasonable to simulate the load effect by a relatively small area of piston load on the sample during the CBR test. Because of these reasons, CBR tests have certain drawbacks and are not very reliable and accurate.

The tests proposed are based on the techniques of piezoelectric sensors. The technique of using piezoelectric sensors in soil property determination has been used successfully in the past. In comparison to CBR test, this method is much more accurate and reliable. It is non-destructive and non-intrusive. It measures resilient modulus as well as Poisson's ratio directly without using any empirical relationships.

With the introduction of the new method for testing resilient modulus and Poisson's ratio and the possibility of widely use in the future, certain technical improvement must be made to acquire accurate data more efficiently. Since the wave transmissions depend mostly on the vibration of the sensors that are pushed into the soil, the sensors are in intimate contact with the clay. Since the cohesion of the compacted clay and the soil pressure on the sensors are relatively large, it inevitably makes it harder for the sensors to vibrate compared with sand during the signal transmission. Therefore, it is common to observe weaker and fuzzier signals than those in sand tests.

REFERENCES

- Bowles, J.E. (1992). “*Engineering Properties of Soils and Their Measurement.*” Fourth Edition, McGraw-Hill, Inc. New Jersey.
- Dyvik, R. and C.Madshus (1985). “Lab Measurements of G_{max} Using Bender Elements.” *Advances in the Art of Testing Soils under Cyclic Conditions*. ASCE Conference, Detroit, MI, Geotechnical Engineering Division, New York, pp.186-196.
- Hryciw, R. D., and T.G. Thomann (1993). “Stress-History-Based Model for Ge of Cohesionless Soils.” *ASCE Journal of Geotechnical Engineering*, Vol.119, No.7, pp.1073-1093.
- Jovicic, V., Coop, M.R., and M. Simic (1996). “Objective Criteria for Determining G_{max} from Bender Element Tests.” *Geotechnique*, London, Vol.46, No.2, pp.357-362.
- Jovicic, V., and M.R. Coop (1998). “The Measurement of Stiffness of Clays with Bender Element Tests in the Triaxial Apparatus.” *Geotechnical Testing Journal*, ASTM, Vol.21, No.1, pp.3-10.
- Leong, E.C., J. Cahyadi, and H.Rahardjo (2009). “Measuring Shear and Compression Wave Velocities of Soil using Bender-Extender Elements.” NRC Research Press.
- Thomann, T. G., and R.D. Hryciw (1990). “Laboratory Measurement of Small Strain Shear Modulus under K_0 Conditions.” *Geotechnical Testing Journal*, ASTM, Vol.13, No.2, pp.97-105.
- Viggiani, G., and J.H. Atkinson, J. H. (1995). “Interpretation of Bender Element Tests.” *Geotechnique*, Vol.45, No.1, pp.149-154.
- Zeng, X. and B.Ni (1998). “Application of Bender Elements in Measuring G_{max} of Sand under K_0 Condition.” *Geotechnical Testing Journal*, ASTM, Vol.21, No.3, pp.251-263.
- Zeng, X. and B.Ni (1999). “Stress-Induced Anisotropic G_{max} of Sands and Its Measurements.” *ASCE Journal of Geotechnical and Geoenvironmental Engineering*, Vol.125, No.9, pp.741-749.
- Zeng, X., Figueroa, J.L. and L. Fu. (2003). “Measurement of Base and Subgrade Layer Stiffness Using Bender Element Technique.” ASCE Geotechnical Special Publication: Recent Advances in Materials Characterization and Modeling of Pavement Systems.

Numerical Analysis of Dynamic Response and Influence Factors on PCC Pile Composite Foundation of High Speed Railway

Qiang Fu¹, Xuanming Ding², Hanlong Liu³, Gangqiang Kong⁴

¹Doctoral student, Key Laboratory of Ministry of Education for Geomechanics and Embankment Engineering, Hohai University, Nanjing 210098, China. Email: fuqutdhhu@163.com

²Associate professor, National Engineering Research Center of Water Resources Efficient Utilization and Engineering Safety, Hohai University, Nanjing 210098, China. E-mail: dxmhhu@163.com

³Professor, Key Laboratory of Ministry of Education for Geomechanics and Embankment Engineering, Geotechnical Research Institute, Hohai University, Nanjing 210098, China. E-mail: hliuhhu@163.com

⁴Associate professor, Key Laboratory of Ministry of Education for Geomechanics and Embankment Engineering, Hohai University, Nanjing 210098, China. gqkong1@163.com

ABSTRACT: In this paper, a reasonable train dynamic loading form is determined, and a finite element model of PCC pile composite foundation for high speed railway is established using ABAQUS software. The dynamic response is simulated on subgrade and pile-soil composite foundation under different train speeds. The dynamic stress and acceleration changes of composite foundation are analyzed by changing the modulus of the roadbed surface layer and cushion. The results show that the changes of train speed, stiffness of roadbed and cushion layer react differently according to the laws of distribution and dispersion for dynamic stress, acceleration response of subgrade and pile-soil composite foundation. The dynamic stress and acceleration in roadbed surface increase with the increase of train speed. The changes in stiffness of roadbed have little effect on dynamic stress of the lower pile area, while the cushion is significantly influenced, by as much as 90%. The cushion has the effect on adjusting pile and soil dynamic stress ratio which may result in up to a 50% change in difference. A dynamic stress arch effect appears in the cushion under the dynamic interaction of the pile and cushion layer, which is similar to the static soil pressure arch effect.

INTRODUCTION

China's rapidly accelerating economy in recent years has been accompanied by a gradually advancing high speed railway system, urging the need of low deformation in the subgrade to ensure smooth operating. The study and analysis of the dynamic response characteristics of the subgrade under traffic loading is one of the major topics in soil dynamics (Xuecheng Bian, 2011; Bo Huang, 2011). Domestic scholars have studied the distribution of dynamic stress, strain, and acceleration in railway subgrade, and compared the effects of the train speed, load, and subgrade parameters through in-

situ tests of subgrade and laboratory model tests (Junliang Zong, 2007; Changjing Wang, 2008; Yongxiang Zhan, 2010). Yang Wang (Yang Wang, 2010) and Longcai Yang (Longcai Yang, Quanmei Gong, 2009) has studied the dynamic response based on CFG pile composite foundation, involving analysis of the subgrade and foundation surface. The piles and soils are not involved, hence excluding aspects such as stress wave reflection and superposition and the dynamic stress arc effect. The most common waves to simulate traffic load are sine and half sine wave (KAYNIA A M, 2000). Bo Huang (Bo Huang, 2011) has adopted the sine and half sine wave approach to simulate high speed train loads. Yang Wang (Yang Wang, 2010) has constructed the impact loading of the wheel rail based on the train's axle load and speed. Longcai Yang (Longcai Yang, 2009) has calculated the load spectra of wheel rail according to the ZK loading pattern. Quanmei Gong (Quanmei Gong, 2009) has obtained the dynamic stress of the subgrade bed based on the actual measurement of the Shanghai-Nanjing Railway using a conventional formula. Further dynamic tri-axial testing has led to pleasing results.

The new type of Cast-in-place Concrete large-diameter pile (termed as PCC pile) (H. L. Liu, Charles W. W. Ng, and K. Fei, 2007), a new technology for soft soil foundation treatment, has been applied in the Nanjing section of the Beijing-Shanghai high speed railway. Some of the main advantages it bears include: characterizing rapid prototyping, improvement in bearing capacity and it being economically resourceful. The dynamic response of pile soil composite foundation under the vibration load is studied, taking into consideration three various speeds of 252km/h, 300 km/h and 350 km/h. Different modulus changes of subgrade and cushion are also included and incorporate the rules that apply to dynamic stress transmitting. It also serves the purpose of providing theoretical basis and reference data for the design of dynamic stress of PCC pile composite foundation in soft soil areas.

MODEL DESIGN

The Beijing-Shanghai high speed railway consists of a standard single track as shown in FIG.1. The pile has an outside diameter of 1.0m, an inside diameter of 0.76m; the distance between piles is 2.0m and the subgrade has a width of 3.6m at the top and 11.7m at the bottom. A plane simplified axisymmetric model of the subgrade is established, with a width of 60m and depth of 33.5m.

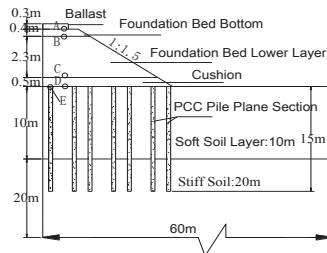


FIG.1. Structure of PCC Pile Composite Foundation: Not to Scale

As is shown in Figure 1, in order to study the propagation and attenuation of the

subgrade, taking five typical points A,B,C,D,E as monitoring points which are corresponding to five different material types. The parameters are shown in Table 1. The calculation schedule is shown in Table 2. The dynamic response of the whole model can be calculated using dynamic finite element method.

Table1. Material parameters

| Material Type | Thickness & length(m) | Dynamic Elastic Modulus(MPa) | Poisson's Ratio | Density (kg/m ³) | Damping Ratio |
|-----------------------|-----------------------|------------------------------|-----------------|------------------------------|---------------|
| Concrete Slab | 0.3 | 45000 | 0.17 | 2500 | - |
| Foundation bed top | 0.4 | 240 | 0.35 | 2000 | 0.1 |
| Foundation bed Bottom | 2.3 | 320 | 0.35 | 2000 | 0.1 |
| Cushion | 0.5 | 240 | 0.4 | 2000 | 0.1 |
| Pile | 15 | 20000 | 0.3 | 2300 | 0.05 |
| Soft Soil | 10 | 20 | 0.4 | 1350 | 0.2 |
| Stiffer Soil | 20 | 30 | 0.3 | 1700 | 0.15 |

Table 2. Calculation Scheme

| Item | Ballast modulus(MPa) | | | | Cushion Modulus(MPa)* | | | | |
|---------------------|----------------------|----------------|----------------|----------------|-----------------------|------------------|------------------|------------------|------------------|
| | E ₁ | E ₂ | E ₃ | E ₄ | E ₁ * | E ₂ * | E ₃ * | E ₄ * | E ₅ * |
| Train Speed(km/h) | | | | | | | | | |
| V ₁ =252 | 240 | 320 | 400 | 480 | 240 | 320 | 400 | 480 | 1000 |
| V ₂ =300 | 240 | 320 | 400 | 480 | 240 | 320 | 400 | 480 | 1000 |
| V ₃ =350 | 240 | 320 | 400 | 480 | 240 | 320 | 400 | 480 | 1000 |

The wheel distance, train speed and running time is determined based on the complexity of the train and wheel load system. Suppose that the dynamic wave on one point is a composite half-sine loading wave when each carriage passes it, a modified loading wave is then established. This is according to the vibration waves in previous research (Quanmei Gong, 2009) whereby the maximum amplitude is 80kPa. Three train speeds are designed as V₁=252 km/h, V₂=300 km/h, V₃=350km/h. The load wave is determined based on the train structures and train speeds, resulting in T₁=0.3657s for one train carriage with a length of 25.6m for V₁=252 km/h. Five train carriages are analyzed in the calculation, and the resultant loading wave is illustrated in FIG.2.

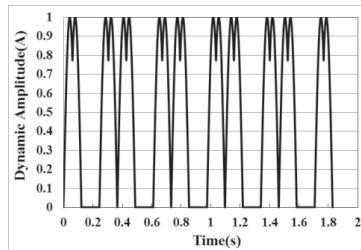


FIG.2. Composite Half-Sine Loading Wave ($V_I=252\text{km/h}$)

TIME-HISTORY CURVES OF DYNAMIC RESPONSE

FIG.3 displays typical dynamic response time history curves in the case of V_I-E_I . It must also be noted that the dynamic response curve of the subgrade surface is similar to the loading curve, as shown in FIG.3 (a). The dynamic stress response under vibration load is expressed by the dynamic waves; the maximum point value is the dynamic response when the train loads pass it. This is determined by the loading frequency and vibration load, and it decreases along the subgrade depth, namely along the key points *A, B, C, D, E*. The maximum stress at *A* and *B* is approximately 40kPa and 30kPa, while points *C* and *D* experience a maximum stress of 5kPa. As is shown in FIG.3 (b), the dynamic acceleration value is not significantly large as a whole, and decreases along the depth of the subgrade.

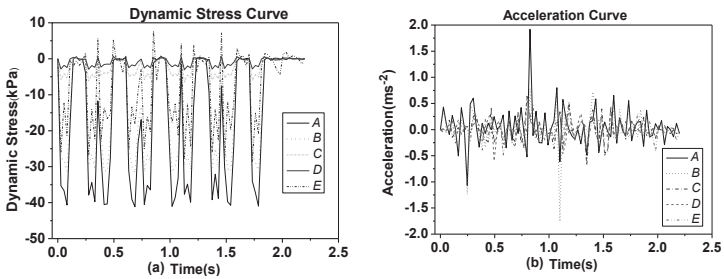


FIG.3. Time-history curves of dynamic response ($V_I=252\text{km/h}$)

FIG.4 (a) illustrates the relationship between the dynamic stress of the subgrade and the train speed; an increase in one, leads to an increase in the other. However, compared to fig 3, the increase in the subgrade is not as prominent. Stress fluctuates with the time, and dynamic stress rebounds in the cushion area with a maximum value of 30kPa. The stress of *E* is increased by a factor of 2, for the reason of the dynamic interaction between the piles and cushion at the speed of 350km/h. As is shown in FIG.4 (b), an increase in the train speed obviously leads to an increase in acceleration, of which the density and amplitude are higher than the case of V_I , and has a maximum value of 5m/s^2 at point *A*. The maximum acceleration of the subgrade decreases along the subgrade depth, reaches a value around 1m/s^2 at point *D*. Thus, we can assume that

the dynamic energy of the subgrade increases with the increase in train speed; this energy is reflected through dynamic stress, dynamic acceleration, and the subgrade itself can effectively reduce the vibration influence of the train load.

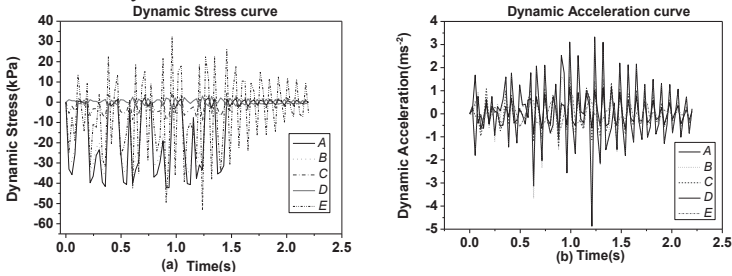


FIG.4. Time-history curves of dynamic response ($V_3=350\text{km/h}$)

DYNAMIC RESPONSE AND INFLUENCE FACTORS ANALYSIS

As is shown in FIG.5, the dynamic stress is not influenced as significantly by the increase of train speed. Instead, it decreases linearly along the subgrade until reaching the subgrade lower area, whereby the maximum stress is approximately 42kPa, and the rate of decay decreases by half. Thus, the changes in modulus of the subgrade bed between 240MP-480MPa have little impact on the dynamic stress; the thickness of the subgrade is small enough to have an insignificant impact.

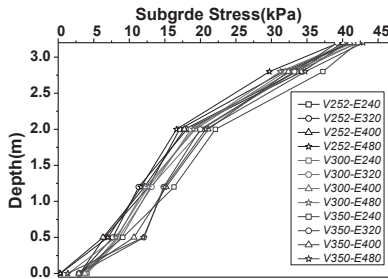


FIG.5. Comparison Curves of Dynamic Stress varying with Depth from the top of the embankment

FIG.6 demonstrates two relationships: an increasing train speed coupled by an increasing acceleration, and an increasing acceleration resulting in a decrease of the modulus of the subgrade bed. Superposition effect of acceleration occurs under the condition of reciprocating movement of dynamic stress waves between piles, cushion and the subgrade bed. The maximum acceleration on subgrade surface for V_2 , V_3 is 3.4m/s^2 , 4.87m/s^2 respectively. The acceleration rapidly decreases along the subgrade bed, by up to 60% at a depth of 2m, and then gradually slowing down until a depth of 1.2m is reached. The results discussed in this paper regarding the weakening tendency of dynamic stress and acceleration is consistent with the measured results in previous

literature articles (Binglong Wang, 2000).

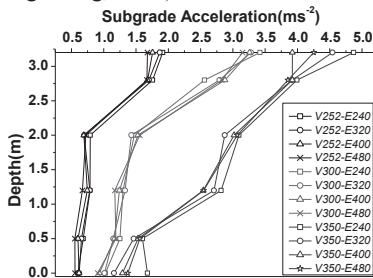


FIG.6. Comparison Curves of Acceleration of subgrade varying with Depth

Dynamic Response of Pile

Dynamic stress with varying pile length and soil dynamic stresses with varying depth are calculated using dynamic loading based on the changes in modulus of subgrade bed and cushion. As shown in FIG.7, the dynamic stress at the pile top increases significantly with the increase of train speed. A maximum value of approximately 52, 69, 99kPa is reached, corresponding to V_1 , V_2 , V_3 . The decay curves of the former two speeds are similar to each other, while the third one is larger than the former two. The dynamic stress of piles decreases rapidly in the initial 1.5m, gradually decreases in the following 3m, and continues to accelerate again, until reaching a minimum value of 5kPa at the pile bottom. On another note, the improvement of modulus of subgrade bed has little impact on the stress of piles.

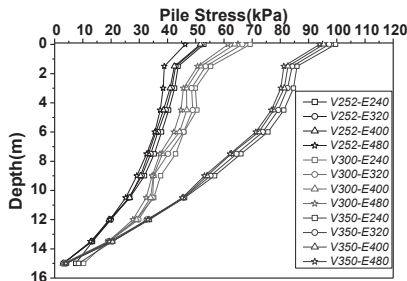


FIG.7. Curves of pile stress based on the changes in modulus of subgrade

FIG.8 illustrates various curves of dynamic stress of piles based on the changes in modulus of cushion. From the graph, it is evident that the pile stress is affected by the cushion, a result of the interaction effect between pile and cushion. The V_1 case of soft cushion has low effect, while the concrete plate can decrease the dynamic stress up to 15%. The dynamic stress of the pile top decreases in the cases of V_2 and V_3 which involve concrete plate, thus it can be concluded that concrete plates can bear larger dynamic load than soft cushion layer and reduce the pile stress effectively.

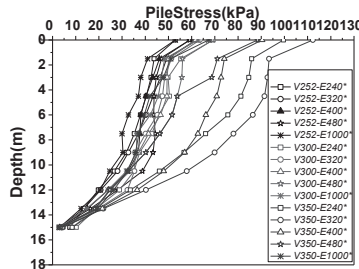


FIG.8. Curves of Pile Stress based on the changes in modulus of cushion

DYNAMIC STRESS ARCH EFFECT

FIG.9 displays the dynamic stresses in cushions at various times, under the condition of $V_3=350\text{km/h}$ and $E_1=240\text{MPa}$. The dynamic stress on the pile top is larger than soils due to the difference in dynamic interaction. The dynamic interaction between pile and cushion is larger than that between soil and cushion; hence the maximum value on the pile top is 40kPa, with only 3kPa in the soil areas adjacent the pile. The pile and cushion play important roles in the equitable distribution of dynamic stress, which assist in improving the dynamic and static stability of subgrade in soft soil areas.

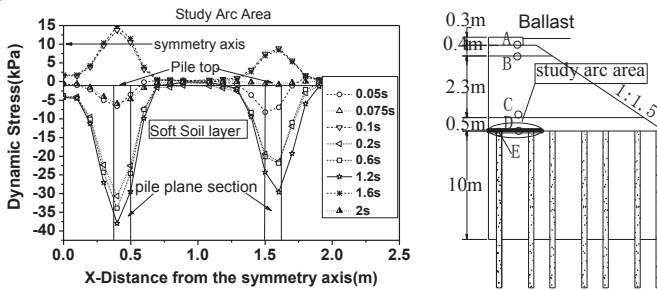


FIG.9. Curves of Dynamic Stress Arch effect in Cushion

CONCLUSIONS

Results are obtained based upon dynamic response analysis. The increase of train speed enhances the dynamic stress and acceleration on the subgrade bed. The modulus of the subgrade bed increases accordingly to the increase of stress, although the stress increases in small increments. Consequently, the decreasing amplitude of acceleration is lower than the increasing amplitude of the subgrade bed. Improvements in thickness can decrease the dynamic stress in the case of increasing the modulus of the subgrade bed. In the case of improving the modulus of the subgrade bed, there is a declining tendency for the acceleration to increase with the increase of the train speed and subgrade depth. The increase in modulus of the subgrade bed surface has little impact on the stress of the pile's lower area, whereas the cushion can experience up to 90%

more impact. The pile-soil composite foundation serves the purpose of effectively decreasing static and dynamic stress. The dynamic stress wave arc, which is induced during the interaction between pile and cushion, is similar to the static soil pressure arc effect, and can weaken the dynamic effect on soft soil.

ACKNOWLEDGMENTS

The authors appreciate the support of the National Natural Science Fund & High speed fund key Project No.U1134207 and Program for Changjiang Scholars and Innovative Research Team in University NO. IRT1125

REFERENCES

- Xuecheng Bian, Hongguang Jiang, Wenming Shen, et al(2011)."Study of accumulative deformation of high-speed railways based on physical model." *CHINA CIVIL ENGINEERING JOURNAL*, Vol.44 (6): 112-119.
- Bo Huang, Hao Ding, Yunmin Chen (2011). "Simulation of high-speed train load by dynamic triaxial tests." *Chinese Journal of Geotechnical Engineering*, Vol.33 (2): 195-202.
- Junliang Zong, Tao Liu, Quanmei Gong, et al(2007)."Dynamic Response Study on speed Increase Subgrade of Existing Railway." *CHINA RAIL WAY SCIENCE*, Vol.28 (4): 7-11.
- Changjing Wang, Yunmin Chen.(2008)."Influence of ground shear modulus on train-induced dynamic stresses." *Rock and soil Mechanics*, Vol.28: 611-614.
- Yongxiang Zhan, Guanlu Jiang. (2010) "Study of dynamic characteristics of soil subgrade bed for ballastless track." *Rock and Soil Mechanics*, Vol.31 (2):392-396.
- Yang Wang, Meng Zhou, Quanmei Gong, et al(2010)."An Analysis on Design Parameters of CFG Pile-net Composite Structure of High-speed Railway" *Journal of East China Jiaotong University*, Vol. 27(6):17-22.
- Longcai Yang, Quanmei Gong, Shengying Peng, et al(2009)"Dynamic FEM Analysis on CFG Pile Composite Foundation of Low Embankment." *Railway Engineering*, Vol.7: 27-30.
- KAYNIA A M, MADSHUS C, ZACKRISSON P. (2000) "Ground vibration from high-speed trains: prediction and countermeasure." *Journal of Geo technical and Geoenvironmental Engineering, ASCE*, Vol.126 (6): 531-537.
- Quanmei Gong, Zhe Luo, Jianyi Yuan.(2009) "Experimental Study on Long-term Cumulative Settlement and Equivalent Cyclic Load of Speed-up Railway Subgrade Soil" *Journal of Railway Society*,31(2):88-93.
- H.L.Liu , Charles W. W. Ng , and K. Fei.(2007)"Performance of a Geogrid-Reinforced and Pile-Supported Highway Embankment over Soft Clay: Case Study" *Journal of Geotechnical and Geoenvironmental Engineering, ASCE*, Vol. 133 (12) pp: 1483-1493.
- Binglong Wang, Shaofeng Yu, et al. (2000) "Analysis of Subgrade Dynamic Stress under Increasing Speed." *Journal of the China Railway Society*, Vol. 22(suppl.): 79-81.

Analysis on Deformation Mechanism of PCC Pile Composite Foundation Under Train Vibration Load

Qiang Fu¹, Xuanming Ding², Hanlong Liu³, Kong Gangqiang⁴

¹Doctoral student, Key Laboratory of Ministry of Education for Geomechanics and Embankment Engineering, Hohai University, Nanjing, 210098, China. Email: fuqtdhhu@163.com

²Associate professor, National Engineering Research Center of Water Resources Efficient Utilization and Engineering Safety, Hohai University Hohai University, Nanjing 210098,China.. E-mail: dxmhhu@163.com

³Professor, Key Laboratory of Ministry of Education for Geomechanics and Embankment Engineering, Geotechnical Research Institute, Hohai University, Nanjing 210098, China. E-mail: hliuhhu@163.com

⁴Associate professor, National Engineering Research Center of Water Resources Efficient Utilization and Engineering Safety, Hohai University, Nanjing,210098, China E-mail:gqkong1@163.com

ABSTRACT: In this paper, a three-dimensional dynamic coupling finite element model of tracks of embankment pile-soil composite foundation has been established. The dynamic displacement of pile composite foundation is analyzed based on modulus parameter changes of foundation bed, pile, cushion layer and foundation. The results show that the interface area between cushion and pile increases with the decreasing of pipe pile top, the load-sharing ratio of the PCC pile increases significantly, and the load that the soil bears also decreases. The magnitude and scope of dynamic displacement for subgrade also decreases. It is worth noting that the dynamic interaction between PCC piles and cushion layer is greater than that between soils and the cushion layer. Rigid piles tend to penetrate into the cushion layer; the dynamic curve along the cushion layer surface is similar to type 'W'. An increase in modulus of the cushion enhances the dynamic interaction effects between PCC pile and the cushion, which, to some degree, encourages PCC piles to share more bearing responsibilities. This mechanism magnifies the dynamic displacement of pile top and body, whilst simultaneously reducing upward penetration deformations.

INTRODUCTION

In today's rapidly developing high-speed network, it is difficult avoiding soft soil terrain for high speed train systems. The high speed running of trains requires a smooth and stable track foundation meaning that a high quality of stability for the settlement is absolutely essential. Plastic accumulative deformation occurs with repeated dynamic loading, generated by the operation of high-speed train on the railway and foundation structure (Xuecheng Bian, 2011; Bo Huang, 2011). This produces a vast amount of post-construction settlement and can prevent smooth

operating of the train, as well as the comfort and safety. In order to reduce the settlement and improve riding comfort, a significantly costly viaduct is used to pass through soft soil area. The method of the pile-soil composite foundation increases the bearing capacity of foundation soil, and reduces post- construction settlement and costs. A new type of Cast-in-place Concrete large-diameter pile (termed PCC pile) developed independently by Hanlong Liu of GeoHohai (2011) has been patented in China, and has been applied in the Nanjing section of Beijing-Shanghai high speed railway. It effectively controls lateral displacement as well as the total settlement of the foundation. Another advantage is the increased bearing capacity and stability of the soil foundation. However, the transmission of ground vibrations from a moving train to the surroundings is a complex problem which is dependent on a great number of factors. The theories and methods surrounding high speed subgrade settlement control for soft soils are very premature. The high speed railway subgrade system includes rails, sleepers, ballast, foundation bed, cushion, pile and soil bearing the train load. A three-dimensional dynamic coupling finite element model of the tracks embankment pile-soil composite foundation has been established using finite element program ABAQUS. The dynamic displacement of pile composite foundation are also analyzed based on modulus parameter changes of foundation bed, pile, cushion layer and foundation, thereby providing data references and a theoretical basis for the design of PCC pile composite foundation of high speed railway in soft soil areas.

LOADING MODEL

Loading of trains is a complex issue, which is dependent upon many factors such as the axle weight, suspension system, traveling speed, track structure and geometric irregularity of lines (Lars Hall, 2003). In-situ dynamic response testing has been established on British railway subgrade by Dawn and Stanworth (1976), and it can be concluded that the train load on the subgrade mimics the shape of the pulse stress wave. A new train load combined with the wheel-sets form is created by Li Junshi (1995) based on the wave superimposition theory, which is expressed by Fourier series and is suitable for wave transmission. This paper incorporates vibrational function, as presented by Changshi Pan (1984) to simulate train load, which involves static load and dynamic load generated by superposition of a series of sine functions. This is demonstrated in Formula 1:

$$F(t) = P_0 + P_1 \sin \omega_1 t + P_2 \sin \omega_2 t + P_3 \sin \omega_3 t \quad (1)$$

Where $F(t)$ is train dynamic load, P_0 is wheel static load, P_1, P_2, P_3 are dynamic load correspond to certain frequency, the corresponding load amplitude is:

$$P_i = M_0 a_i \omega^2 \quad (2)$$

Where M_0 is the unsprung mass, a_i is typical vector height, ω is the circular frequency under corresponding train speeds and irregularity vibration wave length, which is calculated as

$$\omega_i = 2\pi \frac{v}{L_i} \quad (3)$$

Where v is the train speed, L_i is the corresponding typical wave length. As the harmony train's axle load is 17 tonne, the side load is 85KN, and M_0 is 2 tonne. When

taking into consideration the additional dynamic load generated by high speed train load for velocity and assuming it to be 324km/h, the irregular vibration wave that corresponds to low and medium frequency can be calculated. The vibration load curve within a time step of 0.05s is shown in FIG.1.

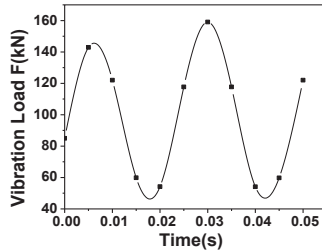


FIG.1. Relationship between train vibration load and time

CALCULATION MODEL

For dynamic calculations, five sleepers and rail connecting bodies are taken into consideration whereby the vertical dynamic load is applied but the horizontal is not. A three dimensional model of high speed railway pile-soil composite foundation is established based on the design criteria of a typical subgrade section of the Beijing-Shanghai high speed railway. The model has a width along the transverse direction of 25m and the foundation has a depth of 40m. The pile has a length of 15m with an inside and outside dimension of 0.76m and 1m respectfully, while the pile spacing is 2.5m. The top 0.5m is filled with concrete to enhance the contact effect of the pile and subgrade. The bottom boundary of the model is fully fixed, as are the surrounding boundaries (left, right, front and back) which are fixed along the horizontal direction. The model is meshed into 422,058 elements, and the final three-dimensional dynamic coupling finite element model is shown in FIG.2.

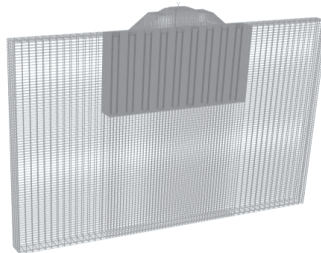


FIG.2. Three-dimensional finite element model of soil pile composite foundation

The rail, ballast, foundation bed, sleeper and piles are regarded as line elastomers, while the foundation is considered a viscoelastic body. The calculation parameters of model design conditions are shown in Table 1.

MECHANISM ANALYSIS ON DYNAMIC DISPLACEMENT OF SUBGRADE

The deformed meshes of the displacement, magnified with a factor of 500 for soil

pile composite foundation are shown in FIG.3. The dynamic load at the rail transfers downward to the subgrade, resulting in a gradual decrease in the transient dynamic displacement from the center outwards. This then fluctuates along the subgrade to the center of the pile area. The cushion passes the majority of the dynamic load to piles of higher stiffness. As piles have a larger rigidity than cushion, the piles have a tendency to penetrate upwards into the cushion; this behavior is based on the dynamic coordination interaction between piles and cushion.

Table1. Calculation Parameters

| Parameter Material | Thickness & Length(m) | Elastic Modulus E(MPa) | Poisson's Ratio μ | density $\rho(\text{kg} \cdot \text{m}^{-3})$ |
|---------------------------------|-----------------------|-------------------------|-----------------------|---|
| Rail Beam | 3 | 210000000 | 0.2 | 7800 |
| Sleeper | 0.22 | 30000 | 0.2 | 2500 |
| Ballast | 0.628 | 200 | 0.2 | 2200 |
| Surface Layer of Foundation Bed | 0.7 | 50 100 150 200 | 0.3 | 2000 |
| Bottom layer of foundation Bed | 1.8 | 30 | 0.3 | 1800 |
| Cushion | 0.5 | 50 100 200 | 0.25 | 1800 |
| Soft Soil Layer | 15 | 5 10 | 0.35 | 1200 |
| Supporting Layer | 25 | 20 | 0.3 | 1500 |
| PCC Pile | 15 | 5 10 15 20 | 0.2 | 2200 |



FIG.3. Deformed nephogram of displacement magnified with a factor of 500 from finite analyses of dynamic response of soil pile composite foundation

As shown in FIG.4, the dynamic displacement of subgrade increases gradually over time, resulting in the weakening of the wave form along the top to the bottom of

the subgrade. The dynamic displacement waves in sleepers are similar to vibration waves of trains, of which the maximum value is 0.0028m. The dynamic displacement of piles and cushion is influenced by vibration time and size, of which the minimum value is approximately 0.012m. FIG.5 demonstrates the compatibility effect between the piles and the surrounding soil; it is evident that the dynamic displacement of cushion on the top of the center pile is smaller than that of the pile soil. As discussed previously, the dynamic curve along the cushion layer surface is similar to type 'W'; that is the dynamic displacement decreases from the center pile outwards, gradually approaching 0 at the foot of the embankment.

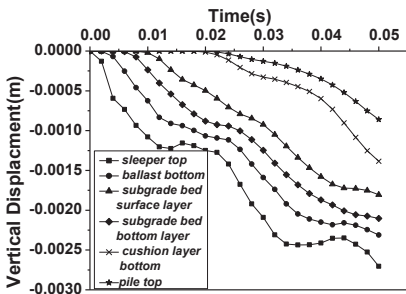


FIG.4. Time history curve of dynamic displacement of subgrade

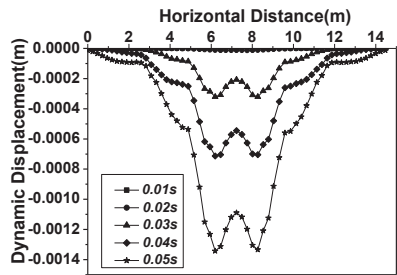


FIG.5. Comparison of cushion dynamic displacement at different time

INFLUENCING FACTORS ANALYSIS

Effect of Foundation Bed Modulus

As is shown in FIG.6, the maximum dynamic displacement of the ballast is 0.0025m, which is larger than that of the cushion with a value of 0.0012m. As the dynamic displacement of ballast and cushion decrease with the increase of ballast modulus, the dynamic displacement variation is relatively small, ranging between 50 and 100MPa, and decreasing considerably at the point of 150MPa. This is due to the fact that the dynamic displacement of ballast and cushion generated by vibration load decreases gradually. FIG.7 demonstrates the modulus difference between piles and soils, whereby the piles bear the majority of the load. Firstly, dynamic displacement occurs, which is very much similar to the development rule of the cushion. The affects by the foundation bed modulus are quite insignificant, thus reflect upon the mechanism of deformation coordination between piles and soil.

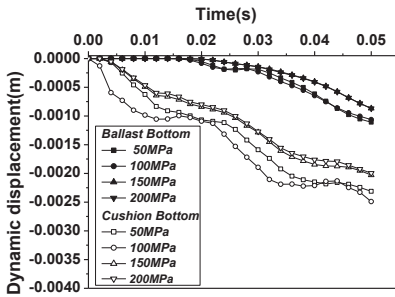


FIG.6. Influence of modulus of bed on ballast and cushion dynamic displacement

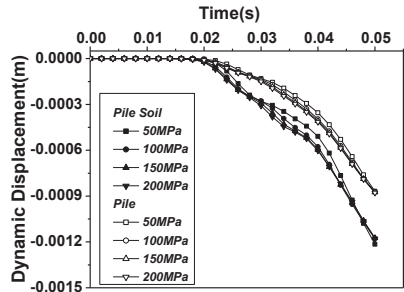


FIG.7. Influence of modulus of bed on pile and soil dynamic displacement

Effect of Pile Modulus

As is shown in FIG.8 and FIG.9, the displacement changes between 10 and 20GPa of pile modulus are less notable. For one, the dynamic displacement of piles increases with the increase of the pile modulus. A decrease in the cushion does not majorly affect the top ballast; piles with higher stiffness bear greater loads and are therefore subject to greater effects to the deformation of adjacent contacting bodies.

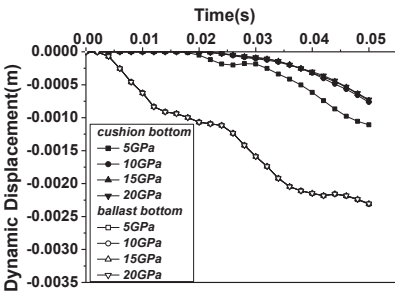


FIG.8. Influence of modulus of pile on ballast and cushion dynamic displacement

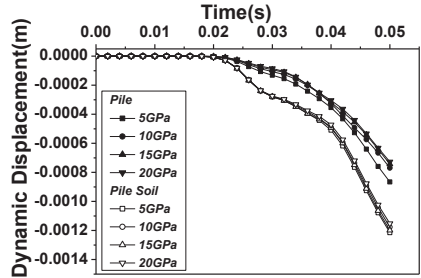


FIG.9. Influence of modulus of pile on pile and Soil dynamic displacement

Effect of Foundation Soil Modulus

FIG.10 illustrates the relationship between a decrease in the dynamic displacement of cushion and the increase of soil modulus, by which the ballast is less affected. Based on the condition of displacement coordination of soil and cushion, the modulus increase of soil can effectively reduce dynamic deformation of the cushion. As shown in FIG.11, the soil bearing capacity is dramatically improved with the

increase of the soil modulus and a decrease in the dynamic displacement of soil. However, this does not apply to the pile, hence it is less affected.

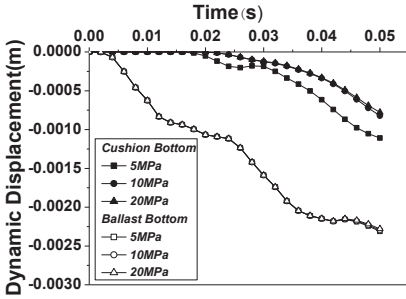


FIG.10. Influence of modulus of soil on ballast and cushion displacement

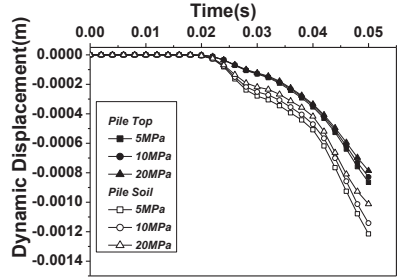


FIG.11. Influence of modulus of soil on pile and soil dynamic displacement

Effect of Cushion Modulus

FIG.12 shows the improvement in the resistance ability of the cushion against dynamic deformation, which has been aided by the improvement of the modulus of cushion. This has hence led to an improvement in the displacement coordination ability between the pile and cushion. Another fact worth noting is the simultaneous increase of the pile top, which illustrates the strong dynamic coordination between the pile and cushion.

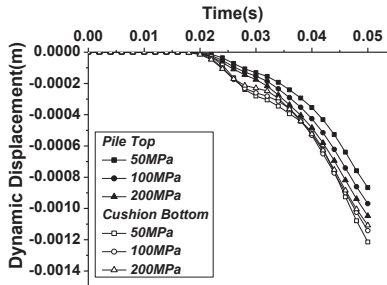


FIG.12. Influence of modulus of cushion on pile displacement

CONCLUSIONS

There exists an indirectly proportional relationship between the subgrade and modulus of the pile and soil; as the dynamic displacement of subgrade decreases, the modulus of pile and soil increases. The dynamic displacement waves in sleepers are similar to the vibration waves of trains, of which the maximum value is 0.0028m. The dynamic displacement of piles and cushion is influenced by vibration time and size, of which the minimum value is approximately 0.012m. The dynamic curve along the cushion layer surface is similar to type 'W', whereby the dynamic displacement

decreases from the center pile outward, gradually approaching 0 at the foot of the embankment. As the rigidity of the pile larger than that of the cushion, it has the tendency for upward penetration into the cushion, which can be explained by the theory behind dynamic deformation coordination between piles and cushion. An increase in modulus of the cushion enhances dynamic interaction effects between PCC pile and the cushion, which to some degree, encourages PCC piles to share more bearing responsibilities. This results in an increase in the dynamic displacement between the pile top and the pile body.

ACKNOWLEDGMENTS

The authors appreciate the support of National Science Joint High Speed Railway Foundation of China No.U1134207 and Program for Changjiang Scholars and Innovative Research Team in University No. U1134207.

REFERENCES

- Xuecheng Bian, Hongguang Jiang, Wenming Shen, et al. (2011) "Study of accumulative deformation of high-speed railways based on physical model testing." *China Civil Engineering Journal*, vol. 44(6): 112-119.
- Bo Huang, Hao Ding, et al. (2011) "Simulation of high-speed train load by dynamic triaxial tests." *Chinese Journal of Geotechnical Engineering*, vol. 33(2): 195-202.
- Xuanming Ding, Hanlong Liu, Yumin Chen. (2011) "Compilation and Explanation of Technical Specification for Composite Foundation of Cast-in-place Concrete Large-diameter Pipe pile." *JGJ/T213-2010 Construction Technology*, vol. 40 (2): 91-94.
- Lars Hall. (2003) "Simulations and analyses of train-induced ground vibrations in finite element models" *Soil Dynamics and Earthquake Engineering*, vol. 23 (5): 403-413.
- Gutowski, Dym. (1976) "Propagation of ground vibration: a review" *Journal of Sound and Vibration*, vol. 49 (2): 179-193
- Junshi Li, Kechuan Li. (1995) "Finite element analysis for dynamic response of roadbed of high speed railway." *Journal of the China Railway Society*, vol. 17 (1): 65-75.
- Changshi Pan, G.N. Pande. (1984) "Preliminary Deterministic finite element study on a tunnel driven in loess subjected to train loading." *China Civil Engineering Journal*, vol. 17 (4): 19-28.

Study on Formation Mechanism of Liujiawan Landslide Triggered by Wenchuan Earthquake

Yonghong Luo¹, Yunsheng Wang¹, Ronghua Fu¹, Jie Liu²

¹State Key Laboratory of Geohazard Prevention and Geoenvironment Protection, Chendu University of Technology, Chengdu, Sichuan, 610059; lyh445890689@qq.com.

²Sichuan Province Coal Field Geological Engineering Survey and Design Institute; 034466692@qq.com.

ABSTRACT: Since May 12th 2008, it has been already determined that tens of thousands of landslides were triggered by Wenchuan earthquake. However, the fully understanding on mechanism of seismic landslides is still unclear due to the complex geological condition and dynamic action of seismic wave. This paper presents the Liu jiawan landslide accumulation characteristic and intends to analyze the formation mechanism under the Wenchuan earthquake. Based on field investigation, an unique geological condition of Liu jiawan landslide appears two stage platform accumulations with different lithology, which have an obvious landslide boundary in lithological interface and unloading weathering zone. This characteristics is hardly found in other types of landslide. In the meanwhile, a numerical model displays tension stress concentration on the lithology boundary surface. From the results, it can be concluded that the seismic waves propagate through the different physical properties of interface and structure plane, which mutated strong dynamic stress and induced slope failure. The dynamic stress mutations should be considered as the triggering factor of Liu jiawan slope failure.

INTRODUCTION

May 12th, 2008 Ms8.0 Wenchuan Earthquake strided north western of Sichuan province, China. It has caused dramatic damaged to the lives and properties in those areas. From the geological point of view, Longmen mountain areas is an abnormal fragile geological environment, and the Wenchuan earthquake has a characteristic of high intensity and long duration, the earthquake is easy to induce the mountain slope failure. Some investigations showed that types of slope instability were controlled by lithology: slope collapses occurred more landslides in granitic and dioritic areas, while large-scale landslides were well developed in the layered

epimetamorphic rock, meanwhile rockfalls and landslides were generated in the overburden and strong weathered zone in the middle-lower part of slope (e.g., Wang and Luo 2010). Geo-hazards of Wenchuan earthquake were well developed in various types of stratum, which were the most developed in the hard rock strata such as magmatic rock, carbonate rock and sand conglomerate. Geo-hazards density of soft rock strata such as sandy slate, phyllite, shale was the second place (e.g., Huang and Li 2008).

According to slope seismic response investigation, Wenchuan earthquake triggered different types of rock mass structure slope deformation and failure. Among them seismic dynamic failure with intermittent structure rock and fragmental structure rock were the strongest. Mechanism simulation experiment showed that complex rock structure slopes exist in natural joints, fault and other structure defects, in the strong seismic waves action process, no matter whether the rock (rock mass) or joint could bear tension, compression, shear. Because joints and rock mass have lower shear strength and tensile strength, those tension fracture and shear sliding controlled the whole slump process(e.g., Wang 2009). After the earthquake, a preliminary investigation of landslides were carried out in the wide area along the quake fault such as Dujiangyan, Beichuan and Qingchuan areas. In this paper, it chose a typical seismic landslide in Liujiawan study area. It is located in Donghekou Qingchuan County. From the features of the landslide accumulation observed in the field, the rock mass structure characteristics were surveyed, moreover by different model numerical analysis comparison, it can be concluded that strong dynamic stress mutations of rock mass during the main shock triggered the slope failure.

GEOLOGICAL BACKGROUND

It has been studied that under strong cutting effect, the mountain areas form a deep canyon topography. Because of the topographic relief, the elevation difference of the study area is bigger than hilly region. The highest elevation of the study area is about 1420m, and relative height of the terrain is about 750m.

Show in Fig.1, the mainly outcropping stratas of the landslide area are the first formation of Yuanji Group (Z_y^1) and Hujia Zhai Group (Zh), Sinian System. Among them, Z_y^1 lithology is composed of light grey dolomite with silicon strip and silicon dolostone. The lithology of Hujia Zhai Group is sericite quartz phyllite, rhyolitic tuff and tuffaceous phyllite. Field survey results showed that the landslide material contains silicon dolomite and sericite quartz phyllite. In regional tectonic, the study area is near the branch fracture of Yingxiu~Beichuan fracture (the central fracture), the linear image of main central fracture is explicit and active tectonic landforms are preserved intactly, all phenomena show that regional tectonic activity is strong active.

LIUJIAWAN LANDSLIDE

Liujiaowan landslide is located in Shibangou village, Qingchuan county, about 3.2km northwest of Donghekou landslide (Fig.2). This landslide originated from a protruding ridge, where the highest elevation on the source area is about 1420m , a watershed of Liujia mountain. Under the strong seismic energy of Wenchuan earthquake this slope severely responded and eventually formed seismic landslide-hazards. Several houses were buried by this landslide completely, and more than 40 people were killed. Field investigation showed that the rock mass of the slope from the source area was movement about 0.8km along the valley and was blocked by No.2 Liujiaowan landslide (Fig.2). So the movement distance of Liujiaowan landslide was less than that of Donghekou landslide. The total volume of Liujiaowan landslide accumulation is about $2.5 \times 10^6 \text{m}^3$.

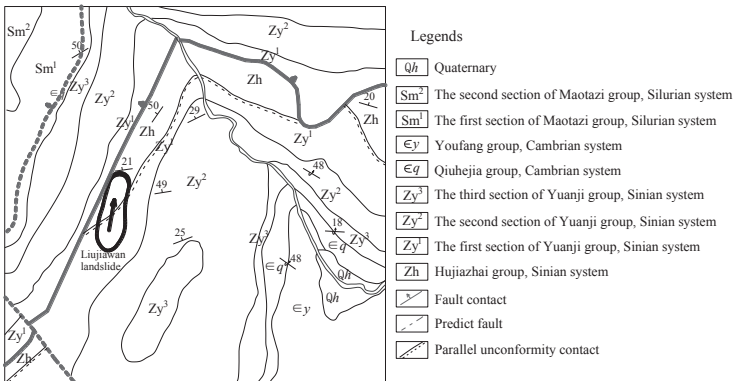


FIG. 1. Geologic map of study area

According to the investigation of Liujiaowan landslide, the landslide was composed by two stages accumulation (Fig.3). The first stage platform elevation is about 926m, of which the altitude difference is 458m from the slide source area. The accumulation is about 450m in length, 100m in width and 10m in thickness, with volume about $0.45 \times 10^6 \text{m}^3$. This accumulation is mainly composed by schistose stone which lithology is phyllite (Fig. 4a and 4b). The size of the rock mass is about 1~2m. The maximum and the minimum size of the rock mass are 3.0m and 0.1m respectively. And it could be easily break the rock mass with geological hammer, which shows that the compressive strength of this lithology is lower than 15Mpa.

The platform elevation of the second accumulation is between 1150m and 1100m, which the altitude is 170m~220m difference from the first platform. Field measurement shows that this accumulation platform is about 370 m in length, 350 m in width and 15m in thickness, which the volume is about $2.05 \times 10^6 \text{m}^3$. This accumulation is mainly composed by irregular megalith and rubble which lithology

is dolomite (Fig. 4c and 4d). The general size of the rock mass is between 2m and 5m and the maximum rock block volume is up to $10.0 \times 4.0 \times 9.0 \text{ m}^3$, which the particle volume of the accumulation is bigger than the first platform. And the rock mass surface always has rust stain or calcification phenomenon, it proofs that these area experienced unloading and weathering. Also the rock mass strength is harder than phyllite so that it could not be easy break it with the geological hammer.

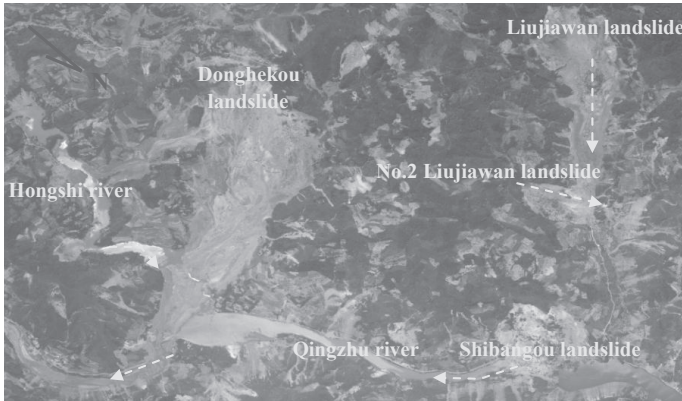


FIG. 2. The spatial relationship of Liujiawan landslide with other landslides

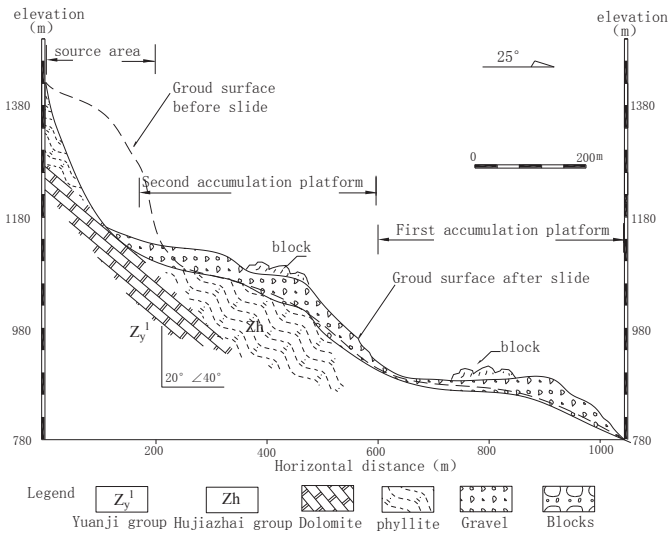
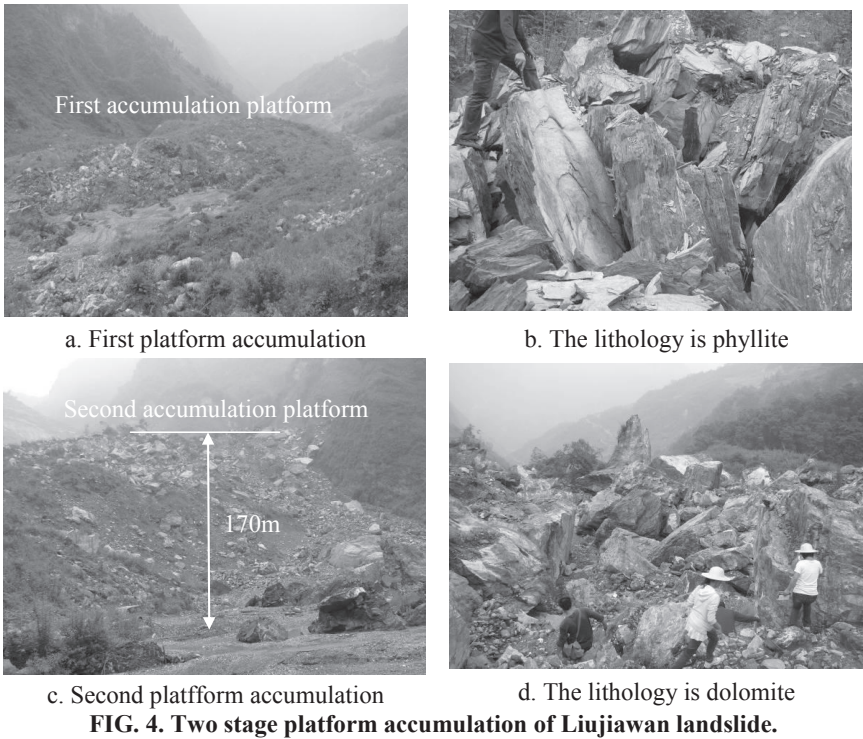


FIG. 3. The profile of Liujiawan landslide.

According to comparing the two accumulation, it is found that this landslide was composed by different lithology, and under strong earthquake it formed two stage platforms distinguished by different lithology. This phenomenon may show

that some information that during Wenchuan earthquake the lithology interface and structure plane of the slope were respectively play an important role in rock mass stability.



GENETIC MECHANISM

It has been studied widely that the Wenchuan earthquake is the direct triggering factor for a large number of landslides. The mechanism research of Donghekou landslide showed that under seismic shock, the horizontal and vertical cracks combination formed slipping surface (e.g., GIS PARK 2011), the strong seismic shaking lead to the failure of materials in source area (e.g., Wang and Kamai 2010). The favorable rock mass structure and special lithology combination lead to seismic wave obvious amplification, and finally induced Shibangou landslide (e.g., Xu 2010). Liujiawan landslide is adjacent to Donghekou and Shibangou landslides. It has been studied that due to the weathering and unloading effect or diagenesis, the slope is always composed by different physical properties lithology, and there are macroscopic geological interfaces, just as the weathering interface and lithologic interface. When the seismic stress wave propagates through those geological

interfaces, it produces reflection and refraction waves. Therefore, the seismic wave will produce significant dynamic stress mutations. When incoming wave propagates from a relative hard rock mass into a soft rock, and the reflected wave is the tensile wave at the interface, which will produce tensile stress. And the opening or being filled cracks are the part of rock mass characteristics mutations, so it will produce a reflected wave stress, and promote fracture surface cracking. Just as this reflected mechanism, it produces complex dynamic differentiation effect near various rock mass structure surface or lithology interface (e.g., Zhang and Wang 1980). According to detailed geological field investigation, it was found that Liujia wan landslide had different lithology and the rock surface had obvious weathering and unloading feature, it was inferred that strong seismic movement during the main shock, which resulted in dynamic stress mutations on the geological interface, this effect produced strong tensile stress which induced this slope failure.

NUMERICAL ANALYSIS

The numerical analysis of the geological interface dynamic differentiation effect was performed by using the ANSYS element simulation software developed by ANSYS company. The numerical analysis was based on the “time history analysis method”. The seismic wave selection of Wolong station of Wenchuan earthquake as power acceleration input calculation (Fig.5). Meanwhile interception 13.5s of time-history waveform as calculation, the peak acceleration is at 10.52s which is 963Gal, unit time step is 0.02s.

The parameters of the numerical analysis were based on comprehensive report of geo-hazards exploration results in Wenchuan earthquake disaster areas. Phyllite: the density is $2,570 \text{ kg/m}^3$, the elastic modulus is 2.295 Gpa, the poisson's ratio is 0.23, the friction angle is 17° , the cohesive strength is 4 MPa. Dolomite: the density is $2,700 \text{ kg/m}^3$, the elastic modulus is 35.61 GPa, the poisson's ratio is 0.19, the friction angle is 35° , the cohesive strength is 24MPa. The boundary conditions of calculation models follow those principles: ①Assumption of horizontal and vertical direction of bottom boundary is fixed. ②Assumption of vertical direction of lateral boundary is fixed, the horizontal is freedom. ③The top boundary is free. Ansys unit of damping matrix used Rayleigh damping. Model first order natural frequency of vibration is as the damping constant for calculation. Two numerical models were built as a comparison (Fig.6).

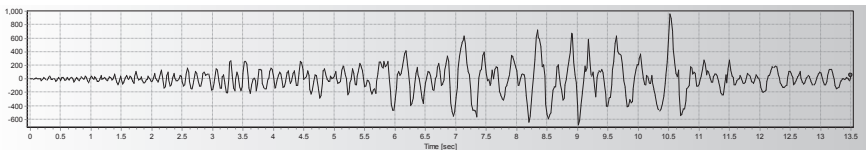


FIG. 5. Horizontal seismic acceleration time curve (EW, PGA=963Gal)

Rock slope had large plastic deformation under the Wenchuan earthquake which was not prone to convergence in the calculation process, so it is only considered the elastic analysis and the interface dynamic mutations characteristic is the major objective. Numerical dynamic analysis results of 10.52s are shown in Fig.7.

The comparison analysis shows that the stress and the strain of lithologic combination have obvious mutations along the lithologic interface. The X-component tensile stress of combination model mutated to be compressive stress when the stress wave was through the lithologic interface (Fig.7a). The Y-component stress was generated concentration on the lithologic interface (Fig.7b). The lithologic interfaces lead to strain differentiation (Fig.7c, Fig.7d), Meanwhile the stress and strain value of the combination model are bigger than that of single lithology model.

CONCLUSIONS

May 12th, 2008 Ms8.0 Wenchuan Earthquake caused tens of thousands of seismic landslides. An unique geological condition of Liujiawan landslide appears two stage platform accumulations with different lithology, which have an obvious landslide boundary in lithological interface and unloading weathering zone. Based on the field investigation and a numerical model analysis, it was found that the slope lithologic interface had obvious dynamic mutation effect, and this lithologic interface constitutes the boundary of the first stage landslide. The second stage landslide failed along the rock mass structure and unloading zone. Comprehensive research shows that the geological interface of Liujiawan slope is an important control factor, when the seismic waves propagates through the different physical properties of interfaces and structure planes, it could form a large number of secondary seismic waves by the strong reflection and refraction effects. These generated strongly dynamic tensile stress and triggered the slope failure.

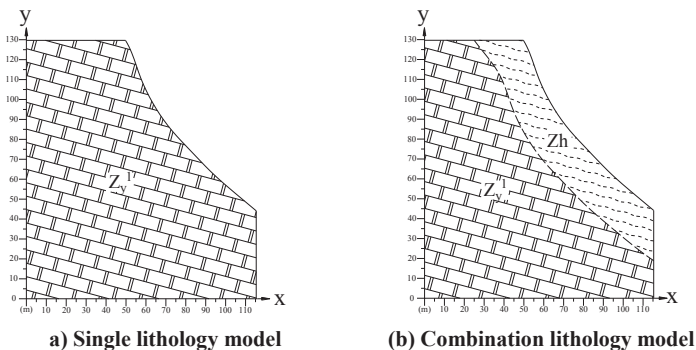
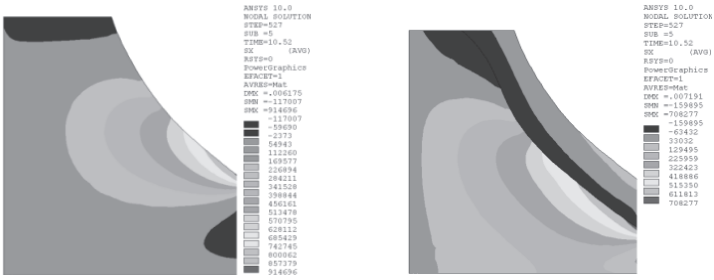
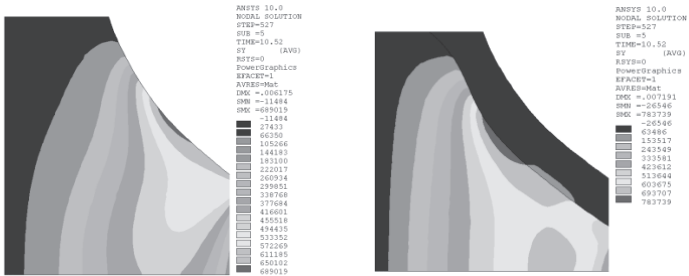


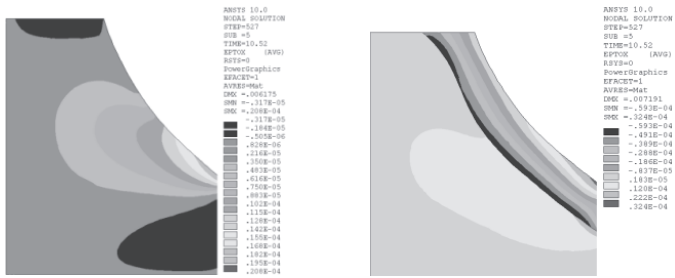
FIG.6. Two models as a comparison



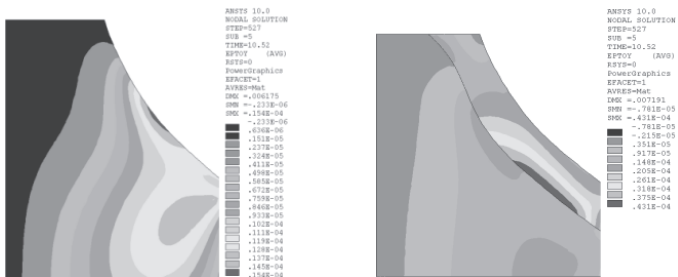
(a) X-component of stress comparison



(b) Y-component of stress comparison



(c) X-component of total strain comparison



(d) Y-component of total strain comparison

FIG. 7. Stress and total strain comparison of two models

ACKNOWLEDGMENTS

The authors would like to thank Li Shun, Liu Sili, Fu Rong for their help and support in carrying out the field investigation. Also the authors would like to thank Dr. Simeng Dong for her help in English correction of the paper. This work has been supported by National Natural Science Foundation for the youth (Grant No.41202211, Grant No.41202210); The open fund on "Study on slope seismic topography effect and observation on mountain areas" provided by the State Key Laboratory of Geohazard Prevention and Geoenvironment Protection; China Geological Survey Bureau (Grant No. 1212010914010 and 1212011220154);

REFERENCES

- G. Wang & T. Kamai. (2010). "A large landslide triggered by the 2008 Wenchuan (Ms8.0) earthquake: Insights for seismic motion. " *Geologically Active*, Taylor & Francis Group, London, ISBN 978-0-415-60034-7.
- Laigu Wang. (2009). "Simulation experiment research on slope mechanism under the condition of strong earthquakes." *Geo-hazards research of Wenchuan Earthquake*. 298-339 (in Chinese).
- Runqiu Huang, Weile Li. (2008). "Research on development and distribution rules of geohazards induced by wenchuan earthquake on 12th May." *Rock mechanics and engineering journal*. 27 (12):2585-2592 (in Chinese).
- Qiang Xu. (2009). "The formation mechanism research of Shibao Gou landslide." *Geo-hazards research of Wenchuan Earthquake*. 235-245(in Chinese).
- Yunsheng Wang, Yonghong Luo, Hongbiao Xu. (2010). "Analysis of the factors controlling slope instability in the mountainous epicenter zone of the Wenchuan Earthquake." *Geologically Active-Volume of papers from the 11th Congress of the International Association for Engineering Geology and the Environment* (781-787).
- Zhuoyuan Zhang, Shitian Wang. (1980). "Analysis principle of engineering geology. " *Geological Publishing House*, 95-96 (in Chinese).

Study on the Classification of Loess Ground in Tunnel Engineering

Qing-guo Liang^{1,2}, Lili Wang^{1,2}, De-wu Li^{1,2},

¹ School of Civil Engineering, Lanzhou Jiaotong University, Lanzhou, Gansu 730070, P. R. China; lqg_39@163.com

² Key Laboratory of Road & Bridge and Underground Engineering of Gansu Province, Lanzhou, Gansu 730070, P. R. China

ABSTRACT: Based on 346 complete data sets collected from 27 loess tunnels along the Zhengzhou-Xi'an Passenger Dedicated Railway, a new method for classification of loess ground is proposed by using multidimensional scaling (MDS) and principal component analysis (PCA). The comparative studies are conducted by the use of either only 7 tested indices or all 12 indices (i.e. 7 tested indices plus 5 deduced indices). Both the MDS and PCA provide similar but reasonable explanation of links between different indices. The first principal component (F1 or FPC) is adopted as a classification index to separate the total data into 5 groups according to the frequency distribution of F1 by using the golden section concept. The better and more reasonable results can be obtained from the classification by F1 from 7-index PCA than those by 12-index PCA, which not only verified both the importance of independence among indices to classification results and cohesion to loess characterization, but also revealed the clear boundaries of different classifications of loess ground from the statistical perspective. This study indicates that the cohesion should be considered as an optimum index to reflect the intrinsic strength characteristic of loess.

INTRODUCTION

Loess can be classified according to different purposes and indices such as chronological ages, grain size distribution, plasticity index (PI), collapsibility (δ), water content (ω) and liquidity index (LI) (Liu et al, 2004). The first classification dedicated to loess cavern and tunnels had been proposed in 1970's in China, where all four types of loess are classified into three categories mainly based on their chronological ages, geological conditions and the related geotechnical parameters (Wang et al, 1990). Although Q_1 and Q_2 loess are classified into IV, and Q_3 and Q_4 loess into V respectively, the associated parameters of them are not suggested like other grounds (e.g. *Code for design of railway tunnel*, 2005). A similar classification has also been suggested for the classification of loess ground based on three different hierarchical indices, namely chronological ages, plasticity index and water content with the consideration of burial depth of tunnels below the ground surface as

modification factor (Zhao et al, 2011). Another new classification of soils has been proposed for highway tunnel engineering in China (*Guidelines for Design of Highway Tunnel*, 2010). This classification considers mainly clayey soil, sandy soil and gravel soil, besides loess based on the large samples with basic classification index of *LL*, mass density (ρ) and *PI* (e.g. 4980 sets for cohesive soil, see Wang et al, 2009). Based on the existing methods above, this research will seek for a comprehensive index which not only can represent the multi-facet characteristics of loess reflected by multiple indices, but also reveal the intrinsic links of the physical parameters of loess to its mechanical parameters as far as the given sample data sets concerned.

SELECTION OF BASIC INDICES FOR ANALYSIS

The most widely used indices to characterize soils can usually be classified into 2 groups, i.e. tested index and deduced index. The tested parameters used in classification of loess ground in tunnel engineering can be as follows: **density** (ρ), **water content** (ω), **plastic limit** (ω_p), **liquid limit** (*LL*), **compressive coefficient** (*CC*), **cohesion** (*c*), and **internal friction angle** (ϕ), i.e. seven parameters. The deduced parameters, such as **bulk dry density** (ρ_d), **void ratio** (*e*), **degree of saturation** (S_r), **plasticity index** (*PI*), **liquidity index** (*LI*), are sometimes used to evaluate and classify loess too. Since they are considered as the indices closely linked to the mechanical behaviours of loess, all 12 indices were also used for a statistical analysis with 346 data sets of loess.

DATA

The source data were mainly from 27 tunnels in loess on the Zhengzhou-Xi'an Passenger Dedicated Railway (350 km long) located in the middle-eastern part of famous **Loess Plateau** in China (Zhao et al, 2011). In order to investigate the interrelationships among 12 different indices, only 346 complete data sets were adopted, where Q_1 and Q_2 loess cover 74.8% of all the loess ground, but only 97 sets of data of Q_1 and Q_2 loess can be used in the following analysis.

CORRELATIONS BETWEEN BASIC INDICES

The Pearson coefficients of correlation (Tang, 2010) between any two indices were listed in Table 1. For the first 7 measured indices, the maximum positive coefficient of correlation i.e. 0.83, was between *PL* and *LL*, followed by between ρ and ω (0.81). When all the 12 indices were considered, the maximum coefficient of correlation was -0.99, between ρ_d and *e*, implying these two can actually be considered as one independent index followed by ω vs *LI* (0.97), and ρ vs ρ_d (0.95), respectively.

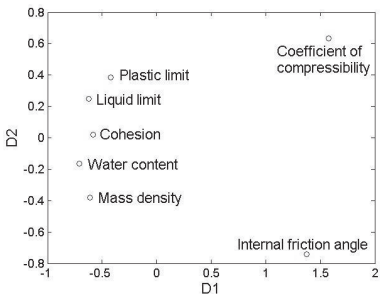
If the first 7 indices were considered, only *c*, to the limited extents, correlated well with several physical indices, namely by *LL* (0.66), ρ (0.57) and ω (0.55), respectively. But *CC* and ϕ had no any meaningful correlations with other indices. However, in the 12 indices analysis, not only the highest correlation is changed between *c* and *PI* (0.70) rather than *c* and *LL* (0.66), but the new and 'better' correlation occurred, for example, between *CC* and *e* (0.46) and *CC* and ρ_d (-0.44). These correlation orders in magnitude can be meaningful in qualitatively describing the interrelationships among

the geotechnical indices given the sample size of 346.

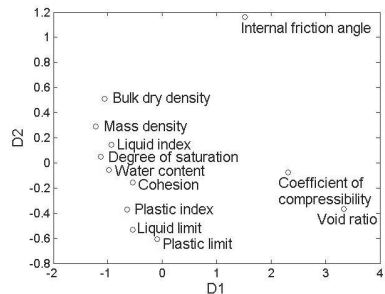
Table 1 Correlations matrix of 12 indices

| SN | Index | ρ | ω | PL | LL | CC | c | ϕ | ρ_d | e | S_r | PI | LI |
|----|----------|-------------|-------------|-------------|-------------|-------|-------|--------|--------------|-------|-------|------|------|
| 1 | ρ | 1.00 | | | | | | | | | | | |
| 2 | ω | 0.81 | 1.00 | | | | | | | | | | |
| 3 | PL | 0.32 | 0.42 | 1.00 | | | | | | | | | |
| 4 | LL | 0.52 | 0.63 | 0.83 | 1.00 | | | | | | | | |
| 5 | CC | -0.38 | -0.17 | -0.04 | -0.10 | 1.00 | | | | | | | |
| 6 | c | 0.57 | 0.55 | 0.41 | 0.66 | -0.19 | 1.00 | | | | | | |
| 7 | ϕ | 0.00 | -0.09 | -0.12 | -0.20 | -0.07 | -0.17 | 1.00 | | | | | |
| 8 | ρ_d | 0.95 | 0.57 | 0.20 | 0.37 | -0.43 | 0.49 | 0.05 | 1.00 | | | | |
| 9 | e | -0.93 | -0.54 | -0.18 | -0.34 | 0.46 | -0.46 | -0.06 | -0.99 | 1.00 | | | |
| 10 | S_r | 0.94 | 0.95 | 0.41 | 0.63 | -0.27 | 0.62 | -0.05 | 0.79 | -0.75 | 1.00 | | |
| 11 | PI | 0.56 | 0.64 | 0.53 | 0.92 | -0.13 | 0.70 | -0.21 | 0.42 | -0.38 | 0.65 | 1.00 | |
| 12 | LI | 0.79 | 0.97 | 0.24 | 0.49 | -0.16 | 0.49 | -0.08 | 0.57 | -0.54 | 0.92 | 0.57 | 1.00 |

The above correlations in Table 1 can also be more visually and conveniently expressed in a plane by using multidimensional scaling (MDS) method as showed in Fig 1, where the coefficients of correlation in Table 1 were further processed by reducing the multidimensional space (i.e. 7×7 matrix or 12×12 matrix) into a two-dimensional plane with the most information about the original matrix kept and represented equivalently. The accuracy of this approximate transformation is usually measured by the Kruskal stress. The lower the Kruskal stress is, the better the calculated result is. The details of the principle and algorithm about MDS can be found in *Multidimensional Scaling* (Trevor F. Cox et al, 2001).



(a) 7-index (Kruskal stress = 0.0040)



(b) 12-index (Kruskal stress = 0.0083)

FIG. 1. Relationships among different indices

It was clearly indicated in Fig 1 that the MDS results from either 7 indices or 12 indices in Table 1 were all at the satisfied level with Kruskal stresses of 0.0040 and 0.0083, respectively. In the two-dimensional plane, most indices clustered on the left half, while coefficient of compressibility and internal friction angle were far way from other indices, indicating their lowest correlations with the others. But as for void ratio, its nearest distance to coefficient of compressibility reflected their close relationships on the one hand, but its distance much far away from others, especially from bulk dry density and mass density should be interpreted as their negatively but very highly correlated relationships on the other hand (Fig 1 (b)). In the D2 direction, the index with the smallest distance to D2 axis was cohesion, closely neighbored by liquid limit and water content (instead of mass density) for 7-index MDS (Fig 1 (a)), while for 12-index MDS, degree of saturation was closely surrounded by water content and liquidity index (Fig 1 (b)). The distances between cohesion and water content were the smallest compared with other variables either from 7-index MDS (0.051) or 12-index MDS (0.049), which can correctly reveal the most significant influence of water content on the cohesion of loess. Nevertheless, both the quantitative calculated correlations in Table 1 and qualitative visualized expression in Fig 1 can easily conclude that the interrelationships amongst all the indices can be properly explained by the fewer indices on the left side. These will be further discussed later.

PRINCIPAL COMPONENT ANALYSIS (PCA)

Principal Component Analysis (PCA) is another dimension reduction method widely used for the data analysis of large samples with multiple variables. The principles and algorithms of PCA can be found in mathematical books or manuals (e.g. Tang, 2010) and will not be discussed here due to the space limitations. It is suggested that the first PC (F1) mainly correlates with the original indices more quantitatively at the given contribution level, while the other PCs might be related more to the shape or structure of total samples (Tang, 2010). As more specifically for this research, the first three components (F1, F2 and F3) contributed to 90.8%, 5.1% and 3.0% to the total engenvalues from 7-index PCA, and 82.0%, 16.1% and 1.1% from 12-index PCA, respectively. So, F1 might be the best index to classify the original samples since the engenvalue of F1 covers more than 80% of the total engenvalues. The regression constants for calculating the first three PCs are listed in Table 2, which can be used to obtain the related PCs. For example, the F1 in 7-index PCA can be calculated by linear combination of original indices as follows:

$$F1 = 0.0066\rho + 0.1630\omega + 0.0284PL + 0.0944LL - 0.0020CC + 0.9811c - 0.0321\varphi$$

The largest absolute value of the constant usually means the maximum contribution from the original index to the corresponding PC. For instance, the constant absolute value of c for F1 from 7-index analysis is 0.9811, much higher than others, which implied that F1 mainly depends on c and then followed by ω , while as for F2 and F3, the maximum contributions might be dominated by ω and φ . This clearly suggested that c might be the most significant indices to characterize the properties of loess in this research if based on the results from 7-index PCA, closely followed by ω . But for the 12-index PCA, the indices with most contribution to F1 were S_r and c , different from those in 7-index PCA, which highlighted the importance of S_r and then of c to

the whole samples. These quantitative relationships from PCA agreed very well with the patterns presented by using MDS in Fig 1, where the correlations among and clustering of indices in plane actually formed two central points with minimum distances to D2 axis, i.e. cohesion ($D1 = -0.584$, $D2 = -0.020$) in 7-index MDS and degree of saturation ($D1 = -1.131$, $D2 = -0.050$) in 12-index MDS. So the classification based on F1 values calculated either from 7-index or 12-index can be both reasonable and acceptable in that it includes the importance of water content to loess as widely studied preciously. Therefore, the most significant factors in describing the whole source data in dimension reduced F1 direction were c for 7-index PCA and S_r for 12-index PCA, respectively, implying the much difference between 7-index and 12-index method.

Table 2. Principal component constants from 7-index PCA and 12-index PCA

| Indices | Unit | 7-index PCA | | | 12-index PCA | | |
|-----------|-------------------|---------------|---------|---------|----------------|---------|---------|
| | | F1 | F2 | F3 | F1 | F2 | F3 |
| ρ | g/cm^3 | 0.0066 | -0.0257 | 0.0070 | -0.0064 | 0.0038 | -0.0044 |
| ω | % | 0.1630 | -0.9577 | 0.0345 | -0.1623 | 0.1131 | 0.1110 |
| PL | % | 0.0284 | -0.0794 | -0.0293 | -0.0190 | -0.0097 | 0.0495 |
| LL | % | 0.0944 | -0.2069 | -0.0830 | -0.0617 | -0.0374 | 0.1356 |
| CC | Mpa^{-1} | -0.0020 | 0.0026 | -0.0060 | 0.0018 | -0.0005 | 0.0063 |
| c | kPa | 0.9811 | 0.1817 | 0.0356 | -0.4943 | -0.8644 | -0.0538 |
| φ | $^\circ$ | -0.0321 | 0.0073 | 0.9948 | 0.0113 | 0.0433 | -0.9778 |
| ρ_d | g/cm^3 | | | | -0.0034 | 0.0019 | -0.0053 |
| e | - | | | | 0.0039 | -0.0023 | 0.0070 |
| S_r | % | | | | -0.8502 | 0.4856 | -0.0182 |
| PI | - | | | | -0.0427 | -0.0277 | 0.0861 |
| LI | - | | | | -0.0148 | 0.0123 | 0.0080 |

CLASSIFICATION AND RESULTS

Since F1 has been determined and selected as the major classification index, the next key parameters would be the division values to classify the whole sample into several groups. Fig 2 shows the accumulative distribution of F1 values. The percentage of the curve means the proportions in all the samples with its value larger than that in horizontal axis. The first step is to divide the total sample into 2 groups based on the accumulated distribution curve of F1 (see Fig 2), where one group has higher values than the mean value of the total sample, while the other group has lower values than the mean value of total sample. The mean value of F1 from 7-index PCA was 35.2 and there was 39.9% samples had the value higher than the mean value, which seems to fit to the golden section scale quite well. The higher F1 is positively correlated with higher values in mass density and cohesion, indicating the 'better quality' of loess. So this group can be classified as the 'better part' of all the samples. The other 60.1% samples can be considered as the 'worse part'. As for F1 from 12-index PCA, only 34.4% samples had the lower values than the mean value, i.e. -60.1,

but the lower values (higher if in absolute values) in F1 from 12-index PCA corresponded to higher mass density and cohesion. Thus the first division value between better group and worse group from F1 in 12-index PCA was determined as about -58.4 corresponding to 35% samples classified as the ‘better part’, and the remaining 65% as the ‘worse part’.

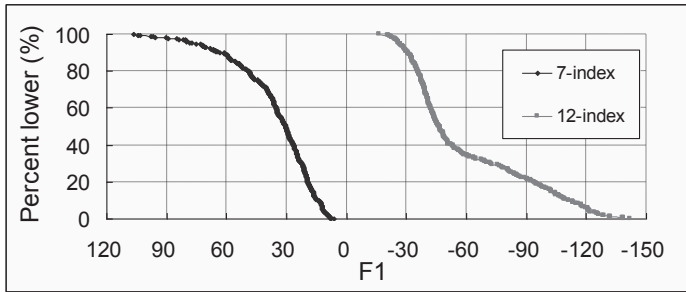


FIG. 2. Accumulative distribution of F1 from 7-index PCA and 12-index PCA

The second step is to further divide the above two groups into more subgroups. For the ‘better part’ samples in 7-index PCA, the subdivision values was adopted as 15% or 25% (corresponding value was 55.5) but not the commonly used dichotomy values of 20%. The former (i.e. 15% with the highest F1 values) also approximately coincides with the golden section scale of 40%, as the total sample distribution implied. Thus the samples with the F1 values from 7-index PCA higher than 55.5 (covering 15% of all the samples) can be classified as c1, i.e. the best part of all the samples, and the remaining parts then was classified as c2. The worse part of all the samples can also be determined by the method of golden section scale but 3 subgroups might be required in that the most loess are distributed on the ground surface with lower strengthen due to environmental variations, especially precipitation. So the subdivision boundaries were determined as 40% and 15%, respectively, which means the worst parts also accounted for the 15% of all the samples. The division values and corresponding percent in all the samples are presented in Table 3, so the samples can then be classified into 5 groups.

Table 3. Division values of F1 for classification and sample distribution

| Classification | 7-index PCA | | | | 12-index PCA | | | |
|----------------|-------------|------------------|----|------|--------------|---------------------|----|------|
| | Division | Ranges | n | (%) | Division | Ranges | n | (%) |
| c1 | IVa* | F1 ≥ 55.5 | 53 | 15.3 | | F1 < -102.4 | 54 | 15.6 |
| c2 | IVb | 35.2 ≤ F1 < 55.5 | 86 | 24.9 | 85% | -102.4 ≤ F1 < -58.4 | 69 | 19.9 |
| c3 | Va | 26.6 ≤ F1 < 35.2 | 69 | 19.9 | 65% | -58.4 ≤ F1 < -42.3 | 87 | 25.1 |
| | | 16.9 ≤ F1 < 26.6 | 86 | 24.9 | 40% | -42.3 ≤ F1 < -33.4 | 84 | 24.3 |
| c4 | Vb | F1 < 16.9 | 52 | 15.0 | 15% | F1 ≥ -33.4 | 52 | 15.0 |
| c5 | VI | | | | | | | |

Note: * corresponding to the sub-classification in Code for design of railway tunnel (TB 10003-2005).

The mean value and standard deviation of original indices were obtained after classification by 7-index PCA and 12-index PCA and summarized in Table 4. It can be seen that although the distributions of ρ_d , ω , φ did not show obvious patterns with either c or S_r , the ranges of c classified by F1 from 7-index PCA are both rational and distinguishable. As Table 4 indicated, for c1 classification, the majority S_r values of c1 are higher than 60%, while the S_r of c5 classification are lower than 60%. There are no obvious patterns for other subclasses. The LI and PI of different classifications by both 7-index and 12-index PCA show similar patterns with most of LI and PI of c1 classification higher than 0 and 10, but most of them of c5 classification lower than 0 and 10, respectively. The comparative analyses both on classification method and on results clearly indicated that 7-index PCA can distinguish the samples better than 12-index PCA in terms of variation of S_r with c .

Table 4. Mean and standard deviation of different classifications by F1

| Index | PCA | c1 | c2 | c3 | c4 | c5 |
|--|-----|-----------------|-----------------|-----------------|-----------------|-----------------|
| ρ (g/cm^3) | 7* | 1.97 ± 0.17 | 1.74 ± 0.22 | 1.67 ± 0.18 | 1.60 ± 0.17 | 1.56 ± 0.11 |
| | 12 | 2.02 ± 0.07 | 1.90 ± 0.12 | 1.62 ± 0.10 | 1.55 ± 0.10 | 1.49 ± 0.09 |
| ω (%) | 7 | 20.0 ± 4.4 | 13.9 ± 5.7 | 12.3 ± 4.8 | 10.9 ± 3.9 | 9.7 ± 3.0 |
| | 12 | 22.0 ± 2.7 | 17.6 ± 3.1 | 10.9 ± 2.5 | 9.5 ± 1.9 | 7.5 ± 1.5 |
| PL (%) | 7 | 19.2 ± 1.6 | 18.1 ± 1.2 | 18.0 ± 1.1 | 17.6 ± 1.0 | 17.2 ± 0.9 |
| | 12 | 19.4 ± 1.6 | 17.9 ± 1.1 | 17.7 ± 1.0 | 17.8 ± 1.0 | 17.3 ± 1.0 |
| LL (%) | 7 | 32.1 ± 2.9 | 28.4 ± 2.4 | 27.6 ± 1.6 | 26.9 ± 1.4 | 26.0 ± 1.4 |
| | 12 | 32.5 ± 3.0 | 28.2 ± 2.0 | 27.2 ± 1.5 | 27.3 ± 1.5 | 26.2 ± 1.5 |
| CC (MPa^{-1}) | 7 | 0.12 ± 0.05 | 0.22 ± 0.19 | 0.20 ± 0.20 | 0.25 ± 0.27 | 0.23 ± 0.17 |
| | 12 | 0.12 ± 0.05 | 0.17 ± 0.14 | 0.21 ± 0.18 | 0.26 ± 0.27 | 0.28 ± 0.25 |
| c (kPa) | 7 | 67.6 ± 13.8 | 39.4 ± 6.1 | 27.1 ± 2.9 | 18.3 ± 2.8 | 9.3 ± 3.0 |
| | 12 | 63.3 ± 18.2 | 34.2 ± 13.3 | 29.6 ± 12.8 | 21.7 ± 8.0 | 13.9 ± 7.0 |
| φ ($^\circ$) | 7 | 26.1 ± 4.3 | 25.9 ± 4.0 | 27.4 ± 3.4 | 27.7 ± 3.4 | 28.3 ± 2.2 |
| | 12 | 25.9 ± 4.4 | 27.6 ± 3.5 | 26.3 ± 3.6 | 27.1 ± 3.5 | 28.5 ± 2.8 |
| ρ_d (g/cm^3) | 7 | 1.64 ± 0.11 | 1.52 ± 0.14 | 1.49 ± 0.12 | 1.44 ± 0.13 | 1.42 ± 0.09 |
| | 12 | 1.65 ± 0.07 | 1.62 ± 0.11 | 1.46 ± 0.09 | 1.41 ± 0.11 | 1.38 ± 0.08 |
| e | 7 | 0.66 ± 0.12 | 0.79 ± 0.17 | 0.83 ± 0.15 | 0.88 ± 0.16 | 0.91 ± 0.12 |
| | 12 | 0.64 ± 0.07 | 0.68 ± 0.12 | 0.86 ± 0.12 | 0.92 ± 0.15 | 0.96 ± 0.11 |
| S_r (%) | 7 | 85.1 ± 21.2 | 51.6 ± 27.4 | 42.6 ± 21.5 | 35.0 ± 17.2 | 29.5 ± 10.3 |
| | 12 | 93.0 ± 8.6 | 71.1 ± 14.2 | 34.8 ± 8.2 | 28.1 ± 4.1 | 21.3 ± 4.6 |
| PI | 7 | 12.9 ± 2.1 | 10.3 ± 1.5 | 9.6 ± 1.0 | 9.4 ± 0.7 | 8.7 ± 0.7 |
| | 12 | 13.1 ± 2.2 | 10.3 ± 1.4 | 9.5 ± 0.8 | 9.5 ± 0.7 | 8.9 ± 0.7 |
| LI | 7 | 0.03 ± 0.4 | -0.44 ± 0.5 | -0.60 ± 0.5 | -0.72 ± 0.4 | -0.87 ± 0.4 |
| | 12 | 0.19 ± 0.3 | -0.04 ± 0.3 | -0.71 ± 0.3 | -0.88 ± 0.2 | -1.10 ± 0.2 |

Note: * 7 means 7-index PCA, and 12 means 12-index PCA.

DISCUSSIONS AND RECOMMENDATIONS

Because S_r is a calculated index based on ρ , G_s , and ω , its variation is mainly dominated by ω but generally higher than that of ω due to the accumulated variations. So ω can be considered as a primary indicator for the precise nature of loess as discussed and verified by numerous researches and practices. Cohesion together with internal friction angle is of much importance to the tunnel stability according to the Elasto-plastic theory given the specified support pressures (e.g. Cantieni et al, 2009). So the classification method by using F1 from 7-index PCA is both rational and acceptable not only in quantitatively reflecting the basic features of loess but in qualitatively expressing the most important connections between mechanical behaviors (mainly by c) and physical properties (mainly by ω). The suggested parameters for the classification of loess based on above analyses (see Table 4) can then be summarized in Table 5 and used if there is no enough testing data available.

Table 5. Suggested parameters for loess as ground based on 7-index PCA

| Classification | $\rho(\text{g/cm}^3)$ | PI | $c(\text{kPa})$ | $\varphi(^{\circ})$ | $\rho_d(\text{g/cm}^3)$ |
|----------------|-----------------------|-----------|-----------------|---------------------|-------------------------|
| 1 | ≥ 1.86 | ≥ 12 | ≥ 51 | ≥ 30 | ≥ 1.60 |
| 2 | 1.76~1.85 | 10~12 | 33~50 | 27~29 | 1.51~1.59 |
| 3 | 1.66~1.75 | 8~11 | 23~32 | 23~26 | 1.46~1.50 |
| 4 | 1.56~1.65 | 8~11 | 16~22 | 19~22 | 1.41~1.45 |
| 5 | ≤ 1.55 | ≤ 8 | ≤ 15 | ≤ 18 | ≤ 1.40 |

Note: the ranges of c were mainly from the actual classification results, while others were modified accordingly from the mean values and standard variations in Table 4.

It is extremely important to note that the classifications in Table 5 should be firstly determined mainly by cohesion with the consideration of both the mass density and the water content of given loess sample other than the bulk dry density or degree of saturation, which means the higher bulk density and lower water content coincide to the higher strength parameters in the same classification. Compared with the existing classification method for loess or other soils, the method proposed in this research is more reasonable and acceptable in that not only the classification index has the theoretical basis by using the MDS and PFC method, but also the parameter ranges have clear physical meanings since F1 represents the overall characteristics of loess with the emphasis on cohesion. In a word, this new method is supported by theoretical basis and data sample, which could be also used to quantitatively analyze the similar problems associated with multi-variables.

CONCLUSIONS

Based on the results presented above, the following conclusions can be drawn:

1. Both the MDS and PCA showed similar patterns of the interrelationships among the basic indices of loess whether 7 indices or 12 indices were adopted, but the major contributions of original indices to F1 by 7-index PCA were much differed with those

by 12-index PCA in that 7-index PCA is from cohesion while 12-index PCA is from degree of saturation.

2. The comparative analyses of 7-index PCA and 12-index PCA indicated that the former can give the better and more reliable classification results. In spite of the ambiguous ranges and boundaries of most parameters such as φ , ω , ρ and *et al*, the classification of loess ground by 7-index PCA are rational and acceptable in that not only the most important influencing factors has been verified to be cohesion rather than degree of saturation, but also the results can reasonably represent the main characteristic of loess from different classifications.

3. The cohesion of loess can be considered as the optimum index to reflect the intrinsic and strength characteristic of loess. F1 by 7-index PCA was used to classify the loess into 5 types from the statistical perspective, which might obey the philosophy and principle of ground classifications.

ACKNOWLEDGMENTS

The authors appreciate the support of National Science Foundation of China (41262010), 'Qing Lan' Talent Engineering Funds (QL-08-19A) of Lanzhou Jiaotong University and the Program for Changjiang Scholars and Innovative Research Team in University (IRT1139), China.

REFERENCES

- Cantiemi L., Anagnostou G.(2009). "The effect of the stress path on squeezing behavior in tunnelling." *Rock Mech. Rock Eng.* Vol.42, 289-318.
- Chinese Railway Standard. (2005)."Code for design of railway tunnel (TB 10003-2005)." China Railway Publishing House, Beijing.
- Industrial recommended standard of People's Republic of China. (2010). "Guidelines for Design of Highway Tunnel (JTG/T D70-2010)." People's Jiaotong Publishing House, Beijing.
- Liu Z.D.(1996)."Loess Mechanics and Engineering." Shanxi Science and Technology Publishing House, Xi'an.
- Tang Q.Y.(2010). "DPS[©] Data Processing System-Experimental Design Statistical Analysis and Data Mining (Second edition)." Science Press, Beijing.
- Trevor F. Cox., Michael A. A. Cox. (2001). "Multidimensional Scaling (Second Edition)." Chapman & Hall/CRC, USA (eBook ISBN: 978-1-4200-3612-1).
- Wang M.M., Wei L.H., Li H.J., Liu B. (2009). "Research on mechanical parameters of subclassification rock mass of highway tunnel." *Chn. J. Rock Mech. Rock Eng.* Vol.27 (11), 2252-2259.
- Wang Y.Y, Lin Z.G.(1990). "Structural Characteristics, Physical and Mechanical Properties of Loess in China." Science Press, Beijing.
- Xie D.Y.(2001). "Exploration of some new tendencies in research of loess mechanics." *Chn. J. Geotech. Eng.* Vol.23(1),3-13.
- Zhao Y., LI G.L. and YU Y.(2011)."Loess Tunnel Engineering." China Railway Publishing House, Beijing.

Shear Strength Characteristics of an Artificially Cemented Sand-Gravel Mixture

Younes Amini¹, Amir Hamidi² and Ebrahim Asghari³

¹ School of Engineering, Kharazmi University, Tehran, Iran, y.amini@tmu.ac.ir

² School of Engineering, Kharazmi University, Tehran, Iran, hamidi@tmu.ac.ir

³ Faculty of Natural Science, University of Tabriz, Tabriz, Iran, e-asghari@tabrizu.ac.ir

ABSTRACT: Over the years, a number of researches have been carried out to describe the behavior of granular soils. However, the mechanical behavior of cemented granular soils is not well understood. Indeed, shear strength and dilation characteristics are different from uncemented soils. The lack of experimental data for illustration of the mechanical behavior of cemented soils is more obvious for cemented sand-gravel mixtures.

In this paper, shear strength-dilation behavior of artificially cemented sand-gravel mixtures has been studied using large direct shear tests. The soil consists of fine sand mixed with 30% uni-sized gravel particles with maximum size of 12.5 mm. Large direct shear tests have been conducted using saturated samples in a 300×300×170 mm shear box. Samples were prepared in four different relative densities of 30, 50, 70 and 90% and three cement contents of 0, 1 and 2% and were tested under two surcharge pressures of 77 and 150 kPa. Cemented samples were cured in direct shear box for seven days under a low water head to prevent degradation of cemented bonds. After curing, shear loading was applied at a constant rate of 0.1 mm/min. Both horizontal and vertical displacements besides shear stresses were recorded during loading process. Shear strength, friction angle and cohesion intercept of cemented samples were calculated and it was indicated that shear strength of cemented sand-gravel mixtures increase with cement content and relative density. However, dilation of cemented samples reduced with increase in surcharge pressure.

Keywords: Cemented soil, shear strength, sand-gravel mixture, relative density, dilation.

INTRODUCTION

Geotechnical engineers often deal with soils that have different behaviors. These soils have much higher strength and dilation compared to the same remolded soils in laboratory. The reason for this type of behavior is cemented bonds. Cementation is usually due to the chemical effects of material deposition from groundwater. Carbonates, Silicates and iron oxides are usual natural cementing agents. There are

many researches that deal with cementation in soils. Experimental studies have been conducted with various cement agents including Portland cement, gypsum, hydrated lime and different base soils. Indeed artificially cemented samples are widely used in experimental studies because of difficulties in undisturbed sampling from naturally cemented coarse-grained soils. Clough et al. (1981), Leroeil and Vaughan (1990), Gens and Nova (1993), Coop and Atkinson (1993), Consoli et al. (1998), Malandraki and Toll (2001) and Rotta et al. (2003) extended the basic concepts of the behavior of cemented sands.

Yasrebi and Asghari (2002) performed direct shear tests on uncemented and artificially cemented gravely sand using hydrated lime as the cementing agent. Hamidi and Haeri (2005) conducted consolidated drained and consolidated undrained triaxial tests on Tehran alluvium equivalent gradation using gypsum as the cementing agent. In a parallel study, Haeri and Hosseini (2005) performed a series of triaxial tests on the same soil using Portland cement as cementing agent. According to the results of these studies, stress-strain behavior, stiffness characteristics, dilatancy and pore pressure generation in cemented soil are affected by the type and amount of cement content (Haeri et al., 2006). Also cementation increases cohesion intercept, friction angle and cohesion intercept of gravely sand.

EXPERIMENTAL PROGRAM

Tested soil consists of uniform sand which is a clean and uniform quartz beach sand with sub-rounded to sub-angular particles from the shores of the Caspian sea mixed with 30% of uni-sized gravel particles with maximum size of 12.5 mm. Figure 1 shows the gradation distribution curve of the base soil and Table 1 lists its physical properties. Large direct shear tests have been conducted on saturated samples using a 300×300×170 mm shear box under consolidated drained condition. Samples were prepared in four different relative densities of 30, 50, 70 and 90% using three Portland cement contents of 0, 1 and 2% and were tested under two surcharge pressures of 77 and 150 kPa.

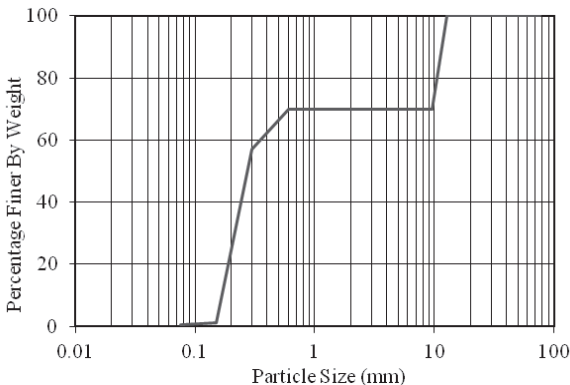


FIG. 1. Gradation distribution curve of sand-gravel mixture (base soil).

Table 1. Physical properties of the base soil

| Parameter | Soil group | C_u | C_c | e_{max} | e_{min} | G_s | D_{60} (mm) | D_{10} (mm) |
|-----------|------------|-------|-------|-----------|-----------|-------|---------------|---------------|
| Value | SP | 1.88 | 0.89 | 0.48 | 0.39 | 2.71 | 0.32 | 0.17 |

SAMPLE PREPRATION

Cemented samples were prepared by mixing the soil, Portland cement type II and 7% distilled water. After mixing, samples were prepared in shear box in three layers using under compaction method and were cured for 48 hours in wet condition to reach the initial strength of cement. The samples were completely saturated using a very low static pressure head to prevent bond degradation. After seven days cemented samples were sheared similar in a constant rate of 0.1 mm/min. Horizontal and vertical displacements besides shear stresses were recorded during loading process in both cemented and uncemented samples. Some pictures of testing apparatus and tested samples are shown in Figure 2.



FIG. 2. Cured and tested cemented samples in large direct shear apparatus.

ANALYSIS OF THE RESULTS

A summary of test results for cemented and uncemented samples are shown in Table 2. Figures 3 and 4 are shown shear stress–shear displacement and vertical displacement–shear displacement curves for different surcharge pressures, cement contents and relative densities. As the figures shows, shear strength increased with increase in relative density and surcharge pressure. Increase in maximum friction angle with relative density was more obvious for the uncemented samples compared to the cemented ones. However, cohesion intercept clearly increased with increase of relative density and cement content for cemented samples.

Table 2. Results of large direct shear tests

| Cement Content (%) | Relative Density (%) | Normal Stress (kPa) | Max. Shear Stress(kPa) | Cohesion Intercept (kPa) | Friction Angle (degree) |
|--------------------|----------------------|---------------------|------------------------|--------------------------|-------------------------|
| 0 | 30 | 77 | 51.8 | 0 | 34.0 |
| | 50 | 77 | 54.6 | 0 | 35.3 |
| | 70 | 77 | 60.5 | 0 | 38.2 |
| | 90 | 77 | 61.6 | 0 | 38.7 |
| 1 | 30 | 77 | 100.4 | 35.0 | 40.4 |
| | 30 | 150 | 162.4 | | |
| | 50 | 77 | 110.0 | 42.0 | 41.5 |
| | 50 | 150 | 174.4 | | |
| | 70 | 77 | 119.6 | 55.0 | 41.9 |
| | 70 | 150 | 185.0 | | |
| 90 | 77 | 130.3 | 60.7 | 42.1 | |
| 90 | 150 | 196.3 | | | |
| 2 | 30 | 77 | 123.6 | 60.7 | 40.9 |
| | 30 | 150 | 186.9 | | |
| | 50 | 77 | 147.8 | 78.1 | 42.2 |
| | 50 | 150 | 213.9 | | |
| | 70 | 77 | 157.8 | 86.7 | 42.8 |
| | 70 | 150 | 225.3 | | |
| 90 | 77 | 166.8 | 95.4 | 42.9 | |
| 90 | 150 | 234.6 | | | |

Uncemented samples indicated a strain hardening behavior but cemented samples showed a prominent peak followed by strain softening behavior up to the ultimate state of the stress. Both cemented and uncemented samples underwent dilation during shear loading, however, dilation of cemented samples was more than uncemented ones. Dilatancy decreased with increase of surcharge pressure in all samples.

In Figure 5 failure envelope for cemented samples under different relative densities are shown. According to this figure failure, envelope increased with cement content. Variation of shear strength with relative densities and cement content in different surcharge pressures had shown in Figure 6 and indicated that increase in relative density and cement content caused increase in shear strength.

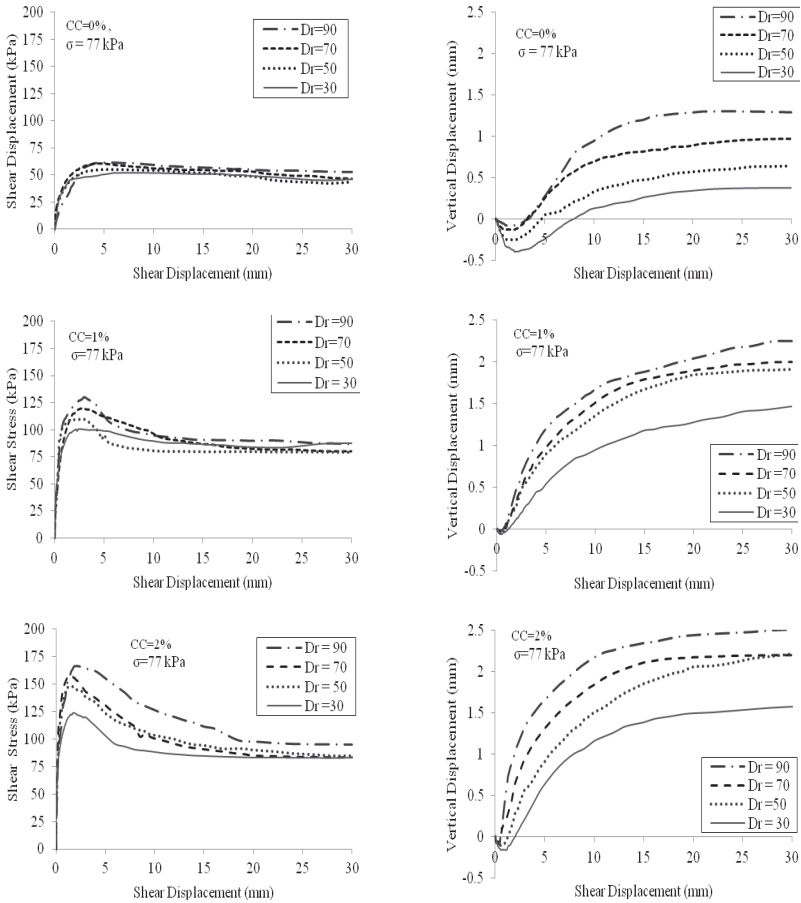


FIG. 3. Large direct shear test results on sand mixed with 30% gravel in different densities and cement contents under surcharge pressure of 77 kPa.

Variation of maximum friction angle and cohesion intercept with relative density and cement content had shown in Figure 7. By adding one percent of cement agent in soil maximum friction angle increased suddenly, however increase in relative density decreased jump of maximum friction angle. According to the Figure 7, effect of increase in relative density and cement content in cemented soil had not much higher, but these parameters had higher effect on cohesion intercept. This phenomena reported by different researchers include Yasrebi and Asghari (2002), Hamidi and Haeri (2005) and Hosseini and Haeri (2005).

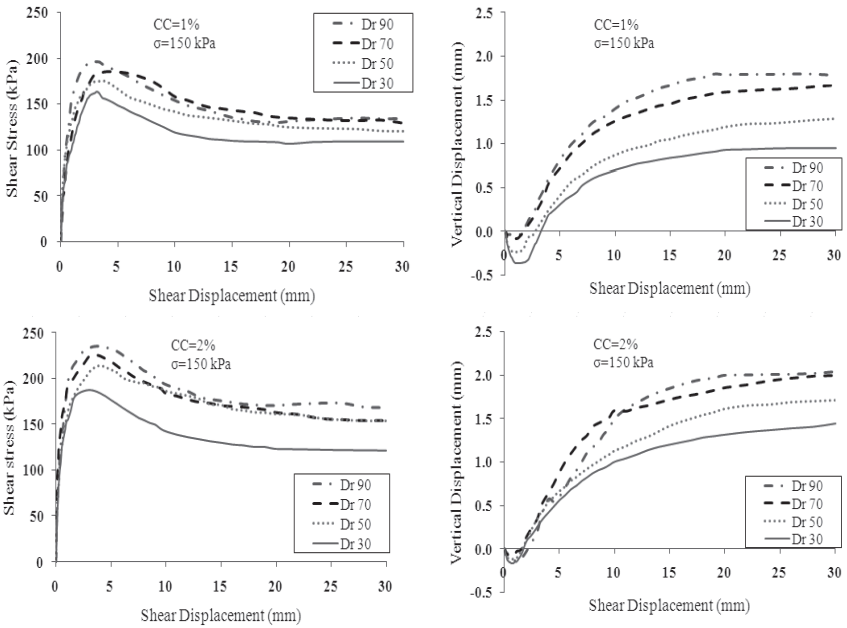


FIG. 4. Large direct shear test results on sand mixed with 30% gravel in different densities and cement contents under surcharge pressure of 150 kPa.

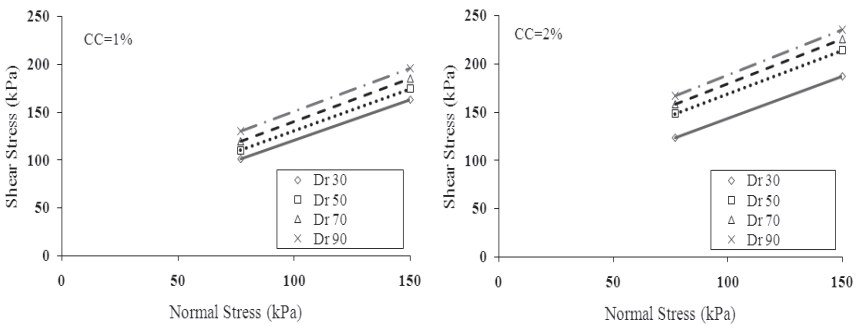


FIG. 5. Failure envelopes of soil with different cement content at each relative density.

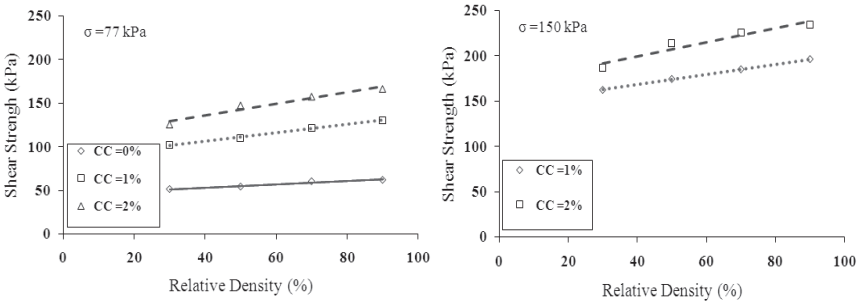


FIG. 6. Variation of shear strength with relative densities and cement content in different surcharge pressures.

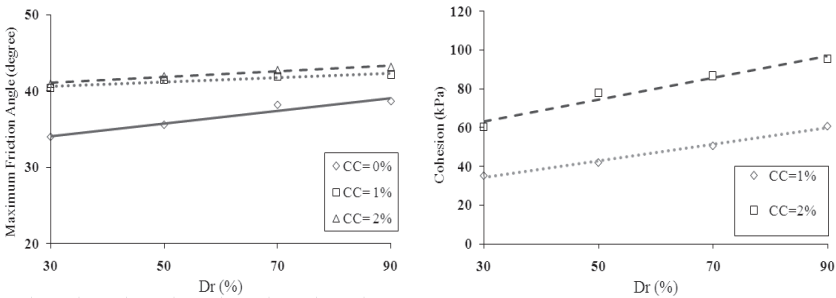


FIG. 7. Variation of maximum friction angle and cohesion with relative densities in different cement content.

CONCLUSIONS

Regarding to the results of experiments conducted in this present study, the following results were obtained:

1. Cementation increased the shear strength, cohesion intercept, dilatancy and maximum friction angle of the soil.
2. Increasing in relative density caused increase in maximum friction angle, shear stress and dilatancy. Increasing of surcharge pressure is decreased dilatancy in cemented soil.
3. Increasing in relative density results in a more obvious change in friction angle for the uncemented samples compared to the cemented ones.
4. Cemented samples have shown a strain softening behavior associated to more dilatancy compared to uncemented samples.

5. Adding small percent of cement agent on soils had shown suddenly increase in maximum friction angle in different relative density.
6. Maximum friction angle in cemented soils had not large variation with relative density and cement content, but cohesion intercepts increased with increase of cement content and relative density.

REFERENCES

- Clough, G. W., Sitar, N., Bachaus, R.C. and Rad, N. S. (1981). Cemented Sands under Static Loading, *Journal of Geotechnical Engineering, ASCE*, Vol. 107, No. 6: 799-817.
- Consoli, N. C., Prietto, D.M. and Ulbrich, L.A. (1998). Influence of fiber and cement addition on behavior of sandy soil, *Journal of Geotechnical and Geoenvironmental Engineering, ASCE*, Vol. 124, No. 12: 1211-1214.
- Coop, M. R. and Atkinson, J.H. (1993). The mechanics of cemented carbonate sands, *Geotechnique*, Vol. 43, No. 1: 53-67.
- Gens, A. and Nova, R. (1993). Conceptual bases for a constitutive model for bonded soils and weak rocks, *Proceedings of International Symposium on Geotechnical Engineering of Hard Soils-Soft Rocks, Balkema*, The Netherlands, Vol. 1: 485-494.
- Haeri, S.M., Yasrobi, S. and Asghari, E. (2002). Effects of cementation on the shear strength parameters of Tehran alluvium using the large direct shear test, *9th IAEG Congress, South Africa*: 519-525.
- Haeri, S. M., Hosseini, S.M., Toll, D. G., and Yasrebi, S.S. (2005). The behavior of an artificially cemented sandy gravel, *Journal of Geotechnical and Geological Engineering*, Vol. 23, No. 3: 537-560.
- Haeri, S.M., Hamidi, A., Hosseini, S.M., Asghari, E. and Toll, D. G. (2006). Effect of cement type on the mechanical behavior of gravely sand, *Journal of Geotechnical and Geological Engineering*, Vol. 24, No. 2: 335-360.
- Hamidi, A., Haeri, S. M., (2005). Critical state concepts for a cemented gravely sand, *Electronic Journal of Geotechnical Engineering*, Vol. 10, Bundle E: 1-12.
- Leroueil, S. and Vaughan, P.R. (1990). The general and congruent effects of structure in natural soils and weak rocks, *Geotechnique*, Vol. 40, No., 30: 467-488.
- Malandraki, V. and Toll, D.G. (2001). Triaxial tests on a weakly bonded soil with changes in stress path, *Journal of Geotechnical and Geoenvironmental Engineering, ASCE*, Vol. 127, No. 3: 282-291.
- Rotta, G. V., Consoli, N.C., Prietto, P.D.M., Coop, M.R. and Graham, J. (2003). Isotropic yielding in an artificially cemented soil cured under stress, *Geotechnique*, Vol. 53, No. 5: 493-501.
- Yasrebi, S. and Asghari, E. (2002). Influence of cementation on the shear strength of a gravely sand using large direct shear test, *55th Canadian Geotechnical Conference, Niagara Falls, Ontario, Canada*: 109-114

Key Factors of Subgrade Influencing Dynamic Wheel/Rail Loads at Railway Transition Zones

Hanbing Hu¹, Hans Brinkman²

¹Senior engineer, Key Laboratory of Geotechnical Mechanics and Engineering of the Ministry of Water Resources, Changjiang River Scientific Research Institute, Wuhan 430010, China; huhb@mail.crsri.cn

²Senior consultant, Deltares, P.O. Box 177, 2600 MH Delft, the Netherlands; hans.brinkman@deltares.nl

ABSTRACT: It is widely believed that differential settlement at railway transition zones is the result of dynamic wheel/rail force, and the stiffness difference between embankment and fixed structures is believed to be one of the major causes of high wheel/rail forces. A dynamic simulation model, which takes into account both a varying subgrade stiffness and track settlement, and incorporates the dynamic characteristics of railway vehicles, was applied to analyze the influences of subgrade stiffness on dynamic loads at railway transition zones. The studies reveal that stiffness variation at transitions is of minor influence over dynamic wheel/rail forces, and the overall dynamic effect is dominated by track settlement differences at transitions and the stiffness of fixed structures.

INTRODUCTION

At locations where embankments change to engineering structures, the railway track exhibits abrupt changes in the vertical support conditions which are often associated with uneven stiffness and differential settlement in longitudinal direction, bumps at the transitions, accelerated rates of geometry and component degradation, high maintenance demand, and poor ride quality.

According to ProRail (Dutch rail infrastructure provider), the maintenance frequency at transitions is 4-8 times higher than at regular track. The accompanying costs are 25% of ProRail's total maintenance budget for position maintenance (Hopman and Hölscher, 2007).

The differential settlement due to subsoil consolidation and creep cannot fully explain the excessive maintenance. It is expected that an uneven track surface and stiffness difference at transitions result in high vertical accelerations and dynamic wheel/rail loads, and these effects have influences on the degree of foundation compaction (Meijers and Hölscher, 2007). Therefore, the purpose of this study is to

investigate the behavior of an existing railway transition zone under dynamic load of a train passage, and to determine the influence of subgrade stiffness on dynamic axle forces for the studied transition zone.

STUDY OBJECTIVES

This study is part of the Delft Cluster research program ‘Railway Transition Zones’, and is based on a real case of railway transition between embankment and culvert structure.

The transition is situated along the Utrecht - Rotterdam/the Hague railway line in the western part of the Netherlands, near railway station Gouda Goverwelle. The transition lies at a typical soft soil area where the subsoil consists of peat layers with varying thickness. A typical soil layer profile at the transition is listed in Table 1. The railway crosses a concrete culvert which encloses a concrete square box of 2.40 m × 2.15 m with a wall thickness of 0.2 m. Four tracks cross the culvert. Eight approach slabs (one slab for each rail) are installed at both ends of the culvert. Dimensions of the approach slab are: length 4 m, width 1.20 m, thickness 0.3 m. On the culvert, rail tracks lie upon the ballast (thickness 1.0 m) and are not attached to the culvert.

Table 1. Soil layers at the transition

| No. | Soil layers | Thickness (m) | E (MPa) |
|-----|-------------|---------------|---------|
| 1 | Ballast | 1.00 | 50 |
| 2 | Sand | 0.70 | 130 |
| 3 | Sand | 1.30 | 146 |
| 4 | Clay | 0.40 | 30.9 |
| 5 | Peat | 4.30 | 5.48 |
| 6 | Clay | 1.45 | 25.4 |
| 7 | Peat | 2.20 | 5.84 |
| 8 | Clay | 0.45 | 30.9 |
| 9 | Sand | 3.40 | 360 |

At the transition site, four local and eight intercity trains pass by each direction in every hour with train speeds up to 160 km/h. Heavy freight trains also pass by. Maintenance of the transition zone is frequent (4 to 6 times a year). Maintenance will be carried out if a rail height difference of more than 1.5 mm is measured (Hopman and Hölischer, 2007).

SUBGRADE STIFFNESS OF THE TRANSITION ZONE

Subgrade stiffness of railway is one of the parameters measuring the quality and safety condition of rails. It is defined as the supporting force per unit length of rail per unit deflection. It excludes the flexural stiffness of the rail and is concerned only with the support condition below the rail.

It is commonly believed that stiffness difference is one of the major causes of high

wheel-rail force and track degradation at transition zones. Accordingly, the stiffness variation at the studied transition zone is determined, as shown in Fig. 1, using the numerical FEM program PLAXIS and Mtrack 3D model (Hu, 2008) which is based on elastic foundation theory. The following main conclusions can be drawn for the studied transition zone:

- 1) The subgrade stiffness of normal embankment track and the track on culvert are 43.01 MN/m/m and 133.33 MN/m/m respectively.
- 2) The stiffness ratio between the structure and normal track is about a factor of three.
- 3) The length of stiffness variation is about 15 m.

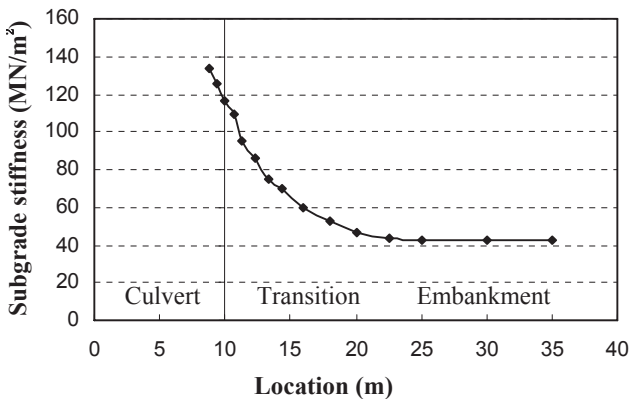


FIG. 1. Longitudinal variation of subgrade stiffness.

DYNAMIC RESPONSE OF THE TRANSITION ZONE

The dynamic response of vehicle-track interaction at the transition zone is simulated with a program developed by Professor Newland and Dr Hunt from Cambridge University in 1995 (hereafter called Cambridge Model).

Theoretical Basis of Cambridge Model

Track Description—the ‘Ramp’ Model

The ramp model is an analytical representation of an Euler beam resting on the prescribed foundation which takes into account a varying subgrade stiffness and track settlement, as shown in Fig. 2.

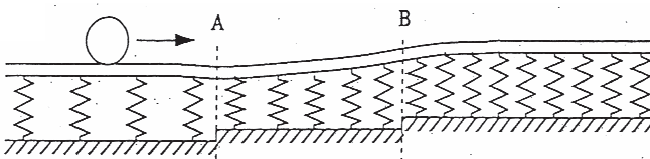


FIG. 2. The sketch of rail model

The calculation procedure works by dividing the beam into four segments as shown in Fig. 3. The left segment is a semi-infinite beam on uniform Winkler subgrade. The next is a short segment of beam on a uniform subgrade, but it is necessary to separate these first two segments so that the action of the applied vertical force P can be accounted for at the junction of these two beams. The third segment is a ramp one in which subgrade stiffness varies linearly. The fourth segment is again a semi-infinite beam resting on a uniform subgrade. As described, the force is to the left of the ramp segment and the four types of segment are "infinite-uniform-ramp-infinite". For calculating the deflected shape, when the force is within the ramp then the four segment types need to be "infinite-ramp-ramp-infinite" and for a load to the right of the ramp the segments are "infinite-ramp-uniform-infinite".

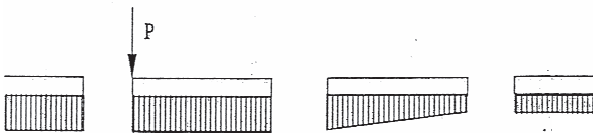


FIG. 3. Sketch of rail segments (load acts to the left of transition zone)

The deflected shape of a beam resting on a uniform Winkler foundation has the form of Eq.(1):

$$w = C \cos(\alpha x) + D \sin(\alpha x) + E \cosh(\alpha x) + F \sinh(\alpha x) \quad (1)$$

and for a beam on a foundation whose stiffness is linearly increasing with distance, the form can be expressed by Eq.(2):

$$w = GF_1(\alpha x) + HF_2(\alpha x) + IF_3(\alpha x) + JF_4(\alpha x) \quad (2)$$

But the functions 'cos', 'sin', 'cosh' and 'sinh' are replaced by four functions F_1 , F_2 , F_3 and F_4 which can be calculated by trigonometric functions.

The deflected shape of a beam resting on a semi-infinite uniform Winkler foundation has the form of Eq.(3) for a beam extending infinitely to the left ($x \rightarrow -\infty$) and the form of Eq.(4) for a beam extending infinitely to the right ($x \rightarrow +\infty$) respectively.

$$w = (A \cos(\alpha x) + B \sin(\alpha x))e^{\alpha x} \quad (3)$$

$$w = (K \cos(\alpha x) + L \sin(\alpha x))e^{-\alpha x} \quad (4)$$

The derivatives of each of the above equations are used to calculate the slope, bending moment and shear force within the beam segments and they can be pieced together by computing compatibility conditions at each of the three junctions, then the 12 unknown constants A , B , C , D , E , F , G , H , I , J , K and L are found and the shape of the rail is determined.

Vehicle Model

The vehicle is separated into wheel, bogie and carriage, as shown in Fig. 4, which allows bogie and body inertia and the primary and secondary suspension to be included separately. According to the validation of Cambridge model performed by Wiersma and Dirks (2005), it can represent the vehicle dynamics appropriately, and can give good simulations.

Model Parameters

Subgrade Stiffness

According to the analytic results, the subgrade stiffness of the track on structure and normal track is 133.33 MN/m/m and 43.01 MN/m/m respectively. The ratio between them is 3.1. The length of stiffness variation is 15 m, and approximation curve of the variation of subgrade stiffness is linear.

Initial Rail Surface

In order to put our emphasis on the influence of subgrade stiffness over the dynamic wheel/rail force, a horizontal rail surface (no track settlement) is assumed first, then differential settlements are also taken into account at parametric studies.

Vehicle Parameters

The parameters chosen for the vehicle model are based on the locomotive Eloc 1700 which is a widely used vehicle in the Netherlands and relatively a heavy vehicle.

Traveling Speed and Direction

A traveling speed of 150 km/h is used in this study, which is supposed to be the most typical vehicle speed on this line, and the train traveling through a stiffening subgrade (from embankment to structure) is simulated first, then different traveling speeds and direction are also taken into account at parametric studies.

Results Analysis

Because the dynamic wheel/rail force is the major concern of this study, the analysis results are expressed as the ratio between the calculated dynamic force P_d applied by the axle to each rail and the static wheel load P_s . Fig. 5 shows the variation of wheel-rail force when the train passes the studied transition zone.

Fig. 5 reveals that for the case of a train passing a horizontal rail surface (no track settlement) with stiffening subgrade (from embankment to culvert) at a speed of 150 km/h, the difference between dynamic axle force and static wheel load is relatively small, if normalized to static wheel load, the peak overload is only 0.3%.

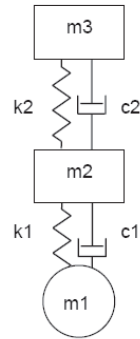


FIG. 4. Vehicle model

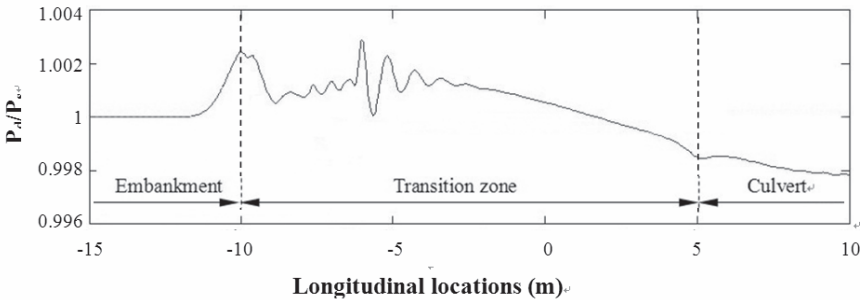


FIG. 5. Variation of wheel-rail force when the train passes the transition zone

Parametric Studies

Main parameters which may have influences over dynamic track forces are studied using Cambridge model.

Train Velocity

The effect of train velocity over the peak axle load is presented in Fig. 6. A clear trend of increasing dynamic forces with increasing velocity can be observed. While as a whole, even when the train speed reaches 250 km/h, the peak axle force is only 0.7 percent larger than the static load, which means that the dynamic effect which caused solely by subgrade stiffness difference is very small.

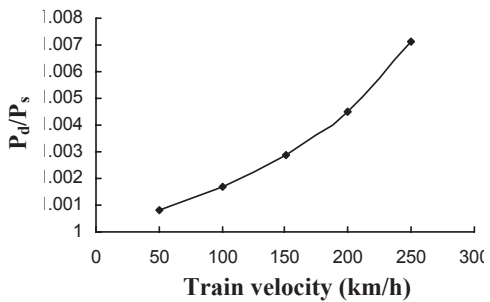


FIG. 6. Influence of train velocity on dynamic effect

Direction of Traveling

In Fig. 7, we can see that the peak axle forces of traveling forward (from embankment to structure) are larger than those of traveling backward (from structure to embankment) at the same traveling velocity. It is also revealed that at the softer side (embankment side), the dynamic axle force is always larger than the static wheel load, while at the stiffer side (culvert

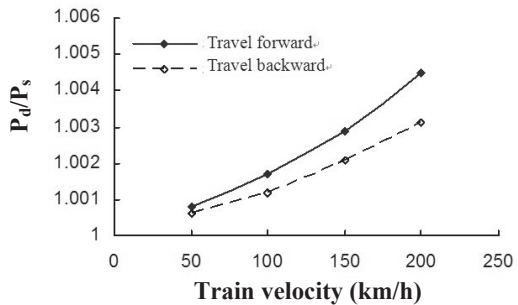


FIG. 7. Influence of train direction on dynamic effect

side), the dynamic axle force is always smaller than the static wheel load. This means that no matter in which direction the train travels, the ballast at the embankment side near the culvert always subjects to additional load, which might results in extra ballast compaction.

Length of Subgrade Stiffness Variation

The influence of stiffness variation length over the peak axle force is presented in Fig. 8. It shows clearly that for different lengths of stiffness variation, the peak axle forces are almost the same. Therefore, it is not difficult to conclude that the stiffness variation length has little influence on the dynamic axle force.

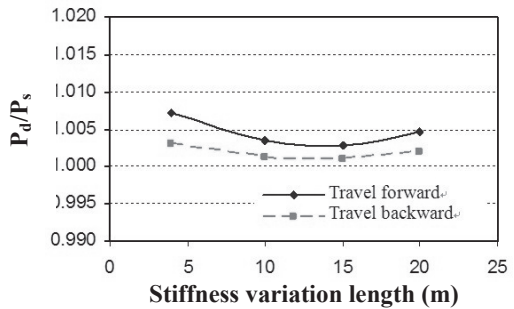


FIG. 8. Influence of transition length on dynamic effect

Track Settlement

The influence of track settlement over the peak axle force when the train travels from the embankment to the culvert at a speed of 150 km/h is presented in Fig. 9. It demonstrates a linearly increasing trend with increasing track settlement, which means that the influence of track settlement is significant.

When there is a 10 mm differential settlement at the transition, the peak dynamic axle force would be 18.5 percent larger than the static load. When the differential settlement reaches 25 mm, the peak dynamic axle force would be as great as 1.5 times of the static load.

Therefore, in order to reduce the dynamic overload, it is important to ensure that the track is leveled to a close tolerance and the track settlement is not allowed to develop. Bigger settlement leads to bigger axle force. Then additional deformation may occur, and settlement difference may develop further, which will form a vicious circle.

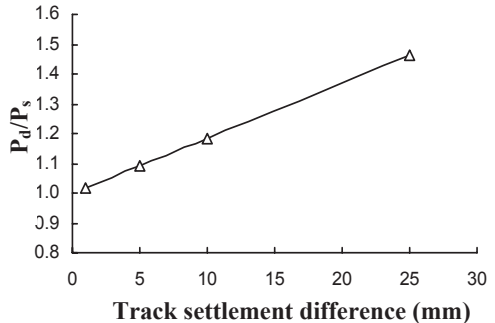


FIG. 9. Influence of differential settlement on dynamic effect

Subgrade Stiffness

In order to find out the main cause of increasing dynamic forces with respect to subgrade stiffness, the peak axle forces for the transition cases which have the same stiffness of culvert k_C , but have different embankment stiffness k_A , were compared

and plotted in Fig. 10, in which w_0 represents the track settlement difference. It shows obviously that the magnitude of embankment stiffness k_A has little influence on dynamic load, while a clear trend of increasing dynamic forces with increasing structure stiffness k_C can be observed, and for the case of larger track settlement, peak axle forces increase more rapidly with increasing ratio k_C/k_A .

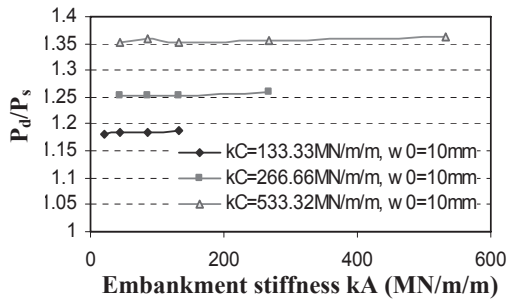


FIG. 10. Influence of stiffness k_A on dynamic effect

The comparison of the peak axle forces when the train travels through the uniform embankment, the transition zone with stiffening subgrade and the uniform structure at a speed of 150 km/h is presented in Fig. 11.

Fig.10 and Fig.11 display clearly that for the cases with same k_C value, the amplitude of k_A value has little influence on the peak axle force. Therefore, it is the stiffness amplitude of the stiffer side that dominates the overall dynamic behavior of the transition zone; the softer side has little influence.

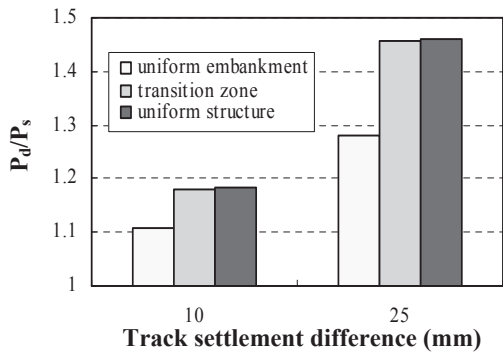


FIG. 11. Influence of stiffness on dynamic effect

It can be inferred from above analysis that one of the most effective measures of reducing the dynamic effect of transition zones is lowering the stiffness of structures.

CONCLUSIONS AND RECOMMENDATIONS

This study reveals that the subgrade stiffness difference between embankment and structures is of minor influence over dynamic axle forces, and the overall dynamic behavior of transitions is dominated by the track settlement difference of transitions and the stiffness of fixed structures.

Therefore, the peak dynamic forces at transitions due to the passage of trains can be reduced by two main measures: one is reducing the track settlement difference; the other is lowering the stiffness of the structure.

REFERENCES

- D.E. Newland and H.E.M. Hunt (1995). "Theoretical investigation of track dynamic settlement". July 1995.
- Hu Hanbing (2008). "Behavior of railway transition zone under dynamic loading", UNESCO-IHE & Deltares, MSc. Thesis, April 2008.
- P.K. Wiersma and B. Dirks (2005). "AEAT/03/3600113/007. Vervolgstudie Cambridgemodel deelonderzoek 2: validatie van het mathematisch model". April 2005.
- P. Meijers and P. Hölscher (2007). "Lasting flat roads and railways / Literature study of knowledge and experience of transition zones", GeoDelft, 415990-0011 v02.
- V. Hopman and P. Hölscher (2007). Delft Cluster Project Railway Transition Zones and Switches / Monitoring Plan of Field Test. GeoDelft, 415990-0024 v02 Draft, December, 2007.

Dynamic Characteristics of Subgrade Bed for Ballastless Track

KONG Xianghui¹, JIANG Guanlu², XIAO Dong², LI Anhong³

¹School of Transportation Engineering, Shandong Jianzhu University, Jinan, Shandong 250101, China; kongxh2009@163.com

²School of Civil Engineering, Southwest Jiaotong University, Chengdu, Sichuan 610031, China

³China Railway Eryuan Engineering Group Co. Ltd, Chengdu, Sichuan 610031, China

ABSTRACT: In order to study the characteristics of dynamic stress in subgrade bed, large-scale ballastless track dynamic model test was made based on Suining-Chongqing high-speed railway. The results indicate that the dynamic stress has an uneven distribution along subgrade cross section, and the unevenness is more and more obvious as the dynamic loading increases. Along the depth direction, the dynamic stress in the surface layer of subgrade bed decays more rapidly than in the base layer. The dynamic stress can be calculated by Odemark and Elasticity theory as its distribution under foundation slab of ballastless track is simplified uniform along lateral direction, and triangular along longitudinal direction. On the premise of dynamic stress was known, this paper assumed each soil layer of subgrade to be one-dimensional compression model and determined the limited thickness of compression layer. Based on this, an approach of conversion from multi-layer system to the equivalent Winkler foundation was explored, and the coefficient of subgrade reaction in different working conditions can be acquired.

1 INTRODUCTION

The development trend of railway in the world is high speed and heavy duty, both of which can significantly increase the dynamic interaction between vehicle and railway. In order to improve the stability and riding comfort, and to reduce maintenance of the track, the world railway scholars have carried out the research of ballastless track since the beginning of 1960s, substituting overall curing track composed with concrete and asphalt mixture for granular ballast. Today, some countries have taken the technology of ballastless track as a main policy. The distribution law of subgrade dynamic stress and the value of coefficient of subgrade reaction is an prerequisite for establishing reasonable subgrade support stiffness (Heath 1972, JIANG 1997, CAI 1999, BIAN 2007, Auersch 2008). In general, the

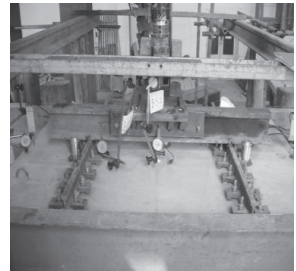
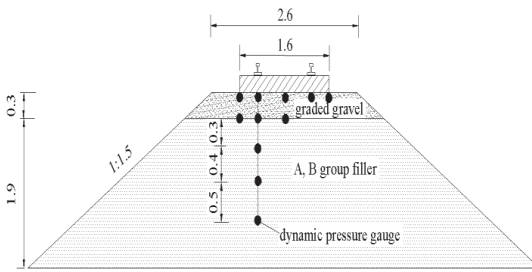
subgrade support stiffness and coefficient of subgrade reaction still presents obvious nonlinear relationship even in the elastic field. The main reasons of the nonlinearity can be summarized as the following three points: ① Loading range; ② Deformation range; ③ Length of loading time (JIANG 2010).

To solve these problems mentioned above, the dynamic characteristics of subgrade must be grasped, especially within the subgrade bed. Combination the test section of ballastless track in Suining-Chongqing railway, this paper studied the distribution property of dynamic stress both along the cross section and the depth direction of subgrade through the ballastless track dynamic model test indoor. Based on this, the theory solutions of dynamic stress and coefficient of subgrade reaction is discussed respectively.

2 DYNAMIC MODEL TEST OF SUBGRADE BED

2.1 Test Introduction

Fig. 1 shows structural dimensions, instrument layout and loading device of ballastless track dynamic model. The height of subgrade bed model is 2.2m, with its surface width of 2.6m and slope of 1:1.5. The horizontal width of concrete foundation slab is 1.6m, with longitudinal length of 1.12m and thickness of 0.2m. The surface layer and base layer of subgrade bed is composed of graded gravel, A,B group filler, respectively. The model boundary conditions is considered as a problem of plain strain, and fixed with steel retaining wall. Cyclic loading is divided into 9 levels which are 41.5-51.5 kN, 36.5-56.5 kN, 31.5-61.5 kN, 26.5-66.5 kN, 21.5-71.5 kN, 16.5-76.5 kN, 11.5-81.5 kN, 6.5-86.5 kN and 0-93 kN. The vibration numbers of each level of loading are 6000 (FENG 2008).



(a) Model Structure (Unit: m)

(b) Loading Device

FIG1. Subgrade bed of dynamic model test.

2.2 Test Results

Fig. 2(a) shows the lateral distribution form of dynamic stress in the subgrade

surface under each level of dynamic loading. It can be seen that the dynamic stress is constantly increasing with the improvement of applied loading. The results also indicate that the dynamic stress has an uneven distribution along subgrade cross section, and the unevenness is more and more obvious as the dynamic loading increases. The largest dynamic stress takes place under the concrete slab at the track position, while the dynamic stress under the midline and the edge of the slab is small. This type of distribution is also called saddle form.

From Fig. 2(b), it can be seen that the dynamic stress gradually decreases along the depth direction of subgrade in each level of dynamic loading, and its value in the surface layer of subgrade bed decays faster than that in the base layer. The dynamic stress in the interface between the surface layer and the base layer of subgrade bed is about 50%~65% of the subgrade surface, which means the dynamic stress has been decayed by 35%~50% in the field of surface layer of subgrade bed. It indicates that the surface layer bears most of the dynamic action, and puts forward higher requirements to its filler.

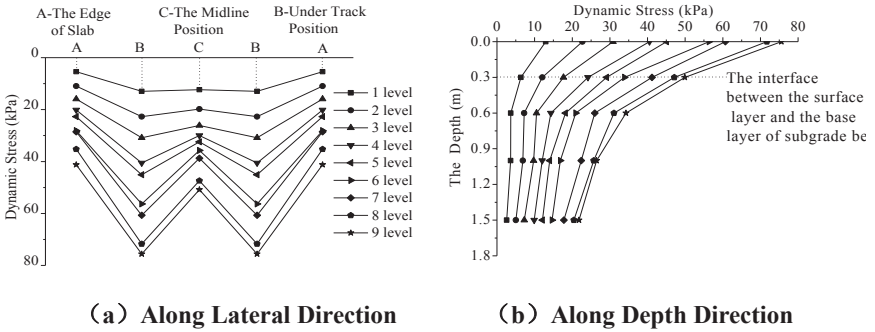


FIG2. Distribution law of dynamic stress of subgrade.

3 CALCULATION METHOD OF DYNAMIC STRESS

For the structure of ballast track, Wang Q. C. introduced a method to calculate the dynamic stress by associating Odemark and Elasticity theory (WANG 1999). Zhang Q. L. pointed out that the calculation results were more accurate if the effective supporting length of sleeper was 1.1m (ZHANG 2005). The first part of (1) is Odemark modulus and thickness equivalent conversion formula, the second part is the Boussinesq stress solution.

$$h_e = h \sqrt[3]{\frac{E_i}{E_0}}, \quad \sigma_z = \frac{P_0}{2\pi} \left[\frac{m \times n}{\sqrt{1+m^2+n^2}} \times \frac{1+m^2+2n^2}{(1+n^2)(m^2+n^2)} + \arctan \frac{m}{n\sqrt{1+m^2+n^2}} \right] \quad (1)$$

Here, E_i is the modulus of layer i , E_0 is the modulus of bottom layer, h_e is conversion thickness, P_0 is the dynamic stress of sleeper bottom. In addition, $m=L/B$, $n=z/B$, where L is the length of loading area, B is the width of loading area, z is the depth under load corner.

For the structure of ballastless track, the method mentioned above is effective if the distribution of dynamic stress under foundation slab is known. Although the dynamic stress is uneven in the lateral distribution, the form of load only affects the stress in the vicinity according to the Saint-Venant principle. In order to facilitate the calculation, the distribution of dynamic stress under foundation slab was simplified uniform along cross section, and triangular along longitudinal direction (DONG 2008). Fig. 3 shows the calculation and test results of subgrade bed model, and the two results have a good agreement.

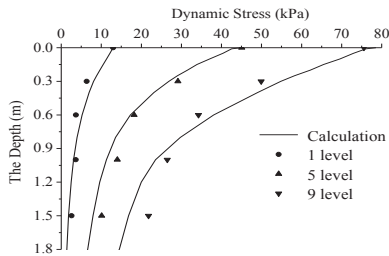


FIG.3. Calculated and measured values of dynamic stress.

4 THE COEFFICIENT OF SUBGRADE REACTION

The Winkler foundation model has been adopted in the structural design of ballastless track on soil subgrade. It assumes that the pressure of any point underside the slab is proportional to its displacement, namely, $p=ks$, here k is the coefficient of subgrade reaction, and its correct value or not directly affects the rationality of design. The value of k is usually be determined by the following methods. ①Large load board test; ②The relationship between k and K_{30} ; ③Experience value. However, these methods all have their own shortcomings.

On the premise of dynamic stress was known, this paper proposed a method of calculating the value of k based on the elastic parameters and thickness of each soil layer.

4.1 The Process of Derivation

The railway subgrade is a multi-layer structure, so the elastic modulus and Poisson's ratio in different layers are not the same. The primary task of calculation of k is converting the multi-layer system into a homogeneous single layer. Assumed each soil layer of subgrade to be one-dimensional compression model, the

compression modulus of each soil layer (E_{si}) can be calculated by (2).

$$E_{si} = \frac{E_i(1-\nu_i)}{(1+\nu_i)(1-2\nu_i)} \tag{2}$$

(3) is used to define the average compression modulus of the whole subgrade (E_s^*).

$$E_s^* = \frac{\sum \sigma_{di}}{\varepsilon} = \frac{\sum \sigma_{di}}{\sum \varepsilon_i}, \quad \sigma_{di} = \frac{1}{H_i} \int_{H_i}^{H_{i-1}} \sigma_d dh, \quad \varepsilon_i = \sigma_{di} / E_{si} \tag{3}$$

Where σ_{di} , ε_i , H_i and E_{si} is average dynamic stress, dynamic strain, thickness and compression modulus of i layer soil, respectively.

Both dynamic stress and deformation decreases along the depth direction of subgrade. From a practical point of view, the deformation can be approximated as zero below a certain depth, i.e. the thickness of limited compression layer (H_0), determined by the formula: $\sigma_d/\gamma H_0=0.1$. Here, γ is soil bulk density. It should be noted that H_0 equals H if H_0 is greater than the actual soil thickness H .

Then the multi-layer system can be converted into a homogeneous single layer through (3), showed in Fig. 4.

The homogeneous single layer is divided into some sheet with small thickness, the stress, strain and thickness of each sheet are represented by σ_{dj} , ε_j and h_j . The total deformation of subgrade can be calculated by (4), its calculation schematic diagram showed in Fig. 5. Here, A_e is the area of region OBCD.

$$s = \sum (\varepsilon_j h_j) = \sum \left(\frac{\sigma_{dj} h_j}{E_{sj}} \right) = \frac{1}{E_s^*} \sum (\sigma_{dj} h_j) = \frac{1}{E_s^*} \int_0^{H_0} \sigma_d dh = \frac{1}{E_s^*} A_e \tag{4}$$

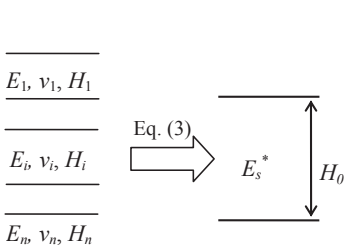


FIG4. Multi-layer system be converted to a homogeneous single layer.

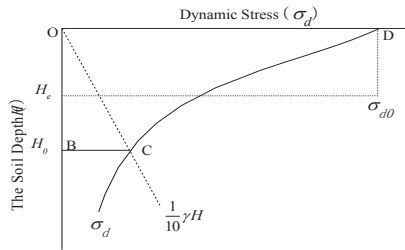


FIG5. Distribution of dynamic stress in homogeneous single layer.

The total deformation in Winkler model can be obtained by (5), here, H_e is equivalent depth; σ_{d0} is the dynamic stress of subgrade surface.

$$s = \sum (\varepsilon_j h_j) = \frac{\sigma_{d0}}{E_s^*} H_e, \quad H_e = A_e / \sigma_{d0} \tag{5}$$

Then, the coefficient of subgrade reaction k can be calculated by (6).

$$k = \sigma_{d0} / s = E_s^* / H_e \tag{6}$$

Fig. 6 shows the process of conversion from single layer be to the equivalent Winkler foundation.

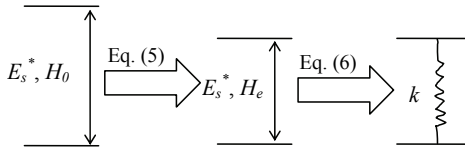


FIG.6. Single layer converted to the equivalent Winkler foundation.

4.2 Experimental Verification

Table 1 shows the calculated and measured values of k in different loading conditions for 2 layers subgrade. For graded gravel, $E=180\text{MPa}$, $\nu=0.3$; for A, B group filler, $E=110\text{MPa}$, $\nu=0.3$. It can be seen that the deviation between calculated results and measured results is in the range of 1%~9%, a good agreement demonstrates that the method proposed above is effective.

Table 1. Calculated and Measured Values of k

| Loads | k (kPa/mm) | | Loads | k (kPa/mm) | |
|---------|--------------|------|---------|--------------|------|
| | Calculation | Test | | Calculation | Test |
| 1 level | 316 | 341 | 6 level | 221 | 203 |
| 2 level | 279 | 303 | 7 level | 213 | 196 |
| 3 level | 268 | 266 | 8 level | 203 | 190 |
| 4 level | 257 | 253 | 9 level | 197 | 183 |
| 5 level | 235 | 218 | | | |

5 CONCLUSIONS

The dynamic stress is constantly increasing with the improvement of applied loading, and it has an uneven distribution along subgrade cross section, and gradually decreases along the depth direction. The value in the surface layer decays faster than that in the base layer of subgrade bed.

The values of dynamic stress can be calculated by Odemark and Elasticity theory,

and they have a good agreement with the test results. It should be noted that the distribution of dynamic stress under foundation slab of ballastless track is simplified uniform along lateral direction, and triangular along longitudinal direction.

On the premise of dynamic stress was known, this paper assumed each soil layer of subgrade to be one-dimensional compression model, and determined the limited thickness of compression layer. On this base, the theoretical approach of conversion from multi-layer system to the equivalent Winkler foundation was explored. The coefficient of subgrade reaction can be acquired by employing the method mentioned above in different working conditions, and a good agreement with the measured results demonstrates that the method is effective.

REFERENCES

- Auersch L. (2008). "Dynamic Interaction of Various Beams With the Underlying Soil-finite and Infinite, Half-space and Winkler Models." *European Journal of Mechanics (A/Solids)*, (27): 933-958.
- BIAN Xuecheng. (2007). "Characteristics of Layered Ground Responses Under Train Moving Loads." *Chinese Journal of Rock Mechanics and Engineering*. 26(1): 182-189.
- CAI Ying. (1999). "Study of the Critical Dynamic Stress and Permanent Strain of the Subgrade-soil Under the Repeated Load." *Journal of Southwest Jiaotong University*, 31 (4): 1-5.
- DONG Liang. (2008). "Experimental Validation of A Numerical Model for Prediction of the Dynamic Response of Ballastless Subgrade of High-speed Railways." *China Civil Engineering Journal*, 41 (10): 81-86.
- FENG Lichen. (2008). "Experimental Study on Dynamic Characteristics for Ballastless Track Subgrade Bed of High Speed Railway." *Railway Engineering*, (8): 78-81.
- Heath D L. (1972). "Design of Conventional Rail Track Foundation." *Proc. of the Institution of Civil Engineers*, 51 (3): 49-57.
- JIANG G L. (1997). "Inherent and Stress-state-induced Anisotropy in Very Small Strain Stiffness of a Sandy Gravel." *Geotechnique*, 47 (3): 509-521.
- JIANG Guanlu. (2010). "Dynamic Characteristics of Soil Subgrade Bed for Ballastless Track." *Journal of Southwest Jiaotong University*, 45 (6): 855-862.
- WANG Qichang. (1999). "Civil Engineering of High-speed Railway." Chengdu: Southwest Jiaotong University Press.
- ZHANG Qianli. (2005). "Structural Analysis and Design Method for Subgrade Bed of High-speed Railway." *China Railway Science*, 26 (6): 53-57.

Study on Seepage-Induced Debris Flows Initiation under the Rainfall Action for Loose Soil

Chi LI¹, Wenhui ZHU¹ and Xiaobing LU²

¹ College of Civil Engineering, Inner Mongolia University of Technology, 49 Aimin Road, Huhhot, 010051, Inner Mongolia, China; tjdxlch2003@126.com

² Institute of Mechanics, Chinese Academy of Science, 15 Beisihuan West Road, Beijing, 100084, China; xblu@sina.com

ABSTRACT: Test soils were collected from debris flow source area in the Weijia groove, Beichuan county, Sichuan province. Indoor artificial rainfall model tank test has been designed; it can be used to simulate the process of debris flow initiation for slope loose soil under the rainfall action. The debris flow starting condition and confluence process have been measured in this test, through the analyzing the relationship of the rainfall intensity, duration time before the starting, and the total rainfall capacity at the starting moment, the relationship between the volume of production flow and the water to soil ratio in production flow. All these research results can be used to simulate debris flow initiation mechanism obtained from model test focused on the seepage-induced action and its influence factors.

INTRODUCTION

When it mentions to the research of debris flow, one of the main concerns is how debris flows are initiated. It is the basis of disaster prevention and reduction. Previous research has proven that the earthquake zone usually is the zone of most frequent debris flow activity in the world (USGS, 2011).

Iverson, et al. (1989), applying the growth and dissipation of pore water pressure in soil mechanics theory, studied the mechanisms of growth, dissipation, and maintenance of pore water pressure during the initiation and movement of debris flows (Iverson, R. M., 1997a; Iverson, R. M., 1997b; Iverson, R. M. et. al., 1989). Most previous research works focused on the mechanisms of rainfall induced slope failures (Sladen, J. A., et. al., 1985; Fleming, R. W., et. al., 1989; Sasitharan, S., et. al., 1994; Anderson, S. A., et. al., 1995; Zhu, J. H., et. al., 1998). The transformation to flows from rainfall-induced slides was commonly simulated by tests on anisotropically consolidated-undrained and constant-shear drained saturated specimens. Their test results showed that most failures involved some relatively slow initial deformation, followed by a rapid transformation of the soil mass into a viscous liquid. The development of a debris flow was separated into two different mechanisms, the initial

drained slope failure followed by undrained mobilization of the flow.

Applying the unsaturated soil shear strength theory, the causes of rainfall-induced debris flow and its formation process has been studied. Brand (1981) postulated that the decrease of suction in the soil causes a reduction in effective normal stress on the potential failure surface, which in turn lowers the shear strength. The rainfall action mechanism and mechanical property change characteristics have been revealed for loose detrital material. The influence factors of the matrix attraction of unsaturated soil slope, such as intensity of rainfall, duration of rainfall, and saturated permeability coefficient of soil have been analyzed through numerical simulation. Above research showed the main factor contributing to rainfall-type debris flow initiation is the significant loss of attraction from the soil matrix due to rainfall infiltration (Chen, H., et. al., 2004; Take, W. A., et. al., 2003).

This paper focuses on the Wenchuan earthquake of May 12, 2008, which took place in the Beichuan County, Sichuan province. Weijia groove, which located in the Beichuan County, have steep terrain landform plus loose material accumulated on the slope after the earthquake, it can be provides the beneficial terrain conditions and abundant material source for debris flow initiation. After the earthquake, rain storms or strong rain have taken place in the Beichuan County in the next two months, these have contributed a plentiful water source to the initiation of debris flows, it became a main side effect or secondary disaster following the earthquake. As the research object, the landslide translating into debris flow under rainfall in the Beichuan County has been studied by author through numerical simulation (Li, C., et. al., 2010; Cui, P., 1992; Cui, P., 1993). The effects of the slope ratio, rainfall strength and soil moisture conditions have been analyzed. The initiation expansion of the plastic zone and the development of the tensile stress zone in the slope under rainfall have been investigated. It indicated that the zone with the high pore water pressure mainly near the slope toe with one fifth of the slope height. The pore water pressure at the slope toe was the highest, and decreased from the toe to top. The large horizontal displacements of the slope were mainly near the slope toe with one fifth of the slope height, and debris flow initiation under rainfall first began at the slope toe. Therefore, with the increase of the slope angle and rain strength and saturation degree, the stability of the slope decreased gradually to trigger the debris flow initiation. But the process of debris flow initiation for slope soil, especially, for loose soil with certain content of fine particle, need to be simulate under the rainfall action, with the purpose of understanding the humidifying process from unsaturated soil to saturated soil. In this study, we will focus the process of debris flow initiation for slope soil under the rainfall action, the indoor artificial rainfall model tank test will be designed; it can be used to simulate the process of debris flow initiation for loose soil under the rainfall action. All these research results can be used to present debris flow initiation mechanism originated from the seepage-induced action and its influence factors.

EXPERIMENT

The soil used in this study is collected from the loose soil in the Weijia groove debris flow source area. A grain-size analysis test was done on the retrieved soil. In this process, some particles with a grain size greater than 5mm are taken away, the

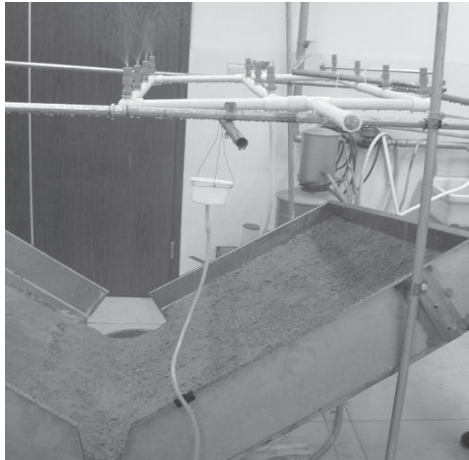


FIG. 2. Model tank device.

Experimental Method and Procedure

Be as the experimental variables, the rainfall intensity, the unit weight of cumulative production flow and the water to soil mass ratio can be measured in the test, the relationship between these experimental variables is analyzed after the test.

Firstly, the soil masses which the dry unit weight is 1005 kg/m^3 and water masses which the original water content maintains 8.4% are weighted, respectively. Next, some dry soil masses and water masses are mixed together until the mixture is uniform, and the mixture is placed into the model tank in five layers for compaction, compacted and galled with each layer, and the same is done for a total of five layers. Furthermore, we prepare the artificial rainfall test using three different kinds of rainfall, the starting time and the finish time, the soil deformation and landslide are observed in each test. After each test, the rainfall intensity which means the rainfall within unit time are measured, the unit weight of cumulative production flow are tested, and the water to soil mass ratio can be calculated after drying in oven.

EXPERIMENTAL RESULTS AND DISCUSSION

Test Observations

Some interesting phenomena are found in this artificial rainfall test. During the rainfall, the soils begin to slide from the slope toe firstly, the length of slider is about 1/5 or so of the slope width along the slope width direction, we can see it in Fig.3 (a). After that, block of soil around the slope toe goes to slide, and corrode gradually in the form of convex arc shape upward, shown in Fig.3 (b). Especially, fluidal water can't form on the slope surface when the rainfall intensity is small. The soils slide integrity with piece by piece. The fluidal water accumulate on the slope surface when the

rainfall intensity is greater, the soil sliding more easily, and the top soil with liquefied or softening condition slide firstly.

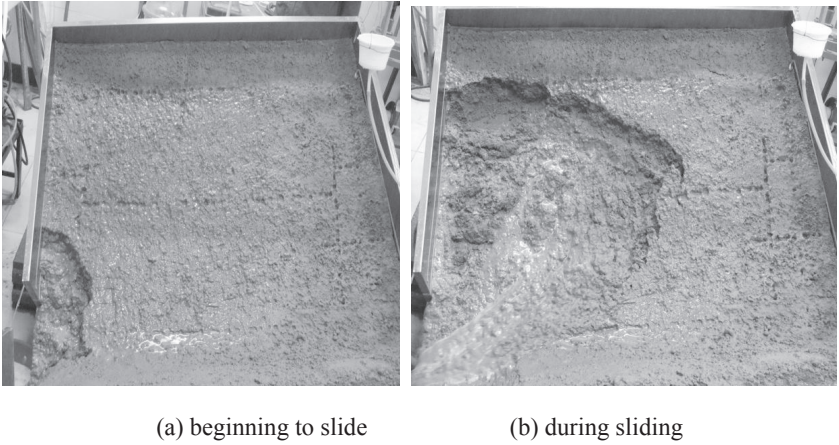


FIG.3. Test observations during the soil sliding.

Relationship between Experimental Variables

The relationship between slide starting time and the total rainfall is analyzed according to the three kind of different rainfall intensity, shown in Fig.4.

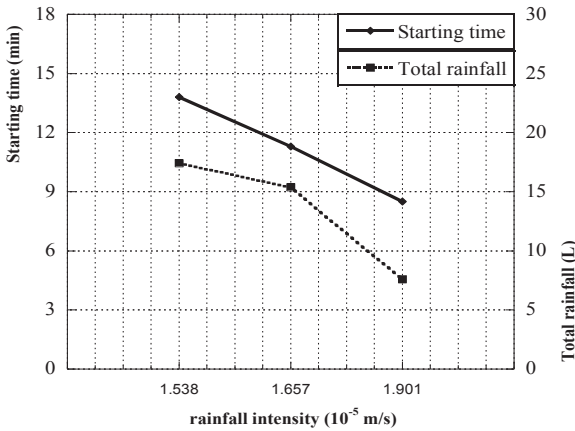


FIG.4. Relationship between starting time, the total rainfall and rainfall intensity.

From the Fig.4, we can see the starting time for the stable soil to slide shorten with the rainfall intensity increase, and the total rainfall also decrease. It shows that the scouring action from raindrop has a bad effect on the slope stability. This kind of

scouring action act the component force on the slope soil along inclined slope surface, and the component force increases with the increasing of rainfall intensity, the slope loose soil trend to slide with strong rainfall intensity, but the total rainfall is not large.

The relationship between rainfall intensity, cumulative production flow and water to soil mass ratio of cumulative production flow is analyzed, shown in Fig.5, Fig.6 and Fig.7, respectively. From these figures, we can see cumulative production flow increase with the increasing of rainfall intensity during the same rainfall duration, that is, the speed of production flow is faster with the greater rainfall intensity. But the water to soil mass ratio of cumulative production flow decrease with the rainfall duration developed. This shows that the slope soil needs more water source to trigger to product flow at the beginning of rainfall, however, at the end of rainfall, a small amount of water can stimulate the soil production flow. During the whole rainfall process, the soil cumulative production flow unit weight increase first, then decrease, the maximum cumulative production flow unit weight decrease gradually with the increasing of rainfall intensity.

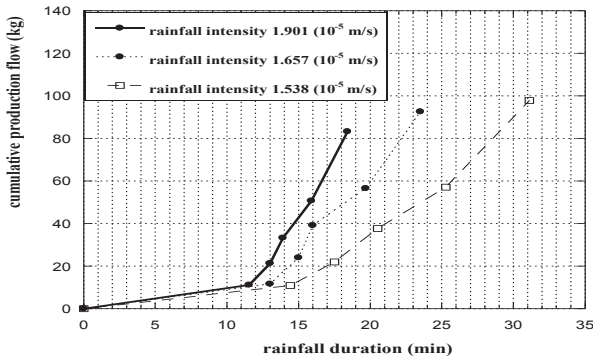


FIG. 5. Relationship between rainfall intensity and cumulative production flow.

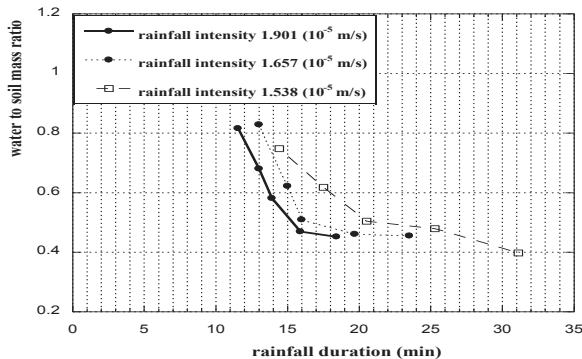


FIG.6. Relationship between rainfall intensity and the water to soil mass ratio of the cumulative total production flow.

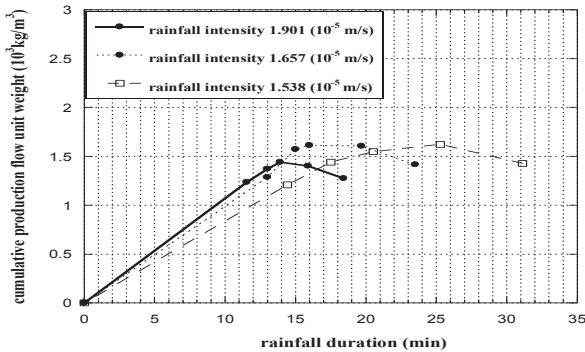


FIG.7. Relationship between rainfall intensity and the cumulative production flow unit weight.

CONCLUSIONS

Through the indoor artificial rainfall test, the process of debris flow initiation for the soil accumulated on the slope has been simulated under the rainfall action. The relationship between rainfall intensity, duration time before the starting and the total rainfall at the starting moment have been analyzed. The debris flow starting condition and confluence process have been measured in this test. All these research results can be used to present debris flow initiation mechanism originated from the seepage-induced action and its influence factors. Study on debris flow initiation through field observation and field experiment need to conduct further for the objective of the debris flow initiation mechanism.

ACKNOWLEDGEMENTS

This article's topic is based on the National Project 973 "Wenchuan earthquake mountain hazards formation mechanism and risk control" (2008CB425800), a project of the Chinese Academy of Sciences Mountain Hazards and a joint project of the Environment Institute and the Chinese Academy of Mechanics.

The authors acknowledge the project supported by the program for New Century Excellent Talents in University of Ministry of Education of China (NCET-11-1016), and supported by the program for Young Talents of Science and Technology in Universities of Inner Mongolia Autonomous Region (YTST).

REFERENCES

- Anderson, S. A., and Sitar, N. (1995). "Analysis of rainfall-induced debris flows." *J. Geotech. Eng.*, Vol. 121(7): 544-552.
- Brand, E. W., (1981). "Some thoughts on rain-induced slope failures." *Proc., 10th Int. Conf. on Soil and Mechanical Foundation Engineering*, Stockholm, Sweden, Vol. 3:

373-376.

- Cui, P. (1992). "Studies on Condition and Mechanism of Debris Flow by Means of Experiment." *Chinese Science Bulletin*, Vol. 37(9): 759-763.
- Cui, P. (1993). "The sudden change properties of debris flow initiation." *Journal of Natural Disasters*, Vol. 2 (1): 53-61.
- Chen, H., Lee, C. F. and Law, K. T. (2004). "Causative mechanisms of rainfall-induced fill slope failures." *Journal of Geotechnical and Geoenvironmental Engineering*, Vol. 130(6): 593-602.
- Fleming, R. W., Ellen, S. D., and Albus, M. A. (1989). "Transformation of dilative and contractive landslide debris into debris flow-An example from Marin County," *California. Eng. Geol.*, Amsterdam, Vol. 27: 201-223.
- Iverson, R. M. and Lahusen, R. G. (1989). "Dynamic pore-pressure fluctuations in rapidly shearing granular materials." *Science*. Vol. 246: 796-799.
- Iverson, R. M. (1997a). "The physics of debris flows." *Reviews of Geophysics*, Vol. 35(3): 245-296.
- Iverson, R. M., Reid, M. E. and LaHusen, R. G. (1997b). "Debris-flow mobilization from landslides." *Annual Review of Earth and Planetary, Sciences*. Vol. 25: 85-138.
- Li, C., Zhu, W. H., Lu, X. B. and Cui, P. (2010). "Studied on landslide translating into debris flow under rainfall." *China Civil Engineering Journal*, Vol. 43: 371-376.
- Sladen, J. A., Hollander, R. D., and Krahm, J. (1985). "The liquefaction of sand, a collapse surface approach." *Canadian Geotechnical Journal*, Vol. 22(4): 564-578.
- Sasitharan, S., Robertson, P. K., Segoo, D. C., and Morgenstern, N. R. (1994). "State-boundary surface for very loose sand and its practical implications." *Canadian Geotechnical Journal*, Vol. 31(3): 321-334.
- Take, W. A. and Bolton, M. D. (2003). "Tensiometer saturation and the reliable measurement of soil suction," *Géotechnique*, Vol. 53(2):159-172.
- Zhu, J. H., and Anderson, S. A. (1998). "Determination of shear strength of Hawaiian residual soil subjected to rainfall-induced landslides." *Geotechnique*, Vol. 48(1): 73-82.

The Reasonable Layout of Cross Passages for Qianjiang River Tunnel based on seismic analysis

Qizhu Jiao¹, Di Zhang², Shaoming Liao³, Yizhi Xu⁴

¹China Railway No.4 Survey and Design Group Co., Ltd., 745 Peace Avenue, Wuhan 430063, P. R. China; jfocus@163.com

²China Railway No.4 Survey and Design Group Co., Ltd., 745 Peace Avenue, Wuhan 430063, P. R. China; zdiok@126.com

³Department of Geotechnical Engineering, Tongji University, 1239 Siping Road, Shanghai 200092, P. R.China; engcent@tongji.edu.cn

⁴Department of Geotechnical Engineering, Tongji University, 1239 Siping Road, Shanghai 200092, P. R.China; xyz.61533@yahoo.com.cn

ABSTRACT: Numerical modeling and Response Displacement Method are applied to assess the effects of the presence of cross passages and geology formations on the seismic responses of the Qianjiang River tunnel, in order to determine the proper locations of cross passages. The numerical analysis shows that the presence of cross passages affects the longitudinal seismic response of the main tunnel significantly within 25m distance from the intersections of cross passages with main tunnels. So the possible local failure of the intersections will be a major concern. This is largely attributed to the complicated geologic formations and irregular ground conditions. The analysis based on the Response Displacement Method indicates that cross passages in flat and uniform ground layers can mitigate the local failure at the intersections. Optimal location for cross passages are proposed based on the detailed analysis of the geologic profiles of Qianjiang River Tunnel.

INTRODUCTION

There has been a serious dispute among the tunnel engineers in China since 2003 over whether the cross passages should be constructed for Qianjiang River Tunnel, especially the risks associated with constructing cross passages in saturated soft ground. The catastrophic failure of the No. 4 route in Shanghai happened during the last step excavating a cross passage under Huangpu river taught a major lesson. Another great concern is the effect of cross passages on the structural safety of tunnels during earthquakes. The local failure at the intersections of under river cross passages in soft ground can cause it to collapse, which can result in severe

catastrophic failure of the whole tunnel. These made the layout of the cross passages a crucial task in design.

Damages of tunnels during recent earthquakes, i.e., the 1999 Chi-Chi, Taiwan earthquake (Wang 2002), have revived the interest in studying the safety of tunnel structures subjected to earthquake shaking. Significant amount of researches have been conducted to estimate the seismic responses of tunnel lining along the transverse direction over the past decades (Hashash et al. 2005, Park 2009, Chen 2011). However, the longitudinal responses (bending, axial compression and extension) are also essential to the safety of tunnel during seismic excitation (He and Koizumi 1999).

Regarding the longitudinal seismic response of shield tunnel, Yukio SHIBA, Kazuhiko KAVASHIMA, Naomi OBINATA and Takashi KANO evaluated the axial force and bending moment in linings subjected to ground displacement with sinusoidal distribution along the tunnel axis by assuming the linings to be uniform beams (Yukio et al. 1989). He and Koizumi (1999) studied the dynamic responses in the longitudinal direction of shield tunnel in non-uniform ground under axial and transverse seismic loads. The study revealed the adverse consequences for shield tunnel located in irregular ground.

In the previous studies, the Response Displacement Method were usually used as a simplified approximation with and the inertia of the structure ignored. As some studies have pointed out, tunnels were designed to accommodate the free-field ground deformations for tunnels constructed in stiff ground. But for tunnels in soft soils, the soil-structure interactions should be considered (Shahrour et al. 2010). The criteria of whether soil-structure interaction should be considered can be checked via the flexibility index, F , which measures the ability of the lining to resist distortion from the ground (Wang 1993):

$$F = \frac{2E_m(1-\nu_l^2)R^3}{E_l(1+\nu_m)t_s^3} \quad (1)$$

where E_m is Yong's modulus of the surrounding soil, E_l is Yong's modulus of the structure material, ν_m is Poisson's ratio of the surrounding soil, ν_l is Poisson's ratio of the structure material, t_s is the thickness of the cross-section, and R is the structure radius (Kouretzis et al. 2006).

A sound engineering approach is to ignore overall the soil-structure interaction (SSI) only if values of the calculated flexibility index is higher than 20 (Hendron and Fernandez 1983, O'Rourke and Liu 1999).

In this research, the impact of the longitudinal seismic response of the main tunnels by the cross passages is firstly analyzed with a simplified numerical simulation, then the Response Displacement Method is employed to study the stresses of the intersections under different geology conditions and seismic forces. Finally optimal locations for cross passages of the tunnel are proposed.

PROJECT BACKGROUND

The ground formations that the tunnel passes through are generally silty clay, sandy silt, silty sand, mucky silty clay, clayed silt and silty clay, according to the geological investigation reports. The physical and mechanical properties of these formations are summarized in Table 1. And the longitudinal and typical transverse geology profiles are shown in FIG.1 and FIG.2.

Table 1. The properties of soil layers

| Soil layer No. | Soil description | Cohesion (kPa) | Angle of friction (°) | Shear velocity V_s (m/s) | Categories of soil layers |
|----------------|------------------|----------------|-----------------------|----------------------------|---------------------------|
| 1 | Plain fill | / | / | 92.7 | soft Topsoil |
| 2-2 | Silty clay | 15 | 19.8 | 94.0 | |
| 3-1 | Sandy silt | | | 130.5 | Soft soil |
| 3-2 | Silty sand | 15.2 | 19.1 | 155.0 | |
| 4-1 | Mucky silty clay | 16.3 | 16.4 | 139.3 | |
| 5-1 | Silty clay | | | 181.0 | Medium-soft soil |
| 5-2 | Silty clay | 24.8 | 20.1 | 240.0 | |
| 6-3 | Silty clay | / | / | 313.7 | Medium-hard soil |

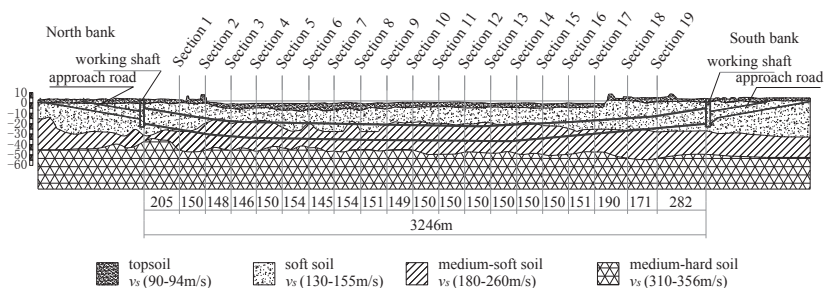


FIG.1. Geologic formation along the longitudinal direction of the tunnel

THE EFFECT OF THE PRESENCE OF CROSS PASSAGES

The dynamic analysis module of FLAC^{3D} program is employed to evaluate the effects of cross passages to the longitudinal seismic response of the main tunnels. The calculation is based on the explicit finite difference scheme to solve the full

equation of motion, using lumped grid point masses derived from the real density of surrounding zones (rather than fictitious masses used for static solution). This formulation can be coupled to the structural element model, thus permitting dynamic analysis of soil-structure interaction. No slip is considered between the tunnel structure and the surrounding soil mass, and the tunnel lining are simulated as continuum structure for simplified analysis in this study.

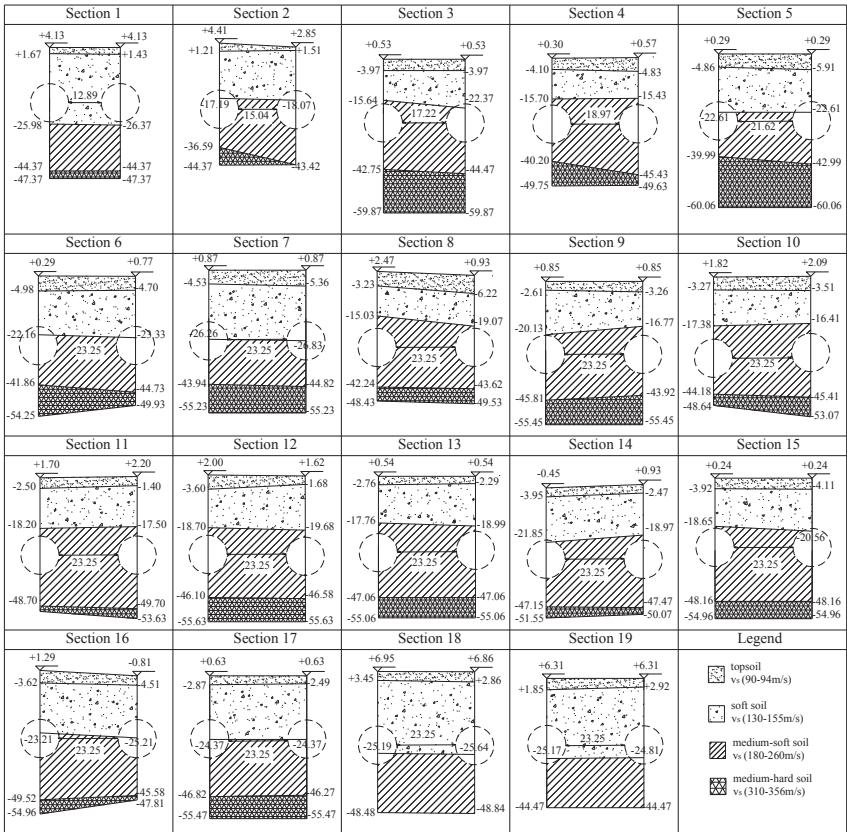


FIG.2. Typical sections of geologic formations along the Qianjiang River tunnel

For convenience, the nodes and the elements of the numerical model is created using FEM program ANSYS, which is extremely powerful in pre-processing, and then be imported into FLAC^{3D}. FIG.3, FIG.4, FIG.5 and FIG.6 show the detailed information about the model. The global model is excited at grid points at the base by a uniform Cosine curve type of acceleration along the axis of cross passage (to simulate the shear wave excitation).

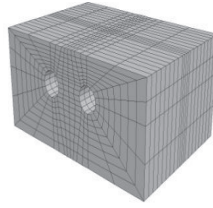
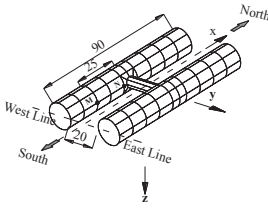


FIG3. cross passage FIG4. Meshed model FIG5. Meshed tunnel lining

The soil mass is considered to be mohr-coulomb material with specific weight $\gamma = 19 \text{ KN/m}^3$, friction angle $\phi = 15^\circ$, and cohesion $c = 20 \text{ KN}$. The tunnel linings are simulated as isotropic linear elastic material with Young’s modulus $E = 30 \text{ GPa}$ and Possion’s ratio of $\nu = 0.2$. The damping of the whole model is neglected, so the effect of the presence of cross passage is analyzed conservatively in this study.

Point M, shown in FIG3, 25m (4.17 times the diameter of cross passage) away from the intersection, was chosen for analysis. FIG.6 compares the acceleration-time responses of the main tunnel under two conditions (i.e., “tunnel with cross passage” and “tunnel without cross passage”) at point M. The curves show that the presence of cross passage even reduce the response longitudinal accelerations of the main tunnel compared with “tunnel without cross passage”, despite that the effect is not so significant (within 10% at the largest gap). However, as shown in FIG.7, the response shear stresses at the intersection is much bigger due to the stress concentration effect. The result indicates that the presence of cross passage even makes the main tunnel safer at a certain distance away from the cross passage, and the local failure of the intersection may be the primary problem rather than the overall seismic response.

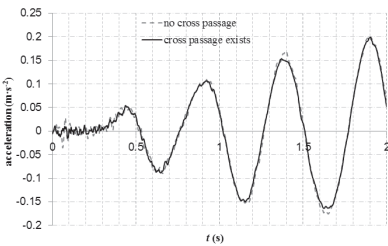


FIG6. Seismic response(point M)

| FLAC3D 3.00 | |
|----------------------------|----------------|
| Step 21/22 | Batch Progress |
| 10/10/2012 Mon am 17:02:13 | |
| Center | Origin |
| X = 1.000e+001 | Y = 0.000e+000 |
| Y = 1.000e+001 | Z = 0.000e+000 |
| Z = 1.000e+001 | Aug. 12.000 |
| Time 1.000e+001 | Step 1.001 |
| Iteration 1.000e+001 | Aug. 12.000 |
| Nodes 1.000e+001 | |
| El. 1.000e+001 | |
| SE1: Pressure-1 | |
| Min/Max = 1.000e+001 | |
| 1.4200e+001 to 2.000e+001 | |
| 2.000e+001 to 3.000e+001 | |
| 3.000e+001 to 4.000e+001 | |
| 4.000e+001 to 5.000e+001 | |
| 5.000e+001 to 6.000e+001 | |
| 6.000e+001 to 7.000e+001 | |
| 7.000e+001 to 8.000e+001 | |
| 8.000e+001 to 9.000e+001 | |
| 9.000e+001 to 1.000e+002 | |
| Min/Max = 1.00e+000 | |
| 1.000e+000 to 2.000e+000 | |
| 2.000e+000 to 3.000e+000 | |
| 3.000e+000 to 4.000e+000 | |
| 4.000e+000 to 5.000e+000 | |
| 5.000e+000 to 6.000e+000 | |
| 6.000e+000 to 7.000e+000 | |
| 7.000e+000 to 8.000e+000 | |
| 8.000e+000 to 9.000e+000 | |
| 9.000e+000 to 1.000e+001 | |
| Min/Max = 1.00e+000 | |
| 1.000e+000 to 2.000e+000 | |
| 2.000e+000 to 3.000e+000 | |
| 3.000e+000 to 4.000e+000 | |
| 4.000e+000 to 5.000e+000 | |
| 5.000e+000 to 6.000e+000 | |
| 6.000e+000 to 7.000e+000 | |
| 7.000e+000 to 8.000e+000 | |
| 8.000e+000 to 9.000e+000 | |
| 9.000e+000 to 1.000e+001 | |

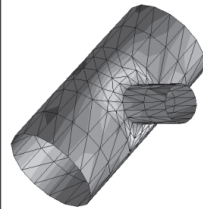


FIG7. stress concentration effect

THE EFFECTS OF GEOLOGICAL FORMATIONS

Response Displacement Method was employed here to assess the effects of geological formations on the response of the main tunnels. In Response Displacement Method, a “bed rock” layer whose shear wave velocity V_s is larger than 300m/s, usually needs to be determined first. Vibration of the soil layers above the

“bed rock” is assumed as a Cosine curve which culminates at the ground surface (shown as FIG.8a).

If a twin-tunnel with cross passages locates on a declining “bed rock” plane at an angle α from the horizontal plane along the transverse direction, the displacement response of the two tunnels will not be synchronous due to the diversities of their distances to the “bed rock” (shown as FIG.8a). Then extra tensions/shears for the cross passage will be induced, aggravating the stress states at the junction.

Because the distance of the main tunnel to “bed rock” ($C \cdot \tan(\alpha)$) increased with the increase of inclination of the “bed rock” plane, it is advisable to locate the cross passage at sections of the tunnel with small inclination.

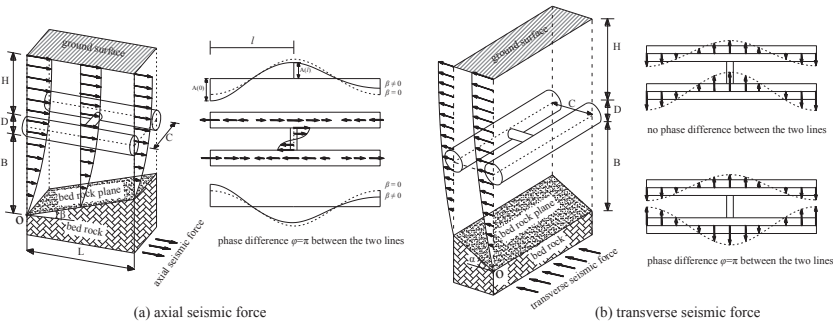


FIG.8. Tunnels acted by seismic forces(After He and Koizumi, 1999)

Similarly, as shown in FIG.8b, in case of an inclined “bed rock” plane, the peak magnitude of axial displacements will be somewhat different at different points along the longitudinal direction. It is also that the smaller of the β , the safer of the intersection of cross passage and local junction.

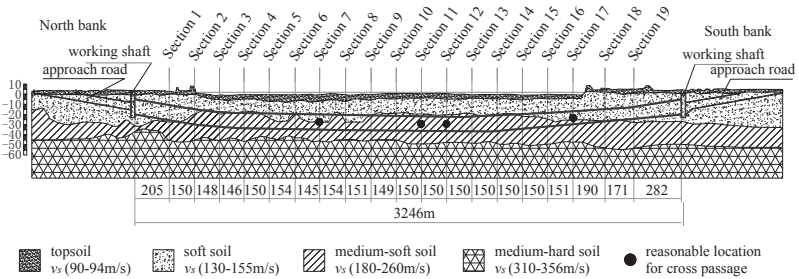


FIG.9. Reasonable locations for cross passage based on seismic analysis

Extending the above key ideas to a more general sense, reasonable locations for cross passages should be “uniform” and “regular” ground layers. In this regard, for Qianjiang River Tunnel, Section 7, Section 11, Section 12 and Section 17(FIG.10) are good choices both for the longitudinal and transverse direction according to FIG.1 and FIG.2. Additionally, the distance between adjacent cross passages needs to

consider factors such as emergency evacuation.

CONCLUSIONS AND DISCUSSIONS

The aim of this research was to study the seismic response of parallel twin-tunnel with cross passages along the longitudinal direction under earthquake shaking, and to provide advices on reasonable locations of cross passages for Qianjiang River Tunnel. The following conclusions are obtained based on computational and conceptual analyses:

Firstly, preventing the local failure of the intersections at cross passages should be the primary concern in design.

Secondly, the complicated formations of geology impose significant effects on stability and dynamic responses of the intersections at cross passages. Reasonable locations of cross passages can be decided on according to the inclinations of the “bed rock”. Another concern about the geological condition is the thick layer of silty sand at the south bank of the Qianjiang River, which is very prone to liquefaction under seismic action. It is therefore advised to avoid locating the cross passage in this area. Otherwise, measures should be taken to improve the ground to prevent the liquefaction.

Generally speaking, the regular space between cross passages required by evacuation in fire has a large weight in determining the distance of cross passages, but this factor alone is insufficient for determining the location of cross passages. Many factors should be considered in determining the location of cross passages. The optimal location needs to be set based on a comprehensive evaluation of all the relevant factors.

ACKNOWLEDGMENTS

The research funds provided by National Science Foundation of China (NSFC Grant No. 51078292), Ministry of Transport of China (Grant No. 2009-353-333-340), Kwang-hua Funds for College of Civil Engineering at Tongji University are acknowledged.

REFERENCES

- Chen Cheng-Hsun, Wang Tai-Tien, Jeng Fu-Shu, Huang Tsan-Hwei (2011). “Mechanisms causing seismic damage of tunnels at different depths.” *Tunneling and Underground Space Technology*, Vol.28:31-40.
- Hashash Youssef M.A., Park Duhee, Yao John I-Chiang (2005). “Ovaling deformations of circular tunnels under seismic loading, an update on seismic design and analysis of underground structures.” *Tunneling and Underground Space Technology*, Vol.20(5): 435-441.

- HE Chuan, KOIZUMI Atsushi (1999). A Study on the Seismic Behavior in the Longitudinal Direction of Shield Tunnels, Report of Science and technology, Waseda University.
- HE Chuan, KOIZUMI Atsushi (1999). A study on the Dynamic Behavior in Longitudinal Direction of Shield Tunnel in Non-uniform Depth Ground under Axial Seismic Force, *Journal of Structural Engineering*, JSCE (In Japanese) .,Vol.45A:1553-1564.
- HE Chuan, KOIZUMI Atsushi (1999). A Study on the Dynamic Behavior in Longitudinal Direction of Shield Tunnel in Non-uniform Depth Ground under Transverse Seismic Force, *Journal of Structural Engineering*, JSCE (In Japanese) .,Vol.45A:1565-1574.
- Hendron AJ Jr, Fernandez G. (1983). Dynamic and static considerations for underground chambers. Seismic design of embankments and caverns. New York: 157-197.
- Kouretzis George P., Bouckovalas George D., Gantes Charis J. (2006). "3-D shell analysis of cylindrical underground structures under seismic shear (S) wave action." *Soil Dynamics and Earthquake Engineering* .,Vol.26: 909-921.
- O'Rourke MJ, Liu X. (1999). Response of buried pipelines subjected to earthquake effects. Monograph Series MCEER.
- Park Kyung-Ho, Kullachai Tantayopin, Tontavanich Bituporn, Owatsiriwong Adisorn (2009). "analytical solution for seismic-induced ovaling of circular tunnel lining under no-slip interface conditions: A revisit." *Tunneling and Underground Space Technology*.,Vol.24(2): 231-235.
- Shahrour I., Khoshnoudian F., Sadek M., Mroueh H. (2010). "Elastoplastic analysis of the seismic response of tunnels in soft soils." *Tunneling and Underground Space Technology* .,Vol.25: 478-482.
- Wang JN. (1993). *Seismic design of tunnels*. Parsons Brinckerhoff Monograph.
- Wang W.L., Wang T.T., Su J.J., Lin C.H., Seng C.R., Huang T.H. (2001). "Assessment of damage in mountain tunnels due to the Taiwan Chi-Chi earthquake." *Tunneling and Underground Space Technology*.,Vol.16(3): 133-150.
- YUKIO Shiba, KAZUHIKO Kavashima, NAOMI obinata, TAKASHI kano (1989). "Evaluation procedure for seismic stress developed in shield tunnels based on seismic deformation method." *Proceedings of the Japan Society of Civil Engineers*.,Vol.404: 385-392.

Study on Stability and Failure Mode of Bedding Rock Slope Affected by Rock Mass Structural Plane Parameters

S Huang¹, B Song²

¹School of Civil and Environment Engineering, University of Science and Technology Beijing, P.O.Box 396, Beijing ST Xueyuan; PH 15210716603; FAX (010) 62334929; email:huangshuai3395@163.com

²School of Civil and Environment Engineering, University of Science and Technology Beijing, P.O.Box 396, Beijing ST Xueyuan; PH (010) 62334929; FAX (010) 62334929; email: b20100038@xs.ustb.edu.cn

ABSTRACT: Based on the discrete element numerical simulation, the change rules of safety factor and failure modes of slope influenced by parameters of rock mass structural plane is studied. Based on the principle of variance analysis of orthogonal experiment, significance of the rock structural plane parameters to the stability of slope is studied. It is shown that slope safety factor is linear increase in a certain range with the increase of the strength of the rock mass structural plane, and the failure modes shift gradually from the bedding sliding failure modes to the sliding-bending failure modes. Extent of variation of safety factors changes very little with the increasing of the normal and shear stiffness and spacing of rock structural plane, and the slope failure modes are mainly sliding failure modes. Slope safety factor firstly decreases and then increases and finally decreases with the increase of the rock structural plane dip angle, and failure modes shift from shearing slip failure modes to shearing slip and buckling failure modes and finally to the tilting failure modes. The impact of the rock structural plane cohesion to the slope stability is the greatest, and the stiffness is the least.

INTRODUCTION

Due to the difficulty in predicting landslide hazards, its occurrences cause great losses of lives and property. Landslide has always been and is still a major research focus in the field of geological hazards. Past engineering practices show that the bedding rock slope is most likely to be failure in the rock slopes, and it causes enormous loss of the engineering project and brings great losses of lives and property. Bedding rock slope influenced by spacing, dip angle, cohesion, internal friction angle

and stiffness of structural plane shows different degree of stability, and structural plane parameters play a decisive role on the stability of slope. Lin et al (2010) studied the relationship of structural plane dip angle and stability of slope. Lu et al (2011) studied the influence of cohesion and internal friction angle of structural plane on the slope stability. Wei et al (2011) studied the relationship of structural plane spacing and slope failure modes, and instability position of slope is at the foot of the slopes. However most of the studies focused on the influence of certain parameters of the structural plane on the slope stability and the significance of structural plane parameters on the stability of the slope is not studied. Besides, because of the division of structural plane to the rock mass, rock mass is three-phase medium of heterogeneous, anisotropy and discrete, thus, sliding surface is difficult to be determined, and the traditional limit equilibrium method is not suitable for bedding slope. Based on the strength reduction method, influence rules of rock structural plane parameters to safety factor and failure mode are studied, and significance of structural plane parameters on the stability of the slope is studied, which could provide guidance for the judgment of the stability of bedding rock slope.

PRINCIPLE OF STRENGTH REDUCTION METHOD

The principle of strength reduction method is that the shear strength indexes C and ϕ of rock mass are multiplied by a reduction factor, and then the reduced shear strength indexes C_F and ϕ_F of rock mass substitute the original shear strength indexes. The initial value of the reduction factor should be sufficiently small to guarantee for being elasticity at the beginning of reduction. The value of the reduction factor is then continuously increased, and the shear strength indexes decrease gradually until the slope is unstable. The reduction factor just before the instability of slope is the safety factor of slope, namely the ratio of practical shear strength indexes and reduced shear strength indexes, when the slope is instability, shown in Eq.(1) and Eq. (2).

$$C_F = C / F_s \quad (1)$$

$$\phi_F = \tan^{-1}((\tan\phi) / F_s) \quad (2)$$

Where C_F is the reduced cohesion, ϕ_F is the reduced internal friction angle.

NUMERICAL SIMULATION ANALYSIS of SLOPE

Numerical Simulation Model

Total length of Huaihua-Chongqing Railway is about 600km, and the terrain is complicated. After excavation, there are different forms of slope and the angles of slopes are more in the range of 20°~60°. The poor geological conditions that the slope confronts include bedding landslide etc, as shown in Fig.1. There are more than

200 bedding landslides, which occupied 14% of the main line length of the railway. The structural plane of the slope presents different forms including different spacing, different angle and different shear strength index, which becomes the important factors restricting the construction of railway engineering. Thus, selecting bedding rock slope along the railway line as the research object, the height of the slope is taken as 32m, and the slope angle is 45° . Horizontal displacements of the model lateral boundaries are constrained, and level and vertical displacements at the bottom boundary are constrained. The computation model is shown in Fig.1. The parameters of the bedding rock slope which are shown in Table 1. This paper focuses on the analysis of the stability of the slope affected by rock structural plane, thus, the parameters of rock structural plane are as the variables. The dip angle of rock structural plane is the minimum angle between rock structural plane and horizontal plane.

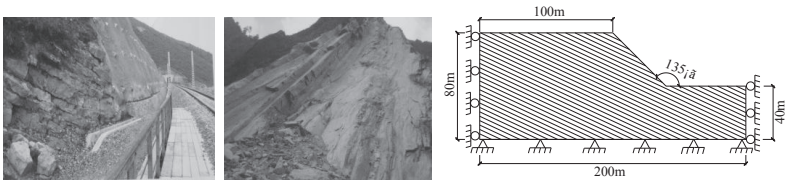


Fig.1. Computation model of the bedding rock slope

Table 1. Parameters of the Slope Rock Mass

| Object | Poisson ratio | Density ($\text{kg} \cdot \text{m}^{-3}$) | Bulk modulus (GPa) | Shear modulus (GPa) | Cohesion (MPa) | Internal friction angle ($^\circ$) | Tensile strength (MPa) |
|-----------|---------------|---|--------------------|---------------------|----------------|--------------------------------------|------------------------|
| Rock Mass | 0.3 | 2550 | 14.17 | 6.54 | 0.14 | 29 | 2.1 |

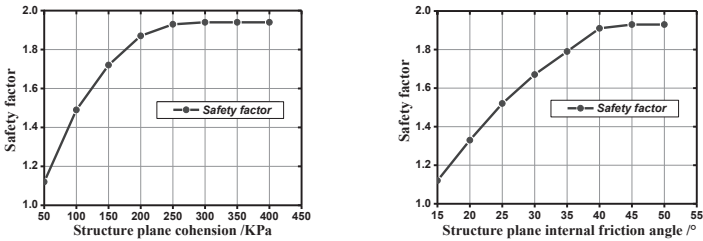
Stability Analysis of Slope Affected by Rock structural Plane

To study the change rules of safety factor and failure modes of bedding rock slope affected by rock structural plane parameters which are as the variables, the numerical procedure is shown in Table 2. When one of the parameters of rock structural plane is variable, values of other parameters will be the values of first numerical procedure.

Based on the numerical simulation analysis, influence rule of structural plane parameters to the slope safety factor is shown in Fig.2.

Table 2. Numerical Procedure of Rock Structural Plane Parameters

| Numerical procedure | Spacing (m) | Dip angle (°) | Cohesion (kPa) | Internal friction angle (°) | Normal stiffness (GPa · m ⁻¹) | shear stiffness (GPa · m ⁻¹) |
|---------------------|-------------|---------------|----------------|-----------------------------|---|--|
| 1 | 3 | 25 | 50 | 15 | 1 | 1 |
| 2 | 5 | 35 | 100 | 25 | 6 | 6 |
| 3 | 7 | 45 | 150 | 35 | 11 | 11 |
| 4 | 9 | 55 | 200 | 45 | 16 | 16 |
| 5 | 11 | 60 | 250 | 50 | 21 | 21 |
| 6 | 13 | 65 | 300 | 55 | 26 | 26 |
| 7 | 15 | 70 | 350 | 60 | 31 | 31 |
| 8 | 17 | 75 | 400 | 65 | 36 | 36 |

**Fig.2 Influence rule of structural plane strength parameters to safety factor**

As shown in Fig.2, when structural plane strength parameters values are less than the rock mass strength parameter values, safety factor increases linearly with the increase in the structural plane strength parameter values. When structural plane strength parameters values are greater than the rock mass strength parameter values, increasing extent of the safety factor reduces gradually. Until structural plane strength parameters values are more than a certain value of rock mass strength parameters values, the slope safety factor tends to be unchanged. When structural plane cohesion value is 1.78 times the rock mass cohesion, the safety factor tends to be unchanged. When structural plane internal friction angle is 1.4 times the rock mass internal friction angle, the safety factor tends to be unchanged.

When structural plane cohesion values are less than the rock mass cohesion values, the failure modes of slope are bedding sliding failure modes. When structural plane cohesion values are greater than the rock mass cohesion values, the failure modes shift gradually from the bedding sliding failure modes to the sliding-bending failure modes, and the sliding surface shift from plane to the circular arc surface. When structural plane cohesion values and rock mass cohesion values are equal, the change begins. The influence of structural plane internal friction angle on slope failure mode

is the same with the influence of the rock mass internal friction angle. When structural plane internal friction angle value and rock mass internal friction angle value are equal, the slope failure mode begins to change.

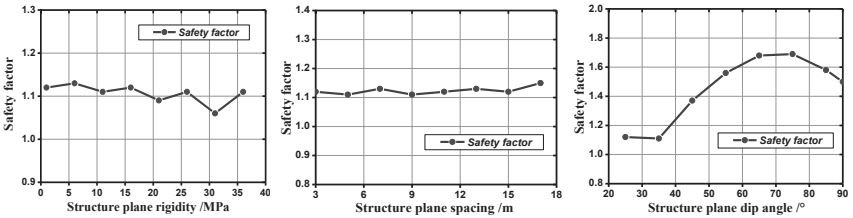


Fig.3 Influence of stiffness and spacing and dip angle on safety factor

As shown in Fig.3, the safety factor varies weakly with the increase of structural plane stiffness and spacing, and the maximum variation rates are 6.6% and 3.6% respectively, which shows that there is little impact of structural plane stiffness and spacing on safety factor. When structural plane dip angle is less than the slope angle, the safety factor decreases with the increase in the structural plane dip angle. When the dip angle of structural plane is greater than the slope angle, the safety factor increases with the increase in the structural plane dip angle. When the structural plane dip angle is 75° , the safety factor reaches a maximum value of 1.69, but then, the safety factor decreases with the increase of the structural plane dip angle.

Failures of rock mass bedding slope mainly display the shearing slip failure modes with the increase of structural plane stiffness which is influenced by gravity, while the slope display the shearing slip with the increase of structural plane spacing. It is shown that there is no influence on slope failure modes. When structural plane dip angle is less than slope angle, the failures of rock mass bedding slope mainly display wedge sliding failure modes. When structural plane dip angle is greater than slope angle, stress concentration and yield appears at the toe of slope, and the displacement is greater, and failure modes shift from shearing slip failure modes to shearing slip and buckling failure modes. When structural plane dip angle reaches 85° , failure modes shift from shearing slip and buckling failure modes to tilting failure mode, which verifies that the accuracy of influence rules of dip angle to slope safety factor.

SIGNIFICANCE ANALYSIS OF STRUCTURAL PLANE FACTORS

The significance of structural plane parameters to slope stability is different, thus, it is necessary to determine the significance of structural plane parameters to the slope stability. There are five parameters of the structural plane, and orthogonal experiment could be used[6].

Numerical Simulation Based on Orthogonal Experiment

Based on numerical simulation of orthogonal experiment, the significant of spacing(A), dip angle(B), cohesion(C), internal friction angle(D), stiffness(E) of structural plane on slope stability is studied. Based on assumption that the factors have no influence on each other, four levels and five factors table is used, and it is experimented at least 16 times, namely L16(4⁵)orthogonal test table, shown in Table 3 and Table 4.

Table 3. Factor Value and Level Table

| Orthogonal level | Spacing (m) | Dip angle (°) | Cohesion (kPa) | Internal friction angle (°) | Normal and shear stiffness (GPa·m ⁻¹) |
|------------------|-------------|---------------|----------------|-----------------------------|---|
| 1 | 3 | 25 | 50 | 15 | 1 |
| 2 | 5 | 35 | 100 | 25 | 6 |
| 3 | 7 | 45 | 150 | 35 | 11 |
| 4 | 9 | 55 | 200 | 45 | 16 |

Table 4. Orthogonal Scheme

| Orthogonal scheme | Spacing (m) | Dip angle (°) | Cohesion (kPa) | Internal friction angle (°) | Normal and shear stiffness (GPa·m ⁻¹) | Safety factor |
|-------------------|-------------|---------------|----------------|-----------------------------|---|---------------|
| 1 | 3 | 25 | 50 | 15 | 1 | 1.12 |
| 2 | 3 | 35 | 100 | 25 | 6 | 1.73 |
| 3 | 3 | 45 | 150 | 35 | 11 | 1.92 |
| 4 | 3 | 55 | 200 | 45 | 16 | 1.92 |
| 5 | 5 | 25 | 100 | 35 | 16 | 1.91 |
| 6 | 5 | 35 | 50 | 45 | 11 | 1.75 |
| 7 | 5 | 45 | 200 | 15 | 6 | 1.88 |
| 8 | 5 | 55 | 150 | 25 | 1 | 1.91 |
| 9 | 7 | 25 | 150 | 45 | 6 | 1.92 |
| 10 | 7 | 35 | 200 | 35 | 1 | 1.89 |
| 11 | 7 | 45 | 50 | 25 | 16 | 1.62 |
| 12 | 7 | 55 | 100 | 15 | 11 | 1.79 |
| 13 | 9 | 25 | 200 | 25 | 11 | 1.92 |
| 14 | 9 | 35 | 150 | 15 | 16 | 1.74 |
| 15 | 9 | 45 | 100 | 45 | 1 | 1.91 |
| 16 | 9 | 55 | 50 | 35 | 6 | 1.80 |

Based on the numerical simulation, safety factor of slope could be obtained under the different combination of various factors, and the experiment results by rang analysis are analyzed, shown in Fig.4 and Fig.5.

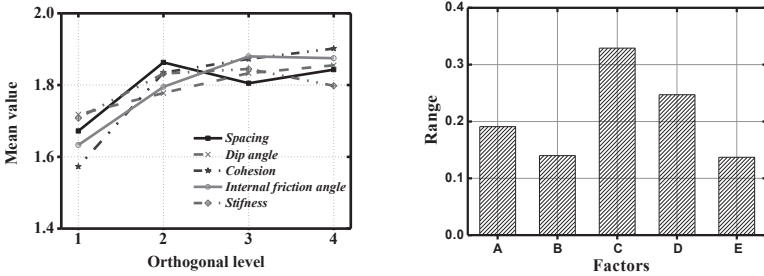


Fig.4 Mean value of Structural Plane parameters Fig.5 Range of parameters

As shown in Fig.4, the slope is most stable under the combination scheme $A_2B_4C_4D_3E_3$, and least stable under the combination scheme $A_1B_1C_1D_1E_1$. Also, it is found that the trend of the influence of structural plane parameters on safety factor of slope based on orthogonal experiment is similar to the result of previous publications, which verifies the accuracy of the influence rule of structural plane parameters to stability of bedding rock slope.

As shown in Fig.5, the important order of structural plane parameters affecting the stability of bedding slope is: $R_C > R_D > R_A > R_B > R_E$, which shows that influence of structural plane cohesion on stability of slope is the strongest in the five factors of structural plane parameters, followed by internal friction angle, dip angle, spacing and stiffness.

CONCLUSIONS

Based on the strength reduction method, influence rules of structural plane parameters to safety factor and failure modes of slope are studied, and based on orthogonal experiment, the significance of structural plane parameters to slope stability is studied in this paper. The main conclusions are as follows:

(1)With the increase of strength parameter values (cohesion and internal friction angle) of structural plane, the safety factor linearly increases initially and then the increment extent decreases and finally tends to be unchanged, and the failure modes shift gradually from the bedding sliding failure modes to the sliding-bending failure modes, and the sliding surface shifts from plane to the circular arc surface.

(2)There are little impact of structural plane stiffness and spacing on safety factor. The failures of rock mass bedding slope mainly display the shearing slip influenced by stiffness and spacing.

(3)With the increase of structural plane dip angle, the safety factor decreases initially and then increases and finally decreases. The failures of rock mass bedding

slope mainly display bedding sliding failure, sliding-bending failure and toppling failure.

(4)Based on the orthogonal experiment, it is shown that the important order of structural plane parameters affecting the stability of bedding slopes is: cohesion, internal friction angle, dip angle, spacing and stiffness.

ACKNOWLEDGMENTS

This work is financially supported by the Natural Science Foundation of China (51078033) and the Natural Science Foundation of China (51178045) and the Overseas Teacher Project of the Ministry of Education of the People's Republic of China (MS2011BJKJ005). State Key Laboratory for Track Technology of High-speed Railway, (Contract No: 2012SKL01) ,China Academy of Railway Sciences.

REFERENCES

- Anhong L and Depei Z et al. (2011). "Assistant designed and stability analysis of rock mass bedding slope." *China Communications Press*.
- Hang L and Ping C et al. (2010). "Numerical analysis of failure modes and stability of stratified rock slopes." *Rock and Soil Mechanics*, Vol 31(10):3301-3304.
- Dunhua L and Wei Q et al (2011). "Three dimensional analysis for effect of structural plane strength parameters on stratified slope stability." *Journal of Central South University*, Vol 42(1): 147-150.
- Junqi W and Lizhen W. (2011). "Study on Stability Analysis and Stress Monitoring of Bedded Rock Slope." *Journal of Water Resources and Architectural Engineering*, Vol 9(6): 44- 47.
- Haibo L and Keqiang X et al. (2007). "Factor of safety analysis of bedding rock slope under seismic load." *Chinese Journal of Rock Mechanics and Engineering*, Vol 2007,26(12): 2386-2392.
- Hongyuan F and Jianhua L et al.(2011). " Dynamic stability analysis for rock slope based on orthogonal test." *Journal of Central South University*, Vol 42(9): 2853-2859.

Numerical Analysis of Failure Mode of Geocell Flexible Retaining Wall

Fei Song¹, Geng-Ren Cao², Lu-Yu Zhang³ and Xiu-Mei Tan⁴

¹Associate Professor, Institute of Geotechnical Engineering, School of Highway Engineering, Chang'an University, Xi'an, 710064, P.R. China; songfei05@tsinghua.org.cn

²Postgraduate, School of Civil Engineering and Architecture, Chongqing Jiaotong University, Chongqing, 400074, P.R. China; summergengren@hotmail.com

³Senior Engineer, the 9th General Team of Airport Construction of China, Chengdu, 611430, P. R. China; zly1974@gmail.com

⁴Postgraduate, School of River and Ocean Engineering, Chongqing Jiaotong University, Chongqing, 400074, P.R. China; summer-txm@hotmail.com

ABSTRACT: The geocell flexible retaining wall has a broad application prospect in the road slope protection. However, its failure mechanism is not systematically investigated. In this paper, by employing the FEM software Plaxis, the failure mode of the geocell flexible retaining wall is studied by the numerical analysis. The effects of soil strength, geocell structure strength, and location of high strength geocell structure layer on the failure mode are investigated based on the analysis of the numerical results. The research results indicate that the sliding surface is a curved surface which passes through the wall toe and intersects with the wall, which differs from the planar one in the Coulomb's soil wedge theory. Both soil strength and geocell structure strength have great effects on the location where the sliding surface intersects with the top of the backfill surface. However, their effects on the location where the sliding surface intersects with the wall back are not significant. In addition, the failure mode of the wall with the lower half part constructed by means of high strength geocell is almost the same with that of the whole wall constructed with high strength geocell. The results in the study will be useful for the determination of the sliding surface of the geocell flexible retaining wall when evaluating the earth pressures against it.

INTRODUCTION

With the rapid development of highway construction in China, embankments and road cutting which have effects on the ecological environment are inevitably adopted for the part of highway routes in the mountains. Retaining structures are widely used for the protection of road slopes. In comparison with other retaining structures, the geocell flexible retaining wall has the advantages of light structure, simple construction, low cost, ecological protection and landscape beautification. Therefore, it has a broad application prospect in the road slope protection as a new type of retaining structure. A lot of researches have been done on the work mechanism and

deformation characteristics of geocell flexible retaining wall. Fu (2002), Lv (2003), Gu (2004), and Yang (2005) investigated the mechanical properties of geocell structures by triaxial shear tests, large scale direct shear tests, compression tests and tensile tests. Yao (2005) analyzed the deformation characteristics of the geocell flexible retaining wall through the centrifugal model tests. Ma (2009) summarized the construction technologies and test method of engineering quality based on the project of the geocell flexible retaining wall in Jingkun Highway. Wang (2004), Xie and Yang (2009), Qu et al. (2009) studied the deformation characteristics and the effect of design parameters on earth pressures by the FEM numerical simulation. Qu et al. (2010), Xu (2010) proposed the method to calculate the active earth pressures against geocell flexible retaining wall. Nevertheless, the failure surface in the analysis is simplified and assumed to be the same planar one in the Coulomb's soil wedge theory, which is not consistent with experimental results and the practices. Song et al. (2011) analyzed the effects of H/B , defined as the ratio of wall height to wall width, slope ratio and surcharges on the deformation behavior of the flexible retaining wall based on the numerical analysis.

However, the effect of soil strength and geocell strength on the failure mode of geocell flexible retaining wall, which is required in the calculation of earth pressures, has not been investigated systematically and is still not clear. In this paper, the effect of soil strength and geocell strength on the failure surface is studied by employing the geotechnical FEM software Plaxis. In addition, the effect of location of high strength geocell structure layer on the failure surface and the safety factor is also investigated by the numerical analysis. Based on the analysis of the numerical calculation results, some valuable conclusions are drawn.

PRINCIPLE AND PARAMETERS OF CALCULATION

Constitutive Model of Material

In the computation, Mohr-Coulomb model is adopted for the backfill, the geocell structure and the foundation. The 15-node triangular element is employed in this analysis to model soil and geocell structure layers. The interface element is set between each geocell structure layer, between the wall back and backfill to model the interaction between the structure and the soil. Besides, there is also interface element between the foundation and the soil.

Interface Element

According to Plaxis 2D Reference Manual Version 9, an elastic-plastic model is used to describe the behavior of interfaces for the modeling of soil-structure interaction. When using 15-node soil elements, the corresponding interface elements are defined by five pairs of nodes. The Coulomb criterion is used to distinguish between elastic behavior, where small displacements can occur within the interface, and plastic interface behavior when permanent slip may occur. The roughness of the interaction is modeled by choosing a suitable value for the strength reduction factor in the interface (R_{inter}). This factor relates the interface strength (wall friction and adhesion) to the soil strength (friction angle and cohesion).

For the interface to remain elastic the shear stress τ is given by:

$$|\tau| < \sigma_n \tan \phi_i + c_i \quad (1)$$

For plastic behavior τ is given by:

$$|\tau| = \sigma_n \tan \phi_i + c_i \quad (2)$$

where ϕ_i and c_i are the friction angle and cohesion (adhesion) of the interface. The strength properties of interfaces are linked to the strength properties of a soil layer. Each data set has an associated strength reduction factor for interfaces (R_{inter}). The interface properties are calculated from the soil properties in the associated data set and the strength reduction factor by applying the following rules:

$$c_i = R_{inter} c_{soil} \quad (3)$$

$$\tan \phi_i = R_{inter} \tan \phi_{soil} \leq \tan \phi_{soil} \quad (4)$$

Phi-C Reduction Method

With reference to Plaxis 2D Reference Manual Version 9, Phi-c reduction in Plaxis is used to compute failure surface and safety factors. In the Phi-c reduction approach, the strength parameters $\tan \phi$ and c of the soil are successively reduced until failure of the structure occurs. The strength of interfaces, if used, is reduced in the same way.

The total multiplier $\sum M_{sf}$ is used to define the value of the soil strength parameters at a given stage in the analysis:

$$\sum M_{sf} = \frac{\tan \phi_{input}}{\tan \phi_{reduced}} = \frac{c_{input}}{c_{reduced}} \quad (5)$$

where the strength parameters with the subscript 'input' refer to the properties entered in the material sets and parameters with the subscript 'reduced' refer to the reduced values used in the analysis, which are the smallest values to maintain the equilibrium state. $\sum M_{sf}$ is set to 1.0 at the start of a calculation to set all material strengths to their unreduced values.

A Phi-c reduction calculation continues until a failure mechanism has been fully developed. The factor of safety is given by:

$$F_s = \frac{\text{available strength}}{\text{strength at failure}} = \text{value of } \sum M_{sf} \text{ at failure} \quad (6)$$

To capture the failure of the structure accurately, the use of *Arc-length control* in the iteration procedure is required.

When the factor of safety is determined by the Phi-c reduction, the sliding

surface can be calculated at the same time. It is known to all that the deformation of the soil wedge surrounded by the sliding surface is substantially larger than that of the soil outside the sliding surface. According to this, the sliding surface can be determined, as is shown in Fig. 1.

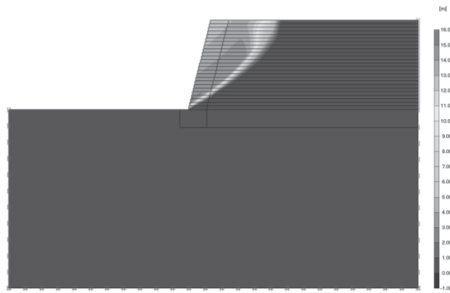


FIG.1. The sliding surface of the geocell flexible retaining wall.

CALCULATION MODEL AND PARAMETERS

When geocell is used for building retaining wall for slope protection, each structure layer composed of geocell and the filler is placed according to a certain slope ratio. The model wall in the calculation is shown in Fig. 2.

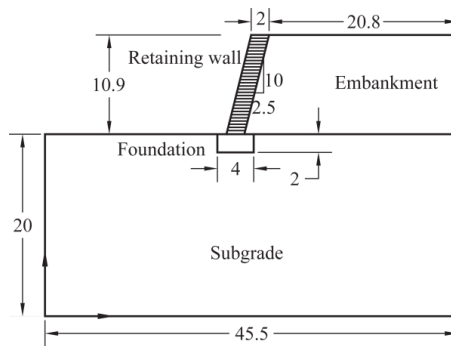


FIG. 2. Sketch of calculation model (unit: m).

The calculation parameters in this study are determined according to the researches results of mechanical property tests by Fu (2002), Gu (2004) and Yang (2005), combined with the experiences in engineering practices. The calculation parameters adopted by Wang (2004), Xie and Yang (2009) are also referred to for this study. The cases in the centrifuge model tests conducted by the authors are simulated by employing the geotechnical FEM software Plaxis. The failure mode predicted by the numerical simulation is compared with the measured one in the centrifuge model tests. In the centrifuge model test, $H/B=5.45$, the slope ratio is 0.25 and the wall fails until the centrifuge acceleration is increased to 57g. At the same

time, marked points made of hobnails and plastic insulating tape are laid on the side of the backfill near the transparent plexiglass of the soil box and photographs of the model are taken during the increase of the acceleration. The displacement field and the failure surface of the wall and backfill are measured on the basis of the analysis of displacements of the marked points by comparison of the photographs at different accelerations.

After trial calculation, it is found that the computation results are consistent with the experimental results when the computation parameters are listed in the table 1.

Table 1. Calculation Parameters of Model

| Material | $\gamma /(\text{kN}/\text{m}^3)$ | $\gamma_{sat} /(\text{kN}/\text{m}^3)$ | c/kPa | $\varphi /(^{\circ})$ | E/MPa | ν | R_{inter} |
|------------|----------------------------------|--|----------------|-----------------------|----------------|-------|-------------|
| Wall Body | 18 | 20.5 | 62 | 42 | 60 | 0.25 | 0.67 |
| Foundation | 20 | 22.0 | 70 | 45 | 65 | 0.20 | 0.67 |
| Backfill | 17 | 20.0 | 60 | 40 | 30 | 0.35 | 0.67 |

COMPARISON WITH THE CENTRIFUGAL MODEL TEST RESULTS

The comparison of the calculation and the experimental results on the sliding surface is illustrated in Fig. 3, where H and B are the height and width of the wall respectively, x and z are the horizontal and vertical distances respectively. The horizontal and vertical coordinate are divided by the wall height in order to make the comparison feasible and convenient.

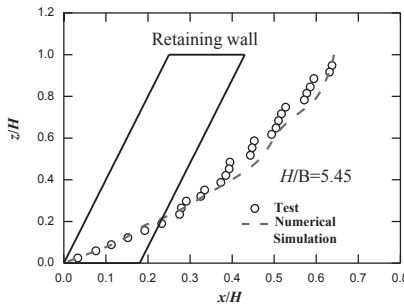


FIG. 3. Comparison of the failure mode predicted by the numerical simulation and measured in the test.

It can be seen from Fig. 3 that the curved sliding surface passes through the wall toe, intersects with the wall back and eventually reaches some place on the backfill surface near the wall top, which differs from the planar one adopted in the Coulomb’s soil wedge theory. The mathematical formulation of the sliding surface may be expressed in the following equation:

$$y = Ax^2 + Bx + C \tag{7}$$

in which A , B , and C are three parameters determining the location and shape of the sliding surface. The coordinates of three points on the sliding surface such as the wall toe, the locations where the surface intersects with the wall back and the backfill surface can be substituted into Eq. (7) to calculate the parameters A , B , and C . Then the sliding surface can be determined quantitatively by Eq. (7).

EFFECT OF SOIL STRENGTH ON THE FAILURE MODE

The failure mode of the geocell flexible retaining wall with different soil strength is computed and investigated by numerical analysis. In the computation, $H/B=5.45$, the slope ratio is 1:0.25, and the strength parameters of geocell structure are the ones in Table 1, while the soil strength parameters are reduced by 20%, 40%, 50%, 60%. The calculation results are illustrated in Fig.4, from which it can be seen that the size of the sliding soil wedge gradually increases with the reduction of the soil strength parameters. The distance between the wall top and the place where the sliding surface intersects with backfill surface enlarges with the reduction of the soil strength. However, the location where the sliding surface intersects with the wall remains almost the same place and is not sensitive to the change of the soil strength. In comparison with the effect of height-width ratio of the wall, the effect of soil strength on the location where the sliding surface intersects with wall back is not so significant. Therefore, when calculating the earth pressures against the wall, the assumption can be made that the location where the sliding surface intersects with wall back is not affected strongly by the soil strength in order to make the analysis simple and convenient.

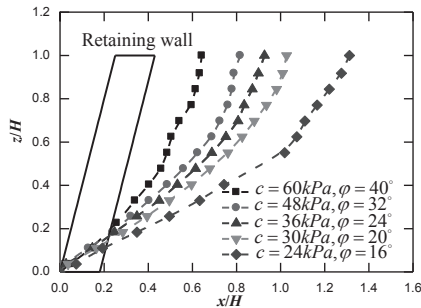


FIG. 4. Effect of soil strength on the failure mode of the wall.

EFFECT OF GEOCELL STRUCTURE STRENGTH ON THE FAILURE MODE

In order to increase the stability and safety factor of geocell flexible retaining walls, geocell with high strength are employed in engineering practices. The effect of geocell structure strength on the failure mode of the wall is computed and analyzed in this paper. The calculation results are illustrated in Fig. 5, in which c and ϕ are the soil strength parameters while c_1 and ϕ_1 are the geocell structure strength parameters.

In the calculation, $c = 30kPa, \varphi = 20^\circ$ while c_1 and φ_1 increase by 20%, 30%, 50% and 60% of the soil strength. The other calculation parameters are the same as shown in Table 1. It can be seen from Fig. 5 that the range of sliding soil gradually increases with the increase of geocell structure strength, which is because the mechanical properties of the wall approach those of the rigid retaining wall and the deflection deformation of the wall body decreases with the increase of geocell structure strength. The distance between the wall top and the place where the sliding surface intersects with backfill surface enlarges with the increase of the geocell structure strength. However, the location where the sliding surface intersects with the wall is not affected by the change of the geocell structure strength, which is the same case with the effect of soil strength. When the increase of strength of geocell structure is greater than 50% of the soil, the failure mode doesn't change.

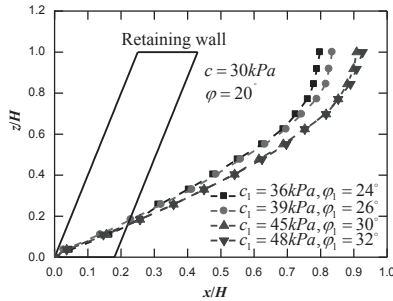


FIG. 5. Effect of strength of geocell structure on the failure mode of the wall.

The effect of the geocell structure strength on the safety factor is also computed and shown in Fig. 6, in which the ratio of geocell structure strength to soil strength is defined as $strength_g/strength_s$. It can be seen from Fig. 6 that the safety factor increases with the geocell structure strength but it keeps the same constant after the value of $strength_g/strength_s$ is greater than 2.8.

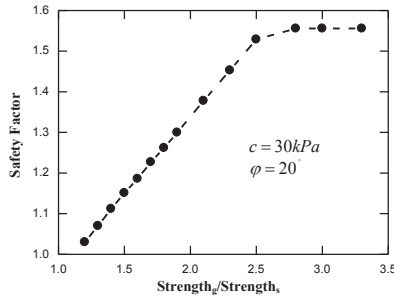


FIG. 6. Effect of strength of geocell structure on the safety factor.

EFFECT OF LOCATION OF HIGH STRENGTH GEOCELL STRUCTURE ON THE FAILURE MODE

As is known to all, the lateral earth pressures against the lower $H/3$ of the wall is larger than that against its rest part. Therefore, geocell structure with high strength is always placed in the lower part of the wall, which is an effective method to raise the stability and safety factor of the wall. In order to investigate the effect of proportion and location of high strength geocell structure on the failure mode, two kinds of geocell structures with different strength are selected in this study and four cases are calculated. One kind is the ordinary geocell structure with strength parameters, $c_1 = 36kPa$, $\varphi = 24^\circ$, which are increased 20% of the backfill strength, the other is the high strength geocell structure with parameters $c_1 = 48kPa$, $\varphi = 32^\circ$, which are increased 60% of the backfill strength. The four cases in this study are shown in Fig. 7, in which H_1 represents the height of the geocell structure with high strength.

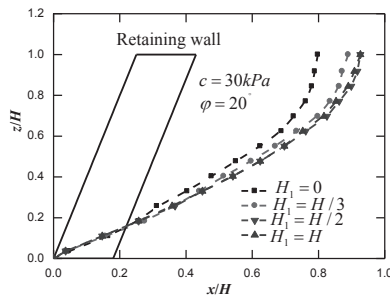


FIG. 7. Effect of location of high strength geocell on the failure mode of the wall.

As is shown in Fig.7, the first case is $H_1 = 0$, which means that the geocell with ordinary strength is used for the whole wall. The second one is $H_1 = H/3$, which means that the geocell with high strength is used for the lower 1/3 part of the wall. The third one is $H_1 = H/2$, which means that the geocell with high strength is used for the lower 1/2 part of the wall. The last one is $H_1 = H$, which means that the geocell with high strength is used for the whole wall. As is shown in Fig. 7, the failure mode is almost the same with $H_1 = H$ and does not change when $H_1 \geq H/2$.

Variation of the safety factor with the location of high strength geocell structure is shown in Fig. 8, from which it can be seen that the safety factor increases with H_1 but maintains a constant when $H_1 \geq H/2$. Therefore, in order to save the material and reduce the engineering cost, it is recommended to place the geocell with high strength only at the lower half part of the wall while construct the rest of the wall by means of geocell with ordinary strength.

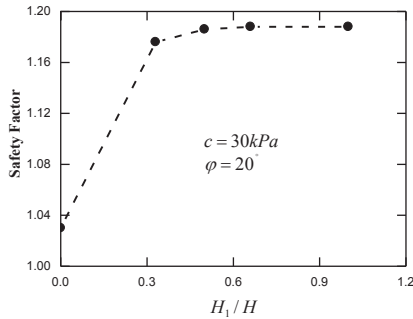


FIG. 8. Effect of location of high strength geocell structure layer on the safety factor.

CONCLUSIONS

In this paper, the effects of soil strength, geocell structure strength, and location of high strength geocell structure layer on the failure mode and the safety factor of geocell flexible retaining wall are investigated by numerical analysis. On the basis of the calculation results and discussions, the following conclusions may be drawn primarily:

- (1) The distance between the wall top and the place where the sliding surface intersects with backfill surface enlarges with the reduction of the soil strength and the increase of the geocell structure strength. However, the effect of soil strength and geocell structure strength on the location where the sliding surface intersects with the wall back is not significant.
- (2) When the increase of strength of geocell structure is greater than 50% of the soil, the failure mode doesn't change. The failure mode of the wall with the lower half part constructed by means of high strength geocell is almost the same with that of the entire wall constructed with high strength geocell.
- (3) The safety factor increases with the geocell structure strength but keeps the same value after the ratio of geocell structure strength to soil strength is greater than 2.8. Besides, the safety factor increases with the proportion of high strength geocell in the whole structure but maintains a constant when the lower half part of the wall is constructed with high strength geocell.

ACKNOWLEDGMENTS

The authors wish to acknowledge the Youth Project supported by National Natural Science Foundation of China (No. 51109006 and 51109112) for the financial support.

REFERENCES

- Brinkgreve R.B.J., Broere W., Waterman D. "Plaxis 2D Reference Manual Version 9", Delft University of Technology and PLAXIS b.v., The Netherlands, 2008.
- Fu J.F. (2002). "Experimental study on the mechanical properties of geocell flexible structure layers." *M. Eng. Thesis*, Geotechnical and Tunneling Department, School of Highway, Chang'an University, Xi'an, China.
- Gu L.J. (2004). "Experimental study on the engineering behavior of geocell structure layers." *M. Eng. Thesis*, Geotechnical and Tunneling Department, School of Highway, Chang'an University, Xi'an, China.
- Lv D.X. (2003). "Study on the engineering behavior of geocell ecological wall." *M. Eng. Thesis*, Geotechnical and Tunneling Department, School of Highway, Chang'an University, Xi'an, China.
- Ma X. Y. (2008). "Study on the deformation behavior of cut type geocell flexible retaining wall." *M. Eng. Thesis*, Geotechnical and Tunneling Department, School of Highway, Chang'an University, Xi'an, China.
- Qu Z.H., Xie Y.L., Yang X.H. (2009). "Influence of design parameters of flexible wall on earth pressure by numerical analysis." *Journal of Chang'an University (Natural Science Edition)*, 29 (6): 6-9.
- Qu Z.H., Xie Y.L., Yuan F.F., et al. (2010). "Calculation method of active earth pressure under limit state for geocell flexible retaining wall." *Journal of Traffic and Transportation Engineering*, 10 (1): 24–28.
- Song F., Xu W.Q., Zhang L. Y., et al. (2011). "Numerical analysis of deformation behavior of geocell flexible retaining wall." *Rock and Soil Mechanics*, 32 (supp.1): 738-742.
- Wang L.P. (2004). "Simulation analysis of engineering behavior of geocell flexible retaining wall." *M. Eng. Thesis*, Geotechnical and Tunneling Department, School of Highway, Chang'an University, Xi'an, China.
- Xie Y.L., Yang X.H (2009). "Characteristics of a new-type geocell flexible retaining wall." *Journal of Materials in Civil Engineering*, ASCE, 21(4): 171–175.
- Xu W.Q. (2010). "Study on calculating methods of active earth pressure for geocell flexible retaining wall." *M. Eng. Thesis*, Geotechnical and Tunneling Department, School of Highway, Chang'an University, Xi'an, China.
- Yang X.H. (2005). "Study on engineering character and applied technique of geocell." *Ph.D. Thesis*, Geotechnical and Tunneling Department, School of Highway, Chang'an University, Xi'an, China.
- Yao H. Z. (2005). "Centrifugal model study on the engineering behavior of geocell flexible retaining wall." *M. Eng. Thesis*, Geotechnical and Tunneling Department, School of Highway, Chang'an University, Xi'an, China.

Shear Modeled from Random Particle Movement

Paul G. Joseph¹, M. ASCE, P.E.

¹President, Engineering Solutions, 38 Blanchard Rd., Boxboro, MA 01719, USA; pjoseph@gmail.com

ABSTRACT: Dynamical systems based soil shear holds that rates of change of shear stress, effective normal stress of a sheared mass of particles are proportional to applied values of shear and effective normal stress; initial proportionality values decay exponentially with strain to become zero at the steady-state condition. This behavior results from an underlying stochastic process in which load carrying particles in the shear zone move into the steady-state at random shear strains, causing the number of load carrying particles in the shear zone which are not in the steady-state to decay exponentially with shear strain. This note proposes a reason for why load carrying particles move into the steady-state configuration at random shear strains, and for why as the number of particles in the shear zone that are not in the steady-state decay exponentially, so too does their total inter-particle contact area. The reason is that all load carrying particles in the shear zone move at random during shear. If this is the case then, further, entropic considerations show that the percent number load carrying particles must distribute exponentially against inter-particle contact area for load carrying particles not in the steady-state and uniformly for those in the steady-state.

INTRODUCTION

A soil when sheared at a constant strain-rate starts from an initial condition, and ultimately reaches the steady-state condition. This paper uses the word “steady-state” strictly as defined by Poulos (1981). The steady-state of deformation occurs in a particulate mass for any loading and drainage condition where the shear stress breaks down the original structure and puts it into a new “flow” structure. It is the result of a continuous process that starts with the first small increase of shear stress and ends when the soil reaches a steady-state of deformation, with all trace of the original structure lost, and with a statistically constant “flow-structure.”

The steady-state condition is not the same as the critical-state condition. As described in Poulos (1981) there are two key differences between the steady-state and the critical-state condition. First, the steady-state has a requirement that the deformation explicitly occurs at a constant deformation velocity (which can be any velocity that does not cause inertial effects), and not as in the case of the critical-state, the near zero, i.e., pseudo-static velocity. Second, at the steady-state the soil grains

position themselves in the steady-state flow structure that remains statistically constant with continued shear strain. No such restrictions apply to the critical-state.

Soil particles move continuously during shear; even in the steady-state flow-structure, for elongated particles, there can be small, continual, and random up and down movement, while for bulky grains, there can be random grain rotations. However, the steady-state flow-structure is statistically constant in that the movements of these individual particles result in negligible changes in the shear stress, normal effective stress, volume, and velocity observed with continued straining at the steady-state (Poulos, 1981, 2010).

As described in Joseph (2012) particles (a single soil grain or cluster of soil grains) transfer applied stresses through their contacts with other particles. Due to the change in load on the soil these inter-particle stresses change, causing particles to move from their initial position to eventually reach the steady-state position with its associated flow-structure.

Since a soil is but a mass of particles with or without surface chemistry (clays and sands respectively), the mechanisms described in this note and in Joseph (2012) also apply to particulate media in general where the particles are sufficiently dense to be considered to act as solids en-masse.

As particles move to the steady-state flow structure, the material's structure changes, and consequently, its ability to support shear and normal stresses. This change in material structure manifests as the resulting stress-strain curves. Were no such repositioning of load carrying particles needed, shear would proceed at the initial constant shear and normal stresses and would not change with shear strain, i.e. the shear, effective normal stress and void ratio would already be at their steady-state values.

For monotonic shear, Joseph (2009, 2010) showed that the rates of change of the shear stress and the effective normal stress and void-ratio are proportional to their applied values, with the proportionality values decaying exponentially with shear strain to reach ultimately a value of zero at the steady-state condition.

Joseph (2012) describes a micro-structural process that provided the physical basis for this behavior: particles move into the steady-state flow-structure at random shear strains. For any process where particles leave at random intervals (one example is radioactivity), then the number of remaining particles decays exponentially. Likewise, in the case of soils, if particles move at random shear strains into the steady-state flow-structure, then the number of particles not in the steady-state position decays exponentially with strain. Joseph (2012) also assumed that as the number of particles in the shear zone that were not in the steady-state decayed exponentially with shear strain, so too did their total inter-particle contact area.

The resulting model closely fit, with orderly varying model parameters, a range of shear tests from 130 drained and undrained tests on sands, silts, clays at various densities and OCRs, along various different stress-paths, and exhibiting strain-hardening or strain-softening behavior.

However, not explained in Joseph (2012) were the reasons why a) particles move into the steady state position at random shear strains and b) why the total inter-particle contact area decreases as the number of particles. This note shows that the reason for both these behaviors is that particles in the shear zone that carry the load, move at

random during shear.

BASIS

Physical considerations suggest that for particles to move into the steady-state flow-structure at random shear strains, they must first move randomly. In other words, it is the random movement of load carrying particles in the shear zone that causes particles move into the steady state position at random shear strains. More rigorously, if load carrying particles in the shear zone are moving randomly, then this means that any given particle will move into the flow-structure at some random shear strain, and that the shear strain for which the load carrying particle is not in the flow-structure can be denoted as a continuous, positive random variable X . That movement into the steady-state flow structure occurs at some random X in turn requires that the probability of this event occurring at any shear strain is the same i.e. that:

$$Prob\{X > \gamma + h \mid X > \gamma\} = Prob\{X > h\} \dots\dots\dots(1)$$

where shear strain h occurs after shear strain γ .

This is exactly analogous to the case of radioactive decay where radioactive particles leave the radioactive material at random times. For such processes, particle are not in the flow-structure with a probability $e^{-\lambda\gamma}$, and in the flow-structure with a probability $1 - e^{-\lambda\gamma}$, where λ is the rate (per unit strain) at which particles move into the flow-structure.

This results in a binomial distribution where for an initial N_0 particles, independent, and identically distributed in X , the probability of N_γ particles not being in the flow-structure at shear strain γ is:

$$Prob\{N_\gamma = n\} = \frac{N_0!}{n!(N_0 - n)!} \exp(-n\lambda\gamma)[1 - \exp(-\lambda\gamma)]^{N_0-n} \dots\dots\dots(2)$$

where N_γ is the number of load carrying particles in the shear zone that are not in the steady-state position at shear strain γ . So, the expected value $E[N_\gamma]$ is:

$$E[N_\gamma] = N_0 \exp(-\lambda\gamma) \dots\dots\dots(3)$$

Joseph (2012) assumed that as the number of particles N_γ decays exponentially, so also does the total inter-particle contact area of the particles that constitute N_γ . This assumption implies that on average, the inter-particle contact area between any two individual particles not in the steady-state position is always the same as shear proceeds and that consequently, total inter-particle area of the particles not in the steady-state decreases in step with the number of particles that are not in the steady-state, i.e., also decays exponentially.

This can happen only if the particles are load carrying particles that move into the

steady-state in proportion to the number of particles corresponding to any given inter-particle contact area, during the shear process, thereby maintaining the same average inter-particle contact area for the distribution as a whole. This movement to the steady-state can happen in this uniform manner across the entire distribution of inter-particle contact areas only if the probability of it happening at any given value of inter-particle contact area is the same for any inter-particle contact area. This in turn implies that this probability is the same for any given particle, i.e., that movement to the steady-state position of any given particle occurs at a random shear strain, as previously defined by Equation (1).

More rigorously, at any given strain, the percent number of load carrying particles not in the steady-state position has some distribution with respect to the inter-particle contact area of these individual particles. Let this distribution be as follows:

$$P_n = f(a).....(4)$$

where: P_n is the percent number of particles that have inter-particle contact area a .

Let the expected value $E[a]$ of this distribution be a_{avg} , the expected value of the distribution P_n defined in Equation (4). The assumption in Joseph (2012) is that a_{avg} remains unchanged through the shear process. This can only happen if the distribution defined by Equation (4) remains unchanged with shear, i.e., that P_n remain the same throughout the shear process. This can only be possible if the number of load carrying particles moving into the steady-state is in the same proportion as the original number of load carrying particles not in the steady-state corresponding to any given inter-particle contact area. This is exactly what would occur if, load carrying particles are moving into the steady-state at random shear strains, as per Equations (1).

To help clarify this, consider the highly artificial example of 100 load carrying particles in the shear zone that are not in the steady-state position and with only 2 inter-particle contact areas a_1 and a_2 with 90% of these particles with inter-particle contact area a_1 and the remaining 10% with inter-particle contact area a_2 . With shear, in order for the average inter-particle contact area to remain the same, the percent distribution P_n must remain the same. This requires that at any given strain, the numbers of load carrying particles corresponding to a_1 and a_2 that move to the steady state be in the same proportion as their original numbers.

As an example, at some arbitrary strain, let us assume that 50 of these particles have moved to the steady-state. In order for the remaining 50% particles to have the same distribution P_n , it requires that the percent number of particles corresponding to a_1 and a_2 remain unchanged at 90% and 10% respectively or at 45 and 5 respectively. Correspondingly, this requires that the number of particles that did move into the steady-state during the shear till this strain were also 45 and 5, i.e., each exactly in the same proportion (50%) as their original values. This can only occur is that if the movement is happening uniformly for all particles at any given inter-particle contact area a . This uniformity in turn can occur only if each particle has the exact same probability of moving into the steady-state, i.e., behaves as per Equation (1).

The specific type of distribution i.e., the specific form P_n has does not matter for purposes of the analysis. As particles move into the steady-state position from randomly within this distribution, because of the randomness, statistically, equal numbers of particles for each inter-particle contact area will move into the steady-state flow-structure with the result that the distribution itself—the percent number of particles not in the steady-state position with respect to the inter-particle contact area—remains unchanged with shear. Since the distribution remains unchanged with shear, so also the expected value of the inter-particle contact area between individual particles remains unchanged. Consequently, though the number of load carrying particles in the shear zone decreases with shear, the mean value of inter-particle contact area between individual load carrying particles remains unchanged with shear (equal to the expected value of the distribution), while at the same time, the total absolute inter-particle contact area between all the load carrying particles decreases.

Before the start of shear let the shear zone contain N_q and N_p independent, identically distributed load carrying particles per unit volume of the sample that are not in the steady-state flow structure and whose movement into the steady-state flow-structure affects q and \bar{p} respectively. Joseph (2012) showed that as shear proceeds these particles move into the steady-state position at rates λ_q and λ_p per unit strain that for any given shear strain γ the expected value of the number of particles that effect q and which are not in the flow structure are $N_q e^{-\lambda_q \gamma}$ and $N_p e^{-\lambda_p \gamma}$ corresponding to the shear and normal stresses q and \bar{p} . Likewise, the expected value of the number of particles that effect \bar{p} which are not in the flow-structure are $N_p e^{-\lambda_q \gamma}$ and $N_p e^{-\lambda_p \gamma}$ corresponding to the shear and normal stresses q and \bar{p} .

As described above, each load carrying particle has the same expected value for inter-particle contact area—that of the distribution of which it is a part. Consequently, the total inter-particle area corresponding to N_q and N_p particles decreases as N_q and N_p . In other words, if the initial total inter-particle contact areas corresponding to N_q and N_p load carrying particles in the shear zone be J_q and J_p respectively, then these inter-particle contact areas at any given shear strain γ that affects q are $J_q e^{-\lambda_q \gamma}$ and $J_p e^{-\lambda_p \gamma}$ and that affects \bar{p} are $J_p e^{-\lambda_q \gamma}$ and $J_p e^{-\lambda_p \gamma}$. From this follows the model proposed in Joseph (2012) whose governing equations are:

$$dq / d\gamma = J_q [\bar{p} \tan \alpha_q \exp(-\lambda_p \gamma) - q \exp(-\lambda_q \gamma)] \dots\dots\dots(5a)$$

$$d\bar{p} / d\gamma = J_p [\bar{p} \tan \alpha_p \exp(-\lambda_p \gamma) - q \exp(-\lambda_q \gamma)] \dots\dots\dots(5b)$$

Where α_q and α_p are the secant friction angles of the particles whose movement into the flow-structure cause changes in q and \bar{p} respectively. The right-hand side of these equations describe the operation of simple friction over the inter-particle area available at any given shear strain γ .

Though the specific distribution of the percent number of load carrying particles not in the steady-state position with respect to the inter-particle contact area does not impact the analysis presented above, the Maximum Entropy Production Principle indicates what this distribution should be. The Maximum Entropy Production Principle states that a system tries to maximize its entropy at all times. An important result that follows from this is by Jaynes (1957), who showed that in order to maximize entropy, any system that is varying such that the mean is positive and constant, must follow an exponential distribution—see for example Gokhale (1975) for the detailed derivation. This means that the number of load carrying particles decays exponentially as their corresponding inter-particle contact area increases. Figure 1 schematically shows this distribution.

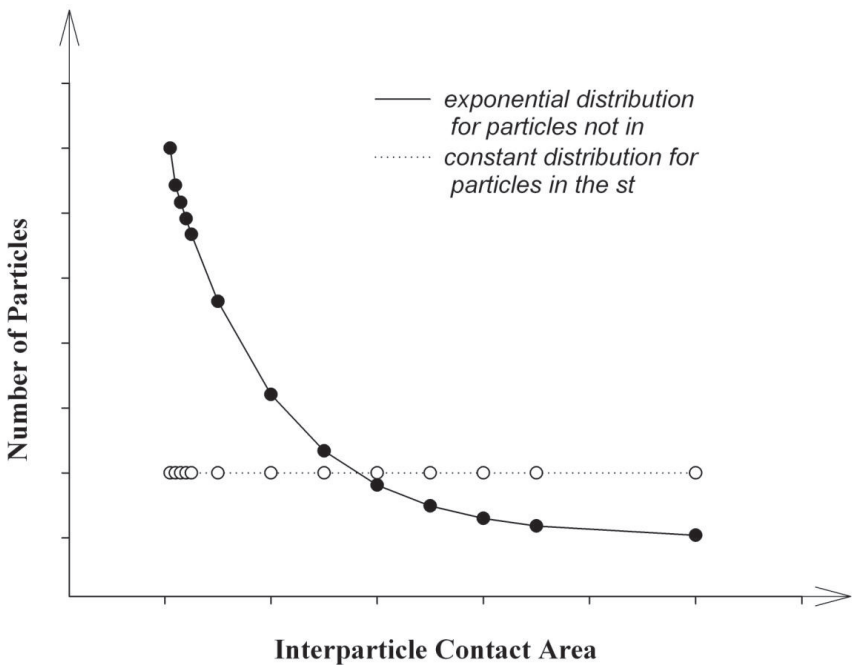


FIG. 1. Schematic of number of load carrying particles vs. inter-particle contact area.

Particles in the steady-state do not have this requirement that the mean value of the distribution be constant and in this case, again following from Jaynes (1957), Gokhale (1975), to maximize entropy, the percent number of particles varies uniformly with inter-particle contact area as also shown schematically in Figure 1. Physical considerations indicate that at the random steady-state flow-structure, this must indeed be the case.

CONCLUSIONS

This note proposes that load carrying particles in the shear zone move at random. This in turn implies that a) load carrying particles in the shear zone move into the steady-state position at random shear strains and b) the expected value of the inter-particle contact area between load carrying particles that are not in the steady-state position remain unchanged with shear. Joseph (2012) showed that the consequence of particles in the shear zone moving into the steady state at random shear strains is that the number of load carrying particles in the shear zone that are not in the steady-state position decays exponentially with strain. The consequence of the expected value of the inter-particle contact area between any two particles in the distribution of load carrying particles in the shear zone not in the steady-state position remaining constant as shear proceeds is that the total inter-particle contact area of these particles decays as the number of these particles.

This random movement of these load carrying particles during shear provides the underlying basis of the model proposed by Joseph (2012) that closely fit, with orderly varying model parameters, a range of shear tests from 130 drained and undrained tests on sands, silts, clays at various densities and OCRs, along various different stress-paths, and with strain-hardening or strain-softening behavior.

Additionally this note uses entropic considerations to show that the percent number load carrying particles is distributed exponentially against inter-particle contact area for particles not in the steady-state and uniformly for particles in the steady-state

NOTATION

This paper uses the following symbols:

\bar{p} = effective normal/confining stress, defined as $(\bar{\sigma}_a + \bar{\sigma}_r)/2$ for a triaxial test and as $(\bar{\sigma}_1 + \bar{\sigma}_2 + \bar{\sigma}_3)/3$ for a true-triaxial test

q = shear stress, defined as $(\bar{\sigma}_a - \bar{\sigma}_r)/2$ for a triaxial test and as $1/3[(\bar{\sigma}_1 - \bar{\sigma}_2)^2 + (\bar{\sigma}_2 - \bar{\sigma}_3)^2 + (\bar{\sigma}_3 - \bar{\sigma}_1)^2]^{1/2}$ for a true-triaxial test

a, a_1, a_2 = inter-particle contact areas of particles not in the steady-state position

h = increment of shear strain (%)

J_q, J_p = initial non-dimensional inter-particle contact area of load carrying particles in the shear zone that are not in the steady-state configuration, corresponding to N_q and N_p respectively, per unit area of the sample.

N_q, N_p = initial number of independent, identically distributed load carrying particles in the shear zone that are not in the steady-state position, per unit area of the sample corresponding to q and \bar{p} respectively

X = strain for which a particle is not in the steady-state flow-structure (random variable) (%)

α_q, α_p = secant friction angles corresponding to q and \bar{p} respectively

γ = shear strain (%)

λ_q, λ_p = rate of movement of particles into the steady-state configuration per unit strain corresponding to q and \bar{p} respectively

$\bar{\sigma}_a, \bar{\sigma}_r$ = effective axial and radial stresses respectively

$\bar{\sigma}_1, \bar{\sigma}_2, \bar{\sigma}_3$ = principal effective stresses

REFERENCES

- Gokhale, D. V. (1975), "Maximum *Entropy Characterization of Some Distributions*," In *Statistical Distributions in Scientific Work*, Patil, Kotz and Ord. Eds., Boston, M.A. Reidel, Vol. 3, pp 299-304.
- Jaynes, E. T. (1957), "*Information theory and statistical mechanics*," Phys. Rev. 106, pp 620-630.
- Joseph, P. G. (2009), "*A Constitutive Model of Soil Based on a Dynamical Systems Approach*," Journal of Geotechnical and Environmental Engineering, Vol. 135, No. 8, August 1
- Joseph, P. G. (2010), "*A Dynamical Systems Based Approach to Soil Shear*," Geotechnique, Vol. LX, Number 10, pp 807-812.
- Joseph, P. G. (2012), "*Physical basis and validation of a constitutive model for soil shear derived from micro-structural changes*," International Journal of Geomechanics, ASCE, (accepted for publication and available at: [http://dx.doi.org/10.1061/\(ASCE\)GM.1943-5622.0000209](http://dx.doi.org/10.1061/(ASCE)GM.1943-5622.0000209)).
- Poulos, S. G. (1981), "*The Steady State of Deformation*," Journal of Geotechnical Engineering, ASCE, Vol. 107, GT5, pp 553-562.
- Poulos, S. G. 2010. Personal communication to the author dated Oct. 14th, 2010.

A Stability Analysis Method for Arbitrary Slip Block Based on Finite Element Method

Xikang Liu¹, Jianhai Zhang² and Wenguang Zhao³, P.E.

¹Master Degree Student, State Key Laboratory of Hydraulics and Mountain River Development and Protection, College of Water Resources & Hydropower, Sichuan University, No. 24 South Section 1, Yihuan Road, Chengdu, China, 610065; E-mail: lxksu@163.com

²Professor, State Key Laboratory of Hydraulics and Mountain River Development and Protection, College of Water Resources & Hydropower, Sichuan University, No. 24 South Section 1, Yihuan Road, Chengdu, China, 610065; E-mail: Z3257@263.net

³Chief Engineer, China Hydropower Engineering Consulting Group Chengdu Design & Research Institute, No. 1 North Huanhua Road, Chengdu, China, 610072; E-mail: zwgcky@163.com

ABSTRACT: The stability of slip blocks on arch dam abutment under earthquake is of great importance for the safety of the dam. In order to analyze static and dynamic stability of arch dam blocks, a hybrid method incorporating the advantage of finite element method and rigid body limit equilibrium method is proposed. A scheme is presented by which any arbitrary slip block defined can be obtained from topography of the studied region, and then the 3D slip block is meshed. Based on stress field of static and dynamic FEM calculation, the stress field of all blocks is obtained by interpolating stress on block mesh. By integrating stress on block faces and using the idea of limit equilibrium method, the safety factor of slip block is computed and dynamic stability of arch dam block is evaluated. The proposed method can provide instant stability of slip block during the whole seismic action, which cannot be obtained with traditional limit equilibrium method. Take Shapai arch dam as an example, the dynamic stability of Shapai arch dam abutment under Wenchuan “5.12” earthquake is analyzed. The method gives a new way for analytical technique of dam abutment stability evaluation.

INTRODUCTION

Arch dam is a kind of dam with high security which is material saving and cost saving. It is widely used in the world because of the advantages it owns. It is essential to keep the dam abutment stable while the dam transmits huge water pressure to the rock foundation. Up to now, limit equilibrium method (LEM) is still the most widely used method in the assessment of safety of slip block on dam foundation (Zhang and Chen 2011). The advantages of LEM lay in simple model, quick analysis in which no rock deformation is considered. But LEM can hardly be used in seismic analysis to evaluate the instant safety factor of dam abutment block.

Different from LEM, finite element method (FEM) can give out both deformation

and stress distribution on any point of dam-foundation system. But it is not very straight forward to assess the safety state of a dam abutment block from the stress field obtained from FEM. To solve the problem, the idea to use the advantages of LEM and other numerical method is proposed. For example, Zhang and Fan (1999) suggested a method which combines the rigid body element and LEM. The method can be used to evaluate the stability of arch dam blocks. But it can't cut arbitrary slip block. The structural plane must be the interface of element in calculation model. This character makes the generation of calculation mesh more difficult. After that, a method using strength reduction is proposed (Song and Zhen 2006). It has the same difficulty with the method proposed by Zhang and Fan. Because of the randomness of structural planes, the slip blocks on dam abutment can be very complex with many kinds of structural combination, this will strongly affect the generation of calculation mesh. For complex blocks on arch dam abutment, the generation of calculation mesh will be a time consuming job. Bao and Yang (2011) describes a method called Multi-grid Method to calculate safety factor. The basic concept of the method is based on stress interpolation. But Multi-grid Method has not been extended to dynamic safety factor computation. Bao and Xu (2011) proposed an idea of using block displacement and node stress to calculate internal force on slip surface, and then to obtain safety factor. But it also takes block mesh as a part of FEM calculation mesh.

To overcome the disadvantages that many methods which are used to calculate safety factor of arch dam blocks commonly own, that is, the block mesh must be a part of calculation mesh. A method with automatic mesh generation for slip blocks and safety factor calculation is proposed. In this new method, dam slip blocks of arbitrary joint face combination are cut firstly from topographical data, then they are meshed. To assess the dynamic factor of safety, the stress field results of each moment of dynamic FEM calculation is used. In addition, the change of sliding direction of arch dam blocks during earthquake and seepage force are also considered.

THEORETICAL BASIS

To bring the proposed method into practice, the generation of arbitrary slip block mesh and to interpolate stress field in FEM mesh are two main problems. The following section will give out detail for slip block mesh generation and interpolation.

Algorithm of Automatic Mesh Generation for Slip Block

Blocks on arch dam abutment formed by structural planes is three-dimensional and always have many kinds of shapes, so it is hard to form block mesh artificially. The Grid-Based Approach (Huang and Zhao 2009) is difficult to generate element with reasonable size for dam abutment slip block. In order to solve the problem, an improved algorithm called virtual grid is proposed. The process of virtual grid method is shown in the following steps:

- (1) Input of topography triangulation network and structural plane data.
- (2) Get intersection line of every two structural plane to form intersection line set $LP(L_1, L_2 \dots L_n)$.

(3) Choose an intersection line L_i with the direction from upstream to downstream.

(4) Equally divide L_i to obtain divide point set $p(p_1, p_2 \dots p_n)$, cut the block with plane which is perpendicular to L_i and across point p_i to form section set $Ap(A_1, A_2 \dots A_n)$.

(5) Cycle every two adjacent sections $(A_{i-1}, A_i), i = 2 \dots n$. Judge whether topography changes fast.

(6) If topography changes fast, the grid outside the target area will be trimmed. The step is called trimming. Otherwise, two point on the edge will be treated as coincide with each other. This is called contracting.

(7) Form virtual grid of two adjacent sections. If any other two adjacent sections need to be processed, then cycle to step (5).

(8) Group all virtual grids of adjacent two sections to form total block mesh.

Contracting and trimming are two main operations when the original regular grid is transformed into virtual grid. The modified grid does not maintain its original regular shape, but adapt to the change of ground surface. To show the effect of the algorithm, two blocks on the abutment of Shapai arch dam are meshed and shown in Fig. 1.

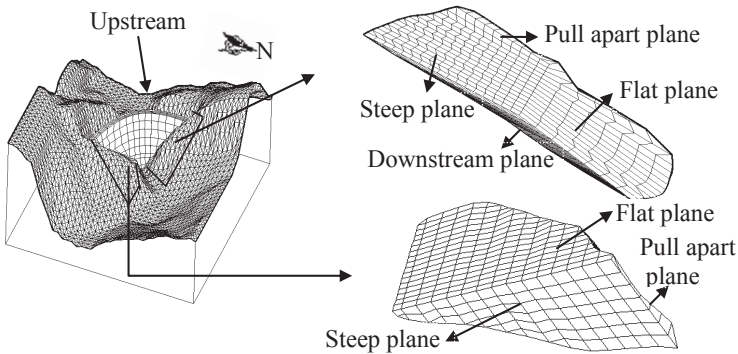


FIG. 1. Two blocks on left and right abutment of Shapai arch dam.

Interpolation of Stress on Slip Body and Safety Factor Definition

The main idea of the method proposed in this paper is interpolation. Two meshes are used in the procedure. One is the calculation mesh of FEM, and another is block mesh. The calculation mesh is used for FEM static or dynamic analysis which provides results for later use. The block mesh is used for interpolation of stress or other interested physical parameters, thus to obtain the stress field of blocks in every dynamic calculation step. The process of interpolating stress on slip body and integrating forces to obtain total slip force and anti-slip force is presented in Fig. 2. The following paragraphs will list main equations used in this process.

When iso-parametric element is used, the coordinate of node point $NB_i(x_i, y_i, z_i)$ of block mesh can be expressed as Eq. 1.

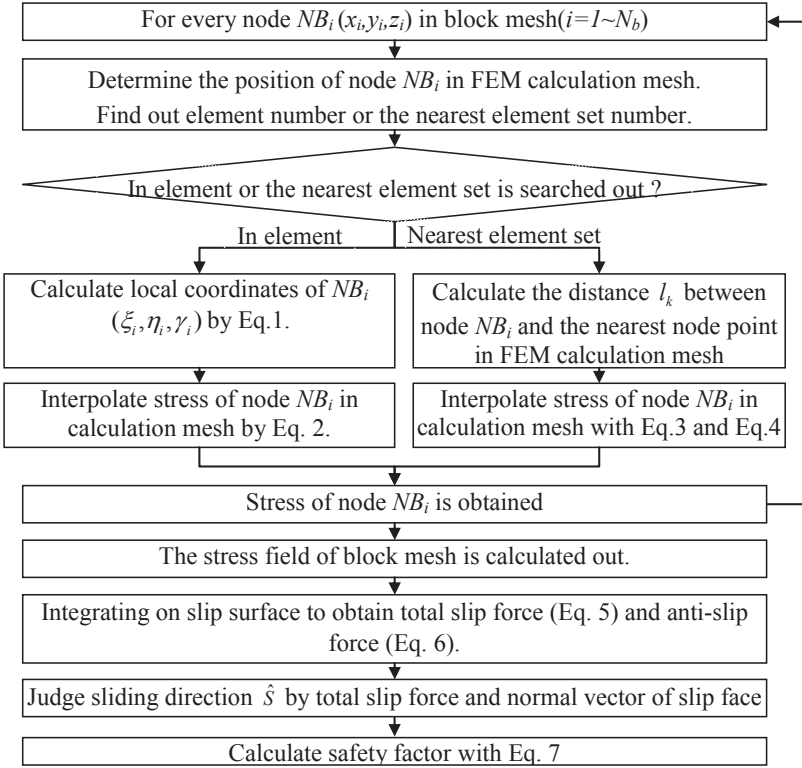


FIG. 2. Computation of factor of safety for a slip block.

$$x_i = \sum_{j=1}^m N_j x_j, y_i = \sum_{j=1}^m N_j y_j, z_i = \sum_{j=1}^m N_j z_j \quad (1)$$

Where, $N_j = \frac{1}{8}(1 + \xi_j \xi_i)(1 + \eta_j \eta_i)(1 + \gamma_j \gamma_i)$ is the shape function of hexahedron.

(x_j, y_j, z_j) is the node coordinates of element in FEM calculation mesh.

Two kinds of interpolation forms are used to obtain stress field of block mesh. When node point NB_i of block mesh is inside an element of FEM mesh, interpolation form shown in Eq. 2 is used to obtain its stress state:

$$[\sigma_A] = \sum_{k=1}^{nip} [\sigma_k] N_k \quad (2)$$

Where, N_k is the value of shape function on gauss point k . It can be calculated by Eq.1

When the node of block mesh is outside any element of FEM calculation mesh, interpolation Eq.3 and Eq.4 are employed:

$$[\sigma_A] = \sum_{k=1}^{nip} [\sigma_k] s_k \tag{3}$$

$$s_k = \frac{1}{l_k^n} \quad t = \sum_{k=1}^{nip} \frac{1}{l_k^n} \tag{4}$$

Where nip is a given number of Gauss point near point NB_{i_s} , here $nip=8$. l_k is the distance between interpolation point to Gauss point which is numbered by k . n is a given power parameter decided by user, usually $n=1$ or 2 . Bao and Yang (2011) recommended that n is better to be assigned to 2 . $[\sigma_k]$ is stress matrix on Gauss point k . $[\sigma_A]$ is stress matrix that is obtained by interpolation.

After stress interpolation, the stress state of all nodes on slip block is known. Then integration of stress to calculate total slip force and anti-slip force on the slip surface will be done by Eq. 5 and Eq. 6 respectively.

$$\vec{r} = \sum_{i=1}^n \vec{r}_i = \sum_{i=1}^n \left(\int_{a_c} \vec{i} da \right) = \sum_{i=1}^n \left(\int_{a_c} \sigma \vec{n} da \right) \tag{5}$$

Where, \vec{r} is the resultant force on face a_c . \vec{r}_i is the component of resultant force. n is the total face number of a block. σ is the stress tensor on the node of sliding surface. \vec{n} is the normal vector of sliding face.

Anti-sliding force can be calculated by integrating the stress on block surface. Anti-sliding force can be calculated by Eq. 6.

$$F_Z = \int_{ac} (C + (\sigma_n - p) f) da \tag{6}$$

Where, C is cohesion. σ_n is normal stress on sliding face. p is seepage force on the nodes of block surface. f is the coefficient of friction.

Goodman and Shi(1985) describes the judging of sliding direction. With sliding direction \hat{S} , the safety factor will be calculated by Eq.7 in every dynamic step and finally the time-safety factor curve of arch dam blocks will be formed.

$$K_s = \frac{F_Z(t)}{F_H(t)} = \frac{F_Z(t)}{\vec{r} \cdot \hat{S}} \tag{7}$$

Where, $F_Z(t)$ is anti-sliding force. It can be calculated by Eq. 6. \vec{r} is the resultant force.

EXAMPLES

To realize the idea proposed in this paper, a program with concise inputs for safety analysis is developed. A simple example and an engineering example are demonstrated to show the applicability and reliability of the program.

A cube which is 10m length, 10m width and 10m height is shown in Fig. 3. The load considered is gravity. Young’s modulus of elasticity is 20GPa, Poisson’s ratio is 0.3 and density $\rho=2400\text{kg/m}^3$. It is meshed and the stress field is obtained by using ANSYS. A block with single slip surface and a block with double slip surface are formed independently and meshed with tetrahedron element. They are shown in Fig.4

together with the FEM calculation mesh. The physical parameters on slip surfaces is $C'=15\text{kPa}$, $f'=0.94$.

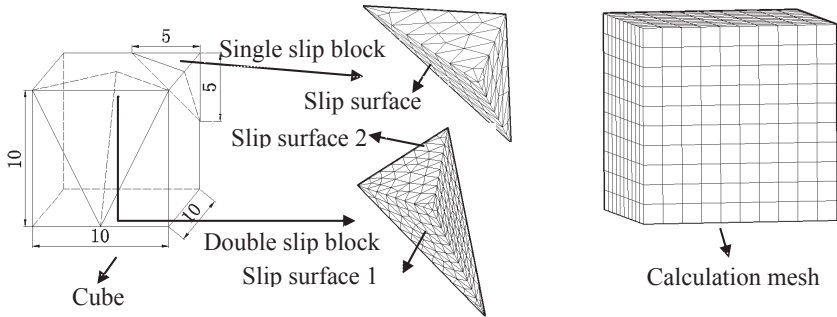


FIG. 3. FEM mesh and block mesh for a single slip block and a double slip block.

According to the theory of limit equilibrium method, factor of safety for block with single slip surface and double slip surfaces are $K_s = 1.477$ and $K_s = 1.342$ respectively. By using the method presented in this paper. Factor of safety calculated is $K_s = 1.473$ and $K_s = 1.335$ respectively. The error between LEM and hybrid FEM-LEM method proposed is less than 0.3% and 0.6% for single slip block and double slip block discussed here.

The program is further applied to the dynamic stability analysis of Shapai arch dam under Wenchuan “5.12” earthquake. During Wenchuan earthquake, the water level of Shapai arch dam is at its normal storage level. After the earthquake, site inspection found that except the destructed power house on left bank by falling stones and a few cracks on the up-stream dam face, no obvious damage is found on anti-sliding rock foundation, so the dam abutment kept stable (Wang and Shao 2009). Take Shapai arch dam as an example, stability analysis for slip blocks on both left and right dam abutment is done. To save space, only the governing slip block on left abutment (steep plane: $N50^\circ E/SE \angle 75^\circ$, $C'=0.54\text{MPa}$, $f'=0.89$; flat plane: $N30^\circ E/SE \angle 30^\circ$, $C'=0.68\text{MPa}$, $f'=0.99$; downstream plane: $N60^\circ W/SW \angle 70^\circ$, $C'=0.54\text{MPa}$, $f'=0.89$) and governing slip block on right abutment (steep plane: $N30^\circ E/NW \angle 60^\circ$, $C'=0.55\text{MPa}$, $f'=0.89$; flat plane: $N45^\circ W/NE \angle 30^\circ$, $C'=0.70\text{MPa}$, $f'=0.99$) are discussed here. Fig.4 shows the FEM calculation mesh and the relation between surfaces of the two blocks and arch dam. The entity graph of the two blocks is shown in Fig.1.

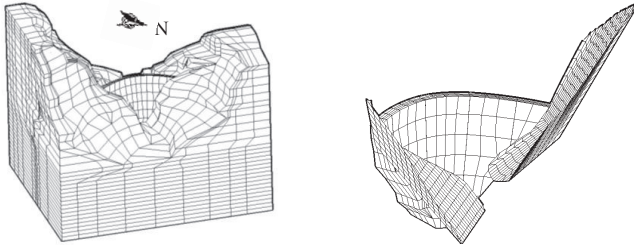


FIG. 4. The calculation model and block surface mesh of Shapai arch dam.

Firstly, FEM dynamic analysis is done for Shapai arch dam by using time domain analysis. For lack of wave record on dam site, Shifang earthquake wave record with peak acceleration as 5.47m/s^2 during Wenchuan “5.12” earthquake is used. The load acted on the dam is normal storage water level of the dam (Elv1866m), gravity and earthquake wave. After dynamic FEM calculation, stability of the two governing blocks on left and right dam abutment are calculated by using the method proposed in this paper. Fig. 5 shows the obtained dynamic safety factor curve of block on left dam abutment.

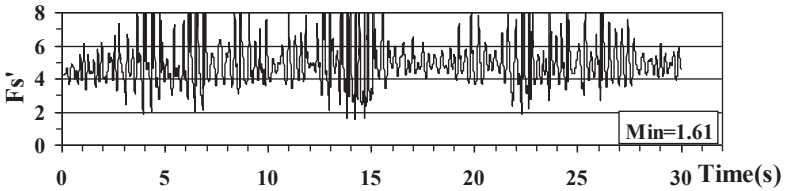


FIG.5. Time-safety factor curve of governing block on left dam abutment.

From the curve shown in Fig. 5, it can be seen that the minimum dynamic safety factor of governing block on left abutment is $K_d=1.61$. By the same process, the minimum dynamic safety factor of governing slip block on right abutment can be obtained as $K_d=1.20$, thus it can be concluded that the two governing blocks analyzed here are stable when Wenchuan “5.12” earthquake happened. But if the minimum safety factor of slip block is less than 1.0, the time length during which safety factor is below 1.0 must be considered, which will need further study on what time length will not cause instability.

CONCLUSIONS

A FEM-LEM hybrid method has been proposed to solve the dynamic safety factor of arch dam abutment blocks and reasonable result has been obtained by using this method to analyze dynamic safety of Shapai arch dam under Wenchuan “5.12” earthquake. The proposed method not only overcomes the difficulty of automatic hexahedron mesh generation for arch dam blocks, but also improves the traditional

interpolation style on structural plane. A time-safety factor curve is calculated in the example and the result shows the abutment of Shapai arch dam is stable when Wenchuan "5.12" earthquake happened. The method gives a new way for analytical technique of dam abutment stability evaluation.

ACKNOWLEDGMENTS

China Hydropower Engineering Consulting Group Chengdu Design & Research Institute provides support and basic data for this research, which would not have been possible without the generous input of industry professionals who volunteered their time and advice for this project.

REFERENCES

- Bao, T.F. and Xu, B.S. (2011). "Hybrid method of limit equilibrium and finite element internal force for analysis of arch dam stability against sliding." *J. Sci. China Tech. Sci.*, Vol. 54 (4): 793-798.
- Bao, J.Q., Yang, Q. and Guan, F.H. (2011). "An improved 3-D multi-grid method and its engineering practice." *J. Hydraulic Engineering*, Vol. 30 (2): 112-117. (in Chinese).
- Goodman, R.E. and Shi, G.H. (1985). "Description of block geometric characteristics and stability with vector method." *Block Theory and its Application to Rock Engineering*, Prentice-Hall, Englewood Cliffs, N.J..
- Huang, L.L., Zhao, G.Q. and Ma, X.W. (2009). "A grid-based automatic generation algorithm and optimization of three-dimensional hexahedron meshes." *Chinese J. of Plasticity Engineering*, Vol. 16 (3): 187-191. (in Chinese).
- Song, Y.K. and Zhen, Y.R. (2006). "Application of three-dimensional strength reduction FEM in slope" *Chinese J. of Underground Space and Engineering.*, Vol. 2 (5): 822-827. (in Chinese).
- Wang, R.K. and Shao, J.D. (2009). "Shapai arch dam has withstood Wenchuan earthquake beyond fortification level." *J. Hydroelectric Engineering*, Vol. 28 (5): 92-96. (in Chinese).
- Zhang, B.Y. and Chen, H.Q. (2011). "Analysis on abutment seismic stability by using finite element method and rigid body limit equilibrium method." *Chinese J. of Rock Mechanics and Engineering*, Vol. 20 (5): 665-670. (in Chinese).
- Zhang, J.H., He, J.D. and Fan, J.W. (2001). "Static and dynamic stability assessment of slopes or dam foundations using a rigid body-spring element method." *International J. of Rock Mechanics and Mining Sciences.*, Vol. 38 (8): 1081-1090.

A Similar Cam-clay Model for Sand Based on the Generalized Potential Theory

Yong Wen¹; Guanghua Yang²; Zhihui Zhong³; Xudong Fu⁴ and Yucheng Zhang⁵

¹Corresponding author; Ph.D, School of Civil and Architectural Engineering, Wuhan University, Wuhan 430072; Email: wy876633@163.com

²Professor, Guangdong Research Institute of Water Resources and Hydropower, Guangzhou 510610

³Ph.D, School of Civil and Architectural Engineering, Wuhan University, Wuhan 430072

⁴Professor, School of Civil and Architectural Engineering, Wuhan University, Wuhan 430072

⁵Ph.D, Guangdong Research Institute of Water Resources and Hydropower, Guangzhou 510610

ABSTRACT: In Cam-clay model, the energy equation assumption is lack of theoretical basis and it can not describe the dilatancy of sand. Moreover, it needs to determine the plastic potential functions. In order to improve the Cam-clay model, mathematical principle of the energy equation assumption and the dilatancy equation in Cam-clay model were analyzed and a similar Cam-clay model for sand was proposed based on the generalized potential theory. In the proposed model, mathematical principle of each assumption is clear and only four conventional soil parameters are needed, and the difficulties brought by the determination of plastic potential functions are avoided. Rationality of the proposed model was verified by the test results of sand under different stress paths. The results show that the predicted results of the proposed model agree well with the test ones and the dilatancy of sand can also be described. It proves that the proposed model is more reasonable than Cam-clay model.

INTRODUCTION

At present, Cam-clay model (Roscoe et al., 1963 and 1968) is one of the most widely used models and it needs only three conventional soil parameters. However, the energy equation assumption in Cam-clay model is lack of theoretical basis and it can not describe the dilatancy of sand. Moreover, Cam-clay model needs to determine the plastic potential functions, which brings some difficulties.

In order to improve the Cam-clay model, a similar Cam-clay model was proposed

based on the generalized potential theory (YANG et al., 2013). Mathematical principle of each assumption in this proposed model is clear and it needs no plastic potential functions. However, it is also only suitable for clay. Therefore, in order to further improve the Cam-clay model, a similar Cam-clay model for sand will be proposed in this paper and the rationality of it will be verified by the test results of sand under different stress paths.

MATHEMATICAL PRINCIPLE OF CAM-CLAY MODEL

In order to determine the yield function, an energy equation in Cam-clay model was assumed as (Roscoe et al., 1963)

$$dW^p = Mp \cdot d\bar{\varepsilon} \quad (1)$$

where W^p is the plastic deformation energy; M is the failure constant; p is the average principal stress and $\bar{\varepsilon}$ is the plastic shear strain.

Then, the dilatancy equation of Cam-clay model can be obtained

$$\frac{d\varepsilon_v^p}{d\bar{\varepsilon}^p} = M - \eta \quad (2)$$

where ε_v^p is the plastic volume strain and $\bar{\varepsilon}^p$ is the plastic shear strain; $\eta = q/p$ is the stress ratio (q is the generalized shear stress).

The yield locus of Cam-clay model on p - q plane is shown in FIG. 1 (p_0 is the hardening parameter).

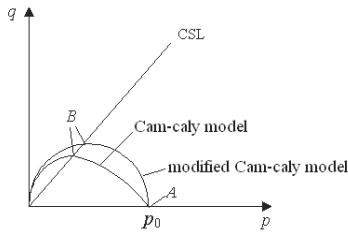


FIG. 1. Yield locus of Cam-clay model and modified Cam-clay model

From FIG. 1 and Eq. 2, it can be seen that at point A, $q=0$ and $\eta=0$,

then $d\bar{\varepsilon}^p = d\varepsilon_v^p/M$. It is unreasonable, because when $dq=0$, $d\bar{\varepsilon}^p = 0$. Therefore, Roscoe et al. (1968) proposed the modified Cam-clay model. The energy equation of the modified Cam-clay model was assumed as

$$dW^p = p\sqrt{(d\varepsilon_v^p)^2 + M^2(d\bar{\varepsilon}^p)^2} \quad (3)$$

Then, the dilatancy equation can be obtained

$$\frac{d\varepsilon_v^p}{d\bar{\varepsilon}^p} = \frac{M^2 - \eta^2}{2\eta} \quad (4)$$

The yield locus on p - q plane of the modified Cam-clay model is shown in FIG. 1.

From FIG. 1 and Eq. 4, it can be seen that at point A, $q=0$ and $\eta=0$, then

$$d\bar{\varepsilon}^p = \frac{2\eta}{M^2 - \eta^2} \cdot d\varepsilon_v^p = 0, \text{ which meets the requirement of orthogonal feature. At}$$

point B, $\eta=M$, then $d\bar{\varepsilon}^p \rightarrow \infty$, which meets the requirement of failure feature. It shows that the modified Cam-clay model is more reasonable than Cam-clay model.

According to the analysis above, it can be seen that the mathematical principle of energy equation assumption in Cam-clay model is to obtain a reasonable dilatancy equation, which should meets the requirements that $d\bar{\varepsilon}^p = 0$ at point A and

$d\bar{\varepsilon}^p \rightarrow \infty$ at point B. It can be solved directly by mathematical method. However,

the energy equation assumption in both Cam-clay model and the modified Cam-clay model is determined by the cut and try method, which is lack of theoretical basis.

On the other hand, the dilatancy is an important characteristic of soil and it can be described by the dilatancy equation $d = d\varepsilon_v^p/d\bar{\varepsilon}^p$, where $d>0$ represents negative dilatancy (volume shrinkage) and $d<0$ represents positive dilatancy (volume expansion, for sand).

According to the analysis above, the dilatancy equation of Cam-clay model and modified Cam-clay model is Eq. 2 and Eq. 4 respectively. Since $M>\eta$, there are always $d>0$ for Eq. 2 and Eq. 4. It means that the Cam-clay model and modified Cam-clay model are not suitable for sand.

IMPROVEMENT OF CAM-CLAY MODEL BASED ON THE GENERALIZED POTENTIAL THEORY

The Generalized Potential Theory

Yang (1991) proposed the generalized potential theory and the constitutive model based on it can be established directly by mathematical methods. It gives a new approach to the study of constitutive model of soil. The following is a simplified constitutive model based on the generalized potential theory.

In p - q space, when the influence caused by the rotation of Lode angle and principal stress axes is neglected, there is

$$\left. \begin{aligned} d\varepsilon_v^p &= Adp + Bdq \\ d\bar{\varepsilon}^p &= Cdp + Ddq \end{aligned} \right\} \quad (5)$$

where A , B , C and D are plasticity coefficients.

In the general stress space, according to the generalized potential theory, the following equations can be obtained (Yang et al., 2007)

$$\{d\varepsilon^p\} = \lambda_1 \left\{ \frac{\partial p}{\partial \sigma} \right\} + \lambda_2 \left\{ \frac{\partial q}{\partial \sigma} \right\} \quad (6)$$

where λ_1 and λ_2 are undetermined coefficients and there is

$$\left. \begin{aligned} \lambda_1 &= d\varepsilon_v^p \\ \lambda_2 &= d\bar{\varepsilon}^p \end{aligned} \right\} \quad (7)$$

Then, the plastic strain can be obtained

$$\{d\varepsilon^p\} = [C_p^\sigma] \{d\sigma\} \quad (8)$$

where $[C_p^\sigma]$ is the plastic flexibility matrix and it can be written as

$$\begin{aligned} [C_p^\sigma] &= A \left\{ \frac{\partial p}{\partial \sigma} \right\} \left\{ \frac{\partial p}{\partial \sigma} \right\}^T + B \left\{ \frac{\partial p}{\partial \sigma} \right\} \left\{ \frac{\partial q}{\partial \sigma} \right\}^T \\ &\quad + C \left\{ \frac{\partial q}{\partial \sigma} \right\} \left\{ \frac{\partial p}{\partial \sigma} \right\}^T + D \left\{ \frac{\partial q}{\partial \sigma} \right\} \left\{ \frac{\partial q}{\partial \sigma} \right\}^T \end{aligned} \quad (9)$$

Therefore, the constitutive equation can be obtained

$$\{d\varepsilon\} = \left([C_e^\sigma] + [C_p^\sigma] \right) \{d\sigma\} \quad (10)$$

where $[C_e^\sigma]$ is the elastic flexibility matrix.

Eq. 10 is called simplified multi-potential surface model (Yang et al., 2007), in which only four coefficients (A , B , C and D) are needed.

Similar Cam-clay Model Based on the Generalized Potential Theory

In order to improve the Cam-clay model, a similar Cam-clay model was proposed based on the generalized potential theory (YANG et al., 2013). It can be written as

$$\left. \begin{aligned} d\varepsilon_v^p &= \frac{A}{\beta} (\beta dp + dq) \\ d\bar{\varepsilon}^p &= \frac{A}{\beta} \left(dp + \frac{1}{\beta} dq \right) \end{aligned} \right\} \quad (11)$$

Where $\beta = d\varepsilon_v^p / d\bar{\varepsilon}^p = (M - \eta) / \eta$; $A = \frac{\lambda - \kappa}{1 + e} \cdot \frac{1}{p} \cdot \left(1 - \left(\frac{\eta}{M} \right)^n \right)$ and the value of n can be obtained by conventional tests; e is the void ratio, λ is the compression index and κ is the swelling index.

In this proposed model, the mathematical principle of each assumption is clear and it needs no plastic potential functions. However, due to the dilatancy equation of similar Cam-clay model is

$$\beta = d\varepsilon_v^p / d\bar{\varepsilon}^p = (M - \eta) / \eta \quad (12)$$

Since $M > \eta$, there is always $d > 0$ for Eq. 12. It means that the similar Cam-clay model above is also not suitable for sand.

Similar Cam-clay Model for Sand Based on the Generalized Potential Theory

In order to describe the dilatancy of sand, Yao et al. (2009) modified the hardening parameter of Cam-clay model and the value of plastic strain was

multiplied by a coefficient $\Omega = \frac{M_d}{M} \frac{M^4 - \eta^4}{M_d^4 - \eta^4}$, where M_d is the phase transformation stress ratio (the separatrix of negative dilatancy and positive dilatancy, see FIG. 2). In this way, the Cam-clay model can be suitable for sand.

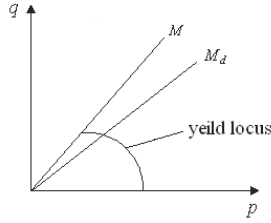


FIG. 2. Peak stress ratio M and characteristic state M_d

In the same way, the parameter M_d will be introduced into the similar Cam-clay model. In order to make the similar Cam-clay model suitable for sand, there should be both $d > 0$ and $d < 0$ for Eq. 12. From mathematical angle, it can assume $AD - BC = 0$ and $B \neq C$, and then the corresponding constitutive equation is

$$\left. \begin{aligned} d\varepsilon_v^p &= Adp + \frac{A}{\beta_1} dq \\ d\bar{\varepsilon}^p &= \frac{A}{\beta_2} dp + \frac{A}{\beta_1\beta_2} dq \end{aligned} \right\} \quad (13)$$

$$\text{where } A = \frac{\lambda - \kappa}{1 + e} \cdot \frac{1}{p} \cdot \left(1 - \left(\frac{\eta}{M} \right)^n \right), \quad \beta_1 = \frac{M - \eta}{\eta} \quad \text{and} \quad \beta_2 = \frac{M_d - \eta}{\eta}.$$

According to Eq. 13, when $0 < \eta < M_d$, $d\varepsilon_v^p > 0$, and when $M_d < \eta < M$, $d\varepsilon_v^p < 0$. Therefore, a similar Cam-clay model for sand is proposed.

TEST VERIFICATION OF THE SIMILAR CAM-CLAY MODEL FOR SAND

To demonstrate the performance of the proposed model, predictions by this model are compared with test results of saturated Toyoura sand under triaxial compression conditions (Nakai, 1989). The tests were started after an initial isotropic compression up to $p=196$ kPa and then kept σ_3 =constant and p =constant respectively. The model parameters are given in Table 1, where e_0 is the initial void ratio and μ is

the Poisson ratio. The value of n is obtained by the conventional triaxial compression tests. Meanwhile, $n=1$ is also considered.

Table 1. Model parameters

| e_0 | λ | κ | M | M_d | μ | n |
|-------|-----------|----------|------|-------|-------|-------|
| 0.68 | 0.0068 | 0.0042 | 1.66 | 0.95 | 0.3 | 2.404 |

The comparisons of results are shown in FIG. 3 and FIG. 4. It can be seen that the predicted results of the similar Cam-clay model agree well with the test ones. The dilatancy of sand is also described reasonably by the similar Cam-clay model, while Cam-clay model and the modified Cam-clay model can not describe it.

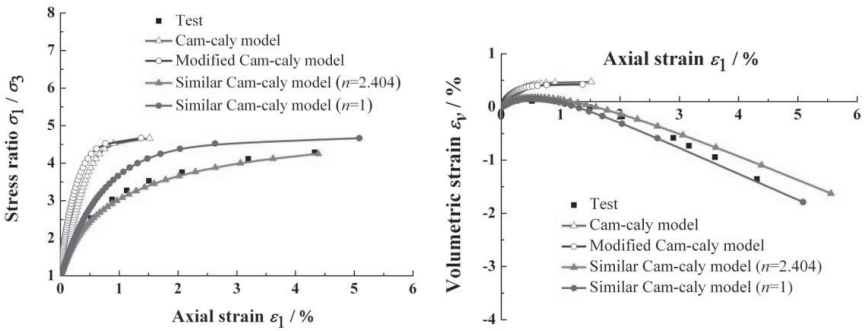


FIG. 3. Comparison between the predicted results of model and test results under conventional triaxial compression condition (sand, $\sigma_3=196$ kPa)

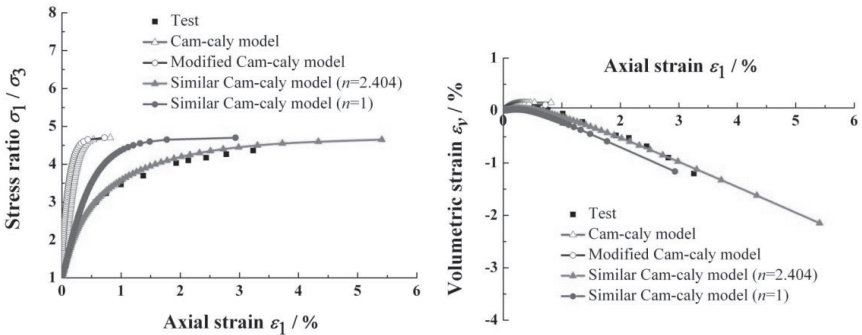


FIG. 4. Comparison between the predicted results of model and test results under triaxial compression condition (sand, $p=196$ kPa)

Therefore, the results above show that the similar Cam-clay model for sand can reasonably describe the stress-strain characteristics of sand, including the dilatancy.

Theoretically, the value of n should be determined by conventional tests. However, when $n=1$, the predicted results of similar Cam-clay model are also of good accuracy.

CONCLUSIONS

In order to improve the Cam-clay model, mathematical principle of the energy equation assumption and the dilatancy equation are analyzed, and a similar Cam-clay model for sand was proposed based on the generalized potential theory. In the proposed model, the mathematical principle of each assumption is clear and only four conventional soil parameters are needed, and the difficulties brought by the determination of plastic potential functions are avoided. The verification results show that the predicted results of the proposed model agree well with the test ones and the dilatancy of sand can also be described, which proves that the proposed model is more reasonable and practical than the Cam-clay model.

ACKNOWLEDGEMENT

The authors appreciate the support of the Fundamental Research Funds for the Central Universities (Project Number: 2012210020203).

REFERENCES

- Roscoe, K. H., Schofield, A. N. and Thurairajah, A. (1963). "Yielding of clays in states wetter than critical." *Geotechnique*, Vol. 13(3): 211-240.
- Roscoe, K. H. and Burland, J. B. (1968). "*On the generalized stress-strain behaviors of an ideal wet clay.*" Engineering Plasticity. Heyman J, Leckie F A, eds. Cambridge University Press: 535-609.
- Yang, G. H., WEN, Y., ZHONG, Z. H. (2013). "Similar Cam-clay model based on the generalized potential theory." *Rock and Soil Mechanics*, Vol. 34(6).
- Yang, G. H. (1991). "The multi-potential constitutive theory of elasto-plasticity for the soil and rock materials." *Chinese Journal of Geotechnical Engineering*, Vol. 13(5): 99-107.
- Yang, G. H., Li, G. X., Jie, Y. X. (2007). "*The general potential theory for soil constitutive model and its application.*" China Waterpower Press: 96-106.
- Yao, Y. P., Hou, W. and Luo, Ti. (2009). "Unified hardening model for soils." *Chinese Journal of Rock Mechanics and Engineering*, Vol. 28(10): 2135-2151.
- Nakai T. (1989). "An isotropic hardening elastoplastic model for sand considering the stress path dependency in three-dimensional stresses." *Soils and Foundations*, Vol. 29(1):119-37.

Stability Behavior of Lime Stabilized Gypseous Soil under Long-Term Soaking

ALDAOOD¹, A. BOUASKER², M. AL-MUKHTAR³, M.

¹Ph.D Student, Research Center in Divided Matter, CRMD, FRE CNRS 3520, Orleans, France;

¹*Department of Civil Engineering, College of Engineering, Mosul University, Al—Majmooh Street, Mosul, Iraq; Abdulrahman.aldaood@etu.univ-orleans.fr*

²Assistance Professor, Research Center in Divided Matter, CRMD, FRE CNRS 3520, Orleans, France; Marwen.bouasker@univ-orleans.fr

³Professor, Research Center in Divided Matter, CRMD, FRE CNRS 3520, Orleans, France; Muzahim@cnsr-orleans.fr

ABSTRACT: This paper aims to study the effect of long-term soaking and leaching on the stability properties of fine-grained soil with and without gypsum content, in relation to changes of the mechanical properties and permeability. The soil samples were stabilized with 3% lime and cured for 28 days at 20°C. The cured samples were subjected to soaking for different period extended to 180 days. Also, permeability values of stabilized and unstabilized soil samples were measured under 30 days of leaching. Results showed that, the long-term soaking has strong effect on the unconfined compressive strength, wave velocity and volume change of the stabilized soil samples. These properties are degraded when compared with initial properties of the unsoaked samples. Moreover, the results indicate that an increase in gypsum content have significant effects on stability properties of soil samples. The leaching test revealed a marked increasing in permeability values of unstabilized soil samples and to a lesser extent in the permeability of stabilized samples. The results also showed that, the permeability of soil samples is highly related to the quantity of gypsum during leaching test, however, the lower gypsum content, the lowest permeability.

INTRODUCTION

Gypseous soils are generally unsuitable for supporting engineering constructions, such as roads, buildings or hydraulic structures. Most risks are related to construction on gypseous soils occurred when these soils subjected to water, causing softening the soil and reducing the shear strength (Razouki and El-Janabi 1999; Al-Zubaydi, 2011; Aldaood et al., 2013). Gypsum can causes serious damages when it acts as cementing agent as dissolution of the cement can result in the destroy of the soil structure, the

leaching of the fine particles and the formation of the soil pipes (Abduljawad and Al-Amoudi, 1995). Gypseous soils are highly soluble materials in their nature, and the types of problems associated with it. The failures include collapse and settlement, which can affect all constructions including buildings, roads and other structures (Cooper 2008).

There are many situations in situ where the soils are subjected to soaking, resulting the soils in fully saturate state or have at least high water content. Soaking can take place in different ways such as local shallow wetting, deep local wetting, slow and uniform rise of ground water level, and the increase of the moisture content of a thick layer of soil resulting from condensation of steam and accumulation of moisture caused by changes in the evaporation process (Razouki et al., 2006).

The mechanical properties of natural soil can be improved by chemical stabilization. Chemical stabilization of soils involves additives such as cement, lime and other chemical additives. Lime stabilization is one of the most economical techniques to improve the engineering behavior of soils. The addition of lime to a soil causes two basic sets of reactions, one being a short-term reaction while the second is long-term reaction. The immediate effect of lime addition to the soil is to cause flocculation and agglomeration of the clay particles caused by cation exchange at the surface of the soil particles. The result of this short-term reaction is to enhance workability and plasticity. The long-term reactions that are accomplished over period of time may require weeks, months or even years for completion of these reactions depending on the rate of chemical decomposition and hydration of the silicates and aluminates. This results in the formation of cementations material, which binds the soil particles together (Little, 1995).

This study was amid to assess the stability behavior of lime stabilized gypseous soil. The effect of gypsum content and long-term soaking on the mechanical properties was investigated. Furthermore, leaching effect on permeability was examined.

MATERIALS AND METHODS OF TESTING

Materials

The soil used in this research work is a fine – grained soil, obtained from borrow pit near Jossigny region in eastern part of Paris – France. Its main geotechnical index properties are liquid limit is (29%), plastic limit (21%) and specific gravity is 2.66. The percentages of clay, silt and sand are 19, 64 and 17% respectively. The soil can be classified as sandy lean clay (CL) per the Unified Soil Classification System (USCS).

The quick lime used in this study, is a very fine lime and passes through an 80 μ m sieve opening. The activity of lime used was 94%. The gypsum used in this study, is a very fine gypsum and passes through an 80 μ m sieve opening, and with purity more than 99%.

Samples Preparation

For preparing the samples, the required amounts of oven-dried soil (2 days at 60°C) were initially mixed with pre-determined quantity of gypsum (0, 5, 15 and 25% by mass

of the dry soil) in dry state. The mixing process continued till obtain uniform color. When no lime was added, the dry soil-gypsum mixtures were directly mixed with the required amount of water, representing the optimum moisture content of the natural soil and the mixture was subsequently put into polyethylene bags. After that the bags were sealed and stored for 24 hrs as mellowing time before compaction. A standard Proctor compaction effort (ASTM D-698) was adopted in the preparation of soil samples. A total of 24 samples of natural (un-stabilized) soil were prepared for unconfined compression test. The soil samples with different gypsum content were stabilized by 3% lime; representing the optimum lime content; based on the Eades and Grim Method (1966). The mixtures were prepared firstly, by thorough mixing of dry predetermined quantities of soil, gypsum and lime to obtain uniform color. Thereafter the aforementioned procedure is used to get a uniform mixture. The mixture was then placed in polyethylene bags and left for 1 hour as mellowing time (Little, 1995).

After that, the soil samples were statically compacted inside a cylindrical stainless steel mold, so that reached the maximum dry unit weight of the natural soil, with a final dimension of soil sample of 50 mm in diameter and 100 mm in height. After the compaction, the soil sample was immediately extracted from the mold, then placed within polyethylene bags to avoid significant variations in moisture content till testing. For the lime stabilized soil samples, these samples were immediately wrapped with cling film and coated with paraffin wax to reduce the moisture loss and cured at room temperature (20°C) for 28 days. A total of 48 samples of stabilized soil were prepared for unconfined compression test.

Soaking Test

At the end of the curing time of 28 days (which represent the initial state), the soil samples were unwrapped of the wax and cling film covering, recorded all dimensions and soaked in water at room temperature (20°C) for 7, 14, 28, 90 and 180 days. The soil samples were subjected to prolonged soaking (i.e. more than 28 days) in order to assess the impact of increasing severity of environmental degrading forces of soaking. The water content of the soil samples were recorded at the end of each soaking period. Volume change variations were considered by measuring the height and diameter of soil samples to evaluate the stability.

The unconfined compressive strength was determined according to the ASTM procedure (D-5102). The wave velocity of soil samples were measured before performance the unconfined compression test. The PUNDIT instrument and two transducers (a transmitter and a receiver) having a frequency of 50 kHz were used.

Leaching Test

During the preparation of soil samples for leaching test, the soil samples were statically compacted inside the stainless steel mold with inside diameter of (97 mm) and

a net height of (38.5 mm), at rate of 1 mm/min. The compaction mold with the soil sample in it was used as part of the leaching apparatus, in order to eliminate disturbance of the sample on extrusion from the mold. Constant head test was adopted to simulate the leaching process. After saturation, the water was allowed to seep through the soil sample under hydraulic gradient of 20 for 30 days. The daily flow water volume was collected in glass vessel for permeability calculations.

RESULTS AND DISCUSSION

Evolution of Unconfined Compressive Strength

The variation of unconfined compressive strength (UCS) of soil samples under different soaking periods is shown in figure (1). Note that it was not possible to determine the effect of soaking on the unconfined compressive strength of unstabilized soil samples as they almost immediately began to collapse when soaked in water. It can be observed that the unconfined compressive strength of soil samples decrease as the soaking period increases. The unconfined compressive strength is less for soil samples having 0% gypsum content at 90 days soaking period and the value was (0.03 Mpa). With the increase in the gypsum content, the unconfined compressive strength of soil samples has been also decreased and the values were (0.38, 0.2 and 0.18 Mpa) for 5, 15 and 25% gypsum content respectively at 90 days of soaking.

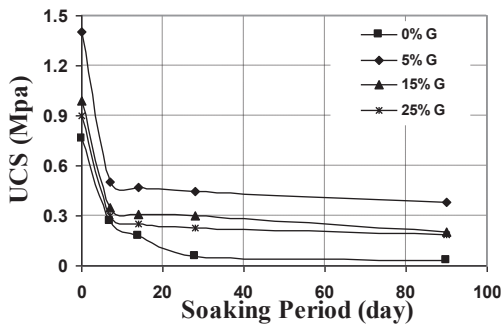


FIG. 1. Unconfined compressive strength variation with soaking periods

The effect of gypsum content was most pronounced on the soil samples having 5% gypsum, demonstrating the largest unconfined compressive strength; small reduction in strength; as shown in figure (1). Another significant result is that, a soaking period of 7 days leads to a significant reduction in unconfined compressive strength of soil samples. In general, the results also showed that the soaking period longer than 7 days does not result in further reduction in unconfined compressive strength. It is worth mentioning

that, all the soil samples became unstable and failed during the soaking at 180 days. In other words, the soil samples did not survive for the unconfined compressive strength at this soaking period. The reason for this failure could be the ineffectiveness of the lime percent and/or due should be gypsum dissolution over a long period of time. The reduction in unconfined compressive strength of soil samples appear to be due the increasing in moisture content, increasing in volume and gypsum dissolution. As known soil is porous media and have ability to absorb and retain water during soaking process. In this stage all available pore space is filled with water and causing reduction in suction forces resulting in the decrease the cohesion between soil particle and unconfined compressive strength.

The amount of water available in soil samples were measured during soaking process, as shown in figure (2), and it was observed that the moisture content increased with increasing soaking period and gypsum content. As the results of the moisture content increasing the volume of the soil samples also increased as presented in figure (3). The increasing in volume is attributed to the expansion of clay particles and presence of ettringite mineral. At the 28 days of curing, ettringite mineral formed, and as well-known ettringite mineral is hydrous mineral and exhibit expansive behavior upon wetting. Moreover, ettringite dehydration was possible contributor to the observed increase volume of gypseous soil samples. Thus, water absorption during soaking led to increase the volume of soil samples by more than (15%) especially for the soil samples having 25% gypsum content.

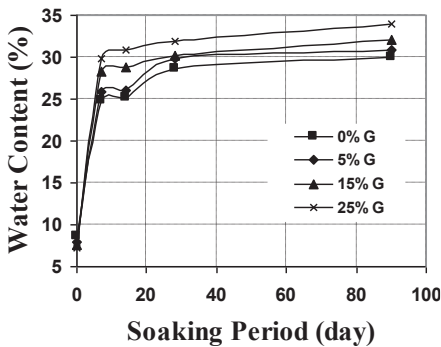


FIG. 2. Water content variation with soaking periods

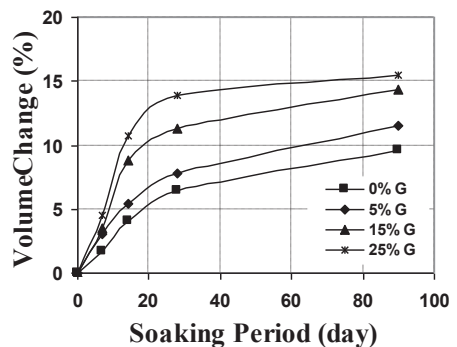


FIG. 3. Volume change variation with soaking periods

The increasing in volume resulted in cracks formation and led to soil samples failed as mentioned previously. Finally, when gypsum adsorbed the water, the cementation property between soil and gypsum particles are destroyed, and the soil structure system change due to particles rearrangement. Also, voids could be formed among soil particles due to gypsum dissolution.

Evolution of Wave Velocity

The variation of wave velocity values of soil samples under soaking are presented in figure (4). It is observed that, there was significant reduction in the wave velocity values of soil samples during soaking, even at 7 days of soaking which represented the most affected period on the wave velocity. The soil samples without gypsum have lowest wave velocity as compared with other soil samples having gypsum content. The effect of soaking as indicated by the reduction in wave velocities increases with increase in gypsum content. This is because more moisture content and cracks formation. Other reason, in a three phase system such as compacted soil, wave transmission occurs through all the phases. Generally, wave velocities in solid are higher than velocities in liquids, which are higher than velocities in gases (McIntire, 1991). Therefore, highest solid and lowest voids in soil samples having 5% gypsum content gave higher wave velocity values as compared with other samples.

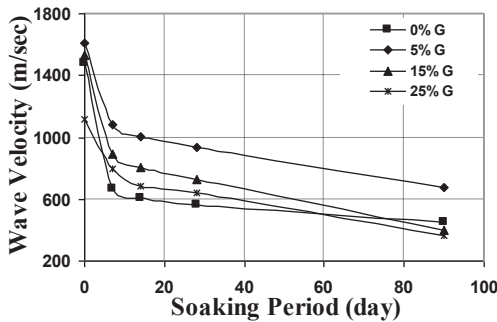


FIG. 4. Wave velocity variation during soaking periods

Evolution of Permeability during Leaching

The measurements of the permeability before and after lime stabilization during leaching process were investigated. Figure (5) present the variation of the permeability values of unstabilized soil samples. It is observed that, gypsum addition marginally reduces the permeability of soil samples. The initial permeability value of soil samples without gypsum decreased from 2.8×10^{-4} cm/sec to 1.3×10^{-4} , 6.7×10^{-5} and 1.65×10^{-5} cm/sec for soil samples having 5, 15 and 25% gypsum content respectively. The change in permeability can be attributed to the variations in grain size distribution of soil samples due to the addition of gypsum.

During leaching process, the permeability values of soil samples increased with increasing leaching time. The permeability of soil samples having 0 and 5% gypsum content increased from 2.8×10^{-4} and 1.3×10^{-4} cm/sec to 9.6×10^{-4} and 1.46×10^{-3} cm/sec respectively, up to 6 days of leaching. After that, the permeability increased rapidly until

reach to 7.3×10^{-3} and 7.54×10^{-3} cm/sec at 10 days of leaching then stabilized. With further increase of gypsum content to 15% and 25% the permeability increased to 7.83×10^{-3} cm/sec up to 5 days of leaching, then will be stabilized. In general, at the early time of leaching (i.e. 2 days), the permeability value of soil samples having 25% gypsum content show an increase in the permeability up to four orders of the permeability of soil samples without gypsum. The leaching of soil samples gives rise to the development of a variety of structural defects such as cavities and microscope voids which lead to increasing permeability. With time these voids become larger and larger, till to be impossible to control the flow of water through the soil samples.

Addition of lime changes the permeability of the soil samples, and during leaching the pattern of change influenced by gypsum added. Figure (6) show the variation of permeability values of soil samples with respect to leaching time. The permeability of soil samples increased with increasing gypsum content. The initial values of stabilized samples were 1.17×10^{-5} , 2.22×10^{-5} , 4.56×10^{-5} and 5.36×10^{-5} cm/sec for 0, 5, 15 and 25% gypsum content respectively. The increasing in permeability with gypsum content is attributed to the changes in micro pores of soil samples during the initial curing time (i.e. 28 days).

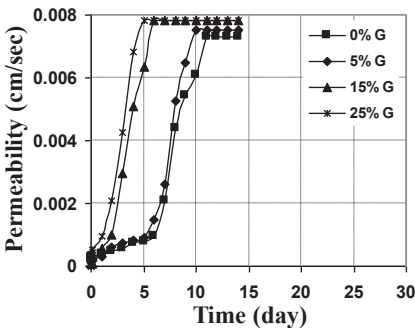


FIG. 5. Permeability variation of unstabilized soil samples during leaching

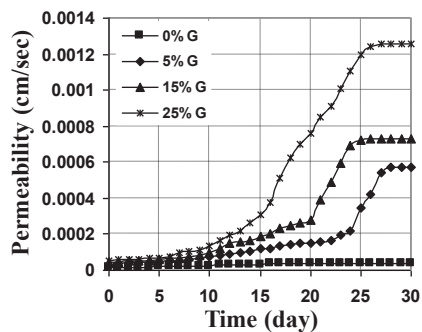


FIG. 6. Permeability variation of stabilized soil samples during leaching

Leaching process increases the permeability of the soil sample having gypsum content, but there is little perceptible change in the permeability of soil samples without gypsum. The permeability value of soil samples without gypsum content increased from 1.17×10^{-5} cm/sec to 4.1×10^{-5} cm/sec after 30 days of leaching. The increasing in permeability can be due to the change in soil structure during curing time and leaching. The continuous leaching which extended to 30 days did not significantly change the permeability of soil samples without gypsum as compared with those having gypsum, and the soil structure remained stable. This is due to more cementing materials could be formed during leaching process.

CONCLUSIONS

The following conclusions can be drawn from this study:

1. Natural soil samples (unstabilized) with and without gypsum content did not sustain the effect of soaking and leaching.
2. The strength and stability properties are considerably enhanced with lime addition.
3. Water soaking led to a significant reduction in the unconfined compressive strength, mainly after 90 days of soaking.
4. Soaking have a detrimental effect on the stability behavior of the soil samples due to more volume change, water content, gypsum dissolution and cavities formation.
5. Leaching is a time-dependent process with a detrimental effect on the stability of soil samples with gypsum. Gypsum content is responsible for the permeability behavior, and as gypsum content leaching time increases the permeability increase.

REFERENCES

- Abduljawwad, S.N. and Al-Amoudi, O.S.B. (1995). "Geotechnical behaviour of saline sabkha soils." *Geotechnique*, Vol. 45 (3): 425-445.
- Ahmad, A.A. (1985). "Lime stabilization of soils containing high soluble salts contents." *M.Sc. Thesis*, College of Engineering, University of Mosul.
- Aldaoood, A. Bouasker M. and Al-Mukhtar M. (2013). "Effect of freezing-thawing cycles on the mechanical properties of lime stabilized gypseous soil." *3rd International Conference on Geotechnical Engineering*: 271-279, Tunisia.
- Al-Zubaydi, A.H. (2011). "Strength and erosion of lime stabilized gypseous soil under different flow conditions." *Al-Rafidain Engrg. J.*, Vol. 19, (2): 12-28.
- Cooper, A.H. (2008). "The classification, recording, data basing and use of information about building damage caused by subsidence and landslides." *Qua. J. of Engrg. Geol. and Hydro.*, Vol. 41 (3): 409-424.
- Eades, J.L. and Grim, R.E. (1966). "A quick test to determine lime requirements for soil stabilization." *Highway Research Record*, No. 139: 61-72.
- Little, D.N. (1995). "Handbook for stabilization of pavement sub- grade and base courses with lime." *National Lime Association*, Iowa, USA.
- McIntire, P. (1991). "Nondestructive testing handbook." *American Society for Nondestructive Testing*, Vol. 7 Ultrasonic Testing, Columbus.
- Razouki, S.S. and El-Janabi, O.A. (1999) "Decreasing in the CBR of a gypsiferous soil due to long-term soaking." *Qua. J. of Engrg. Geol. and Hydro.*, Vol. 31,(1): 87-89.
- Razouki, S.S. Kuttah, D.K. Al-Damluji, O.A. and Nashat, I.H. (2006). "Strength erosion of a fine-grained gypsiferous soil during soaking." *The Arabian Journal for Science and Engineering*, Vol. 32, (1B): 147-152.

The Study on the Influences of Drainage Way Arrangements on the Law of Seepage Flow in the Slope

Bing Yang¹, Chong Wang², Fengtao Wan³, Tao Yang⁴ and Qiurong Yan⁵

¹Associate Professor, School of Civil Engineering, Southwest Jiaotong University, Chengdu, China 610031. E-mail: yangb@home.swjtu.edu.cn

²Graduate Student, School of Civil Engineering, Southwest Jiaotong University, Chengdu, China 610031 E-mail: wangchong546561@163.com

³Graduate Student, School of Civil Engineering, Southwest Jiaotong University, Chengdu, China 610031 E-mail: 764350104@qq.com

⁴Associate Professor, School of Civil Engineering, Southwest Jiaotong University, Chengdu, China 610031 E-mail: yangtao@home.swjtu.edu.cn

⁵Associate Professor, Chongqing Communications Research & Design Institute, Chongqing, China 400067 E-mail: yanqiurong@cmhk.com

ABSTRACT: Rain is an important factor inducing the failure of slope. The existent studies concerning the influence of drainage way arrangement on the seepage flow in the slope are little involved. In this paper the law of seepage flow in the slope exposed to the rain is investigated when the drainage way exists. The mathematical model for seepage flow of rain in the slope is set up, and the finite element method is used to solve the model. The numerical solution of the model is obtained. The results indicate that the drainage way arrangement within the slope has important influences on the distribution of pore water pressure in the slope. The arrangement with the drainage way in the slope and its end extending to the surface of the slope has better effect for the drainage. But the arrangement with the drainage way within the slope along the strike direction of the slope is not good one. The soil between the drainage ways are influenced weakly by the rain, which means that little rain seep into the part of soil.

INTRODUCTION

The main factors of slope failure include rain, earthquake, human inappropriate activity, and so on. Rain is one of the main factors leading to slope failure (Sun 1998; Freeze and Cherry 1979). The seepage flow in the slope exists widely in the medium of rock and soil. The study on the influence of seepage flow on the stability of soil is paid attention by many researchers due to the importance of seepage flow. Freeze and Cherry (1979) discussed the characteristic of seepage flow in the slope with thick overburden layer, and their results show that pore water pressure in the superficial layer with certain depth of the slope increases gradually during the raining. Han and Huang (2012) studied the seepage flow in the soil slope with two layers. Qi et al. (2003) investigated the seepage flow in rock slope due to rain with the method

of numerical simulation, and analyzed the distribution characteristic of pore water pressure in the region of transient saturation. Chen et al. (1998) studied the motion of water and seepage flow in the earth slope under the condition of rain. Zhu et al. (1999) measured the variation of infiltration line and motion of water in the large scale test. Zhan et al. (2003) conducted an in situ test and obtained the variation of pore water pressure, water content, the ratio between horizontal stress and vertical stress of slope, and rate of infiltration with time. It is of important guide significance for existent studies to understand deeply the seepage flow's law in the slope.

In modern transportation engineering, e.g. high speed highway, the slope is usually inevitable. In the slope engineering, all kinds of drainage way are usually installed in the slope, in order to reduce the influence of rainwater on the stability of slope. The drainage way arrangements usually have several options, and how to select the effective drainage way is one of key problems to be solved in the engineering of design. It is important for the selection of effective drainage way to know the characteristic of seepage flow in the slope under the condition of different drainage way arrangement. The existent studies related to the influence of drainage way arrangement on seepage flow in the slope are reported scarcely. In this paper the influences of drainage way arrangements on seepage flow of rainwater in the slope will be investigated, and the characteristic of seepage flow in the slope for different drainage way arrangements will be understood, which can be expected to provide theoretical guideline for drainage design of slope.

GOVERNING EQUATION FOR SEEPAGE FLOW OF RAINWATER IN THE SLOPE

According to the studies available, the seepage flow of water in the soil can be described by Darcy's law, and the governing equation is the following:

$$\frac{\partial}{\partial x} \left(\frac{K_x}{\mu} \frac{\partial p}{\partial x} \right) + \frac{\partial}{\partial y} \left(\frac{K_y}{\mu} \frac{\partial p}{\partial y} \right) + \frac{\partial}{\partial z} \left(\frac{K_z}{\mu} \frac{\partial p}{\partial z} \right) + 2\rho g c_f \frac{K_z}{\mu} \frac{\partial p}{\partial z} + q = \phi c_t \frac{\partial p}{\partial t} \quad (1)$$

The above equation is a two order partial differential equation related to pressure p , and also is the common equation for saturated seepage flow of single-phase flow of water with constant temperature. Where K_x, K_y, K_z are saturation permeability in $x, y,$ and z direction respectively, μ is dynamic viscosity of water, ρ is mass density of water, c_f is compression coefficient of water, $c_t = c_f + c_\phi$ is comprehensive compression coefficient of water, c_ϕ is compression coefficient of pore, g is gravitational acceleration, q is source item.

For the homogeneous medium, permeability, K , is the same in each direction, thus, the partial differential equation with no source is

$$\frac{\partial^2 p}{\partial x^2} + \frac{\partial^2 p}{\partial y^2} + \frac{\partial^2 p}{\partial z^2} + 2\rho g c_f \frac{\partial p}{\partial z} = \frac{\phi \mu c_t}{K} \frac{\partial p}{\partial t} \quad (2)$$

The above governing equation, combined with suitable boundary condition and initial condition constitute the condition of definite solution.

FINITE ELEMENT MODEL OF SEEPAGE FLOW IN THE SLOPE EXPOSED TO RAIN

For most problems, it is difficult to get the analytical solution, and the numerical solution is usually obtained by numerical computation. In this paper the finite element method is employed to solve the partial differential equation of seepage flow and the ABAQUS software is used to conduct the solving process.

The geometry model is shown in Fig.1, which is an abstract model of a construction site of high speed highway in Guizhou Province of China. The size of the model and physical property of soil in the model are nearly consistent with the practical field. The model is 45m long, 25m high. There is a step with a height of 10m in the model of slope. The slope has one layer of soil with a permeability coefficient of 1×10^{-6} m/s. The element type of plain strain, CPE8RP, is employed in the model. Most of elements are quadrilateral and triangular meshes are adopted in some region.

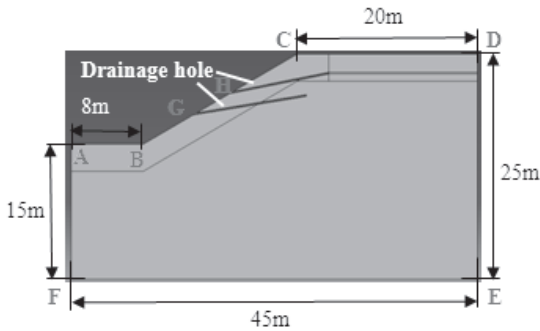


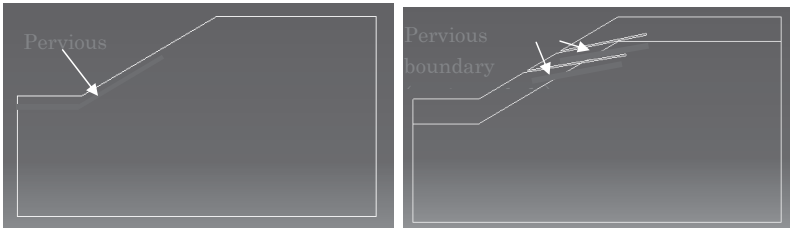
FIG. 1. Geometric model of rainwater's seepage flow.

In the model the displacement of all the grids are fixed. The boundaries of AF , EF , DE , CH are set as impervious boundary, i.e. $\frac{\partial p}{\partial n} = 0$. The boundaries of AB , BG , GH are impervious or pervious according to different drainage way arrangements. The wall of drainage hole is pervious, i.e. $p = 0$. The boundary of CD is inflow boundary and the intensity of inflow is specified at this boundary, i.e. $\frac{\partial p}{\partial n} = \frac{\rho g}{k} V$, V is intensity of inflow. At boundary of CD , V is set as 0.48 m/day.

RESULTS AND DISCUSSION

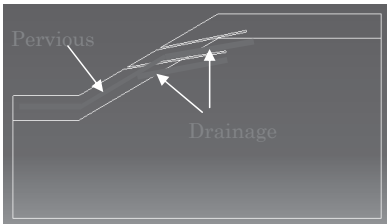
According to the practical cases in the engineering, there exist several kinds of drainage way arrangements in the slope. In this paper, four kinds of drainage way arrangements taken as typical examples are investigated in this paper, which are shown in Fig. 2. The first is that there is no drainage hole in the slope but some section of the slope's surface is pervious. The second is that drainage hole exists in

the slope but the slope's surface is impervious. The third is that drainage hole exists in the slope but some part of the slope's surface is pervious. The fourth is that the slope's surface is impervious but there is a circular cave in the slope.

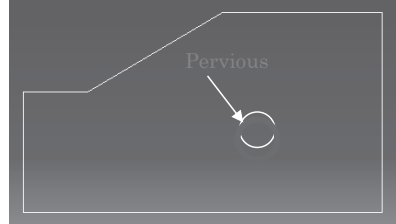


(a) No drainage way in the slope but some section of the slope's surface is pervious

(b) Drainage hole exists in the slope but the slope's surface is impervious



(c) Drainage hole exists in the slope but some section of the slope's surface is pervious



(d) The slope's surface is impervious but there is a circular cave in the slope.

FIG. 2. Schematic of four drainage way arrangements.

Fig. 3 presents the distribution of pore water pressure and seepage flow in the slope at five days after rain for the case of no drainage way in the slope but some section of the slope's surface being pervious. It is shown from Fig. 3 (a) that pore water pressure decreases successively from the top of slope to the outflow surface. The maximum value of pore water pressure occurs at the inflow surface and the minimum one is at the outflow location. At five days after rain the maximal pore water pressure is up to 80 kPa. Several typical streamlines are shown in Fig. 3 (b) and motion tracks of fluid particles in the slope can be seen clearly. The arrow's direction of velocity vector in the seepage flow field represents the direction of fluid particles' motion, and the length of arrow indicates the magnitude of velocity. It can be seen from the figure that the magnitude of fluid velocity has larger value near the inflow surface.

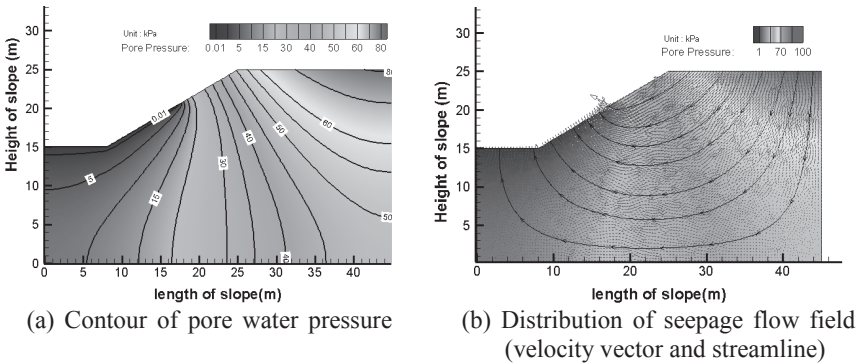
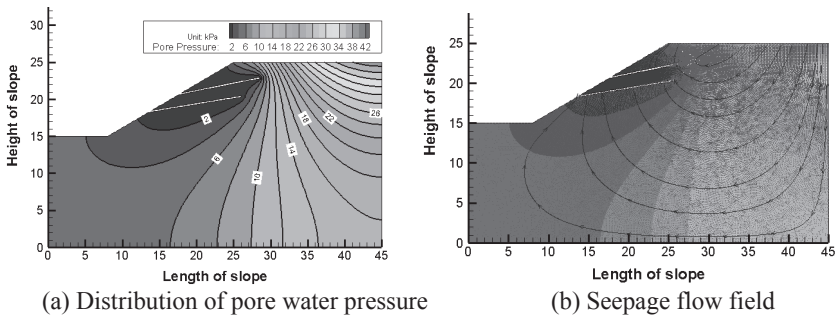
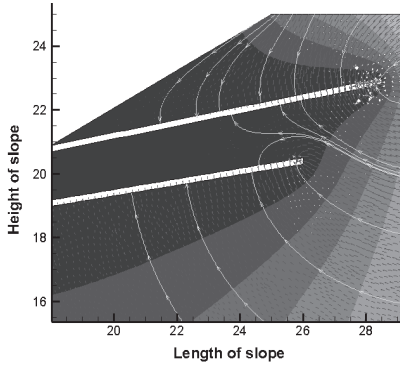


FIG. 3. Distribution of pore water pressure and seepage flow field (no drainage hole in slope, surface of slope is pervious, 5 days after rain).

Fig. 4 shows the distribution of pore water pressure and seepage flow velocity in the slope at five days after rain for the case of existence of drainage hole and slope's surface being impervious. It is indicated from the Fig. 4 (a) that the region where pore water pressure is small mainly locates near the drainage hole due to existence of drainage hole, and the region with higher value of pore water pressure occurs near the right corner of the slope, which is the farthest from the drainage hole. In this case the maximum of pore water pressure is up to 42 kPa. It can be seen from the seepage flow field (see Fig. 4 (b, c)) that the rainwater gathers rapidly at the drainage hole when rainwater infiltrates into the slope. The arrow of flow vector is very intensive at the end of drainage hole (located within the slope), which means more rainwater will flow into the place. It is shown from the streamline diagram that the rainwater infiltrated into the slope will flow out the slope through drainage hole, although it distributes all over the slope. The seepage flow field indicates that the region between two drainage holes almost has no velocity vectors, which means that only small part of rainwater infiltrates into this region and the soil in this region is influenced by seepage flow weakly.

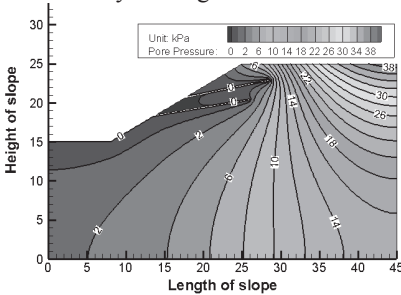




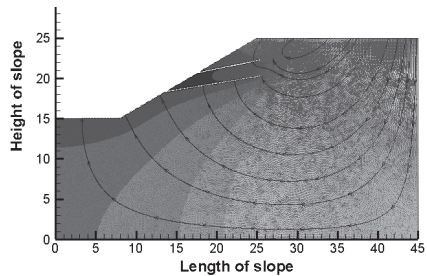
(c) Amplification of local seepage flow field

FIG. 4. Distribution of pore water pressure and seepage flow field (With drainage hole in slope, surface of slope is impervious, 5 days after rain).

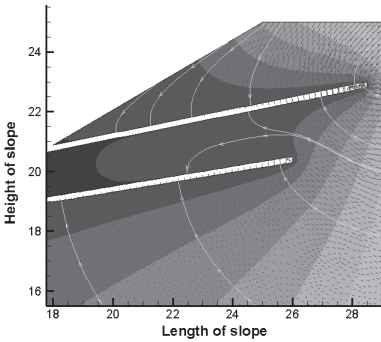
The distribution of pore water pressure and seepage flow velocity field in the slope at five days after rain for the case of existence of drainage hole and slope's surface being pervious are shown in Fig. 5. It is seen from Fig. 5(a) that the size of region with lower value of pore water pressure is notably larger than that for the case of surface being impervious. The rainwater in the slope flow out the slope not only from the drainage hole but also from the surface of the slope (see Fig. 4(b),(c),(d)). By analyzing the results shown in Fig. 4(a) and Fig. 5(a) whether the slope is pervious has little influence on the distribution and the maximum value of pore water pressure for the case of existence of drainage hole. For the case of slope's surface being pervious the maximum value is about 38 kPa and 42 kPa for the impervious one, which means small difference between them. In most region of the slope the characteristic of contour of pore water pressure for the two cases is very similar, which means that the distribution of pore water pressure in the slope is mainly controlled by drainage hole.



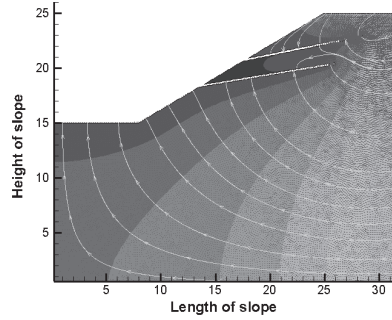
(a) Distribution of pore water pressure



(b) Distribution of seepage flow field



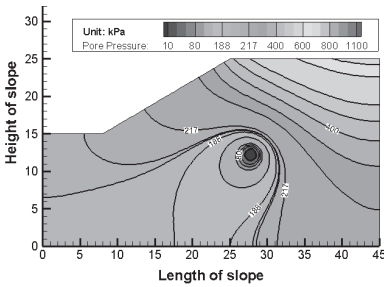
(c) Amplification of local region (1)



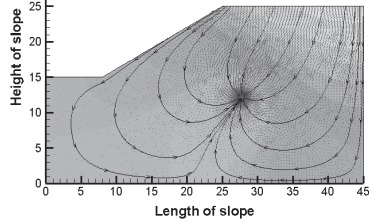
(d) Amplification of local region (2)

FIG. 5. Distribution of pore water pressure and seepage flow field (With drainage hole in slope, surface of slope is pervious, 5 days after rain).

Fig. 6 gives the distribution of pore water pressure and seepage flow velocity field in the slope at five days after rain for the case of existence of only a drainage cave in the slope and slope's surface being impervious. It can be seen from the figure that pore water pressure dissipates slowly and the maximum value reaches to about 1000 kPa. As depicted in Fig 6(b), all the fluid particles gather into the drainage cave.



(a) Distribution of pore water pressure



(b) Distribution of seepage flow field

FIG. 6. Distribution of pore water pressure and seepage flow velocity field in the slope. (Existence of only a drainage cave in the slope, surface of slope is impervious, 5 days after rain).

From the above analysis it can be found that different drainage ways correspond to different distribution of pore water pressure in the slope, and also influence the motion pattern of fluid particles in the slope. The most effective drainage way arrangement is that the drainage hole is laid in the slope and the surface of the slope is impervious.

Fig. 7 presents the variation of pore water pressure at one point in the slope with time for four drainage way arrangements. It is seen from the figure that pore water pressure in the slope increases progressively during the raining. The increasing

amplitude of pore water pressure is larger for the fourth drainage way arrangement, compared with other three arrangements. It means that there is more rainwater accumulated in the slope for the fourth one. However, the other three drainage way arrangements have similar increasing amplitude of pore water pressure.

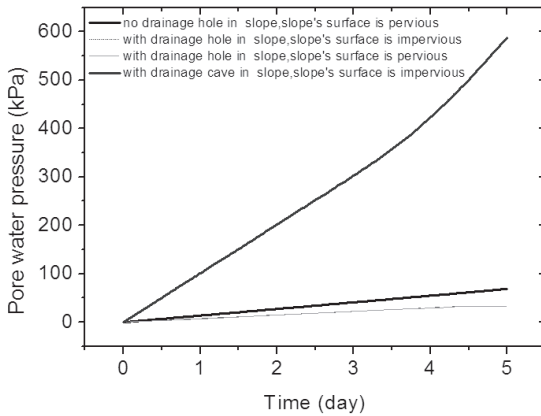


FIG. 7. Variation of pore water pressure with time for different drainage way arrangements.

Distribution of pore water pressure along the line which is 3m distant vertically from the bottom of the step is shown in Fig.8. The pore water pressure has a successive growth from left to right along the line, as indicated in the figure, which is consistent with the distribution of the pore water pressure in the whole slope. While pore water pressure shows a trend at vertical direction that it is higher at upward side and lower at downward side for the case of the first and second drainage way arrangements, it has an opposite trend for the third and fourth ones (see Fig. 9). In Fig. 9 at the abscissa =3m pore water pressure is zero due to the existence of drainage hole, in which it is just at the surface of the hole.

CONCLUDING REMARKS

For the case of existence of drainage hole and slope's surface being impervious, the rainwater gathers rapidly at the drainage hole when rainwater infiltrates into the slope. More rainwater will flow into the place, and only small part of rainwater infiltrates into this region between two drainage holes and the soil in this region is influenced by seepage flow weakly.

Whether the slope is pervious has little influence on the distribution and the maximum value of pore water pressure for the case of existence of drainage hole, and the distribution of pore water pressure in the slope is mainly controlled by drainage hole.

Pore water pressure dissipates slowly for the case of existence of only a drainage cave in the slope and slope's surface being impervious.

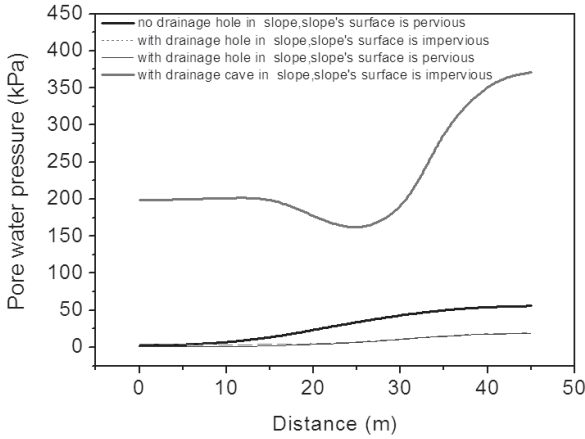
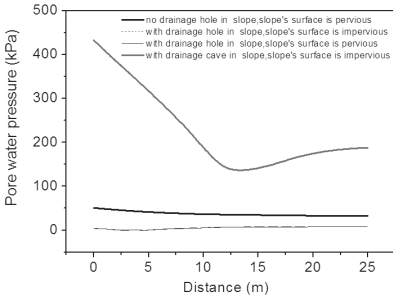
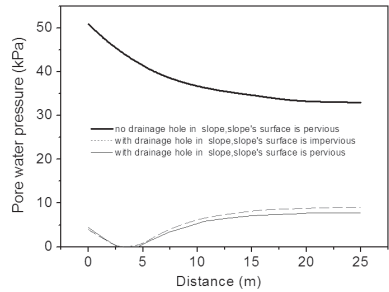


FIG. 8. Variation of pore water pressure with horizontal location (the horizontal line is 3m distant from the bottom of the step, abscissa =0 represents the left end and 45 represents the right end).



(a) Four drainage way arrangements



(b) Three drainage way arrangements (not include the fourth)

FIG. 9. Variation of pore water pressure with vertical location (at $x=25m$, abscissa =0 represents the top and 25 represents the bottom).

Different drainage ways correspond to different distribution of pore water pressure in the slope, and also influence the motion pattern of fluid particles in the slope. The most effective drainage way arrangement is that the drainage hole is laid in the slope and the surface of the slope is impervious.

ACKNOWLEDGEMENT

This project was supported by the National Natural Science Foundation of China (10902112).

REFERENCES

- Chen, S.X. and Chen, S.Y. (1998). "Numerical modeling of the regularity of rain infiltration in unsaturated soil slope." *The 6th National Symposium on Numerical Simulation and Analytical Method of Rock and Soil Mechanics*, 488-493.
- Chen, S.X. and Chen, S.Y. (1998). "Numerical modeling of water motion in soil slope exposed to rain." *The 6th National Symposium on Numerical Simulation and Analytical Method of Rock and Soil Mechanics*, 502-506.
- Han, T.C. and Huang, F.M. (2012). "Rainfall infiltration process and stability analysis of two-layered slope." *Journal of Zhejiang University (Engineering Science)*, Vol. 46 (1): 39-45.
- Jiang, Z.M., Zeng, L., Fu, H.Y. and He Z.M. (2012). "Seepage characteristics of thick coating slope in raining condition." *Journal of Central South University (Science and Technology)*, Vol. 43 (7): 2782-2788.
- Qi, G.Q., et.al (2003). "Numeric simulation on rainfall infiltration on rock slope." *Chinese Journal of Rock Mechanics and Engineering*, Vol. 22 (4): 625-629.
- Freeze, R.A., Cherry, J.A.. (1979). *Ground water, USA: Prentice-Hall, Inc.*
- Sun, G.Z. (1998). *Typical landslides in China, Beijing: Science Press.*
- Zhu, W. et al. (1999). "Stability of river embankment under the seepage of rain or flood." *Chinese Journal of Geotechnical Engineering*, Vol. 21 (4): 414-419.
- Zhan L.T. et al. (2003). "Artificial rainfall infiltration tests on a well-instrumented unsaturated expansive soil slope." *Rock and Soil Mechanics*, Vol. 24 (2): 151-158.

Visualization of Grout Permeation inside Transparent Soil

Jinyuan Liu¹, M. ASCE, Yue Gao², and Wanghua Sui³

¹Associate Professor, Ryerson University, Toronto, Canada jinyuan.liu@ryerson.ca

²Ph.D. Candidate, China University of Mining Technology, Xuzhou, China yuegao.cn@gmail.com

³Professor, China University of Mining Technology, Xuzhou, China suiwanghua@cumt.edu.cn

ABSTRACT: This paper presents an experimental investigation on the permeation process of grout inside soil. The injection of grout inside soil and its permeation process is not well known due to the fact that natural soils are not transparent. In this study, a transparent soil is used to visualize the permeation process. Transparent soil used in this study is made of fused silica and calcium bromide solution with the same refractive index. Geotechnical properties of transparent soil were found to be similar to those of natural sands. A combined grouting and optical measurement system is developed for this study, which consists of a grout injection station with a constant pressure head to inject grout into a transparent soil model, a laser to illuminate the interested cross-section inside the model, and a charge-coupled device (CCD) camera to capture a series of images during the whole grout injection and permeation process. Image processing techniques are used to delineate the fronts of grout body. It was found that the radius of grout body is proportional to the grouting time, which verifies Maag's permeation grouting formula.

INTRODUCTION

The purpose of permeation grouting is to fill voids in a soil or rock mass with a grout fluid at a low injection pressure without destroying the original structure of the soil or rock (Bruce 2005). Permeation grouting has been used to strengthen soil/rock and reduce its permeability for more than two centuries since it was first applied in France in 1802. The first theoretical formula was proposed by Maag (1938) to describe the relationship between the grouting time and the radius of grouting sphere based on assumptions of homogenous and isotropic soils and the grout of a Newtonian fluid. This formula has been widely used in the practice. Recently, Bruce (1994) described the impact factors on the permeation radius, including the pore diameter, Bingham yield stress, and grout pressure. Some special cases, including against

liquefaction and subsurface barrier performance, are studied by other researchers (Finsterle et al. 1997; Sanaz and Behzad 2012). Littlejohn (2003) provided a good summary of the development and applications in practice between 1802 and 2002. In order to investigate the grout movement inside soils, a grout site was exhumed to reveal details of the grout permeation by Dwyer (1994). A similar method was used by Bezuijzen (2007) in the laboratory tests to study the grout movement. Bolisetti (2009) used the acrylic transparent tubes to investigate colloidal silica grout movement. Due to the opacity of natural sands, there is no reported study on visualizing the process of grout injection and permeation process inside soils. This paper presents an experiment to visualize the permeation of grout inside soils by using transparent soil and image processing techniques.

TRANSPARENT SOILS

Transparent soil was first made of silica with a pore fluid with matching refractive indices (Mannheimer and Oswald 1993). It has been used by many researchers in their investigations. Two kinds of amorphous silica were developed before to model sand and clay (Iskander et al. 2002a; 2002b). However, amorphous silica is found to exhibit a higher secondary consolidation and a lower compressibility than natural soils due to its porous particles (Liu et al. 2003).

A new kind of silica called fused silica is used in this study with grain sizes ranging from 0.1 mm to 1.0 mm. Recently, fused silica has been used by other researchers in their model tests (Ezzein and Bathurst 2011). Fused silica used in this study was obtained from Jiansu Kaida Silica Co., Ltd in China without further process. Compared to amorphous silica, fused silica has solid particles with no pores inside, which exhibits a better capacity to model natural sand. Fig. 1 shows the dry fused silica with particle size ranging from 0.1 mm to 1 mm. Physical properties of fused silica used in this study are summarized in Table 1 along with those of Chinese Standard Sand obtained from China ISO Standard Sand Co. LTD., China. The peak friction angle of fused silica is estimated at 32° through a series of triaxial tests on dry medium dense silica. This value of the friction angle is within the normal range reported for natural sands (Holtz et al. 2010). This value is lower than the peak friction angle of $43-44^\circ$ for a similar material reported by Ezzein and Bathurst (2011). The different sources of material and the pore fluids may contribute to this discrepancy.

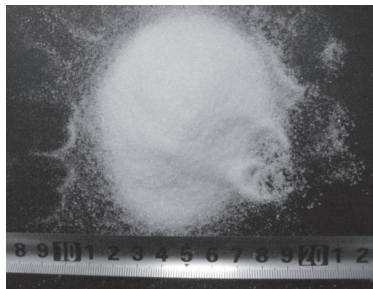


Fig. 1 A picture of fused silica used in this study

A calcium bromide solution is used in this study instead of mineral oils used in other researches due to its easy accessibility. A series of trial and error tests were performed for the calcium bromide solution to achieve the best transparency at a refractive index of 1.4585 with a concentration of approximately 60%. An ink-dyed calcium bromide solution was used as the grout slurry to provide a good contrast for a better visualization of grout permeation inside transparent soil.

Table 1 Physical properties of fused silica and Chinese Standard Sand

| | Gs | e_{\max} | e_{\min} | Dr | e | $k \times 10^{-3} / \text{cm} \cdot \text{s}^{-1}$ |
|-----------------------|-----------|------------|------------|-----------|----------|--|
| Chinese Standard Sand | 2.65 | 0.76 | 0.51 | 30% | 0.68 | 7.00 |
| | | | | 50% | 0.63 | 6.73 |
| | | | | 70% | 0.58 | 6.52 |
| fused silica | 2.21 | 0.80 | 0.51 | 30% | 0.71 | 8.32 |
| | | | | 50% | 0.65 | 7.41 |
| | | | | 70% | 0.59 | 6.39 |

EXPERIMENTAL SETUP

An experimental setup was developed for this study, which consists of a black and white charge-coupled device (CCD) camera and a laser light source. The CCD camera has a resolution of 1024×768 pixels and a maximum frame rate of 30 frames per second (fps). The CCD camera was controlled by the PC through a in-house developed driver in MATLAB®. The 650 nm laser with a power of 65 mW was used to illuminate an interested section inside the transparent soil model. A Plexiglas transparent mold with internal dimension of 50 mm (length) x 50 mm (width) x 50 mm (height) was used with transparent soil filled to the 40 mm deep during testing. A constant pressure grout inject apparatus was set up. The pressure head was about 1500 mm high which approximately equals 15 kPa, a similar device was used by Hayashi (2006). The injection needle was inserted 25 mm into transparent soil. The experimental setup is schematically shown in Fig. 2.

MODEL PREPARATION AND TEST PROCEDURE

The model box was first filled partially with a calcium bromide solution. A total weight of 135 g fused silica was divided into five parts and gradually immersed into the calcium bromide solution. A vacuum pump was applied to de-air the mix until it turned transparent. The above operations were repeated until all fused silica were immersed in the calcium bromide solution to make a transparent soil model. The relative density of fused silica in the sample was estimated to be about $Dr=51.5\%$.

After sample preparation, the injection needle was pushed into the model to a depth of 25 mm below the sample surface. Then, the laser light source was adjusted to

illuminate the interested section immediately passing the injection needle. After that the camera was connected with a frame rate of 30 fps. The background images were taken before the grout injection started. Once the switch on the injection pipe was turned on, a series of images were taken during injection with time data acquired simultaneously into the computer. The tests were stopped after 20 s of grout injection.

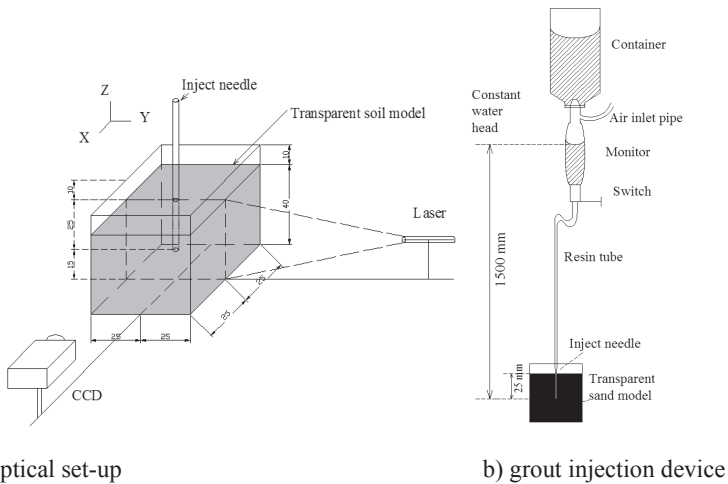


Fig. 2 Schematic diagram of experimental setup for grout permeation test

RESULT ANALYSES AND DISCUSSIONS

A total of 600 images were obtained during the whole grout injection process. A series of 9 images with a time interval of about 1 second were selected for further image processing to visualize the grout permeation process, as shown in Fig. 3.

In order to visualize clearly the movement of grout, an image processing technique called image subtraction was used where the images during injection were subtracted by the background images captured before injection. The improved images can show clearly the movement of grout during injection process, as shown in Fig. 4. It can be found that the grout body is expanding like a sphere from the injection point. It is as expected that the volume of this grout sphere is gradually increasing as the injection time increases.

A linear relationship was proposed by Maag (1938) between the cubic root of grouting time and the radius of grout sphere. This relationship was based on a few assumptions, including soils are homogenous and isotropic with a constant permeability value, the grout slurry is a Newtonian fluid, and a constant the grouting pressure. Based on image analysis, the grout radius was identified by edge detection technique. An excellent linear relationship was obtained with the grout radius and the cubic root of time from image processing of test images, as shown in Fig. 5, where grout body was assumed to be a perfect sphere.

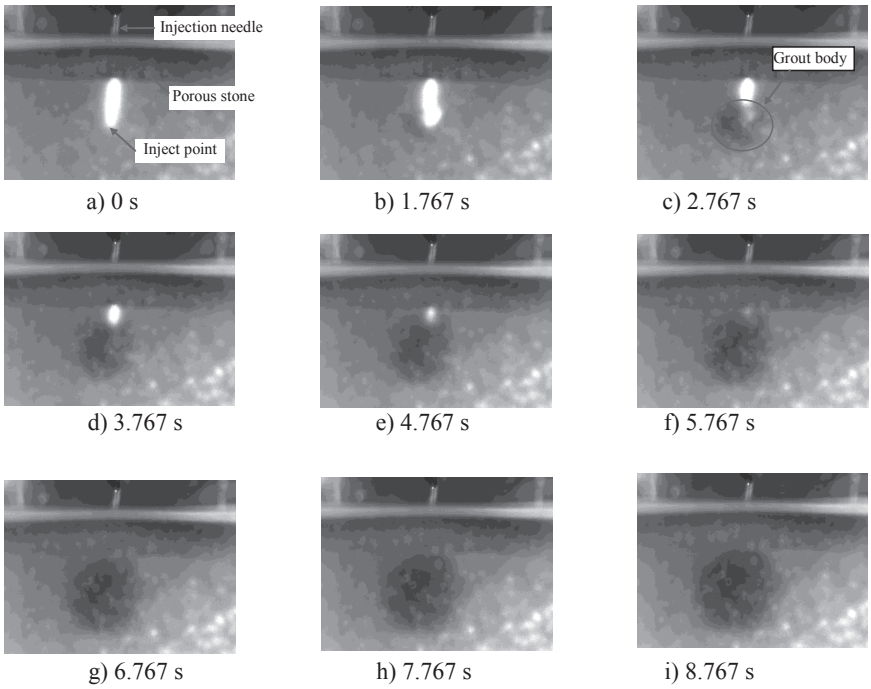


Fig. 3 The series of images captured during grout permeation testing

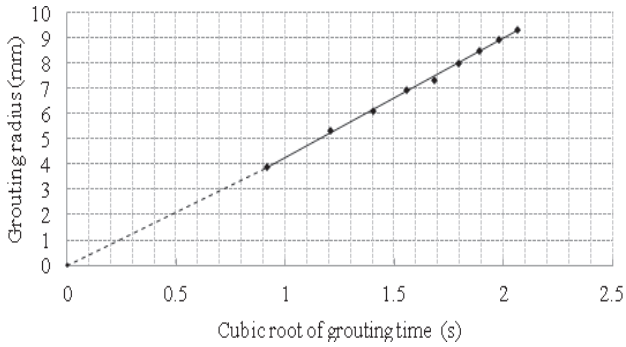


Fig. 5 Relationship between grout radius and grouting time

CONCLUSIONS

This paper presents an experiment to visualize the permeation grouting process

using transparent soil. An optical set-up was developed along with a grouting apparatus. It is as expected that the grout permeates and expands as a sphere as grouting time increases. The image analyses show a linear relationship between the grout radius and the cubic root of time, which verifies the validity of Maag's formula.

There are some limitations found in this study. Due to the degradation of transparent soil model, only a small model was used in this study. A high purity silica and a better fluid are suggested to be able to increase the model size and minimize the boundary effect. An ink-dyed calcium bromide solution was used in this study. A fluid more similar to grout slurry is suggested for further study. One camera was used to provide only two-dimensional images of grout development. Two or more cameras will be used to provide a three-dimensional information of grout in the future.

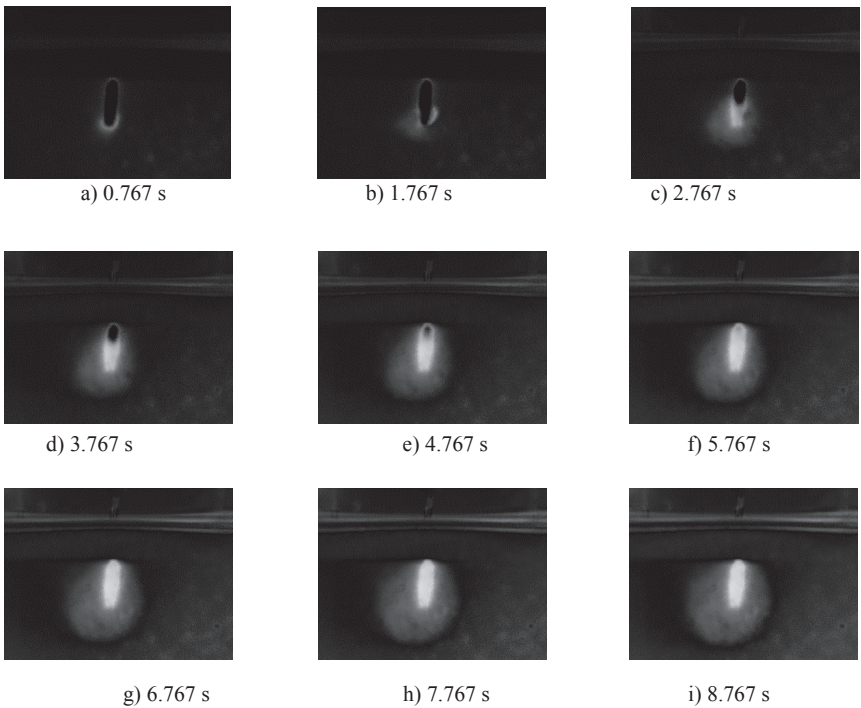


Fig. 4 A clearer view of grout permeation process after image subtraction

ACKNOWLEDGEMENTS

The authors would like to acknowledge the financial support of this research from State Key Laboratory for Geomechanics and Deep Underground Engineering at China University of Mining and Technology (Grant No. SKLGDUEK0903) and the National Natural Science Foundation of China (Grant No. 41072237)

REFERENCES

- Bezuijen, A., Sanders, M. P. M., den Hamer, D., and Van Tol, A. F. (2007). "Laboratory tests on compensation grouting, the influence of grout bleeding." *Proc. 33rd World Tunnel Congress Prague: ITA-AITES*, pp. 395-401.
- Bolisetti, T., Reitsma, S., and Balachandar, R. (2009). "Experimental investigations of colloidal silica grouting in porous media." *J. Geotech. Geoenviron. Eng.*, Vol.135 (5): 697-700.
- Bruce, D. A. (1994). *Ground Improvement and Control*, John Wiley and Sons Inc, New York.
- Bruce, D. A. (2005). "Glossary of grouting terminology." *J. Geotech. Geoenviron. Eng.*, Vol. 131(12): 1534-1542.
- Dwyer B.P. (1994). "Feasibility of permeation grouting for constructing subsurface barriers." *Proc. 33rd Hanford Symposium on Health and the Environment*, Battelle Press, Ohio, pp. 3-36.
- Etzein, F. M., and Bathurst, R. J. (2011). "A transparent sand for geotechnical laboratory modeling," *Geotechnical Testing J.*, Vol. 34(6): 590-601.
- Finsterle, S., Oldenburg, C. M., James, A. L., Pruess, K., and Moridis, G. J. (1997). "Mathematical modeling of permeation grouting and subsurface barrier performance." *Proc., Int. Containment Technology Conf. and Exhibition*, St. Petersburg, Florida, USA, pp. 438-444.
- Hayashi, S., Chai, X. J., Matsunaga, K., and Toki, A. (2006). "Drip injection of chemical grouts: a new apparatus." *Geotechnical Testing J.*, Vol. 29(2): 108-116.
- Holtz, R.D. and Kovacs, W.D. (2010), *An introduction to geotechnical engineering*. Prentice-Hall, Englewood Cliffs, N.J.
- Iskander, M., Liu, J., and Sadek, S. (2002a). "Transparent amorphous silica to model clay." *J. of Geotech. and Geoenv. Eng.*, Vol. 28(3): 262-273.
- Iskander, M., Sadek, S., and Liu, J. (2002b). "Optical measurement of deformation using transparent silica gel to model sand." *Int. J. of Physical Modelling in Geotechnics*, Vol. 2(4): 13-26.
- Littlejohn, S. (2004). "The Development of practice in permeation and compensation grouting: A historical review (1802-2002) Part 1: Permeation grouting." *Proc 3rd Int. Conf. Grouting and Ground Treatment*, ASCE, Reston, VA, pp. 50-99.
- Liu, J., Iskander, M., and Sadek, S. (2003). "Consolidation and permeability of transparent amorphous silica." *Geotechnical Testing J.*, Vol. 26: 390-401.
- Maag, E., 1938, "Ueber die Verfestigung und Dichtung des Baugrundes (Injektionen)," *Erdbaukurs de ETH, Sammlung der Vorträge herausgegeben vom Institut für Erdbauforschung der eidg. Techn. Hochschule Zürich*, Zürich.
- Mannheimer, R. J. and Oswald, C. (1993). "Development of transparent porous media with permeabilities and porosities comparable to soils, aquifers, and petroleum reservoirs." *Ground Water*, Vol. 31: 781-788.
- Sanaz S. and Behzad K. (2012). "Use of grouting method to improve soil stability against liquefaction—A review," *EJGE*, Vol. 17: 1559-1566.

Influence of Curing Time on the Main Mechanical Characteristics of High-Water-Content and Quick-Setting Stones

Hui Xie¹, Changwu Liu², Yu Wang¹, Dingyang Ye¹

¹Graduate Student, State Key Laboratory of Hydraulics and Mountain River Engineering, College of Water Resource and Hydropower, Sichuan University, Chengdu, Sichuan, P. R. China, 610065. E-mail: 463797258@qq.com.

²Professor, State Key Laboratory of Hydraulics and Mountain River Engineering, College of Water Resource and Hydropower, Sichuan University, Chengdu, Sichuan, P. R. China, 610065. E-mail: xxxsd@263.net.

ABSTRACT: High-water-content and quick-setting stones serve as one of the filling materials in the underground goaf, and their water-cement ratio and curing time have significant influence on the main mechanical characteristics. The internal structure of stones was analyzed by scanning electron microscope (SEM), and MTS815 Flex Test GT was used to determine the mechanical parameters. The influence of curing time and water-cement ratio of stones on their main mechanical characteristics was analyzed. The results showed: the microscopic morphology of stones was structure of columnar sticks and mesh; With an increase in water-cement ratio, the internal structure of stones became looser and the compressive strength became lower; With curing time increasing, the strength of stones grew rapidly at the beginning, until reached its maximum at the curing time of 7 days, but then decreased gradually, and finally stabilized; The variation characteristics of elastic modulus and deformation modulus were similar to that of compressive strength; Although there was a small rise at the beginning, Poisson's ratio remained stable on the whole.

INTRODUCTION

Coal is the main energy which people live on in China. With large-scale mining and using of coal resources, surface and shallow underground coal resources gradually dried up, and coal mining is transferring to deep underground. Therefore, the control of ground stress in the goaf has become increasingly prominent, and becomes a major obstacle to safe and efficient deep mining. The problem of goaf surface subsidence has become a major issue restricting the coal mining. Major articles on goaf filling analysis (e.g., Jia Jiancheng, Zhang Miaofeng and Wu Yan 2012. Wang Jin'an, Li Dazhong and

Ma Haitao 2010. Yang Dongwei and Tong Baoguo 2010) describe that goaf filling technique is one of the most effective ways to solve the problem of deep pressure control, maintain goaf stability, improve coal recovery rate, and ensure the safe operation. The economical and feasible filling material is the key factor to the filling technique development. As a new material, which is widely used in various engineering practices, especially in goaf filling, roadway support, and filling the tunnel collapse, High-water-content and quick-setting stones' physical and mechanical properties have called more and more attention. When stones are used as filling materials, the study of their mechanical characteristics is crucial. Meanwhile, the stones can work in the goaf filling to prevent surface subsidence for a long time, so it is very essential to do research about the effect of curing time on the mechanical characteristics of the stones.

These stones have high water content, which are formed by rapid solidification from the mixture of two slurries, so that they are called high-water-content and quick-setting stones. They are usually used in mining engineering as filling materials. Yan Zhiping and Zhu Zanling (2000) describe that the high-water-content and quick-setting materials' blending ratio, confining pressure, water-cement ratio and curing time are the four main factors that significantly affect the physical properties of these stones. With the curing time increasing, strength of stones of different water-cement ratio has a big difference. Hu Hua and Cui Mingyi (2001) describe that the early strength of stones is high, while the late strength is stable. Feng Guangming, Sun Chundong, Wang Chengzhen and Zhou Zhen(2010) describe that the high-water-content and quick-setting stones' early strength is about 20% of the final strength, while 7d compressive strength is up to 60% to 90% of the final strength, and the late strength growth trend is slow. Peng Meixun, Jiang Jianhong, Zhang Xin, Shen Shaohua and Feng Tao (2011) describe that this material is formed by ettringite which contains large amount of crystal water, with the moisture content increasing, the ettringite crystals become tiny, the inner space becomes large as well, and the stones' setting time increases, meanwhile their strength in various curing period reduces accordingly.

The mechanical characteristics of high-water-content and quick-setting stones have great effect on the backfill stability when they are used as goaf filling material, especially the stones' compressive strength, elastic modulus and Poisson's ratio have the most significant effect on deformation and damaging of stones. However, the current study focus on the variation characteristics of strength, while the analysis of the deformation characteristics constants of the material is few, and analysis on influence of curing time and water-cement ratio of the stones on main mechanical characteristics is not comprehensive. Therefore, by the use of SEM、MTS815 and some other test methods, combined with analysis of the internal structure of high-water-content and quick-setting stones, the influence of curing time and water-cement ratio on stones' compressive strength、modulus of elasticity、modulus of deformation、Poisson's ratio and other major mechanical characteristics was studied. What's more, the stress - strain curves of stones cured for different time were researched and the variation mechanical characteristics with curing time increasing were analyzed, thus obtaining the relationship

between the stones' curing time, water-cement ratio and mechanical characteristics.

EXPERIMENT RESULTS AND ANALYSIS

The uniaxial compression test was performed on the MTS815 experimental system in the College of Water Resources and Hydropower, Sichuan University. And the analysis test on the internal structure of stones was performed on the scanning electron microscope (SEM) in Southwest Center for Supervision and Inspection of Mineral Resources, Ministry of Land and Resources. In this experiment, the samples were stones of three different water-cement ratio of 5:1, 6:1, 7:1, and they were respectively cured for 3d, 5d, 7d, 11d, 15d, 25d in water at room temperature before the test.

The Analysis of SEM Results

During the experiment, SEM analysis for stones whose water-cement ratio was 5:1 and 7:1 was respectively conducted. Fig. 1 was SEM images of the stones, and the microscopic morphology of internal structure can be clearly seen from the figure. The microscopic morphology of ettringite which was hydration products included the columnar sticks and mesh, and every stick overlapped disorderly, arranged sparsely with large gap among them. The structure of stones whose water-cement ratio was 7:1 was looser than that of stones whose water-cement ratio was 5:1. With a decrease in water-cement ratio, the internal sticks of stones became compact. Meanwhile, the internal gap of the stones was occupied by water, therefore the material can have high moisture content.

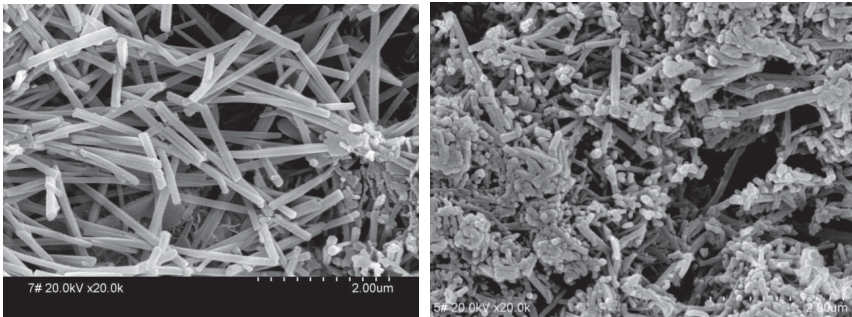


FIG. 1. SEM photograph of stones whose water-cement ratio were 7:1 and 5:1 (20000 times)

The Stress-strain Relationship Curves

Uniaxial compression test was conducted using the standard test pieces of $\Phi 50\text{mm} \times H100\text{mm}$, and the deformation of stones was measured by extensometer

method. According to the measured value of the load and specimen size, the stress - strain curves were drawn in Fig. 2, and the stress-strain curves of stones cured for different time were shown in Fig. 3.

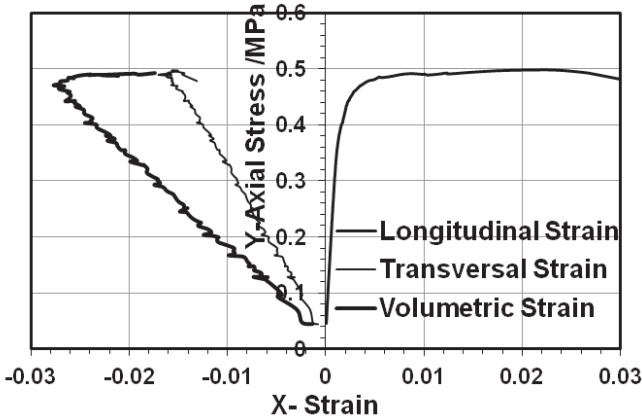


FIG. 2. The stress-strain curves

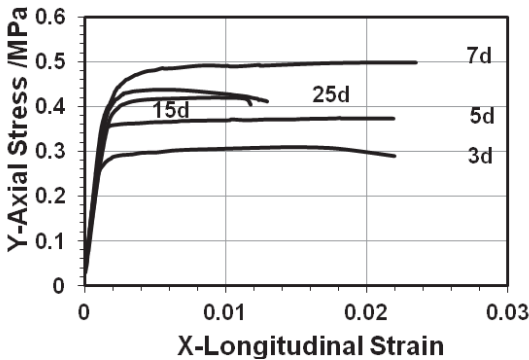


FIG. 3. The stress-strain curves of stones cured for different time

As shown in Fig. 2, the high-water-content and quick-setting stones had elastic-plastic characteristic. Their compression failure process was somewhat different from general rock, while the overall trend was similar. At the very beginning of uniaxial compression, the stress value rose elastically and quickly, while the strain increased slow. When the stress value increased to near the peak load, the longitudinal strain increased rapidly, and while the stress value remained stable for a long period of time, the strain value became larger gradually, and no brittle failure occurred. The stones'

lateral deformation was different from general material. When the material was about to enter the failure stage, the lateral deformation began to decrease, then the transverse contraction appeared, and so as the volume strain. The material's properties of the elastic-plastic deformation with a large deformation were well suited to filling support.

As shown in Fig. 3, it was obvious that the shapes of the curves were the same, and the variation law of various stages was similar. The stress - strain curves had the similar characteristics.

Influence of Curing Time on Stones' Compressive Strength

The variation law of uniaxial compressive strength of three water-cement ratios stones cured for different time was shown in Fig. 4. As shown in Fig. 4, different water-cement ratios stones' compressive strength changed similarly with curing time. With the curing time increasing from 3d to 7d, the material's strength value gradually rose until it reached the maximum at 7d, but then decreased and gradually tended to stabilize. Meanwhile, the stones of different water-cement ratio had big difference in strength. With an increase in water-cement ratio, the strength of the material decreased, which was the same as the characteristics of general materials. Compared with the general concrete, the difference was that the compressive strength of these stones reached maximum at the curing time of 7d, and the strength decreased and stabilized at about 85% of the max compressive strength.

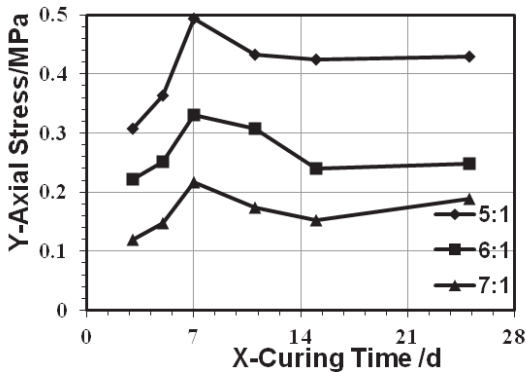


FIG. 4. The variation law of strength of three water-cement ratios stones with curing time

Influence of Curing Time on Stones' Elastic Modulus

Calculation formula for elastic modulus was shown as equation (1), and according to the test data and the stress-strain curve, calculation results were drawn in Fig. 5.

$$E_e = \frac{\Delta\sigma}{\Delta\varepsilon} \quad (1)$$

In the equation, E_e was elastic modulus of the material (GPa); $\Delta\sigma$ was the change of stress value (MPa); and $\Delta\varepsilon$ was the change of strain value corresponded to stress value.

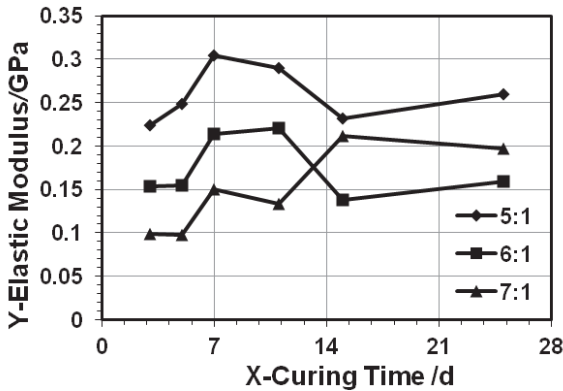


FIG. 5. The variation law of elastic modulus of three water-cement ratios stones with curing time

As shown in Fig. 5, the variation law of elastic modulus of stones whose water-cement ratio were 5:1 and 6:1 were similar, that they all increased with curing time increasing, until they reached maximum at curing time of 7d, but then decreased, and finally a small rise appeared. Although the variation law of elastic modulus of stones whose water-cement ratio was 7:1 was somewhat different from that of the above two, the overall trend was similar. Meanwhile, with an increase in water-cement ratio, the elastic modulus reduced gradually, which was similar to the variation law of stones' compressive strength with curing time.

Influence of Curing Time on Stones' Poisson's Ratio

Calculation formula for Poisson's ratio was shown as equation (2), and calculation results were drawn in Fig. 6.

$$\mu = \frac{\Delta\varepsilon_d}{\Delta\varepsilon_h} \quad (2)$$

In the equation, μ was Poisson's ratio; $\Delta\varepsilon_d$ was the change of transversal stress; and

$\Delta\varepsilon_n$ was the change of longitudinal stress under transversal stress.

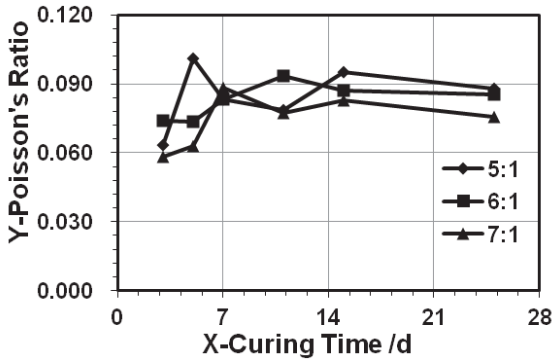


FIG. 6. The variation law of Poisson's ratio of three water-cement ratios stones with curing time

As shown in Fig. 6, the trend of three broken lines was roughly the same obviously. With the curing time increasing, the Poisson's ratio increased, and stabilized around 7d. The change trend of Poisson's ratio of three water-cement ratios stones was the same, without significant difference, which showed the water-cement ratio had little influence on Poisson's ratio. With the curing time increasing, the Poisson's ratio rose up at the beginning by a relatively small change of value, and it was relatively stable on the whole fluctuating around 0.08.

Influence of Curing time on Stones' Deformation Modulus

Calculation formula for deformation modulus was shown as equation (3), and calculation results were drawn in Fig. 7.

$$E_{50} = \frac{\sigma_{50}}{\varepsilon_{50}} \quad (3)$$

In the equation, E_{50} was deformation modulus (secant modulus) of the material (GPa); σ_{50} was stress value which was 50% of compressive strength (MPa); and ε_{50} was Longitudinal strain value under σ_{50} .

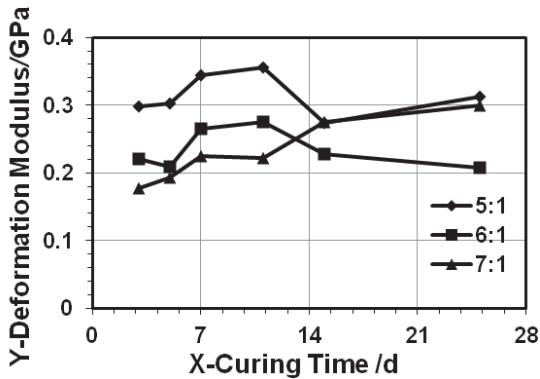


FIG. 7. The variation law of deformation modulus of three water-cement ratios stones with curing time

Compared Fig. 5 with Fig. 7, it could be found that the graphics of elastic modulus and deformation modulus were similar, with the same variation law. And the influence of water-cement ratio and curing time on elastic modulus and deformation modulus was almost the same, while only the value of deformation modulus was slightly larger.

DISCUSSION

According to the internal microscopic structure of stones, there were plenty of gaps among the sticks and brunches of ettringite which was hydration products. Major articles on ettringite analysis (e.g., Feng Guangming 2009. Vahid R. Ouhadi and Raymond N. Yong 2008) showed that its capability of adsorbing water was very high, and the internal gaps were occupied by plenty of crystal water and free water. When stones were under pressure, the gaps were compressed with free water extruded, at the same time, sticks and brunches broke and rearranged. Therefore, large deformation appeared when stones were destroyed with a low compressive strength. What's more, due to the gaps compression and discharging of free water, transverse strain and volumetric strain reduced at late stage of compression. The internal structure of stones whose water-cement ratio was 5:1, with fewer interspaces, was denser than that of stones whose water-cement ratio was 7:1. So the compressive strength of stones whose water-cement ratio was 5:1 was relatively higher.

The stress - strain curve showed that the risen straight segment at the beginning is the elastic stage, with the stress rising fast, while the strain increased slow, and the internal molecular arrangement became compact gradually under compression. The horizontal line segment in the late was the stage of strain growing stably, with the strain growing rapidly, while the stress was relatively stable, and the voids inside stones became smaller under compression, branches structure fractured and rearranged

gradually, until the stones were destroyed under pressure. Although the compressive strength of stones cured for different time varied widely, the process of deformation and failure was similar. The destruction characteristics of high-water-content and quick-setting materials varied little. It's of great significance to grasp the deformation and failure characteristics so as to achieve the security and stability of the works.

The analysis results of the elastic modulus, deformation modulus and Poisson's ratio showed that curing time and water-cement ratio of stones had a large impact on their elastic modulus and deformation modulus. With an increase in water-cement ratio, the elastic modulus and deformation modulus both reduced. Compared with the effect on the compressive strength, curing time had a similar influence on elastic modulus and deformation modulus. However, the Poisson's ratio was almost unaffected by curing time and water-cement ratio. According to the experimental data of elastic modulus, deformation modulus and Poisson's ratio, which were all of small values, the Poisson's ratio remained around 0.08, while the max elastic modulus was 0.304GPa and the max deformation modulus was 0.356GPa, which showed the stones' deformation resistance was poor, with a large deformation under pressure.

With the curing time increasing, the early strength of high-water-content and quick-setting stones grew rapidly, which reached about 60% of the max strength at 3d, while the late strength remained near 85% of the max strength. But the value of stones' strength were small, with the max strength value was about 0.5MPa, and the high water-cement ratio and high moisture content were the main reasons for the low strength values. In engineering applications, it was recommended to use properties of high early strength for roadway temporary support, and took advantages of properties of relatively stable later strength in goaf filling. In order to achieve higher strength, it is recommended to study the appropriate blending ratio and water-cement ratio of stones and analyze the mechanical characteristics of stones under triaxial compression test.

CONCLUSIONS

According to the test results of internal microstructure and compressive strength of stones, the influence of curing time and water-cement ratio on the main mechanical characteristics of stones was analyzed, and main conclusions were drawn as follows:

The microscopic morphology of the high-water-content and quick-setting stones was structure of the columnar sticks and mesh. There were a lot of voids among the structure. With an increase in water-cement ratio, the internal structure of stones became looser with more voids, consequently, the compressive strength of stones became lower and the deformation became larger.

The high-water-content and quick-setting stones presented elastic-plastic damage, with large longitudinal strain, while transverse deformation contracted and volume became smaller when they were destroyed. The stones cured for different time had similar damage characteristics.

With the curing time increasing, the compressive strength of the high-water-content and quick-setting stones increased, and reached maximum at the curing time of 7d, then

gradually decreased, and finally stabilized. The change characteristics of elastic modulus and deformation modulus of stones were similar to that of stones' compressive strength with curing time increasing. With a decrease in water-cement ratio, the stones' compressive strength, elastic modulus and deformation modulus increased, while Poisson's ratio remained stable around 0.08 on the whole, although there was a small rise in the beginning. And the water-cement ratio had no significant effect on Poisson's ratio.

ACKNOWLEDGMENTS

The authors are deeply obliged to the College of Water Resource and Hydropower, Sichuan University for its help under National Basic Research Program of China (973 Program) (2010CB226802) and National Natural Science Foundation Project on Coal Joint Fund (51134018).

REFERENCES

- Jia Jiancheng, Zhang Miaofeng and Wu Yan (2012). "The geological guarantee system for exploiting deep coal resources in safety and high efficiency." *J. Coal Geology & Exploration*, Vol. 40 (6): 1-7.
- Wang Jin'an, Li Dazhong and Ma Haitao (2010). "Study of rheological mechanical model of pillar-roof system in mined-out area." *J. Chinese Journal of Rock Mechanics and Engineering*, Vol. 29 (3): 577-582.
- Yang Dongwei and Tong Baoguo (2010). "Research and application of promoting coal resources achieved on complicat geology." *J. Coal Technology*, Vol. 29 (8): 68-69.
- Yan Zhiping and Zhu Zanling (2000). "Research on the mechanical characteristics of the consolidated soft soil mixed with the high-water-content and quick-setting materials." *J. Journal of South China University of Technology*, Vol. 28 (6): 79-84.
- Hu Hua and Cui Mingyi (2001). "Characteristics of high water content hardening body and analysis on the mechanical mechanism of fill body." *J. Mining Research and Development*, Vol. 21 (5): 23-26.
- Feng Guangming, Sun Chundong, Wang Chengzhen and Zhou Zhen (2010). "Research on goaf filling methods with super high-water material." *J. Journal of China Coal Society*, Vol. 35 (12): 1963-1968.
- Peng Meixun, Jiang Jianhong, Zhang Xin, Shen Shaohua and Feng Tao (2011). "Effect of composition on the performance and microstructures of mining high-water solidified materials." *J. Mineral Engineering Research*, Vol. 26 (3): 56-59.
- Feng Guangming (2009). Research on the superhigh-water packing material and filling mining technology and their application. *PhD Thesis*, China University of Mining and Technology, Xuzhou, Jianguo, 163p.
- Vahid R. Ouhadi and Raymond N. Yong (2008). "Ettringite formation and behaviour in clayey soils." *J. Applied Clay Science*, Vol. 42 (1-2): 258-265.
-

Soil Cementation Generated and Enhanced by Electrokinetics

Julie Q. Shang¹, Ping hui Liu²

¹ Ph. D., P. Eng. Professor, Department of Civil and Environmental Engineering, Western University, Spencer Engineering Building, Room 3082, London, ON, Canada N6A 5B9; jqshang@uwo.ca

² Associate Professor, North China University of Water Resources and Electric Power, Zhengzhou, Henan, China; pinghui.liu@hotmail.com

ABSTRACT: Electrokinetics has been applied in geotechnical engineering, specifically in soil improvement, for near a century. Most engineering applications and research projects have focused on electro-osmotic consolidation generated by the negative pore water pressure, as well as settling of suspended soil solids due to electrophoresis. Although many studies have reported that significant cementation bonds have developed in soils after electrokinetic treatment, a systematic study on the subject, i.e. the mechanism and observations from field and lab experiments, has not been reported. In this review, the cementation developed in marine sediments and offshore calcareous sands is presented along with discussion of the principles of electrokinetic cementation. The study is of particular importance in earthquake engineering for development of soil improvement technologies against seismic loading, because electrokinetics generated cementation of soils may significantly reduce the risk of soil liquefaction.

INTRODUCTION

Electrokinetics has been successfully applied for soil improvement in civil engineering (Casagrande 1952). Research and field applications using electrokinetic (EK) technology to treat soft clays, mine tailings and waste slurry have been successful in field applications and reported extensively (Srinivasaraghavan and Rajasekaran 1994, Wrixon and Cooper 1998, Shang 2000, Lo and Shang 2000, Cundy and Hopkinson 2005, Fourie and Jones 2007). The Helmholtz-Smoluchowski model (H-S model) is widely used to explain electro-osmosis (EO) in soils. This theory is first introduced by Helmholtz (1879) and later refined by Smoluchowski (1921). It has been recognized that the effect of electro-osmosis is attributed to the negative pore water pressure generated at the anode, which leads to soil consolidation. However, the electrochemical effects associated with electrokinetics play important role in the overall treatment, which have been observed by many researchers but not addressed in detail. This paper addresses principles of electrokinetics generated cementation by electrochemical reactions induced by electrical current. Three cases carried out by the

authors' research group are presented to support the discussion.

THEORETICAL BACKGROUND

Electrokinetic treatment is a soil improvement technique used for strengthening fine grained soil. Previous studies have reported the potential of using electrokinetic treatment to generate cementation in soil. Although many studies reported the observation of cementation in the electrokinetic treatment, its mechanisms has not been clearly understood. The cementation process in soil involves many electrochemical reactions, mainly controlled by water pH. Applying an electrical current by electrodes embedded in soil generates oxidation at the anode and reduction at the cathode, i.e.



The protons (H^+) generated at the anode migrate towards the cathode. Simultaneously, the hydroxides (OH^-) generated at the cathode migrate towards the anode, which generate a pH gradient between the anode and cathode. The soil can retard the change in pore fluid pH, which is referred to as acid/base buffering capacity. The soil pH during and after an electrochemical treatment is controlled by the acid buffering capacity. Two predominant sources have been identified as the contributing factors to the cementation during an electrokinetic process, i.e. carbonates and amorphous compounds. The carbonates (CO_3^{2-}) in soil have high acid buffering capacity due to the rapid dissolution, for example,



The effects of carbonates are two folds: to enhance the electro-osmotic flow process by reducing the soil acidity and to generate carbonate cementation bonds in soil. If anodes in the electrokinetic treatment are made of structural steel or other consumable metals as commonly reported in field applications, the anode releases cations, which will precipitate again in soil, serving as amorphous cements. For example, the electrochemical reaction of iron in calcareous soil submerged in water can be illustrated by the pe-pH diagram showing the iron dissolution/precipitation in Fig. 1. The precipitation of cations is controlled by pH and pe. As shown in Fig.1, the ferric and ferrous ions are dissolved at low pH. The precipitation of ferrous ions mainly forms siderite (FeCO_3) in a carbonate rich environment, which is an amorphous compound that serves as a cementing agent:



As discussed, when a soil is subjected to an electric current for a sustained time, cementation bonds develop, which is evidenced by the increase in the soil undrained shear strength, cohesion, and plasticity, as will be demonstrated in the following three case studies.

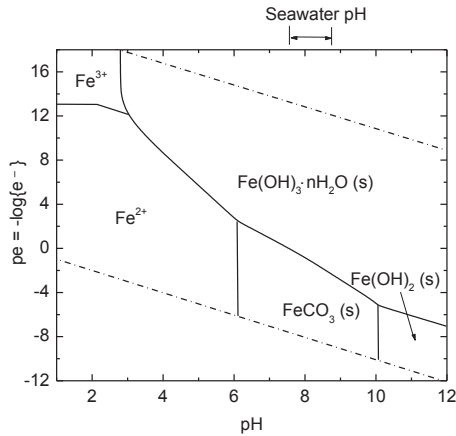


FIG. 1. pe-pH diagram for a Fe-H₂O-O₂-CO₂ system (modified from Whittemore and Langmuir 1975)

CASE STUDIES

1. Improvement of the load-carrying capacity of offshore skirted foundations by electrokinetics (S. Micic, J.Q. Shang, and K.Y. Lo 2003)

A large-scale testing facility was designed to investigate the effect of electrokinetic treatment on the load-carrying capacity of skirted foundations embedded in soft marine deposits. The facility included a model tank, a steel cylinder to simulate a skirted foundation, electrodes connected to a dc power supply, loading equipment, and monitoring device (a pressure transducer, displacement transducer, ammeter, and voltmeter). The model tank was made of electrically insulating poly-propylene with dimensions of 150 cm long, 75 cm wide, and 70 cm high. The tank was divided by a HDPE plate into two identical compartments, i.e., compartment A and Compartment B. Each compartment houses a soil sample of 73 cm * 73 cm * 65 cm (L*W*H). In the first electrokinetic test, compartment A was used for the electrokinetic treatment, while compartment B served as a control without treatment. Compartment B was employed later for the second electrokinetic test. The skirted foundation model was made of a steel cylinder with an outside diameter of 320 mm, inside diameter of 315 mm, and unit weight of 347.5 N/m. These dimensions give a length to diameter ratio of 1.25. Two identical cylinders were embedded in the soil samples, one for electrokinetic treatment and the other for control. The clay used in the study was a dredged river sediment mixed with salt water to simulate a marine sediment.

During the electrokinetic tests, an electric field was generated by electrodes installed both inside and outside of the foundation model. Eight electrodes were installed circularly outside the cylinder and five electrodes installed inside the cylinder. EK test 1 was performed in compartment A. The test was started 26 days after the consolidation pressure of 15 kPa was applied. At that time, the soil in compartments A and B had reached an average degree of consolidation near 90%. The soil in

compartment A was subjected to a dc voltage of 5.2 V for 28 days, i.e., the anode and cathode potentials relative to the ground were +5.2 V and 0 V, respectively. EK test 2 was performed in compartment B after the cylinder was loaded to failure for the control test. The soil around the cylinder in compartment B was remolded to simulate aggressive cyclic loading conditions during a storm. Then the soil was left to reconsolidate for 30 days at a pressure of 15 kPa. EK test 2 was conducted under the same electrical conditions as those in EK test 1.

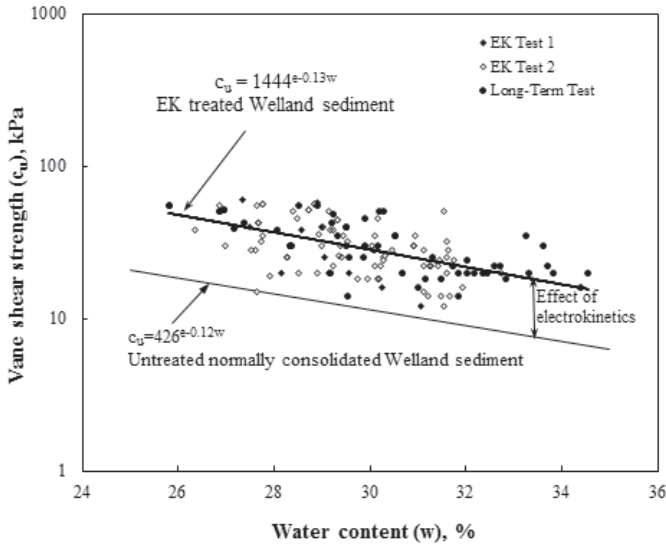


FIG. 2. Undrained shear strength and water content relationship after treatment.

Figure 2 shows the soil undrained shear strength versus water content after the EK tests, along with the undrained shear strength and water content (c_u - w) relationship measured from the untreated normally consolidated river sediment. The figure clearly shows that the application of electrokinetics generated a significant strengthening effect. It indicates that the undrained shear strengths of the treated soil are higher at the same water content than those of the untreated soil. The average shear strength of the treated soil adjacent to the cylinder was 30.5 kPa, indicating an increase of 150% by electrokinetic treatment, compared to the average undrained shear strength of 12.3 kPa of the untreated soil. On the other hand, it is noted that there was only a small decrease in the soil water content after the EK treatment which indicates that the electrokinetic treatment induced development of soil cementation in addition to consolidation and dewatering by electroosmosis. Furthermore, it was observed that a soil layer of about 15 mm thick was firmly attached to the steel cylinder and steel electrodes. The soil attached on the cylinder and electrodes had a very firm to hard consistency. Additional chemical analysis of the soil sample also supported the fact

that amorphous compounds have formed and served as cementing agents. As a result, the overall load carrying capacity increased 200% after the electrokinetic treatment.

2. Electrochemical Cementation of Offshore Calcareous Sand (E. Mohamedelhassan, J.Q. Shang, M.A. ismail, and M.F. Randolph 2005)

A large scale laboratory experimental study was conducted on the electrochemical cementation of calcareous sand from Western Australia coast. The sand is poorly graded with coefficients of uniformity and curvature of 1.84 and 0.94, respectively. Seawater recovered near the sampling site was used in the study. The main cation and anion in the seawater are sodium and chloride. Two identical electrochemical treatment tanks were designed and manufactured for the study. One tank was used to provide the baseline data or the control test, and the other, for that after electrochemical treatment. The tank was made from a steel drum 575 mm in diameter, 750 mm in length and 5 mm in wall thickness. A drainage valve was installed at the base of the tank to facilitate saturation of the calcareous sand. A caisson foundation model, 200 mm in diameter, 400 mm in length and 3 mm in wall thickness, made of a steel cylinder, was embedded in the calcareous sand submerged in seawater recovered near the sampling site. The hollow electrodes were filled with soluble CaCl_2 granules as the cementation agent, which were forced into the calcareous sand by an applied intermittent electric current. A dc voltage of 8 volts with current intermittence and polarity reversal was applied over a period of 7 days. A control test with identical configuration to that of the electrochemical treatment test was also set up to provide baseline data.

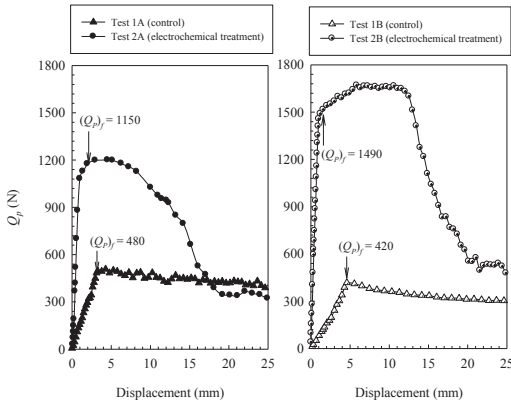


FIG. 3. Pullout resistance, Q_p , vs. displacement of caisson. (Mohamedelhassan and Shang 2005)

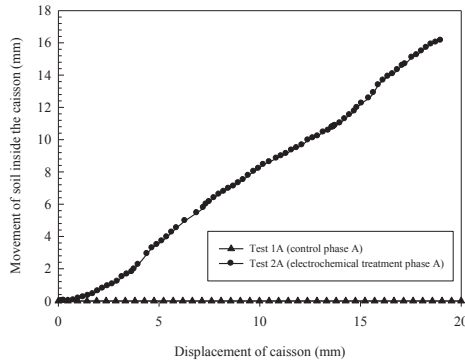


FIG. 4. Movement of soil inside the caisson vs. movement of the caisson (soil plug action) (Mohamedelhasan and Shang 2005).

Fig 3 presents the pullout resistance of the cylinder, Q_p , versus the displacement after electrochemical treatment, compared with the control. The results showed that the pullout resistance of the foundation model increased 140% prior to failure and 255% post-failure after the electrokinetic treatment, as compared with that of the control test. Another important effect observed in the test series is the formation of a soil plug in the caisson, as indicated by the movement of the soil enclosed in the cylinder during the pullout test after electrochemical treatment (Fig. 4.). No soil plug was formed in either of the control tests. This is particularly important in the increase of the caisson's bearing capacity. The results are further supported by chemical analysis of soil samples after treatment. X-ray fluorescence (XRF) analyses were conducted to identify the chemical changes in the calcareous sand, in particular the newly formed compounds, due to electrochemical treatment. XRF analysis showed significant increase in the amount of iron oxide (Fe_2O_3), an amorphous compound known as a natural cementing agent, due to corrosion of the electrodes and caisson during the electrochemical treatment process. In comparison with the control sample, Fe_2O_3 increased by 55% on the soil between the wall of the tank and the cemented column and increased by 677% in the soil between the cemented columns. The percentage of Fe_2O_3 in the sand cemented on the electrodes is about 84 times its weight on the control sample.

3. Improvement of Marine Sediment by Combined Electrokinetic and Chemical Treatment (Pinghui Liu and Shang 2012)

An experimental program was designed and carried out on a marine clay from Korean coast to study the combined chemical and electrokinetic treatment. The chemical admixtures used in the study included sulphate resistant cement, quicklime and coal fly ash. The effectiveness of the combined treatment was evaluated in terms of the soil water content, Atterberg limits, carbonate content, undrained shear strength, compressibility and pore water chemistry. The soil samples were prepared with

dredged marine sediment mixed with synthetic sea water made by sea water crystals. Four electrokinetic tests were performed with different chemical admixtures added to the soil samples under the same testing conditions. In addition, four control tests (with chemical treatment only) were performed with the same surcharge, drainage condition, chemical admixture, and testing duration but without the application of the electrical current.

It was found that both quicklime and cement enhanced the undrained shear strength of the marine sediment, whereas coal fly ash did not achieve the enhancement. Without adding any admixture, the specimen was very soft, with the undrained shear strength of only 2-3.5 kPa, after 7 days consolidation under 5 kPa. The undrained shear strength only increased to 8-12.5 kPa after electrokinetic treatment alone without admixture mixing. The highest shear strength was achieved by adding quicklime up to 58 kPa. Sulphate resistant cement also enhanced the undrained shear strength of the sediment up to 47 kPa. Coal fly ash failed to increase the shear strength of the sediment. After EK treatment the undrained shear strengths (Cu) of sediments were further increased from 14.9% to 300% as compared to chemical treatment only. The highest undrained shear strength was up to 86 kPa at the cathode and 72 kPa at the centre, compared to 45 kPa and 34 kPa from the control. According to the tests results, the combined electrokinetic and chemical treatment for 7 days increased the undrained shear strength of marine sediment up to 200% compared to the chemical treatment only. Moreover, plasticity of the sediment was changed significantly after the treatment, as shown in Figure 5. It is shown that all points of treated samples lie below the A-line, indicating the decrease of plasticity due to EK and chemical treatment in all samples, attributed to the cementation effects.

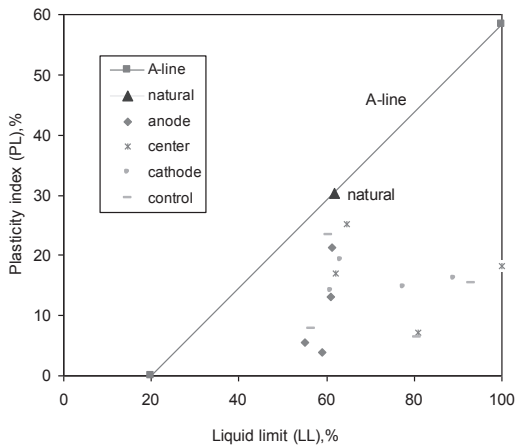


FIG. 5. Plasticity chart before and after the treatment

CONCLUSIONS

The principles of electrokinetic cementation are attributed mainly to carbonates and amorphous compounds generated by electrochemical reactions during electrokinetic treatment. Three case studies are presented to illustrate the cementation generated by

electrokinetics, including a river sediment, a calcareous sand, and a marine sediment. The cementation bonds developed are reflected as the increases in the undrained soil shear strength, pullout resistance of foundation models, and changes in the soil plasticity and chemical composition. These features highlight the possible engineering applications of electrokinetics for soil improvement and foundation applications. We have done research showing EK alone is effective under various conditions. However, it is beyond the scope of this paper.

ACKNOWLEDGMENTS

The research is funded by the Natural Science and Engineering Research Council of Canada and the Science Foundation of North China University of Water Resources & Electric Power.

REFERENCES

- Casagrande, L (1952). "Electro-osmosis stabilization of soils." *Journal Boston Society of Civil Engineers*, Vol 39: 51-83.
- Cundy, AB, and Hopkinson, L (2005). "Electrokinetic iron pan generation in unconsolidated sediments: implications for contaminated land remediation and soil engineering," *Applied Geochemistry*, Vol 20, No 5: 841-848.
- Fourie, A.B., Johns, D.G., and Jones, C.J.F.P. (2007). "Dewatering of mine waste using electrokinetic geosynthetics." *Canadian Geotechnical Journal*, Vol. 44: 160-172.
- Helmholtz, H. (1879). "Studies of electric boundary layers" *Wiedemann's Annalen D. Physik*, Vol.7: 337-382.
- Lo, K.Y., Shang, J.Q., Micic, S. et al. (2000). "Electrokinetic strengthening of soft marine clays." *International Journal of Offshore and Polar Engineers*, Vol 10, No 2: 137-144.
- Liu Pinghui and Shang J.Q. (2012). "Improvement of Marine Sediment by Combined Electrokinetic and Chemical Treatment." *Proceedings of the 22th International Offshore and Polar Engineering Conference*, Vol.2: 618-625.
- Micic, S., Shang, J.Q., and Lo, K.Y. 2003. "Improvement of the load-carrying capacity of offshore skirted foundations by electrokinetics." *Canadian Geotechnical Journal*, Vol. 40: 949-963.
- Mohamedelhasan, E., Shang, J.Q., Ismail, M.A. and Randolph, M.F. (2005). "Electrochemical cementation of calcareous sand for offshore foundations." *International Journal of Offshore and Polar Engineering*, Vol.15: 71-79.
- Smoluchowski, M. (1921). "Handbuch der Elektrizität und des Magnetismus." *L. Graetz .Ed. Barth, Leipzig*, Vol. 2: 379.
- Srinivasaraghavan, R., and Rajasekaran, G. (1994). "Electro-osmotic stabilization of marine clay with chemical piles." *Ocean Engineering*, Vol 21, No 2: 207-219.
- Shang, J.Q. (2000). "Electrokinetics in Geotechnical and Geoenvironmental Engineering Applications." *Canadian Geotechnical Colloquium Speech. Proc 53rd Canadian Geotechnical Conference*, Montreal, Quebec, Vol 1: 5-23.
- Wrixon, R.C. and Cooper, G.A. (1998). "Theoretical and practical application guidelines for using electrokinetics to improve casing support in soft marine sediments." *Proc IASC/SPE Asia Pacific Drilling Technology Conference*, APDT: 77-83.

The Effect of Excavation Disturbance on Rockburst Trigger under Different Horizontal Geostress

ZHANG Ru¹, WU Gang^{2*}, GAO Ming-zhong³,
WEI Jin-bing⁴, ZHANG Yan-fei⁵

¹State Key Laboratory of Hydraulics and Mountain River Engineering, College of Hydraulic and Hydroelectric Engineering, Sichuan University, Chengdu 610065, China; zhangru@scu.edu.cn, gmzh@scu.edu.cn, jbwei@scu.edu.cn, 454813796@qq.com

^{2*}Headmaster's Office, Sichuan University, Chengdu 610065, China; scuwg@scu.edu.cn (corresponding author)

ABSTRACT: Rockburst is one kind of dynamic geological disaster, and the influencing factors are complicated and diversified. Among which the high geostress is the major external cause, the hard brittle rock mass is the major internal cause, and excavation disturbance is the major incentive. The initial horizontal geostress in the surrounding rock significantly affects distribution of secondary stress after excavation, which is closely related to rockburst occurrences. Therefore it is necessary to study the excavation disturbance on rockburst trigger under different horizontal geostress. To accomplish the research goal, the underground powerhouse at Pubugou hydropower station in Sichuan Province, China was taken as an example. The numerical model was set up to simulate the actual excavation steps and predict rockburst intensity based on stress criterion. The analysis indicated that the potential hazard of rockburst increased with the rise of horizontal geostress. When horizontal geostress was more dominant, rockburst usually happened on the roof and bottom of cavern; when vertical geostress was more dominant, rockburst usually happened on the side wall of cavern. Specially, when the ratio of horizontal geostress to vertical geostress was greater than 1.7, we should seriously pay attention to the effect of excavation disturbance on rockburst trigger and take proper measures to prevent and control rockburst.

INTRODUCTION

Rockburst is one kind of dynamic geological disaster under high geostress during underground works excavation. It is a sudden brittle fracture(Wang 2009) caused by internal fracture of rock and release of elastic strain energy, often accompanied by sloughing, burst spalling and even ejection damage to rock mass. Due to its suddenness in time and uncertainty at location, rockburst will cause direct damage to persons and construction equipment, consequently affect construction progress and increase project investment. It has become a significant problem associated with

worldwide underground excavation projects. Especially in recent years, such fields as energy, hydropower, national defense and traffic engineering expand to deeper levels. The depth of underground mining and underground structure arrangement increases each year, for instance, relevant data indicate that many coal mines in China will reach mining depths of 1000 to 1500m in the next 20 years(Xie 2006). Therefore, it is likely that the frequency, intensity, and quantity of rockburst occurrence will increase correspondingly.

However, influencing factors of rockburst are complicated and diversified, which increase the difficulty for this study and prove to be the main reasons that hinder the study progress (Wang 2009). Based on the study of rockburst formation mechanism, statistic analysis of rockburst data from all over the world, and experimental and theoretical demonstration in recent decades, it is considered that rockburst has at least a certain relationship with the following factors, i.e. high geostress, rock structure and properties, excavation depth, geologic structure conditions, shallow supergene transformation, shape and dimensions of cavern excavation, hydrogeological conditions, shake, etc. These factors are not independent but interrelated with each other(Zhou1995,Wu2008, Ortlepp 2005). Under general conditions, high geostress and rock structure and properties are dominant factors for rockburst occurrence, the former is the external cause and the latter is the internal one.

Occurrence environment of high geostress provides the force source for elastic strain energy storage of surrounding rock mass and rockburst occurrence. Two external factors contribute mainly to high geostress, i.e. tectonic stress and burial depth. It can be seen from practical engineering that quantity, frequency and intensity of rockburst gradually increase as burial depth increases. However in areas with intense geologic tectonization, rockburst may also occur in shallow level when lateral pressure ratio $k = \sigma_h / \sigma_v$ (horizontal stress/vertical stress) is high. It is thus clear that magnitude and distribution of initial horizontal geostress are closely related to secondary stress redistribution after excavation and rockburst occurrence, and therefore it is necessary to conduct systematic study on the law of effect on excavation disturbance to rockburst trigger under different initial horizontal geostress.

Based on the review of the distribution rule of geostress in rock mass, this paper, taking underground powerhouse at Pubugou hydropower station as one example, selects different amounts of initial horizontal geostress by numerical modeling to simulate actual excavation steps, analyzes the relationship between secondary stress and initial horizontal geostress, carries out preliminary forecasting of rockburst occurrence intensity, and discusses the effect of excavation disturbance on rockburst trigger under different level of horizontal stress.

DISTRIBUTION RULE OF INITIAL GEOSTRESS IN ROCK MASS

There are many causes for stress occurrence in rock mass, such as tectonic stress generated from tectonic movement, gravity stress caused by the weight of overlying rock mass, temperature stress caused by temperature change, earthquake force, etc. Furthermore, there are other reasons for stress occurrence such as stress redistribution in cavern surrounding rock caused by excavation and additional stress

in rock foundation caused by the weight of large dams and other buildings. Rock mass stresses, regardless of cause, are generally referred to geostress collectively. Traditionally, the geostress existing in rock mass before engineering construction is called initial stress or natural stress such as tectonic stress and gravity stress. The magnitude of initial stress mainly depends on the weight of overlying rock and the type, intensity and duration of tectonization.

The distribution of initial stress in rock mass is extremely complicated. Based on a large number of research results from geostress survey, it is found that the geostress in the shallow level of earth's crust has a complicated distribution rule affected by geologic structure, lithology, topography and landform, etc. However, according to analysis of current existing measured data, the change rule of geostress within 3000m can be concluded as follows:

(1) Geostress field belongs to an unstable stress field. Under general conditions, the geostress field is a three-dimensional anisobaric space stress field and the magnitude and direction of principal stress changes with space and time.

(2) The characteristics of vertical and horizontal geostress. Analysis of a great amount of geostress measured data indicates that vertical stress σ_v is basically equal to the weight of overlying rock γH at a depth of 25 to 2700m, i.e., $\sigma_v \approx \gamma H$, $\gamma = 27\text{kN/m}^3$. Table 1 provides geostress measured data for some project areas.

Table 1 Measured data of horizontal and vertical stress for some project areas

| Measured location | Lithology | Depth (m) | Horizontal stress σ_h (MPa) | Vertical stress σ_v (MPa) | Lateral pressure ratio $k = \frac{\sigma_h}{\sigma_v}$ |
|--|--|-----------|------------------------------------|----------------------------------|--|
| Powerhouse No.2 for 511 Project | thick-bedded sandstone in original state | 98 | 3.86 | 2.57 | 1.50 |
| Yingxiuwan underground powerhouse | Granite and granodiorite | 200 | 12.36 | 9.92 | 1.25 |
| Ertan powerhouse | Granite | 100 | 9.0 | 21.6 | 0.41 |
| 511 Project | Granite | 50~60 | 12.0 | 4.00 | 0.30 |
| Some dam areas of Three Gorges | Thin-bedded medium-thick microcrystalline argillaceous strip | 128 | 15.75 | 6.93 | 2.30 |
| Some dam areas of Three Gorges | Limestone of Longdong Formation | 100 | 8.98 | 4.38 | 2.05 |
| Taipingba cavern No.2 | Huangling granite-diorite | | 20.5 | 10.7 | 1.98 |
| Baishan project | Migmatite | 60 | 45.6 | 17.8 | 2.50 |
| Three-cascade Hydropower Station on the Yili River | Broken basalt | 60 | 1.98 | 2.22 | 0.98 |
| Three-cascade Hydropower Station on the Yili River | Basalt | 175 | 1.99 | 2.38 | 0.87 |
| Three-cascade Hydropower Station on the Yili River | Volcanic breccia | 220 | 8.87 | 7.97 | 1.12 |
| The fourth power plant in Yunnan | Limestone | 0~70 | 1.72~2.40 | 1.28~1.46 | 1.36 |

Horizontal geostress, σ_h , defined as the mean value of two horizontal stress components is mostly greater than vertical stress, σ_v . The lateral pressure ratio is defined as $k = \sigma_h / \sigma_v$, whose value is basically between the relationships given in formula (1):

$$\frac{100}{H} + 0.30 \leq k \leq \frac{1500}{H} + 0.5 \quad (1)$$

H refers to the depth of measured stress (unit: m). The range of the k value is 0.5~3.5 and it decreases as H increases. In the case of a shallow depth (for example, $H < 1000\text{m}$), k is disperse and great. As the depth increases, the dispersity of k gradually decreases, and measured data indicate that k gradually tends to 1. This shows that the stress state is close to hydrostatic pressure state at greater depths.

EFFECT OF EXCAVATION DISTURBANCE ON ROCKBURST UNDER DIFFERENT VALUES OF HORIZONTAL STRESS

As previously mentioned, high geostress conditions in rock mass is an external leading factor to cause rockburst. The occurrence of rockburst is closely related to the distribution and centralization degree of secondary stress after excavation, which is significantly affected by the value of horizontal stress. Therefore, we take the underground caverns of Pubugou hydropower station in south west China as one example to study the effect of horizontal stress on rockburst. First, we establish a plane numerical model to simulate the excavation steps (Fig.3), then input different k values to represent different horizontal stresses. Calculation results are used to analyze the maximum principle stress with the change of k after every excavation step, and to discuss the triggering effect of excavation disturbance on rockburst under different values of horizontal stress.

Introduction of Pubugou Hydropower Station and Rockburst Phenomenon

Pubugou hydropower station is one of the control reservoirs along Daduhe river basin. It is a large water conservancy and hydropower project, mainly for power generation, with the function of flood control and sediment containment. Gross installed capacity of the hydropower station is 3300MW, and 6 mixed flow water turbines with single-machine capacity of 550MW are provided. It comprises core-wall rockfill dams with gravelly soil, an underground workshop system at the left bank, shore-side open spillways, tunnel spillways, vent holes at the right bank and Niger River diversion works. The underground caverns consist of a main workshop, a main transformer chamber, a draft tube gate chamber, 2 non-pressure tailrace tunnels and 6 diversion tunnels which are crossed with each other and have large structures. The size of the main workshop is 208.6m×30.7m×70.175m (length×width×height); the width above the crane beam reaches 30.7m and that under the crane beam is 26.8m. The size of the main transfer cavity is 250.3m×18.3m×25.58m (length×width×height); the size of the draft tube gate chamber is 178.87m×17.4m×53.35m (length×width×height).

The underground caverns of Pubugou hydropower station are located in the mountain at the left bank of downstream and the burial depth is 220 to 360 meters. The overlying rock is granite which is very hard and thick, which provides the main internal condition to trigger rockburst. According to spot test, the maximum initial geostress is 28.3MPa, which provides the main external condition to trigger rockburst.

Rockburst occurred in fresh rock mass during exploration and survey. The locations of rockburst occurrence are as follows, exploratory holes of No.45 which is located at 70m of the downstream along the axis of the dam, 263 to 275m section of main hole, and 70 to 80m section of adit No.4. Especially, adit No.4 had severe rockburst phenomenon, such as splitting and spalling of rock on the abutment and the hole wall, accompanied with the sound of fracturing. The depth of fracturing could reach to 1 to 2 meters.

Rockburst statistics during excavation indicate that most of rockburst took place at an early stage during excavation in 2004. Rockburst occurred in construction adit No.4 and No.9, the underground workshop, the draft tube gate chamber, the tailrace tunnel and the access traffic hole on several occasions. The working platform frame and hand drills were seriously damaged and even operating personnel were injured during rockburst, which greatly affected the construction schedule and caused threat to life of construction personnel. Typical site rockburst photos are shown in Figure 1.



(a) Rockburst in adit No.2 connected to the end of the auxiliary workshop



(b) Wall caving at the transition between tailrace tunnel No.1 and adit No.9

FIG 1 Typical rockburst photos in underground caverns of Pubugou hydropower station

Numerical Model, Calculation Parameters and Proposals

Figure 2 shows calculation grid using finite element method. Based on the geometrical dimensions of the underground caverns at Pubugou hydropower station and the topographic conditions close to the cross section of the unit No.5, the model calculation range is as follows: 6 times of the overall space of 3 caverns in the horizontal direction, in the vertical direction from the ground to around 6 times of the cavity under the main workshop. The model calculation range in horizontal direction and vertical direction is 750m×970m. The number of mesh grid and node is 5665 and 2883, respectively. See Table 2 for calculation parameter values. Mohr-coulomb strength criterion is used and a total of 9 excavation steps is simulated in the model.

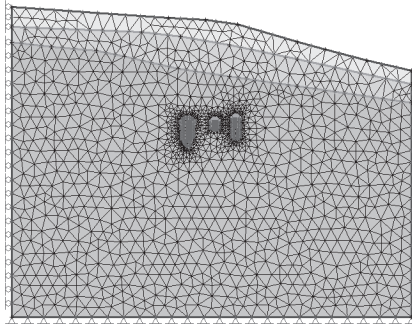


FIG. 2 Calculation grid using finite element method

Table 2 Physical and mechanical parameters of rock mass

| | $\gamma(\text{kN/m}^3)$ | E (GPa) | μ | C (MPa) | φ (°) |
|------------------------------------|-------------------------|---------|-------|---------|---------------|
| Upper layer in Fig3(gray color) | 25.0 | 0.8 | 0.33 | 0.08 | 30.1 |
| Medium layer in Fig3(green color) | 26.1 | 12.0 | 0.25 | 1.0 | 40.4 |
| Bottom layer in Fig3(yellow color) | 26.1 | 17.0 | 0.23 | 1.5 | 42.0 |

According to measured geostress data of some project areas in China, lateral pressure ratio is from 0.3 to 2.5 (Xu 1993). From table 3, according to the measured geostress data in underground caverns of Pubugou hydropower station, there are a total of 6 measuring points, the maximum principal stress is 28.3MPa, and the maximum horizontal stress is 27.01MPa. The value of k for the 6 measured points at Pubugou hydropower station is 1.73, 1.80, 1.41, 1.36, 1.53 and 1.50, resulting in an average value of about 1.55. Therefore, we input 8 different values of k into the calculation model showed in Fig.3, to simulate the different initial horizontal stress conditions and study the effect of excavation disturbance on rockburst trigger. The 8 different values of k are chosen as 1.1, 1.3, 1.7, 2.0, 2.3, 2.5, 2.7, 3.0.

Table 3 Measured site geostress and burial depth of Pubugou hydropower station

| No. of test point | Burial depth of test point (m) | | Test results | | | | | | | | | Calculation results | | | |
|-------------------|--------------------------------|----------|--------------------------|------------|-----------|-------------------------------|------------|-----------|--------------------------|------------|-----------|---------------------|-----------------|----------------|--------------------------------|
| | | | Maximum principle stress | | | Intermediate principle stress | | | Minimum principle stress | | | Horizontal stress | Vertical stress | Gravity stress | Stress ratio % |
| | Horizontal | Vertical | σ_1 | α_1 | β_1 | σ_2 | α_2 | β_2 | σ_3 | α_3 | β_3 | σ_h | σ_v | σ_{sz} | $\frac{\sigma_{sz}}{\sigma_v}$ |
| 1 | 385 | 262 | 16.5 | 54 | 20 | 9.7 | 307 | 39 | 2.8 | 165 | 44 | 15.25 | 8.81 | 6.86 | 77.8 |
| 2 | 300 | 214 | 23.3 | 84 | 15 | 12.9 | 194 | 52 | 9.3 | 344 | 34 | 22.46 | 12.48 | 5.61 | 44.9 |
| 3 | 150 | 165 | 10.1 | 283 | 7 | 7.1 | 54 | 79 | 6.3 | 192 | 8 | 9.99 | 7.11 | 4.32 | 60.7 |
| 4 | 410 | 291 | 21.1 | 81 | 7 | 15.5 | 246 | 32 | 4.8 | 351 | 2 | 21.05 | 15.51 | 7.62 | 49.1 |
| 5 | 460 | 263 | 28.3 | 84 | 29 | 14.9 | 216 | 15 | 2.7 | 340 | 24 | 24.43 | 15.96 | 6.89 | 43.1 |
| 6 | 520 | 315 | 27.3 | 68 | 10 | 23.3 | 168 | 45 | 11.8 | 328 | 43 | 27.01 | 17.96 | 8.25 | 45.9 |

Note: stress in the table is in MPa; angles α and β are in degrees.

Calculation Results and Analyses

The calculation results of the 6th excavation step were used as one example. Distribution of isolines of the maximum main geostress under different lateral pressure ratios, is given in Figure 3.

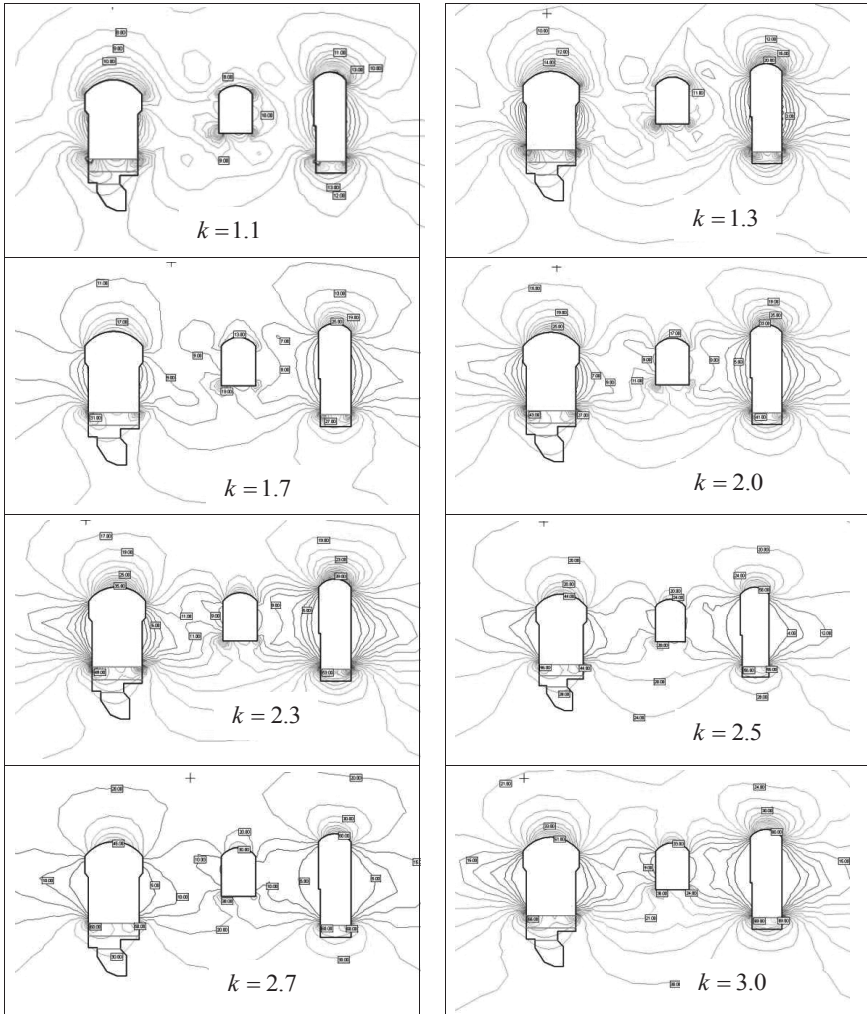


FIG. 3 Isoline map of the maximum main geostress under different lateral pressure ratio ($k = \sigma_h / \sigma_v$) (during excavation of the 6th step)

As to the main powerhouse, the relations between k and σ_1 / σ_c after each

excavation step are plotted in Figure 4.

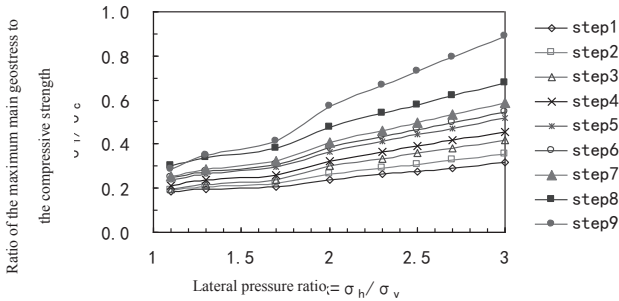


FIG. 4 Values of σ_1/σ_c under different lateral pressure ratio k during 1 to 9 excavation steps in main powerhouse

The maximum main geostress value and the rockburst discrimination results are described in Table 4. The following preliminary conclusions are reached based on the analyses:

(1) During excavation of the 6th step as indicated in Figure 3, the concentration of geostress of the main powerhouse and the draft tube gate chamber becomes more significant compared with that of the main transformer room, which is consistent with the on-site rockburst record, i.e. rockburst in the main powerhouse and the draft tube gate chamber is much more severe than that in the main transformer room. By comparing and studying redistribution of geostress due to excavation disturbance under different k , transfer of the concentration area of geostress in the three main caverns under different horizontal geostress can be indicated. According to Figure 4, when k is small, concentration of geostress at the side wall is quite distinct; when k becomes larger, the concentration area of geostress tends to transfer from the arch support to the crown. It can be concluded that when horizontal geostress dominates, rockburst mainly occurs at the roof and bottom of the cavern; when vertical geostress dominates, there will be great potential risk of rockburst at the side walls. The k of the underground caverns at Pubugou hydropower station is approximately 1.55, which indicates the dominance of horizontal stress. Meanwhile, according to field observation and statistic data during the excavation period, rockburst of the crown is more significant. As a result, it is necessary to strengthen monitoring and focus more on rockburst of the crown part of the surrounding rock.

(2) According to study results shown in Figure 4, and Table 4, the larger k is, the larger the maximum main geostress value after rock mass excavation will be, and the larger the ratio of the maximum main geostress to the compressive strength σ_1/σ_c will be. Based on the geostress criterion brought forward by Wang Lansheng (Wang 2003), the possibility as well as intensity of rockburst will increase along with the σ_1/σ_c value. It indicates that the rise of horizontal geostress will cause increment of potential rockburst risk. Moreover, when k is around 1.7, it seems to be a turning

point. When k becomes higher than 1.7, the increment of secondary geostress of the surrounding rock under excavation disturbance is significant along with the increasing of horizontal stress; when k is less than 1.7, there is no significant change in secondary geostress of the surrounding rock with the increasing of horizontal geostress. This shows that the potential hazard of rockburst increases when the degree of unevenness of geostress in the rock mass rises.

Table 4 Impact of horizontal geostress on rockburst in main powerhouse

| Excavation step | Maximum main geostress and rockburst evaluation (MPa) | Lateral pressure ratio $k = \sigma_h / \sigma_v$ | | | | | | | |
|-----------------|---|--|-------|-------|-------|-------|-------|-------|--------|
| | | 1.1 | 1.3 | 1.7 | 2.0 | 2.3 | 2.5 | 2.7 | 3.0 |
| 1 | $\sigma_{1\max}$ | 22.33 | 23.56 | 24.94 | 28.87 | 31.44 | 33.21 | 35.01 | 38.40 |
| | Evaluation | N | N | N | N | N | N | N | S |
| 2 | $\sigma_{1\max}$ | 22.97 | 24.74 | 26.62 | 31.66 | 34.84 | 37.00 | 39.19 | 42.50 |
| | Evaluation | N | N | N | N | None | S | S | S |
| 3 | $\sigma_{1\max}$ | 23.43 | 26.12 | 28.86 | 35.88 | 40.17 | 43.05 | 45.94 | 50.29 |
| | Evaluation | N | N | N | N | S | S | S | S |
| 4 | $\sigma_{1\max}$ | 25.40 | 28.29 | 31.27 | 38.96 | 43.66 | 46.81 | 49.99 | 54.76 |
| | Evaluation | N | N | N | S | S | S | S | S |
| 5 | $\sigma_{1\max}$ | 28.55 | 31.89 | 35.31 | 44.09 | 49.46 | 53.05 | 56.67 | 62.11 |
| | Evaluation | N | N | N | S | S | S | S | M |
| 6 | $\sigma_{1\max}$ | 29.69 | 33.28 | 36.96 | 46.37 | 52.10 | 55.94 | 59.80 | 65.61 |
| | Evaluation | N | N | N | N | N | S | S | M |
| 7 | $\sigma_{1\max}$ | 30.51 | 34.56 | 38.67 | 49.12 | 55.46 | 59.70 | 63.95 | 70.33 |
| | Evaluation | N | N | S | S | S | S | M | M |
| 8 | $\sigma_{1\max}$ | 36.30 | 40.89 | 45.55 | 57.39 | 64.57 | 69.38 | 74.19 | 81.44 |
| | Evaluation | S | S | S | S | M | M | M | M |
| 9 | $\sigma_{1\max}$ | 34.33 | 41.91 | 49.50 | 68.46 | 79.83 | 87.42 | 95.00 | 106.38 |
| | Evaluation | N | S | S | M | M | I | I | I |

Note: "N" represents none, "S" represents Slight, "M" represents Moderate, "I" represents Intense.

CONCLUSIONS AND SUGGESTIONS

By summarizing the initial horizontal geostress in certain underground projects, it is found that the horizontal geostress relates closely to occurrence of rockburst. By reviewing the distribution law of geostress in rock mass, it is concluded that the lateral pressure ratio, k , varies within the range of 0.5 to 3.5; moreover, the horizontal geostress component is higher than the vertical geostress component in actual survey of many underground works. Therefore, we take the underground caverns of Pubugou hydropower station (k is about 1.55) as an example, to set up a numerical model and study the trigger action of excavation disturbance on rockburst under different horizontal geostress. Main conclusions and suggestions are made as follows:

(1) According to results of the plane numerical simulation study on the impact of horizontal geostress on rockburst, the larger the initial horizontal geostress is, the larger the value of maximum main geostress after excavation will be, which reflects the increase of degree of stress unevenness in the rock mass that can increase potential hazard of rockburst.

(2) When horizontal geostress dominates, rockburst mainly occurs at the roof and floor of the cavern; when vertical geostress dominates, rockburst tends to transfer to the side wall.

(3) When k is around 1.7, it seems to be a turning point. When k becomes higher than 1.7, the increment of secondary geostress of the surrounding rock under excavation disturbance is increased significantly along with the increasing of horizontal stress. When k is less than 1.7, there is no significant change in secondary geostress of the surrounding rock with the increasing of horizontal geostress. It shows that when the horizontal geostress component accounts for a larger proportion, excavation disturbance will intensify unevenness of stress in the rock mass and thus increase potential hazard of rockburst. As a result, it is suggested that in project areas with high actually measured horizontal geostress, especially in areas with $k > 1.7$ ($k = \sigma_h / \sigma_v$, i.e. horizontal geostress / vertical geostress), special attention should be paid to the rockburst trigger action of excavation disturbance and rockburst protection and control measures shall be taken in advance.

ACKNOWLEDGMENTS

The authors are grateful for the financial support from the Natural Science Foundation of China (51204113), the National Key Basic Research Projects of China (2011CB201201, 2010CB226802, 2010CB732005) and Sichuan Youth Science and Technology Foundation (2012JQ0031).

REFERENCES

- Wang Lansheng et al, *High Geostress and Stability of Surrounding Wall of Erlangshan Tunnel* [M]. Beijing: Geological Publish House, 2003.
- Xie Heping, *Engineering Disaster Induced by Exploration of Deep Resources & Basic Science*; Xie Heping, Peng Suping, He Manchao, *Basic Theoretical Research and Engineering Practice of Deep Exploration*. Beijing: Science Press, 2006: 3 – 14.
- Xu Zhiying, *Rock Mechanics* [M]. Beijing: China WaterPower Press, 1993.
- Zhou Depei, Hong Kairong, *Characteristics and Control Measures of Rockburst of Taipingyi Tunnel* [J]. *Chinese Journal of Rock Mechanics and Engineering*, 1995, 14(2): 171 – 178.
- Wu Xuanzheng, Li Mingchuan, Wu Yuteng, *Analysis and Control Measures for Rockburst in the Auxiliary Tunnel Works of Jinping Hydropower Complex* [J]. *Journal of Shandong University (Engineering Science)*, 2008, 38(3): 28 - 33
- W.D. Ortlepp. RaSIM comes of age—a review of the contribution to the understanding and control of mine rockbursts. Sixth International Symposium on Rockburst and Seismicity in Mines Proceedings, 2005: 3 - 20.

Parametric Study on the Effect of Deep Excavation on the Adjacent Metro Station in Suzhou

Shifeng Wei¹, Shaoming Liao², Yanbing Zhu³, Xiang Li⁴ and Yong Tan⁵

¹Department of Geotechnical Engineering, Tongji University, 1239 Siping Road, Shanghai 200092, P. R. China; sfwei@outlook.com

²Department of Geotechnical Engineering, Tongji University, 1239 Siping Road, Shanghai 200092, P. R. China; liaosm@126.com

³China Railway No.4 Survey and Design Group Co., Ltd., 745 Peace Avenue, Wuhan 430063, P. R. China; mic2001@126.com

⁴Department of Geotechnical Engineering, Tongji University, 1239 Siping Road, Shanghai 200092, P. R. China; eric_lixiang@126.com

⁵Department of Geotechnical Engineering, Tongji University, 1239 Siping Road, Shanghai 200092, P. R. China; tanyong21th@tongji.edu.cn

ABSTRACT: This paper examines the response of metro stations adjacent to an excavation via a series of comprehensive finite element parametric studies. The effects of several key factors (e.g., the distance, D , between the existing metro station and the deep excavation, the depth of the excavation, H_e) governing the performance of the metro station were quantified. On the basis of the numerical analysis results, some major findings were obtained: (1) rotation of rail closer to the excavation transformed from the clockwise direction to the anticlockwise direction with the increasing of D / H_e , (2) as D / H_e increased, internal structural forces of juncture at roof slab and right wall decreased gradually and excessive internal structural force occurred when D / H_e was smaller than 0.7, (3) conventional protection criteria of metro stations were not rational because they did not take into account the internal structural forces.

INTRODUCTION

Suzhou is the first prefecture-level city which has opened metro systems in China. Rapid development of urban construction calls for deep excavations adjacent to the existing metro stations in congested areas where space is limited. Effects of ground movement induced by deep excavations would cause the following two potential hazards to the metro stations: (1) structural cracks which might lead to leak and even damage to the metro structures; (2) rail differential displacements which might result in derailment of the trains and loss of lives. Therefore, the deformations of the metro stations should be controlled within acceptable level during excavation of a pit nearby.

Since the publication of Peck (1969), many researchers and engineers have studied the performance of excavations (e.g., Clough and O'Rourke 1990, Liu and

Hou 1997, Hsieh and Ou 1998, Xu 2007, Tan and Wei 2012). However, literatures reporting the effects of deep excavations on the adjacent metro stations are limited. At present, the available studies mainly focused on three kinds of problems: (1) case histories (e.g., Wang 2008), (2) effects of some factors (e.g., Zeng et al. 2005), and (3) protection criteria of the metro stations (e.g., Xie 2005, Li 2009, Li et al. 2011). It is still difficult to have a comprehensive understanding of this subject. Conventional protection criteria for the metro stations in service mainly focus on the rail displacements with little attention paid to the internal structural forces. In practice, excessive internal structural forces would put the metro stations at the risk of crack and leaking. Hence, it is necessary to include the internal structure forces into the existing protection criteria as well. Moreover, the variation characteristics of the internal forces and displacements of the metro-station structures are not clear yet because the effects of relevant factors still remained uncertain so far.

In this study, the behaviors of deformations and internal forces of the metro stations in service induced by bottom-up excavations supported by multi-propped diaphragm walls in Suzhou were investigated. This was achieved by 36 two-dimensional (2D) finite element (FE) analyses, in which the effects of the final excavation depth, H_e , and the distance, D , between the excavation and metro station were comprehensively quantified. Based on the local excavation experience and numerical analysis results, the rationality of conventional protection criteria was discussed. The findings yielded from this study will provide practically useful references for engineers to determine the rational protection criteria of the metro stations and adopt appropriate countermeasures when encountering similar construction conditions.

SUBSURFACE CONDITIONS IN SUZHOU

The soil profiles along with the measured soil properties at the site are presented in Figure 1. In general, Suzhou is characterized by a layer of fill (Layer I) in the upper 2-4 m below ground surface (BGS), followed by a layer of soft to medium silty clay (Layer II) to a depth of 7 to 9 m BGS. Next layer is medium to fine dense silty sand (Layer III) to a depth of 17 to 19 m BGS, underlain by soft clay (Layer IV) to a depth of 21 to 23 m BGS. Beneath Layer IV is a thick layer of medium to dense silty clay (Layer V) to a depth of 41 to 42 m BGS. In the lower layers, medium clay (Layer VI) and very dense silty sand (Layer VII) will be encountered to a depth of 62 to 65 m BGS and the termination depth of 72 m BGS, respectively. The long-term groundwater table in Suzhou is around 1.0 to 1.5 m BGS. The final excavation bottoms in Suzhou are generally in the Layer III and Layer IV. Water inflow and quicksand might occur in Layer III easily during conduction due to the high permeability. The constrained modulus of Layer IV is low, which might induce excessive lateral wall displacements in the final excavation bottom level. The potential adverse effects resulting from these two layers are major concerns for design and construction of deep excavations in Suzhou.

FE-SIMULATION OF METRO STATION AND EXCAVATION

The parametric studies were performed using the two-dimensional finite element

code PLAXIS 8.5. The 2D FE-mesh is showed in Figure 2. To obtain initial structural internal forces and displacements of the investigated metro station, a metro-station excavation constructed by the bottom-up method was modeled at first and then a consolidation analysis for 500 days was carried out prior to conducting the excavation nearby. The new pit had a given width. Its excavation depth, H_e , varied from 9 to 21 m with an increment of 4 m. The distance between the pit and the metro station, D , varied from 5 to 40 m with an increment of 3 to 4 m when D was less than 15 m and an increment of 5 m when D was greater than 15 m. In order to avoid disturbance of boundary conditions, the mesh boundaries were located 120 m from diaphragm walls in all cases. The vertical mesh boundaries were fixed in the horizontal direction and the base was fixed in both horizontal and vertical directions. A surcharge of 20 kPa was applied on the ground surface along the length direction.

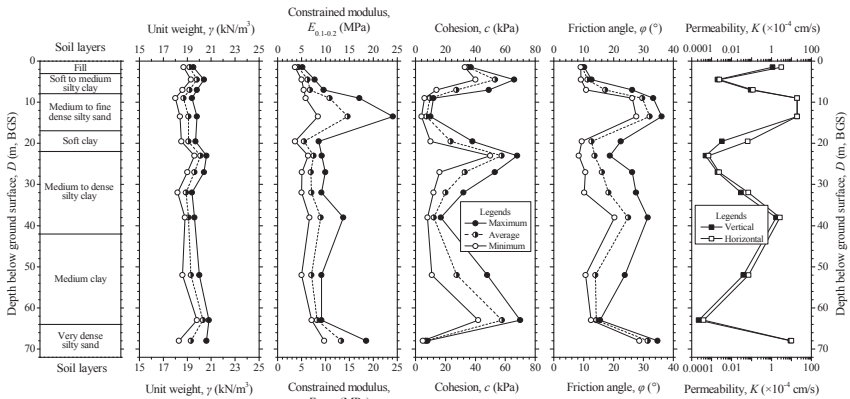


Figure 1. Soil profiles and material properties.

The detailed information regarding the metro station and excavation is summarized in Table 1. Both of them were modeled with elastic structural elements. The struts of excavation at first level were concrete struts and those at the other levels were steel struts, which were simulated by anchor-element model. Diaphragm walls, lining walls, slabs and columns of metro station were simulated by plate-element model. To model clayey soils behavior accurately, Hardening Soil Small-strain (HSS) model (Benz 2006) was employed. Silty sands were characterized by Mohr-Coulomb (MC) model.

MODEL VERIFICATION

Wu et al. (2010) analyzed several case histories of metro-station excavation in Suzhou. The monitoring data showed that the maximum wall deflections ranged from $0.05\%H_e$ to $0.30\%H_e$ with an average magnitude of $0.16\%H_e$. Prior to performing parametric studies, the reliability of the FE simulation was verified by comparing the FE-predicted wall deflections from 60 m wide excavations with H_e was 9 m, 13 m, 17 m, 21 m with those reported by Wu et al. (2010) and the relatively agreement was reached.

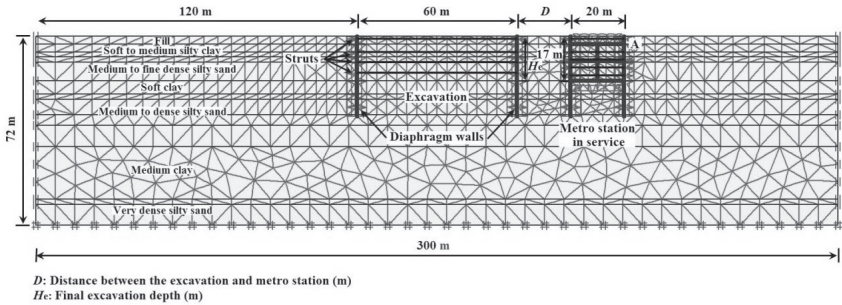


Figure 2. FE-mesh used for parametric studies.

Table 1. Size of each member of metro station and excavation.

| Members | | Unit | Magnitudes | |
|--------------------------|--------------------------|-------------------|------------|-----|
| Metro station in service | Roof slab depth | m (BGS) | 3.0 | |
| | Base slab depth | m (BGS) | 17.0 | |
| | Width | m | 20 | |
| | Penetration ratio | — | 0.8 | |
| | Diaphragm wall thickness | mm | 1000 | |
| | Lining wall thickness | mm | 700 | |
| | Roof slab thickness | mm | 900 | |
| | Middle slab thickness | mm | 400 | |
| | Base slab thickness | mm | 1000 | |
| Column section | mm ² | 700×1000 | | |
| Excavation nearby | Width | m | 60 | |
| | Penetration ratio | — | 0.8 | |
| | Diaphragm wall thickness | mm | 1000 | |
| | Concrete struts section | mm ² | 800×1000 | |
| | Steel struts section | External diameter | mm | 609 |
| | | Thickness | | 16 |

LATERAL MOVEMENT OF DIAPHRAGM WALLS OF THE EXCAVATION

As aforementioned, the maximum deflections of diaphragm walls of the excavation, δ_{hm} , are the same theoretically on two sides and the magnitude is about $0.16\%H_c$ in Suzhou when there is no metro station nearby. In this study where a metro station is considered adjacent to the excavation, δ_{hm} of the right wall closer to the metro station was smaller than the δ_{hm} of left side. It could be attributed to the shielding effect of metro station. Metro station restrained the movement of the soils in right side induced by excavation to some extent because of its large stiffness. Therefore, the fix point of the bracing system of excavation moved rightward from symmetry axis. Figure 3 presents the maximum deflections of diaphragm walls of the excavation. Shielding effect of metro station became significant and weak gradually with the increasing of H_c and D , respectively.

As shown in Figure 3, the maximum lateral deflections of diaphragm walls of the excavations in this study ranged from $0.12\%H_c$ to $0.25\%H_c$ with an average value of

$0.18\%H_e$ which is larger than that reported by Wu et al. (2010). However, the upper and lower limits were within the reported $0.05\%H_e$ - $0.30\%H_e$ by Wu et al. (2010).

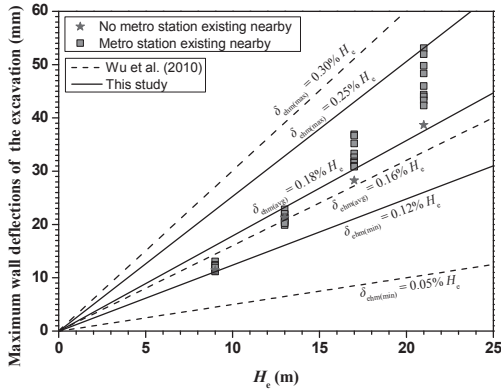


Figure 3. Maximum lateral deflections of diaphragm walls of excavations.

RAIL DISPLACEMENTS

The effect induced by the adjacent excavation on the left rail which was closer to the excavation was more obvious than the right rail which was far away. Figure 4 shows the normalized displacements of the left rail, ω , which is the value of differential displacements between two tracks divided by track gauge. Prior to conducting the adjacent excavation, the left rail had exhibited a slight clockwise rotation. When D / H_e value was small, the clockwise rotation of left rail was relatively serious. In the case, metro station center was located in the decreasing zone of the concave ground settlement profile induced by excavation nearby. As D / H_e became larger, ω turned from negative values to positive values in terms of degrees. After passing by the peak value, ω decreased and trended to zero. This was primarily attributed to the characteristics of concave ground settlement profile. As the distance from excavation became larger, the slope of concave profile decreased gradually in the beginning and then equaled to zero at the location of the maximum ground settlement. Subsequently, the slope increased until the distance was beyond the inflection point. Thereafter, the slope value became smaller and tended to zero.

To protect the rail from potentially detrimental displacement, national standard GB 50299-1999 (Code for construction and acceptance of metro engineering) was enacted in China. According to this code, the differential displacement between two tracks in crosswise section should be no more than 2 mm. Standard track gauge of metro in China is 1435mm. Therefore, the allowable value of the normalized displacements of rail in crosswise section, ω_m , is equal to 139.4×10^{-5} . In this study, although the variation rate of ω at $H_e = 21$ m was larger than the others, the maximum absolute value of ω was 51.7×10^{-5} which is only 1/3-1/2 of the ω_m . Thus, the differential displacement of rail was within the allowable range.

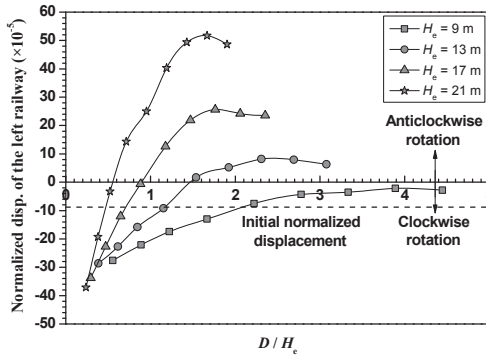


Figure 4. Normalized displacements of the left rail.

INTERNAL STRUCTURAL FORCES OF METRO STATION

In order to prevent the concrete structures from leaking and even failing due to excessively wide crack, national standard GB 50010-2010 (Code for design of concrete structures) was enacted in China. According to this criterion, the grade of the crack control of the metro-station structures can be classified as level III. The allowable width of crack, w_{lim} , on the outer surface and the inner surface of walls are 0.2 mm and 0.3 mm, respectively. Based on the condition of the reinforcement in the concrete structures, the allowable values of internal structural forces corresponding to w_{lim} could be calculated. As marked in Figure 1, section A is located in the juncture at the roof slab and the right wall and its steel reinforcement is listed in Table 2. The allowable bending moment of section A, $M_{q0.2}$, was calculated as 1200.1 kN/m/m.

Table 2. Condition of reinforcement in section A.

| Members | Thickness (mm) | Reinforcement | |
|----------------|----------------|--------------------|-------------------------------|
| | | Outer side | Inner side |
| Diaphragm wall | 1000 | Φ25@300 Φ25@300 | Φ28@150 Φ28@300 Φ28@150 |
| Lining wall | 700 | Φ25@150 Φ28@150 | Φ28@150 |

Figure 5 presents the relationship of the final bending moments of section A, M , and the distance ratio, D / H_e . M became smaller with the increasing of D , while became larger with increasing H_e . It resulted from the variation of the horizontal earth pressure which transformed from passive earth pressure to active earth pressure when D got larger gradually. As shown in Figure 5, M exceeded the $M_{q0.2}$ when D / H_e reduced to 0.7 and a value smaller, which meant metro stations were at the risk of excessively wide crack, leaking and even invalidation. However, in these cases, the lateral deflections of diaphragm walls of the adjacent excavations and the rail displacements of the metro stations were at acceptable levels. This finding indicated that the conventional protection criteria of metro stations which concentrated on rail

displacements with little attention paid to internal structural forces were not rational. The more proper protection criteria needed to be developed.

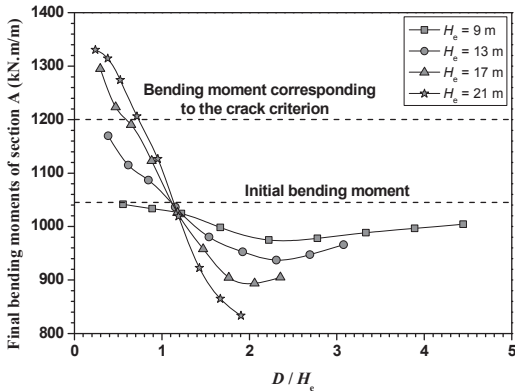


Figure 5. Final bending moments of section A.

CONCLUSIONS

On the basis of the parametric study results on the metro stations close to an excavation by the finite element analyses, the following conclusions and suggestions can be drawn:

1. Rotation of rails closer to the excavation transformed from the clockwise direction to the anticlockwise direction with the increasing of D/H_e , which mainly resulted from the location of the metro station center in the concave ground settlement profile.
2. As D/H_e increased, the internal structural forces of the juncture at the roof slab and the right wall decreased gradually and the reduction rate increased with the increasing of excavation depths.
3. Excessive internal structural forces occurred when the distance ratio, D/H_e , was smaller than 0.7. However, in these cases, the lateral deflections of diaphragm walls of excavations and rail displacements were at acceptable levels. Therefore, the conventional protection criteria of metro stations which concentrated on rail displacements with little attention paid to internal structural forces were not rational. The more proper protection criteria should be developed.
4. The excavation depth and the distance between the excavation and metro station are the key factors affecting the behaviors of the existing metro stations. When D/H_e is smaller than 0.7, relevant countermeasures should be taken to protect the metro stations.

ACKNOWLEDGEMENT

The financial support from the National Natural Science Foundation of China (NSFC Grant No. 51078292) was gratefully acknowledged.

REFERENCES

- Benz, T. (2006). "Small-strain Stiffness of Soils and Its Numerical Consequences." Ph.D. thesis, University of Stuttgart, Germany.
- Clough, G. W., and O' Rourke, T. D. (1990). "Construction induced movements of in situ walls." *Geotechnical Special Publication: Design and Performance of Earth Retaining Structures* (GSP 25), ASCE, Reston, VA: 439-470.
- Hsieh, P. G., and Ou, C. Y. (1998). "Shape of ground surface settlement profiles caused by excavation." *Canadian Geotechnical Journal*, Vol. 35 (6): 1004-1017.
- Li, K., Li, Z. Y., and Gao, B. (2011). "Study of safety evaluation method for existing metro station structures." *Rock and Soil Mechanics*, Vol. 32 (4): 1193-1199. (in Chinese).
- Li, X. X. (2009). "Security analysis of running metro station structure adjacent to foundation excavation." *Rock and Soil Mechanics*, Vol. 30 (Supp. 2): 382-386. (in Chinese).
- Liu, J. H., and Hou, X. Y. (1997). *Excavation engineering handbook*, Chinese Construction Industry, Beijing. (in Chinese).
- Peck, R. B. (1969). "Deep excavations & tunneling in soft ground. State-of-the-art-report." *Proc., 7th Int. Conf. on Soil Mechanics and Foundation Engineering*, International Society for Soil mechanics and Geotechnical Engineering, Mexico, 225-290.
- Tan, Y., and Wei, B. (2012) "Observed behaviors of a long and deep excavation construction by cut-and-cover technique in Shanghai soft clay." *Journal of Geotechnical and Geoenvironmental engineering*, Vol. 138 (1): 69-88.
- Wang, Y. (2008). Displacement analysis of adjacent subway station due to deep excavation and study on protection measure of construction, *Master Degree Thesis*, Tongji University, Shanghai, China. (in Chinese).
- Wu, C. J., Chen, J.J., Ye, G. L., Wang, J. H., and Zhou, H. B. (2010). "Deformation characteristics of foundation pits of subway stations in Suzhou." *Chinese Journal of Geotechnical Engineering*, Vol. 32 (Supp. 1): 458-462. (in Chinese).
- Xie, H. S. (2005). A study on the control of deformation during construction of deep excavation adjoining operating station, *Ph.D. Thesis*, Tongji University, Shanghai, China. (in Chinese).
- Xu, Z. H. (2007). Deformation behavior of deep excavations supported by permanent structures in Shanghai soft deposit, *Ph.D. Thesis*, Shanghai Jiaotong University, Shanghai, China. (in Chinese).
- Zeng, Y., Li, Z. G., and Wang, Y. B. (2005). "Research on influencing factors of deep excavation adjacent to subway station." *Chinese Journal of Underground Space and Engineering*, Vol. 1 (4): 642-645. (in Chinese).

A Visco-Elastic Model with Loading History Dependent Modulus and Damping for Seismic Response Analyses of Soils

Zhiliang Wang¹ and Fenggang Ma².

¹Senior Associate, AMEC Environment & Infrastructure, Inc., Oakland, CA 94612; zhi-liang.wang@amec.com

²Environmental Engineer, Washington State Dept. of Ecology, Dam Safety Office, Spokane, WA 99205

ABSTRACT: It is well established that soils exhibit non-linear behavior even at small strain levels. Yet, most evaluations of the seismic response of soil deposits utilize an equivalent linear methodology, i.e. elastic solutions incorporating constant damping. In such solutions the modulus and damping constants are adjusted by means of an iterative approach to correlate to the maximum strain. In doing so, the smaller amplitude, high-frequency component motions are forced to use the same modulus degradation and damping as that of the lower frequency motions. As a consequence, the computed motions at the surface of a deposit often exhibit unrealistic low amplitudes at high frequencies, when the strong input motions are applied.

This article presents a modified Kelvin model, in which the modulus and damping are treated as loading history dependent coefficients for each loading-unloading branch. This model works in the program FLAC in a time domain integration procedure. Based on the peak strain level experienced in the previous half cycle, the modulus degradation and viscosity are updated for the current branch. Numerical analyses for a soft soil site are presented and compared with those obtained using the equivalent linear method implemented in the program SHAKE for a recorded motion at Treasure Island. The site response analysis of another soft clay site for a higher design input motion shows that the computed PGA and response spectral could be higher than those obtained from a typical equivalent linear analysis.

INTRODUCTION

It is well known that soil response exhibits strong non-linearity during monotonic and cyclic loading. From soil cyclic loading tests, two key parameters are determined: the secant shear modulus and the damping ratio. The secant modulus corresponds to the slope of the diagonal of a cyclic stress-strain loop and the damping ratio from the area of the loop (or energy loss) as shown in Figure 1. The non-linearity of soil is reflected in the degradation of the shear modulus and an increase in the damping ratio as shear strain amplitude increases, i.e. they are both functions of the strain amplitude. Typical shear modulus reduction and associated damping ratio curves for clays as a function of shear strain are shown in Figure 2 (Vucetic, M. and Dobry, R., 1991).

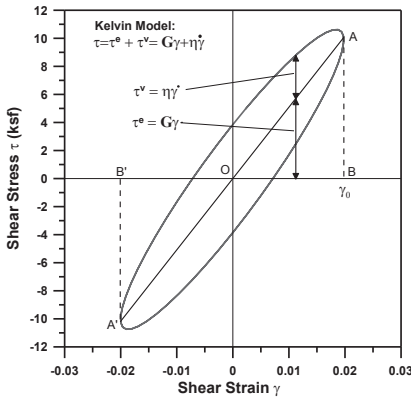


FIG 1. Stress strain loops based on Kelvin model

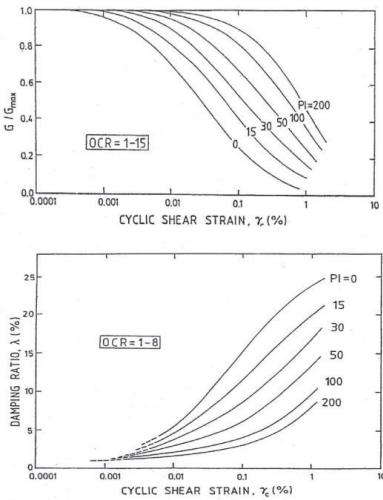


FIG 2. Typical modulus reduction and damping ratio curves of clay (Vucetic and Dobry, 1991)

Program SHAKE is a visco-elastic model with constant modulus and damping ratio (Schnabel, et al, 1972). An initial estimate of the shear modulus and damping ratio is made and the problem solved. From this solution an effective strain is defined as a fraction of the calculated maximum shear strain, typically between 0.5 and 0.7. That effective strain is used to guide a more refined estimate of the dynamic soil properties and the problem rerun. This solution process is repeated until the modulus and damping used is within an acceptable tolerance of strain compatible modulus and damping calculated. The simplicity of the approach and its ability to yield site response predictions that reasonably agree with recorded motions and spectral content have made it the program of choice for most site response analyses. However, there has been a progressive increase in the intensity of strong ground shaking. These greater accelerations are testing the limits of SHAKE and in particular the appropriateness of the effective shear strain scheme to use a constant shear modulus and damping ratio for the duration of shaking. In particular SHAKE results appear to underestimate the response when high input motions induce very high strains in the soft soil layers.

Recently the geotechnical profession has begun investigating other schemes to more realistically model the shear

modulus and damping response of soils in the equivalent linear visco-elastic approach. Kausel and Assimaki (2000) proposed replacing the constant modulus and damping ratio for the entire duration of shaking in an equivalent linear approach with frequency-dependent moduli and damping ratios. At about the same time, another new procedure was proposed based on the time domain integration of the motion equations using the concept of cycle-wise equivalent linear analysis (CELA). In this

procedure (Shiomi et al, 2000, 2008), the equivalent linear method is applied cycle-wise instead of the entire duration of the earthquake. The modulus and damping change for each cycle, based on the peak strain level experienced in the previous cycle. The authors claim ‘this cycle-wise equivalent linear analysis (CELA) should theoretically have better accuracy’.

In the present article, a modified Kelvin model (visco-elastic model) is described. The strain time history is modeled as sets of loading-unloading branches (or, half cycles). The response of the model to each loading-unloading branch is assessed with a time domain integration scheme. The modulus and damping are defined in each loading-unloading branch based on the load induced and shear strain time history experienced prior to the current branch. The model has been written for the program FLAC in both the FISH language and as a compiled dynamic linked library, Kelvin-Wang.FIS and Kelvin-Wang.dll, respectively. To demonstrate the capabilities of the site response analysis, a soft clay site was assessed with both the proposed model and SHAKE. A comparison of the results shows important similarities and notable differences.

CLASSICAL VISCO-ELASTIC MODEL

As a notation convention, we use symbols s_{ij} and e_{ij} to denote deviatoric stress and strain components, i.e.,

$$s_{ij} = \sigma_{ij} - p\delta_{ij}, \quad e_{ij} = \varepsilon_{ij} - \frac{\varepsilon_{kk}}{3}\delta_{ij} \quad (1)$$

$$p = \frac{\sigma_{kk}}{3} \quad (2)$$

Then, the classical Kelvin visco-elastic model is

$$s_{ij} = 2Ge_{ij} + 2\eta\dot{e}_{ij} \quad (3)$$

In which the first term on the right side of the equation is the elastic term representing the resistance of soil to the deformation (e_{ij}). G is the shear modulus of soils. The second term is the soil resistance to the strain rate de_{ij}/dt . Based on the Kelvin model, the total resistance is the summation of the elastic term and viscous term.

The volumetric strain vs. mean stress relation is elastic

$$p = K\varepsilon_{kk} \quad (4)$$

For simplicity, consider a simple shear condition, then, the Kelvin model is

$$\tau = G\gamma + \eta\dot{\gamma} = \tau^e + \tau^v \quad (5)$$

If we apply a sinusoidal strain loading wave $\gamma = \gamma_o \sin(\omega t)$, the viscous resistance is

$$\tau^v = \eta\omega\gamma_o \cos(\omega t) \quad (6)$$

Using the relationship $\sin^2(\omega t) + \cos^2(\omega t) = 1$, we can demonstrate the relation between τ^v and γ is an ellipse:

$$\left(\frac{\tau^v}{\eta\omega\gamma_o}\right)^2 + \left(\frac{\gamma}{\gamma_o}\right)^2 = 1 \quad (7)$$

The area of the ellipse (see Figure 1) is the energy loss, $dW = \pi(\eta\omega\gamma_o)\gamma_o$. The elastic part is completely recoverable and does not contribute to energy losses.

In soil dynamics (Das, 1993), the shear modulus of a soil in cyclic simple shear tests can be determined as

$$G = \frac{\text{amplitude of cyclic shear stress, } \tau}{\text{amplitude of cyclic strain, } \gamma} \quad (8)$$

The damping ratio at a given shear strain amplitude can be obtained from the hysteretic stress-strain properties. Referring to Figure 1 the damping ratio can be expressed as

$$D = \frac{1}{2\pi} \frac{\text{area of the hysteresis loop}}{\text{area of triangle } OAB \text{ and } OA'B'} \quad (9)$$

Now, we have

$$D = \frac{1}{2\pi} \frac{\Delta W}{W} = \frac{\pi\eta\omega\gamma_o\gamma_o}{2\pi G\gamma_o\gamma_o} = \frac{\eta\omega}{2G} = \frac{\eta\pi f}{G} \quad (10)$$

Then, the viscosity can be determined by damping ratio D and period T (frequency f =1/T) by

$$\eta = \frac{DGT}{\pi} \quad (11)$$

MODIFIED VISCO-ELASTIC MODEL

The original Kelvin model has constant modulus and viscosity. In the traditional ‘equivalent linear’ approach, such modulus and damping parameters were determined to correlate to the loading cycle that produces the highest strain amplitude. This is conducted through an iterative procedure as in the program SHAKE. This approach may generate a better simulation of the loading cycle at ‘effective strain’ level (e.g., 65% of the maximum strain), but could be unrealistic for cycles smaller or larger than such cycle.

The alternative approach presented in this paper is as follows:

- First treat the strain loading time history as a sequence of many ‘loading-unloading’ branches in the time domain.
- Each loading-unloading branch is defined as the load path from zero shear strain to a peak strain and the unloading path from the peak strain back to zero strain.
- A complete branch may include a ‘partial loading’ that starts from a nonzero strain and a ‘partial unloading’ that ends with a nonzero strain.
- The modified Kelvin model assumes that modulus and damping parameters can be different for each branch.
- A postulation about soil’s memory is made that the modulus and damping parameters for the current branch are dependent on the loading history prior to this branch. Specifically, the parameters are treated as a function of peak shear strain in the immediate prior loading branch. Note that when strain peak is reached (or unloading starts) in a branch, the strain rate is zero. The peak strain γ_{mi} for the current branch is recorded, and the modulus $G=G(\gamma_{mi})$, damping $D(\gamma_{mi})$ as well as the period $T=4*(t_{mi}-t_i)$ can be determined to modify the Kelvin model in the following manner.
- Modulus G will be changed at the beginning of the next branch, i.e. when zero strain appears. Doing it at this time avoids causing a discontinuity in the computed stress. No modulus reduction is assumed for the first branch, i.e. the modulus is the

maximum modulus assigned the layer (user input value) when starting the computations.

- g) Viscosity will be changed based on Eq. (11), i.e., $\eta_i = \frac{D_i G_i T_i}{\pi}$. In the above equation, damping, modulus and period will be changed at the reverse point indicated by zero shear strain rate, which means it is changed at the peak strain level. It is easy to verify that changing viscosity at zero strain rate level will ensure the continuity of computed stresses. Of course, for the loading part before reaching the current peak, the viscosity is that used in the previous branch.

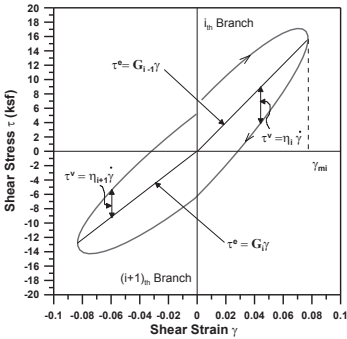


FIG 3. Loading history dependent modulus and damping from the modified Kelvin model

The foregoing is illustrated in Figure 3. The modulus of the i -th loading branch is determined by the peak strain in the $(i-1)$ th loading branch, so that the elastic resistance follows $\tau^e = G_{i-1} \gamma$. When unloading starts, the peak strain for this i -th branch is determined, so are the damping ratio D_i , modulus G_i and Period T_i . Note that the viscosity η is refreshed when un-loading starts from where the strain rate is zero. It will be kept unchanged to the loading part of next $(i+1)$ -th branch while the modulus will be changed in the $(i+1)$ -th branch based on the peak strain at i -th branch G_i .

NUMERICAL IMPLEMENTATION OF MODIFIED KELVIN MODEL

The numerical implementation of the Kelvin model Eq. (3) is described below. Kelvin-Wang.FIS is the subroutine written in FISH (FLAC’s programming language) that implements the modulus and damping rules proposed in the previous section. Although the FLAC manual cites a number of different algorithms to carry out the integration of the model subject to the earthquake time histories, the authors found that the subroutine worked best with the Euler forward method.

The elastic and viscosity part of Eq. (3) are as follows:

$$s_i^e = 2G_i e_{ij} \tag{12}$$

$$s_{ij}^v = \left(\frac{2\eta}{dt} \right) * de_{ij} \tag{13}$$

And
$$s_{ij} = s_{ij}^e + s_{ij}^v \tag{14}$$

In which dt is constant, and de_{ij} is given for each new time step.

The peak strain is measured by

$$e_m = \sqrt{\frac{1}{2} e_{ij} e_{ij}} \tag{15}$$

The ‘strain crossing zero’ is judged by

$$sume = e_{ij} (e_{ij} + de_{ij}) \tag{16}$$

Within the branch, $sume$ is positive. If $sume \leq 0$, then, the strain is defined as having crossed the zero point. Then, the modulus will be changed, and a new loading branch begins. The moment of crossing is the starting time of this branch.

The ‘strain rate crossing zero’ is judged by

$$sumv = e_{ij} de_{ij} \tag{17}$$

If $sumv \leq 0$, an unloading is defined using an index $Load(i) = -1$. Expressing this index for the previous time step as $Load(i-1)$ which is 1 (loading) or -1 (unloading). The reverse time is detected by $Load(i) * Load(i-1) < 0$. At that time, the strain rate is crossing zero, and the viscosity will be changed for the i -th branch based on Eq.(11).

SIMULATION FOR A SOIL ELEMENT UNDER CYCLIC LOADING

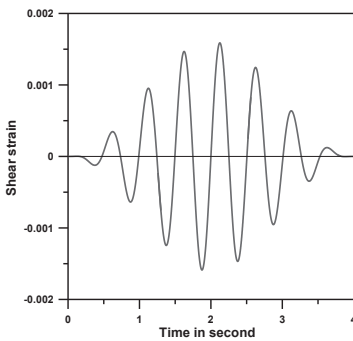


FIG 4. Time history of shear strain as input for one element simple shear

The modified Kelvin model is applied to simulate one zone’s response to a sinusoidal shear strain loading in FLAC. The input shear strain time history is presented in Figure 4. The computed stress-strain loops are shown in Figure 5. It can be seen that when the shear strain amplitude increases for each cycle, the secant modulus reduces and the damping ratio increases. When the peak strain cycle is passed, the shear strain amplitude decreases for each cycle, so that the secant modulus increases and the damping ratio decrease. The modulus and damping ratio time histories are shown in Figure 6. It is demonstrated that the modulus and damping ratio vary for each of the loading branches or half-cycles.

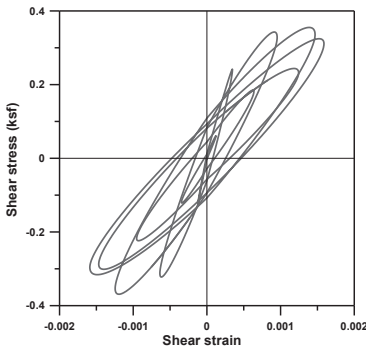


FIG 5. Computed stress strain loops using the modified Kelvin model for one element simple shear

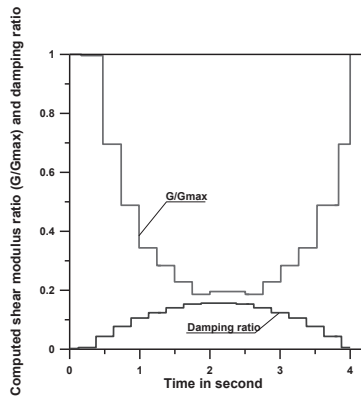


FIG 6. Time histories of computed modulus and damping ratio for one element simple shear

COMPARISON OF COMPUTED RESPONSE WITH RECORDINGS AT TREASURE ISLAND

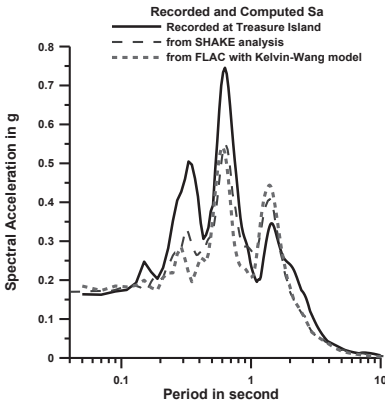


FIG. 7. Comparison of computed (dashed line) and recorded response spectra at Treasure Island

match the values from recordings. The new analysis is expected to be close to the SHAKE results, because the input motion is at a low level ($PGA=0.06g$). Both analyses are reasonably close in this Treasure Island case study as shown in Figures 7.

COMPARISON WITH EQUIVALENT LINEAR METHOD IN A SITE SEISMIC RESPONSE ANALYSIS

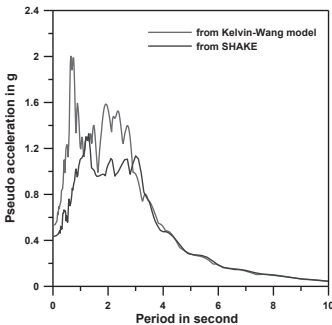


FIG. 8. Computed spectral acceleration at ground surface compared with results from SHAKE analysis

Using the model described above via the program FLAC, a site response analysis was performed. The site conditions are consistent with those at Treasure Island (CSMIP STA 58117). The input motion (090 components) was recorded at Yerba Buena Island (CSMIP STA 58163) which is 2 km to the north and is classified as a ‘rock’ site. The input data for the SHAKE analysis is reported in Long Sen (2012) and used here too for the new analysis using the proposed model.

Figure 7 presents the spectral accelerations computed using the modified Kelvin model and those from the recordings. In the same figure, equivalent linear (SHAKE) results are also included for comparison. It is clear that the analytical results reasonably

A site response analysis was conducted using the equivalent linear method. The profile and all parameters for SHAKE are presented in Tables 1 and 2. These parameters are all applied for this modified Kelvin model and a new response analysis was completed using this model coded for FLAC. The input acceleration has a peak value about 0.6g. The computed ground surface response spectra are presented in Figure 8 together with those from SHAKE. It can be seen that the PGA and higher frequency spectral values obtained using the modified Kelvin model are higher than those obtained from the SHAKE analysis.

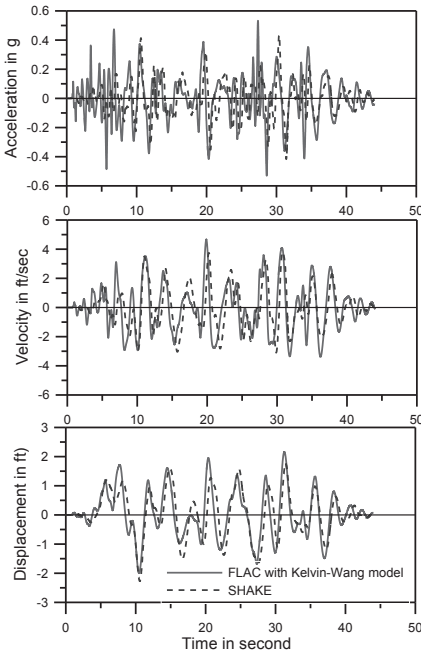


FIG. 9. Computed surface acceleration, velocity and displacement time histories compared with results from SHAKE analysis

The computed surface acceleration, velocity and displacement time histories, compared with those from SHAKE analyses are presented in Figure 9. It is interesting that the peak acceleration values from Kelvin-Wang model are higher than those from SHAKE analyses in general. The time histories for modulus and damping are presented in Figures 10 and 11 while these values are constants in SHAKE. The period for each half cycle is closely dependent on the strain time history.

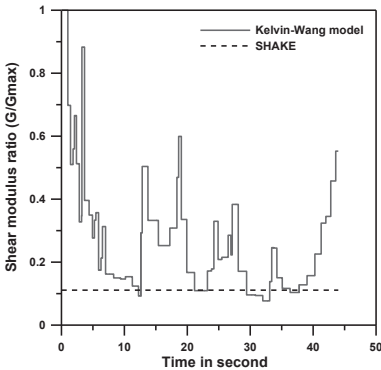


FIG. 10. Computed modulus reduction time history in a layer compared with results from SHAKE analysis

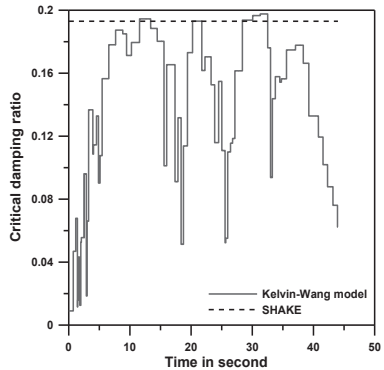


FIG. 11. Computed damping ratio time history in a layer compared with results from SHAKE analysis

Table 1. Soil Profile and Input Parameters for a Site Response Analysis

| Layer No. | Curve No. | Sub layer No. | Thickness, ft | Initial damping | Unit weight, kcf | Vs, fps |
|-----------|-----------|---------------|---------------|-----------------|------------------|---------|
| 1 | 3 | 1 | 3.7 | 0.05 | 0.105 | 300 |
| 2-9 | 3 | 1 | 4 | 0.05 | 0.105 | 300 |
| 10 | 3 | 1 | 3.7 | 0.05 | 0.106 | 306 |
| 11 | 3 | 1 | 4 | 0.05 | 0.106 | 318 |
| 12 | 3 | 1 | 4 | 0.05 | 0.106 | 331 |
| 13 | 3 | 1 | 5 | 0.05 | 0.106 | 346 |
| 14 | 3 | 1 | 5 | 0.05 | 0.106 | 362 |
| 15 | 3 | 1 | 5 | 0.05 | 0.106 | 378 |
| 16 | 3 | 1 | 5 | 0.05 | 0.106 | 395 |
| 17 | 3 | 1 | 5 | 0.05 | 0.106 | 411 |
| 18 | 3 | 1 | 5 | 0.05 | 0.106 | 427 |
| 19 | 3 | 1 | 5 | 0.05 | 0.106 | 443 |
| 20 | 3 | 1 | 5 | 0.05 | 0.106 | 459 |
| 21 | 3 | 1 | 5 | 0.05 | 0.106 | 476 |
| 22 | 3 | 1 | 5 | 0.05 | 0.106 | 492 |
| 23 | 1 | 1 | 5.2 | 0.05 | 0.129 | 880 |
| 24 | 1 | 1 | 5.2 | 0.05 | 0.129 | 897 |
| 25 | 1 | 1 | 5.2 | 0.05 | 0.129 | 913 |
| 26 | 2 | 1 | 6 | 0.05 | 0.129 | 1184 |
| 27 | 2 | 1 | 6 | 0.05 | 0.129 | 1206 |
| 28 | 2 | 1 | 6 | 0.05 | 0.129 | 1226 |
| 29-36 | 4 | 1 | 8 | 0.05 | 0.115 | 900 |
| 37 | 2 | 1 | 7.5 | 0.05 | 0.137 | 1208 |
| 38 | 2 | 1 | 7.5 | 0.05 | 0.137 | 1224 |
| 39 | 2 | 1 | 12 | 0.05 | 0.137 | 1391 |
| 40 | 2 | 1 | 12 | 0.05 | 0.137 | 1417 |
| 41 | 2 | 1 | 13 | 0.05 | 0.137 | 1443 |
| 42 | 5 | 1 | 17.7 | 0.05 | 0.14 | 2875 |
| 43 | 5 | 1 | 17.7 | 0.05 | 0.14 | 3625 |
| 44 | | | | 0.01 | 0.14 | 4000 |

Table 2. Modulus Reduction and Damping Curves

| Soil Type | Curve Number | Curves used in equivalent Linear Analysis (SHAKE) |
|------------------|--------------|--|
| Fill and YBM | 3 | YBM Site-Specific Curves |
| Silty Fine Sand | 1 | Mid-range Sand, Seed & Idriss, 1970 |
| Dense Silty Sand | 2 | Upper G/Gmax, Seed & Idriss, 1970; Damping, Idriss, 1990 |
| OBC | 4 | OBC Site-Specific Curves |
| Fine Sand | 2 | Upper G/Gmax, Seed & Idriss, 1970; Damping, Idriss, 1990 |
| Gravel | 5 | Upper G/Gmax, Seed & Idriss, 1970; Damping, Idriss, 1990 |

CONCLUSIONS

Conventional equivalent linear visco-elastic analysis for seismic response is computed using an iterative procedure to get the modulus and damping correlated to the maximum strain (Schnabel et al., 1972). Such determined parameters are applied to the entire duration, which means the modulus reduction and damping ratio could be overestimated for the cycles smaller than the cycle of effective strain level.

The present article proposes a scheme to update the shear modulus and damping over the course of shaking as a function of time history of loading. These values for the current loading branch (half cycle) are determined by the peak strain level experienced by the soil during the past loading branches (half cycles). Such determined modulus from the current loading branch are delayed and applied to the immediate subsequent loading branch. The viscosity is updated when the strain rate is zero, or at the peak strain level in the current branch when unloading starts. In such a time domain integration algorithm, there is no need for iterations.

Numerical examples are provided for explanations. The site response analysis of a soft clay site using the Kelvin-Wang model shows that the computed PGA and response spectral could be higher than those obtained from a typical equivalent linear SHAKE analysis. Of course, the validity of all computed results should be judged by comparisons with field recordings when they become available.

REFERENCES

- Das, B.M., (1993) "Principles of Soil Dynamics", PWS-KENT Publishing Company.
- Dickenson, S.E. (1994). "The dynamic response of soft and deep cohesive soils during the Loma Prieta earthquake of October 17, 1989," Ph.D. Dissertation, Univ. of California, Berkeley.
- Kausel, E and Assimaki, D., (2002). "Seismic simulation of inelastic soils via frequency-dependent moduli and damping", *J. Engrg. Mech.*, Vol. 128 (1): 34-47.
- Schnabel, P B., Lysmer, J., and Seed, H B. (1972). "SHAKE: A computer program for aeolian soil." *Geomaterial* earthquake response analysis of horizontally layered sites," *Report No. EERC 72-12*, University of California, Berkeley, Calif., Earthquake Engineering Research Centre.
- Seed, H. B., and Idriss, I. M. (1969). "Soil moduli and damping factors for dynamic response analyses." *Report No. EERC 70-10*, Earthquake Research Center, University of California, Berkeley, Calif.
- Sen, Long, (2012.), "Seismic response analysis considering ground motion variability and site property variability", Dissertation, Hong Kong University of Science and Technology.
- Shiomi, T., Chan, A., Nukui, Y., Hijikata, K., and Koyama, K., (2000). "Comparison of equivalent linear analysis and nonlinear analysis for a liquefaction problem". 12th WCEE, Paper 1761.
- Shiomi, T., Nukui, Y., and Yahishita, F., (2008). "Practical effective stress analysis and determination of its dynamic property", 14th WCEE.
- Vucetic, M. and Dobry, R. (1991). Effect of Soil Plasticity on Cyclic Response. *J. Geotechnical & Geoenv. Engrg.*, Vol. 117 (1): 89-107.

Investigation of Influencing Factors on Strain Localization inside Sand Specimens Subjected to Triaxial Loading

Ye Lu ¹

¹ Lecturer, Department of Civil Engineering, Shanghai University, No. 149 Yanchang Road, Shanghai, 200072, China. Email: ye.lu@shu.edu.cn.

ABSTRACT: The initialization and development of strain localization inside a triaxial sand specimen are affected by multiple factors, e.g. membrane stiffness, weak inclusions, particle breakage, slenderness ratio, and etc. To investigate the effect of membrane stiffness, a flexible membrane algorithm was implemented in the discrete element method code (PFC), which allowed both vertical and radial deformations of the specimen. The modeling results showed that the specimen failed with bulging in the middle portion (i.e., presented a barrel-like shape). Comparisons with the rigid membrane algorithm, prominent shear bands could be spotted at microscopic scale for the flexible membrane bounded specimen. Weak inclusions and particle breakage were simulated by reducing particle stiffness and changing particle shape, and their effects on the triaxial sand specimens were examined. Analyses on the modeling results indicated in addition to the primary shear bands, both weak inclusions and particle breakage intrigued a secondary shear band and shear block while imposing no substantial effect on the stress-strain response of the specimens.

INTRODUCTION

As one of the most commonly used and studied laboratory tests in soil mechanics, the axisymmetric triaxial compression test has been the tool to investigate strain localization (or shear banding) in soils for decades. When a soil specimen is subjected to triaxial compression loading, it fails with either some prominent shear bands or bulging shape showing no clearly defined shear bands. However, according to the investigation using X-ray computed tomography (Desrues et al., 1996), some internal structures of strain localization still exist for the failed triaxial specimen with bulging shape. Such internal structures look like a turbine with a cone in the center and a set of shear planes radially aligned.

In addition to laboratory tests, numerical modeling which can extend the scope of experimental investigation is used as a supplementary tool to study strain localization. Among the available numerical modeling methods, the finite element method (FEM) and the discrete element method (DEM) are the most widely adopted ones. Different from FEM, DEM assumes that the soil mass is composed of discrete particles which

can displace independently from one another and interact only at contact points (Cundall and Strack 1979). Considering the discrete nature of soils, DEM can conceptually provide better simulations of particulate behavior (e.g., rotations and relative displacements) at the microscopic scale than continuum models. Consequently, DEM has been used by many researchers to model the specimen behavior under triaxial loading on both macroscopic and microscopic scale (e.g. Thorton, 2000; Zhao and Evans, 2009).

In this paper, the response of dry sands subjected to drained triaxial compression loading was investigated. A series of numerical experiments were performed using the commercial 3D DEM code PFC3D. In order to help strain localization initialize and fully develop, a specially designed flexible membrane algorithm was implemented in the modeling. The modeling results showed that strain localization became more prominent in the flexible membrane bounded specimens than in the rigid membrane bounded specimens. In addition to the membrane stiffness, the influence of weak inclusions and particle breakage on strain localization was investigated.

NUMERICAL SETUP OF TRIAXIAL TESTS

As the effect of membrane stiffness, i.e. flexible versus rigid, on specimen behaviors was the focus of this study, the numerical setup followed the previous investigation on triaxial tests using rigid membrane (Lu and Frost, 2010) – specimen preparation, clump creation, consolidation and specimen shearing. The only modification done in the current study was that the rigid cylindrical wall was replaced with a sheet of flexible membrane after the specimen was consolidated. The flexible membrane was comprised of single spheres of which the displacements in X, Y and Z directions were related. The testing material was sub-rounded quartz sands and simulated by two-sphere clumps. The triaxial specimens were prepared with initial void ratio of 0.580, and the dimension was 70 mm in diameter and 140 mm in height. All the specimens were sheared to the global axial strains of 14% under an initial confining stress of 50 kPa. The detailed model parameters are listed in Table 1. As a total of 15192 specimen particles and more than 8000 membrane particles were generated, the computation time for each simulation run was more than 24 hours.

Table 1. Model parameters of the numerical triaxial tests

| Parameters | Numerical |
|----------------------------------|-----------------------|
| Specimen Height | 140 mm |
| Specimen Width | 70 mm |
| Particle Radii Range | 1.25-2.25 mm |
| Particle Normal Stiffness, k_n | 1.0×10^5 N/m |
| Particle Shear Stiffness, k_s | 0.5×10^5 N/m |
| Particle Friction Coefficient | 0.30 |
| Specific Gravity | 2.67 |
| Platen Stiffness | 1.0×10^8 N/m |
| Membrane Stiffness | 2.0×10^4 N/m |

MODELING RESULTS

Three numerical triaxial tests using the flexible membrane algorithm were performed to investigate the influence of membrane stiffness, weak inclusions, and particle breakage.

Membrane Stiffness

Figures 1(a) and 1(b) show the failed shapes of the specimens which were sheared to 14% axial strain. The specimen bounded with rigid membrane kept the cylindrical shape till the end of loading, while the one bounded with flexible membrane failed with a barrel-like shape. The bulging shape is typical of the triaxial laboratory specimens being sheared to failure, which are bounded with latex membrane. To check the effect of membrane stiffness on material properties at microscopic scale, the rotations and displacements of the particles located in the middle Y-Z plane are plotted in Figure 1. For the rigid membrane case, two symmetrical shear blocks formed at the ends of the specimen and moved toward each other. The particles that underwent large rotations distributed all over the specimen, which was caused by that the rigid membrane restricted the radial deflection of the specimen and thus those particles that tended to move outwards from the specimen center were forced to rotate locally. For the flexible membrane case, the particles around the top and bottom portions of the specimen basically underwent vertical displacements and almost no rotations. By this way, two conical shear blocks formed and moved toward each other. When the two shear blocks met around the middle portion, more than one shear band can be clearly distinguished. Inside the shear bands, the particles rotated and moved radially away from the specimen center. As the flexible membrane did not restrict radial deflection, the particle rotations and lateral displacements resulted in dilation of the middle portion of the specimen. The comparisons based on both visual observation and microscopic behavior proved that the flexible membrane is a much better simulation of the latex membrane used in the laboratory. With the implementation of flexible membrane, the microscopic behavior of triaxial sand specimens can be investigated via PFC simulation.

After the effect of membrane effect was investigated, two more triaxial numerical tests were conducted to check the effect of weak inclusions and particle breakage. The numerical test with flexible membrane presented in this section would be used as a reference test for the following sections.

Weak Inclusion

To investigate the effect of weak inclusion on the initialization and development of strain localization, 52 particles inside a small cubical area close to the lower end of the specimen were replaced with smaller stiffness after specimen consolidation, i.e. $k_n = 1 \times 10^3$ N/m and $k_s = 0.5 \times 10^3$ N/m. These particles of reduced stiffness represented the weak inclusion existing inside the specimen. The specimen was sheared to 14% axial strain, and its stress-strain response and volumetric strain is plotted in Figure 2. It is noticed that the stress-strain response and volumetric strain of the specimen with weak

inclusion did not differ much from the reference test except for the residual stress. However, the difference between the residual stresses was less than 7 kPa, which was very minute. Figure 3 presents the particle rotation and displacement map for the triaxial specimens. Via comparison with the reference test, it shows that the weak inclusion incurred greater particle rotations locally, which resulted in a secondary shear band that extended to the specimen center. The secondary shear band along with the primary shear band formed a secondary shear block which tended to be pushed out of the specimen.

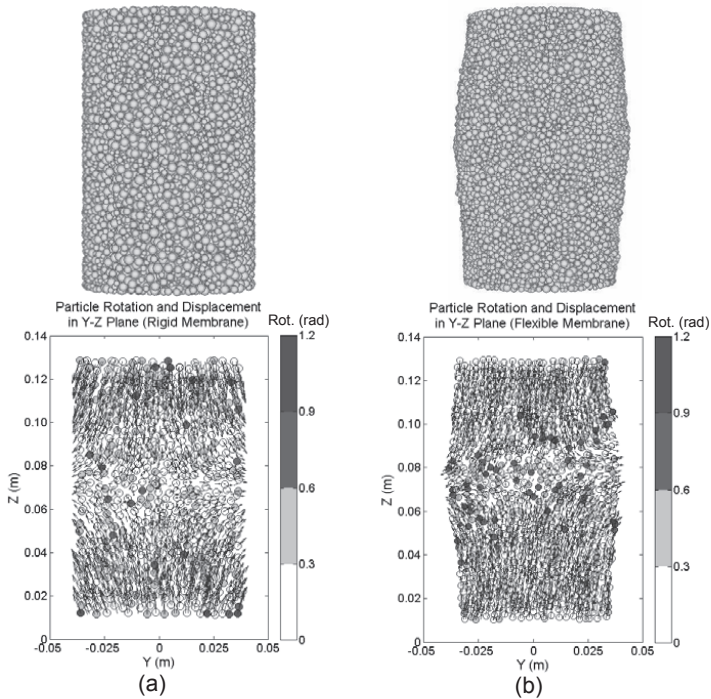


FIG. 1. Failed shapes of triaxial specimens bounded with (a) rigid membrane and (b) flexible membrane.

Particle Breakage

When the particles were subjected to loading, they might be crushed and affect local mechanical and material behaviors. In this study, particle breakage was simulated by replacing each two-sphere clump within a cubical area with two single spheres after specimen consolidation. A total of 86 clumps were replaced, and their stiffness and friction remained the same as before. The stress-strain response in Figure 2 shows that compared with the reference specimen, particle breakage did not affect the initial modulus of the response curve but resulted in the minor reduction of peak stress and residual stress. The stress differences were only 6-7 kPa, which means particle

breakage did not affect the strength of the specimen substantially. However, as the number of particles in the breakage group or the number of breakage groups increase, the effects are expected to become more significant. For the volumetric strain, the specimen containing particle breakage experienced slightly less contraction, but its volumetric strain caught up with that of the reference specimen at dilation stage. The particle rotation and displacement map in Figure 3 indicates similar patterns of strain localization for both specimens with weak inclusion and particle breakage. A secondary shear band and a shear block showed up for the particle-breakage specimen as well. However, replacing clumps with single spheres caused greater particle rotations, and thus the local void ratio increased and this portion of specimen experienced greater dilation.

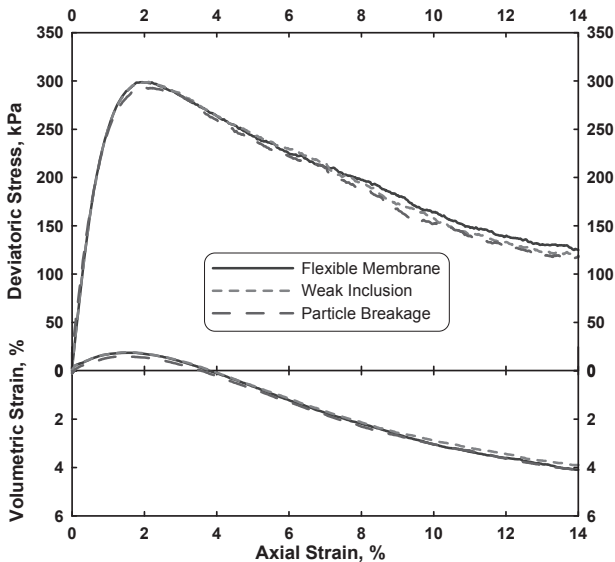


FIG. 2. Stress-strain response and volumetric strain of the triaxial specimens.

CONCLUSIONS

Three numerical tests were performed to investigate the mechanical and material behaviors of sands subjected to triaxial loading. Based on the analyses of the modeling results, the effects of membrane stiffness, weak inclusions and particle breakage on strain localization were characterized, and the following conclusions can be reached:

1. The flexible membrane algorithm implemented in the numerical modeling not only confined the specimen but also allowed longitudinal and radial deformations of the specimen. Therefore, it was a much better simulation of the latex membrane used in the laboratory than the rigid cylindrical wall. The analyses on the microscopic behavior of the triaxial specimens indicated that the flexible membrane facilitated the initialization and development of strain localization.

2. Modeled by a number of particles assigned with less stiffness, the effect of weak inclusions on specimen behaviors was investigated. Via comparison with the reference specimen, it was found that weak inclusion resulted in a secondary shear band and shear block without affecting the mechanical behavior substantially.
3. Particle breakage was simulated by replacing some two-sphere clumps with single spheres. Like the specimen containing weak inclusion, when particle breakage occurred inside the specimen, it intrigued a secondary shear band and shear block while imposing no substantial effect on the stress-strain response. However, particle breakage incurred greater local void ratio than weak inclusion.

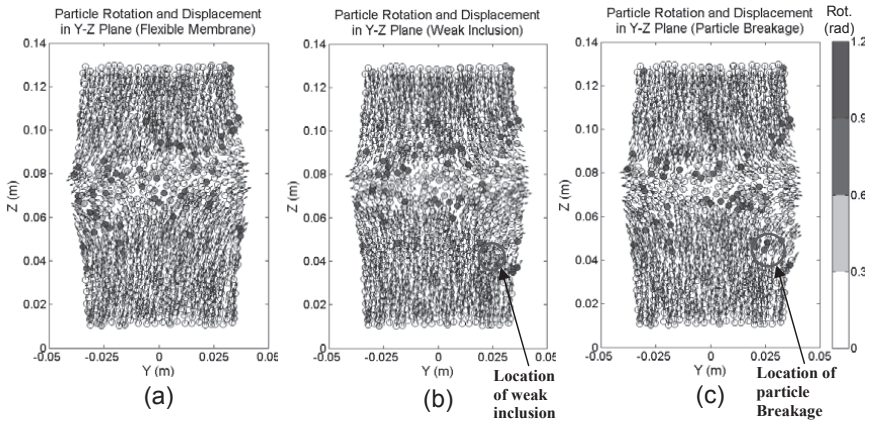


FIG. 3. Particle rotations and displacements for (a) reference specimen, (b) specimen with weak inclusion and (c) specimen with particle breakage.

ACKNOWLEDGMENTS

The financial support from the National Natural Science Foundation of China (NSFC Grant No.51109125) was gratefully acknowledged.

REFERENCES

- Cundall, P.A., and Strack, O.D.L. (1979). "A discrete numerical model for granular assemblies." *Géotechnique*, 29(1): 47-65.
- Desrues, J., Chambon, R., Mokni, M., and Mazerolle, F. (1996). "Void ratio evolution inside shear bands in triaxial sand specimens studied by computed tomography." *Géotechnique*, 46(3): 529-546.
- Lu, Y., and Frost, D. (2010). "Three-Dimensional DEM Modeling of Triaxial Compression on Sands." *GeoShanghai 2010, Geotechnical Special Publication 200 (GSP200)*, ASCE: 220-226.
- Thornton, C. (2000). "Numerical simulations of deviatoric shear deformation of granular media." *Géotechnique*, 50(1): 43-53.
- Zhao, X.L., and Evans, T.M. (2009). "Discrete simulations of laboratory loading conditions." *International Journal of Geomechanics*, ASCE, 9(4): 169-178.

Influential Factors on Slope Stability and Landslide Mobility

Deping Guo¹, Masanori Hamada², Hongyu Jia³

¹Dr. candidate & Research associate, Department of Civil and Environmental Engineering, Waseda University, 3-4-10kubo, Shinjuku-ku, Tokyo 169-8555, Japan; guodeping99@gmail.com

²Professor, Fellow of JSCE and JAEE, Department of Civil and Environmental Engineering, Waseda University, 3-4-10kubo, Shinjuku-ku, Tokyo 169-8555, Japan; hamada@waseda.jp

³Dr. candidate, Department of Civil Engineering, Emei Campus 614202, Southwest Jiaotong University, China; jhy_2010@my.swjtu.edu.cn

ABSTRACT: The 2008 Wenchuan earthquake caused a severe damage by landslide along the Longmenshan thrust belt zone in southwest China. The authors investigated into various influential factors on slope stability and landslide mobility based on 97 landslides in Wenchuan County and 46 long runout landslides in Wenchuan earthquake area, respectively. The results demonstrated that slope height, horizontal peak ground acceleration (PGA) and geological structure were more influential to slope stability than slope angle and rock type. After slope failure, slope height, rock type, field cross angle and landslide volume were the most important influential factors on landslide mobility, and followed by slope angle and horizontal PGA. Two empirical models were developed to estimate landslide volume and landslide mobility, their validities had been verified by the satisfactory agreements between observations and predictions, therefore, they could be useful in Wenchuan earthquake area and the areas with similar geological conditions.

INTRODUCTION

Landslide is one of typical geo-hazard in mountainous area, and earthquake is a main cause to trigger landslide, such as 1999 Chi-chi earthquake, 2005 Kashmir earthquake and 2008 Wenchuan earthquake. The cause of slope failure is a complicated interplay between seismic parameters and geological conditions and topographical conditions. Rapid or long runout landslide may result in heavy loss of life and properties; because persons in the travel path of these types of landslide do not have enough time to evacuate and the kinetic energy is so large that can severely

damage the infrastructure.

After the 2008 Wenchuan earthquake, numerous authors have analyzed the relationships between landslide spatial distribution and influential factors (Huang and Li 2009, Chigira et al. 2010, Qi et al. 2010, Dai et al. 2011, Gorum et al. 2011). However, there are few studies on the comprehensive effectiveness of influential factors on slope stability and landslide mobility. Hence, the authors discussed these issues, intending to clarify which factor/factors had predominant effect on slope stability and landslide mobility for better understanding the whole process from slope failure to landslide movement. In this paper, the authors totally collected 143 landslides to analyze. Firstly, data sources were briefly introduced; secondly, the effectiveness of each influential factor on slope stability would be explored based on 97 landslides in Wenchuan County. Thirdly, the relationship between landslide mobility and influential factors would be discussed according to 46 long runout landslides in Wenchuan earthquake area. Conclusion would be reported at last.

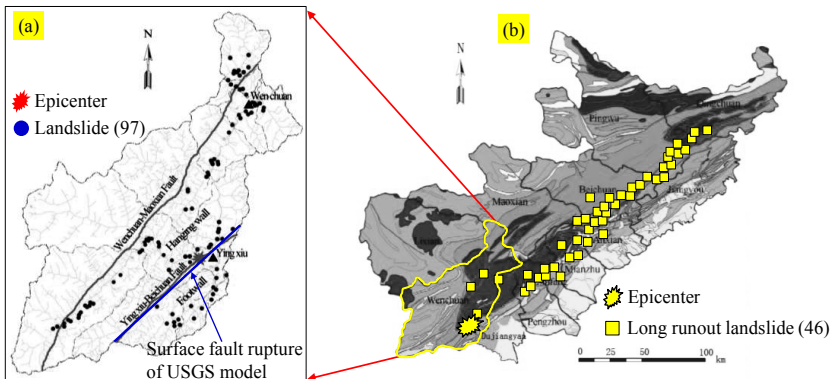


FIG.1 The location of surveyed landslides. (a) 97 landslides in Wenchuan County; (b) 46 long runout landslides in Wenchuan earthquake area (Based on Qi. et al 2011).

There are two data sources. One data source is 97 landslides located in Wenchuan County, as shown in Fig.1 (a), intending to explore the relation between slope stability and influential factors. Each of these landslides was delineated by slope angle (α_1), slope height (h) and geological structures. Because every landslide had parallel or nearly parallel stratigraphic surfaces, hence, geological structures were described by the relationship between slope angle (α_1) and rock bedding inclination angle (β). The other data source includes 46 long runout landslides in Wenchuan

earthquake area, as shown in Fig.1 (b); these landslides travelled on an open slope or partly confined by gentle side slope, when long runout landslides were obstructed by valley and relatively large infrastructures or confined by sharply steep slope, they had been excluded from this data source. Each long runout landslide was delineated by travel distance (L_{max}), landslide height (H_{max}), fährböschung (Heim 1932) or travel distance angle (α) (Hunter and Fell 2003), field cross angle (θ), slope angle (α_1), slope height (h), as illustrated in Fig.2. These 46 long runout landslides were used to discuss the relationship between landslide mobility and influential factors.

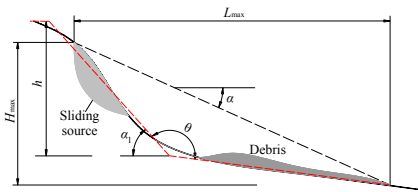


FIG.2 Term definition sketch

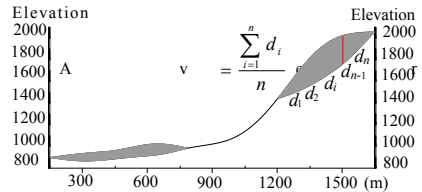


FIG.3 Landslide typical profile

The sliding area of each landslide outlined on the map was calculated by using ArcGIS software, and the sliding volume was estimated by multiplying the sliding area by the average collapse depth of the sliding body. The average collapse depth was obtained from the typical longitudinal profile of slope, as shown in Fig.3. According to rock strength and the degree of weathering, rock materials were assorted into two types and four subclasses, namely, hard rock (RT1, RT2) and soft rock (RT3, RT4). Typical rocks of each type are as follows (Chang et al. 2006):

RT1: Non-weathered or slightly weathered magmatic rock, diorite, basalt, andesite, gneiss and quartzite, etc.

RT2: ①Non-weathered or slightly weathered marble, slate, limestone, dolomite, metamorphic quartz rock, etc.; ②Moderately weathered magmatic rock, diorite, basalt, andesite, gneiss and quartzite, etc.

RT3: ①Non-weathered or slightly weathered tuff, phyllite, marl, sandy mudstone, etc.; ②Moderately or strongly weathered hard rock.

RT4: ①Non-weathered or slightly weathered shale, mudstone, shaly sand, etc.; ②Strongly weathered hard rock; ③Moderately or strongly weathered tuff, phyllite, marl, sandy mudstone, etc.

The horizontal peak ground acceleration of each landslide was estimated by following acceleration attenuation model, as Eq.1, which took hanging-foot wall effect into consideration and was developed on the hanging wall side and footwall side, respectively.

$$\ln PGA = a_1 \ln(D_{rup} + a_2) + a_3 \cdot D_{rup} + a_4 \quad (1)$$

where PGA refers to horizontal peak ground acceleration (cm/s²); D_{rup} represents nearest distance from site to Yingxiu-Beichuan surface fault rupture (km), which was located by USGS data (Ji and Hayes 2008), as shown in Fig.1(b); b_1, b_2, b_3, b_4 are the regression coefficients, listed in Table 1, in which R^2 stands for coefficient of determination.

Table 1. Regression parameters of acceleration attenuation model

| Hanging wall or footwall | b_1 | b_2 | b_3 | b_4 | R^2 |
|--------------------------|---------|--------|---------|--------|-------|
| Hanging wall | -0.8203 | 13.767 | -0.0042 | 9.1689 | 0.639 |
| Footwall | -0.6907 | 5.6180 | -0.0072 | 7.9393 | 0.555 |

INFLUENTIAL FACTORS ON SLOPE STABILITY

Sliding volume is one of the most important outcomes of slope failure; it indicates the affected scope and disaster scale. Based on the assumption of cubic root of sliding volume are linearly correlated with influential factors, multiple linear regression was conducted and a backward elimination approach was applied to obtain an optimization model in the aid of F-test and t-test. The regression procedures and results are shown in Table 2.

Table 2. Multivariable analysis on slope volume

| $LV^{1/3}=c_1h+c_2PGA+c_3\sin\beta+c_4\tan\alpha_1+c_5RT$ | | | | | | | | | | |
|---|--------|-------|-------|-------------|--------------|-------------|-------------------------|-----------------------------|-----------------------------|-------|
| Variable and parameter | c_1 | c_2 | c_3 | c_4 | c_5 | Multiple R | Adjusted R ² | F-stat (F _{0.05}) | t-test (t _{0.05}) | |
| 5 variables | c_i | 0.20 | 3.39 | 23.32 | -6.11 | 0.49 | 0.895 | 0.782 | 74.481 (2.313) | 1.986 |
| | t-stat | 5.97 | 2.28 | 1.85 | -0.66 | 0.16 | | | | |
| | c'_i | 0.55 | 0.18 | 0.18 | -0.06 | 0.01 | | | | |
| 4 variables | c_i | 0.20 | 3.46 | 23.84 | -5.99 | - | 0.895 | 0.785 | 94.080 (2.470) | 1.986 |
| | t-stat | 6.02 | 2.46 | 1.96 | -0.65 | | | | | |
| | c'_i | 0.55 | 0.19 | 0.18 | -0.06 | | | | | |
| 3 variables | c_i | 0.20 | 3.04 | 20.61 | - | - | 0.895 | 0.786 | 126.068 (2.701) | 1.986 |
| | t-stat | 6.01 | 2.44 | 1.86 | | | | | | |
| | c'_i | 0.55 | 0.16 | 0.16 | | | | | | |
| 2 variables | c_i | 0.23 | 4.78 | - | - | - | 0.891 | 0.781 | 182.655 (3.092) | 1.985 |
| | t-stat | 7.79 | 5.77 | | | | | | | |
| | c'_i | 0.63 | 0.26 | | | | | | | |

In Table 2, LV refers to sliding volume (m³); h represents slope height (m); PGA

refers to horizontal peak ground acceleration (m/s^2), estimated from Eq.1; β denotes rock bedding inclination angle ($^\circ$); α_1 represents slope angle ($^\circ$); RT refers to rock type, which was qualitatively considered, 4, 3, 2, and 1 were respectively assigned to RT1, RT2, RT3 and RT4. Multiple R means multiple correlation coefficient, which represents the correlated level between dependent and independent variables. Adjusted R^2 represents adjusted coefficient of multiple determination, namely, adjusted squared multiple correlation, which reveals the goodness of fit. F-stat denotes regressive F-value, $F_{0.05}$ means F-test threshold value with 95% significance level; if F-stat is bigger than $F_{0.05}$, it suggests overall regression satisfies significance level. t-stat denotes regressive t-value of each regression coefficient, $t_{0.05}$ denotes t-test threshold value with 95% significance level; if t-stat is bigger than $t_{0.05}$, it suggests the corresponding regression coefficient (c_i) satisfies coefficient significance level. However, not all regression coefficients are significance during regression procedures; therefore, the variable with smallest absolute t-stat value (italic bold digit in the Table 2) would be eliminated and then re-regressed, step-by-step until overall regression and all regressive coefficients both satisfy the significance level. These procedures are named as backward elimination regression. Since the units of independent variables affect regression coefficients (c_i), the standardized regression coefficients (c'_i) were applied to exclude the influence of the unit dimension so as to have insight into the effectiveness of each independent variable on the dependent variable.

Out of the four models in Table 2, F-tests suggest that the hypothetical models have statistical meaning and satisfy linear assumption. Furthermore, the model with 2 variables satisfies not only overall regression significance but also the significance of regression coefficients. Therefore, the model with 2 variables is more convenient and efficient to be applied for prediction. By using 2 variables' model, predicted sliding volume was compared with observed results, as shown in Fig.4.

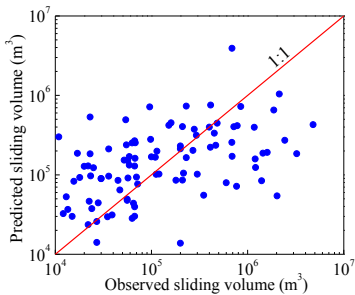


FIG.4 Predicted versus observed sliding volume

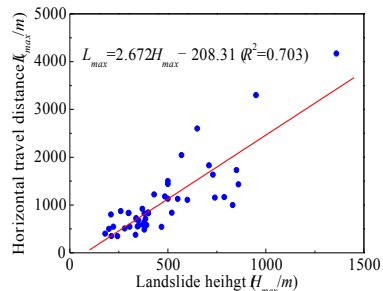


FIG.5 Landslide travel distance related with landslide height

Based on above stepwise regression and analysis, the optimization procedures

and absolute values of standardized regression coefficients in the 5 variables' model both suggest slope height, horizontal PGA and geological structure are more influential to sliding volume than slope angle and rock type. Because sliding volume is one of the most important characteristic of slope instability, hence, this result implies that slope height, horizontal PGA and geological structure are the most important factors on slope stability during earthquake.

INFLUENTIAL FACTORS ON LANDSLIDE MOBILITY

46 long runout landslides were used in this section, and Fig.5 suggests that landslide travel distance (L_{max}) and landslide height (H_{max}) had a significantly linear correlation, hence, landslide mobility might be expressed by an index, $\mu=H_{max}/L_{max}$, which was applied to assess landslide mobile ability after slope failure in the following discussion. In previous studies, this index was termed as equivalent coefficient of friction (Scheidegger 1973), which is equal to the tangent of fahrböschung (Heim 1932) or travel distance angle (α) (Hunter and Fell 2003).

Table 3. Multivariable analysis on landslide mobility

| $\mu=H_{max}/L_{max}=e_1\log h+e_2 RT+e_3 \sin\theta+e_4\log V+e_5\tan\alpha_1+e_6\log PGA$ | | | | | | | | | | | |
|---|--------|-------|-------|--------|--------|--------------|---------------|-------------------------|-----------------------------|-----------------------------|-------|
| Variable and parameter | e_1 | e_2 | e_3 | e_4 | e_5 | e_6 | Multiple R | Adjusted R ² | F-stat (F _{0.05}) | t-test (t _{0.05}) | |
| 6 variables | e_i | 0.375 | 0.064 | -0.337 | -0.083 | 0.123 | -0.088 | 0.971 | 0.910 | 109.57 (2.342) | 2.023 |
| | t-stat | 3.164 | 2.839 | -2.304 | -1.961 | 1.196 | -0.560 | | | | |
| | e'_i | 0.381 | 0.360 | -0.339 | -0.323 | 0.170 | -0.072 | | | | |
| 5 variables | e_i | 0.369 | 0.063 | -0.356 | -0.090 | 0.116 | - | 0.971 | 0.912 | 133.66 (2.449) | 2.021 |
| | t-stat | 3.153 | 2.819 | -2.525 | -2.239 | 1.144 | | | | | |
| | e'_i | 0.375 | 0.353 | -0.358 | -0.350 | 0.160 | | | | | |
| 4 variables | e_i | 0.417 | 0.067 | -0.316 | -0.098 | - | - | 0.970 | 0.912 | 165.52 (2.600) | 2.020 |
| | t-stat | 3.804 | 3.083 | -2.306 | -2.471 | | | | | | |
| | e'_i | 0.424 | 0.380 | -0.319 | -0.381 | | | | | | |

Based on linear assumption, the index of landslide mobility was supposed to be linearly correlated with influential factors and obey the model shown in Table 3. Multiple linear regression was implemented and backward elimination approach was applied to obtain prediction model in the aid of F-test and t-test. The regression procedures are the same as those used in above section, and the results were listed in Table 3.

In Table 3, $\mu=H_{max}/L_{max}$ represents the index of landslide mobility; h denotes slope height (m); RT refers to rock type, it was qualitatively considered, 4, 3, 2, and 1 were respectively assigned to RT1, RT2, RT3 and RT4; θ represents field cross angle

($^{\circ}$); V represents landslide volume (m^3); α_1 denotes slope angle($^{\circ}$); PGA refers to horizontal peak ground acceleration (m/s^2), estimated from Eq.1; the basis of logarithm is 10.

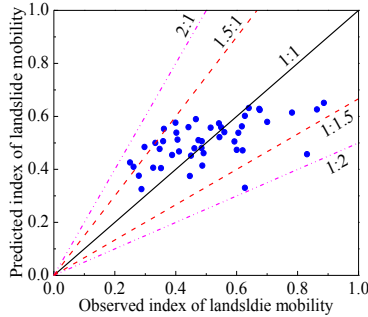


FIG.6 Predicted versus observed index of landslide mobility

Compared four models in Table 3, F-tests suggest that all of these hypothetical models have statistical significance and satisfy linear assumption. Based on the backward elimination procedures and those absolute values of each standardized regression coefficient in 6 variables' model, they suggest that slope height, rock type, field cross angle and landslide volume were the most important influential factors on landslide mobility, and followed by slope angle; horizontal peak ground acceleration had weakest effect on landslide mobility. Furthermore, the model with 4 variables satisfies both overall statistical significance and the significance of each regression coefficient, hence, it was applied to predict the index of landslide mobility. The comparison between predictions and observations was shown in Fig.6, which suggests that this model for predicting landslide mobility yields satisfactory results.

CONCLUSIONS

There are numerous influential factors on slope stability and landslide mobility, some of which are discussed in this paper; however, some other factors are not mentioned here, such as hydro-geological parameters, vegetation and slope aspect, and so on, because it is difficult to gather all of these influential factors. Nevertheless, this paper had explored the effectiveness of various influential factors on landslide volume and mobility, and proposed that slope height, horizontal PGA and geological structure were more influential to slope stability than slope angle and rock type, moreover, slope height, rock type, field cross angle and landslide volume had predominant effect on landslide mobility, and followed by slope angle, horizontal peak ground acceleration had weakest effect on landslide mobility. Even if

the predicted results by multiple linear regression models are not perfect, the stepwise regression demonstrated that these two hypothetical models satisfied both the overall significance level and the significance of regression coefficients, and yielded satisfactory predictive results. Therefore, these two models are reasonable, and might be useful to preliminarily predict landslide volume and its mobility in Wenchuan earthquake area and in the similar geological and topographic areas. Notwithstanding, more researches need to be conducted to further verify their validities and improve them.

REFERENCE

- Chang, S.B., Zhang, S.M., et al. (2006). *Manual of Engineering Geology (Fourth edition)*, China architecture & building press, 17–18.
- Chigira, M., Wu, X.Y., Inokuchi, T., Wang, G. H. (2010). “Landslides induced by the 2008 Wenchuan earthquake, Sichuan, China.” *Geomorphology*, 118:225–238.
- Dai, F.C., Xu, Q., Yao, X., Xu, L., Tu, X.B., Gong, Q.M. (2011). “Spatial distribution of landslides triggered by the 2008 Ms8.0 Wenchuan earthquake, China.” *Journal of Asian Earth Sciences*, 40(4):833–895.
- Gorum, T., Fan, X.M., Westen, C.J., Huang, R.Q. Xu, Q. (2011). “Distribution pattern of earthquake-induced landslides triggered by the 12 May 2008 Wenchuan earthquake.” *Geomorphology*, 133:152–167.
- Heim, A., 1932. *Bergsturz und Menschenleben*. Fretz und Wasmuth, Zurich, p.218.
- Hunter, G., Fell, R., 2003. “Travel distance angle for ‘rapid’ landslides in constructed and natural soil slopes.” *Canadian Geotechnical Journal*, 40:1123–1141.
- Huang, R.Q., Li, W.L. (2009). “Analysis of the geo-hazards triggered by the 12 May 2008 Wenchuan earthquake, China.” *Bulletin of Engineering Geology and the Environment*, 68(3):363–371.
- Ji, C., Hayes, G. (2008). “Finite fault model-preliminary result of the May 12, 2008 Mw7.9 eastern Sichuan, China earthquake.” Information from website: http://earthquake.usgs.gov/earthquakes/eqinthenews/2008/us2008ryan/finite_fault.php
- Qi, S.W., Xu, Q., Lan, H.X., Zhang, B., Liu, J.Y. (2010). “Spatial distribution analysis of landslides triggered by 2008.5.12 Wenchuan earthquake, China.” *Engineering Geology*, 116:95–108.
- Qi, S.W., Xu, Q., Zhang, B., Zhou, Y.D., Lan, H.X., Li, L.H. (2011). “Source characteristics of long runout rock avalanches triggered by the 2008 Wenchuan earthquake, China.” *Journal of Asian Earth Sciences*, 40(3):896–906.
- Scheidegger, A.E. (1973). “On the prediction of the reach and velocity of catastrophic landslides.” *Rock Mechanics*. 5:231–236.

The Test Research Of Dynamic Strength and Deformation on Geogrid Reinforced Cohesive Soil Under Cyclic Loading

Ning Wang¹, Zhixing Han², Wenmei Su³ and Wenxu Li⁴

¹School of Civil Engineering and Architecture, Southwest University of Science and Technology; No.59, Qinglong Middle Road, Mianyang 621010; Tel: (0816)2419237; Fax: (0816)2419237; Email: 1010868946@QQ.com

²School of Civil Engineering and Architecture, Southwest University of Science and Technology; No.59, Qinglong Middle Road, Mianyang 621010; Tel: (0816)2419237; Fax: (0816)2419237; Email: 1289377784@QQ.com

³ChuanJiao Highway Planning Survey and Design Co, Ltd of Mianyang; No.70, YingBing Road, Mianyang 621010; Tel: 13458009786; Email: 289981870@QQ.com

⁴Housing and Urban Construction Bureau of Neijiang; No.88, TaiBai Road; Neijiang 641000; Tel: (0832)2024301; Email: 380229590@QQ.com

ABSTRACT: The results of dynamic triaxial test of reinforced geogrid cohesive soil under cyclic loading indicate that the dynamic strength of reinforced cohesive soil shows good regularity with the change of amplitude of dynamic stress and number of reinforced geogrid layer . The forms of dynamic strength curve of reinforced cohesive soil are basically uniform with different conditions, and the dynamic strength curve can be expressed as $\tau_d = A \ln (-B \ln N_f)$. The axial cumulative strain increases quickly with vibration times increasing under cyclic loading during the earlier stage of the vibration which can reach 60% ~ 70% of the total strain, and it remains stable with vibration times increasing if the dynamic stress is smaller than the limited dynamic stress. But the axial cumulative strain increases slower than the axial cumulative strain during the earlier stage and the curve of the axial cumulative strain is nonlinear totally if the dynamic stress is bigger than the limited dynamic stress and the sample fails eventually for instability. The development of the axial cumulative strain of reinforced cohesive soil shows good regularity along with the change of amplitude of dynamic stress and number of geogrid layers, and the cumulative strain may be described as $\varepsilon_p = A + B N^C$.

INTRODUCTION

In modern transportation, the load conditions of road are becoming more and more complex, and vehicle load is the main load beard by road. So the strength and deformation of the subgrade in cycle load has been drawn extensive attention by researchers. With the development of the technology of geosynthetic materials, geotechnical reinforcement technology in subgrade construction on the geosynthetic materials has been applied widely. The research is focused on static load bearing capacity of the foundation and deformation characteristics at present, while the

research on the dynamic loading characteristics is less at home and abroad. Moreover as the homogeneous sand or sand soil was used in many testes, the experimental research of reinforcement cohesive soil is reported not more so far. In this paper, the dynamic triaxial test of reinforcement cohesive soil has been done, and its dynamic strength and deformation law of development in the cycle dynamic loading has been analyzed.

TEST EQUIPMENT AND METHOD

The test equipment is the electro-hydraulic servo soil dynamic triaxial test machine (SDT 100 model) made by Xian Lichuang Measuring Instrument Co. The samples used of soil are from a reconstruction place in the Mianyan Road in Sichuan province. The samples is low liquid limit silty clay which color is brown yellow and specific gravity is 2.72. Their liquid limit is 42.8%, plastic limit 27.2% and plastic index is 15.6%. The most optimum moisture content is 13.7% and the maximum dry density is 1.8 g/m^3 . The diameter of the prepared samples in the optimum moisture content is 61.8mm, height 125mm. The reinforcement material is the warp knitting geogrid reinforced materials in the Mianyan road whose grid size is 21.0mm x 21.0mm, the mass in unit area is 447 g/m^2 , longitudinal tensile strength is 63.4KN/m and the elongation is 2.80%, transverse tensile strength is 74.5KN/m and the elongation is 2.90%. The materials are arranged and layered horizontally, which a reinforcement layer is in the central part of the sample, and two reinforcement layers are respectively placed in a third place in the sample. The samples are prepared in strict accordance with the soil test execution procedures, and the sample moisture content and density are controlled strictly in the test.

The vehicle dynamic load is simulated with the approximate sine load in the test. The value of vibration frequency refer to the results of related literature, and the test vibration frequency is 1.0Hz. Considering the characteristics of geosynthetic reinforcement engineering and the safety of test results in engineering application, the unconsolidated undrained test (UU test) is adopted. Because of lack of research on cohesive soil reinforcement dynamic load tests, the methods of fatigue-dynamic tests of some rock under dynamic loading are referred. Before this dynamic triaxial test, the static triaxial test based on the same density and the moisture content is done in order to sure the static strength. The stress values in the center of vibration of the dynamic test are the 0.6 times of the static strength values under the corresponding condition. The confining pressures of dynamic test are 100, 200 and 300KPa respectively, The tests of 3 ~ 4 samples are carried on under each confining pressure. Considering the properties of cohesive soil engineering, the failure strain in standard is used in the test that if the cumulative axial strain is up to 5%, the sample is thought failed. The pausing condition of the test is the axial strain more than 5% and the most vibration time is 3000 times.

DYNAMIC SHEAR STRENGTH ANALYSIS

The data collected of the experiment is processed, and dynamic shear strength curves ($\tau_d - lg N_f$) are drawn and fitted to get dynamic strength curve equation.

Dynamic Shear Strength Curve

It can be known from different reinforced geogrid layers in different confining pressure tests of dynamic shear strength curve (Figure 1) that whether the confining pressure is 100, 200 or 300KPa, the change rule of dynamic shear strength curve is nearly same that the curve is steep overall in the early stage of vibration, then it tends to be flattened with vibrations time increasing; the permutation of the curves from top to down is always made up two layers the reinforcement, a layer the reinforcement and soil(not the reinforcement). The test results show that: (1) The geogrid layers on reinforcement of the cohesive soil have obvious influence on the dynamic strength. No matter that the reinforcement a layer or two layers, the dynamic stress of reinforced soil required is far greater than that of the soil to achieve the same damage strain in the same cycle times which shows that the reinforced soil has a good ability in ant-vibration and reinforced material in the arrangement of the cohesive soil can improve the grid soil shear strength, reduce the dynamic soil deformation; (2) With other conditions being the same as the more reinforcement layers, the dynamic shear strength is the greater and the reinforcement effect is the better, taking confining pressure 200KPa as an example, vibration time of the damage being 50 times, the dynamic shear strength of the two reinforcement layers increases about 55% and the dynamic shear strength of the one reinforcement layer increases more about 30% than that of soil (not the reinforcement); (3) The reinforcement effect on the dynamic strength in high confining pressure is better, taking an example, to achieve the same damage strain, the dynamic stress with confining pressure being 300KPa is far bigger than that with 100KPa and 200KPa for different geogrid layers on the same cycle times; (4) The dynamic stress amplitude on the reinforcement soil destruction has significant effects on the number of vibration. under the same confining pressure, the deformation of the sample whose dynamic stress amplitude is bigger in high cycle load increases soon, while the sample can be damaged in smaller time of the vibration, and vice versa.

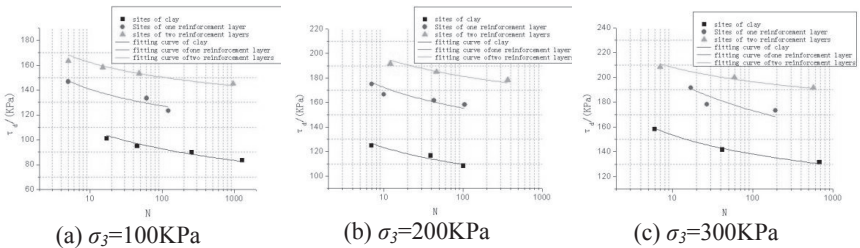


FIG. 1. The dynamic strength curve of different confining pressure.

Dynamic Shear Strength Fitting Curve Equation

The test results of dynamic shear stress and damage of the vibration time are fitted and it is found that dynamic shear stress and damage of the vibration times

with logarithmic function fitting the better, fitting equation can be written as:

$$\tau_d = A \ln(-B \ln N_f)$$

In the function, τ_d is the dynamic shear stress in failure; N_f is vibration times of the corresponding destruction; A and B are the fitting parameters of the equation which are related to the category of soil, the reinforcement layer, the initial stress state and the dynamic stress on amplitude. The parameters in the function of the shear strength curve see Table 1.

Table 1. The Dynamic Strength Curve Fitting Test Results

| Sample state | σ_3 (KPa) | A | B | R ² |
|--------------------------|------------------|---------|-------------|----------------|
| No reinforcement | 100 | -22.647 | -0.00363 | 0.91107 |
| | 200 | -20.419 | -0.00102 | 0.91515 |
| | 300 | -22.813 | -5.11078E-4 | 0.98551 |
| One reinforcement layer | 100 | -19.049 | -2.7151E-4 | 0.90729 |
| | 200 | -24.186 | -3.50218E-4 | 0.71965 |
| | 300 | -36.649 | -0.00192 | 0.67531 |
| Two reinforcement layers | 100 | -16.361 | -2.24521E-5 | 0.90036 |
| | 200 | -21.361 | -4.45533E-5 | 0.84680 |
| | 300 | -16.891 | -1.92364E-6 | 0.92957 |

For 0 ~ 2 layer reinforcement, their R² value are respectively in 0.92 ~ 0.98, 0.68 ~ 0.91 and 0.85 ~ 0.93, and it can explain that the degree of fitting of test data is good. Through putting the damaged vibration time in the test into the fitting formula to calculate the dynamic shear stress of the experiment and calculating and analyzing the dynamic shear stress absolute error, the absolute error range of the soil is between 0.81% ~ 2.79%, the absolute error of one reinforcement layer between 0.33% ~ 4.03%, the absolute error of two reinforcement layers between 0.01% ~ 3.60%. Because fitting parameters are obtained through the test, fitting formula is useful to practical application.

DEFORMATION ANALYSIS

Relationship Between Axial Strain Accumulation and Vibration Time

The development of deformation of the soil in the dynamic loading is in connection with the dynamic stress.

In the test it is found that when the dynamic stress is less than the damage loads, the deformation of samples can not reach its failure strain. In Figure 2 it can be seen that the accumulation axial strain of reinforcement increases with the vibration time increasing, and in the earlier period of the vibration, when the time is 300 or so, accumulation of axial strain increases fast with vibration time increasing as almost linear increasing, and the strain can achieve 60% ~ 70% of total strain. With the vibration time increasing, the increased rate of axial strain becomes very small and

axial strain increment is very slow and axial strain accumulation becomes stable. This deformation law of the reinforcement is consistent with that of cohesive soil under dynamic loading.

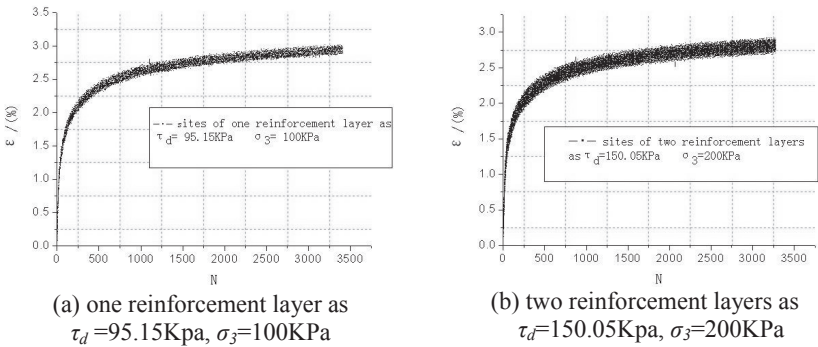


FIG. 2. The relation curves between axial cumulative strain and vibration times.

When the dynamic stress applied is more than dynamic destruction loads, soil samples will be damaged due to big deformation. In Figure 3 it can be seen that when the dynamic stress is bigger than critical dynamic stress, the axial accumulated strain of the reinforcement also increases with the increase of the vibration time. And in the initial about 50 times vibration, the axial strain accumulation can reach 60% ~ 70% of the damage strain; in 100 ~ 200 times vibration, the increased speed of axial accumulative strain is small with nonlinear increase overall, and the deformation of samples can not stable; the axial strain will accumulate more than 5% so that the sample is damaged due to bigger deformation finally.

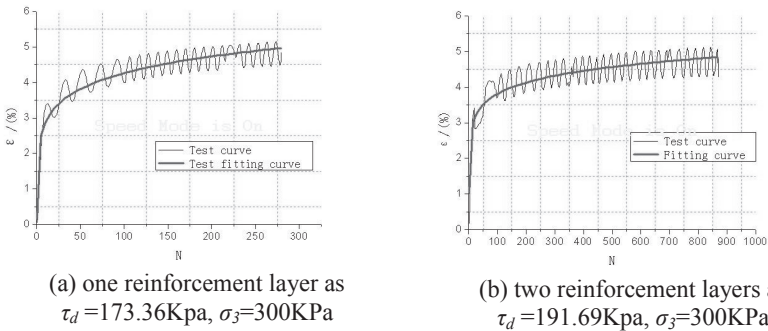


FIG. 3. The relation curves between axial cumulative strain and vibration times.

In Figure 2 and Figure 3, the relationship of axial strain accumulation and vibration time was fitted, and fitting function is:

$$\varepsilon_p = A + BN^C$$

In the function, the ε_p is cumulative plastic strain; N is times of cycle load; A, B and C are the fitting parameters of the equation which are related to the category of soil, the reinforcement layer, the initial stress state and the amplitude of the dynamic stress. The fitting parameters of the sample in Figure 2 and Figure 3 are shown in Table 2.

Table 2 Fitting test results

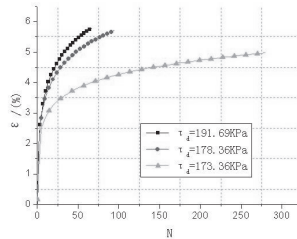
| Parameters | A | B | C | R ² |
|------------|----------|---------|---------|----------------|
| | 0 | 0.94947 | 0.14269 | 0.90680 |
| Value | 0 | 0.93441 | 0.13964 | 0.87129 |
| | -4.11446 | 5.82996 | 0.07876 | 0.80926 |
| | -2.57656 | 4.65449 | 0.06889 | 0.75496 |

The Relationship between Axial Strain Accumulation and Geogrid Layers

Geogrid layers to axial accumulated strain have significant effect. In the same confining pressure and dynamic load conditions, the axial accumulative strain decreases as the increase of geogrid layers. Taking an example, when confining pressure is 200KPa and dynamic shear stress is 108.35KPa, the soil (not the reinforcement) will be failed and the axial strain will be accumulated 5.63% as the vibration times is only 200, but reinforced layers is not damaged in the end of test outage, and the axial strain accumulation is only 2.78%(one reinforced layer) and 0.92%(two reinforced layers). The final cumulative axial strain is only 49.3% and 16.3% of the soil (not the reinforcement) respectively. That means that reinforced soil has good ability in ant-vibration, and arranging geogrid into cohesive soil is a feasible method to improve the dynamic strength of soil, to restrain the axial strain and reduce the accumulation of settlement and deformation.

Relationship between Axial Strain and Dynamic Stress Amplitude

Dynamic stress amplitude has great influences on the axial strain. The relationship between the axial strain of different reinforced geogrid layers and vibration time has similarity. The influence of dynamic stress amplitude to axial cumulative plastic strain is explained using relation curve of the axial accumulated strain of one reinforcement layer with 300KPa confining pressure and different dynamic stress.



One reinforcement layer as
 $\sigma_3=300\text{KPa}$

FIG. 4. The relation curves between axial cumulative plastic strain and vibration times.

In Figure 4 it can be seen that the dynamic stress has great influence on the axial strain accumulation of the reinforcement, and this is similar to the influence of dynamic stress to dynamic strength. Whether or not the reinforcement, the axial strain accumulation increases with the increase of the dynamic stress and vibration time of reaching damaged strain is smaller. This is because each cycle strain energy can be directly related to stress amplitude. When dynamic stress amplitude is greater, the energy in the development of deformation is more, and the development of deformation is faster, and vibration time needed is also less.

CONCLUSIONS

In view of this experiment, the following conclusions may be drawn.

- (1) The dynamic strength of reinforced soil shows good regularity as the amplitude of dynamic stress and reinforced geogrid layers change, and the forms of dynamic strength curve of reinforced soil are basically uniform with different conditions. The dynamic strength curve can be expressed as $\tau_d = A \ln(-B \ln N_f)$;
- (2) The axial cumulative strain increases quickly with vibration times increasing under cyclic loading during the earlier stage of the vibration which can reach 60% ~ 70% of the total strain, and it remains stable with vibration times increasing if the dynamic stress is smaller than the limited dynamic stress; But the axial cumulative strain increases slower than it during the earlier stage and it was nonlinear totally if the dynamic stress is bigger than the limited dynamic stress and the sample fails eventually for instability;
- (3) The development of the axial accumulated strain of reinforcement shows good regularity along with dynamic stress amplitude and geogrid layers change whose relationships may be described as $\varepsilon_p = A + B N^C$.

REFERENCES

- Cai, Y. and Cao, X. W. (1996). "Repeated load subgrade soil under the critical dynamic stress and permanent deformation discussed." *J. Southwest Jiaotong*

University, v.31 (1): 1-5.

- Fu, H., Ling, H., and Cai, Z. Y. (2008). "The experimental research on the factors of reinforced strength." *J. Geotechnical Mechanics*, v.28 (s1): 481-484.
- Ge, X. R., Jiang, Y., Lu, Y. D., and Ren, J. X. (2003). "Cycle load rock deformation characteristics of the experimental studies." *J. Fatigue Rock Mechanics and Engineering*, v.22 (10): 1581 - 1585.
- He, J. Q., Yang, J. S., and J, M. (2008). "The cycle load soil mechanical properties with coal gangue experimental study." *J. Rock Mechanics and Engineering*, v. 27 (1): 199-205.
- Peng, S. Q., Zhao, J. H., and Huang, R. Q. (2002). "Chengdu clay dynamic triaxial test research." *J. Geological Hazard and Environmental Protection*, v. 13 (1): 57-60
- Ren, J. X., Jiang, Y., and Ge, X. R. (2005). "Uniaxial compressive rock fatigue life influence factors were analyzed." *J. Chinese Journal of Geotechnical Engineering*, v. 27 (11): 1282 - 1285.
- Song, X. Y., Luo, R. A., Shan, Y. F., and Cheng, C. J. (2003). "Rock and elastic-plastic fatigue strength test theory analysis preliminary studies." *J. Geotechnical Engineering*, v. 24 (s2): 171 -174.
- Wu, J. H. (2000). "Geosynthetic materials reinforcement sandy soil test." *J. of Geotechnical Engineering*, v. 22 (2): 200-204.
- Xie, W. L., Xue, J. G., and Chang, B. (2008). "Reinforced the dynamics characteristics of triaxial test." *J. Science*, v. 23 (B9): 120 - 124.
- Yang, P., Ye, W. M., and Zhang, Y. W. (2009). "Train for power load power subgrade soil deformation analysis." *J. of Underground Space and Engineering*, v. 5 (6): 1166-1169.
- Yang, Y., Bai, S., and Zhang, J. (2009). "Reinforced the dynamic triaxial test." *J. of Subgrade Engineering Study*, (5): 178-179.
- Zhang, M. X., & Min, X. (2006). "The three-dimensional soil reinforcement. Single characters of triaxial test study." *J. of Geotechnical Engineering*, v. 28 (8): 931-936.

A Numerical Study on Artificial Fill Embankment with Liquefiable Foundation Using FLAC

Genlong Wang¹, S.M. ASCE, Hengxing Lan² and Guoqiang Yu³

¹Associate professor, Xi'an Center of Geological Survey, China Geological Survey, No. 438, East of Youyi Road, Beilin District, Xi'an 710054, China; wang2006@mail.iggcas.ac.cn

²Researcher, Institute of Geographic Sciences and Natural Resources Research, Chinese Academy of Sciences, 11A, Datun Road, Chaoyang District, Beijing 100101, China; lanhx@lreis.ac.ca

³Assistant researcher, Xi'an Center of Geological Survey, China Geological Survey, No. 438, East of Youyi Road, Beilin District, Xi'an 710054, China; yuguoqiang23@163.com

ABSTRACT: The problem of seismic liquefaction related to artificial fill embankment is complicated. In this study, by making using of Finn model, a typical artificial fill embankment was simulated by means of Finn model in FLAC. Numerical simulation results indicated that the pore water pressure of saturated sand soil increased extremely which resulted in the significant decrease of the effective stress. When the effective stress decreased approximately to zero, the liquefaction phenomena occurred. According to the change of pore water pressure at different locations and depths, three rules have been obtained. Firstly, the occurrence time for the first peak of pore water pressure coincided with the seismic peak acceleration of input wave. Secondly, the liquefaction occurred earlier in the upper-layer of saturated sand soil than in the lower-layer below the bottom of slope. However the duration of liquefaction in lower-layer of saturated sand soil was longer than in the upper-layer. Thirdly, the upper-layer of saturated sand soil was almost not liquefiable below the top of slope, while the lower-layer was easily liquefiable with long time duration. In summary, the characteristics of seismic liquefaction in the artificial fill embankment were closely related to the seismic wave, locations and depths of saturated sand soil in a slope.

INTRODUCTION

Earth embankments are constructed for various purposes, such as river dykes, earth dams and road embankments. A large number of earth embankments are prone to partial or total damage, mainly due to the liquefaction of the embankments and/or foundation soils induced by earthquakes (Adalier and Sharp, 2004; Huang et al., 2008), i.e. in the 1975 Tangshan earthquake in China (Fu and Zeng, 2005; Chen et al., 2009), the 1995 Hyogoken-Nambu Earthquake in Japan (Matsuo, 1996), the 1995 Kobe

earthquake in Japan, the 1999 Chi-chi earthquake in Taiwan, the 2001 Bhuj Earthquake in India (Krinitsky and Hynes, 2002) and the 2008 Wenchuan earthquake in China (Zhou et al., 2009; Wang et al., 2013). Earthquake-triggered liquefaction may cause a significant loss of strength of the soil mass with a progressive build-up of pore pressure, resulting in large permanent deformation and even complete failure of the embankments (e.g. Seed et al., 1985; Wang et al., 2010).

Experimental tests and numerical simulation are two major approaches to analyze the stability of earth embankments under earthquake loading. Experimental tests related to these problems include shaking table tests (Koga and Matsuo, 1990; Park et al., 2000) and dynamic centrifuge tests (Koseki et al., 1994; Adalier et al., 1998). Because of high cost for experimental test, the numerical simulation becomes the most useful alternative approach. Numerical simulation approaches have many advantages over physical experimental methods. They can rapidly and efficiently change test conditions and component properties without inordinate setup costs or significant downtime. Numerical simulations for engineering practice have been applied by an increasing number of researchers, especially with advances in computer technology. They have been widely used to solve specific problems of earth embankments under earthquake loading in the past few decades. Pekau and Cui (2004) carried out a comprehensive study of the dynamic behavior of the fractured Koyna dam in India during earthquakes using the distinct element method (DEM). Siyahi and Arslan (2008) used finite element to analyze the dynamic behavior, failure modes and mechanisms of failure of the dam under ground motions. Huang et al. (2012) studied the seismic performance in a numerical model to examine the effect of anti-liquefaction treatments on liquefaction foundation soils during earthquake loading.

This work aims to investigate the characteristics of the accumulation and dissipation for pore water pressure under earthquake loading and the subsequent liquefaction in an artificial fill embankment. The results are valuable to the understanding of liquefaction mechanism in the seismic area.

2. METHODOLOGY

2.1 Finn model

The Finn model for liquefiable soil was employed in this study. This mechanism was well-described by Martin et al. (1975). The empirical equation, which indicates the relation between the increment of volume and shear strain, is given as:

$$\Delta\varepsilon_{vd} = C_1(\gamma - C_2\varepsilon_{vd}) + \frac{C_3\varepsilon_{vd}^2}{\gamma + C_4\varepsilon_{vd}} \quad (1)$$

where $\Delta\varepsilon_{vd}$ is the increment of volume, ε_{vd} is the accumulated irrecoverable volume strain, γ is shear strain, C_1 , C_2 , C_3 and C_4 are constants.

Bryne (1991) proposed an alternative and simpler formula on the basis of Martin's research. It is expressed as:

$$\frac{\Delta \varepsilon_{vd}}{\gamma} = C_1 \exp\left(-C_2 \frac{\varepsilon_{vd}}{\gamma}\right) \quad (2)$$

where C_1 and C_2 are constants with different interpretations from those of Eq. 2. In many cases, $C_2=0.4/C_1$, so Eq. 2 involves only one independent constant.

Bryne noted that the constant, C_1 , can be derived from relative densities, D_r , as follows:

$$C_1 = 7600(D_r)^{-2.5} \quad (3)$$

Further, using an empirical relation between D_r and normalized standard penetration test value $(N_1)_{60}$:

$$D_r = 15\sqrt{(N_1)_{60}} \quad (4)$$

Substituting Eq. 4 into Eq. 3, then,

$$C_1 = 8.7(N_1)_{60}^{-1.25} \quad (5)$$

2.2 Geological model and boundary conditions

According to engineering geological conditions of the fill embankment, the geological model has been simplified as a fill layer, a sand soil layer and a gravel soil layer (see in FIG. 1). The model size has been set to three times the actual size of the embankment for the purpose of decreasing boundary effects. The numerical model was 35 m high and 155 m wide, with 1510 quadrilateral elements. The thickness of sand soil layer (i.e., liquefiable soil) was 12 m, and the gravel soil layer was 18 m. The water table was 1.5 m below the surface.

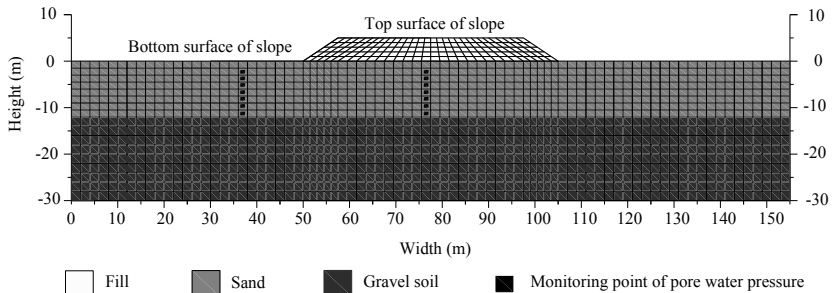


FIG. 1 The model of numerical simulation for the embankment.

FLAC dynamic numerical simulation has strict requirements for element size. The size must be smaller than approximately one-tenth to one-eighth of the wavelength

associated with the highest frequency component of input wave. The element size can be calculated by the Eq. 6

$$\Delta l = \frac{C_s}{A \cdot f} \quad (6)$$

where C_s is the minimum shear wave velocity of fill (m/s), f is the maximum frequency of the input waves (Hz), A equals 10 or 8.

In this study, the minimum shear wave velocity of the fill layer was 150 m/s and the maximum frequency of the input wave was 10 Hz. Therefore, the allowable maximum element size should be in the range of 1.5-1.87 m. In fact, the maximum element size in the numerical model (see in FIG. 1) was 1.8m (>1.5 m and < 1.87 m). At the first stage (static analysis), the vertical displacement at the model's bottom and the horizontal displacement at the model's left and right boundaries were fixed, and then the static equilibrium at the self-weight stress has been obtained. By setting up the water table to the model and the impervious boundary condition at the model's bottom, the pore water pressure was initialized. At the second stage (dynamic analysis), the left and right of the model were set as free-field boundaries, and the bottom was set as vertical displacement boundary and horizontal viscous boundary.

2.3 Parameters

On the basis of indoor soil test and in-situ standard penetration test (SPT), the selected parameters used in numerical simulation are listed in Table 1. In addition, through numerical simulation, the natural frequency of soil strata was calculated to be 0.8 Hz when the damping ratio was 5%.

Table 1. Parameters used in numerical simulation.

| Name of soils | Cohesive force (kPa) | Internal friction angle (°) | Bulk modulus (MPa) | Shear modulus (MPa) |
|---------------|--------------------------------------|--|---------------------------|---------------------|
| Fill | 10 | 25 | 97.6 | 45.0 |
| Sand soil | 0.0 | 28 | 134.6 | 62.9 |
| Gravel soil | 4.9 | 36 | 509.1 | 234.9 |
| Name of soils | Natural density (kg/m ³) | Coefficient of permeability (m ² /Pa·s) | Shear wave velocity (m/s) | Element size (m) |
| Fill | 2 000 | 10 ⁻¹⁰ | 150 | 1.0~1.8 |
| Sand soil | 1 900 | 10 ⁻⁸ | 182 | 1.5~2.0 |
| Gravel soil | 2 200 | 10 ⁻⁷ | 327 | 1.5~2.0 |

2.4 Seismic Input

The characteristics of earthquake motion depend on three major elements: amplitude, spectrum, and duration. We adopted US typical EI Centro earthquake wave

(S-N) as the input wave (as shown in FIG. 2). The peak horizontal acceleration and duration are about 0.3 g and 40 seconds respectively. In order to improve computing speed and calculation accuracy, the high-frequency components (> 10 Hz) have been filtered out. A stress boundary condition has been used by assigning input seismic dynamic loading. A velocity record is transformed into a stress record and applied to a quiet boundary. The initial acceleration wave has been transformed into a velocity wave (FIG. 3) by means of numerical integration method. The conversion formula from velocity wave to shear stress wave can be written as follows:

$$\left. \begin{aligned} \sigma_s &= -2(\rho C_s) V_s \\ C_s &= \sqrt{\frac{G}{\rho}} \end{aligned} \right\} \quad (7)$$

where σ_s is applied shear stress, V_s is input shear wave velocity, G is shear modulus, ρ is mass density, C_s is speed of s-wave propagation through medium.

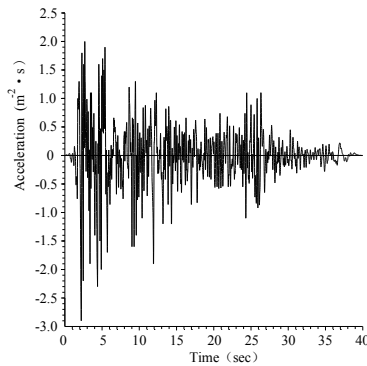


FIG. 2 Input earthquake wave of EI Centro Earthquake (S-N).

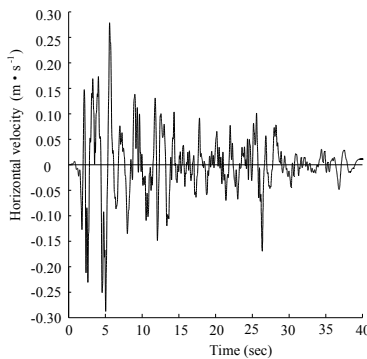


FIG. 3 Input horizontal velocity wave transformed from acceleration wave.

3. RESULTS AND DISCUSSION

For the purpose of studying liquefaction problem of the fill embankment under seismic loading, 14 monitoring points were set below the slope's bottom surface and top surface (FIG. 1). Numerical simulation results show that the pore water pressure of saturated sand soil has increased extremely, and the effective stress has decreased simultaneously. The curve of effective stress indicated that the liquefaction phenomenon has occurred when the monitoring point's effective stress was equal to zero. According to changes of pore water pressure at different locations and depths, the following liquefaction characteristics in the embankment were obtained:

(1) The occurrence time for the first peak of pore water pressure coincided with the seismic peak acceleration of the input wave. FIG. 2 shown the peak acceleration (0.3 g) of input wave occurred after two seconds. As shown in FIG. 4 and FIG. 5, the first peak of pore water pressure also almost occurred at the same time.

(2) The occurrence time of liquefaction for upper-layer of saturated sand soil was earlier than lower-layer below the bottom of slope, but the duration of liquefaction for lower-layer of saturated sand soil was longer than upper-layer. For example, the liquefaction for upper-layer (at depth of 2.3 m) occurred after two seconds, and the duration was less than five seconds (FIG. 4a). By contrast, the liquefaction for lower-layer (at depth of 11.2 m) occurred after 15 seconds, and the duration was more than ten seconds (FIG. 4b).

(3) The upper-layer of saturated sand soil was almost not liquefiable below the top of slope, but the lower-layer was liquefiable and duration was very long. For example, as shown in FIG. 5a, the upper-layer (at depth of 7.2 m) was hardly liquefiable; however, the duration of liquefaction for lower-layer (at depth of 14.7m) was longer (FIG. 5b).

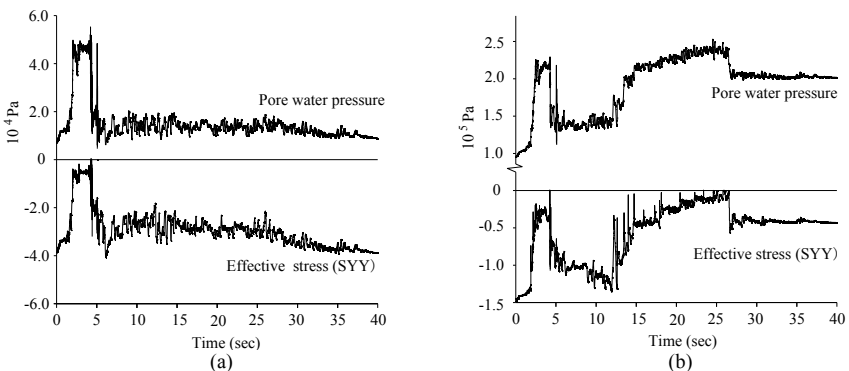


FIG. 4 Time histories of pore water pressure and effective stress under the slope's bottom surface. (a) At depth of 2.3 m; (b) At depth of 11.2 m.

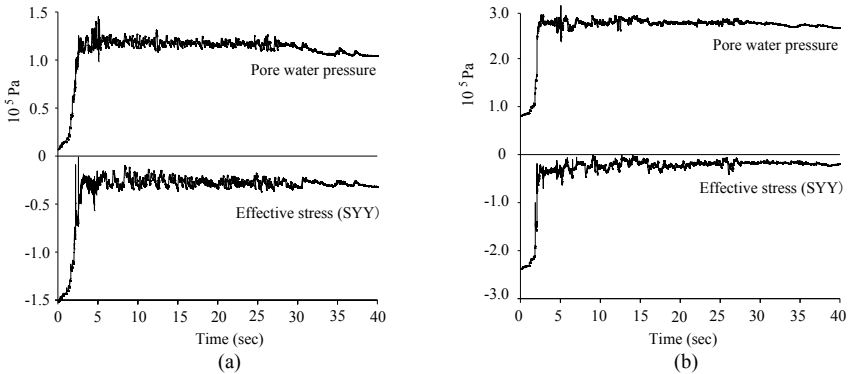


FIG. 5 Time histories of pore water pressure and effective stress under the slope's top surface. (a) At depth of 7.2m; (b) At depth of 14.7m.

4. CONCLUSIONS

Using Finn model for saturated sand soil, a typical fill embankment has been simulated by FLAC. The results shown the occurrence time for the first peak of pore water pressure coincided with the seismic peak acceleration of input wave. The occurrence time of liquefaction in the upper-layer of saturated sand soil was earlier than lower-layer below the bottom of slope while the duration of liquefaction for lower-layer of saturated sand soil was longer than upper-layer. The upper-layer of saturated sand soil was almost not liquefiable below the top of slope, but the lower-layer was liquefiable and duration time was very long. In summary, seismic liquefaction for artificial fill embankment was related to not only the characteristic of input wave, but also the different locations and different depths of saturated sand soil in a slope.

REFERENCES

- Adalier, K., Elgamal, A.W. and Martin, G.R. (1998). "Foundation liquefaction countermeasures for earth embankments." *J. Geotech Geoenviron Eng ASCE*. 123 (6): 500-517.
- Adalier, K. and Sharp, M.K. (2004). "Embankment dam on liquefiable foundation-dynamic behavior and densification remediation." *J. Geotech Geoenviron Eng*. 130 (11): 1214-1224.
- Aydingun, O. and Adalier, K. (2003). "Numerical analysis of seismically induced liquefaction in earth embankment foundations. Part I. Benchmark model." *Can Geotech J*. 40 (4): 753-765.
- Bilge, S. and Haydar, A. (2008). "Nonlinear dynamic finite element simulation of Alibey earth dam." *Environ Geol*. 54: 77-85.
- Byrne, P.A. (1991). "Cyclic shear-volume coupling and pore-pressure model for sand." *Proc. 2th International Conference on Recent Advances in Geotechnical Earthquake Engineering and Soil Dynamics*, Missouri, pp. 47-55.

- Chen, W.H. and Men, F.L. (2002). "Study on FEM to simulate slip and seismic liquefaction of slope-field by theory of two phased dynamics." *Earthquake engineering and engineering vibration*. 22 (1): 132-140. (in Chinese)
- Koga, Y. and Matsuo, O. (1990). "Shaking table tests of embankments resting on liquefiable sandy ground." *Soils Found.* 30 (4): 162-174.
- Koseki, J. Koga, Y. and Takahashi, A. (1994). "Liquefaction of sandy ground and settlement of embankments." *Proc. The International Conference Centrifuge*, Balkema, Rotterdam, pp. 215-220.
- Krinitzsky, E.L. and Hynes, M.E. (2002). "The Bhuj, India, earthquake: lessons learned for earthquake safety of dams on alluvium." *EngGeol.* 66: 163-196.
- Mardin, G.B., Finn, W.D.L. and Seed, H.B. (1975). "Fundamentals of liquefaction under cyclic loading." *J. Geotech, Div ASCE*, 101 (5): 423-438.
- Matsuo, O. (1996). "Damage to river dikes." *Soils Found.* 36 (1): 235-240.
- Park, Y.H., Kim, S.R., Kim, S.H. and Kim, M.M. (2000). "Liquefaction of embankments on sandy soils and the optimum countermeasure against the liquefaction." *Proc. 12th World Conference on Earthquake Engineering*. Auckland, Paper No. 1170.
- Pekau, O.A. and Cui, Y.Z. (2004). "Failure analysis of fractured dams during earthquakes by DEM." *Eng Struct.* 26 (10): 1483-1502.
- Ren, H.M., Lv, X.L. and Li, P.Z. (2007). "Advances in liquefaction research on saturated soils." *Earthquake engineering and engineering vibration*. 27 (6): 166-175. (in Chinese)
- Seed, H.B., and Idriss, I.M. (1971). "Simplified procedure for evaluating soil liquefaction potential." *Journal of Soil Mechanics & Foundations Division, ASCE*, 97 (SM9): 1249-1273.
- Wang, J., Yao, L.K. and Wu, W. (2010). "Research on seismic dynamic mode and dynamic characteristics of road embankment." *Rock and Soil Mechanics*. 31 (12): 3801-3808. (in Chinese)
- Wang, G.L., Liu, H.Y. and Wu, F.Q. (2013). "NCEER method and application of an embankment slope with liquefaction problem in coastal area." *New Frontiers in Engineering Geology and the Environment*. 9: 187-190.
- Huang, Y., Yashima, A., Sawada, K. and Zhang, F. (2008). "Numerical assessment of the seismic response of an earth embankment on liquefiable soils." *Bull Eng Geol Environ.* 67: 31-39.
- Huang, Y., Zheng, H. and Zhuang, Z.J. (2012). "Seismic liquefaction analysis of a reservoir dam foundation in the South-North Water Diversion Project in China. Part II: seismic response simulation." *Nat Hazards*. 60:1313-1324.
- Zhou, Y.G., Chen, Y.M. and Ling, D.S. (2009). "Shear wave velocity-based liquefaction evaluation in the great Wenchuan earthquake: a preliminary case study." *Earthquake Engineering and Engineering Vibration*. 8 (2): 231-239. (in Chinese)

Reference Strain γ_r in Hyperbolic Modeling of Dynamic Shear Modulus of Soils

Zhijia Wang¹, Gang Fan¹, Jianwei Han², Weiming Liao², and Jianjing Zhang³

¹ Ph.D candidate, School of Civil Engineering, Southwest JiaoTong University; P.O. Box 610031, ChengDu; PH 18708186626; FAX (086) 028-87600612; email: 344963551@qq.com; fg113112@126.com;

² Master candidate, School of Civil Engineering, Southwest JiaoTong University; P.O. Box 610031, ChengDu; PH 18382405719; FAX (086) 028-87600612; email: 477925591@qq.com; 464039003@qq.com;

³ Professor, School of Civil Engineering, Southwest JiaoTong University; P.O. Box 610031, ChengDu; PH 13438840756; FAX (086) 028-87600612; email: jianzhang1102@swjtu.edu.cn.

ABSTRACT: Hardin-Drnevich, Stokoe and Davidenkov models all belong to hyperbolic models which are commonly used to describe the relationship between dynamic shear modulus ratio versus shear strain of soils. However, few studies have been performed on the parameters of these models. To understand the meaning of the parameters, the three models were analyzed by using test data from remolded, disturbed and undisturbed soils, and then by using fitting approach, the parameters of the three models were derived. After comparing the fitting parameters with the reference strain γ_r from dynamic triaxial test, it is found that the fitted parameter γ_0 in the Davidenkov model has same meaning with the reference strain γ_r . Furthermore, the factors of impacting the reference strain were performed by changing confining pressure and loading rates and the effects of the reference strain on dynamic shear modulus ratio were discussed. By using the results derived from the study, a range of reference strains for clay, silty clay, silt, muddy clay and sand was recommended.

INTRODUCTION

The maximum dynamic shear modulus G_{max} (at zero strain) and reference strain γ_r are two of key parameters to characterize the behaviour of soil under cyclic loading conditions. The first study on the parameters was performed by Hardin and Drnevich (Hardin and Drnevich 1972). Their study suggested that the shear modulus ratio could be evaluated by the relationship: $G/G_{max} = 1/(1 + \gamma/\gamma_r)$, and stress-strain relationship under cyclic loading conditions can be determined once the values of G_{max} and γ_r were obtained. Currently, the maximum shear modulus can be determined accurately by means of in-situ test, laboratory test and empirical equation. But the study on the reference strain is relatively few. Under the situation, the paper focuses on studying the reference strain γ_r . In the following sections, effects of confining pressures, loading frequency, and dynamic shear modulus ratio on the reference strain

in the Davidenkov model are discussed and a range of the reference strain was recommended.

THE MEANING OF γ_0 IN DAVIDENKOV MODEL

Davidenkov model is a hyperbolic model for $G/G_{max} \sim \gamma$ relationship proposed by Martin and Seed (Martin and Seed 1982). The model is described as :

$$\frac{G}{G_{max}} = 1 - \left[\frac{(\gamma/\gamma_0)^B}{1 + (\gamma/\gamma_0)^B} \right]^A \quad (1)$$

Where: G is dynamic shear modulus, G_{max} is the maximum dynamic shear modulus, γ is strain; A, B, γ_0 are parameters.

Normally, the physical meaning of the parameter γ_0 is equivocal, and is usually regarded as a test parameter (Guoxing Chen 2007) or a fitted parameter that describes soil characteristics (Dingyi Xie 2007). Therefore, it is necessary to explore the relationship between γ_0 and γ_r . Currently, two steps of the work are carried out. The first step is to compute the reference strain by using equation $\gamma_r = \tau_{max} / G_{max}$ and compare it with the fitting parameter γ_0 in the Davidenkov model. The second step is to use the test data to evaluate the reference strain γ_r in the Hardin model and Stokoe model, and by using fitting approach to obtain γ_0 in the Davidenkov model, and then studying the relationship between γ_r and γ_0 are performed.

Comparison between Fitting Parametre γ_0 and Computed γ_r

To explore the meaning of γ_0 in the Davidenkov model, dynamic triaxial test on reconstituted clays has been performed under different confined pressure levels and loading rates. All specimens in the experiment have a diameter of 39.1mm and length of 80mm. The clays are from the Chengdu South Railway Station, and the sands are from Jiulidi Quarry and water, which are used as sample materials.

The fitting parameters A, B, γ_0 in the Davidenkov model are computed by using the test data, and the $G/G_{max} \sim \gamma$ curve can be expressed as Eq.(1), Where A equal 1.02, B equal 0.91, γ_0 equal 0.0007, and the fitting results are shown in Fig.1. In general, dynamic triaxial test is useful for measuring dynamic shear modulus under moderate to relatively high strain, while the result under low strain is estimated by the Davidenkov model.

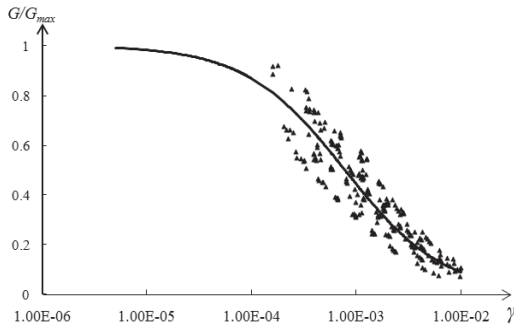


FIG. 1. Variation of shear modulus ratio with shear strain for reconstituted soil

Based on the test data, reference strains are computed by equation $\gamma_r = \tau_{max} / G_{max}$, where τ_{max} is the maximum shear stress, G_{max} is the maximum shear modulus. For reconstituted soils, the reference strains are 0.00067, 0.000677, 0.000681, 0.000709 under confined pressures of 50kpa, 100kpa, 150kpa, 200kpa.

By analyzing the computed values, it can be found that the fitting parameter γ_0 in the Davidenkov model is almost the same as the reference strain that are computed by equation for the same soils. Therefore, the meaning of γ_0 in the Davidenkov model is actually the reference strain γ_r , and it is apparent that the reference strain values computed by equation are quite similar to the value obtained by statistical method.

Comparison between Fitting Parameter γ_0 and Statistical Representative Values γ_r in the Hardin and Stokoe Models

Hardin and Drnevich proposed that a hyperbolic relationship can be used to describe the relationship between shear modulus and shear strain in modeling dynamic soil behavior. The hyperbolic model was expressed as:

$$\frac{G}{G_{max}} = \frac{1}{1 + \gamma / \gamma_r} \quad (2)$$

Where G is shear modulus, G_{max} is the maximum shear modulus, γ is shear strain, and γ_r is a reference strain.

Based on the Hardin and Drnevich work, Stokoe (Stokoe1999) proposed a new relationship and was expressed as

$$\frac{G}{G_{max}} = \frac{1}{1 + (\gamma / \gamma_r)^a} \quad (3)$$

Where γ_r is a reference strain, and a is curvature coefficient.

To explore the relationship between fitting parameter γ_0 in the Davidenkov model and the reference strain γ_r in the Hardin and Stokoe models, numerous test data on dynamic shear modulus from published papers had been collected, and a database was established. Then, γ_0 and γ_r in different empirical models were determined through fitting based on the database. The parameters of the fitting curves for clay and sand are provided in Table 1, and the fitting curves for different models are shown in Fig.2 and Fig.3.

Table 1. Fitting Parameters in Different Models for Clay

| | Davidenkov model | | Hardin model | | Stokoe model | |
|------|------------------|---------|--------------|---------|--------------|---------|
| Clay | γ_0 | 0.00078 | γ_r | 0.00077 | γ_r | 0.0008 |
| | A | 0.97 | - | - | a | 0.83 |
| | B | 0.85 | - | - | - | - |
| Sand | γ_0 | 0.00069 | γ_r | 0.00067 | γ_r | 0.00065 |
| | A | 0.97 | - | - | a | 0.83 |
| | B | 0.85 | - | - | - | - |

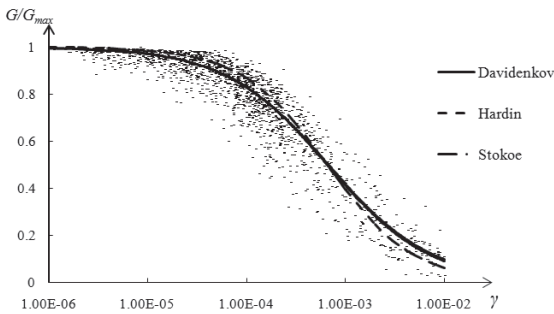


FIG. 2. Fitting Curves of $G/G_{max} \sim \gamma$ for clay with different models

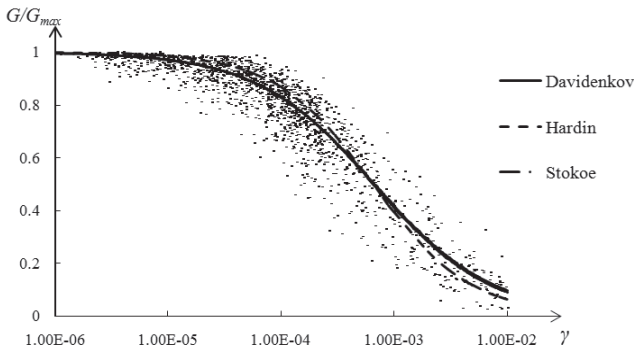


FIG. 3. Fitting Curves of $G/G_{max} \sim \gamma$ for sand with different models

Results for clay in Table 1 and Fig. 2 illustrate that the reference strain in the Hardin and Stokoe models are nearly same as the value of γ_0 in the Davidenkov model, Therefore, it is reasonable to consider γ_0 in the Davidenkov model represents the reference strain for clay.

Results for sand in Table 1 and Fig. 3 show that the reference strain values in the Hardin and Stokoe Models are very close to the reference strain from the Hardin and Stokoe models. Therefore, it is reasonable to consider that γ_0 represents the reference strain γ_r .

In addition, Fig.2 and Fig.3 also illustrate that the fitting curves of the Davidenkov and Stokoe models are almost coincide with each other, while the Stokoe model has few fitting values than the Davidenkov model. The Stokoe model is simple and has higher accuracy for regression. Therefore, it is recommended to use the Stokoe model in dynamic stress-strain study.

RELATIONSHIP BETWEEN SHEAR MODULUS, PRESSURE LEVELS, LOADING FREQUENCY AND REFERENCE STRAIN

Relationship between Shear Modulus and Reference Strain

In the Stokoe model, dynamic shear modulus ratio is strongly influenced by the curvature coefficient and reference strain. The effect of the reference strain on G/G_{max} is illustrated by the result in Fig.4, from which it can be concluded that the higher the reference strain is, the larger the G/G_{max} becomes.

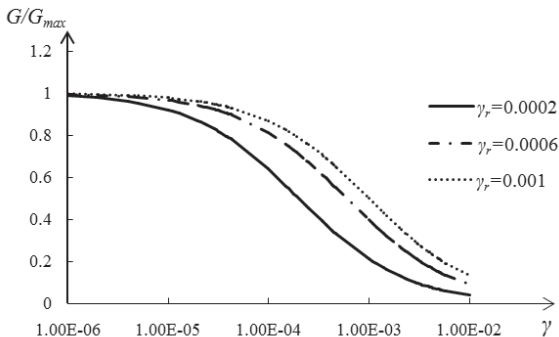


FIG. 4. Effect of reference strain on G/G_{max}

By further analyzing, the result that G/G_{max} can be limited by different reference strain values are also presented in Fig.4, meanwhile, a significant result is obtained that the range of G/G_{max} can be represented by the reference strain values, and a parameter which is used to reflect the range of G/G_{max} is discovered.

Relationship between Pressure Levels, Loading Frequency and Reference Strain

To compare the effect of confined pressure and frequency on γ_r , a systematic investigation on the reconstituted clays at different confined pressure levels and loading frequency has been performed. The reference strain change of the specimen is presented in Fig.5. The change indicates that there is a significant influence for the value of reference strain at these pressure and frequency levels.

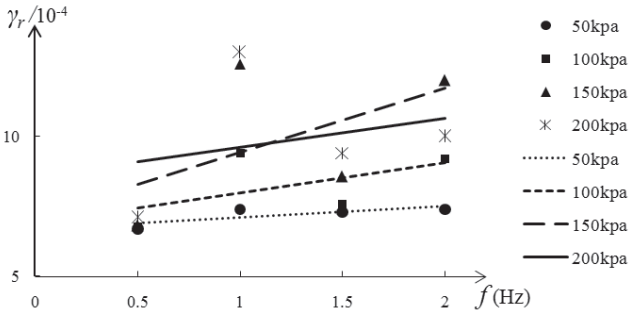


FIG. 5. The relationship between pressure, frequency and reference strain

Reference strain, γ_r , increases with increasing effective confining pressure as shown in Fig.5, and the relationship is approximately linear. The effect of excitation frequency, f , on γ_r is also suggested in this figure. The tendency of γ_r change is increased with increasing loading rates, and the higher the pressure level is, the more obvious loading effects.

RANGE OF REFERENCE STRAIN FOR DIFFERENT TYPE OF SOILS

Based on the database of the dynamic shear modulus and the Stokoe model, the fitting curves of $G/G_{max} \sim \gamma$ for clay, silty clay, silt, muddy clay and sand are obtained. The fitting parameter values of a and γ_r are presented in Table 2.

Table 2. Fitting parameter values of $G/G_{max} \sim \gamma$ for different soils

| | clay | silty clay | silt | muddy clay | sand |
|-----------------------------|--------|------------|--------|------------|---------|
| curvature coefficient a | 0.83 | 0.95 | 0.84 | 0.82 | 0.83 |
| reference strain γ_r | 0.0008 | 0.00065 | 0.0005 | 0.0006 | 0.00065 |

A constant value of 0.92 was suggested for the curvature coefficient a by Darendeli (Darendeli 2001). However, the a values in this paper are approximate to 0.83 for each kind of soils except silty clay ($a=0.95$). All specimens are taken from California, Carolina and Taiwan China in the experiment of Darendeli, while the database of G/G_{max} is almost from China, and the dynamic shear modulus measured at different locations is typically different.

In this study, a constant value of 0.83 (0.95 for silty clay) is suggested for the a value in China, and it is founded that G/G_{max} and γ_r are related by Eq.(3), where $a=0.83$, so that the ranges of G/G_{max} are expressed through the ranges of the reference strain. The range curves of γ_r can be illustrated by the results in Fig. 6(a-e) which are computed using the relationship between G/G_{max} and γ_r , and the γ_r values are presented in Table 3.

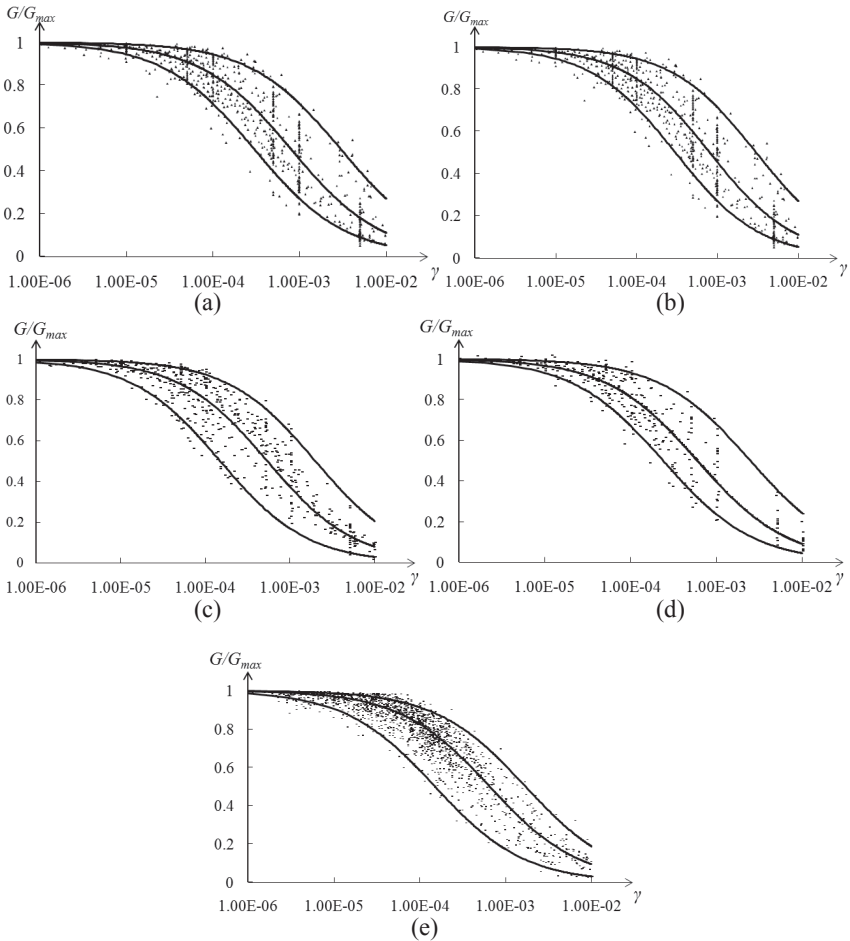


FIG. 6. The range curves of reference strain for different soils: (a) clay; (b) silty clay; (c) silt; (d) muddy clay; (e) sand

Table 3. Range of γ_r for different soils

| parameters in Stokoe model | clay | silty clay | silt | muddy clay | sand |
|----------------------------|--------|------------|---------|------------|---------|
| γ_r | 0.0008 | 0.00065 | 0.00054 | 0.0006 | 0.00065 |
| $\gamma_{r\max}$ | 0.003 | 0.0011 | 0.002 | 0.0025 | 0.0017 |
| $\gamma_{r\min}$ | 0.0003 | 0.00032 | 0.00015 | 0.00024 | 0.00015 |
| a | 0.83 | 0.95 | 0.83 | 0.83 | 0.83 |

CONCLUSIONS

- (1) By comparing the computed values of the reference strain with fitting parameters in different empirical models, the results show that the value of γ_0 in the Davidenkov model is the same as the reference strain, which make the sense of the parametre γ_0 in the Davidenkov model clear. This result would provide a useful guidance for engineering application.
- (2) Based on the comparison between the Davidenkov model and the Stokoe model, the Stokoe model is more simplicity and accuracy.
- (3) The correlation analysis of dynamic shear moduli, confining pressure and frequency shows that the reference strain increases with the increase of dynamic shear moduli, confining pressure and frequency.
- (4) It is proposed to use the reference strain to estimate soil dynamic shear moduli ratio. This paper provides the recommended range values of clay, silty clay, silt, muddy clay and sand.

REFERENCES

- Darendeli, B.M.(2001) . Development of a New Family of Normalized Modulus Reduction and Material Damping Curves. *Ph.D. dissertation*, University of Texas at Austin, Austin.
- Xie, DY. (2007). *Soil dynamics*. Beijing, China.
- Chen, GX. (2007). *Geotechnical earthquake engineering*. Beijing, China.
- Hardin, B.O. and Drnevich, V.P. (1972). "Shear modulus and damping of soils: measurement and parameter effects." *Journal of Soil Mechanics and Foundation Division*, 98 (SM6): 603-624.
- Martin, P.P. and Seed, H.B. (1982). "One-dimensional dynamic ground response analyses." *Journal of the geotechnical engineering division*, 108(7): 935-952.
- Stokoe, K.H. Darendeli, M.B. Andrus, R.D. and Brown, L.T. (1999). "Dynamic soil properties: Laboratory, field and correlation studies." *Proc.2nd Intl. conference on Earthquake Geotechnical Engrg*, Rotter-dam, Netherlands.

Physical and Analytical Modeling of Tire Mat Reinforced Vegetated Slope

Cheng Zhou¹, Jiao Liu², Yao-Wen Xing³, Hong-Liang Zhu⁴, Zhi-Gang Rao⁵

¹Professor, College of Hydraulic and Hydroelectric Eng. and Key Laboratory of Hydraulic and Mountain River Engineering, Sichuan Univ., Chengdu, 610065.China; czhou@scu.edu.cn

²Master Student, College of Hydraulic and Hydroelectric Eng. and Key Laboratory of Hydraulic and Mountain River Engineering, Sichuan Univ., Chengdu, 610065.China; 289295053@qq.com

³Engineer, Design and Investigation Institute of Nanning city, Guangxi Zhujiang Water Resource Commission, Nanning, 530007.China; 915519030@qq.com

⁴Director, Changzhou Waterway Administrative Bureau of Jiangsu Province, Changzhou, 213004.China; 915519030@qq.com

⁵Co-director, Changzhou Waterway Administrative Bureau of Jiangsu Province, Changzhou, 213004.China; 915519030@qq.com

ABSTRACT: Waste tire mat like geo-cells can be used as containers filled with soil and planted with vetiver grass. Waste tire and vetiver grass root reinforced soil are uniaxial and triaxial compressed to study the strength and deformation behavior. Test results indicate that tires and vetiver grass root can increase shear strength and improve ductility of soils. An in situ demonstration test is also conducted by waste tire mat filled with soil and vetiver grass in bioengineering stabilization of a fully weathered mud rock slope. Nonlinear viscosity of the slope soil is taken account into Bingham model that indicates the composite slope soil is fully or partially saturated. The concept of shear layer can be easily emerged by the formula without any assumption; as a result the progressive deformation of the waste tire mat and vetiver grass root reinforced slope soil is described.

INTRODUCTION

Waste tires are produced at increasing rates every year, particularly in metropolitan areas. They require a large amount of space for storage. The potential fire hazard and consequent environmental damage can also be posed. Consequently, there is an urgency to develop new, energy-efficient, beneficial ways to reuse large volumes of waste tires. A tire has very high tensile strength, flexibility, resiliency, and high frictional compaction resistance. If tires are tied together to make a mat, filled with soil, they can be used as a reinforced flexible cover for slope and can provide a practical alternative for the use of this waste. This conventional construction technique is similar to that employed in the use of geo-cells for slope soil reinforcement which is well accepted in engineering practice. In addition, laboratory tests and field monitoring with waste tires above the water table indicates that insignificant adverse effects on groundwater quality had occurred over a period of 2 years (Williams et al,

1990; O'Shaughnessy and Garga, 2000; Garga and O'Shaughnessy, 2000).

Large displacements of waste tires to fully mobilize the ultimate pull-out capacity can be compatible with flexible deformation and high strength behavior of vetiver grass roots. Vetiver introduced by the World Bank in the 1980's, has evolved strongly in recent decades to become an important soil bioengineering tool (Xu, 2003). Engineers conventionally rely on the use of 'hard' or 'inert' material such as mortared riprap and shot-concrete to prevent water infiltration (Shields, 1991; Shields and Gray, 1993; Zhou, 2008). People resort to vegetation to help strengthen 1.5 m deep slope soil that is prone to slippage (Gray and Sotir 1992, 1996; Greenway et al, 1984; Roering et al, 2003; Pollen, 2007). Models based on physiology and ecology had been developed to approximate the contribution of tree roots to slope stability (Abe, 1990; Abe and Ziemer 1991; Wu et al, 1988; Wu and Beal 1988; Wu and Watson, 1998; Watson and Dakessian, 1981; Watson and O'loughlin, 1985; Mickovskiet al., 2011).

Gravitational creep flow of slope soil is often encountered in natural slope (Angeli, et al, 1996). Based on field observation, Desai et al (1995) developed an elastic viscoplastic model and assumed a more reasonable variety of velocities that a shear zone exists up to a certain depth. Cristescu et al (2002) introduced a power function in description of slow movement of soil slope so that there is a shear layer in the movement profile of the slope.

In this paper, Waste tire and vetiver grass root reinforced soil are uniaxial and triaxial compressed to study the strength and deformation behavior. An in situ demonstration test is also conducted by waste tire mat filled with soil and vetiver grass in bioengineering stabilization of a fully weathered mud rock slope. Based on Bingham model with a nonlinear viscosity of the slope soil, the progressive deformation of the waste tire mat and vetiver grass root reinforced slope soil is described.

TEST ON WASTE TIRE CONFINED SOIL COLUMNS

Uniaxial compression (UC, tires with 42cm outer diameter) and triaxial compression (TC, sample with 30cm diameter and 60cm height) tests are performed on the waste tire reinforced clay and gravel columns to study the strength and deformation of tire stabilized slope soil. The physical properties of tire confined soils are listed in Tables. 1 and 2. For the gravel the non-uniform coefficient C_u is 50, and the coefficient of curvature C_c of gravel is 2.8. Three layers of tires with 10cm vertical space under 0.3MPa, 0.5MPa, 0.8MPa, and 1MPa cell pressure are adopted in TC tests.

Table 1. Properties of Waste Tire Reinforced Soil Column in UC Test

| Samples | | Density (g/cm ³) | Water Content (%) | Column area (cm ²) | Column height (cm) |
|---------|----|---------------------------------|----------------------|-----------------------------------|-----------------------|
| Clay | C1 | 2.01 | 10.94 | 1452.2 | 63.50 |
| | C2 | 2.61 | 8.04 | 1452.2 | 63.00 |
| | C3 | 2.27 | 10.29 | 1452.2 | 60.00 |
| Gravel | G1 | 2.35 | — | 1452.2 | 58.00 |
| | G2 | 2.35 | — | 1452.2 | 58.80 |

Table 2. Particle Size and Amount of Gravel in TC Test

| Particle Size(mm) | 40 | 20 | 10 | 5 | 2 | 1 | 0.5 | 0.1 | 0.05 |
|-------------------|-----|------|------|------|------|------|------|-----|------|
| Accumulation(%) | 100 | 75.3 | 55.5 | 40.5 | 28.3 | 19.9 | 15.8 | 7.6 | 2.5 |

The uniaxial compression stress-strain curve of tire confined clay and gravel columns are shown in Figs. 1 (a) and (b).

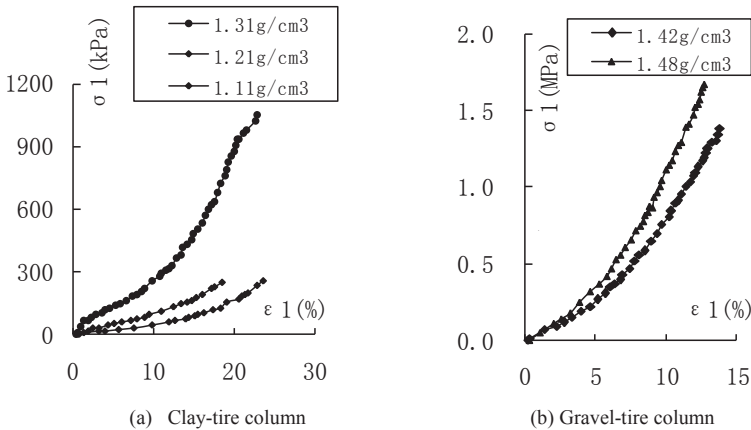


FIG.1 Axial stress-strain curve of tire confined clay and gravel in UC test

The large triaxial compression (TC) stress-strain curve of the waste tire confined gravel columns are shown in Figs. 2 (a) and (b).

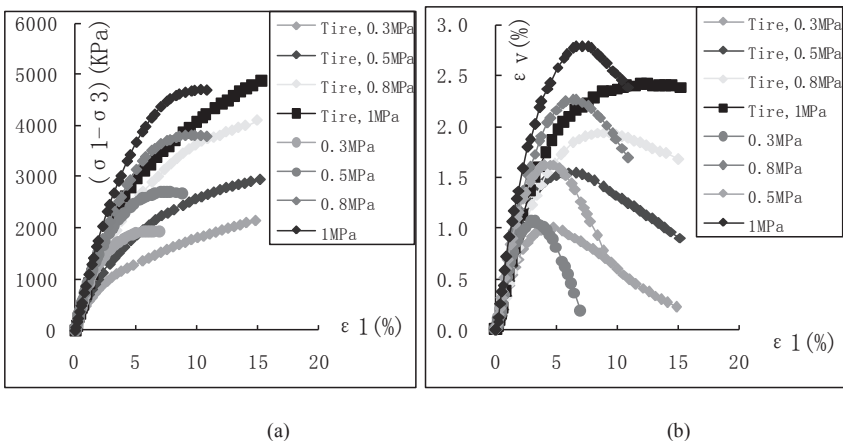


FIG.2 (a) Deviator stress vs. axial strain, (b) volumetric strain vs. axial strain of gravel column with and without tire confinement in TC test

It can be seen from Figs. 1 and 2 that tires confinement result in larger failure strain and higher strength of soil, i.e., the friction angle is 41° and apparent cohesion increase from 170kPa (gravel) to 220kPa (gravel-tire mat). This reinforcement effect is more obvious when cell pressure is lower. Dilation and ductility is also obvious with tire confinement. Considering the reinforcement of tire mat to slope soil, an in situ demonstration test is conducted by waste tire mat filled with soil and vetiver grass in bioengineering stabilization of a fully weathered mud rock slope, as shown in Fig.3.

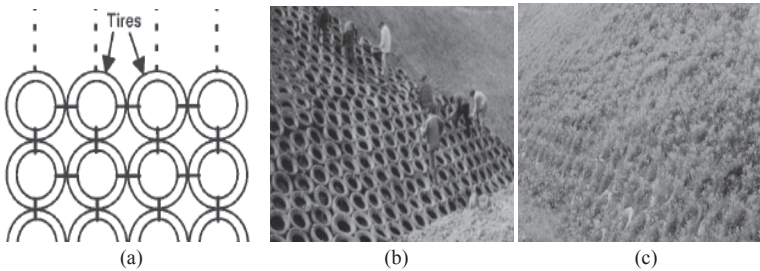


FIG. 3 Tire mat vegetated with vetiver grass in bioengineering stabilization of a fully weathered mud rock slope

TEST ON VETIVER GRASS ROOT REINFORCED SOIL

Considering root as fiber and by means of fiber- soil test method, 1mm thin and 1 to 2 cm long vetiver grass roots are mixed with soil. Uniaxial compression (UC) and triaxial compression (TC) tests are performed on these composite soils to study the effect of root on stabilization of slope soil. In laboratory tests, weight ratio between vetiver grass live fibre root and soil was desired as 1.5%. Root fiber length is 1 and 2 cm. Physical properties of the clay are: $w_l = 30.8\%$, $w_p = 19.2\%$, $I_p = 11.6\%$, $G_s = 2.72$, $w_{op} = 16.0\%$, $\gamma_{d,max} = 1.8\text{g/cm}^3$. The uniaxial compression (UC) and triaxial compression (TC) stress-strain curves of root reinforced clay are shown in Figs. 4 (a) and (b), where in TC test only the result under cell pressure 200kPa is shown.

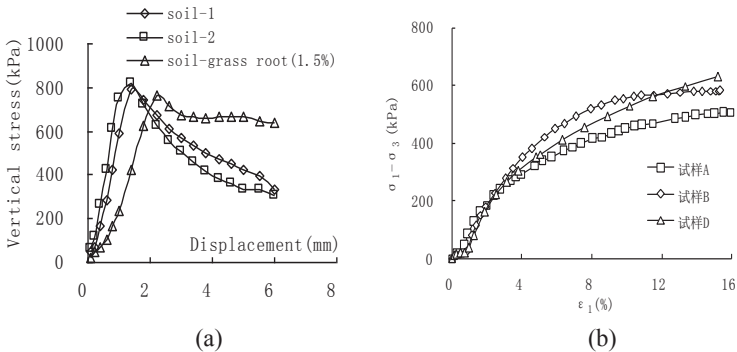


FIG.4. UC (a) and TC (b) stress-strain (deformation) curves of root reinforce soil

It can be seen from the UC test result (Fig.4a) that the peak strengths are similar between soil samples with and without root. Vetiver roots can improve the ductility and shear resistance of soil. The TC test results indicate that, root increases the cohesion of soil obviously, and the higher the amount of fibre root, the larger the increases of strength, as shown in Fig.4b and Table 3. Vetiver grass root helps to maintain progressive deformation of slope soil rather than brittle failure.

Table 3. Shear Strength of Vetiver Grass Root Reinforced Soil

| Sample | A (0%) | B(1.5%, 1cm) | C (1.5%, 2cm) |
|-----------------------|--------|--------------|---------------|
| c (kPa) | 26.2 | 39.0 | 44.0 |
| ϕ ($^{\circ}$) | 31.0 | 32.0 | 32.1 |

ANALYTICAL SOLUTION TO THE PROGRESSIVE DEFORMATION OF VEGETATED SLOPE

In Bingham model the viscous resistance which is directly proportional to the gradient of velocity v . It can be expressed by $\eta \frac{\partial v}{\partial z}$, where η is the viscosity coefficient of soil, and z is the depth of slope soil. Thus for the moveable soil with a total thickness of h , the overall resistance τ_f is $c' + \sigma' \tan \phi' + \eta \frac{\partial v}{\partial z} + \Delta S$, where ΔS is the shear strength of root. Along the depth of slope, the difference of driving and resistance forces can be shown as $\tau - \left(c' + \sigma' \tan \phi' + \eta \frac{\partial v}{\partial z} + \Delta S \right)$, where $\tau = \gamma(h-z) \sin \beta$ is the driving stress. For a certain laminate of soil along the slope, there is $\frac{\partial}{\partial z} \left[\tau - \left(c' + \sigma' \tan \phi' + \eta \frac{\partial v}{\partial z} + \Delta S \right) \right]$. By analyzing the stress of the laminate based on the Newton's second law of motion, we can formulize the problem about the motion of the vegetated slope soil as the following basic equation:

$$\frac{\partial}{\partial z} \left[\tau - \left(c' + \sigma' \tan \phi' + \eta \frac{\partial v}{\partial z} + \Delta S \right) \right] = -\rho \frac{\partial v}{\partial t} \quad (1)$$

where β is the slope angle, t represent time and ρ is the density of soil. Root strength along slope depth is $\Delta S = T_r (\sin \beta + \cos \beta \tan \phi') \times kz^2$, in which k is a parameter and T_r is the tensile strength of the root.

The boundary and initial conditions are described as: (a) $t=0, v=0$; (b) $z=0, v=0$; (c) $z=h, \frac{\partial v}{\partial z} = 0$ (that means a rigid mobility of the surface slope soil with the beneath shear layer). Equation (1) can be rewritten as (2):

$$\rho \frac{\partial v}{\partial t} = \frac{\partial}{\partial z} \left(\eta \frac{\partial v}{\partial z} + T_r (\sin \beta + \cos \beta \tan \phi') \times kz^2 \right) + C \quad (2)$$

where $C = \gamma(\sin \beta - \cos \beta \tan \phi) - \gamma_w \cos \beta \tan \phi$, ($t \geq 0, 0 \leq z \leq h$).

Assuming that $\eta = \eta_0 z^b$, where the exponent b is used to describe the influence of pore water pressure along slope depth, i.e., the composite slope soil is fully or partially saturated. Further with integral of time, the displacement of vegetated slope soil can be calculated as following equation (3):

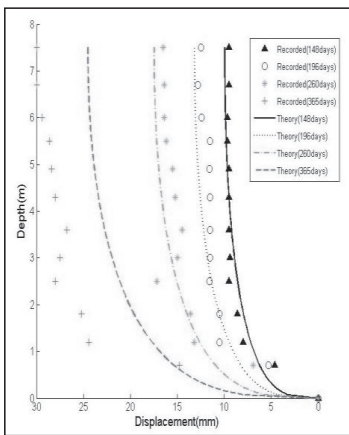
$$u(z, t) = \frac{32Ch^{\frac{3-b}{2}}}{\eta_0} \sum_{m=1}^{\infty} B_m z^{\frac{1-b}{2}} J_{1-b}(\mu_m \sqrt{z/h}) \{t + 4\rho h[\exp(-\frac{\eta_0 \mu_m^2}{4\rho h} t) - 1]/(\eta_0 \mu_m^2)\} \quad (3)$$

where the zero points μ_m can be automatically calculated by Bessel equation such as $J_{-b}(x) = 0$.

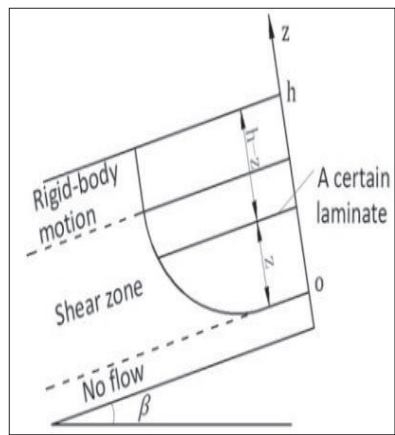
In the vegetated slope in Fig. 3, it is assumed that the top slope soil layer in rigid motion is about 6m and shear zone is about 1.5m. The adopted model parameters are listed in Table 4. The calculated and measured progressive displacement is shown in Fig.5.

Table 4. Analytical Model Parameters

| Tr(kN/m) | η_0 (Pa·s) | b | k | ϕ (°) |
|----------|-------------------|-----|----------------------|------------|
| 10 | 1.1×10^7 | 0.7 | 5.0×10^{-3} | 31 |



(a)



(b)

FIG. 5 (a) The calculated and measured progressive displacement profile after a period of: $t = 148$ days, 196 days, 260 days, and 365 days, (b) Schematic of soil mobility along slope depth corresponding to (a).

CONCLUSIONS

The effect of waste tire-mat and vetiver grass roots was characterized on progressive deformation of slope soil via laboratory and analytical study. The reinforcement available from the tire-mat and vetiver grass roots was identified. Studies demonstrated how results from experimental tests and analytical modeling may be used to estimate the potential reinforcement effects available from the tire-mat and vetiver grass roots within the slope soil. Some conclusions can be drawn from the preliminary test and analysis:

(1) Soil could be reinforced by tire-mat and vetiver grass root confinement. The reinforcement effect could be described by means of increases of apparent cohesion or shear strength.

(2) Tire mat and vetiver grass root can also improve ductility of soils via confinement. Therefore tire-mat and vetiver grass roots can help change the deformation and failure mode of slope soils from a catastrophic failure case to progressive failure case.

(3) The analytical solution developed from Bingham model can simulate the shear layer and describe the slow progressive deformation of the waste tire mat and vetiver grass root reinforced slope soil.

ACKNOWLEDGMENTS

The authors appreciate the support of the Public Non-profit Welfare Project from China Ministry of Water Resources (No. 1261330210053) and Research Fund from Jiangsu Province Waterway Communication and Transportation Bureau (No. 2011Z01-1). The writers would also like to acknowledge the reviewers' comment on this paper.

REFERENCES

- Abe, K. (1990). "Simulation model for the distribution of tree roots: application to a slope stability". *Journal of Japanese Forestry Society*, 72: 375-387.
- Abe, K. and Ziemer, R. R. (1991). "Effect of tree roots on a shear zone: modeling reinforced shear stress". *Canadian Journal of Forest Resources*, 21: 1012-1019.
- Angeli, M.G., Gasparetto, P., Menotti, R.M., Pasuto, A., Silvano, S., (1996). "A viscoplastic model for slope analysis applied to a mudslide in Cortina d'Ampezzo, Italy". *Q. J. Eng. Geol.* 29,233-240.
- Cristescu, N.D., Cazacu, O., Cristescu, C., (2002). "A model for slow motion of natural slopes". *Canadian Geotechnical Journal*.39: 924-937.
- Desai, C.S., Samtani, N.C., and Vulliet, L. (1995). "Constitutive modeling and analysis of creeping slopes". *Journal of Geotechnical Engineering*, ASCE, 121: 43-56.
- Garga, V.K., and O'Shaughnessy, V. (2000). "Tire-reinforced earthfill. Part 1:

- Construction of a test fill, performance, and retaining wall design". *Canadian Geotechnical Journal*, 37: 75–96.
- Gray, D.H. and Sotir, R. (1992). "Biotechnical stabilization of a highway cut". *Journal of Geotechnical Engineering*, ASCE, 118(GT10): 335-353.
- Gray D. H. and Sotir R. B., (1996), "Biotechnical and soil bioengineering slope stabilization: a practical guide for erosion control", John Wiley & Sons, Inc.
- Greenway, D. R. Anderson, M. G. and Brian-Boys, K. C. (1984). "Influence of vegetation on slope stability in Hong Kong". In: *Proceedings of the 4th International Symposium on Landslides*, Toronto, Vol.1, pp. 399-404.
- Pollen N, (2007). "Temporal and spatial variability in root reinforcement of streambanks: accounting for soil shear strength and moisture". *Catena* 69:197–205
- Roering J. J, Schmidt K. M., Stock J D., Dietrich W. E., and Montgomery D. R. (2003). "Shallow landsliding, root reinforcement, and the spatial distribution of trees in the Oregon Coast Range", *Canadian Geotechnical Journal*, 40: 237–253.
- Shields, F. D. (1991). "Woody vegetation and riprap stability along the Sacramento River mile 84 to 119". *Water Resources Bulletin*, 27(3): 527-536.
- Shields, F. D. and Gray, D. H. (1993). "Effects of woody vegetation on the structural integrity of sandy levees". *Water Resources Bulletin*, 28(5): 917-931.
- Slobodan B. Mickovski, Alexia Stokes, Rens van Beek, Murielle Ghestem, Thierry Fourcaud, (2011). "Simulation of direct shear tests on rooted and non-rooted soil using finite element analysis". *Ecological Engineering*, 37: 1523-1532.
- Watson, L. J. and Dakessian, S. (1981). "Soil reinforcement by roots: calculation of increased soil shear resistance from root properties". *Soil Science*, 132(6): 427-435.
- Watson, A.J. and O'loughlin C.L. (1985). "Morphology, strength and biomass of Manuka roots and their influence on slope stability". *New Zealand Journal of Forestry Science*, 15(3):337-348.
- Wu, T.H., Macomber R.M., Erb R.T., and Beal P.E. (1988). "Study of soil-root interaction". *Journal of Geotechnical Engineering* (ASCE) 114(12):1351- 1375.
- Wu, T.H., and Beal P.E (1988). "In-situ shear test of soil-root systems". *Journal of Geotechnical Engineering* (ASCE) 114(12):1376-1394.
- Wu T H. and Watson A. (1998). "In situ shear tests of soil blocks with roots", *Canadian Geotechnical Journal*, 35: 579–590.
- Xu L.Y., (2003). "Research and application of vetiver system in China". The International Asia Pacific Publishing Co., Ltd. (In Chinese).
- Zhou C. (2008). "Calculation Method for vegetated slope". Beijing: China Water Power Press. (In Chinese)
- O'Shaughnessy, V., and Garga, V.K. (2000a). "Tire-reinforced earthfill. Part 2: Pull-out behaviour and reinforced slope design". *Canadian Geotechnical Journal*, 37: 97–116.
- O'Shaughnessy, V., and Garga, V.K. (2000b). "Tire-reinforced earthfill. Part 3: Environmental assessment". *Canadian Geotechnical Journal*, 37: 117–131.
- Williams, P.T., Besler, S., and Taylor, D.T. (1990). "The pyrolysis of scrap automotive tyres: the influence of temperature and heating rate on product composition". *Fuel*, 69: 1474–1482.

Experimental Study on Compression Modulus of Sandy Soil

YANG Qi¹, LENG Wu-ming², ZHANG Sheng³, NIE Ru-song⁴

¹Lecturer, School of Civil Engineering and Mobile Post-doctoral Stations of Traffic and Transportation Engineering, Central South University, Changsha P.R. China 410075, E-mail: qiyang433@163.com

²Professor, School of Civil Engineering, Central South University, Changsha P.R. China 410075, E-mail: lwm123456@126.com

³Associate Professor, School of Civil Engineering, Central South University, Changsha P.R. China 410075, E-mail: 446434884@qq.com

⁴Lecturer, School of Civil Engineering, Central South University, Changsha P.R. China 410075, E-mail: 316798150@qq.com

ABSTRACT: The compression modulus is a key parameter for evaluating compression behavior of soil layer and for predicting foundation settlement. High-pressure confined compression test and the standard penetration test were performed to investigate the compression characteristics of sandy soil layers beneath pile toe, and to obtain the relationship of compression modulus with depth and overburden pressure. The experimental results indicated that the compression modulus of sandy soil increased with pressure, but its increasing rate gradually reduced. The compression modulus almost linearly increased with embedded depth. The ratio of compression modulus under the pressure ranging from 100kPa to 200kPa to that under the pressure in the range of overburden pressure to the additional stress plus overburden pressure ($E_s/E_{s_{0.1-0.2}}$) ranged from 2.1 to 4.2. The empirical formula of the $E_s/E_{s_{0.1-0.2}}$ ratio with overburden pressure was established to give a reference to predict compression modulus of sandy soil under actual pressure, as its overburden pressure was known. At last, the basic principles of how to determinate the value of compression modulus were proposed for design of pile foundation.

INTRODUCTION

The compression modulus, a key parameter for evaluating the compression behavior of soil layer and for predicting the foundation settlement, was defined as the ratio of vertical additional stress increment to corresponding strain increment under confined condition. The prediction precision of the foundation settlement depended on the reliability of the value of compression modulus from the lab or field test (Leng 2011). With the large-scale construction of high-rise buildings and the long-span bridges, the long pile are widely adopted for increasing high capacity and for reducing settlement. Especially in the deep soft soil ground in coastal area,

the pile has extended to a length of 100m and more. For example, the pile of the Huangdu mansion has a length of 98m. The pile length of the sixth QianTang River bridge is 114m and the No.30~32 pier pile foundations of the WEN Zao-ban great bridge of the Beijing-Shanghai high speed railway have the lengths of 71m ,73m and 73m respectively (Yang 2011).The high speed railway has stricter limitation for settlement than the ordinary railway, and so more accurate soil parameter from the lab or field test are required (Danno 2009, TB 10621-2009,Xue 2011). The geologic reports only provide the value of compression modulus under the pressure ranging from 100kPa to 200kPa ($E_{s_{0.1-0.2}}$), while the stress in the soil layer beneath the long pile is frequently greater than 800kPa ,which greatly exceeds the pressure conducted in the common compression test. At the same time, the value of compression modulus from the consolidation test also tends to be low due to stress release of soil samples and other factors. Therefore, it is significant in engineering application to perform research on test method and on how to determinate compression modulus.

Many test investigations on compression modulus of soil can be found in published literatures. Determination of the compression modulus of soils from compression-test data for calculation of pile-foundation settlements was studied (Bakholdin 1999). The consolidation tests on collapsible loess, remolded soil and undisturbed soil were conducted to study the changing law of the compression modulus with overburden pressure (Ma 2006). A theoretical method was presented to determinate compression modulus based on the e-p curve from the confined compression test (Deng 1996). The calculating method of compression modulus was proposed based on the e-p curve and e-log(p) curve, when the vertical stress on the soil was known(Liu 2004,Mei 2003). The accuracy of predicting foundation settlement was improved through the advanced method of determination of the compression modulus(Fu 2012).The evolution law and mechanism of compression modulus of normally consolidated and overconsolidated soil with pressure and time were studied(Zhou 2010). A new estimation formula between compression modulus of soil with the deep was presented (Aziz 2012).

How to determine the empirical value of the compression modulus from in-situ tests is always an important research. A empirical formula was derived to calculate the value of compression modulus from the static cone penetration test and the in-situ standard penetration test (Huang 1997, Li 2001, Chen 2003, Ji 2011).The regression analysis method was adopted to study the relationship between compression modulus and other physico-mechanical parameters, and the regression equations were established to predict the compression modulus value(Yang 1997).

From the above-mentioned literatures, it can be found that little attention was paid to the compression behavior of sandy soil. In this paper, high-pressure confined compression test and the standard penetration test were performed to investigate the compression characteristics of sandy soil layer beneath long pile and the relationship of compression modulus with depth and overburden pressure. The mathematical statistics method was adopted to establish the empirical formula between $E_{s_{0.1-0.2}}$ and E_s . The basic principles of how to determinate the value of compression modulus were presented for the design of pile foundation.

TEST METHOD

The field of exploring the soil samples was located in the No.31~32 pier pile foundation of the WEN Zao-ban great bridge of the Beijing-Shanghai high speed railway. As shown in Fig 1, the length of the piles of was 73m. The soil layer beneath the pile toe was silty sand containing clay with thickness of 4m, and its underlying stratum was silty sand containing medium and coarse sand. Fourteen soil samples were obtained from the depths of 2m, 3m, 5m, 11m, 17 m, 23 m and 29m below pile toe. The results of 9(1) silty sand containing clay and 9(2) silty sand containing medium and coarse sand from the sieve analysis tests are listed in Table.1 and shown in Fig.2~3 separately. The physico-mechanical properties of them are listed in Table.2. The consolidation test was conducted in confined compression test apparatus, where the dimensions of the cylindrical sample were height of 2cm and base area of 30cm². The load was applied suddenly in the load stages of 25kPa, 50kPa, 100kPa, 200kPa, 400kPa, 800kPa, 1600kPa, 2400kPa and 3200kPa, respectively. At each stage, it was considered to reach the final and stable deformation when the rate of deformation was no greater than 0.005mm/d, and then the next-step loading was applied. The elapsed time for each loading was 24 hours, the environmental temperature was held constant to 23°C±3°C during tests.

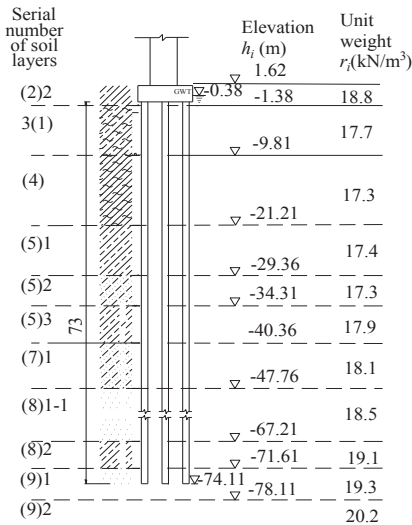


Fig.1 The layout of soil profile

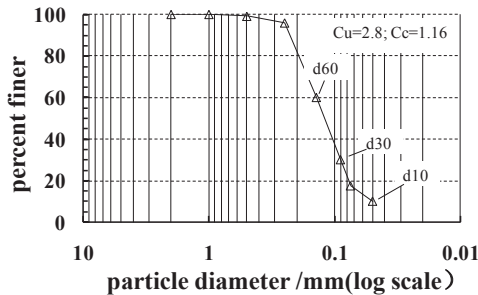


FIG.2 Grain size distribution of 9(1) sandy soil layer

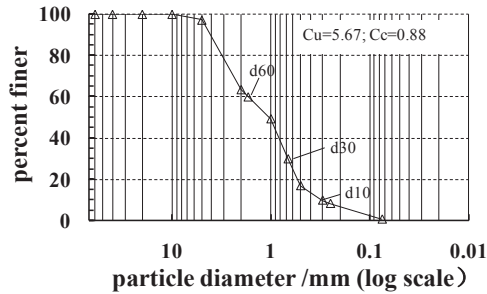


FIG.3 Grain size distribution of 9(2) sandy soil layer

Table.1 Grain size distribution

| Serial number of soil layer | Grain group(mm) | | | | | | | |
|-----------------------------|-----------------|-------|-------|-------|----------|------------|--------|-------------|
| | 10-5 | 5-2 | 2-1 | 1-0.5 | 0.5-0.25 | 0.25-0.075 | <0.075 | 0.075-0.005 |
| 9(1) | 0.00 | 0.00 | 0.00 | 0.00 | 3.20 | 78.50 | 17.40 | 0.00 |
| 9(2) | 2.80 | 33.70 | 14.10 | 32.30 | 8.60 | 7.60 | 0.80 | 0.00 |

Table.2 Physico-mechanical properties of sandy soil

| Serial number of soil layer | Unit weight r (kN/m^3) | Gravity of soil solids G_s | Void ratio e | Water content w (%) | Cohesion c (kPa) | Friction angle ϕ ($^\circ$) |
|-----------------------------|-------------------------------------|------------------------------|----------------|-----------------------|--------------------|------------------------------------|
| 9(1) | 19.3 | 2.68 | 0.49 | 19.87 | 10 | 35.7 |
| 9(2) | 20.2 | 2.64 | 0.52 | 18.36 | 0 | 41.1 |

THE EMPIRICAL RELATIONSHIP BETWEEN $E_{S0.1-0.2}$ AND E_s

In order to establish the empirical relationship between $E_{S0.1-0.2}$ and E_s of sandy soil located the depth of 0m ~ 30m below the pile toe, the sandy soil samples were explored in the depths of 2m,3m,5m,11m, 17m, 23m and 29m below the pile toe, and tests were conducted in high-pressure confined compression test apparatus. The relationship between the ratio of $E_s/E_{S0.1-0.2}$ and the depth of soil sample was shown in Fig.4.

As observed from Fig.4, the relationship between the ratio of $E_s/E_{S0.1-0.2}$ and depth of soil sample below the pile toe was not apparent, but the ratio of E_s to $E_{S0.1-0.2}$ ranged from 2.1 to 4.2 by the statistical analysis, so the empirical formula between $E_{S0.1-0.2}$ and E_s could be expressed as follows

$$E_s = (2.1 \sim 4.2) \times E_{S0.1-0.2} \tag{1}$$

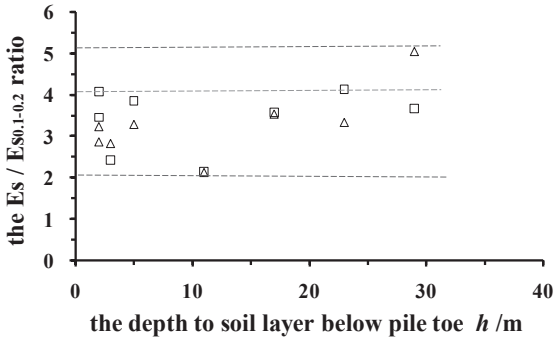


FIG.4 The relationship between the $E_s / E_{s0.1-0.2}$ ratio and its depth

THE RELATIONSHIP OF E_s WITH DEPTH BELOW THE GROUND SURFACE AND OVERBURDEN PRESSURE

For the 9(2) silty sand containing medium and coarse sand, the relationship of the compression modulus E_s with depth below the ground surface and its fitting curve were presented in Fig.5

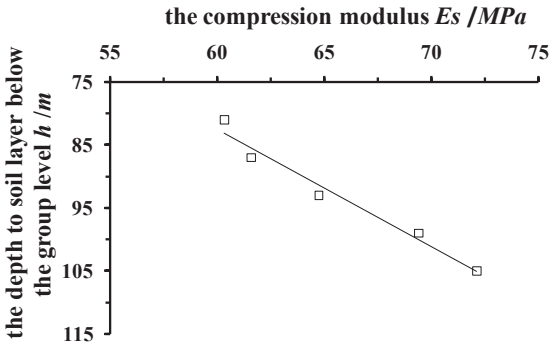


FIG.5 The curve for compression modulus of 9(2) sandy soil with its depth

It was indicated that the variable of E_s and depth had satisfactory linear relationship from the Fig.5, the fitting formula could be written as

$$E_s = 0.523h + 16.98 \quad (2)$$

where h is the depth to the sample below the ground surface

The Fig.5 illustrated that the compression modulus almost linearly increased with the depth. The main reason for this result was that the deeper the sand soil was, the

denser the sand soil was because of the greater overlying stress. The similar formula was established by Burland . (Burland 1986, Tomlinson 2004)

The expression of calculating overburden pressure is $\sigma_z = \sum_{i=1}^n (h_{i+1} - h_i) \gamma_i$, where h_i is the elevation of the upper surface of the i th soil layer; γ_i is the unit weight of the i th soil layer in the Fig 1. It is noted that the unit weight of each soil layer is replaced by its the effective unit weight, when it is below GWT(the groundwater table). The relationship between the $E_s/E_{s0.1-0.2}$ ratio and overburden pressure could be described in Fig.6 by the statistical analysis.

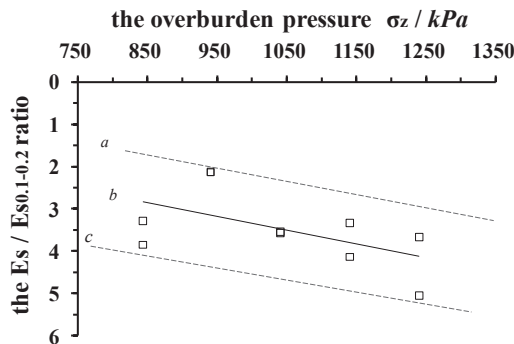


FIG.6 The relationship between the $E_s/E_{s0.1-0.2}$ ratio and overburden pressure for 9(2) sandy soil layer

It was indicated that the $E_s/E_{s0.1-0.2}$ ratio increased with the overburden pressure σ_z , and the relationship formula was expressed as

$$E_s = (0.0032\sigma_z + 0.119)E_{s0.1-0.2} \tag{3}$$

The compression modulus under the actual stress could be approximatively determined from the Eq.(3) when $E_{s0.1-0.2}$ was known. It could arrive at the conclusion that the greater error would occur if E_s was replaced by $E_{s0.1-0.2}$, when the settlement of pile foundation should be calculated during design of pile foundation.

THE EVOLUTION LAW OF COMPRESSION MODULUS WITH PRESSURE

According to the value of the compression modulus under different test pressures, the curves for the compression modulus with pressure of soil samples from different depth of 9(1) and 9(2) sandy soil layer (E_s -P) were shown in Fig.7~8.

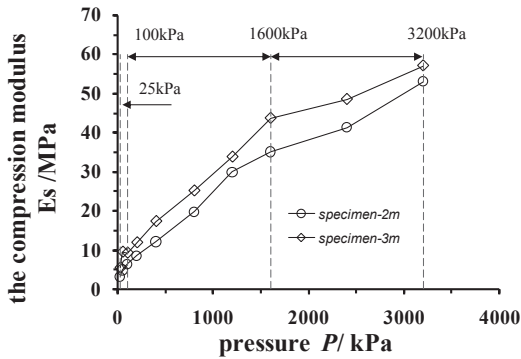


FIG.7 The curves for the compression modulus with pressure of 9(1) sandy soil layer

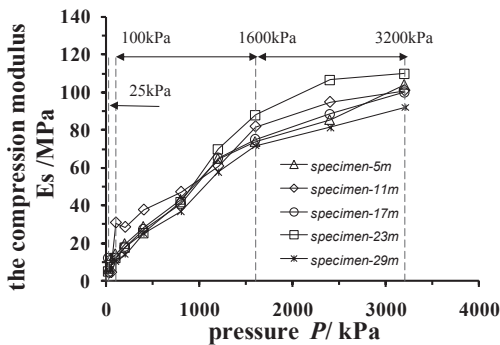


FIG.8 The curves for the compression modulus with pressure of 9(2) sandy soil layer

From Fig.7 and 8, the following results can be found: (1) The compression modulus of 9(1) and 9(2) sand soil layer increased with pressure, and the curve for compression modulus with pressure followed three-broken-line for the corresponding three-stage pressures were 25~100 kPa, 100~1600 kPa and 1600~3200 kPa; (2) The increasing rate of the compression modulus with pressure gradually decreased, because the compressibility of sand soil reduced with the increase of overlying stress applied on it; (3) The above laws obtained from Fig.7~8 further verified the conclusion that the compression modulus appeared to linearly increase with depth for the greater overburden stress, leading to the denser sand soil.

THE COMPRESSION MODULUS FROM IN-SITU TEST

The values of compressibility index obtained from lab test on the undisturbed soil

often deviate from the actual one and the discreteness of data is obvious, because the soil sample is disturbed to some extent and its original stress condition are changed when the sample was explored, carried and made. These factors have impact on the compressibility of soil sample and the reliability of results from the lab test. The compression modulus cannot be directly obtained from the in-situ test such as the static sounding and the dynamic sounding. However, the relationship between in-situ test index and the compression modulus has good correlativity. The standard penetration test was conducted in the location of No.31~32 pier pile foundation of the WEN Zao-ban great bridge of the Beijing-Shanghai high speed railway. The N-value of penetration of 9(1) and 9(2) sand soil layer were 54 and 66, respectively. The formula for estimating the compression modulus based on the N-index of standard penetration test, which was suitable to sandy soil of Shanghai area, was expressed by (2002, Shi)

$$E_s' = 1.2 \times N \quad (4)$$

where N was the blows of standard penetration test.

As listed in the Table 3, the values of compression modulus of 9(1) and 9(2) sand soil layer obtained from Eq.4 were 65MPa and 79MPa, respectively, while the ones obtained from lab test were 52MPa and 66.7MPa, respectively. It was found that the former were slightly greater. Further considering the disturbance of sand sample, the value of compression modulus from standard penetration test was recommended to evaluate the compression behavior of soil layer and to be adopted to predict foundation settlement. It was consistent with the conclusion that the value of compression modulus should be properly increased when the one was obtained from high pressure confined compression test reported by Chen(Chen 2001).

Table.3 the value of compression modulus of soil layers beneath pile toe

| Serial number of soil layer | Depth below the pile toe H(m) | Compression modulus from lab test E_s (MPa) | Compression modulus from SPT E_s' (MPa) | The E_s'/E_s ratio |
|-----------------------------|-------------------------------|---|---|----------------------|
| 9(1) | 2 | 52 | 65 | 1.23 |
| 9(2) | 5 | 60 | 79 | 1.18 |
| | 11 | 62 | | |
| | 17 | 65 | | |
| | 23 | 69 | | |
| | 29 | 72 | | |

CONCLUSIONS

High-pressure confined compression tests and the standard penetration tests were performed to investigate compression behavior of sandy soil layer beneath long pile

toe, and the relationship of compression modulus with embedded depth and overburden pressure were studied. The main conclusions from this research were as follows:

(1) The compression modulus of sandy soil increased with overburden pressure, and the curve for compression modulus with pressure followed three-broken-line. The changing rate of the compression modulus gradually decreased with pressure, because its compressibility reduced with the increase of overburden pressure.

(2) The $E_s/E_{s0.1-0.2}$ ratio ranged from 2.1 to 4.2. The compression modulus almost linearly increased with the depth, because the deeper the sand soil embedded and greater the overburden stress was, the denser the sand soil layer was. The relationship formula of the $E_s/E_{s0.1-0.2}$ ratio with the overburden pressure σ_z was obtained to determine the value of compression modulus under the actual stress.

(3) When prediction of the pile foundation settlement was conducted, the in-situ test such as standard penetration test was preferentially recommended to determinate the compression modulus, while the one from high pressure confined compression test should be properly increased.

ACKNOWLEDGMENTS

This paper is financially supported by the National Nature Science Foundation of China (Grants No. 51208518, 51208519 and 51108464), the Special Fund for Basic Scientific Research of Central Colleges grants 2012QNZT050 and the Post Doctor Foundation of Central South University.

REFERENCES

- Leng W.M, Yang Q.Nei R.S,Yue J.(2011). "Study of post-construction settlement combination forecast method of high-speed railway bridge pile foundation." *Rock and Soil Mechanics*. 32(11): 3341-3348
- Yang Qi. (2011). "Study on deformation behavior test and settlement after acceptance of high-speed railway bridge pile foundation." *Ph.D. dissertation*, Central South University ,Changsha
- Danno K, Kimura M.(2009). "Evaluation of long-term displacements of pile foundation using coupled fem and centrifuge model test." *Soils and Foundations*.49(6):941-958
- TB 10621-2009.(2009).The code for high seep railway. Beijing: China railway Publishing House.
- Xue F.C, Ma J. L, Yan L.P. (2011). "Three-dimensional fem analysis of bridge pile group settlement in soft soils." *Geotechnical Special Publication No. 220*, ASCE.2011:135-143
- Bakhholdin B. V ,Chashchikhina L. P .(1999). "Determination of the compression modulus of soils from compression-test data for calculation of pile-foundation

- settlements ." *Soil Mechanics and Foundation Engineering* . 36 (1): 9-12
- Ma L.X.(2006). " Research on changing law of compressing module of soil." *Site Investigation Science and Technology*. (3):42-44
- Deng W.L, Zhou Z.M.(2011). "A calculation method for soil's modulus of compressibility". *Industrial Constitution* .26(10):34-36
- Liu Z.T, Mei G.X , Zai J.M.(2004). "Calculation of oedometric modulus of soil and its application based on the routine soil test."*Journal of Nanjing University of Technology*.26(1):5-8
- Mei G.X, Zai J.M, Zhao W.B.(2003). "A simplified calculation method of oedometric modulus of soil and its application." *Rock and Soil Mechanics*.24(6):1057-1060
- Fu T.Y, Chen Z.L, Chen C,Pan L.Y, Yu C.(2012). "Computations on compression modulus and its application." *Low Temperature Architecture Technology*. (4):72-74
- Zhou C.Y, Lin C.Y, Lin L.S Yang X.L. (2010). "Research on dynamic evolution law of compression modulus of soft clay under external loads." *Rock and Soil Mechanics*.31(7):2040-2044
- Aziz H Y, Ma J L.(2012). " Deep foundation numerical analysis using modified compression modulus ." *The Open Civil Engineering Journal*, Vol .(6): 65-86
- Huang T.(1997). "A method of direct determination of the compression modulus of silt and sand using SPT blow counts." *Site Investigation Science and Technology*. (5):11-14.
- Li H.B, Zhou X.C. (2001). "Discussion on relationship between compression modulus of red clay ground and standard penetration test blow count." *Railway Investigation and Survey*.1 (2):55- 57
- Chen R.P, Ling D.S, Chen Y.M.(2003). "Some problems in the calculation for settlement of pile-group foundation." *China Civil Engineering Journal*. 36(9): 89-84
- Ji F.Q, Jing F, Liu Z.B, Ju J.(2011) . "Determination of compressive modulus for foundation soils from the piezocone penetration test(CPTU) ." *Journal of Engineering Geology*.19 (6):882-886
- Yang H.Y, Shi Z.M.(1997). "Regression analysis of the forecast of modulus of compressibility of soil."*Shanghai Geology*. (3):44-49
- Tomlinson M. J (2004). "Pile design and construction practice." London: E & FN SPON
- Burland J. B, Kalra J.C.(1986). "Queen elizabeth conference centre II : geotechnical aspects." *Proceedings of the Institution of Civil Engineer*. 80 (6): 1479–1503
- Shi,P.D.(2008). "Manual of pile foundation." Beijing: The People Jiao-Tong Press

Model Test Study on Force and Deformation Characteristics of Steel Tubular Composite Piles

Min Zhang¹, Jianlin Ma², Weisheng Wu³, and Hongbing Xie⁴

¹Ph. D Can, College of Civil Engineering, Southwest Jiaotong University, Chengdu 610031, Sichuan, China; zhangminswjtu@126.com

²Professor, College of Civil Engineering, Southwest Jiaotong University, Chengdu 610031, Sichuan, China; majianlin01@126.com

³Senior eng. and Prof., CCCC Highway Consultants CO., Ltd, Beijing 100088, China; wws@163.com

⁴Senior eng. and Prof., Hong Kong-Zhuhai-Macao Bridge Authority, Zhuhai 519015, Guangdong, China; hzmbo@hzmbo.com

ABSTRACT: To investigate the effects of shear ring, drilling mud skin and anti-corrosion coating on force and deformation characteristics of Steel Tubular Composite (STC) piles, seven model tests with different combinations of shear ring, drilling mud skin and anticorrosion coating were conducted. Based on test results, the relationship between the shear ring spacing and STC pile bending stiffness is studied. The results obtained from the tests show that the capacity for lateral deformation of STC piles is greatly influenced by drilling mud skin, anti-corrosion coating and shear ring. Drilling mud skin and anti-corrosion coating reduces the bond strength between steel tube and concrete. On the contrary, shear ring can effectively transfer the stress from concrete to steel and consequently the bearing capacity for lateral deformation of STC pile is improved. This also causes the strain distribution along the cross section to be “inverse-v” or “m” shaped. The reinforcement of shear ring can completely overcome the adverse influence of drilling mud skin and anti-corrosion coating, when the spaced distance is less than $2D$ (D is pile diameter). Finally, the relationship between the increment of bending rigidity of STC pile and shear ring spacing is formulated.

INTRODUCTION

In recent years, large diameter steel pipe piles have gained popularity in oversize bridges due to their advantages of providing large bearing capacity, relatively simple pile driving process, amount of smaller dump and good flexural capacity. Due to the increase of China's steel production, researches and developments of new technologies and new materials for the preservation of steel pipe piles, steel pipe pile increasingly subjects to the attention of designers. So far, various experimental and analytical studies have been performed on steel pipe piles (L. Kappes(2012), Pan H. M.(2007), Jia Q.(2011), Zhang M. Y.(2012), KWAK K(2010), Liu R.(2009)). But

these studies did not relate to the residual drilling mud skin on inner wall of steel pipe caused by the construction, the issue about the anti-corrosion protection of steel pipe inner wall, shear ring arranged on the inner wall of Steel pipe in order to increase the bond strength between concrete and steel tube. Therefore, the research on working performance of steel pipe pile under the action of shear ring, drilling mud skin and anti-corrosion coating is necessarily to be carried out.

Based on the construction of the Hong Kong-Zhuhai-Macao Bridge, to investigate mechanical and deformation characteristics of high platform pile with shear ring, drilling mud skin and anti-corrosion coating under axial load-bending moment-lateral load, seven specimens were tested. According to the test results, relationship between the shear ring spacing and STC pile bending rigidity was studied.

EXPERIMENTAL PROGRAM

Model test design

All the specimens had the same size: 0.3m diameter and 4.1m in length totally, where the length L used for testing is 2.5 m, the load applied length is 1.2m, the anchor length is 0.4m. The dimensions and characterizations of test specimens are as shown in Table 1.

In Table 1, D is diameter of the test specimen; t is thickness of the steel tube; α is ratio of the cross-section area of steel and concrete.

Table 1. Dimensions and characterizations of test specimens

| Specimen | Details of Specimen | Shear Ring Spacing /number | D /mm | t /mm | α | D/t |
|----------|--|----------------------------|-------|-------|----------|-----|
| 1 | Anti-corrosion coating | | 300 | 3 | 4% | 100 |
| 2 | Drilling mud +anti-corrosion coating | | 300 | 3 | 4% | 100 |
| 3 | Drilling mud | | 300 | 3 | 4% | 100 |
| 4 | Shear ring +anti-corrosion coating | 30cm/8 | 300 | 3 | 4% | 100 |
| 5 | Shear ring+drilling mud +anti-corrosion coating | 45cm/6 | 300 | 3 | 4% | 100 |
| 6 | Shear ring+drilling mud +anti-corrosion coating | 60cm/4 | 300 | 3 | 4% | 100 |
| 7 | Shear ring+drilling mud skin +anti-corrosion coating | 90cm/3 | 300 | 3 | 4% | 100 |

Materials

The concrete was supplied by a local firm, with the yield stress being 45MPa. For all specimens the diameter of longitudinal reinforcement and spiral stirrups were respectively 8mm and 2mm. The ratio of longitudinal reinforcement was constant for

all specimens and equal to 0.5%, with the yield stress being 335MPa. The stirrups spacing was 25mm, with the yield stress being 235MPa. The outside diameter and thickness of steel tubes were respectively 300mm and 3mm, with the yield stress being 345MPa.

The shear ring was composed with a width of 6mm, and thickness of 3mm rectangular steel, with yield stress being 345MPa, and spacing of 1D(=30cm), 1.5D(=45cm), 2D(=60cm) and 3D(=90cm) (see in FIG.1(c)).

Six specimens were coated with anti-corrosion coating completed by the Institute of Metal Research, Chinese Academy of Sciences, as shown in FIG. 1(a).

Five specimens were brushed with drilling mud skin (see in FIG.1(b)), with thickness of 0.1mm, which was made up of bentonite and Neptune polymer additives by a certain ratio. The quality ratio of additive and water was 0.11%, and volume ratio of water and bentonite was 10.

After welding shear ring on the inner wall of steel tube, and then besmear anti-corrosion coating and drilling mud. At last pour concrete and artificial stirring at the same time. So a steel tubular composite pile is built.

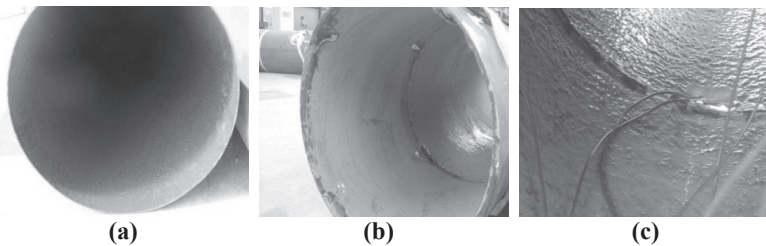


FIG. 1. Anti-corrosion coating, drilling mud skin and shear ring on the inner wall of steel tube

Arrangement of sensors

To measure the longitudinal strain of steel tube, twenty seven gauges were applied on the surface of each specimen, three in the axial at the cross-section. Fifteen concrete strain gauges were applied for each specimen, three in the axial at the cross-section, to monitor the core concrete strain. Arrangement of test position for each specimen was as illustrated in FIG. 2. The lateral displacement of all specimens was also measured by micrometer gauge (see FIG.3).

Test procedure

The test specimens were loaded up to 1.7P (P was the design load) by YES-5000 -type digital display presses and MTS that had the capacity of 5000kN. The employed MTS enable to apply lateral load (v) and moment (moment produced by a group couple f). The lateral displacement, steel strain and concrete strain were record by a TDS-303 automatic static data acquisition system.

The bottom of the specimen was fixed without deformation in all directions and the axial load was applied through a steel cap with greater diameter, which was placed on

the top surface of the specimen. The photograph of the test setup is shown in FIG. 3.

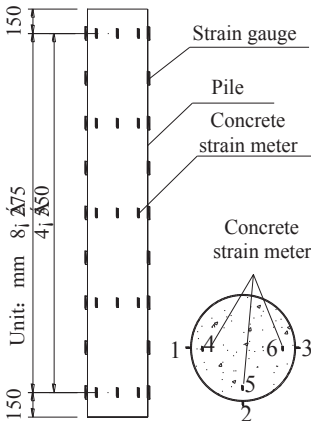


FIG. 2. Layout of measuring point of specimens

FIG. 3. Test setup

TEST RESULTS AND ANALYSIS

No obvious damage was observed during all tests. In order to verify the influence of anti-corrosion, drilling mud skin and shear ring on the behavior of STC piles, the lateral displacement of pile top, steel strain and cross-section deformation of all specimens are discussed, respectively.

The experimental results and the maximum applicable load are reported in Table 2.

Table 2. Experimental results

| Specimens | Axial load/bending moment/lateral load (kN/kNm/kN) | Lateral displacement /mm | Steel strain | | Concrete strain/ $\mu\epsilon$ |
|-----------|--|--------------------------|-----------------------------------|-------------------------------|--------------------------------|
| | | | Compression strain/ $\mu\epsilon$ | Tensile strain/ $\mu\epsilon$ | |
| 1 | 402/67/53 | 5.06 | -721 | 526 | -441 |
| 2 | 132/50/42 | 4.59 | -581 | 589 | -156 |
| 3 | 132/50/42 | 4.50 | -465 | 306 | -169 |
| 4 | 402/67/53 | 4.61 | -769 | 744 | -688 |
| 5 | 132/50/42 | 4.30 | -550 | 750 | -198 |
| 6 | 402/67/53 | 4.68 | -797 | 544 | -395 |
| 7 | 402/67/53 | 4.78 | -916 | 145 | -692 |

From Table 2, it is found that the maximum of lateral displacement is 5.06mm, and the maximums of steel compression and tensile strain are 916 $\mu\epsilon$ and 744 $\mu\epsilon$, respectively. As for concrete, the maximum of concrete strain is 692 $\mu\epsilon$. The maximum strains of steel and concrete are less than their yield strains. Based on the reference (Liu W.(2005)), it is evident that in all specimens the force and deformation

are in elastic-plastic state.

According to Table 2, in the case of the same load, the lateral displacements of specimens with shear ring are smaller than piles without shear ring.

The curves of lateral Load-lateral displacement

The curves of lateral displacement versus lateral load for seven specimens are plotted in FIG. 4.

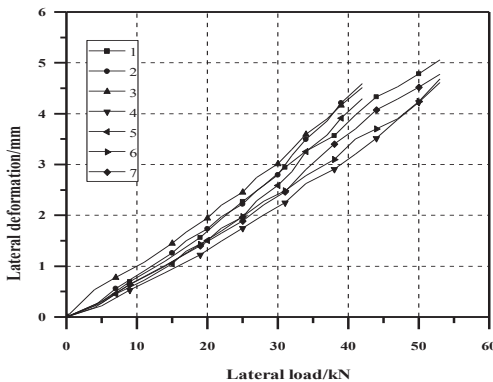


FIG. 4. Curves of lateral load – lateral displacement

It can be observed from FIG. 4 that the curves of lateral displacement versus lateral load do not possess obvious inflection point, and the lateral displacement is linear increase along with the change of lateral load. Thus, it can be concluded that the force and deformation of all specimens are in elastic-plastic state.

From FIG. 4 and Table 2, it can be seen that: under the same load conditions, the lateral displacements of STC piles with shear ring are less than STC piles' without shear ring. Consequently, it can be concluded that shear ring effectively make lateral deformation of STC piles reduce. At the same time, the capacity for lateral deformation is improved. The reason can be that the reinforcement of shear ring may enhance the bond strength between the steel tube and the core concrete, while, the drilling mud skin and anti-corrosion coating lead to the bond strength weakening.

With the increase of load, the growth rate of lateral deformation of specimen 4(the spacing of shear ring is 30cm) is less than specimen 6(the spacing of shear ring is 60cm), which is less than specimen 7(the spacing of shear ring is 90cm). Therefore, it is perceived that lateral displacement increases with the increasing of the shear ring spacing.

Strain distribution along the cross section

FIG. 5 shows the longitudinal strain distribution along the cross - section of STC piles.

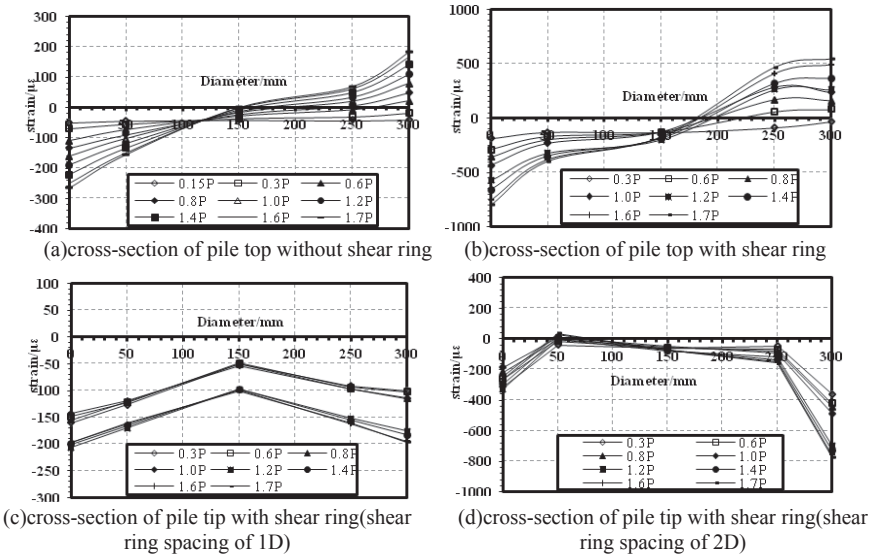


FIG. 5. The longitudinal strain distribution along the cross-section of specimens

Based on the comparison of FIG.5 (a) and (b), it can be seen that the cross-section deformation of piles without shear ring matches the plane-section assumption, when the load is less than 0.8P (P is the design load). With the increase of the load, the cross-section deformation does not meet the plane-section assumption, and then the steel deformation does coordinate with the concrete. However, the cross-section deformation of piles with shear ring obeys the plane-section assumption until 1.0P.

According to FIG.5 (b), (c) and (d), it is found that the steel strain of pile end significantly increase, resulting that the strain distribution at the cross-section is “inverse-v” or “m” shaped. Therefore, the cross-section deformation of STC pile end with shear ring does not meet the plane-section assumption.

Steel tube strain varies with the location and load

Together under axial load–bending moment–lateral load, the stress state of each cross-section at different positions is different, so that the strain of steel tube varies with the locations. The steel average longitudinal strain versus the location curves from the test results, when the load is 1.0P and 1.7P, are plotted in FIG.6.

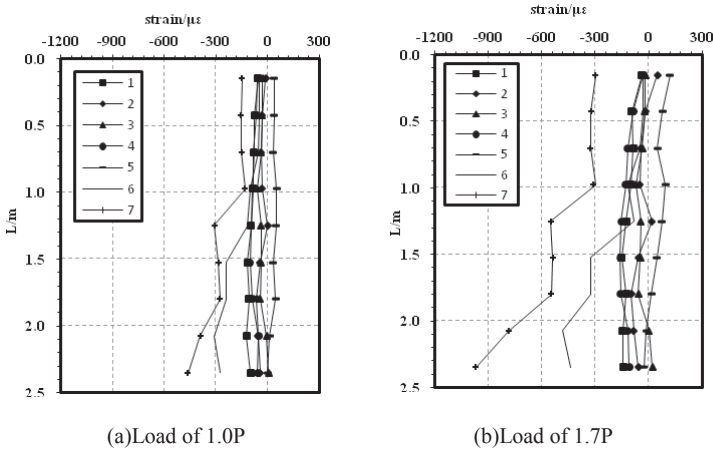


FIG. 6. Curves of steel pipe average longitudinal strain-load

With the increase of the load, the steel tube strains of specimen 6 (shear ring spacing of 60cm) and specimen 7 (shear ring spacing of 90cm) increase greatly than specimen 5 (shear ring spacing of 45cm), respectively, however, the steel tube strains of the other specimens are substantially no significant changes. Meanwhile, under the same load conditions, the steel pipe strain of specimen 6 and 7 gradually increases along the location, reaching the maximum of steel tube strain of the pile end.

In summary, the shear ring improves the force characteristic of steel tube, and thus, this contributes to improvement in performance of STC piles. As the load increases, when the spacing of shear ring is $2D$ or $3D$, the steel tube deformation of STC pile below $2/5$ position increase significantly.

STC PILE BENDING RIGIDITY ANALYSIS

Based on the principles of classical mechanics, and the experimental results, mechanics analysis on STC pile is studied. In addition to follow the basic assumptions of the theory of classical mechanics, the following assumptions are supposed:

- (1) In the elastic stage, steel tube and core concrete work together, deformation compatibility;
- (2) The shape of cross-section remains round; its area is exactly the same as before the deformation of STCP happens;
- (3) The radial pressure of steel tube is far less than the longitudinal and hoop stress, which can be ignored.

Equation proposed for STC pile bending rigidity

The calculation method of the steel pipe pile bending rigidity has been frequently adopted by the domestic and foreign relevant current specifications and design, as

follows:

$$EI = E_s I_s + \phi E_c I_c \quad (1)$$

Where: ϕ is a reducing factor for $E_c I_c$ due to the cracking of concrete, its value in the range of 0.2~0.8(AIJ 1997, AISC 2005, BS5400 2005, EC4 2004, DB12-51-2003).

Based on the results of model test, to investigate the effect of drilling mud skin, shear ring and anti-corrosion coating on STC pile's bending rigidity. In the elastic stage, the bending rigidity equation of STC pile may be proposed as follows:

$$EI = k_{ws} E_s I_s + k_{wc} E_c I_c \quad (2)$$

Where: k_{ws} is a reducing factor for $E_s I_s$ due to the long-term corrosion in a marine environment, in this test $k_{ws} = 1$.

k_{wc} is a parameter which represents the effects of drilling mud skin, ant-corrosion coating and shear ring. Its equation can be proposed as follows:

$$k_{wc} = k_{wN} \cdot k_{wJ} \cdot k_{wF} \quad (3)$$

Where: k_{wN} is a reducing factor due to the weakening effect of the drilling mud skin. When the effect of the drilling mud skin (thickness of 0.1mm) is considered, the value of k_{wN} is less than 1, otherwise, equal to 1.

k_{wJ} is the increasing factor related to the reinforcement of the shear ring. When the specimen with shear ring, the value of k_{wJ} is more than 1, otherwise, equal to 1.

k_{wF} is a reducing factor because of the weakening effect of the anti-corrosion coating. When the effect of the anti-corrosion coating is taken into account, the value of k_{wF} is less than 1, otherwise, equal to 1.

In the elastic stage, based on the principles of material mechanics, combining with the lateral deformation of pile top, the proposed Eq. (4) is used to determine the bending rigidity of STC pile.

$$S = \frac{VL^3}{3EI} - \frac{ML^2}{2EI} \quad (4)$$

Where: S is the lateral deformation of pile top; V , M are the lateral load and moment, respectively; L the length used for testing, with a value of 2.5m; EI is the bending rigidity of STC pile.

The calculation for the bending rigidity of STC pile

Based on the above analysis, the test results are adopted to calculate the bending rigidity of STC piles with or without shear ring when the load is 1.0P or 0.8P.

Eq. (4) and Eq. (2) are respectively used to determine the bending rigidity and its expression of STC pile.

The bending rigidity expressions of STC piles and the values of parameter k_{wc} are as shown in Table 3.

From Table 3, it is observed that the k_{wc} is affected by the effects of shear ring, drilling mud skin and anti-corrosion coating.

The k_{wc} is decreased by drilling mud skin and anti-corrosion, because they make the bond strength between the steel tube and the concrete weaken. Its value ranges from 0.90 to 0.92, when the specimen is without shear ring.

Table 3. Bending rigidity expressions of specimens and k_{wc}

| Specimens | Spacing of shear ring/cm | Correction coefficient/ k_{wc} | Expressions of bending stiffness/ EI |
|-----------|--------------------------|----------------------------------|--|
| 1 | | 0.91 | $E_s I_s + 0.91 E_c I_c$ |
| 2 | | 0.90 | $E_s I_s + 0.90 E_c I_c$ |
| 3 | | 0.92 | $E_s I_s + 0.92 E_c I_c$ |
| 4 | 30 | 1.14 | $E_s I_s + 1.14 E_c I_c$ |
| 5 | 45 | 1.03 | $E_s I_s + 1.03 E_c I_c$ |
| 6 | 60 | 1.013 | $E_s I_s + 1.013 E_c I_c$ |
| 7 | 90 | 0.99 | $E_s I_s + 0.99 E_c I_c$ |

The shear ring is the most important factor, which can make k_{wc} increased for its reinforcement. It can be seen from Table 3 that the k_{wc} value of specimens with shear ring ranges from 0.99 to 1.14, and also it decreases with the increasing of shear ring spacing.

When the spacing of shear ring is less than $2D$, the k_{wc} value is greater than 1, meanwhile the effects of the drilling mud skin and anti-corrosion coating can be completely ignored. Thus, it is concluded that the bending rigidity is increased by the reinforcement of shear ring, and then which contributes to improvement in properties of STC piles.

The following mainly discuss the influence of shear ring on steel composite pile.

Discussion on the reinforcement of shear ring

Based on the analysis of experimental results, it is assumed that the bending rigidity relation equation between the STC pile with or without shear ring is:

$$(EI)_J = (1 + \xi)(EI)_w \quad (5)$$

Where: $(EI)_J$ and $(EI)_w$ are the bending rigidity of STC piles with or without shear ring, respectively. ξ is the correction coefficient related with shear ring spacing for $(EI)_w$. Table 4 shows the calculations of ξ based on the results of this experiment.

Table 4. Calculations of ξ

| Specimens | Shear ring spacing/ S_J | ξ | $1 + \xi$ |
|-----------|---------------------------|-------|-----------|
| 4 | 1D | 0.25 | 1.25 |
| 5 | 1.5D | 0.15 | 1.15 |
| 6 | 2D | 0.13 | 1.13 |
| 7 | 3D | 0.08 | 1.08 |

According to Table 4, it can be seen that when the shear ring spacing S_J is between $1D$ and $3D$, the values of ξ ranges from 0.25 to 0.08. Thus, it is found that the correction factor ξ decreases with the increasing of shear ring spacing. The fitted

curve for $1+\xi$ is shown in FIG. 7, and the correlation coefficient between observed data and fitted curve of $1+\xi$ is $R^2=0.95$, which means that the fitted curve matches the analytical results well. The equation for expressing the relation between the two is as follows:

$$\xi = \frac{1}{4\beta}, \quad \beta = \frac{S_J}{D} \tag{6}$$

Where:

β is the ratio between shear ring spacing and diameter and a dimensionless parameter. The value of β should be in the range of $0.5 \leq \beta \leq 5$.

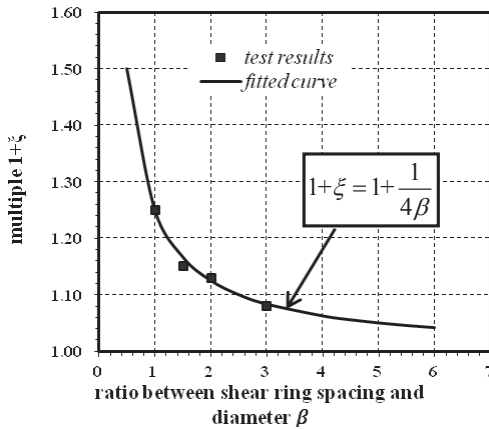


FIG. 7 β versus $1+\xi$

The equation applied to describe the relation between $(EI)_J$ and $(EI)_w$ is obtained by substituting Eq. (6) into Eq. (5) as follows.

$$(EI)_J = (1+\xi)(EI)_w = (1 + \frac{1}{4S_J})(EI)_w \tag{7}$$

Therefore, the Eq. (7) will be used to calculate the bending rigidity of STC piles with shear ring, directly. Meanwhile, this can provide a reliable basis for the design and optimization of the shear ring spacing.

CONCLUSIONS

The results of a large experimental program were presented in order to show the drilling mud skin, anti-corrosion and shear ring that affect the behavior of STC piles under axial load-bending moment-lateral load. The following conclusions can be drawn from the study:

1. Based on the analysis of the experimental results, it is verified that the effects of drilling mud skin and anti-corrosion coating lead to the deformation of STC piles increase; however, deformation is decreased due to the reinforcement of shear ring.
2. The reinforcement of shear ring causes significant steel strain increase, with the result that the strain distribution along the cross section is “inverse-v” or “m” shaped.
3. According to the results of the investigations, the calculation formulas for

bending rigidity of STC piles are achieved. It is indicated that the bending rigidity is observably affected by shear ring spacing. At last, an equation for bending rigidity and shear ring spacing is proposed, the validation results of calculated values against experimental values proved that the equation is advisable.

REFERENCES

- L. Kappes, M. Berry, J. Stephens, L. McKittrick(2012). "Concrete Filled Steel Tube Piles to Concrete Pile-Cap Connections". *ASCE Structure Congress*.
- Pan, H. M., Guo, Y. L., Liang S., ect (2007). "A Stability Analysis of Major Diameter Thin-walled Tube Beam-columns". *China Civil Engineering Journal*, Vol. 40(3): 11-17(in Chinese).
- Jia, Q., Zhang, A. Q., Zhang, X. (2011). "Test Study and Numerical Analysis of Stability of High-level Cap Steel Tubular Pile under Compression Loads". *Rock and Soil Mechanics*, Vol. 32(6): 1736-1740(in Chinese).
- Zhang, M. Y., Song, H. Z., Li, B., Li, Y. (2012). "Prediction for Bearing Capacity of Lager-diameter and Super-long Steel Pipe Pile Based on ICA-SVM". *Rock and Soil Mechanics*, Vol. 33(9): 2759-2764(in Chinese).
- KWAK K, KIM K J(2010). "Reliability-based calibration of resistance factors for static bearing capacity of driven steel piles". *Canadian Geotechnical Journal*, 47(5): 528-538.
- Liu, R., Yan, S. W., Li, Z. H. (2009). "Soil plug effect prediction and pile drivability analysis for large-diameter steel piles in ocean engineering". *China Ocean Engineering*, Vol. 23(1): 107-118(in Chinese).
- AIJ, 1997. "Recommendations for design and construction of concrete filled steel tubular structures". *Architectural Institute of Japan (AIJ), Tokyo, Japan*
- ANSI/AISC 360-05, 2005. "Specification for structural steel buildings". *American Institute of Steel Construction (AISC), Chicago, USA*
- British Standards Institutions BS 5400, 2005. "Steel, concrete and composite bridges, Part 5: Code of practice for design of composite bridges". *London, UK*
- Euro code 4(EC4), 2004. "Design of steel and concrete structures-Part-1: General rules and rules for building". EN 1994-1-1: 2004, Brussels, *European Committee for Standardization*.
- DB12-51-2003(2004). "Technical Specification for Concrete Filled Steel Tubular Structures". *Department of Construction of Fujian Province*.
- Liu, W. (2005). "Research on mechanism of concrete-filled steel tubers subjected to local compression". *Fuzhou University*, (in Chinese).

The Chemical-Physical Combined Method for Improving Clay Slurry in Land Reclamation

Dong Qing Wu¹, Wen Yu Xu¹, Dan Ping Zhu¹

¹Chemilink R&D Centre, Chemilink Technologies Group, 20 Kuanji Road, Singapore 739462, Emails: wu@chemilink.com; wenyu_xu@chemilink.com and danping_zhu@chemilink.com

ABSTRACT: The paper has concentrated on technical effectiveness of Physical-Chemical Combined Method (CPCM) through a series of laboratory tests. The chemical stabilization method was used to investigate two slurry groups, one initially with lower water content w ($w < 2LL$; LL-liquid limit); and the other with higher initial water content ($w \geq 2 \sim 6LL$) which is within the water content range of dredged clay slurry. The final water content, shear strength C_u of clay slurry achieved and their relationship after chemical pre-treatment were set up for the two groups at different chemical dosages, while some vacuum preloading (VP) tests using pure clay slurry were also conducted for comparison. When the initial water content is lower ($w < 2LL$), the achieved shear strength with the chemical treatment can be higher than that of pure clay slurry treated by VP with drains. However the shear strength after the chemical treatment is generally poorer when the initial water content is higher ($w \geq 2 \sim 6LL$). In order to achieve better or higher performances, the VP with drains was introduced during the chemical stabilization. The achieved higher strengths with this combined method have proven that CPCM for improvement of clay slurry is not only academically effective but also very potential for engineering applications.

Keywords: Sustainable, Green and Eco-Friendly, Chemical-Physical Combined Method (CPCM), Clay Slurry, Soil Improvement, Land Reclamation, Chemical Stabilization, Vacuum Preloading (VP)

INTRODUCTION

Conventional filling materials such as natural sands and hill-cut materials have been used for land reclamation for hundred or even thousand years. As faster international economic development for past few decades, the demand on reclaimed land has become higher and higher. Some dredged marine clay slurry and cement-treated dredged clay are used in recent time because this approach for land reclamation by fully utilizing the dredged or excavated soft clays which are normally treated as waste materials is sustainable, green and eco-friendly with relatively lower cost. How to effectively improve the clay slurry using different engineering methods to maximize the performances of the reclaimed land becomes very critical and is also a new challenge to both academic research and engineering practice.

Physical or mechanical preloading either by surcharge or vacuum incorporated with vertical drains is the most commonly-used methods to enhance the load bearing capacity of reclaimed land using very soft clay or clay slurry. Some research works have been conducted in universities by using dredged or excavated marine clays as filled materials for land reclamation. However, these academic studies mainly focused on their theoretical analysis, physical properties and mechanical behavior, such as the study of Non-linear Finite Strain Consolidation (Wu, 1994). The real engineering application issues are still not well addressed and resolved. Vacuum preloading (VP) with drains has been widely used in China to strengthen the soft land reclaimed by dredged materials in coastal cities for past about 10 years but the ultimate bearing capacity achieved is limited (6 to 8 t/m²) which may often require further soil improvement in order to achieve higher bearing capacities for reclaimed land. Some chemical treatment studies were reported (Zhang et al, 2008). Cement treated dredged clay at low initial water content with the Pneumatic Flow Mixing Method had been used to reclaim land in Japan for the construction of an international airport (Sato & Kato, 2002) and it was one of few full scale projects with successfully applying chemical treatment, where the range of liquid limit (LL) of dredged clay is 49~88%; initial water content 48~84% or 0.88~1.21LL; dosage of cement 5~9% and achieved UCS (unconfined compressive strength) around 100~350kPa. However, the chemical treatment for the most dredged marine clays or clay slurries with higher initial water content such as more than 2~4LL are generally ineffective even with higher dosage of chemical binders.

So far, none of the academic research or engineering application has explored into combining chemical treatments and physical methods to more efficiently improve the properties of the soft to slurry-type materials for civil engineering purposes especially land reclamation. This paper is a premier trial to disclose the concept of the Chemical-Physical Combined Method (CPCM) for improvement of clay slurry, which was proposed by Chemilink in an internal report earlier and an initial trail similar to CPCM can be traced back to early 1990 (Wu et al, 1992). The technical effectiveness and performance of CPCM have been concentrated in this paper through a series of laboratory tests. It could be an innovative solution, by using CPCM to achieve higher strengths and performances, to the challenge of effective improvement of clay slurry in both fields of academic research and engineering application. Furthermore CPCM may also provide a strong technical platform to study how to use clay slurry incorporated with chemical binders and possible physical approaches to treat some solid wastes with various solid waste materials for land reclamation, which may be discussed in a separate paper.

CLAY SLURRY IMPROVED BY VACUUM PRELOADING (VP)

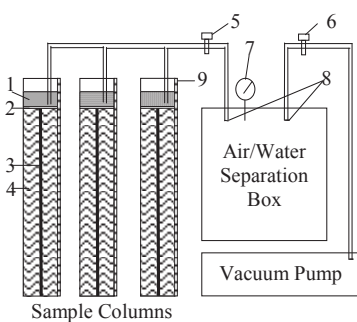
The representative Singapore marine clay (MC) was selected for the study and its typical basic properties are given in Table 1. The general range of LL for Singapore MC is around 50% to 95% and its plastic index (PI) around 30% to 65% (Arulrajah & Bo, 2008).

Table 1: Typical Basic Properties of Singapore Marine Clay (MC)

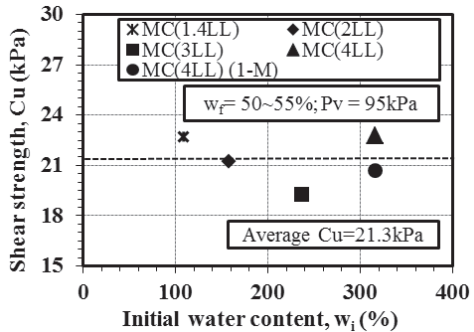
| No | Properties | Value | No | Properties | Value |
|----|----------------------------|-------|----|-------------------------|-------|
| 1 | Specific Gravity, G_s | 2.66 | 6 | Organic Content | 3.8% |
| 2 | Natural Water Content, w | 60% | 7 | Grain Size Distribution | |
| 3 | Liquid Limit, LL | 79% | | a) Sand | 3% |
| 4 | Plastic Limit, PL | 34% | | b) Silt | 48% |
| 5 | Plastic Index, PI | 45% | | c) Clay | 49% |

A series of 3-dimensional (3-D) consolidation tests were conducted (Fig. 1a) with clay slurries at different initial water contents of 1.4LL, 2.0LL, 3.0LL and 4.0LL. An additional slurry sample with initial water content at 4.0LL was purposely soaked under sea water for a month in order to simulate field situation and investigate the influence from soaking. It should be noted that in order to reflect real engineering conditions, sea water has been always used for all tests presented in this paper. The fall cone test was selected to determine the undrained shear strength (C_u).

A constant VP at 95kPa was applied instantly because of no instability issue and upon the completion of consolidation the water contents along each sample height were further checked to be a constant during C_u tests layer by layer. The final water contents for the fully consolidated samples are quite similar within a small range of 50% to 55%. Generally the C_u values achieved for different samples are quite close each other and the average is about 21kPa (Fig. 1b) for the used Singapore MC. The results indicate that the final consolidated results are almost the same for all samples with different initial water contents even up to 4.0LL and there is not much difference between the soaked and un-soaked for the used pure MCs.



(a) 3-D consolidation tests device



(b) Achieved C_u vs. initial water content

FIG. 1. 3-D consolidation test by VP

Note: In (a), 1: Sand; 2: Geotextile; 3: Vertical drain; 4: Clay samples; 5: Pressure control valve; 6: Vacuum control valve; 7: Pressure Meter; 8: Tubes; 9: Ruler.

CHEMICAL STABILIZATION FOR CLAY SLURRY

A group of specially designed chemical binders (SS-300 series) have been employed to the both tests with chemical stabilization (SS-310 sub-series) and with CPCM (SS-330 sub-series) in this paper. The sub-series products SS-311E & H were selected for

a group of chemical stabilization tests with both different initial water contents: 2LL, 3LL and 4LL; and different chemical dosages: 4%, 6% and 8% (% by dry soil weight) under different curing time at 7 and 28 days. The soil samples mixed with SS-311H were placed under sea water for curing and then at different curing days, the fall cone test was used to determine the C_u value (Fig. 2).

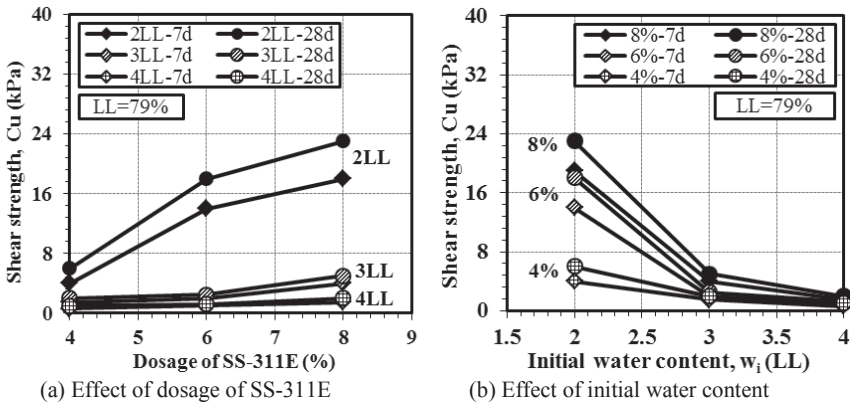


FIG. 2. Affecting factors on C_u at different curing time

From Fig. 2 it can be found that the lower initial water content, the higher C_u value is achieved, while the higher dosage, the higher C_u value is obtained. It is also very obvious that C_u value increases as the curing time increases. However even with higher dosage at 28 days, the C_u values for those with the higher initial water contents ($>3LL$ or 237%) are still extremely low ($<5kPa$). The chemical stabilization looks quite effective when the initial water content is low (especially lower than 2LL) but is ineffective when the initial water content is higher than 3LL.

When the initial water content is lower than 2LL, the increasing rate of C_u becomes faster as shown in Fig. 3, which strongly indicates that 2LL could be the turning point to identify the applicable range of the chemical stabilization. Further investigations in the paper were thus concentrated on more samples with the initial water content not higher than 2LL.

More binders with different chemical formulas (SS-311 sub series and cement) at a fixed dosage of 6% were used to stabilize MC; and the initial water content was set at 2LL in order to investigate the stabilization effectiveness of each chemical binder as shown in Fig. 4a. As expected, the C_u value of pure MC has no much change while cement stabilization effect looks very poor at 28 days. The C_u values stabilized by some chemicals look encouraging within a short time of 28 days and the average C_u achieved is around 18~20kPa which is closer to what VP achieved (Fig. 1). SS-311H was selected for the long-term tests and pure MC is investigated as a testing reference (Fig. 4b). It is beyond the expectation that the C_u value can continuously increase to about 40kPa at 120 days, which is close to 2 times of what vacuum preloading can achieve and the minimum ultimate bearing capacity for SS-311H stabilized MC is estimated to be around 200kPa or $20t/m^2$ which could be sufficient for most ordinary

foundations.

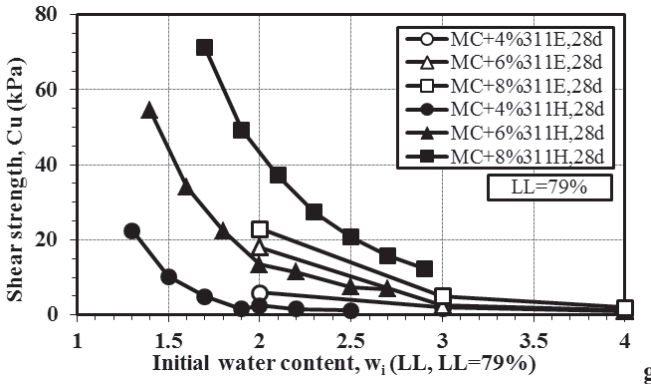


FIG. 3. Cu achieved with different initial water contents and chemical dosages

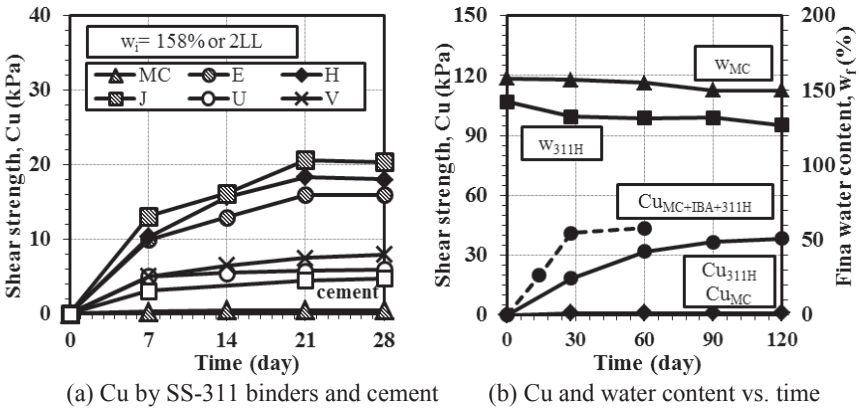


FIG. 4. Cu vs. curing time

Note: In (a), E: MC+311E; H: MC+311H; J: MC+311J; U: MC+311U; V: MC+311V; cement: MC+cement.

The shear strength of the pure MC without chemical stabilization remains as almost zero. Furthermore the water contents for both samples were also measured at different time together with Cu value (Fig. 4b). The water content of MC at different time has a very little reduction mainly due to the effect of Self-Weight Consolidation (Wu, 1994), while the water content of MC stabilized by the chemical has been reduced more because of introduction of the powder chemical at beginning and then chemical reactions. It could be therefore another surprise that even with the 2LL initial water content, the MC stabilized by chemical can still achieve significant high shear strength. As curing time increases, the Cu value has a trend to increase further.

CHEMICAL-PHYSICAL COMBINED METHOD (CPCM)

It is a logical but brave reasoning that if water content of MC stabilized by chemical can be reduced by some physical ways, which will function like the compaction in conventional chemical soil stabilization (Suhaimi & Wu, 2003), the mixture of MC and chemical will be compacted by squeezing water out so that the mixture structure becomes denser with lower water content; the chemical reactions will be more effective as mixture particles are closer each other; and thus strengths can be greatly increased.

Therefore a large number of in-house tests mainly using the 3-D consolidation cells were carried out to verify the validity of this new CPCM by combining chemical stabilization and VP with drains together for more effective improvement of MC with higher initial water content. Some of the testing results on Singapore MC with different initial water content at 2LL, 3LL and 4LL are given in Fig. 5a, where the applied VP was fixed at 95kPa for 9 days. For easy comparison, the average Cu value of pure MC achieved by VP (about 21kPa) is used as the reference basis. The Cu values achieved after CMCP with the selected chemical binders are generally 2 to 3 times of that of pure MC under the same VP condition. Therefore it proves that CPCM can achieve much higher strength than what vacuum preloading does.

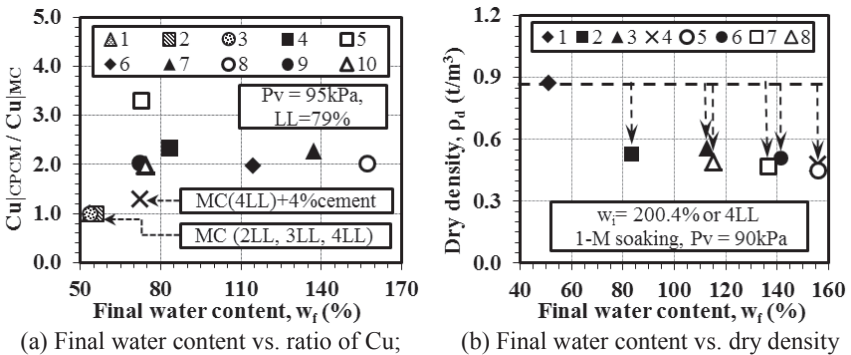


FIG. 5. Testing results of Singapore MC by CPCM

Note: In (a), 1: MC(2LL); 2: MC(3LL); 3: MC(4LL); 4: MC(2LL)+4%331E(6-M soaking); 5: MC(2LL)+4%331E+20%IBA(6-M soaking); 6: MC(4LL)+8%331D(1-M soaking); 7: MC(4LL)+8%331E(7-M soaking); 8: MC(4LL)+8%331H(1-M soaking); 9: MC(4LL)+4%331H; 10: MC(3LL)+4%331H. In (b), 1: MC; 2: MC+4%331H; 3: MC+6%331H; 4: MC+8%331H; 5: MC+8%331A; 6: MC+8%331B; 7: MC+8%331C; 8: MC+8%331D

In order to simulate field situation, parts of samples were soaked under sea water for 1~7 months and the Cu values achieved have no much dereferences, which strongly indicates that the selected chemical binders have good applicability. Though the initial water contents have big differences among the tested samples, the final result seems quite closer each other. It should be noted that though the Cu values are similar, the different samples have very much different final water contents. Thus the final water content and its corresponding dry density were investigated (Fig. 5b). The higher dosage was applied the higher final water content remained and lower dry density is resulted. This behavior clearly indicates a fact that the original MC has lost its original characters and developed to be a new structure with new chemical and physical properties under chemical reaction and physical compaction. As a result of these reactions, the original Singapore MC has been transformed into a totally new MC

called “Transformed Soil” and it is a part of “Singapore Newsoil” which was proposed as the environment-safe and engineering-capable materials transformed from various solid wastes. This transformed soil has light-weight but higher strength, which is greatly different from conventional understandings on consolidation of natural soils and may have great potential impacts to both technical and commercial aspects. The details about such complicated changes have to be studied further.

In addition, a higher figure of relative Cu (>3) can be seen in Fig. 5a which was achieved by a MC mixture with additional 20% of IBA (incineration bottom ash) and SS-311E. Disregard of environmental and chemical effects of IBA, the higher Cu value resulted by introducing the IBA with sand-size range indicate that at the same conditions, the coarser the mixture, the higher the strength can be resulted.

No sample with initial water content higher than 4LL was prepared based on the concept of Fluid Limit (FL) which corresponds to a state when the soil particles first start to interact and the FL for Singapore MC was determined to be 4LL (Wu, 1994). It deems that MC at 4LL can be a representative for others with higher water content in the study.

A Chinese Zhujiang MC was selected to verify the effectiveness and universal property of application of CPCM. Its LL, PI and clay content are 50.4%, 25% and 34.5% respectively, which are lower than those of Singapore MC. The initial water content of each MC sample was fixed at 4LL. The Cu values achieved are averagely about 3 times of that of pure MC by VP. It has proven again that CPCM is capable to achieve much higher strength than what vacuum preloading can and the universal property of applying CPCM is confirmed by a different material source. The average increment is higher than what was achieved for Singapore MC (averagely about 2 times). It could be caused by that China MC has lower liquid limit, less clay content, different mineral & chemical contents and others in addition to different binders used, which will be studied further. It should be noted that the LL after CPCM has increased for China MC from 50.4% to 55~70% and this change also supports the fact of the new transformed soil after CPCM found with Singapore MC.

CONCLUSIONS

1. VP with drains is one of few proven engineering approaches to improve soft clay with higher water content because it has no instability issue.
2. Chemical stabilization is applicable to Singapore MC when its initial water content is not higher than 2LL. It can achieve 40kPa or higher shear strength which could be sufficient to the bearing capacity of most ordinary foundations.
3. CPCM is a totally new methodology for very soft clay and slurry and it has been proven to be more effective in increasing the strength of very soft reclaimed foundations; furthermore a new material after applying CPCM has been transformed and this transformed soil has light-weight but higher strength.
4. Further studies on CPCM in both laboratory- and field-scale have to be conducted in order to investigate the details in mechanism of the chemical-physical reactions;

application range; optical chemical binders and so on with different soil sources.

ACKNOWLEDGEMENTS

The paper is a part of the R&D project, titled "Creating a Marine Clay Matrix with Incineration Bottom Ash (IBA) for Land Reclamation", under the Innovation for Environmental Sustainability (IES) Fund from National Environment Agency (NEA) of Singapore (ETO/CF/3/1). Authors would like to thank NEA for allowing them releasing the data while appreciation also goes to Engineering Technology Research Co., Ltd of CCCC Fourth Harbor Engineering Co., Ltd for testing data sharing.

REFERENCES

- Arulrajah, A. and Bo, M.W. (2008). "Characteristics of Singapore marine clay at Changi" *Geotechnical and Geological Engineering*, Vol. 26: 431-441.
- Sato, T. and Kato, H. (2002). "Application of the pneumatic flow mixing method to land development for central Japan international airport." *Underwater technology*, Proceedings of the 2002 International symposium on date of conference: 2002: 93-98.
- Suhaimi, H.G. and Wu, D.Q. (2003). "Review of Chemical Stabilization Technologies and Applications for Public Roads in Brunei Darussalam." *REAAA Journal* (The Journal of Road Engineering Association of Asia & Australia), Vol. 10 (1): 42-53.
- Wu, D.Q. (1994). "Improvement of Clay Slurry for Land Reclamation." School of Civil and Structural Engineering, doctoral dissertation, Nanyang Technological University, Singapore, 280 pp.
- Wu, D.Q., Broms, B.B. and Choa, V. (1992). "Stabilization of soft clay with fly-ash and by vacuum preloading for land reclamation." *International Conference on Geotechnical Engineering*, April 21-23, 1992, Johor Bahru, Malaysia.
- Zhang, C.L., Wang, S.C., Zhu, W., Liu, Q.S. and Ohki, T. (2008). "Influence of initial water content on cement solidification effect of dredged material." *Rock and Soil Mechanics*, Vol. 29 (Supp.): 567-570.

Research on New Dam Structure for High Earth Core Rockfill Dam on Thick Overburden

Han Xu¹, Bin Huang², Xibao Rao³, Jiajun Pan⁴, Yun Chen⁵

Key Laboratory of Geotechnical Mechanics and Engineering of the Ministry of Water Resources, Changjiang River Scientific Research Institute, Wuhan 430010, China

¹mechanics007@yahoo.com.cn, ²36269283@qq.com, ³raoxibao8899@126.com,

⁴511074651@qq.com, ⁵56764018@qq.com

ABSTRACT: For high earth core rockfill dam constructed on thick overburden, traditional anti-seepage system design and construction is to construct the foundation seepage cut-off wall first, and then build a rigid or soft-connected grouting gallery on top of seepage cut-off wall, and then cover the gallery with high plastic clay. Therefore, after the construction, the high dam body transmits great pressure to the seepage cut-off wall through the gallery. For this reason, a new type of structure for high earth core rockfill dam constructed on thick overburden is proposed, namely constructing a “concrete slab” with a large dimension gallery on the overburden, so that the seepage cut-off wall can be constructed from the inside of the large dimension gallery during or after construction of the dam body to reduce the stresses in the cut-off wall. The cut-off wall and the concrete slab on the overburden, together with the upper dam body, form a complete anti-seepage system, but it has not been used in actual dam construction. In this paper, two-dimensional finite element stress and deformation analyses were carried out to assess the effects of the proposed concrete slab and cut-off wall construction sequence on a 223-meter high earth core rockfill dam constructed on thick overburden. The stresses and deformations of the concrete slab are obtained, and its structural safety and suitability for use in earth core rockfill dam are also evaluated. According to research results, by rationally adjusting the construction order of the dam body and the cut-off wall, the compressive stresses on the cut-off wall can be controlled, which has been a big problem for traditional structures. It reflects the advantage of the new structure.

INTRODUCTION

For high earth core rockfill dam constructed on thick overburden, traditional

anti-seepage system design and construction is to construct the foundation seepage cut-off wall first, and then build a rigid or soft-connected grouting gallery on top of the cut-off wall, and finally cover the gallery with high plastic clay, as shown in Figure 1. However, it has been difficult to extend such traditional anti-seepage structure to over 200-meter high earth core rockfill dams built on 100-meter-thick overburden.

The reason is that direct dam construction without removing overburden will result in large differential settlement between the cut-off wall and the over 100-meter-thick overburden, and friction between the two will cause huge compressive stresses on the cut-off wall. In addition, since the dam is over 200-meter high, pressure transmitted through gallery to the cut-off wall is also massive. In another word, self weight, friction from surrounding compressible soils, combined with the gravity and water pressure from the dam would create a huge stress on the cut-off wall, which could surpass the maximum compressive strength of the concrete cut-off wall, and cause compression failure of the cut-off wall.

THOUGHTS ON THE NEW STRUCTURE

From the above, the new structure needs to overcome the following two problems of traditional structures.

(1) Over 223-meter high dam built on over 100-meter-thick overburden causes excessive compressive stresses on cut-off wall.

(2) In the construction sequence of traditional structure, the dams can not be constructed until the cut-off wall is finished, so the construction period is too long.

In order to solve the above problems, a new gallery structure is proposed. By building up a “concrete slab” with large dimension gallery on the overburden, the cut-off wall can be constructed inside the large dimension gallery. Cut-off wall and concrete slab on the overburden and the upper dam body altogether constitute a complete anti-seepage system. The structure diagram is as shown in Figure 2. This new structure has not been used in actual dam construction.

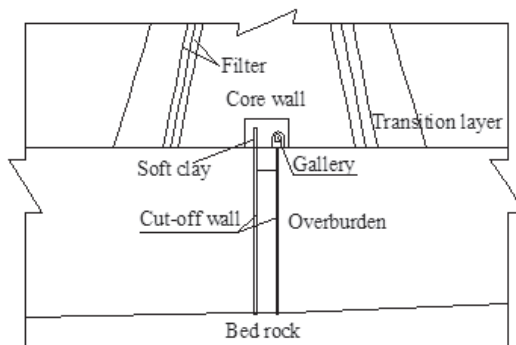


FIG. 1. Sketch map of traditional structure.

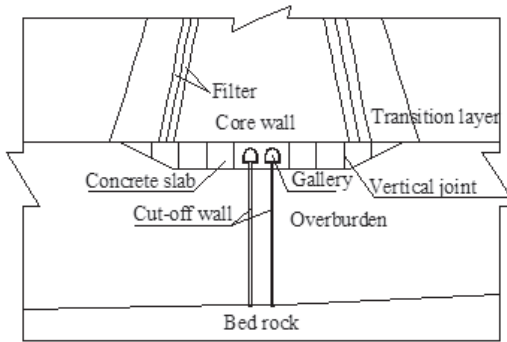


FIG. 2. Sketch map of new structure.

CALCULATION MODEL AND PARAMETERS

Calculation is conducted on a 223-meter high earth core rockfill dam constructed on a 100-meter-thick overburden, as shown in Figure 2. The geology of the overburden is all granular material.

The elevation of dam bottom (overburden top surface) is 0; crest elevation is 223m; reservoir water level elevation is 215m; upstream slope ratio of the dam body is 1V: 2.25H and that of the downstream is 1V: 2H. Two 1.2-meter-thick cut-off walls are set up, with their bottom penetrating 1m into the bedrock, and the space between the two cut-off walls is 12m. Concrete slab is 20m high and is distributed along the bottom of the core wall with a length of about 100m. There is a vertical joints every 15m. Upstream and downstream gradient of the cover plate is 1: 2. Two large dimension galleries are 7m wide and 7m high.

The Duncan-Zhang E-B stress-strain model is used for the material of dam body and overburden, and the calculation parameters of dam body are selected according to large dimension triaxial test. Finite element method is applied to study the stress and deformation characteristics of the dam body and concrete slab in various new dam structure design plans, and evaluate their structural safety under high stress and high water head. In order to accurately calculate the interaction between cut-off wall and overburden, the following contact friction elements are set up on multiple interfaces with discontinuous stiffness. Zero-thickness contact friction element simulates the mechanical property of dam body with different stiffness. Be based on actual testing data the friction angle between overburden and cut-off wall is 11° .

DEFORMATION OF DAM

First, the initial stress field of the overburden is set up in the computer model, and then the dam body is constructed in the model. Construction of the dam is simulated in 23 lifts, with each lift of about 10m thick of the dam fill. The

reservoir storage loading is simulated in 5 stages, and the buoyancy of the upstream dam body caused by rising phreatic surface is also taken into account.

The contours of the dam body's horizontal and vertical displacements are shown in Figure 3 and 4, respectively. The computed maximum vertical and horizontal displacements are 4.5m and 1.6m, respectively. Due to the 100-meter-thick overburden and the large weight of the dam body, the overburden has a large settlement with a maximum of about 2.9m; dam body's own settlement is about 2.4m. Therefore, differential settlement between the overburden and the cut-off wall can cause high compressive stresses of the cut-off wall.

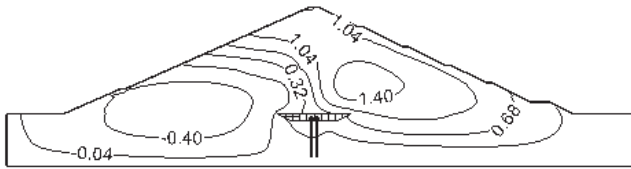


FIG. 3. Contour of horizontal displacement (m)

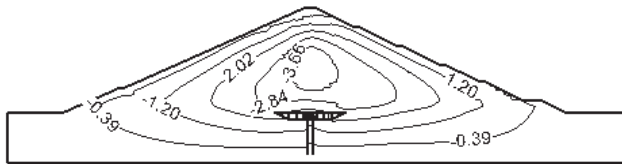


FIG. 4. Contour of vertical displacement (m).

STRESS OF TRADITIONAL CUT-OFF WALL

In the traditional method, stiff-connected gallery is adopted for concrete cut-off wall and then covered by high plastic clay. Therefore, the maximum compressive stress of the cut-off wall at the end of dam construction is calculated as 68MPa, and the compressive stress increases to 75MPa after reservoir filling. This greatly exceeds the material's compressive strength, and can cause compression failure of the cut-off wall.

STRESS AND DISPLACEMENT OF NEW CUT-OFF WALL

New structure enables construction of cut-off wall inside the gallery. Therefore, construction of the dam body and the cut-off wall can be carried out independently. In order to study the impact of construction order on the cut-off wall and the concrete slab, the following three calculation schemes are established and compared. Details are shown in Table 1. By conducting nonlinear finite element method, the interaction between the concrete slab and the cut-off wall can be discussed in detail, and the impact of the concrete slab and its surrounding dam body on the stress change of concrete cut-off wall can be systematically studies.

Table 1. Calculation Scheme for New Structure with Concrete Slab

| Scheme | Construction Order |
|----------------|--|
| Working mode 1 | First construct cut-off wall, and then dam body |
| Working mode 2 | First construct 1/2 of the dam body, and then construct cut-off wall |
| Working mode 3 | First construct the dam body and then cut-off wall |

The displacement curves and the state of stresses of the cut-off wall after reservoir filling under the above 3 working modes are shown in Figure 5 and 6, and Figure 6(a) also shows the vertical stress of the cut-off wall at the end of construction. The negative sign means compressive stresses in Figure 6.

It is shown that the maximum horizontal displacement of the cut-off wall is 42cm, independent of the working modes. This is because for all the working modes, the horizontal displacement of the cut-off wall is mainly caused by water pressure during the reservoir period, and the reservoir water pressure of all the working modes are basically the same. Therefore, it is shown that that the cut-off wall construction order has little impact on the horizontal displacement of the cut-off wall.

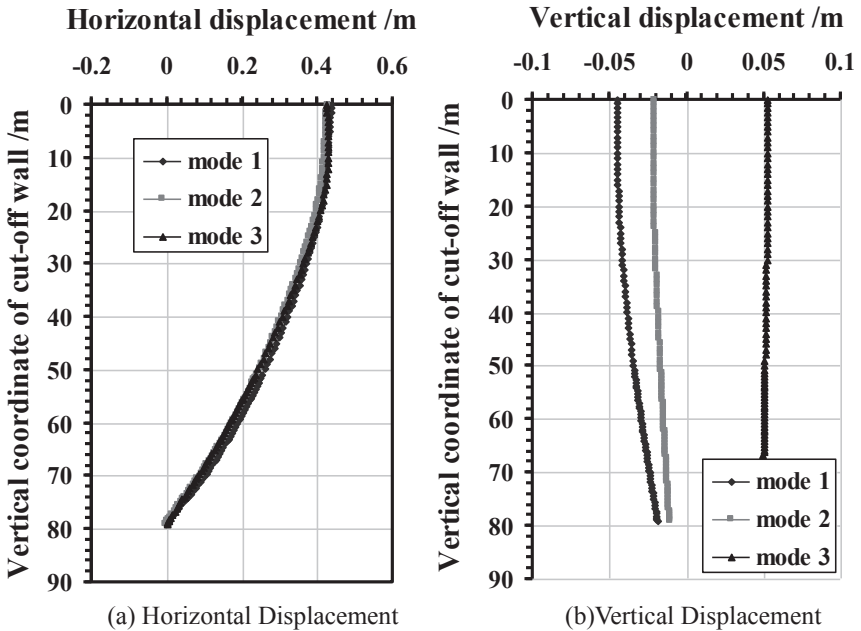


FIG. 5. Displacement curve of cut-off wall during the storage period (m): (a) horizontal displacement; (b) vertical displacement.

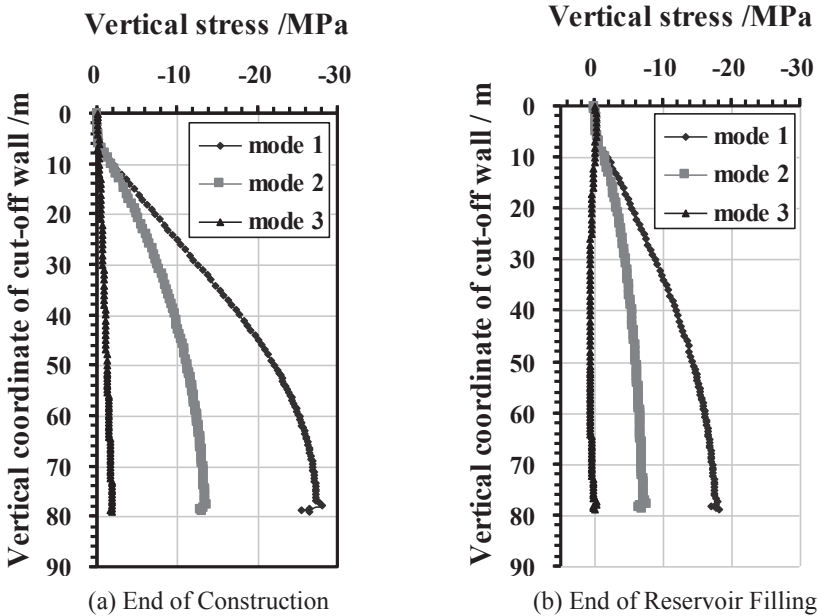


FIG. 6. Vertical stress curve of cut-off wall: (a) end of construction; (b) end of reservoir filling.

For working mode 3, due to relatively small vertical stress on the cut-off wall at the end of construction, the hydrostatic water pressure at the end of reservoir filling turns the cut-off wall into an eccentric tension member, which results in larger tensile stress with maximum of 2.0MPa. Evidently, this working mode fails to satisfy the design requirements of limited tensile stress of in the cut-off wall, thus this working mode cannot be adopted.

Under working mode 1 and 2, before reservoir filling, settlements of the overburdens adjacent to the cut-off walls leads to certain vertical stresses on the cut-off walls. After reservoir filling, despite of large hydrostatic pressure, the cut-off wall remains an eccentric compression member without too large tensile stress. In addition, under working mode 1, the relative displacement between the overburden and the cut-off wall is larger than that under working mode 2, therefore the frictional stress on the cut-off wall under working mode 1 is also larger than that under working mode 2. From the perspective of controlling the frictional stresses on the cut-off wall, it may be a better choice to construct the dam body to a certain height before constructing the cut-off wall.

From above, it can be seen that the new structure enables control of the frictional stresses to the cut-off wall by changing the construction order, and thus reduce the compressive stresses on the cut-off wall.

STRESS AND DISPLACEMENT OF CONCRETE SLAB

The distribution of horizontal and vertical stresses on the concrete slab is shown in Figure 7. The stresses at the crowns of the galleries are complicated, but the state of stress is little influenced by the construction order of the cut-off wall. Under the three working modes, the extreme values of the stress at the crowns of the galleries remain similar between the end of construction and the end of reservoir filling. At the crown and area between the two galleries, tensile stresses are observed, indicating some bending has occurred in these areas. However, as long as the concrete above the gallery crown has certain thickness, the tensile stress can be under control within a reasonable range.

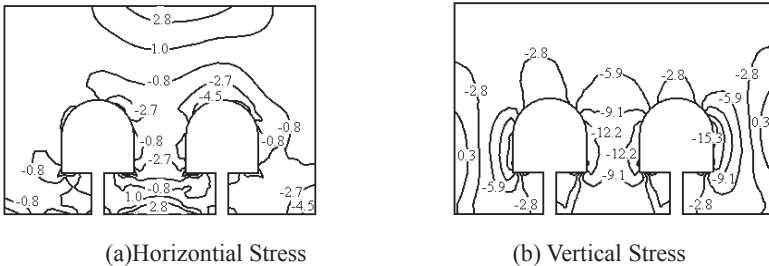


FIG. 7. Contour of concrete slab stress (MPa): (a) horizontal stress; (b) vertical stress.

The maximum alternate displacement between each vertical joints of concrete slab is 5cm, while maximum tension displacement is 2cm; according to the control standard of sealing design of current hydro-structure, the alternate displacement and tension displacement are both within acceptable range in engineering. Therefore, as long as the concrete slab has reasonable joints, its stress and deformation will also be acceptable. However, any tension cracks in the concrete slab or along the concrete slab joints will cause concerns to seepage, in order to ensure the safety of concrete slab, the potential seepage effect of this structure will be examined and optimized carefully in the next stage.

CONCLUSIONS

(1) The main advantage of the new structure is that it avoids excessive compressive stress on top of the cut-off wall transmitted from upper dam body, and it greatly reduces stress on the cut-off wall; it also enables construction of the cut-off wall from the inside of the gallery. Therefore, it is a positive approach in terms of structural behavior and construction organization;

(2) Before water storage, it is beneficial to maintain certain pressure stress on the cut-off wall, for it ensures cut-off wall as eccentric compression member under the reservoir load, which ensures not too much tensile stress. According to the

calculation results, it indicates that under the working mode 2, i.e. constructing the dam body to 1/2 before constructing the cut-off wall, the stress on the cut-off wall at the end of construction and reservoir filling remains within the acceptable range in engineering, and it demonstrates the advantage of the new structure.

(3) However, any tension cracks in the concrete slab or along the concrete slab joints will cause concerns to seepage, in order to ensure the safety of concrete slab, the potential seepage effect of this structure will be examined and optimized carefully in the next stage.

ACKNOWLEDGMENTS

This research is financially supported by Ministry of Water Resources' Special Funds for Scientific Research on Public Causes of China(Grant No. 201201039) and National Natural Science Foundation of China(Grant No. 51109013).

REFERENCES

- Li, N.H., Mi, Z.K., Li, G.Y., et al. (2004). "Numerical Analysis of Stress Deformation Behavior of Concrete Diaphragm Wall in Super-deep Overburden of Yele Hydropower Station. " *Hydro-Science and Engineering*, Vol. (1): 18-23.
- Li, N.H., Sun, D.W., Mi, Z.K., et al. (2005). "Optimization Analysis on Length of Connection Slab for High Concrete Faced Rockfill Dam on Deep Alluvium Deposit". *Water Resources and Hydropower Engineering*, Vol. 36 (7): 81-85.
- Wei, Z.R.. (2002). "Kan'erqi Bituminous Concrete Core Dam Built in Deep Overburden". *Experiences and Problems in the Construction of Earth and Rock Dam*, Shaanxi People's Publishing House, Vol. 9: 315-318.
- Pan, J.J., WANG, M.Y., Xu, H. (2009). "Three-dimensional Finite Element Analysis of High Earth Core Rockfill Dam on Deep Overburden". *Modern Rockfill Dams-2009*, China Water Conservancy and Hydropower Press.
- Wang, B.L. (2004). "Chinese Contemporary Earth and Rock Dam Project". China Water Power Press.

Shear Strength Characteristic of Fissure Plane in Expansive Soil

Hu Bo¹ and Sun Hui²

¹Senior Engineer, Yangtze River Scientific Research Institute, Jiangda Road, Wuhan, Hubei, China 86-27-82927141, woshihubo135@sina.com

²Doctor, Yangtze River Scientific Research Institute, Jiangda Road, Wuhan, Hubei, China 86-27-82820427, sunhui_hust@126.com

ABSTRACT: Fissures generally exist in all of expansive soils. It always results in failure of expansive soil slope. Shear strength characteristics of fissure plane is studied and a new triaxial test method is recommended with typical expansive soil taken from Nanyang section of middle route of the South-to-North Water Transfer Project (SNWTP). The computed tomography technology is firstly introduced to shear strength test of fissure plane. The real failure stress of fissure plane is analyzed accurately through measurement of the fissure plane's real occurrence by CT scanning and shear strength parameters determined method is provided for triaxial test of fissure plane. The test results show that peak strength of fissure plane is much lower than that of bilateral expansive soil without fissures, and even smaller than residual strength of bilateral expansive soil without fissures. The reasons of these phenomena are that gray clay in fissures has higher water content, smectite content and particles orientation degree.

INTRODUCTION

Investigations by Skempton et al. (1969) and Skempton (1977) indicate that the development of a fissure can result in softening of surrounding overconsolidated clay. The softening corresponds to an increase in water content caused by soil dilation under the imposed shear stress. Softening reduces the effective stress cohesion component of the Mohr-Coulomb shear strength parameters but does not cause orientation of clay particles or reduction in friction angle (Skempton 1970). In a material with randomly oriented fissuring the larger the sample the higher the probability that the failure plane will contain properly oriented fissures and it has been demonstrated by Skempton and Piltley (1967), Lo(1970) that in fissured clays the size of the test specimen has a major effect on shear strength.

In macroscopic view, strength of expansive soil includes strength of soil block without fissure plane, strength of fissure plane and strength of soil mass. Strength of expansive soil mass is an integral index reflecting strength of expansive soil block and strength of fissure plane. However, factors such as distribution range, spacing, gradient, orientation, shape of fissures and coarseness or unevenness of fissure plane,

and quality of integral soil block between fissures, etc. contribute to the impacts on strength of soil mass; in addition, owing to the uneven distribution of fissure, shear strength of expansive soil reveals an intensively anisotropic feature.

Fissures generally exist in expansive soils. Fissures in expansive soil include initial and secondary fissures, currently there is uncertainty for generative mechanism of initial fissures. Liu (1997) pointed out that initial fissures referred to fissures resulted from actions of geological forces due to temperature, humidity and uneven effects of expansion and contraction during soil formation; while secondary fissures referred to newly generated ones resulted from soil weathering, drying and wetting cycle and other change for ambient environment. Initial fissures in expansive soils become waxen in color, and most of them are filled with gray clay. Major papers on fissure analyses that initial fissures in expansive soils have significant impact on strength of expansive soil mass, strength of fissure depends on strength of gray clay filled into fissures, and most fissures existing in expansive soils always result in failure of expansive soil slope, which occurs along such kind of fissure plane (Liu 1997; Feng and Wang 1993). Many landslides occurred in succession at Nanyang section of middle route for SNWTP during excavation and test, and sequential geological surveys still proved that sliding plane is mostly composed of weak bed plane or fissure plane in expansive soil or of through-run fissure plane in expansive soil.

In view of control of fissure plane over stability of expansive soil slope, many scholars studied on strength of fissure plane in expansive soil. Liao (1984) have conducted unconfined compression tests on natural expansive soils with different diameters after sampling from several areas, and then managed to figure out impact of fissure plane on strength of expansive soil based on dimensional effect of expansive soil strength. Similarly, site shear test method was adopted to test strength of expansive soil with large scale samples, attempting to reflect strength of expansive soil mass with a single strength index. Hu (1994) elaborated formation and distribution of fissure and analyzed impacts of inclination angle, fissure quantity, thickness of fissure clay and other factors on fissure clay strength in Chengdu area based on triaxial test. In view of failure to division of strength of expansive soil into strength of expansive soil block and strength of fissure plane, such study only exquisitely specified impact of fissure on strength of expansive soil, so it failed to make deep and quantitative analysis or to make separate study on strength of fissure plane in expansive soil. Owing to less thick fissure plane in expansion soil and curved distribution of fissures except some flat fissures, shear plane is usually hard to fully extend along fissure plane during fissure strength test via direct shear method. In light of these above, Bao and Liu (1990) specially expressed strength of expansive soil by the following formula.

$$\tau_{fm} = s \times \tau_{ff} + (1 - s) \times \tau_{fb} \quad (1)$$

where τ_{fm} 、 τ_{ff} 、 τ_{fb} are shear strength of expansive soil mass, fissure plane and expansive soil block without fissure plane, respectively, s is the ratio of area of well-sheared fissure to total area of shear plane. Such formula's proposition plays a positive role in understanding strength of expansive soil mass, strength of fissure plane, strength of soil block and their correlation. However, in application of this formula, strength of expansive soil mass, strength of soil block and ratio of soil block area to

total shear area should be determined before obtaining strength of fissure plane, so it fails to directly test strength of fissure plane in expansive soil. In this article, initial expansive soil taken from Nanyang section of middle route for SNWTP was selected and direct shear test method was adopted to test strength of flat fissure plane of expansive soil; then a new method to conduct triaxial test on fissure plane and determine strength parameters was proposed based on determining the inclination angle of non-flat fissure plane by CT 3D images, while analysis on strength characteristic of fissure plane in expansive soil was also carried out.

Direct Shear Test of Fissure plane in Expansive Soil

The sample was the typical expansive soil taken from Nanyang section of middle route for SNWTP under the conditions of natural water content. When preparing undisturbed soil for direct shear, flat fissure plane was selected for shear according to fissure orientation to ensure that both the upper and the lower soil sample was 10mm in thickness, thus a set of slow direct shear test of fissure plane can be conducted; and at the same time, a set of repeated direct shear test of expansive soil without fissure can be carried out. The free expansion rate of expansive soil without fissure was 61%, its moisture content was 23%, and the moisture content of gray clay in fissure plane was 32%. The sample size: diameter 61.8mm, height 20mm. The saturation of the sample was 90% and the dry density was 1.62g/cm^3 . The test equipment is Electric Strain-controlled Direct Shear Apparatus. Shear rate of the direct shear test is 0.015mm/min , and consolidation pressure is 100, 200, 300 and 400kPa, respectively. The consolidation settlement of the sample was estimated before loading, and the bottom of the sample was filled up with a corresponding permeable plastic sheet so that the shear could be strictly carried out along fissure plane. After the test, the shear plane of the sample was photographed.

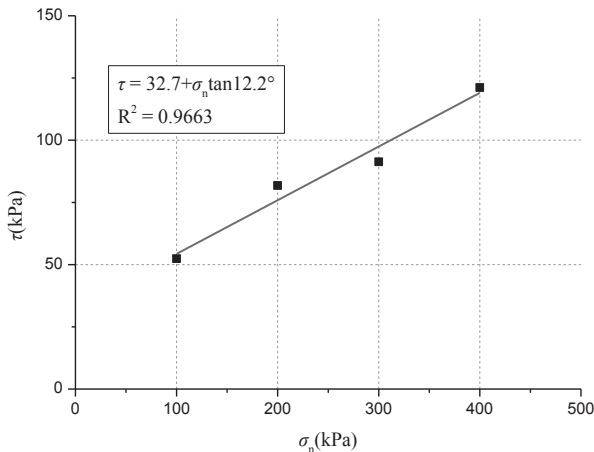


FIG. 1. Mohr-Coulomb curve of fissure plane filled with gray clay.

Figure 1 shows Mohr-Coulomb curve of fissure plane filled with gray clay. Figure 1

shows that cohesion c of fissure plane filled with gray clay is 32.7kPa, internal friction angle $\varphi = 12.2^\circ$. Figure 2 shows the photo of fissure plane filled with gray clay after direct shear test. It is known from Figure 2 that the fissure planes of the four samples are filled evenly with gray clay, the shear process is carried out along fissure plane filled with gray clay, and the strength of direct shear tests is the one of fissure plane filled with gray clay.

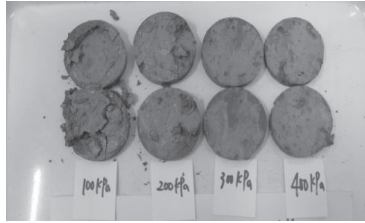


FIG. 2. Photo of fissure plane filled with gray clay after direct shear test.

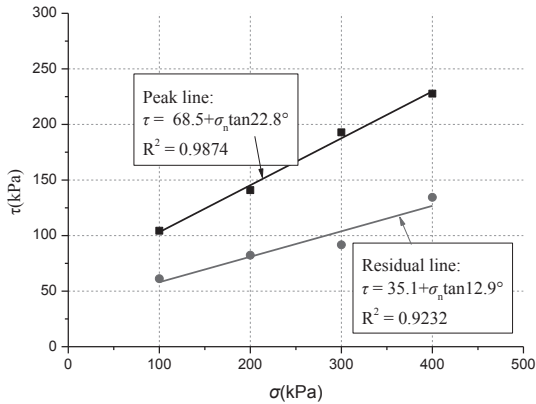


FIG. 3. Peak and residual strength Mohr-Coulomb curves of expansive soil without fissure.

Expansive soil without fissure at the same place of the fissure plane was sampled for repeated direct shear tests. There was a total of six shear test process, the shear displacement of each process was 8cm. Peak strength Mohr-Coulomb curve can be gained based on the peak of the curve of the first shear-way shear stress vs. shear displacement; and residual strength Mohr-Coulomb curve can be obtained as well based on the stable value of the curve of the six shear-way shear stress vs. shear displacement, as is shown in Figure 3. Figure 3 shows that the sample's peak strength cohesion c of expansive soil without fissure is 68.5kPa, internal friction angle $\varphi = 22.8^\circ$; cohesion c of residual strength is 35.1kPa, internal friction angle $\varphi = 12.9^\circ$.

Triaxial Test of Fissure plane in Expansive Soil

The shear plane of direct shear tests (including laboratory direct shear test and site large shear test) is fixed between the upper direct shear box and the lower one, but the shear plane is usually hard to fully extend along fissure plane via direct shear test of non-flat fissure planes. Hence, triaxial test is recommended with its advantages of overcoming the above-mentioned shortcoming and ensuring the shear plane extending along the weakest fissure plane.

A triaxial test of fissure plane was carried out with typical expansive soil taken from Nanyang section of middle route project for South-to-North Water Transfer. Sample size: diameter 39.1mm, height 80mm. Shear rate of the sample was 0.015mm/min. When preparing undisturbed soil for triaxial test, the fissure should be in the middle of the sample as much as possible. Make sure to take pictures and CT scan the fissure of the sample before sample loading, and its failure mode be photographed and recorded after the test. At the same time, the sample should be CT scanned for the reconstruction of its orthographic views via its three-dimensional CT images and the determination of the angle of inclination between the fissure plane and the horizon. Figure 4 shows the photo of Siemens Sensation40 CT apparatus used by Key Laboratory of Geotechnical Mechanics and Engineering of the Ministry of Water Resource.



FIG. 4. Siemens Sensation40 CT apparatus.

Figure 5 shows the typical photos of fissure plane filled with gray clay before and after triaxial test. It can be seen that the shear plane extends along the fissure plane filled with gray clay. It can be concluded that the shear strength obtained from the test is the strength of the fissure plane. Figure 6 shows CT photo of fissure plane filled with gray clay, and the angle between the shear plane and the horizontal plane can be measured from the photo. Based on the above-mentioned test methods, the new triaxial test data processing method is as follows: peak stress ($\sigma_{1f}-\sigma_{3f}$) of the sample being damaged can be obtained via stress-strain curve of triaxial test results. On the basis of static equilibrium conditions, normal stress σ_n and shear stress τ_f of the fissure plane being damaged can be calculated by using equation (2) and (3), respectively.

$$\sigma_n = \frac{(\sigma_{1f} + \sigma_{3f})}{2} + \frac{(\sigma_{1f} - \sigma_{3f})}{2} \cos 2\alpha \quad (2)$$

$$\tau = \frac{(\sigma_{1f} - \sigma_{3f})}{2} \sin 2\alpha \quad (3)$$

Shear strength parameters c and φ of the fissure plane can be obtained via arranging the relationship curve between normal stress and shear stress in the light of Mohr-Coulomb's law. In Eq. (2) and (3), σ_n is normal stress and τ_f is shear stress of shear failure plane; σ_{1f} is the peak major principal stress; σ_{3f} is the peak minor principal stress; and α is the angle between the shear failure plane and the horizon, it can be obtained from the CT image.

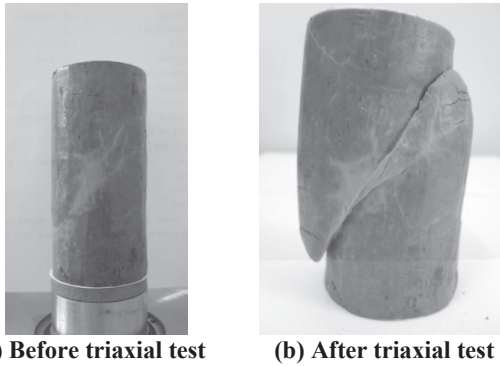


FIG. 5. Typical photos of fissure plane filled with gray clay: (a) before triaxial test; (b) after triaxial test.

Through a large number of triaxial tests on fissure plane filled with gray clay, we can get a curve reflecting the relationship between normal stress σ_n of the fissure plane and shear stress τ_f of the fissure plane as is shown in Figure 7. It can be seen from Figure 7 that cohesion c of the fissure plane filled with gray clay is 29.5kPa, while internal friction angle $\varphi = 11.9^\circ$.

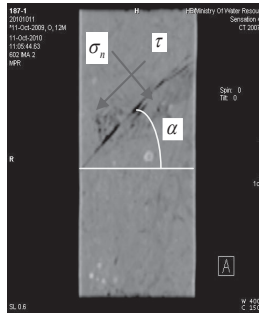


FIG. 6. CT photo and stresses of fissure plane.

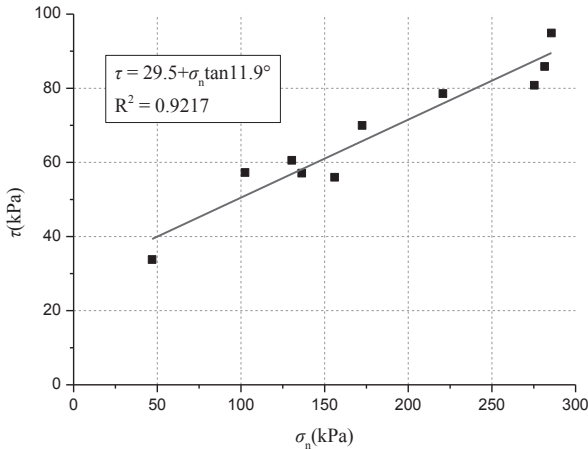


FIG. 7. Relationship between σ_n and τ_f of fissure plane filled with gray clay.

STRENGTH CHARACTERISTICS ANALYSIS OF EXPANSIVE SOIL

Table 1 shows strength parameter indexes of expansive soil with fissure. The strength index of fissure plane filled with gray clay via triaxial tests is very close in value to that of direct shear tests. Specifically, direct shear test on strength of fissure plane must be carried out on the premise that flat fissure plane must be sampled for shear and that the shear plane of the sample and the fissure plane be completely overlapped. In addition, the peak cohesion and internal friction angle of fissure plane filled with gray clay is much smaller than peak strength parameters of expansive soil without fissure. Low strength of fissure plane in expansive soil owes to the following three aspects: (1) Water content of gray clay in fissure plane is 9% higher than that of bilateral expansive soil without fissure. Existing research (Tan and Kong 2006; Kong 1994) suggests that the water content of the fissure planes of expansive soil in Yunnan and Chengdu clay is significantly higher than that of bilateral soil mass. (2) The montmorillonite content of the gray clay in fissure plane is relatively high.

Table 1. Shear strength parameters of expansive soil with fissures

| Strength Parameters | $\phi(^{\circ})$ | c(kPa) |
|--|------------------|--------|
| Peak strength parameters of fissure plane filled with gray clay (Direct shear test) | 12.2 | 32.7 |
| Peak strength parameters of fissure plane filled with gray clay (Triaxial test) | 11.9 | 29.5 |
| Peak strength parameters of expansive soil block without fissure (Direct shear test) | 22.8 | 68.5 |
| Residual strength parameters of expansive soil block without fissure (Direct shear test) | 12.9 | 35.1 |

Table 2 shows the mineral composition analysis of Nanyang expansive soil. It can be seen from Table 2 that the montmorillonite content of the gray clay in fissure plane is 26.5%, while that of bilateral soil mass is 22.9%. Montmorillonite content affects shear strength of clay significantly. Feng and Yan (1977) carried out shear strength tests on montmorillonite, kaolinite and illite as well as on the mixture of different proportions. The results showed that internal friction angle began to reduce when montmorillonite content reached 5% or more. As for the mixed sample of montmorillonite and kaolinite, when montmorillonite content exceeded 30%, internal friction angle was mainly decided by montmorillonite, and kaolinite had minimal impact; in the mixed sample of montmorillonite and illite, when montmorillonite content exceeded 20%, montmorillonite played the major role on deciding internal friction angle of the mixed sample. (3)The fissure plane filled with gray clay had higher particles orientation degree, so it presented a highly directional arrangement structure.

Table 2. Mineral composition analysis of Nanyang expansive soil

| Mineral composition (%) | Bilateral soil | Fissure clay |
|--------------------------------|-----------------------|---------------------|
| Quartz | 33 | 29 |
| Feldspar | 14 | 10 |
| Calcite | 0 | 8 |
| Amphibole | 2 | 0 |
| Monrmorillonite | 22.9 | 26.5 |
| Illite | 15.3 | 13.3 |
| Kaolinite | 10.2 | 10.6 |
| Chlorite | 2.6 | 2.7 |

Table 3. Chemical composition analysis of Nanyang expansive soil

| Chemical composition (%) | Bilateral soil | Fissure clay |
|---------------------------------|-----------------------|---------------------|
| SiO ₂ | 65.12 | 59.12 |
| Al ₂ O ₃ | 14.88 | 16.19 |
| Fe ₂ O ₃ | 5.93 | 3.84 |
| CaO | 0.97 | 4.92 |
| MgO | 1.36 | 1.48 |
| K ₂ O | 2.58 | 2.41 |
| Na ₂ O | 0.96 | 0.82 |
| TiO ₂ | 0.71 | 0.75 |
| P ₂ O ₃ | 0.13 | 0.07 |
| MnO ₂ | 0.14 | 0.03 |
| Ignition loss | 6.88 | 10.32 |

At the same time, it can be seen from Table 1 that both peak cohesion and internal friction angle of fissure plane filled with gray clay is slightly lower than residual strength parameters of expansive soil without fissure. Previously researchers have thought that intensity of fissure plane in expansive soil or intensity of weak structural

plane was close to residual strength of expansive soil, and thus concluded that residual strength of expansive soil must be the lower limit of strength of expansive soil accordingly. However, the mineral and chemical composition analysis from Table 2 and 3 proved that gray filling material in fissure plane and bilateral expansive soil is two completely different sorts of soils in mechanical properties; there is therefore no comparability between the two in theory. Kong (1994) validated via experimental studies the possibility of bilateral parent soil turning into gray clay through long-term leaching behavior of groundwater in weakly alkaline conditions. In microscopic view, leaching changes ferric iron oxide in expansive soil to ferrous oxide and that results in gray clay in fissures whose color is different from expansive soil besides fissures, and Table 3 shows that iron oxide content of gray clay in fissures is significantly higher than that of bilateral expansive soil; In mesoscopic view, mineral composition and particles arrangement of expansive soil have been modified by leaching and filling material in fissures have higher smectite content and particles orientation degree; In macroscopic view, factors mentioned above result in significant difference in strength characteristic between fissure plane and bilateral expansive soil, which is also the reason why peak intensity of fissure plane is lower than residual strength of expansive soil.

CONCLUSIONS

1. Shear plane of direct shear tests (including laboratory direct shear test and site large shear test) is fixed between the upper direct shear box and the lower one, and thus shear plane is usually hard to fully extend along fissure plane in the process of test. As to this problem, CT technology is firstly introduced to shear strength test of fissure plane. The real failure stress of fissure plane is analyzed accurately through measurement of the fissure plane's real occurrence by CT scanning and shear strength parameters determined method is provided for triaxial test of fissure plane.

2. The comparison between direct shear test results and triaxial test results shows that peak strength of fissure plane filled with gray clay in Nanyang is much lower than that of bilateral expansive soil, and even smaller than the residual strength of bilateral expansive soil. The reasons of these phenomena are that gray clay in fissures has higher water content, smectite content and particles orientation degree.

3. In microscopic view, leaching changes ferric iron oxide in expansive soil to ferrous oxide and that results in gray clay in fissures whose color is different from expansive soil besides fissures; In mesoscopic view, mineral composition and particles arrangement of expansive soil have been modified by leaching and filling material in fissures have higher smectite content and particles orientation degree; In macroscopic view, factors mentioned above result in significant difference between fissure plane and bilateral expansive soil in mechanical strength.

ACKNOWLEDGMENTS

The support of the Chinese National Natural Science Fund through research grant 51008035 and 51108042 is gratefully acknowledged.

REFERENCES

- Bao, C. G. and Liu, T. H.(1990). "Shear strength of swelling soil in Nanyang district, Henan province." *Journal of Yangtze River Scientific Research Institute*, 7(2):1~8.
- Cheng, Z. L., Li, Q. Y., Guo, X. L., and Gong, B. W. (2011). "Study on the stability of expansive soil slope." *Journal of Yangtze River Scientific Research Institute*, Vol. 28(10): 3-11.
- Feng, G. Y., and Wang, X. F.(1993). "Stability of expansive soil canal slopes of Middle Route Project for South-to-North Water Transfer." *Yangtze River*, 24(3):9-14.
- Feng, G. Y., and Yan, Y. F.(1977). "Shear Strength of kaolin, illite, montmorillonite clay and its mixtures. *Yangtze River Press*, Wuhan.
- Hu, X. W., Liu, Q. F. and Zhao, Z. S.(1994). "Mechanical properties of fissured clay." *Chinese Journal of Geotechnical Engineering*, 16(4):81~88.
- Kong, D. F.(1994). "Fissured clay." *Geology Press*, Beijing.
- Liu, T. H.(1997). "Expansive soil problems in engineering construction." *China Architecture and Building Press*, Beijing.
- Liao, S. W.(1984). "Expansive Soil and Railway Engineering." *China Railway Publishing House*, Beijing.
- Lo, K. Y.,(1970). "The operational strength of fissured clays." *Geotechnique*, 20(1):57-74.
- Skempton, A.W., and Petley, D. J.(1967). "The strength along structural discontinuities in stiff clays." *Proc. Geotech. Conf.*, Oslo 2: 29-46.
- Skempton, A.W., Schuster, R. L., and Petley, D. J.(1969). "Joints and fissures in the London clay at Wraysburg and Edware." *Geotechnique*, 19(2):205-217.
- Skempton, A.W. (1970). "First-time slides in over-consolidated clay." *Geotechnique*, 20(3):320-324.
- Skempton, A.W. (1977). "Slope stability of cuttings in brown London clay." *Proc. 9th Int. Conf. Soil Mech. and Found. Engrg.*, Tokyo, 3, 261-270.
- Tan, L. R., and Kong, L.W.(2006). "Soil texture theory of special geotechnical engineering." *China Science Press*, Beijing.

Dynamic Model of Subgrade Using a Coupled Vehicle-Track-Subgrade Method

Xue Ning Ma^{1,2*}, Xu Wang^{1,2}, Bo Liang³, Song Hong Yan^{1,2}

¹Lanzhou Jiaotong University, Key Laboratory of Road & Bridge and Underground Engineering of Gansu Province, Lanzhou, 730000, China

²School of Civil Engineering, Lanzhou Jiaotong University, Lanzhou, 730070, China

³School of Civil Engineering, Chongqing Jiaotong University, Chongqing 400074, China

*Corresponding author, PH (86)13519611942; email: mxn1974@163.com

ABSTRACT

It is very critical to understand the dynamic interaction of vehicle-track-subgrade for high speed railway development. This paper presents a dynamic interaction model of vehicle-slab track-subgrade system, in which a slab track-subgrade structure is put forward as a substructure and is studied considering track irregularity excitation and displacement compatibility condition. In this model both the actual structure of a vehicle and vibration characteristic of the substructure including slab track, subgrade and foundation are considered. This model not only reflects the interaction between vehicle and substructure completely, but also provides a theoretical foundation for determining design parameters of high speed railway (especially for design parameters of track and subgrade). Research results can provide technical reference for design and construction of slab ballastless track and subgrade structure of high speed railway.

INTRODUCTION

High speed railway emerges as an efficient transportation tool with the advantages of high-speed, safety and comfort. In China, high speed railway in service and under construction is built using ballastless track technique instead of ballasted track. It has been evident to railway industry that the traditional ballasted track has poor stability and growing deformation after long term repeated train load. And ballast can be easily worn and powdered after certain years of service. It is difficult for ballasted track to maintain a good geometric condition due to discontinuity of rail support point. Ballastless track can easily overcome the above problem, which represents a high strength structure behaving like a rigid structure and maintains a good geometric shape in service. The stability can be greatly improved and the amount of maintenance work is greatly reduced too. Because the study on ballastless track paved on soil subgrade just started, one of the key techniques to be solved is how to control residual deformation of soil subgrade for meeting ballastless track paving and long-term

operation.

For a long time, study on ballastless track is always limited in statics analysis, and the study on its dynamic behavior is less. During the past few decades, some progress has been made in understanding dynamic behavior of the ballastless track and vehicle-ballastless track-subgrade. Most of these existing researches have been focused on vehicle-track structural dynamic interaction and coupled vibration of vehicle-structure system. NIELSEN, et al.(1995) investigated the vertical dynamic behavior for a railway bogie moving on a rail which is discretely supported, via rail pads, by sleepers resting on an elastic foundation. KNOTHE, et al.(1993) established the modeling of railway track and vehicle/track interaction at high frequencies. VERBIC B(1997) built up a vertical analyzing model of ballastless track to study its dynamic properties according to boundary finite element method. ZHAI, et al.(1999) depended on wheel-rail system dynamic theory, simplified the track structure into some beams with finite length, and built vibration equations of slab track by using modality method. HE, et al.(2006) studied the dynamic properties of ballastless track by using finite stripe method. Little effort has been devoted to the dynamic properties of subgrade. The existing theoretical analyses and studies can't completely meet the requirements of design, construction and maintenance of high speed railway subgrade. FENG, et al.(2008) studied vibration of high-speed railway tracks with geometric irregularities. XIANG, et al.(2007) studied the effects of dynamic parameters on vertical vibration responses based on the vertical vibration theory of high speed train and slab ballastless track time-varying system. XU, et al.(2011) established a dynamic model of a train-ballast track-subgrade coupled system. It can be seen that current research is mainly focused on the wheel/rail interaction relationship and the characteristics of vehicle. The subgrade is still overly simplified as an elastic ground or as a spring-damping-lumped mass system based on the classical theory. As a result, the subgrade system is simplified as a point and is not a clear point in the mechanical model. However, when high speed railway subgrade is designed, the dynamic response distribution, propagation and attenuation within a certain depth range should not be considered as a point. Therefore, ballastless track and subgrade structure of high speed railway should be designed based on the actual conditions of subgrade in order to obtain reasonable design parameters of subgrade structure. The spatial characteristics of subgrade should be fully taken into account and a dynamic analysis of subgrade-track interaction be conducted. In this paper, a vertical coupling dynamic model of vehicle-ballastless track-subgrade under secondary suspension is established based on the actual operation condition of train, in which vehicle, rail, fastener and pad, slab track, and subgrade are considered as a whole. The dynamic responses of slab ballastless track and subgrade structure were investigated.

DYNAMIC MODEL OF VEHICLE-SLAB TRACK-SUBGRADE SYSTEM

Vehicle Model. The mechanical model used to describe vehicle-track interaction varies with the classifications of vehicle structures, suspension characteristics and track structure types. This system was considered as a multi-body system, and the following assumptions were made: 1) The car body, trusses and wheel pairs are rigid, even-mass-distributed, and vibrate in small displacement from the equilibrium

position; 2) Damping between all the suspension systems are viscous, springs between the primary and secondary suspension are linear; 3) The vehicle moves along the rail line in uniform speed, without the longitudinal dynamic effect; 4) the wheel set of vehicle always cling to the rail surface during operation, as shown in Fig.1. The ups/downs Z_c and nodding φ_c movements of the car body, the ups/downs (Z_{t1}, Z_{t2}) and nodding ($\varphi_{t1}, \varphi_{t2}$) movements of the front and back bogie frame and the vertical vibration of four wheel pairs ($Z_{wi}, i=1\sim 4$) are considered in the model, which have ten degrees of freedom. Moreover, the vertical vibration of wheel pairs bounded by rails is not an independent freedom. Therefore the vertical displacement of wheel pairs can be determined based on the relationship of the rail displacement and track irregularity in vertical direction.

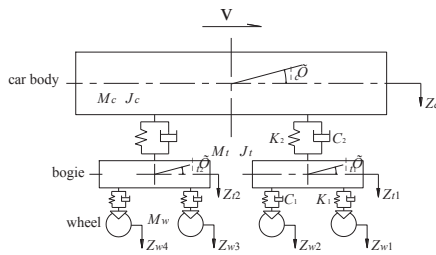


FIG.1. Vertical vibration model of vehicle

According to D'Alembert principle, the system equations can be established.

For the i th car body, dynamic equilibrium equation of the ups/downs and the nodding of the car body is given by

$$M_{ci}\ddot{Z}_{ci} + \sum_{j=1}^2 C_{2ij}(\dot{Z}_{ci} - \dot{Z}_{tij}) + \sum_{j=1}^2 K_{2ij}(Z_{ci} - Z_{tij}) = 0 \tag{1.a}$$

$$J_{ci}\ddot{\varphi}_{ci} + \sum_{j=1}^2 C_{2ij}(l_{ci}^2\dot{\varphi}_{ci} - \eta_{ij}l_{ci}\dot{Z}_{tij}) + \sum_{j=1}^2 K_{2ij}(l_{ci}^2\varphi_{ci} - \eta_{ij}l_{ci}Z_{tij}) = 0 \tag{1.b}$$

The matrix form of Eq.1 is Eq.2.

$$\begin{bmatrix} M_{ci} & 0 \\ 0 & J_{ci} \end{bmatrix} \begin{Bmatrix} \ddot{Z}_{ci} \\ \ddot{\varphi}_{ci} \end{Bmatrix} + \begin{bmatrix} C_{czi} & 0 \\ 0 & C_{c\varphi i} \end{bmatrix} \begin{Bmatrix} \dot{Z}_{ci} \\ \dot{\varphi}_{ci} \end{Bmatrix} + \begin{bmatrix} K_{czi} & 0 \\ 0 & K_{c\varphi i} \end{bmatrix} \begin{Bmatrix} Z_{ci} \\ \varphi_{ci} \end{Bmatrix} - \begin{bmatrix} C_{2i} & C_{2i} \\ C_{2i}l_{ci} & -C_{2i}l_{ci} \end{bmatrix} \begin{Bmatrix} \dot{Z}_{t1} \\ \dot{Z}_{t2} \end{Bmatrix} - \begin{bmatrix} K_{2i} & K_{2i} \\ K_{2i}l_{ci} & -K_{2i}l_{ci} \end{bmatrix} \begin{Bmatrix} Z_{t1} \\ Z_{t2} \end{Bmatrix} = 0 \tag{2}$$

where M_{ci} and J_{ci} are the mass and nodding inertia moment of the i th car-body; K_{czi} and C_{czi} are the general stiffness and general damping of the ups/downs of the i th vehicle respectively; $K_{c\varphi i}$ and $C_{c\varphi i}$ are the general stiffness and general damping of the nodding of the i th vehicle respectively; K_{2i} and C_{2i} are the vertical stiffness and damping of the bogie of the i th vehicle; Z_{ci} , \dot{Z}_{ci} and \ddot{Z}_{ci} are referred to the vertical displacement, velocity and acceleration of the centroid of the i th vehicle respectively;

φ_{ci} , $\dot{\varphi}_{ci}$ and $\ddot{\varphi}_{ci}$ are referred to the angle, angular velocity and angular acceleration of the centroid of the i th vehicle respectively; Z_{ij} and \dot{Z}_{ij} are referred to the vertical displacement and velocity of the centroid of the j th bogie of the i th vehicle respectively; l_{ci} is referred to the distance of the half-vehicle.

For the j th bogie of the i th vehicle, the matrix form of dynamic equilibrium equation is given by

$$\begin{bmatrix} M_{ij} & 0 \\ 0 & J_{ij} \end{bmatrix} \begin{Bmatrix} \ddot{Z}_{ij} \\ \ddot{\varphi}_{ij} \end{Bmatrix} + \begin{bmatrix} C_{zij} & 0 \\ 0 & C_{\varphi ij} \end{bmatrix} \begin{Bmatrix} \dot{Z}_{ij} \\ \dot{\varphi}_{ij} \end{Bmatrix} + \begin{bmatrix} K_{zij} & 0 \\ 0 & K_{\varphi ij} \end{bmatrix} \begin{Bmatrix} Z_{ij} \\ \varphi_{ij} \end{Bmatrix} - \begin{bmatrix} C_{2i} & \eta_j C_{2l_{ci}} \\ 0 & 0 \end{bmatrix} \begin{Bmatrix} \dot{Z}_{ci} \\ \dot{\varphi}_{ci} \end{Bmatrix} - \begin{bmatrix} K_{2i} & \eta_j K_{2l_{ci}} \\ 0 & 0 \end{bmatrix} \begin{Bmatrix} Z_{ci} \\ \varphi_{ci} \end{Bmatrix} = \begin{Bmatrix} \sum_{i=1}^{N_k} [(K_{li} Z_{wi} + C_{li} \dot{Z}_{wi})] \\ \sum_{i=1}^{N_k} 2\eta_l l_w (K_{li} Z_{wi} + C_{li} \dot{Z}_{wi}) \end{Bmatrix} \quad (3)$$

where M_{ij} and J_{ij} are the mass and nodding inertia moment of the j th bogie of the i th vehicle; K_{zij} and C_{zij} are the general stiffness and general damping of the ups/downs of the j th bogie of the i th vehicle; $K_{\varphi ij}$ and $C_{\varphi ij}$ are the general stiffness and general damping of the nodding of the j th bogie of the i th vehicle; K_{li} and C_{li} are the vertical stiffness and damping of the wheel pair of the i th vehicle; \ddot{Z}_{ij} is the vertical acceleration of the centroid of the j th bogie of the i th vehicle; φ_{ij} , $\dot{\varphi}_{ij}$ and $\ddot{\varphi}_{ij}$ are the angle, angular velocity and angular acceleration of the centroid of the j th bogie of the i th vehicle; Z_{wi} and \dot{Z}_{wi} are the vertical displacement and velocity of the i th wheel pair; η_j is the symbol function of the wheel; η_j is the symbol function of the bogie; l_w is the half distance between axles of a bogie; N_k is the number of the wheel of each bogie.

As the motion equations of wheel pair are dependent, the matrix form of motion equation for the i th car-body and two bogies are given by

$$[M_c] \{\ddot{X}_c\} + [C_c] \{\dot{X}_c\} + [K_c] \{X_c\} = \{P_c\} \quad (4)$$

where $[M_c]$, $[C_c]$ and $[K_c]$ are mass matrix, damping matrix and stiffness matrix of vehicle, respectively; $\{\ddot{X}_c\}$, $\{\dot{X}_c\}$ and $\{X_c\}$ represent acceleration vector, velocity vector and displacement vector of vehicle, respectively; $\{P_c\}$ is the load vector acting on vehicle.

Mechanics Model for Slab Ballastless Track and Subgrade. High-speed railway subgrade is a multi-layer system generally consisting of three or more layers. Multi-layer subgrade system model can reflect actual working condition. Generally analytical solutions can be only obtained under certain simple conditions. For complex constraints and loading conditions, the mechanical behavior of multi-layer subgrade can be better simulated using numerical methods, such as finite element method (FEM). In this paper, subgrade is assumed to be composed of multi-layers.

Slab track-subgrade system consists of the rails, pads and fasteners, track slab, CA mortar (cement-asphalt mortar), base, and subgrade. In the finite element model, the rail is modeled by using beam elements, pads and fasteners are simulated by using spring-damper elements. Track slab, CA mortar, base and subgrade are discretized using quadrilateral elements.

Based on the above mentioned conditions, the FEM model for slab track-subgrade is shown in Fig.2. Horizontal constraint at both sides of subgrade is fixed in the normal direction and bottom surface is completely fixed.

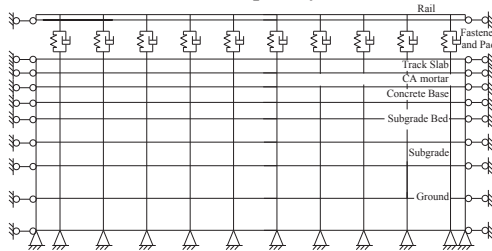


FIG.2. Finite element model of slab track and subgrade

The dynamic equilibrium equation of ballastless track-subgrade is given as Eq.5 based on the Principle of Virtual Work.

$$[M_r]\{\ddot{\delta}_r\} + [C_r]\{\dot{\delta}_r\} + [K_r]\{\delta_r\} = \{P_r\} \tag{5}$$

where, $[M_r]$, $[C_r]$ and $[K_r]$ are mass matrix, damping matrix and stiffness matrix; $\{\ddot{\delta}_r\}$, $\{\dot{\delta}_r\}$ and $\{\delta_r\}$ are the total acceleration vector, velocity vector and displacement vector; $\{P_r\}$ is the external force vector (the wheel-pair force due to running train acts on the track).

For numerical model of slab track-subgrade interaction, degrees of freedom might be large, and the workload will be great if it is coupled with the vehicle vibration equation. In order to reduce the calculation of degrees of freedom, modal synthetic technique is adopted, such as method of generalized coordinate discretization (established based on substructure method). Firstly, the frequency and vibration mode of the structure under free vibration are calculated, then the motion equations of hundreds of coupling nodes are decoupled through the orthogonal of different vibration modes. Thus it leads to a separate modal system of equations. As the dynamic response of structure is controlled by the first several vibration modes with low frequency, only the first few vibration modes are chosen for calculation, which greatly reduce the computational work. Because vehicle and track only contact at the rail surface, in each vibration mode only the nodes at the contact surface of wheel pair and rail were selected.

Decoupling of Dynamic Equations. As discussed earlier, the track-subgrade interaction model can be decomposed into independent modal equations with the

substructure method. And several low vibration modes can be selected for dynamic analysis of vehicle-slab track-subgrade system. However, it is very challenging to integrate dynamic equations of track-subgrade interaction model and vehicle model together and solve it simultaneously. Previous dynamic coupling of wheel/rail interaction is achieved through the Hertz non-linear contact theory. In this paper, decoupling is achieved based on displacement compatibility of vehicle, track and subgrade vibration.

It is assumed that wheel and rail always contact each other when vehicle runs on the rails. The vertical displacement of wheel and rail couples with each other. The vertical displacement of rail consists of two parts, which are track vertical irregularity and vertical displacement induced by vibration. Therefore, it can be expressed as follows:

$$Z_{wrij} = Z_r(x) + Z_s(x) \quad (13)$$

where $Z_r(x)$ is the vertical displacement at any cross-section x in track-subgrade model and can be superposed by vibration mode function. $Z_s(x)$ denotes the vertical track irregularity at track surface x .

Dynamic Equation of Coupling System. Combining the motion equation of vehicle with the modal equation of ballastless track-subgrade (Eq.4 and Eq.12) and inserting displacement compatibility Eq.13, the dynamic equation of system can be obtained:

$$\begin{bmatrix} M_{cc} & 0 \\ 0 & M_{rr} \end{bmatrix} \begin{Bmatrix} \ddot{X}_c \\ \ddot{X}_r \end{Bmatrix} + \begin{bmatrix} C_{cc} & C_{cr} \\ C_{rc} & C_{rr} \end{bmatrix} \begin{Bmatrix} \dot{X}_c \\ \dot{X}_r \end{Bmatrix} + \begin{bmatrix} K_{cc} & K_{cr} \\ K_{rc} & K_{rr} \end{bmatrix} \begin{Bmatrix} X_c \\ X_r \end{Bmatrix} = \begin{Bmatrix} F_c \\ F_r \end{Bmatrix} \quad (14)$$

The subscript c and r stands for vehicle and ballastless track-subgrade, respectively.

If there are N_v vehicles in service being analyzed, and each vehicle has N_l bogies, the displacement sub-vector can be expressed as

$$X_c = [X_{c1} \quad X_{c2} \quad \cdots \quad X_{cN_v}]^T \quad (15)$$

where, $X_{ci} = [v_{ci}, v_{t_{i1}}, v_{t_{i2}}]^T$;

$$v_{ci} = [Z_{ci}, \phi_{ci}]^T; v_{t_{i1}} = [Z_{t_{i1}}, \phi_{t_{i1}}]^T; v_{t_{i2}} = [Z_{t_{i2}}, \phi_{t_{i2}}]^T; i = 1, 2, \dots, N_v$$

If N_f is the number of vibration modes during the calculation, the generalized displacement sub-vector of slab track-subgrade is presented as follows:

$$X_r = [A_1 \quad A_2 \quad \cdots \quad A_{N_f}]^T \quad (16)$$

If the external force of system (such as wind load and earthquake load) is not considered, the load vector of system can be expressed by:

(1) Force vector acting on the vehicle

$$F_c = [F_{c1} \quad F_{c2} \quad \dots \quad F_{cN_v}]^T \tag{17}$$

in which,
$$F_{ci} = \begin{bmatrix} 0 \\ F_{ci}^{t_1} \\ F_{ci}^{t_2} \end{bmatrix}$$

$$F_{ci}^{t_j} = \sum_{i=1}^{N_{ki}} \left\{ \begin{matrix} K_{ij}Z_s(x) + C_{ij}\dot{Z}_s(x) \\ 2\eta_l l_w [K_{ij}Z_s(x) + C_{ij}\dot{Z}_s(x)] \end{matrix} \right\} (i=1,2,\dots,N_v, j=1,2)$$

where $Z_s(x)$ and $\dot{Z}_s(x)$ represent the vertical irregularity value and derivative of track at the rail surface x ; N_{ki} stands for the number of wheel pair of each bogie; l_w stands for the half of the fixed wheelbase of bogie.

(2) Force vector acting on the slab track-subgrade

$$F_r = [F_{r1} \quad F_{r2} \quad \dots \quad F_{rN_r}]^T \tag{18}$$

in which,

$$F_{rn} = \sum_{i=1}^{N_v} \sum_{j=1}^{N_l} \sum_{l=1}^{N_{kl}} \{ \Phi_{vijl}^n K_{lij} Z_s(x) + \Phi_{vijl}^n g [M_{wi} + (0.5M_{ci} + M_{ij}) / N_{kl}] \} \quad (n = 1, 2, \dots, N_r)$$

where M_{wi} is the mass of the wheel pair of the i th vehicle; Φ_{vijl}^n is the n th vibration mode function corresponding to the rail surface.

The coefficient Φ_{vijl}^n reflects the coupling relationship among vehicle, slab track-subgrade structure, and different vibration mode of slab track-subgrade. Totally there are $[2 * N_v(1 + N_l) + N_r]$ equations. When the train passes the calculated line, location of each wheel changes continuously and the coefficient Φ changes too. The dynamic equation set of the system is a second-order linear differential one with time-variable coefficients. The equations can be solved by Newmark- β method.

By solving the motion equation of system, the following theoretical calculation values can be obtained.

(1) Car-body acceleration of the i th vehicle

$$a_i = \left(\ddot{z}_{ci} + \frac{l_p}{l_u} \cdot \ddot{\phi}_{ci} \right) \tag{19}$$

where l_p stands for the distance from the center of the body, and l_u stands for the distance between the center of wheel pair and the body.

(2) Wheel load reducing rate of the j th wheel pair of the i th vehicle

$$D_j = \frac{P_{jw} - P_{js}}{P_{js}} = \frac{P_{jw}}{P_{js}} - 1 \quad (20)$$

Where p_{jw} stands for the weight of moving wheels; p_{js} stands for the average weight of static wheels.

(3) Dynamic deflection at the rail surface $x = x_p$ is given by

$$z_r(x) = \sum_n^N A_n \phi_n(x) |_{x=x_p} \quad (21)$$

Where A_n is the generalized coordinate corresponding to the n th vibration mode, $\phi_n(x)$ is the function for the n th vibration mode.

CONCLUSIONS

Based on engineering practice the vertical coupling dynamic model of vehicle-slab track-subgrade is established. Through analyzing with this model the following conclusions are drawn:

(1) The dynamic properties of system can be reflected completely in dynamic analysis considering slab track-subgrade as a part of vibration structure of vehicle-track-subgrade.

(2) Slab track-subgrade is regarded as a part of the vibration structure of vehicle model, which can fully reflect the interaction between the vehicle and the substructure under track. So it can provide theory basis for determining relevant design parameters.

(3) In the model the effects of some subgrade design parameters (including subgrade stiffness, sleeper spacing, foundation condition and track surface maintenance standard) on vehicle operation quality (including vehicle comfortable degree and safety) are considered. It can provide analysis basis for solving the matching between substructure under track and vehicle system in track transportation.

ACKNOWLEDGEMENTS

The research was supported by Program for Changjiang Scholars and Innovative Research Team in University (IRT1139) and the National Natural Science Foundation Project(51268030), China.

REFERENCES

- NIELSEN J.C.O, IGELAND A.(1995). "Vertical dynamic interaction between train and track influence of wheel and track imperfections". *Journal of Sound and Vibration*. Vol.187:825-839.
- KNOTHE KL, GRASSIE SL.(1993). "Modeling of Railway Track and Vehicle/Track Interaction at High Frequencies". *Vehicle system Dynamics*. Vol.22:209-262.
- VERBIC B.(1997). "Investigating The Dynamic Behavior of Rigid Track". *Railway Gazette International*. Vol.153(9):585-586.

- ZHAI WM, HAN WJ, CAI CB, et al.(1999). “Dynamic Properties of High-speed Railway Slab Tracks.” *Journal of the China Railway Society*, Vol.21(6), 65-69.
- HE D, XIANG J, GUO GJ, et al.(2006). “The Effect of Stiffness and Damping of Cement Asphalt Mortar on The Vertical Vibration of The High-Speed Train and Slab Track Time-Dependent System”. *Journal of Railway Science and Engineering*, Vol. 3:26-30.
- FENG QS, LEI XY & LIAN SL.(2008). “Vibration Analysis of High-Speed Railway Tracks with Geometric Irregularities”. *Journal of Vibration Engineering* Vol.6:559-564.
- XIANG J, CAO Y, LIU BG.(2007). “Dynamic Parameters of Slab Track of Passenger Transport Line”. *Journal of Central South University*.Vol.5:981-986.
- XU P, CAI CB.(2011). “Spatial Dynamic Model of Train-Ballast Track-Subgrade Coupled System”. *Engineering Mechanics*.Vol.3:191-197.

Reliability Analysis on Anti-overturning Stability of Supporting Structure of Excavation Using Monte-Carlo Method

Hu Weiming¹, Ma Jianlin², Peng Xiongzhi³ and Li Leilei⁴

¹Ph.D. candidate, Department of Geotechnical engineering, Southwest Jiaotong University, Chengdu, Sichuan 610031, China; stone.hoo@hotmail.com

²Professor, Department of Geotechnical engineering, Southwest Jiaotong University, Chengdu, Sichuan 610031, China

³Associate professor, Department of Geotechnical engineering, Southwest Jiaotong University, Chengdu, Sichuan 610031, China

⁴Engineer, Sichuan Suiguangsuixi Expressway Co., Ltd., Chengdu, Sichuan 629000, China

ABSTRACT: Engineering characteristics of soil are different at dissimilar layers and regions because of the variability of geological origin, earth history, environment condition, etc. Traditional safety factor method, which is usually used in design and calculation of geotechnical engineering, cannot reflect this variability and uncertainty of soil scientifically because characteristics of soil are often influenced by sampling and experimental condition. In this paper, reliability analysis method, based on probability and statistics, was applied to analysis anti-overturning stability of supporting structure of excavation. Anti-overturning limit status function, in which layered soil was considered, is derived using equivalent beam method. In the process of computation, geometric dimension of supporting structure was deemed as constant such as excavation depth, anchored depth of pile, pile spacing and so on; and soil parameters, gravity, cohesive force, internal friction angle of soil, were regarded as random variable. At last, the open excavated tunnel of Chengdu-Dujiangyan railway was taken for example to discuss anti-overturning stability of supporting structure influenced by loads nearby excavation.

INTRODUCTION

The stability of the supporting structure should be checked in design according to the Industry Standard of the People's Republic of China (1999), which mainly includes overall stability, anti-overturning stability and basal stability. Huang (1999) pointed out that anchored depth of pile, determined by anti-overturning stability, is larger than that determined by overall stability and basal stability in design of pile wall plus inner supporting structure. Thus, if anti-overturning stability is met in checking calculation, overall stability and basal stability are fulfilled naturally.

At present, safety factor method is still used widely to check excavation stability, in which all of soil mechanical parameters (such as unit weight γ , cohesion c , and internal friction angle φ) and computing pattern are considered as certainty. Huang

et al. (2009) looked upon above mentioned parameters and computing method as uncertainty. Although the safety factor method has accumulated a wealth of experience, this method dealt with uncertain problems through certain method, which did not take into account variability in parameters, and could not reflect degree of safety of supporting structure scientifically and quantitatively (Whitman 2010). Reliability analysis, based on probability and statistics theory, is able to obtain degree of safety of supporting structure through taking variability and uncertainty of parameters into account. Most of existing theoretical research of excavation stability considered soil as single layer (Tang 1998, Liu et al. 1998, Huang et al. 2009, Huang 2010). Research about effects of variability of each layer, among multilayers of soil, on excavation stability was few (Luo et al. 2006, Li et al. 2011). In this paper, research considering variability of each layer among multi-layers focuses on the effect of load near excavation and the variability on excavation stability.

LIMITING STATUS FUNCTION OF ANTI-OVERTURNING STABILITY

Fundamental Assumption

In order to highlight the research emphasis, assumptions are made as follows.

- (1) Geometric dimension of supporting structure is defined as constant, for example, excavation depth, anchored depth of pile, and pile spacing;
- (2) Mechanical properties of soil, such as unit weight, cohesive force, internal friction angle, are regarded as random variable;
- (3) Soil above top of retaining pile, considered as uniform load, takes part in calculation; and
- (4) Building load acts on surface of ground whose depth equals to top of retaining pile because building load is transferred to a certain depth under the ground through foundation which is complex and hard to describe exactly.

Limiting Status Function of Anti-overturning Stability

In this paper, equivalent beam method was used in calculation of supporting structure, and calculating sketch was illustrated in Fig. 1. Limiting status of anti-overturning stability is that soil pressure in front of retaining wall plus axial force of supports equals to soil pressure behind retaining wall. Under the action of multilayers, force situation of retaining structure should be calculated dividedly according to soil pressure of each layer. Furthermore, layers should be divided further because of the point of action of building load (Points A and B in Fig. 1) and underground water. According the factors above mentioned, limiting status function of anti- overturning stability, in which layered soil was considered, was derived (process is omitted), as shown in Eq. (1) through (5).

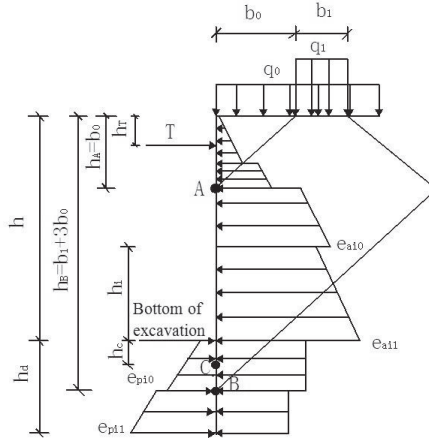


FIG.1. Calculating sketch.

$$Z = R - S = M_T + M_{ep} - M_{ea} \tag{1}$$

$$M_T = T(h + h_d - h_r) \tag{2}$$

$$T = \frac{\sum_{i=1}^m e_{ai} h_i \left(h_c + h - \sum_{j=1}^{i-1} h_j - \frac{h_i}{2} \right) + \sum_{i=1}^m \Delta e_{ai} \frac{h_i}{2} \left(h_c + h - \sum_{j=1}^{i-1} h_j - \frac{2h_i}{3} \right)}{h + h_c - h_r} \tag{3}$$

$$+ \frac{\sum_{i=m+1}^{k-1} (e_{ai} - e_{pi0}) h_i \left(h_c - \sum_{j=m+1}^{i-1} h_j - \frac{h_i}{2} \right) + (e_{ak} - e_{pk0}) \frac{\left(h_c - \sum_{i=m+1}^{k-1} h_i \right)^2}{2}}{h + h_c - h_r}$$

$$- \frac{\sum_{i=m+1}^{k-1} \Delta e_{pi} \frac{h_i}{2} \left(h_c - \sum_{j=m+1}^{i-1} h_j - \frac{2h_i}{3} \right) - (e_{pc} - e_{pk0}) \frac{\left(h_c - \sum_{i=m+1}^{k-1} h_i \right)^2}{6}}{h + h_c - h_r}$$

$$M_{ep} = \sum_{i=m+1}^n e_{pi0} h_i \left(h_d - \sum_{j=m+1}^{i-1} h_j - \frac{h_i}{2} \right) L + \sum_{i=m+1}^n \Delta e_{pi} \frac{h_i}{2} \left(h_d - \sum_{j=m+1}^{i-1} h_j - \frac{2h_i}{3} \right) L \tag{4}$$

$$M_{ea} = \sum_{j=1}^m e_{ai0} h_i \left(h + h_d - \sum_{j=1}^{i-1} h_j - \frac{h_i}{2} \right) L + \sum_{i=1}^m \Delta e_{ai} \frac{h_i}{2} \left(h + h_d - \sum_{j=1}^{i-1} h_j - \frac{2h_i}{3} \right) L \tag{5}$$

$$+ \sum_{i=m+1}^n e_{ai} h_i \left(h_d - \sum_{j=m+1}^{i-1} h_j - \frac{h_i}{2} \right) L$$

where

b_1 is width of building load.

- b_0 is distance between inside of building and excavation.
- e_{ak} is active earth pressure of the k^{th} layer.
- e_{pk} is passive earth pressure of the k^{th} layer.
- k is identifier of layer where point of inflection is located.
- h_d is anchored depth of retaining pile.
- h_k is thickness of the k^{th} layer.
- h_T is distance between steel support and the top of retaining pile.
- L is pile spacing.

Description of Uncertainty

Probability statistics method is used to describe uncertainty usually. Mathematical and statistic feature of each variables are obtained by statistical analysis of data through this method. Existing research results show that unit weight γ and internal friction angle φ of soil followed normal distribution and cohesive c followed lognormal distribution (Baroth and Malecot 2010) and the Industry Standard of the People's Republic of China (1994).

Reliability analysis method is based on the independence among variables. By the statistical analysis of the soil test results, Huang et al. (2009) found that c and φ of soil at the same layer were negatively correlated random variables. Therefore, they were supposed to be transformed into uncorrelated random variables.

Sampling Calculation and Reliability Index

Monte-Carlo method is used in sampling calculations, in which variables follow above mentioned distribution. After a number of random sampling calculations, the structural failure probability is obtained.

Reliability index β is a dimensionless coefficient which is used to measure the reliability of engineering structures. P_f is failure probability. There is a corresponding relationship between β and P_f . The reliability index β , used to measure reliability of structure internationally, increases with drop of P_f .

PROJECT EXAMPLE AND PARAMETER VALUES

Project Overview

The new railway branch line, length of 3241.1m, from Chengdu to Dujiangyan, located beneath the Dujiangyan city roads. The whole tunnel was constructed using a cut-and-cover technology, the standard width of the tunnel was 12.1m, and the excavation depth was 14.5m. The well dewatering was used throughout the whole construction of main project. The precipitation depth was not less than the standard scale which is 0.5m below the excavation face. Row of piles and internal supporting structure were used as the retaining structure. Diameter of pile was 1.2m, and distance between the piles was 2.4m. Steel pipe which was used as the supporting

structure were arranged vertically in two tiers. Vertical distance of the two tiers was 6.1m and horizontal distance was 4m.

A church, with the estimated load $q_1=64.29\text{kN/m}^2$, was 2.3m away from the excavation where is the worst section. Anchored depth of retaining pile in this section was 6m.

Parameter Values

The soil near the section was divided into four layers: (1) Artificial fill soil, whose thickness is 1~1.5m; (2) Fine sand, whose thickness is 2m.; (3) Loose pebble soil, whose thickness is 6.5m; (4) Dense pebble soil, whose thickness is 11m. Artificial fill soil was located above the top of supporting pile, and this layer was excavated through step-slope method. During the calculation, this layer was defined as a uniform load $q_0=19\text{kN/m}^2$. Laboratory tests were carried out on the samples from the rest soil layers and results were shown in Table. 1.

Table 1. Soil parameters of layers

| Fine sand | | | Loose pebble soil | | | Dense pebble soil | | |
|---------------------------------|------------------------|---------------------------|---------------------------------|-------------------------|---------------------------|---------------------------------|-------------------------|---------------------------|
| γ (kN/m^3) | C (kP) | φ ($^\circ$) | γ (kN/m^3) | C (kPa) | φ ($^\circ$) | γ (kN/m^3) | C (kPa) | φ ($^\circ$) |
| 17 | 2 | 28 | 20 | 2 | 38 | 25 | 0 | 49 |
| 21 | 0 | 31 | 18 | 1 | 47 | 21 | 5 | 36 |
| 18 | 3 | 25 | 23 | 0 | 39 | 23 | 1 | 39 |
| 17 | 0 | 28 | 20 | 1 | 35 | 27 | 0 | 48 |
| 19 | 5 | 26 | 19 | 3 | 40 | 23 | 4 | 42 |
| 18 | 0 | 33 | 22 | 1 | 45 | 21 | 0 | 51 |
| 22 | 1 | 35 | 25 | 2 | 46 | 20 | 3 | 47 |
| 18 | 4 | 29 | 19 | 0 | 50 | 25 | 0 | 35 |
| 17 | 0 | 32 | 21 | 1 | 37 | 25 | 0 | 46 |
| 19 | 0 | 37 | 23 | 4 | 45 | 21 | 3 | 55 |

Statistic feature of soil parameters, after orthogonal transformation, were listed in Table 2.

Table 2. Statistic feature of soil parameters in situation of multilayer

| | μ_γ (kN/m^3) | σ_γ (kN/m^3) | μ_c (kPa) | σ_c (kPa) | μ_φ ($^\circ$) | σ_φ ($^\circ$) |
|-------------------|-------------------------------------|--|-----------------------------|--------------------------------|-------------------------------|----------------------------------|
| Fine sand | 18.6 | 1.71 | 1.5 | 1.90 | 30.4 | 3.89 |
| Loose pebble soil | 21.0 | 2.21 | 1.5 | 1.26 | 42.2 | 5.00 |
| Dense pebble soil | 23.1 | 2.33 | 1.6 | 1.95 | 44.8 | 6.60 |

In order to compare with the situation which considers soil behind retaining structure as a single layer, soil parameters were done by thickness weighted-average

of above mentioned soil layers. Then statistic feature of these parameters, in situation of single layer, was shown in Table 3.

Table 3. Statistic feature of soil parameters in situation of single layer

| | μ_γ (kN/m ³) | σ_γ (kN/m ³) | μ_c (kPa) | σ_c (kPa) | μ_ϕ (°) | σ_ϕ (°) |
|--------------|--------------------------------------|---|------------------|---------------------|-------------------|----------------------|
| Single layer | 21.9 | 1.04 | 1.55 | 1.38 | 42.4 | 3.93 |

RESULTS AND DISCUSSIONS

On the situation of multilayers and single layer, distance between inside of building and supporting structure was changed to analyze the effect of the distance on anti-overturning stability of excavation, separately. Results were shown in Fig. 2.

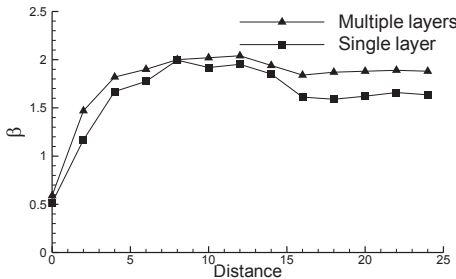


FIG. 2. Effect of distance between building and excavation on reliability index.

Fig. 2 shows that anti-overturning stability of excavation is minimal when building closes to supporting structure, which means $b_0=0$. In this situation, overturning moment is maximal because of effect of building load on retaining structure. While b_0 increases from 0 to 12m, point A and B move downward, and overturning moment of supporting structure grows rapidly at beginning and then slowly. The influence curve likes logarithmic curve approximately. When $b_0=12$ m, reliability index β reaches maximum. By this time, point A and B are in the region of anchored part of pile, and provide anti-overturning movement. Then, β drops a little while b_0 increases unceasingly. When b_0 is longer than length of pile, 19.5m, β no longer has obvious change.

When the distance between building and excavation is constant, reliability index which was calculated though single layer is lower than that though multilayers. This is because that compactness of soil in anchored part of pile is better than that in the shallow soils. Weighted average is equivalent to the weakening of soil properties, so the result tends to be conservative.

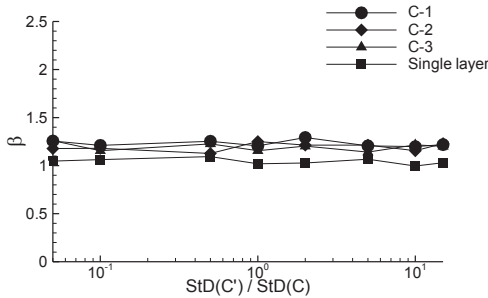


FIG. 3. Effect of variability of cohesion on reliability index.

Variability of soil parameters increases with the growth of standard deviation. So in this paper, standard deviation of each kind of soil parameter was expanded and reduced several times to discuss the effect of variability of soil parameters on reliability index. Results were shown in Fig. 3 through Fig. 5. In order to make results intuitive, logarithmic coordinates was used in the horizontal axis. In the legend, *parameter* - 1 (-2, -3) mean the parameters of the first (second, third) layer from top of pile.

As illustrated in Fig. 3, no matter the result is calculated from multilayers or single layer, reliability index changes a little with increase of variability of cohesive. This means that anti-overturning stability of excavation is not sensitive to cohesive of soil.

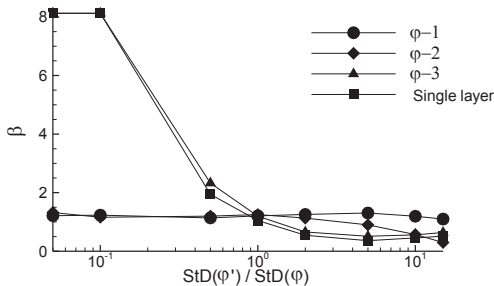


FIG. 4. Effect of variability of internal friction angle on reliability index.

From Fig. 4, reliability index β drops rapidly with increase of variability of internal friction angle φ in single layer. However, in multilayers, β only performs same change with growth of variability of φ of layer in which anchored part of pile locates. Effect of variability of φ of the rest layer is smaller comparatively. It means that anti-overturning stability of excavation is sensitive to variability of φ of layer in which anchored part of pile locates, and the rest layers above make less effect on it. If calculation is only done in single layer, above characteristic cannot be found.

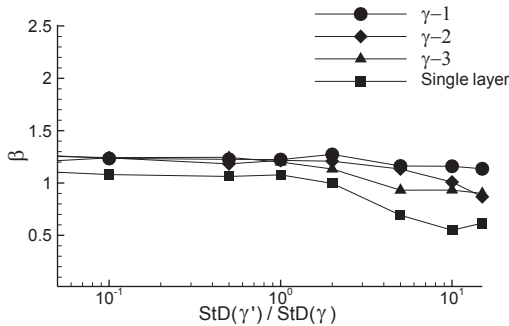


FIG. 5. Effect of variability of unit weight on reliability index.

Fig. 5 shows that reliability index β drops gradually with increase of variability of unit weight, and in situation of multilayers, the effect of under layers is larger than upper layers.

Overall, variability of internal friction angle and unit weight of soil causes a certain degree of influence on anti-overturning stability of excavation. Thus, supplementary investigation is very necessary, to reduce variability of soil parameters, for estimating reliability of anti-overturning of excavation.

CONCLUSIONS

1. While distance between building and supporting structure b_0 is shorter than depth of excavation, the influence on reliability index β curve likes logarithmic curve approximately. When b_0 is longer than length of pile, β no longer has obvious change.

2. Effect of variability of cohesive on anti-overturning stability of excavation is not obvious. It is sensitive to variability of internal friction angle and unit weight of soil.

3. Considering soil behind retaining structure as single layer cannot reflect actual situation in field and calculative result tends to be conservative.

4. Anti-overturning stability of excavation is sensitive to variability of soil parameters of layer in which anchored part of pile locates, and the rest layers above make less effect on it.

The detailed analysis on the critical value of reliability index β in assessment of excavation stability may be the scope in future research.

REFERENCES

- Baroth, J. and Malecot, Y. (2010). "Probabilistic analysis of the inverse analysis of an excavation problem." *Computers and Geotechnics*, Vol. 37: 391-398.
- Huang Guanglong, Gong Xiaonan, Xiao Ming (2010). "Random field model of soil property and analysis of variability of pile-settlement". *Rock and Soil*

- Mechanics*, Vol. 21 (4): 311-315.
- Huang Guanglong, Wei Min and Li Juan (2010) "Analysis of influence of parameters variability on retaining structure stability." *Rock and Soil Mechanics*, Vol. 26 (3): 2484-2489.
- Huang Shenggen (1999). Foundation treatment and foundation pit supporting engineering. China University of Geosciences Press.
- Huang Zhiquan et al. (2009). Reliability analysis and numerical simulation of deep foundation pit support engineering. The Yellow River Water Conservancy Press.
- The Industry Standard of the People's Republic of China (1994). Water conservancy and hydropower engineering structure reliability design standard (GB50199-1994) (1994). China Plans Press.
- The Industry Standard of the People's Republic of China (1999). Building foundation pit supporting technical regulations (JGJ 120-99). Metallurgical Industry Press.
- Li Junsong and Qiu Wenge (2011). "Instability risk analysis and management for tunnel foundation pit close to building." *China Railway Science*, Vol. 32 (6): 0076-0081.
- Liu Guobin, Shen Jianming and Hou Xueyuan (1998). "Reliability Analysis of Braced Structures of Deep excavation." *Journal of Tongji University*, Vol. 31 (8): 260-264.
- Luo Xiaohui, Li Zaiguang and He Lihong (2006). "Evaluation on stability of trench strengthened with soil nail based on reliability analysis." *Chinese Journal of Geotechnical Engineering*, Vol. 28 (4): 0480-0485.
- Tang Yugeng (1998). "Reliability analysis of deflection of diaphragm walls caused by deep excavation." *Chinese Journal of Geotechnical Engineering*, Vol. 32 (2): 0179-0183.
- Whitman, R.V. (2010). "Organizing and evaluating uncertainty in geotechnical engineering." *Journal of Geotechnical and Geoenvironmental Engineering*, Vol. 7: 583-593.

Foundation Treatment Methods of Metro Station on Geological Sensitive Area

Chao Zou¹, Yi-Min Wang², Wen-Ming Song³ and Yin-Lin Tang³

¹Ph.D., State Key Laboratory of Subtropical Building Science, South China University of Technology, Guangzhou, Guangdong, 510641, P. R. China; zouchao226@gmail.com.

²Professor, State Key Laboratory of Subtropical Building Science, South China University of Technology, Guangzhou, Guangdong, 510641, P. R. China; ctymwang@scut.edu.cn.

³Master, State Key Laboratory of Subtropical Building Science, South China University of Technology, Guangzhou, Guangdong, 510641, P. R. China; songwenming1983@163.com.
m15017547358@163.com.

ABSTRACT: The vital geological risk factors including in saturated soft clay stratum, water-rich fracture zone, Karst stratum with abundant soil caves and saturated sand stratum on the safety of metro station are discussed. The successful experiences of controlling the geological risks in metro projects are summarized. The design methods of metro station foundation and main structure at geological sensitive area are presented. It is concluded that: Hazards of foundation settlement, pit collapsing, and water gushing are more easily taken place in metro station with saturated soft clay stratum. Failure of soil and water inrush is often happened owing to the water-rich fracture zone. Collapse and subsidence are frequently come up at the area of Karst stratum with abundant soil caves. The water bursting and sand flowing is usually broken out at the foundation pit with saturated sand stratum. The safety of metro station with above mentioned defective geological factors can be controlled and ensured through targeted design schemes and construction methods.

INTRODUCTION

It has been reported that the safety of metro station is sensitively affected by geological hazards, such as subsidence, collapse, water gushing, and building cracking or toppling (Zhao et al. 2009). These scenarios lead to stoppages requiring corrective measures, and higher construction costs, not to mention the risk to life and damage to property (Jordi et al. 2011). Therefore, choosing the reasonable foundation treatment methods is very important to ensure the safety and improve the investment efficiency.

In this paper, several metro-station projects with vital geological risk factors including in saturated soft clay stratum, water-rich fracture zone, Karst stratum with abundant soil caves and saturated sand stratum are presented. The successful experiences of controlling the geological risks are summarized and discussed. The output of this article hopefully provides reference to the design and construction application of metro stations with similar geological conditions.

ANALYSIS OF POOR GEOLOGICAL CONDITION ON METRO STATION

Saturated Soft Clay Stratum

The saturated soft clay stratum is characterized with high water content, large void ratio, high compressibility, low bearing capacity, small internal friction angle, and small permeability coefficient. When metro station is built on the saturated soft soil area, the hazards of settlement deformation, foundation pit collapsing or sliding, and the water gushing can be easily taken place during the construction.

Settlement deformation is one of the most frequently happened problems on the soft ground. If the settlement of a structure exceeds its allowable value, it will seriously affect the safety and function of the building and even result in the structural damage. Taking the Shenzhen metro line one as an example (Huang et al. 2012), land subsidence incidents occupied around 25% of the total accidents during the construction period, and the maximum surface settlement reached 300mm. Similar problems had happened in Saint-Lazare station of the EOLE subway line in Paris (Fruneau et al. 2005). Due to water pumping method for keeping construction field in dry condition, the surface settlement had taken place.

Foundation pit collapsing or sliding failure is stability problem of the foundation. An accident was occurred during its construction at Xianghu Station of Subway Line 1, Hangzhou City. A 100 m-long and 50 m-wide section of a foundation pit collapsed. A number of people were buried under the rubble and many of whom die. The accident showed that stability of depth of pile and wall must be considered, including subsidence of pile and wall, destruction of uplift and "skirting" (Ma et al. 2012).

According to a lot of analysis of instability and deformation instance of foundation pit showed that groundwater processing was the key to project success. It was reported by Lee et al. (2010) that a disastrous ground failure accompanied by the groundwater leakage occurred at the construction site of Station O2 of Kaohsiung Mass Rapid Transit in Taiwan.

Water-rich Fracture Zone

Water-rich fracture zone has the features of mixed different particle sizes, poor sorting, good connectivity and both sides of the rock masses with significant differences in the physical and mechanical properties; It is easy to form dynamic flowing water path and create a "snow ball effect" (Barton, 2000). High inflows drag soft materials that increase permeability and connectivity with the rest of the aquifer and cause the accidents of collapse of the station and water gushing. Such collapses interrupted boring tasks and led to costly delays during the construction of the Santa Coloma Sector of Line 9 of the Barcelona Subway which was crossed by subvertical strike-slip faults (Jordi et al. 2011).

Karst Stratum

The Karst stratum with abundant soil caves is mainly caused by dissolution, water erosion, sub-ground erosion, collapse, and other mechanical erosions. Most of Karst caves are irregular and rock surface and downs, they are difficult to be detected accurately and easily cause foundation deformation uneven; The cave roof

deformation easily cause foundation instability; In addition, the engineering activities (such as the extraction of groundwater, etc.) lead to the dynamic change of Karst water will in turn affect the construction and function of the station adversely. Taking Metro Line 6 at Datansha in Guangzhou City as an example (Zhao et al. 2009), the maximum height of a single cave reaches up to 21 m. The water permeability coefficient of Karst caves was 112.2~135.5 m/d. The maximum prediction value of water inflow was 608.8~814.7 m³/d.

Saturated Sand Stratum

The saturated sand stratum has the features of large void ratio, loose structure, easily connecting with the surface runoff and underground seepage. The hazards of water bursting and sand flowing can be easily happened in the foundation pit with saturated sand stratum. When negative layer of Linhexi Station of Guangzhou Metro was excavated to 7m, the dome appeared water gushing and flowing sand. While the flowing sand was controlled through the timely rescue, but surface subsidence values had relatively large (Li 2004).

FOUNDATION REINFORCEMENT METHODS OF METRO STATION ON ADVERSE GEOLOGICAL CONDITION

Saturated Soft Clay Stratum

The treatment method of the saturated soft clay stratum base on reinforcement mechanism and construction methods can be divided into seven aspects: replacement and fill cushion, preloading foundation, compacted foundation, tamping foundation, composite foundation, grouting reinforcement and micro-pile. At present, the design and construction process of retaining structure are not the same in different places. Steel sheet (pipe) pile, precast concrete pile, bored pile, digging filling pile, deep mixing pile, high-pressure rotary jet grouting pile, SMW (Soil Mixing Wall) method, diaphragm wall and caisson method are used widely. It is important to consider security and economic effect of engineering to select engineering solutions. Table 1 had summarized retaining structure options in different excavation depth by Shi (2006).

Foundation soil of South Xizang Road Station of Shanghai Metro which was mainly composed of 70m saturated clay, silt and sand. The excavation depth of foundation pit which has five internal bracing was 15.8m. Retaining structure used 1.0m diameter bored piles combined with 180° directional rotary jet grouting pile for preventing groundwater, and foundation reinforcement selected high-pressure rotary jet grouting pile to cover the entire foundation. Through the monitoring of foundation pit, Ding et al. (2008) had got the relationship between the maximum lateral displacement of retaining structure ($\delta_{h,max}$) with excavation depth (H), as showed in Fig. 1. The result showed that the ratio of $\delta_{h,max}$ to the H ranged from 0.1% to 0.2%, and the average value was about 0.145%, basically met the requirement of specification for excavation in Shanghai Metro construction of 0.14%. Ding et al. had compared the results with the Wang et al. (2005) and Xu (2007), as showed in Fig. 1(a). Wang et al. (2005) collected the measured data of the six stations of Shanghai Metro, the retaining structure of all stations were diaphragm wall. A database of 39 case of deep excavations in Shanghai soft deposit was presented by Xu (2007). The 39 deep excavations can be divided into

three categories: type I, the excavations which were supported by permanent structure, retaining structure was diaphragm wall; type II, the excavations which used normal construction method and used diaphragm wall as retaining structure; type III, the excavations which used normal construction method and used SMW method.) The result showed that the ratio of $\delta_{h,max}$ of Wang's and Xu's to the H ranged from 0.04% to 0.6%, and the average value was about 0.3%, the discreteness of the data was relatively larger than Ding's. Similar results was reported from five metro stations at Iran-Ahwaz metro which used diaphragm wall for preventing groundwater (Fig. 1b). It can be seen that the data $\delta_{h,max}$ fall between (0.25-0.35)% H (Mohammad et al. 2013). Therefore, the construction method of bored piles combined with rotary jet grouting pile for cutting off groundwater was generally proved to be more effective in controlling deformation of deep excavations than diaphragm wall or SMW method.

Table 1. Retaining structure options in different excavation depth

| Excavation depth | Retaining structure options |
|------------------|--|
| ≤ 6 m | Mixing pile retaining wall |
| | Bored pile or digging filling pile combine with mixing pile or rotary jet grouting pile for cutting off groundwater, one bracing |
| | Steel sheet pile or precast concrete pile, one or two bracing |
| 6-11 m | Bored pile or digging filling pile combine with mixing pile or rotary jet grouting pile for cutting off groundwater, one or two bracing |
| | Diaphragm wall combine with bracing (if the retaining structure doubles as a permanent structure) |
| | Steel sheet pile, two or three bracing |
| | SMW method |
| 11-14 m | Bored pile or digging filling pile combine with mixing pile or rotary jet grouting pile for cutting off groundwater, three or four bracing |
| | Diaphragm wall combine with bracing (if the retaining structure doubles as a permanent structure), construction method: top-down method or semi-inverse method |
| | SMW method |
| | Caisson method |
| > 14 m | Diaphragm wall combine with bracing, construction method: normal construction method, top-down method or semi-inverse method |
| | Bored pile or digging filling pile combine with mixing pile or rotary jet grouting pile for cutting off groundwater, more than five bracing |

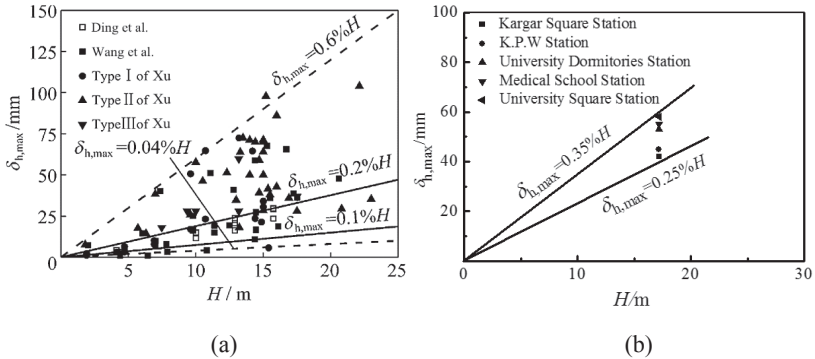


FIG. 1. Relationship between maximum lateral displacements of retaining structure with excavation depth: (a) metro stations at Shanghai Metro; (b) metro stations at Iran-Ahwaz metro.

Water-rich Fracture Zone

The station should try to avoid fracture zones in the engineering design and construction. Otherwise, it should take appropriate reinforcement and seepage control measures.

The retaining structure of foundation pit which uses open cut method can select row piles combine with sealing up curtaining or diaphragm wall combines with bracing. The diaphragm wall is advised to use the strongly weathered or moderately weathered bedrock as bearing layer. The embedding depth of the foundation should deepen appropriately to prevent groundwater flowing to make the diaphragm wall overturning along the fracture zone. Subsurface excavation construction often relies on reinforcement measures for the lining supports. For the fracture zone of smaller scale and less affected to the foundation, it can excavate surface and fill concrete; For the fracture zone of large scale, it generally require to dig cogging and set anti-slide pile; For the fracture zone of larger scale, it can pour concrete or set up reinforced concrete arch, reinforced concrete beam or reinforced concrete pile; For the fracture zone of good groutability, it can use cement consolidation grouting to reinforce. It had been reported by An et al. (2003) that Xinjiaonan Station of Guangzhou Metro crossed Guang-San fracture zone, and the fracture zone and its influence zone were rich water aquifer and developed with tectonic joints and weathering fissure. In this case, the station used open excavation order method to construct. Retaining structure selected bored piles combined with rotary jet grouting pile for preventing groundwater, and foundation pit equipped with steel pipe support system. During construction, surface subsidence around foundation pit was controlled in less than 30mm and the foundation pit had no obvious water gushing.

Seepage control usually through excavate vertical shaft or inclined shaft along the dip of fault at the intersection of the fracture zone with axis of impervious curtain, and clear weak broken material and backfill concrete, and grout the contact surface of the concrete and the fault bedrock to form a concrete cutoff wall to deal with, but the construction is difficult. In order to reduce the difficulty of construct, it tends to use large-diameter drilling to pour chain impervious wall of concrete or

use high-pressure perfusion slurry of cement or chemical materials slurry to form an impervious curtain. Although above methods can achieve a certain effect, but the impact on the surrounding environment in the urban built-up areas is usually relatively large. Therefore, artificial ground freezing method can be utilized to solve the problem (Li et al. 2006)). Dr. Sun Yat-sen's Memorial Hall Station of Guangzhou Metro crossed Qingquanjie fracture zone. It used shallow mining method to excavate and used horizontal freezing method as auxiliary construction methods to freeze full-face curtain. In the early of froze, it took quick cooling and freezing measure to reduce the impact of frost heaving and thawing during the construction on ground subsidence. When the frozen wall melting, it grouted timely once the settlement exceeded the allowed values. Compared to the impervious curtain above, the freezing method costs higher, but the construction process was relatively simple, and more effective on sealing and subsidence control.

Karst Stratum

The treatment methods of the Karst stratum mainly are dredging, filling, across and reinforcement. Treatment for Karst water should take the dredging as the essential measurement, and the measures such as drainage hole, pipeline and open ditch are used commonly. For shallow cave, it can dig out weak filler and fill gravel, crushed rock, rubble, sand or concrete, and the filter layer should be set on the filler to prevent scouring. For deep buried cave or the roof of cave unstable, it can use grillage foundation, long beam foundation, or great rigidity raft foundation to cross cave. The fulcrum of the foundation must be placed in the rock or reliable bearing stratum. For larger or more layers of development and to bear a larger load cave, it can use cement mortar or cement clay mixed slurry to instill in the Karst fissure or cave, or use pile foundation to pass through or to avoid cave, or use composite foundation to compact loose soil and increase the carrying capacity, such as sand column, lime column, deep mixing pile, steel pipe pile and so on.

Site investigation identified the presence of a number of unfavorable geological bodies around the Huangzhuang station of Beijing by Fang et al. (2011), such as loose zone, cave, water bearing zone and some other unidentified structures, among which cavity was most common (Fig. 2). For the treatment of cavities, cement grouting was utilized to fill up the void space (Fig. 3). After treatment, the ground surface settlement for all the monitoring points was successfully controlled below 75 mm.

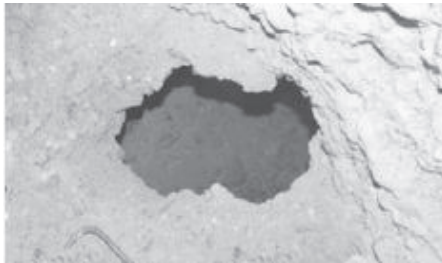


FIG. 2. Cave of Huangzhuang station.

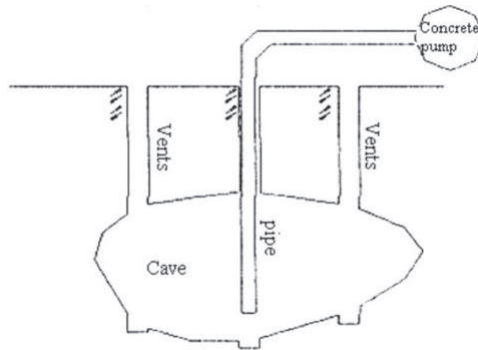


FIG. 3. Sketch of filling a cave.

Saturated Sand Stratum

Dig and replace, encryption, supercharged, enclosed drainage and deep foundations are effective measures to deal with the sand liquefcent. For processing problems of water bursting, the methods are similar to the treatment methods of the saturated soft clay stratum. A field construction using jet grout column was conducted to improve the ground in the foundation pit of a metro station of Line 9, Seoul, Korea which site was in saturated sand stratum. The admixture of grout-soil can be gelled within 5 to 10 seconds, and the ground can be quickly solidified, providing a three-fold increase in work efficiency (Shen et al. 2013).

CONCLUSIONS

Since metro systems have been developed rapidly, it is inevitable to build metro stations on geologically sensitive areas. Taking serious considerations on engineering geological conditions and the construction environment to determinate the right foundation treatment method is very important for the project to reach the goal of safety and economy. The major results are summarized as follows:

(1)The saturated soft clay stratum will lead to the hazards of settlement deformation, foundation pit collapsing or sliding, and the water gushing can be easily taken place during the construction. The treatment method of this stratum base on reinforcement mechanism and construction methods can be divided into seven aspects. It should consider security and economic effect of engineering to select engineering solutions.

(2)Water-rich fracture zone is easily to form dynamic flowing water path, and cause the accidents of changeable water pressure and water inrush. The station should try to avoid the fracture zone in the engineering design and construction, otherwise, it should take appropriate reinforcement and seepage control measures.

(3)The Karst stratum with abundant soil caves are difficult to be detected accurately and easily cause the collapse and subsidence accidents. Dredging, filling, across and reinforcement are widely used to deal with this stratum.

(4)The water bursting and sand flowing hazards can be easily happened in the foundation pit on saturated sand stratum. For processing problems of water

bursting, the methods are similar to the treatment methods of the saturated soft clay stratum. Dig and replace, encryption, supercharged, enclosed drainage and deep foundations are effective measures to deal with the sand flowing.

REFERENCES

- An G.F., Yin K.L. and Tang H.M. (2003). "Design of foundation pit support in Xinjiaonan Station of Guangzhou Metro." *Underground Space*, Vol. 23(3):265-267.
- Barton, N. (2000). *TBM Tunnelling in Jointed and Faulted Rock*. Brookfield, VT: Balkema, cop, Rotterdam.
- Ding Y.C., Wang J.H., Xu Z.H. and Chen J.J. (2008). "Deformation characteristics of deep excavations for metro stations in Shanghai soft soil deposits." *Journal of Shanghai Jiao Tong University*, Vol. 42(11):1871-1875.
- Fruneau B., Deffontaines B., Rudant J.P. and Parmentier A. L. (2005). "Monitoring vertical deformation due to water pumping in the city of Paris (France) with differential interferometry." *C. R. Geoscience*, Vol.337: 1173-1183.
- Fang Q., Zhang D.L. and Wong L.N.Y. (2011). "Environmental risk management for a cross interchange subway station construction in China." *Tunnelling and Underground Space Technology*, Vol.26:750-763.
- Huang M.S., Wang W.D. and Zheng G. (2012). "A review of recent advances in the underground engineering and deep excavations in soft soils." *China Civil Engineering Journal*, Vol.45 (6):146-161.
- Jordi F.C., Enric V.S., Carrera J. and et al. (2011). "Groundwater inflow prediction in urban tunneling with a tunnel boring machine (TBM)." *Engineering Geology*, Vol.121:46-54.
- Li Y. (2004). "Construction technology of the shallow excavation subway air duct in the water-rich sand stratum." *Tunnel Construction*, Vol.24 (2): 25-28.
- Li S.Y., Lai Y.M., Zhang M.Y. and Zhang S.J. (2006). "Minimum ground pre-freezing time before excavation of Guangzhou subway tunnel." *Cold Regions Science and Technology*, Vol.46:181-191.
- Lee W.F., and Ishihara K. (2010). "Forensic diagnosis of a shield tunnel failure." *Engineering Structures*, Vol.32: 1830-1837.
- Ma Y.C., Jong M.D., Koppenjan J., and et al. (2012). "Explaining the organizational and contractual context of subway construction disasters in China: The case of Hangzhou." *Policy and Society*, Vol.31:87-103.
- Pakbaz M. S., Imanzadeh S. and Bagherinia K.H. (2013). "Characteristics of diaphragm wall lateral deformations and ground surface settlements: Case study in Iran-Ahwaz metro." *Tunnelling and Underground Space Technology*, Vol.35:109-121.
- Shi J.H. (2006). Research and analysis of main structural supporting design and construction methods in the dark base hole project of line 3rd of Tianjin Subway. *M.E Thesis*, College of Construction Engineering, Jilin University, Changchun, Jilin, 85p.
- Shen S.L., Wang Z.F., Horpibulsuk S., and Kim Y.H. (2013). "Jet grouting with a newly developed technology: The Twin-Jet method." *Engineering Geology*, Vol.152:87-95.
- Wang Z.W., Ng C.W.W. and Liu G.B. (2005). "Characteristics of wall deflections and ground surface settlements in Shanghai." *Canadian Geotechnical Journal*,

Vol.42 (5): 1243-1254.

- Xu Z.H. (2007). Deformation behavior of deep excavations supported by permanent structure in Shanghai soft deposit. *Eng. D Thesis*, School of Naval Architecture, Ocean and Civil Engineering, Shanghai Jiao Tong University, Shanghai, 316.
- Zhao Q., Lin H., Jiang L.M. and et al. (2009). "A Study of Ground Deformation in the Guangzhou Urban Area with Persistent Scatterer Interferometry." *Sensors*, Vol.9:503-518.

Field comparative tests for studying the vertical loading performance of piles due to water level periodical fluctuation in foundation soils

NIE Ru-song¹, and LENG Wu-ming², YANG Qi³

¹Lecturer, Department of Geotechnical Engineering, School of Civil Engineering, Central South University, Shaoshan Road No.68, Changsha, Hunan Province, China; nierusong97@163.com

²Professor, Department of Geotechnical Engineering, School of Civil Engineering, Central South University, Shaoshan Road No.68, Changsha, Hunan Province, China; lwm123456@126.com

³Lecturer, Mobile Post-doctoral Stations of Traffic and Transportation Engineering, Department of Geotechnical Engineering, School of Civil Engineering, Central South University, Shaoshan Road No.68, Changsha, Hunan Province, China; qiyang433@163.com

ABSTRACT: The water level in the reservoir of the Three Gorge Dam rises from 145m to 175m since the dam is in full operation. The periodical fluctuation of the water level changes the water environment of the reservoir banks. The water saturation and drying cycles affects the strength and stiffness of original rock and soil mass. These changes have led to problems such as the instability of ancient landslide, the safety of buildings supported on pile foundations whose bearing stratum is affected by the changing water levels. Seven 8-storey height buildings supported on pile foundations in Fengjie county in Chongqing Municipality had been facing such threats. A series of field direct shear tests and pile loading tests were conducted to study the influence of capacity of foundation soils due to water level fluctuations. The results indicated that after water soaking, the cohesion strength of the foundation soil decreases significantly, while the internal friction angle is relatively stable. The weaken ratio of the internal friction angle which is the ratio of strength parameters before and after water soaking into the gravel soil is mainly between 0.78-1.0 and the weaken ratio of cohesion strength is around 0.4 to 0.8. The capacity of pile decreased when the water submerged the pile tip. Field calibration and indoor calibration have proved the availability of the O-cell boxes designed and produced by ourselves in pile static loading tests. The observations provided important support for evaluating the safety of seven 8-storey height buildings.

INTRODUCTION

Water is one of the key factors to affect the mechanical properties of soils. The periodical fluctuations of the water level in the Yangtze River controlled by the Three Gorge Dam changes water environment of the reservoir banks, which is affecting the strength and stiffness of original rock and soil mass through constant alternation

from water saturation to air drying. These changes have led to some serious problems such as the instability of ancient landslides, the safety of buildings supported on pile foundations whose bearing stratum is in the changing water levels. The Sanma hill community, as the commercial and administrative center of Fengjie County in Chongqing Municipality is located on the Hou zishi landslide which has been strengthened and testified to stay stable by monitoring data of inclinometers. Figure 1 was the photo of Fengjie wharf and the Yangtze River water level was about 137m. And the water level of 145m and the highest water level, 175m, were shown in the photo. Along the wharf, one of the seven 8-storey buildings shown by yellow rectangular, was facing the threats from the periodical water level fluctuation.



FIG.1. The photo of Fengjie wharf

LI Wei-shu(2003) did a series of loading plate tests to study the bearing capacity of debris foundation in new Fengjie City. He (2006, 2007) also studied shear strength degeneration of soil and rock mixture in Three Gorges Reservoir bank slopes under influence of impounding. KONG Wei-xue(2005,2007) did a lot of direct shear tests in lab to study the bearing capacity and weakening effect of water on gravel soil. In order to ensure the security of the buildings, a clear understanding of the ultimate bearing capacities and settlements in such conditions is needed. Field tests are the most reliable methods and field direct shear tests and pile loading tests of two piles were conducted to study the influence of bearing capacity of foundation soils due to the water saturation and drying cycles.

INVESTIGATION

According to the materials of the seven 8-storey buildings, the soil profile at the site consists of about 15m to 20m of gravelly soil overlying stone block and there are

no clear boundaries between the two soil layers. The soils are in middle dense to dense state. The physical and mechanical properties are in high variability. Figure 2 shows the result of sieve analysis of the soils. The maximum size of the soil particles is less than 100 mm and the percentage of silt and clay are very little. The mechanical properties of the soils are listed in Table 1. f_a is the bearing capacity characteristic value of soil.

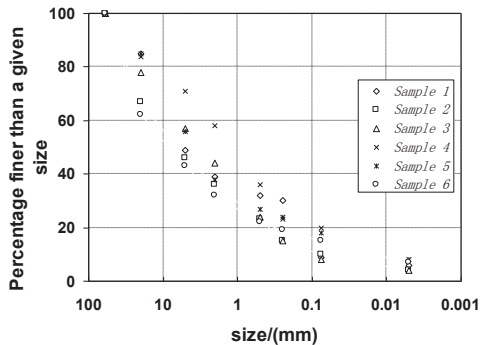


FIG.2. Particle size distribution

Table 1. The mechanical properties of the soils

| soils | f_a /(kPa) | c /(kPa) | φ /($^{\circ}$) | E_s /(MPa) |
|---------------|--------------|------------|---------------------------|--------------|
| gravelly soil | 220 | 30 | 25 | 15 |
| stone block | 400 | 50 | 35 | 20 |

The foundations of buildings are 0.8m~1.2m diameter artificial dig-hole piles which are mostly embedded on gravelly soils and stone blocks. The pile-tip levels are about 10m to 20m below the highest water level. Piles are about 18m to 30m long. The concrete label of piles is C20.

DIRECT SHEAR TESTS

Field direct shear tests were conducted on the landslide to explore the attenuation rule of the soils in two states: the natural state and the saturation state. The saturation state means that the specimens in the direct shear boxes were flooded for at least 24 hours. Most of the direct shear tests were conducted during the time of strengthening the landslide. Figure 3 and figure 4 show the results of the direct shear tests of specimens at different depth. Compared with the natural specimens, the “ φ ” and cohesion strength of saturation specimens were smaller. The parameters of soil strength with the depth were discrete. The “ φ ” scatters in 10° to 35° and the cohesion strength scatters in 2 kPa to 80 kPa. Below statistics results of “ φ ” and cohesion strength are listed in table 2.

Two parameters are defined to describe the attenuation rule of the gravelly soils.

The weaken ratio of cohesion strength: $\eta_c = \frac{c_{sat}}{c_{nat}}$

The weaken ratio of internal friction angle: $\eta_\phi = \frac{\phi_{sat}}{\phi_{nat}}$

Figure 5 shows the results of “ η_ϕ ” and “ η_c ”. Most of “ η_ϕ ” scatter from 0.78 to 1.0 and most of “ η_c ” scatter from 0.4 to 0.8. The average of “ η_ϕ ” and “ η_c ” are 0.82 and 0.60 respectively. The standard deviation of them are 0.12 and 0.18 respectively.

Table 2. The statistics results of field direct shear tests

| Soil | c/(kPa) | | phi/(°) | |
|------------|---------|--------------------|---------|--------------------|
| | average | standard deviation | average | standard deviation |
| natural | 34.21 | 17.14 | 23.41 | 4.97 |
| saturation | 21.94 | 13.77 | 19.35 | 5.02 |

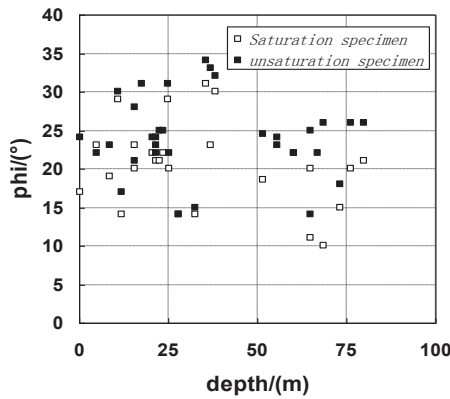


FIG.3. The internal friction angle with depth

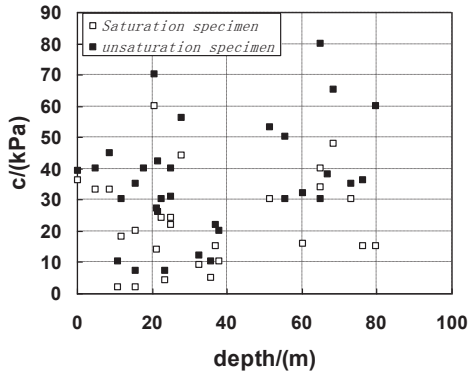


FIG.4. The cohesion strength with depth

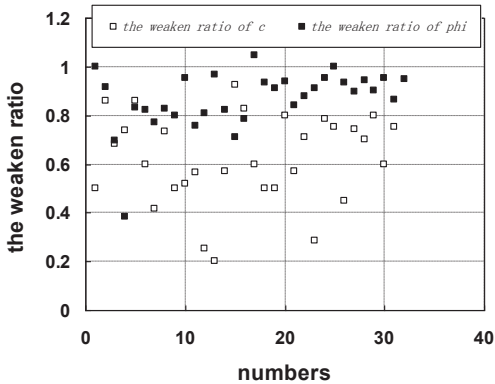


FIG.5. The weaken ratio of soil strength

DESIGN OF TWO PILES

Two artificial dig-hole piles were designed and constructed on the narrow platform of the landslide shown in FIG.1 and FIG.6. to investigate the capacity and settlement of piles. Figure 6 shows the site of two piles located on the narrow platform whose elevation is 175m. The piles were made 0.86m in diameter, 0.15m in dado thickness, 18m in length and 5m in pile spacing. In order not to affect the stability of the landslide and because of economic reasons, the static loading tests for piles employ the Osterberg cell method. In pile A two steel pipes with holes on pipe wall for water seepage to soils were buried in breast wall to soak the soils around the pile. Before static loading test, the soils were soaked for 3 days and the water level was measured 1.5m above the pile tip. Figure 7 shows water is soaking the soils through two steel pipes. Figure 8 shows the details of the arrangement of the strain gauges and the location of O-cell boxes. The O-cell boxes were designed and made by our team. The

diameter of the O-cell boxes is 0.78m and the height is 0.3m. Indoor calibrations were done before O-cell boxes were fixed.



FIG.6. The site of two piles



FIG.7. Water soaking soils around the pile through two steel pipes.

FIELD CALIBRATION OF O-CELL BOXES

O-cell boxes are the most important loading device in O-cell static loading test. It is hard and important work to calibrate the o-cell boxes indoor. The basic principle of O-cell working is Pascal principle of liquid pressure. In fact, oil pumps are usually used to provide oil pressure to O-cell boxes, the liquid pressure multiplied the area in O-cell boxes oil pressure acted on, is to determine the output load of O-cell boxes. The equipment includes O-cell boxes, oil pumps and oil pipelines. There are many uncertain factors when O-cell boxes work. Calibrating O-cell box is necessary to determine the relationship between pump oil pressure and the output pressure of O-cell box. Two methods including indoor method and field method have been applied to calibrate the O-cell boxes. Field calibration process is the process of loading and unloading the piles. The elastic modulus of pile concrete is tested in lab and the average elastic modulus value of concrete is 17.8GPa. The diameter of pile is taken to be 0.86, neglecting the influence of the dado thickness. The curves of axial force on section H and the output of O-cell box are shown as FIG.9.

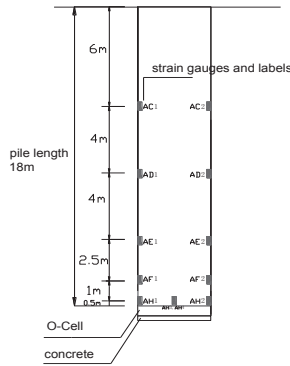


FIG.8 strain gauges arrangement for piles

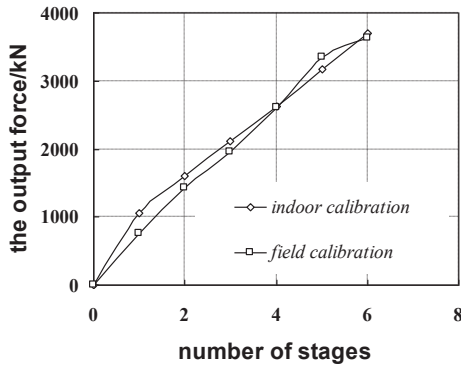


FIG.9. Calibration of O-cell box

Figure 9 shows that field calibration and indoor calibration have similar linear relationships. At the former load steps, the axial forces of section H are slightly lower than the output load of O-cell box. That is because the shaft resistance between the section H and the O-cell box works. As the output load of O-cell increases, the shaft resistance is fully mobilized and become a constant value. The shaft resistance occupying the output load is falling from 27.71% to 0.55%. Two calibration methods are proved correct and the O-cell boxes in piles operate reliably.

Q-S CURVES OF TWO PILES

In spite of the similar foundation conditions, the similar construction technology and the same loading methods, the capacities of Pile B and pile A are impossible to be the same. Even if is such, they still provide important reference to know the capacities of piles before soaking and after soaking.

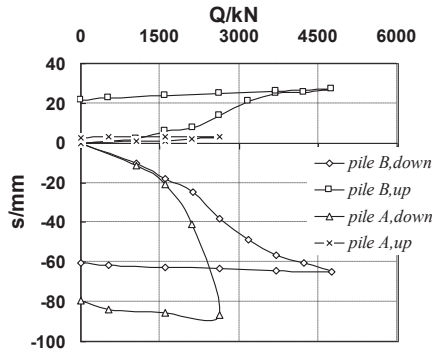


Fig.10. The curves of Q – S of two piles

Figure 10 shows the Q-S curve of pile A and pile B. Q represents the output force of O-cell boxes and S is the movement of the top and base plates of O-cell box. The Q-S curve of pile A after soaking is obviously different from the Q-S curve of pile B without soaking. The toe resistance and shaft resistance of pile B is higher than that of pile A. For pile B, O-cell box below the tip of pile does not fully mobilize the toe resistance and shaft resistance. The curves indicate that there is soft mat below the tip. If the capacity of pile is defined as the corresponding load on the top of pile being pressured down 40 mm and the pile shortenings are not included, the base capacity of pile B is 2630 kN and the shaft capacity is larger than 2630 kN. The capacity of pile B is larger than 5260 kN. Similarly the capacity of pile A is larger than 4240 kN.

THE AXIAL FORCE OF PILES

Figure 11 and figure 12 show the axial forces in pile A and pile B. The axial force curves of two piles increase steadily from pile top to tip. From pile top to 10m, the shaft resistances are not fully mobilized. The main cause is that the toe resistance of piles can not provide enough counter-force to mobilize the shaft resistances. Here using the β method to estimate the capacities of the two piles. Above the O-cell boxes, there are short shafts where the shaft resistances are fully mobilized. Corresponding to the down movement of O-cell boxes, 40mm, the shaft resistances are used to calculate β to be 0.517 for pile B and $\beta=0.45$ for pile A. The capacity of Pile B was about 7155 kN and Pile A was about 6050 kN. The base capacity and shaft capacity of pile A are 2120 kN and 3930 respectively while pile B's are 2630 kN and 4525 kN. If the capacities are taken to be the same before three days' soaking, the capacity of pile A is about 84.55% of Pile B's. The weaken ratio of shaft capacity and base capacity are 86.85% and 80.61% respectively after three days' soaking.

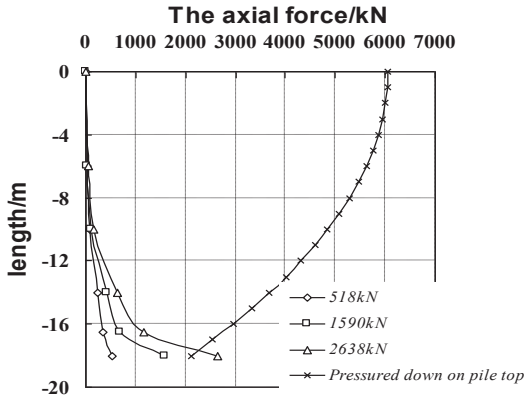


Fig. 11. Distribution of axial force of pile A

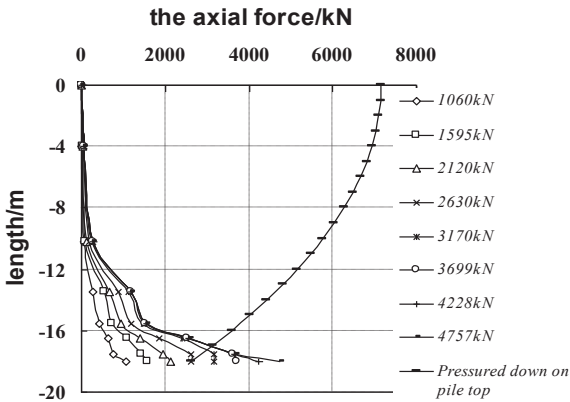


Fig. 12. Distribution of axial force of pile B

CONCLUSIONS

The periodical fluctuation of the water level affects the mechanical properties of soils and rocks of the bank slopes along the Yangtze River. Field direct shear tests and pile static loading tests of two piles indicate that the gravel soils have strong weakening effect during the water soaking process. The cohesion strength of the foundation soil decreases significantly, while the internal friction angle is relatively stable. The capacity of pile in soaking conditions also decreases compared with those in natural conditions. O-cell boxes are important devices in static loading test and field calibration and indoor calibration have proved the availability of the O-cell

boxes designed and produced by ourselves.

The researches have been supported by Natural Science Foundation of China (51108464,51208518) and the Fundamental Research Funds for the Central Universities (2011QNZT106)

REFERENCES

- LI Wei-shu, LIU Jiang-zhong(2003). "Study on bearing capacity of debris foundation in new Fengjie city." *Journal of Yangtze River Scientific Research Institute*, Vol. 20(2):61-64.
- LI Wei-shu, WU Ai-qing, DING Xiu-li(2006). "Study on influencing factors of shearing strength parameters of slide zone clay in Three Gorges Reservoir area." *Rock and Soil Mechanics*, Vol.27(1):56-60.
- LI Wei-shu, DING Xiu-li, Wu Ai-qing, et(2007). "Shear strength degeneration of soil and rock mixture in three Gorges Reservoir bank slopes under influence of impounding." *Rock and Soil Mechanics*, Vol.28(7):1338-1342.
- LIU Wen-ping, SHI Wei-min, KONG Wei-xue, ZHENG Ying-ren(2005). "Weakening effect of water on gravel-soil in Three Gorges Reservoir area." *Rock and Soil Mechanics*, Vol.26(11): 1857-1861.
- KONG Wei-xue, ZHENG Ying-ren.(2005) "Study on bearing capacity of foundation of saturated gravelly soil in the reservoir zone of the Changjiang gorges." *Industrial Construction*, Vol.35(4):62-64.

Simulation of the dangerous area by PFC for the Lvchunba crag body

Jun Xu¹, Anhong Li², Yongxin Wei³, Chugen Li⁴ and Yang Liu⁵

¹Senior engineer, China Railway Eryuan Engineering Group Co. Ltd, Chengdu, Sichuan, P.R.China, 610031; jesse525@126.com

²Professor of engineering, China Railway Eryuan Engineering Group Co. Ltd, Chengdu, Sichuan, P.R.China, 610031; Liyd4321@sina.com

³Professor of engineering, China Railway Eryuan Engineering Group Co. Ltd, Chengdu, Sichuan, P.R.China, 610031; yonxing@vip.sina.com

⁴Professor of engineering, China Railway Eryuan Engineering Group Co. Ltd, Chengdu, Sichuan, P.R.China, 610031; lichg8789@163.com

⁵Professor of engineering, China Railway Eryuan Engineering Group Co. Ltd, Chengdu, Sichuan, P.R.China, 610031; ly870702@126.com

ABSTRACT: The crag body at the slope of the Lvchunba tunnel entrance is so larger that it's necessary the dangerous area and minor dangerous area is determined firstly in the design, and then the proper and economical treatment is adopted. There isn't division method of dangerous area in current codes and standards, so field test is adopted for inverse analysis of the numerical parameters. After then the rock-fall motion path is simulated for all of the sections by particle flow code. At last the dangerous area and minor dangerous area is determined according to the influencing range and degree of rock-fall on all of the sections. Based on the particle flow code, the 2-D visual simulation of rock-fall motion path is realized, and the motion style of free fall, bouncing and rolling can be obtained, and then it's feasible to analyze the dangerous area of crag body. Also the motion velocity and displacement of the rock-fall at anytime can be gained so that the reference is presented for calculating the energy or impact force of rock-fall at different position. The simulation method of particle flow code can be used as a reference for the design of similar railway engineering.

INTRODUCTION

Crag as one of the three severe natural disasters in mountainous areas of China has become the key restriction factor for the western development policy and the great development in railway and road traffic construction. Crag disaster includes definition and content of dangerous rock, collapsing rock, rockfall and rolling stone, etc, of which the rockfall refers to a dynamic geological disaster that the rock-soil body is cut by joint fissure under action of gravity or other external forces and suddenly separated

away from the rock matrix or collapsed down from its original position(Hu 1989). Portal sections of tunnel in mountainous area are always located in geologically vulnerable sections with steep terrain and fractured rock body. In addition, slope cutting and blasting, etc. for construction also put the portal sections of tunnel into serious risk of rockfall. Thus, the rockfall disaster at tunnel portals becomes increasingly prominent(Ye 2008). At present, the simple open-cut tunnel portal is generally employed for tunnels in China railway system at rockfall sections in accordance with the requirements of relevant specification and code(TB10003 2005; CREEC 1999).

Prevention and control technology for crag rockfall depends on studies on simulation and calculation of rockfall movement trajectory, impact characteristics of rockfall and identification of hazardous area of crag body, etc. Dangerous areas of crag body may be understood as the integration of areas crossed by the route of rockfall movement on each cross-section of crag body. In such areas, all engineering structures, construction equipment, infrastructure and personnel will be endangered by the rockfall disaster. Therefore, the classification of dangerous area of crag body is very important for engineering structure design, construction safety and land acquisition and planning, etc. The determination of hazardous areas mainly includes investigation on historical rockfalls, field test and rockfall movement calculation and simulation, etc. Currently, in China, the determination of hazardous areas is still based on investigation on historical rockfalls. And in foreign countries, it is generally based on some empirical methods. For examples, Hungr et al.(1988) proposed dangerous area of rockfall disaster based on investigation of colluvium slope; and Azzoni et al. (1995) proposed the range of lateral rockfall movement from a single slope is 10% of the slope length according to the dangerous area of rockfall disaster gained from field test. In recent years, Jaboyedoff et al.(2003) has predicted dangerous area of rockfall disaster by GIS and rock pile characteristics; and F. Guzzetti et al.(2003) has carried out 3-D simulation on dangerous area of rockfall disaster in Yosemite Valley of California, U.S.A. by STONE simulation software, digital elevation system and GIS. Calculation of rockfall movement trajectory is the basis of analysis of hazardous areas, including common methods such as empirical method, test method and calculation of rockfalls. The empirical method is to study and conclude the relationship between rockfalls and slope based on field investigation data or a great many of tests and studies. The test method includes two kinds of tests i.e. field test and model test, in which the field test is the best way to determine the rockfall movement trajectory(Huang et al. 2007). The calculation of rockfalls includes mathematical mode and numerical simulation mode(L.K.A.Dorren 2003). The former includes the imported semi-empirical and semi-theoretical formula of H.M. Ройнишвили (former Soviet Union) used in China as well as similar formulae and numerous improved formulae(Chen et al. 2004; Tang et al. 2003). As required by simulation of disintegration and collision, some numerical analysis methods are proposed, such as the discrete element method (DEM) created by Cundall(1971).

In general, based on the empirical design, the analysis and study on crag body by methods such as numerical simulation and field test, etc. are feasible and reliable. The hazardous areas of crag body at the portals of Lvchunba tunnel of Chongqing-Lichuan(Yuli, namely) Railway are analyzed herein in combination with field test and

numerical simulation, providing reference and basis for engineering design.

OVERVIEW OF CRAG BODY ON LVCHUNBA SITE

The working site is located at the upside of the portal of Lvchunba tunnel of Yuli Railway. The entrance of Lvchunba tunnel is connected to the double-track super major bridge in the Lvchunba and the exit to the Longhe River Bridge. The entrance and exit of the tunnel are next to and located at the front of the Jiangma Road, with extremely poor portal geological conditions and complicated components of crags. The vault of the entrance section is surrounded by several crag groups, shown as Figure 1. The relative height difference between the mountaintop section with an altitude of 380~480 m and the portal ground (inner rail top) is greater than 200 m and crags are close to the cliff. The rock body is seriously fractured and the most of rock bodies are cut vertically with a crack width more than 20 cm and in an obvious trend of sliding down, forming several free faces. Such rock body which may drop down at any time is significantly a kind of potential safety hazard, shown as Figure 2. For stability of the working site, the focus is put on the stabilities of slope surface, cliff top boulder and cliff surface crag body. Therefore, the crag body on the cliff slope shall be removed.



FIG. 1. The crag body on Lvchunba

FIG. 2. The broken rocks and cracks

FIELD TEST AND ANALYSIS

In order to ensure reliable results of numerical simulation analysis, the required parameters shall be subject to inversion calculation according to field test. Therefore, a field test point has been set at a working site of Lvchunba in crag and rockfall area, and a small scale of basting of crag has been carried out with filming in the whole course based on simulation of actual construction conditions, so as to gain a representative rockfall movement trajectory from analysis. See Classification of Hazardous Areas (Figure 5) for typical location of rockfall in field test site.

Test conditions

Blasting place: On the cliff nearby the axial section No.5, with a ground elevation about 460 m; and

Parameters of blasting test: Drilling depth: 1.0~1.5 m; spacing of holes: 0.6~0.8 m; number of holes: 11; charge: 0.5 kg for a single hole, 5.5 kg in total; and quantities of earthwork and stonework being blasted: 20 m³.

Test results

Movement trajectory of main flyrocks and rolling rocks: After blasting, flyrocks are scattered around through horizontal throwing, inclined throwing and free falling. Most of rockfalls fall on the lower platform of the cliff. Blocks with larger diameter (about 20~35 cm) finally stop at the gentle slope toe of maintain through dropping on the platform and rolling and jumping along the slope surface in a sector shape. The ground elevation of the place where the rolling rocks have stopped is a bout 245 m. In the first stage (horizontal throwing), the vertical displacement of rockfalls is measured as 100 m and the horizontal displacement as 50 m. In the second stage (jumping and rolling movements), the vertical displacement is measured as 115 m and the horizontal displacement as 150 m.

NUMERICAL SIMULATION ANALYSIS

Numerical analysis on flyrock movement trajectory after blasting has been carried out based on data collected from field test. The simulation of a block with a diameter of 1.0 m has been conducted from dropping on the rock pile after being thrown from different places and finally stopping through jumping and rolling. Moreover, the moving velocity, energy and impact force of the block at various places have been calculated.

Particle flow simulation analysis programme (PFC)

PFC3D (Particle Flow Code in 3 Dimensions) is an effective way to simulate the movement and interaction of circular particle mediums by the Discrete Element Method and then to gradually simulate issues about solid mechanics and particle flow(Cundall 1971). Main steps(Zhen et al. 2008)) of numerical simulation by PFC include: (1) Defining the simulation target and developing detailed programme according to the simulation purpose; (2) Establishing basic concept of mechanical model to form the preliminary concept on characteristics of the analysis target under certain initial conditions and then to determine and describe the general characteristics of the model; (3) Constructing and operating the simplified model; (4) Supplementing data of simulation target and choosing reasonable parameter study range to provide information for further test; (5) Further preparation for operation of the simulation, such as determining the time required by each time step, saving the operation state of the model and arrangement of adequate monitoring points (such as place with changed parameters and unbalanced force, etc.); (6) Operating calculation model and carrying out some test models prior to formal operation of the simulation model, suspending the operations, verifying whether the simulation results are reasonable according to field test conditions or theoretical calculation result, and linking all data documents to conduct calculation after determining that the operation of the simulation model is correct; and (7) Interpreting the results and analyzing and comparing the calculation results and the measured data.

Particle flow analysis model

(1)Slope surface: The slope surface model is mainly used for defining the geometric

shape of the slope surface and properties of interaction of the slope surface and rockfall. The geometric shape of the slope surface is subject to piecewise linear definition and the slope is described through the unit of combined wall. The properties of the wall include geometrical features, shear stiffness, normal stiffness and friction coefficient, etc.

(2)Rockfall: In general, rockfalls are assumed as balls during rockfall movement analysis. However, the rockfalls are actually in various shapes and a rockfall is always cracked into several smaller rockfalls during movement. Therefore, several particle combinations (Cluster) are used in the PFC to simulate rockfalls in various shapes (according to quantities of different balls and parameters of different combinations). All particles react with each other through bonding and the strength of the bonding determines whether the particles will be disintegrated or not during movement.

(3)Constitutive models required by rockfall simulation are contact constitutive models, including contact stiffness constitutive model, sliding constitutive model and bonding constitutive model. The contact stiffness constitutive model is mainly to simulate the ball-ball contact and relative displacement relationship. During rockfall disaster simulation, the linear contact stiffness constitutive model is used.

Particle flow simulation analysis

Calculation model

In order to analyze the hazardous areas of crag body in Lvchunba, the PFC3D programme is employed for establishment of calculation models for cross-sections within the range of crag body. Due to limited space, the calculation of one cross-section (Axis No.5) is taken as the only one example herein for introducing the analysis procedure. During simulation, only gravity of the rockfall (PFC: set g 0 0 - 9.81) and friction force and impact force between the rockfall and slope surface are considered, excluding the resistances of air and trees on the slope surface. The rockfall is composed of two balls with a given radius of 0.5 m, and the slope surface is simulated based on the wall generated by slope surface points in the CAD cross-section view. In order to realize such procedure, two fish functions are compiled: One to generate block function (make_cluster) and the other to generate slope surface function (make_mountain). In order to consider the initial conditions of block after blasting, the fish statement (ini) of PFC programme is employed for assignment of initial velocity of the rockfall (ini xvel 12.0 yvel 0 zvel 0 xdisp 0 ydisp 0 zdisp 0 range rock_body, only the average initial velocity is considered herein). For recording of rockfall movement trajectory, position of the rockfall at any time is recorded herein (his id=11 ball xpos id=1/plot add his 11) and the animation of simulation is saved (movie avi_open file lcb5.avi/movie step 100 1 file lcb5.avi/cycle 200000/movie avi_close file lcb5.avi). The established PFC3D rockfall movement calculation model is shown as Figure 3.

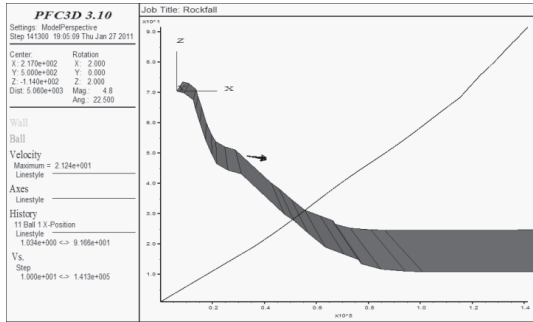


FIG. 3. The PFC3D rockfall movement calculation model on Axis No.5

Calculation results

In order to ensure that the rockfall movement trajectory gained from the numerical simulation analysis is basically consistent with that from the field test, the viscous damping coefficient of the particle flow at the working site is finalized through repeated simulations, by which the rockfall movement trajectory on each cross-section can be gained. See figure 4 for the final rockfall movement trajectory on Axis No.5. The rockfall started to move with the initial velocity of 12 m/s, and flew just like free falling with the motion of projectiles. When met with the slope surface, the rockfall jumped and started to fly again. At last, due to the friction of slope surface, the rockfall gradually ceased.

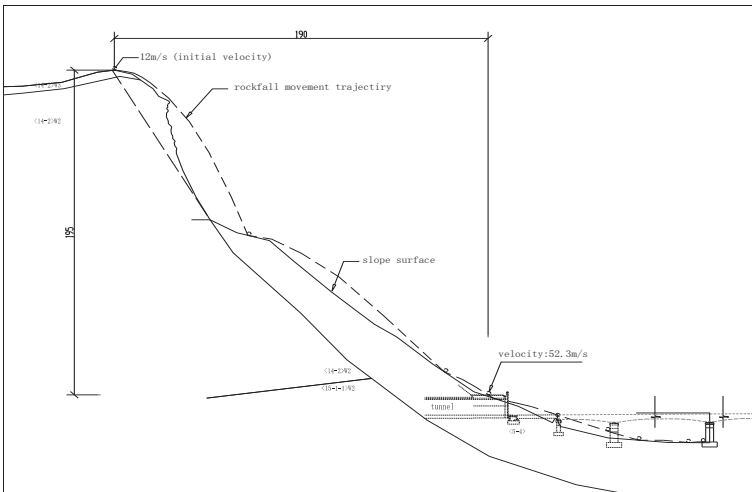


FIG. 4. The final rockfall movement trajectory on Axis No.5

Seen from the rockfall movement trajectory, the numerical simulation analysis

method based on particle flow can get the velocity at any place on the movement trajectory, thereby the energy and impact force at such place can be gained. In the calculation example given herein, the velocity of the rockfall at the tunnel portal is 52.3 m/s and the rockfall impact force is estimated as 77 t according to the reference(Ye et al. 2010). In order to ensure the structural safety of the tunnel portal and bridge deck, measures shall be taken to remove the overhead crag body.

Classification of hazardous areas

(1) Determination of displacement ratio of rockfall movement

The rockfall movement route gained from the numerical simulation analysis is a 2D movement route, only reflecting the status of movement along the cross-section for calculation. However, as the actual rockfall is a 3-D movement, the hazardous area shall be a special and geographical area. For the abovementioned, the displacement ratio of rockfall from the cross-section for calculation shall be clearly defined; thereby, the hazardous areas of rockfall can be determined. According to the reference(Ye 2008), the displacement ratio of rockfall movement is $\eta=0.3$ in the tunnel portal area with Level I risk. Therefore, the corresponding hazardous area in isosceles triangle in any cross-section for calculation can be defined (if the height is assumed as H , the length of the bottom side shall be $2*0.3H=0.6H$).

(2) Analysis of hazardous areas

According to the rockfall movement trajectory on each cross-section gained from the numerical simulation analysis and in combination with the results of field test, the analysis results are as follows: From Axis No.1 to Axis No.3, the rockfall jumping trajectory in Area A-D has no impact on the bridge deck, but has impact on the bridge pier within the rolling range with an affected area of D8K163+990~D8K164+100 along the line. Therefore, the Area A-D is classified as a secondary dangerous area. From Axis No.4 to Axis No.10, the rockfall jumping in Area C-F endangers the deck system of the double-track super major bridge of Yuli Railway in Lvchunba, bridge piers No.20-23 and the tunnel portal, with an affected area of D8K164+000~D8K164+355 along the line. Therefore, the Area C-D is classified as a dangerous area. As Area E-H is the extended excavation range meeting the requirements of slope excavation, the rockfall movement trajectory has no impact on the works. Thus the Area E-H is classified as a secondary dangerous area (or called as the affected area). See Figure 5 for the final classification of dangerous areas of crag body.

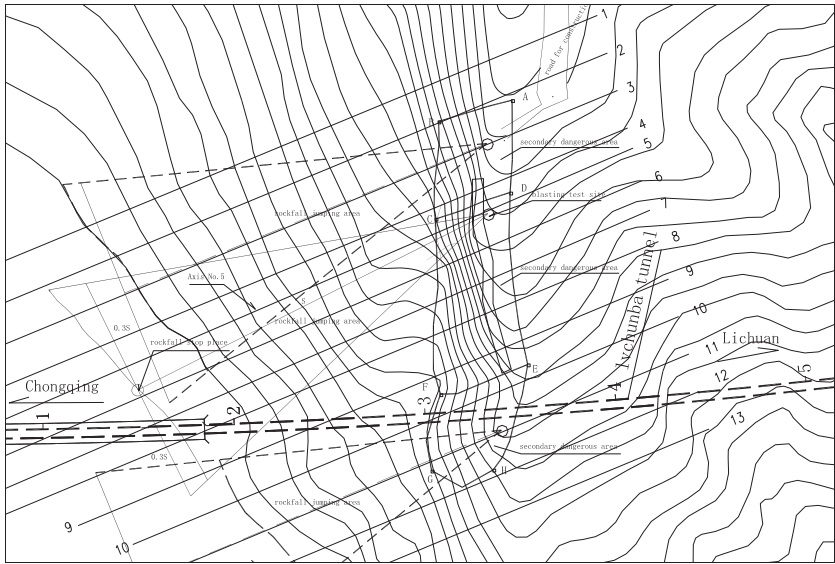


FIG. 5. The final classification of dangerous areas of crag body

CONCLUSIONS

According to the results of field test, the PFC3D numerical analysis software platform based on particle flow is employed for 3-D numerical simulation analysis of the crag body in Lvchunba. Through combination of ball units of the particle flow, rockfalls are generated capable of simulating crags in various shapes and of different characteristics. The simulation of slope surface is conducted by defining wall unit. Ball-ball and ball-wall contact models such as contact-modulus model, parallel bonding model, sliding model are selected to reflect the action of rockfall and inner parts on the slope surface during rockfall movement, so as to realize the 3-D numerical simulation of rockfall from crag body, and gain rockfall movement trajectory on each cross-section and the velocity, energy and impact force of the rockfall at any position. Moreover, the dangerous areas of crag body are identified accordingly to provide reference and basis of crag body rockfall prevention and control design for railways in mountainous areas. The analysis method based on PFC is proposed herein only for hazardous areas of crag body. In order to accurately simulate the rockfall movement trajectory and analyze hazardous areas, it is necessary to establish a real 3-D ground model. Moreover, a further study on selection of parameters for the model and aerodynamics impact during movement with high velocity shall be conducted. (Parameters gained from the field test which are mentioned herein shall be used for each cross-section and be different from the actual ones. Also, parameters of parts in the same cross-section may be different from each other.)

REFERENCES

- Hu, H.T. (1989). "Collapse and Rockfall." *China Railway Press*, Beijing: 78-105(in Chinese)
- Ye, S.Q. (2008). "Research and Mitigation of Rockfall Hazards at Tunnel Entrance and Exit." *Dissertation for PhD of Southwest Jiaotong University*. (in Chinese)
- Industrial Code of the People's Republic of China. (2005). "Code for design on tunnel of railway(TB10003-2005).", 42-44(in Chinese)
- China Railway Eryuan Engineering Group Co., Ltd. (1999) "Technology Reference for Design Manual:Tunnel." *China Railway Press*, Beijing: 141-191(in Chinese)
- Hungr, O., Evans, S.G. (1988). "Engineering evaluation of fragmental rockfall hazards." *Proceedings of the 5th International Symposium on Landslides in Lausanne*. Rotterdam:Balkema, 685-690
- Azzoni, A., Barbera, G.L., Zaninetti, A. (1995). "Analysis and Prediction of rockfalls using a mathematical model." *International Journal of Rock Mechanics and Mining Science*, Vol. 32(7): 709-724
- Jaboyedoff, M., Labiouse, V. (2003). "Preliminary assessment of rockfall hazard based on GIS data." *ISRM2003-Technology roadmap for rock mechanics*, South African,575-578
- F.Guzzetti, P. Reichenbach, G.F. Wieczorek. (2003). "Rockfall hazard and risk assessment in the Yosemite Valley California, USA." *Natural Hazards and Earth System Sciences*, Vol. 3: 491-503
- Huang, R.Q., Liu, W.H., Zhou, J.P., and Pei, X.J. (2007). "Rolling tests on movement characteristics of rock blocks." *Chinese Journal of Geotechnical Engineering*, Vol. 29(9): 1296-1302(in Chinese)
- L.K.A.Dorren. (2003). "A review of rockfall mechanics and modeling approaches." *Progress in Physical Geography*, Vol. 27(1): 69-87
- Chen, H.K., Tang, H.M., Ye, S.Q., Yi, P.Y., and Hu, M. (2004). "Research on Both Bond Mechanism for Unstable Rock to Develop and Move Path for Unstable Rock to Avalanche in the Three Gorges Reservoir Area." *Proceedings of the 8th China National Congress on Rock Mechanics and Engineering*, Science Press, Beijing: 820-825(in Chinese)
- Tang, H.M., Yi, P.Y. (2003). "Research on Dangerous Rock Movement Route." *Journal of Chongqing Architecture University*, Vol. 25(1): 17-23(in Chinese)
- Cundall P A. (1971). "A computer model for simulating progressive large scale movements in blocky rock system." *Proceedings of the ISRM Symposium on Rock Fracture*, Nancy: 129-136
- Zheng, Z.N., Zhang, Y.X., Dong, Q., and Ling, T.Q. (2008). "Visual simulation of rock-fall of slope based on particle flow theory." *The Chinese Journal of Geological Hazard and Control*, Vol. 12(3): 46-49(in Chinese)
- Ye, S.Q., Chen, H.K., Tang, H.M. (2010). "Comparative research on impact force calculation methods for rockfalls." *Hydrogeology & Engineering Geology*, Vol. 37(2): 59-64(in Chinese)

Stability Assessments of the Slope Controlled by Deep Seated Concentrating Belts of Unloading Fractures in Dagangshan (China): a Case Study

Mingli Xiao¹, Hongqiang Xie^{1*}, Jiangda He¹, Baiyu Xiang², Hualin Yang¹

¹College of Water Resource & Hydropower, Sichuan University, Chengdu 610065, China; xiaomingli@scu.edu.cn

²Chengdu Hydroelectric Investigation and Design Institute, China Hydropower Consulting Group Corporation, Chengdu 610072, China

ABSTRACT: This paper presents a case history detailing the two concentrating belts of unloading fractures found in the right bank slope of Dagangshan Hydropower station, China. Based on the analyses about potential sliding modes which controlled by the unloading fracture belts, cause of the three in-situ crack cases are discussed. The results of numerical calculation illustrate the stability of excavation slope and rock mass failure trend, verify development patterns of the in-situ cracks and instability mode of hazard sliding blocks, offer references for reinforcement. The most appropriate and feasible method of stabilizing slopes with deep seated fractures is to construct synthetic reinforced galleries system and combine them with grouting and prestressed anchoring.

INTRODUCTION

A number of hydropower stations are being constructed on the eastern slope of the Qinghai-Tibet Plateau. Deep valleys, rivers of steep gradient, abundant precipitation and sparse population offer ideal sites for hydropower development. However, the complex geological formation also increase safety risks and project investment. The slopes which contain deep discontinuous planes within the rock mass are one of the most common problems in some constructions.

This paper presents a stability analysis for the right bank slope of Dagangshan Hydropower Station where deep seated fractures are dominant. The geotechnical models of limit equilibrium method (LEM) and finite element method (FEM) were used to simulate the different slope enforcement scenarios for the proposed dam site.

GEOLOGICAL CONDITIONS

Located on the middle reach of the Dadu River, southwestern China, Dagangshan Hydropower Station is under construction and will generate some 2,600MW. A 210m-tall double-curvature arch dam will impound water to 1130m asl from 952.6m asl. The slopes at right bank rise more than 600m at an angle of 40°~50° below 1220m asl, above which they are 35°~40° (Fig. 1).

The main strata of the right slope consists of incanus/reddish medium-grain biotite monzonitic granites ($\gamma_{4.1}^2$) showing weathering-unloading phenomena. The diabase (β) and aplite-granitic (γ_L) dykes are widely embedded in the strata. The tectonic patterns of rock mass are featured by faults, joints, fractures and compresso-crushed zones along with dykes. Exploration (CHIDI 2010) reveals 78 diabase and 8 granite dykes developing at the right slope (Fig. 1). The majority of faults are generated along with diabase dykes of the NNW or NE strike which dip with a steep angle and are facing toward the slope. In the 5 sets fractures on the right slope, Set 2 with NNW strike and Set 5 with NE strike are relatively more developed. Above 1200m asl, the base rock is covered by grayish yellow rubbles with soil (Q_4^{col+dl}).

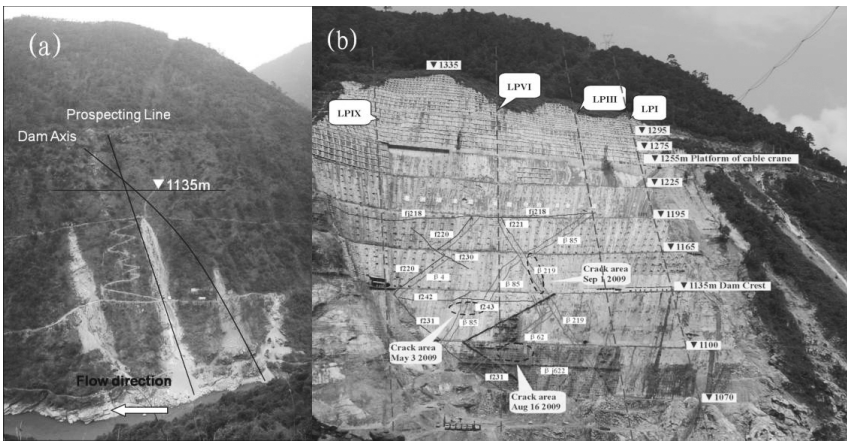


FIG 1 The right slope of the proposed arch dam
(a) natural slope; (b) Excavation and discontinuous plates exposed on the surface

CHARACTERISTICS OF DEEP SEATED FRACNTURES

Compared to a more commonly observed individual fractures that are sparsely spaced, Set 5 fractures are closely spaced and interconnected. Several or more than 10 tension fractures intensively develop in the thick range of 2~15m, and show the obviously thickly banded pattern. Furthermore, the cover depth of the fractures (the maximum 140m) is also worth noticing. Hence, they are referred to as “deep seated concentrated belt of unloading fractures”. Based on the characteristics of distribution and development, it can be separated to two concentrated belts: XL_{316-1} and XL_{9-15} .

XL_{316-1} is discovered from LPI-I to LPIX-IX developing at about 1180m~1400m asl (Fig. 2). The cover depth is about 60m~140m from the natural slope surface, 60~120m from the excavated face. It is parallel to surface slope with an occurrence of $N90^\circ \angle 40^\circ \sim 50^\circ$. The general thickness of XL_{316-1} is 2~5m, and the maximum is about 14m (LPI-I). It appears intensive unloading-relaxation phenomena, where the open and closed fractures distribute alternatively as a beading nodules structure (Fig. 3a). The aperture is relatively small when passing through $\gamma_{1.5}$. Above 1250m asl, tension fractures are well penetrated with more steep inclination.

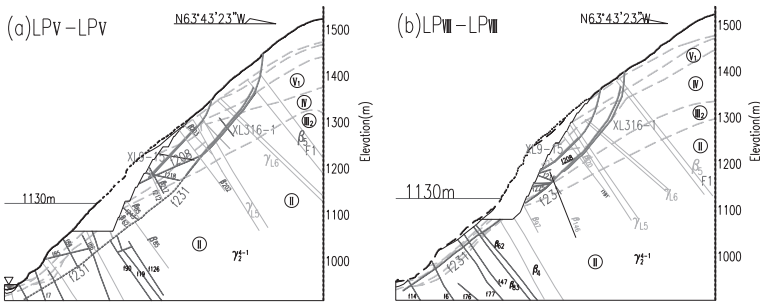


FIG.2 Typical cross sections of the right bank slope:a PLV-V; b PLVIII-VIII



FIG. 3 Shape of unloading fracture belts: (a) XL₃₁₆₋₁, PD316 +100m side wall; (b) XL₉₋₁₅, PD322 adit +90m side wall

The occurrence of XL₉₋₁₅ is N80°∠47°~52°, almost parallel to XL₃₁₆₋₁ (Fig. 2). The natural cover depth is about 50m~80m (approximately 25~60m over XL₃₁₆₋₁); it exposes on the excavated slope surface at about 1160m asl.. It extends over 350m in length with 1~3m thickness in general. XL₉₋₁₅ develops in the lower wall of γ_{L5} , and also appears as beading nodules structure (Fig 3b). It consists of tension fractures with a good penetrability above 1200m asl.

Table 1 Potential hazard sliding block in the right slope

| Num | Bottom slide surface | Rear surface downstream side surface | Upstream side surface | Range |
|-----|---|--------------------------------------|---|------------------|
| T1 | XL ₃₁₆₋₁ (f ₂₀₈ , f ₂₃₁) | β_5 (F ₁) | f ₂₀₂ | LP I downstream |
| T2 | | | β_{209} (f ₂₀₅)、 β_{219} (f ₂₂₁) | LPIII downstream |
| T3 | | | β_{316-5} (f ₃₁₆₋₇)、 β_{316-6} (f ₃₁₆₋₁₁) | LPVI downstream |
| T4 | XL ₀₉₋₁₅ | γ_{L5} | f ₂₀₂ | LP I downstream |
| T5 | | | β_{209} (f ₂₀₅)、 β_{219} (f ₂₂₁) | LPIII downstream |
| T6 | | | β_{316-5} (f ₃₁₆₋₇)、 β_{316-6} (f ₃₁₆₋₁₁) | LPVI downstream |
| L1 | f ₂₃₁ | β_4 | β_{219} | LPIV-LPVIII |
| L2 | f ₂₃₁ | β_{85} | β_{219} | LPIV-LPVII |
| L3 | f ₂₃₁ | β_{62} | β_{j622} , β_{j608} or Set 4 fractures | LPIV-LPVI |
| L4 | f ₂₃₁ | f ₂₄₂ (β_{601}) | Set 4 fractures | LPVI-LPVIII |

Deep seated fracture belts XL₃₁₆₋₁ and XL₉₋₁₅ heavily damage the integrity of rock mass of the slope. With the adjacent faults, such as f₂₃₁ and f₂₀₈, the stability of slope

rock mass may be significantly reduced. Analyzing for the global failure mode of the right slope, XL_{316-1} and XL_{9-15} are considered as the key bottom slide surfaces. Other discontinuities can be considered as rear cutting surfaces or side boundaries. Thereby, a number of likely global slide blocks are identified (Block T1~T6 in Table 1). Besides the global slide mode, several partial unstable blocks that threaten the slope stability should be analyzed (Table 1, Block L1-L4). f_{231} is the bottom slide surface for all of these partial blocks, but their rear surfaces are variable with several parallel dykes dipped inward toward the slope.

IN-SITE CRACKS

During the excavation of the right slope, there are three incidents of in-situ crack development at surface rock mass (CHIDI 2010, Table 2 and Fig. 1).

- May 3rd 2009: EL 1124-1127m asl, Dam 0+095~0+113m, 3 cracks along β_{j601} rived spray concrete reinforced with steel mesh.
- August 16th 2009: EL 1075-1092m asl, Dam 0+069~0+088m, 4 cracks developed at the slope surface. Meanwhile, 9 cracks (Fig 4) were found at PD314 (1107m asl), and relaxation phenomenon is measured at the crushed zone along with f_{231} .
- September 1st 2009, EL 1135-1165m asl, Dam 0+040m~0+050m, several longitudinal cracks appeared along β_{219} with loud shattering sound. There are also cracks shown between 1100m~1135m asl.

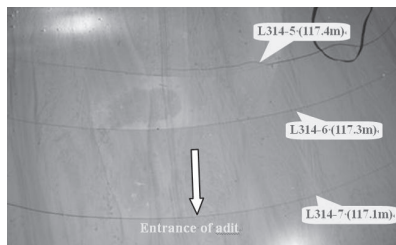


FIG. 4 The cracks on the floor of PD314 (EL 1107m asl, the upper wall of f_{231})

Analyzing the potential slide modes, the in-situ cracks of May 3rd are related to Block L4. The front shear outlets of L4 exposed during excavating. As a result, β_{j601} (the rear surface of L4) suffers bend-rip effect, led to the slip deformation and cracks.

Both of cracks developed on Aug 16th and Sep 1st are along the boundaries of Blocks L1~L3 which are controlled by f_{231} and diabase dykes. Firstly, because of the deformation of Block L3, the tensile cracks emerged on β_{62} and Set 4 fractures (Aug 16th). As the deformation of Block L3 increasing, Block L1/L2 lost the lower support and tended to slide down, which made the cracks along β_{219} and f_{231} on Sep 1st.

Additionally, it is notable that the three in-situ cracks happened during the local rainy season. Not only the decreasing of the mechanical parameters of rock mass and structural planes by the rainfall infiltration, additional hydrostatic pressure excited by seepage water may trigger slope failure.

As described above, due to the readjustment of gravity following the excavation, some key discontinuities (f_{231} , β_{62} , β_{j601} and β_{219}) of possible partial slide blocks are

tensioned and yielded, in-situ cracks emerged. Then, the integrity of slope rock mass may damage gradually. Furthermore, the failure of key structural surfaces leads to the hazard partial blocks in a critical stable state. If the key partial blocks fail, the right slope may globally collapses as the next step.

Table 2 Cracks at the right bank slope

| Num. | Aperture(mm) | Elevation(m) | Length(m) | type | Characters | Notes | |
|-------------------------|--------------|--------------|-----------|--------------------------------|----------------------|--|--|
| Date: 2009.05.03 | | | | | | | |
| L1-1/2/3 | 10 | 1125 | 2.2/4/11 | Lateral crack | — | Along with β_{601} | |
| Date: 2009.08.16 | | | | | | | |
| L2-1/2 | 1~2 | 1087/1092 | 4.2/6.6 | Lateral crack | | | |
| L2-3 | 15~20 | 1089~1092 | 10.00 | | | Along with β_{62} | |
| L2-4 | | 1088~1093 | 6.30 | Longitudinal crack | | | |
| L314-1/2 | 1~4 | 1107 | | Camber (center toward outside) | Calcium bulged | Downstream side at β_4 | |
| L314-3 | 2~3 | | | Line (vertical with adit axis) | Inner side higher | aperture on upstream crown | |
| L314-4/5 | 1~3 | | | Camber (center toward inside) | Inner side higher | | |
| L314-5 | 1~3 | | | Camber (center toward inside) | Inner side higher | At the upper wall of F_{231} , F_{231} relaxation status with aperture | |
| L314-6 | 1~2 | | | | Outboard side higher | | |
| L314-7 | 1~3 | | | | | | |
| L314-8 | 2~4 | | | Straight line | | Inner side higher | Downstream side located at β_{314-6} |
| L314-9 | 2 | | | | | | |
| Date: 2009.09.01 | | | | | | | |
| L3-1 | 10~20 | 1136~1146 | 0.5~3 | 5 opening spalling | | Along with β_{219} | |
| L3-2 | 1~2 | 1134 | 5.30 | waviness | | | |
| L3-3 | 5 | 1120~1130 | 0.5~1 | 5 opening spalling | | Along with β_{219} | |
| L3-4 | 1 | 1103~1108 | 1~3 | Slightly waviness | | | |
| L3-5/6 | 1~3/2~5 | 1101~1110 | 0.5~1 | 4 opening spalling | | Along with β_{219} | |

STABILITY ANALYSES

As described above, the stability of the right bank slope is threatened by deep seated concentrating belts of unloading fractures, and it further deteriorates with excavation. The 2D LEM (Sarma approach (Sarma 1979, Chen et al. 2003) and the transmitting coefficient approach) and the 3D interfacial stress integration approach (Griffiths 1999, He et al. 2004) based on FEM were adopted to determine the factor of safety (FOS) of the slope. The minimum of permissible FOS is 1.25 under the normal condition, and 1.15 under the heavy rain condition.

9 typical cross sections (LPI-I to LPIX-IX) in which deep unloading fractures had developed were selected to build 2D LEM models, and the block FOS of each section were calculated. Based on the sizes and extent of each slide blocks, the comprehensive FOS of blocks was obtained by weighted mean in order to evaluate the stability of slope. The 3D elastic-plastic FEM model was built by simulating the terrain, stratum, main discontinuities, excavation and remedial works (FIG. 5).

According to the RMR system, the rock mass of the right slope is classified into four grades: II~V, with grades III and V further divided into III₁, III₂ and V₁, V₂. Based on results of laboratory and in-situ tests, rock mass structure and geological condition, a summary of the mechanical parameters for each grade is given in Table 3. Because of the intermittent distribution in unloading fractures, the equivalent shear strength parameters of slide surfaces are given in Table 3 in which considered the mechanical parameters and interconnecting rate (e.g. 0.60 for XL₃₁₆₋₁/XL₀₉₋₁₅) of discontinuities and corresponding rock mass.

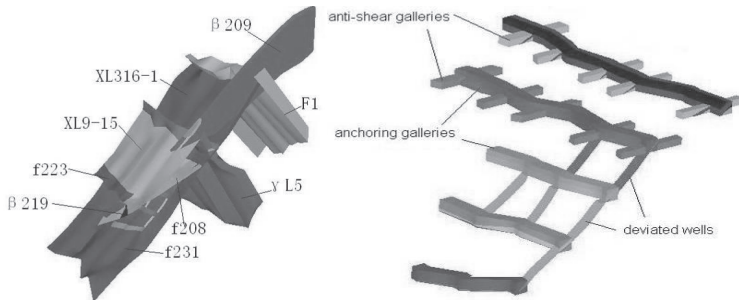


FIG. 5 The 3D FEM mesh of the right slope
(a)Discontinuity Planes; (b)Reinforced structure

Table 3 Parameters of rock mass and discontinuities used in stability analysis

| Grade | Friction angle, ϕ (°) | | Cohesion, c' (MPa) | | Vol. weight (kN/m ³) | Def. modules, E(GPa) | | Poisson ratio, ν |
|------------------------|----------------------------|--------------------------|----------------------|-----------------------------|----------------------------------|----------------------|--|----------------------|
| | nat./sat. | | Nat./sat. | | | horizontal | vertical | |
| Rock mass | | | | | | | | |
| II | 52.5/50.5 | | 2.0/1.8 | | 26.5/27.5 | 22.0 | 20.0 | 0.25 |
| III1 | 50.2/48.2 | | 1.5/1.35 | | 26.2/27.2 | 10 | 7.0 | 0.27 |
| III2 | 45.0/43.0 | | 1.0/0.9 | | 26.2/27.2 | 7.5 | 5.0 | 0.30 |
| IV | 38.6/36.6 | | 0.7/0.63 | | 25.8/26.8 | 3.0 | 1.25 | 0.35 |
| V 1 | 26.5/24.5 | | 0.2/0.18 | | 24.5/25.5 | 0.375 | 0.25 | 0.40 |
| V 2 | 21.8/19.8 | | 0.175/0.16 | | 22.1/23.1 | 0.2 | | 0.42 |
| col+dIQ4 | 30.0/28.0 | | 0.025/0.023 | | 20.0/21 | 0.05 | | 0.42 |
| Discontinuities | | | | | Features and Composition | | | |
| XL316-1 | III ₁ : 38/35 | III ₂ : 35/33 | IV: 31.8/29.8 | III ₁ : 0.6/0.54 | III ₂ : 0.4/0.36 | IV: 0.28/0.26 | Rock 40%, A2(open rigid discontinuities) 60% | |
| f208 | 19.3/17.3 | | | 0.05/0.04 | | | B2(weak discontinuities, rock debris mixed with mud) | |
| | 16.7/14.7 | | | 0.02/0.015 | | | B3(weak discontinuities, mud mixed with rock debris) | |
| f231 | 25.2/20.6 | | | 0.09/0.07 | | | B1(rock block with rock debris) and B2 (weak discontinuities, rock debris mixed with mud) | |

Table 4 Stability analysis result of possible slide blocks (FOS)

| Block Num. | 2D Sarma method | | | | 2D transmitting coefficient method | | | | 3D FEM integration method | |
|------------|------------------|-----------|----------------------|-------------|------------------------------------|-------------|----------------------|-------------|---------------------------|-------------|
| | Normal Condition | | Heavy rain Condition | | Normal Condition | | Heavy rain Condition | | Normal Condition | |
| | Bef. Reinf. | Af Reinf. | Bef. Reinf. | Bef. Reinf. | Bef. Reinf. | Bef. Reinf. | Bef. Reinf. | Bef. Reinf. | Bef. Reinf. | Bef. Reinf. |
| T1 | 1.11 | 1.33 | 1.04 | 1.25 | 1.03 | 1.26 | 0.96 | 1.20 | 1.00 | 1.29 |
| T2 | 0.88 | 1.19 | 0.80 | 1.13 | 0.86 | 1.14 | 0.79 | 1.08 | 0.91 | 1.21 |
| T3 | 0.93 | 1.25 | 0.85 | 1.21 | 0.91 | 1.19 | 0.85 | 1.12 | 0.97 | 1.26 |
| T4 | 1.62 | 1.77 | 1.57 | 1.73 | 1.52 | 1.66 | 1.46 | 1.58 | 1.68 | 1.79 |
| T5 | 1.45 | 1.62 | 1.34 | 1.50 | 1.43 | 1.61 | 1.32 | 1.50 | 1.52 | 1.67 |
| T6 | 1.37 | 1.56 | 1.25 | 1.45 | 1.30 | 1.53 | 1.21 | 1.45 | 1.38 | 1.55 |
| L1 | 0.98 | 1.38 | 0.92 | 1.30 | 0.93 | 1.24 | 0.87 | 1.18 | — | — |
| L2 | 1.12 | 1.41 | 1.07 | 1.34 | 1.09 | 1.37 | 0.99 | 1.28 | — | — |
| L3 | 1.28 | 2.13 | 1.20 | 2.06 | 1.12 | 1.92 | 1.01 | 1.83 | — | — |
| L4 | 1.13 | 1.52 | 1.02 | 1.43 | 1.05 | 1.46 | 0.96 | 1.35 | — | — |

Table 4 shows the stability of hazard slide blocks which have been analyzed. The results indicate that the FOS of blocks T4, T5 and T6 which are controlled by XL₉₋₁₅ are relatively high, and a conventional support can meet the requirements of stability. However, blocks T1, T2 and T3 controlled by XL₃₁₆₋₁ have lower FOS. Especially, the most dangerous block T2 only has FOS of 0.86~0.91 under the normal condition and 0.79~0.80 under heavy rain condition, which shows the block is unstable. The partial blocks L1~L4 have FOS of 0.93~1.28 under the normal condition, and 0.87~1.20 under heavy rain condition, which means they stay in a critical stable state.

3D elastic-plastic FEM was adopted to study the spatial stress status and rupture developing process of slope rock mass. Fig. 6 illustrates the failure distribution of rock mass after excavation to 1170m asl at cross section PLV-V. When XL_{316-1} passes through grade IV rock mass, the failure along it is not obviously developed. It means that the global blocks which are controlled by XL_{316-1} stay in the basically stable status. But the faults (e.g. f_{231}) and crushed dykes (e.g. β_4 , β_{62} and β_{85}) have completely failed by shear stress, which means that a penetrating rupture zone along the surfaces of partial blocks has formed. This result suggests that there is a probability of partial losing of the slope and the consequent risk of global slide. The slide mode of the right bank can be summed up as follows: tensile failure of rear dykes — shear failure of outlet section of key bottom slide surface — sliding of partial block(s) — sliding of the whole slope. Furthermore, according to stress projection and integrity on the slide surfaces, the corresponding FOS was solved. Similarly to the results of LEM, the FOS of blocks related XL_{9-15} is satisfactory, while the FOS of blocks related XL_{316-1} are lower than requirement (e.g. FOS of Block T2 is 0.91 under the normal condition).

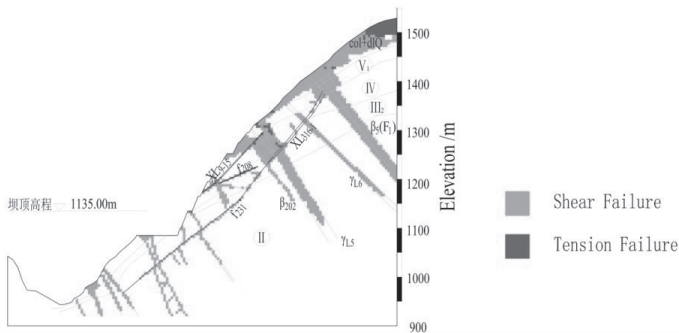


FIG. 6 Failures of rock mass based on 3D FEM (Cross Section PLV-V)

REMEDIAL WORKS

As studied above, the non-support excavation right slope is not mathematically stable to ensure its safety. XL_{316-1} , XL_{9-15} , f_{231} , f_{208} and several crushed dykes are threatening its stability as the main structural planes. Among them, XL_{9-15} , β_4 , β_{62} , β_{85} and lower section of f_{231} can be reinforced by anchoring because of their shallow depth. But since the cover depth of XL_{316-1} which exceeds the effective range of anchoring and the huge volume of its cut blocks, there is little anchoring effect. Furthermore, due to the wide extent, large local aperture, connection with other discontinuities and the significant thickness, the effect of single grouting is also limited. As a result the synthetic spatial reinforced structure was adopted to improve the mechanical parameter of XL_{316-1} and upper section of f_{231} which is made by reinforced concrete anti-shear galleries, anchoring galleries and deviated wells with gallery consolidation grouting (Fig.5b).

The LEM and FEM were used to simulate and evaluate the remedial effect of reinforced structure. The results show that the FOS of these hazard slide blocks is

prominently increased. Especially for partial blocks L1~L4, because of their relatively small volumes, the FOS of them are dramatically improved after reinforcement. The synthetic spatial reinforced structure also improves the stability of the global blocks. The FOS of the most dangerous block T2 was 0.86~0.91 and increased to 1.14~1.21 under the normal condition, 0.79~0.80 and increased to 1.08~1.13 under the heavy rain condition.

The result of 3D FEM shows enhanced mechanical parameters of reinforced zones cause a stress redistribution of slope rock mass. Reinforced galleries restrain the development of shear failure along the bottom slide surfaces (XL_{316-1} , f_{231}), thus obstruct the continuous failure in rock mass. The modification of failure distribution reveals the slope stability is improved after reinforcement.

CONCLUSIONS

Two deep seated concentrating belts of unloading fractures lie in the right slope of Dagangshan Hydropower Station, which are paralleled with slope surfaces with the features of the deep cover depth, wide extent, low mechanical parameter, and large thickness. Combined with other discontinuities, they may play significant roles in a number of potential slide modes. It can clarify the mechanism of the three in-situ slope crack cases during the rainy season of 2009.

The 2D LEM and 3D FEM were used to evaluate the global and local stability of the right slope. The results demonstrate the non-support excavated slope is marginally stable, especially under the rainfall condition. It also verifies the causes of the in-situ cracks and the necessity of reinforced measures. In view of the location and properties, a synthetic spatial reinforced galleries structure combined with anchoring and grouting was recommended. The study shows that it can effectively block the main slide channels and significantly improve the stability of the right bank slope.

ACKNOWLEDGEMENTS

The authors are grateful for the support from the China Natural Science Foundation under the grant of No. 51079092. The authors wish to thank Professor Chi-hua Huang for his instructive suggestion.

REFERENCE

- Chen, J., Yin, J.H., et al. (2003). "Upper bound limit analysis of slope stability using rigid finite elements and nonlinear programming." *Canadian Geotechnical J.*, 40(4): 742-752.
- CHIDI (Chengdu Hydroelectric Investigation and Design of Institute) (2010). "Engineering geology report of stability research for the right slope of arch dam, Dagangshan Hydropower Station, Dadu River." (In Chinese)
- Griffiths, D.V., Lane, P.A. (1999). "Slope stability analysis by finite elements." *Geotechnique* 49(3): 387-403.
- He, J., Xie, H., Fan, J, and Wang, Q. (2004). "Brittle elastoplasticity model of rockmasses during unloading and its application to high slope excavation." *Chinese J of Rock Mechanics and Engineering*, (07): 1082-1086.
- Sarma, S.K. (1979). "Stability Analysis of Embankments and Slopes." *J of the Geotechnical Engineering Division-ASCE*, 105(12): 1511-1524.

Shallow Slope Stability Analysis Method for Vegetated Slope

Junyun Zhang

School of Civil Engineering, Southwest Jiaotong University, Chengdu, China, 610031; zjy74@126.com

ABSTRACT: Based on direct shear tests of soil samples with roots, the empirical formula of roots' contribution to soil's shear strength is summarized. In consideration of the effects of sliding surface depth, sliding mass width, sliding mass shape and roots, shallow slope stability analysis method for vegetated slope is suggested by mechanical equilibrium analysis of shallow sliding mass. According to the analysis of factors affecting shallow slope stabilization, it is shown that the factor's importance descending order is sliding mass width, sliding surface depth and sliding mass shape in turn. Results of shallow slope stability analysis proposed by the paper are reasonable in comparison to the plane analysis method because more factors are taken into account.

INTRODUCTION

Numerous researchers have verified that plant roots can increase the shear strength of shallow soils, thereby enhance the stability of shallow slope (e.g., Gray 1978; Wu 1979; Waldron 1981; Abe 1991). Many researchers have also derived various analytical models of soil-root interaction and shallow slope stability. However, they are mostly focused on the influence of vertical roots on shallow slope stability, and analyze the shallow slope stability by the plane method (e.g., Koler 1998; Sidle 1992; Ekanayake 1999; Zhao 2006; Qi 2006; Deng 2007). In fact, vertical roots can not reach the failure surface, therefore, they do not significantly improve the stability of shallow slope in most cases. In recent years, people have realized that lateral roots can improve the stability of shallow slope (e.g. Zhou 1997). Nevertheless, the analytical method is far from mature. We summarize the empirical formula of roots' contribution to soil's shear strength, then put forward shallow slope stability analysis method for vegetated slope according to mechanical analysis of shallow sliding mass.

INFLUENCE OF PLANT ROOTS ON SOIL'S SHEAR STRENGTH

Direct shear tests and results

Prior to the test, we screen sandy clay with 2 mm soil samples sieve, then put sieved soil into different pots and compact them, finally remodel the soil by water addition. In

addition, we select fine roots of cynodon dactylon, which is approximately 7 month old and root diameter is 0.60 mm. When conducting the test, we take soil sample with cutting ring, and prick fine pores into the sample, then insert air dried root into fine pore. The number of roots ranges from 10 to 40 according to the gradient. The density of soil sample is adjusted by its weight and water content. Two kinds of water content's samples are used in direct shear tests, which are 25.8% and 32.9% respectively. Direct shear tests are conducted using a standard, laboratory direct shear apparatus. The normal stresses are 50, 100, 150, 200 and 250 kPa respectively. Table 1 shows the test results of the shear strength of soil samples with 25.8% water content and Table 2 shows the test results of the shear strength of soil samples with 32.9% water content.

Table 1 The shear strength of soil samples (Water content is 25.8%)

| Type of soil sample | Shear strength S (kPa) | | | | |
|---------------------|--------------------------|------------------|------------------|------------------|------------------|
| | $\sigma=50$ kPa | $\sigma=100$ kPa | $\sigma=150$ kPa | $\sigma=200$ kPa | $\sigma=250$ kPa |
| No root | 34.3 | 56.4 | 80.9 | 102.9 | 125.0 |
| With 10 roots | 39.2 | 66.2 | 93.1 | 117.6 | 144.6 |
| With 20 roots | 41.7 | 71.1 | 100.5 | 127.4 | 151.9 |
| With 30 roots | 44.1 | 73.5 | 100.5 | 129.9 | 159.3 |
| With 40 roots | 46.6 | 78.4 | 107.8 | 137.2 | 166.6 |

Table 2 The shear strength of soil samples (Water content is 32.9%)

| Type of soil sample | Shear strength S (kPa) | | | | |
|---------------------|--------------------------|------------------|------------------|------------------|------------------|
| | $\sigma=50$ kPa | $\sigma=100$ kPa | $\sigma=150$ kPa | $\sigma=200$ kPa | $\sigma=250$ kPa |
| No root | 31.9 | 53.9 | 76.0 | 98.0 | 120.1 |
| With 10 roots | 36.8 | 61.3 | 85.8 | 110.3 | 134.8 |
| With 20 roots | 39.2 | 68.6 | 95.6 | 122.5 | 149.5 |
| With 30 roots | 41.7 | 71.1 | 100.5 | 127.4 | 156.8 |
| With 40 roots | 44.1 | 73.5 | 102.9 | 132.3 | 161.7 |

Contribution of plant roots to soil's shear strength

The number of roots in test samples is reflected by root area ratio (RAR). RAR is the percentage of all of roots' cross sectional area (A_R) and soil sample shear area (A). RAR ranges from 0 to 0.377% in direct shear tests, and the root number per soil sample is from 0 to 40 correspondingly. Fitting soil shear strength and RAR, we can get the formula as shown in Table 3 and Table 4.

Table 3 and Table 4 show that the relationship between the shear strength of soil-root composites and RAR is linear. It can be expressed as

$$S = a \frac{A_R}{A} + b \quad (1)$$

Where a and b are indeterminate coefficients. Comparing indeterminate coefficient b to the shear strength of soil, we can find that there is little difference between them. Here, we regard the coefficient b as the shear strength of soil. The contribution of roots to the shear strength of soil is estimated by the following expression

$$S_R = a \frac{A_R}{A} \quad (2)$$

Table 3 The fitting formula of shear strength (Water content is 25.8%)

| σ (kPa) | Shear strength of soil-root composites S (kPa) | Correlation coefficient R | Shear strength of soil S (kPa) | Roots' contribution S_R (kPa) |
|----------------|--|-----------------------------|----------------------------------|------------------------------------|
| 50 | $S = 31.28 \frac{A_R}{A} + 35.29$ | 0.986 | 34.3 | $S_R \approx 31.28 \frac{A_R}{A}$ |
| 100 | $S = 54.38 \frac{A_R}{A} + 58.87$ | 0.970 | 56.4 | $S_R \approx 54.38 \frac{A_R}{A}$ |
| 150 | $S = 64.86 \frac{A_R}{A} + 84.34$ | 0.950 | 80.9 | $S_R \approx 64.86 \frac{A_R}{A}$ |
| 200 | $S = 85.75 \frac{A_R}{A} + 106.84$ | 0.965 | 102.9 | $S_R \approx 85.75 \frac{A_R}{A}$ |
| 250 | $S = 103.79 \frac{A_R}{A} + 129.93$ | 0.970 | 129.3 | $S_R \approx 103.79 \frac{A_R}{A}$ |

Table 4 The fitting formula of shear strength (Water content is 32.9%)

| σ (kPa) | Shear strength of soil-root composites S (kPa) | Correlation coefficient R | Shear strength of soil S (kPa) | Roots' contribution S_R (kPa) |
|----------------|--|-----------------------------|----------------------------------|------------------------------------|
| 50 | $S = 31.07 \frac{A_R}{A} + 32.89$ | 0.986 | 31.9 | $S_R \approx 31.07 \frac{A_R}{A}$ |
| 100 | $S = 51.95 \frac{A_R}{A} + 55.89$ | 0.966 | 53.9 | $S_R \approx 51.95 \frac{A_R}{A}$ |
| 150 | $S = 72.62 \frac{A_R}{A} + 78.48$ | 0.970 | 76.0 | $S_R \approx 72.68 \frac{A_R}{A}$ |
| 200 | $S = 90.86 \frac{A_R}{A} + 100.98$ | 0.975 | 98.0 | $S_R \approx 90.86 \frac{A_R}{A}$ |
| 250 | $S = 111.53 \frac{A_R}{A} + 123.57$ | 0.970 | 120.1 | $S_R \approx 111.53 \frac{A_R}{A}$ |

It is easy to estimate contribution of roots to the shear strength of soil samples by the formula (2). As shown in Table 3 and Table 4, the coefficient a is apparently related to the normal stress σ . Fitting the coefficient a and the normal stress σ , we can achieve the formula as following

$$\text{Water content is 25.8\%, } a = 0.353\sigma + 15.095 \quad R = 0.995 \quad (3)$$

$$\text{Water content is 32.9\%, } a = 0.400\sigma + 11.669 \quad R = 1.000 \quad (4)$$

Contribution of roots of different depth and various plant to the shear strength of soil is different, which is mainly reflected by indeterminate coefficient a . Its determination method is as follows

(1) Take soil samples with roots in the field, conduct direct shear tests, and obtain the shear strength of soil-root composites.

(2) Record the number and the diameter of roots through shear surface in every soil sample, and then calculate its RAR.

(3) Take fallow soil sample in the same depth near soil samples with roots, conduct direct shear tests, and obtain the shear strength of soil sample under the condition of different normal stress.

(4) The value of S_R is the difference of the shear strength of soil-root composite and fallow soil. A set of coefficient a can be determined by formula (2) under the corresponding normal stress. Fitting coefficient a and normal stress σ , the formula of

coefficient a , similar to formula (3) and formula (4), can be obtained.

SHALLOW SLOPE STABILITY ANALYSIS

Fundamental assumptions

Sliding surface is a plane and parallel to slope surface, as shown in Fig.1 (a).

Sliding mass shape is simplified to the rectangle, as shown in Fig.1 (b).

Ground water level is deep, so the influence of groundwater is not considered.

Soil failure follows Mohr-Coulomb criterion.

Stability analysis

Sliding force of shallow sliding mass is

$$T = W \sin \alpha = \gamma A_b z \cos \alpha \sin \alpha = \gamma L B z \cos \alpha \sin \alpha \quad (5)$$

Resistance force of shallow sliding mass is

$$R = R_b + R_l \quad (6)$$

Where, T is sliding force; W is weight of sliding mass; α is slope angle; γ is unit weight of sliding mass; A_b is sliding surface area, $A_b = L \cdot B$; z is depth of sliding surface; L is length of sliding mass; B is width of sliding mass; R is resistance force; R_b and R_l are resistance forces acting at the base of the mass and on the sidewalls, respectively.

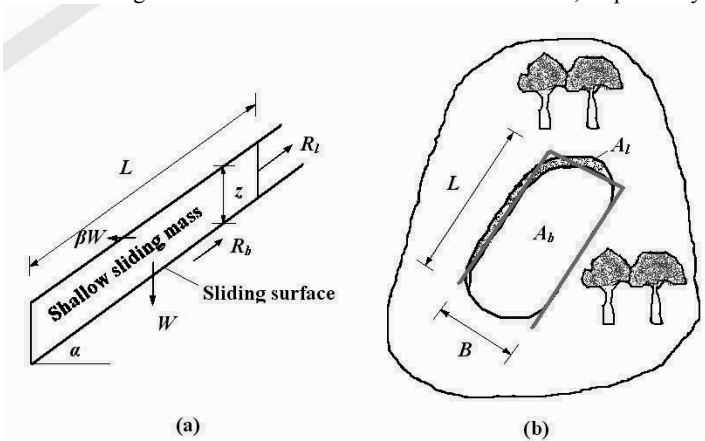


FIG. 1 The sliding surface and shape of shallow sliding mass

According to Mohr-Coulomb criterion, resistance force R_b and R_l can be obtained from the following equations

$$R_b = S_b A_b = (c + \sigma \tan \varphi + S_{Rb}) \cdot L B \quad (7)$$

$$R_l = S_l A_l = (c + S_{Rl}) \cdot (2L + B) \cdot z \quad (8)$$

Where, S_b and S_l is shear strength of soil mass acting at the base of the mass and on the

sidewalls, respectively; c is soil cohesion; φ is angle of internal friction; A_b is basal area, $A_b = LB$; A_l is side area of sliding mass, $A_l = (2L + B) \cdot z$; S_{Rb} and S_{Rl} is contribution of roots to the shear strength of soil acting at the base of the mass and on the sidewalls, respectively; σ is normal stress acting on sliding surface, and can be written as

$$\sigma = \gamma z \cos^2 \alpha \quad (9)$$

Substituting equation (9) into equation (7), and assuming that failure surface is deeper than vertical depth of roots, that is, $S_{Rb} = 0$, equation (7) becomes

$$R_b = (c + \gamma z \cos^2 \alpha \tan \varphi) \cdot LB \quad (10)$$

Substituting equation (2) into equation (8), equation (8) becomes

$$R_l = \left(c + a \frac{A_R}{A} \right) \cdot (2L + B) \cdot z \quad (11)$$

Substituting (10) and (11) into equation (6), equation (6) becomes

$$R = (c + \gamma z \cos^2 \alpha \tan \varphi) \cdot LB + \left(c + a \frac{A_R}{A} \right) \cdot (2L + B) \cdot z \quad (12)$$

If we define F_s as the coefficient of shallow slope stability, $F_s = R/T$, then by substitution of equation (5) and equation (12) for R and T , F_s is

$$F_s = \frac{R}{T} = \frac{(c + \gamma z \cos^2 \alpha \tan \varphi) \cdot LB + \left(c + a \frac{A_R}{A} \right) \cdot (2L + B) \cdot z}{\gamma LBz \cos \alpha \sin \alpha} \quad (13)$$

$$= \frac{(c + \gamma z \cos^2 \alpha \tan \varphi) \cdot B + \left(c + a \frac{A_R}{A} \right) \cdot \left(2 + \frac{B}{L} \right) \cdot z}{\gamma Bz \cos \alpha \sin \alpha}$$

If the length of shallow landslide is considerably larger than the width of sliding mass, it is unnecessary to consider the contribution of roots on the sidewalls of sliding mass. Then equation (13) can be written as

$$F_s = \frac{(c + \gamma z \cos^2 \alpha \tan \varphi) + 2 \cdot \left(c + a \frac{A_R}{A} \right) \cdot z}{\gamma z \cos \alpha \sin \alpha} \quad (14)$$

According to equation (13) or (14), shallow slope stability can be determined. If $F_s > 1$, shallow slope is in a stable state, and if $F_s = 1$, shallow slope is in the limit equilibrium state, or it is in an unstable state.

INFLUENCING FACTORS OF SHALLOW SLOPE STABILITY

As showed in equation (13), the coefficient of shallow slope stability F_s is not only related to slope angle (α), physical and mechanical parameters of soil (γ , c , φ), distribution of roots and their contribution on shear strength of the soil, but also related to potential sliding range and sliding shape (z , B , B/L). For a given slope, F_s is mainly affected by potential sliding range, sliding shape and roots.

Before influencing factors of shallow slope stability are analyzed, initial parameters

given are: $\alpha = 45^\circ$, $\gamma = 17 \text{ kN/m}^3$, $c = 10 \text{ kPa}$, $\phi = 20^\circ$, $z = 0.5 \text{ m}$, $B = 1.0 \text{ m}$, $B/L = 1.0$, $a = 10$, and $A_r/A = 0.1\%$. Then it is calculated that initial F_s is 6.60. Changing one of parameters and remaining the others, we can analyze the influence of different parameter on shallow slope stability.

Fig.2 is variation of F_s with sliding face depth; Fig.3 is variation of F_s with sliding mass width; Fig.4 is variation of F_s with sliding mass shape; and Fig.5 is variation of F_s with RAR. In the figures, the depth of sliding surface ranges from 0.5 m to 3.0 m; the width of sliding mass ranges from 1.0 m to 10.0 m; the shape of sliding mass B/L ranges from 0.01 to 1.0; and RAR ranges from 0.1% to 0.5%.

Fig.2 and Fig.3 show that the coefficient of shallow slope stability F_s will decrease exponentially as the depth of sliding surface and the width of sliding mass increase. However, compared to the width of sliding mass, the depth of sliding surface has more effect on F_s . As the depth of sliding surface increases from 0.5 m to 3.0 m, F_s decreases from 6.60 to 4.64, and the percentage of decrease rate is 29.7%. As the width of sliding mass increases from 1.0 m to 10.0 m, F_s decreases from 6.60 to 3.11, and the percentage of decrease rate is 52.9%. Therefore, if the influence of the width of sliding mass is ignored, the calculated F_s tends to be unsafe. However, it is unnecessary to adopt too large value of the width of sliding mass. In this case, as the width of sliding mass width exceeds 6.0 m, the influence of the width of sliding mass on F_s has been small.

Fig.4 and Fig.5 show that the coefficient of shallow slope stability F_s will linearly increase as sliding mass shape (B/L) and RAR (A_r/A) increase. As B/L increases from 0.01 to 1.0, F_s increases from 5.32 to 6.60, and the percentage of increase rate is 24.1%. As A_r/A increases from 0.1% to 0.5%, F_s increases from 6.60 to 8.01, and the percentage of increase rate is 21.4%. Therefore, choosing deep rooted plants can improve shallow slope stability.

Through the previous analysis, the depth of sliding surface, the width of sliding mass and the shape of sliding mass all can affect the coefficient of shallow slope stability. The factor's importance descending order is sliding mass width, sliding face depth and sliding mass shape in turn.

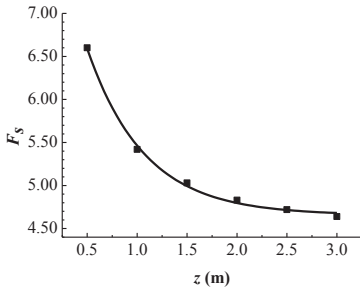


FIG. 2 Variation of $F_s r$ with sliding surface depth

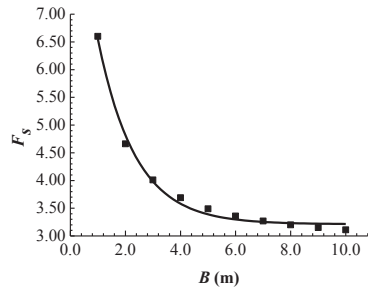


FIG. 3 Variation of F_s with sliding mass width

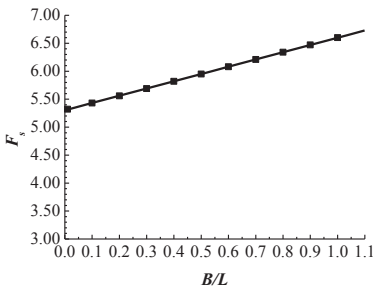


FIG. 4 Variation of F_s with sliding mass shape

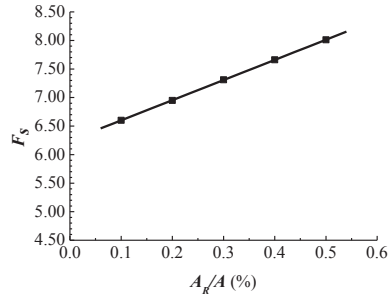


FIG. 5 Variation of F_s with root area ratio

CONCLUSIONS

Plant roots can enhance the shear strength of soil, but what they quantificationally contribute to the shear strength of soil is very difficult. Based on direct shear tests, the paper proposes the fitting equation of roots' contribution to the shear strength of soil S_R . Because the fitting equation needs fewer parameters, and moreover, the parameters are easily obtained, it would be conveniently used. In addition, compared to the plane analysis method, the paper's shallow slope stability analysis method is more realistic because of considering the depth of sliding surface, the width of sliding mass and the shape of sliding mass.

ACKNOWLEDGMENTS

The author appreciates the support of the National Science Foundation of China (50508037).

REFERENCES

- Abe, K., Ziemer, R. R. (1991). Effect of tree roots on a shear zone: modeling reinforced shear stress. *Canadian Journal Forest Research*, Vol. 21(7): 1012-1019
- Deng Wei-dong, Zhou Qun-hua, Yan Qiu-rong. (2007). Test and calculation of effect of plant root on slope consolidation. *Chinese Journal of Highway and Transport*, Vol. 20(5): 7-12
- Ekanayake, J. C., Phillips, C. J. (1999). A method for stability analysis of vegetated hillslopes: an energy approach. *Canadian Geotechnical Journal*, Vol. 36(6): 1172-1184
- Gray, D. H. (1978). Reinforcement and stabilization of soil by vegetation. *ASCE Journal of the Geotechnical Engineering Division*, Vol. 100(G6): 695-699
- Koler, T. E. (1998). Evaluating slope stability in forest uplands with deterministic and probabilistic models. *Environmental and Engineering Geoscience*, Vol. 4(2): 185-194
- Sidle, R. C. (1992). A theoretical model of the effects of timber harvesting on slope stability. *Water Resources Research*, Vol. 28(7): 1897-1910
- Qi Guo-qing, Hu Li-wen. (2006). Study on mechanism and application of slope protection with vegetation. *Chinese Journal of Rock Mechanics and Engineering*, Vol. 25(11): 2220-2225
- Waldron, L. J., Dakessian, S. (1981). Soil reinforcement by roots: calculation of increased soil shear resistance from root properties. *Soil Science*, Vol. 132(6): 427-435
- Wu, T. H., McKinnel, W. P., Swanston, D. N. (1979). Strength of tree roots and landslides on Prince of Wales Island, Alaska. *Canadian Geotechnical Journal*, Vol. 16(1):19-33
- Zhao Zhi-ming, Wu Guang, Wang Xi-hua. (2006). Research on greening protection mechanism for engineering slope. *Chinese Journal of Rock Mechanics and Engineering*, Vol. 25(2): 299-305
- Zhou Y., Watts, D., Cheng X. P. (1997). The traction effect of lateral roots of *Pinus yunnanensis* on soil reinforcement: a direct in situ test. *Plant and Soil*, Vol. 190(1): 77-86

Research on the Settlement Behavior of Ram-compacted Piles with Bearing Base

Chen Hongyun¹, Ma Jianlin², Zhao Guotang³ and Xu Zailiang⁴

¹Ph.D, Geotechnical Engineering Department, Southwest Jiaotong University, Chengdu 610031, China; 278709407@qq.com

²Professor, Geotechnical Engineering Department, Southwest Jiaotong University, Chengdu 610031, China; majianlin01@126.com

³Professor, Beijing-Shanghai High Speed Railway Co. Ltd., Beijing 100038, China;

⁴Professor, 3rd Railway Survey and Design Group Co., Ltd., Tianjin 300142, China; xuzailiang@tsdig.com

ABSTRACT: In order to study the settlement characteristic of ram-compacted piles with bearing base (RPBB) and pile-raft composite foundation in high-speed railway, RPBB and Cement Fly-ash Gravel (CFG) piles were tested and compared under the Beijing-Shanghai high speed railway. Using hydrostatic levels, the settlements of test sections were monitored over the long-term. Results show, because of the formation conditions and the construction technology of RPBB, the reinforced depth of RPBB is limited. Consequently the settlement of RPBB is bigger than CFG. It also takes longer to reach stable settlement for RPBB. In addition, based on measured and modified soil compression modulus, the thicknesses of compressed layers and the settlements were calculated using control strain method and control stress method. The calculated results using control strain method and modified soil compression modulus are reasonably close to the testing data. This proves that the modified soil compression modulus can improve the precision and reliability of the settlement estimation. This can overcome the limitations of existing Chinese code.

INTRODUCTION

Bearing base of RPBB consists of three parts; concrete, compacted fill material, compacted soil of three parts, as shown in Fig. 1 (JGJ 135-2007). RPBB differs from ordinary rammed expanded pile in that RPBB uses the cheap building waste as fill material of bearing base, such as broken bricks, gravel, stone and so on, instead of concrete (Qiu 2002a). Due to quick construction speed, high load carrying capacity, good construction quality, low cost, good environmental effects, etc., RPBB has been widely used (Wang 2002b). In the past the applications of RPBB focused on the buildings and the research focused on the carrying capacity (Qiu 2001; Gao 2012b; Li 2011a; Su 2011b; Yang and Chu 2012a), but the high-speed railway foundation settlement requirement is stricter than the building foundation. This is the first time

that the RPBB is applied to high-speed railway foundation reinforcement, so the engineering experience is lack, and the technology theory can't be transfer simply, then it is necessary to conduct research on high-speed railway RPBB composite foundation settlement characteristics.

In recent years, CFG pile is widely used and researched in various engineering, including the high-speed railway foundation reinforcement, and results have been achieved (Xue 2012c; Yan and Zhang 2006; Zhang 2011c), so the comparative study with CFG pile can clearly reflect the RPBB relevant characteristics. In order to study the settlement characteristics of RPBB composite foundation under embankment, the on-site tests of the RPBB and CFG pile composite foundation settlement had been carried out in the test section of the Beijing-Shanghai high-speed railway Langfang soft ground, and the settlement of RPBB composite foundation is calculated.

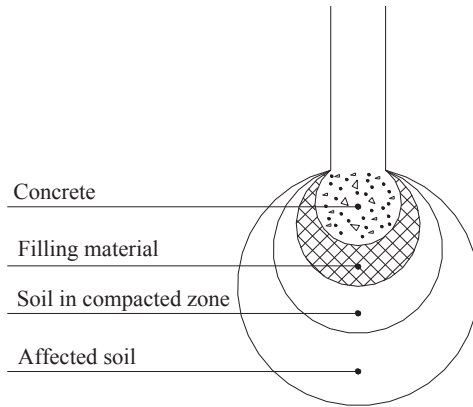


Fig. 1 Schematic Diagram of Bearing Base

TEST SITUATIONS

Engineering Geological Conditions of Test Site

The test sites locate in the Beijing-Shanghai high-speed railway Langfang station, where groundwater is 0.05 to 3.4m deep quaternary pore phreatic water which is mainly recharged by meteoric and the water level varies 2 to 3m seasonally. The main strata are quaternary Holocene artificial accumulation layer (Q_4^{mf}), quaternary Holocene alluvium layer (Q_4^{al}) and quaternary Pleistocene alluvium (Q_3^{al}) from top to bottom. The soft silty clay and clay layer is 6 m below the top of the pile, and a layer of dense fine sand is in the range of 6 ~ 9m, then soft silty clay soil and clay interaction layer is more below.

Designing Scheme

According to the technology Characteristics of the RPBB, the Bearing Base of the RPBB is designed in dense sand layer at a depth of 6 ~ 9m. The RPBB pile length is 6.5m, the pile diameter is 0.43m, pile spacing is 2m, 16 piles per row. The

CFG pile length is 22.6m, the pile diameter is 0.4m, pile spacing is 1.6m, 17 piles per row. Each test section pile top order 0.15m thick gravel bedding, a 0.5m thick cast-in-place reinforced concrete raft, 2.2m thick base bed base, 3.5m thick preload soil.

FIELD TEST

Testing Program

Shown in Fig. 2, hydrostatic levels had been fixed along the center to the sideline of roadbed in the test cross-section to monitor the surface settlement of the composite foundation. A hydrostatic level had been fixed above the soil around the center of roadbed, and other hydrostatic levels had been fixed above the piles.



Fig. 2. Hydrostatic Levels

Test Results

The measured data are plotted as settlement-load-time curves shown in Fig. 3 and Fig. 4. In the figures, S represents the hydrostatic level above the soil and P represents the hydrostatic levels above the piles, then the sizes in parenthesis content is the distance from the midline of the roadbed to the hydrostatic levels.

In the figures, the load is derived from the material and the quantity of the structure. By construction sequence, followed by laying gravel cushion, pouring reinforced concrete raft, filling bottom layer of foundation bed, preloading soil, unloading preloading soil, paving the structure including surface layer of foundation bed and track panels.

Fig. 3 shows in the RPBB test section preloading lasted only 50 days which is a short time. When loading, the settlement increased significantly. After unloading, the settlement did not quickly stabilize and became stable until 150 days later. When monitoring end, the settlements are stable and the maximum pile settlement is 95 mm located in the roadbed center (P (0m)). The soil settlement is 100 mm. The settlement

increased mainly during the preloading.

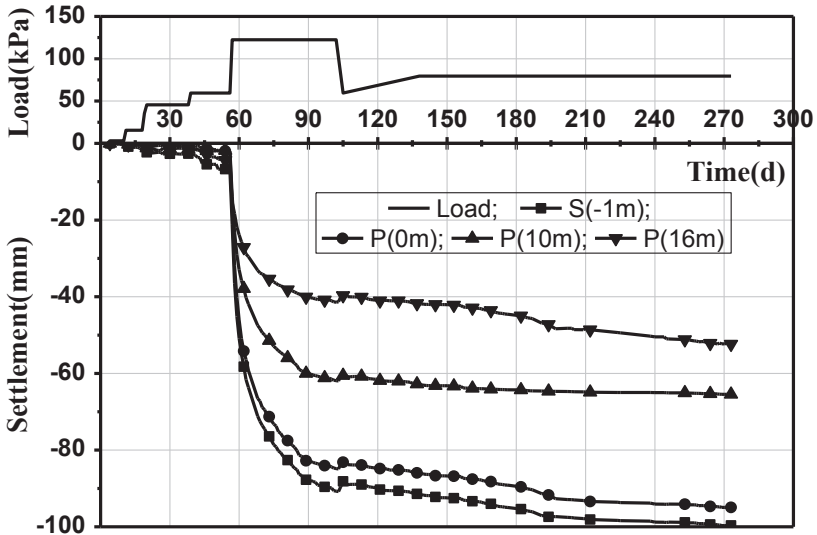


Fig. 3 Settlement-Load-Time Curves of RPBB

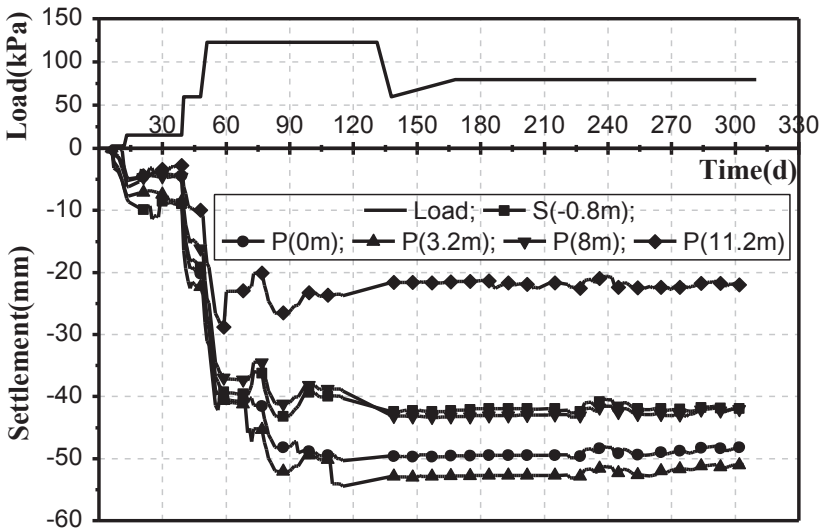


Fig. 4 Settlement-Load-Time Curves of CFG

Fig. 4 shows in the CFG test section preloading lasted 80 days. After unloading,

the settlement was stable. When monitoring end, the maximum pile settlement is 51 mm located in the pile which is 3.2 m away from the roadbed center (P (3.2m)). The soil settlement is 42 mm.

Above all, the CFG pile settlement is less than the RPBB, about half of the RPBB. A reason is the RPBB reinforced depth is limited by the construction process, and then the RPBB length is short (6.5m). Another reason is the formation conditions that below fine sand layer in bearing base, there is weak substratum, and under loading, the consolidation settlement of weak substratum requires a longer time. The CFG pile length is longer than the RPBB (22.6m), and CFG piles penetrate a weak substratum below fine sand layer, so the settlement and stable time of CFG pile is less than the RPBB.

SETTLEMENT CALCULATION

In the high speed railway, the settlement is strictly controlled, so it is very important to calculate the settlement accurately. In the last part, the real settlement of RPBB composite foundation in the high speed railway is measured. In this part, the settlement of RPBB is calculated and checked via the real settlement.

Correctional Compression Modulus

In general, the soil compression modulus increases with depth, but in engineering the soil compression modulus is mostly tested under 0.1 ~ 0.2MPa vertical pressure. If the settlement is calculated by using the same soil pressure compression modulus in different soil depth, it would make a large difference between the calculation result and the actual value. The soil test compression modulus should be corrected by the depth to solve this problem, and then the correctional soil compression modulus can be applied to the theoretical analysis and calculation of the settlement. The compression modulus is not corrected in the current specification, and the settlement calculation empirical coefficient ψ_p is introduced to make up. But the coefficient range is too broad (0.2 to 1.4) whose difference is up to 7 times as large, which make difficult to calculate the settlement accurately for the inexperienced engineers. Especially in the high-speed railway, the settlement after construction is controlled strictly and the large difference is not allowed such that.

In order to improve the reliability and accuracy of the calculation results and narrow the range of empirical correction factors, on the basis of the soil test compression modulus $E_{s,0.1-0.2}$, a compression modulus correction formula related to the depth is presented.

$$E_{s,z} = E_{s,0.1-0.2} \cdot (z / h_0)^{1/\beta}$$

Where β is parameter (see table 1), z is depth, h_0 is referenced thickness (preferred value $h_0 = 1\text{m}$), $E_{s,0.1-0.2}$ is the compression modulus under 0.1~0.2

MPa vertical pressure.

Table 1. Value of β

| Vaule of β | Soil and characteristic |
|------------------|---|
| 2.5~3.5 | Cohesive soil, silt: hard, rigid-plastic; Sandy soil: medium-density; Gravel soil: well graded; |
| 3.5~5 | Cohesive soil, silt: waxiness; Sandy soil: slightly-medium density; Gravel soil: bad graded; |
| 5~8.0 | Cohesive soil, silt: waxiness-molliplast; Sandy soil: loose-slightly density; |
| 8.0~10.0 | Cohesive soil, silt: molliplast and less. |

Note: the better and the harder the soil is, the smaller the value of β is.

The formula is closely related to soil depth, so the deeper, the better the result of settlement calculation.

Calculating Parameter

In order to check the compression modulus correction formula, in particular the compression moduli of the soil in RPBB section are corrected by the formula to calculated the settlement and then compared with the calculated settlement with the uncorrected soil compression modulus. The calculation parameters are shown in Table 2 and Table 3.

For contrasting with the real settlement, the load in construction is only considered in calculation, including the rubble cushion, the reinforced concrete raft, the bedding filling and the preloading soil.

The soil compression modulus are determined by the soil compression test in 0.1~0.2MPa, and the correctional compression modulus are determined by the soil compression modulus and other features in the soil test paper based on Table 1.

Table 2. Geometric Parameters

| Designation | Size |
|---|-----------|
| Ground water depth | 1.1m |
| Pile top depth | 2.3m |
| Pile bottom depth | 8.8m |
| Bearing base bottom depth | 10.8m |
| Equivalent calculation distance ΔR | 0.8m |
| Load | 117.25kPa |
| Raft width | 31m |
| The lateral pile body vertical projection width B_0 | 30.5m |
| Base load equivalent width | 32.1m |

Table 3. Soil Parameters

| Soils | Thic kness (m) | Natural density (kN/m ³) | Standard values of ultimate flank resistance(kPa) | Compression modulus (MPa) | Correctional compression modulus(MPa) |
|--------------------|----------------|--------------------------------------|---|---------------------------|---------------------------------------|
| Miscellaneous fill | 4.7 | 18.6 | 28 | — | — |
| Silty clay | 1.4 | 20.1 | 38 | — | — |
| Clay | 1.3 | 18.3 | 53 | — | — |
| Silty clay | 0.9 | 18.6 | 53 | — | — |
| Fine sand | 3.6 | 20.5 | 86 | 46 | 91.9 |
| Silty clay | 1.1 | 20.3 | 66 | 7.48 | 12.4 |
| Clay | 1.1 | 18.3 | 66 | 5.54 | 9.3 |
| Silty clay | 2.2 | 20.2 | 53 | 5.56 | 9.6 |
| Clay | 1.4 | 18.9 | 66 | 5 | 8.8 |
| Silt | 0.8 | 20.5 | 64 | 50 | 89.1 |
| Silty clay | 0.9 | 20.1 | 53 | 4.87 | 11.3 |
| Clay | 1.6 | 19.5 | 66 | 4.65 | 11.0 |
| Silty clay | 1.6 | 20.2 | 82 | 10 | 24.1 |
| Fine sand | 1.8 | 20.5 | 86 | 50 | 123.0 |
| Silt | 2.4 | 19.9 | 82 | 23.76 | 59.9 |
| Silty clay | 7.5 | 20.4 | 59 | 6.06 | 16.1 |
| Clay | 8.8 | 19.7 | 74 | 5 | 10.4 |

Result

Refer to the relevant regulation (JGJ 135-2007) and norm (GB 50007-2002), the calculation is performed based on equivalent body foundation. The unidirectional compression layered summation method is chosen as the calculation method. The Equivalent active surface is under the bearing base, below the pile body 2 m. Equivalent calculated area is the body projection area formed by RPBB. The equivalent body side length is the projection side length of outside pile plus 2 times RPBB equivalent calculated distance.

The settlement calculation formula is as follows:

$$s = \psi_p p_0 \sum_{i=1}^n \frac{z_i \bar{\alpha}_i - z_{i-1} \bar{\alpha}_{i-1}}{E_{si}}$$

If in the strip foundation, p_0 is

$$p_0 = \frac{F' + G_k' - \gamma d_h B_0 - 2 \sum q_{sia} l_i}{B_0 + 2\Delta R}$$

Where

s is the pile final settlement.

ψ_p is the empirical coefficient of settlement calculation, determined by the

regional the settlement observations and experience, if not, determined by the code (GB 50007-2002).

p_0 is the additional pressure on the top of compression soil layer, corresponding to load effect quasi-permanent combination

n is the number of soil layers, within the Soil calculation depth of pile foundation settlement.

z_i 、 z_{i-1} is the distance from the RPBB settlement calculation surface to the bottom of i th and $i-1$ th soil layer.

$\bar{\alpha}_i$ 、 $\bar{\alpha}_{i-1}$ is the average additional stress coefficient from the calculated point on the bottom of RPBB foundation to the bottom of i th and $i-1$ th soil layer, carried out by the code (GB 50007-2002).

E_{si} is the compression modulus of i th layer soil within pile settlement calculation, taking the pressure range from soil weight pressure to the sum of soil weight pressure and additional pressure.

q_{sia} is the eigenvalue of pile skin resistance.

A is the cushion cap area.

d_h is the cushion cap depth.

F' is the vertical force per meter on apron piece from upper structure as load effect quasi-permanent combination, corresponding to the serviceability state.

G' is the weight standard value per meter of the cushion cap and the soil on cushion cap.

B_0 is the vertical projected length of the outermost piles.

ΔR is the equivalent distance for calculating, always 0.6~1m, which is determined by the code of RPBB.

L_Z is the height of bearing base, always 2m.

l is the length of the pile.

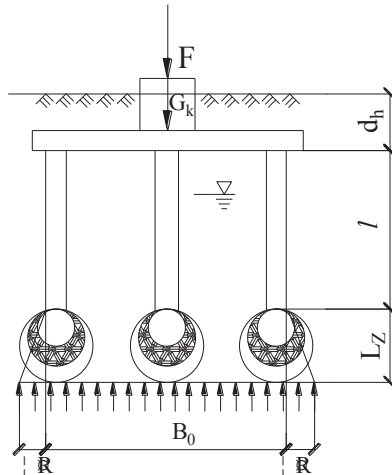


Fig. 5 Schematic Diagram of Settlement Calculation

The compression layer thickness is determined in control stress method by controlling the additional and gravitational stress ratio is not more than 10%. The compression layer thickness is determined in control strain method by controlling the above 1 m and total deformation ratio is not more than 0.025. Then the settlement is calculated. The calculation results are shown in Table 4.

Table 4 The contrast of calculation results

| | Control stress method | | Control strain method | |
|---------------------------------------|-----------------------|----------------------------------|-----------------------|----------------------------------|
| | Compression modulus | Correctional compression modulus | Compression modulus | Correctional compression modulus |
| Compression layer thickness (m) | 25.2 | 25.2 | 35.2 | 35 |
| Settlement (mm) | 163 | 76 | 225 | 105 |
| Empirical coefficient ψ_p | 0.69 | — | 0.72 | — |
| Empirical coefficient settlement (mm) | 112 | — | 162 | — |

The soil compression modulus do not relate to The compression layer thickness determined by control stress method, so different compression moduli make no effect on the calculated compression layer thickness. The soil compression modulus relates to the compression layer thickness determined by control strain method. Deeper soil compression modulus improves when compression modulus is corrected, so the compression layer thickness is thinner when compression modulus is corrected.

Settlement calculation results using different methods are quite different in the test section. The modulus is corrected which leads to increase modulus and then the calculated settlement decreases. The settlement of modulus is more than twice as correctional modulus. The compressed layer thickness determined by of different control methods differs by 10 m in the test section, and then the settlement results are quite different.

At the end of the on-site monitoring, the measured maximum pile settlement is 95mm in the RPBB test section, which is close to the calculation results (105mm) of control strain method combined with the correctional modulus.

CONCLUSION

This paper describes the advancement of a research on the RPBB used in the high speed railway. Based on compared field tests on RPBB and CFG composite foundations of the Beijing-Shanghai high speed railway, a good insight has been acquired with regard to the settlement behaviour of RPBB.

(1) Within this field test research, RPBB is able to control the ground settlement effectively to meet the standard of high-speed railway settlement after construction.

(2) Preloading can accelerate soil consolidation settlement under foundation observably. The settlements occur mainly in the preloading early in the test sections. After preloading lasted 30 days, the settlements reached 76% of the total settlements.

(3) Compared with RPBB and CFG in this field test, the result shows, because of the pile length, the settlement of RPBB is more than twice as CFG.

(4) Based on the national regulation and norm, the settlement calculation method combined with control strain method and the correctional soil compression modulus is quite suitable for the engineering similar as this test section.

REFERENCES

- JGJ 135-2007. (2007). Specification for design of ram-compacted piles with bearing base. Beijing: *China Architecture and Building Press*. (in Chinese)
- Qiu, K.B. (2001) Study of rammed enlarged composite bearer pile, Beijing: *Tsinghua University*. (in Chinese)
- Qiu, K.B., Jie, Y.X., Li, G.X., and Wang, J.Z. (2002a). "Finite element analysis of bearing capacity properties for rammed enlarged composite bearer piles." *Engineering Mechanics*, Vol. 19(3):90-94. (in Chinese)
- Gao, C.R., Yang, Q.A., and Qi, X.Y. (2012b). "Research and analysis on influence factors of bearing capacity of pile with bearing base in design and construction." *Construction Technology*, Vol. 41(4):63-66. (in Chinese)
- Li, R., Feng, Z.Y., and Yang, Q.A. (2011a). "Field test of vertical load-bearing characteristic of ram-compaction piles with composite bearing base composite foundation in soft soil areas." *Building Structure*, Vol. 41(2):101-105. (in Chinese)
- Su, Y.S. (2011b). "Application of vector piles technology in collapsible loess area." *Building Science*, Vol. 27(3):97-99. (in Chinese)
- Wang, J.Z., Lin, Z.Y., and Zhang, L.X. (2002b). "Study and application of composite-carrier punner-enlarging pile." *Construction Technology*, Vol. 31(1):47-48. (in Chinese)
- Xue, X.H., Wei, Y.X., Yang, X.G., Li, H.T., and Yu, C. (2012c). "Indoor model test study on CFG pile composite foundation." *China Railway Science*, 2):7-12. (in Chinese)
- Yan, M.L., and Zhang, D.G. (2006) Technology and engineering practice of CFG composite foundation, Beijing: *China Water Conservancy Press*. (in Chinese)
- Yang, Q.A., and Chu, Z.H. (2012a). "Bearing mechanism analysis and research on ram-compacted piles with bearing base and composite foundation under the soil foundation." *Geotechnical Investigation & Surveying*, Vol. 40(11):44-49. (in Chinese)
- Zhang, J.W., Zeng, J.C., Tu, Y.M., and Tong, X.D. (2011c). "Experimental study on CFG pile-raft composite foundation of Beijing-Shanghai high-speed railway." *Journal of the China Railway Society*, Vol. 33(1):83-88. (in Chinese)
- GB 50007-2002. (2002c). Code for design of building foundation. Beijing: *China Building Industry Press*. (in Chinese)

Imaging the graben structure based on microtremor with H/V spectral ratio

Zhang Qian¹, Zhao Boming², Liu Jianda³, Xu Hangang³, Gao Zhibing³

¹ Doctoral candidate, School of Civil Engineering, Beijing Jiaotong University, Beijing 100044, China;

² Professor, School of Civil Engineering, Beijing Jiaotong University, Beijing 100044, China; bmzhao@bjtu.edu.cn;

³ Earthquake Administration of Jiangsu, Nanjing, 210000, Jiangsu, China; Jsdzjjs@163.com

ABSTRACT: The long period spectrum characteristics of microtremor have been used in investigating dynamic parameters and speculating the graben structure. This paper reports the results from a microtremor observation profile crossing the Xuzhou city to deduce the graben structure of the Xuzhou Basin, and investigate the predominated period in the H/V spectral ratio method. When the equivalent shear wave velocity is constant, the result shows good corresponding relationship between predominant period and sedimentary thickness. The theoretical calculation of the microtremor characteristics base on wave propagation theory validates the analysis results from the observation. The method, imaging the graben structure based on microtremor with H/V spectral ratio is credible, and the predominant period obtained from H/V spectral ratio is more precise than horizontal power spectrum.

1 INTRODUCTION

Microtremor is continuous periodic tiny ground motion. The systematic measurements of microtremor have been carried out at several thousand places in Japan. The source characteristics of microtremor, wave propagation characteristic and site effect are discussed by many views. Horike (1985) studied the main composition of microtremor. Kanai *et al* (1951, 1954 and 1965) studied of microtremor to be use in engineering field. Scientists selected the test sites with different geological structures to make research. The results showed that solid characteristics of site, the stiffness and thickness of soil layer, are responded by spectrum (Takeuchi 1993, Seo 1997). In the same site conditions, microtremor and strong ground motion have a similar predominant period (Hiroshi 1986, Aki 1988). The observation method is convenient and economical. In the foreign country, analyzing microtremor observation data as an efficient and reliable method to speculate underground structure has been used to earthquake engineering and earthquake resistance design.

The spectral ratio which was proposed by Nakamura (1989), between the horizontal component of a microtremor relative to the vertical component at the single site, H/V , is the same as the shear wave of the surface layer. It is more effective and robust in calculating the period of a stratum than other methods (Zhao 1998, 2007). Compared with horizontal power spectrum, H/V spectral ratio method eliminates the influence of the source and path effects (Katsuaki 1998).

Based on the result, admitting the presupposition that the microtremor's H/V spectral value is the same as the predominant period of a given stratigraphic structure, we studied the graben structure of the deep strata in the Xuzhou Basin through the predominant frequency value of the H/V ratio based on V_S provided by the exploration data.

2 MICROTREMOR OBSERVATIONS

Xuzhou Basin is located in the south of the North China Plain. Most of it is plain, while the central and eastern zone is hills. Depth of the sedimentary layer is intricate. The seismic exploration result showed that there are large scale quaternary active faults beneath the Xuzhou City.

Two main faults are expressed by two dark dotted lines in FIG.1. One is Waste Yellow River fault, which is a concealed fault. The overall trend NWW, tend to SW, elongation at rupture direction is similar with Waste Yellow River development direction. Terrain fault broken bandwidth about 2 km. Both sides of the fracture topography showed a variety of forms, including mountain fault break, beaded drainage phenomenon. The other one is Shao Floor fault, which span 28 km in the area from north to south by 55° into 10° .

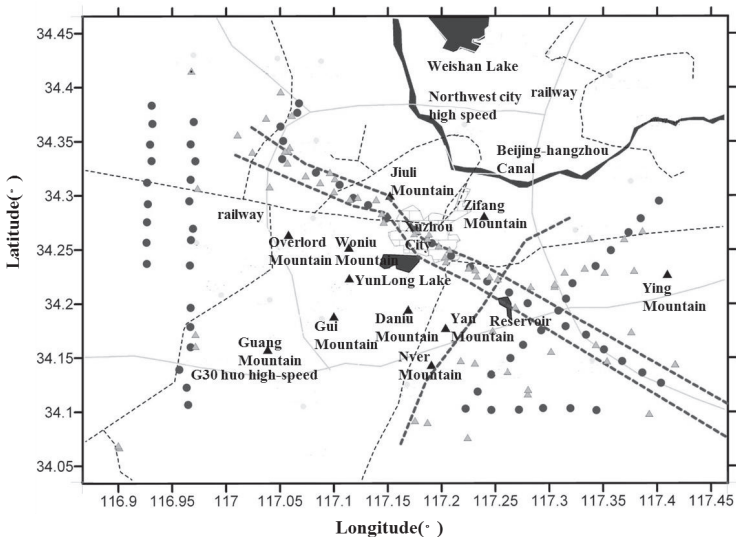


FIG. 1. The location of microtremor observation sites in Xuzhou Basin.

As shown in FIG.1, the black dots are the microtremor observation sites; the light triangles are some borehole points. The microtremor observation main profile set along with NW-SE direction, which is near to borehole points, based on the trend of Waste Yellow River fault. Some other observation profile set to increase the east and west data, a total of 68 observation sites. Spacing between two adjacent observation sites are 1 km or 2 km. Each observation keep three times, and more than 15 minutes. Observation equipment is K2 digital seismograph that can capture low frequency signals well.

3 THE RESULT OF H/V SPECTRA

Xuzhou exploration data gives the borehole shear wave velocities, some of them are collected near the microtremor observation sites. The V_s of entire sedimentary layer are basically the same. So the predominant frequency variation reflects the undulating variation of the basin basement. Usually, the higher the frequency, the thinner the sedimentary thickness is, and vice versa.

The spectrum results are shown in FIG.2. No.3 and no.6 come from western zone, no.31 and no.35 come from central zone, and no.48 and no.60 come from eastern zone. Considering the microtremor is a kind of low frequency vibration, the effective frequency range is determined between 0.1 Hz and 10 Hz. To avoid the influence of the source, four data with same time duration are selected by different observed time. In FIG.2, the horizontal axis is frequency, the right vertical axis is the H/V spectrum ratio and the left vertical axis is the horizontal power spectrum. The corresponding position in the horizontal axis for the solid black dot is the predominant frequency, which is in the highest peak value of graph, in H/V spectrum ratio, and the open dot is the predominant frequency in the horizontal power spectrum. The analysis results show that the frequency obtained from the H/V ratio is different from horizontal power spectrum. No.31 is located in downtown, influenced by surrounding or underground structure, the predominant frequency value of which is the second peak.

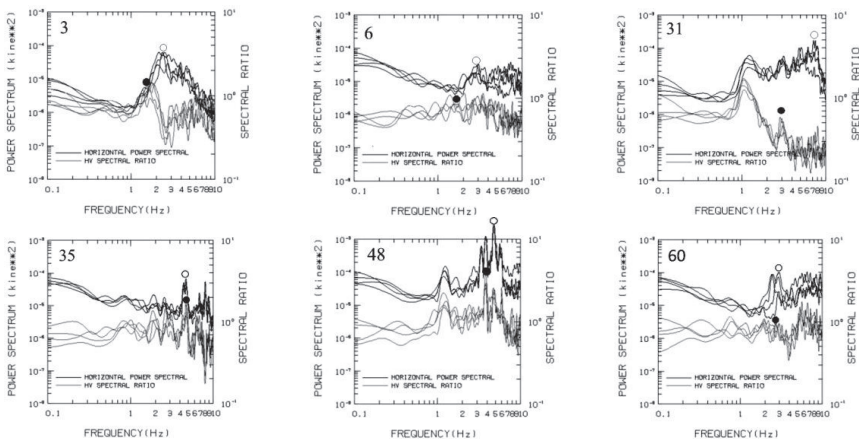


FIG.2. Calculation results of microtremor by different zone.

The sedimentary thickness of observation sites is determined by exploration data along with main profile. In FIG.3, (a) is the relationship between the thickness and predominant period values obtained from H/V spectrum ratio between no.21 and no.37, and (b) is that obtained from horizontal power spectrum. Comparing (a) with (b), the corresponding relationship in the first figure is more obvious, whereas the second data is scattered. As shown in FIG.3 (a), the predominant periods of observation sites in the western are high, and in central and eastern zone, that are steady and low. Those show that in the western zoon the sedimentary layer is thick, and in the central and eastern zone it is thin. The borehole data have verified.

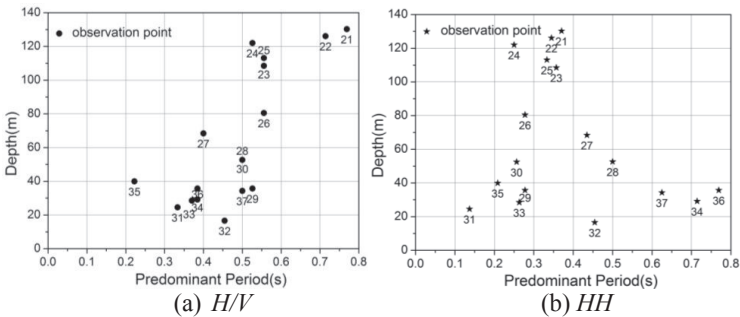


FIG.3. The relationship between the thickness and predominant frequency values by different methods along with trend of Waste Yellow River fault.

To further understand the relationship between the predominant period and sedimentary thickness, the Xuzhou Basin is divided into different zone according to the landform, the position of microtremor observation sites and borehole points. The subsurface in mountains is mainly rock, the velocity structure is similar and special, no considering. The zoning is shown in FIG.4. The solid black dots are the microtremor observation sites, gray areas is mountains.

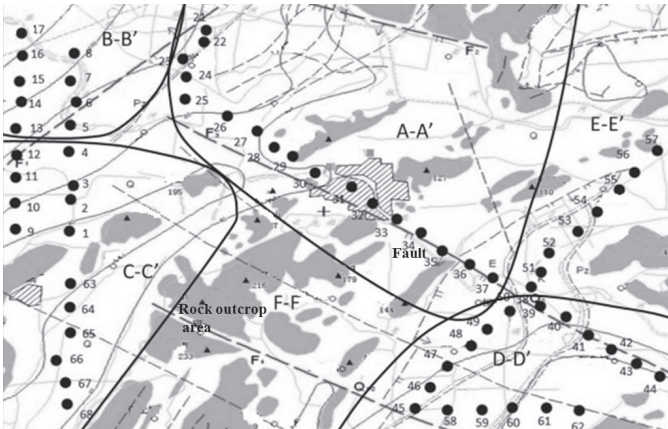


FIG.4. Zoning in Xuzhou Basin.

The regression curve between predominant period obtained from the H/V ratio and thickness in different zone is shown in FIG.5. With the exception of A-A' zone, the borehole points are sparse, thus the thickness is referred to nearby borehole data and A-A' regression curve. After drawing the corresponding curve, the final thickness of observation sites is determined by the period in curve corresponds to the depth. In FIG.5, the thickness is high in B-B' zone. Along the direction of observation line west to east in A-A' zone, the thickness is decreasing gradually. In C-C', D-D' and E-E' zone, the thickness is low. The results are just close to the borehole data, the sedimentary layer is thick in northwest, some parts reach 130 km, and in the central and eastern zone that is thin, between 20 km and 60 km. The predominant period in the E-E' zone is large, but the thickness is low. The different slope of curve owns to dynamic stiffness of the underlying sediment

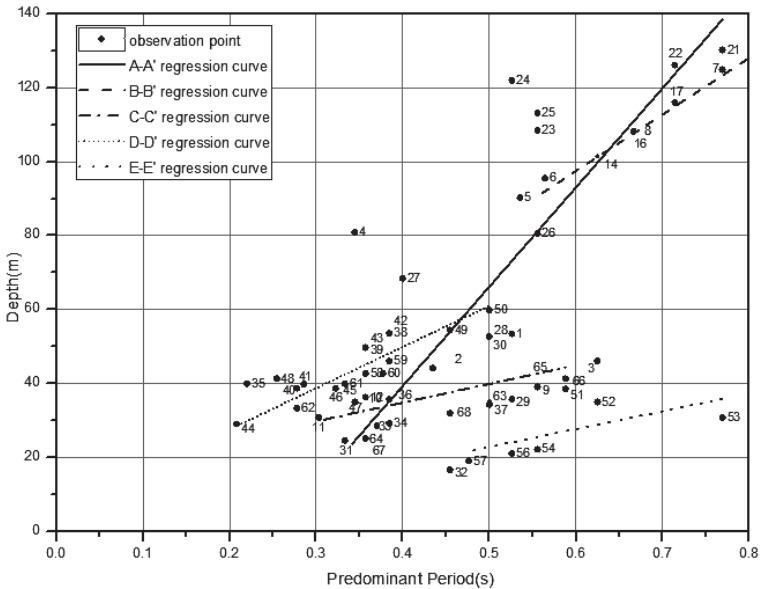


FIG.5. Regression curve between predominant period and depth in different zone.

To validate that imaging the graben structure based on microtremor with H/V spectral ratio is credible. The inferred graben structure results is compared with those obtained from seismic explorations, borehole and survey line data, along with a NW-SE profile, which through the most complicated geological conditions. As is shown in FIG.6, the grey rectangles are borehole column, the dot dash line is final depth of sedimentary layer from exploration data, and the solid dots are the depth which comes from the corresponding thickness, according to the regression curve, deducting the depth of the earth's surface. Plain connected with real line, and hills with dotted line. Both depth and variation tendency are the same basically.

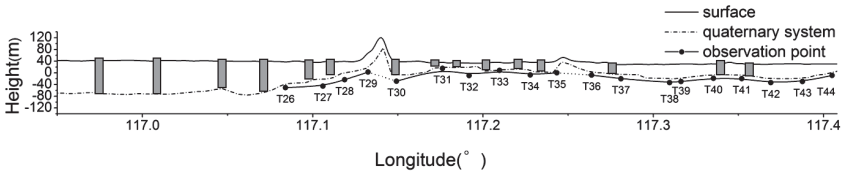


FIG.6. Contrast curve between depths obtained by microtremor and exploration along the profile crossing from NW to SE.

4 THEORETICAL CALCULATION

The inferred graben structure results in turn prove that the predominant frequency obtained from the H/V ratio is exact. We have chosen three observation sites: no.39, no.43 and no.57 to conduct further comparison with theoretical prediction at these sites. The wave propagation theory is used to calculate the Rayleigh wave dispersion curve for the previous research shows that most microtremor consist of surface wave. The H/V ratio of the surface wave is compared with the observed microtremor H/V value. In the theoretical calculation, it is assumed that the sedimentary layer of the Xuzhou Basin is stratified horizontally. The calculating method is a compound-matrix that is more precise than the traditional Thomson-Haskell (1953) determinant equation.

The bedrock is assumed to be an elastic half space, and it is overlaid by five layers, Q3、Q2、Q1、Q and R, as the four formations are all assumed to be horizontal flat layers. The thickness, density, shear wave velocity and compressional velocity of each later are obtained from the exploration data. As shown in Table 1.

Table 1. Parameters of Theoretical Calculation

| Point | Layer | Depth (m) | ρ (kg/m ³) | V_S (m/s) | V_P (m/s) |
|-------|-------|-----------|-----------------------------|-------------|-------------|
| No.39 | Q3 | 6 | 1.75 | 230 | 1000 |
| | Q2 | 12 | 1.85 | 470 | 1900 |
| | Q1 | 50 | 1.9 | 690 | 3200 |
| | Q | 104 | 2.2 | 1700 | 4500 |
| | R | - | 2.5 | 3200 | 5000 |
| No.43 | Q3 | 2 | 1.75 | 230 | 1000 |
| | Q2 | 15 | 1.85 | 380 | 1900 |
| | Q1 | 39 | 1.90 | 570 | 3200 |
| | Q | 100 | 2.20 | 1000 | 4500 |
| | R | - | 2.50 | 3200 | 5000 |
| No.57 | Q3 | 5 | 1.75 | 230 | 1000 |
| | Q2 | 10 | 1.85 | 375 | 1900 |
| | Q1 | 33 | 1.90 | 570 | 3200 |
| | Q | 69 | 2.20 | 1000 | 4500 |
| | R | - | 2.50 | 3200 | 5000 |

The three comparison results are shown in FIG.6. The single black solid line is the theoretical calculation and the four black solid lines are the observed results by H/V ratio. It is shown that, in general, the location of peak corresponding frequency of calculated results is agreed with the predominant frequency by observation result. The magnitude of peak value is different owing to the theoretical method is simple, not considering the influence of body wave and damping.

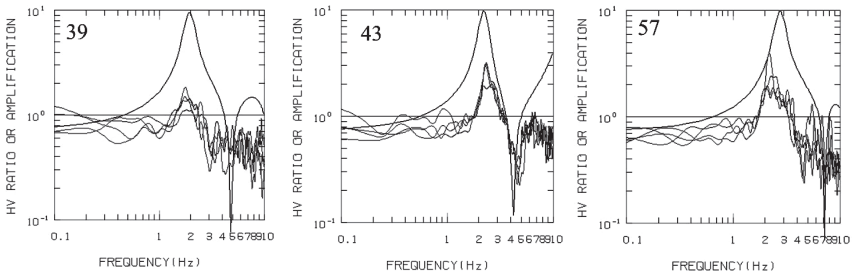


FIG.7. Comparison of the result of theoretical calculation and observation

5 CONCLUSIONS

A number of conclusions can be drawn from the present study on using the microtremor data.

(1) The predominant period obtained from H/V spectral ratio is more accurately represent the variation of sedimentary thickness than horizontal power spectrum in Xuzhou Basin.

(2) When V_S is a constant, the predominant period is consistent with the sedimentary thickness. Predominant period value near the thickest point of the basin is the highest.

(3) In the different zone, the corresponding relationship between predominant period value and thickness is different owing to variable geology.

(4) The H/V value can reflect the tectonic variation in the basin with a reasonable precision. Long period microtremor observation is a viable way to study the garben structure in the deep basin where the Xuzhou City is located

ACKNOWLEDGMENTS

The authors appreciate the support of the National Natural Science Foundation of China (Grant No. 51278045).

REFERENCES

- Kanai K (1951). "Relation between the nature of surface layer and the amplitudes of earthquake motions. I" *Bull. Earthq. Res. Inst. Univ. Tokyo*, Vol. 30: 31-37.
- Kanai K, Osada T and Tanaka T (1954). "Measurement of the microtremor." *Bull. Earthq. Res. Inst. Univ. Tokyo*, Vol. 32: 199-209.

- Kanai K and Tanaka T (1961). "On microtremors. VIII" *Bull. Earthq.Res.Inst. ; Univ. Tokyo*, Vol. 39: 97-114.
- Horike M (1985). "Inversion of phase velocity of long-period microtremor to the S-wave-velocity structure down to the basement in urbanized areas." *Phys. Earth*, Vol. 1(33): 59-96.
- Hiroshi Kagami et al (1986). "Observation of 1 to 5 Second microtremors and their application to earthquake engineering. part III:A two-dimensional study of site effects in the san fernando valley." *Bull. Seis. Soc. Am.*, Vol. 76(6): 1801-1812..
- Aki K (1988). "Local Site Effects On Strong Motion." *Proc. Earthquake Engineering Soil Dynamic II*, Vol. 1: 103-155.
- Nakamura Y (1989). "A method for dynamic characteristics estimation of subsurface using microtremor on the ground surface." *QR of RTRI* 30, No.1: 25-33.
- Takeuchi Y (1993). "A study on application of microtremor to evaluate the characteristics of ground motions during earthquakes." *Grant-in-Aid for developmental scientific research (No.05558047)*, the Ministry of Education, Science and Culture.
- Seo K (1997). "Comparison of measured microtremors with damage distribution." *JICA Research and Development Project on Earthquake Disaster Prevention*.
- Katsuaki K and Tatsuo O (1998). "Ground-motion characteristics estimated from spectral ratio between horizontal and vertical components of microtremor." *Bull. Seis. Soc. Am*, Vol. 88(1): 228-241.
- Haskell NA (1953). "The dispersion of surface waves on multilayered media." *Bull. Seis. Soc. Am.*, Vol. 43: 17-34.
- Zhao B M, Horike M, and Takeuchi Y (1998). "Which site-specific characteristics estimated from microtremors are useful?" *Journal of Struct. Constr. Eng. Architectural Inst. Japan (AIJ)*, Vol. 509: 69-75. (in Japanese with English abstract)
- Zhao B M and Xie XF (2007). "Imaging the graben structure in the deep basin with a microtremor profile crossing the Yinchuan city." *J. Geophys. Eng.* 4, 293-300.

Measuring Shear and Compression Wave Velocities in Laboratory Triaxial Tests Using Disk Shaped Composite P/S Piezoelectric Transducer

Muhammad Irfan¹, and Taro Uchimura²

¹PhD Candidate, Department of Civil Engineering, The University of Tokyo, Japan;
mirfan1@msn.com

²Associate Professor, Department of Civil Engineering, The University of Tokyo, Japan;
uchimura@civil.t.u-tokyo.ac.jp

ABSTRACT: The fundamental construction of disk type p/s composite piezoelectric transducer, which is capable of measuring both shear and compression wave velocities simultaneously in triaxial testing conditions, is discussed. Performance evaluation of wave measurement system was conducted by studying the effects of crosstalk, quality of transmission cables and features of recording unit. The evaluation showed that crosstalk deterioration can successfully be eliminated through proper grounding, and the use of low-noise coaxial cables can significantly enhance signal to noise ratio of received signals. Use of wave recorder with low inherent noise, and high analogue to digital (A/D) conversion resolution, sampling rate, and voltage sensitivity can considerably improve the overall performance and signal interpretation of received signals. Combined monitoring of shear and compression waves by using disk transducer was also found to assist the identification of near-field effects in shear wave receiver signals. Based on this work disk type piezoelectric transducers show significant future potential for laboratory determination of shear modulus and constrained compression modulus of soil because of their robustness and noninvasive nature.

INTRODUCTION

The use of piezoelectric elements for geotechnical engineering applications was first introduced by Lawrence (1963). Since then, various types of piezoelectric transducers are being used for laboratory studies of geomaterials properties; some of them include the bender elements (Shirley, 1978), frictional/pulsate bender elements (Fioravante, 2000), and bender/extender elements (Lings & Greening, 2001; Leong et al., 2009), etc. Among these, bender elements for the determination of shear wave (*S*-wave) velocities have gained outright popularity. However, the usage of piezoelectric transducers for dilatational/compression wave (*P*-wave) determination is not as widespread because for soil, which is mostly loaded in the shear mode, the deformation behavior is better explained by shear modulus. Also, the inability to

measure P -wave velocity in saturated soils (as P -wave travels faster through the water phase than through the soil skeleton), restricts the usage of P -wave piezoelectric transducers (Leong et al., 2009). However, with the emerging interest in unsaturated soil mechanics, the measurement of P -wave velocity is becoming more meaningful as it can provide an assessment of the saturation ratio as well as the porosity of unsaturated soil specimen (Brignoli et al., 1996). Various researchers have worked on the idea of combined determination of shear and compression wave velocities by using separate pairs of S -wave and P -wave piezoelectric transducers mounted in the same apparatus (Bates, 1989; Brignoli et al., 1996; Nakagawa et al., 1996; Lings & Greening, 2001; Lee & Huang, 2007; Uchimura, 2011). However, all of these transducers were essentially modifications of the original bender element which penetrated into the soil causing disturbance to soil specimen.

This paper describes the construction and use of a new flat shaped piezoelectric transducer, called *disk transducer*, for combined determination of P -wave and S -wave velocity in triaxial specimen. Performance evaluation of transducer and the measuring system in terms of resolution of analogue to digital (A/D) recorder and connecting cables, and a note on the ambiguities caused by near-field effect in shear wave arrival time are discussed hereinafter.

P/S COMPOSITE PIEZOELECTRIC TRANSDUCER

Lawrence (1963) was the first one to employ piezoelectric plate elements for the determination of S -wave velocity in clay and sand specimen. However, their use has been limited because of their large size and a requirement of greater driving voltage. Plate type piezoelectric elements, similar to the ones used by Lawrence (1963), but more versatile and much smaller in size were used in this study. A pair of compression (P -type) and a pair of shear (S -type) ceramic plate transducers, manufactured by Fuji ceramics corp. were employed in this study. Both P and S type plates (20 mm diameter; 2 mm and 5 mm thick respectively) were bonded together with araldite (a two-component epoxy glue) and were encapsulated in a metal housing. Space in the top of metal housing was filled with silicon rubber to allow easy movement of S -type piezo disk. A thin layer of araldite coated on the surface of transducer made it waterproof and also protected it against direct exposure of testing material. The completed assembly, as shown in Fig. 1(a), was thus capable of measuring both P -

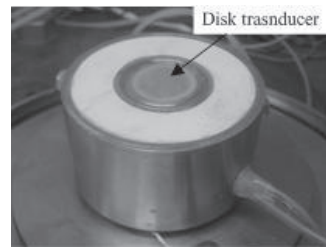
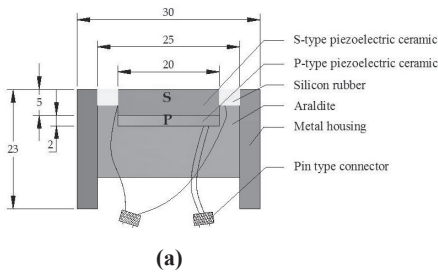


FIG. 1: Disk transducer; (a) schematic diagram (b) fixed in base pedestal of triaxial apparatus.

wave and *S*-wave velocity and was named as *disk transducer*. The metal housing supporting the disk transducer was then fixed at the center of triaxial cell base pedestal by means of an O-ring, as shown in Fig. 1(b). Further construction details can be found in (Irfan & Uchimura, 2013a, 2013b).

A single pulse of 4.5 *Vpp* (V_{pp} = peak-to-peak voltage) sinusoidal signal generated by function generator (Tektronix, AFG3022B) and amplified to 90 *Vpp* by power amplifier (NF Corp. model HSA4012) was used to excite transmitter disk transducer. Sinusoidal pulse was preferred over square wave input as it causes less distortion of the received signal, hence simplifying the determination of first arrival time (Irfan & Uchimura, 2013a). The wave transmitted through the soil specimen was received at top cap by receiver disk transducer which transferred the signal to recording unit. Input signal from power amplifier was fed to the recording unit through a monitoring channel. The recording unit thus recorded both the input and output signals simultaneously. Edosaki sand (natural sand with 10% fines) specimens of diameter 75 mm and 150 mm height were used in this study (basic soil properties of test material can be found in Irfan and Uchimura (2013a).

DISK TRANSDUCER - PERFORMANCE ANALYSIS

Due to the noninvasive nature of disk transducers, the amplitude of received signals is lower as compared to bender elements, under similar test conditions. Any source of electromagnetic or external noise would therefore decrease the signal to noise ratio, hence making signal interpretation difficult. Discussed hereinafter is the performance analysis of disk transducers with respect to crosstalk, quality of transmission cables, and resolution of recording unit.

Electromagnetic Coupling – Crosstalk

Electromagnetic coupling between source and receiver piezoelectric transducer causes the deterioration of output signal in the form of an early component which is quasi-simultaneous with the input signal, known as “crosstalk”. Figure 2 shows typical

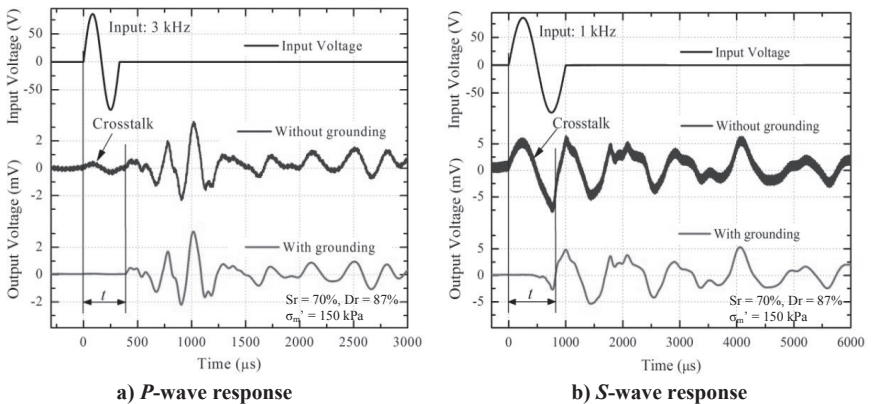


FIG. 2: Crosstalk effect in (a) *P*-wave and, (b) *S*-wave signals.

example of crosstalk in disk transducer signals. The actual arrival point of received signals in Fig. 2 is masked by crosstalk. As a result, the first arrival appears at a time later than the actual arrival time; consequently the computed wave velocity is lower than the actual value. Crosstalk in disk transducers is found to be removed by grounding the transmitter disk transducer. It was also observed that 50 Hz noise from commercial power supply can be eliminated by grounding the receiver disk transducer. For grounding, the negative terminals of both P and S transducers were connected to a grounded cable. Both transmitter and receiver disk transducers were therefore, properly grounded in all subsequent tests conducted in this study.

Quality of Transmission Cables

Very low amplitude receiver signals are prone not only to external noise interference, but also to the self-induced noise within the cable. Standard coaxial cables are susceptible to self-induced noise, due to vibration, bending, twisting, friction and fluctuation of pressure, a phenomenon known as triboelectric noise. The performance of ordinary coaxial cables in receiving low-amplitude disk transducer signals was compared with low noise coaxial cables (Fuji ceramics model LN-030). Low noise cables had special fluorinated ethylene propylene (*FEP*) sheathing to reduce self-induced cable noise. Use of low noise coaxial cables significantly reduced the noise generated within the cable, thereby increasing signal to noise ratio (*SNR*) of received signal by about 2.5 times (Fig. 3). The signal to noise ratio in decibels is given by:

$$SNR = 20 \log \frac{\text{Signal Amplitude}}{\text{Signal Noise}} \quad (1)$$

Resolution of Signal Recorder

Quality of signal recording unit directly affects the received signals. The effect of recording unit quality on disk transducer received signals is evaluated by comparing signals recorded by a data logger (Keyence NR-500 data logger with NR-HA08 hi-speed measurement unit) and a digital oscilloscope (Hioki 8860-50 digital oscilloscope with model 8957 hi-resolution measurement unit).

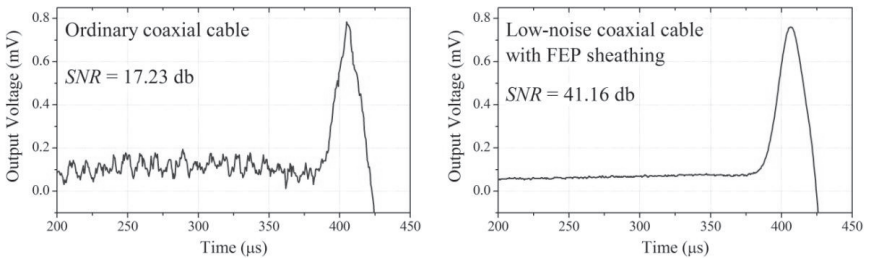


FIG. 3: Receiver disk transducer signals (zoomed-in) showing the effect of quality of transmission cables.

Figure 4(a) shows typical *S*-wave receiver signals in Edosaki sand specimen ($S_r = 70\%$; isotropic stress = 50 kPa), recorded on both Keyence NR-500 data logger and Hioki 8860-50 oscilloscope and their corresponding frequency spectrum. Although the frequency spectrum of both recorders show a similar dominant frequency but the signal to noise ratio as well as amplitude of signal recorded by Hioki 8860-50 oscilloscope is much higher. Moreover, the signal obtained through Hioki 8860-50 oscilloscope is much clearer compared to its counterpart making travel time determination rather easy. Typical *P*-wave receiver signals in the same Edosaki sand specimen obtained through both recorders and their corresponding frequency spectrum are shown in Fig. 4(b). *P*-wave signal received by Hioki 8860-50 oscilloscope is again much clearer than the signal obtained by Keyence NR-500 data logging unit. High levels of noise in Keyence NR-500 data logger signals mean a very low signal to noise ratio, resultantly no dominant frequency can be observed from its frequency spectrum. On the contrary, a dominant frequency of about 15 kHz, similar to the excitation frequency, can be observed from the frequency spectrum of signal recorded by Hioki 8860-50 oscilloscope.

Besides a higher analog to digital (A/D) conversion resolution (16 bit versus 14 bit), Hioki 8860-50 oscilloscope offers a much higher sampling rate (50 ns/S versus 2 μ s/S) resulting in a smoother signal. The voltage sensitivity of recorder is expressed in terms of least significant bit (*LSB*) voltage, which is the minimum voltage discernible by the recorder. The *LSB* voltage of Keyence NR-500 was limited to 0.01 mV as compared to 3.125 μ V for Hioki 8860-50 oscilloscope; hence any change in voltage smaller than 0.01 mV could not be detected by NR-500 data logger, as can be seen in Fig. 4. In order to determine the inherent noise level, both recorders were fed with 0 V input (i.e. short-circuited) and the resulting signal was recorded. Keyence NR-500 data logger possessed a very high inherent noise of about 0.08 mV as compared to 0.001 mV of Hioki 8860-50 oscilloscope. Hence, signals recorded by Keyence NR-500 data logger having peak-to-peak amplitude of less than 0.08 mV would be difficult to observe as being masked by inherent noise. Therefore, a recording unit with high A/D conversion resolution, sampling rate, voltage resolution; and low inherent noise is necessary for disk transducer element tests.

COMBINED MEASUREMENT OF *P*-WAVE AND *S*-WAVE VELOCITY

The ability of disk transducer to measure both *P*-wave and *S*-wave velocity over the same travel path in the triaxial specimen makes it suitable for studying the near-field effect (i.e. a *P*-wave component of opposite polarity associated with *S*-wave propagation (Brignoli et al., 1996)). Near-field effect obscures the actual arrival point of *S*-wave and adds to the complexity of *S*-wave velocity determination. To identify near-field component in *S*-wave propagation, both *P*-type and *S*-type response of receiver disk transducer due to shearing excitation of transmitter disk transducer are recorded, as shown in Fig. 5. A comparison with received signals from compression excitation confirms that the initial deflection of *S*-wave signal represents the arrival of *P*-wave instead. Also the *P*-wave velocity obtained through shear excitation and compression excitation is found to exhibit no significant difference in Edosaki sand specimen subjected to varying isotropic confining pressure as shown in Fig. 6.

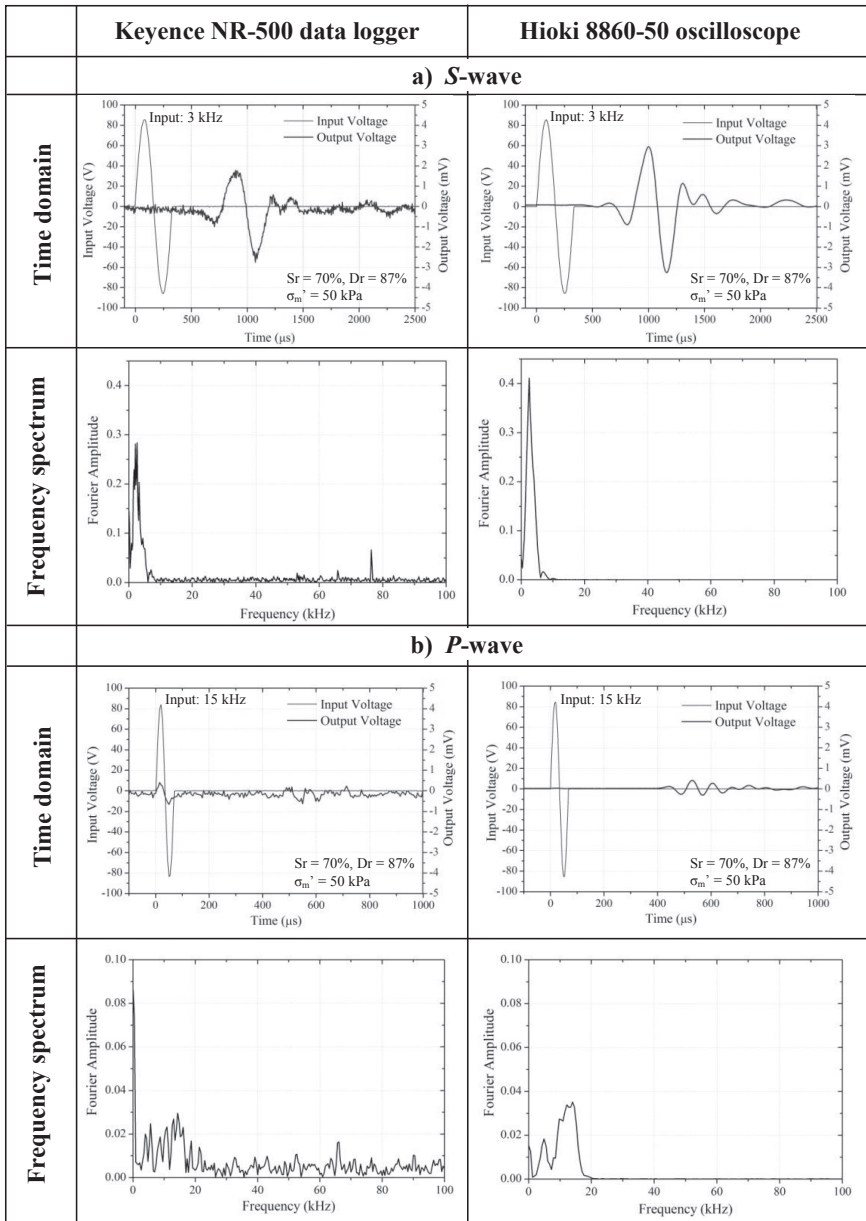


Figure 4: Typical (a) shear wave (S-wave), and (b) compression wave (P-wave) signals recorded on Keyence NR-500 data logger and Hioki 8860-50 oscilloscope and their corresponding frequency response function.

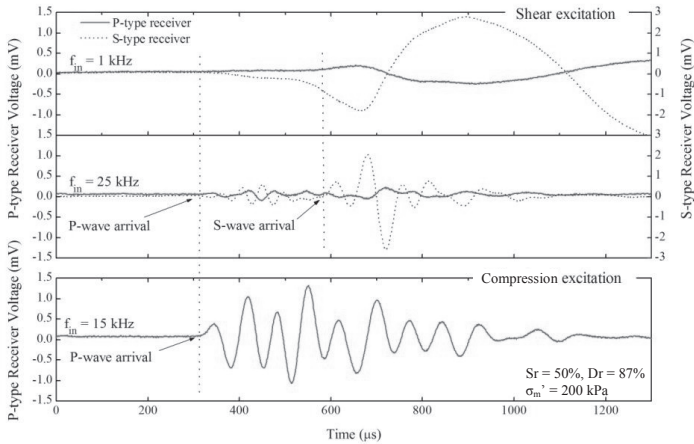


Figure 5: Wave velocity measurements in Edosaki sand ($S_r = 50\%$; isotropic stress = 200 kPa) illustrating transverse motion before shear wave arrival.

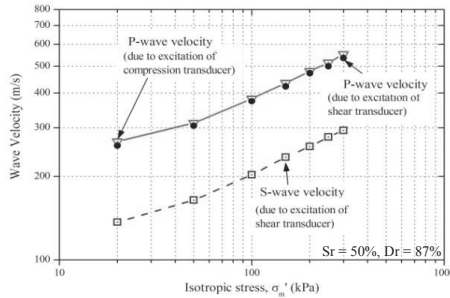


Figure 6: Compression and shear wave velocity measurements in 50% saturated Edosaki sand specimen.

CONCLUSIONS

A new disk shaped piezoelectric transducer that enables both shear and compression wave velocities to be determined by using a single pair of transducers mounted across a soil specimen is described. The proposed disk transducer is advantageous over conventional bender elements due to its non-invasive nature. Performance of disk transducer with respect to resolution of A/D recorder, quality of transmission cables, and grounding conditions is analyzed and the following conclusions are drawn;

- Receiver signals were found to be distorted by crosstalk, which could effectively be removed by grounding both transmitter and receiver disk transducers.
- Use of low noise coaxial cables reduced the self-induced cables noise and improved signal to noise ratio of received signals by 2.5 times compared with

ordinary coaxial cables.

- For disk transducer element tests, the use of recording unit with low inherent noise is essential. Signal recording unit with high A/D conversion resolution, sampling rate and voltage sensitivity is found to facilitate signal interpretation.
- Disk transducer has made possible combined monitoring of *P*-wave and *S*-wave response which can assist in eliminating ambiguities caused by near-field effects in determination of shear wave arrival time.
- Arrival time of *P*-wave does not appear to be affected by the mode of excitation (i.e. shear or compression).

REFERENCES

- Bates, C. (1989). Dynamic soil property measurements during triaxial testing. *Geotechnique*, 39(4): 721-726.
- Brignoli, E. G. M., Gotti, M., & Stokoe, K. H. (1996). Measurement of Shear Waves in Laboratory Specimens by Means of Piezoelectric Transducers. *Geotechnical Testing Journal*, GTJODJ, 19(4), 384-397. doi: 10.1520/GTJ10716J
- Fioravante, V. (2000). Anisotropy of small strain stiffness of Ticino and Kenya sands from seismic wave propagation measured in triaxial testing. *Soils and foundations*, 40(4), 129-142.
- Irfan, M., & Uchimura, T. (2013a). *Criteria for determining Gmax in laboratory element tests using disk type piezoelectric transducers*. Proceedings, 10th International Conference on Urban Earthquake Engineering Tokyo, Japan. 555-560
- Irfan, M., & Uchimura, T. (2013b). *A modified triaxial apparatus for measurement of shear and compression waves during water injection in unsaturated soils*. Proceedings, 13th National Conference on Geotechnical Engineering, 2013, Lahore, Pakistan. 20-28
- Lawrence, F. V. (1963). Propagation of ultrasonic waves through sand. *Massachusetts Institute of Technology, Boston, Report R63-08*.
- Lee, C. J., & Huang, H. Y. (2007). Wave velocities and their relation to fabric evolution during the shearing of sands. *Soil Dynamics and Earthquake Engineering*, 27(1), 1-13. doi: 10.1016/j.soildyn.2006.05.006
- Leong, E. C., Cahyadi, J., & Rahardjo, H. (2009). Measuring shear and compression wave velocities of soil using bender-extender elements. *Canadian Geotechnical Journal*, 46(7), 792-812. doi: 10.1139/t09-026
- Lings, M., & Greening, P. (2001). A novel bender/extender element for soil testing. *Geotechnique*, 51(8), 713-717.
- Nakagawa, Soga, K., & Mitchell. (1996). Pulse Transmission System for Measuring Wave Propagation in Soils. *Journal of Geotechnical Engineering*, 122(4), 302-308. doi: 10.1061/(ASCE)0733-9410(1996)122:4(302)
- Shirley, D. J. (1978). An improved shear wave transducer. *The Journal of the Acoustical Society of America*, 63, 1643.
- Uchimura, T. (2011). *Wave velocity in unsaturated slopes in relation to moisture and stability*. Proceedings, The 14th Asian Regional Conference on Soil Mechanics and Geotechnical Engineering, Hong Kong. 194-217

Analysis of Elastic Support Beam on Dynamic Load

LIU Yang¹, WANG Ming-yang² and SONG Chun-Ming³

¹PHD student, Engineering Institute of PLA University of Science and Technology, Qinhuai District, Haifuxiang 1, Nanjing, nanjb821045@163.com

²Professor, Engineering Institute of PLA University of Science and Technology, Qinhuai District, Haifuxiang 1, Nanjing, wmyrf@163.com

³Doctor, Engineering Institute of PLA University of Science and Technology, Qinhuai District, Haifuxiang 1, Nanjing, ming1979@126.com

ABSTRACT: The differences of boundary restraints do directly affect the dynamic responses and bearing capacity. The mechanics models of beams with flexible supports were established, and elastic supports, lumped masses at the beams ends and non-symmetric supports were taken into account. Numerical analysis of the model was conducted by using the Euler-Bernoulli's theory and Lagrange method. The characteristic equation and the eigen-functions of the supported beam were derived. The responses of beams subjected to any dynamic loads were explored. Through the comparison with results from the existing references calculation results, the accuracy of the present method is validated. Then the effect of the boundary restrained stiffness on the dynamic responses of beams is analyzed, the analyses show that flexible supports have great effects on the performances of beams, both horizontal and vertical elastic supports can reduce the dynamic coefficient of displacement. The optimization of added masses and their positions on the beam can improve the impact resistance of beam.

INTRODUCTION

Beams are ubiquitous structural elements that appear in many different forms and comprise many different artifacts. Bearing capacity of RC beams calculated by using typical dynamic computing methods is always smaller than the practical value. The main reason is that the deformations of surrounding members and the flexible supports are not taken into account. Practically, flexible supports have great effects on inner forces and deformations of structures, and theories based on condition of rigid support are completely not in agreement with engineering practice. Therefore, it is of great importance both in practice and theoretically to investigate the dynamic analysis of beams with flexible supports.

Supports are not only expected to hold a structure firmly, but can also be designed to improve the structural performance. This problem has been performed by several researchers (Xia et al. 2010; De Rosa et al. 1995). Kenny (1954) studied an infinite beam on Winkler foundation. The beam was idealized using the Euler-Bernoulli beam

theory and the effect of viscous damping was also investigated; Song et al. (2008) studied the dynamic response of beams with flexible supports subjected to transversal impact; Fryba et al. (1993) presented a solution for the problem of a constant moving load along an infinite beam on an elastic foundation considering all values of viscous damping; Yau et al. (2001) analyzed the impact response of bridges with elastic bearings from a series of moving loads, the bearings were modeled by linear transverse springs. There exists other literature on the vibration of beams with elastic supports (Xia et al. 1991; Biler 1986, De et al. 1984; Goswami 1982).

In this paper, the study on vibration characteristics of beams with arbitrary boundary conditions is carried out, the free vibration characteristics of beam with arbitrary boundaries are analyzed, the effect of the boundary restraining stiffness on the dynamic response of beam is studied, and the general rule for the effect of stiffness is also presented.

MATHEMATICAL FORMULATION

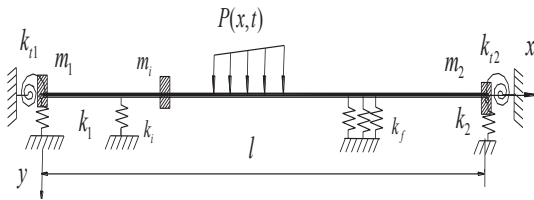


FIG. 1. The mechanics model of beam

As shown in Fig. 1, a beam of length l is considered in this study. A translational spring with stiffness $k_i(N/m)$ and a mass m_i are attached to the beam at in-span locations $x = l_s, 0 \leq l_s \leq l$ and $x = l_m, 0 \leq l_m \leq l$, respectively, where $k_i(N/m)$ is the spring constant per unit length of the foundation $k_f(N/m^2)$. At the left end ($x = 0$), the beam is restrained by a translation spring k_1 and a torsion spring k_{t1} . At the right end ($x = l$), the beam is restrained by a translation spring k_2 and a torsion spring k_{t2} . In addition, the left and right ends are attached with a mass m_1 and a mass m_2 , respectively. The differential equation of motion can be written as

$$EI \frac{\partial^4 y(x,t)}{\partial x^4} + m \frac{\partial^2 y(x,t)}{\partial t^2} = P(x,t) \tag{1}$$

where b, h are the cross-sectional width and height, respectively; m is the mass per unit length of the beam, EI is the rigidity of the beam.

The kinetic energy of the system can be expressed as:

$$T = \frac{1}{2} m_1 \dot{y}_1^2 + \frac{1}{2} m_2 \dot{y}_2^2 + \frac{1}{2} m_i \left(\frac{\partial y(l_m,t)}{\partial t} \right)^2 + \frac{m}{2} \int_0^l \left(\frac{\partial y(x,t)}{\partial t} \right)^2 dx \tag{2}$$

The potential energy of the system can be expressed as

$$V = \frac{1}{2}k_1y(0,t)^2 + \frac{1}{2}k_2y(l,t)^2 + \frac{1}{2}k_{i1}\left(\frac{\partial y(0,t)}{\partial x}\right)^2 + \frac{1}{2}k_{i2}\left(\frac{\partial y(l,t)}{\partial x}\right)^2 + \frac{1}{2}k_i\left(\frac{\partial y(l_i,t)}{\partial x}\right)^2 + \frac{1}{2}k_j\int_0^l\left[\frac{\partial^2 y(x,t)}{\partial x^2}\right]^2 dx + \frac{EI}{2}\int_0^l\left[\frac{\partial^2 y(x,t)}{\partial x^2}\right]^2 dx \quad (3)$$

The external work is:

$$W = \int_0^l P(x,t)y(x,t)dx \quad (4)$$

Substitute the data obtained from kinetics analysis into the Lagrange equation (general parameters are $q_i, u_1(t), u_2(t), g_i(t)$).

$$\frac{d}{dt}\left(\frac{\partial T}{\partial \dot{q}_i}\right) - \frac{\partial T}{\partial q_i} + \frac{\partial V}{\partial q_i} = \frac{\partial W}{\partial q_i} \quad (5)$$

Introducing the following non dimensional parameters

$$u = \frac{x}{l}, \tau = \frac{t}{t_0}, w(u, \tau) = \frac{y(x, t)}{l}, F(u, \tau) = \frac{P(x, t)l^3}{EI}, M_i = \frac{m_i}{m_b},$$

$$\eta_i = \frac{k_{i1}l}{EI}, \xi_i = \frac{k_{i2}l^3}{EI}, i = 1, 2, \quad t_0^2 = \frac{ml^4}{EI}, m_b = ml$$

The non dimensional form of Eq. 1 becomes

$$\frac{\partial^4 w}{\partial u^4} + \frac{\partial^2 w}{\partial \tau^2} = F(u, \tau) \quad (6)$$

The response of the beam is represented as a series expansion in terms of the eigen-functions

$$w(u, \tau) = \sum_{n=1}^{\infty} Y_n(u)\varphi_n(\tau) \quad (7)$$

The boundary conditions and the initial conditions for the general beam are:

$$\left\{ \begin{aligned} \frac{d^3 Y}{du^3} &= (-\eta_1 + M_1\lambda^4)Y, \frac{d^2 Y}{du^2} = \xi_1 \frac{dY}{du} & u = 0 \\ \frac{d^3 Y}{du^3} &= (\eta_2 - M_2\lambda^4)Y, \frac{d^2 Y}{du^2} = -\xi_2 \frac{dY}{du} & u = 1 \end{aligned} \right. \quad (8)$$

The eigen-functions of the continuum can be expressed as

$$Y(u) = C_1 \sin(\lambda u) + C_2 \cos(\lambda u) + C_3 \sin h(\lambda u) + C_4 \cos h(\lambda u) \quad (9)$$

where C_i are arbitrary constants and can be defined from the boundary conditions of the beam, $\lambda^4 = \frac{m\omega^2 l^4}{EI}$, $\omega = 2\pi f$ is the circular frequency.

FREE AND FORCED VIBRATIONS

Substituting Eq. 7 into Eq. 6 and solving for the nontrivial solution leads to the characteristic equation

$$z_1(\cos \lambda_n \sinh \lambda_n + \sin \lambda_n \cosh \lambda_n) + z_2(\cos \lambda_n \sinh \lambda_n - \sin \lambda_n \cosh \lambda_n) - 2z_3 \sin \lambda_n \sinh \lambda_n + z_4(\cos \lambda_n \cosh \lambda_n - 1) + z_5(\cos \lambda_n \cosh \lambda_n + 1) + 2z_6 \cos \lambda_n \cosh \lambda_n = 0 \quad (10)$$

$$\begin{aligned} \text{where } z_1 &= b_{1n} b_{2n} (a_{1n} + a_{2n}) + b_{1n} - b_{2n}, & z_2 &= a_{1n} a_{2n} (b_{1n} - b_{2n}) - a_{1n} - a_{2n}, \\ z_3 &= a_{1n} a_{2n} + b_{1n} b_{2n}, & z_4 &= 1 - a_{1n} a_{2n} b_{1n} b_{2n}, & z_5 &= a_{2n} b_{2n} - a_{1n} b_{1n}, & z_6 &= a_{1n} b_{2n} - a_{2n} b_{1n}, \\ a_{1n} &= \frac{\xi_1 - M_1 \lambda_n^4}{\lambda_n^3}, & a_{2n} &= \frac{\xi_2 - M_2 \lambda_n^4}{\lambda_n^3}, & b_{1n} &= \frac{\eta_1}{\lambda_n}, & b_{2n} &= -\frac{\eta_2}{\lambda_n}. \end{aligned}$$

Mode shapes are:

$$Y_n(u) = C_n [Q(\lambda_n u) - a_{1n} T(\lambda_n u)] + R(\lambda_n u) + b_{1n} S(\lambda_n u) \quad (11)$$

$$\text{where } C_n = \frac{a_{2n} R(\lambda_n) + (a_{2n} b_{1n} - 1) S(\lambda_n) - b_{1n} T(\lambda_n)}{R(\lambda_n) - (a_{1n} + a_{2n}) Q(\lambda_n) + a_{1n} a_{2n} T(\lambda_n)}, \quad Q(u) = [\cos(u) + \cosh(u)]/2,$$

$$R(u) = [\sin(u) + \sinh(u)]/2, \quad S(u) = [\cosh(u) - \cos(u)]/2, \quad T(u) = [\sinh(u) - \sin(u)]/2$$

This method can deal with many combinations of boundary conditions and in-span attachments. For example, if we were to divide Eq. 11 by k_1, k_{i1} and let $k_1 \rightarrow \infty$ and $k_{i1} \rightarrow \infty$, we have the case of a clamped end. Conversely, when $k_1 = 0$ and $k_{i1} = 0$, we have the case of a free end. When $m1 = m2 = 0$, $k1 = k2 = 0$, Eq. 10 becomes

$$(a_{1n} + a_{2n})(\cos \lambda_n \sinh \lambda_n - \sin \lambda_n \cosh \lambda_n) + 2a_{1n} a_{2n} \sin \lambda_n \sinh \lambda_n - (\cos \lambda_n \cosh \lambda_n - 1) = 0$$

which is consistent with the frequency equation of the same elastic support beams in the reference (Peng et al. 2002).

If we assume that the initial conditions are zero, then the solution to the governing equation and boundary conditions is of the form

$$w(u, \tau) = \sum_{n=1}^{\infty} \frac{Y_n(u)}{\lambda_n^2 N_n} \int_0^{\tau} F(u, \tau') Y_n(u) \sin[\lambda_n(\tau - \tau')] d\tau' du \tag{12}$$

where the function $Y_n(u)$ is the corresponding orthogonal mode shape that satisfies the boundary conditions, and $N_n = \int_0^1 Y_n^2(u) du$ is a function of the square of Y_n .

NUMERICAL EXAMPLE AND DISCUSSION

Many familiar classical boundary conditions can be obtained by assuming the translational and rotational spring constant and mass to be extremely large or small. The non-dimensional frequency coefficient $\lambda = \sqrt{\omega l^2 \frac{m}{EI}}$ for different combinations of boundary conditions listed in Table 1. It shows that the natural frequency is proportional to translational and elastic coefficient η_1, ξ_1 . The lower frequencies are significant affected when stiffness of the translational spring at both ends is small.

Table 1. The first non-dimensional frequency coefficients

| $\xi_1 = \xi_2$ | $\eta_1 = \eta_2$ | λ_1 | λ_2 | λ_3 | λ_4 |
|-----------------|-------------------|-------------|-------------|-------------|-------------|
| ∞ | 0 | 3.142 | 6.283 | 9.425 | 12.566 |
| ∞ | 1.0 | 3.398 | 6.427 | 9.524 | 12.642 |
| ∞ | 5.0 | 3.897 | 6.808 | 9.825 | 12.889 |
| ∞ | 10 | 4.156 | 7.068 | 10.066 | 13.105 |
| ∞ | 100 | 4.641 | 7.710 | 10.801 | 13.894 |
| ∞ | 10^6 | 4.730 | 7.853 | 10.995 | 14.137 |
| ∞ | ∞ | 4.730 | 7.853 | 10.996 | 14.137 |
| 1.0 | 0 | 1.310 | 3.943 | 7.071 | 10.211 |
| 10.0 | 0 | 2.231 | 4.095 | 7.097 | 10.220 |
| 50 | 0 | 2.849 | 4.685 | 7.221 | 10.257 |
| 100 | 0 | 2.989 | 5.148 | 7.387 | 10.310 |
| 10000 | 0 | 3.140 | 6.271 | 9.382 | 12.460 |

Consider an impulse force of magnitude f_0 that is applied at $u = \eta_s (0 < \eta_s < 1)$ and at $\tau = 0$. This type of applied force is represented as

$$F(u, \tau) = f_0 \delta(u - \eta_s) \delta(\tau)$$

Substituting into Eq.12 gives

$$w(u, \tau) = f_0 \sum_{n=1}^{\infty} \frac{Y_n(u) Y_n(\eta_s)}{\lambda_n^2 N_n} \sin(\lambda_n^2 \tau)$$

The stiffness of the translational and rotational springs is then taken equal to: $k_{r1} = k_{r2}$ and $k_1 = k_2$, respectively, $f_0 = 1, \tau = 1.2, \eta_s = 0.4$. The eleventh modes are

included in the simulated responses. Fig. 2 is the dimensionless dynamic response of the beam with elastic supports under impulse force. It shows that the elastic support beam displacement is smaller than the simply supported conditions, and the displacement w increases as the elastic supporting coefficient ξ increases. Hence, when ξ is relatively large, the influence of the amplitude variation is quite insignificant.

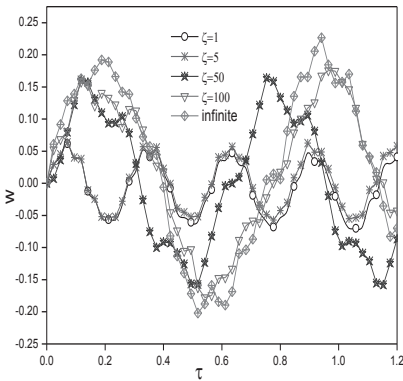


FIG. 2. The displacement response curves for different ξ .

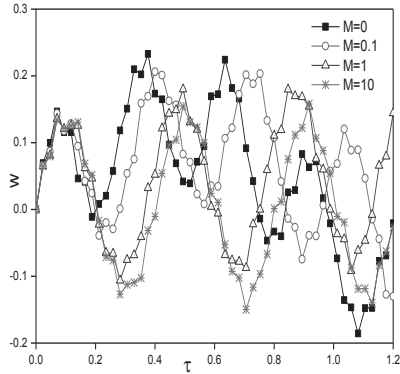


FIG. 3. The displacement response curves for different η .

The results for the dynamic response in mid-span deflections are shown in Fig. 3. It is interesting to note that the rotatable elastic support beam displacement w is significantly smaller than the simply supported beam, and w decreases as the rotational coefficient η increases.

In order to study the influence of added mass of beam on its dynamic response, the mass ratio of 0.1, 1, 10 is considered. For each case, the dynamic response on the mid-span deflections is shown in Fig. 4. It can be seen that w decrease as the mass ratio increases, which indicates that the added mass has a significant effect on the response of the beam, the effect becomes large along with the increasing of the mass ratio. It is shown that the optimization of added masses and their positions on the beam can improve the impact resistance of components.

The elastic support beam under impulse loads with long and short durations are analyzed, which are shown in Fig. 5. The translation spring k_1, k_2 and torsion spring k_{t1}, k_{t2} and attached mass m_1 and m_2 are considered ($\xi_i = 10, \eta_i = 10, M = 0.1$). It can be seen that w increases with the non dimensional time τ , and the fluctuation amplitude significant increases when the duration time is short. Therefore, the beams with elastic supports have strong impact resistance when the time is short.

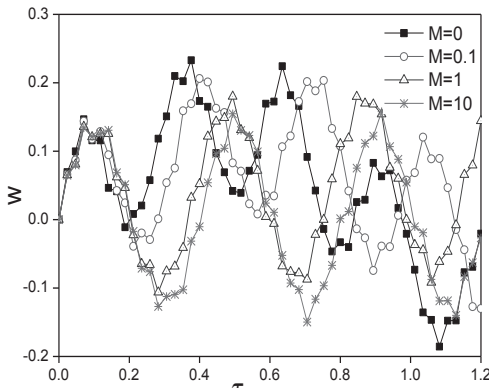


FIG. 4. The displacement response curves for different M .

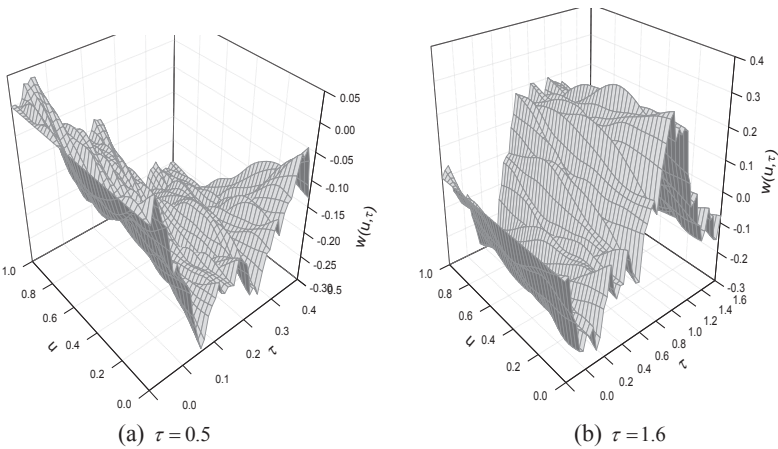


FIG. 5. The displacement response curves for different persist time under impulse loads.

CONCLUSIONS

The mechanics models were established with flexible supports, which include vertical elastic and rotatable elastic supports. The dynamic responses of beam under impulsive loading were explored, and the effects of flexible supports on impulsive resistant capabilities were analyzed. The analysis shows that flexible supports have great effects on impulsive resistant capabilities of beam, and different supports have distinctly different influence.

The dynamic displacement of beam increases with increasing stiffness coefficient ξ , but the trend tends to be ease up as supporting stiffness increasing. The dynamic displacement of beam decreases with the increasing stiffness coefficient η . Both the translational spring and rotational spring can improve the bearing capacities of beams. Even small added mass may affect dynamic characteristic of the beam, which may result in the amplifying of beam response and the falling of response frequency of the beam. The beam with elastic support can make the dynamic displacement decrease obviously, therefore, the bearing capacity to resist impulse loads can be relatively increased, but the effectiveness lies on the stiffness of elastic support and actuation duration of impulsive loading. The resistance of beams can be increased effectively in the case of impulsive loads with short duration.

ACKNOWLEDGMENTS

The project is supported by Science Found for Creative Research Groups of the National Natural Science Foundation of China (No.51021001).

REFERENCES

- Biler, P. (1986). "Remark on the decay for damped string and beam equations." *Nonlinear Analysis-theory Methods & Application*, Vol. 10 (9): 839 - 842.
- De Brito, E.H. (1984). "Decay estimates for the generalized damped extensible string and beam equations." *Nonlinear Analysis-theory Methods & Application*, Vol. 8 (12): 1489 - 1496.
- De Rosa, M. A., Belles, P.M., and Maurizi, M.J. (1995). "Free vibrations of stepped beams with intermediate elastic supports." *Journal of Sound and Vibration*. Vol. 181 (5): 909-910.
- Fryba, L., Nakagiri, S., and Yoshikawa, N. (1993). "Stochastic finite elements for a beam on a random foundation with uncertain damping under a moving force." *Journal of Sound and Vibration*, Vol. 163 (1): 31-35.
- Goswami, M. M. (1982). "Natural frequency of a beam on elastic supports." *Journal of the Institution of Engineers (India)*, 1982, 62: 372-375.
- Kenney, J.T. (1954). "Steady state vibrations of beam on elastic foundation for moving load." *Journal of Applied Mechanics*, Transactions ASME 21: 359-364.
- Peng Ru-hai and Liu Jie (2002). "Elastic beam method for mode analysis of rigid frame." *Journal of Hohai University; Natural Science*, Vol. 30 (2): 9-13.
- Song Chun-ming, Wang Ming-yang and Tang Zheng-guo (2008). "Dynamic responses of beams with flexible supports subject to transversal impact." *Journal of PLA University of Science and Technology*, Vol. 9 (2): 151-155.
- Xia He and Zhu Mu-cheng (1991). "Dynamic response of a flexible arch stiffened truss under train loads." Proc, EASEC-3, 4.
- Xia Ji, Zhu Mu-cheng and Ma De-yi (2010). "Analysis of lateral natural vibration of beams with lumped masses and elastic supports." *Mechanics In Engineering*, Vol. 22 (5): 27-30.
- Yau, J.D., Wu, Y.S., and Yang, Y. B. (2001). "Impact response of bridges with elastic bearings to moving loads." *Journal of Sound and Vibration*, Vol. 248 (1): 9-30.

Field Deformation Study on Enclosure Structure and Environment of Subway Shaft Construction under Complex Conditions

Aijun Yao¹, Hu Peng², Huanfang Chen² Fangduan Ning²

¹ Professor, Institute of Geotechnical and Underground Engineering; Beijing University of Technology; Beijing, China, 100124; yaj@bjut.edu.cn

² Master candidate, Institute of Geotechnical and Underground Engineering; Beijing University of Technology; Beijing, China, 100124; penghu_1988@163.com, 20111004_echol@sina.com, ngfangduan@163.com

ABSTRACT: Shaft plays an important role in subway construction, some shafts will be retained and used as an important part of the permanent subway structure after the excavation. More knowledge about the deformation mechanism of shaft construction are needed, as it has a great influence on the safety of the subway construction. Based on a shaft construction of Changchun Metro1, this paper systematically analyzes the impact of various factors on the enclosure structure and its surrounding areas by examining a large number of monitoring data obtained in real-time during the shaft construction. The results show that the inverted side-wall method is appropriate for shaft construction under complex conditions, as this method of construction would provide a good control over the deformations of the shaft enclosure structure and the surrounding layers; The real time monitoring data show that the ground settlements during shaft construction are greatly influenced by local loads and construction traffic applied on the ground surface, e.g. the ground are adjacent to the shaft loaded with excavation muck piles settled significantly more than the other side that were not or less loaded. In addition rapid change of groundwater level during construction dewatering could also significantly impact the shaft structure and its surrounding environment, especially for the surrounding ground settlement. The result of this study could provide some useful information for the design and construction of similar engineering structures.

INTRODUCTION

Shaft construction is one of the important parts of the subway station excavation construction. Completing the Shaft Construction quickly and efficiently can not only

reduce the construction duration, but also can save the project cost. In order to improve the safety and economy of the shaft construction, we should optimize the design and construction process. On-site real time monitoring plays an important role in the subway design and construction. The shaft construction described in this paper is in soil-rock composite formation and it was constructed by inverted side-wall method in a narrow construction site. Through the real time on-site monitoring of the whole shaft construction process, the characteristics of the deformations of the shaft structure and its surrounding environment were analyzed and studied. The results of the analysis and study show that inverted side-wall method is a more appropriate method for shaft construction under complex conditions, as it could provide a good control over the deformation of the shaft enclosure structure and surrounding environment.

THE ENGINEERING SITUATION AND GEOTECHNICAL CONDITIONS

Engineering Situation

The study area is a station shaft of Changchun City Metro Line one. The shaft is 15.45 meters long, 7.1 meters wide and 28.126 meters deep, and it was constructed by inverted side-wall method. The so called inverted side-wall method of shaft construction is that it should build a reinforced concrete foundation beam on the ground first, then excavate and support layer by layer and every layer of support should be connected by the extended steel bars. The support constitutes by shotcrete, steel mesh and steel grating (Joist steel). Well-point dewatering method is used in the construction dewatering of this shaft, the arrangement plan of the dewatering well is shown in Figure2. When the shaft has been completed, break the ingate and begin the duct construction. A cross section profile of the shaft is shown in Figure 1.

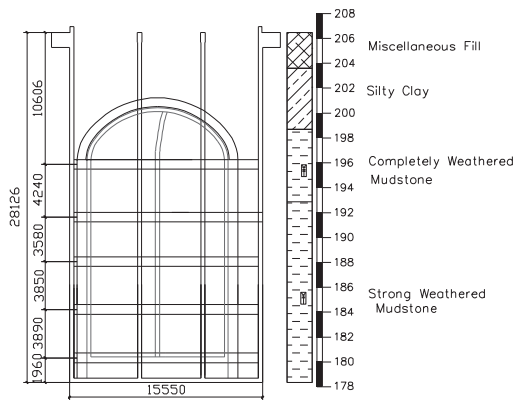


FIG. 1. Cross Section Profile of the Shaft

Geotechnical Conditions

According to site investigation results, the soil layer of the engineering site within the scope of investigation could be divided into Quaternary Holocene Artificial soil layer(Q4ml), Quaternary Pleistocene Alluvial clay(Q2al+pl) and cretaceous mudstone(K). According to the formation lithology and its physical and mechanical properties, it could be further divided into seven layers containing three groundwater tables in various subsoil layers and bedrock. Soil basic physical and mechanical parameters are shown in Table 1.

Table 1. Physical-Mechanics Parameter of Soils

| Number | Soil Layer | Thickness (m) | Gravity (KN/m ³) | Cohesion (KPa) | Internal Friction Angle (°) | Load Eigenvalue (Kpa) |
|--------|-------------------------------|---------------|------------------------------|----------------|-----------------------------|-----------------------|
| ① | Miscellaneous Fill | 2.9 | 18.5 | 8 | 10 | — |
| ② | Silty Clay | 4.9 | 19.9 | 34 | 14 | 140 |
| ③ | Completely Weathered Mudstone | 5.8 | 18.8 | 70 | 20 | 330 |
| ④ | Strong Weathered Mudstone | 15.0 | 19.2 | 80 | 20 | 500 |
| ⑤ | Medium Weathered Mudstone | 21.0 | 22.9 | 100 | 25 | 700 |

Monitoring Program

According to the design and construction requirements, the main monitoring project included monitoring of the surrounding ground surface and building subsidence, the supporting structure's vertical displacement, the shaft wall clearance convergence, lateral soil pressure monitoring, groundwater level. Considering the Changchun City frozen soil depth is 1.7 meters, the ground surface subsidence monitoring points were all buried to a depth of two meters. The arrangement plan of the monitoring points is shown in Figure2.

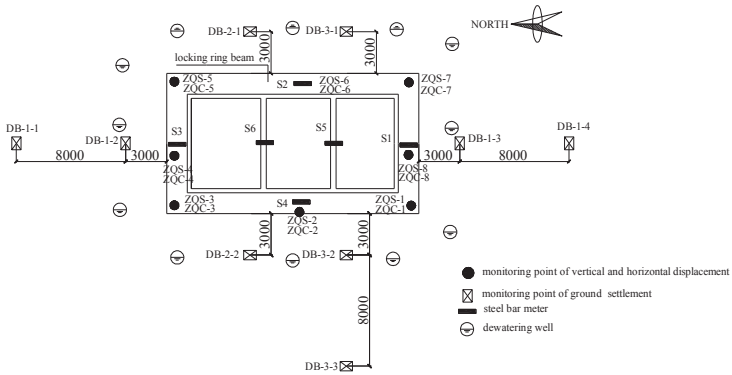


FIG. 2. Layout Plan of Monitoring Points

ANALYSIS OF MONITORING RESULTS

Analysis of the Observed Surrounding Ground Settlements

The layout of the ground settlement monitoring points is shown in Figure 2. The ground settlement control value is 30mm at the end of the construction. The maximum ground settlement is 9.98mm observed at DB-3-2. Taking a typical monitoring point, its duration curve is shown in Figure 3. Comparing the monitoring data and engineering experience in the past, it is seen that inverted side-wall method for shaft construction in this field area have a good effect on ground settlement control, primarily due to the soil-rock complex formation, where 7.8 meters below the ground surface is weathered mudstone with small compressibility. In addition, groundwater drawdown was not that effective during the construction, so that ground settlement due to loss of groundwater was relatively small.

Part of the cavern was excavated to the bottom by July 18th, and the back cover construction completed on July 26. From Figure 3 we can see that settlement data at each monitoring point become stabilized after July 18.

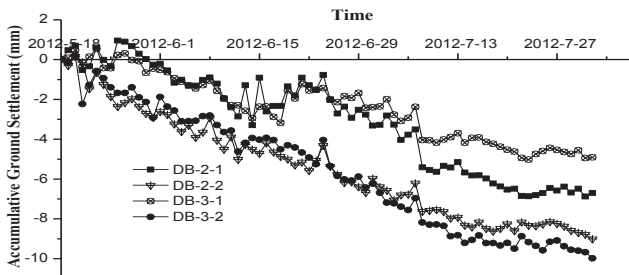


FIG. 3. Curves of ground settlement

From Figure 2 and 3, we can see that more settlement occurred on the west side of the shaft than the east side (i.e. settlement monitoring points DB-2-1, DB-3-1 vs. DB-2-2, DB-3-2). At the construction site there were excavation muck piles stored, at the west side of the shaft about 5 meters away from the borehole wall while other conditions were basically the same. Therefore, it is considered that the main reason for more settlement observed at the west side is the muck pile load around the shaft and dynamic loading of the long-term operation of the muck cars.

In the monitoring process, we found that in the evening of June 26th the deformation rate of monitoring points DB-1-1 to DB-1-4, DB-2-1, DB-3-1 were more than the warning value and reached to -2.52 mm/d ~-3.68 mm/d, the warning value is 1.7mm / d, the negative value indicates sinking and the positive value indicates rising. In the daytime of June 27th, the deformation rate of monitoring points DB-1-1 to DB-1-3, DB-2-1, DB-3-1 were more than the warning level and reached to 2.06 ~ 4.49mm/d. On that day most constructions conditions were as usual, but during the night of June 26th, the water pumps were all replaced on the north, south and east sides of the shaft except the west side, so the dewatering rate has been greatly enhanced on the north, south and east sides. This caused more settlements at points DB-1-1 to DB-1-4, DB-2-1, DB-3-1(Fig.2). In the daytime of June 27th, part of the new replaced water pumps stopped pumping for checking, which led to the ground water level rising and the ground at the nearby monitoring points also began to rise. The monitoring data are shown in Table 2. From the phenomenon we could know that strict attention must be paid for the dewatering scale and rate in foundation construction, the rapid change of dewatering scale and rate will have significant impacts on the ground settlement.

Table 2. Deformation Rate of ground settlement

| Deformation Rate (mm/d) | | | | |
|----------------------------|-------------------|---------------------|-------------------|---------------------|
| Number of Monitoring Point | June 26th Daytime | June 26th Nighttime | June 27th Daytime | June 27th Nighttime |
| DB-1-1 | -0.85 | -3.68 | 4.44 | -0.05 |
| DB-1-2 | -0.57 | -3.68 | 4.49 | -0.02 |
| DB-1-3 | -0.48 | -3.49 | 2.06 | 1.04 |
| DB-1-4 | -0.33 | -2.52 | 0.82 | 0.37 |
| DB-2-1 | -1.10 | -2.70 | 3.39 | 0.54 |
| DB-2-2 | 0.49 | 0.04 | -0.85 | -0.40 |
| DB-3-1 | -0.69 | -3.68 | 4.29 | 0.30 |
| DB-3-2 | -0.01 | 0.66 | -1.00 | -0.27 |

Analysis of the Observed Surrounding Buildings Settlements

There is a 6-storey shopping mall building about 27 m north of the shaft, two building monitoring points JCJ-1, JCJ-2 were installed at the building side close to the excavation pit. The maximum settlement of the mall building by the end of the construction is -1.35mm, it is far less than the building settlement control value 20mm. It indicates that inverted side-wall method for shaft construction in this area has little impact on the buildings that are 20 m away from the shaft. Building settlement duration curve is shown in Figure 4. As shown in the figure, during the middle of the shaft construction, the settlement of the building had big fluctuation, and a certain differential settlement existed. However, during the later stage of the construction, the fluctuation of the settlement reduced and the settlement of the two points became consistent. After the bottom sealing of the shaft was completely constructed on July 26th, the settlement of the building was basically level-off.

Analysis of the Vertical Displacement Monitoring of Supporting Structure

In the construction by inverted side-wall method, locking ring beam, the friction of the borehole wall and soil, grouting catheter, all of them bear the weight of the wall body. As the monitoring data shows, the total vertical displacement of the borehole wall is small. In the end of the construction, the minimum settlement is 9.47mm, the largest settlement is 11.24mm, and the vertical displacement of the borehole wall is relatively uniform. The above indicates that locking ring beam, the friction of the borehole wall and soil and grouting catheter could hang the borehole wall effectively and prevent it sinking seriously due to its own gravity and other external factors. In the monitoring process, it was found that timely steel grating installation and concrete injection could effectively reduce the settlement of the locking ring beam. The vertical displacement duration curve of the supporting structure is shown in Figure 5. From the figure we could see that the settlement of locking ring beam began to stabilize after the shaft has been excavated to bottom on July 18th.

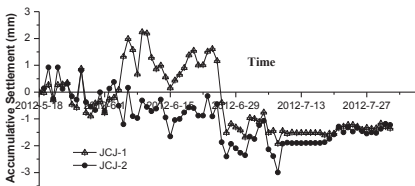


FIG. 4. Settlement curves of the building

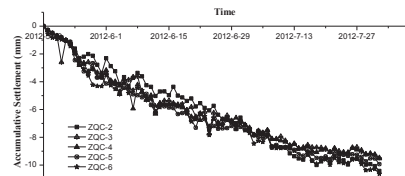


FIG. 5. Vertical displacement curves of the supporting structure

Analysis of Soil Pressure Monitoring

The soil pressure monitoring was completed by DY-110 single film soil pressure cell, it was installed between the soil and shaft wall, the max pressure range of the pressure cell is 0.4 MPa. According to the need of monitoring, two soil pressure cells numbered 642# and 632# had been installed in the middle of S2 side with depth of 8 meters and 15 meters, respectively. Another soil pressure cell numbered 599# had been installed in the middle of S4 side with depth of 8 meters. The monitoring data shows that during the shaft construction, the soil pressure between the supporting structure and the lateral soil is smaller. The maximum soil pressure of a soil pressure cell numbered 599# is 0.011Mpa.

Combining the stratigraphic condition and construction technology, the main reason is that the process of the shaft construction did not coordinate, lots of the formation stress was released before the supporting structure installed, namely, the soil basically stabilized before the steel grating installed and the concrete sprayed. Additionally, the following about 7meters of the formation is weathered mudstone, the strength and stability of this formation is much better. The soil pressure duration curve is shown in Figure 6.

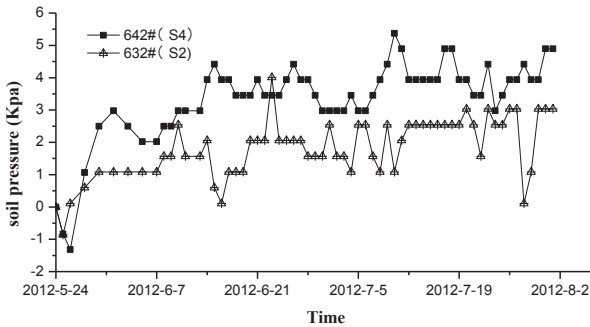


FIG. 6. Duration curves of soil pressure monitoring

CONCLUSIONS

Combining the working conditions and the monitoring data, the following conclusions can be drawn:

(1) During the shaft excavation, the surrounding stockpile of excavated soils and movement of muck vehicles will have significant influence on the shaft deformation, so sustained operation of heavy vehicles near the shaft should be avoided, and any temporary muck piles from the excavation should be placed at a safe distance from the shaft.

(2) From the abnormal change of ground settlement caused by replacement of water pumps, it is known that strict attention should be paid for the precipitation scale and rate in foundation construction, the rapid change of the precipitation scale

and rate will have significant impacts on the ground settlement.

(3) The shaft described in this paper is constructed by inverted side-wall method, its supporting system consist of steel grating, small grouting catheter and sprayed concrete. Based on the monitoring results, it is shown that the method of this shaft construction is a feasible method in this region, because of its quick construction, environment-friendly and higher structure security.

REFERENCES

- Aijun Yao, Xindong Zhang. (2011). "Influence of asymmetric lode on supporting deformation for deep foundation pit" J. Rock and Soil Mechanics, Vol. 32 (2): 378-382.
- Zhongwei Wang, Guobin Liu, etal. (2006). "Study on the deformation of a deep metro excavation under complex environment" J. Chinese Journal of Geotechnical Engineering, Vol. 28 (10):1263-1266.
- Jianxue Song, Yi Zheng, etal. (2006). "Deformation monitoring and alerting technology of foundation pits" J. Chinese Journal of Geotechnical Engineering , Vol. 28 Supp: 1889-1891.
- Xindong Zhang, Aijun Yao. (2011). "Monitoring and Numerical Simulation of Behaviour of Supporting Piles in a Deep Foundation Pit" J. Chinese Journal of Underground Space and Engineering, Vol. 7 (6): 1138-1141.
- Jian Jia, Xiaolin Xie. (2009). "Unloading Deformation Mechanism of Deep-large Excavation in Shanghai Clay Area" J. Journal of Shanghai Jiaotong University , Vol. 43 (6): 1005-1009.
- Xiaorong Jin, Jianlin Yu, etal. (2009). "Analysis of behaviors of settlement of pit's surrounding soils by dewatering" J. Rock and Soil Mechanics, Vol. 26 (10):1575-1580.

Effect analysis of soft rock slope reinforced by bolts under blasting dynamic load

Zou Xinkuan¹, Zhang Jichun², Shi Hongchao³, Wang Zhongda⁴

¹Doctoral candidate, Department of Geotechnical engineering, Southwest Jiaotong University; Chengdu, P. R. of china, 610031 E-mail: zou1017@163.com

²Professor, Department of Geotechnical engineering, Southwest Jiaotong University, Chengdu, P. R. of china, 610031 E-mail: Jczhang2004@163.com

³Doctoral candidate, Department of Geotechnical engineering, Southwest Jiaotong University, Chengdu, P. R. of china, 610031

⁴Qingdao Geotechnical Investigation & Surveying Research Institute, Qingdao, P. R. of china, 266033

ABSTRACT: This paper took the excavation of gravity type anchor ingot deep foundation of Nan-xi Yangtze River Bridge as the research object. A typical section of the northern slope was selected to make a 3-D numerical model. Through the equilibrium method and the numerical calculation software FLAC^{3D}, dynamic stability of the slope, before and after reinforced by bolts, was calculated and analyzed. Both the stress and displacement variations of the slope were compared, and the dynamic response characteristics of the slope and bolts were explored. The results show that both the maximum tensile stress and shear stress of the slope decreased, the dynamic disturbance degree of the slope inner layer mitigated observably, the latent sliding plane migrated toward the empty face and the dynamic stability safety factor increased when the slope is supported by bolts. However, as the head of the lowest bolt located in the fine sand layer and close to the explosive source, it will shake more intensively and cause partial mortar damaged and the reinforcement effect of bolts decreased.

Keywords: slope stability, blasting load, bolt, dynamic response

INTRODUCTION

Security of deep excavation slope is always attached great importance to the deep excavation engineering. Especially, as drilling and blasting method is used for excavating bedrock, frequent blasting operation would cause the rock mass in the slope surface gets more and more relaxed. The high slope stability would become more and more difficult to forecast. In order to avoid the deep excavation slope failed during the excavation process, fully bonded type bolts are widely used to reinforce the deep excavation slope (Larbi Siad 2001). Currently, the reinforcement effect of bolts on slope has been mainly studied by several quasi-static methods such as pull-out bond test(Eligehause R et al. 1993), analogy simulation test(Wei Si-jiang et al. 2012), numerical analysis method(Cao 2003). Compared to static load, dynamic load caused by blasting or earthquake is more complex (Zhang et al. 2006), and the interaction between bolts and rock mass is more intricate. Thus there is only a few researches about the reinforcement effect of bolts suffering dynamic load, and these researches are major focused on the separate response of slope and bolts(GISLE S 1998 and Dong 2008), and the stability of slope after reinforced by bolts is rarely involved.

In fact, the mainly contents of the reinforcement effect of bolts on deep excavation slope include the dynamic mechanical of rock and bolts and the stability variation of the slope. To figure out the reinforcement mechanism of bolts and the slope stability

variation after reinforced by bolts under blasting load, this thesis set up a finite difference computation model of the northern slope of the gravity anchorage excavation in the north bank of NanXi Yangtze River Bridge with FLAC^{3D} program. Through analyzing and contrasting the dynamic response characteristics of the slope and bolts, the reinforcement effect and mechanism of bolts on the slope under blasting load were discussed. And at last, gained the respective stability factors of the slope before and after reinforced by bolts based on the pseudo-static method.

THE EXCAVATION SLOPE NUMERICAL MODEL

Site and geology descriptions

This study took place during the construction of the gravity anchorage foundation of Nanxi Yangtze River Bridge, located at a hillside on the northern bank of Yangtze River in Sichuan province, China. Length of the foundation excavation is 60 m, and its width is 50 m. When the foundation's northern part excavated to the bottom a slope about 60 meters height formed, and the slope gradient is within 1:0.75~1:0.3. The upper layer of the slope combined with poor stability silt clay, fine sand and pebble soil, and its bedrock is sandy mudstone. The gradient of sandy mudstone distributed as single and incline shape, and its attitude is $145^\circ \angle 16^\circ$. After the sandy mudstone excavated, a layer rock dip slope would be created. The frame girder of reinforced concrete anchor bar is applied to reinforce the 1st and 2nd step slopes. The anchor bar is fully bonded type bolt with no pre-stress, and the bolts interval is $3\text{ m} \times 3\text{ m}$, obliquity angle is 20° . The bolts length, from top to bottom of the slope, are 30 m, 30 m, 25 m, 25 m, 18 m and 18 m, respectively, drilling diameter of boreholes is 110 millimeters, and mortar is grouted in these holes. Geotechnical properties of the intact rock are described in Table 1. Table 2 lists the mechanical parameters of bolts and mortar.

Table 1. Summary Results of Laboratory Testing: Geo-mechanical Properties

| Rock Type | Elasticity Modulus (MPa) | Poisson Ratio | Natural Bulk Density (kg/m^3) | Cohesive Force (kPa) | Internal Friction Angle ($^\circ$) |
|------------------------|--------------------------|---------------|---|----------------------|--------------------------------------|
| Land Pebble | 70 | 0.25 | 2.24 | 15 | 38 |
| Fine Sand | 10 | 0.24 | 1.84 | 11.5 | 36 |
| Intense Weathered Rock | 600 | 0.22 | 2.39 | 40 | 42 |
| Weekly Weathered Rock | 1000 | 0.20 | 2.51 | 80 | 45 |

Table 2. Mechanical Parameters of Bolt and Mortar

| Bolts | | | | Mortar | | |
|-------------------------|-----------------------|---------------|------------------------------------|-------------------------|---------------------|-------------------------------------|
| Elasticity modulus (Pa) | Tensile strength (Pa) | Diameter (mm) | Density (kg/m^3) | Shearing Stiffness (Pa) | Cohesion Force (Pa) | Internal Friction Angle($^\circ$) |
| 2×10^9 | 310×10^3 | 32 | 7850 | 2×10^7 | 8×10^4 | 25 |

Computational model

In this thesis numerical simulation is used to analyze the dynamic response of the deep excavation slope, when the 3rd rocky step slope in the center of the foundation's north part is excavated by blasting. The location of excavation ranges is comparatively large, and the relative impact of spatial effects can be ignored. Then establish a simplified 3-D numerical model with the same thickness of bolts horizontal spacing. The model calculation range is 92 m×65 m×3 m, and the bolts are installed at the 1/2 thickness of the model. During the simulation computation process, cable element is used to simulate the fully bonded type bolt. All the materials of slope rock, the interface materials of bolts-mortar and mortar-rock are assumed as elastic-plastic and characterized by Mohr-Coulomb strength criterion, and deformation of bolts is allowed until reach to its yield state. Specified the lateral and bottom boundary and the blasting excavation boundary as viscous boundary, and constrained the Y-direction displacement of bottom. Local damping, contain in FLAC^{3D}, is selected in the numerical model. According to calculation trials, the local damping coefficient is set to 0.157 at last. Fig.1 shows the slope dynamic analysis model sketch.

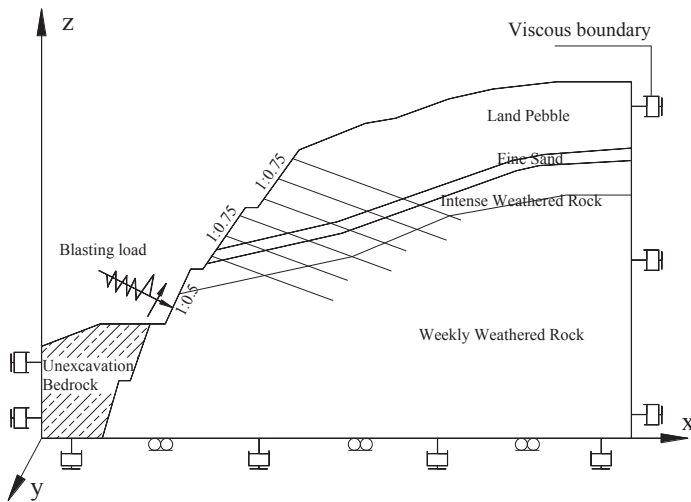


Fig. 1 The slope dynamic analysis model sketch.

Blasting load

How to determine the input dynamic load reasonably is the basis for slope dynamic stability analysis when blasting excavation is performed. Usually, blasting load is simplified as triangular impulsive load with a linear ascent stage and descent stage, according to the explosive charge and its distance between the load input location. However, the simplified blasting load is quite different from the engineering practice, and it could not realistically simulate vibration response, what was truly happening in

a rocky slope. To stop this from happening and get more reasonable results, a section of measured time-history curve of blasting vibration velocity, which is largest in a test near the excavation slope, was selected as the input blasting load waveform. Fig.3 is the measured vibration waveform, and the input blasting loads are shown as Eq. (1) and Eq. (2).

$$\sigma_n = 2(\rho c_p)v_n \quad (1)$$

$$\sigma_s = 2(\rho c_s)v_s \quad (2)$$

Where σ_n and σ_s are the input normal stress and tangential stress of particles, respectively. ρ is the density of rock mass. c_p and c_s are the longitudinal wave velocity and shear wave propagation velocity of rock, respectively. v_n and v_s are the measured particle tangential vibration velocity and normal vibration velocity, respectively, their values are showed in Fig.3. As shown in Fig.1, the range blasting loads acting on it is 3 meters from the slope toe.

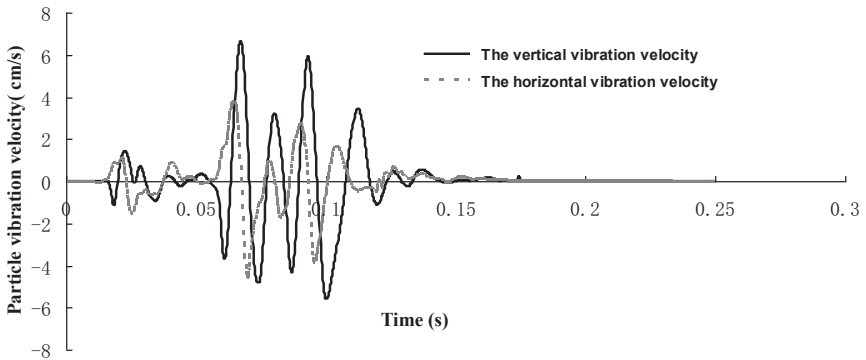


Fig. 2 The in-situ measured waveform of blasting vibration velocity.

RESULTS OF ANALYSES AND DISCUSSIONS

The slope stress analyses

After excavation blasting, the distribution of the maximum principal stress and the shear stress of the slope before and after reinforced by bolts are showed in Fig. 3 and Fig.4, respectively. Fig.3 shows that the tensile zone of the slope after reinforced is larger compared with the unreinforced slope. Before bolts embedded in the slope, tensile stress occurs in the berm of the 2nd and the 3rd grade slope, and the maximum value of tensile stress is 13.9 kPa. After the slope reinforced by bolts, the slope maximum tensile stress would reduce to 8.34 kPa. According to Fig.4 we can see obvious shear stress concentration appears at the 3rd grade slope toe. Generally speaking, excessive shear stress would cause partial failure, mechanical properties varied near the excavation face, and even the overall stability of the slope will be effected. Therefore, in order to decrease the concentration degree of shear stress and

ensure the slope's stability and safety, it's necessary to support the slope timely. After reinforced, the maximum shear stress of the 3rd grade slope toe is decreased, but not obviously. Stress state of the slope has been improved after reinforced by bolts, both tensile and shear stress of the slope layer are reduced, effectively prevent partial failure due to shear stress concentration.

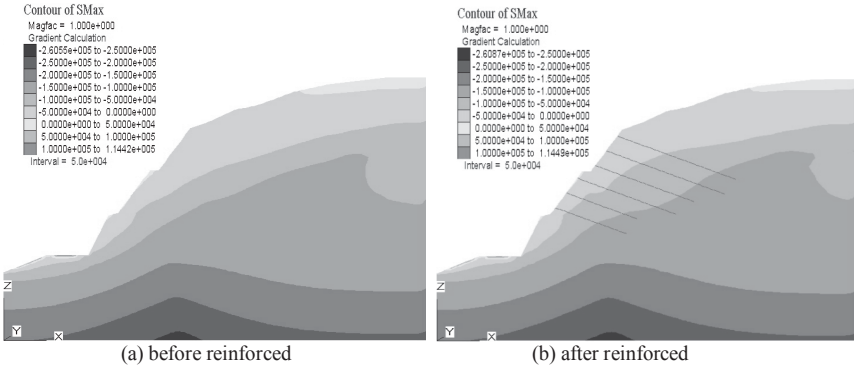


Fig. 3 The maximum principal stress distribution.

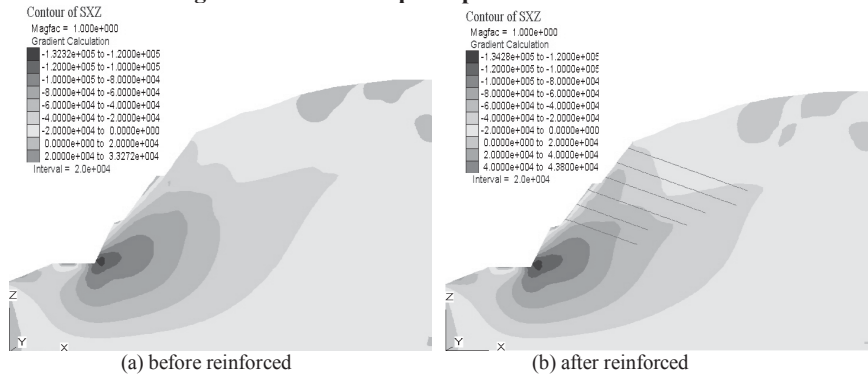


Fig. 4 The shear stress distribution.

The slope displacement analysis

Fig.5 is the slope horizontal displacement contours before and after excavated by blasting method. Whether the excavation slope reinforced or not, the empty face displacement distribution is basically no distinctive change. Under the blasting load, displacement is mainly appeared in the surface of the 3rd grade slope near the location where blasting load applied on. Before reinforced by bolts, the slope displacement values are less than 1 mm. There is permanent displacement towards the empty face direction appeared at the 2nd grade slope toe, due to it is near to the explosive source and weak fine sand distributed in, and its value is 0.17 mm. After the slope reinforced, the inside-body and surface displacement of the slope rock reduced and limited effectively.

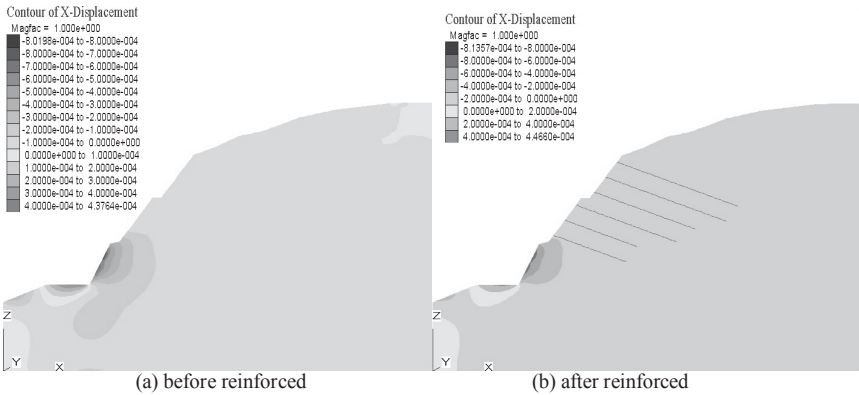


Fig. 5 The slope horizontal displacement contours.

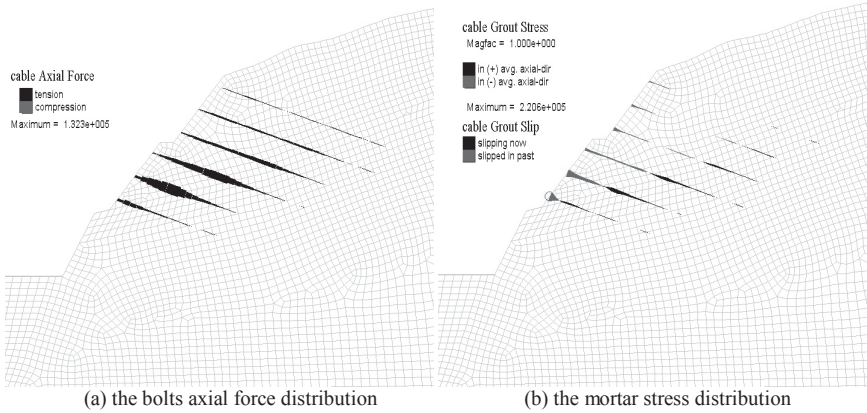


Fig. 6 The bolts axial force and the mortar stress distribution.

Bolt dynamic response analysis

Fig.6 shows the axial force distribution of the bolts and the mortar stress after blasting excavation. The axial force distribution of each bolt is like a date pit with only one peak point in the middle. From Fig. 6(a), the maximum peak value of all the bolts is 132.3 kN, and it is appears in the 5th row bolt. And it also can be found that the line, connecting the spots where the maximum value of each bolt located on, approximates to the potential slip surface of the slope after reinforced. Fig. 6(b) shows that after excavation blasting the maximum mortar stress appeared at the end of the 6th row bolt, where the mortar stress is up to 220.6 kPa and exceeds its yield stress, and bring about the mortar slipped on the bolt-end. This indicates that the shallow holes blasting excavation will not cause excessive axial force in bolts and make bolts invalid. However, because the 6th row bolt is nearest to the explosive source blasting load would get the bolt-head shake intensive, cause partial mortar damaged and decrease

the anchoring effect of bolts.

The bolt axial force and mortar shear stress time response of 130[#] element in the 6th row bolt, as shown in Fig.7, are selected to study and analyze. Under the blasting load, both bolt axial force and mortar stress increase, and their growth trends are almost consistently. The reinforcement effect of bolts could work effectively, owing to the interaction between bolts and mortar before the mortar yield.

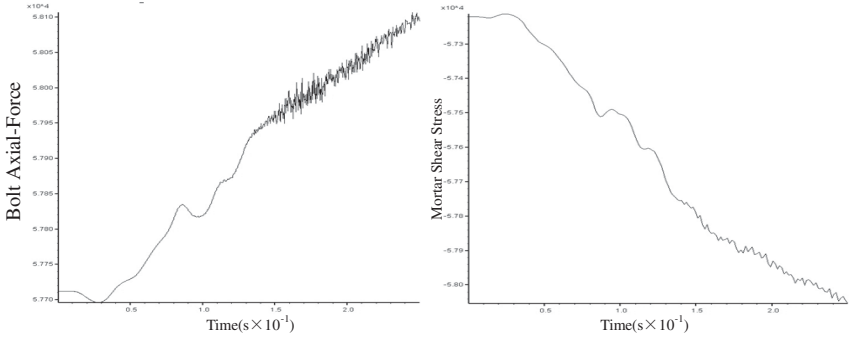


FIG. 7 The bolt axial force and mortar shear stress VS time curve of 130[#] element.

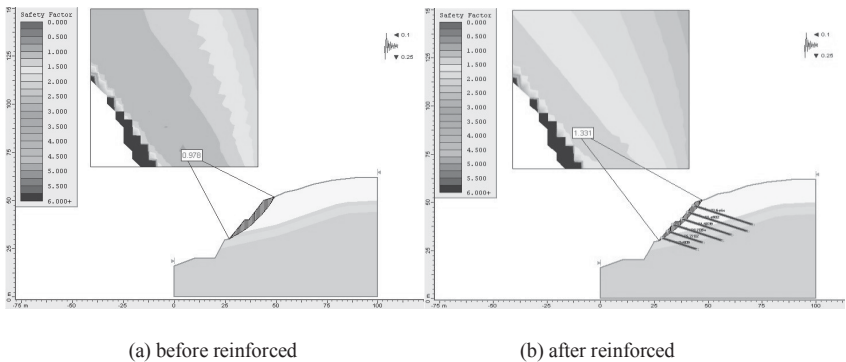


FIG. 8 The dangerous potential sliding surface of the slope.

SLOPE DYNAMIC STABILITY ANALYSIS

Using the Slide Code, a 2-D numerical simulation is carried out to calculate and analyze the stability factor of the slope before and after reinforced by bolts, based on the pseudo-static method. In this method, blasting load is replaced by equivalent static loads in horizontal direction and vertical direction, and evaluate the slope stability according to the slice method, which is on the basis of the limit equilibrium theory. The typical cross-section, which is same to the finite-difference model above, is selected as the calculation model. And the circle slice method was applied to search the potential slip surface automatically. Fig.8 shows the dangerous potential sliding

surface of the excavation slope before and after reinforced. Simulation calculation and analysis gain that the stability safety factor of the slope before and after reinforced by are 0.98 and 1.33 respectively, after reinforced the slope dynamic stability would be raised by 36.1%, the reinforcement effect of bolts is obvious.

CONCLUSION AND RECOMMENDATIONS

Compared with the unreinforced slope, both the maximum tensile stress and shear stress of the slope will decreased, the dynamic disturbance degree of the slope inner layer will mitigated observably, the displacement of the slope surface will controlled and the latent sliding plane will migrate toward to the empty face when the slope reinforced by bolts. Based on quasi-static method, calculation and analysis gained that stability safety factor of the slope before and after reinforced are 0.98 and 1.33 respectively, the bolts do have apparent reinforcement effect on the slope. However, great attention should be paid to the accumulative effect of the soft rock slope and the supporting structure caused by frequent excavation blasting.

Under blasting load, both bolt axial force and mortar stress are increasing, and their growth trends are almost consistently. After blasting, the axial force distribution of each bolt is like a date pit with only one peak point in the middle and the line used to connect the maximum axial force point of each bolts is close to the potential slip surface of the slope after reinforced. One thing to note is that the blasting load do have significant impact on the lowest bolt. Due to the bolt-head located in the fine sand layer and close to the explosive source , lead this part vibrate more vigorously and partial mortar yield and slip off the bolt.

REFERENCES

- Cai Fei and UGAI K.(2003). "Reinforcing mechanism of anchors in slopes: a numerical comparison of results of LEM and FEM." *Int J Numer Anal Meth Geomech.* Vol. 27(7) : 549-564.
- Larbi Siad.(2001). "Stability analysis of joint rock slopes reinforced by passive fully grouted bolts. " *Computers and Geotechnics.* Vol. 2001(28): 325-347.
- Wei Si-jiang and GOU Pan-feng.(2012). " Analogy simulation test on strengthening effect for pretention of bolts on anchorage body." *China Journal of Coal Science & Engineering.* Vol. 37(12) 1987-1993. (in Chinese)
- Zhang C-S, Zou D-H and M ADENGA V. (2006). "Numerical simulation of wave propagation in g routed rock bolts and the effects of mesh density and wave frequency." *International Journal of Rock Mechanics and Mining Sciences.* Vol. 43(4) : 634-639.
- Dong Jian-hua, ZHU Yan-peng.(2008)."Analysis of response of slope supported with framed anchor to earthquake." *Journal of Lanzhou University of Technolog.* Vol. 34 (2): 118-124. (in Chinese).
- Gisle S and Arne M.(1998)."The influence of blasting on grouted rock bolts." *Tunnelling and Underground Space Technology.*Vol. 13(1): 65-70.
- Ausilio E, Conte E and Dente G.(2000). "Seismic stability analysis of reinforced slopes." *Soil dynamics and Earthquake Engineering.*Vol. 19(13): 159-172.
- Zhang Ji-chun.(2001). "Vibration Characteristics of Blasting in Bed Rock Mass at

Sanxia Project." *Explosion and shock waves*. Vol. 21(2):131-137. (in Chinese).
Zheng Ying-ren, YE Hai-lin and HUANG Run-qiu.(2009) "Analysis and discussion of failure mechanism and fracture surface of slope under earthquake. "*Chinese Journal of Rock Mechanics and Engineering*. Vol. 28(8): 1714-1723. (in Chinese)

The Mechanism of Ground Subsidence Induced by EPB Tunneling in Sand and Cobble Stratum

Gao Mingzhong¹, Zhang Ru^{2*} and Wang Man³

¹State Key Laboratory of Hydraulics and Mountain River Engineering, College of Water Resource and Hydropower, Sichuan University, Chengdu, Sichuan, 610065 China; gaomingzhong@163.com

²State Key Laboratory of Hydraulics and Mountain River Engineering, College of Water Resource and Hydropower, Sichuan University, Chengdu, Sichuan, 610065 China; zhangru@scu.edu.cn

(Corresponding author)

³College of Water Resource and Hydropower, Sichuan University, Chengdu, Sichuan, 610065 China; 29473577@qq.com

ABSTRACT: Sand and cobble stratum in Chengdu Metro Line 1 present challenging tunneling ground conditions with high water levels, and high strength large diameter cobbles that result in excessive wear of tunnel boring machine cutters. In general, the stratum is self-supporting for extended periods of time making real-time monitoring for ground subsidence difficult to detect. In the process of tunneling the traffic along roadways over the tunnel bore had to be restricted because of ground subsidence or multiple ground collapses, which have serious implications on the surrounding environment. From some ground collapse cases, the excavation parameters and real time monitoring data were investigated to understand the ground subsidence mechanism. The research shows that: ① Under the condition where the stratum has high water levels, non-uniform densities and higher permeability coefficients, the sand and cobble soil is in a plastic state. ② Alone, the stratum cannot maintain earth pressure balance for EPB tunneling. ③ Additionally, once the stratum is disturbed by dynamic loads, the self-supporting nature of the ground degrades progressively. ④ Finally, the subsidence manifests at the surface as ground collapse. Our study further investigates the major factors of ground subsidence induced by EPB tunneling in such stratum. In order to prevent ground subsidence, some valid measures that were verified by previous projects were advised. The results are helpful for improving the understanding of the mechanism for ground subsidence, avoiding ground collapse and environmental impacts, and maintaining surface safety.

INTRODUCTION

Currently, tunnel boring machines (TBM) include a high degree of automatization to optimize the rate of tunneling, maintain safe operating conditions, reduce the costs

of labor, minimize ground settlement, reduce the impacts to the surrounding environment, create a uniform bore and precise grade, etc. The shield TBM construction method has many technical and economic advantages for constructing long, deep, tunnels in a dense urban area with complex geological stratum and high groundwater levels (Thuro, K. 1997; Hu 2006). Therefore, this tunneling method is regarded as quick and effective. It has been an indispensable tool in urban subway and tunnel construction. Shield TBMs have been used in China since the 1960s (Wang 2009). In 1966, the full face TBM (SJ34) with 3.4m diameter was assembled as part of a nation key research project (Zhang 2003.). This machine was successfully tested at the hydropower tunnel of Xi'er River hydroelectric station in Xiaguan, Yunnan Province within a granite-gneiss geology. The advance rate was satisfactory with an advance per month of up to 48.5m. Also in 1966, the grid TBM with a 10.2m diameter was jointly designed by Institute of Shanghai tunnel Designing and the Factory of Jiangnan Shipbuilding. In 2001, the National Ministry of Science and Technology put a priority on China's TBM manufacturing capabilities as part of the state key project plan. A research group was established and featured key members from the industrial, academic and private sector. These members included the China Railway Tunnel Group and Shanghai Tunnel Engineering Company. This program is the largest simulating experimental multifunction platform for TBMs in the world. Two TBM industrialization bases were built in Xinxiang and Shanghai (Huang 2006). In 2004, the first domestically built shield TBM for metro, named Xianxinhao, was manufactured by Shanghai Tunnel Engineering Company, who owns intellectual property rights.

After nearly 20 years of development, shield TBMs have proven to be effective in a variety of geological conditions, from hard rock to soft soil tunneling, and in constructing different bore geometries, from circular to rectangular (Zhao 2006). But the geological condition, in turn, has a large impact on the efficiency of a shield TBM (Gong 2005; Zhao 2007). Construction of tunnels in hard rock and soft strata using a TBM is quite common and has many advantages over the drill-and-blast or other tunneling methods (Xi 2005). However, when the work face is the sand and cobble stratum that was encountered for the Chengdu Metro Line 1, this mixed-face condition (i.e., the simultaneous occurrence of two or more types of ground each with sufficient area and significantly different penetration properties) makes a shield TBM less effective (Dong 2006). According to the ISO (International Standardization Organization) 14688-1, the definition for boulder, cobble and gravel are particle size between 200mm to 630mm, 63mm to 200mm and 2.0mm to 63mm, respectively.

The first phase of the Chengdu metro line 1 has an overall length of 15.15 km and includes 13 stations. In total, 11.92 km of the line is underground. The metro line 1 under Renmin Road runs from south to north of Chengdu city through the highly developed downtown, commercial center and with a myriad of existing underground infrastructure. The line passes several important transport hubs such as North Railway Station, Luoma Shi, City Sport Center, Tianfu Plaza, the Gymnasium, South Railway Station, Exposition Centre of Century City, etc. The ground along Chengdu metro line 1 is mainly Quaternary deposits. Generally, the ground water elevations are high, and there are many high-strength, large-diameter cobbles. Under such

conditions, tunneling using an Earth Pressure Balance (EPB) TBM is challenging in construction practice. In general, it has been demonstrated that use of an EPB TBM in such conditions can result in excessive wear to the cutterhead, jammed roller cutterhead, damage to the screw conveyor, subsidence and ground settlement at the surface, that cause project delays and/or impact budget. Moreover, subsidence and ground settlement have serious impacts to traffic and the surrounding environment. In order to research the main reasons and mechanism of ground subsidence induced by EPB tunneling in sand and cobble stratum, this study considers the field investigation and monitoring data collected from one section in Chengdu metro No. 1 line. Based on this study, corresponding preventive measures were put forward. The results are to be applied to future tunneling projects where such ground conditions will be encountered.

THE GEOLOGY FEATURES OF CHENGDU METRO LINE 1

The project is located in Chengdu plain. The topography of the area is relatively flat sloping southeast. The seismic peak ground acceleration in Chengdu city is 0.01g, the characteristic period of the seismic response spectrum is 0.40s, and the basic intensity is categorized as degree VIII according to the “seismic ground motion parameter zonation map of China” (GB 18306-2001). With the action of the Longmenshan fault and Longquanshan fault, the Chengdu NE rift-subsidence basin was formed, which constitutes the large and thick Quaternary-age fan deposits in western Longmenshan. The maximum thickness of sand and cobble deposited in Chengdu plain reaches 540m and the minimum is only 15~40m (Survey and mapping institute of chengdu 2005). In general, EPB-type TBM must overcome high water pressures.

Based on field explorations and the engineering geology, the first phase project of the Chengdu metro line 1 is in an area with Quaternary system unconsolidated sediments (Q_4). Most of the surface is covered with artificial fill (Q_4^{ml}) about 5m thick. The poorly graded, high strength cobbles of the covering layer (Holocene-age) are comprised of limestone, sandstone and quartzite (Fig. 1)(Chen 2009).



FIG. 1. The geological situation of Chengdu Metro Line 1

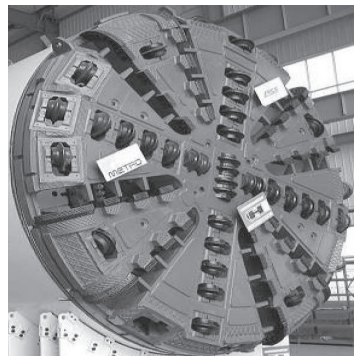


FIG. 2. The cutterhead layout

The main geology features of Chengdu metro line 1 are as follows:

- 1) High cobble content with cobbles being large diameter and high strength

According to the author's PhD thesis research in Chengdu metro line 1, the maximum cobble content reaches 76%, and ranges from between 10mm and 80mm in diameter. Based on laboratory testing, the maximum diameter is 512mm and the maximum strength of cobble is 200 MPa (Gao 2009.).

- 2) The stratum exhibits poor rippability resulting in serious wear to the cutterhead of the EPB TBM.

Due to the poor rippability, the muck always locks the cutterhead. Soon afterwards, the large cobbles settle to the bottom of the cutterhead chamber hindering muck removal. In the process of EPB tunneling, the muck is too viscous and cannot discharge beyond the cutterhead chamber. In an attempt to clear the muck, the thrust and torque of the EPB-type TBM is increased by the operator, resulting in excessive cutter and screw conveyor wear.

- 3) The stratum with high water content and less stability

The 13.5~25.8 m-thick water bearing stratum exhibits high permeability and EPB tunneling is difficult under such conditions. During tunneling, the ground can flow unless it is dewatered.

THE PARAMETER OF EPB

The cutterhead layout

This paper deals with the collapsing zone in order to study the mechanism of ground subsidence. The shield TBM used in one section of Chengdu metro line 1 has a 50t gross weight, 6280mm diameter, and was manufactured by Herrenknecht of Germany. The structure of the EPB TBM cutterhead is as shown in Fig. 2. There are eight holes for foam, water or bentonite slurry to jet in the face of cutterhead. The cutter head configuration consists of 4 center cutters (432mm or 17" double-edged roller cutter), 32 single-blade cutters, 28 shovel cutters, and 8 peripheral scraper cutters (expanding cutter) (Zhang 2009) .

The EPB TBM Operation

To a certain extent, the operation of the EPB TBM in the various stratum is a key factor for tunneling safely and efficiently. It is necessary to adjust EPB TBM operation to the local conditions to increase efficiency in the sand and cobble stratum. The abnormally fast rotation speed and increased torque of the cutterhead lead to excessive wear and damage of the EPB TBM. The operation of the EPB TBM must be adjusted in real time based on the geologic conditions encountered. For example, when the torque on the cutterhead fluctuates or increases suddenly and the advance rate is slow, the direction of cutterhead rotation should be changed to discharge the mud cake from the cutter head, enlarge the bore, and improve the advance rate (Guo 2009). Combining practice experience, it draws a reasonable conclusion about tunneling parameter of EPB:

- 1) The speed of cutterhead rotation should be less than 1.5 revolutions/min (1 rev/min normally).
- 2) The thrust of cutterhead should not be very much larger than 1800t (1500 t normally).

- 3) Penetration rate (PR) is the excavation distance of TBM per boring unit time. PR is generally expressed in meters per hour (m/h). PR is a parameter indicating the interaction between rock mass and TBM. It also indicates whether the selection of TBM in a project is suitable or not. The penetration rate should be greater than 20 mm/h.

CASE STUDY ABOUT GROUND SUBSIDENCE

Ground subsidence occurred in one section of Chengdu metro line 1 in January 2008 while tunneling ring No. 200 where the distance between the surface and the top of EPB TBM cutterhead is about 12.5m. The maximum diameter of subsidence area reaches 4.8m (Fig.3) . The center of the subsidence area is 3~5m behind the cutterhead. The surface traffic had to be halted completely and conventional EPB construction of the tunnel was no longer possible.



FIG. 3. The ground subsidence

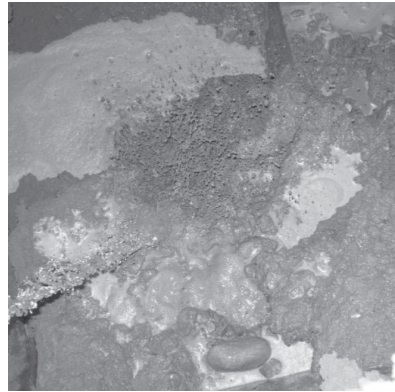


FIG. 4. The soil located in place of ground subsidence

Based on the field investigation, the geological situation is as shown in Fig.4. The soil is in a plastic state as a result of the high permeability coefficient, high water pressure, and the inconsistent density of the sand and cobble stratum. These conditions make it difficult to maintain ground stability and keep the pressure balance between the ground at the excavation face and the muck inside the cutterhead chamber. By theoretical calculation before tunneling, 1.8 bar pressure of slurry can maintain the pressure balance, but according to the real-time monitoring data, this flows into the ground when the pressure of the slurry is between 0.7~0.9 bar (Yang 2007). Therefore, the pressurization of the slurry cannot guarantee the pressure balance to maintain stability, resulting in the formation of voids or “chimneys” above the tunnel. Under the high water pressures and loading, these “chimneys” should be near their critical state. However, for sand and cobble stratum, which exhibit self-supporting behavior, these chimneys gradually progress upward until they manifest at the ground surface. Therefore, the time for recognizing ground subsidence is delayed much later than the passing of the EPB TBM. The settlement curve is as shown in Fig. 5 during normal tunneling (Tao 2009).

- 1) It has less impact on the ground longitudinal deformation ahead of the EPB

TBM while tunneling. The affected zone is about 6m, close to covering depth.

- 2) In the scope of tunneling influence, the longitudinal settlement is observed to be about 20mm and maximum 40mm in monitoring zone.
- 3) The settlement curve from the excavation face or “cut” to the shield tail presents a concave parabolic shape. The ground deformation in middle of shield is maximum and decreases gradually going to the sides.
- 4) The ground deformation in shield tail is relative large, but after 5 rings of tunneling from the shield tail, ground subsidence is clearly leveling off at about 5mm.

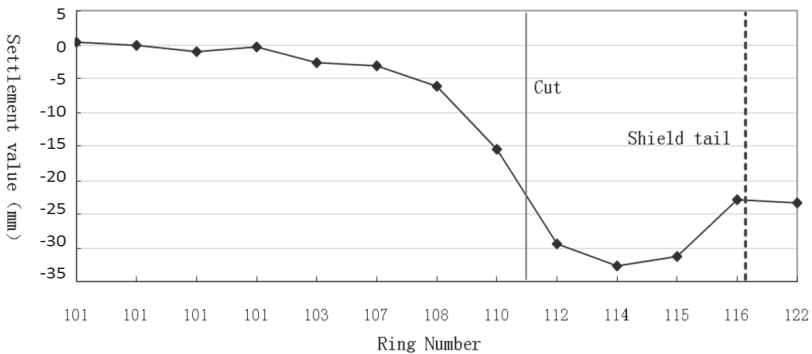


FIG. 5. The settlement curve

THE MECHANISM OF GROUND SUBSIDENCE

The overall design philosophy for EPB tunneling is to balance the pressures between the cutterhead chamber and the working face in order maintain ground stability. The rate of muck extraction compared to the advance rate is used to regulate the pressure balance. In the process of tunneling, the loose sand and cobble from chimneys will enter into the cuttinghead chamber due to gravity while the cutterhead is rotating and cutting. For the sand and cobble, it is nearly impossible to squeeze them to the outside of the cutterhead by simply increasing the pressure in the cuttinghead chamber, so some degree of overexcavation is unavoidable (Xu 2010).

In general, many believe ground subsidence induced by shield TBM tunneling is inevitable. The time response for the ground subsidence to occur is significantly different in different geologic conditions (Luo 2010). For the water-rich sandy cobble stratum in Chengdu that exhibits longer stand-up times, the monitoring data cannot report the real situation of ground loss because of the lag time of ground subsidence. According to the real time monitoring data in one section of Chengdu metro line 1, the lag time of ground subsidence varies from several days to several months (Luo 2010). Therefore, the engineer must deduce the deformation considering the real situation for such stratum. In general, the main reasons of ground subsidence that occurred during tunnel construction for the Chengdu metro line 1 are as follows.

- 1) The overexcavation always happens when the proper pressure balance between the cuttinghead chamber and the working face is not maintained.
- 2) The stratum is disturbed or collapses during changing cutter tools. Because of

the high quartz content in such stratum, the cutter wear is excessive. Much time and energy is required to change cutter tools.

- 3) When considering only monitoring results, these may mislead engineers to guide construction or decide the parameters of tunneling.
- 4) The rippability of soils is very poor.

CONCLUSIONS AND ADVISES

For shield tunneling, the affecting factors on buildings and environment come mainly from ground disturbance induced by EPB tunneling. Especially for the water-rich sandy cobble stratum of Chengdu, the ground subsidence occurred much later than what would be expected from tunneling within a single geological stratum. This lag time is due to the unique physical and mechanical properties that result in the short-term self-support of the sand and cobble stratum. Consequently, the monitoring data cannot report the real situation of the stratum. To mitigate the ground subsidence in these water-rich sandy cobble stratum, prevention and control measures are put forward based on local site experience. The research results are to be applied to a tunneling project with similar geologic conditions to avoid ground subsidence, and also provide some theoretical basis for deciding EPB operation methods.

- 1) The TBM should be suitable to geologic conditions. The type and parameters of TBM determine the advance rate completely. For Chengdu situation, the cobble should be discharged directly rather than broken. So a large diameter screw conveyor and large opening ratio of cutterhead are required. This would not only lead to less cutter wear but also help to avoid cutterhead jam.
- 2) It is very important to design the reasonable side cutter and the cutterhead with preventing vault collapse to avoid the ground subsidence.
- 3) Replacing cutting-tools with pressure of EPB shield in water-rich and pebbly sand stratum is safe and feasible.
- 4) Grouting can improve the mechanical properties of the stratum encountered under poor geologic conditions.
- 5) The grouting pressure and grouting volume should be strictly controlled based on optimum tunneling parameters of the test results.
- 6) The soil conditioning is essential to improve the soil liquidity through mixing into the bentonite, foam etc.

ACKNOWLEDGEMENTS

This work was financially supported by National Natural Science Foundation of China No. 51204112 and by National Basic Research Program of China (973 Program, 2011CB201201) .

REFERENCES

- Thuro, K. 1997. Geological influences in hard rock drill and blast tunnelling. *International Journal of Earth Sciences* 86 (2): 426-438.
- Hu Qian. Feasibility analysis of shield driving method used in interzone tunnel in Chengdu metro[D], Southwest Jiaotong University, Chengdu, 2006.
- Wang Shuhua. EPB TBM adaptable for sand and cobble stratum in chengdu city[J]. *Modern tunneling technology*, 2009, 46(1): 73-77.

- Zhang Zhaohuang. Full face TBM and the broken rock theory by its cutter[M]. *China railway publishing house*, Beijing,2003.
- Huang Xujiu. Discussion on ShieldMachine Development[J]. *Equipment Manufacturing Technology*, 2006, 34(2): 3-7.
- Zhao, J. 2006. The challenge of TBM excavation in rock. *Tunnels and Tunnelling International* 38 (9): 27-29.
- Gong, Q.M., Zhao, J. & Jiao, Y.Y. 2005. Numerical modeling of the effects of joint orientation on rock fragmentation by TBM cutters. *Tunnelling and Underground Space Technology* 20 (2): 183-191.
- Zhao, J., Gong, Q.M. & Eisensten, Z. 2007. Tunnelling through a frequently changing and mixed ground: A case history in Singapore. *Tunnelling and Underground Space Technology* 22 (4): 388-400.
- XI Zhongwei. Advance of Transport Tunnel Engineering and Construction Technique in China[J].*Journal of Beijing Polytechnic University*,2005,2031(2002):2035-2040.
- Dong, A., Ma, G., Gong, Q. etc. Numerical simulation on rock cutter performance in mixed ground. *Geotechnical Special Publication*, Shanghai, 2006.
- Survey and mapping institute of chengdu. *Geotechnical engineering investigation report [R]*. Chengdu, 2005.
- Tao Jianxun. Shield structural construction technical measures in the sand cobble layer in Chengdu[J]. *Shanxi Architecture*,2009, 2035 (2010): 2302-2303.
- Gao M.Z. TBM tunnelling mechanism in Chengdu cobblestone-soil ground and cobblestone-soil matrix deformation performance research[D]. SiChuan University, PhD thesis, 2009.
- Zhang Longguan, Chen Kui. Key technologies of earth pressure balance shield in Chengdu metro construction[J]. *Construction Mechanization*,2009, (2012): 2062-2065.
- Guo Jiaqing. Selection of shield cutterhead and tool for Chengdu sand-pebble layer[J]. *Construction Mechanization*,2009(2002): 2056-2058.
- Yang Shujiang. Slurry Shield Construction Technology for Launching Section of South Railway Station~ Provincial Stadium Running Tunnel of ChengduMetro[J]. *Tunnel Construction*,2007, 2027 (2006): 2043-2046.
- Xu Runze. A simple analysis of Shield Construction Sand and Gravel stratum in Chengdu[J]. *Technology Innovation Herald*,2010, (2013): 2086-2087.
- Luo S., Zhang H.R. Discussion on Prevention and Control ofDelayed Settlement Induced by Shield Tunneling inWater[J]. *Tunnel Construction*, 2010, 30 (03): 317-320.

Study on the Movement of Soil and Rock Mass Resulted from Underground Excavation of Horizontal Rectangle Section

Qiao Shi-Fan¹, Zhang Xi-Bao^{1,2}, SUN Xiao¹, LIU Bao-Chen¹

¹School of Civil Engineering, Central South University, Changsha 410075, China; qiaosf@csu.edu.cn

²The Urban Rail Transportation Engineering Company, China Railway No.5 Engineering Group CO., LTD Changsha 410000, China

ABSTRACT: Underground excavation will influence the safety of the geotechnical surroundings. Based on the stochastic medium theory, influence on the surrounding rock and soil by underground excavation is studied. Formula for predicting movement and deformation of rock and soil mass caused by excavation are deduced, and especially for those with horizontal rectangle section, semi-analytic solution for this problem is put forward. Furthermore, a computer program is developed to compute the movement and deformation of the rock and soil mass resulted from excavation. The theory is applied in an engineering example, which shows that the results of the research are reasonable and the developed solutions can be used for safety evaluation of underground excavations.

INTRODUCTION

Research on ground movements caused by underground excavation originates from underground mining. As an additive effect of engineering excavation, the research on mining subsidence has a long history and there are many theories to explain the reason of subsidence from mining, such as perpendicular line theory, arched theory and stochastic medium theory founded by Litwiniszyn^[1], which is used very popular to predict the movement of ground caused by mining in China.

The stochastic medium theory was introduced into China by Liu Baochen in 1962^[2] and has become one of the main methods to predict mining subsidence^[3-9]. However, because of the difficulties of mathematics, it is only used to solve the 1-D problem of ground movement prediction. In this article, using an advanced computer program, the 3-D problem of ground movement prediction caused by underground excavation is studied further.

THE STOCHASTIC MEDIUM THEORY

For the underground excavation problem, the subsidence basin of ground induced by excavation can be regarded as the effect caused by infinitesimal unit excavation. Therefore an excavation with an infinitesimal unit width, length and thickness

(1 × 1 × 1) is called the elementary excavation. The subsidence and horizontal displacement of any point in the elementary basin are called the elementary subsidence W_e and the elementary horizontal displacement U_e respectively^[3].

As shown in Fig.1, the displacement or deformation induced by the random shape excavation area Ω is

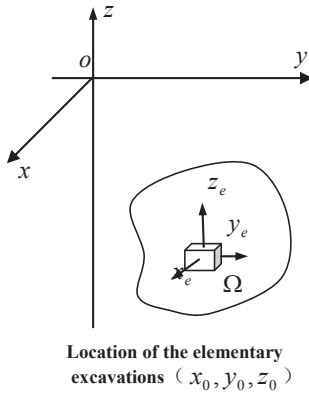


FIG. 1. Elementary excavation

$$F = \iiint_{\Omega} F_e dv \tag{1}$$

where F is the displacement or deformation induced by the whole excavation and F_e is the displacement or deformation correspondingly induced by the elementary excavation, which represents W_e and U_e .

The equations of vertical displacement and horizontal displacement induced by the elementary excavation are deduced^[2,3], which is

$$\begin{cases} W_e = \frac{1}{r_1(z)} \exp\left[-\pi \frac{x^2}{r_1^2(z)}\right] \cdot \frac{1}{r_2(z)} \exp\left[-\pi \frac{[y - \rho(z)]^2}{r_2^2(z)}\right] \\ U_{ex} = -\frac{x}{r_1(z)} \frac{dr_1(z)}{dz} \frac{1}{r_1(z)} \exp\left[-\pi \frac{x^2}{r_1^2(z)}\right] \cdot \frac{1}{r_2(z)} \exp\left[-\pi \frac{[y - \rho(z)]^2}{r_2^2(z)}\right] \\ U_{ey} = -\left\{ \frac{[y - \rho(z)]}{r_2(z)} \frac{dr_2(z)}{dz} + \frac{d\rho(z)}{dz} \right\} \frac{1}{r_1(z)} \exp\left[-\pi \frac{x^2}{r_1^2(z)}\right] \cdot \frac{1}{r_2(z)} \exp\left[-\pi \frac{[y - \rho(z)]^2}{r_2^2(z)}\right] \end{cases} \tag{2}$$

where H is the excavation depth, $r_1(z)$ and $r_2(z)$ are the main influence radius along the X and Y directions at the level z , which are

$$r_1(z) = \left(\frac{H}{H-z}\right)^{n-1} \frac{H}{\tan \beta_1}, \quad r_2(z) = \left(\frac{H}{H-z}\right)^{n-1} \frac{H}{\tan \beta_2} \tag{3}$$

$$b_1(z) = \left(\frac{H}{H-z}\right)^{n-1} b_1, \quad b_2(z) = \left(\frac{H}{H-z}\right)^{n-1} b_2 \tag{4}$$

where $\tan \beta_1$, $\tan \beta_2$, b_1 , b_2 , θ and n are the basic parameters of the rock mass movements, whose meaning are as follows:

$\tan \beta_1$ and $\tan \beta_2$, b_1 and b_2 are the tangent of the main influence angle and the horizontal displacement coefficient along the X and Y directions respectively; θ is transfer angle of the effects caused by excavation; n is the main influence range index.

THE MOVEMENT OF SOIL AND ROCK MASS RESULTED FROM UNDERGROUND EXCAVATION OF HORIZONTAL RECTANGEL SECTION

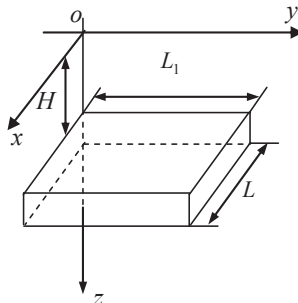


FIG. 2. Horizontal rectangle excavation with thin layer

As shown in Fig. 2, there is an underground excavation of thin layer with horizontal rectangle section, which has depth H , length L and width L_1 .

For this problem, the elementary excavation is horizontal which locates the point (x_0, y_0, z_0) , according to the stochastic medium theory, transfer angle θ becomes $\pi / 2$, $r_1(z) = r_2(z) = r(z)$ and $b_1 = b_2$. Therefore, Eq. (2) becomes

$$\left\{ \begin{array}{l} W_e = \frac{1}{r^2(z)} \exp\left[\frac{-\pi(x-x_0)^2}{r^2(z)}\right] \exp\left[\frac{-\pi[y-y_0]^2}{r^2(z)}\right] \\ U_{ex} = \frac{(x-x_0)}{r(z)} 2\pi b W_e \\ U_{ey} = \frac{(y-y_0)}{r(z)} 2\pi b W_e \end{array} \right. \tag{5}$$

From Eq.(1) and Eq.(5), the movement of soil and rock mass for 3-D problem is

$$\begin{cases} W(x, y, z) = \int_{s_1}^{s_2} \int_{q_1}^{q_2} \frac{1}{r^2(z)} \exp\left[\frac{-\pi(x-s)^2}{r^2(z)}\right] \frac{1}{r(z)} \exp\left[\frac{-\pi(y-q)^2}{r^2(z)}\right] dsdq \\ U(x, y, z) = \int_{s_1}^{s_2} \int_{q_1}^{q_2} \frac{2\pi b_1}{r^2(z)} (x-s) \exp\left[\frac{-\pi(x-s)^2}{r_1^2(z)}\right] \exp\left[\frac{-\pi(y-q)^2}{r_2^2(z)}\right] dsdq \end{cases} \quad (6)$$

Generally because the variable s and q are correlative, the doubly integrating in Eq. (6) has mathematical difficulties, which is the reason why the stochastic medium theory is often used to solve 1-D problem of ground movement prediction before. However, if the variable s and q are unrelated, the doubly integrating in Eq.(6) can be solved according to the method of variables separation.

For underground excavation of thin layer with horizontal rectangle section shown in Fig. 2, the two integral directions are unrelated, so according to Eq.(1) and Eq.(5), the movement of soil and rock mass is^[4]

$$\begin{cases} W(x, y, z) = \frac{1}{r^2(z)} \int_0^L \exp\left[\frac{-\pi(x-s)^2}{r^2(z)}\right] ds \int_0^{L_1} \exp\left[\frac{-\pi(y-q)^2}{r^2(z)}\right] dq \\ U(x, y, z) = \frac{2\pi b}{r^2(z)} \int_0^L (x-s) \exp\left[\frac{-\pi(x-s)^2}{r^2(z)}\right] ds \int_0^{L_1} \exp\left[\frac{-\pi(y-q)^2}{r^2(z)}\right] dq \end{cases} \quad (7)$$

For geotechnical safety assessment problem, the deformation of soil and rock mass is more important than its movement. From Eq. (7), the deformation of soil and rock mass is

$$\begin{cases} T_x(x, y, z) = \frac{\partial W(x, y, z)}{\partial x} \\ E_x(x, y, z) = \frac{\partial U(x, y, z)}{\partial x} \end{cases} \quad (8)$$

where T_x is the ground inclination along axis x and E_x is the ground horizontal deformation along axis x .

In the above equations, β and b can be obtained by spot measurement data. Since the above formulas cannot be directly integrated, numerical integration must be used. Procedure SurMov developed by the authors have been carried out to compute ground movement and deformation successfully, in which the functions including all the formulas in the article are defined. it is convenient to plot lines on some section in an area with the relevant functions.

For underground excavation of thick layer with horizontal rectangle section, it can be regarded as excavations of many thin layers. For every layer excavation, Eq.(7)

and Eq.(8) can be used to compute ground movement or deformation. Then according to the superposition principle, the movement and deformation of soil and rock mass induced from the whole thick rectangle excavation can be obtained.

ENGINEERING EXAMPLE

An example is shown as follows to explain the successful use of the stochastic medium theory in mining engineering.

In Fig.3, the depth M of coal seam is 2.0~2.3m. The top boundary of mining area is 109m far from ground surface. In order to study the rules of ground movement, the survey net is built, shown as Fig.3 .

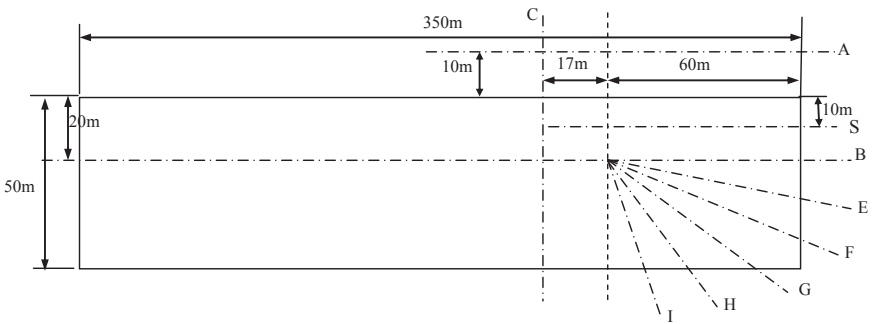


FIG. 3. The survey net of the working face 1213 in some coal mine

According to the survey data, the basic parameters of ground movement are as below

$$W_{max} = 1442 \text{ mm}, \tan \beta = 1.3, b = 0.33, h = 109 \text{ m}$$

The prediction of ground deformations induced by mining on the working is shown in Fig.4~Fig.5.

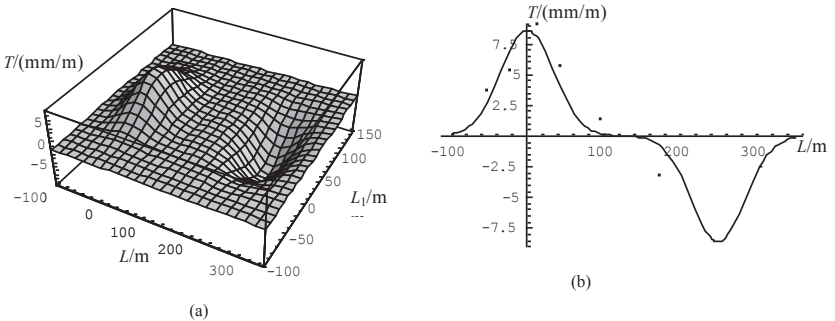


FIG. 4. Ground inclination

Prediction of the ground inclination along the strike direction is shown in Fig.4. In Fig.4, (a) is three-dimensional figure and (b) is the changing of inclination along the Survey Line B, whose dots are survey data. From Fig.4, the inclination at the mining boundary is great, which inclines to the middle of mining area. The maximum of inclination is ± 8 mm/m and the inclination at the middle of mining area is zero, which shows that the mining is sufficient mining along the strike direction.

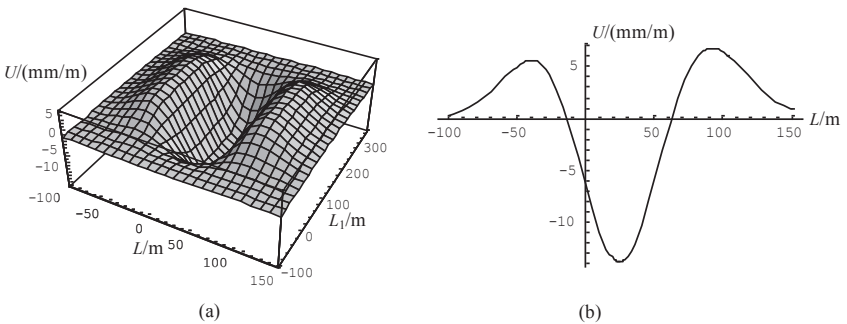


FIG. 5. Ground horizontal deformation

Prediction of the ground horizontal deformation along strike direction is shown in Fig.5. In Fig.5, (a) is three-dimensional figure and (b) is the changing of horizontal deformation along the Survey Line B. From Fig.5, the maximum of horizontal drawing deformation outside mining area is 5mm/m and the minimum of horizontal compression deformation above the mining area is 14 mm/m.

CONCLUSION

1) Theoretical basis of the stochastic medium theory is introduced. Formula for predicting soil and rock mass movements induced by rectangle shape excavation are proposed. For rectangle shape excavation, because the two integral directions are unrelated, the mathematical difficulties to get the explicit formulation of ground movement are solved, which can be used to compute 3-D problems of ground movement.

2) A computer program is developed to compute the movement and deformation of the ground and rock mass, in which the functions include all the formulas defined in the article. In the process of computing, it is convenient to plot lines on some section in an area with the relevant functions

3) From the results of an engineering example, the method of predicting the ground movement based on stochastic media theory is very reasonable and acceptable results are obtained.

ACKNOWLEDGEMENT

This work is sponsored by National Basic Research Program of China (973

Program, No.: 2011CB710601), -Research Project of the Traffic Bureaus of Huan Province (No.: 200810) and China Scholarship Council and National Science Foundation of China (No.: 50708116)

REFERENCES:

- Litwiniszyn J (1957). "The theories and model research of movements of ground masses." *In Proc. Eur. Congr. Ground Movement*, Leeds, UK:203-209
- Liu Bao-chen (1962). "Motion of rock masses due to advancing exploitation butt in the light of the theory of Stochastic media. " *Bull. Pol. Acad. Sci.* Vol. X. No.4, 1962
- Liu Baochen, Zhang Jiasheng, Liao guo hua (2004). "Application of the stochastic medium in mining". *Hunan science and technology publisher*, Changsha. (in Chinese)
- Qiao Shifan, Fang Ligang, Liu Baochen (2006). "Prediction of Ground Displacement and Deformation Induced by Large Diameter Piles." In: *Robert L. Parsons, Limin Zhang, et al, eds. Foundation Analysis And Design Innovative Methods*. New York: ASCE: 293-299
- Shifan Qiao, Baochen Liu (2006). "Prediction of Ground Displacement and Deformation Induced by Dewatering." In *Hehua Zhu, Feng Zhang, et al, eds. Underground Construction and Ground Movement*. New York: ASCE:73-79
- QIAO Shifan (2006). "Study on the Deformation Failure Criterion of Stochastic Medium and Its Applications." *Ph.D. Thesis*. Changsha: Central South University. (in Chinese)
- QIAO Shi-fan, LIU Bao-chen (2010). "Deformation Failure Criterion of Stochastic Medium." *Chinese Journal of Geotechnical Engineering*. Vol. 32(2):165-171. (in Chinese)
- GU O Qi-lin, QIAO Shi-fan, LIU Bao-chen (2011). "The Movement and Deformation of Soil and Rock Mass Resulted from Mining Activity." *Journal of Mining & Safety Engineering*, Vol. 28(1):109-114. (in Chinese)
- GUO Qi-Lin, QIAO Shi-Fan, WANG Lu (2012). "Deformation Calculation in Soil and Rock Mass of Slope in Open-pit Mining and Its Safety Evaluation." *Journal of Mining & Safety Engineering*, Vol. 29(5):679-684. (in Chinese)

Discussion on superposition empirical formula of ultimate bearing capacity based on the upper bound limit analysis theory

ZHAO Lianheng¹, YANG Feng^{2#}, HUANG Fu³, LEN Wuming⁴

¹Lecturer, School of Civil Engineering and Mobile Post-doctoral Stations of Traffic and Transportation Engineering, Central South University, Changsha P.R. China 410075, E-mail: zlh8076@163.com

²Lecturer, School of Civil Engineering and Mobile Post-doctoral Stations of Traffic and Transportation Engineering, Central South University, Changsha P.R. China 410075, E-mail: yf5754@126.com

³Lecturer, School of Civil Engineering and Architecture, Changsha University of Science and Technology, Changsha 410004, China, E-mail: hfnzdx2002@yahoo.com.cn

⁴Professor, School of Civil Engineering, Central South University, Changsha P.R. China 410075, E-mail: lwm123456@126.com

ABSTRACT: Traditional Terzaghi foundation bearing capacity superposition empirical formula dose not consider the nonlinear effect of the soil unit weight on the ultimate bearing capacity and its failure mode, which is only a kind of approximate method. Therefore, error occurs when unit weight is taken into account. The relatively complete two dimensional conversion velocity field based on slip-line field and the basic method and principle of corresponding failure mechanism were introduced in this paper. Compared with the existing upper bound failure mechanism, this failure mechanism adds a one-dimensional optimization freedom degree, which can reflect the real failure mode, and thus obtain better upper bound solutions. The results indicate that the traditional superposition empirical formula stress on safty, and the error caused by traditional superposition method will increase with the increase of the internal friction angle; the failure range derived from non-superposition method is between the failure range determined by using superposition method to solve the analysis coefficient N_γ and N_c (or N_q), which reflects the influence of soil unit weight on the failure mechanism.

INTRODUCTION

Ultimate bearing capacity of shallow foundation is one of the three classic problems of soil mechanics. In engineering, Terzaghi's (1943) foundation bearing capacity expression is generally used:

$$P_u = 1/2 \cdot B \gamma N_\gamma + c N_c + q N_q \quad (1)$$

N_c 、 N_q and N_γ represent the influence coefficients of soil cohesion c , overload q and soil unit weight γ . In the calculation, making $c = 0$, $q = 0$, the soil unit weight coefficient N_γ is obtained. Moreover, making $\gamma = 0$, $q = 0$, and $c = 0$, $\gamma = 0$, the cohesion coefficient N_c and the overload coefficient N_q can also be obtained.

The theory of slip line field was applied to study the effects of gravity on the bearing capacity of the soil (Sokolovskii 1965). The research shows in the case of $\gamma > 0$, although its stress slip line equation is same with the zero gravity slip line equation, the correlations of these two stress slip lines is different. Therefore, the solution of the ultimate bearing capacity cannot be expressed by Eq. (1), which means capacity coefficient N_c 、 N_q 、 N_γ cannot be separated.

The major reason of its adoption is that: because the application of the traditional limit equilibrium theory encounters the difficulty of mathematics solving. Therefore the effect of different soil parameters on the foundation bearing capacity was computed respectively, and then the ultimate bearing capacity of shallow foundation was analyzed by using the superposition principle. The effect of soil unit weight on the plastic bearing capacity of foundation still needs to be evaluated by establishing a limit equilibrium differential equation and implement numerical integration. Thus, for the general bearing capacity of weightness c - ϕ type soil, the stepwise solving way is employed. The process is as following: firstly, assuming the soil is a weightless c - ϕ type material, and using the closed form solution (the slip line field theory, Prandtl 1920; the limit equilibrium theory, the limit upper bound theory, Reissner 1924; Terzaghi 1943; Meyerhof 1951) to get the first part of the bearing capacity $cN_c + qN_q$. And then assuming that the soil as within weightness ϕ type material, and using the incomplete stress solution form (partial stress slip line field solution, Cox 1962; Lundgren 1953; Hansen 1969; half diagram solution, Ohde 1938; diagram solution, De Jong 1957; numerical integration solution, Sokolovskii 1965) to get the second part of the bearing capacity $1/2B\gamma N_\gamma$ with empirical or semi-empirical method.

In these solutions: the first part bearing capacity $cN_c + qN_q$ has already got the exact solutions; while the second part bearing capacity of bearing coefficient N_γ related to the unit weight has been still studied. It was Martin (2005) who used high density of slip line grid, based on the slip-line field theory, and firstly got the real answers of the N_γ within the weightness ϕ type soil materials. However, since the soil property of plastic zone for weight soil in actual failure mode is nonlinear, the applicability to use the foundation bearing capacity superposition method in weightness c - ϕ type soil still requires to be further discussed.

For the limitations of the superposition method for bearing capacity of foundation, while avoiding the complexity of construction stress field in differential equations and different schemes in the slip line field theory, Chen (1975), Soubra (1997,1999), Michalowski (1997), Donald and Chen (1995,1997,2002), Zhu (2000) are discussed the issue by using upper bound theorem of limit analysis. When constructing collapse mechanism, these studies, are all based on the slip-line field in one-dimension simplified condition. Although it is possible to get the closer results, there is still some distance from the real answer, especially the soil bulk density are taken into account, this situation is even more pronounced. Based on the failure

mechanism established by Donald and Chen (1995,1997), Wang (2001) studied this issue. Due to the limitations of the failure mechanism, their results are still not precise enough.

Based on two reasons, this paper constructs a complete velocity field based on the slip-line field to analyze the problem and enrich the field of limit analysis upper bound analysis of content. The velocity field actually transforms from the slip line method under the two dimensional condition. Compared with the existing upper bound failure mechanism, it adds one-dimensional optimization degree of freedom which reflects the failure mode is better. Therefore, this mechanism can obtain the better upper bound solution. On that basis, this paper further discusses the applicability to use the superposition method in calculating the foundation bearing capacity.

THE EFFECT OF SOIL WEIGHT ON THE SLIP-LINE NETWORK

The complete slip line velocity field for weightless soil includes three parts: two uniform stress velocity fields and a simple stress velocity field corresponding to two uniform stress field and a simple stress field, i.e. the uniform velocity field area I, III and the simple velocity field area II as shown in Fig. 1(a).

According to the definition of the slip line stress field and velocity field and one of its basic properties: for the weightness $c-\varphi$ type geomaterial, the existence of the cohesion does not affect the shape and angle of these two slip lines, the weight does not affect the angle between these two slip lines, but it affects the shape of slip lines. When considering the unit weight of the geomaterial, the slip line field shape will change correspondingly, as shown in Fig. 1 (b) and 2 (b). Comparing Fig.1 with Fig.2, it can be found that the wedge located in the basement is curve shape for weightness soil, and is no longer the straight wedge shape under the condition of weightless soil. The connected curve CD in the radiation shear area is also no longer an angle φ logarithmic spiral line. In fact, according to the research of Chen (1975), when $\varphi \neq 0$, the partial area of the connected curve CD is between an spiral line of angle φ and circular arc; and when $\varphi=0$, the connected curve CD is arc shape.

Therefore, both the currently used combination failure mechanism of line and logarithmic spiral constructed by Chen (1975) (Fig. 3(a)), or the multi-wedge failure mechanism failure mechanisms constructed by Soubra (1997, 1999), Michalowski (1997), Donald and Chen (1995, 1997, 2002), Zhu (2000), Wang (2001) (Fig. 4(a,b)) cannot truly reflect the actual failure mode of the foundation, especially for the simulation of the curve wedge below the basement. So that it cannot achieve a precise solution of the weightness-soil foundation bearing capacity by using the upper bound velocity field constructed based on the weightless-soil foundation slip line field (Fig. 3 and Fig. 4).

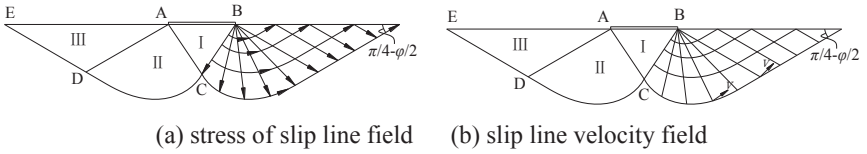


FIG. 1 Weightless $c-\phi$ soil stress of slip line field

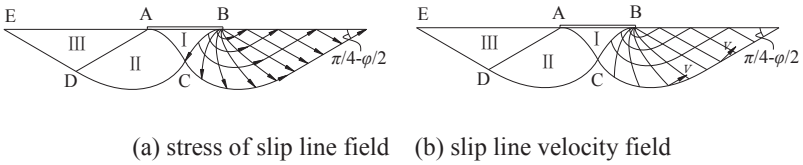


FIG. 2 Weightness $c-\phi$ soil stress of slip line field

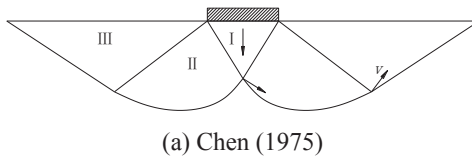


FIG.3 Prandtl failure mechanism for rough foundation (Mechanism 1)

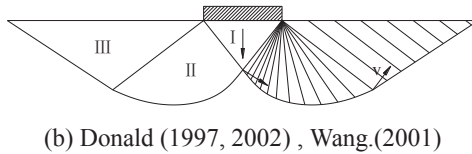
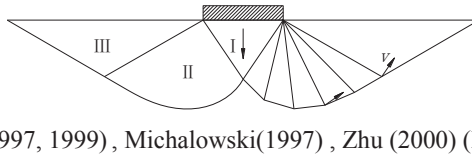


FIG.4 Multi-wedge failure mechanism for rough foundation

CONSTRUCTION OF THE UPPER BOUND VELOCITY MECHANISM BASED ON THE SLIP LINE FIELD

According to the basic properties of the weight-soil slip line, this paper simulates the slip-line net with piecewise line (i.e. velocity broken line) at the slip-line intersection when constructing the upper bound velocity field based on the weightness-soil slip line field, and forming a series of rigid block in the radial direction, which is shown in Fig. 5.

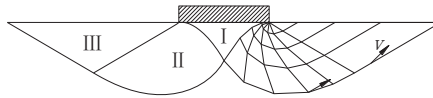
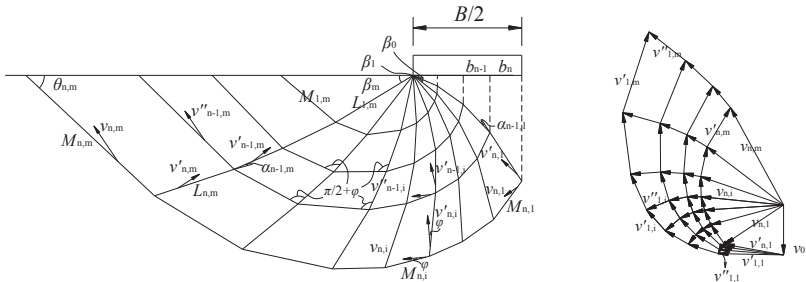


FIG.5 The two dimensional velocity field construction based on the slip-line method for rough foundation

Comparing Fig.3 and Fig.4 with Fig.5, it can be found that the grid-type velocity broken line based on the weightness-soil slip line net, on the one hand, the grid-type failure mechanism makes the construction of the velocity field become relatively perfect so that the velocity field can change in the radial direction; on the other hand, the failure modes and failure ranges of area I, II and III more approximate to the real failure state under the limit condition, and then obtains better solution of the weighness-soil foundation bearing capacity.

The two dimensional failure mechanism and corresponding velocity field based on the slip-line method for rough foundation is shown in Fig. 6. The detailed calculation and comparative analysis process can be found in Zhao (2009), Yang. (2009), Zhao et al (2010) and Zhao and Yang (2013) in detail.



(a) failure mechanism

(b) the velocity field

FIG.6 The two-dimensional transformation collapse mechanism and its corresponding closing velocity field (Mechanism 3)

DISCUSSION ON SUPERPOSITION METHOD OF BEARING CAPACITY EMPIRICAL FORMULA FOR ROUGH FOUNDATION

All traditional limit bearing capacity formulas (Terzaghi 1943; Hansen 1968; Vesic 1970; Meyerhof 1963; Muhs 1971) use the superposition empirical formulas. Since the superposition does not consider the nonlinear effect of the unit weight on the ultimate bearing capacity of the foundation and its failure mode, the superposition is only an approximate method. For the plane strain problems concerned in this paper, the corresponding failure mode and range are the same when solving N_c and N_q , so the superposition method is accurate. However, the failure

mode and range corresponding to N_γ is obviously less than that of N_c and N_q ; In fact, for the $c-\phi$ type weightness soil, it should use the same failure mechanism to determine N_c , N_q and N_γ . It is inevitable to cause certain errors if using simplified superposition method. Table 1 gives the values of ultimate bearing capacity derived from the three failure mechanisms described in this paper with the parameters $B=4\text{m}$, $\gamma=20\text{kN/m}^3$, $c=30\text{kPa}$, $q=25\text{kPa}$, and ϕ varying from 0° to 40° . This table also lists the relative error of the ultimate bearing capacity of the foundation between the superposition method and non-superposition method.

Table.1 Comparison of ultimate bearing capacity values for rough footing with superposition method and non-superposition method

| Calculation methods | Superposition method | | | | Non-superposition method | Relative error (%) | |
|---------------------|----------------------|---------|------------|---|--------------------------|---------------------------------------|---------|
| | N_c | N_q | N_γ | $P_u = cN_c + qN_q + 1/2B\gamma N_\gamma$ | P'_u | $\frac{P'_u - P_u}{P_u} \times 100\%$ | |
| $\phi = 0^\circ$ | Martin (2005) | 5.1416 | 1.0000 | 0.0000 | 179.248 | -- | -- |
| | Wang (2001) | -- | -- | -- | -- | -- | -- |
| | Mechanism 1 | 5.1416 | 1.0000 | 0.0000 | 179.248 | 179.260 | 0.0067 |
| | Mechanism 2 | 5.1436 | 1.0000 | 0.0000 | 179.308 | 179.334 | 0.0145 |
| | Mechanism 3 | 5.1426 | 1.0000 | 0.0000 | 179.278 | 179.288 | 0.0057 |
| $\phi = 10^\circ$ | Martin (2005) | 8.3449 | 2.4714 | 0.4332 | 329.460 | -- | -- |
| | Wang (2001) | 8.6400 | 2.6300 | 1.6700 | 391.750 | 438.100 | 11.8315 |
| | Mechanism 1 | 8.3449 | 2.4714 | 1.1645 | 358.712 | 366.640 | 2.2101 |
| | Mechanism 2 | 8.3498 | 2.4729 | 0.7070 | 340.597 | 364.438 | 7.0000 |
| | Mechanism 3 | 8.3481 | 2.4728 | 0.4675 | 330.963 | 362.723 | 9.5962 |
| $\phi = 20^\circ$ | Martin (2005) | 14.8347 | 6.3994 | 2.8389 | 718.582 | -- | -- |
| | Wang (2001) | 15.0000 | 6.4700 | 6.5600 | 874.150 | 949.550 | 8.6255 |
| | Mechanism 1 | 14.8347 | 6.3994 | 5.8711 | 839.870 | 861.420 | 2.5659 |
| | Mechanism 2 | 14.8428 | 6.4244 | 4.4776 | 784.998 | 844.435 | 7.5717 |
| | Mechanism 3 | 14.8410 | 6.4184 | 2.9158 | 722.322 | 832.376 | 15.2361 |
| $\phi = 30^\circ$ | Martin (2005) | 30.1396 | 18.401 | 14.754 | 1954.373 | -- | -- |
| | Wang (2001) | 30.2000 | 18.5000 | 24.2100 | 2336.900 | 2458.550 | 5.2056 |
| | Mechanism 1 | 30.1396 | 18.401 | 26.7026 | 2432.317 | 2488.138 | 2.2950 |
| | Mechanism 2 | 30.1621 | 18.4157 | 21.4108 | 2221.688 | 2388.079 | 7.4894 |
| | Mechanism 3 | 30.1594 | 18.4343 | 14.9571 | 1963.924 | 2318.881 | 18.0739 |
| $\phi = 40^\circ$ | Martin (2005) | 75.3131 | 64.195 | 85.566 | 7286.908 | -- | -- |
| | Wang (2001) | 75.9000 | 64.9000 | 122.9500 | 8817.500 | 9518.700 | 7.9524 |
| | Mechanism 1 | 75.3131 | 64.195 | 146.7658 | 9734.900 | 9905.910 | 1.7567 |
| | Mechanism 2 | 75.4066 | 64.2736 | 118.9080 | 8625.358 | 9196.135 | 6.6174 |
| | Mechanism 3 | 75.4008 | 64.3813 | 86.7592 | 7341.925 | 8720.937 | 18.7827 |

Table 1 indicates when the superposition method is employed, the ultimate bearing capacity of the foundation derived from the failure mechanism proposed in the paper mostly approximates to the high-precision characteristic line solution (Martin 2005), and the relative error is less than 0.8%; in the basis of three failure mechanisms used in this paper, the calculation results by non-superposition method are all bigger than those by superposition method. Furthermore, when using two-dimension transformation failure mechanism constructed in this paper, relative error is the maximum. When $\varphi=40^\circ$, the relative error is more than 18.5%. Although the similar research by Wang (2001) can reflect the same trend, due to the limitation of the failure mode, his solution is not optimal. The comparative analysis indicates that the error caused by the superposition empirical formula emphasis on safety, and the error increases with the increase of the internal frictional angel.

When $B=4\text{m}$, $\gamma=20\text{kN/m}^3$, $c=30\text{kPa}$, $q=25\text{kPa}$, $\varphi=30^\circ$, the failure ranges obtained by non-superposition method and superposition method to solve N_γ and N_c (or N_q) are shown in Fig. 7.

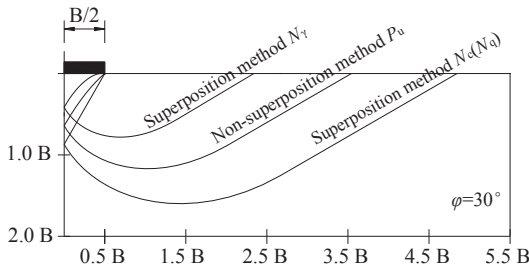


FIG.7 Comparison of failure range for rough foundation with superposition method and non-superposition method

Fig.7 shows that the failure range obtained by non-superposition is between the failure range derived from superposition method to solve N_γ and N_c (or N_q). The difference exactly reflects the effect of soil unit weight on the failure mechanism.

CONCLUSIONS

(1) Taking the construction method of the rough foundation bearing capacity velocity field as an example, the basic principle of two-dimension transformation grid type upper bound failure mechanism based on the slip line field has been illustrated; the difference between the one-dimension and two-dimension transformation failure mechanism has been analyzed; case study in this paper demonstrates the correctness and effectiveness of two-dimension transformation grid type upper bound failure mechanism based on the slip line field.

(2) The contrast analysis between the foundation bearing capacity coefficient N_c , N_q and N_γ in this paper and the latest achievements show that: without

considering the unit weight ($m=30, n=30$), the errors between N_c, N_q and theoretical solutions and the high precision characteristic line solution by Martin (2005) are rather small, and the maximum error is less than 1.5%. When considering the unit weight, the solution of N_γ in this paper is obviously superior to the similar one-dimension transformation upper bound solution, and the error between this solution and the solution by Martin (2005) is rather small. When the division of the rigid block reaches a certain density ($m=30, n=30$), the absolute maximum error is less than 4.0%, and it will decrease with the increase of the rigid block division density.

(3) As traditional superposition empirical formula does not consider the nonlinear effect of the soil unit weight on the ultimate bearing capacity of the foundation, it is only an approximate method, which will inevitably cause a certain error. The failure range obtained by non-superposition is between the failure range which obtained from solve N_γ and N_c (or N_q) by superposition method. The difference exactly reflects the effect of soil unit weight on the failure mechanism.

(4) For the engineering practice, the traditional superposition empirical formula stress on safety, and the error caused by traditional superposition method will increase with the increase of the internal friction angle.

ACKNOWLEDGMENTS

The present work was sponsored by the National Natural Science Foundation of China (No. 51078359, 51208522), the freedom explore Program of Central South University (No. 201012200197), the Postdoctoral Science Foundation of China (No. 20110491269, 2012T50708) and the Postdoctoral Science Foundation of Central South University. The financial supports are greatly appreciated. Special thanks should go to Zhang Ting and Gao Yueyue who have made constant help for authors.

REFERENCES:

- Chen W.F.(1975). "Limit analysis and soil plasticity". Amsterdam: Elsevier.
- Martin C.M.(2005). "Exact bearing capacity calculations using the method of characteristics". Proceedings of the 11th International Conference of IACMAG, Turin: 441-450.
- Soubra A.H.(1997). "Seismic bearing capacity of shallow strip footing in seismic conditions". Proceedings of the Institution of Civil Engineers, Geotechnical Engineering, Vol. 125(4): 230-241.
- Soubra A.H.(1999). "Upper-bound solution for bearing capacity of foundations". Journal of Geotechnical and Geoenvironmental Engineering, ASCE, Vol. 125(1): 59-64.
- Michałowski R.L.(1997). "An estimate of the influence of soil weight on bearing capacity using limit analysis". Soils and Foundations, Vol. 37(4): 57-64.
- Donald I.B, Chen Z.Y.(1995). "Upper Bound Solutions in Geomechanics". Computational Plasticity, Fundamentals and Applications. In: Proc 4th Int Conf

- Comp Plas. Barcelona, Spain: 1797-1808.
- Chen Z.Y, Donald I.B.(1995). "Comparison between the limit equilibrium and limit analysis method". PP Proceedings of the 10th Asian Regional Conference on Soil Mechanics and Foundation Engineer: 267-270.
- Chen Z.Y. (1997). " Numerical analysis of bearing capacity of Foundation method. Journal of geotechnical engineering, Vol. 19(5): 6-13.
- Chen Z.Y. (1997). "Soil mechanics classical lower boundlimit analysis of the problem, solutions ". Journal of geotechnical engineering, Vol. 24(1): 1-11.
- Zhu D. (2000). "The least upper-bound solution for the bearing capacity factor N_γ ". Soils and Foundations, Vol. 40(1): 123-129.
- Wang Y.J., Yin J.H., Chen Z.Y. (2001). "Failure mechanisms and calculation of bearing capacity of a strip footing on soil considering joined influences of cohesion, surcharge and gravity". Chinese Journal of Rock Mechanics and Engineering(Chinese Journal of rock mechanics and engineering), Vol. 20(4): 481-491.
- Соколовский В.В. (160). Статика сыпучей среды. The third edition (in the second edition of the translation, the translator of Xu Zhiying, Geological Publishing House, 1956).
- Zhang X.Y. (1993) "Plasticity of rock and soil mechanics". Beijing: people's transport Publishing House.
- Zhao L.H. (2009) "Energy analysis study on slope stability and reinforcing design". Changsha: Central south university.
- Yang F. (2009) "Investigation of shallow tunnel stability using upper bound solution of limit analysis. Changsha: Central south university.
- Zhao L.H., Yang F., Li L., Zhou J. (2010) "Upper bound multi-rigid-body limit analysis on positive soil pressure based on the slip-line field theory". Hong kong: 2010 International Conference on Modeling and Computation in Engineering (CMCE 2010), CRC Press / Balkema.
- Zhao L.H., Yang F. (2013). "Construction of improved rigid blocks failure mechanism for ultimate bearing capacity caculation based on slip-line field theory". Journal of Central South University of Technology, Vol. 20(4): 1047-1057.
- Hjjaj M., Lyamin A.V., Sloan S.W. (2005). "Numerical limit analysis solutions for the bearing capacity factor N_γ ". International Journal of Solids and Structures, Vol. 42(5-6): 1681-1704.

Back Analysis of Landslide Deposit Basal Failure Plane Residual Shear Strength

N. Matasovic¹, F. ASCE, C. Conkle¹, M. ASCE, A. F. Witthoeft, M. ASCE¹, A. Stern¹, and T. Hadj-Hamou, M. ASCE²

¹ Geosyntec Consultants, 2100 Main Street, Suite 150, Huntington Beach, California 92648
(nmatasovic@geosyntec.com)

² Strategic Engineering and Science, 17701 Cowan, Suite 210, Irvine, California 92614

ABSTRACT: Landslide deposits are geologic features that show signs of movement (“failure”) which occurred outside the historical record. Unlike recent landslides, they do not show evidence of recent movement such as a defined head scarp, tension cracking, and/or bulging at the toe, but are identified by geomorphic evidence of past movement. Back analysis of landslides is a common technique used to assess shear strengths for design wherein a factor of safety (FS) equal to 1.0 is assumed along a pre-defined failure surface. However, as landslide deposits may no longer be “at the verge” of failure, a back analysis with an assumed FS equal to 1.0 may result in excessively conservative shear strength properties. Therefore, back analysis of landslide deposits should be performed assuming a FS greater than 1.0. As there is no consensus on how much higher than unity FS should be, values typically used in practice range between FS = 1.05 and 1.25 with little, if any, justification provided for FS selected. Consensus on seismic FS and/or calculated maximum permanent seismic displacement for use in back analysis is similarly lacking. In this paper we evaluate parameters that affect back analysis of landslide deposits and provide illustration using a recent case history from our practice.

INTRODUCTION

Geotechnical engineers are often faced with the problem of how to evaluate the shear strength parameters of landslide deposits, especially if a distinct shear plane can be identified within those deposits. Options include:

1. Assessment of shear strength parameters based upon engineering correlations;
2. Specialty geotechnical laboratory testing; and/or
3. Back analysis.

Back analysis is commonly believed to be one of the most reliable ways to estimate shear strength along a pre-defined shear plane and hence is the focus of this paper. The shear strength parameters obtained in this process are assumed to correspond to

the residual shear strength of the material interface along the assumed (or observed) shear plane.

The back analysis approach to evaluate in-situ shear strength parameters is popular because there are significant limitations in the use of laboratory and in-situ test results to accurately characterize a soil and/or formational material profile. This is especially true when evaluating stability of slope configurations in formational materials where the stability is often controlled by shear strength of relatively thin (millimeters-thick) clay seams which are difficult to sample and test at representative stresses and shear strain levels.

Numerous studies have addressed and discussed the limitations of back-analyses in soils. These studies include papers by Leroueil and Tavenas (1981), Azzouz et al. (1981), Leonards (1982), Duncan and Stark (1992), Gilbert et al. (1998), Tang et al. (1998), Stark and Eid (1998) and Deschamps and Yankey (2006) and discuss the pitfalls of back analysis. Although these authors provide discussion no consensus is reached and no consistent recommendations on when and how to perform a back analysis are made. It is not clear when design should be based upon a back analysis rather than results of laboratory testing and/or engineering correlations.

FACTORS THAT INFLUENCE SHEAR STRENGTH INTERPRETED FROM BACK ANALYSIS

Deschamps and Yankey (2006) summarize and discuss the factors that influence interpretation of shear strength as a part of Back Analyses. They, however, limit their discussion to static evaluations and address the following:

1. The relative strength of materials in heterogeneous (often formational materials) profiles impacts interpretations of the target material strength. Often it is desirable to back-calculate the strength of a weak layer or seam. However, to accurately back-calculate the strength of the desired material, the strength of all other materials must be known.
2. The slip surface analyzed must be the same as the actual rupture surface to effectively back-calculate the strength of the material along the slip surface. Leonards (1982) describes several cases where a back analysis was reported to show a safety factor near 1.0 using laboratory or in situ determined shear strengths, but the failure surface in the analysis is not consistent with the actual rupture surface. Conclusions are sometimes drawn that the limit equilibrium method used with shear strengths obtained by some specific approach can predict the failure, but not the actual slip surface. This logic is flawed because the actual slip surface will demonstrate different back-calculated strengths than the "critical" surface obtained from analyses. A significant challenge in this regard is that the actual rupture surface may only be known at only a few locations, if any.

3. Another example of uncertainty in the slip surface is the presence of a tension crack, its depth, and whether it is full of water. For materials that are characterized as having relatively high cohesive strength, the assumption of a tension crack will have a significant influence on interpreted stability, and therefore, the back-calculated strength.
4. Knowledge of the pore water pressure is required to determine effective stresses, and therefore strength. Sometimes there are pre-failure piezometric data at select locations, sometimes measurements are made post-failure, and other times pore pressures are estimated. However, it must be recognized that the actual distribution of water pressure can be complicated, and that the operable pore pressures at failure, including shear-induced pore pressures, cannot be reliably measured.
5. Practically all slopes have a three-dimensional component. Neglecting this component in a back analysis will lead to an over-estimation of shear strength. However, "end effects" are not easily accounted for because the influence on stability can vary over a broad range. Azzouz et al. (1981) and Stark and Eid (1998) provide estimates of the influence of three-dimensional factors in stability analyses. In general, for soil slopes and embankments the end effects appear to increase the calculated stability by 5% to 30%.
6. Progressive failure in strain softening materials will also affect interpretation of strength. If the back-calculated strength is to be used for similar slopes in similar stratigraphy, the back-calculated strength may be useful (Duncan and Stark 1992). However, if the loading condition induces a significantly different stress path, the back-calculated strength from another stress path or geometry may be misleading. For example, using strength back-calculated from slope failures may not be appropriate in foundation design.
7. Mohr-Coulomb strength is defined by a friction angle and a cohesion intercept. Determination of these parameters individually is typically not possible unless significant redundant data is available (Duncan and Stark 1992).

At landslide deposit locations where historic records of strong ground shaking are available this information can assist in the back analysis of shear strength parameters. Considerations here include:

1. Intensity of strong ground shaking

The intensity is commonly interpreted as seismic coefficient. Seismic coefficient is, in turn, an empirical constant. Occasionally, seismic coefficient is evaluated as a fraction of Peak Horizontal Acceleration (PGA/g). Although relatively simple, the seismic coefficient approach has significant drawbacks as there are no universally-accepted relationships between PGA/g and seismic

coefficient and duration of shaking is completely ignored. An approach is to evaluate the seismic coefficient from calculated normalized shear stress following the procedure of Makdisi and Seed (1978) is also available. This approach, although significantly more accurate, requires a set of advanced input parameters for evaluation. These input parameters include a set of representative ground motions, shear wave velocity and unit weight profiles, and sets of nonlinear parameters for soils/materials within the profile (i.e., modulus reduction and damping curves). Therefore, evaluation of seismic coefficient from the results of site response analysis is hence used less frequently than its empirical constant approach counterpart.

2. The duration and frequency content of strong ground shaking

These parameters are required for a back analysis performed based upon the principles of performance-based design. This includes the Newmark-type approach (Newmark, 1965) which is based upon processing of design ground motions selected to match the estimated PGA, frequency content (i.e., acceleration response spectrum), and duration of strong ground shaking.

3. Stability criteria

Factors of safety used for back analysis where loading is interpreted as a seismic coefficient may range from 1.05 to 1.25 depending on the practitioner. Again, a consistent approach here is lacking.

Where a Newmark-type seismic displacement analysis is used it is not clear what magnitude of seismic displacement should be targeted by the calculations. This is particularly true if the slope was subject to multiple events in the past and if there are no observational data about the actual movement that slope experienced. For landslide deposits, in lack of observational data, most engineers assume 25 to 150 mm of permanent seismic displacement for back analysis of residual shear strength based upon the Newmark principles.

The considerations above are illustrated below using the example of a current project in Southern California.

CASE HISTORY – LANDSLIDE DEPOSIT IN SOUTHERN CALIFORNIA

Introduction

The case history is a landslide deposit that is approximately 1 km long and up to approximately 100 m thick. The deposit is derived from the Capistrano formation which is widely regarded as one of Southern California's most unstable formations. Detailed geologic description of the Capistrano formation, including information of typical modes of failure, can be found in Terres (1992). The groundwater is

approximately 45 m above the landslide deposit basal shear plane. The basal shear plane is composed of an approximately 25 mm-thick layer of bentonite clay. The site is in an area of high seismicity and was subjected to several seismic events in the past.

Site Conditions

The evaluation of the landslide deposit consisted of geologic mapping, geophysical measurements, and geotechnical laboratory testing of basal shear plane shear strength parameters. Figure 1 shows a representative cross-section through the landslide deposit and includes the locations of boreholes advanced through the landslide deposit, interpretation of groundwater conditions, and the interpreted basal failure surface. The groundwater elevation shown was estimated based upon groundwater elevation measurements and results of geophysical measurements. The failure surface was interpreted based upon site geomorphology and interpretation of borehole logs. Representative samples of the basal shear plane were recovered from a depth of approximately 90 m below ground surface (b.g.s.) and extracted from a 60-mm diameter core. Index testing indicated a clay content of 40% - 60% with a Liquid Limit of 90% and a Plasticity Index of 60.

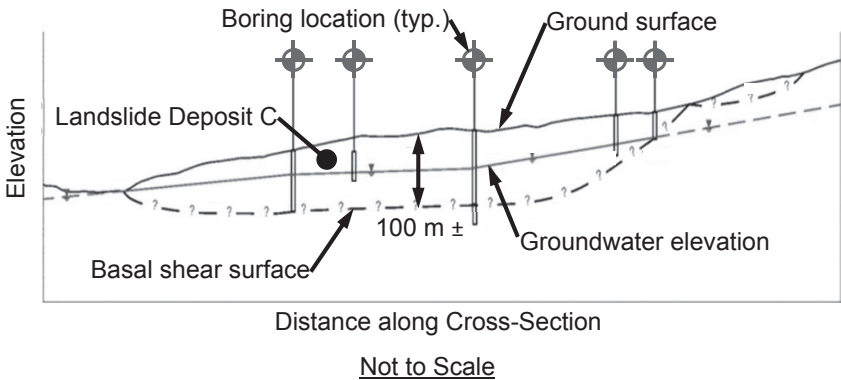


Fig. 1: Longitudinal cross-section through the subject landslide deposit with indicated boring locations.

Torsional Ring Shear Testing and Engineering Correlations for Shear Strength Characterization

Materials recovered from the basal shear surface were tested in a torsional ring shear apparatus. The testing results are presented in Figure 2 along with the results of ring shear testing performed by another consultant for remediation of a landslide within

relative vicinity. The interpreted friction angles ranged from 4.0 to 8.0 degrees, with an average value of approximately 6.0 degrees for both landslide deposits. Assuming the upper bound value of friction angle of 8.0 degrees as representative, the calculated FS ranged from $FS = 0.8$ to $FS = 0.9$ (i.e., less than 1.0) for the geometry assumed in Figure 1. The same results were found regardless of the unit weight profile, the shear strength of landslide deposit mass itself, and method of analysis employed (i.e., Spencer, Janbu, Morgenstern-Price, 2-D and/or 3-D). As the landslide deposit did not show signs of slope instability (e.g., bulging or cracking) it appeared that laboratory results should not serve as the sole basis for establishing shear strength parameters in this case.

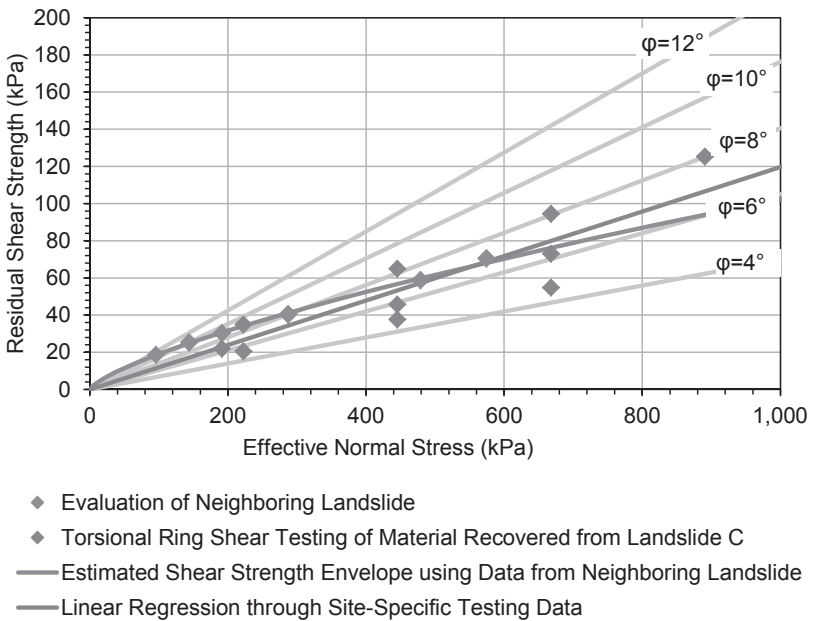


Fig. 2: Results of torsional ring shear testing for Landslide Deposit C compared to the results of similar testing program for a nearby landslide deposit in the same geologic formation.

The lower than expected residual shear strength as indicated by torsional ring shear testing may have several combined causes:

1. These specialty tests could not be performed at appropriate range of stresses (equivalent to 90 m of overburden) due to the testing equipment limitations

2. Pre-existing shear planes likely underwent healing or strength gain over the past several thousands of years, (see, Stark et al., 2001 for discussion)
3. Torsional ring shear testing is typically performed on scalped, milled, remolded samples and as such results in lower strength estimates.

Engineering correlations that relate liquid limit and clay content to residual (secant) friction angle have been developed by several researchers. These correlations typically ignore a cohesion intercept for the drained residual strength envelope. That is because the particle contact and bonding that leads to a cohesion strength parameter greater than zero are significantly reduced or removed by the shear displacement required to reach a residual strength condition. This results in only a frictional shear resistance that is represented by a residual friction angle and the effective normal stress acting on the shear surface.

A recent correlation by Stark et al. (2005) indicates the residual friction angle along the subject basal shear plane may range from 6 to 12 degrees, with an average value of 9 degrees. However, Stark et al. (2005) note that their testing results do not capture strength gain due to healing which may occur at the relatively high stress levels representative of the basal plane of this landslide deposit.

Back Analysis

Finally several back analyses of Landslide Deposit C were as performed. The static and pseudostatic back-analyses were performed conservatively assuming an in-situ FS of 1.1. This assumption was justified by lack of observable signs of slope movement, such as bulging at the toe and/or cracking along the postulated head scarp. The pseudostatic back-analyses were performed with seismic coefficient evaluated as an empirical constant (0.025 – 0.05). The seismic back analyses were performed assuming a target calculated permanent seismic displacement in the range of 25 to 150 mm.

Both static and pseudostatic evaluations were performed in two and three dimensions (2-D and 3-D, respectively). The 3-D model was developed from interpreted basal surface with 9 longitudinal and two transversal cross sections. A variety of analysis methods was used, and the results were reported for the lowest calculated FS. Figure 3 shows one of the back analysis models developed using the software SVSlope (www.soilvision.com).

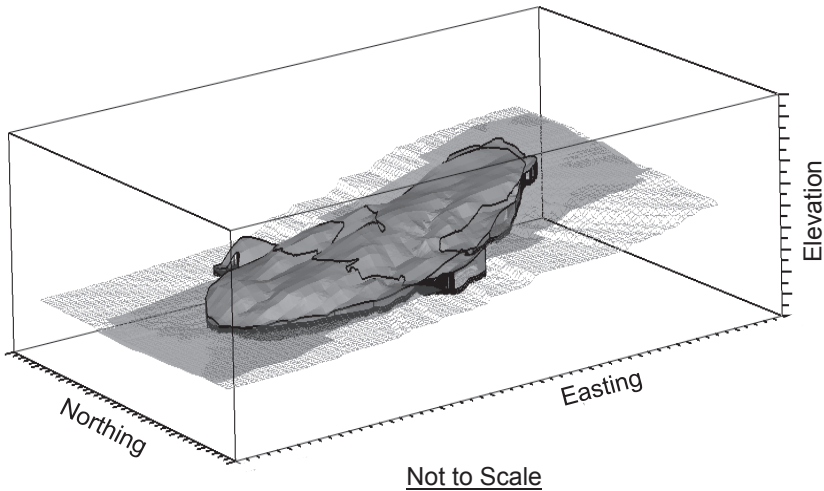


Fig. 3: Three-dimensional model of Landslide Deposit C for back analysis of the basal shear plane residual shear strength parameters under static, pseudostatic, and performance-based seismic conditions.

Comparison of Back Analysis to Other Methods

The back-calculated friction angle for the landslide basal shear surface under static loading conditions was approximately 10 degrees. This value is approximately 25% higher than the friction angle estimated from torsional ring shear testing and approximately 13% higher than the an average value estimated from engineering correlations.

The values back-calculated by the means of pseudostatic analysis with a seismic coefficient equal to 0.025 were approximately 5% higher than their static counterparts, with even higher values when the intensity of seismic coefficient was increased to 0.05. The range of back-calculated friction angle for performance-based seismic evaluations varied within a broad range with the results depended mostly upon the assumption of the target calculated permanent seismic displacement.

Additional factors in this variability included the number of accelerograms considered. All of the back-calculated values of the residual friction angle were higher than the average value of the Stark et al. (2005) correlation, with values back-calculated based upon seismic conditions slightly above the upper bound of value of 12 degrees predicted by the correlation.

CONCLUSIONS

This case study confirms that back analysis is an appropriate way to evaluate the residual shear strength parameters of landslide deposits (where no observations of recent movement but geomorphologic evidences of movement exist). The results of this study further confirm that the shear strength parameters estimated from back analysis may be significantly affected by a number of disparate factors. As such, results of a back analyses should always be considered alongside other means of evaluating of residual shear strength, such as laboratory testing and engineering correlations.

The evaluations documented herein illustrate that assumptions which are conservative in design are un-conservative in back analysis. This is especially true with respect to the assumption of FS for back analysis (both static and pseudostatic), and especially for the target maximum permanent seismic displacement which is an essential input into the performance-based back analysis. The selection of target displacement merits further evaluation as landsliding in soils and formational materials is frequently seismically-induced.

As more accurate back analysis tools are developed over time, including computer codes, geophysical methods for assessment of slide geometry, and improvements in our ability to estimate past ground motions, the results of these analyses should be evaluated with the application of appropriate engineering judgment.

REFERENCES

- Azzouz, A. S., Baligh, M. M., and Ladd, C. C. (1981). "Three-dimensional stability analyses of four embankment failures." *Proc., 10th Int. Conf. on Soil Mechanics and Foundation Engineering*, Balkema, Rotterdam, The Netherlands, Vol. 3: 343–346.
- Deschamps, R. and Yankey, G. (2006). "Limitations in the back analysis of strength from failures." *J. of Geotech. Geoenviron. Eng.*, Vol 132 (4): 532-536.
- Deschamps, R., Hynes, C., and Wigh, R. (1999). "Analysis and stabilization of a failing earth dam founded on claystone." *J. Perform. Constr. Facil.* Vol. 13 (4): 143–151.
- Duncan, J. M. and Stark, T. (1992). "Soil strengths from back analysis of slope failures." *Proc. Stability and Performance of Slopes and Embankments II*, ASCE, New York, 890–904.
- Gilbert, R. B., Wright, S. G., and Liedtke, E. (1998). "Uncertainty in back analysis of slopes: Kettleman Hills case history." *J. Geotech. Geoenviron. Eng.*, Vol. 124 (12): 1167–1176.

- Leroueil, S., and Tavenas, F. (1981). "Pitfalls of back analysis." *Proc. 10th Int. Conf. on Soil Mechanics and Foundation Engineering*, Balkema, Rotterdam, The Netherlands, Vol. 1: 185–190.
- Makdisi, F. I. and Seed, H. B. (1978), "Simplified Procedure for Estimating Dam and Embankment Earthquake-Induced Deformations." *Journal of Geotechnical Engineering Division*, ASCE Vol. 104 (GT7): 849-867.
- Newmark, N. M. (1965), "Effects of Earthquakes on Dams and Embankments." *Geotechnique* 15, No. 2, 139-160.
- Stark, T. D. and Eid, H. T. (1998). "Performance of three-dimensional slope stability methods in practice." *J. of Geotech. and Geoenviron. Eng.*, Vol. 124 (11): 1049–1060.
- Stark, T. D., Choi H. and McCone S. (2005), "Drained shear strength parameters for analysis of landslides." *J. of Geotech. and Geoenviron. Eng.*, ASCE, May 2005, Vol. 131: 575-588.
- Tang, W. H., Stark, T. D., and Angulo, M. (1998). "Reliability in back analysis of slope failures." *Soils and Foundations*, Vol. 39 (5): 73–80.
- Terres, D. A. (1992). "Landslides in the Capistrano Formation, Orange County, California." In: *Engineering Geology Field Trips: Orange County, Santa Monica Mountains and Malibu*, Proc. 35th Annual Meeting, Association of Engineering Geologists, Southern California Section, Los Angeles, California.

Study on the Modified Coefficient of Dynamic Penetration Rod Length

Zuo yongzhen¹, Cheng zhanlin², Ding hongshun³, Liao jianhui⁴

Yangtze River Scientific Research Institute. Key Laboratory of Geotechnical Mechanics and Engineering of the Ministry of Water Resources. WuHan,430015, China.

¹zuoyongzh@163.com, ²chengl@mail.crsri.cn, ³Ding2005628@sina.com, ⁴liaojianhui1219@126.com

ABSTRACT: Dynamic penetration test (DPT) is one of those widely applied in situ test techniques. The rod length during operation could be as large as hundreds of meters, calling for length modification in practical applications. Two major methods were proposed in the most recent specifications for the modification of dynamic penetration rod length. These two methods were based on Newton elastic collision theory and elastic rod waving theory respectively, and derived totally different correction coefficients. How to applying rod length modifications to the results of dynamic penetration tests, have become a major issue that affects the reliability of its application. In this study, indoor model tests were conducted to evaluate the length corrections. A variety of heavy dynamic penetration model were conducted on sand and gravel soil with different of rod lengths (2.0m, 8.9m, 16.4m, 23.4m, 30.0m, 36.0m). The modification coefficient of heavy dynamic penetration rod length was obtained from there experiments. The results indicated that the modification coefficient for the length of penetration rod followed the description of Newton elastic collision theory, and was independent of the material properties.

INTRODUCTION

During the construction of hydropower stations in western areas, the overburden depths of the riverbed were mostly tens to hundreds of meters, and 300m of maximum. Those overburden layers were formed by geological alluvial of sands and gravel stones from different ages. They were complex in compositions, and possessed large spatial variations. Determination to the mechanical properties of deep overburden layer is one of the key technical problems for constructing a dam onto it. The accuracy and reasonability were directly related to the project cost and construction safety.

In situ detections, such as dynamic penetration, were often employed for measuring the mechanical properties of overburden layers, as those cohesionless granular sands and conglomerates in the riverbed overburden caused depth-sampling difficulties. The dynamic penetration method determined the mechanical properties by measuring the

accessibility of penetration into the soil.

In those dynamic penetration to deep layers, the length of rod posed increasingly significant influences to the hammering count N , as the rod went deeper. Thus the N varied with different rod lengths, requiring for a rod length modification.

For quite long a time, the Newton elastic collision theory and Elastic rod waving theory were existed and erived different correction coefficients, since direct measurement by experiments were not available.

The first modification was grounded on the Newton collision theory, instead of field data. Typical modifications based on it were *Code for design of building foundation* (Chinese National Standards , GBJ7—89, 1989) and the Shanghai Gujiwei effective energy modification equation stated in *Specification for geological exploration in highway constructions* (Chinese Industry Standards , JTJ064-98, 1998).

The second modification was established up the basis of elastic rod waving theory. Typical modifications were the SPT test principles proposed on International Summit of Penetration Tests (ISOPT-1, 1988), and the *Test Method for Stress Wave Energy Measurement for Dynamic Penetrometer Testing Systems* (ASTM , D4633-1986, 1986) published by ASTM, USA.

The different modification coefficients with rod lengths were shown in Figure 1. By doing a comparison between they two, quite obvious differences were found between the coefficients based on Newton's theory and the elastic rod theory. As described by the Newton elastic collision theory, the modification coefficient decreased as rods went longer, while those under elastic rod waving increased. Such a diversion indicated the necessity as well as practical meanings of studying modification to rod length.

The coefficients listed above all laid in the single parameter relationship with the rod lengths. Its correlation to hammering counts were separately given by *Code for investigation in geotechnical constructions* (Chinese National Standard GB50021-2001,2009 edition) and *Code for design of building foundation* (Chinese National Standard , GB50007-2011, 2011) , up to 20m in length. In general, the coefficients in Table 1 are both related to rod lengths and hammering counts.

Table 1. Modification coefficients to hammering counts

| $N_{63.5}$ L (m) | 5 | 10 | 15 | 20 | 25 | 30 | 35 | 40 | ≥ 50 |
|---------------------|------|------|------|------|------|------|------|------|-----------|
| 2 | 1.00 | 1.00 | 1.00 | 1.00 | 1.00 | 1.00 | 1.00 | 1.00 | |
| 4 | 0.96 | 0.95 | 0.93 | 0.92 | 0.90 | 0.89 | 0.87 | 0.86 | 0.84 |
| 6 | 0.93 | 0.90 | 0.88 | 0.85 | 0.83 | 0.81 | 0.79 | 0.78 | 0.75 |
| 8 | 0.90 | 0.86 | 0.83 | 0.80 | 0.77 | 0.75 | 0.73 | 0.71 | 0.67 |
| 10 | 0.88 | 0.83 | 0.79 | 0.75 | 0.72 | 0.69 | 0.67 | 0.64 | 0.61 |
| 12 | 0.85 | 0.79 | 0.75 | 0.70 | 0.67 | 0.64 | 0.61 | 0.59 | 0.55 |
| 14 | 0.82 | 0.76 | 0.71 | 0.66 | 0.62 | 0.58 | 0.56 | 0.53 | 0.50 |
| 16 | 0.79 | 0.73 | 0.67 | 0.62 | 0.57 | 0.54 | 0.51 | 0.48 | 0.45 |
| 18 | 0.77 | 0.70 | 0.63 | 0.57 | 0.53 | 0.49 | 0.46 | 0.43 | 0.40 |
| 20 | 0.75 | 0.67 | 0.59 | 0.53 | 0.48 | 0.44 | 0.41 | 0.39 | 0.36 |

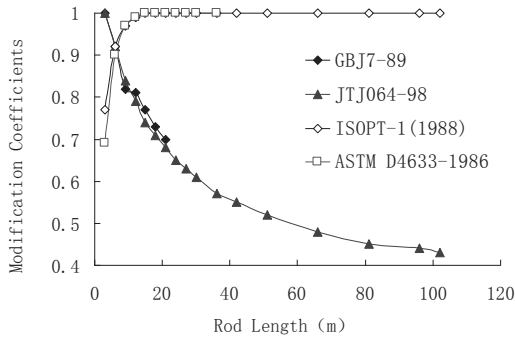


FIG.1. The correlation curve between coefficients and rod length

DESIGN OF THE TESTING SYSTEM

The test system was consisted up by two major components, namely the model testing system and the in-situ testing system.

The model system was consisting of model box and a pressurizing system, as shown in Figure 2 and 3. The model box was welded by steel plates of 60mm thickness. Its internal dimension was 0.82m×0.84m×1.20m (length x width x height). Specimens were filled into the box layer by layer, forming a homogeneous foundation. Four 75T jacks were placed between the cover and the pressure plate as the pressurizing system. Self-balanced pressure was applied to the surface of the model to simulate the self-weight stress from the structure from those on the foundation. Coaxial holes were made on both the cover and the pressure plate, for further dynamic penetration tests.

The in-situ test system was installed in a stairwell of a 11 storied building, as shown in Figure 4. The model system was placed in the bottom of the stairwell, along with the penetration rod in vertical fashion. Hammering points were set on different heights to meet the rod lengths of 2m, 8.9m, 16.4m, 23.4m, 30m and 36m.

Upon one individual classification and dry density, substances were pressed by layers into a homogeneous model foundation, in accordance of one specific foundation soil. Constant upward pressures were applied on the surface of those foundations for complete solidification (under 240kPa for 12h). Dynamic penetration tests were conducted with different rod lengths to each model. For each special foundation model, the correlation from mechanical properties to both rod lengths hammering counts were then obtained, and further derived in to the rod modification coefficients. It was first time that physical field tests were conducted to measure the rod modification coefficient. The reliability of those results was sound and was then used for validating the theories.

THE MATERIAL USED IN TESTS

Experiments were conducted in two groups, with soil samples be of homogeneous medium grained sands and gravels.

Homogeneous sands were grains size within 0.5-1.0mm, their maximum and

minimum dry density were 1.63 g/cm^3 and 1.31 g/cm^3 respectively. The experimental dry density was 1.45 g/cm^3 , relatively in 0.50, as for medium density.

Gravels were maximum 60mm in grain sizes. They were continuous in gradation, coefficient of curvature is 2.2, coefficient of uniformity is 45.7. The max dry density was 2.31 g/cm^3 . The experimental value was 2.12 g/cm^3 , porosity was 8% (92% compacted).

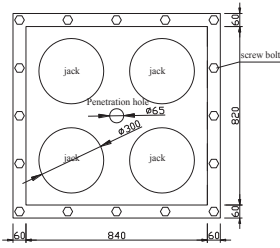


FIG.2. The plans of model box(mm)

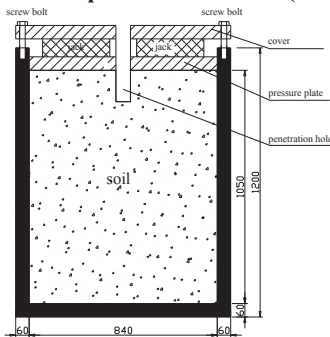


FIG.3. The sections of model box(mm)

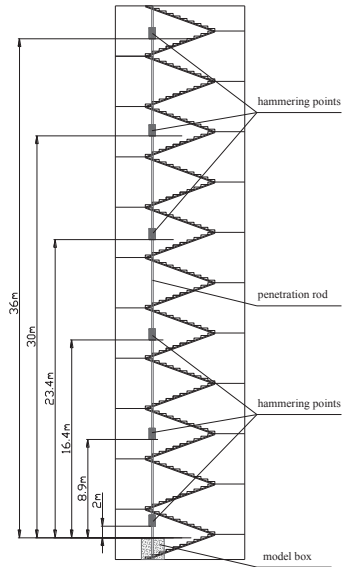


FIG.4. The distribution figure of dynamic penetration hammering points

TESTS OF DYNAMIC PENETRATION AND DATA ANALYSIS

Models were applied with pressures and solidified after the completion of making. Dynamic penetration tests were then conducted to them. Heavy penetrations were applied with every penetration went no less than 40cm. Each depth was recorded, and plotted into the correlation curve with hammering counts. The steady part of the curve was then put into fitting, for calculating the hammering counts when reaching 100mm. The number was taken as the hammering count $N_{63.5}$ for dynamic penetration. The representative curve for dynamic penetration was at last shown in figure 5.

Following contents described the major procedures taken in the heave dynamic penetration experiments:

- (1) Steady install the penetration frame before any test, ensure the maximum deviation of verticality is less than 2%. Ensure the penetration rod is fastened in vertical position.
- (2) The free fall distance of hammer is controlled at $0.76 \pm 0.02 \text{ m}$.

(3) Set hammering rate to 15-30 per minute. Continuous hammering is more preferred. Any interval longer than 5 min must be noted in the records.

(4) Timely record the hammering counts for every penetration of 0.10m. Regularly the counts are noted at a certain time interval, and then converted into counts per 0.10m.

(5) When the total counts for 0.10m are three times in a row exceeding 50, stop the test.

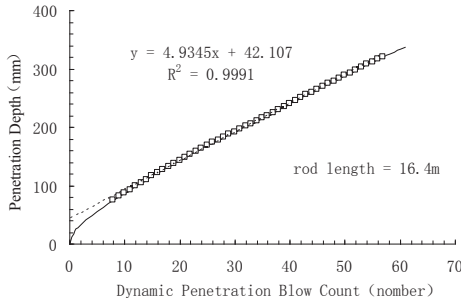


FIG.5. A typical test curve of dynamic penetration

TEST RESULTS AND ANALYSIS

Tests were conducted in two groups. Factors including the gradation of foundation soils, experimental densities and upward pressures were kept unchanged throughout each group. For heavy dynamic penetration in homogeneous sands, parallel tests were done with rod length ranging 2m, 8.9m, 16.4m, 23.4m and 30m, with 10 effective spots taken for each of them. The results were shown in table 2. For gravel group, the rod lengths were 2m, 8.9m, 16.4m, 23.4m, 30m and 36m; number of effective spots was 11. The results were also shown in table 2.

Seen from table 2, the hammering count for every 100mm progress increased for longer rods. Taken the value from gravels as an example, the $N_{63.5}$ for 2m was 15.0, and increased to 27.3 for 26m (increase of 82%). It surely revealed the significant influence from rod lengths to hammering counts.

For regular modifications, the operation starts from where rod length is 2-3m. When adopt it to the tests in the paper, assume the $N_{63.5}$ taken from 2m rod was the standard value, as the start point for modification. The modification coefficient was then defined as the ratio between hammering counts taken from rod with length of i , to the $N_{63.5}$ taken on 2m rod.

Guided by this rule, the calculated modification coefficients for both homogeneous sands and gravels, with different rod lengths, were listed in table 3 respectively.

The correlation curves for the modification coefficient and rod lengths were plotted and shown in both figure 6 and 7. Theoretical coefficients from both Newton's elastic collision and elastic rod waving theory were also given in the figures for references. Further inspection indicated that measured datum were better in consistence with the Newton's theory. Those modification coefficients were mostly complied to the *Code for design of building foundation* (GBJ7—89) and the Shanghai Gujiwei effective

energy modification equation stated in *Specification for geological exploration in highway constructions (JTJ064-98)*, and valid for different foundation soils.

Table 2. The DP* results in homogeneous sands and gravels

| Rod lengths (m) | homogeneous sands | | | gravels | | |
|-----------------|-------------------|------------------|---------|---------|------------------|---------|
| | No. | count $N_{63.5}$ | | No. | count $N_{63.5}$ | |
| | | Individual | Average | | Individual | Average |
| 2 | B1 | 13.9 | 12.1 | S1 | 15.2 | 15.0 |
| | B2 | 10.3 | | S2 | 14.8 | |
| 8.9 | B3 | 13.7 | 14.1 | S3 | 18.4 | 17.7 |
| | B4 | 14.6 | | S4 | 16.9 | |
| 16.4 | B5 | 15.6 | 15.6 | S5 | 20.3 | 20.3 |
| | B6 | 15.7 | | -- | -- | |
| 23.4 | B7 | 16.6 | 16.9 | S6 | 22.2 | 21.7 |
| | B8 | 17.3 | | S7 | 21.1 | |
| 30 | B9 | 18.6 | 18.9 | S8 | 24.0 | 25.2 |
| | B10 | 19.2 | | S9 | 26.3 | |
| 36 | -- | -- | | S10 | 27.9 | 27.3 |
| | -- | -- | | S11 | 26.7 | |

*DP = Dynamic Penetration

Table 3. The rod length Modif. Coeff. in homogeneous sands and gravels

| Rod length (m) | | 2.0 | 8.9 | 16.4 | 23.4 | 30.0 | 36.0 |
|-------------------|----------------|------|------|------|------|------|------|
| homogeneous sands | $N_{63.5}$ | 12.1 | 14.1 | 15.6 | 16.9 | 18.9 | |
| | Modif. Coeff.* | 1.00 | 0.86 | 0.78 | 0.72 | 0.64 | |
| gravels | $N_{63.5}$ | 15.0 | 17.7 | 20.3 | 21.7 | 25.2 | 27.3 |
| | Modif. Coeff. | 1.00 | 0.85 | 0.74 | 0.69 | 0.60 | 0.55 |

*Modif. Coeff. = Modification Coefficient

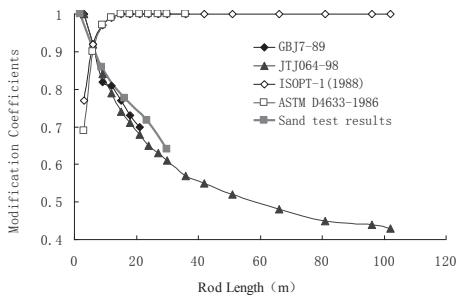


FIG.6. The correlation between rod lengths and Modif. Coeff. for sands

Late the obtained results went through rod length modifications, with references

from the data given by *Code for investigation in geotechnical constructions* (GB50021-2001) (2009 edition, shown in Table 1) . Comparisons with other results were made and displayed in figure 8.

And seen from the figure 8, the test results were found to be larger when compared to those rod length modification coefficients given by the Code GB50021-2001. But for test results themselves, no significant deviations were observed between the data from homogeneous sands and gravels. Conclusion was drawn here, as say approximately the coefficient still obeyed the same law even the foundation materials were altered.

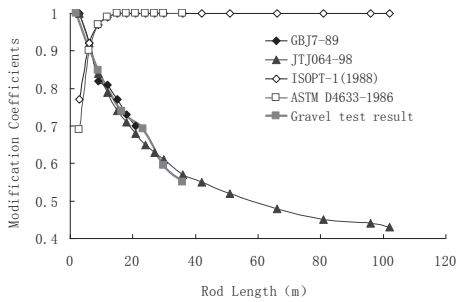


FIG.7. The correlation between rod lengths and Modif. Coeff. for gravels

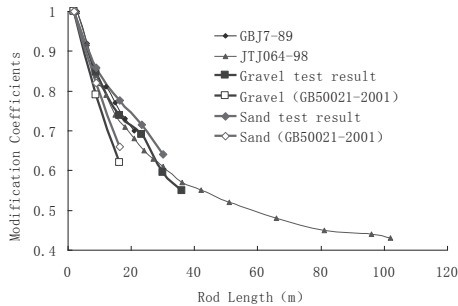


FIG.8. The comparison of rod length Modif. Coeff. from sands and gravels

CONCLUSIONS

A series of heave dynamic penetration tests were conducted indoor on two different foundation materials, in the purpose of studying the correlation of rod lengths and hammering counts. The modification coefficients for heavy dynamic penetration were then obtained. This test is a beneficial try to the modified coefficient of dynamic penetration rod length.

(1) The modification coefficients for heavy dynamic penetration were general in consistent to Newton's elastic collision theory. When rod length extended, the coefficient gradually dropped.

(2) Those modification coefficients were mostly complied to the *Code for design of building foundation* (GBJ7—89) and the Shanghai Gujiwei effective energy modification equation stated in *Specification for geological exploration in highway constructions* (JTJ064-98).

(3) Although the longest rod employed in the heavy dynamic penetration was exceeding the limited 21m, to 36m, its $N_{63.5}$ was still effective in revealing the mechanical properties of the soil being tested.

(4) The modification coefficient remained obeying the same law even the foundation materials were altered. No significant deviation was detected when changing from gravels to homogeneous sands.

ACKNOWLEDGMENTS

This research is financially supported by the central public research institutes for basic research funds of Yangtze River Scientific Research Institute(Grant No. CKSF2012022/YT) and Ministry of Water Resources' Special Funds for Scientific Research on Public Causes of China(Grant No. 201201039).

REFERENCES

- National Standards. (1989). *Code for design of building foundation* (GBJ7-89).[S]. Beijing.
- Industry Standards. (1998) *Specification for geological exploration in highway constructions* (JTJ064-98)[S]. Beijing, China Communications Press.
- ASTM. (1986). *Standard Test Method for Stress Wave Energy Measurement for Dynamic Penetrometer Testing Systems* (D4633-1986) [S]. American.
- National Standard. (2009). *Code for investigation in geotechnical constructions* (GB50021-2001)(2009 edition). Beijing, China Architecture and Building Press.
- National Standard. (2011). *Code for design of building foundation* (GB50007-2011). Beijing, China Architecture and Building Press.

Study on Hydrodynamic Pressure and Dynamic Response of Pier under Long-period Earthquakes

Bo Song¹ and Shuai Huang²

¹School of Civil and Environment Engineering, University of Science and Technology Beijing, P.O.Box 396, Beijing ST Xueyuan; PH 18811348935; Email: b20100038@xs.ustb.edu.cn

²School of Civil and Environment Engineering, University of Science and Technology Beijing, P.O.Box 396, Beijing ST Xueyuan; PH 15210716603; Email: huangshuai28@yahoo.cn

ABSTRACT: Based on shaking table test and finite element method, the influence of water on the natural vibration characteristics of the pier was studied. Then, the effect of long-period ground motions to hydrodynamic pressure of the pier under various water depths was discussed. As the same time, seismic responses of the pier were also analyzed under the condition of different water depths. Finally, the first order natural frequency and the distribution of acceleration peak values along the pier height were compared between the shaking table test and finite element method. The results show that, the influence of the water on the natural vibration characteristic of the pier should be considered. When the water depth exceeds a critical value, the hydrodynamic pressure has different tendency along the pier under different ground motions. The peak values of bending moment and shear force at the bottom of the pier and the acceleration and displacement on the top of the pier increase with the rise of water depth. The calculated values from model test and finite element calculation are in good agreement.

INTRODUCTION

Parameters of long-period ground motions are different from short ground motions. Also, the response spectrum of long-period earthquakes no matter from form or value has a large difference from present code. Considering the impact of earthquakes, designing spectrum given by the code is obvious deficiency. Thus, when choosing seismic waves or design spectrum, the influence of long-period ground motions on structure should be considered.

In recent years, examples of the destruction of structure under long-period ground motions sometimes happened, such as, Great Kanto earthquake of Japan happened in 1983 led to thirteen oil tanks damage, however the distance was about 270km far away from the epicenter. South Yellow Sea earthquake happened in 1996, five root trolleys of the Oriental Pearl Television Tower which was 160km far away from epicenter were broken. These examples indicate that disasters mechanism caused by the long-period earthquakes need to be further researched. Xie et al (1990) studied the influence of site condition, distance and magnitude to the long-period earthquakes. Zang et al (2010) studied the seismic wave spectrum characteristics by choosing two typical long-period earthquakes. Wu et al (2011)

studied the response of a top frame structure under long-period earthquakes. Once the important structures are damaged, the losses will be huge. Also, because of the limitation of seismic code to long-period earthquakes, to study the destructiveness of long-period earthquakes is particularly important.

However, due to the lack of reliable records of long-period earthquakes, the research in china and abroad is not enough. The research of the effect of the long-period ground motions to hydrodynamic pressure and dynamic response of rectangular piers were less. Thus, based on shaking table test and finite element method, hydrodynamic pressure and dynamic response under long-period ground motions and short-period ground motions along the pier in different water depths were studied.

FINITE ELEMENT MODELING OF RECTANGULAR PIER

The subject is a typical entity pier of a large span bridge. The section of the pier is rectangular with size $10\text{m} \times 2.5\text{m}$ and height 24m . The water depth is 20m , and the quality of pier of the top is 495t . Site class is II. Water range is 20 times as wide as pier which is 50m to realize the influence of reasonable range of water on dynamic reaction of the structure in the seismic loading direction and the vertical direction. The modal is shown in Fig. 1.

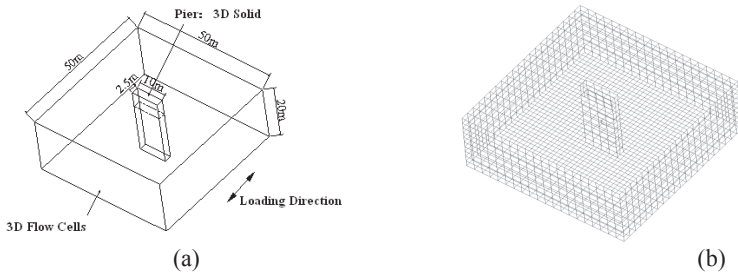


FIG. 1. Analysis model of rectangular pier: (a) model Size (b) modal of numerical analysis.

The calculation system of hydrodynamic-pier in this paper is based on potential flow theory. Pier is simulated by three-dimensional solid elements, and water is simulated by potential fluid elements. When free vibration frequency of cylindrical structures is within 0.5Hz to 2Hz , there is no influence of compressibility of fluid on hydrodynamic pressure of the structure and the compressibility of fluid could be ignored. Method of computation is New Mark β , and damping used is Rayleigh damping. Damping ratio of the structure is 5% . At the same time, reinforced concrete was assumed to be as homogeneous material for equivalent treatment. Elasticity modulus of fluid E_V is $2.2 \times 10^3 \text{Mpa}$, and density ρ is 1000Kg/m^3 .

Selection of Earthquakes.

Highway bridges designed against seismic intensity 8 are seismically crucial. Thus, the design basic earthquake acceleration is 400gal (i.e., 0.4g). Table 1 lists the characteristics of four seismic waves in the time domain. The acceleration time- histories of the four seismic waves are shown in Fig. 2.

Table 1. Contrast of Characteristics of Seismic Waves in Time Domain

| Category | Earthquakes | Magnitude | Station | PGA (gal) | PGV (cm/s) | PGD (cm) |
|-----------------------------|----------------------|-----------|----------|-----------|------------|----------|
| Long-period ground motions | Chi-Chi 1999 | 7.6 | TCU006 | 76 | / | / |
| | Chi-Chi 1999 | 7.6 | TCU115 | 115 | 39 | 33 |
| Short-period ground motions | Imperial Valley 1940 | 7.0 | I-ELC180 | 313 | 30 | 13 |
| | Kern County | 7.4 | TAF021 | 156 | 15 | 9 |

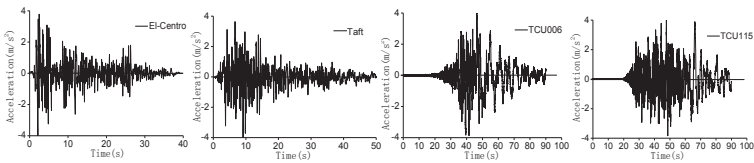


FIG. 2. Acceleration time-histories of long-period and short-period earthquakes.

INFLUENCE OF WATER ON THE NATURAL VIBRATION CHARACTERISTIC OF THE PIER

Natural vibration characteristics of the pier in the air and water were calculated. The first and second vibration modes in 20m deep water are shown in Fig. 3. Change laws of the first natural vibration period under different depth of water were studied as shown Fig. 3.

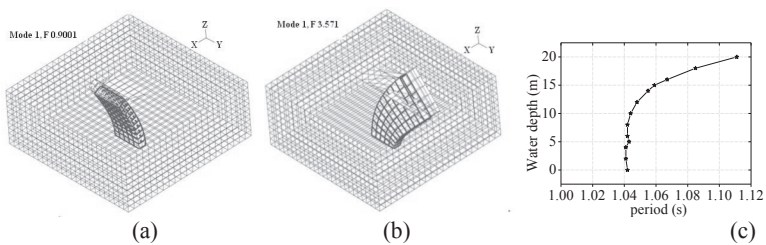


FIG. 3. First 2-modal of the pier under 20 m deep water: (a) first modal; (b) second modal; (c) change of the first modal period with water depth.

As shown in Fig. 3, the first modal period of the pier increases with the increasing of the water depth. When the water depth is 40% of the full depth (below the 8m water depth, the first modal period increases slowly, and when the water depth is more than 8m, the first modal period increases faster. The first modal period of the pier in 20m water increases by 6.62% compared with the pier in the air. Thus, 40% of the full depth is a critical point, and the influence of the water on the natural vibration characteristic is little, when the water depth is below the critical point. However, the effect of the water to the natural vibration

characteristic of the rectangular pier should be considered, when the water depth exceeds a critical value.

Analysis of the Hydrodynamic Pressure under Long-period Ground Motions

The effect of long-period and short-period ground motions to hydrodynamic pressure of the pier through the finite element were calculated, and hydrodynamic pressure was calculated accordance with *Guidelines for Seismic Design of Highway Bridges (JTG/T B02-01-2008) of China* and *Japan Road association 2012, Specification for Highway Bridge, Part V: Seismic Design* as shown in Eq.1 for $\frac{b}{h} \leq 2$:

$$p(z) = k_h w_0 A_0 \frac{b}{a} \left(1 - \frac{b}{4h}\right) \sqrt[3]{\frac{z}{h}} \tag{1}$$

where p is the hydrodynamic pressure on unit length pier (kN/m), k_h is the horizontal seismic scale, w_0 is the weight per unit volume of water (N/m³), h is the water depth (m), A_0 is the cross-section area of pier (m²), b is the pier size in vertical direction of the hydrodynamic pressure (m), a is the pier size in direction of the hydrodynamic pressure (m).

The effect of hydrodynamic pressure to the pier could be calculated by studying on the distribution regularities of the hydrodynamic pressure under earthquakes. The hydrodynamic pressure of the pier in the direction facing the water is shown in Fig 4.

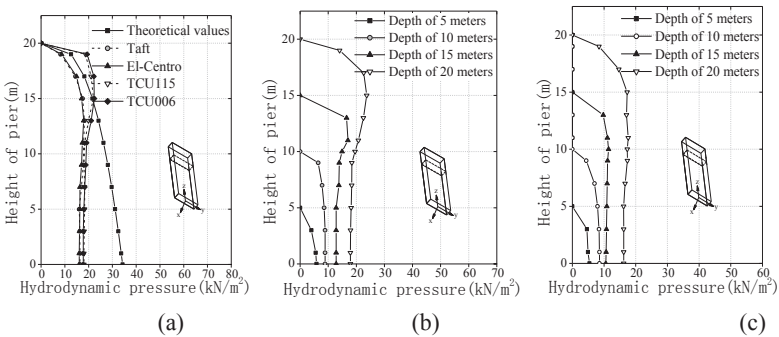


FIG. 4. Tendency of the hydrodynamic pressure along the pier: (a) hydrodynamic pressure under different earthquakes in the 20m deep water; (b) hydrodynamic pressure under long-period ground motions; (c) hydrodynamic pressure under short-period ground motions.

Hydrodynamic pressure affected by different earthquakes along the pier shows different regularities in Fig. 4. When the water depth is 20m, with the pier height decreasing, the hydrodynamic pressure under long-period earthquakes increases along the pier up to 15m and starts to reduce until the bottom of the pier. However, the tendency of the short-period earthquakes is not obvious. As shown in Fig. 4(b) and (c), the hydrodynamic pressure under long-period earthquakes and

short-period earthquakes maintain basically tendency of increasing in the 5m and 10m and 15m deep water. When the height of pier is above 15m, the values of the long-period earthquakes using the finite element method are greater than theoretical calculating values, and the maximum deviation rate is 21.89%. When the height of pier is below 15m, the theoretical calculating values are greater than that of the finite element method, and the maximum deviation rate is 77%. However, the calculation values of the short-period earthquakes using the finite element method are less than the theoretical calculating values. In a word, the effect of the long-period earthquakes to the hydrodynamic pressure of the pier is greater than that of short-period earthquakes, especially when the depth of water reaches 20m, the hydrodynamic pressure under the long-period earthquakes has a obvious peak on the pier of the upper-middle position, which could cause bridge disaster more easily. Thus, it is necessary to consider the effect of long-period earthquakes to the rectangular pier in deep water.

Dynamic Response of the Bridge Pier

The dynamic characteristics of the structure are reflected directly by the acceleration and section force. In order to compare the dynamic response of the pier under long-period ground motions and short-period ground motions, an influence coefficient R was used to express the influence of long-period ground motions on the dynamic response of the pier, which is defined as: $R = (\text{dynamic response of pier under long-period ground motions} - \text{dynamic response of pier under short-period ground motions}) / \text{dynamic response of pier under short-period ground motions}$.

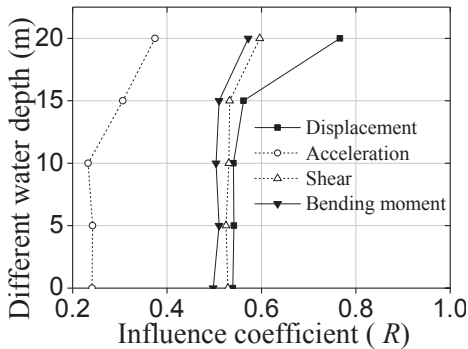


FIG. 5. Influence coefficient.

As shown in Fig. 5 that the influence coefficient R increases with the increasing of water depth. The maximum values of the influence coefficient R of the displacement and acceleration reached 0.77 and 0.38 in the 20m deep water. The maximum values of the influence coefficient R of the bending moment and shearing force reached 0.57 and 0.60 in the 20m deep water. And the effect of the long-period ground motions to the displacement at the bottom of the pier was greatest, while the effect to the maximum acceleration on the top of the pier is the least.

COMPARED OF SHAKING TABLE TEST AND FINITE ELEMENT METHOD

Constant frequency vibration test and sweep frequency vibration test can be done using shaking table. Shaking table and monitoring equipment were shown in Fig. 6.

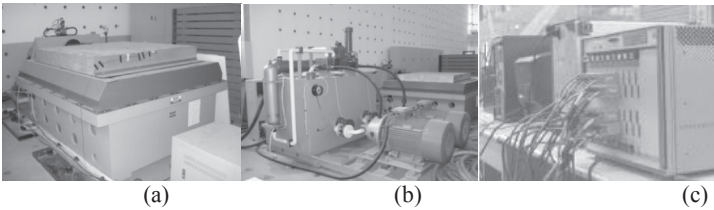


FIG. 6. Vibration equipment: (a) shaking table; (b) hydraulic oil pump vibration; (c) monitoring equipment.

The water tank was fixed on vibration table surface. The pier was fixed at the bottom of the water tank. The size of the water tank is $2.0m \times 1.3m \times 1.5m$. Weight is about 300 kg, as shown in Fig. 7.

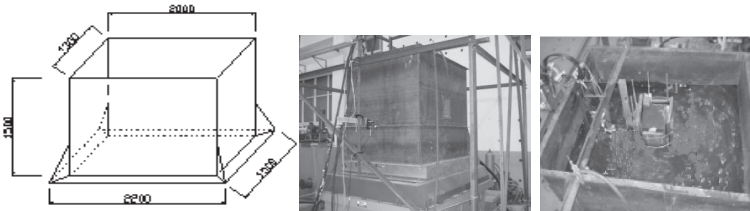


FIG. 7. Physical diagram of pile cap model with water.

In order to make the model test results reflect the character of prototype structure, the similarity which includes geometric shape and material characteristic and boundary conditions and external load and initial movement' conditions should be considered between the test model and the prototype structure, as shown in Table 2.

Table 2. Main Physical Similarity Relation of Dynamic Model

| Category | Physical quantity | Similarity coefficient | Model | Remark |
|---------------------|-------------------|------------------------------|--------|----------------------|
| Material properties | strain ϵ | $\lambda_\epsilon = 1.0$ | 1 | |
| | stress σ | $\lambda_\sigma = \lambda_E$ | 1/6.87 | |
| | Elastic modulus E | λ_E | 1/6.87 | Model design control |
| | Poisson's ratio | $\lambda_\mu = 1.0$ | 1 | |

| | | | | |
|----------------------------|----------------|--|---------|----------------------|
| | μ | | | |
| | Density ρ | λ_ρ | 7.85 | Model design control |
| Geometrical characteristic | length L | λ_l | 1/50 | Model design control |
| Dynamic property | quality m | $\lambda_m = \lambda_\rho \lambda_l^3$ | 1/15924 | |
| | time t | $\lambda_t = \lambda_l (\lambda_\rho / \lambda_E)^{1/2}$ | 0.03 | Dynamic load control |
| | frequency f | $\lambda_f = 1 / \lambda_l$ | 33.5 | Dynamic load control |
| | velocity v | $\lambda_v = \lambda_l / \lambda_t$ | 0.667 | |
| | acceleration a | $\lambda_a = \lambda_l^{-1} \lambda_\rho^{-1} \lambda_E$ | 1 | Dynamic load control |

Dynamic characteristics of the pier in the air and water were analyzed by hammer free attenuation and sine wave frequency sweep test. The first natural vibration frequency was shown in Table 3.

Table 3. The Model Test Results of Dynamic Characteristics

| Category | Natural vibration frequency (Hz) | Period(s) |
|----------|----------------------------------|-----------|
| water | 10.10 | 0.099 |
| No water | 9.21 | 0.109 |

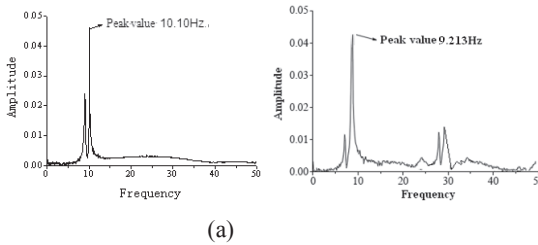


FIG. 8. Dynamic free attenuation fourier spectrum of pier model: (a) in the water; (b) in the air.

It can be seen in Fig. 8, the model natural vibration frequency reduced by 8.8% and the natural period increased by 9.6% compared the test results of pier model in the air and water. Due to the operation error in the experiment, there was somewhat different between the experimental results and the finite element results.

Dynamic Response Analysis of Test Modal

Relative acceleration peak values on the top of bridge pier in the air and water were calculated under sine wave with frequencies of 1Hz and 7Hz, TCU006 and EL-Centro based on the shaking table test and finite element method, which are shown in Fig. 9, Fig. 10 and Fig. 11.

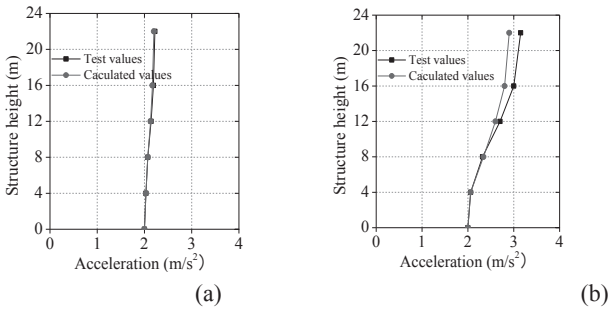


FIG. 9. Relative horizontal acceleration peak values under sine wave which is 200 Gal: (a) 1 Hz; (b) 7 Hz.

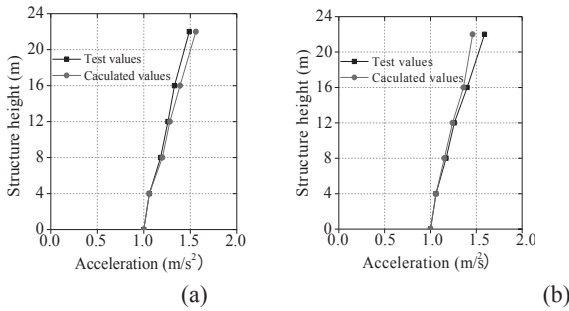


FIG. 10. Horizontal acceleration peak values for 100 Gal under: (a) TCU006; (b) El-Centro.

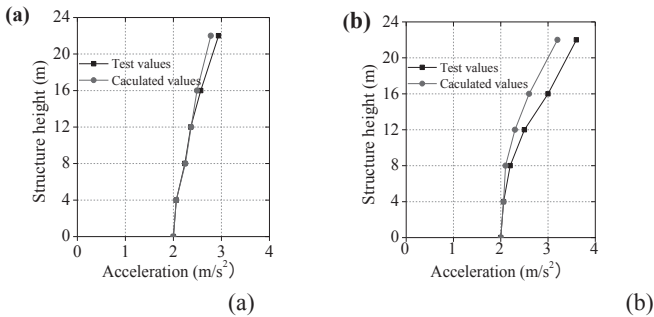


FIG. 11. Horizontal acceleration peak values for 200 Gal under: (a) TCU006; (b) El-Centro.

As shown from Fig. 9 to Fig. 11, dynamic simulation results and experimental results are consistent, and deviation exists only in severalty conditions. The maximum deviation was 10.49% under sine wave which were 7Hz of 200Gal. The maximum deviations were 8.99% and 12.5% under TCU006 and EL-Centro, which were mainly due to the shortcomings of the shaking table to input high frequency dynamic loading. In general, the results from model test and finite element method were in good agreement, which proved the research of the influence of water on

pier under dynamic loads using the finite element method in this paper was reliable.

CONCLUSIONS

(1) The first modal period of the pier increases with the increasing of the water depth. The effect of the water to the natural vibration characteristic of the pier should be considered, when the water depth exceeds a critical value.

(2) The effect of the long-period ground motions to hydrodynamic pressure is greater than that of short-period ground motions in different water depths. There appears obvious peak on the pier of the upper-middle position under long-period ground motions which makes the action point of the hydrodynamic pressure towards the top of pier, and makes the pier of the bottom produce greater bending moment. Thus, ignoring the effect of long-period earthquakes is unsafe to structures.

(3) The maximum shearing force and bending moment at the bottom and the maximum acceleration and displacement on the top of the pier are increased with the increasing of water depth. Greater bending moment and shear force are produced on the pier under the long-period ground motions which make bridge superstructure produce greater dynamic response. Thus it is necessary to consider the effects of the long period earthquakes to the internal force of structure.

(4) The first order natural frequency and the distribution of acceleration peak value along the pier height are compared between the shaking table test and finite element method. The results show that the calculated values from model test and from finite element method are in good agreement, which proves the research of the influence of water on pier under dynamic loads using the finite element method in this paper is reliability.

ACKNOWLEDGEMENTS

This work is financially supported by the Natural Science Foundation of China (51078033) and the Natural Science Foundation of China (51178045).

REFERENCES

- K Y Zhuang and Y L Xu et al. (1997). "Study on the effects to Shanghai under long period earthquakes of TaiWan." *Acta Seismologica Sinica*, Vol. 19(6):634-639.
- S Q Liao and X Z Pi et al. (2005). "Elastic-plastic Analysis of Earthquake Response of Structures Under the Long-period Earthquake Motion." *Building Structure*, Vol. 35(5):24-27
- L I Xie and Y N Zhou et al. (1990). "Characteristics of Response Spectra of Longperiod Earthquake Ground Motion." *Earthquake Engineering and Engineering Vibration*, Vol.10(1): 1-18.
- M M Zang and Q J Chen. (2010). "Site Effect of Long-Period Ground Motion and Dynamic Analysis of Long-Span Bridge Structures." *Structural Engineers*, Vol. 26(1): 118-125.
- Q Wu and Q J Chen. (2011). "Analysis on Long-Period Seismic Responses for High-Rise Frame Structures." *Structural Engineers*, Vol. 27(1): 79-84.

Seismic Damage Rules and Seismic Risk of Tunnel Portals Based on Fuzzy Comprehensive Evaluation Method

ZANG Wan-Jun¹, WANG Zheng-Zheng²

¹ School of Civil Engineering, Fujian University of Technology, No3 Xueyuan Road, University Town, Minhou, Fuzhou City, Fujian Province, China; zwj8810@sohu.com

² School of Civil Engineering, Dalian University of Technology, No.2 Linggong Road, Ganjingzi District, Dalian City, Liaoning Province, China; 66540325@qq.com

ABSTRACT: A fuzzy comprehensive evaluation method was put forward to study the seismic risk of tunnel portals. Through collecting and analyzing information of seismic damage of the tunnel portals after Wenchuan Earthquake, the main influence factors of tunnel damage and its function law were summarized. The risk factors' weight and the membership degree to the risk level were calculated respectively by AHP and trapezoidal membership function and semantic subordinate function. Seismic risk level of tunnel portals was concluded through fuzzy transformation principle and weighted average method. At last, a case was done on a built tunnel by fuzzy comprehensive evaluation. The conclusion could be used to take corresponding measures to reduce seismic risk.

INTRODUCTION

Seismic damage investigation at home and abroad^[1-5] shows that tunnel portals are most vulnerable to earthquake, but is difficult to evaluate seismic risk accurately. People often use such fuzzy language description as "probably", "may". Fuzzy Theory can base the seismic risk analysis and evaluation on science, make ambiguity more quantitative. However, Fuzzy Theory does not rule out subjective question, it deals with the problem of quantitative by fuzzy set theory.

Through collecting and analyzing information of seismic damage of tunnel portals after Wenchuan Earthquake, the main influence factors of seismic are identified and taken as influence factors. The seismic risk level of mountain tunnel portals is concluded through fuzzy comprehensive calculation with AHP and membership function. Finally the fuzzy comprehensive evaluation method is applied in actual engineering earthquake risk assessment.

SEISMIC RISK FACTOR IDENTIFICATION OF TUNNEL PORTALS

Mountain Tunnel Portals Damage in Sichuan due to Wenchuan Earthquake

The author made seismic damage investigation and analysis to 59 mountain tunnels in Sichuan province after Wenchuan Earthquake, laying emphasis on tunnel portals and fault fracture zone section. Seismic damage severity and its classification standard of tunnel portals is described in table 1 and shown in Fig 1. Facts have proved that tunnel portal is one of the weak links and it is a realistic and urgent problem to carry out tunnel portal seismic risk management in high intensity seismic zone.

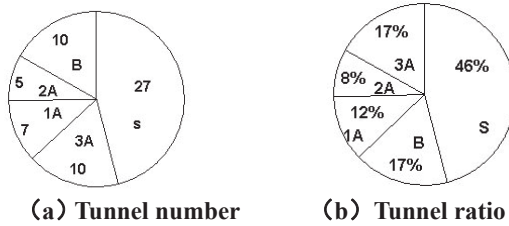


FIG.1 Statistics of seismic damage of tunnel portals in Wenchuan earthquake

Table 1 Degree of seismic damage in tunnel portals

| Level | Description | Tunnel portals | | |
|-------|-------------|---|---|---|
| | | Mountain, rock | Tunnel lining | Walls |
| S | Intact | No collapses and landslides | Intact | Intact, stable |
| B | Light | No collapses and landslides | Local aliation, exfoliating, not interfere with traffic | Slight cracking, tilt or sink, etc, not interfere with traffic |
| A | 1A | Moderate Existing landslide, collapse of the initial signs, not endanger traffic | A small amount of aliation, cracking, may interfere with traffic | Locally cracking, tilt or sink, etc, may interfere with traffic |
| | 2A | More serious Mountain craze, slide, rock mass crack, fail, threaten the traffic | Lots of aliation, exfoliating, cracking, interfere with traffic | Cracking, tilt or sink is more serious, Threaten the traffic |
| | 3A | Serious Mountain craze, slide, rock tumble and block tunnel entrance, threaten the traffic | There are aliation, exfoliating and rock falling at the top of tunnel, interfere with traffic | Cracking, tilt or sink is extensive. Threaten the traffic |

Seismic Risk Factors of Tunnel Portals

When make seismic risk assessment of tunnel portals, it need to make seismic risk factors identification at first.

Seismic Factors

Two seismic factors, seismic intensity and epicenter distance, are considered as part of risk factors in terms of seismic effect. According to the statistics of seismic fortification intensity and practical seismic intensity of 15 tunnels which have happened severe seismic damage or more during Wenchuan earthquake, the real seismic intensity is far bigger than seismic fortification intensity, the biggest difference is 4. Statistically analyze the relationship between tunnel portals and seismic faults during Wenchuan earthquake, shown in Fig 2.

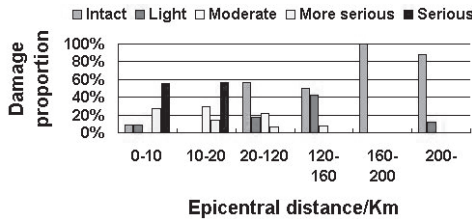


FIG.2 Relationship between tunnel damage degree and the epicenter or seismogenic fault distance.

Tunnels are mainly within 20km whose portals happened more serious damage or more, a total of 14, accounting for 93% of a total of 15 tunnels whose portals happened more serious seismic damage or more; and 82% of a total of tunnels are within the epicenter of 10 km. Damage severity drops off rapidly with the increasing of epicentral distance, and there are basically no more serious damage or more over 20 km. So, epicentral distance is important seismic risk influence factors for tunnel portals.

Engineering Geological Conditions

Slope conditions of tunnel, surrounding rock quality, fault and katamorphic zone are the risk factors reflecting the tunnel portal geological conditions. Tunnel portals and slope section are the weakest parts vulnerable to earthquake. There are 40.5% of tunnel portals which have induced seismic damage to tunnels due to secondary disasters during Wenchuan earthquake. Therefore, when make seismic risk assessment, great importance should be attached.

Overall, the worse surrounding rock quality is the more serious tunnel damage is. Counting up 8 tunnels damaged seriously in Wenchuan Earthquake , total length of

tunnel portals is 1879m, and damaged length is 1387m, of which grade V surrounding rock is 51%, grade IV is 37%, grade III is 8% and grade II is 4%.

It can be seen from Fig.3 that seismic damage rate of tunnel portals is up to 72% in fault fracture zone.

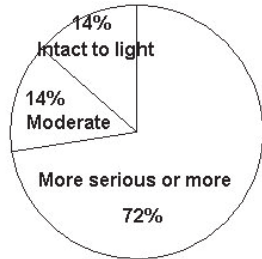


FIG.3 Seismic damage distribution of tunnel portals in fault and fracture zone

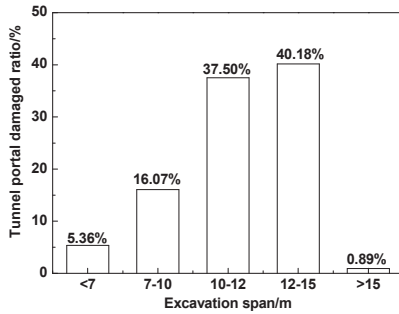


FIG4 Proportional relationship between excavation span and number of tunnel portals damaged

Tunnel Structures Conditions

The risk factors related to tunnel structure conditions include tunnel portal type, cross-section size and shape, supporting structure and stiffness, construction situation, and burial depth. Take the 15 x 2 tunnels damaged seriously during Wenchuan Earthquake as an example^[6], tunnel portal type are as followings: 9 end wall ,1 wing wall ,3 post, 7 bench, 6 cutting face ,4 no portals. Tunnels with cutting face portal are roughly well such as Wenchuan end of Long dong zi tunnel; end wall and post tunnel portal damage most ,a total of 12; tunnels whose portals not yet applied are serious.

Seismic safety of tunnels with round curved wall cross-section is obviously advantageous over that with the rectangular straight one. The greater the basal area is the worse the aseismic performance is for the tunnel with same cross-section shape. According to the literature (Wangt, et. al, 2012), it can be seen that damage ratio is eight times when excavation span is 12 to 15 m than 7 m. They are not counted when the span is more than 15 m because of the small sample, shown in Figure 4.

From statistics material about damage of tunnel portals in Wenchuan Earthquake within 50 km seismogenic fault, the ratio that tunnel portals without invert having suffered more serious damage or more is 43.75%, moderate seismic damage ratio is 37.5%. Damage degree of tunnel with lining is obviously less than without lining.

Construction methods affect integrity of tunnel and surrounding rock system. NATM can better protect surrounding rock than Mining Method and make them share loading. Construction defects are also important factors affecting tunnel aseismic performance. Tunnels in VI degree seismic intensity area also occurred more serious damage. Data shows that the tunnels construction had seriously

defective, furthermore, the flaws paragraph highly tallied with the paragraphs where damage happened.

Generally speaking, burial depth of tunnel and damage severity is negatively related. According to Wang zheng zheng's literature, when burial depth is within 30m, tunnel portal stays basically damaged(94.65%); more than 40m, tunnel portal is essentially in good condition, only nearly 1% damaged.

In addition, formation lithology has influence on tunnel seismic dynamic response, and ground stress is also a factor that may cause seismic damage to the tunnel. Due to the lack of enough data, this paper ignores these factors.

FUZZY COMPREHENSIVE ANALYSIS OF SEISMIC RISK

Factor Set of Evaluation Model

Three primary factors strongly influencing seismic damage are selected to set up factor set.

First level factor set:

$$U=\{U_1, U_2, U_3\} \quad (1)$$

U_1 、 U_2 、 U_3 in the formula are tunnel structure conditions, ground motion parameter, engineering geology conditions separately.

Second level factor set:

$$U_1=\{u_{11},u_{12},u_{13},u_{14},u_{15}\}, U_2=\{u_{21},u_{22}\}, U_3=\{u_{31},u_{32},u_{33}\} \quad (2)$$

In the formulae, u_{11} 、 u_{12} 、 u_{13} 、 u_{14} 、 u_{15} are tunnel portal type, construction situation, supporting structure and stiffness, cross-section size and shape, burial depth separately; u_{21} 、 u_{22} are seismic fortification intensity, epicenter distance or seismogenic fault distance separately; u_{31} 、 u_{32} 、 u_{33} are slope conditions, fault and katamorphic zone, surrounding rock grade separately.

Weight Value of Risk Factors

Fuzzy A represents set of weights, which is a combination of each weight, and is called factor weight set, weight set for short.

$$A=\{a_1, a_2, \dots, a_m\} \quad (3)$$

Some conditions should be needed by each weight:

$$\sum_{i=1}^m (a_i = 1), a_i \geq 0, (i = 1, 2, \dots, m) \quad (4)$$

Calculate value of the weight of risk factors with AHP method. Usually take nine indicators for relative importance comparison.

Evaluation Set of Model

Refer to "Highway bridge and tunnel engineering design safety risk assessment guide (for trial implementation)" and related seismic risk evaluation literature of tunnel, risk assessment is divided into 5 levels, see table 2.

Table 2 Risk gradation

| Risk grade | Very low | Low | Medium | High | Extremely high |
|------------|----------|-----|--------|------|----------------|
| Risk index | 1 | 2 | 3 | 4 | 5 |

Tunnel risk evaluation set can be represented as the letter V by the risk level of tunnel.

$$\begin{aligned}
 V &= \{V_1, V_2, V_3, V_4, V_5\} \\
 &= \{ \text{Very low, low, medium, high, very high} \} \\
 &= \{1, 2, 3, 4, 5\}
 \end{aligned}$$

Membership Function of Risk Factors

According to the expert experience and many investigations, trapezoidal membership function is adopted for its convenient and good consistency between assessment result and field test results. Seven seismic influence factors as tunnel portal type, cross-section size and shape, burial depth, seismic fortification intensity, epicenter distance or seismogenic fault distance, fault and katamorphic zone, surrounding rock grade have good quantitative regularity. Their trapezoidal membership functions are calculated according to the following formula:

$$r_{ij(k)}(x) = \begin{cases} \frac{x-a_1}{a_2-a_1} & a_1 \leq x \leq a_2 \\ 1 & a_2 < x \leq a_3 \\ \frac{x-a_3}{a_3-a_4} & a_3 < x \leq a_4 \\ 0 & a_1 > x \text{ or } x > a_4 \end{cases} \quad (5)$$

In the formula, $r_{ij(k)}$ is corresponding membership of No. ij risk factors and No. k risk level; $a_i (i=1,2,3,4)$ is reference limit values of assessment index to assessment standard.

For construction situation, supporting structure and stiffness, slope conditions three factors, because their regularity is not easy to quantify or lack of statistical data, semantic subordinate function is referred^[8] to effectively convert semantic variable value into related fuzzy number that decision-making personnel offers.

Calculate the membership value of seismic risk factors of tunnel portal and get the seismic risk judgment matrix based on the first level risk factors:

$$R_m = \begin{bmatrix} r_{11} & \cdots & r_{1k} \\ \vdots & & \vdots \\ r_{n1} & \cdots & r_{nk} \end{bmatrix} \quad (6)$$

In this formula, $m=1, 2, 3$ represents tunnel structure conditions, ground motion parameter, engineering geology conditions separately; r_{ik} is the corresponding membership of NO. i secondary risk factors k level risk grade of some primary risk

factor .

Fuzzy Comprehensive Evaluation

Make fuzzy comprehensive evaluation to relevant risk factors of tunnel portals seismic risk by application of fuzzy transformation principle and weighted average method, and get fuzzy comprehensive evaluation set B.

Fuzzy comprehensive evaluation set of first class risk factor $B_m = A_m \circ R_m$

In this formula, A_m is factor weight set for second class factors under first class risk factor.

Construct matrix R ,

$$R = \begin{bmatrix} B_1 \\ B_2 \\ B_3 \end{bmatrix}, \text{ so } B = A \circ R \tag{7}$$

A is first class risk factor weight set.

Process the assessment results with weighted average method and get:

$$V = \sum_{j=1}^n b_j v_j / \sum_{j=1}^n b_j \tag{8}$$

APPLICATION EXAMPLE

Lingshan tunnel is a double hole separated tunnel at Yalu highway, crossing Anninghe fault zone many a time with □ degree seismic fortification intensity and 0.3g seismic peak acceleration, it is necessary to carry on seismic risk assessment.

Seismic risk factor parameter of Lingshan tunnel portal is shown in table 3. Make fuzzy comprehensive evaluation calculation, evaluation results are shown in table 4.

Table 3 Seismic risk factors of Ling Shan tunnel portals

| Tunnel portal | Risk factors | | | | |
|---------------|-------------------|---------------------------------|----------------|------------------------|-------------------|
| | Seismic intensity | Surrounding rock classification | Burial depth/m | Construction situation | Excavation span/m |
| Entrance | □ | □ | 4.1 | Basically standard | 12 |
| Exit | | | 1.2 | | |

(continued)

| Tunnel portal | Risk factors | | | | |
|---------------|------------------------------------|--------------------------------|-----------------------------|--------------|----------------------------|
| | Supporting structure and stiffness | Seismogenic fault distance /km | Slope conditions | Portal type | Fault and katamorphic zone |
| Entrance | Basically reasonable | 3.3 | Exiting soil rock interface | Cutting face | No |
| Exit | | | | | Yes |

Table 4 Evaluation result of seismic risk of Ling Shan tunnel portals

| Tunnel portal | Risk index | Risk levels |
|---------------|------------|----------------|
| Entrance | 3.644 | High |
| Exit | 4.741 | Extremely high |

Seismic risk management for Ling Shan tunnel portals should be strengthened for its high and extremely high seismic risk levels of import and export respectively, and shock absorption measures should be taken to reduce seismic risk.

CONCLUSIONS

(1) 10 seismic risk factors of portals were selected by two levels through the analysis of seismic damage of mountain tunnel portals in Wenchuan earthquake.

(2) Weights of risk factors were calculated with AHP, and seismic risk multistage fuzzy comprehensive evaluation is carried out to the risk factors related of tunnel portals by the application of fuzzy transformation principle and weighted average method taking trapezoidal membership function and semantic membership function.

(3) Fuzzy comprehensive evaluation model is applied to existing tunnel to assess seismic risk of portal and provide the reference for operation risk management.

REFERENCES

- Dowing C.H. and Rozen A. (1978). "Damage to rock tunnels from earthquakes shaking." *Journal of the geotechnical engineering Division*.104(1):175-191.
- LI TIAN-bin. (2008). "Failure characteristics and influence factor analysis of Mountain tunnels at epicenter zones of great Wenchuan Earthquake." *Journal of Engineering Geology*, 16(6):742-750.
- WANG Zheng-zheng, GAO Bo, JIANG Yuan-jun, et al. (2008). "Investigation and assessment on mountain tunnels and geotechnical damage after the Wenchuan earthquake." *Science in China Series E: Technological Sciences*, 52(2): 546-558.
- Wang W L, Wang T T, Su J J, et al. (2001). "Assessment of damage in mountain tunnels due to the Taiwan Chi-Chi earthquake." *Tunneling and Underground Space*

Technology.16(1): 133–150.

Yoursself M.A. Hashish, Jeffrey J.Hook, el al. (2001). “Seismic design and analysis of underground structures.” *Tunneling and Underground Space Technology*. 16: 247–293.

ZHENG Qing, GAO Bo, SHEN Yu-sheng. (2010). “Investigation of Mountain Tunnel Earthquake Damage and Study on Remedial Measures.” *JOURNAL OF SHI JIA ZHUANG TIEDAO UNIVERSITY(NATURAL SCIENCE)* .23(4): 46–47.

WANG Zheng-zheng, ZHANG Zhe, GAO Bo, et al. (2012). “Factors of seismic damage and fuzzy synthetic evaluation on seismic risk of mountain tunnel portals.” *Journal of Central South University (Science and Technology)*.43(3): 1122–1129.

Gwo-Hshiung Tzeng, Jih-jeng Huang. (2011). “Multiple Attribute Decision Making: Methods and Applications.” *Boca Raton: CRC Press*,:55-67.

Influence of Overlying Goaf Dip Angle on Stability of Highway Tunnel during Excavation

Ya-peng Fu¹, Yong Fang², Ge Cui¹ and Bin Yang¹

¹Master candidate, Key Laboratory of Transportation Tunnel Engineering, Ministry of Education, Dept. of Civil Engineering, Southwest Jiaotong University, Chengdu 610031, China, Email: fyp19900328@foxmail.com, cui114@126.com, 285525675@qq.com

²Associate Professor, Key Laboratory of Transportation Tunnel Engineering, Ministry of Education, Dept. of Civil Engineering, Southwest Jiaotong University, Chengdu 610031, China, Email: fy980220@swjtu.cn

ABSTRACT: In order to study the influence rule of the security and stability under different goaf dip angles during the tunnel excavation when the highway tunnel is approaching to the goaf, the computation models are built and simulated numerically with the finite difference software of FLAC, relying on the Tian Pingzhai tunnel of Dazhou-Wanzhou highway. Under the condition of the certain tunnel buried depth, thickness of coal seam and distance, a comparative analysis on the displacement and axial force of primary support resulted from the changement of the overlying goaf dip angle has been conducted. The impact on the displacement and deformation of surrounding rock for different goaf dip angles are also further explored. The simulation results indicate: with the increasing of dip angle, the added forces acting on primary structure will decrease and when the dip angle is less than 5°, the impact on the added forces are most significant. The changement of the overlying goaf dip angle brings remarkable impact to vault settlement and horizontal convergence and the influence on left hance which is close to the mined-out area is greater than the right hance but it has little impact on the displacement of arch bottom. It is suggested that Pre-firming and Treatment for mined-out areas should be used.

INTRODUCTION

Today, along with the development of our country's highway construction, road network becomes more and more intensive, and the route will inevitably go through the unavoidable routing factors, such as the goaf. Because of the uneven settlement and deformation of overlying strata, it is very easy to cause the deformation and crack of the highway tunnel lining structure and the fluctuation in road surface, which pose a serious security hidden danger and potential hazard for the highway

tunnel normal operation, maintenance and repair. Any disturbance to the surrounding rock is likely to break stable state of the current goaf and then the abandoned mine goaf becomes activity. The close-spaced tunnel construction will cause the deformation of the surrounding strata and then change the stress performance of the structure.

Goaf is produced by the manmade excavation or natural geological movement. If the probe is not clear and the preparation for construction is inadequate, it will bring certain difficulty to construction when the expressway tunnel passes through the mined-out region. Right now, there are many test results about the mined-out region in our country. Jinqi XIANG, et al. (1999), puts forward some measures to deal with the tunnel settlements and cracking problems based on the analysis of the mined-out area how to affect the Jiang Jiawan tunnel. Using the finite element numerical simulation, Zhipei ZHANG, et al. (2006) makes a study on the tunnel surrounding rock stress and deformation characteristics when tunnel passes through the mined-out region. Shuren WANG, et al. (2008), illustrates the underlying goaf tunnel deformation characteristics. Zhisheng CUI, et al. (2011), makes a study of the effects of tunnel lining structure at various intervals between the tunnel and the underlying mined-out region. Based on the indoor test, Zhixiang ZHANG, et al. (2011), makes a research on the stability of underlying goaf under the action of traffic load.

From the general situation of domestic researches, it can be found that many scholars treat the goaf as the cavity. In fact, the mined-out area is divided into three zones (caving zone, fractured zone and bent zone), which are filled with the broken rock. The author intend to make it equivalent to the homogeneous rock mass, but the material parameters are less than the original rock mass. The influence rule of the tunnel structure resulted from the different overlying goaf dip angles can be obtained by the finite difference numerical method.

NUMERICAL MODEL AND CALCULATION PARAMETER

Based on the design drawing, the tunnel depth is about 250m. The width of the coal seam which has influence on the Tian Pingzhai tunnel is about 0.3-0.6m. In the model, the coal thickness is 0.5m, the distance between the caving zone and the tunnel is 2m.

Model Establishment and Calculation Condition

According to the previous tunnel mechanics experience, the conditions of the model selection are as follows: the distance between the lateral boundary and the tunnel boundary is about 3-5 times of the tunnel diameter, the distance from the lower boundary to the bottom of tunnel is approximately 2-3 times of the tunnel diameter. With Tian Pingzhai tunnel as the research object to establish numerical model, due to the goaf parallel to the longitudinal direction of the tunnel, there is no need to build 3D numerical model, meanwhile considering the influence resulted

from the tunnel excavation and the Boundary Effect, tunnel's buried depth is 250m, and the model is 140m wide, 1m long, 320m high, as is shown in Fig.1. Vertical displacement constraints are imposed in the lower boundary, the level displacement constraints are applied in the left and right boundary and the axis displacement constraints are applied in the front and behind boundary of the model.

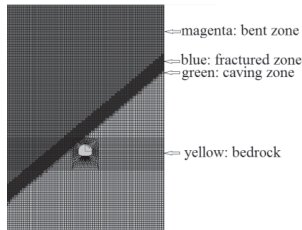


FIG. 1 The numerical simulation model

According to the research purpose, the distance between the tunnel and the caving zone is fixed, and with the changing of the overlying goaf dip angle, the influence rule of stability of surrounding rock and tunnel structure during the tunnel excavation can be deduced.

Calculation Parameter Selection

Mechanics Parameter Selection

Numerical simulation calculations contain the simplification of the types of the rock mass and the appropriate mechanical parameters' selection. According to the geological investigation date for the Tian Pingzhai tunnel and the design specification of highway tunnel, the property parameters are shown in the following Table 1.

Table 1. Material parameters of numerical model

| contents | E/(GPa) | V | ρ /($\text{kg}\cdot\text{m}^{-3}$) | C/(kPa) | φ (°) |
|-----------------|---------|------|---|---------|---------------|
| bedrock | 2 | 0.45 | 2000 | 200 | 27 |
| caving zone | 1 | 0.35 | 1700 | 0 | 20 |
| fractured zone | 1.5 | 0.4 | 1850 | 125 | 23 |
| bent zone | 2 | 0.45 | 2000 | 200 | 27 |
| Primary support | 29.3 | 0.2 | 2480 | - | - |

Height of Goaf "three zones"

Presently, the height of the goaf "three zones" can be obtained by empirical formulas. This paper aims to study the coal seam named K6-1 which has influence on this tunnel and makes assumptions that this coal production way is the single-layer exploitation and the thickness of this coal seam is 0.5m.

(1). the height of caving zone

a) gentle inclined ($0^\circ\sim 35^\circ$)and middle lean ($36^\circ\sim 54^\circ$)coal seams

$$h_m = m/[(k-1)\cos\alpha] \quad (1)$$

Where h_m is the thickness of caving zone (m), m is the coal-seam thickness (m), k is the coefficient of bulk increase, the value is 1.4 and α is the coal seam dip angle.
 b) steep inclined coal seams ($55^\circ\sim 90^\circ$)

$$H_m = (0.4 \sim 0.5)H_{li} \tag{2}$$

Where, H_m is the thickness of caving zone (m) and H_{li} is the thickness of fractured zone (m).

(2). the height of fractured zone

Based on the Tian Pingzhai tunnel design dates, the level of surrounding rock is V, thus the empirical formula used to calculate the height of fractured zone is as follows:

a) gentle inclined ($0^\circ\sim 35^\circ$)and middle lean ($36^\circ\sim 54^\circ$)coal seams

$$h_1 = 10(\sum m)^{0.5} + 5 \tag{3}$$

Where, h_1 is the height of fractured zone (m), m is the coal seam thickness (m).

b) steep inclined coal seams ($55^\circ\sim 90^\circ$)

$$H_{li} = 100Mh/(7.5h + 293) \pm 7.3 \tag{4}$$

Where, H_{li} is the height of fractured zone (m), M is the coal seam thickness (m), and h is the vertical dimension to the mining coal face and the value is 2m.

(3). the height of bent zone

The height of bend zone is mainly affected by the mining depth, generally from the upper of the fractured zone to the surface. The bent zone height is far greater than the sum of the other two when the mining depth is great. Based on the above calculation formulas, the heights of “three zones” are as shown in Table 2:

Table 2. Heights of “three zones”

| dip angle/(°) | caving zone height/(m) | fractured zone height/(m) | bend zone height/(m) |
|---------------|------------------------|---------------------------|----------------------|
| 0 | 1.250 | 12.071 | |
| 5 | 1.255 | 12.071 | |
| 10 | 1.269 | 12.071 | |
| 15 | 1.294 | 12.071 | |
| 20 | 1.330 | 12.071 | from the upper |
| 25 | 1.379 | 12.071 | of |
| 30 | 1.443 | 12.071 | the fractured zone |
| 35 | 1.526 | 12.071 | to the surface |
| 40 | 1.632 | 12.071 | |
| 45 | 1.768 | 12.071 | |
| 50 | 1.945 | 12.071 | |
| 55~90 | 3.812 | 7.625 | |

ANALYSIS OF THE CALCULATION RESULTS

Analysis of the Displacement

The vault settlement, convergence displacement and arch bottom uplift are selected as analysis section. The monitoring section is shown in Fig.2. The

calculation results explain that the vault settlement is 3.945cm, the arch bottom uplift is 4.530cm and the convergence displacement is 9.021cm without goaf. The situation in which the displacement of vault, arch bottom, left hance and right hance changed with dip angle is shown in Fig.3, and the Fig.4 is used to show the tunnel displacement difference between the overlying goaf layer and the same normal strata.

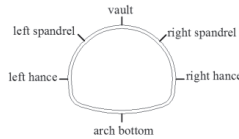


FIG. 2. The monitoring section

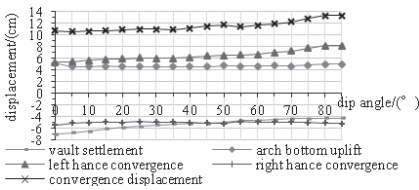


FIG. 3. The displacement in different position

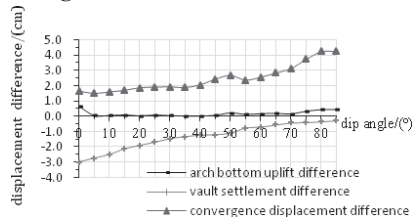


FIG. 4. The displacement difference in different position

On the basis of the Fig.3, under the condition of the certain tunnel buried depth, the coal seam thickness and distance, the dip angle of overlying goaf has significant influence on the convergence displacement and vault settlement. Along with the gradually increased overlying goaf dip angle, the vault settlement decreases slowly, while the arch bottom uplift and the right hance convergence are almost remained the same, but the left hance convergence increases linearly. It is demonstrated that the overlying goaf has influence on the displacement of surrounding rock. For the entire, the vertical displacement reduces relatively, while the horizontal displacement increases. Especially, the displacement approaching the goaf changes greatly, hence, the lining structure in this position deforms relatively large which is bad for the lining structure. As a result, Pre-firming and Treatment for goaf areas should be used.

From the Fig.4, the vault settlement difference almost decreases linearly and finally the value is approaching zero which is demonstrated that the increase of dip angle brings less impact to vault settlement. But the increase of dip angle brings greater impact to convergence displacement.

Finally, according to the design specification of highway tunnel, the allowable convergence value is 20cm under such circumstances. From the simulation results, the maximum convergence value is 13.291cm; therefore, the lining structure meets the design requirements.

Analysis of internal force of primary support

Analysis of axial force of primary support

The axial force of vault and arch bottom are selected as analysis section. As can be seen from the calculation results, the axial force of vault is 5931kN and the arch bottom is 2540kN without goaf. The situation in which the axial force of vault and arch bottom changed with dip angle is shown in Fig.5, and the Fig.6 is used to show the axial force difference between the overlying goaf layer and the same normal strata.

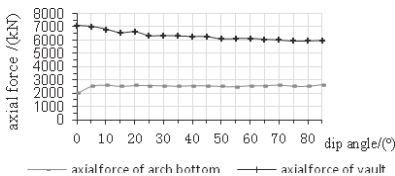


FIG. 5. The axial force of vault and arch bottom

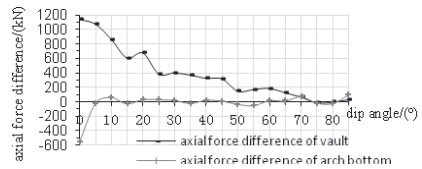


FIG. 6. The axial force difference of vault and arch bottom

As can be seen from Fig.5 and Fig.6, under the condition of the certain tunnel buried depth, the coal seam thickness and distance, the existence of overlying goaf brings a certain impact to the axial force of primary support. When the dip angle is increased from 0° to 5°, the axial force of arch bottom increases significantly, but when the dip angle is larger than 5°, the axial force of arch bottom tends to be stable and the axial force difference of arch bottom is relative small, thus the influence upon axial force of arch bottom can be neglected. Otherwise, along with the dip angle is increased gradually, the axial force of vault decreases slowly and finally its value is increasingly approaching to the axial force of vault in the normal layer. Hence, in case of the overlying goaf, it should ensure the mechanical properties of the upper structure.

Analysis of axial force of bolt

The vault, left spandrel, right spandrel, left hance and right hance are selected as the bolt axial force monitoring position. When the goaf is not present, the calculation results have illustrated that the axial force of bolt in vault, left spandrel, right spandrel, left hance and right hance are, in order, 0.7107kN, 2.817kN, 3.026kN, 10.24kN, 10.35kN. The situation in which the axial force of bolt changed with dip angle is shown in Fig.7, and the Fig.8 is used to show the axial force difference of bolt between the overlying goaf layer and the same normal strata.

As can be illustrated from Fig.7, the dip angle of overlying goaf has little influence on axial force of bolt in right spandrel. When the dip angle is less than 5°, the changement of dip angle brings great impact to axial force of bolt in vault, left hance and right hance and the all three almost increase linearly. Nevertheless, when the dip

angle changes from 5° to 25° , the axial force of bolt in vault presents a tendency of linear decrease and after the dip angle is greater than 25° , it almost remains stable. When the dip angle changes from 5° to 55° , along with the gradually increased dip angle, the axial force of bolt in left hance is decreased slowly, but after the dip angle is greater than 55° , the axial force of bolt in left hance increases linearly greatly and the added value is 12.684kN. With the increase of the dip angle, the axial force of bolt in left spandrel increases when the dip angle is less than 45° , but after the dip angle is bigger than 45° , it decreases slowly and becomes stable finally.

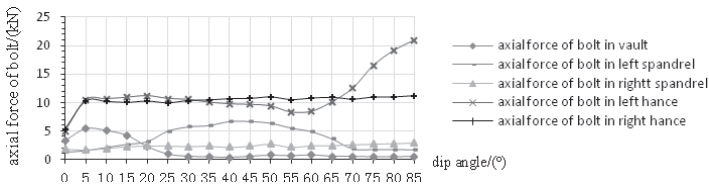


FIG. 7. The axial force of bolt

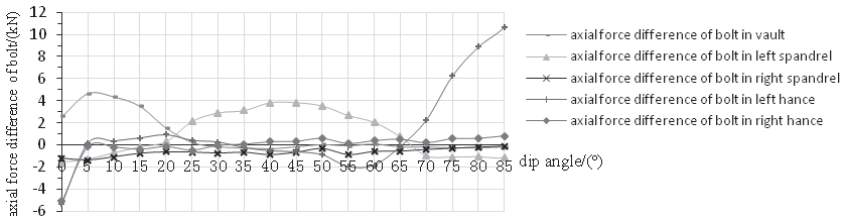


FIG. 8. The axial force difference of bolt

Based on the Fig.8, it is also illustrated that the changement of the overlying goaf dip angle brings remarkable impact to the axial force of bolt in vault, left spandrel and left hance. Instead, it has little influence on the axial force of bolt in right spandrel and right hance. Therefore, Pre-firming and Treatment for goaf areas should be used when tunnel approaching to the goaf layer. This figure has further demonstrated the above conclusions.

CONCLUSION

This paper regards the overlying goaf rock mass as the homogeneous rock mass. Under the condition of the certain tunnel buried depth, the coal seam thickness and distance, some conclusions can be deduced:

Firstly, the changement of the overlying goaf dip angle brings remarkable impact to vault settlement and horizontal convergence. Meanwhile, the influence on left hance which is close to the mined-out area is greater than the right hance, thus the

convergence displacement mainly come from the left hance. Besides, it has little impact on the displacement of arch bottom.

Secondly, the chagement of the overlying goaf dip angle brings remarkable impact to the axial force of upper lining structure. But when the dip angle is less than 5° , the impact on the bottom is always significant. Therefore, under the condition of small dip angle, axial force should be controlled within the allowable value.

Above all, Pre-firming and Treatment for mined-out areas should be used or the bearing capacity of lining structure should be improved so as to meet the design and application requirements.

ACKNOWLEDGEMENTS

This paper is supported by: the National Natural Science Foundation of China (No: 51278422, 50925830); National 973 Plan Topics of China (No: 2010CB732105); National Science and Technology Pillar Program of China (No: 2012BAG05B03); Sichuan Youth Science and Technology Foundation, China (No: 2012JQ0021).

REFERENCES

- The Industry Standard of the People's Republic of China. (2004). "Code for Design of Road Tunnel (JTG D70—2004)" *M. Beijing: China Communications Press.*
- Xiang Jinqi, Qin Zhenggang, Wei Xiangyang. (1999). "Effect and treatment measures associated with mined-up regions for Railway tunnels." *J. West-China Exploration Engineering*, (5): 177-178.
- Wang Shaobin. (2005). "Stability Analysis of Underlying Goaf in Bo Shudi Railway Tunnel Construction." *J. Railway Construction*, (12): 30-31.
- Liu Jinghua, Wang Zhuwen, Zhu Shi, Weng Aihua, Xia Anying. (2005). "The geophysical exploration about exhausted area and sinking area in coal mine." *J. Journal of China Coal Society*, 30(6): 715-719.
- Wang Shu-ren, Shen Nai-qi, Zhang Hai-qing, Song Li-zhi. (2008). "Numerical analysis of deformation characteristics for highway tunnels through the mined-up regions." *J. China Mining Magazine*, 17(3):76-81
- Cui Zhisheng, Zhao Kai, Gong Jianwu. (2011). "Numerical Simulation Analysis on Effect of Underlying Goaf in Road Tunnel Construction." *J. Exploration Engineering (Rock & Soil Drilling and Tunneling)*, (07): 76-79
- Zhang Zhixiang; Zhang Yongbo; Zhao Zhihui; Chen Long. (2011). "Experimental Study on the Stability Analysis of Goaf Beneath Tunnel under Traffic Load." *J. Journal of Taiyuan University of Technology*, (05): 534-538
- Zhang Zhipei; Peng Hui; Yang Xiping. (2011). "Analysis and Study on Stability When Xikouchi Tunnel Excavated Through Mine Goaf." *J. Coal Engineering*, (7):70-72.

Stability Analysis of Landslide Dam under Rainfall

Pei-Hsun Tsai¹, Zheng-Yi Feng², Fan-Chieh Yu³ and Jian-Han Lin⁴

¹ Associate Professor, Department of Construction Engineering, Chaoyang University of Technology, 168 Jifong E. Rd., Wufong District, Taichung, 41349, Taiwan; phtsai@cyut.edu.tw

² Professor, Department of Soil and Water Conservation, National Chung Hsing University, 250, Kuo-Kuang Rd. Taichung, 40227, Taiwan; tonyfeng@nchu.edu.tw

³ Professor, Department of Soil and Water Conservation, National Chung Hsing University, 250, Kuo-Kuang Rd. Taichung, 40227, Taiwan; fcyu@nchu.edu.tw

⁴ Graduate Student, Department of Construction Engineering, Chaoyang University of Technology, 168 Jifong E. Rd., Wufong District, Taichung, 41349, Taiwan; jonuslarry@yahoo.com.tw

ABSTRACT: Failure of a landslide dam might occur by river discharge or rainfall. A rise of the upstream water level of a landslide dam and rain infiltration into the dam body increase pore water pressure and the weight of the dam. In this study, transient seepage analysis of rainfall infiltration and dam stability analysis are performed. A two-phase flow simulation using the FLAC finite difference code is adopted to analyze unsaturated seepage flow in transient fluid-mechanical calculations. The safety factor of dam stability is evaluated using the shear strength reduction technique. The parameters discussed in this study include the rising speed of the water level, rain infiltration, and the hydraulic conductivity of soil. The results show that the time to slope failure of the dam is approximately 247 min when only the effect of the rising upstream water level of the dam is considered. The failure time decreases to 189 min when the rain infiltration and rising upstream water level of the dam are considered. The results also indicate that the hydraulic conductivity of the dam affects dam failure time.

INTRODUCTION

Landslides and debris flows commonly occur after heavy rainfall. Waste materials resulting from landslides and avalanches can obstruct a river and create a landslide dam. Unlike manmade dams with a compacting process and filtering materials, a landslide dam is formed by a mixture of unconsolidated soil and rock in a naturally unstable state. The water level typically rises rapidly upstream of a landslide dam because of continuous rainfall. Landslide dams are often unstable and dangerous because flash floods might occur downstream if the landslide dam fails. Sliding failure can occur in the dam body because of an increase in pore water pressure. When rainfall occurs or the water level rises upstream, the water infiltrating into the dam

causes an increase in water content and pore water pressure, which is caused by transient seepage flow in unsaturated soils. The pore water pressure profile can be analyzed using a numerical transient analysis of a saturated-unsaturated seepage flow model. For stability analysis of landslide dams, the shear strength reduction technique is used to obtain the safety factor of the dams and to locate the corresponding critical slip surface. In numerous studies, the finite difference and finite element methods were used to perform 2D transient seepage flow analyses using the saturated-unsaturated seepage theory (Ng et al., 1998; Xu et al., 2003; Huang and Jia, 2009; Fu and Jin, 2009). Experimental testing regarding the stability analysis of an unsaturated slope has been studied using small-scale models (Orense et al., 2004; Tohari et al., 2007; Schnellmann et al., 2010; Egeli and Pulat, 2011).

The influence of the hydraulic conductivity of dam and rising speed of the water level on the dam failure time has not been fully examined. In this study, the relationship between the dam stability and the distribution of moisture inside the dam induced by influencing parameters was examined using a transient analysis. In addition, a parametric study was performed by varying the rising speed of the water level and the saturated hydraulic conductivity of soil.

NUMERICAL MODEL

Landslide Dam Configuration

A FLAC code with a two-phase flow model was adopted to analyze the timing of the slope failure when the water level rose upstream of the dam. A typical configuration and finite difference mesh for the landslide dam is shown in Fig. 1. The dam, with a height of 4 m and a length of 14 m, was assumed to be situated above a riverbed. The slope angles of the upstream and downstream faces of the dam were set as 34° , which is close to the angle of repose of the dam materials.

To analyze the influence of the rising speed of the upstream water level on dam stability, three water level rising speeds ($v = 3.33 \times 10^{-3}$, 6.66×10^{-3} and 13.33×10^{-3} m/s) were studied. To estimate the effects of the hydraulic conductivity of soil on the stability of the landslide dam, three saturated hydraulic conductivities of soil ($K_s = 8.57 \times 10^{-3}$, 8.57×10^{-4} and 8.57×10^{-5} m/s) were used for analyses.

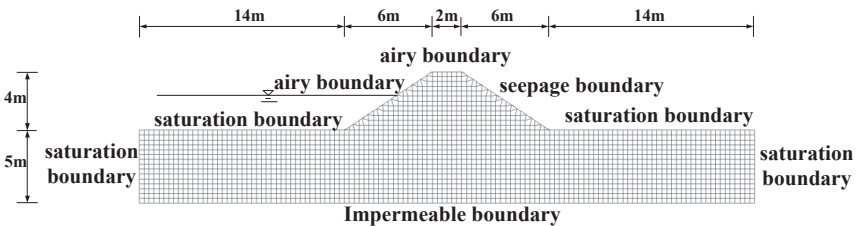


FIG. 1. Typical finite difference mesh for landslide dam.

Seepage Flow Modeling of Unsaturated Soil

The transient seepage flow analysis of the dam after the upstream water level rises is

described by Richards' equation (1931).

$$C \frac{\partial h}{\partial t} = \frac{\partial}{\partial x} \left(K_x(h) \frac{\partial h}{\partial x} \right) + \frac{\partial}{\partial y} \left(K_y(h) \frac{\partial h}{\partial y} + 1 \right), \quad (1)$$

where h is the water pressure head, and $K_x(h)$ and $K_y(h)$ are the hydraulic conductivity in the x and y directions, respectively. C is the specific moisture capacity, t is time, x is the horizontal coordinate, and y is the vertical coordinate.

A model proposed by van Genuchten (1980) is used to determine the relationship between water pressure head, moisture content, and hydraulic conductivity. The relationship between soil moisture and water pressure head is expressed as:

$$S_e = \begin{cases} \frac{1}{\left(1 + |\alpha h|^\eta\right)^m} & \text{for } h < 0 \\ 1 & \text{for } h \geq 0 \end{cases} \quad (2)$$

where α and η are constant parameters that express the matric potential of soil, $m = 1 - (1/\eta)$, and S_e is the effective saturation, which is defined as:

$$S_e = \frac{\theta - \theta_r}{\theta_s - \theta_r}, \quad (3)$$

where θ_s and θ_r are the saturated and residual moisture content, respectively. The relationship between effective saturation and unsaturated hydraulic conductivity is expressed as:

$$K = \begin{cases} K_s S_e^{0.5} \left[1 - \left(1 - S_e^{1/m} \right)^m \right]^2 & \text{for } h < 0 \\ K_s & \text{for } h \geq 0 \end{cases} \quad (4)$$

where K_s is the saturated hydraulic conductivity. For the numerical analysis, the landslide dam and riverbed sediments were assumed to satisfy the Mohr-Coulomb failure criteria. The engineering properties of the landslide dam and riverbed sediment for the simulation are listed in Table 1. The landslide dam is assumed to be an isotropic medium, and the parametric values of the unsaturated soil model are set as follows: $\alpha = 1$, $\eta = 1.5$, $m = 0.333$, $\theta_s = 0.412$ and $\theta_r = 0.0185$.

Simulation Procedures

First, the initial values of the water pressure head and moisture content in the dam were specified in transient seepage flow analysis. The bottom of the riverbed sediment was assumed to be a no-flow boundary. The pressure head and saturation of the dam surface under the water level upstream and the upper, left, and right side of the riverbed sediment must be specified. The seepage boundary was on the downstream

side of the dam, which indicated that water left the soil and that the water pressure head was zero. The height of the seepage face at the seepage boundary was not initially known. The upstream side above the water level and the upper side of the dam were airy boundaries. For the rainfall infiltration case, the infiltration rates at the airy and seepage boundaries were assumed to be the product of rainfall intensity and the cosine of the angle of the boundary face to the horizontal. This is because the direction of the discharge normal to the surface of the slope was specified on the boundaries, but the rainfall direction was assumed to be vertical. In mechanical analysis, the bottom and the 2 sides of the riverbed sediment were assumed to be fixed (i.e., the deformability was constrained and sliding was prevented).

Table 1. The material parameters of the landslide dam and riverbed sediment

| Zone | Density (kg/m ³) | Bulk Modulus (MPa) | Shear Modulus (MPa) | Cohesion (kPa) | Friction Angle (°) | Saturated Hydraulic Conductivity (m/s) |
|----------|---------------------------------|--------------------------|---------------------------|-------------------|--------------------------|---|
| Dam | 1900 | 49 | 19 | 1 | 35 | 8.57×10^{-4} |
| Riverbed | 2000 | 49 | 19 | 3 | 38 | 8.57×10^{-5} |

The initial static equilibrium in the dam body was established during the forming process of the landslide dam. An initial stress state in the dam can be obtained before the transient seepage flow analysis is conducted. A rising water level upstream was simulated for the case in which the river was blocked by landslide materials. To estimate the failure time of the landslide dam, the safety factors of dam stability were calculated for 10 different water levels during the river blocked stage. The simulation of various water levels was conducted to ensure a reasonable pressure head and saturation distribution in the dam. The boundary values of the pressure head and saturation at the upstream boundary were re-specified for each water level. Transient seepage analysis with a time step of 0.5 s was performed separately from the mechanical analysis. The static equilibrium stress field of the dam was recomputed after each transient seepage analysis. The shear strength reduction technique was used to obtain the safety factor of dam stability and to locate the corresponding critical slip surface of each water level rise. To maintain the stability of the dam, a safety factor of one was assumed.

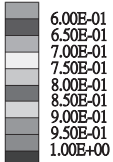
NUMERICAL ANALYSES RESULTS

Transient Seepage Results of a Dam Undergoing Rising Water Levels

The rising speed of the water level upstream was assumed to be 6.66×10^{-3} m/s. The water level reached the top of dam (height $H = 4$ m) after 10 min. The upstream water level was held constant at the level of the dam crest. The calculated saturation and pore water pressure profiles from the numerical analysis of the landslide dam at 200 min are shown in Fig. 2. The computed saturated zone of the soil occurring upstream of the dam and the range of saturation downstream is between 0.5 and 1.0. Fig. 2(a)

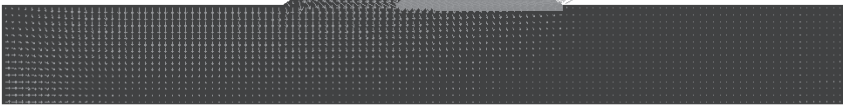
shows the wetting speed of the unsaturated soil is high in the bottom of the dam, possibly because of the effect of gravity. The positive pore water pressure is induced by rising water level upstream of dam, as shown in Fig. 2(b). Because the soil was in an unsaturated state, negative pore water pressure developed in the upper portion downstream of the dam.

Saturation contours



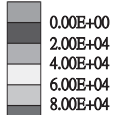
Flow vectors

Max vector = 6.966E-04



(a)

Pore pressure contours



Unit: N/m²

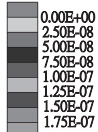
Flow vectors

Max vector = 6.966E-04



(b)

Max. shear strain-rate

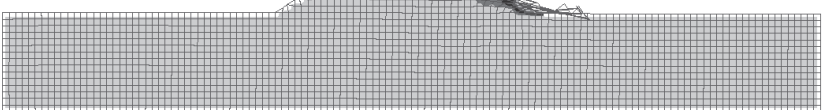


FS=0.99

Exaggerated Grid Distortion

Magnification = 2.864E+03

Max Disp = 1.164E-03m



(c)

FIG. 2. Contours when the time is 200 minutes: (a) saturation (b) pore water pressure and (c) maximum shear strain rate.

Influence of the Rising Speed of the Water Level on Dam Stability

To study the influence of the rising speed of the water level on the safety factor of dam stability, the saturated hydraulic conductivity of soil was fixed at $K_s = 8.57 \times 10^{-4}$ m/s, and the three rising speeds were assumed to be 3.33×10^{-3} , 6.66×10^{-3} , and 13.33×10^{-3} m/s. The comparison of the simulated results under these water level rising speeds are shown in Fig. 3, which indicates that the safety factors of dam stability decrease with increasing time after 50 min. However, the influence of the water level rising speed on dam stability is insignificant because the variation is not obvious, possibly because the rain infiltration in the dam body from upstream to downstream is more rapid than the rise of the water level; therefore, the pore water pressure profiles under these water level rising speeds are similar.

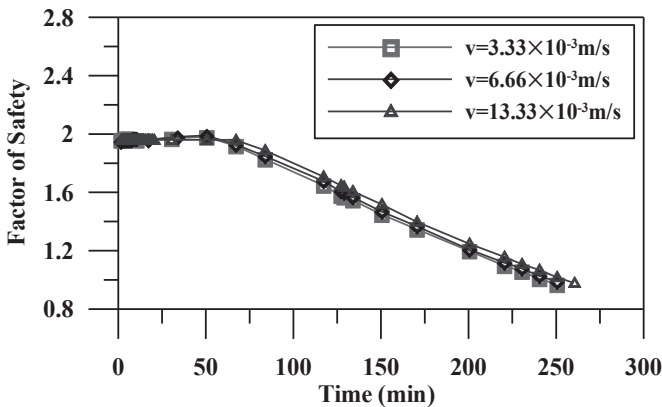


FIG. 3. Influence of rising speed of water level on dam stability.

Influence of the Saturated Hydraulic Conductivity of Soil on Dam Stability

To study the influence of the saturated hydraulic conductivity on the safety factor of dam stability, two additional hydraulic conductivities were estimated, $K_s = 8.57 \times 10^{-3}$ and $K_s = 8.57 \times 10^{-5}$ m/s; Fig. 4 shows a comparison of the simulated results. The variation of the safety factor is small before a threshold time is reached, and, after the threshold time, the safety factor of dam stability decreases when the time increases. The threshold time indicates that the time is when seepage starts to affect the slope stability of the dam. The results also imply that the threshold time and the dam failure time increase when the saturated hydraulic conductivity of the dam is reduced.

Influence of Rain Infiltration on Dam Stability

Fig. 5 shows that the slope failure time of the dam is approximately 247 min when only the effect of rising water level upstream is considered; however, it is 189 min

when the rain infiltration condition is added to the rising water level. The coupling of the rising water level with rainfall infiltration enlarges the saturated soil zone and increases the wetting speed of the unsaturated soil. Therefore, the dam fails more quickly when both the rain infiltration and the rising water level are considered than when only the rising water level is considered.

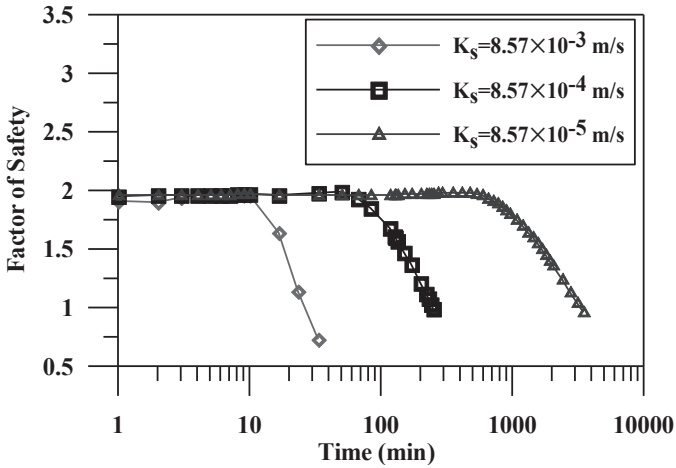


FIG. 4. Influence of saturated hydraulic conductivity of soil on dam stability.

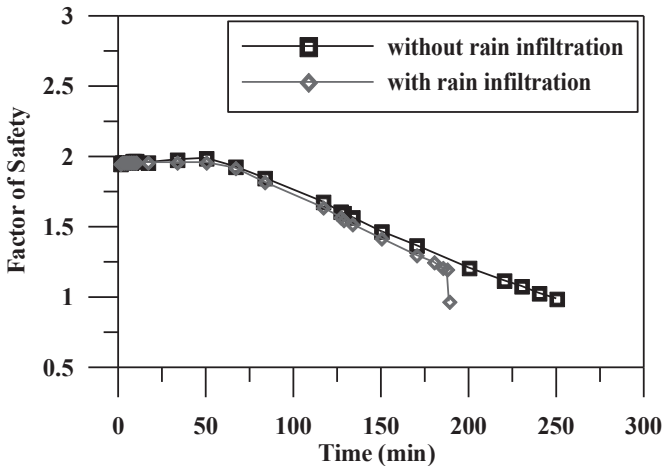


FIG. 5. Influence of adding rain infiltration on dam stability.

CONCLUSIONS

This study used FLAC to analyze the stability of a landslide dam assuming a rising water level upstream. The influencing parameters discussed include the rising speed of the water level and the hydraulic conductivity of the soil. Based on the numerical analyses presented in this study, the following conclusions are made:

1. The influence of the rising speed of the water level on the safety factors of dam stability is less significant than that of varying the hydraulic conductivity of the soil.
2. The dam stability is reduced when saturated hydraulic conductivity is increased.
3. The dam failure is more rapid when both rainfall infiltration and rising water level are considered than when rising water level alone is considered.

ACKNOWLEDGMENTS

This study was supported by research funding from the National Science Council of Taiwan (NSC99-2625-M-005-009-MY3; NSC99-2625-M-005-004-MY3). Their support is gratefully appreciated.

REFERENCES

- Egeli, I. and Pulat, H.F. (2011). "Mechanism and modelling of shallow soil slope stability during high intensity and short duration rainfall." *Scientia Iranica*, Vol. 18(6): 1179–1187.
- Fu, J.F. and Jin, S. (2009). "A study on unsteady seepage flow through dam." *Journal of Hydrodynamics*, Vol. 21(4): 499–504.
- Huang, M. and Jia, C.Q. (2009). "Strength reduction FEM in stability analysis of soil slopes subjected to transient unsaturated seepage." *Computes and Geotechnics*, Vol. 36(1): 93–101.
- Ng, C.W.W. and Shi, Q. (1998). "A numerical investigation of the stability of unsaturated soil slopes subjected to transient seepage." *Computes and Geotechnics*, Vol. 22(1): 1–28.
- Orense, R.P., Shimoma, S., Maeda, K. and Towhata, I. (2004). "Instrumented model slope failure due to water seepage." *J. Nat. Disaster Sci.*, Vol. 26 (1): 15-26.
- Richards, L.A. (1931). "Capillary conduction of liquids through porous mediums." *Physics*, Vol. 1: 318–333.
- Schnellmann, R., Busslinger, M., Schneider, H.R. and Rahardjo, H. (2010). "Effect of rising water table in an unsaturated slope." *Engineering Geology*, Vol. 114: 71–83.
- Tohari, A., Nishigaki, M. and Komatsu, M. (2007). "Laboratory rainfall-induced slope failure with moisture content measurement." *Journal of Geotechnical and Geoenvironmental Engineering*, ASCE, Vol. 133 (5), 575–587.
- van Genuchten, M.Th. (1980). "A close-form equation for predicting the hydraulic conductivity of unsaturated soil." *Soil Sci. Soc. Am. J.*, Vol. 44: 892–898.
- Xu, Y.Q., Unami, K. and Kawachi, T. (2003). "Optimal hydraulic design of earth dam cross section using saturated–unsaturated seepage flow model." *Advances in Water Resources*, Vol. 26(1): 1–7.

Experimental Study on Strength and Deformation Characteristics of the Gassy Muddy Clay with Thin Silt Interlayers

Wang Yong¹, Mu Kun², and Wang Yanli³

¹Associate research fellow, State Key Laboratory of Geomechanics and Geotechnical Engineering, Institute of Rock and Soil Mechanics, Chinese Academy of Sciences, Wuhan, Hubei 430071, China; wang831yong@163.com

²Doctoral candidate, State Key Laboratory of Geomechanics and Geotechnical Engineering, Institute of Rock and Soil Mechanics, Chinese Academy of Sciences, Wuhan, Hubei 430071, China; chn_008@sina.com

³Engineer, Key Laboratory of Geotechnical Mechanics and Engineering of the Ministry of Water Resources, Yangtze River Scientific Research Institute, Wuhan 430010, China; wyldhh@126.com

ABSTRACT: The effects of moisture content on strength and deformation characteristics of gassy muddy clay with thin silt interlayers obtained from a tideland reclamation area in Cangnan are analyzed by conducting triaxial and consolidation tests. Results show that the moisture content of the clay significantly affects the shear strength of the soil. The total cohesion of the clay presents a ladder-type steep reduction as soil moisture content increases, while the internal friction angle is almost free from the influence of moisture content. Soils with different moisture content exhibit relatively linear elastic properties at a small strain. The stress-strain curve alternates between mild strain hardening and mild strain softening as soil moisture content varies. The overall shear strength of the soil is determined by the combined action of the muddy clay and the thin silt interlayers, but the strength of the interlayers is more sensitive to changes with variation of the average soil moisture content than the muddy clay. The overall deformation characteristics of the soil are mainly determined by mechanical properties of the muddy clay. The thin silt interlayers and the average moisture content slightly influence the soil deformation.

INTRODUCTION

Shallow gas refers to the gas buried at depths < 1500 m with a small scale of reserves generally distributed in Quaternary and Tertiary strata (Ding et al. 1996). Drilling engineering industries in oilfields, bays of deltas, and continental shelves often encounter shallow gas (Garcia et al. 2007; Jiang et al. 2003). Shallow gas is usually exploited as clean energy, but it has caused many accidents worldwide because it is a colorless, tasteless, inflammable, and explosive gas that possibly causes blowouts (Adams et al. 1991; Zimmerman 2009). Shallow gas is also a potentially disaster geology for engineering that adversely affects the construction of bridges,

tunnels, hydraulic structures, and foundation pits, thereby causing serious accidents (Xie 2005; Ye et al. 2008; Guo et al. 2012). With the development of massive infrastructure construction, some of these industries along Yangtze River and the southeastern coast of China have also encountered the shallow gas geology in succession (Kong et al. 2004; Feng et al. 2006; Huang et al. 2008). But so far, the knowledge on basic properties of the soil containing shallow gas is very limited. Some studies have focused on continental and marine sedimentary gassy sand and fluffy soft soil with large bubbles on the seabed (Wheeler 1988; Sills et al. 2001; Bernard et al. 2005; Wang et al. 2010). Other studies have investigated varved clay (Stermac et al. 1967; George 1986; Eigenbrod et al. 1991; Hughen and Zolitschka 2007). However, such soil as the muddy clay with thin silt interlayers containing shallow gas has been barely studied.

In this study, a series of triaxial and consolidation tests in different moisture content were conducted to investigate the strength and deformation characteristics of the gassy muddy clay with thin silt interlayers found in Cangnan, Wenzhou City, China, and their variation with the different average moisture content were also determined.

SHEAR STRENGTH TESTS OF THE MUDDY CLAY WITH THIN SILT INTERLAYERS

Basic physical properties of the soil

The muddy clay with thin silt interlayers used in the tests was obtained from a region with buried shallow gas in a tideland reclamation area in Cangnan, Wenzhou City in the southernmost coastal region in Zhejiang Province, China. Shallow gas is found in some regions during construction.

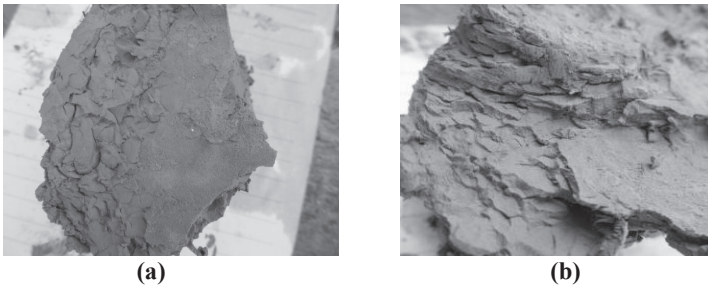


FIG. 1. Samples of muddy clay with thin silt interlayers.

The shallow gas is a typical Quaternary ultra-shallow methane biogas (Lin et al. 2009) mainly distributed at 22.7 m to 32.6 m below the seafloor. The muddy clay with thin silt interlayers is the natural reservoir of shallow gas. This soil appears as a “multilayer pie” called varved clay. The thickness of the silt interlayers ranges from 0.1 mm to 3.0 mm. The samples of the muddy clay with thin silt interlayers from the site are shown in Fig. 1. The following properties were determined based on the basic physical property test: specific gravity of the clay particle (G_s) = 2.68; natural density

(ρ_0) = 1.77 g/cm³; initial moisture content (ω_0) = 62.7%; porous ratio (e_0) = 1.74; liquid limit (ω_L) = 61.2%; plastic limit = 25%; and plastic index (I_p) = 36.2.

Sample preparation and test plan

Given that the muddy clay with thin silt interlayers is the reservoir of shallow gas, the original state of the soil contains different moisture levels because of different gas pressures in the soil. Due to the shallow gas is easy to escape in field sampling, it is difficult to get the proper undisturbed samples. A method to prepare soil samples into the state of different moisture content was adopted to nearly simulate the different initial state of the gassy muddy clay with thin silt interlayers. And a series of constant moisture content triaxial and consolidation tests were carried out to investigate their shear strength and deformation characteristics. There were four groups of undisturbed soil samples with different moisture contents to be prepared in the following tests. The first group is composed of the saturated soil sample with a moisture content of 68.5%. The second group is composed of the soil sample with a natural moisture content of 62.7%. The remaining two groups of the soil samples were prepared in a box at constant temperature and humidity. These soil samples were then dehumidified evenly with a drying time of 24 h and 48 h, respectively. And the soil samples in these two groups were measured their final average moisture content after the soil water balance. The detailed information of soil sample properties and their final average moisture contents are shown in Table 1.

Table 1. Soil Sample Properties

| Soil Sample Type | Dry Density (g/cm ³) | Average Moisture Content (%) | Method for Sample Preparation |
|---------------------------------------|----------------------------------|------------------------------|-------------------------------|
| Muddy Clay with Thin Silt Interlayers | 1.10 | 68.5 | Saturation |
| | | 62.7 | Natural Moisture Content |
| | | 55.6 | Dehumidified for 24 h |
| | | 45.7 | Dehumidified for 48 h |

The constant moisture content triaxial tests were carried out with a shear rate of 0.0022 mm/min. The size of the test soil samples was ϕ 61.8 mm \times 125.0 mm. The confining pressures were 100, 200, 300, and 400 kPa. And the termination condition of tests is the axial strain at 15%.

Test results and analysis

The results of the shear strength test on the muddy clay with thin silt interlayers in different moisture contents are shown in Table 2. As saturation decreases, the total cohesion (c) of the muddy clay with thin silt interlayers gradually increases from 14.1 kPa in the saturated state to 37.5 kPa at a moisture content of 45.7%. By contrast, the internal friction angle (ϕ) only slightly changes as moisture content varies. These variations in c and ϕ as moisture content changes are shown in Fig. 2. The cohesion c

of the soil is greatly influenced by moisture content, showing a ladder-type steep reduction as soil moisture content increases. However, the curve of ϕ is almost a straight line, indicating a weaker correlation between ϕ and moisture content.

Table 2. Shear Strength Index of Muddy Clay with Thin Silt Interlayers in Different Moisture Contents

| Average Moisture Content (%) | Saturation (%) | Index of Shear Strength | |
|------------------------------|----------------|-----------------------------|---------------------------------------|
| | | Total Cohesion (c ; kPa) | Internal Friction Angle (ϕ ; °) |
| 68.5 | 100 | 14.1 | 9.5 |
| 62.7 | 96.6 | 18.0 | 9.6 |
| 55.6 | 85.6 | 29.5 | 9.3 |
| 45.7 | 70.4 | 37.5 | 9.4 |

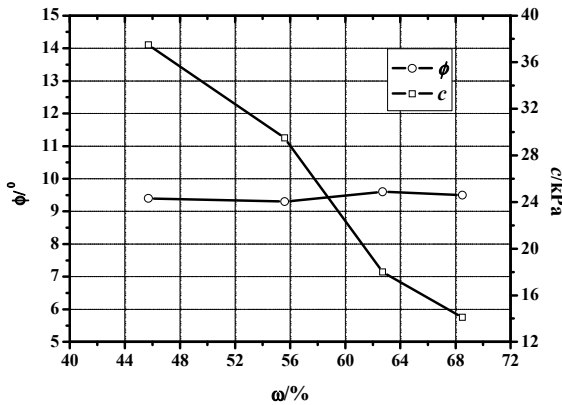


FIG. 2. Strength index variation curve with moisture content.

Fig. 3 shows the stress-strain relationship curve of the muddy clay with thin silt interlayers in different moisture contents. Properties close to the linear elastic are observed for a small strain ($\epsilon_a \leq 3\%$). The stress-strain curve alternates between mild strain hardening and mild strain softening as soil moisture content varies. At the same stress level, the stress-strain relationship curve of the muddy clay with thin silt interlayers initially changes from mild strain hardening in a saturated state to mild strain softening type as moisture content decreases. As moisture content further decreases to $\omega = 45.7\%$, the stress-strain relationship shows the same shape of mild strain hardening. This phenomenon suggests that the shear strength properties of the muddy clay with thin silt interlayers are attributed to different behaviours of the muddy clay and the thin silt interlayers with variation of the average moisture content. As the average moisture content decreases, the silt interlayer shows a comparatively greater loss of moisture content than the muddy clay (which has a relatively smaller

loss of moisture content). The increase in overall strength of the soil is mainly come from the increased part of the thin silt interlayer as moisture content decreases. The increase in strength of the thin silt interlayers determines whether the overall mechanical property of the muddy clay with thin silt interlayers presents a strain-hardening type or a strain-softening type. As the average moisture content further decreases, the strength of the muddy clay gradually increases. Thus, the overall mechanical properties of the muddy clay with thin silt interlayers recover the shape of mild strain hardening.

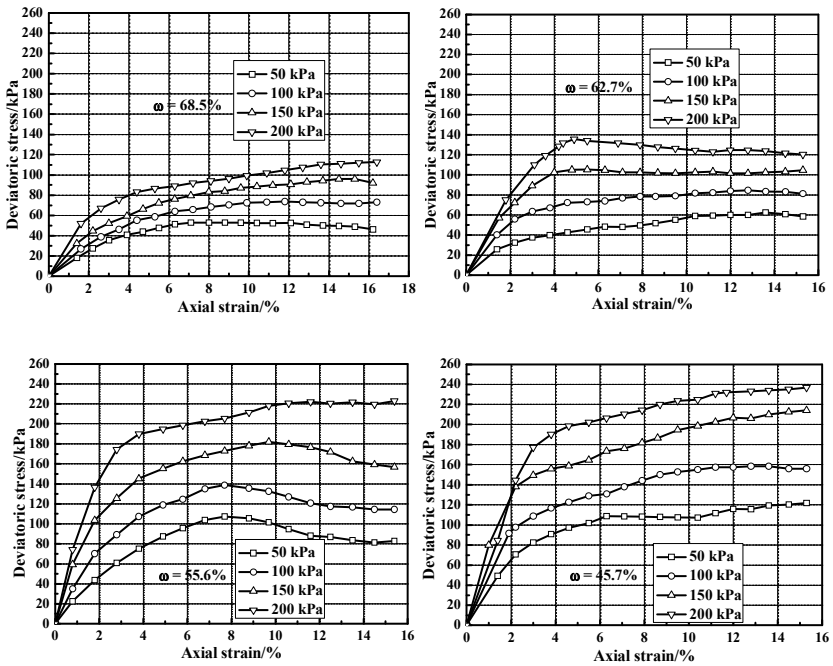


FIG. 3. Stress-strain relationship curves of the muddy clay with thin silt interlayers at different water contents.

DEFORMATION CHARACTERISTICS OF THE MUDDY CLAY WITH THIN SILT INTERLAYERS

To provide predictive parameters for foundation deformation analysis of the construction, consolidation tests are conducted using the muddy clay with thin silt interlayers in different moisture contents. The primary soil deformation indexes are obtained. Table 3 shows the results of the consolidation test of the muddy clay with thin silt interlayers in different moisture contents. Their corresponding e -log p curves are shown in Fig. 4.

The compression modulus (E_s) of the muddy clay with thin silt interlayers is small

and consistent with that of the muddy clay. As moisture content decreases, E_s of the soil increases from 1.41 MPa in a saturated state to 3.17 MPa at $\omega = 45.7\%$, indicating that moisture content influences the deformation characteristics of the muddy clay with thin silt interlayers.

Table 3. Deformation Indexes of the Muddy Clay with Thin Silt Interlayers

| Soil Sample | Average Moisture Content (%) | Saturation (%) | Coefficient of Compressibility $a_{1-2}(\text{MPa}^{-1})$ | Modulus of Compression E_s (MPa) |
|---------------------------------------|------------------------------|----------------|---|------------------------------------|
| Muddy Clay with Thin Silt Interlayers | 68.5 | 100 | 1.79 | 1.41 |
| | 62.7 | 96.6 | 1.48 | 1.72 |
| | 55.6 | 85.6 | 1.05 | 2.43 |
| | 45.7 | 70.4 | 0.81 | 3.17 |

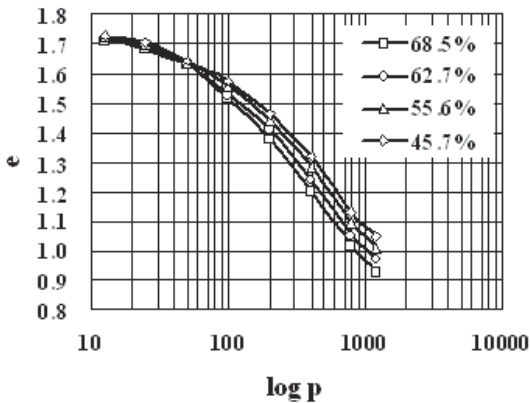


FIG. 4. e-log p curve of the muddy clay with thin silt interlayers.

At consolidation stress < 50 kPa, the moisture content only slightly influences soil deformation characteristics. As the consolidation stress increases, the effect of the moisture content on the muddy clay with thin silt interlayers gradually becomes evident and stable. Therefore, the deformation characteristics of the muddy clay with thin silt interlayers are mainly determined by the mechanical properties of the muddy clay. The thin silt interlayers and the average moisture content only slightly influence the overall deformation characteristics of the clay.

CONCLUSION

The effects of moisture content on strength and deformation characteristics of the muddy clay with thin silt interlayers obtained from a tideland reclamation area in

Cangnan County, Wenzhou City, China are determined by conducting triaxial and consolidation tests based on different moisture contents. The main conclusions of the study are obtained.

(1) Different water-bearing states caused by shallow gas in reservoirs significantly affect the shear strength of the muddy clay with thin silt interlayers. c of the soil presents a ladder-type steep reduction as soil moisture content increases, but ϕ has a weaker correlation with the moisture content.

(2) The overall strength characteristics of the muddy clay with thin silt interlayers are determined by the combined action of the muddy clay and the thin silt interlayers. The soil with different moisture contents presents relatively linear elastic properties at a small strain. The stress-strain curve of the soil alternates between mild strain hardening and mild strain softening as soil moisture content varies.

(3) As moisture content decreases, E_s of the muddy clay with thin silt interlayers gradually increases, but the coefficient of compressibility decreases. The average moisture content and the thin silt interlayers slightly influence the overall deformation characteristics of the soil.

ACKNOWLEDGMENTS

This work was financially by the National Natural Science Foundation of China (51109208), the Foundation of State Key Laboratory for Geomechanics and Deep Underground Engineering (SKLGDUEK1110), the Natural Science Foundation of Hubei Province, China (2011CDB407).

REFERENCES

- Adams, N. and Kuhlman, L.G. (1991). "How to prevent or minimize shallow gas blowouts." *World Oil*, 212(5): 51-60.
- Bernard, P.B., Chris, A. and Bruce, D.J. (2005). "Bubble growth and rise in soft sediments". *Geological Society of America*, 33(6): 517-520.
- Ding, G.S., and Tian, X.Y. (1996). "China's shallow gas resources and exploration prospects". *Oil & Gas Geology*, 17(3): 226-231.
- Eigenbrod, K.D and Burak, J.B. (1991). "Effective stress paths and pore-pressure responses during undrained shear along the bedding planes of varved Fort William Clay.". *Canadian Geotechnical Journal*, 28(6): 804-811.
- Feng, M.Z., Ji, J. (2006). "The geological hazard evaluation by shallow layered natural gas in Shanghai region". *Shanghai Geology*, 100(4): 44-47.
- Garcia, G.A., Orange, D.L., and Miserochic, S., et al. (2007). "What controls the distribution of shallow gas in the Western Adriatic Sea? " *Continental Shelf Research*, 27(3-4): 359-374.
- George, H. (1986). "Characteristics of varved clays of the Elk Valley, British Columbia, Canada." *Engineering Geology*, 23(1): 59-74.
- Guo, A.G., Kong, L.W., and Shen, L.C., et al. (2013). "Study of disaster countermeasures of shallow gas in metro construction. " *Rock and Soil Mechanics*, 34(3): 769-775.
- Huang, J.M, Gu, Y., and Mao, H.M. (2008). "Study on construction technology for jacking of concrete pipe through shallow gas stratum". *Building Construction*,

30(3): 222-225.

- Hughen, K.A., and Zolitschka, B. (2007). "Varved marine sediments.". *Encyclopedia of Quaternary Science*, Elsevier Science Ltd, Kidlington: 3114-3132.
- Jiang, Y., Tian, M.Y. (2003). "Prediction of subsidence caused by exploiting oil and gas." *Journal of Liaoning Technical University*, 22(6): 746-748.
- Kong, L.W., Guo, A.G., Chen, S.Y., and et al. (2004). "Influence of shallow natural gas blow out on stratum damage and hazard analysis of pile foundation". *Journal of Disaster Prevention and Mitigation Engineering*, 24(4): 375-381.
- Lin, C.M., Li, Y.L., Zhuo, H.C., and Zhang, Z.P., et al. (2009). "Geology and pore-water pressure sealing of shallow biogenic gas in the Qiantang River incised valley fills". *Journal of Palaeogeography*, 11(3): 314-329.
- Sills, G.C., and Gonzalez, R. (2001). "Consolidation of naturally gassy soft soil". *Geotechnique*, 51(7): 629-639.
- Stermac, A.G., Lo, K.Y., and Barsvary, A.K.(1967). "The performance of an embankment on a deep deposit of varved clay". *Canadian Geotechnical Journal*, 4(1): 45-61.
- Wheeler, S.J. (1988). "A conceptual model for soils containing large gas bubbles". *Geotechnique*, 38(3): 389-397.
- Wang, Y., Kong, L.W., Guo, A.G., et al. (2010). "Effects of gas release rate on gas-water migration in shallow gas reservoir". *Journal of Zhejiang University (Engineering Science)*, 44(10): 1883-1889.
- Xie, C.Y. (2005). "Shallow gas along the Yangtze river in Anhui province and its effects on hydraulic structures". *Express of Water Resources & Hydropower Information*, 21(10): 11-16.
- Ye, N.J., Li, G.J. (2008). " Research on influence of shallow-buried natural gas on pile foundation of bridge and its countermeasures". *Highway*, (12): 61-64.
- Zimmerman, D. (2009). "Investigation report of oil and gas leasing in the outer continental shelf". Northcoast Ocean and River Protection Association.
- Zolitschka, B. (2007). "Varved lake sediments.". *Encyclopedia of Quaternary Science*, Elsevier Science Ltd, Kidlington: 3105-3114.

Analysis of Surrounding Rock Displacement Induced by Tunnel Excavation in Horizontal Interbedding Rock Mass

Yong Fang¹, Ya-peng Fu², Bin Yang², Ge Cui², Xiao-min Wang²

¹Associate Professor, Key Laboratory of Transportation Tunnel Engineering, Ministry of Education, Dept. of Civil Engineering, Southwest Jiaotong University, Chengdu 610031, China, Email: fy980220@swjtu.cn

²Master candidate, Key Laboratory of Transportation Tunnel Engineering, Ministry of Education, Dept. of Civil Engineering, Southwest Jiaotong University, Chengdu 610031, China, Email: fyp19900328@foxmail.com, 285525675@qq.com, cuige114@126.com, 410504236@qq.com

ABSTRACT: Material properties of horizontal sandstone and mudstone interbedding rock mass have significant differences in the horizontal and vertical directions. It is difficult to reveal the characteristic of surrounding rock displacement induced by tunnel excavation in horizontal interbedding rock mass by numerical methods based on isotropic constitutive models. Regarded as transversely isotropic medium, material parameters such as density, elastic modulus, poisson ratio etc. of interbedding rock mass are deduced. As an example, transversely isotropic constitutive model is taken into consideration in three dimensional numerical model of Luan Jiayan tunnel on Guanran highway. The process of tunnel excavation is simulated in this model, and ground displacement distribution and variation with excavation steps are obtained. For the purpose of comparison, field tests of vault settlement and side wall convergence caused by tunnel construction are carried out. It is shown that compared with isotropic constitutive model, transversely isotropic constitutive model can reflect the physical difference in horizontal and vertical directions for interbedding rock mass of sandstone and mudstone. But transversely isotropic model is elastic, and plastic zone caused by tunnel excavation can't be obtained. So there exist some differences from actual situation when this model is applied.

INTRODUCTION

In general, we regard sedimentary rock whose stratum bedding-plane is approximately level as horizontal stratum, and the altitude of the same rock formation for horizontal stratum is basically the same. In the process of Guangyuan-Nanchong expressway construction, tunnels are built to pass through mountainous region in the Sichuan Basin. Stratigraphic dip angle in tunnel site area is low and nearly horizontal;

rock strata is sandstone and mudstone interbedding rock mass, the differences of rock properties are significant, and the rock stratum possesses typical transverse isotropic characteristics. During the excavation of tunnel, the deformation mechanism of surrounding rock and the mechanical behavior characteristics of lining structure are rather different from common rock.

Xian Mowen (1995) verified the stability and feasibility of excavation scheme of four parallel canal tunnel through Limestone and shale interbedding rock mass. B.L.Chu (2007) took the conditions of homogeneous surrounding rock, 2-layer surrounding rock and 3-layer surrounding rock into consideration, conducted the model and numerical experiments of two circular tunnel excavation, analyzed the mechanical behavior of the cavern after excavation. Based on the construction monitoring results, Guan Huiping (2008) analyzed the reasons and characteristics of the surrounding rock deformation for horizontal rock tunnel surrounding rock deformation, and discussed the classifications of the deformation stages. YanLi (2009) regarded each rock stratum as the isotropic continuous medium, considered the influence of rock stratum interface, performed the numerical model and discussed the stability of middle rock pillar. In addition, the influences of the different net distances between two tunnels and the various surrounding rock conditions on the stability of middle rock pillar are studied. Based on Biot's theory of consolidation, the time-dependent analytical solutions of stress, displacement and pore pressure induced by circular tunnel excavation in a transversely isotropic and saturated soil were obtained by Liu Ganbin (2003) in the Laplace transform domain. The anisotropic elastoplastic model of layered soil was established by Zhu Yanzhi (2005) to solve seismic response analysis of shield tunnel systems in layered soil. Transversely isotropic characteristics of the segment structure were taken into consideration, and impacts on the existing tunnel caused by the construction of parallel and undercrossing shield tunnels was simulated by Fang Yong (2007).

Due to the numerous structure planes of horizontal sandstone and mudstone interbedding rock mass (2006,2010) and the typical transversely isotropic characteristics, it is difficult to reveal the characteristic of surrounding rock displacement induced by tunnel excavation in horizontal interbedding rock mass by numerical methods based on isotropic constitutive models. In this paper, by introducing transversely isotropic theory, surrounding rock displacement induced by excavation is studied when the tunnel passes through horizontal sandstone and mudstone interbedding strata.

TRANSVERSELY ISOTROPIC CONSTITUTIVE MODEL

Basic Assumptions

For horizontal soft-hard interbedding rock layer, each individual layer possesses approximately isotropic characteristics, but from the overall point of view, elastic modulus are greatly different in the horizontal and vertical directions, which means that interbedding stratum owns transversely isotropic characteristics. To deduce the constitutive model of horizontal soft-hard interbedding rock mass, the following assumptions are necessary.

①The rock layers bond firmly and don't produce sliding displacements, which is in accordance with the consistent deformation theory ;

②each individual layer is isotropic medium.

The equivalent model of nearly horizontal strata includes three equivalent physical parameters, namely density, elastic modulus and poisson ratio.

Surrounding Rock Density

According to the fact that the total weight and volume of equivalent surrounding rock are equal to the original interbedding surrounding rock, there is such formula as follows:

$$\sum_{i=1}^n \rho_i g h_i = \rho g h \tag{1}$$

The equivalent stratum density is:

$$\rho = \frac{\sum_{i=1}^n \rho_i h_i}{\left(\sum_{i=1}^n h_i\right)} = \sum_{i=1}^n \rho_i h_i / h \tag{2}$$

Where, ρ_i and h_i are the density and thickness of each stratum, h is the thickness of equivalent stratum, n is the number of strata, and ρ is equivalent density.

Elastic Modulus

(1) E_v : equivalent elastic modulus in the vertical direction.

Figure 1 shows the derivation for equivalent elastic modulus in the vertical direction. Where, E_i is the elastic modulus of surrounding rock, and E_v is the equivalent elastic modulus.

By the action of a vertical unit load F on interbedding strata and equivalent stratum, according to the fact that vertical compression displacements of two models produced by the unit load are equal, there is such formula as follows:

$$\sum_{i=1}^n [F / (E_i L / h_i)] = F / (E_v L / h) \tag{3}$$

The calculation formula for vertical elastic modulus is

$$E_v = h / \left(\sum_{i=1}^n h_i / E_i\right) \tag{4}$$

(2) E_h : equivalent elastic modulus in the horizontal direction.

Figure 2 shows the derivation for equivalent elastic modulus in the horizontal direction. Where, E_i is the elastic modulus of surrounding rock, and E_h is the equivalent elastic modulus.

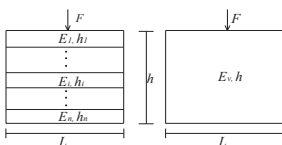


Fig. 1 Vertical elastic modulus

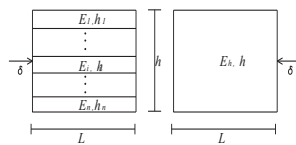


Fig. 2 Horizontal elastic modulus

By the action of a horizontal unit displacement δ on originally interbedding strata and equivalent stratum, this displacement would result in horizontal pressure, and according to the fact that the horizontal pressure of two models produced by the unit displacement are equal, there is such formula as follows:

$$E_h h \delta / L = \sum_{i=1}^n E_i h_i \delta / L \tag{5}$$

The calculation formula for horizontal elastic modulus is

$$E_h = (\sum_{i=1}^n E_i h_i) / h \tag{6}$$

Poisson Ratio

In the transversely isotropic medium, the poisson ratio includes two parameters: and, which respectively represent the poisson ratio in the vertical and horizontal directions. Poisson ratio of equivalent model can be calculated according to the horizontal pressure and vertical pressure ratio. In the transversely isotropic elastic medium, lateral pressure coefficient is defined as:

$$\lambda' = \sigma_x / \sigma_y = E_h v_{vh} / [E_v (1 - v_{hh})] \tag{7}$$

Figure 3 shows the equivalent model of poisson ratio. Both of the original soil and equivalent soil are under vertical pressure F , two sides are restricted by the horizontal constraints, and bottom is restricted by vertical constraints.

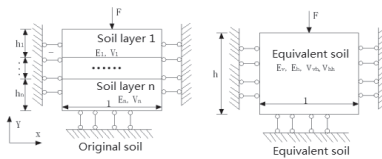


Fig. 3 Equivalent model 1 of poisson ratio

In the boundary conditions, the horizontal total pressure of interbedding strata is: $\sum_{i=1}^n (\lambda_i F h_i) / L$, the horizontal total pressure of equivalent stratum is: $(\lambda' F h) / L$. In theory, they are equal to each other.

$$\sum_{i=1}^n (\lambda_i F h_i) / L = (\lambda' F h) / L \tag{8}$$

Where is the lateral pressure coefficient, the further result is as follow:

$$v_{vh} / (1 - v_{hh}) = h \sum_{i=1}^n [v_i h_i / (1 - v_i)] / [(\sum_{i=1}^n E_i h_i) (\sum_{i=1}^n \frac{h_i}{E_i})] \tag{9}$$

Similarly, horizontal compression displacements of the equivalent stratum model and all original strata are δ , as is shown in figure 4, the left side is restricted by the horizontal constraints, top and bottom by vertical constraints.

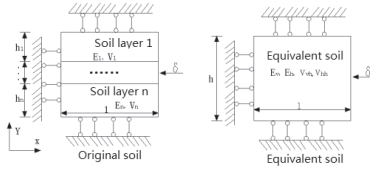


Fig. 4 Equivalent model 2 of Poisson ratio

Using the same method, we can get the following formula:

$$v_{vh}(1 + v_{hh}) / (1 - v_{vh}^2) = \left(\sum_{i=1}^n E_i h_i \right) \left(\sum_{i=1}^n \frac{h_i}{E_i} \right) / \left\{ h \left[\sum_{i=1}^n \frac{h_i (1 - \nu_i)}{\nu_i} \right] \right\} \tag{10}$$

The above two equations are simultaneously solved, the poisson ratio in the horizontal direction is:

$$v_{vh} = \left\{ -1 + \left[1 + B(B - A^{-1}) \right]^{0.5} \right\} / (B - A^{-1}) \tag{11}$$

And the poisson ratio in the vertical direction:

$$v_{hh} = \left\{ AB - \left[1 + B(B - A^{-1}) \right]^{0.5} \right\} / (AB - 1) \tag{12}$$

Where, $A = \left(\sum_{i=1}^n \lambda_i h_i \right) / R$, $B = R / \left[\sum_{i=1}^n (h_i / \lambda_i) \right]$, $R = \left(\sum_{i=1}^n E_i h_i \right) \left(\sum_{i=1}^n h_i / E_i \right) / h$, $\lambda_i = \nu_i / (1 - \nu_i)$, $i = 1, 2, \dots, n$

CONSTRUCTION SIMULATION OF TUNNEL EXCAVATION

Model Establishment

Luan Jiayan tunnel of Guangnan highway is 3265 meters long, which is located in north-central Sichuan basin. As for the construction conditions the layers are nearly flat, the attitude of rocks at the tunnel entrance is 280~320° ∠1~3°, the rock is mainly composed of thin-middle siltstone and mudstone interbedding rock mass, and interlayer bonding is poor. With Luan Jiayan tunnel as the research object to establish numerical model, tunnel’s buried depth is 150m, and the model is 200m wide, 150m long, and 210m high, every 4m is divided into a unit in longitudinal direction. Vertical displacement constraints are imposed in the lower boundary, the level displacement constraints are applied in the left and right boundary and the axis displacement constraints are applied in the front and behind boundary of the model, as is shown in Figure 5.



Fig. 5 Three dimensional numerical model

According to the geological investigation date for the Luan Jiayan tunnel and the design specification of highway tunnel, there is no groundwater, the property parameters of stratum and primary support are shown in the following Table 1.

Table. 1 Material parameters of numerical model

| name | E/MPa | Poisson ratio ν | $\gamma/\text{kN}\cdot\text{m}^{-3}$ | C/MPa | Φ | ratio % |
|-----------------|-------|---------------------|--------------------------------------|-------|--------|---------|
| Mudstone | 1500 | 0.35 | 19.7 | 0.14 | 25 | 37.5 |
| Siltstone | 2800 | 0.32 | 22.8 | 0.4 | 33 | 62.5 |
| primary support | 23000 | 0.2 | 22 | -- | -- | -- |

By putting the above data into the front of the formula, properties of the equivalent formation can be obtained. The physical property parameters are as following:

$$E_v=2113\text{MPa}; E_h=2312\text{MPa}; \nu_{vh}=0.4095; \nu_{hh}=0.1764; \gamma=21.64\text{kN/m}^3$$

Excavation Simulation

The benching tunneling construction method is applied in the Luan Jiayan highway tunnel excavation. Compared with the down steps, the up steps are beyond 40 meters. Simulation of the excavation is shown in Figure 6. During the construction, in order to prevent the horizontal rock from blocking and collapsing, the initial support parameters are as follows:

The level of the sprayed concrete: C20

Thickness: 25cm

I-steel model: I18

Interval: 1.0m

The initial support parameters are viewed as an equivalent average shell and then applied to this model. The equivalent physical parameters are shown in Table 1.

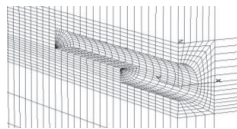


Fig. 6 Simulation of the excavation

Generally, there are 2-blasting cycle every day and there is a drilling and blasting operation cycle almost every 2 meters in the construction, and the initial support must be immediately applied after every time of blasting operation. In the numerical

calculation, it selects 8 meters as an excavation calculation cycle step. Through the construction process simulation, this paper is intended to study the rule of the surrounding rock displacement caused by highway tunnel excavation in the horizontal sandstone and mudstone interbedding rock mass.

Result Analysis

In order to eliminate the influence of the boundary effect, the model longitudinal intermediate position is selected, $Y = 100\text{ m}$, as monitoring section. The situation in which the displacement of the vault, sidewall and inverted arch changed with excavation steps is shown in Figure 7. As can be seen, because the settlement of the vault resulted from the excavation of the upper bench makes up 70% of the total settlements and the uplift quantity in the inverted arch takes up 55% of the total uplift quantities, the excavation of the upper bench would lead to settlement in the vault and uplift in the inverted arch significantly. Likewise, because the convergence magnitude of the sidewall resulted from the excavation of the lower bench makes up 70% of the total convergence displacements, the excavation of the lower bench would lead to the increment of the sidewall convergence. Under the initial support, the final displacements of edges of tunnel are as follows:

Vault: -19.11mm; Sidewall: -9.45mm; Inverted arch: 6.82mm

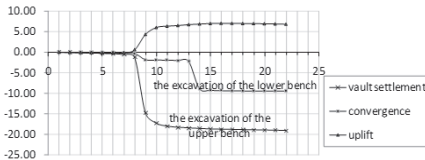


Fig.7 Displacement variation with tunnel excavation

In the model monitoring section, $Y=100\text{m}$, the vertical displacement contours in the final state under the initial support are shown in Figure 8, and the Figure 9 is used to show the horizontal displacement contours.

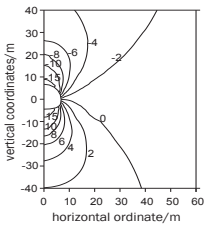


Fig.8 Displacement in vertical direction

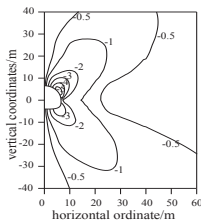


Fig.9 Displacement in horizontal direction

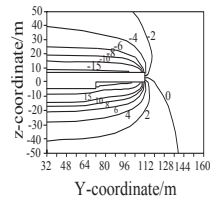


Fig.10 Vertical displacement in the plan $x=0$

On the basis of the Figure 8 and Figure 9, it can be concluded that the biggest vertical displacement in the model longitudinal direction usually occurs in the $X=0$ plane. When the tunnel is dug through completely, the strata displacement on the longitudinal section reaches the maximum, but the displacement in the longitudinal is uniformly distributed, the uneven displacement is smaller. The strata uneven displacement appears in the excavation stage, especially near the excavation face. When the upper stair excavation surface is located in $Y = 112$ m, the distribution of vertical displacement in the $X=0$ plane is shown in Figure 10. As can be seen, the vertical displacement near the upper stair excavation surface changes greatly and the vertical displacement at the distance of three times of diameter to the down stair excavation surface is basically stable.

ANALYSIS OF FIELD TEST RESULTS

It selects cross-section of ZK87+295 mileages which is located in Luan Jiayan tunnel to launch the field testing of displacement around the hole. The buried depth of this cross-section is about 150 meters and the benching tunneling construction method is used to excavate this cross-section. Three measuring points, located in this test cross-section, are used to measure the changes of vault settlement and horizontal convergence in tunnel excavation. Three measuring points are shown in Figure 11.

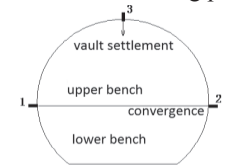


Fig.11 Displacement measuring point around tunnel

After the slag is carried away, the measuring point would be arranged with the steel arch being erected. Initial reading could not be acquired until the shotcreting-bolting support is completed, which does not include the displacement value before shotcreting-bolting support is finished. The measuring point is welded on the steel arch so as to ensure that it completely bond on the frame of initial support. Test frequencies are as follows: early days: once a day and then gradually transit to once two days or once seven days, finally after the inverted arch is closed, the displacement became stable, and test frequency changes to once a month.

The situations in which the settlement of the vault and the horizontal convergence change with excavation steps are shown in Figure 12 and 13. As can be seen, the settlement of the vault and the horizontal convergence mainly are resulted from the excavation of the upper bench. With the advance of the excavated surface, the displacement rate decreases gradually and tends to be stable. The monitoring data shows that the design of the initial support is reasonable. So the initial support can ensure the displacement tend to be stable. After the excavation of the lower bench, the

settlement of the vault and the horizontal convergence would further increase. But after the excavation of the lower bench, the inverted arch is closed shortly, so it can restrain the development of displacement. After the inverted arch is closed, the displacement would tend to be stable basically.

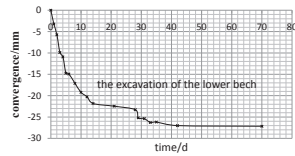
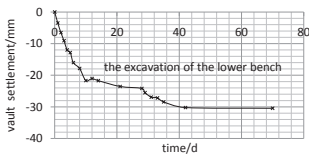


Fig.12 Settlement in the vault during the excavation

Fig.13 Convergence in sidewall during the excavation

In comparison with the measured value, it can be found that the displacement resulted from the measured value is bigger than the numerical calculated result. The actual measured cumulative settlement in the vault is about 30 mm. Before the measurement, the settlement in the vault has been finished partly, so the accumulation of surrounding rock actual settlement is greater than 30 mm, which is far more than the numerical calculated result.

CONCLUSION

This paper regards the horizontal sandstone and mudstone interbedding rock mass as the transversely isotropic rock. Based on the principles of mechanics, the property parameters of the density, elastic modulus and Poisson's ratio of this equivalent rock can be deduced. The study takes the Luan Jiayan tunnel of Guangnan highway as the subject. By using the transversely isotropic parameter of the equivalent strata to establish 3D numerical model and simulating the process of tunnel excavation, it can get the regularity of the strata displacement resulted from the advance of the excavation section. Meanwhile, field test is carried out, which can obtain the situation in which the displacement of the vault and the convergence of the sidewall change with the time.

Compared with the model of isotropic homogeneous formation, the transversely isotropic constitutive model can reflect the difference of the sandstone and mudstone layer in the horizontal direction and the vertical direction and can more truly describe the real formation characteristics,. But the transverse isotropic constitutive model is still the elastic model, which can't get the tunnel surrounding rock plastic zone caused by the tunnel excavation. As a result, this model can't achieve ideal result in soft stratum.

The numerical and field test results show that under the condition of the horizontal sandstone and mudstone interbedding rock mass, the displacement of surrounding rock mainly originates from the excavation of the upper bench. Due to the excavation of the lower bench, the displacement of surrounding rock would further increase. But

as the inverted arch is closed, the displacement would soon tend to be stable and convergent.

ACKNOWLEDGEMENTS

This paper was supported by: the National Natural Science Foundation of China (Nos: 51278422, 50925830); National 973 Plan Topics of China (No: 2010CB732105); National Science and Technology Pillar Program of China (2012BAG05B03); Sichuan Youth Science and Technology Foundation, China (2012JQ0021).

REFERENCES

- XIE Mowen, YANG Shuqing, LIAO Yelan. (1995). "Study and practice of stability for tunnel group in alternative stratified rocks." *J. Chinese Journal of Rock Mechanics and Engineering*, 14(2): 131-137.
- CHU B L, HSU S C, CHANG Y L, et al. (2007). "Mechanical behavior of a twin-tunnel in multi-layered formations." *J. Tunnelling and Underground Space Technology*, 22: 351-362.
- GUAN Hui-ping, XIONG Jun-nan, TAO Shuang-jiang etc. (2008). "Deformation Monitoring of Surrounding Rocks and Stability Analysis of Approximate Horizontal Rock Tunnel" *J. ROCK AND MINERAL ANALYSIS*, 27(5): 357-362
- YAN Li, YANG Junsheng, ZHANG Xuemin. (2009). "STABILITY ANALYSIS OF MIDDLE ROCK PILLAR IN PARALLEL TUNNELS IN HORIZONTALLY INTERBEDDING ROCK MASS." *J. Chinese Journal of Rock Mechanics and Engineering*, 28(S1):2898-2904
- LIU Ganbin, XIE Kanghe, SHI Zuyuan. (2003) "Analysis of stress and displacement around a deep circular tunnel in transversely isotropic soil." *J. Chinese Journal of Geotechnical Engineering*, 25(6): 727-731
- ZHU Yan-zhi, FENG Zi-liang, FANG Zhi. (2005). "Numerical simulation of shield tunnel dynamic response to earth motions taking account of anisotropy of layered soil." *J. Rock and Soil Mechanics*, 26(5): 711-716
- FANG Yong, HE Chuan. (2007). "Analysis of Influence of Undercrossing Subway Shield Tunneling Construction on the Overlying Tunnel." *J. JOURNAL OF THE CHINA RAILWAY SOCIETY*, 29(2):83-88
- FANG Yong, HE Chuan. (2007). "Numerical Analysis of Parallel Shield Tunnel Construction Affecting on The Existent One." *J. Rock and Soil Mechanics*, 28(7):1402-1406
- HAN Tong-chun, ZHENG Jun-qing, ZHU Jian-cai etc. (2010). "Monitoring analysis of outlet section of tunnels with small clear-distance in half-hard and half-soft rock strata." *J. Rock and Soil Mechanics*, 31(S2): 303-307
- DENG Shaojun. (2006). "Study on the surrounding rock stability and optimization of bolting parameters under horizontal strata" *D. Changsha: Central South University*.

A transversely isotropic Cosserat continuum model and its numerical application

Zhaolong HU¹, Hongxiang TANG^{1,*}

¹Postgraduate student, School of Civil Engineering, State Key Laboratory of Costal and Offshore Engineering, Dalian University of Technology, Dalian 116024, China; Email: hzlllzh@126.com

^{1,*}Corresponding author, associate Professor, School of Civil Engineering, State Key Laboratory of Costal and Offshore Engineering, Dalian University of Technology, Dalian 116024, China; Email: tanghx@dlut.edu.cn

ABSTRACT: A transversely isotropic Cosserat continuum model is developed based on the Cosserat continuum theory and transversely isotropic elastic theory in three-dimensional condition. The finite element program based on this model is developed to analysis the stress and deformation of a transversely isotropic layered soils subjected to a loading on an elastic rectangular plate. It illustrates that the transversely isotropic model can reflect the soil's property more realistically than the isotropic one in some practical engineering, and that the proposed transversely isotropic Cosserat continuum model can describe micro-scale mechanical property of soils and simulate the mechanical behavior of the transversely isotropic soils effectively.

INTRODUCTION

During a long historical depositional aggregation of granular particles, the arrangement of soil grains shows a strong directivity, which causes the material property in vertical direction (or the direction in which the grains were accumulated) different from in horizontal direction, so it will reflect the mechanical nature better to regard soil as a transversely isotropic continuum rather than a homogeneous isotropic continuum. Many scholars have taken plenty of researches on the mechanical properties of transversely isotropic continuum. Liao and Wang derived and presented the complete closed-form of the displacements and stress subjected to a point load in a transversely isotropic elastic half-space (Liao and Wang 1998). Bonet and Burton presented a simple orthotropic, transversely isotropic hyperelastic constitutive equation for large strain computations, which can be used to model fiber oriented elastic materials in the fully nonlinear range (Bonet and Burtonm 1998). Ai and Cao studied the analytical solution of stresses and displacements of transversely isotropic soils under the elastic rectangular plate, and carried out a numerical calculation at the same time (Ai and Cao 2011). However, these works are mainly discussed in the fame of classical continuum theory. Considering the character of the Cosserat continuum theory, this paper presents a transversely isotropic model under Cosserat theory.

Since the beginning of last century, Cosserat theory has been studied widely in the world. In geotechnical engineering field, it is mainly used to simulate the localization phenomena and calculate the progressive failure in soils (De Borst and Sluys 1991; Li and Tang 2005). Another important application of Cosserat theory in geotechnical engineering problems is to simulate jointed rock by homogenization method (Riahi and Curran 2009). By introducing the internal length scale, which can be treated as the "characteristic dimension" of material, into Cosserat theory, it is possible to reflect the micro-scale mechanical properties of soils, such as the strain gradient or strain localization phenomena, which is beyond the capacity of classical continuum theory. In most researches above, soil is treated as homogeneous isotropic body which does not truly reflect its material property. In order to reveal the soil's nature more authentically and make a better understanding through numerical analysis, it is necessary to consider soil as transversely isotropic Cosserat continuum.

THREE-DIMENSIONAL COSSERAT CONTINUUM THEORY

Compared with the classical continuum theory, Cosserat continuum theory assumes that there are six independent degrees of freedom at each material point, among which three degrees-of-freedom (u_x , u_y , u_z) are associated with the displacement and the other three degrees-of-freedom (ω_x , ω_y , ω_z) are associated with the local rotation. The subscript of the translational degrees-of-freedom represents the direction of the displacement, and the subscript of the rotational degrees-of-freedom represents the axis around which the rotation revolves. Accordingly, the mechanical variables include nine conventional stresses and nine couple-stresses are shown in Fig.1, where two parallelepipeds represent the same micro-unit.

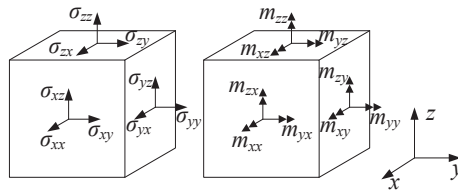


FIG.1. 3D representation of stress and couple stress measures.

The notation adopted for stress components is the same as the standard notation of the classical continuum theory, however it is different from measures of the couple stresses. The first subscript of couple stress component refers to the axis around which it rotates, while the second subscript denotes the surface on which the couple-stress acts. This intuitive representation is the same as the expression in Riahi's research (Riahi and Curran 2009), which makes it easier understood. In the three-dimensional Cosserat continuum theory, the components of the strains and micro-curvatures can be written as follows (Tang and Hu 2012)

$$\epsilon_{ij} = u_{j,i} - e_{ijk}\omega_k, \quad \kappa_{ij} = \omega_{i,j} \tag{1}$$

Here, the tensor equations above are also called the geometric equations of the Cosserat continuum, e_{ijk} is the permutation symbol. It is obviously that the conjugate shear strains will not be equal to each other in the Cosserat theory, that means the equivalent theorem of shear stress will not exist, which is an essential distinction with the classical theory. According to Truesdell’s study (Truesdell and Toupin 1960), taking the momentum balance and angular momentum balance into consideration, the equilibrium equation of the micro-unit can be expressed as follows

$$\begin{cases} \sigma_{ij,j} + b_j = 0 \\ m_{kj,j} + e_{kij}\sigma_{ij} + c_k = 0 \end{cases} \tag{2}$$

in which b_j represents the body force and c_k represents the couples.

ELASTIC MECHANICS OF TRANSVERSELY ISOTROPIC BODY

In the transversely isotropic continuum shown in Fig.2, it assumes that coordinate z -axis represents the elastic symmetric axis, and xoy -plane represents the isotropic plane. So based on the material properties of transversely isotropic body, points in the xoy -plane have the same elasticity, however the elasticity along z -axis are not the same, and there are five independent elastic parameters in the classical transversely isotropic continuum theory.

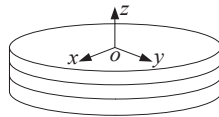


FIG.2. The material direction of transversely isotropic continuum.

In the transversely isotropic Cosserat continuum as shown in Fig.1, couple-stresses $m_{xx}, m_{yy}, m_{xy}, m_{yx}$ act in the isotropic plane so that they follow the horizontal constitutive relationship with their conjugated micro-curvatures, and the other five couple-stresses, including a torsional couple-stress and four curving couple-stresses, follow the vertical constitutive relationship with conjugated micro-curvatures. Employing the strain energy equation, we present the constitutive equation for the elastic transversely isotropic Cosserat continuum as follows

$$\sigma = D_e \epsilon \tag{3}$$

where the stress vector and strain vector can be written respectively as

$$\sigma = \{ \sigma_{xx} \quad \sigma_{yy} \quad \sigma_{zz} \quad \sigma_{xy} \quad \sigma_{yx} \quad \sigma_{yz} \quad \sigma_{zy} \quad \sigma_{zx} \quad \sigma_{xz}$$

$$\left. \begin{array}{c} \frac{m_{xx}}{l_t} \quad \frac{m_{yy}}{l_t} \quad \frac{m_{zz}}{l_t} \quad \frac{m_{xy}}{l_b} \quad \frac{m_{xz}}{l_b} \quad \frac{m_{yx}}{l_b} \quad \frac{m_{yz}}{l_b} \quad \frac{m_{zx}}{l_b} \quad \frac{m_{zy}}{l_b} \end{array} \right\}^T \quad (4)$$

$$\begin{aligned} \boldsymbol{\varepsilon} &= \left\{ \varepsilon_{xx} \quad \varepsilon_{yy} \quad \varepsilon_{zz} \quad \varepsilon_{xy} \quad \varepsilon_{yx} \quad \varepsilon_{yz} \quad \varepsilon_{zy} \quad \varepsilon_{zx} \quad \varepsilon_{xz} \right. \\ \kappa_{xx}l_t \quad \kappa_{yy}l_t \quad \kappa_{zz}l_t \quad \kappa_{xy}l_b \quad \kappa_{xz}l_b \quad \kappa_{yx}l_b \quad \kappa_{yz}l_b \quad \kappa_{zx}l_b \quad \kappa_{zy}l_b \end{aligned} \left. \right\}^T \quad (5)$$

and the elastic material matrix

$$\mathbf{D}_e = \begin{pmatrix} \mathbf{D}_u & \mathbf{0} \\ \mathbf{0} & \mathbf{D}_\omega \end{pmatrix} \quad (6)$$

in which \mathbf{D}_u and \mathbf{D}_ω are the fourth order tensors and can also be expressed as

$$\mathbf{D}_u = \begin{pmatrix} d_{11} & d_{12} & d_{13} & 0 & 0 & 0 & 0 & 0 & 0 & 0 \\ d_{12} & d_{11} & d_{13} & 0 & 0 & 0 & 0 & 0 & 0 & 0 \\ d_{13} & d_{13} & d_{33} & 0 & 0 & 0 & 0 & 0 & 0 & 0 \\ 0 & 0 & 0 & G_1 + G_c & G_1 - G_c & 0 & 0 & 0 & 0 & 0 \\ 0 & 0 & 0 & G_1 - G_c & G_1 + G_c & 0 & 0 & 0 & 0 & 0 \\ 0 & 0 & 0 & 0 & 0 & G_2 + G_c & G_2 - G_c & 0 & 0 & 0 \\ 0 & 0 & 0 & 0 & 0 & G_2 - G_c & G_2 + G_c & 0 & 0 & 0 \\ 0 & 0 & 0 & 0 & 0 & 0 & 0 & G_2 + G_c & G_2 - G_c & 0 \\ 0 & 0 & 0 & 0 & 0 & 0 & 0 & G_2 - G_c & G_2 + G_c & 0 \end{pmatrix} \quad (7)$$

$$\mathbf{D}_\omega = \begin{pmatrix} 2G_1 & 0 & 0 & 0 & 0 & 0 & 0 & 0 & 0 & 0 \\ 0 & 2G_1 & 0 & 0 & 0 & 0 & 0 & 0 & 0 & 0 \\ 0 & 0 & 2G_2 & 0 & 0 & 0 & 0 & 0 & 0 & 0 \\ 0 & 0 & 0 & 2G_1 & 0 & 0 & 0 & 0 & 0 & 0 \\ 0 & 0 & 0 & 0 & 2G_2 & 0 & 0 & 0 & 0 & 0 \\ 0 & 0 & 0 & 0 & 0 & 2G_1 & 0 & 0 & 0 & 0 \\ 0 & 0 & 0 & 0 & 0 & 0 & 2G_2 & 0 & 0 & 0 \\ 0 & 0 & 0 & 0 & 0 & 0 & 0 & 2G_2 & 0 & 0 \\ 0 & 0 & 0 & 0 & 0 & 0 & 0 & 0 & 2G_2 & 0 \end{pmatrix} \quad (8)$$

To make the expression consistently, the internal length scales, l_t and l_b , are written in the stress vector and strain vector so that the dimensions of couple-stresses and micro-curvatures are the same as the conventional stresses and strains respectively. Here, l_t and l_b are related to the torsion and bending respectively, and these two internal length scales can be computed from the torsion of circular cylinder and bending of a plate, respectively. The relationship between the internal length scales and the micro-polar elastic constants are as follows (Gauthier and Jahsman 1975)

$$l_t = \left(\frac{\lambda_4 + \lambda_5}{2\lambda_2 + \lambda_3} \right)^{1/2}, \quad l_b = \left(\frac{\lambda_6}{2(2\lambda_2 + \lambda_3)} \right)^{1/2} \tag{9}$$

where λ_2 is the classical Lamé constant, and the remaining four are new micro-polar constants. The dimension of λ_2 and λ_3 are force/length², and λ_4 , λ_5 and λ_6 are the force (couple/length).

In the elastic material matrix shown in Eq.7 and Eq.8, G_c is the Cosserat shear modulus, and based on the elasticity theory, other components of the elastic material matrix can be computed as follows

$$d_{11} = \frac{1 - m\nu_2^2}{(1 + \nu_1)(1 - \nu_1 - 2m\nu_2^2)} E_1, \quad d_{12} = \frac{\nu_1 + m\nu_2^2}{(1 + \nu_1)(1 - \nu_1 - 2m\nu_2^2)} E_1,$$

$$d_{13} = \frac{\nu_2}{1 - \nu_1 - 2m\nu_2^2} E_1, \quad d_{33} = \frac{1 - \nu_1}{1 - \nu_1 - 2m\nu_2^2} E_1, \quad G_1 = \frac{E_1}{2(1 + \nu_1)}, \quad m = \frac{E_1}{E_2} \tag{10}$$

Here, E_1 , ν_1 and G_1 represent the elastic modulus, Poisson's ratio and shear modulus in the isotropic plane, respectively. E_2 , ν_2 and G_2 are independent with each other and represent the elastic modulus, Poisson's ratio and shear modulus at the elastic symmetric direction, respectively. It can be seen that the elastic transversely isotropic Cosserat continuum also has five elastic parameters if the Cosserat shear modulus is neglected.

NUMERICAL EXAMPLE

In order to test the effectiveness of the proposed transversely isotropic Cosserat continuum model, a FE analysis of the stress and deformation of transversely isotropic layered soils subjected to a loading by an elastic rectangular plate is taken here. In the present work, the twenty noded displacement-based solid isoparametric element interpolation approximation, as can be seen in Fig.3, is simply employed for the six degrees-of-freedom in the 3D Cosserat continuum.

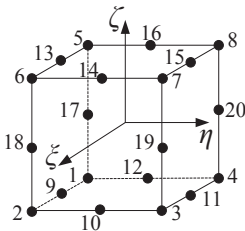


FIG.3. Twenty noded solid finite element for 3D Cosserat continuum.

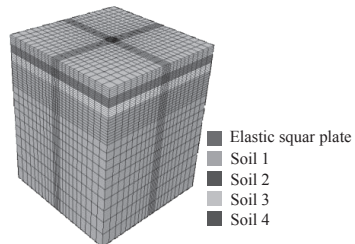


FIG.4. FE model of the layered soil foundation.

The example here is a little different from which is in Ai’s research (Ai and Cao 2011), except for the material parameters of soils. The FE model of this example is shown in Fig.4, the half-side length and thickness of the elastic square plate are 3m and 0.5m, respectively. The rigidity of the plate is defined as follow (Milovic 1992)

$$k = \frac{E_b}{E_{v4}}(1 - \nu_{v4}^2)(h/a)^3 \tag{11}$$

where a is the half-side length of the elastic square plate, h is its thickness, E_b is the elastic modulus of the rectangular plate, E_{v4} and ν_{v4} are vertical elastic modulus and Poisson’s ratio of the fourth layered soil respectively. The Poisson’s ratio of the rectangular plate $\nu_b=0.25$. We use the vertical normal stress factor I_z and vertical surface displacement factor I_w to describe the features of stress and deformation of the layer foundation, and the formulas can be found in Ai’s paper (Ai and Cao 2011).

The elastic material parameters of each layered soil are shown in Table 1. In the analysis, the soils are considered as isotropic body and transversely isotropic body respectively. If the soil is considered as homogeneous isotropic body, then make $E_2=E_1$, $\nu_2=\nu_1$ and $G_2=G_1$ in the FE program. The Cosserat continuum can be degraded into classical one by setting the internal length scale or the Cosserat shear modulus as zero. The results of I_z and I_w in different conditions are shown in Fig.5 and Fig.6.

Table 1. The elastic material parameters of each layered soil

| soil | E_1 (MPa) | ν_1 | E_2 (MPa) | ν_2 | G_2 (MPa) | h (m) |
|------|-------------|---------|-------------|---------|-------------|---------|
| 1 | 3 | 0.25 | 6 | 0.35 | 4 | 5 |
| 2 | 16 | 0.25 | 8 | 0.3 | 5.4 | 5 |
| 3 | 5 | 0.25 | 9 | 0.35 | 8 | 5 |
| 4 | 12 | 0.25 | 12 | 0.25 | 10 | 80 |

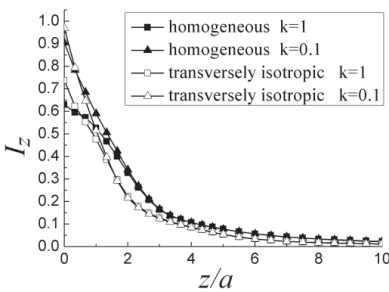


FIG.5. Vertical normal stress factors I_z under the center of the plate of homogeneous and transversely isotropic layered soils for different values of rigidity k .

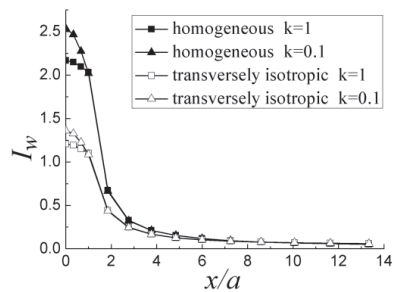


FIG.6. Vertical surface displacement factors I_w along the x-coordinate of homogeneous and transversely isotropic layered soils for different values of rigidity k .

From Fig.5 and Fig.6, it can be seen that the value of the vertical normal stress factors I_z decreases with increase of the depth of soil foundation and also the value of the vertical surface displacement factors I_w decreases as the distance from the center of the plate increases in the horizontal direction. It is also obviously that under the same loading condition, the calculated results of vertical stress and displacement are markedly different when the soils are assumed as different models. It illustrates that what hypothesis adopted for the soil model will markedly influence the calculated accuracy of the stress and settlement of soil foundation. So it is meaningful and necessary to consider the soil as a transversely isotropic model in some circumstance.

Further, consider the soil as transversely isotropic Cosserat continuum and compare the results of I_z and I_w for different internal length scale. The rigidity of the rectangular plate is chosen as $k=1$, and the internal length $l_c(=l_b=l_t)=0.05, 0.1$ and 0.2m respectively. The calculated curves of I_z and I_w are shown in Fig.7 and Fig.8.

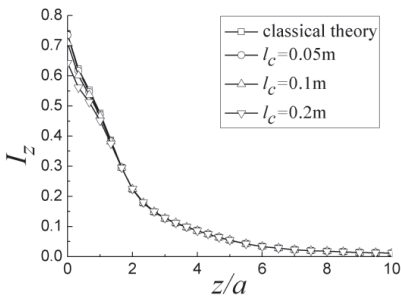


FIG.7. Vertical normal stress factors I_z under the center of the plate in classical theory and Cosserat theory.

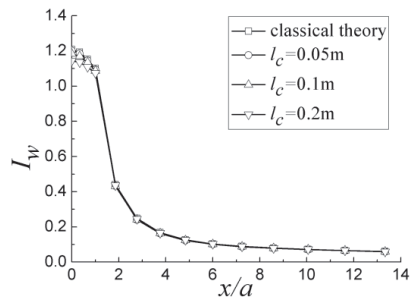


FIG.8. Vertical surface displacement factors I_w along the x-coordinate in classical theory and Cosserat theory.

It can be seen that the values of stress and settlement calculated by the Cosserat continuum are a little lower than the results of classical one, and become smaller as the internal length scales increase. From the perspective of energy, the reason of this phenomenon is that, in the Cosserat continuum, the work done by external forces changes into two parts, one is the classical strain energy and the other is the energy related to the local rotation of micro-structure, and the latter improves the loading capacity of material as the internal length scale increases. This shows Cosserat theory is able to describe micro-scale mechanical property of soils. It also demonstrates that the results based on Cosserat theory will be the same as the classical one's when the internal length scales are zero, which confirms the conclusion above.

CONCLUSIONS

This paper develops an elastic transversely isotropic model in the frame of Cosserat theory. The finite element program based on this model is developed to analysis the stress and deformation of a transversely isotropic layered soils subjected to a loading on an elastic rectangular plate. Two main conclusions can be acquired:

- (1) Compared with the isotropic model, different results will be obtained when regard the soil as transversely isotropic one, so, in order to ensure the calculated accuracy, it's necessary to adopt the transversely isotropic model, which is more consistent with the soil's property in practical engineering.
- (2) Different values of internal length scales in Cosserat model will influence the calculated results of stress and deformation of the layered soil foundation, which reflects the capacity of Cosserat theory in describing micro-scale mechanical property of soils (or other materials). By contrast, the classical theory has inability in this respect.

ACKNOWLEDGMENTS

This work was financially supported by the National Natural Science Fund of China (50808033), the Fundamental Research Funds for the Central Universities (DUT11LK37), and the National Key Basic Research and Development Program (973 Program, 2010CB731500).

REFERENCES

- Ai, Z.Y., and Cao, G.J. (2011). "Analysis of transversely isotropic layered soils under an elastic rectangle plate." *Rock and Soil Mechanics(Supp.2)*, 32, 59-63.
- Bonet, J., and Burton, A.J. (1998). "A simple orthotropic, transversely isotropic hyperelastic constitutive equation for large strain computations." *Computer methods in applied mechanics and engineering*, 162(1), 151-164.
- De Borst, R., and Sluys, L. J. (1991). "Localisation in a Cosserat continuum under static and dynamic loading conditions." *Computer Methods in Applied Mechanics and Engineering*, 90(1), 805-827.
- Gauthier, R.D., and Jahsman, W.E. (1975). "A quest for micropolar elastic constants." *Journal of Applied Mechanics*, 42, 369-374.
- Li, X.K., and Tang, H.X. (2005). "A consistent return mapping algorithm for pressure-dependent elastoplastic Cosserat continua and modelling of strain localisation." *Computers and structures*, 83(1), 1-10.
- Liao, J.J., and Wang, C.D. (1998). "Elastic solutions for a transversely isotropic half-space subjected to a point load." *International Journal for Numerical and Analytical Methods in Geomechanics*, 22(6), 425-447.
- Milovic, D. (1992). "Stresses and Displacements for Shallow Foundations." Amsterdam: Elsevier Publishing Company.
- Riahi, A., and Curran, J.H. (2009). "Full 3D finite element Cosserat formulation with application in layered structures." *Applied Mathematical Modelling*, 33(8), 3450-3464.
- Tang, H.X., and Hu, Z.L. (2012). "Three Dimensional Cosserat Continuum Model and its Application to Analysis for the Cantilever Beam." *Applied Mechanics and Materials*, 117, 438-442.
- Truesdell, C., and Toupin, R. (1960). "The classical field theories." *Handbuch der Physik*, 3(1), 226-793.

3-D Masing Behavior of a Parallel Iwan Model

Ethan Dawson¹, A.M. ASCE, Wolfgang Roth¹, M. ASCE, G.E.
and Bei Su¹, A.M. ASCE, P.E.

¹URS Corporation, 915 Wilshire Blvd, Suite 700, Los Angeles, CA, 90017-3437; PH (213) 996-2000; FAX (213) 996-2374; email: ethan.dawson@urs.com

ABSTRACT: A plasticity model for simulating 3-D hysteretic behavior of frictional materials is presented. The model, implemented in the program FLAC^{3D}, is a generalization of the 1-D parallel Iwan model, in which a number of components are connected in parallel, each component consisting of a linear elastic spring in series with a perfectly plastic slider. This simple arrangement produces non-linear stress-strain curves and hysteretic, Masing behavior for 1-D cyclic loading. Remarkably, this approach also works for 3-D cyclic loading. For generalization to 3-D, the constitutive model consists of a number of 3-D linear-elastic perfectly-plastic components with Drucker-Prager yield conditions. All components are subjected to the same strain, with the global stress defined as the average of the component stresses. This simple framework is straightforward to implement numerically, leading to a robust tool for analysis of general 3-D stress paths. The 3-D Masing behavior of the Iwan model is demonstrated for simultaneous cyclic loading in two and three orthogonal directions. The interaction between stress-strain loops in orthogonal directions is explored. Further work is required to validate the predicted interaction against laboratory experiments.

INTRODUCTION

For three-dimensional (3-D) dynamic analyses involving complex loading paths, it is useful to have a reliable, numerically robust soil model capable of simulating Masing (hysteretic) behavior in multiple dimensions. This paper explores the performance of a 3-D plasticity model for frictional soils which is a generalization of the 1-D Iwan parallel-series model. Because of their simplicity, parallel Iwan models are widely used in structural engineering to represent hysteretic behavior of individual components or connections, and are also used in earthquake engineering and seismology for 1-D site response studies. Remarkably, this simple technique can also be adapted for use in 3-D plasticity models for simulating general nonproportional cyclic loading (Chiang, 1992 and Chiang & Beck, 1994).

Parallel Iwan models have been shown to be capable of accurately simulating complex non-proportional cyclic strain paths for metal plasticity (Chiang, 1992;

Chiang & Beck, 1994; Dawson, 2011). However, metals have a large linear elastic range, while soils exhibit plastic yielding even at very low strains. Thus, it is not clear that a model useful for metal plasticity would be equally useful for soil plasticity.

The aim of this paper is to demonstrate that parallel Iwan models are potentially capable of modeling complex non-proportional cyclic stress paths for soils - specifically, for the type of cyclic-strain paths relevant for 3-D seismic analyses. These paths involve simultaneous cyclic straining in multiple directions with cycle amplitudes varying over several orders of magnitude. The 3-D Masing behavior of the Iwan model is demonstrated by applying cyclic loading in two and three orthogonal directions and observing the model response. The interaction between stress-strain loops in orthogonal directions is explored.

IWAN MODELS

Iwan (1966, 1967) explored the idea that a material exhibiting hysteretic behavior can be thought of as consisting of a large number of elastic, perfectly-plastic components having different yield levels. He investigated the hysteretic behavior of assemblies of elastic springs and plastic sliders, considering both a series-parallel arrangement and a parallel-series arrangement. For the series-parallel model, the elastoplastic components are arranged in a series, thus, each component has the same stress. For the parallel-series model, the components are arranged in parallel, thus, each component has the same strain. Iwan demonstrated that these systems exhibit a Bauschinger effect and follow Masing rules, so that the cyclic behavior is completely determined if the monotonic loading behavior is known.

To extend these 1-D ideas into 3-D plasticity, Iwan focused on the series-parallel arrangement, which he felt had similarities with the concept of kinematic hardening which had been developed at the time. Iwan proposed a collection of nested yield surfaces, with each surface translating according to its own linear work-hardening rule. Since then, nested-surface models have been used extensively in soil plasticity. However, these models are quite complicated with many moving parts. In addition to kinematic hardening rules, translation rules are required to move the nested yield surfaces while preventing them from overlapping, and additional logic is required to determine which yield surface is active at any particular instant.

Chiang (1992) and Chiang and Beck (1994) demonstrated that a much simpler 3-D plasticity model can be developed based on the parallel-series model, rather than the series-parallel model. This has also been demonstrated by Einav (2005) and Einav and Collins (2008). The constitutive model consists of a number of 3-D linear-elastic, perfectly-plastic components acting in parallel. All components are subjected to the same strain, with the global stress defined as the average of the component stresses. The yield surfaces of the components remain fixed – they do not translate in stress space. Thus, numerical implementation of the model is extremely simple.

THE IWAN PARALLEL-SERIES MODEL

The 1-D Iwan parallel-series model is illustrated in Figure 1. A number of components are connected in parallel, each component consisting of a linear elastic

spring with stiffness E_i in series with a perfectly plastic slider which yields at stress, σ_i^* . Each component is subject to the same strain, and the resulting global stress for the system is the average stress of the individual components. If all components start from an unstressed state, the initial loading curve is given by:

$$\sigma = \frac{1}{N} \left[\sum_{i=1}^m \underbrace{\sigma_i^*}_{\text{yielding}} + \sum_{i=m+1}^N \underbrace{E_i \varepsilon}_{\text{elastic}} \right] \tag{1}$$

where the components are arranged in order of increasing yield force, and m is the number of components at their yield state. There are two contributions to the global stress, those components at yield, and those components still remaining in their elastic range. It can be shown that this simple arrangement produces hysteretic Masing behavior for cyclic loading. Although both the yield stress and elastic stiffness can vary between components, most applications of the Iwan model have used a constant elastic stiffness, varying only the yield strength.

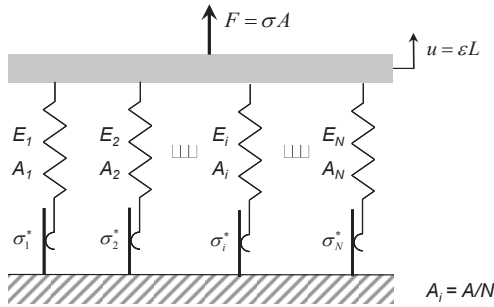


FIG. 1. The 1-D Iwan parallel-series model.

To adapt this model to 3-D plasticity, the 1-D spring-slider components are replaced with 3-D linear-elastic, perfectly-plastic components, each with their own stress tensor and yield strength. For this study, the components are given a Drucker-Prager yield condition

$$f(I_1, J_2) = \alpha I_1 + \sqrt{J_2} = 0 \tag{2}$$

where I_1 is the first invariant of the stress tensor; J_2 is the second invariant of the deviatoric stress tensor; and α is the strength parameter. As in the 1-D model, all components are subject to the same strain, and the global stress is the average of the component stresses.

FLAC^{3D} NUMERICAL IMPLEMENTATION

The Iwan parallel scheme described above was implemented in FLAC^{3D} (Itasca 2009) as a C++ DLL. The constitutive model internally stores a separate stress tensor and yield strength for each Iwan component. The strain increment supplied by FLAC^{3D} at each time step is passed down to the components, and the updated stress state returned by the components is then averaged to compute the global stress. Since 10 to 20 Iwan components are required to smoothly approximate the backbone loading curve, the memory requirements of the Iwan model are substantial, although no larger than those for nested-surface models.

MODEL RESPONSE FOR SIMULTANEOUS CYCLIC LOADING IN ORTHOGONAL DIRECTIONS

The model was fit to a backbone curve corresponding to the G/G_{\max} relation of Vucetic and Dobry (1991) for $PI = 0$. As shown in Figure 2, twenty components were necessary to approximate the target curve over roughly three orders of magnitude of strain. The fitting process consisted simply of selecting the strength parameter, α , for each component. The shear modulus and Poisson ratio (118 MPa and 0.3) were the same for each component. There are no other model parameters. Example stress-strain loops produced with this fit are shown in Figure 3.

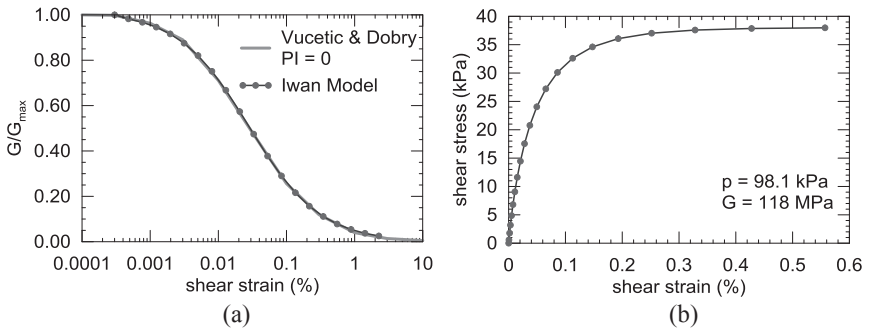


FIG. 2. Model performance: (a) G/G_{\max} of a 20-component Iwan Drucker-Prager model fit to Vucetic and Dobry (1991) curve for $PI = 0$; (b) the resulting ‘backbone’ stress-strain curve for initial loading for a confining pressure, $p = 98.1$ kPa.

To demonstrate the model’s performance for simultaneous cyclic loading in multiple directions, cyclic shear strain loading was applied in two and three orthogonal directions. Simulations were performed at a constant pressure of 98.1 kPa. Histories of shear stress are shown in Figure 4 for simultaneous application of cyclic strains of 0.1%, 0.02% and 0.005% in three orthogonal directions. Figure 5 shows stress-strain loops for the largest amplitude cycle, while Figure 6 shows stress-strain loops for the two smaller amplitude cycles. These stress-strain loops are then shown

more clearly in Figure 7 for a small portion of the simulation. The model is clearly able to produce simultaneous hysteretic behavior in multiple directions, with significant interaction between the orthogonal cycles being predicted.

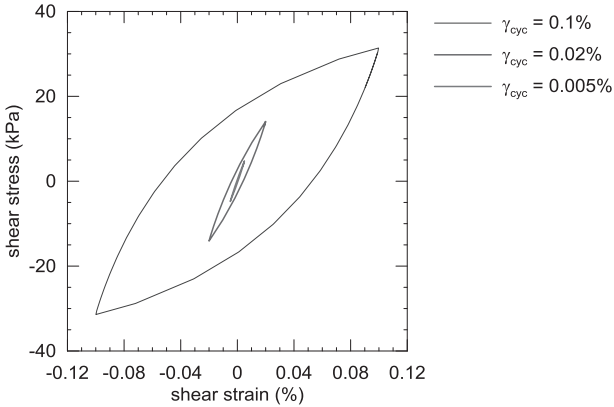


FIG. 3. Stress-strain loops for 1-D cyclic loading.

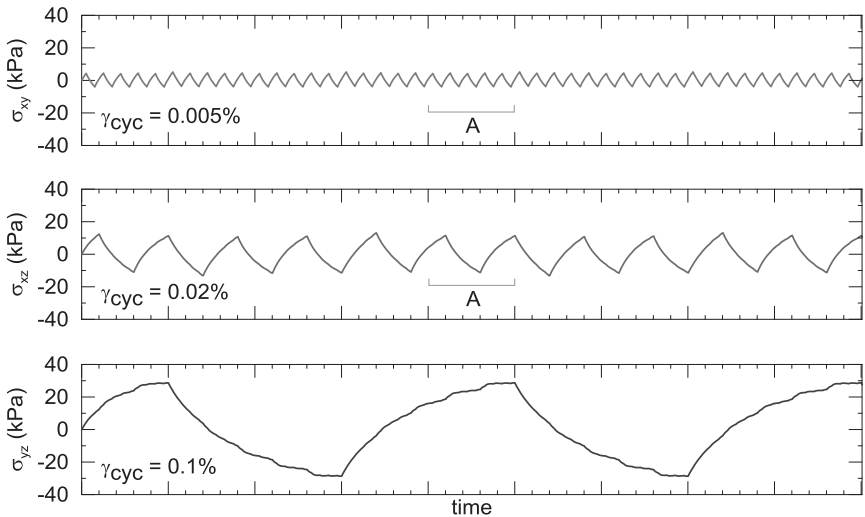


FIG. 4. Stress histories for shear strain cycles applied simultaneously in three orthogonal directions.

To further explore the interaction between stress-strain loops in orthogonal directions, analyses were performed in which low amplitude (0.005%) strain cycles were applied in one direction while a constant shear stress was applied in an orthogonal direction. Figure 8 shows computed strain histories for three different

values of the orthogonal constant shear stress. As the constant shear stress is increased, shear strains in this direction induced by the small orthogonal strain cycles increase significantly. This behavior is generally consistent with the stress probe experiments on sand specimens performed by Pradel et al. (1990) and by Gutierrez et al. (1991).

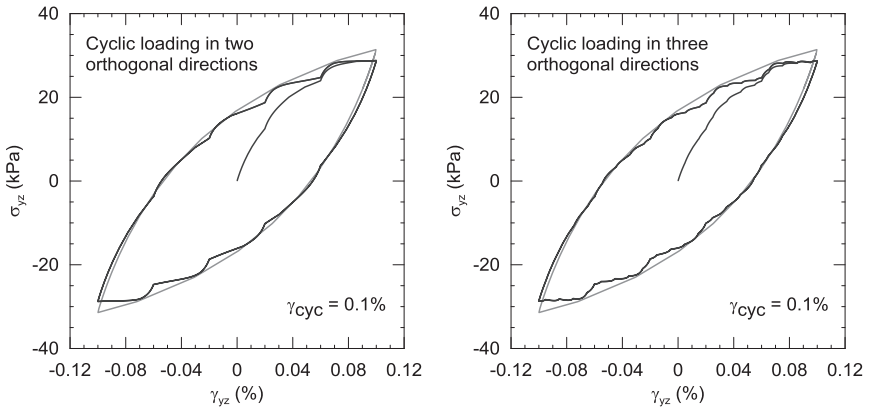


FIG. 5. Stress-strain loops for the largest amplitude cycle. Cyclic loading applied simultaneously in two and three orthogonal directions. Loop for 1-D cycling is shown in gray.

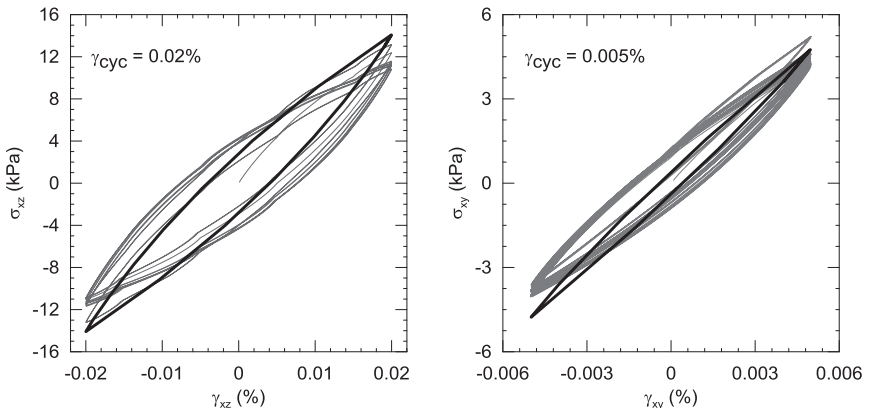


FIG. 6. Stress-strain loops for the two smaller amplitude cycles when cyclic loading is applied simultaneously in three orthogonal directions. Stress-strain histories are shown for the entire duration of the simulation. The loop for 1-D cycling is shown in black. Note that the left and right graphs are plotted at different scales.

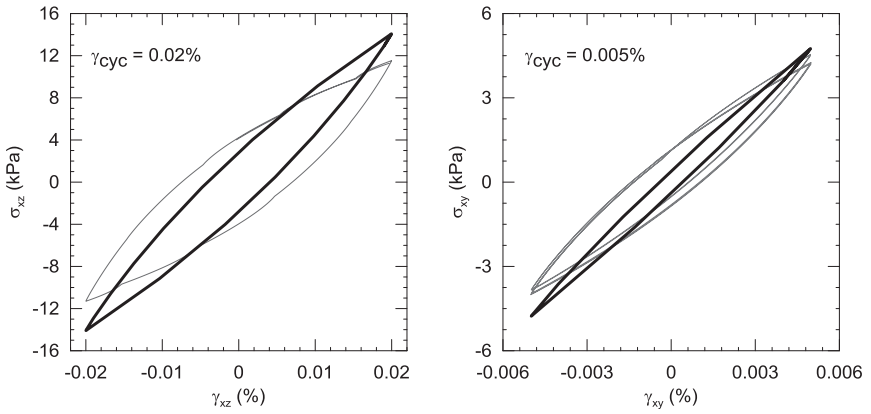


FIG. 7. Stress-strain loops for the two smaller amplitude cycles for the portion of the simulation denoted ‘A’ in Figure 4.

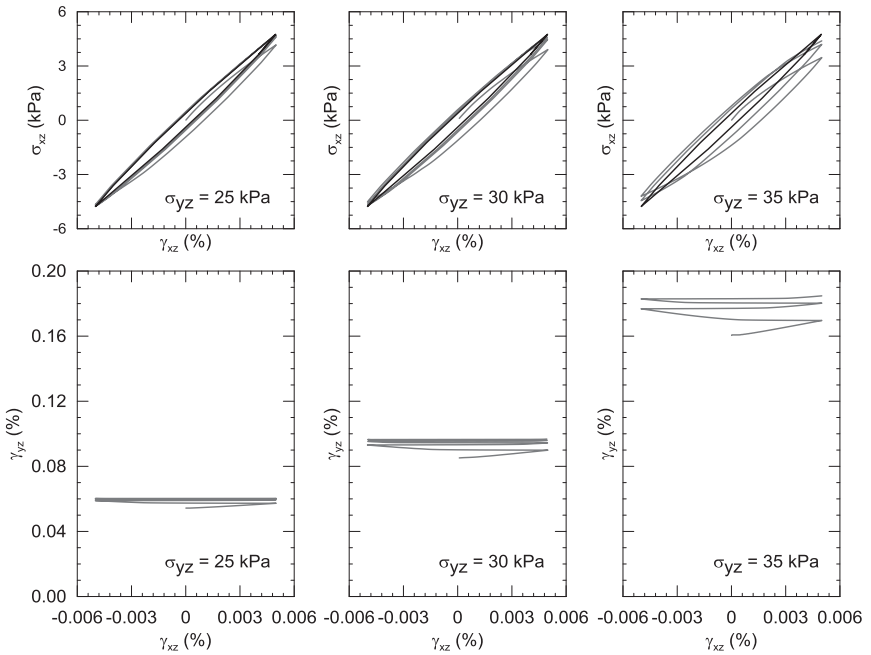


FIG. 8. Stress-strain loops and shear strains when a constant shear stress is applied in a direction orthogonal to the strain cycles. Cyclic strain is 0.005%.

CONCLUSION

The 3-D Masing behavior of a parallel Iwan model for frictional soils has been demonstrated for simultaneous cyclic loading in two and three orthogonal directions. The model is clearly capable of simulating simultaneous hysteretic behavior in multiple directions, with significant interaction between the orthogonal cycles being predicted. Assessing how realistic the predicted interaction is will require further investigation and detailed comparison with experimental results. Nevertheless, the basic model behavior does appear plausible, corresponding to what one would expect from this type of plasticity model.

These complex results were produced by a very simple model that is easy to implement and is numerically robust and reliable. Results shown here suggest that the parallel Iwan model is a promising tool for 3-D dynamic analyses involving cyclic loading in multiple directions. Much further work is required to determine how realistic the response predicted by the Iwan parallel model is.

REFERENCES

- Chiang, D.Y. (1992). "Parsimonious modeling of inelastic systems." *Report No. EERL 92-02*, California Institute of Technology, Pasadena.
- Chiang, D.Y. and Beck, J.L. (1994). "A new class of DEM for cyclic plasticity – I. Theory and application." *Int. J. Solids Structures* 31(4): 485-496.
- Dawson, E.M. (2011). "A parallel Iwan model for 3D cyclic loading of cohesive materials." *Continuum and Distinct Element Numerical Modeling in Geomechanics – 2011 – Sainsbury, Hart, Detournay & Nelson (eds.) Paper: 13-04.*
- Einav, I. (2005). "A second look at strain space plasticity and latest applications." *Proc. 18th Australian conference on the mechanics of structures and materials (ACMSM). Perth. Vol. 1 :225-231.*
- Einav, I. and Collins, I.F. (2008). "A thermo-mechanical framework of plasticity based on probabilistic micro-mechanics." *J. Mech. Mater. Structures* 3(5): 867-92.
- Gutierrez, M., Ishihara, K. and Towhata, I. (1991). "Flow theory for sand during rotation of principal stress direction." *Soils and Foundations*. Vol. 31(4):121-132.
- Itasca Consulting Group, Inc. (2009). *FLAC3D – Fast Lagrangian Analysis of Continua in 3 Dimensions, Ver. 4.0 User's Manual*. Itasca, Minneapolis/MN.
- Iwan, W.D. (1966). "A distributed element model for hysteresis and its steady state response." *J. Appl. Mech. ASME* 33(4): 893-900.
- Iwan, W.D. (1967). "On a class of models for the yielding behavior of continuous and composite systems." *J. Appl. Mech. ASME* 34(2): 612-617.
- Pradel, D., Ishihara, K. and Gutierrez, M. (1990). "Yielding and flow of sand under principal stress rotation." *Soils and Foundations*. 30 (1):87-99.
- Vucetic, M. and Dobry, R. (1991). "Effect of soil plasticity on cyclic response." *J. Geotechnical Engrg.* 117(1): 89-107.

Soil - Pile - Structure Interaction in Earthquake Engineering

Yingcai Han¹, M. ASCE and Shin-Tower Wang², M. ASCE

¹Technical Director, Fluor Canada, 1075 W. Georgia Street, Vancouver, BC V6E 4M7 Canada
yingcai.han@fluor.com

²President, Ensoft Inc, 3003 West Howard Lane, Austin, Texas, 78728, USA
stw@ensoftinc.com

ABSTRACT: The advances on soil-pile-structure interaction are described in this study. The nonlinearity of soil is accounted for approximately by a boundary zone model, and the curves of stiffness and damping of the nonlinear soil-pile system are provided. The coupled horizontal and rocking vibration of an embedded foundation (including pile cap) is analyzed by four parameters rather than the traditional six parameters. The radiation damping is corrected based on many dynamic tests in the field. The effects of soil-pile-structure interaction on dynamic behaviour are examined based on an engineering case. Three conditions are considered, (1) the soil-pile-structure interaction is accounted for fully, (2) the soil-pile system is flexible but the structure is assumed to be rigid, and (3) the structure is flexible but the base foundation is assumed to be rigid. For practical applications, a tower structure supported on piled foundation was examined under seismic loads. The earthquake forces and response were calculated using the time history analysis and response spectrum analysis, and compared with those using the method of equivalent static loads.

INTRODUCTION

Many researchers have made contributions to the subject of soil-pile-structure interaction, such as Dobry & Gazetas (1988), Roesset et al (1986), Luco (1982), Gazetas & Makris (1991), Benerjee & Sen (1987) and Wolf (1988). Different approaches are available to account for dynamic soil-pile interaction but they are usually based on the assumptions that the soil behavior is governed by the law of linear elasticity or visco-elasticity, and that the soil is perfectly bonded to a pile. In practice, however, the bonding between the soil and the pile is rarely perfect, and slippage or even separation often occurs in the contact area. Furthermore, the soil region immediately adjacent to the pile can undergo a large degree of straining, which would cause the soil-pile system to behave in a nonlinear manner. A lot of efforts have been made to model the soil-pile interaction using the 3D FEM. However, it is too complex, especially for pile groups in nonlinear soil. A rigorous approach to the nonlinearity of a soil-pile system is extremely difficult and time consuming.

Great advances have been developed on the study of soil-pile-structure interaction, and the importance of such interaction is recognized widely in the dynamic or seismic design. However, some of the problems are still remained and concerned in practice. One of the interesting subjects is how to account for the nonlinearity of soil in an earthquake environment. The plane strain model of soil-pile system has been improved by a boundary zone model and a computer program DYNAN is developed. The curves of stiffness and damping of pile foundations are proposed, which vary with the ratio of shear modulus G_i / G_0 to indicate the nonlinear properties of soil.

Another interesting subject is the coupled horizontal and rocking vibration of an embedded foundation (including pile cap). A simplified mathematical model was proposed to analyze the coupled vibration using four parameters rather than the traditional six parameters. The radiation damping is also very important subject to soil-pile-structure interaction and was discussed in this study.

The effect of soil-pile-structure interaction is estimated based on an engineering case. The different conditions are considered. In the first case, the soil-pile-structure interaction is accounted for fully, that is, all of the soil, pile and structure are flexible. In the second case, the soil-pile system is flexible, but the structure is assumed to be rigid (no deformation in the superstructure). In the third case, the structure is flexible but fixed (or pinned) to a rigid base, no deformation in base soil (without SSI).

As practical applications, a vacuum tower structure was examined in severe seismic zone as a typical industrial structure supported on pile foundation. The vacuum tower sets on a steel frame with height of 20 m. There are 25 steel piles in the foundation. Three different base conditions were assumed to illustrate the soil-pile-structure interaction: rigid base (i.e. no deformation in the foundation), linear soil-pile system, and nonlinear soil-pile system. The case of liquefaction of sand layer was also discussed for the pile foundation. The seismic response were calculated from the response spectrum analysis and time history analysis considering the soil-pile-structure interaction, and compared with the method of equivalent static loads.

NONLINEAR SOIL - PILE SYSTEM WITH BOUNDARY ZONE MODEL

As an approximate analysis, a procedure was developed using a combination of the analytical solution and the numerical solution, rather than using the general FEM. This procedure is considered as an efficient technique for solving the nonlinear soil-pile system. The relationship between the foundation vibration and the resistance of the side soil layers was derived using elastic theory by Baranov (1967). Both theoretical and experimental studies have shown that the dynamic response of piles is very sensitive to the properties of the soil in the vicinity of the pile shaft as indicated by Han and Novak (1988). A model of inner weakened zone or so called boundary zone includes a cylindrical annulus of softer soil around the pile in plane strain analysis. One of the simplifications involved in the original boundary zone model was that the mass of the inner zone was neglected to avoid the wave reflections from the interface between the inner boundary zone and the outer zone. Velestos and Dotson (1988) proposed a scheme that can account for the mass of the boundary zone. Some of the effects of the boundary zone mass were investigated by Novak and Han (1990), who found that a homogeneous boundary zone with a non-zero mass yields undulation

impedance due to wave reflections from the fictitious interface between the two media.

The ideal model for the boundary zone should have properties smoothly approaching those of the outer zone to alleviate wave reflections from the interface. Consequently, Han and Sabin (1995) proposed a model for the boundary zone with a non-reflective interface. The complex shear modulus, $G(r)$, varies parabolically. G_i and G_o are the shear modulus of the inner and outer zones, and the modulus ratio is an approximate indicator for the nonlinear behavior of soil. It should be explained that the method described here is not a rigorous approach to model the nonlinearity of a soil-pile system. It is an equivalent linear method with a lower value of G_i and a higher value of damping β_i in the boundary zone. With such a model, the analytical solutions can be obtained for the impedance functions of a pile.

The group effect of piles is accounted for using the method of interaction factors. The static interaction factors are based on the study by Poulos and Davis (1980). The dynamic interaction factors are derived from the static interaction factors multiplied by a frequency variation. The frequency variation of interaction factors is based on the charts of Kaynia and Kausel (1982).

There are six degrees of freedom for the rigid mat, and lateral vibration is coupled with rocking vibration. It should be explained that the foundations (or caps on piles) are assumed to be rigid. However, in most cases, the superstructures are flexible rather than rigid. The effects of soil-pile-structure interaction on dynamic response were discussed by Han (2008).

For the pile foundation under static lateral loads, the differential equation for a beam-column can be solved using nonlinear soil resistance (p - y) curves. Nonlinear lateral load-transfer from the foundation to the soil has been modeled widely by using p - y curves for various types of soil. Unfortunately, the dynamic behavior of soil-pile system can not be solved analytically by using the nonlinear p - y curves, which are derived primarily based on static conditions. An approximate analysis has to be used for the dynamic analysis of pile foundations.

The normalized stiffness and damping of pile foundation varied with G_i / G_o as shown in Figure 1 and Figure 2 respectively. The values of stiffness and damping were generated, and applicable to general pile foundations, no matter concrete or steel piles.

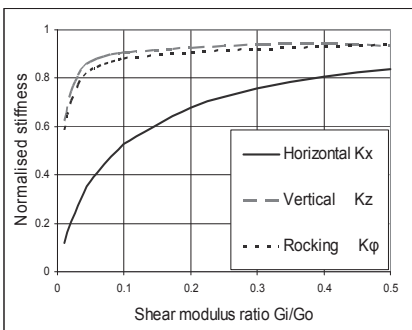


FIG. 1. Normalized stiffness of piles vs G_i / G_o

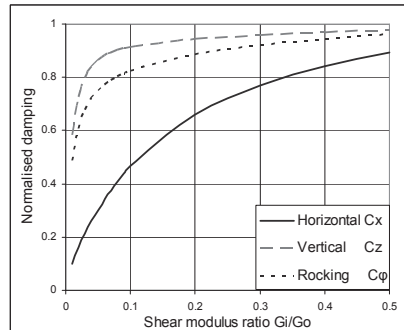


FIG. 2. Normalized damping of piles vs G_i / G_o

The stiffness and damping are generated in low frequency (6 Hz). The dynamic stiffness approach to the static one in the low frequency as $G_i / G_0 = 1.0$. The values of stiffness and damping were normalized to show the effects of G_i / G_0 . The normalized stiffness and damping are defined as the dynamic stiffness and damping to be divided by static values. It should be explained that the static stiffness can not be generated directly from the program, and the values of stiffness and damping in very low frequency domain such as 0.01 Hz were assumed to be close to as static values.

From Figures 1 and 2, it can be seen that the variation of stiffness and damping is larger for horizontal vibration than those for vertical and rocking vibration. It is concluded that the effects of G_i / G_0 are more significant on lateral impedances than those on vertical and rocking impedances. Also, it is noted that the stiffness and damping vary gently as $G_i / G_0 = 0.25 - 0.5$, and vary sharply as $G_i / G_0 < 0.25$. As $G_i / G_0 < 0.1$, the stiffness and damping are reduced seriously for all of the vibration modes such as under seismic loads.

COUPLED VIBRATION OF EMBEDDED FOUNDATION (PILE CAP)

The problem of coupled horizontal and rocking vibration of an embedded foundation is complex in practice. The relationship between the foundation vibration and the resistance of side soil layers can be derived using the elastic theory. Then, the solutions of coupled horizontal and rocking vibration of embedded footings were formulated. Six vibration parameters -horizontal stiffness K_x , and damping C_x , rocking stiffness K_ϕ and damping C_ϕ , and cross coupled stiffness $K_{x\phi}$ and $C_{x\phi}$ —are included in the displacement expression. An inverse problem is often met in experimental research: all the parameters of the embedded foundation are to be determined, while the dynamic response is given from measurements. It is difficult to back-calculate for the six parameters in the displacement expressions.

A simplified mathematical model of the coupled horizontal and rocking vibration of an embedded foundation was proposed by Han (1989). Vibration tests of the foundation with different embedment were conducted and compared with different methods. Based on this method, only four parameters are required in the displacement

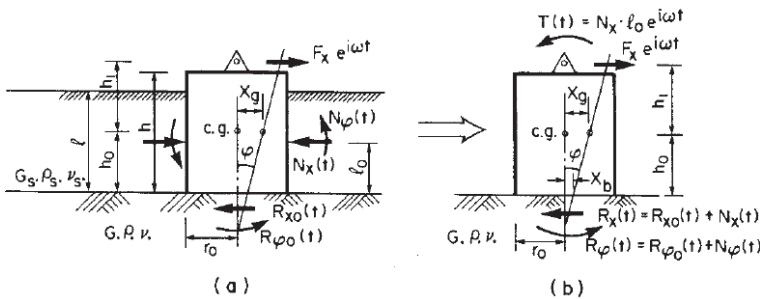


FIG.3. Simplified mathematics model of coupled horizontal and rocking vibration of embedded foundation (pile cap) (a) exciting force and reaction forces acting on the embedded footing (b) equivalent foundation rested on the surface of elastic half-space. (After Han, 1989)

expression but six parameters are required in Novak's method. The four parameters can be back-calculated from the dynamic response of the foundation using this method. The results by the present method agree with the measured data for the foundation with different embedment. The benefit of using only four parameters for foundation impedances is significant because the cross coupled stiffness and damping are inconvenient to be included in structural modeling.

The radiation damping is also very important subject to the soil-pile-structure interaction. The elastic-wave energy from foundation vibration dissipates in three dimensions and forms the radiation damping. The radiation damping is the dominant energy dissipation mechanism in most dynamically loaded foundation systems. The formula of radiation damping was derived based on the elastic theory in which the soil is assumed to a homogeneous isotropic medium. As a matter of fact, however, the soil is not a perfect linear elastic medium as assumed. A series of dynamic experiments have been done and indicated that the damping is overestimated in the elastic theory. The values of radiation damping have been modified and reduced in DYNAN program based on the measurements in dynamic tests.

EFFECTS OF SOIL-PILE-STRUCTURE INTERACTION

Classical empirical methods of dynamic analysis assume that the foundation acts as a rigid body, such as Barkan model (1962). However, three conditions of soil-pile-structure system were considered in this study. In the first case, the soil-pile-structure interaction is accounted for fully, that is, all of the soil, pile and structure are flexible. In the second case, the soil-pile system is flexible, but the table top structure is assumed to be rigid (no deformation in the superstructure). Normally the dynamic analysis for foundations supporting vibrating equipment is conducted in this way. In the third case, the columns of table top structure are flexible but fixed (or pinned) to the rigid base, no deformation in base soil (without SSI). In early years the seismic analysis was generally conducted in this way.

A practical case of a table top structure with a reciprocating compressor foundation is examined to illustrate the effects of soil-pile-structure interaction. 47 concrete piles were used in the foundation, and pile diameter is 0.6 m with length of 49 m. The dimension of mat foundation (pile cap) is 16.6 m by 14.35 m, with thickness of 1.5 m. The shear modulus ratio $G_i / G_o = 0.5$ was assumed to indicate the non-linear behavior of soil. The stiffness and damping of piles were generated by the program as shown in Table 1.

Table 1 Stiffness and Damping of Pile Foundation

| Stiffness | | | Damping | | |
|---------------------|---------------------|------------------------|---------------------|---------------------|--------------------------|
| K_x (kN/m) | K_z (kN/m) | K_ϕ (kN.m/rad) | C_x (kN/m/s) | C_z (kN/m/s) | C_ϕ (kN.m/rad/s) |
| 2.226×10^6 | 3.227×10^6 | 4.586×10^8 | 1.125×10^5 | 2.667×10^5 | 7.073×10^6 |

Where K_x , K_z , and K_ϕ are stiffness in the horizontal, vertical and rocking directions, and C_x , C_z , and C_ϕ are damping constants in the same directions.

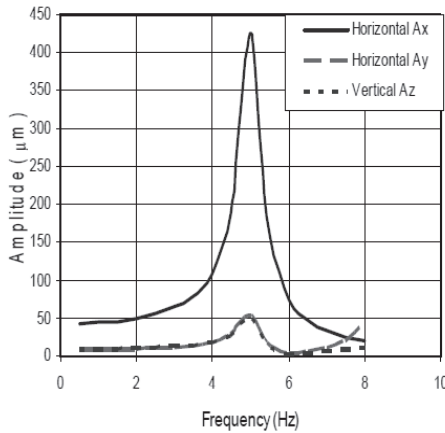


FIG. 4 Dynamic response of structure with soil-pile-structure interaction

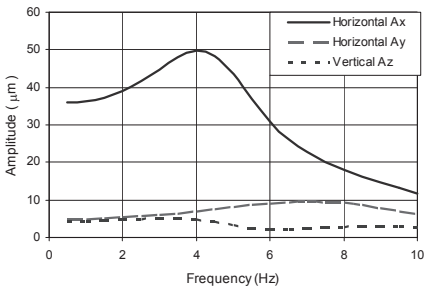


FIG. 5. Rigid structure rest on flexible piles

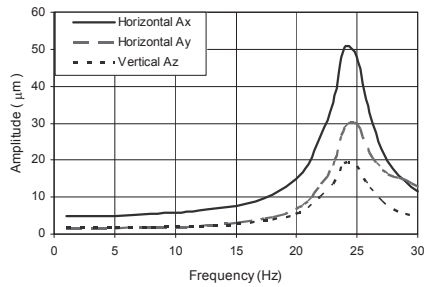


FIG. 6. Flexible structure rest on rigid base (without SSI)

The dynamic response of table top structure was analyzed by using the finite element model from SAP 2000 with the input of foundation parameter stiffness and damping as listed in Table 1. The displacement curves calculated at the corners of deck slab are shown in Fig. 4. It should be explained that the response of foundation is a coupled vibration between three translational and three rotational modes, although only horizontal and vertical behavior are described herein. It can be seen that the peak value of amplitude is $A_x = 426 \mu\text{m}$ at frequency 5.0 Hz. Amplitude $A_x = 47 \mu\text{m}$ at operating speed of 6.67 Hz (400 rpm).

For the second case, the deformation of base soil is accounted, but the table top structure is assumed to be rigid. The stiffness and damping of piles are generated as the same as in the first case. The same loads are applied to the structure. The displacement curves calculated at the same points is shown in Fig. 5. It can be seen that the peak

value of amplitude is $A_x = 50 \mu\text{m}$ at frequency 4 Hz. Amplitude $A_x = 25 \mu\text{m}$ at operating speed. The deformation of superstructure is not considered since it is assumed to be rigid. It can be seen that the resonant frequency is close or a little lower to that in Fig. 4, but the dynamic response is underestimated significantly.

For the third case, the columns of table top structure were pinned to the rigid base (no SSI). The superstructure is flexible but the deformation of base soil was ignored. The structure is subjected to the same loads, and modeled by the same FEM model. The displacement curves calculated at the same points are shown in Fig. 6. It can be seen that the peak value of amplitude is $A_x = 51 \mu\text{m}$ at frequency 24 Hz. Amplitude $A_x = 5.0 \mu\text{m}$ at operating speed. In this case, the resonant frequency is very high since the soil-structure interaction is ignored. The vibration is produced only in the superstructure, and no deformation is considered in the soil-foundation portion. Obviously, it is not true in real situations. The stiffness of structure is overestimated since it was fixed to the rigid base. The damping is underestimated since the energy of vibration transferred through soil (radiation damping) is ignored.

From the above comparison it can be seen that the dynamic response of structure with varied conditions is quite different. Not only the amplitudes are varied at operating speed, but also the resonant frequencies and peak values are very different. As shown in Fig. 4, the peak value is much high and strong vibration is predicted in the resonant frequency domain. The vibration occurred in the entire superstructure (table top structure) and the soil-foundation portion. It is interesting to note that the values of amplitude calculated with the soil-pile-structure interaction (Fig. 4) are close to that calculated with the rigid superstructure and the flexible soil-pile system (Fig. 5) in a very lower frequency range, such as 0.5 to 2 Hz. However, the difference between the two curves becomes large with frequency increasing. The higher values of amplitudes in Fig. 4 come from some higher modes at some locations of the superstructure.

With the comparisons above, the role of soil, piles and structure in the dynamic response can be identified. The range of material damping ratio for concrete structures is 0.02 to 0.05. The damping ratio was taken as 0.02 for all of the three cases. A higher damping is involved with soil-pile interaction, and the damping comes mainly from the radiation damping of soil.

SEISMIC RESPONSE OF VACUUM TOWER STRUCTURE

A vacuum tower structure was constructed in a seismically active area. At the site, surface soil is soft clay with a depth of 2 m, underlain by a layer of saturate fine sand with a depth of 2 m, followed by some silty clay and dense sand layers with depths of 4 to 8 m in each layer, then bedrock. The depth to bedrock is about 30 m. Soil properties vary with depth and are characterized by the shear wave velocity and unit weight, as shown in Table 2.

The concrete mat foundation is 12 x 12 m with a thickness of 1.2 m. The piles are steel HP 360 x 108 with length of 30 m driven to bedrock. Twenty-five piles in a square pattern were fixed to the mat foundation. The stiffness and damping of the pile foundation were calculated for different base conditions. In the first case a linear soil-pile system is assumed, that is, the soil layers are homogeneous, without the weakened zone. In the second case, a nonlinear soil-pile system is assumed, and the boundary zone is considered around the piles. The parameters of the boundary zone were selected as: $G_i / G_o = 0.25$.

In the third case, liquefaction was assumed in the saturated fine sand layer, and the top layer of soft clay has not yielded. Both stiffness and damping are frequency dependent. Since the fundamental period of the structure is closed to 1.0 second, the stiffness and damping were calculated at a frequency of 1.0 Hz. The stiffness and damping calculated are shown in Table 3. Where, K_x , K_z , and K_ϕ are stiffness in the horizontal, vertical and rocking directions, and C_x , C_z , and C_ϕ are damping constants in the same directions. It can be seen that both stiffness and damping are lower in the nonlinear case than those in the linear case.

Table 2. Soil Properties

| Depth (m) | Soil | Unit Weight (kN/m^3) | Shear Wave Velocity (m/s) |
|-----------|-----------------|---------------------------------|---------------------------|
| 0 - 2 | Soft Clay | 18 | 130 |
| 2 - 4 | Fine Sand | 18 | 140 |
| 4 - 12 | Stiff Clay | 20 | 300 |
| 12 - 16 | Silty Sand | 19 | 240 |
| 16 - 20 | Silty Clay | 18 | 300 |
| 20 - 25 | Weathered Shale | 18 | 200 |
| 25 - 30 | Dense Sand | 20 | 300 |
| Below 30 | Soft Rock | 21.5 | 370 |

Table 3. Stiffness and Damping of Pile Foundation

| Soil status | Stiffness | | | Damping | | |
|--------------|---------------------|---------------------|-----------------------|---------------------|---------------------|--------------------------|
| | K_x (kN/m) | K_z (kN/m) | K_ϕ (kN.m/ra) | C_x (kN/m/s) | C_z (kN/m/s) | C_ϕ (kN.m/rad/s) |
| Linear | 1.283×10^6 | 3.215×10^6 | 1.333×10^8 | 1.244×10^4 | 1.803×10^4 | 6.411×10^5 |
| Nonlinear | 0.646×10^6 | 2.877×10^6 | 1.160×10^8 | 0.998×10^4 | 1.005×10^4 | 3.171×10^5 |
| Liquefaction | 0.180×10^6 | 2.527×10^6 | 1.006×10^8 | 0.749×10^4 | 0.943×10^4 | 2.787×10^5 |

A record of horizontal ground acceleration from an earthquake was employed for the time history analysis. The time step is 0.005 second, and duration is 80 second in the earthquake record. To investigate the influence of foundation flexibility on the superstructure, the seismic analysis of the structure was conducted for three different base conditions: rigid base, linear and nonlinear soil-pile systems. The seismic response and forces of the structure were analyzed using a FEM model. The vacuum vessel was modeled as an elastic column with the mass distributed uniformly along its height. The steel structure was modeled using frame elements and the mat foundation was modeled using shell elements. The stiffness and damping of the pile foundation were generated for the three base conditions. The deflection, base shear and overturning moment are shown in Table 4.

Table 4. Seismic Response and Seismic Forces of Tower Structure

| Base Conditions | Amplitude at Top of Tower (mm) | Base Shear (kN) | Overturn Moment (kN-m) |
|-----------------|--------------------------------|-----------------|------------------------|
| Fixed Base | 22.05 | 807 | 19,630 |
| Linear Soil | 26.30 | 598 | 14,980 |
| Nonlinear Soil | 26.05 | 545 | 14,120 |

From Table 4, it can be seen that the earthquake forces for the fixed base condition are larger than those for the cases with the soil-structure interaction. The theoretical prediction does not represent the real seismic response, since the stiffness is overestimated and the damping is underestimated for a structure fixed on a rigid base. From the comparison, it can be seen that the maximum values and time histories for the seismic forces and seismic response are different when the foundation is considered as a fixed base or a flexible base.

The seismic response and seismic forces were calculated, and the comparison of results from the time history analysis, the response spectrum analysis and the method of equivalent static forces are shown in Table 5. It can be seen that the results calculated from different method are conformable.

Table 5. Comparison of Seismic Forces and Response by Different Analysis

| Method of analysis | Amplitude at Top of Tower (mm) | Base Shear (kN) | Overturning Moment (kN-m) |
|--------------------------|--------------------------------|-----------------|---------------------------|
| Time history | 22.05 | 807 | 19,630 |
| Response spectrum | 24.1 | 897 | 21,349 |
| Equivalent static forces | 20.9 | 862 | 20,516 |

CONCLUSIONS

The computer programs are available to applications in practice for soil-pile-structure interaction. The engineering cases are examined, and the following conclusions can be made.

1. The soil-pile interaction is an important factor which affects to the stiffness and damping of the foundation, and also to the dynamic behavior of structure.
2. The dynamic response of complex structures can be calculated consider the soil-pile-structure interaction fully. If a rigid based were assumed, the damping would be underestimated and the stiffness would be overestimated. If the superstructure were assumed to be rigid, the dynamic response would be underestimated significantly in some case, since the contribution from high modes of structure is ignored.
3. The predicted seismic response and earthquake forces are conformable for three different analytical methods, including the time history analysis, response spectrum analysis and equivalent static forces.

REFERENCES

- Banerjee, P.K. and Sen, R. (1987). "Dynamic behavior of axially and laterally loaded piles and pile groups." Chapter 3 in *Dynamic Behavior of Foundations and Buried Structures*, Elsevier App. Sc., London, 95-133.
- Baranov, V.A., (1967). "On the calculation of excited vibrations of an embedded foundation." *Voprosy Dynamiki Prochnosti*, No.14, 195-209, (in Russian).
- Barkan, D.D. (1962). "Dynamics of bases and foundations." McGraw-Hill Book Co., New York.
- Dobry, R. and Gazetas, G. (1988). "Simple method for dynamic stiffness and damping of floating pile groups." *Geotechnique*, Vol.38, No.4, 557- 574.
- El-Marsafawi, H., Han, Y.C. and Novak, M. (1992). "Dynamic experiments on two pile groups." *J. Geotech. Eng.*, ASCE, 118 (4), 576-592.
- Gazetas, G. and Makris, N. (1991). "Dynamic pile-soil-pile interaction. I: Analysis of Axial Vibration." *J. Earthq. Eng. and Struct. Dyn.* Vol. 20, No.2.
- Han, Y.C., (2008). "Study of vibrating foundation considering soil-pile-structure interaction for practical applications." *J. of Earthquake Engineering and Engineering Vibration*, Vol.7, No.3, 321-327.
- Han, Y.C. and Sabin, G. (1995). "Impedances for radially inhomogeneous soil media with a non- reflective boundary." *J. of Engineering Mechanics*, ASCE, 121(9), 939-947.
- Han, Y.C. (1989). "Coupled vibration of embedded foundation." *J. Geotech. Eng.*, ASCE, 115 (9), 1227-1238.
- Han, Y.C. and Novak, M. (1988). "Dynamic behavior of single piles under strong harmonic excitation." *Canadian Geotechnical Journal*, 25(3), 523-534.
- Kaynia, A.M. and Kausel, E. (1982). "Dynamic behavior of pile groups. 2nd Int. Conf. On Num." *Methods in Offshore Piling*, Austin, TX, 509-532.
- Luco, J.E. (1982). "Linear soil – structure interaction: A Review". *Applied Mech. Div.*, Vol.53, ASME, 41-57.
- Novak, M. and Han, Y.C. (1990). "Impedances of soil layer with boundary zone." *J. Geotechnical Engineering*, ASCE, 116(6), 1008-1014.
- Poulos, H.G. and Davis, E.H. (1980). "Pile foundations analysis and design." John Wiley and Sons, P. 397.
- Roesset, J.M., Stokoe, K.H., Baka, J.E. and Kwok, S.T. (1986). "Dynamic response of vertical loaded small-scale piles in sand." *Proc. 8th European Conf. Earthq. Eng.*, Lisbon, Vol. 2, 5.6/65-72.
- Veletsos, A.S. and Dotson, K.W. (1988). "Vertical and torsional vibration of foundation in inhomogeneous media." *J. Geotech. Eng.*, ASCE, 114(9), 1002-1021.
- Wolf, J.P. (1988). "Soil – structure interaction analysis in time domain." *Englewood Cliffs*, NJ: Printice-Hall, 446p.

Application of Soil-Structure Interaction (SSI) in The Analysis of Flexible Retaining Walls

Shin-Tower Wang¹, M., ASCE, Luis Vasquez², M., ASCE, and Daqing Xu³

¹ President, Ensoft, Inc. 3003 W Howard Lane, Austin, Texas 78728, stw@ensoftinc.com

² Project Manager, Ensoft, Inc. 3003 W Howard Lane, Austin, Texas 78728, gonzalo@ensoftinc.com

³ Project Engineer, Ensoft, Inc. 3003 W Howard Lane, Austin, Texas 78728, daqingxu@gmail.com

ABSTRACT: One of the most important features of flexible retaining walls is that wall deformations highly influence the distribution of earth pressures on the wall. The deflection of flexible retaining walls is controlled by the flexural rigidity of the wall and the soil pressure generated based on the permissible movement of the wall. The conventional method of design for flexible retaining walls is based on a limit-equilibrium theory that searches the force equilibrium by assuming the soils engaged around the wall are all in the limit state. The limit-equilibrium analysis does not take into account the nonlinear mobilization of soil reaction with wall deflection.

The application of soil-structure interaction (SSI) to the design of flexible retaining walls means that the deformation of the structural system is analyzed based on the mobilized earth pressure and soil resistance along the wall. Such analyses will result in the most appropriate selection of the size and configuration of the wall, and for the tieback, while ensuring that deformations throughout the system are acceptable.

The method introduced in this paper is to model the structural elements in terms of overall behavior and to use nonlinear p-y curves for modeling the passive resistance of soils due to lateral deformation of embedded wall sections. This paper will discuss the modifications of p-y curves that are needed to take into account the configuration of the wall system (group effects), the unsymmetrical driving forces in the backfill side, the soil resistance in the penetration side, and the long-term effect from the sustained loads.

INTRODUCTION

Flexible retaining structures have received much attention since 1940 because of their widespread use in engineering construction. Flexible retaining walls, in contrast to rigid gravity walls, usually have a single row of piles, likely made of timber, reinforced concrete, or sheet steel, driven so that their lower ends are embedded in soil. The flexural retaining structures also include secant-pile and tangent-pile walls

(drilled-shaft walls), and other innovative cast-in-place concrete walls (slurry walls or diaphragm walls) for basement construction. One of the most important features of flexible retaining walls is that wall deformations highly influence the distribution of earth pressures on the wall. The deflection of flexible retaining walls is controlled by the flexural rigidity of the wall and the soil pressure generated based on the permissible movement of the wall.

The classical soil mechanics procedures based on the active and the passive earth pressure in the limit state have been used in the past for determining the required depth of penetration and factor of safety, extensively for sheet-pile walls. It is no doubt that the success of design by using the classical method has been achieved and recognized in the engineering practice. However, new methods, which provide better capabilities in handling complex nonlinear soil behavior in multi-layers formation and analyzing the deformation of the system based on the mobilized soil resistance along the wall, have been introduced in recent years. Especially, the new method based on the soil-structure-interaction (SSI) concept is most welcomed because it includes the nonlinear resistance-displacement relationship of soil, structural properties, spacing between structural units, penetration depth, and other restraining components in the analysis.

The application of soil-structure interaction (SSI) to a foundation system means that the deformation of the system can be predicted throughout the full range of loading. Appropriate use of SSI allows compatibility to be achieved between the foundation soils and the structural members, in terms of both deformations and forces. The method incorporates the principle that the loading (stress) on each component of the retaining-wall system will result in a deformation. The solution, using SSI, allows the engineer to compute the movement of each increment along the length of the wall under the stage construction, along with the deformation of the tieback system, if used. By applying the loading incrementally, including surcharge and earth pressure, the engineer may analyze the critical load at which failure would occur in certain components, such as excessive bending moment in steel, maximum load on tieback, or excessive deflection at some point in the system. Such analyses will result in the most appropriate selection of the size and configuration of the wall, and for the tieback, while ensuring that deformations throughout the system are acceptable.

The method being used in this paper and in a range of problems in geotechnical engineering for solving problems in SSI is to model the structural elements in terms of overall behavior and to use nonlinear load-transfer functions to model the soil. The principal load-transfer functions in use are p-y curves for modeling the behavior of soils due to deformation of embedded wall sections. This paper will discuss the modifications of p-y curves that are needed to take into account the configuration of the wall system (group effects), the unsymmetrical pressure distribution, the soil resistance in the excavation side, and the long-term effect from the sustained loads.

AVAILABLE METHODS OF DESIGN AND ANALYSIS FOR FLEXIBLE RETAINING STRUCTURES

Brief review of available methods of design and analysis for flexible retaining

structures can help readers understand the advantages and disadvantages of each method. At least four different design methods can be identified based on the recent developments, which include: 1. Limit-equilibrium analysis (classical design method), 2. Subgrade reaction method, 3. Finite-element method, and 4. Nonlinear p-y curve method. The best suitable design method can be selected based on several factors, such as the available engineering data (particularly on subsurface condition), the engineering schedule, the computation tools, and the influence of wall deformation to the neighboring buildings or structures.

The interactions between the structure and the soil on retaining walls will be governed by the retained soil at the back, supporting soil in the front, as well as the structure itself. The response of the soil is a function of the soil-structure system and of the permissible deflections of this system. The limit-equilibrium analysis does not take into account the nonlinear mobilization of soil reaction with wall deflection in the analysis. The subgrade method takes into account the soil-structure interaction based on the assumption of soils with linear-elastic behavior. This model will not realistically capture the ultimate (or yield) soil resistance.

The use of finite-element methods has allowed attempts at a complete solution of retaining-wall problems, including the computation of stresses and deformations in both the wall and the adjoining soil. The finite-element method shows promise in handling the complicated stress-strain relationship for the retaining system. Although the finite-element analysis has been developed far enough to be used for design purposes, it requires soil parameters from sophisticated laboratory tests, significant engineer's time in preparation of the model, and devoted efforts in interpreting the computed results. Even with such high demanding factors, some interesting problems have been solved by using this complicated method.

Recently, the method of analysis for beams or piles on nonlinear foundations employs the soil response curves derived from full-scale experiments and has been accepted as a rational design method by many engineers. The method commonly is referred to as the p-y method and has been successful in aiding the design of laterally loaded piles. Many researches and field loading tests have been performed in the past 40 years worldwide to provide guidance on how to estimate the nonlinear soil resistance (p) versus the pile deflection (y) for a broad range of soil and rock formations. A flexible earth-retaining structure is similar to piles loaded by lateral forces. The original p-y curves were derived mostly for soil response on a single pile (Matlock, 1970; Reese et al., 1974; Reese et al., 1975; Reese and Welch, 1975). The p-y curves need some modifications such as the group effect related to the spacing between the wall units, the difference of the overburden pressure on each side of the wall, the time dependent factor on the soil response due to sustained loading, and others. However, the structural model for analyzing a beam on a nonlinear foundation (in the form of p-y curves) is familiar to many engineers. The benefit of using this method is significant because the engineer can intuitively check the solution by using basic engineering background on the simplified soil-structural model. The design and analysis cycles are dramatically reduced because of the ready-available soil parameters and the validated form of nonlinear soil resistance (Chen et al., 2010).

PRACTICAL APPROACH FOR APPLYING EARTH-PRESSURE LOADS AND P-Y CURVES ON FLEXIBLE RETAINING WALL

The numerical model for the SSI method is based on the so-called “Winkler” foundation, where the active earth pressure is considered as external loads and the soil below the excavation level is modeled by a series of nonlinear p-y springs to provide passive resistance (Figure 1). For practical reasons the method considers the driving force from the active earth pressure as external loads on the wall. However, the active earth pressure above the excavation level should take into account the tributary width (W_a) formed by concrete facing/timber lagging. As defined in Figure 1, W_a is the center to center spacing for a pile-wall system and W_p is the unit width (equivalent diameter) for representing the structural member in the analysis model.

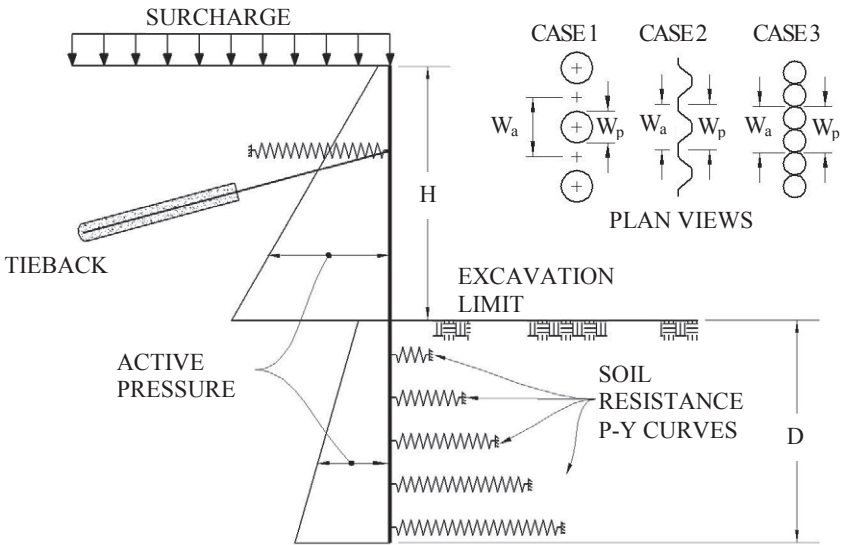


FIG. 1. Practical Approach for Applying Earth Pressure and p-y Curves on the Flexible Retaining Structures.

For continuous sheet-pile walls, the tributary width (W_a) is equal to the unit width of sheet-pile wall (W_p) because no spacing is between the sheet piles. Since no concrete facing/timber lagging is formed below the excavation level, the unit width used in computing the active earth pressure and passive resistance below the excavation level should be equal to the diameter (W_p) of the pile wall only.

The p-y curves, representing the soil reaction, could be specified as nonlinear springs at each wall increment below the excavation level as shown in Figure 1. The

nonlinear soil support developed on the flexible retaining wall below the dredge line (or below the excavation surface) is similar to the nonlinear soil reaction on laterally-loaded piles. A typical p-y curve for sand is shown in Figure 2. The characteristics of p-y curves typically include an initial linear-elastic section, which show a straight-line relationship between p (soil resistance) and y (pile deflection). The second portion of the p-y curve represents the transition of soil resistance from linear to nonlinear behavior. The ultimate soil resistance as a function of pile dimensions and soil properties can be represented as P_u in the final portion of the curve.

The p-y curves (soil resistance) will be calculated based on the width of the wall (as the equivalent pile diameter), W_p . The reduction of soil resistance (p value) due to group effect should be considered in the analysis, especially for sheet-pile and soldier-pile walls. It should be noted that the depth or overburden pressure is a factor in calculation of p-y curves. The overburden pressure on the backfill side is much greater than the excavation side at the same depth. Therefore, the p-y curves below the excavation level become unsymmetrical, which usually indicates that the soil resistance at the backfill side is much higher than those in the excavation side.

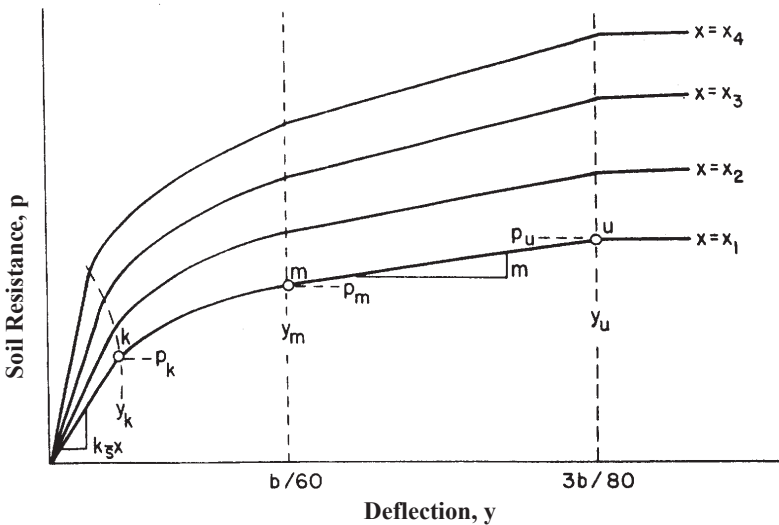


FIG. 2. Characteristic Shape of a Family of p-y Curves for Sand

Most of the conventional methods employ the equivalent hydrostatic pressure distribution theory in the limit-equilibrium analysis. It is difficult to use the limit-equilibrium analysis on flexible retaining walls with multiple anchors because the problem involved is statically indeterminate. The SSI approach presented here solves all components automatically with either case and no assumption is needed about the nature of the support along the wall. The anchor or tieback can be modeled by specifying the stiffness of an equivalent lateral spring at the tieback location. The

It is reasonable to assume that there is no significant difference in the load-carrying capacity of each pile with respect to its position in the same row when designing a retaining wall structure. Their data show that group efficiency does not reach unity until the spacing is nearly four pile diameters. In general, group reduction is not required for timber-lagging systems if the spacing between two adjacent H-piles is greater than four pile diameters. It should be noted that the existing p-y criteria were developed based on a single pile. If the spacing between drilled shafts used in a wall system is less than 4 pile diameters, the designer should consider the group-pile efficiency (β) on p values of the p-y curves based on Figure 3 in the analysis. If a sheet-pile wall is analyzed by using the p-y method, the group-pile efficiency (β) of 0.5 (lower bound) to 0.7 (upper bound) should be considered on p values, calculated directly based on the existing p-y criteria, because of no spacing between the sheet-pile units.

For permanent retaining walls with the earth pressure acting as sustained loads, some of the p-y curves should take into account of effects of the long-term deformation, such as soil lateral movement from consolidation of cohesive soils or soil creep. It is a common practice by increasing y values on the p-y curves for softening the soil resistance due to the long-term effect. The designer may apply modifiers on y values of the generated p-y data to increase the wall deflection until it reaches the deflection level consistent to the field experience on the long-term behavior observed in the past.

CASE STUDIES

An example, which illustrated design of an anchored sheet-pile wall using the p-y curve method for static and seismic loading, was present in National Cooperative Highway Research Program (NCHRP) in 2008. The same example was used and re-analyzed here using the latest criteria of p-y curves and group-pile reduction factors for validation. The wall to be analyzed is presented in Figure 4, along with the soil layer information. The wall for this example is 7.6 m above the finished grade and involves a single unit of homogeneous sandy soil behind the wall as well as the foundation soils below the excavation grade. The unit weight of the sand is assumed to be 18.9 kN/m^3 and the internal friction angle is 32 degrees. The sheet pile selected for the analysis has bending stiffness (EI) of $15,507 \text{ m}^2\text{-kN/m}$ and yield stress of 344,700 kPa. Similar to the method for cantilever sheet-pile walls, the loading condition is based on the active earth pressure theory. Using the Rankine earth pressure theory with $\phi = 32^\circ$, the static active pressure coefficient (K_a) was calculated to be 0.307. The tieback anchor increases the wall/soil stiffness, which leads to an increase in the earth pressure. A load factor of 1.3 is generally applied to the active earth pressure above the finished grade as the external load on the anchored walls and the earth pressure was arranged as the trapezoidal earth pressure distribution as shown in Figure 4.

In conjunction with the trapezoidal earth pressure above the excavation level, an additional loading from the active earth pressure should be considered for the portion of the anchored pile wall beneath the excavation level. This set of earth-pressure

loads increases from 44.1 kPa ($=0.307 \cdot 18.9 \cdot 7.6$) at the excavation level to 55.7 kPa ($=0.307 \cdot 18.9 \cdot 9.6$) at the tip of the wall. The load was calculated using the static Rankine active earth pressure theory without a 1.3 amplification factor. Wall friction angle (δ) was assumed to be zero on the active side. The unit width of the sheet-pile wall selected in the analysis is 0.305 m (1 ft). The p-y curves, which were calculated at depth of 1.9 m below the excavation level, indicate that the soil resistance at the backfill side (800 kN/m) is much higher than those at the excavation side (88 kN).

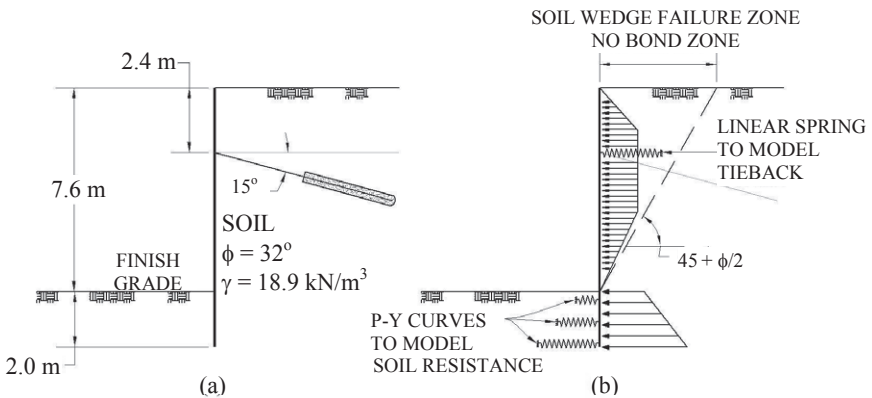


FIG. 4. (a) Geometry and Soil Information for Anchored Sheet-Pile Wall; (b) Static Earth Pressure Distribution.

The total load from the active earth pressure above the excavation level is 66.4 kN ($=0.5 \cdot 44.1 \cdot 7.6 \cdot 1.3 \cdot 0.305$) per unit wall width. Assuming a lateral spacing between anchors of 2.438 m, the design load would be 531 kN ($=66.4 \times 2.438/0.305$) per anchor. The anchors are assumed to be constructed using steel strands with an ultimate tensile strength of 1,861,380 kPa. In addition to the basic design load 531 kN for the anchor, the design load also needs to evaluate loads associated with proof testing. A factor at about 1.5 is typically specified for the proof test condition. After proof testing to this higher load 797 kN, the anchors are relaxed to the theoretical lockoff design load 531 kN. The high strength reduction factor (0.8) is used for the required cross-section area under the temporary load. Therefore, the required cross section area (A_{proof}) for temporary proof test will be equal to 5.35 cm^2 , i.e. $A_{\text{proof}} = 1.5 \cdot 531 \text{ kN} / (0.8 \cdot 1861380 \text{ kPa})$.

The area of 5.35 cm^2 (0.833 in^2) will be used in calculating the stiffness of the anchor spring k , based on $k = AE/L$. The length parameter L needs to be estimated based on the unbounded length of the anchor as shown in the right side of Figure 4. Based on the Rankine active failure wedge, the lateral distance on the ground surface needs to be at least 4.2 m for this example. An unbounded length of 4.57 m was assumed for this example. The boundary line of the Rankine failure wedge under

seismic influence is indicated by a dashed line and the anchor should have sufficient unbounded length passing through the active failure zone. Following conventional practice, the upper bound horizontal stiffness estimated for the anchor would be:

K (per anchor) = $\cos(\theta) AE/L = (\cos 15^\circ) (0.000535) \cdot (200 \times 10^6) / (4.57) = 22616$ kN/m. Since the unit width of sheet pile used in the analysis is 0.305 m, the upper bound stiffness estimated per each anchor should be distributed to each unit width of the analytical model accordingly:

$$K \text{ (per unit width of wall)} = 22,616 \cdot 2.44 / 0.305 = 2,827 \text{ kN/m.}$$

In addition to the static earth pressure shown in Figure 4, the incremental earth pressure for various horizontal seismic coefficients (k_{\max}) can be calculated by following the procedures and Mononobe-Okabe equations as shown in Table 1. Similar to the static loading condition, the conventional dynamic active pressure is increased by 30 percent to account for the stiffer anchor system on the earth pressure distribution above the excavation level.

Table 1. Summary of Active Earth Pressure on the Wall from Seismic Load

| Seismic Coefficient, k_{\max} | 0.1 | 0.2 | 0.4 |
|--|-------|-------|-------|
| $K_{a, \text{static}}$ | 0.307 | 0.307 | 0.307 |
| $K_{a, \text{seismic}}$ (from M-O equations) | 0.37 | 0.44 | 0.65 |
| $K_{a, \text{net}}$ | 0.063 | 0.133 | 0.343 |
| Total active load from $K_{a, \text{net}}$ (seismic – static) = $(1/2)(K_{a, \text{net}})(\gamma)(H)^2(1.3)(0.305 \text{ m})$ (kN/per unit width) | 13.7 | 28.9 | 75.6 |
| Uniformly Distributed Pressure over 7.6 m per unit width (kN/m) | 1.80 | 3.79 | 9.8 |

Figure 5 presents the results of the p-y curve method for the anchored wall under static and cyclic loading conditions. The p-y analyses indicate that the anchor forces would be 443 kN, 527 kN, 622 kN, 903 kN per anchor (2.438 m spacing) for (1) static load case, (2) seismic case with $k_{\max} = 0.1g$, (3) seismic case with $k_{\max} = 0.2g$, and (4) seismic case with $k_{\max} = 0.4g$, respectively. The anchor force under the seismic loading of 0.4g is over the anchor capacity of 797 kN and the anchor would be overloaded in this case. The maximum bending moment is 62.8 kN-m at depth of 5.73 m below the top of the sheet pile for the seismic case with $k_{\max} = 0.4g$, comparing with 28.7 kN-m at 5.33 m below the top of the sheet pile from the static case (approximately 220% increase).

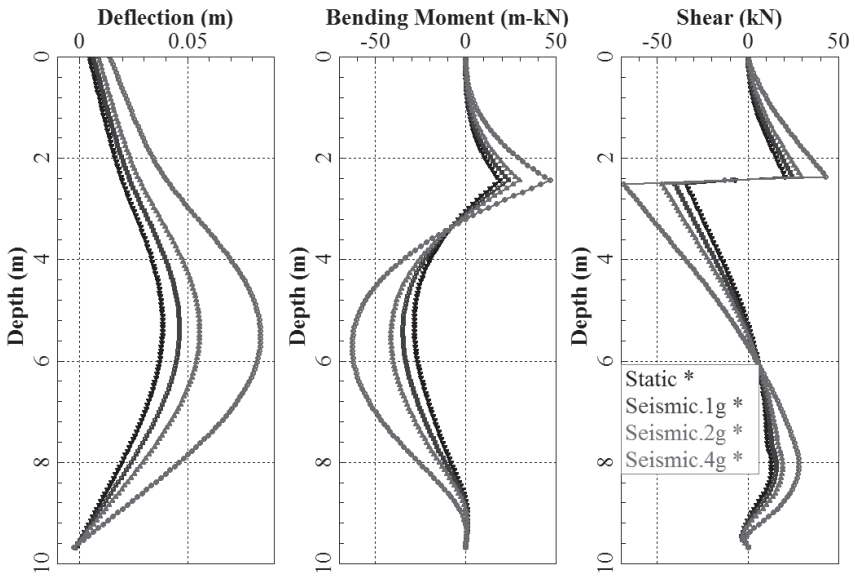


FIG. 5. Computed Deflection Curve, Shear Diagram, and Bending Moment Curves Based on the SSI Method for Anchored Wall

CONCLUSIONS AND RECCOMENDATIONS

1. The p-y curve method was developed based on the commonly-recognized structural theory. With the p-y curve method, both equilibrium and compatibility are automatically satisfied when the solution converges. The distribution of the soil pressure and soil resistance is rational based on the p-y curve method. Engineers can receive the information, such as the maximum bending moment, maximum shear, and the deflection profile, easily for the final design. The limit equilibrium method will have difficulties in computing the deflection curve correctly because it is based on the limit-state soil resistance instead of the mobilized soil resistance.
2. The results show that the p-y Curve method for design of anchored sheet-pile wall is rational and can also be adaptable for seismic conditions. It provides a reliable way to aid the designer in obtaining a more refined evaluation of the actual performance of anchored retaining walls, especially for the cases with seismic loading.
3. The field tests and monitoring programs can provide engineers with valuable data for improvement of the proposed method, especially for the soil resistance curves under the long-term condition.

REFERENCES

- Brown, D. A., Reese, L.C., and O'Neill, M.W., (1987) "Cyclic Lateral Loading of a Large-Scale Pile Group," *Journal of the Geotechnical Engineering Division*, American Society of Civil Engineers, Vol. 113, No. 11.
- Chen, J., Farouz, E., and Landers, P. (2010) "Development of Project-Specific p-y Curves for Drilled Shaft Retaining Wall Design," Proceedings of Earth Retention Conference 3, ASCE, Bellevue, Washington, pp. 162-169.
- Matlock, H. (1970) "Correlations for Design of Laterally Loaded Piles in Soft Clay," *Proceedings, Offshore Technology Conference*, Houston, Texas, Vol. I, Paper No. 1204, pp. 577-594.
- Mononobe, N. and Matsuo, M., (1929) "On the Determination of Earth Pressures During Earthquakes," *Proceedings, World engineering Conference*, Vol.9., pp.176.
- National Cooperative Highway Research Program (NCHRP), (2008), *Seismic Analysis and Design of Retaining Walls, Buried Structures, Slopes, and Embankments*, Report 611, Transportation Research Board of the National Academies, Washington, D.C.
- Reese, L. C., Cox, W.R., and Koop, F.D., (1974) "Analysis of Laterally Loaded Piles in Sand," *Proceedings, Offshore Technology Conference*, Houston, Texas, Vol. II, Paper No. 2080, pp. 473-484.
- Reese, L. C., Cox, W.R., and Koop, F.D., (1975) "Field Testing and Analysis of Laterally Loaded Piles in Stiff Clay," *Proceedings, Offshore Technology Conference*, Houston, Texas, Paper No. 2312, pp. 671-690.
- Reese, L. C. and Welch, R.C., (1975) "Lateral Loading of Deep Foundations in Stiff Clay," *Journal of the Geotechnical Engineering Division*, American Society of Civil Engineers, Vol. 101, No. GT7, pp. 633-649.
- Reese, L. C., and Van Impe, W.F., (2001) Single Piles and Pile Groups Under Lateral Loading," *Balkema, Rotterdam*.

Mechanistic Empirical Pavement Design Guide Input Parameters for Unbound Aggregates in Oklahoma

Zahid Hossain¹, A.M. ASCE, Musharraf Zaman², F. ASCE, and Curtis Doiron³

¹Assistant Professor (Corresponding Author), School of Civil Engineering, Arkansas State University, PO Box 1740, State University, AR 72467; PH: (870) 680-4299; E-mail: mhossain@astate.edu

²David Ross Boyd Professor and Aaron Alexander Professor of Civil Engineering, 202 W. Boyd Street, #107, The University of Oklahoma, Norman, OK 73019; PH: (405) 325-2626; E-Mail: zaman@ou.edu

³Former Undergraduate Assistant, Deans Office, College of Engineering, 202 W. Boyd Street, #107, The University of Oklahoma, Norman, OK 73019; Email: cdoiron@ou.edu

ABSTRACT: This study analyzed resilient modulus (M_r) and other routine properties (gradation, LA Abrasion loss, standard Proctor, and unconfined compressive strength (UCS)) of commonly used limestone and sandstone aggregates in Oklahoma. A total of four stress-based regression models were evaluated using a statistical software package (“SPSS”, Version 17), and material constants (k_1 , k_2 , and k_3) for these aggregates were determined. The octahedral model was found to outperform the other models and is recommended for use in Level 1 analysis. Correlation equations for material constants, required for Level 2, were developed using routine aggregate properties, and the universal model was found to be the “best fit” model with a R^2 value of 0.57. The estimated M_r values obtained from different models were in agreement with each other, and the variations of M_r values were within 4%. However, all of these models would result in conservative designs compared to the MEPDG recommended typical values. The findings of this study are expected to be helpful in the implementation of the MEPDG in Oklahoma and elsewhere.

INTRODUCTION

The new Mechanistic-Empirical Pavement Design Guide (MEPDG), developed under the National Cooperative Highway Research Program (NCHRP) project 1-37A, is less empirical than the 1993 American Association of State Highway and Transportation Officials (AASHTO) Design Guide [Kim et al., 2009]. Among others, resilient modulus (M_r) of granular base is an important input parameter in all three hierarchical levels of the MEPDG (NCHRP, 2004). Level 1 requires material constants (k_1 , k_2 , and k_3) from M_r test data, and it provides the highest level of design reliability. Level 2 uses correlations to determine M_r from other aggregate properties, and gives an intermediate level of reliability. Level 3 gives the lowest reliability level.

In the past, researchers around the globe conducted significant amounts of studies to

evaluate resilient properties of subgrade soils, but there had been a limited number of studies that focused on evaluating aggregates for the MEPDG input. A previous study by Zaman et al. (1998) examined M_r of limestone and sandstone aggregates in Oklahoma and used the bulk stress ($k-\theta$) model to estimate M_r of aggregates. These researchers also established direct correlation equations of M_r with unconfined compressive strength (UCS) and elastic modulus (EM) for selective stress levels.

Richardson et al. (2009) tested five unbound granular base materials in Missouri. The base materials were tested at two different gradations (as-delivered and with an increased amount of percent passing No. 200 Sieve (P200) than the former). These researchers used the MEPDG-recommended octahedral model to determine the material constants. It was reported that all of the individual samples' coefficient of correlation (R^2) values were greater than 0.90, thus satisfying the recommendations of the MEPDG. These researchers also observed very good repeatability of test results among replicate samples. It was recommended that the reported material constants be used as inputs for Level 1 analysis and design for tested aggregates.

Yohannes et al. (2009) characterized several unbound granular materials from Minnesota for pavement applications, including the MEPDG, by conducting M_r tests. These researchers also used a 3-D discrete element method (DEM)-based model, capable of accounting for aggregate shape, coefficient of friction, gradation, stiffness, and other properties, to estimate M_r . The simulation results were in a good agreement with the experimental observations.

A recent study by Xiao et al. (2011) established correlations between M_r and aggregate physical properties by utilizing Minnesota aggregate property database containing M_r data of 376 aggregate specimens (four types of aggregates). It was reported that some basic aggregate parameters, namely P200, moisture content (MC) and dry density (MDD), were somewhat correlated with M_r . However, aggregate particle surface properties (e.g., angularity index, and surface texture index) were also found to be highly correlated predictor variables. Without surface properties of the aggregates, the R^2 values of correlation equations of k_1 , k_2 , and k_3 were found to be only 0.14, 0.32, and 0.39, respectively. It was reported that the R^2 values of the correlations increased significantly when aggregate surface properties were used with aggregate physical properties. Thus, the R^2 values of correlation equations of k_1 , k_2 , and k_3 were reported as 0.58, 0.50, and 0.53, respectively.

The default values and correlations for M_r provided by the MEPDG are based on a limited number of tests and climatic conditions. However, aggregate morphology, mineralogy, and textural characteristics play a significant role on M_r of aggregate materials (Tutumluer and Pan, 2008). Since the morphological, mineralogical, and textural characteristics of Oklahoma aggregates are different from those in the literature, default values and correlations may not be applicable for Oklahoma.

As noted earlier, several state departments of transportation have already created or are in the process of creating M_r databases for local aggregates. These agencies have found their M_r databases to be useful tools for improving pavement designs and analyses using the MEPDG (Titi et al., 2006; Wang, 2009). The Oklahoma Department of Transportation (ODOT) is actively working toward implementing the MEPDG for flexible pavements. A successful implementation of the MEPDG will require a comprehensive database and its assessment. The present study is expected to

provide useful data and correlations that can be used to calibrate the MEPDG according to Oklahoma's conditions and materials.

TEST MATERIALS AND METHODOLOGY

M_r test (AASHTO T 307) data for 105 samples of two commonly used aggregates (limestone and sandstone) in Oklahoma were analyzed in this study. Of which, 65 were limestone and the remaining were sandstone. The limestone aggregates were obtained from quarries at Meridian in Marshal County, and Richard Spurs (RS) in Comanche County. Sandstone aggregate in this study was obtained from a quarry at Sawyer in Choctaw County. Other test data included in the database were sieve analysis (AASHTO T 11 and T 27), LA Abrasion loss (AASHTO T 96), standard Proctor (AASHTO T 180), and unconfined compressive strength (AASHTO T 208). The gradation (average of three replicates) data for these aggregates, along with the ODOT requirements, are shown in Table 1. The specimens for M_r tests were compacted at optimum moisture content (OMC) and at or above 95% MDD. The MDD values were obtained from the moisture-density tests (AASHTO T 180). According to AASHTO M 145, these aggregates were classified as A-2-4.

TABLE 1 Grain size distributions of tested aggregates

| US Standard Sieve Size or No | Sieve Opening (mm) | % Passing of Limestone at Meridian | % Passing of Limestone at Richard Spurs | % Passing of Sandstone at Sawyer | ODOT limit % Passing for Coarser | ODOT limit % Passing for Finer | ODOT limit % Passing for Median |
|------------------------------|--------------------|------------------------------------|---|----------------------------------|----------------------------------|--------------------------------|---------------------------------|
| 1-1/2 in | 38.1 | 98.2 | 100 | 100 | 100 | 100 | 100 |
| 1-1/4 in | 31.75 | 91.8 | 98.1 | 95.0 | 85 | 100 | 90 |
| 1.0 in | 25.4 | 81.5 | 91.2 | 84.0 | 60 | 100 | 80 |
| 0.75 in | 19.0 | 71.4 | 79.5 | 70.0 | 40 | 100 | 70 |
| 0.5 in | 12.7 | 58.8 | 63.8 | 54.8 | 35 | 85 | 60 |
| 0.375 in | 9.5 | 51.7 | 59.3 | 47.8 | 30 | 75 | 52.5 |
| No. 4 | 4.75 | 38.6 | 48.6 | 34.5 | 25 | 60 | 42.5 |
| No. 40 | 0.425 | 14.2 | 14.8 | 20.3 | 8 | 26 | 17 |
| No. 200 | 0.075 | 6.3 | 5.6 | 4.8 | 4 | 12 | 8 |

Since the estimated coefficients of a regression analysis can be profoundly influenced by outliers, these observations were identified and discarded from further analyses. To this end, M_r data located outside the range of ± 1.5 standard deviations from the average M_r value of a given sequence for each aggregate type were treated as outliers. Thus, about 5% of the M_r data was found to be outliers. It is well-known that a normally distributed dataset is desired for developing good statistical models and correlations. Hence, basic statistical parameters (minimum, maximum, mean, and standard deviation) along with two other factors (skewness and kurtosis) were selected to determine distributions of the routine aggregate test data (Table 2). The statistical parameters of the M_r and routine test data of each of 15 sequences for the development datasets are presented in Table 3. Based on skewness, kurtosis values, and other

statistical parameters, the distribution of the M_r data can be treated as normally distributed.

Table 2 Basic statistical parameters for tested aggregate samples

| Parameter | Minimum | Maximum | Mean | Standard Deviation | Skewness | Kurtosis |
|-------------------------------|----------------|----------------|----------------|--------------------|----------|----------|
| Sp. Gr. | 2.47 | 2.70 | 2.63 | 0.08 | -0.45 | -1.48 |
| LA | 24.00 | 37.70 | 26.93 | 3.76 | 1.48 | 1.80 |
| P_4 | 34.50 | 48.60 | 41.99 | 6.70 | -0.08 | -1.94 |
| P_{40} | 14.20 | 20.30 | 16.82 | 2.75 | 0.48 | -1.78 |
| P_{200} | 4.80 | 6.30 | 5.38 | 0.51 | 0.20 | -0.98 |
| LL | 13.00 | 21.90 | 16.18 | 3.19 | 0.38 | -1.27 |
| PI | 2.60 | 8.50 | 3.86 | 1.74 | 2.09 | 3.12 |
| UCS, psi (kPa) | 17.49 (120.60) | 45.91 (316.60) | 34.41 (237.28) | 8.25 (57.56) | -0.44 | -1.00 |
| MDD, pcf (kN/m ³) | 133.05 (20.90) | 148.96 (23.40) | 142.47 (22.38) | 5.67 (0.89) | -0.16 | -1.40 |
| OMC (%) | 4.60 | 7.50 | 5.53 | 0.93 | 0.67 | -0.56 |

Table 3 Basic statistical parameters of resilient modulus of tested aggregates

| Development Dataset | | | | | | | | |
|---------------------|------------------|------------------|------------|----------|-----------|-----------|------------|------------|
| Seq. No. | σ_3 (kPa) | σ_d (kPa) | Mean (MPa) | SD (MPa) | Min (MPa) | Max (MPa) | Skew (MPa) | Kurt (MPa) |
| 1 | 41.4 | 13.8 | 74.50 | 35.43 | 15.59 | 176.09 | 1.03 | 0.66 |
| 2 | 41.4 | 27.6 | 93.88 | 33.03 | 39.74 | 179.97 | 0.63 | -0.45 |
| 3 | 41.4 | 41.4 | 104.30 | 40.86 | 33.95 | 275.6 | 1.32 | 2.60 |
| 4 | 41.4 | 55.2 | 106.40 | 49.74 | 27.67 | 305.09 | 1.33 | 2.73 |
| 5 | 41.4 | 68.9 | 118.78 | 44.48 | 58.77 | 257.55 | 1.08 | 0.82 |
| 6 | 27.6 | 13.8 | 139.57 | 47.64 | 69.38 | 277.05 | 0.80 | 0.13 |
| 7 | 27.6 | 27.6 | 153.35 | 63.32 | 39.68 | 356.21 | 0.86 | 0.37 |
| 8 | 27.6 | 41.4 | 170.53 | 64.40 | 76.55 | 373.71 | 1.09 | 1.07 |
| 9 | 27.6 | 55.2 | 177.76 | 62.28 | 88.67 | 359.45 | 0.73 | -0.05 |
| 10 | 27.6 | 68.9 | 163.11 | 66.97 | 43.06 | 397.48 | 0.88 | 0.85 |
| 11 | 13.8 | 13.8 | 187.29 | 71.68 | 56.17 | 400.58 | 0.89 | 0.51 |
| 12 | 13.8 | 27.6 | 209.20 | 74.25 | 91.71 | 418.02 | 0.78 | 0.13 |
| 13 | 13.8 | 41.4 | 202.95 | 77.92 | 59.25 | 462.53 | 1.06 | 0.95 |
| 14 | 13.8 | 55.2 | 219.39 | 80.87 | 72.55 | 462.87 | 0.93 | 0.56 |
| 15 | 13.8 | 68.9 | 249.63 | 83.92 | 80.11 | 478.37 | 0.59 | -0.14 |

REGRESSION MODELING

Among the several stress-based models available in the literature for characterizing resilient response of unbound granular base materials, four commonly used and relatively simple models were considered in this study. The *bulk stress* ($k-\theta$) model

(Model 1; Equation 1), referenced by Hicks and Monismith (1971), was used in related previous studies (e.g., Zaman et al., 1998) to estimate M_r of limestone and sandstone aggregates. The $k\sim\theta$ model was recommended in the 1986 AASHTO Guide (NCHRP, 2004). The major limitations of the $k\sim\theta$ model are that it neglects the important effects of shear stress on M_r (Thompson et al., 1998). Also, the $k\sim\theta$ model can only represent a very limited range of stress paths, and is thus expected to give erroneous results. The basic two-parameter [$k\sim f(\sigma_d, \sigma_3)$] model, also known as *UT-Austin model* (Model 2; Equation 2), introduced by Pezo (1993) and referenced by Andrei et al. (2004), is based on confining and deviatoric stresses and is being used by several state agencies. The $k\sim f(\sigma_d, \sigma_3)$ model was an outcome of regression analyses of expressing the axial strain in terms of applied confining and deviatoric stresses from laboratory tests. Von Quintus and Killingsworth (1997) recommended the *universal* (bulk stress and deviatoric stress-based [$k\sim f(\theta, \sigma_3)$] model (Model 3; Equation 3) for estimating M_r values required in the 1993 AASHTO Guide. It was introduced by Uzan (1985). The $k\sim f(\theta, \sigma_3)$ model, which includes the shear stress effects, is an improvement of the $k\sim\theta$ model. An extended stress-based model, the *octahedral* ($k\sim\tau_{oct}$) model (Model 4; Equation 4), has been recommended by the MEPDG.

$$M_r = k_1 P_a \left(\frac{\theta}{P_a} \right)^{k_2} \quad (1)$$

$$M_r = k_1 P_a \left(\frac{\sigma_3}{P_a} \right)^{k_2} \left(\frac{\sigma_d}{P_a} \right)^{k_3} \quad (2)$$

$$M_r = k_1 P_a \left(\frac{\theta}{P_a} \right)^{k_2} \left(\frac{\sigma_d}{P_a} \right)^{k_3} \quad (3)$$

$$M_r = k_1 P_a \left(\frac{\theta}{P_a} \right)^{k_2} \left(\frac{\tau_{oct}}{P_a} + 1 \right)^{k_3} \quad (4)$$

where, θ = bulk stress, and P_a = atmospheric pressure (14.7 psi [101 kPa]).

Using the aforementioned four models nonlinear regressions were performed, thus giving four sets of regression constants for each sample. It can be noted that Model 1 has only two regression constants (k_1 and k_2). Average regression constants (material constants) along with other important statistical parameters (maximum, minimum, and standard deviation) for the aggregate samples, satisfying the MEPDG recommended R^2 criterion (≥ 0.9), were calculated. The lowest number of samples (57%; 60 out of 105) satisfied the R^2 requirement in the case of Model 1. The largest number of samples (about 74%; 78 out of 105) fulfilled the aforementioned R^2 criterion in the case of Model 2, followed by Model 3 (72%), which was followed by Model 4 (64%). The reason for relatively low percentages (up to 74%) of samples satisfying these models could be related to "poor" quality laboratory test data. In general, quality M_r test data is expected to provide higher R^2 value.

Validations of these models were done with average material constants obtained from the evaluation dataset. The measured and predicted M_r values for limestone and sandstone aggregates were then plotted, as shown in Figure 1. Based on the R^2 values, all of the selected models showed similar performances for both aggregates. However,

the F-values and corresponding probabilities (p-values) showed some variations in the “overall significance” of the models. In general, limestone data were found to be better “fit” and more “explainable” than sandstone, irrespective of the type of model. Even though there were insignificant variations in performance among these models, based on the R^2 value, and the proximity of data points to the equality lines for limestone aggregate, Model 4 (*octahedral model*) outperformed Model 2, followed by Model 3, and then Model 1. For sandstone aggregate, Model 1 showed the best performance, followed by Model 4, and then Model 2 and Model 3. However, based on the individual sample count that satisfied the MEPDG requirement for R^2 value, as mentioned earlier, Model 1 could not be recommended for sandstone aggregate. Therefore, Model 4 (*octahedral model*) was ranked as the “best fit” model, irrespective of aggregate type. Model 2 and Model 3 were ranked as the “second best fit” and “third best fit” models, respectively.

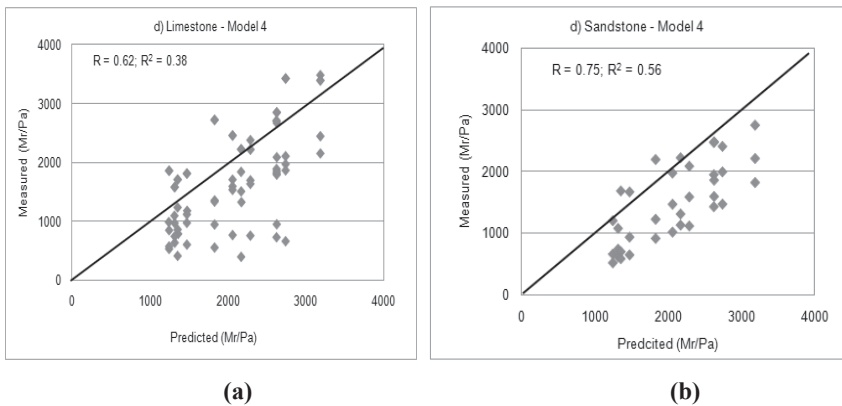


FIG. 1 Predicted versus measured M_r/P_a values from regression analysis for model 4: (a) limestone; and (b) sandstone. Note: F-values along with probabilities for limestone and sandstone are 1.82 ($p = 0.006$), 1.03 ($p = 0.467$), respectively.

CORRELATIONS

To correlate M_r values of an aggregate with index properties, various multiple linear regression models have been used in the past. Tian et al. (1998) established a correlation ($M_r/P_a = A_0 + A_1 * \theta/P_a + A_2 * MC + A_3 * P_{200}$; where, A_0 , A_1 , A_2 , and A_3 are model parameters) to predict M_r values of both limestone and sandstone aggregates. Even though a “good fit” was reported, and high standard deviations in the model parameters were reported. In another study by Pandey et al. (1998), M_r was correlated with UCS and EM. It also reported very low R^2 values (0.28 to 0.41), which suggests a “poor fit.” Further, neither of these studies considered stress-based models. Consistent with the goal of the current study, correlation equations (Equations 5 through 7) for k_1 , k_2 , and k_3 were developed based on aggregate parameters, and Model 3 was found to outperform the others. The R^2 values of the equations of k_1 , k_2 , and k_3 are found to be 0.38, 0.78, and 0.42, respectively. The measured versus predicted M_r/P_a values are

plotted in Figure 2. Relatively low R^2 values of the established correlations indicate further research need and other parameters (e.g., surface properties) can be considered.

$$k_1 = 259.440 * P_{200} - 1.951 * UCs \quad (5)$$

$$k_2 = 0.530 - 0.902 * k_3 \quad (6)$$

$$k_3 = -0.044 * OMC + 0.087 * PI \quad (7)$$

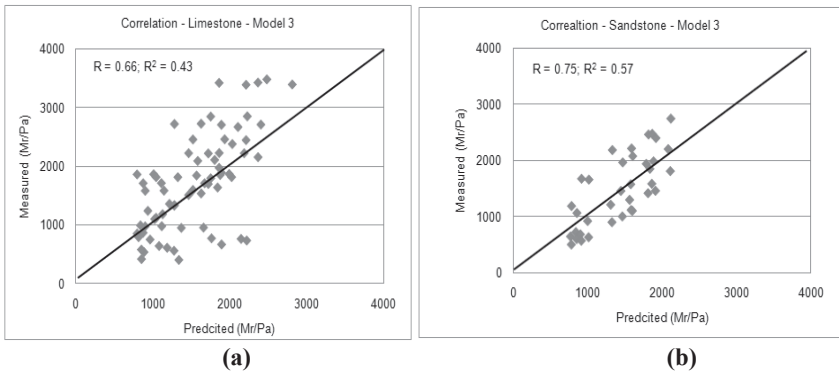


FIG. 2 Predicted versus measured M_r/P_a values from stress-based correlations (a) limestone, and (b) sandstone. Note: F-values along with probabilities of limestone and sandstone are 2.61 ($p = 1.0e-04$) and sandstone 2.06 ($p = 0.018$), respectively.

CONCLUSIONS

Among the four selected models, the octahedral model (Equation 4) was found to perform better than the others and is recommended for use in Level 1. From the perspective of correlations, the universal model (Equation 3) was found to outperform the other models. The established correlation equations can be used to estimate material constants for Level 2 analysis and design. Also, it was observed that limestone aggregate showed higher (51%) M_r values than sandstone aggregate. These observations may be justified by the fact that the limestone aggregate contained bigger sized particles, which provides more interlocking potential than sandstone.

ACKNOWLEDGMENTS

The authors would like to express their sincere appreciation to the Oklahoma Department of Transportation for providing financial support for this project. Assistance given by the Oklahoma Transportation Center is greatly appreciated.

REFERENCES

- Andrei, D., Witzcak, M. W., Schwartz, C. W., and Uzan, J. Harmonized Resilient Modulus Test 50 Method for Unbound Pavement Materials, In *Transportation Research Record*, No. 1874, Washington, D.C., 2004, pp. 29 - 37.
- Hicks, R. G., and Monismith, C. L. "Factors Influencing the Resilient Properties of Granular Materials," *Transportation Research Record* 345, Transportation Research

- Board of the National Academies, Washington D.C., 1971, pp. 15-31.
- Kim, S., Gopalakrishnan, K., and Ceylan, H. Iowa's Rubbilized Pavements: Design Properties of Rubbilized PCC layers. In the 88th TRB Annual Meeting, Paper No. 09-3249 CD-ROM, Transportation Research Board, Washington D.C., 2009.
- NCHRP. *Guide for Mechanistic-Empirical Design of Pavement Structures: Part 2 – Design Inputs*. ARA, Inc., ERES Consultants Division, Champaign, IL, 2004.
- Pandey, K., Zaman, M., and Laguros, J. G. *Resilient Moduli of Raw and Stabilized Aggregate Bases and Evaluation of Layer Coefficients for AASHTO Flexible Pavement Design*. Volume III, ORA 125-4262, ODOT, Oklahoma City, OK, 1998.
- Pezo, R. F. A General Method of Reporting Resilient Modulus Tests of Soils – A Pavement Engineer's Point of View. Paper No. 93082, TRB 72nd Annual Meeting, Transportation Research Board, Washington D.C., 1993.
- Richardson, D. N., Petry, T. M., Ge, L., Han, Y., and Lusher S. M. *Resilient Moduli of Typical Missouri Soils and Unbound Granular Base Materials*. Final Report, No.: OR09-016, Missouri Department of Transportation, Jefferson City, MO, 2009.
- Thompson, M. R., Tutumluer, E., and Bejarano, M. *Granular Material and Soil Moduli Review of the Literature*. Technical Research Report, Center for Excellence, Under Grant No. DOT 95-C-001, Federal Aviation Administration, 1998.
- Tian, P., Zaman, M., and Laguros, J. G. *Resilient Moduli of Raw and Stabilized Aggregate Bases and Evaluation of Layer Coefficients for AASHTO Flexible Pavement Design*. Volume II, Final Report, Item 2199; ORA 125-4262, Oklahoma Department of Transportation, Oklahoma City, OK, 1998.
- Titi, H., Elias, M., and Helwany, S. *Determination of Typical Resilient Modulus Values for Selected Soils in Wisconsin*. Final Report, *Wisconsin Highway Research Program*, Project ID 0092-03-11, Milwaukee, WI, 2006.
- Tutumluer, E. and Pan, T. Aggregate Morphology Affecting Strength and Permanent Deformation Behavior of Unbound Aggregate Materials. In *ASCE Journal of Materials in Civil Engineering*, Vol. 20, No. 9, 2008, pp.1-11
- Uzan, J. Characterization of Granular Material. in *Transportation Research Record*, No. 1022, Washington, D.C., 1985, pp. 52-59.
- Von Quintus, H.L., and Killingsworth, B. (1997). "Analyses Relating to Pavement Material Characterizations and Their Effects on Pavement Performance," FHWA-RD-97-085, *Federal Highway Administration*, Washington, D.C.
- Wang, K. Database Preparation for MEPDG PrepME. Presentation Slides, 2009 *Southeastern Pavement Conference*, New Orleans, Louisiana, 2009.
- Witczak, M. K., and Uzan, J. *The Universal Airport Pavement Design System*. Report I of V: Granular Material Characterization, Department of Civil Engineering, University of Maryland, MD, 1988.
- Xiao, Y., Tutumluer, E., Siekmeier, J. Resilient Modulus Behavior Estimated from Aggregate Source Properties. In *Proceedings of Geo-Frontiers*, Dallas, TX, 2011.
- Yohannes, B., Hill, K., and Khazanovich, L. *Mechanistic Modeling of Unbound Granular Materials*. Research Report MN/RC 2009-21, Minnesota Department of Transportation, St. Paul, MN, 2009.
- Zaman, M., Laguros J., Tian P., Zhu J., and Pandey K. *Resilient Moduli of Raw and Stabilized Aggregate Bases and evaluations of Layer Coefficients for AASHTO Flexible Pavement Design*. Final report, ORA 125-4262, ODOT, Oklahoma, 1998.

Large-Span Rock-Anchored Beam Safety Pre-warning Method and Its Application in Underground Powerhouse

Gao Chunyu and Deng Jianhui¹

¹State Key Laboratory of Hydraulics and Mountain River Engineering, College of Water Resource and Hydropower, Sichuan University, Chengdu, Sichuan, 610065 China, chygao@scu.edu.cn

ABSTRACT: A statistical analysis of the displacement monitoring data, the rock bolt stress and the joint meter opening degree during construction has been performed based on the monitoring data of five large-span rock-anchored beams of underground powerhouses, such as Pubugou Hydropower Station. It is proposed to classify the displacements of rock-anchored beams into large, medium and small types based on the average displacements of greater than 20mm, 10mm-20mm and less than 10mm, respectively. When the average displacement of the rock-anchor beam is within the large displacement range, pre-warning shall be given. The rock bolt-joint meter correlation pre-warning method is put forward here, which says that the maximum allowable deformation of the rock bolt is derived from the design tensile strength of the rock bolt and the unanchored length of the rock bolt and compared with the joint meter opening degree monitoring data in actual projects. The results show that the allowable deformation range coincides with the rock bolt deformations in different projects. The calculated allowable deformation can be regarded as a very important reference value in pre-warning of the joint meter opening degree. The rock bolt-joint meter correlation pre-warning method may be used in similar projects.

INTRODUCTION

Rock-anchored beam has two advantages (Wang 1988). First, it reduces the plant span; second, it can shorten the construction period. So it is widely used in the underground powerhouse. More than twenty years have passed since the rock-anchored beam was used in the Lubuge powerhouse. Rock-anchored beam design is still dependent on experience and engineering analysis (Weng 2010). Expanding the size of the underground excavation (referred to as a cavern), increases the span of rock-anchored beam, and results in a deeper cavern and higher ground stress. A few of the underground powerhouse rock-anchored beams appeared to have problems during construction (Wang 2007, Tang 2009, Fu 2010, Gong 2011). To ensure safety during construction and operation, real-time monitoring is performed to monitor displacement, bolt stress and concrete joints

of the rock-anchored beam. There is a question of how to judge rock-anchored beam safety reasonably based on these data.

The rock-anchored beam structure is employed in almost all underground powerhouses under construction and planned for construction, making such an in-depth study urgent for engineering. Previous study is based on a single project (Peng 2007, Huang 2011), while here we consider statistics and analysis of monitoring data collected during excavation of the rock-anchored beams of the underground powerhouse cavern groups of five large-scale hydropower stations, including the Guandi Hydropower Station in the Yalong River Basin, the Jinping-I Hydropower Station, the powerhouses at the left and right banks of Xiluodu Hydropower Station in the Jinsha River Basin and the Pubugou Hydropower Station in the Dadu River Basin. In spite of differences in rock formation lithology, geological structure and ground stress conditions, they share the following characteristics: first, the main powerhouse, the main transformer room and the tail surge chamber are arranged in parallel; second, the spans of the main powerhouses are all about 30m; third, the surrounding rocks are Class II-III hard rocks (The Ministry of Water Resources, 2011) with minor seepage; and fourth, the rock-anchored beams are used in all the main powerhouses.

DISPLACEMENT, BOLT STRESS AND JOINT METER STATISTICS

Displacement characteristics

The five large cavern groups have many common characteristics, but their displacements are different. The displacement characteristics of the rock-anchored beams in the caverns, mainly consisting of Class II and III type surrounding rocks, are analyzed based on statistical method with a lot of monitoring data. All the monitoring data were obtained after completing the excavations for the three caverns of the underground powerhouses.

30 rock-anchored beam displacement monitoring sections are distributed in the five large powerhouses, which include 58 sets of multi-point displacement meters. Both the maximum and average displacement of 105.39mm and 35.86mm, respectively, occur at Pubugou Underground Powerhouse (see Table 1). For the various underground caverns and main powerhouse, rock displacements are all concentrated on the rock-anchored beams and the high walls of the caverns (Huang 2011, Wei 2010). The rock-anchored beam part exhibits large displacements in the main powerhouses.

According to the statistics of the average displacement of the underground powerhouse, the rock-anchored beams of the five large underground powerhouses are classified into large, medium and small displacement types. The rock-anchored beams with large displacements include Jinping rock-anchored beams and Pubugou rock-anchored beams, with average displacements greater than 20mm; the rock-anchored beams with medium displacements are Guandi rock-anchored beams, with average displacements from 10mm-20mm; and the rock-anchored beams with small displacements include Xiluodu left bank and right bank rock-anchored beams, with average displacements less than 10mm.

Table 1. Rock-Anchored Beam Displacement Statistics

| Underground Powerhouse | Section Amount (a) | Multipoint Displacement Meter (group) | Displacement Range (mm) | Average Displacement (mm) | Maximum Displacement (mm) |
|------------------------|--------------------|---------------------------------------|-------------------------|---------------------------|---------------------------|
| Jinping | 4 | 8 | 2.9~77.0 | 29.96 | 77.0 |
| Pubugou | 10 | 19 | 4.08~105.39 | 35.86 | 105.39 |
| Xiluodu(left) | 6 | 11 | 1.3~14.6 | 6.62 | 14.6 |
| Xiluodu (right) | 6 | 12 | 1.3~14.7 | 6.17 | 14.7 |
| Guandi | 4 | 8 | 7.66~34.53 | 16.91 | 34.53 |

Bolt stress characteristics

The model test results show that when the rock-anchored beam is overloaded, the damage progresses in the following sequence: the tension rock bolt yields, the beam rotates about its lower edge and the lower concrete begins to yield from compression. The yield failure of the tension rock bolt is the most possible factor resulting in failure of the rock-anchored beam, so the stress of the tension rock bolt shall be scrutinized in the statistical analysis. All the rock-anchored beams of the five large powerhouses include two rows of tie rods and one row of compression rods to accommodate the stress that develops within the structure. The upper and lower rows of tie rods are collectively called tie rods and the lower row of compression rods are called compression rods.

The statistics of the rock bolt stress measured by stressometers of the rock-anchored beam rock bolts of the five large underground powerhouses are given in Table 2. In total, the five main powerhouses have 56 rock-anchored beam monitoring sections, 226 groups of rock bolt stressometers, 331 tie rod monitoring points and 137 compression rod monitoring points, including 30 tie rod over-range measuring points, accounting for 9.06% of total measuring points.

Table 2. Rock-Anchored Beam Bolts Stress Statistics

| Underground Powerhouse | Data Deadline | Monitoring Section (a) | Bolt Stress Meter (group) | Tension Bolt Point Number(a) | Over Range of Tension Bolt(a) | Compression Bolt Point Number(a) |
|------------------------|---------------|------------------------|---------------------------|------------------------------|-------------------------------|----------------------------------|
| Jinping | 2010-12-19 | 29 | 85 | 96 | 16 | 46 |
| Pubugou | 2009-10-25 | 8 | 57 | 64 | 7 | 15 |
| Xiluodu (Left) | 2010-5-24 | 7 | 32 | 56 | 2 | 28 |
| Xiluodu (Right) | 2010-5-22 | 7 | 32 | 56 | 1 | 28 |
| Guandi | 2010-7-23 | 5 | 20 | 59 | 4 | 20 |
| total | | 56 | 226 | 331 | 30 | 137 |

The tie rod stress results of the rock-anchored beam rock bolt stressometers of the main powerhouses of the five large underground powerhouses are given in Table 3. The statistical data show that 93.03% of the rock bolt measuring points are in tension; the tensile stresses are mainly within the range of 0-150MPa, accounting for 66.26% of total measuring points; overrange measuring points account for 9.34%, and 5.42% of the measuring points are damaged without readings. Measuring points with values greater than 100MPa at the downstream side account for 43.21%, while measuring points of the same order at the upstream side account for 25.31%, which is notably less when compared with the downstream side.

Table 3. Rock-Anchored Beam Tension Bolts Stress Statistics

| Bolt Stress (MPa) | Point Total | Percentage (%) | Upstream Points Total | Percentage (%) | Downstream Points Total | Percentage (%) |
|-------------------|-------------|----------------|-----------------------|----------------|-------------------------|----------------|
| -150~-100 | 1 | 0.30 | 1 | 0.59 | 0 | 0.00 |
| -100~0 | 22 | 6.63 | 19 | 11.18 | 3 | 1.85 |
| 0~100 | 178 | 53.61 | 103 | 60.59 | 75 | 46.30 |
| 100~150 | 42 | 12.65 | 19 | 11.18 | 23 | 14.20 |
| 150~200 | 22 | 6.63 | 8 | 4.71 | 14 | 8.64 |
| 200~300 | 18 | 5.42 | 8 | 4.71 | 10 | 6.17 |
| ≥300MPa | 31 | 9.34 | 8 | 4.71 | 23 | 14.20 |
| No data | 18 | 5.42 | 4 | 2.35 | 14 | 8.64 |
| total | 332 | 100.00 | 170 | 100.00 | 162 | 100.00 |

The statistics of the stress range are given in Table 4. The average stress of rock-anchored beams located upstream of the main powerhouse is generally less than those of rock-anchored beams located downstream, and the maximum stress upstream is less than that downstream, except for Guandi Powerhouse.

Table 4. Rock-Anchored Beam Tension Bolts Stress Range Statistics (MPa)

| | Jinping | Pubugou | Xiluodu(Left) | Xiluodu(Right) | Guandi |
|------------------------------|-------------|---------------|---------------|----------------|--------------|
| Upstream Bolt Stress Range | -80.6~237.5 | -141.6~359.51 | 41.33~180.39 | 10.4~222.96 | 0.53~519.5 |
| Upstream Average Stress | 25.37 | 57.19 | 91.96 | 85.57 | 89.25 |
| Downstream Bolt Stress Range | 11.3~473 | -15.59~346.6 | 2.71~319.6 | 29.06~304.7 | -1.74~369.01 |
| Downstream Average Stress | 207.77 | 79.62 | 99.94 | 119.28 | 52.82 |

Relationship among Joint Meter Value, Displacement and Bolt Stress

The statistics of the joint meter opening degree orders of the rock-anchored beams of the five large underground powerhouses, and the statistics of the joint meter opening degrees, respectively, are given in Table 5 and 6.

As can be seen from the statistical results of the displacements and the joint meter opening degrees, the larger the displacement is, the larger the joint meter opening degree is, and vice versa. Among the five large underground powerhouses, the displacements of rock-anchored beam parts of Xiluodu left and right bank underground powerhouses with small displacements are all less than 15mm and corresponding joint meter opening degrees are all smaller than 1mm for Xiluodu left bank rock-anchored beams and all below 2mm for Xiluodu right bank rock-anchored beams, and only 5.56% opening degrees are greater than 1mm. For Jinping Underground Powerhouse and Pubugou Underground Powerhouse with large displacements, the maximum displacements of the rock-anchored beam parts, particularly the downstream rock-anchored beam parts, are all greater than 70mm, and corresponding joint meter opening degrees are much greater than those of Xiluodu left and right bank powerhouses, and the joint meters with opening degrees greater than 5mm account for 6.06% and 5%, respectively. For the rock-anchored beams of Guandi Underground Powerhouse with medium displacements, no opening degree greater than 5mm occurs. It can be seen that the displacements of the rock-anchored beam parts and the opening degrees of the rock-anchored beams have a good corresponding relationship.

The rock bolt stress and the joint meter value also have a good corresponding relationship. The stresses of the tie rods of the rock-anchored beams of the five large powerhouses less than 200MPa account for 79.17% for Jinping, 62.50% for Pubugou, 92.86% for Xiluodu left bank, 94.64% for Xiluodu right bank and 77.97% for Guandi. Jinping's rock-anchored beams were constructed during the fifth excavation step of the main powerhouse. While the other four rock-anchored beams were constructed during the fourth excavation step. Jinping's rock bolt stress was included in the range less than 70% because the impact of construction lagging. The corresponding opening degrees are respectively less than 2mm for Xiluodu left and right banks and less than 5mm for Guandi, and certain proportion of opening degree values is greater than 5mm for Jinping and Pubugou.

Table 5. Joint Meter Measured Value Proportion Statistics

| Measured Value Range (mm) | Jinping | | Pubugou | | Xiluodu (Left) | | Xiluodu (Right) | | Guandi | |
|---------------------------|---------|-------|---------|--------|----------------|--------|-----------------|--------|--------|-------|
| | Amount | % | Amount | % | Amount | % | Amount | % | Amount | % |
| ≤0 | 4 | 12.12 | 1 | 5.00 | 3 | 15.00 | 3 | 8.33 | 0 | 0.00 |
| 0~0.5 | 17 | 51.52 | 11 | 55.00 | 15 | 75.00 | 23 | 63.89 | 1 | 5.00 |
| 0.5~1 | 6 | 18.18 | 2 | 10.00 | 2 | 10.00 | 5 | 13.89 | 13 | 65.00 |
| 1~2 | 2 | 6.06 | 3 | 15.00 | 0 | 0.00 | 2 | 5.56 | 5 | 25.00 |
| 2~5 | 2 | 6.06 | 0 | 0.00 | 0 | 0.00 | 0 | 0.00 | 1 | 5.00 |
| >5 | 2 | 6.06 | 1 | 5.00 | 0 | 0.00 | 0 | 0.00 | 0 | 0.00 |
| No Data | 0 | 0.00 | 2 | 10.00 | 0 | 0.00 | 3 | 8.33 | 0 | 0.00 |
| Total | 33 | 100.0 | 20 | 100.00 | 20 | 100.00 | 36 | 100.00 | 20 | 100.0 |

Table 6. Joint Meter Measured Value Range Statistics (mm)

| Location | | Jinping | Pubugou | Xiluodu (Left) | Xiluodu (Right) | Guandi |
|------------|---------|---------|------------|----------------|-----------------|-----------|
| Upstream | Range | 0~3.3 | -0.18~1.85 | -0.05~0.56 | -0.14~0.69 | 0.7~2.11 |
| | Average | 0.56 | 0.35 | 0.22 | 0.20 | 1.26 |
| Downstream | Range | 0~10.1 | 0.03~7.31 | -0.18~0.35 | -0.05~1.24 | 0.27~1.54 |
| | Average | 1.59 | 1.13 | 0.12 | 0.13 | 0.75 |

The statistical table 7 indicates that the relationships among the joint meter, the displacement and the stress are obtained in combination with analysis on their characteristics. It is suggested that the average displacement of the surrounding rock at the rock-anchored beam part greater than 20mm should be included in the pre-warning range. Whether the displacement falls in the hazardous range or not can be determined according to the displacement change rate of the specific part in engineering application.

Table 7. Statistics Relationship among Joint Meter Measured Value, Displacement and Bolts Stress

| Monitoring Value | Jinping and Pubugou | Guandi | Xiluodu (Left and right) |
|-----------------------------------|---------------------|-----------|--------------------------|
| Average Displacement | >20mm | 10mm~20mm | <10mm |
| Bolt Stress (< 200MPa Percentage) | <70% | 70%~80% | >90% |
| Joint Meter Measured Value | >5mm, >5% | <5mm | <2mm |

SAFETY PRE-WARNING

Bolt deformation constraint

In order to better judge the safety conditions of the rock-anchored beams, the rock bolt-joint meter correlation pre-warning method is proposed here. The most possible failure form of the rock-anchored beams is the yielding of the rock bolts occurring near the contact surfaces, so measuring the deformations of the rock bolts is the most direct method (Jin 2003). In engineering safety monitoring, joint meters are arranged between the beams and the rock walls and their measuring values may be approximately taken as the deformation values of the rock bolts in the case of small deformations.

In order to prevent stress concentration, the rock bolts are arranged with unanchored sections near the contact surfaces between the rock-anchored beams and the surrounding rock, and the rock bolts of such sections are not bonded, so their deformations are much greater than those of the anchored sections. According to sensitivity analysis results, an unanchored length within 2.0m is reasonable (Zhang 2010, Zhao 2007). When the design value is determined, the allowable deformation values of the rock bolts may be deemed as fixed. To

guarantee safety of the rock-anchored beams, the joint meter readings shall be less than the allowable deformations of the rock bolts. Such measuring values are fixed upon submission of the design results, which can be used as pre-warning reference for the joint meter readings.

Under the condition of the rotating balance equation, the allowable deformation of the bolt is defined as follows,

$$[\Delta] = LS_1^0 / E \quad \text{or} \quad [\Delta] = LS_2^0 / E \quad (1)$$

and, Maximum deformation of bolt should meet the following expression:

$$\Delta_{\max} \leq [\Delta] \quad (2)$$

where L is the unanchored length of the tension bolt, E is the elastic modulus of bolt, S_1^0 and S_2^0 are the design tensile strength of the two rows of tie rods, $[\Delta]$ is the allowable deformation based on the allowable tensile strength, Δ_{\max} is the maximum deformation of the bolt, and it is available from joint meter value in the actual project.

Project examples

Table 8 provides the allowable deformation values of rocks bolts with different unanchored lengths calculated according to formula (1). When the unanchored length L of the rock bolt has the maximum value within the reasonable range, i.e. 2.0m, $[\Delta]=4.88\text{mm}$.

Table 8. Acceptable Deformation of the Bolt

| Unanchored Length (m) | 0.5 | 1.0 | 1.5 | 2.0 |
|--|------|------|------|------|
| Acceptable Deformation $[\Delta]$ (mm) | 1.22 | 2.44 | 3.66 | 4.88 |

For the rock-anchored beams at Jinping, Pubugou, Guandi and Xiluodu left and right banks, 1.5m long rock bolts coated with bitumen in the rock walls are used and the allowable deformation values calculated according to formula (1) shall be within 3.66mm.

As can be seen from the monitoring data collected during construction of the rock-anchored beams of Pubugou Underground Powerhouse and Jinping-I Underground Powerhouse with partial or overall deformation problems, certain quantity of joint meter measuring values greater than 5mm occurred during construction period, accounting for 6.06% and 5% of the total quantity, respectively. All opening degrees of joint meters for Xiluodu Left and Right Powerhouses are below 2.0mm, only 1 joint meter at Guandi has a reading greater than 2.0mm (the opening degree is 2.11mm), and the rock-anchored beams of the three powerhouses haven't generated any cracks affecting the safety. It can be seen that the unanchored rock bolt lengths can be used to calculate the allowable deformation values of the rock bolts, which corresponds well to the actual engineering monitoring values, such calculated allowable deformation values have reference significance in pre-warning of the joint meter opening degrees and thus

the rock bolt-joint meter correlation pre-warning method is feasible.

The allowable deformation $[\Delta]$ can be obtained after determination of the rock bolt design value. When any engineering part shows any opening degree exceeding such reference value, pre-warning should be given for such part and high attention paid to it, and countermeasures to control the deformation of the rock bolt should be developed. However, in specific engineering applications, while selecting the pre-warning value for joint meter opening degree based on the allowable deformation $[\Delta]$ of the rock bolt, actual conditions such as the geology of the underground powerhouse and the deformation rate should also be considered.

CONCLUSIONS

(1) According to the average displacement of the underground powerhouses, the rock-anchored beams of the five large underground powerhouses are classified into large, medium and small displacement types. Jinping and Pubugou rock-anchored beams, with an average displacement greater than 20mm, belong to the large displacement type; Guandi rock-anchored beams are of medium displacement type, with an average displacement ranging from 10mm to 20mm; while Xiluodu left and right bank rock-anchored beams are classified as small displacement type, with an average displacement less than 10mm.

(2) The displacement, the rock bolt stress and the joint meter monitoring value are well correlated. According to the statistical results and actual engineering conditions, it is suggested that when the average displacement of the rock-anchored beam part is greater than 20mm, it enters the surrounding rock displacement pre-warning range, and in actual engineering applications the displacement change rate of the specific part should also be taken into account to determine whether the displacement enters the hazardous range.

(3) The rock bolt-joint meter correlation pre-warning method is proposed here: the maximum allowable deformation of the rock bolt is derived from the design tensile strength of the rock bolt and the unanchored length of the rock bolt and compared with the joint meter opening degree data actually monitored in projects. It has been shown that the allowable deformation range coincides with the rock bolt deformations and states in different projects, indicating the calculated allowable deformation has reference significance in pre-warning of the joint meter opening degree, and the rock bolt-joint meter correlation pre-warning method is feasible and may be used for pre-warning in similar projects during construction period.

ACKNOWLEDGMENTS

This work was financially supported by National Natural Science Foundation of China (No. 51079093, No. 51204112).

REFERENCES

- Wang, Y.X. (1988). "Rock anchor beam design of Lubuge hydropower station underground powerhouse." *Water Power*, Vol. (12): 52-54.
- Weng, Y.M.(2010). "Bearing mechanism research and design improvement of rock-anchored crane beam." *Water power*, Vol. 36 (8):22-24.
- Wang, D.K. (2007). "Cause analysis of cracking of rock-bolted crane girder in an underground powerhouses." *Chinese Journal of Rock Mechanics and Engineering*, Vol. 26 (10):2125-2129.
- Tang, J.F. (2009). "Cause analysis of longitudinal cracks of rock-anchored beam and its developmental trend in underground powerhouses." *Chinese Journal of Rock Mechanics and Engineering*, Vol. 28 (5): 1000-1009.
- Fu, J. (2010). "Cause and processing of crack of rock anchor beam in Goupitan hydropower station underground powerhouse." *Guizhou Water Power*, Vol. 20 (4): 34-37.
- Gong, S.H. (2011) "Cause analysis and processing of crack of rock anchor beam in underground powerhouse." *Shanxi Architecture*, Vol. 37 (34): 67-68.
- Peng, Q. (2007). "Analysis of surrounding rock deformation characteristics in underground powerhouse." *Chinese Journal of Rock Mechanics and Engineering*, Vol. 26 (12): 2583-2587.
- Huang, Z.P. (2011). "Loading experimental research of rock-anchored beam of Jinping I Hydropowerstation underground powerhouse." *Rock and Soil Mechanics*, Vol. 32 (4): 471-475.
- The Ministry of Water Resources of People's Republic of China. (1994). "Standard for engineering classification of rock masses (GB 50218-94)." *Press of China Plans*.
- Huang, Q.X. and Deng, J.H. (2011). "Displacement characteristics analysis of surrounding rock in underground powerhouse chambers at pubugou hydropower station during construction." *Chinese Journal of Rock Mechanics and Engineering*, Vol. 30 (S1): 3032-3042.
- Wei, J.B. and Deng, J.H. (2010). "Characterization of deformation and fracture for rockmass in underground powerhouse of jinping i hydropower station." *Chinese Journal of Rock Mechanics and Engineering*, Vol. 181 (9): 52-54.
- Jin, F.N. (2003). "Probing into some problems of rock bolt crane beam in underground engineering." *Chinese Journal of Rock Mechanics and Engineering*, Vol. 22 (s1): 2187-2191
- Zhang, P.B. (2010). "Sensitivity analysis of length of bolt sleeves in crane beams on rock walls." *China Rural Water and Hydropower*, Vol. (9): 80-83.
- Zhao, Z.R. (2007). "The model test of crane girder bolted to rock in underground powerhouse in xiaowan hydropower station." *Yunnan Water Power*, Vol. 23 (4): 39-43.
-

Consolidation Behavior of Ultra-soft slurry and 1-D Consolidation Model Considering Viscosity

Jun Tong¹, Noriyuki Yasufuku² and Kiyoshi Omine³

¹Doctor, Changjiang River Scientific Research Institute, Jiangda Road, Wuhan, Hubei, China, +86-27-82927645, tongjun888@gmail.com

²Professor, Department of Civil Engineering, Kyushu University, Fukuoka, Japan, +81-92-612-8292; Email: yasufuku@civil.kyushu-u.ac.jp

³Professor, Department of Civil Engineering, Nagasaki University, Nagasaki, Japan, +81-95-819-2621; Email: omine@nagasaki-u.ac.jp

Abstract: The ultra-soft slurry exhibits significant initially viscous and subsequently elasto-plastic consolidation behavior. In order to investigate the different consolidation response at the viscous stage (VS) and elasto-plastic stage (EPS), a series of element consolidation tests were carried out in the modified light-capped oedometer. Test results show that the consolidation coefficient and permeability at VS and EPS vary significantly, which would bring in non-negligible error to the consolidation prediction with the ordinary assumptions. A simplified 1-D consolidation model considering the significant behavior difference in the VS and EPS was developed. The suction pressure proposed by Hong (2007, 2010) was employed to identify the consecutive stages in the model. Then the consolidation tests for ultra-soft clay under different loadings were conducted in the small-scale consolidometer and the test results are simulated with the proposed model. The model can describe the progressive consolidation well from the VS to EPS. It provides an easy-accessible and reasonable alternative for the prediction of the consolidation behavior for the ultra-soft slurry.

INTRODUCTION

Every year huge amount of dredging ultra-soft clay is generated all around the world (Krizek, 2000). The material can be a valuable fill resource for embankment although much of it is currently disposed because of economic, logistical or environmental constraints. The key to an effective utilization of the ultra-soft clay as filling material is the thorough understanding of the consolidation behavior. It has

been pointed out that the consolidation behavior of slurry-like soil upon additional load is not well understood (Bo M. W., 1999). At the initially viscous stage, as explained by Sill (1995), soil particles may be bonded together loosely in flocs and aggregates with a very open structure due to electro-chemical interaction. Then the ultra-soft clay generally behaves differently from the initially viscous state to the subsequent elasto-plastic state owing to the gradual formation of soil structure. In this paper, firstly, the oedometer tests starting from a low consolidation stress are conducted to investigate the consolidation behavior difference of the ultra-soft clay at different effective stresses. In order to obtain a better understanding of the progressive consolidation transferring from the viscous to plastic state for the ultra-soft clay, consolidation model tests were performed in the small-scale consolidometer equipped with pore-pressure transducers along the profile of the soil column. Consolidation behavior was monitored with both settlement and pore-pressure measurement. The influence of the magnitude of the initial vacuum pressure was investigated. Based on the oedometer test, 1-D consolidation model considering the significant change of the consolidation behavior at the respective viscous and plastic consolidation stages is proposed and verified by the model test results.

TEST SCHEME

The tests scheme includes the oedometer and small-scale consolidation tests. The oedometer tests were conducted at different consolidation stages. The diameter and height of test sample are 60mm and 30mm, respectively. A series of small-scale vacuum consolidation tests are conducted to comparatively investigate the consolidation behavior under the magnitude of 30, 60 and 80 kPa vacuum pressure, respectively. The initial water contents of the sample for all the above tests are 93.5 % (1.2 times of I_L), which are the representative value of natural water content of the dredged slurry. The initial height and diameter of the specimen are 20cm and 10cm, respectively.

TEST SOIL, APPARATUS AND METHOD

Test Soil

The test sample used in the study was retrieved from the reclamation site of Island city Port, Fukuoka city, Japan. Its specific gravity is 2.673 and the natural water content is around 93.5%. The liquid and plastic limits are 77.9% and 36.7%, respectively. The soil sample contains more than 25% clay particle (<0.005mm) and 60% silt particle (0.005~0.05mm). According to Soil Classification System specified by Chinese Specification of Soil Test (SL237-1999), the soil sample is categorized as MH.

Sample Preparation and Saturation

The soil was taken from the silt pond with the grab machine and stored in the plastic tanks. The natural water content of the slurry was 89.4~93.1%, which is around 1.1~1.2 times of the liquid limit. Before the consolidation tests, the slurry was passing through a 2 mm sieve to remove the gravels and other impurities. Then the distilled water was added to approach the targeted water content and agitated by the electrical stirrer to thoroughly remove the entrapped air and bubbles in the slurry.

Test Apparatus

For the oedometer tests, in order to apply very low stress to the ultra-soft clay initially, the self-made perspex light cap is made to replace the original one to make the application of low consolidation stress available.

The small-scale consolidation test apparatus is shown in Fig. 1. The vacuum line is connected to a vacuum gauge. The regulated vacuum pressure is connected with a valve to the water connection tank, which in turn is connected to the bottom of the vacuum cell. Thus, the regulated vacuum pressure is applied to the bottom of the soil specimen. The consolidometer cell is made of 4 layers of the perspex cylinder. The inner diameter of cell is 10 cm, and the maximum accommodated specimen height is 25cm. 3 PWP transducers are equipped on the wall of the cell with the height of 6cm, 11cm and 15cm away from the drainage boundary at the bottom to measure the pore water pressure at 3 different elevation of the soil sample. The light rigid cap is placed on the top of the soil to ensure the uniform strain deformation. An electronic dial gauge mounted on the rigid cap on the sample top is connected to the data acquisition system to monitor the settlement with time. All the readings of the above transducers are recorded by the data acquisition system.

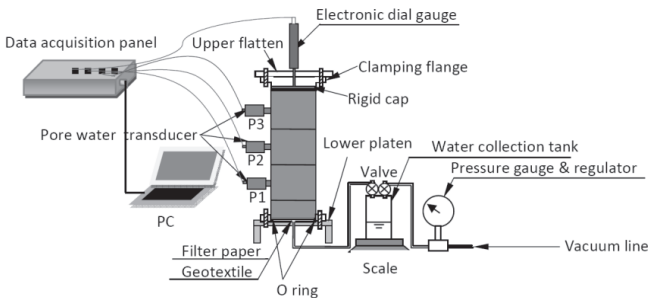


Fig. 1. Schematic diagram for the small-scale consolidation tests.

Test Method

Initially, the geotextile as drainage material and the tube lines were examined and

saturated with distilled water. Then the geotextile was placed at the base of the cell followed by a piece of filter paper. The inner cell surface is lubricated with silicon grease which could significantly reduce the friction between the sample and inner wall. Then the reconstituted sample was carefully placed in small patches in the cell and gently agitated with a thin rod to remove any noticeable air voids. Then it was followed by another wet filter paper and the second saturated geotextile. The piston was lubricated and pushed carefully into the upper part of the cell. Then the piston was pushed gently to rest at the upper geotextile. The settlement gauge, pressure transducer were connected to the data acquisition system. After adjusting the vacuum preloading pressure to the desired value, the valve between the vacuum line and the volume change tube was opened. It is more reasonable to apply the loading instantaneously in the laboratory tests, as in the field, as the excess pore water pressure would not dissipate in the beginning 11 months (M.W.Bo, et al. 2002). The drained water expelled from the soil sample was monitored during the test period through the scale and recorded as a double check. The tests were continued until the primary consolidation was completed, which identified by the flattening of the excess pore-water pressure and settlement versus time curves.

CONSOLIDATION BEHAVIOR AT DIFFERENT EFFECTIVE STRESSES

Most of the previous research is based on the constant permeability and linear void ratio and effective stress relationship that are unlikely to be true for the soil especially at low effective stress (M.W.Bo, et al. 2002; Berry, P.L., et al. 1969; Chen et al. 2004). Hence, the varying coefficient of consolidation and permeability must be included in the theoretical models to provide an acceptable evaluation of the performance of ultra-soft clay. It is imperative to conduct the oedometer tests on thin sample to investigate the fundamental compression behavior of the ultra-soft starting from the low to high effective stresses.

Fig. 2 shows the e - $\log p$ curve obtained from the oedometer consolidation test. There is an obvious turning point on the curve, of which the corresponding water content is around the liquid limit. The corresponding effective stress has been defined as the *suction pressure* by Hong (2010), which is similar to the yield stress of the structural natural clay, indicating the transition point of the “s” shape e - $\log p$ curve for the high water content clay. The suction pressure for the studied clay is $R = 3.9$ kPa. The compression index from 100 to 1256kPa is 0.37, which falls in the typical range of compression coefficient C_c for the normally consolidated soft soil from 0.35~0.75(TONG J., 2007). The corresponding void ratio is very close to that with the water content of the liquid limit (77.9%).

Fig. 3 shows the change of the coefficient of consolidation C_v obtained by the best fit of settlement curves at different consolidation pressures. Fig. 4 shows the change of permeability k with the effective stresses according to the value of C_v and the

corresponding void ratio e and effective stress. It indicates that when the effective stress is lower than the suction pressure, C_v and k is significantly greater than that when effective stress exceeds the suction pressure. As the permeability change index C_k is common index to measure the change in void ratio e with respect to the change of the permeability. Fig. 5 shows the variations in void ratio with permeability. The curve can be obviously divided into 2 segments with the permeability change indices of C_k , which the turning point is around the void ratio with the corresponding water content of w_L . The average C_k in the two sections are 0.22 and 0.37, respectively. All the transitional points obtained from the above curves are consistent, which correspond to the void ratio of 2.0 or the water content of the liquid limit.

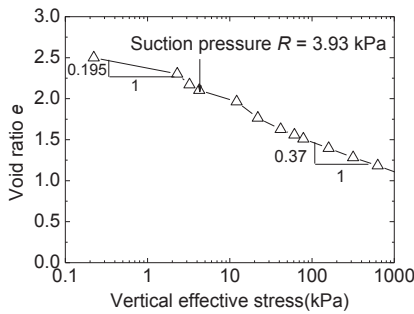


Fig. 2. e -log p curve.

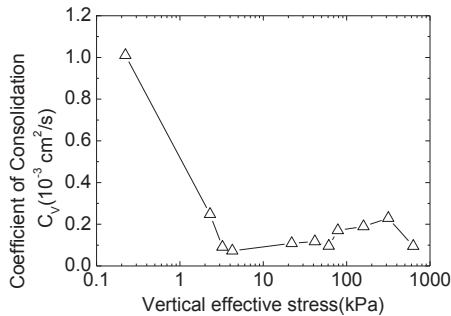


Fig. 3. C_v -log p curve.

SETTLEMENT AND PORE WATER PRESSURE RESPONSE DURING PROGRESSIVE CONSOLIDATION

Fig. 6 shows settlement versus time with vacuum pressures of 30, 60 and 80kPa. The variation of the settlement with the time in the vacuum shows no significantly distinct response to the magnitude of the vacuum pressure in the initial 200 minutes. However, thereafter the settlements subjected to greater negative pressure become

gradually greater than that subjected to less vacuum pressure. The final strains of the soil column are proportional to the magnitude of pressures, which are 23%, 26%, 27%, correspondingly. The elapsed time at 90% consolidation, as commonly expressed as t_{90} for 30, 60 and 80 kPa negative pressure are 9500 min, 6600 min and 3130 min, respectively, suggesting the settlements increase with the magnitudes of the negative pressures.

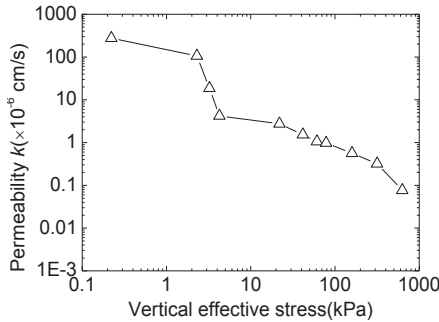


Fig. 4. k -log p curve.

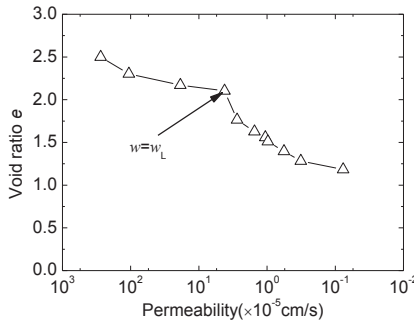


Fig. 5. e -log k curve.

Pore pressures are measured at three different height of the soil column, which have been indicated as P1, P2, and P3 from bottom to top, as shown in Fig. 1. Fig. 7 shows isochronous curves of the PWP under 30 kPa vacuum pressure. Every curve contains 3 data points, indicating the pore water pressures at the point P1, P2, and P3 at the time of 22h, 43h and 153h, respectively. The variation magnitudes of the pore pressure during the intervals (from 22h, 44h to 153h) at P1, P2 and P3 decrease successively. Notably, the pore pressure at P3 shows little variation. It seems that there is a moving consolidation boundary during the slurry consolidation process.

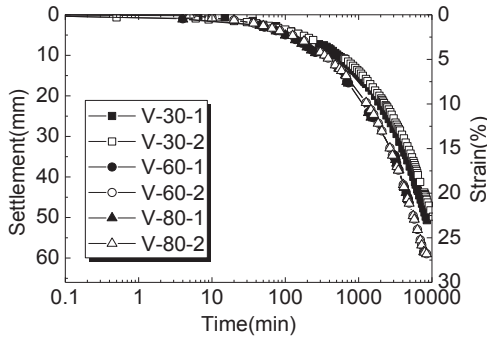


Fig. 6. Comparison of settlement versus time with different magnitudes of vacuum pressures.

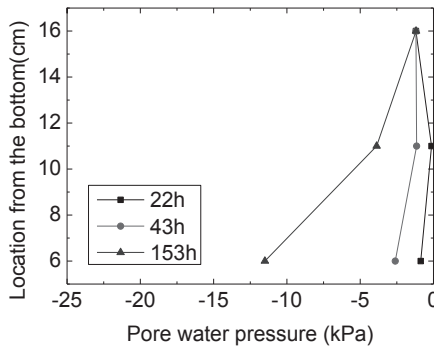


Fig. 7. Isochronous curves of the PWP under 30 kPa vacuum pressure.

1-D SIMPLIFIED CONSOLIDATION MODEL FOR THE ULTRA-SOFT CLAY

In order to describe the initially viscous and subsequent plastic consolidation behavior of the ultra-soft slurry, 1-D simplified consolidation model for ultra-soft clay considering the significant change of the consolidation behavior at the viscous and plastic consolidation stage is developed. The model is based on the Terzaghi governing equation, however, the permeability and the coefficients of consolidation at initial viscous and subsequent plastic stage are considered as the stage-dependent constants, in contrast to the constant consolidation parameters in the Terzaghi assumption. The derivation of the solution for the proposed model is similar to that for predicting the consolidation of sensitive structural soft clay proposed by Chen (2004). Due to the page limitation, detailed explanation of the proposed theory can be referenced in TONG (2012).

The small-scale consolidation test results in section 5 were employed to verify the

proposed model. Fig. 8 shows the development of the moving boundary surface with elapsed time. The scatters could be obtained from small-scale consolidation tests, identified by the elapsed time when the effective stress is greater than the suction pressure, which can be indicated by the pore water pressure. It shows that the moving boundary between the viscous mud and Terzaghi soil can be predicted well by the proposed model. Fig. 9 shows the comparison of U_t-t curve by moving boundary consolidation theory and conventional Terzaghi consolidation theory for the 60 kPa small-scale vacuum consolidation tests. The test data is between the 2 theoretical consolidation curves, which can be obtain from the initial and subsequent coefficients of consolidation by the Terzaghi theory. It indicates that the consolidation rate obtained by the proposed theory is between the rate calculated with the consolidation parameters in the viscous and plastic stage using the Terzaghi consolidation theory. So the conventional Terzaghi theory would overestimate the degree of consolidation result in the unsafe design for the engineering problem.

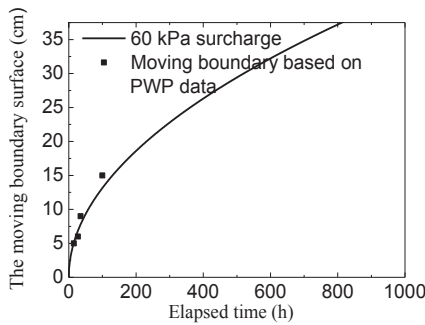


Fig. 8. Development of the moving boundary surface with elapsed time.

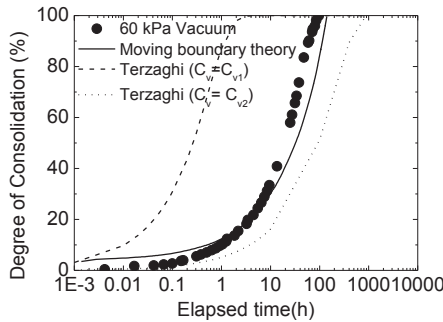


Fig. 9. Comparison of U_t-t curve by different consolidation theory.

CONCLUSIONS

A series of oedometer and small-scale consolidation tests were performed to investigate the viscous and elasto-plastic behavior, the conclusions can be drawn as follows.

1. There is a distinctly sharp transitional point on the e - $\log p$ curve, of which the corresponding water content is around the liquid limit w_L . The consolidation behavior at low stress level shows significantly different response to that at high stress level. The coefficients of consolidation and permeability before and after the transitional point could be as much as 10 times difference.

2. On the basis of the conventional Terzaghi consolidation theory and the test results in this paper, a simplified consolidation model was introduced to incorporate the significant change of consolidation behavior of ultra-soft clay at the initially viscous and subsequent plastic consolidation stage, respectively. The proposed 1-D model can predict the consolidation behavior of the ultra-soft soil well.

3. Further study may be carried out to propose more reasonable consolidation constitutive relationship during the viscous and elasto-plastic stages to simulate the consolidation behavior of the ultra-soft clay more accurately.

REFERENCES

- Berry, P.L., Wilkinson, W.B. (1969). "The radial consolidation of clay soils." *Geotechnique*, 19(2), 253-284.
- Bo, M. W., V. Choa and K.S. Wong (2002). "Compression tests on a slurry using a small-scale consolidometer." *Canadian Geotechnical Journal*, 39(2), 388-398.
- Bo M. W., V Choa, A. Arulrajah and Na Y.M. (1999). "One-dimension compression of slurry with radial drainage." *Soils and Foundations*, 39(4), 9-17.
- Chen Yun-Min, TANG X.-W., Jun Wang (2004). "An analytical solution of one-dimensional consolidation for soft sensitive soil ground." *International Journal for Numerical and Analytical Methods in Geomechanics* 28, 919-930.
- Hong, Z. (2007). "Void ratio–suction behavior of remolded Ariake clays." *Geotech. Testing J*, 30(3), 234–239.
- Hong, Z.S., J. YIN, Y.J. Cui (2010). "Compression behaviour of reconstituted soils at high initial water contents." *Geotechnique*, 60(9), 691-700.
- Krizek, R. J. (2000). "Geotechnics of High Water Content Materials." Special Technical Publication 1374, ASTM.
- Sills G. C. (1995). "Time dependent processes in soil consolidation." *Compression and consolidation of clayey soils*. Yoshikuni H. and Kusakabe O. (eds.), Balkema, Rotterdam, 875-890.
- TONG J. (2007). Experimental study on the consolidation behavior of soft clay under vacuum preloading. *MSc thesis*, Dept. of Civil Engineering and Architecture,

Zhejiang University, Hangzhou, 21p.(In Chinese)

TONG J. (2012). Consolidation behavior of ultra-soft clay and its improvement by siphon method with horizontal layered drainage system. *Doctor thesis*, Dept. of Civil and Structural Engineering, Kyushu University, Fukuoka, p.114-118.

The Settlement Behavior of Piled Raft Interaction in Undrained Soil

Abbasali Taghavi Ghalesari¹; Amin Barari², A.M. ASCE; Pedram Fardad Amini³ and Lars Bo Ibsen⁴, M. ASCE

¹Graduate Student, Department of Civil Engineering, Babol University of Technology, Babol, Iran; Abbasali.Taghavi@yahoo.com

²Postdoctoral Fellow, Department of Civil Engineering, Aalborg University, Sohngårdsholmsvej 57, 9000 Aalborg, Aalborg, Denmark; ab@civil.aau.dk, amin78404@yahoo.com

³Graduate Student, Department of Civil Engineering, Babol University of Technology, Babol, Iran; p.fardadamini@gmail.com

⁴Professor, Department of Civil Engineering, Aalborg University, Sohngårdsholmsvej 57, 9000 Aalborg, Aalborg, Denmark; lbi@civil.aau.dk

ABSTRACT: Offshore piled raft foundations are one of the most commonly used foundations in offshore structures. When a raft foundation alone does not satisfy the design requirements, the addition of piles may improve both the ultimate load capacity and the settlement performance of the raft. In this paper, the behavior of a piled raft on undrained soil is studied based on a series of parametric studies on the average and differential settlement of piled raft using three dimensional finite element analysis. The settlement behavior is found to be dependent on the number of piles and raft thickness.

INTRODUCTION

The concept of enhanced raft foundation with deep foundation elements namely piled rafts has received much attention recently. Piled raft foundation consists of three carrying elements: soil, raft and pile, which the interaction between the elements may cause some complexity in prediction of this composite foundation.

On the basis of the design requirements to be satisfied, Russo and Viggiani (1998) grouped piled rafts into two broad categories. The first group involves small piled rafts, which the width of the raft B_R , is generally small in comparison to the length L of the piles and the bearing capacity of the unpiled raft in this category is insufficient, and thus the primary reason to add the piles is to achieve a suitable safety factor. The second group involves large piled rafts, which the width B_R of the raft is relatively large in comparison to the length of the piles and the bearing capacity is sufficient to

carry the total load with a reasonable margin, so that the addition of piles is usually intended to reduce settlement.

In order to address the requirements for design of piled raft systems, much attention has been given to the development of analytical models followed by numerical, laboratory and field studies investigating the influence of system geometry and soil properties on the performance of piled rafts (Poulos 1994; Horikoshi and Randolph 1996; Oh et al. 2008).

Hooper (1973) was among the first authors who used Finite Element Method to analyze a piled raft and considered the stiffening effect of the superstructure on the behavior of the piled raft by introducing an equivalent raft thickness. Later on, it was found that the use of piles to reduce raft settlements and differential settlements can lead to an economical design without compromising the safety and performance of the foundation (Poulos 2001). The required pile group-raft area ratio for minimizing differential settlement in soft clay was found slightly larger than that of stiff clay in the same pile array, as suggested by Cho et al. (2012) for square piled raft.

Generally, the loading of an offshore structure consists of two components: vertical structural loads and lateral wave loads. The combinations of these two loading components have a significant impact on how the pile reacts and the way the moments are distributed throughout the pile (Eicher et al. 2003). Therefore, the overall objective of this study is to investigate the settlement behavior of a large piled raft on clayey soil under vertical structural loading by using three-dimensional finite element analysis considering the pile-soil slip interface model.

FINITE ELEMENT MODELING

Finite element mesh and boundary conditions

The behavior of the piled raft was investigated by carrying out 3D numerical analysis. Six-node triangular elements were used to represent piled raft elements. Fig. (1) shows a typical finite element mesh used in this numerical study. The parameters for a series of the static finite element analyses are raft and pile sizes and number of piles. Material properties of piled raft and undrained soil parameters are tabulated in Table 1.

Table 1. Material properties used for analysis

| Material | E (MPa) | ν | γ (kN/m ³) | C (kPa) | ϕ (deg) |
|----------|--------------|-------|----------------------------------|--------------|-----------------|
| Soil | 14 | 0.18 | 18 | 20 | 35 |
| Pile | 25000 | 0.20 | 24 | - | - |
| Raft | 25000 | 0.20 | 24 | - | - |

The pile head was connected to the raft rigidly. Special interface element was used at the pile-soil and raft-soil interface. A relatively fine mesh was used near the structural components while a coarser mesh was used further from the piles and raft.

Lateral boundaries were only restrained against horizontal translations to allow downward movement of the soil layers and the beneath of the model was fixed in three orthogonal directions. For the far-field boundaries, the distance of the boundary from the edge of the raft was greater than the pile length. This limit prevents the effects of boundaries on the analysis (Lee et al. 2010). After initial equilibrium, the vertical loading was applied on the top of the raft surface. Since modeling of the entire pile installation process is rather complicated, the pile was assumed to be in a stress-free state (wished in place) at the start of the analysis (Jeong et al. 2004).

Constitutive modeling

The material behavior of the soil was modeled with a Mohr-Coulomb model, and to simplify the analysis process, average values of material parameters (as mentioned in Table 1) were adopted for the soil layer. Since the raft and piles have great Young’s modulus in comparison with the soil, they remain in elastic range. Due to the aforementioned reason, they were modeled with a non-porous linear elastic model.

The modeling techniques used for the pile-soil interface were generally divided into two types: thin layer element and slip element. The former was used by Jeong et al. (2004) and Lee et al. (2010), in which the slip behavior between the adjacent surfaces could be considered. The latter was used by Reul and Randolph (2004) and a middle layer is used to model the interface using the behavior of the soil. In this case when a slide occurs, the shear stress (τ) will be created in the interface and the relationship between shear force and normal pressure P' is governed by a modified Coulomb’s friction theory. In this paper, the pile-soil interface was modeled by slip elements. The schematic diagram of pile-soil interface elements with undrained parameters is shown in Fig. (2).

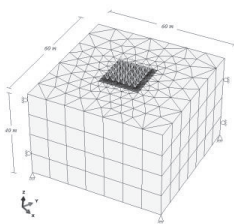


FIG. 1. Typical finite element mesh

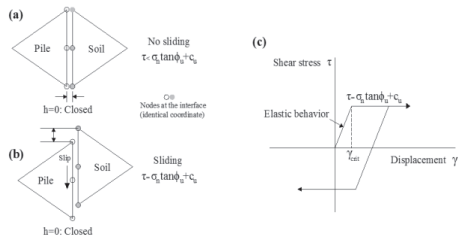


FIG. 2. Pile-soil interface modeling technique: (a) no slip; (b) slip; (c) Coulomb’s frictional law (Jeong et al. 2004)

VALIDATION OF THE NUMERICAL MODEL

The finite element model is validated using centrifuge test data reported by Horikoshi and Randolph (1998). The total number of piles was nine with a length of 15 m and diameter of 0.32 m, which were located under a 14 m diameter circular raft with a thickness of 0.05 m. A soil depth of 25 m was taken into account. The results are given in Table 2.

Table 2. Comparison of the results with the test data

| Results (applied load of 12 MN) | Average Settlement, S_{avg}(mm) | Load taken by piles (%) |
|--|---|--|
| Horikoshi and Randolph (1998) | 22 | 19 |
| Present Study | 21.67 | 23.55 |

PARAMETRIC STUDY

Different parameters affect the behavior of offshore piled raft in the design procedure. To provide a more accurate and effective design for offshore foundation systems under vertical loads, a parametric study is performed to examine the effects of these parameters including soil, raft and pile configurations, different sizes and distances, number of piles and raft stiffness. Table 3 lists the mentioned parameters employed for the piled raft analyses. The pile arrangements used in this study are outlined in Fig. (3).

Table 3. System configuration for parametric study

| | | |
|-------------|---------------------------------|--|
| Pile | Length | 20 m |
| | Diameter | 1 m |
| | Distance | $S/D= 3,4, 5$ |
| | Arrangement | Centered-Uniform |
| Raft | Thickness | 0.5, 1, 1.5 m |
| | Width | 18 by 18 m |
| Load | Uniform | 100 , 150 kN/m ² |
| | Concentrated (Point) | 32.4, 48.6 MN equal to uniform load, respectively (on the location of piles) |

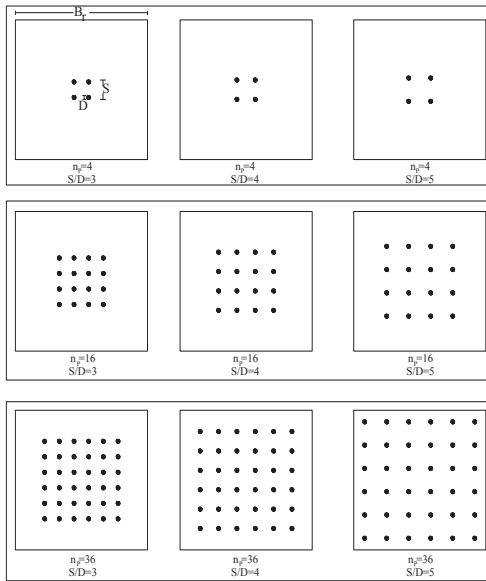


FIG. 3. Pile arrangements used for the parametric study

The majority of the previous studies have considered evenly distributed superstructure loads rather than column loads acting on the piled rafts. The latter load type is more commonly encountered in practice, especially for typical urban structures. Hence, there is still a lack of understanding of the behavior of piled rafts under point loading conditions and the effect of several design variables on the piled raft performance. Therefore, uniform loading studies have been compared with point loading. Point loads, and the equivalent magnitude of the distributed loads in the two different loading conditions were the same. At the first stage, initial stresses were generated and in the second stage, raft and piles were defined as structural components. Finally, vertical loads were applied. The use of undrained soil is preferred because the piled raft location is offshore.

RESULTS AND DISCUSSION

Average settlement

Figure (4) shows the variation of the normalized average settlement, $R_{avg} = S_{PR,avg} / B_r$ with the ratio of pile spacing to diameter (S/D), for piled rafts subjected to vertical uniform and point loads. Each value of this parameter therefore introduces a new configuration. The average settlement is calculated using Eq. (1) according to Davis and Taylor (1962):

$$S_{ave} \approx \frac{1}{3}(2S_{center} + S_{corner}) \quad (1)$$

where S_{center} is the settlement at the raft center and S_{corner} is settlement at the raft corner.

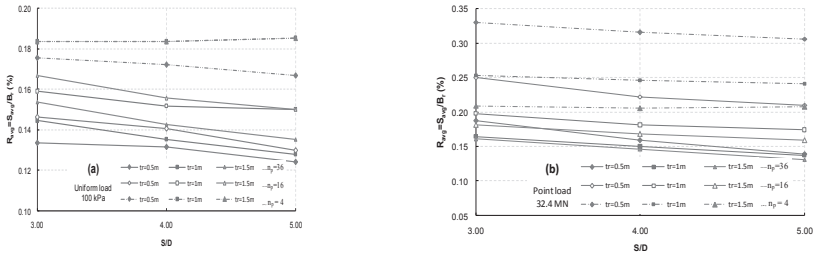


FIG. 4. Variation of normalized average settlement with the ratio of S/D
(a) Uniform load: 100 kPa (b) Point load: 32.4 MN, equal to 100 kPa uniform load

The average settlement is reduced with increasing the S/D ratio. The decrease is more pronounced for piled rafts with larger number of piles and smaller raft thickness (Fig. (4a)). Adding the number of piles for a piled raft system with the thickness of 0.5 m results in significant reduction in observed settlement. Piled raft system was similarly subjected to a uniform loading of 150 kPa and as expected, when the load level increased, the corresponding average settlement of the piled raft increased. The case $S/D=5$ displayed the best performance for different load levels. Another point that realized from the numerical analysis using uniform loading is that increasing in raft thickness may lead to relative increase in average settlement, and the range of values increased with increasing load levels. The raft thickness of 1 m shows acceptable performance between different thicknesses.

Fig. (4b) shows the settlement behavior of piled raft system under point loading for different raft thicknesses and pile numbers. As S/D ratio increases, R_{avg} decreases and the variation of R_{avg} due to point loading is relatively higher than the average settlement caused by uniform loading in most cases.

Center to corner differential settlement

Figure (5) shows the variation of the normalized differential settlement, S_d , with B_g / B_r (pile group to raft width ratio). The normalized differential settlement is calculated from Eq. (2).

$$S_d = \frac{\Delta S_{c-c} E_s}{q \cdot B_r} \tag{2}$$

where ΔS_{c-c} is differential settlement, E_s is modulus of elasticity for the soil, q is applied load and B_r is raft width.

In addition to the standard cases, cases with different raft thicknesses, pile configurations and loading conditions are shown. In this case, raft thickness of 0.5 m does not act so well and shows significant differential settlement especially under point loading. As observed, when the load applied in certain point (on the piles), significant local displacement occurred and made remarkable differential settlement. It is immediately obvious that differential settlement began to level off as the B_g/B_r ratio increases until the B_g/B_r ratio is equal to the 0.45-0.6 for most piled rafts, similar to the observation by Horikoshi and Randolph (1997).

The minimum differential settlement is related to the 1.5 m raft thickness and the raft thickness of 1 m showed the satisfactory performance by reducing the differential settlement in comparison to the thickness of 0.5 m; though using thick raft ($t_r=1.5$ m) just to decrease the differential settlement is not recommended due to the economical issue. Similarly, for uniform loading, a value of 150 kPa was modeled. It is immediately observed that piled raft under uniform loading experienced an increase of normalized differential settlement with increasing load level.

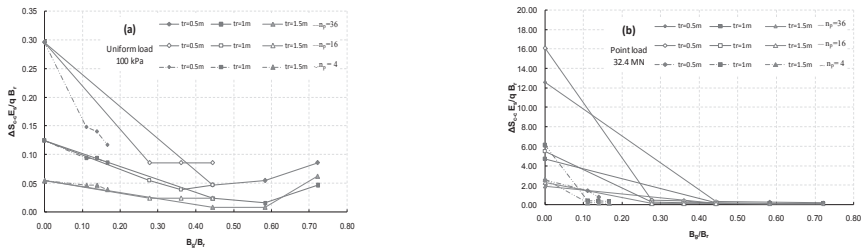


FIG.5. Variation of normalized differential settlement with the ratio of B_g/B_r , (a) Uniform load: 100 kPa (b) Point load: 32.4 MN, equal to 100 kPa uniform load

According to Fig. (5b), when the piled rafts were subjected to point loads, the differential settlement was reduced at low B_g/B_r ratio and leveled off to a relatively zero value beyond a certain value of B_g/B_r ratio. Therefore, increasing the B_g/B_r ratio beyond a certain normalized width value has no considerable effect on differential settlement.

CONCLUSIONS

A series of numerical analyses were conducted to investigate the behavior of a square piled raft subjected to different loading states. In this study, the 3D elasto-plastic FE analyses with slip interface model of pile-soil contact were carried out with undrained shear parameters for a cohesive soil. According to the behavior observed, the discrepancies in Figs. (4) and (5) can be ascribed to the dependency of the settlement behavior of piled raft on the raft thickness, number of piles and loading

conditions. A decrease in normalized differential settlement with increasing raft thickness was recognized from the numerical analysis using uniform loading in Fig. (5a), although it was more pronounced for lower B_g/B_r ratios. This behavior is in contrast with observations from normalized average settlement. In this study, a considerable increase in average settlement was observed when the value of t_r increased towards a value of 1.5 as number of piles decreased. As a conclusion, the normalized pile spacing $S/D=5$ was capable of reducing the computed displacements with variations of n_p and t_r within the load path followed.

REFERENCES

- Russo, G. and Viggiani, C. (1998). "Factors controlling soil-structure interaction for piled rafts." *Int. Conf. on Soil-Structure Interaction in Urban Civil Engineering*, 297-322.
- Poulos, H.G. (2001). "Piled raft foundations: design and applications." *Géotechnique*, Vol. 51: 95-113.
- Cho, J., Lee, J., Jeong, S. and Lee, J. (2012). "The settlement behavior of piled raft in clay soils." *Ocean Engineering*, Vol. 53: 153-163.
- Hooper, J.A. (1973). "Observations on the behaviour of a piled-raft foundation on London Clay." *Inst. Civ. Engrs*, Vol. 55: 855-877.
- Horikoshi, K. and Randolph, M. F. (1996). "Centrifuge modelling of piled raft foundations on clay." *Geotechnique*, London, Vol. 46 (4): 741-752.
- Oh, E., Huang, M., Surarak, C., Adamec, R. and Balasurbamian, A.S. (2008). "Finite element modeling for piled raft foundation in sand." *Paper presented at the EASEC-11*, Taiwan.
- Poulos, H. G. (1994). "An approximate numerical analysis of pile-raft interaction." *Int. J. Numerical and Analytical Methods in Geomechanics*, Vol. 18 (2): 73-92.
- Jeong, S., Lee, J. and Lee, C. (2004). "Slip effect at the pile-soil interface on dragload." *Computers and Geotechnics*, Vol. 31:115-126.
- Eicher, J.A., Guan, H. and Jeng, D.S. (2003). "Stress and deformation of offshore piles under structural and wave loading." *Ocean Engineering*, Vol. 30: 369-385.
- Lee, J., Kim, Y. and Jeong, S. (2010). "Three-dimensional analysis of bearing behavior of piled raft on soft clay." *Computers and Geotechnics*, Vol. 37: 103-114.
- Horikoshi, K. and Randolph, M.F. (1998). "A contribution to the optimum design of piled rafts." *Géotechnique*, Vol. 48 (2): 301-317.
- Davis, E.H. and Taylor, H. (1962). "The movement of bridge approaches and abutments on soft foundation soils." *Proc.1st Biennial Conf. Australian Road Research Board*, p 740.
- Reul, O., Randolph, M.F. (2004). "Design Strategies for Piled Rafts Subjected to Nonuniform Vertical Loading." *Journal of Geotechnical and Geoenvironmental Engineering*, Vol. 130: 1-10.

Pile Foundation Seismic Design Approach for the Padma Bridge, Bangladesh

Suraj De Silva¹, Ph.D., CPEng., Chao Li², Ph.D., M. ASCE, and
Yu, GuoXiong¹, Ph.D

¹ Associate Director AECOM Asia Co. Ltd., Hong Kong, 20F Grand Central Plaza, Shatin, Hong Kong, +852 39228672 suraj.desilva@aecom.com .

² Principal Engineer, Benaim, Hong Kong, chao.li@gmail.com

ABSTRACT: Padma River is 6km wide at the location of the proposed bridge. The estimated riverbed scour is 62m deep with a return period of 100 years. Due to the proximity of Bangladesh to the tectonic plate contact zones of the Himalayas, the site is prone to seismic events. The deep scour and seismicity made the foundation design very challenging. A detailed state-of-the-art ground investigation was carried out down to a depth of about 160 m in the predominant micaceous sands encountered to establish the static and dynamic soil parameters. Undisturbed samples of sand were recovered using the GEL PUSH sampling technique. State-of-the-art insitu tests, the self-boring insitu friction tests (SBIFTs), cross-hole seismic shear wave and compression wave tomography, self-boring pressuremeter tests, and flat plate dilatometer tests were carried out. Cyclic triaxial loading tests, bender element tests, K_0 -consolidated stress path compression and extension tests were carried out.

A structural numerical model developed using MIDAS software comprising six 150m long spans was developed including the piles at each pier. Using the dynamic design soil parameters the ground response was determined using SHAKE, with strong ground motions corresponding to a 475 year return period earthquake event, and they were then input into the MIDAS dynamic soil-structure interaction model with the Penzien Method to design the piles and the superstructure, taking due note of the deep design scour depths. The analyses demonstrate that six 3 m diameter steel raking piles driven down to about 120m are needed to support each bridge pier with the 150 m span truss girders placed on seismic isolation bearings.

INTRODUCTION

Padma River is one of the largest rivers in the world, with a catchment encompassing the southern foothills of the Himalayas, extending from the west to east across the Indian sub-continent. A very large body of water and a massive sediment

load is therefore, transported in the river, particularly during the monsoon seasons.

The Padma Multipurpose Bridge, carrying highway, rail and utilities, will be constructed across the 6km wide Padma River at Mawa, about 50 km to the southwest of Dhaka, Bangladesh. The project site, and hence the design was challenging due to deep riverbed scour, high seismicity and extremely deep deltaic sedimentary deposits comprising mainly of sand with bedrock expected at a depth of about 12km below ground, and heavy design loads due to freight trains, dead loads of the super and the substructure. Design Consultant, AECOM, with the assistance of Bangladesh University of Engineering and Technology (BUET) carried out a detailed site specific seismic hazard assessment and NHC in association with AECOM carried out river bed scour assessment. Based on these assessments design seismic events and scour depths were identified and analyses of the piles were carried out to design foundations that are both economic and robust.

This paper presents in brief the ground investigations that were carried out, the seismic design approach and parameters used, and pile design methodology adopted. In the dynamic model the springs were connected through dashpots to masses that represent the free field; the technique being based on the modified Penzien Method. The variations in the river bed with scour were hence represented by the depth of application of the springs, masses and dashpots along the piles. The design strong ground motions have then been imposed on the model at the stipulated depth to simulate the earthquake events for the dynamic analyses load cases. The design forces and stresses derived from the model have then been used in the structural design of the piles.



Fig. 1 A view of Padma Multipurpose Bridge from the riverbank

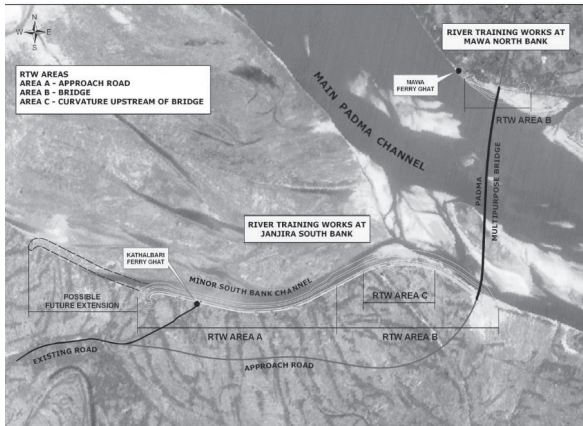


Fig. 2 Proposed Padma Multipurpose Bridge Alignment

SEISMIC HAZARD ANALYSIS

Site Seismicity

The site specific seismic hazard assessment was carried out using the earthquake database available at the Earthquake Engineering Department at the BUET University. From this study the maximum PGAs derived using the Abrahamson & Silva attenuation relationship were recommended as the design PGA values to be adopted at an depth (at an elevation of -120 m PWD considered to be stiff ground or the “pseudo bedrock”) in the Padma Bridge design. These recommended values are presented in Table 3.

Table 3: Seismic Design Parameters

| Earthquake Return Period (Years) | Recommended Horizontal PGA in cm/s^2 (Abraham and Silva 2008) at -120m PWD | Recommended Horizontal PGA in terms of “g” at -120m PWD | Recommended Horizontal PGA in terms of “g” at riverbed/ground level |
|----------------------------------|---|---|---|
| 2 | 4 | 0.004 | 0.008 |
| 10 | 11 | 0.011 | 0.022 |
| 50 | 32 | 0.032 | 0.064 |
| 100 | 51 | 0.051 | 0.102 |
| 200 | 80 | 0.080 | 0.160 |
| 475 | 141 | 0.141 | 0.282 |
| 1000 | 230 | 0.230 | 0.460 |

Ground Motions

The ground motions adopted in design contain both those from the seismic hazard analysis and strong ground motions from the Japanese Codes (see Fig. 3).

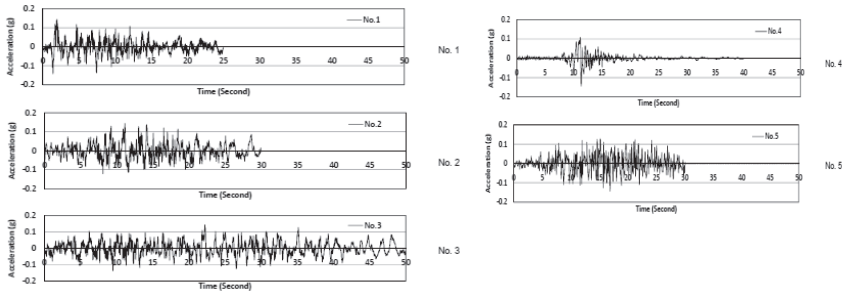


Fig. 3. Input ground motion at -120 mPD for ground response analyses

GEOTECHNICAL GROUND INVESTIGATION

The site investigation program for this project was undertaken in two phases. Phase 1 comprised 5 marine boreholes to 120m depth with Standard Penetration Tests (SPTs). The Phase 2 ground investigation program comprised 19 additional boreholes down to 130m depth, 6 boreholes down to 85 to 90m depth, and 6 cross-hole geophysics boreholes down to 150 m to 160m depth, and Piezocone Penetration Tests down to about 60m depth. In the 19 boreholes down to 130m depth, SPTs, conventional sampling, self boring pressuremeter tests, high pressure dilatometer tests and Flat Plate Dilatometer Tests were carried out. In the 6 boreholes down to 90m, state-of-the-art GEL PUSH sampling and Self Boring Internal Friction Tests (SBIFTs) were carried out along with SPTs. Cross-hole geophysical surveys were carried out down to 160m depth to determine the shear and compression wave velocities and hence the dynamic soil parameters such as the initial/maximum shear moduli, G_0 , of the soil strata.

The high quality undisturbed GEL PUSH samples recovered were sent to Japan for laboratory testing. In addition to the index tests and conventional tests such as particle size distribution tests, specific gravity, mica content tests, consolidated undrained triaxial compression and extension tests, K_0 -consolidated undrained triaxial tests, Cyclic Triaxial Tests, and Bender Element tests were undertaken for the determination of soil dynamic curves including shear modulus degradation curves and damping curves for various soil layers, and to obtain the initial/maximum shear moduli, G_0 , of the soil strata.

Geological Profile

The location of the proposed bridge alignment lies across the river between Mawa and Janjira (Fig. 2). From Phase 1 and 2 Ground investigation program, the geological profile of the site was established (Fig. 4). The design parameters of major soil units are shown in Table 1.

Table 1: Soil Parameters for Static Analyses

| Soil Type | Soil Type | SPT N-Values | Bulk Density (kN/m ³) | Friction Angle ϕ' |
|-------------|----------------|------------------|-----------------------------------|------------------------|
| Unit 1a | Clay | $0 < N \leq 10$ | 16 | - |
| Unit 1b | | $10 < N \leq 17$ | 17 | - |
| Unit 2a & b | Micaceous Sand | $0 < N \leq 10$ | 17.5 | 25 |
| Unit 2c | | $10 < N \leq 17$ | 17.5 | 25 |
| Unit 2d | | $17 < N \leq 32$ | 19 | 28 |
| Unit 2e | | $32 < N \leq 50$ | 19 | 30 |
| Unit 2f | | $N > 50$ | 19.5 | 32 |
| Unit 3e | Micaceous | $32 < N \leq 50$ | 19 | 30 |
| Unit 3f | Gravelly Sand | $N > 50$ | 19.5 | 32 |

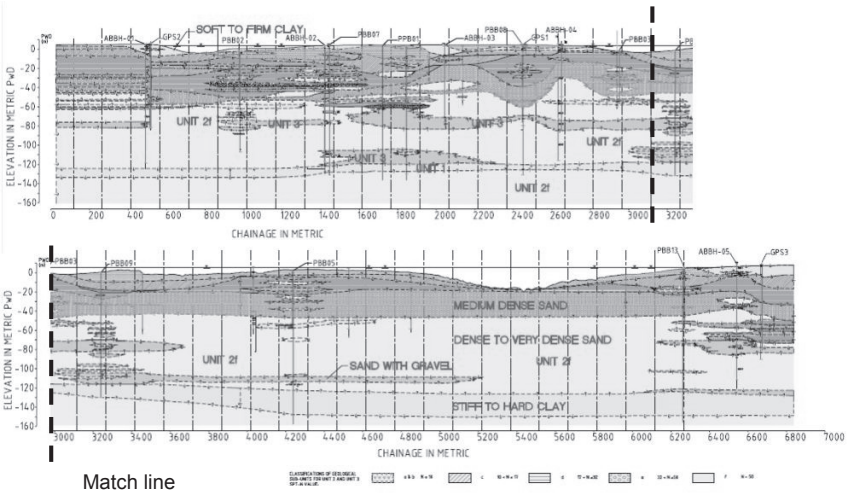


Fig. 4 Geological Section Along Bridge Alignment Across Padma River showing Geological Units

The soil within the main bridge area is predominantly micaceous sand with an average mica content of about 8 to 10 % interspersed with occasional thin layers of clay/silt. A layer of clay and silt is present at the banks, with Unit 2 (fine to medium grained medium to very dense sand with less than 20% fines) extending down to depths of 120 to 130 m, below which a stiff to hard mottled clay layer was encountered. Very dense sand is once again encountered below the stiff to hard clay layer. Approximate 20m thick layer of very dense sand with some gravel (Unit 3 soil with less than 20% fines with some gravel) stratum is identified generally between -60m PWD to -90m PWD. In general, SPT-N values increase with depth. Loose fine grained sand and silty sand was encountered down to a depth of about 10m to 15m. The stratigraphy of sub-units

change with depth but the south bank generally shows lower SPT-N values than the north bank at similar depths, down to about 20m. More fine cohesive materials are evident on the Mawa side.

DYNAMIC SOIL PARAMETERS

Initial/Maximum Shear Modulus, G_0

In this project, various techniques were used to determine initial/maximum shear moduli. These techniques included both in-situ methods and laboratory method. The in-situ methods can be further divided into methods through empirical correlation, and direct measurement from geophysical methods.

Empirical correlations between SPT and CPT tests and shear wave velocity, V_s , have been developed through historical data. In-situ direct measurement of shear wave velocity usually is by geophysical methods such as cross-hole, down-hole geophysical surveys, and the SAWS method. For this project, SPT Tests and cross-hole Geophysics Surveys were carried out as in-situ tests. Laboratory methods included Bender Element Tests and Cyclic Triaxial Tests.

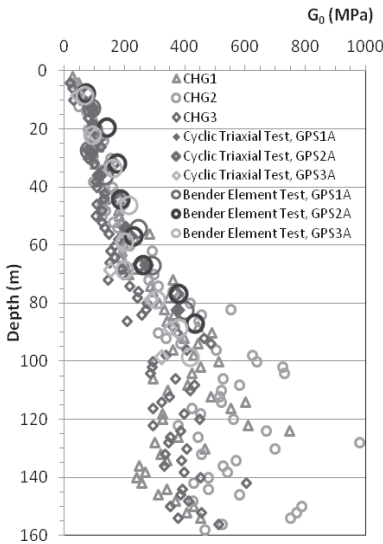


Fig. 5 Combined plot of G_0 from different tests

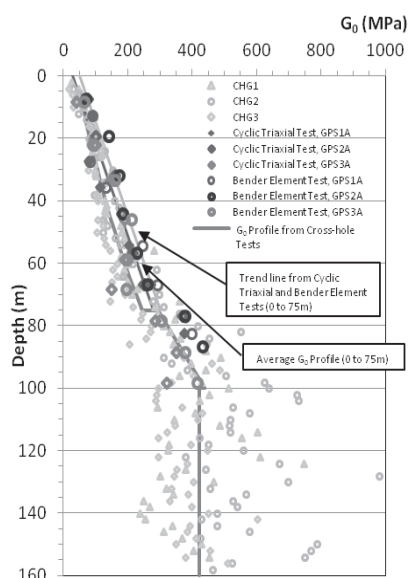


Fig. 6 Combined plot of G_0 from different tests

The results from all types of tests quite consistently showed a trend of increasing initial/maximum shear modulus with depth. The initial/maximum shear modulus at shallow depth (0m to 20m) ranges from 50 MPa to 150 MPa, and at greater depths (100m to 120m), the initial/maximum shear modulus increased to 300 MPa to 700

MPa. The G_0 obtained from different tests are plotted together in **Fig. 5**, in which the profile is divided into 3 depth ranges, i.e., 0~75m, 75~100m and 100~160m. For depth range of 0~75m, data from cyclic triaxial tests, bender element tests and cross-hole geophysical surveys are available. Due to the fact that cross-hole tests provide most data, results from cross-hole tests are considered as one data set, while results from bender element and cyclic triaxial tests are grouped together to form another data set. In **Fig. 6**, the green line is the trend line for cross-hole tests and the pink line is for data from bender element tests and cyclic triaxial tests. An average line (red line) between the two trend lines was recommended as the design G_0 profile for the Padma Bridge Project for the depth range 0~75m.

For the depth range 75~100m, the trend line from cross-hole tests is a good fit to the data points from other two tests as well and is thus used as the recommended design G_0 profile. For depth range 100~160m, the G_0 is taken as constant.

Determination of Shear Modulus Degradation($\frac{G}{G_0}$) and damping Ratios with

Shear Strain (γ) of Soil

Cyclic triaxial tests as per the Japanese Standard Test method Nos. JGS 0542 and JGS 0543 were carried out to determine the deformation properties; the Shear Moduli with shear strain and the Damping Ratio with shear strain, of the sandy soils. The samples were prepared as per JGS 0520. These tests were undertaken in Japan by Kiso-Jiban in their Tokyo laboratory. Upon isotropically consolidating the samples, axial stress controlled sinusoidal cyclic load was imposed at a frequency of 0.1 Hz for a particular axial deviator stress change ($\pm\Delta q$) for a duration of 10 load cycles under undrained conditions, while measuring the axial strain of the sample. After the 10 load cycles were imposed, the cyclic deviator stress magnitude, ($\pm\Delta q$), was increased and a further 10 load cycles was imposed. This cyclic loading process was continued for various deviator stress change values. The data acquisition system of the test was set to capture 120 data point per loading cycle in order to clearly define the cyclic stress strain curves, and hence to determine the G_{eq} , the hysteresis loops and the Damping Ratios. The results obtained from these tests are presented in **Figs. 6** and **7**. The data from cyclic triaxial test results on shear modulus degradation and the laboratory curves of the 4 depth ranges are plotted together in **Fig. 7**. The general trend of the larger G/G_0 ratio at the same shear strain for greater depth and higher confining stress can be seen in the plot. However, the lab-derived curve of 75 – 90m drops faster than the 36 – 75m curve at larger shear strain, which may due to the existence of gravel content. The damping ratios with shear strain determined from the energy loss in the hysteresis loops in the cyclic loadings for the various depth ranges is shown in **Fig. 8**.

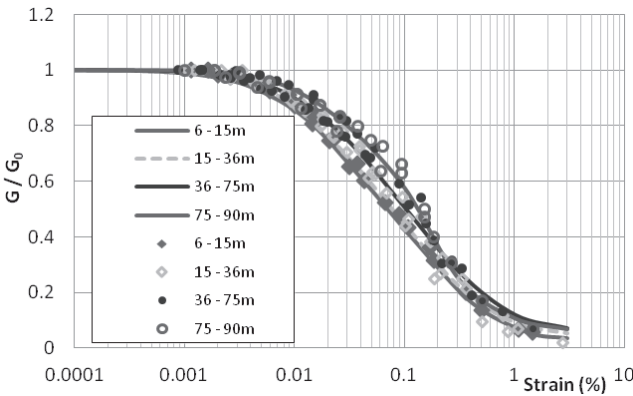


Fig. 7 Shear modulus degradation curves

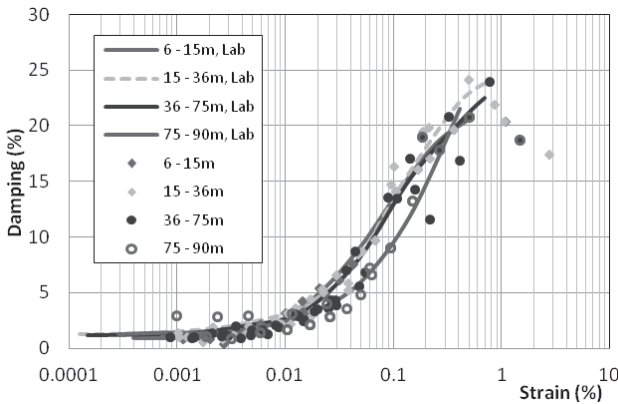


Fig. 8 Damping curves

SEISMIC DESIGN OF PILES

Pile Design Approach

The approach to pile design in this assignment can be summarised as follows; (1) A six span (900m long) structural module was developed using the structural analyses program MIDAS. The various load cases were imposed on this model, including the dynamic load cases (ship impact and seismic) to determine the loadings on the pile caps. (2) Another structural model using MIDAS was developed for a single pier with the soil/structure interaction modelled as springs and dashpots following the Penzien Method. (3) The forces and bending moments obtained from the 900 m long structural model is then imposed on the single pier structural model and the strong ground

motions are imposed at the base of the spring-dashpot column (representing the free field) at -120 m PWD to simulate strong ground motions. The results from these seismic load case analyses and the other load cases are compared to generate a force and bending moment envelopes for the piles; which was then used for the structural design of the piles. (4) PIGLET foundation pile models were also developed to better model the static soil structure interactions. The forces and the moments obtained from the 900 m long structural module was then imposed on the PIGLET model to obtain the settlement and lateral deflection of the pile group at the individual pier locations, and to obtain the loads and bending moments of the individual piles. These were compared with those from the structural model and larger values were used in the geotechnical design of the piles. The following factors of safety were adopted for the various load cases when determining the geotechnical capacity of the piles.

Table 6: Geotechnical Factors of Safety used for Various Load Cases when Designing Piles

| Load Case | Load Case | FOS on Skin Friction in Compression | FOS on Skin Friction in Tension | FOS on End Bearing |
|-----------|--|-------------------------------------|---------------------------------|--------------------|
| 1 | SW + SDL + LL | 1.5 | 3 | 3 |
| 2 | SW + SDL + Ship Impact | 1.25 | 2.5 | 2.4 |
| 3 | SW + SDL + LL + W | 1.25 | 2.5 | 2.4 |
| 4 | SW + SDL + LL + Ship Impact + 10 yr Scour | 1.25 | 2.5 | 2.25 |
| 5 | SW + SDL + 1/3 HA (1 lane) + RL + 100 yr Earthquake + 100 yr Scour | 1.25 | 2.5 | 2.4 |
| 6 | SW + SDL + 1/3 HA (1 lane) + RL + 475 yr Earthquake + 100 yr Scour | 1.1 | 2.2 | 1.1 |
| 7 | SW + SDL + Check Flood Scour (500 yr scour) down to -70 m PWD | 1.25 | 2.5 | 2.4 |

SW – Self Weight; SDL – Superimposed Dead Load; LL – Live Load; W – Wind Load; HA – Highway Loading; RL – Railway Loading

Geotechnical Design of Piles

This main bridge behaves in a complicated manner due to its height (120m) and the large mass of the superstructure, the pile cap and the piles. A three dimensional non-linear time history dynamic analysis, using a modified Penzien model (see **Fig. 11**), has been adopted for carrying out the detailed design. This model is divided into two parts, the structure and the free field soil. The interactions between the structure and the free field are simulated by lateral springs attached to masses. Related to the free field part, in order to determine the equivalent mobilised shear moduli, G , and effective damping ratio, D , at each layer of soil, free field analyses of the soil columns was carried out beforehand using the program SHAKE to determine the ground response. Subsequently, 3-dimensional dynamic analyses were carried out using the equivalent shear moduli and effective damping ratios obtained from the SHAKE analyses as input data in the structural MIDAS model. The dynamic soil parameters obtained from the ground investigation, the Initial Shear Moduli, G_0 , the variation of G with shear strain, and the variation of the Damping Ratio, D with shear strain, were used in the SHAKE Analyses as input parameters.

In the dynamic model the springs were connected through dashpots to masses that

represent the free field; the technique being based on the modified Penzien Method. The variations in the river bed with scour were hence represented by the depth of the springs, masses and dashpots along the piles. The design strong ground motions have then been imposed on the model at the stipulated depth to simulate the earthquake events for the dynamic analyses load cases (refer to **Figs. 9 to 11**).

The design forces and stresses derived from the model have then been used in the structural design of the piles. Each of the cases represents a different combination of scour for an individual bridge module. Through in this exercise bending moments were examined along the pile to make sure conformance and economy of design. It was observed that for piers with deep scour, large bending moments extend a long way down the pile, making it necessary to maintain the structural steel thickness of pile piles with depth.

The forces from the structural model have also been imposed on a model of the foundations using the soil-pile interaction program PIGLET, to determine the overall group behaviour of the piles, the settlement of the pile cap, the individual pile settlements, lateral deflections and the bending moments. The axial forces on the piles determined from PIGLET were then used to carry out the geotechnical design of the piles - to determine the pile lengths and the required geotechnical capacities of the piles. The soil parameters, particularly the elastic and shear moduli, were obtained from the pressuremeter tests, CPTs, Flat Plate Dilatometer tests. Table 7 summarises the pile design for the piers. All river based piles are 3m diameter driven steel tubular piles installed at a 1H:6V rake; and requiring 6 piles for each pier. Bored piles, 3m in diameter are required at the land based transition piers (transition from steel truss bridge to viaducts). The bridge trusses were placed on seismic isolation bearings to reduce the number of piles. The API guidelines and design approach was used when designing the driven steel piles. When designing the bored piles an ultimate end bearing pressure of 10,000 kPa and the skin friction was determined by the following equation with a limiting value of 96 kPa, with these values to be confirmed by trial preliminary pile load tests at the construction stage.

$$f_s = K\sigma'_v \tan \delta \quad \text{where } f_s \leq 96 \text{ kPa} \quad \dots\dots\dots(5)$$

- And where f_s - Pile-soil interface frictional resistance (ultimate)
- K - Coefficient of lateral earth pressure,
- $K = 0.4$ for bored piles in dense to very dense sand
- δ - Soil-pile interface friction angle
- $\delta = \phi' - 3$ (Limited to 29 degrees in Units 2f and 3f)

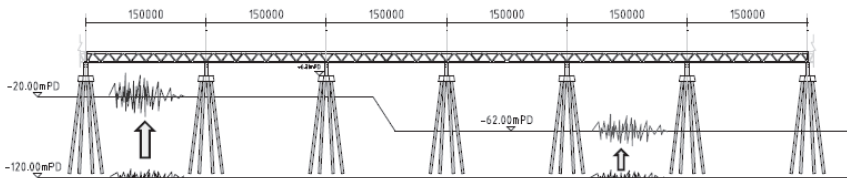


Fig. 9. Application of seismic motions to global model

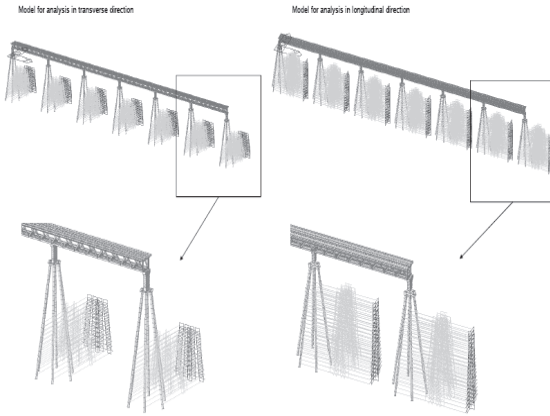


Fig. 10 Global modelling of the piers including the deck structure

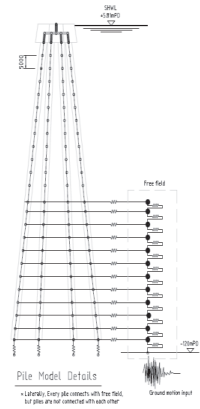


Fig. 11 Modelling of Individual Piers using the Penzien Method

Table 7: Summary of the Geotechnical Pile Design

| | Near Banks - 6 Piles with seismic Isolation bearings | Mid river - 6 Piles with seismic Isolation bearings | Transition Piers at Banks (3m vertical bored piles without seismic Isolation) |
|---|--|---|---|
| Type of Piles | Steel Raking | Steel Raking | Vertical Concrete |
| No. of Piles | 6 | 6 | 12 |
| Diameter (m) | 3 | 3 | 3 |
| Scour Level(100-year return period scour) | -62mPWD | -50mPWD | No scour |
| Scour Level(500-year Flood) | -70mPWD | -55mPWD | No scour |
| Pile Founding Level (m PWD) | -114mPWD | -98mPWD | -80mPWD |
| Critical Axial Load (MN) | 87.6 | 84.5 | 81.0 |

CONCLUSIONS

The difficult ground conditions and severe environmental conditions have made the foundations for the Padma Multipurpose Bridge one of the most challenging aspects of the design. Deep scour combined with earthquake loading, requires piles to be designed for large lateral loads with the piles unsupported for a length of 65m. In developing suitable design solutions, AECOM has utilised the state-of-the-art geotechnical and structural technology, to provide the bridge with a robust foundation system that should require minimal maintenance in future.

ACKNOWLEDGMENTS

This paper is submitted with the permission of the Bangladesh Bridge Authority, the Government of Bangladesh.

REFERENCES

- Sham, S.H.R. & Tapley, M.J. 2010. The design of Padma Multipurpose Bridge – challenges and solutions in design of the river spans. *Proc. IABSE-JSCE Conference, Dhaka, 10-12 August 2010*
- De Silva, S., Wightman, N.R. & Kamruzzaman, Md. 2010. Geotechnical ground investigation for Padma Main Bridge. *Proc. IABSE – JSCE Conference, Dhaka, 10-12 August 2010.*

Aseismic Analysis of Circular Deep Grouting for Tunnel Surrounding Rock in Strong Earthquake Zone

Shen Yusheng¹, Gao Bo², Joshua Li³, Wen Yumin⁴ and Kelvin C.P. Wang⁵

¹ Associate professor, Key Laboratory of Transportation Tunnel Engineering, Ministry of Education, Southwest Jiaotong University, Chengdu, 610031, China; sys1997@163.com

² Dean and Professor, Key Laboratory of Transportation Tunnel Engineering, Ministry of Education, Southwest Jiaotong University, Chengdu, 610031, China; prgaobo@vip.sina.com

³ Research Assistant Professor, School of Civil and Environmental Engineering, Oklahoma State University, Stillwater, OK 74078 United States; qiang.li@okstate.edu

⁴ Lecturer, Key Laboratory of Transportation Tunnel Engineering, Ministry of Education, Southwest Jiaotong University, Chengdu, 610031, China; wym@home.swjtu.edu.cn

⁵ Chair Professor, School of Civil and Environmental Engineering, Oklahoma State University, Stillwater, OK 74078 United States; kelvin.wang@okstate.edu

ABSTRACT: Many tunnels were severely damaged during high intensity earthquakes in recent years, especially for those in mountainous areas. This paper analyzes the seismic responses of the circular deep grouting technique for mountain tunnels with surrounding rocks. Eight circular deep grouting pre-reinforcement schemes are simulated using 3D Finite Element Method and the deformation and stress characteristic and dynamic responses of the tunnel structure analyzed. Results demonstrate that different grouting schemes should be applied for tunnel structure in the high intensity areas. A new seismic performance evaluation approach is proposed in the paper based on the maximum relative displacements of adjacent locations on the tunnel lining. This evaluation method provides a better interpretation of the tensile and compressive states of tunnel structures that are subject to strong ground motion during an earthquake. The approach described in the paper provides guidance to seismic design and construction of tunnels in seismic active mountainous area.

Keywords: Seismic analysis; circular deep grouting technique; performance evaluation; mountain tunnel; strong earthquake zone

1. INTRODUCTION

As man-made tunnels are structurally integrated into existing natural environment, they generally have good seismic performance. Therefore, it is agreed that the seismic design of tunnel is not necessary for tunnels built within stable ground conditions (Asakura 2000 and Tateishi 2005). However, in recent years the seismic damages of tunnel engineering are disastrous during strong earthquakes (Lanzano 2008 and Qian 2009). Examples include the 1995 Kobe, Japan earthquake, the 1999 Chi-Chi, Taiwan earthquake and the 1999 Kocaeli, Turkey earthquake

(Lanzano 2008 and Kontogianni and Stathis 2003 and Li 2008). Particularly, it is reported that (Wang et al., Shen et al., and Gao et al. 2009), 52 tunnels were damaged in the Wenchuan earthquake in 2008, among which 11.5% tunnel extremely severe damaged, 5.8% tunnels severe damaged, 19.2% tunnels moderate damaged, 44.2% tunnels slight damaged, and only 19.3% tunnels no damage. In China, a large number of the existing tunnels are located in seismic-active zones. Since we are currently in the fifth seismic active period (Qian et al. 2009), there is an urgently need to address on how to improve the seismic performance of tunnels within seismic-active zones.

Traditionally, three types of seismic adaptation strategies are used for mountain tunnels in strong earthquake zone: (1) to improve aseismic performance of tunnel structures by improving the stiffness, quality, strength, damping of tunnel lining structure; (2) to design shock absorption layer(s) between tunnel structure and strata; and (3) to pre-reinforce surrounding rock using grouting techniques, due to the understanding that the dynamic response of tunnel structure depends heavily on the seismic response of the surrounding rock mass (Qian et al. 2009).

Mechanistic analysis of using grouting techniques in tunnels for aseismic purpose is rarely done. This paper attempts to analyze the dynamic responses of the grouting pre-reinforcement technique for tunnel surrounding rock. Following is an outline of the paper. First, three grouting methodologies are reviewed and the circular deep grouting is further explored in the paper due to its superior seismic performance. Second, the computation modeling of a mountain tunnel in the strong earthquake zone is established using 3D finite element analysis (FEA) method. Consequently, seven grouting approaches are established and simulated. The dynamic response of the tunnel structure in the longitudinal direction is analyzed and compared. A new seismic performance evaluation method is then proposed. Finally, different grouting pre-reinforcement schemes are recommended for different tunnel positions based on the simulation results so as to improve the seismic performance of tunnel structures.

2. GROUTING PRE-REINFORCEMENT TECHNIQUES

Traditional seismic design of tunnel structure grouts is only at the local weak locations in surrounding rock, as shown in Figure 1a. This method generates an abrupt transition from the grouting zone to non-grouting area in weak areas of surrounding rock, and may not improve the seismic performance of tunnel.

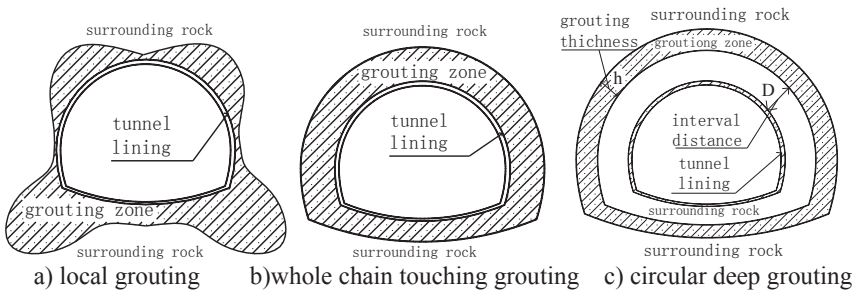


FIG. 1. Pre-reinforcement distribution sketch map of surrounding rock.

Inertial interaction and movement interaction are observed between tunnel and surrounding rock during the earthquake (Wang et al. 2012), the former depends on their density, while the latter relies on the stiffness between them. Based on the stiffness match principle in tunnel seismic design, two types of pre-reinforcement grouting techniques are introduced to change the tunnel structure--surrounding rock system for better seismic performance of tunnel, as shown in Figure 1b or c. The whole chain touching grouting scheme is a structure--grouting ring-- surrounding rock system, while the circular deep grouting scheme (CDGS) is a structure--surrounding rock--grouting ring--surrounding rock system.

Dynamic responses of these three structures have been studied by the author (Xia, et al. 2008) and comparisons were made to investigate the seismic performance of the three methods. It was found that the CDGS approach had better seismic performance over the other two approaches. However, this previous study is limited on very few parameters. In this paper the radial grouting range of the CDGS will be analyzed further aiming to provide guidance for tunnel design and construction in the strong earthquake zone.

3. CIRCULAR DEEP GROUTING SIMULATION

3.1 Methodology

Based on wave propagation theory, the implicit direct integration method for solving the equations of motion is adopted in terms of the Hilber-Hughes-Taylor method (Wang et al. 2011). The motion balance equation of the system is defined as follows at time $t = t + \Delta t$:

$$M\ddot{u}_{t+\Delta t} + I_{t+\Delta t} = P_{t+\Delta t} \quad (1)$$

Where M denotes the general mass matrix of the system; \ddot{u} denotes the node acceleration vector of system; I denotes the internal force vector acting on node; P denotes the external force vector of the equivalent node load transformed.

Using Newmark approach to solve the Hilber-Hughes-Taylor problem, the increment formula is established:

$$u_{t+\Delta t} = u_t + \dot{u}_t \Delta t + \left[\left(\frac{1}{2} - \gamma \right) \ddot{u}_t + \gamma \ddot{u}_{t+\Delta t} \right] (\Delta t)^2 \quad (2)$$

$$\dot{u}_{t+\Delta t} = \dot{u}_t + [(1 - \delta) \ddot{u}_t + \delta \ddot{u}_{t+\Delta t}] \Delta t \quad (3)$$

Where u, \dot{u} denotes the node displacement and velocity vector of system, δ, γ denotes the integration constant, general value is 0.5 and 0.25 respectively.

This calculation method requires iterative computation for every time step, until the displacement increment vector Δu^i converges.

3.2 Computation Model

The infinite regional simulation is conducted by designing artificial boundary near the model boundary. Visco-elastic boundary conditions are applied to the model boundaries. The model is based on a real mountain highway tunnel in the strong earthquake zone in Wenchuan (Shen et al. 2009). The dimension of the model is 120m in width at the horizontal direction, 118m in length along the tunnel axis and

100m in height, with the maximum and minimum buried depths of the tunnel 42m and 12m, respectively. Totally 110,046 solid elements are included in the FEA model (Figure 2a). Detail tunnel structure model are obtained from the field as shown in Figure 2b.

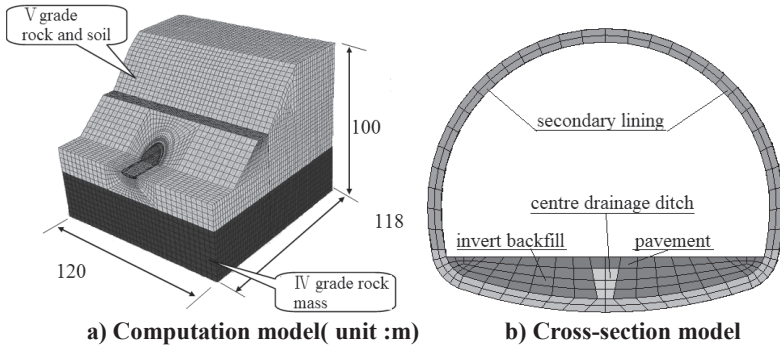


FIG. 2. Tunnel computation model.

Physical mechanics parameters for the tunnel after the improved grouting scheme are shown in Table1 (Shen et al. 2011).

Table1. Physical mechanics parameters of tunnel lining and surrounding rock

| parameter items | Density (Kg/m^3) | Elastic modulus (GPa) | Poisson's ratio | Cohesion (kPa) | Internal friction angle ($^\circ$) |
|----------------------|-----------------------------|-----------------------|-----------------|----------------|--------------------------------------|
| Vgrade rock and soil | 1850 | 1.2 | 0.4 | 200 | 30 |
| IVgrade rock mass | 2200 | 3.1 | 0.3 | 400 | 40 |
| Secondary lining | 2500 | 30 | 0.2 | — | — |
| Invert backfill | 2300 | 24 | 0.25 | — | — |
| Pavement | 2300 | 30 | 0.3 | — | — |
| Grouting zone | 2400 | 30 | 0.25 | 270 | 31 |

3.3 Cases

The computation model is designed based on two parameters: interval distance D and grouting thickness h , for the grouting of surrounding rock, as shown in Figure 1c. Eight simulation cases, as shown in Table 2, are established: two interval distance (2.0m and 3.0m), and four grouting thickness from 1m to 4m with 1.0m increment.

Table 2. Schedule of circular deep grouting cases

| Case | Radial Grouting range parameter | Case | Radial Grouting range parameter |
|------|---|------|---|
| 0 | No grouting | 4 | Interval $D=2\text{m}$, grouting $h=4\text{m}$ |
| 1 | Interval $D=2\text{m}$, grouting $h=1\text{m}$ | 5 | Interval $D=3\text{m}$, grouting $h=1\text{m}$ |
| 2 | Interval $D=2\text{m}$, grouting $h=2\text{m}$ | 6 | Interval $D=3\text{m}$, grouting $h=2\text{m}$ |

| | | | |
|---|-------------------------------|---|-------------------------------|
| 3 | Interval D =2m, grouting h=3m | 7 | Interval D =3m, grouting h=3m |
|---|-------------------------------|---|-------------------------------|

3.4 Seismic Wave Input

The seismic wave adopted in this paper is a synthesis artificial wave based on the response spectrum of the tunnel site conditions, whose maximum amplitude of seismic acceleration is 0.42g. The Time-frequency decomposition map is reconstructed using the Hilbert–Huang transformation method (Shen et al. 2011), as shown in Figure 3a. It is found that most seismic energy appears in 15 seconds. Therefore, the acceleration time-history curve of seismic wave in 15 seconds is adopted for the computation modeling, as shown in Figure 3b.

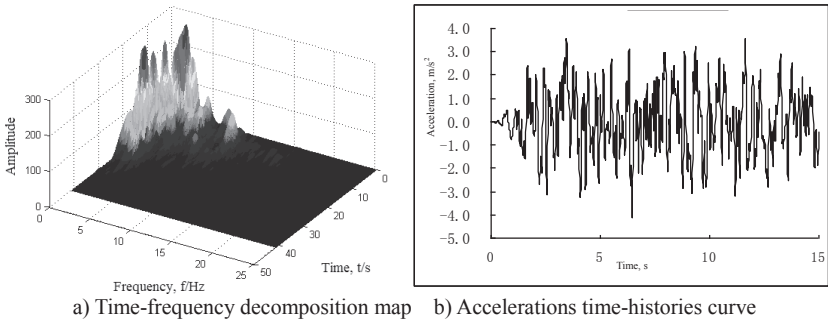


FIG. 3. Accelerations curve of seismic wave.

4. DEFORMATION EVALUATION METHOD

In the earthquake, tunnel structure will undergo repeatedly the tensile and compressive deformation as seismic wave propagates. The particles of structure are not always move in the same direction under the seismic motion, but behaves in the successive reciprocate manner surrounding a certain balance point. In addition, the deformation of structure is depending on and following against the surrounding rock. Therefore, it is important to obtain the maximum stress or relative displacement variation between the adjacent points in tunnel structure.

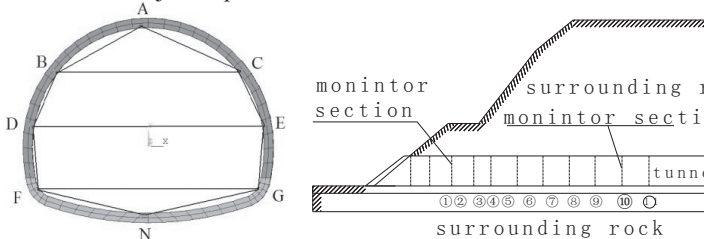


FIG. 4. Distribution of research objective.

This paper proposes a maximum allowable relative displacement method to evaluate the dynamic deformation capacity of the tunnel structure, namely, the

relative displacement peak value (RDPV) of the adjacent monitoring points on the tunnel lining. Eight monitoring points are designed along the lining in the model to evaluate the deformation characteristic of structure under the seismic load, and each point can be connected to two or three measuring lines, as shown in Figure 4a. If the RDPV is a positive value, the deformation between two monitoring points is in a "tensile" state (deformation increase); otherwise, the two adjacent points are in a "compressive" state (deformation decrease). As a result, the deformation characteristic of the structure is obtained based on the RDPV between points.

In addition, eleven sub-sections are monitored in the paper, to study the dynamic response of tunnel structure along the axis direction, as shown in Figure 4b.

5. DYNAMIC RESPONSE ANALYSIS

5.1 Relative Displacement Analysis

Based on the Wenchuan earthquake tunnel damage investigation results and previous research (Li 2008; Qian et al. 2009 and Shen et al. 2009), the upper part of tunnel structure is most liable to be damaged and subjected to repeated compressive and tensile stress cycles. Due to length limitations, this paper only focuses on the investigation of the most critical three measuring lines AB、BC and CE, as shown in Figure 4a.

As shown in Figure 5a, the RDPV of line AB always has negative values, which indicates the structure deformation between two points is under compressive state for all simulation cases under the seismic load. Case 3 and case 4 produce less deformation than those of case 0 (without grouting). The RDPV of line AB in case 4 has minimum (5.7mm) values. For monitoring section 1, the RDPV of case 4 is reduced by 53.3% in comparison with that of case 0, and that of case 3 is reduced by 27.9%. By contrast, the RDPV of the rest cases are larger than that of case 0. In other words, case 3 and case 4 will enhance the seismic performance of the tunnel; while other cases will not strengthen the aseismic performance of tunnel structure, but increase the deformation levels and result in more damage potential. Combined with the tunnel portal surface landform, it is suggested that the case 4 (h=2m, D=4m) grouting pre-reinforcement measure should be adopted from tunnel portal to up to 30m (near the ninth monitoring section).

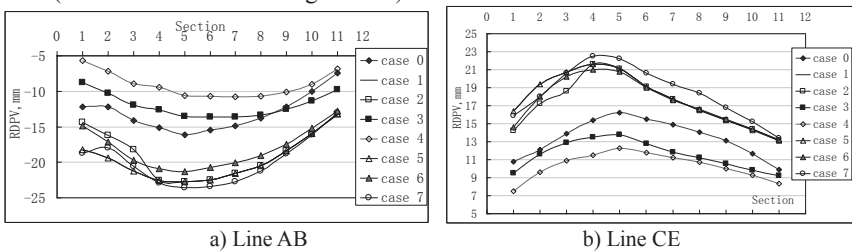
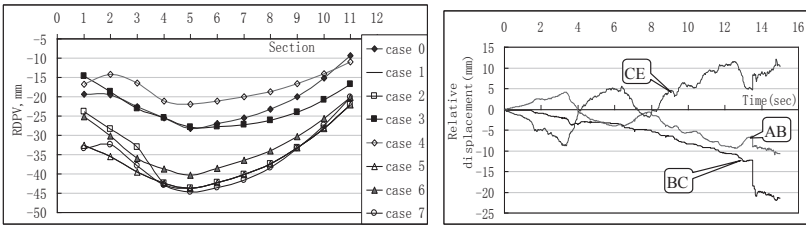


FIG. 5. RDPV curves in various cases along tunnel axis.

From Figure 5b, the RDPV of line CE always has positive value which indicates the structure deformation is in tensile state for all cases. Similarly, the RDPV of case

3 and case 4 are less than other cases, and the RDPV of line CE for case 4 is the minimum (7.5mm) of all cases. For monitoring section 1, the RDPV of case 4 is reduced by 30.6% in comparison with that of case 0, and that of case 3 is reduced by 11.9%. The relative displacement variation of line CE is basically in good agreement with that of the line AB. The RDPV of case 4 at section 6 and section 11 only decreases by 10.6% and 9.1% in comparison with case 0, respectively. Therefore, the case 3 grouting scheme is recommended to be adopted for deep-buried tunnels.

From Figure 6a, the RDPV of measuring line BC are always negative values which indicate the structure deformation is in compressive state for all cases. The RDPV in case 4 has minimum value (21.9mm). For the monitoring section 2, the RDPV of case 4 is reduced by 27% than that of case 0, while the case 3 scheme has minor effect on the structure. The RDPV of other cases exceed that of the case 0.



a) RDPV curve of line BC along tunnel axis b) Time-history curve of relative displacement at section 5

FIG. 6. Relative displacement curves of measuring line.

The RDPV of all the three lines reach the maximum values at the shallow and deep-buried tunnel (section 5). The RDPV time-history of line AB and CE at section 5 indicate that RDPV repeatedly experience positive or negative values under the seismic load. In addition, the final RDPV don't return back zero (Figure 6b). In other words, the tunnel structure remains additional strain residuals due to either tensile or compressive deformation of structure during the earthquake, which could result in tunnel crown collapse and sidewall damage.

Through a comprehensive comparison of relative displacement analysis of various measuring lines, it is recommended that the case 4 grouting scheme should be recommended from tunnel portal to monitoring section 7 and the case 3 scheme should be used from monitoring section 7 to 9.

5.2 Principal stress analysis

This paper only includes point A (crown) and G (sidewall bottom) in this analysis to study the dynamic response of the tunnel structure, as shown in Figure 4a.

As shown in Figure 7 and Figure 8, the peak stress value (PSV) of the tunnel structure in case 4 is less than that of all other cases at the tunnel portal. This indicates that case 4 scheme could improve the seismic performance of structure at the tunnel crown (point A) with regards to the σ_1 and σ_3 stress variety. However, it doesn't significantly strengthen the seismic effect of tunnel structure at the sidewall bottom (point G).

The σ_1 PSV of point A in case 4 is reduced by 45% at tunnel crown in comparison

with the case 0, and the σ_3 PSV is reduced by 18.5%, as shown in Table 3. The case 3 scheme also has a significant effect on the tunnel crown in terms of principal stress, and the PSV of σ_1 and σ_3 is reduced by 34.1% and 14.7% respectively.

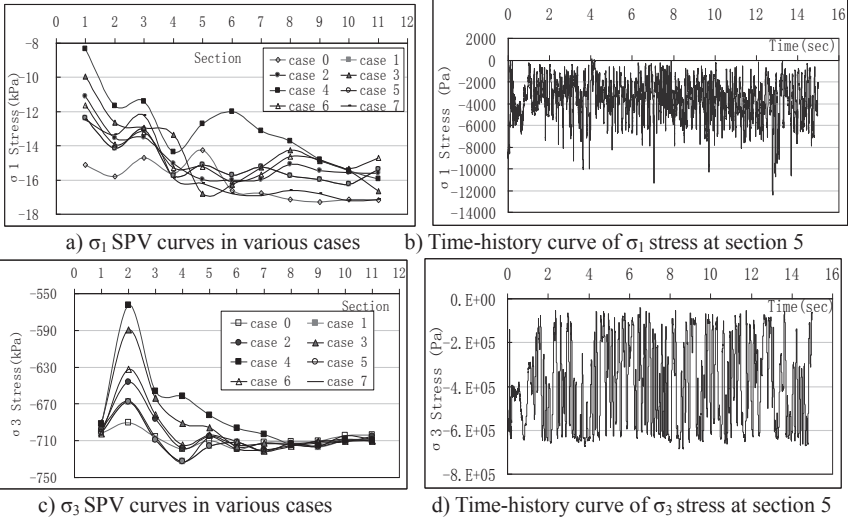


FIG. 7. Stress peak curve of point A in different sections.

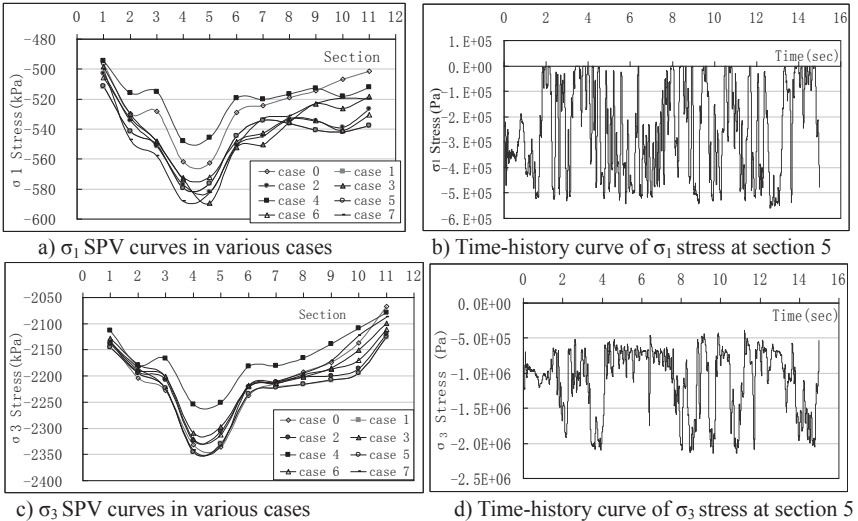


FIG. 8. Stress peak curve of point G in different sections.

Table 3. Percentage of SPV on various points compared with the case 0

| Points | Case 1 | Case 2 | Case 3 | Case 4 | Case 5 | Case 6 | Case 7 | |
|--------|------------|--------|--------|--------|--------|--------|--------|-------|
| A | σ_1 | 18.2% | 26.5% | 34.1% | 45% | 18.1% | 23.1% | 17.5% |
| | σ_3 | 3.4% | 6.4% | 14.7% | 18.5% | 3.4% | 8.5% | 3.6% |
| G | σ_1 | -7.2% | -6.3% | -5.0% | 3.0% | -7.2% | -6.7% | -4.8% |
| | σ_3 | -2.9% | -2.6% | -1.5% | 3.6% | -2.8% | -2.1% | -1.0% |

Note: The positive value indicates that principal stress decrease percentage of this case in comparison with the case 0, whereas it is principal stress increase percentage.

The structural stress concentration appears at both sidewall bottoms (point G) during the strong earthquake, which is the main cause of both tunnel sidewall bottoms damage. As shown in Table 3, only case 4 could attenuate the dynamic responses of the sidewall bottom, and the maximum value of σ_1 and σ_3 is reduced by the 3% (548kPa) and 3.6% (2254kPa) respectively. It is therefore recommended that case 4 grouting scheme should be adopted from tunnel sidewall bottom to crown.

CONCLUSIONS

In this paper, the dynamic responses of a real-world tunnel structure are simulated for eight different circular deep grouting schemes. The following conclusions can be drawn:

(1) According to the seismic wave propagation along the tunnel axis and the vibration characteristics of the particles at the tunnel lining, a new seismic performance evaluation method is proposed based on the RDPV of the adjacent monitoring points. The relative displacements of three measuring lines are analyzed. It is found that various measuring lines are always in tensile or compressive state during the earthquake. This method better explains the deformation characteristic of tunnel structure under the strong ground motion.

(2) The maximum principal stress of the example tunnel structure generally appears at both tunnel sidewall bottoms. This stress concentration is the main cause of the sidewall damage during earthquake. Not all the schemes have positive impacts on seismic performance of the tunnel structure, thus it is important to select favorable grouting scheme in a strong earthquake zone.

(3) Based on the deformation and stress analysis results for eight grouting pre-reinforcement schemes, it is recommended that different schemes should be used at different locations of a tunnel. For tunnel portal, it is recommended that case 4 scheme should be adopted from sidewall bottom to crown at the cross-section of tunnel. In the longitudinal direction, it is suggested that case 4 scheme should be implemented from tunnel portal to monitoring section 7 and case 3 scheme from monitoring section 7 to 9.

ACKNOWLEDGEMENTS

The authors appreciate the support of the National Natural Science Foundation of China (No. 41102220 and No. 51178398) and the Fundamental Research Funds for

the Central Universities (No. SWJTUCX014 and No. SWJTU11ZT33) and Development plan for Ministry of Education Innovation team (No. IRT0955) .

REFERENCES:

- Akira Tateishi, Akire (2005). "A study on seismic analysis methods in the cross section of underground structures using static finite element method." *Structural Eng./Earthquake Eng.*, JSCE, Vol. 22, No.1, 41s. 53s.
- Asakura, T., Tsukanda, K. et al. (2000). "Damage to mountain tunnels by earthquake and its mechanism." *Proceedings-Japan Society of Civil Engineers*, pp. 27-38.
- Lanzano, G., Bilotta, E. and Russo G. (2008). "Tunnels under seismic loading: a review of damage case histories and protection method." *In Workshop of Mitigation of the Earthquake Effects in Towns and in Industrial Regional Districts*.
- Qian Qihu, He Chuan, and Yan Qixiang (2009). "Analysis and investigation on seismic damages of projects subjected to Wenchuan earthquake." *Study on Engineering Damage in Wenchuan Earthquake*, pp: 608-618
- Li Tianbin (2008). "Failure characteristics and influence factor analysis of mountain tunnels at epicenter zones of great Wenchuan earthquake." *Journal of Engineering Geology*, Vol.16 (6): 742-750;
- Kontogianni, Villy A., and Stiros, Stathis C. (2003). "Earthquakes and Seismic Faulting Effects on Tunnels." *Turkish Journal of Earth Sciences* (Turkish J. Earth Sci.), Vol. 12: 153-156.
- Shen Yusheng, Gao Bo et al. (2011). "Study on the interval grouting pre-reinforcement scheme of mountain tunnel surrounding rock in high-intensity earthquake zone." *Journal of Chinese Civil Engineering*, Vol. 44 (s1): 186-192.
- Shen Yusheng, Gao Bo, and Wang Yingxue. (2009). "Analyses on Tunnel Failure Mode and Mechanism During Wenchuan Earthquake." *International Conference on Earthquake Engineering*, 5: 568-573.
- Shen Yusheng, Gao Bo (2009). "Dynamic behavior of portal part of traffic tunnel in high-intensity earthquake area." *The Second International Conference of Transportation Engineering*, 07: 3417-3422.
- Xia Zanou (2008). Optimized research on the grouting measure of the portal sect of cheyang tunnel in Ya'lu speedway, Chengdu: Southwest Jiaotong University.
- Wang Zhengzheng, Wang Zhengsong, and Gao Bo (2011). "Research on seismic measures of double-arch tunnel portals in high-intensity earthquake zone." *Chinese Journal of Highway and Transport*, Vol. 24 (6): 80-85.
- Wang Zhengzheng, Zhu Weizhi and Zhang Zhe (2012). "Seismic isolation effect of a tunnel covered with a buffer layer." *Disaster Advances*, Vol. 5 (4): 1372-1376.

Investigation of Liquefaction Potential of Alluvium underneath an Earth Embankment Dam

Jiaer Wu¹, PhD, PE, GE, M. ASCE, Lelio Mejia², PhD, PE, GE, M. ASCE, Erik Newman³, PhD, M. ASCE, Michael Mooers⁴, PE.

¹Senior Geotechnical Engineer, URS Corporation, Oakland, CA 94612; jerry.wu@urs.com

²Principal Engineer, URS Corporation, Oakland, CA 94612; lelio.mejia@urs.com

³Geotechnical Engineer, URS Corporation, Oakland, CA 94612; erik.newman@urs.com

⁴Project Manager, Santa Clara Valley Water District, San Jose, CA 95118; MMooers@valleywater.org

ABSTRACT: The Santa Clara Valley Water District (SCVWD) owns and operates the Calero Dam facilities, which include the Main and Auxiliary Dams. The Main Dam is about 98 feet high and straddles a former wide stream valley. A large part of the downstream embankment is underlain by coarse grained alluvium (CGA) that is potentially liquefiable during strong earthquake shaking. The liquefaction potential of the CGA was evaluated using SPT- based methods. Validating analyses with the Loma Prieta event suggest the SPT-based liquefaction evaluation methods satisfactorily explain the lack of liquefaction observation during the event. The influence of embankment overburden on the liquefaction potential of foundation alluvium was investigated as part of the study. The findings indicate that the presence of the embankment likely had only minor effects on the liquefaction resistance of the CGA.

INTRODUCTION

Calero Reservoir is located about 13 miles southeast of the City of San Jose, in the seismically active San Francisco Bay Area. At the spillway crest level, the reservoir has a capacity of approximately 10,000 acre-feet. The SCVWD uses the reservoir to store storm runoff and imported water, conserve groundwater and replenish wells, and supply water treatment plants. Calero Reservoir is also used for recreational purposes.

The dam is located across Calero Creek and is about 98 feet high. The spillway crest is about 5.8 feet below the crest elevation of the dam. The dam was built in 1935 and was designed as a compacted earthfill embankment with “impervious” upstream and “pervious” downstream embankment zones. However, the majority of the fill came from a single borrow source and therefore the embankment is nearly homogeneous.

Calero Dam is under the jurisdiction of the California Division of Safety of Dams (DSOD), which requires regular monitoring and inspection of the dam and periodic evaluation of its safety. Previous studies in the 1970s and 1980s found that the dam met then-current dam safety criteria. The ground motion criteria and safety evaluation

procedures have since advanced significantly. Recently the DSOD requested new seismic safety evaluation of the dam be performed. This paper describes the findings from the investigation of the liquefaction potential of the foundation CGA underneath the dam embankment.

GEOLOGIC SETTING AND SITE CONDITIONS

The San Francisco Bay Area lies within a geologically complex, tectonically and seismically active region between the Pacific plate on the west and the Sierran micro-plate on the east. The dam is situated on the southwest side of the Santa Clara Valley, between the San Andreas fault on the west and the Calaveras fault on the east (Figure 1). Both faults are part of the San Andreas system of strike-slip faults. Numerous active or conditionally active faults have been mapped in the dam site vicinity. These faults have slip rates that range from low-to-moderate to very high. Based on the site-to-source distances and earthquake magnitudes, the faults are considered likely to induce the largest ground motions at the site and thus they were all considered in the ground motion analysis performed for the dam.

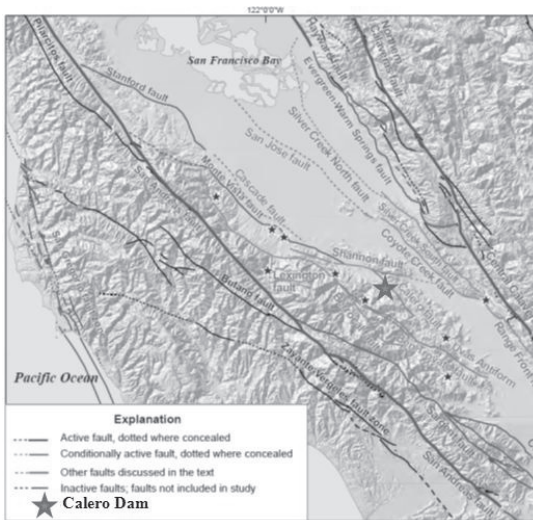


FIG. 1. Location of Calero Dam and seismic sources

The dam straddles a former wide stream valley. Professor Tolman (1934) performed a detail geologic study for the site prior to the dam construction. The Tolman study and subsequent studies by others showed that the valley alluvium consists of an upper stratum of fine-grained clayey soils (Upper Alluvium) that transition into coarse-grained soils with a lower stratum of relatively pervious, gravelly material (CGA) overlying bedrock. Before placement of fill, a cutoff trench was excavated upstream of the crest and the alluvium was stripped from under the embankment upstream of the cutoff trench to reduce seepage. However, alluvium downstream of the cutoff trench

was largely left in place to function as a blanket drain beneath the embankment. Figure 2 presents the plan of the dam showing the geologic unit Qal (alluvium) and Qc (colluvium) in the foundation. The CGA materials are shown as the shaded zones on the maximum cross section on Figure 2.

The bedrock at the site consists predominantly of Franciscan Complex sedimentary rock: greywacke, interbedded sandstone, siltstone, and shale, with shearing of shale beds forming a local mélangé matrix. Franciscan volcanics are present within the upper portion of the right abutment. The Calero fault, striking north-northwest, passes directly under the embankment near the right abutment. Although cultural modification around the dam site made observations of the location of the fault difficult, several lines of evidence support the interpretation that the Calero fault is inactive. A limited investigation was performed in this study in the rugged topography southeast of the reservoir, which demonstrated evidence of no active deformation along the mapped fault trace within the past few to several tens of thousands of years. It was thus concluded that the Calero fault is inactive and poses no threat of surface rupture to the dam.

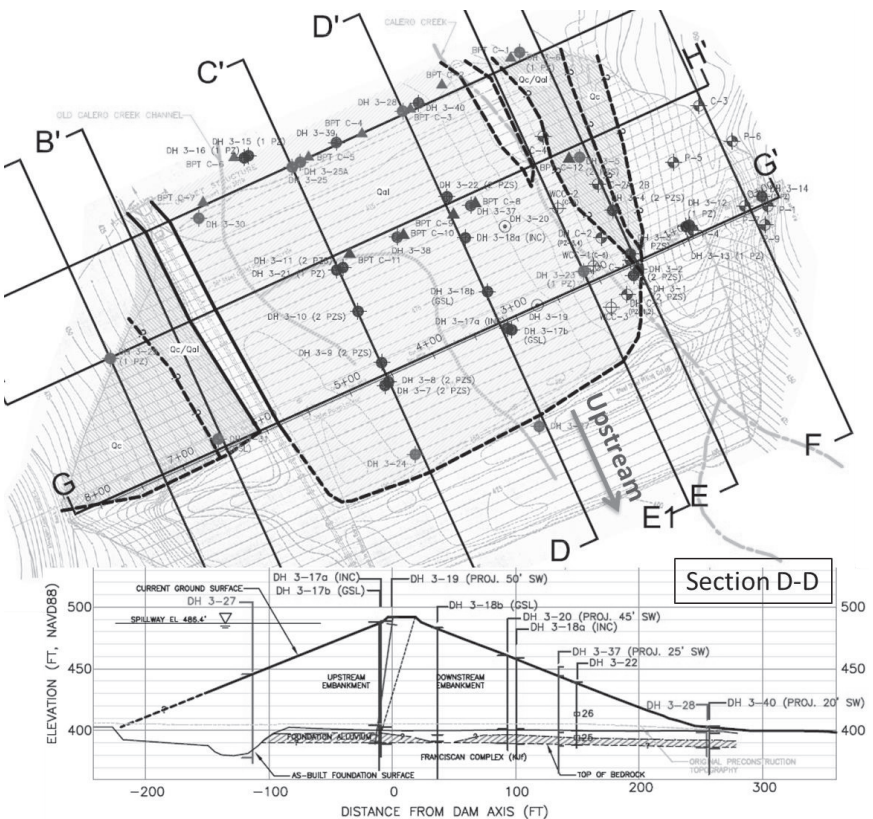


FIG. 2. Plan and section of Calero Dam and foundation

DESIGN EARTHQUAKE MOTIONS

The ground motions for the MCE's on the faults were estimated using the Next Generation Attenuation (NGA) models recently developed for tectonically active regions such as the western U.S. These new attenuation relationships were published in *Earthquake Spectra*, Volume 24, Issue 1, by the Earthquake Engineering Research Institute.

For each fault, the 84th-percentile response spectrum was calculated with the Next Generation Attenuation (NGA) models. For periods shorter than about 3 seconds, the spectral ordinates for the Shannon fault, which is within 2 miles of the dam, are the highest. For periods greater than 3 seconds, the spectral ordinates for the San Andreas fault, which is about 13 miles from the dam, are the highest. Therefore, the maximum credible earthquakes (MCE's) on the Shannon and San Andreas faults were adopted as the controlling MCE's for the dam. These two MCE's were termed the Local Fault Event (LFE) and the San Andreas Event (SFE).

Due to the close proximity of the dam to these faults, two types of the effects of fault rupture directivity were considered: average amplification due to forward directivity and amplification due to orientation with respect to fault strike. The latter results in stronger long-period motions in the direction normal to fault strike than in the direction parallel to strike.

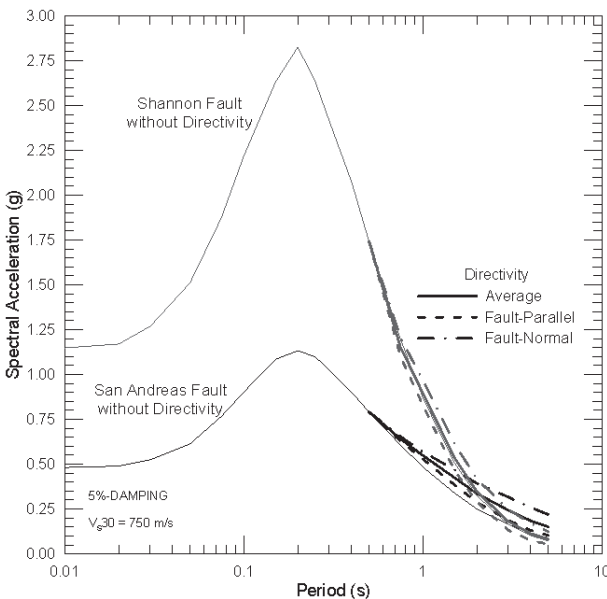


FIG. 3. Design response spectra for SFE and LFE

Figure 3 shows the 84th-percentile response spectra for the controlling MCE's, and the spectra adjustments for near-field directivity effects. The approach to account for fault rupture directivity effects is consistent with the DSOD's guidelines (Fraser and

Howard, 2002). The Somerville et al. (1997) model as modified by Abrahamson (2000) was selected to calculate directivity effects. In applying the model, it is assumed that the portion of the fault that ruptures towards the site is 40% of the total rupture length.

The acceleration time histories for analysis of the dam were developed by 1) selecting seed time histories from worldwide databases that offered the best match to the design earthquake parameters; 2) rotating the seed time histories into the fault-parallel and fault-normal components; 3) modifying the fault-parallel and fault-normal components using a time-domain approach to obtain a reasonably close match to the target fault-normal and fault-parallel response spectra shown in Figure 3. A total of six time histories were developed to represent the SFE and LFE ground motions. These time histories were corrected for base-line shift and checked for Arias Intensity before being applied in the dynamic analyses.

FIELD AND LABORATORY INVESTIGATIONS

Field investigations for the dam were performed in two phases. The first phase included drilling and sampling 11 borings throughout the dam in 2010 using mud rotary techniques on land and from a barge in the reservoir. The borings encountered in-place alluvium underneath the embankment downstream of the cutoff trench. The upper portion of the alluvium consists of finer-grained clayey soils including sandy clay and clayey sand with between 25 and 65 percent of low to medium plasticity fines. The lower unit of the alluvium consists of relatively pervious sand and gravels with 10 to 20 percent fines of similar plasticity to the upper alluvium. This lower unit, called the CGA zone, directly overlies the bedrock and is believed to be the cause of the observed low piezometric surface within the dam foundation. The average gravel content of the CGA material is 40 percent, which is expected to have significant influence on the reliability of the SPT blow counts. Therefore, to assess and supplement the SPT blow counts, seven Becker Penetration Test (BPT) soundings were advanced at locations adjacent to selected borings near the downstream toe of the dam to obtain large-diameter penetration resistance data in the alluvium.

The second phase was completed in 2012 to further investigate the properties of the alluvial soils under the downstream slope of the dam. In the supplemental investigation, four borings were drilled at the toe and on the downstream slope of the dam. The supplemental investigation also included advancing five BPT soundings from locations on the downstream slope of the dam to obtain additional BPT data in the foundation alluvium. The locations of these explorations are shown on Figure 2.

All BPT soundings were performed using a truck-mounted AP1000 Becker Hammer drill equipped with a supercharged diesel hammer. The Becker hammer testing was performed following the procedures recommended by Harder and Seed (1986). Blow counts and bounce chamber pressures were recorded for every foot of penetration. The BPT soundings located at the toe were advanced using a 6.625-inch crowd-out closed bit through the surface fill, in-place foundation soil and bedrock to total depths ranging from 19 feet to 25 feet. The BPT soundings located on the slope were advanced through the embankment zone with a 6.625-inch crowd-in open bit. In order to reduce the casing friction in the embankment, the hole was reamed each time the

driving was stopped to add an additional pipe segment. For reaming, the drill pipes were withdrawn about eight to 10 feet then lowered back into the hole and driven (if necessary) to the bottom while water and pressurized air were injected to carry cuttings up the pipe and out to a cyclone. About 5 feet above the anticipated foundation contact, the BPT drilling was switched to a crowd-out closed bit and the Becker penetration testing was then performed in the standard manner to the final depth. During the BPT advancement in the foundation, re-drive tests were performed at about 5 foot intervals to measure casing friction during the tests. Casing friction measurements generally were very low.

Both investigations also included conducting SPT and BPT hammer energy measurements, performing down-hole geophysical suspension (OYO) logging in borings, surveying the boring locations, and conducting laboratory tests on selected samples. The laboratory tests performed included moisture/density measurements, Atterberg limits, particle size analysis, specific gravity, one-dimensional consolidation, and isotropically consolidated undrained triaxial compression (TX-ICU) tests with pore pressure measurements.

PENETRATION RESISTANCE OF FOUNDATION ALLUVIUM

SPT Data The liquefaction resistance of the foundation material can be estimated by correlating with penetration resistance using the Standard Penetration Test (SPT). In the past, the correlations were developed based on the field SPT blow counts (N_{field}). However, the current practice has migrated to newer correlations based on the normalized SPT blow count ($(N_1)_{60}$). The $(N_1)_{60}$ value represents the number of blows required to advance a 2-inch outside diameter, 1.375-inch inside diameter, split spoon sampler for a depth of 1 foot (30 cm) at 60 percent hammer energy efficiency, and corrected to an effective overburden pressure of 1 atmosphere.

Gravel particles tend to increase the field blow counts while driving the relatively small diameter SPT sampler. To account for these effects, the field SPT blow counts were recorded in blows per inch (2.54 cm) of penetration, plotted cumulatively, and then individually examined and corrected to account for the presence of gravel. The correction is based on the assumption that the cumulative blow counts will plot as a straight line (representing a constant penetration distance for each blow) for samples not affected by gravel. Thus, the gravel-corrected blow count (N) was estimated by extrapolating the straight-line segment of the cumulative blow counts plot through the last 12 inches of the sampler drive, as shown in the example on Figure 4.

The other corrections for hammer energy (C_E), overburden pressure (C_N), rod length (C_R), sampling method (C_S), sampler type ($C_{S,\text{sampler}}$) were performed in accordance with the recommendations of Youd et al. (2001). The average measured SPT hammer energy for a manual-operated rope-and-cathead type hammer was 69 percent. The average measured hammer energy for six different automatic trip hammers were 50, 74, 77, 84, 84 and 86 percent, respectively. The hammer energy measurements show no apparent dynamic inefficiencies associated with a "short rod" length, within the range tested. Thus a constant C_R of 1.0 is used for all SPT sampling depths in the study. The normalized SPT blow counts, $(N_1)_{60}$, in the CGA zone are presented in Figure 5.

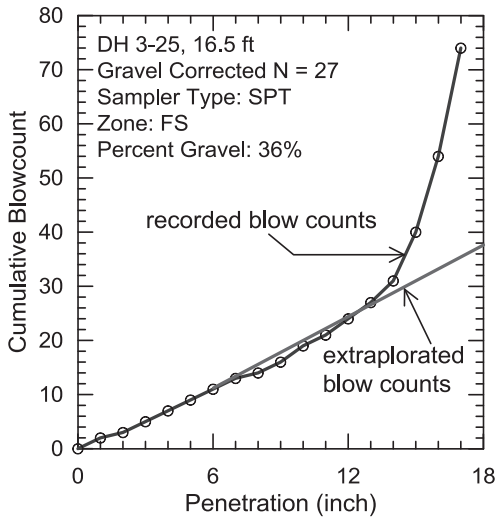


FIG. 4. Example of gravel correction for field blow counts

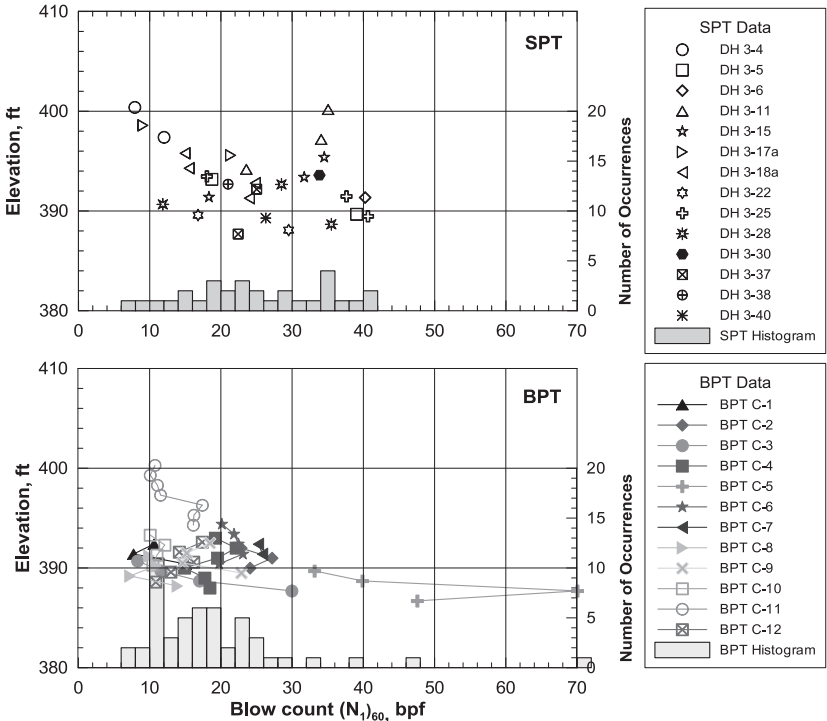


FIG. 5. Summary of normalized SPT Resistance (N_{60}) in CGA Zone

BPT Data A total of 12 BPT soundings were performed at the dam. BPTs C-1 through C-7 are located at near the toe of the dam, and BPTs C-8 through C-12 were performed from the access road bench on the downstream slope of the dam.

The field BPT blow count data were reduced using the Harder and Seed (1986) approach based on the adjusted bounce chamber pressure measurements. Figure 6 shows a summary of the BPT-converted equivalent SPT blow counts using this approach. In general, the gravel-corrected blow counts from the SPT borings are higher than those obtained from the adjacent BPT soundings.

Figure 6 presents, as an example, the equivalent SPT blow counts obtained from a pair of SPT and BPT borings located within about 3 m distance. The BPT blow count data were also reduced using the Sy and Campanella (1994) approach, which is based on direct energy measurements. In this study, the SPT-equivalent blow counts obtained using the two approaches were in good agreement.

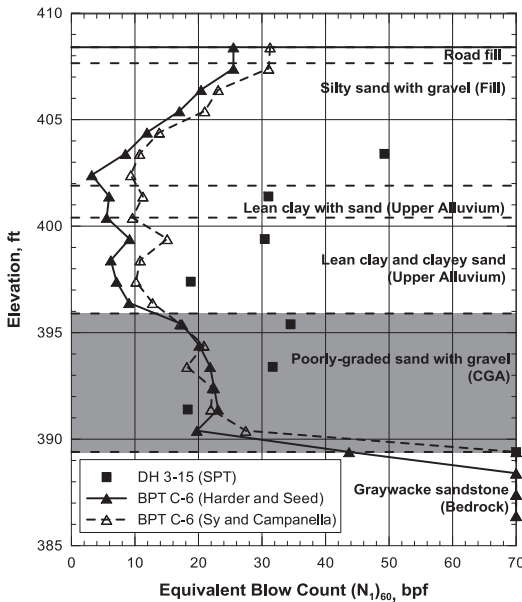


FIG. 6. An example of equivalent (N₁)₆₀ comparison between an SPT boring and a BPT sounding

LIQUEFACTION POTENTIAL ASSESSMENT

Liquefaction Evaluation Methods

In this study, the methods presented in Youd et al. (2001) and Idriss and Boulanger (2008) were used to evaluate the liquefaction potential of the CGA. Both methods are based on the original procedure of Seed and Idriss (1982), in which the liquefaction potential is evaluated by comparing the earthquake-induced cyclic shear stress ratio, CSR, (typically obtained from a dynamic response analysis) with the cyclic resistance

ratio, CRR, of the liquefiable soils. The CRR is defined as the uniform cyclic stress ratio required to trigger liquefaction for a given earthquake magnitude. Both methods correlate CRR with the SPT resistance $(N_1)_{60cs}$ and have slightly different correction factors for earthquake magnitude (MSF), fines content (ΔFC), and effective overburden stress (K_σ). The correction factor for initial static shear stress ratio (K_α) proposed by Idriss and Boulanger (2008) was applied in both methods to adjust for an initial shear stress ratio, $\alpha = \tau_{st}/\sigma'_v$, other than zero.

To estimate the earthquake-induced stresses and accelerations within the embankment and foundation during the MCE events, dynamic analyses was performed for the maximum embankment cross section with the program QUAD4M (Hudson et al., 1994). The input motions were applied in the transverse (upstream-downstream) direction at the bottom of a two-dimensional, plane-strain, finite-element mesh. The potential for liquefaction was evaluated by comparing the CRR for each SPT/BPT data point within the CGA with the CSR calculated for each input motion. The factor of safety against liquefaction (FS_{liq}) was calculated as the ratio of CRR and CSR.

Verification against Loma Prieta Earthquake Performance

The dam experienced the 1989 Loma Prieta earthquake with only minor (about 1 inch or less) settlement and transverse displacements. The San Jose – Santa Teresa Hills station (CGS-CSMIP Station No.57563), which is located within 2 miles of the dam and has site conditions similar to those at the dam site, recorded an outcrop motion during the event. Because the horizontal components were recorded at 225 and 315 degrees azimuths and the axis of the dam is at about 246 degrees, the recorded 225-deg and 315-deg motions were combined and rotated to calculate the 336-deg component, which corresponds to the transverse direction for the dam. The rotated 336-deg component has a peak horizontal acceleration (PHA) of 0.27g and was used as input to the model.

The dynamic response analyses showed that during the Loma Prieta earthquake, the computed peak CSR values within the CGA vary from 0.12 beneath the crest to 0.25 in the downstream free field. The liquefaction evaluation indicated no or minimal liquefaction of the CGA at the locations of most borings. However, liquefaction of limited extent with the CGA was calculated at 6 BPT locations (two beneath the toe and four beneath the bench). The two liquefaction analysis procedures produced approximately the same results for the Loma Prieta earthquake.

Liquefaction Risk in Scenario Design Earthquake Events

Compared to the Loma Prieta event, the scenario design earthquakes are much more demanding. QUAD4M analyses with LFE time histories showed that the peak CSR values during the LFE would roughly quadruple those during the Loma Prieta event. As a result, the calculated extent of liquefaction is much greater for the LFE than for the Loma Prieta earthquake. The analyses predicted ‘substantial or throughout liquefaction’ of the CGA at the locations of many borings and BPTs.

QUAD4M analyses with SFE time histories showed that the peak CSR values during the SFE would roughly double those during the Loma Prieta event. Although the SFE would cause smaller CSR values than the LFE, its larger magnitude (Mw 7.9 for the SFE compared to Mw 6.7 of the LFE) would largely compensate for it. Thus

the estimated extents of liquefaction for the LFE and SFE are similar.

On the above basis, it is concluded that a large portion of the CGA underneath the embankment and at the downstream toe is likely to liquefy during the design events.

INFLUENCE OF EMBANKMENT OVERBURDEN

The influence of embankment overburden on the liquefaction potential of the foundation alluvium is discussed here. It may be intuitive to think that the overburden stress from the embankment would cause consolidation in the alluvium and an accompanying increase in density and liquefaction resistance.

In this study, we assessed the penetration resistance of the CGA using the BPT-based data. The BPT data, as presented in Figure 5, suggest that the CGA under the downstream embankment slope has similar equivalent $(N_1)_{60}$ values compared with the CGA at the downstream toe.

The shear wave velocity measurements were also used to evaluate the effects of the embankment. Figure 7 summarizes the normalized shear wave velocities (V_{s1}) of the foundation soils encountered in a total of seven exploratory borings. Measured V_{s1} values range from 700 to 1,200 ft/s, with higher values within a few feet of bedrock. Approximately the same range of values was measured at the toe as beneath the downstream slope and beneath the crest. The data indicate that the V_{s1} for the alluvium, including the CGA, falls within the same range independent of the locations of the profiles.

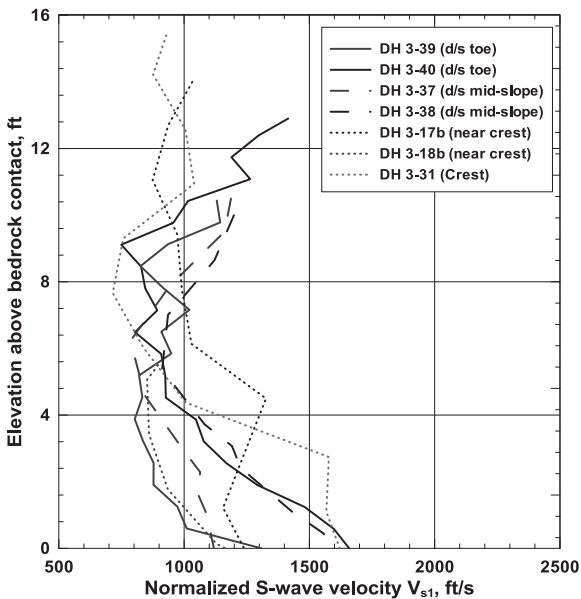


FIG. 7. Normalized shear wave velocities in foundation CGA

Additionally, we performed settlement analyses to estimate the compression of the foundation alluvium under the embankment weight. Consolidation analyses were performed to estimate the settlement in the upper alluvium using the laboratory measured compression index C_c , the recompression index C_r , and the preconsolidation stress. Based on the consolidation analyses, the calculated range of vertical strain in the upper alluvium was between 2.1 and 6.6 percent. The compression of the CGA under the embankment was estimated using two different moduli derived from the shear wave velocity (small strain) and the SPT blow counts (large strain), respectively. Calculations with the small-strain modulus computed a very small amount of compression in the CGA (less than 0.1 percent), while calculations with the large-strain modulus computed less than one percent compression. On the basis of the compressibility analyses, the effects of the embankment presence on the foundation CGA are considered relatively minor.

CONCLUSIONS

A large part of the Calero Dam embankment is underlain by coarse grained alluvium that is potentially liquefiable during strong earthquake shaking. In this study, the liquefaction potential of the CGA was evaluated using SPT- based methods. Normalized $(N_1)_{60}$ values were obtained from SPT borings and BPT soundings and the BPT-converted data tends to be somewhat lower on average. Validating analyses with the Loma Prieta event suggest that the SPT-based liquefaction evaluation methods satisfactorily explain the lack of liquefaction observations during the event. The influence of embankment overburden on the liquefaction potential of foundation alluvium was investigated as part of the study. The findings indicate that the presence of the embankment likely has only minor effects on the liquefaction resistance of the foundation alluvium.

REFERENCES

- Abrahamson, N.A., 2000, Effects of rupture directivity on probabilistic seismic hazard analysis: Proceedings of the 6th International Conference on Seismic Zonation, Palm Springs, California.
- Fraser, W.A., and Howard, J.K., 2002, Guidelines for use of the Consequence-Hazard Matrix and selection of ground motion parameters, The Resources Agency, Department of Water Resources, Division of Safety of Dams.
- Harder, L.F. and Seed, H.B., 1986, Determination of Penetration Resistance of Coarse-grained Soils using the Becker Hammer Drill, Earthquake Engineering Research Center, Report No. UCB/EERC-86/06, Univ. of California, Berkeley.
- Hudson, M., Idriss, I.M., and Beikae, 1994, QUAD4M User's Manual for a Computer Program to Evaluate the Seismic Response of Soil Structures Using Finite-Element Procedures and Incorporating a Compliant Base: Center for Geotechnical Modeling, Univ. of California, Davis.
- Idriss, I.M. and Boulanger, R.W., 2008, Soil Liquefaction during Earthquakes, EERI special publication, Monograph No. 12.

- Tolman, C.F., 1934, Geological Report on the Calero, Almaden, and Guadalupe Damsites, August 31.
- Seed, H.B., and Idriss, I.M., 1982, Ground motion and soil liquefaction during earthquakes: Earthquake Engineering Research Institute (EERI), University of California, Berkeley, EERI Monograph.
- Somerville, P.G., Smith, N.F., Graves, R.W., and Abrahamson, N.A., 1997, Modification of empirical strong ground motion attenuation relations to include the amplitude and duration effects of rupture directivity, *Seismological Research Letters*, V. 68, n.1, pp. 199-222.
- Sy, A. and Campanella, R.G. 1994, Becker and standard penetration tests (BPT-SPT) correlations with consideration of casing friction, *Canadian Geotechnical Journal*, V. 31, 343-356.
- Youd, T.L., Idriss, I.M., et al., Liquefaction Resistance of Soils: Summary Report from the 1996 NCEER and 1998 NCEER/NSF Workshops on Evaluation of Liquefaction Resistance of Soils. *Journal of Geotechnical and Geoenvironmental Engineering*, Vol. 127, No. 10, October.

Centrifuge Model Tests of Settling characteristics about Extremely Deep Soft Subgrade Reinforcement by Composite Pile

Chunhui Su¹, Jianlin Ma², Yanqing Huang³ and Zhongbo Hu⁴

¹Ph.D, Southwest Jiaotong University, Chengdu, Sichuan 610031, China; sch3977@163.com

²Professor, Southwest Jiaotong University, Chengdu, Sichuan 610031, China; majianlin01@126.com

³Senior Engineer, China Zhongtie Major Bridge Reconnaissance & Design Institute Co. Ltd, Wuhan, Hubei 430050, China;

⁴Ph.D, Southwest Jiaotong University, Chengdu, Sichuan 610031, China; huzhongbo87@163.com

ABSTRACT: The building of cross-sea bridge on deep soft soil in the deep sea requires the thick soft soil reinforcement in advance. To this end, centrifuge model tests on the composite pile foundation were conducted. In the tests, the pile lengths were 18cm and 9cm respectively, the diameter was 8mm, and the pile spacing were 3d, 5d and 8d, respectively. The test results indicate that the foundation settlement value with raft can be effectively reduced by the raft between stress balance layer and basement. Corresponding to pile length of 18cm, the foundation settlement value with raft was 39.1% of the one without raft. When the pile length was 9cm, and the pile spacing were 3d, 5d and 8d respectively, foundation settlement values with raft were about 13.4%, 35.2%, and 52.9% of the settlement value without piles and raft; Settlement value with the pile spacing of 8d was almost the same with the raft foundation settlement without pile. Corresponding to the pile spacing of 3d, 5d, and 8d, when the pile length was 18 cm, the settlement values were 12.5%, 76.5%, and 90.1% of the one without piles, respectively. When the pile spacing was 8d, raft foundation settlement with pile length of 18cm was less 30% than the settlement with pile length of 9 cm. According to the test results, relationship between settlement and pile spacing in 2 different conditions based on whether the raft is involved. Through nine groups of centrifuge model test of foundation reinforcement with steel composite piles, settling characteristics and the effects of pile spacing, pile length and raft on foundation settlement were studied. The results of this study provide important reference for theory research and engineering applications of foundation reinforcement of extremely deep soft soil for sea-cross bridge.

INTRODUCTION

Soft soil foundation reinforcement using composite pile, which was introduced by Japanese scholars in early 1960s, is a form of composite foundation treatment. A variety of composite foundations exist, noted that flexible and rigid pile composite foundation are specified in this paper according to their reinforcing properties. With the foundation treatment techniques' thriving, its concept is significantly enriched. The design method of rigid-pile composite foundation is introduced by academician Huang Xiling in China

Academy of Building Research (CABR). And then, CFG pile composite foundation, which is the earliest rigid-pile composite foundation, was developed successfully in 1992 by Institute of Foundation Engineering of CABR. Rigid-pile composite foundation has gained increasing popularity in practical engineering when treating the soft soil subgrade in the last 20 years. Development can also be seen in diversities of foundation forms and in material field with low-strength concrete pile imported. Progresses are made by numerous researchers in 10 years in rigid-pile foundation treatment:

Li Ning(2001) gave analysis about mattress layer's reinforcement effect and its mechanism in composite foundation by using numerical experiment. Starting from settlement and deformation mode of CFG pile composite foundation, Dong Bichang (2002) introduced a settlement calculation method considering mutual effect between pile, soil and layer. Chi Yuejun (2003) put forward the two-layer stress method to calculate settlement, by discussing the settlement calculation method of rigid-pile composite foundation suggested in Code for Design of Building Foundation. By setting the cushion between pile and raft, Liang Fayun etc.(2003) developed a new concept named piled raft composite foundation, with the further research about factors affecting settlement. Zheng Gang (2006) presented the research progress of rigid-pile foundation performances with different mattress layer's thicknesses. Qiao Jingsheng (2008) conducted the research of composite foundation depending on model test and numerical simulation, and provided "method of pile settlement" to calculate foundation settlement. Based on undisturbed soil tangent modulus method, Yang Guanghua (2009) introduced a new method to calculate rigid-pile composite foundation settlement. Qi Le (2011) analyzed piercing deformation of pile in his research. Rigid-pile composite foundation has been developed significantly in theory study and engineering practice, but it's worth noted that some limitations still exist, because the previous research mainly focused on traditional and well-developed CFG pile method, and cushion layer thickness ranged from 15cm to 60cm. Stimulated by high-speed railway's marching, composite foundation forms are diversified. For instance, piled-raft structure (impose raft on gravel cushion), developed as a new foundation form, is currently applied in subgrade and other flexible foundation.

E. Bourgeois etc. (2012) have performed the settlement analysis of piled-raft foundations, but cushion effect is not taken into consideration. In this paper, to strengthen the thick soft soil in deep water, author conducted the centrifuge test with composite foundation simulated, using composite pile (steel tube concrete pile), and set gravel cushion (called stress balance layer in this paper) as 10mm between pile and foundation (thickness can be converted to 1m based on model ratio). Different groups of models are simulated in the test, by combining factors involving pile length of 9cm and 18cm, pile spacing of 3d, 5d and 8d, and whether there's a raft on the stress balance layer. And then, the author conducted research and analysis about settlement of different models with different factors considered, including pile length, spacing and raft, so as to

provide the theoretical support of soft soil composite foundation in deep water for further study.

PRINCIPLE OF THE GEOTECHNICAL CENTRIFUGE MODEL TEST

Loading and stress of the geotechnical structure are the main reasons of deformation and destruction, which are mainly generated by the gravity of the rock and soil. It is a significant feature in the geotechnical engineering. Therefore, it is particularly important to study geotechnical structure deformation and failure characteristics of rock and soil under gravity. In engineering practice, engineers often do the indoor small-scale physical model testing and field testing to verify the correctness of the theory and solve practical problems in engineering. Gravitational stress of the conventional small-scale model is far lower than the prototype, and thus it can't reproduce the characteristics of the prototype. It can be learned that model can present stress - strain relationship which is similar or identical to the prototype, the test results which is consistent with the prototype can be obtained, when the gravitational stress of indoor model is same to geotechnical structures. The basic principle of the centrifuge test is that the geotechnical model in the high-speed rotation of centrifuges is subjected to the effect with a centrifugal acceleration which is greater than the acceleration of gravity, to compensate the geotechnical structures for weight loss resulted by the model size reduction. The inertial force is absolutely equivalent to gravity, and a high acceleration does not change the nature of engineering materials, so that the stress and strain of the model is equal to the stress and strain of prototype, the deformation of the model is similar to the deformation of the prototype, and their damage mechanisms are the same. Centrifuge test reproduces prototype properties with the stress level in site so that the geotechnical working state can be predicted. As a result of this, centrifuge test is widely applied in geotechnical engineering including the studies of soft ground and consolidation settlement, and structure - geotechnical interaction, which simulates traits of geotechnical structures to weight gravity as the main load. A centrifuge model test for soft clay foundation was conducted by Feng Guangyu in 1987, since then it has been conducted by many authors, including Du Jiancheng(1997), Dong Yun (2007), and many others. Li Mei (1995) has conducted Centrifugal model test of the interaction between the foundation of beam-pillar offshore platform and the soil. Zeng Youjin (2005) has studied centrifuge model tests of mini-pile foundation in soft soil.

TEST DEVICE AND MAIN TEST COMPONENTS

The device mainly adopted in this test is TLJ-2-100g-t centrifuge, which equips with advanced automatic data acquisition system and high-performance computer (including peripherals) and complete sets of software, to collect and process the data effectively. The device adopts digital serial transmission mode, firstly amplifying the signal, then

processing, then outputting, as well as high-quality and reliably durable gold slip ring, therefore, the data transmission quality is ensured. The chosen model box is three-wall aluminum alloy (left, right and back wall), with an organic glass wall at one side (front wall) structure. The thickness of aluminum is 20mm, and 30mm thick for organic box. What's more, the front wall is fixed by 18mm bolt group to ensure the stability. Centrifuge as shown in **fig. 1**.

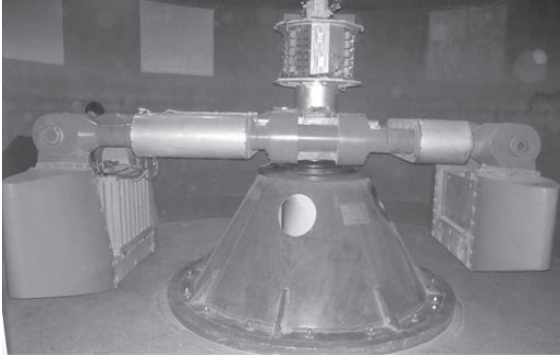


Fig.1. TLJ-2-100g-t centrifuge

The main test components adopted are super-miniature electrical resistance displacement meters and soil pressure box designed especially for civil engineering indoor test. Displacement meter range is 25mm, soil pressure box range is 200kPa~1Mpa. Displacement meters are fixed on the model surface and foundation surface (foundation and additional load are simulated with steel cylinder and sheets steel).

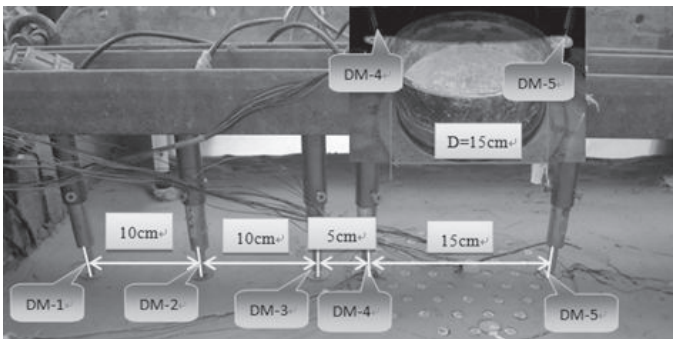


FIG. 2. Displacement Meters arrangement

Specific Settings as shown in **fig. 2** (DM represents the displacement meter). In the process of consolidation, displacement meters are all fixed on the model surface, displacement meters No.4 and 5 are symmetrically fixed on the two sides of foundation edge position (consolidation without foundation) separately. Displacement meters No.3, 2 and 1 are fixed in turn. Because of symmetric model, displacement meters are fixed on one side. The distance between No.3 and No.4 is 5 cm, the distance between No.2 and No.3 is 10 cm, the distance between No.1 and No.2 is 10 cm. When consolidation is finished, putting the sand cushion on soil before foundation and load are imposed for the next stage of test. Displacement meter No.4 and 5 are fixed on the top of the foundation to measure the settlement due to additional load, other No.1, 2 and 3 measure the surface settlement on different positions.

DESIGN AND KEY POINTS OF CENTRIFUGE MODEL TEST

The settlement of bridge foundation reinforced by composite piles is generally considered to be effected by series of factors including: pile space, pile size, pile characteristics (rigid pile or soft pile), thickness of stress balance layer, presence of raft, soil strength parameter, as well as friction coefficient of pile side and soil. This study will focus on settlements by conducting the contrast tests, considering the factors including: unreinforced foundation, changing steel pipe composite pile(STCP) spacing, changing pile length, rafts between stress balance layer and caps, and combination effect between raft and STCP.

Centrifuge Model Test Design and Main Process

According to the study aim, tests consist of 9 groups in total, including 2 groups of natural foundation and 7 groups of STCP with foundation reinforcement. The model size and test materials are chosen with comprehensive consideration involving boundary conditions and size effect (Xu Guangming (1996)). Model length is 80cm, width is 60cm and height is 45cm. Model materials are made of soil grains sieved by 1mm screen, then adding right amount of water to the reconstituted soil already of certain water content before fully mixing them; the gravel stress balance layer is simulated by silt sand; cushion cap is simulated by organic glass (D=19cm) which thickness is 3 cm; foundation is simulated by steel cylinder (D=15cm); piles are aluminum alloy tubes (D=8mm) filled with mortar; pile spacing include 3d, 5d and 8d. Piles length are l=18cm and l=9cm. Testing scheme are shown in table 1, composite foundation model elevation is shown in fig. 3. For every test, the water are added which heights are 2 cm on the model surface after completing the model, and then consolidation is conducted with 100g centrifugal acceleration. The stress balance layer are put, then steel cylinder and sheets steel are put on the cushion after centrifuge running stop. When the

preparation work is done, centrifuge runs at 70g acceleration until the settlement is stabilized. Related data is collected constantly during test.

Table 1. Planning for Centrifuge Model Test

| Models | Diameter (mm) | Pile length (cm) | Pile spacing (mm) | Thickness of the stress balancing layer (cm) | Thickness of raft (mm) | Depth of Water (cm) | Model scale (g) |
|---------|---------------|------------------|-------------------|--|------------------------|---------------------|-----------------|
| Model 1 | No pile | No pile | No pile | 2 | 0 | 2 | 70 |
| Model 2 | 8 | 18 | 3d | 2 | 0 | 2 | 70 |
| Model 3 | 8 | 18 | 5d | 2 | 0 | 2 | 70 |
| Model 4 | 8 | 18 | 8d | 2 | 0 | 2 | 70 |
| Model 5 | 8 | 18 | 8d | 2 | 3 | 2 | 70 |
| Model 6 | No pile | No pile | No pile | 2 | 3 | 2 | 70 |
| Model 7 | 8 | 9 | 8d | 2 | 3 | 2 | 70 |
| Model 8 | 8 | 9 | 5d | 2 | 3 | 2 | 70 |
| Model 9 | 8 | 9 | 3d | 2 | 3 | 2 | 70 |

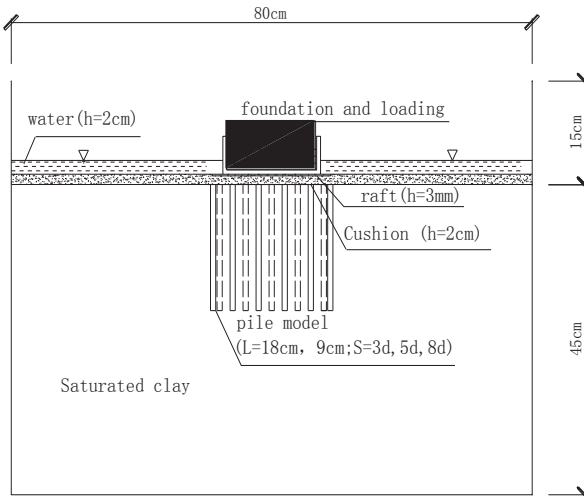


FIG. 3. Planning for Centrifuge Model Test

Key Points of Centrifuge Model Test

1. Simulation of thick soft soil layer: The thickness of soft soil under piles bottom are 27cm and 36cm, 1.5 or 4 times of pile length. Through the bottom stress test, bottom of model box impose little effects on the test results, therefore this test can simulate the thick layer of soft soil foundation situation. Specific test scheme is shown as table 1 and Fig. 3.

2. Soil models: water content and density impose obvious impact on settlement. In order to simplify the comparison, water content and density are set as controlled parameters during the model making. During the model making, moisture and density of soil are basically the same which should be strictly controlled. Test soil's liquid limit is 52.5, plastic limit is 20.9, and the optimal water content is 21.3%. Soil models are made with water content of 28%, forming density of 1.8g/cm³ as well as compaction thickness of 3cm. In the meantime, the soil pressure boxes are embedded according to the test plan, and the model's height should be compacted to what is designed with the surface smoothed. The physical and mechanical parameter can be seen as table 2.

3. Simulated piles: the key problems of pile foundation simulation involve: a, deformation characteristics of pile foundation should be in accordance with requirements and prototypes; b, friction characteristics of pile foundation and soil around should be consistent with requirements and prototypes. This test adopts the aluminum alloy pipes to simulate steel tube piles, and coats the pile surfaces with epoxy resin, to better the pile-soil contact simulation. Moreover, the piles are stunk with a layer of thin slurry to further simulating the project practice in pile shape, stiffness and soil side friction.

Table 2. Model Soil of Physical and Mechanical Parameters

| Description of soil | Layer thickness (cm) | w(%) | γ (kN/m³) | Es (MPa) | Ψ (°) | c (kPa) |
|----------------------------|-----------------------------|-------------|---|-----------------|------------------------------|----------------|
| Clay | 45 | 28 | 19 | 6~8.0 | 15~18 | 30~45 |

TESTING RESULTS ANALYSIS

Testing Results

Settlement increases rapidly as the acceleration increases, and still remains increasing at a slower speed but finally stabilized when the acceleration becomes stable. When acceleration is 70g, the settlement of different schemes with the changing process of the time is shown in Fig. 4. The summary of final settlements is shown in table 3. According to table 3 for the final settlement of each scheme caused by additional load, the results are analyzed and compared:

Settlement of nature foundation with raft is 9.53 mm, while nature foundation without raft is 17.59mm, so their ratio to settlement is 54.2%. Due to the large stiffness of the raft and the raft area is 40% larger than the base area, upper loads "disperse" to the stress balance layer in the first place, and then further transmits to the soil. The area of substrate soil bearing the load increases, so additional stress goes down and settlement reduces by 45.8% than non-raft nature foundation. Settlement analysis of comparison groups with same pile spacing but different pile length indicate: When pile spacing is set as 5d and 8d, foundation settlement of model with raft and pile length of 9 cm is smaller than what is of no raft, but whose pile length is 18cm. A contrast analysis of settlement shows that model settlement with raft accounts for 39.1% of the non-raft under condition that pile length is 18cm.

The foundation settlement (pile length is 18cm, pile spacing is 3d) is 12.5% of the nature foundation settlement, which decreases by 87.5%. The settlement of model with pile length of 18cm as well as pile spacing of 5d and 8d accounts for 76.5% and 90.1% of nature foundation respectively. Note that when pile spacing increases, settlement decrease becomes slower.

Raft is arranged on the stress balance of the centrifuge model with 9cm in pile length. Contrast study of settlement is conducted between the foundation with different pile spacing and foundation only reinforced with raft. The piled-foundation settlement (2.36mm, 6.2mm, 9.3mm with spacing of 3d, 5d 8d respectively) accounts for 24.8%, 65.1%, 97.6% of raft-reinforced-natural foundation. Note that 8d pile spacing foundation settlement is almost equal to nature foundation equipped with raft.

There is a raft on stress balance layer, and pile spacing is 8d. Foundation settlement (6.2mm) for the pile length of 18cm is less 3.1mm than foundation settlement (9.3mm) for the pile length of 9cm; settlement reduces by 30% with double pile length.

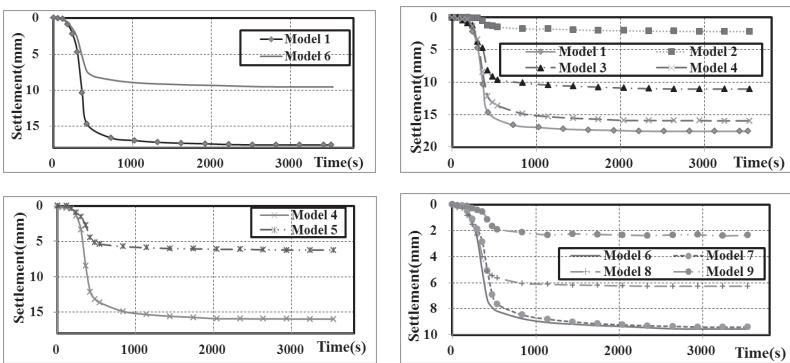


FIG. 4. The Comparative Curves of Time-settlement, $a=70g$

Table 3. Final Settlement Caused by Surcharge Loads, $a=70g$

| schemes | Settlement (mm) | Settlement ratio of composite foundation to raft foundation (%) | Settlement ratio of composite foundation to natural foundation (%) |
|---------|-----------------|---|--|
| model1 | 17.59 | - | 100 |
| model2 | 2.2 | - | 12.5 |
| model3 | 13.45 | - | 76.5 |
| model4 | 15.85 | - | 90.1 |
| model5 | 6.2 | - | 35.2 |
| model6 | 9.53 | 100 | 54.2 |
| model7 | 9.3 | 97.6 | 52.9 |
| model8 | 6.2 | 65.1 | 35.2 |
| model9 | 2.36 | 24.8 | 13.4 |

Fitting Curve and Analysis of Result

The curve of the settlement-pile spacing is obtained from experiment or by fitting the experimental data of graph. If pile length is 9cm, formula (1) accords with the fitting curve 1; while Pile length is 18cm, formula (2) accords with the fitting curve 2.

$$S' = 7.1 \ln(s) - 20.1 \quad (1)$$

$$S' = -201359(1/s)^3 + 16.66 \quad (2)$$

Where S' is the value of settlement, s is the value of pile spacing.

The values of settlement calculated according to Formula (1) and (2) are shown in **table 4**. The pile spacing - settlement curves are shown in **Fig. 5**.

Table 4. The Settlement according Pile Spacing and Pile Length

| Pile length (cm) | Diameter of the pile (mm) | Pile spacing (d) | Calculated value of settlement (mm) | Measured value of settlement (mm) |
|------------------|---------------------------|------------------|-------------------------------------|-----------------------------------|
| 9 | 8 | 3d | 2.46 | 2.36 |
| | | 5d | 6.09 | 6.2 |
| | | 8d | 9.43 | 9.3 |
| 18 | 8 | 3d | 2.09 | 2.2 |
| | | 5d | 13.51 | 13.45 |
| | | 8d | 15.89 | 15.85 |

As shown in **table 4**, contrast study between calculated and measured settlement value are performed. When foundation pile spacing are 3d, 5d and 8d where raft is involved and pile length is 9cm, calculation difference calculated using formula (1) are 4.41%, -1.76% and 1.38%; When no raft is put, and pile length is 18 cm, calculation error calculated using formula (2) are -5.0%, 0.44% and 0.23% correspondingly. All the maximum differences are less than 5%, therefore Formula (1) and Formula (2) can reasonably be used to estimate the effect of pile spacing on the settlement, which provides experimental support for engineering purpose.

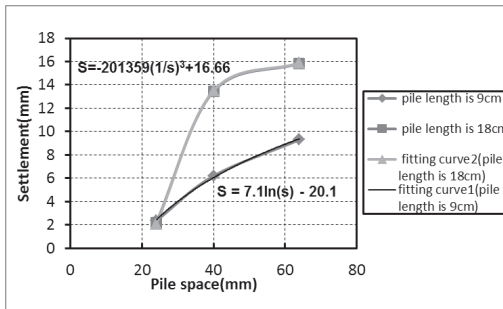


FIG. 5. Curves of Pile Spacing–settlement

CONCLUSION

According to above analysis, following conclusions can be drawn based on the tests:

1. Raft - Base - stress balance layer interactions significantly reduce the settlement. The raft foundation settlement is 45.8% smaller than the non-raft foundation settlement; when pile length is 18cm, settlement of the raft foundation is 39.1% of non- raft foundation. Setting the raft, the length of pile can be appropriately reduced.
2. Influence of pile spacing on the settlement: When pile length is 18 cm, and pile spacing are 3d, 5d and 8d, the settlement values of raft foundation are 12.5%, 76.5% and 90.1% of the no raft foundation, respectively. While pile length is 9cm, and pile spacing are 3d, 5d and 8d, the settlement values of raft foundation are 24.8%, 65.1% and 97.6% of the raft foundation, respectively.
3. Influence of pile length on the settlement: because of setting raft, the foundation with pile length of 18cm is 66.7% of settlement with the pile length of 9cm.
4. When pile spacing satisfies $3d \leq s \leq 8d$, and pile length is 9cm, relationship

between raft foundation settlement and pile spacing can be represented by Equation (1). While pile length is 18cm, the relationship between no raft foundation settlement and pile spacing can be represented by Equation (2). The relationship between settlement and spacing with raft or non-raft is different.

ACKNOWLEDGMENTS

The work reported here is supported by The Central College Foundation of China. The authors wish to express their gratitude for the financial assistance. The anonymous reviewers' comments are also greatly acknowledged.

REFERENCES:

- Li, N. and Han, X. (2001). Study on Mechanism of Cushion in Composite Pile Foundation. *China Civil Engineering Journal*. Vol.34 (2): 68-73, 83.
- Chi, Y.J., Song, E.X. and Chen, Z.Y. (2003). An Simplified Method for Settlement of Rigid-Pile Composite Foundation. *China Civil Engineering Journal*. Vol.36 (11): 19-23.
- Liang, Y.F., Chen, L.Z. and Shi, X.G. (2003). Numerical analysis of composite piled raft with cushion subjected to vertical load. *Computers and Geotechnics*. Vol.30: 443-453.
- Zheng, G., Liu, S.J. and Wu, Z.C. (2006). Study on behavior of rigid pile composite ground with different cushion thicknesses. *Rock and Soil Mechanics*, Vol.27(8): 1357-1360.
- Qiao, J.S., Tao, L.G. and Liu, B., et al (2008). New method for settlement calculation of composite foundation-pile settlement method. *Journal of Liaoning Technical University (Natural Science)* Vol.27 (1): 63-65
- Yang, G.h., Su B.k. and Qiao, Y.L. (2009). Method for calculating settlement of rigid-pile composite foundation. *Chinese Journal of Rock Mechanics and Engineering*, Vol.28 (11): 2193-2200.
- Qi, L, Shi J.Y. and Hou, Q. (2011). Research on pile penetration into cushion of composite ground. *Rock and Soil Mechanics*. Vol.32 (3): 815-820.
- Bourgeois, E., Buhan, P. de and Hassen, G. (2012). Settlement analysis of piled-raft foundations by means of a multiphase model accounting for soil-pile interactions. *Computers and Geotechnics*. Vol.46: 26-38.
- Feng, G.Y. (1987). "A centrifuge model test for soft clay foundation of Dai-Huang highway." *Journal of Yangtze River Scientific Research Institute*, (2): 72-81.
- Du, J.C. and Zhang, L.M. (1997). "Centrifuge modeling study on soft foundation treatment of Guang-Gang station." *Sichuan Architectural*, Vol. 17(3) : 44-45.
- Dong, Y., Chai, H.J., and Yan, Z.L. (2007). "Centrifugal model test study on the settlement character of the rock-soil filled roadbed." *Journal of Highway and*

Transportation Research and Development, Vol. 24(3) : 25-29.

- Li, M., Bao, C.G. and Ren, S. (1995). "Centrifugal model test of the interaction between the foundation of beam-pillar offshore platform and the soil." Chinese Journal of Geotechnical Engineering, Vol. 17(5): 1-6.
- Zeng, Y.J., Wang, N.X. and Zhang, W.M. (2003). "Study on centrifuge model tests of mini-pile foundation in soft soil." Chinese Journal of Geotechnical Engineering, Vol. 25(2): 242-245.
- Xu, G.M. and Zhang, W.M. (1996). "The study on the particle and boundary effect of centrifuge tests." Chinese Journal of Geotechnical Engineering, Vol. 18(3): 80-86.

On the compressibility of cement stabilized zinc-contaminated kaolin clay

Ning-Jun Jiang¹, Yan-Jun Du*², Song-Yu Liu³, Jing-Jing Zhu⁴

¹ PhD student, Department of Engineering, University of Cambridge, Cambridge, UK, CB2 1PZ; former PhD student, Institute of Geotechnical Engineering, Southeast University; nj263@cam.ac.uk

² Professor, Institute of Geotechnical Engineering, Southeast University, Nanjing, China, 210096; duyanjun@seu.edu.cn (corresponding author)

³ Professor, Institute of Geotechnical Engineering, Southeast University, Nanjing, China, 210096; liusy@seu.edu.cn

⁴ Master student, Institute of Geotechnical Engineering, Southeast University, Nanjing, China, 210096; zhujingjing8809@gmail.com

ABSTRACT: In this study, the one-dimensional compression test was conducted to investigate the effect of zinc concentration on the compressibility of cement solidified zinc-contaminated kaolin clay. Post-yield compression index (C_c) and yield stress (σ_{vy}') of stabilized soils were obtained and correlated with initial zinc concentrations. It has been found that zinc concentration significantly affected the compressibility of stabilized kaolin clay in terms of C_c and σ_{vy}' . C_c decreased marginally and sharply when zinc concentration $\leq 0.1\%$ and $> 0.1\%$, respectively. σ_{vy}' decreased steadily with increased zinc concentration. To quantify the influence of zinc concentration on the cementation structure/bonding and, further, the compression characteristics of the cement stabilized kaolin clay, the concepts of void index (I_v), Intrinsic Compression Line (ICL) and Sedimentation Compression Line (SCL) were used to analyze the compression test data. The locations of compression lines of the stabilized kaolin relative to those of ICL and SCL, were discussed. In addition, the convergence of compression lines of stabilized kaolin with ICL was analyzed as well. The results reveal that as zinc concentration increases, cement stabilized kaolin clay exhibits weakened cementation structure/bonding. It is demonstrated that zinc has a considerably destructive effect on the cementation structure/bonding, which in turn affects the compression characteristics of the cement stabilized zinc contaminated kaolin clay.

INTRODUCTION

It has been widely accepted that soil pollution is one of the major issues that impede sustainable development of modern society. Recently, various physical, chemical and

biological methods have been developed to address the remediation of contaminated lands. Among them, cement-based solidification /stabilization (S/S) is a commonly used technique to treat lands contaminated by toxic substances, heavy metals in particular. Mechanistically, S/S method involves two separate processes: containment and isolation of contaminants physically, and transformation of contaminants speciation chemically (UKEA 2004). With the S/S treatment, leaching of toxic substances, as well as soil permeability, is largely reduced whereas strength of soil is improved to some extent (Du et al. 2012a; Boardman et al. 2004). Laboratory and field studies have shown that the performance of S/S treatment method is controlled by several factors, namely binder type/dosage, contaminant type/concentration, initial moisture content, and curing conditions (Antemir et al. 2010; Boardman et al. 2004). As a large proportion of S/S treated lands is reused for construction of civil infrastructures, mechanical properties of treated soils are of increasing concern. Compressibility is an important parameter used in deformation analysis when the cement solidified heavy metal contaminated soils are used as bearing stratum.

Numerous studies have focused on compressibility of naturally deposited soils (Butterfield 1979; Burland 1990). In addition, compression of chemically treated soils (e.g. cement and lime) has been studied extensively as well (Tremblay et al. 2001; Rotta et al. 2003; Horpibulsuk et al. 2004; Rios et al. 2012). To date, however, studies of compression behavior of cement stabilized contaminated soils are very limited. Indeed, based on the authors' previous investigations on strength characteristics of stabilized heavy metal contaminated soils, high contaminant concentration would lead to a serious destruction of soil-cement matrix, thus resulting in loss of resistance (Du et al. 2012b).

The objective of this study is to present an investigation of compression characteristics of zinc (Zn) contaminated kaolin clay stabilized with cement. A series of oedometer tests were carried out. The effect of Zn concentration on the compressibility was discussed in terms of post-yield compression index (C_c) and yield stress (σ_{vy}'). In addition, to quantify the effect of Zn concentration on the cementation structure/bonding, which in turn affects the compression behavior of stabilized kaolin clay, the concepts of void index (I_v), Intrinsic Compression Line (ICL) and Sedimentation Compression Line (SCL) were introduced. Relative locations of ICL, SCL, and compression lines of tested soils, in a semi-logarithmic scale (I_v - $\log \sigma_v'$), were discussed.

MATERIALS AND METHODS

The basic properties of the kaolin clay are listed in Table 1. XRD analysis showed that it was composed of kaolinite (96%) and quartz (4%). Kaolin clay was utilized in this study since its physicochemical properties have been previously well defined. Locally produced cement (equivalent to Portland cement Type I) was used as the sole binder

while commercial zinc nitrate hydrate ($\text{Zn}(\text{NO}_3)_2 \cdot 6\text{H}_2\text{O}$) was the contaminant source. Nitrate anion (NO_3^-) was selected due to its negligible interactions with both cement and kaolin clay during hydration process (Cuisinier et al. 2011; Sridharan et al. 1986). Five levels of Zn concentrations (0.02%, 0.1%, 0.2%, 0.5%, and 1%, the ratio of weight of Zn ions to dry weight of soil) and one cement content (8%, based on dry weight of soil) were adopted in this study. Besides this, clean kaolin clay with cement treatment was also prepared as a control. To prepare stabilized soil samples, predetermined mass of $\text{Zn}(\text{NO}_3)_2 \cdot 6\text{H}_2\text{O}$ was thoroughly dissolved and then mixed with air-dried kaolin clay powders to achieve a slurry with initial water content of 60% (based on dry weight of soil). A predetermined quantity of cement powder was poured into the initial slurry afterwards, and the binary mixture was agitated thoroughly for another 10 minutes to achieve uniformity. The homogeneous paste was then transferred into oedometer rings with two glass sheets enclosing both open sides. Entrapped air bubbles were carefully eliminated during this procedure, which was achieved by using de-aired water as well as regular tapping during preparation. The preparation procedure was completed within 45 minutes to avoid initial hardening. Soil samples together with rings and glass covers were then wrapped in sealed plastic bags and were cured under controlled environment (20°C and 95% relative humidity) for 7 and 28 days. After curing, samples were soaked under water and then subjected to vacuum for 10 hours to facilitate saturation prior to one-dimensional oedometer test. The incremental loads applied were 12.5, 25, 50, 100, 200, 400, 800, and 1600 kPa and each increment was kept constant for 24 hours.

Table 1. Properties of kaolin clay used in this study

| Index | Value |
|-----------------------------|-------|
| Specific gravity G_s | 2.65 |
| Plastic limit w_p (%) | 23.0 |
| Liquid limit w_L (%) | 34.5 |
| Grain size distribution (%) | |
| clay (<0.005 mm) | 33.0 |
| silt (0.005-0.075 mm) | 63.3 |
| sand (0.075-2 mm) | 3.7 |
| pH | 8.7 |

TEST RESULTS

The relationship between void ratio (e) and vertical load (σ_v') was plotted in a normal scale as shown in Fig. 1. In the figure, legend i - j - k represents the sample spiked with $k\%$ Zn contaminants, stabilized with $j\%$ cement, and cured for i days. It is evident that initial void ratios (e_0) of the samples spanned from 1.35 to 1.50, which can be attributed to the retardant effect of Zn contaminants. With load increments, samples with varied initial Zn concentrations exhibited different e - σ_v' curve patterns, as well as final readings of e corresponding to 1600 kPa. More specifically, for the samples possessing 0, 0.02 and

0.1% Zn concentrations, e had an approximately linear correlation with σ_v' , which was similar to the manner of intact structured natural clays (Purushothama Raj, 2008). The values of the final e for these samples (Zn concentration $\leq 0.1\%$) were 0.97 and 1.08 for 7 and 28 days of curing time, respectively. No significant deviations of final e were observed among samples with these three concentration levels. However, when Zn concentration is $> 0.1\%$, approximately hyperbolic-shape curves were apparent which was similar to the manner of remolded natural clays as reported in Purushothama Raj (2008), except for the sample of 28-8-0.2, which displayed a transitional shape between linear and hyperbolic-shape lines. Correspondingly, the higher the concentration, the steeper the initial tangential slope of the hyperbolic-shape curve and the smaller values of the final e . In addition, it is found that samples cured for 28 days had a higher value of e than those for 7 days in the event of the same Zn concentration. This indicates that increasing the curing time would promote resistance to compression, which has been reported by earlier researchers (Wei et al. 2012).

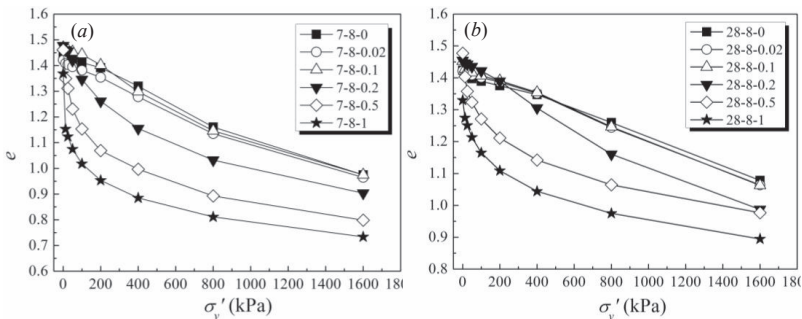


Fig. 1. One-dimensional compression response for cement stabilized Zn contaminated kaolin clay in linear scale: (a) 7 days; (b) 28 days.

Figure 2 shows the e - σ_v' relationship plotted in semi-logarithmic scale. It is evident that the curves of specimens with Zn concentration $\leq 0.1\%$ were almost identical, whose shapes were similar to naturally/artificially cemented soils (e.g. Rotta et al. 2003). The curves were initially flat, which reflected the stiffness of the stabilized soil, and gradual softening occurred as the vertical load increased. Since the initial stiffness of stabilized soil is mainly due to the cementation structure/bonding resulting from the filling of soil pore spaces by cementitious products such as calcium silicate hydrate (C-S-H) (Rotta et al. 2003; Rios et al. 2012), it can be inferred that Zn concentrations less than 0.1% have negligible effect on the stability of the cementation structure/bonding. This point will be further discussed in details in section "Discussion". On the contrary, samples with 0.5% and 1.0% Zn contaminants had very similar curve shapes to weakly structured natural clays, indicating a severe destruction of the cementation structure/bonding. As for the

samples with 0.2% Zn contaminants, they represented a transitionally destructive state of stabilized kaolin clay.

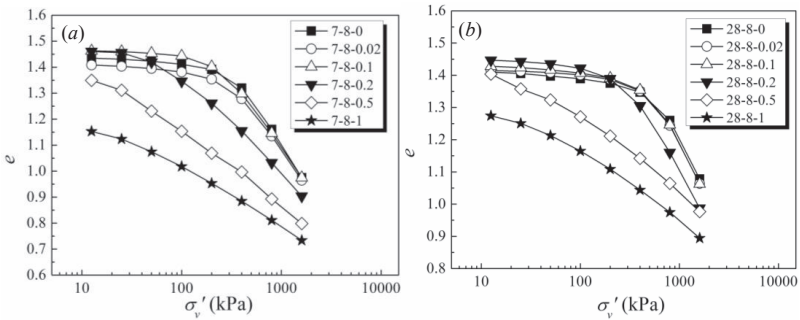


Fig. 2. One-dimensional compression response for cement stabilized Zn contaminated kaolin clay in semi-logarithmic scale: (a) 7 days; (b) 28 days.

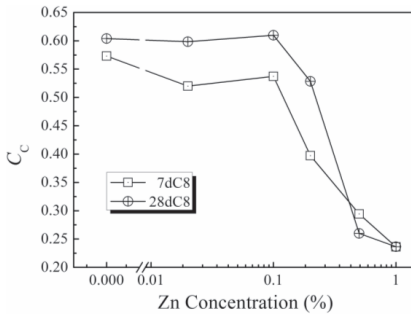


Fig. 3. Effect of initial Zn concentration on compression index (C_c).

From e - $\log \sigma'_v$ curves, values of C_c at varied Zn concentrations were derived. The effect of Zn concentration on C_c is shown in Fig. 3. C_c of various types of structured soil have been extensively investigated. For both cemented sand (Cuccovillo and Coop 1999) and structured clay (Leroueil et al. 1983), C_c of their intact samples were significant larger than that of reconstituted ones, which can be attributed to the structural breakdown associated with greater consolidation pressure than yield stress. As indicated by Leroueil et al. (1983), at the same initial void ratio, C_c of structured clay would increase with increasing sensitivity. Since sensitivity is a widely-used indicator of soil structure or fabric, it is rational to conclude that C_c is positively related to the degree of soil structure/cementation and hence the resistance to

compression. It is apparent that, when Zn concentration is $\leq 0.1\%$, C_c remained around 0.55 and 0.60 at 7 and 28 days of curing, respectively. As summarized by Mitchell and Soga (2005), most naturally intact clays have values of C_c less than 0.5. Therefore, it appears that cement stabilized kaolin clay with low Zn concentrations have greater resistance to compression than most intact natural clays. However, when Zn concentration exceeded 0.1%, a dramatic reduction in C_c was observed regardless of the curing time. The magnitude of C_c decreased to 0.25 at 1% Zn concentration, similar to that of untreated weakly structured natural clays or remolded natural clays as reported by Mitchell and Soga (2005).

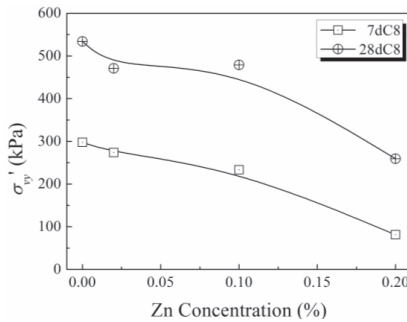


Fig. 4. Effect of initial Zn concentration on yield stresses (σ_{vy}').

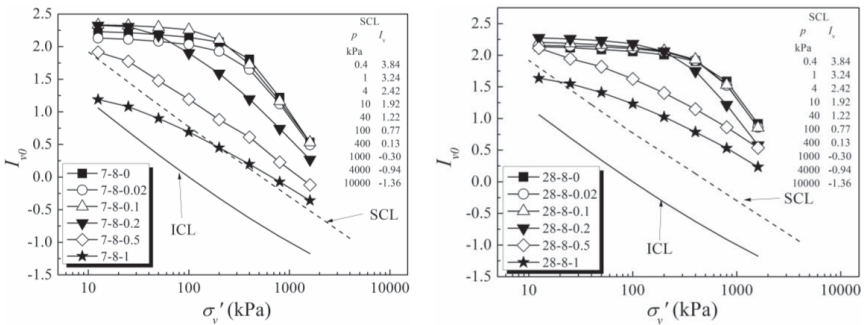


Fig. 5. Relationship between I_v and $\log \sigma_v'$: (a) 7 days; (b) 28 days.

In order to quantitatively investigate σ_{vy}' of stabilized kaolin clay at different initial Zn concentrations, data of compression tests were plotted as the $\ln(1+e)$ versus $\log \sigma_v'$. σ_{vy}' was obtained by employing the method proposed by Butterfield (1979) and its relationship with initial Zn concentration is shown in Fig. 4. Due to the fact that, at 0.5% and 1.0% Zn concentrations, σ_{vy}' were even smaller than the first incremental loading (i.e. 12.5 kPa), it could not be determined using this method. It is evident that with an increase in Zn concentration from 0% to 0.2%, σ_{vy}' decreased steadily from 550 to 270 kPa and from 300 to 100 kPa for 7 and 28 days, respectively. Since yield

marks the commencement of destruction of cementation structure/bonding, variations of σ_{vy}' in this study quantitatively demonstrate that high concentration of Zn contaminants results in lower stress threshold of breakage of cementation structure/bonding of the cement stabilized kaolin samples.

DISCUSSION

As indicated by $e-\sigma_v'$ and $e-\log\sigma_v'$ curves, high Zn concentration is prone to destruction of cementation structure/bonding within cement stabilized kaolin samples. In order to better illustrate the influence of Zn concentration on the destruction, void index (I_v), a normalized parameter proposed by Burland (1990), was introduced in this study, which can be defined by:

$$I_v = \frac{e - e_{100}^*}{e_{100}^* - e_{1000}^*} \quad (1)$$

where e_{100}^* and e_{1000}^* are the void ratios of the reconstituted soil (untreated and uncontaminated kaolin in this study) corresponding to $\sigma_v'=100$ and 1000 kPa, respectively. Empirically, e_{100}^* and e_{1000}^* can be obtained by the following equations (Burland 1990):

$$e_{100}^* = 0.109 + 0.679e_L - 0.089e_L^2 + 0.016e_L^3 \quad (2)$$

$$e_{100}^* - e_{1000}^* = 0.256e_L - 0.04 \quad (3)$$

where e_L is void ratio at liquid limit. In this study, value of e_L was obtained from based on the measured specific gravity and water content of reconstituted untreated uncontaminated pure kaolin at liquid limit.

The concept of ICL, which represents normalized compression characteristics of reconstituted natural clays, is expressed as (Burland 1990):

$$I_v = 2.45 - 1.285x + 0.015x^3 \quad (4)$$

where $x = \log \sigma_v'$. ICL and compression curves in terms of I_v in this study were shown in Fig. 5. ICL has been proved useful for the comparison of compression lines of various soil profiles and the study of one-dimensional compression behavior of structured soils in a normalized way (Burland 1990). As a reference, SCL, which represents a norm for the majority of natural deposited structured clays, is also presented in the figure.

According to Burland (1990), the difference between the locations of the compression line and ICL indicates that the soil exhibits a structured profile. The greater the difference, the more strongly structured the tested soil. Therefore, it is apparent that, under low levels of Zn concentrations ($\leq 0.1\%$), the structures of cement stabilized kaolin clay are almost immune to Zn contaminants. Nevertheless, they

become more vulnerable to destruction at high Zn concentrations (0.5% and 1.0%). Besides this, in terms of SCL, it is found that compression lines of stabilized kaolin clay lie well above the SCL, except for the case of 1% Zn concentration.

Additionally, it is apparent that compression lines of samples with low Zn concentrations ($\leq 0.1\%$) are significantly steeper than ICL at post-yield stage. It can be inferred that these compression lines tend to converge with ICL at higher vertical pressure. This behavior, according to Burland (1990), is attributed to the progressive collapse of structured soil. Hence, it can be concluded that stabilized kaolin clay has an intact structure under low Zn concentrations and thus displays a significant collapse of cementation structure/bonding at post-yield stage. On the other hand, the compression lines of samples with 0.5% and 1.0% Zn concentration almost parallel to ICL. This indicates that the structure of stabilized samples at high Zn concentrations (0.5% and 1.0%) is similar to that of reconstituted natural clays.

CONCLUSIONS

The following conclusions can be drawn from this study:

- (1) Both $e-\sigma_v'$ and $e-\log\sigma_v'$ curves confirm that high concentration of Zn ($>0.1\%$) can significantly deteriorate resistance to compression of cement stabilized kaolin clay at an initial void ratio around 1.45;
- (2) Post-yield compression index (C_c) maintained stable at Zn concentrations $\leq 0.1\%$ but exhibited significantly drop beyond this Zn concentration; yield stress (σ_{vy}') decreased gradually with increased Zn concentration;
- (3) The reduction in resistance to compression at high Zn concentrations is intrinsically attributed to destruction of cementation structure/bonding within stabilized kaolin clay, which was confirmed by the analysis in terms of void index (I_v).
- (4) Further study needs to be initiated to investigate the effect of combination of zinc and other heavy metals on the compression properties of cement stabilized soils.

ACKNOWLEDGMENTS

Majority of the work presented in this paper was funded by the National Natural Science Foundation (No. 51278100) of China, Natural Science Foundation of Jiangsu Province of China (No. BK2010060 and BK2012022), and National High Technology Research and Development Program of China (Grant No. 2013AA06A206). The authors thank Le Wang, Cheng-Xing Mei, Cheng Chen, and Xin-Tao Qiu for their work in relevant laboratory tests.

REFERENCES

- Antemir, A., Hills, C.D., Carey, P.J., Magnié, M-C., and Poletini, A. (2010). "Investigation of 4-year-old stabilised/solidified and accelerated carbonated contaminated soil." *Journal of Hazardous Materials*, Vol. 181 (1-3): 543-555.
- Boardman, D.I., Glendinning, S. and Rogers, C.D.F. (2004). "The influences of iron (III) and lead (II) contaminants on lime-stabilized clay." *Géotechnique*, Vol. 54 (7): 467-486.
- Burland, J.B. (1990). "On the compressibility and shear strength of natural clays." *Géotechnique*, Vol. 40 (3): 329-378.
- Butterfield, R. (1979). "A natural compression law for soils." *Géotechnique*, Vol. 29 (4): 469-480.
- Cuccovillo, T. and Coop, M.R. (1999). "On the mechanics of structured sands." *Géotechnique*, Vol. 49 (6): 741-760.
- Cuisinier, O., Borgne, T.L., Beneele, D., and Masroufi, F. (2011). "Quantification of the effects of nitrates, phosphates and chlorides on soil stabilization with lime and cement." *Engineering Geology*, Vol. 117 (3-4): 229-235.
- Du, Y.-J., Jiang N.-J., Shen, S.-L., and Jin, F. (2012a). "Experimental investigation of influence of acid rain on leaching and hydraulic characteristics of cement-based solidified/stabilized lead contaminated clay." *Journal of Hazardous Materials*, Vol. 225-226: 195-201.
- Du, Y.-J., Jiang, N.-J., Wang, L., and Wei, M.-L. (2012b). "Strength and microstructure characteristics of cement-based solidified/stabilized zinc-contaminated kaolin." *Chinese Journal of Geotechnical Engineering*, Vol. 34 (11): 2114-2120. (in Chinese)
- Horpibulsuk, S., Bergado, D.T. and Lorenzo, G.A. (2004). "Compressibility of cement-admixed clays at high water content." *Géotechnique*, Vol. 54 (2): 151-154.
- Leroueil, S., Tavenas, F., and Le Bihan, J.-P. (1983). "Propriétés caractéristiques des argiles de l'est du Canada." *Canadian Geotechnical Journal*, Vol 20 (4): 681-705.
- Mitchell, J.K. and Soga, K. (2005). *Fundamentals of Soil Behavior*, 3rd Edition. John Wiley & Sons, Hoboken/USA.
- Purushothama Raj, P. (2008). *Soil Mechanics & Foundation Engineering*. Dorling Kindersley (India) Pvt. Ltd, New Delhi/India.
- Rios, S., Viana da Fonseca, A., and Baudet, B. (2012). "Effect of the porosity/cement ratio on the compression of cemented soil." *Journal of Geotechnical and Geoenvironmental Engineering*, Vol. 138 (11): 1422-1426.
- Rotta, G.V., Consoli, N.C., Prietto, P.D.M., Coop, M.R., and Graham, J. (2003). "Isotropic yielding in an artificially cemented soil cured under stress." *Géotechnique*, Vol. 53 (5): 493-501.
- Sridharan, A., Rao, S.M. and Murthy, N.S. (1986). "Compressibility behavior of homoionized bentonites." *Géotechnique*, Vol. 36 (4): 551-564.
- Tremblay, H., Leroueil, S. and Locat, J. (2001). "Mechanical improvement and vertical yield stress prediction of clayey soils from eastern Canada treated with lime or cement." *Canadian Geotechnical Journal*, Vol. 38 (3): 567-579.

- United Kingdom Environment Agency (UKEA). (2004). Review of scientific literature on the use of stabilisation/solidification for the treatment of contaminated soil, solid waste and sludges. Environment Agency, Bristol/UK.
- Wei, M.-L., Du, Y.-J., and Jiang, N.-J. (2012). "Compression behavior of zinc contaminated clayey soils solidified with cement." Geotechnical Special Publication No. 225, *Proceedings of GeoCongress 2012: State of the Art and Practice in Geotechnical Engineering*, Hryciw et al. (Eds.), ASCE, Reston/USA. 4042-4049.

The role of polypropylene fibers and polypropylene geotextile in erosion control

Muawia Dafalla¹ and Ali Obaid²

¹Consultant and an Assistant Professor, BRCES, Civil Engineering, King Saud University. mdafalla@ksu.edu.sa , PO box 800, Riyadh 11421, Kingdom of Saudi Arabia.

²Graduate Student, , BRCES, Civil Engineering, King Saud University.

ABSTRACT: The geotextile industry research and development is growing at a fast rate and new products of variable specifications are now available for earthworks and design engineers. The nature of the material as a filter and the engineering properties of the materials used made it possible to explore a wide range of application. The polypropylene is non-biodegradable and can stand aggressive chemical exposure when placed inside a soil media. This research is conducted on a polypropylene geotextile material locally manufactured in order to gauge the retention capacity for a range of opening sizes. Tests were carried out using an erosion plate subjected to controlled flow for a specific period of time. Erosion loss is computed for different products and different soil material. The results were viewed in relation to the soil grain size distribution and the geotextile material physical properties. The data provides helpful guide for the design of erosion control system using typical geotextile material.

INTRODUCTION

Erosion of sloping ground is a great hazard to earth works and structures. Holding soil material in place against floods and water flow is of real concerns to engineers. This publication is suggesting the use of polypropylene fibers in several forms to control erosion. An erosion plate device introduced by the authors is used in the assessment. Using polypropylene fibers is suggested in two forms; i) adding polypropylene fibers to cement-clay paste and spraying it on surface. ii) using a polypropylene geotextile of certain properties to hold fines from passing away from upper surface of the clay. The first approach is dealt with using the engineering properties of both the fiber mesh and the soil characteristics.

EROSION MEASUREMENT DEVICE

The current study considered a bench based laboratory device (depicted in Fig. 1 and 2) designed to measure the erosion along a plane surface. This device simulates erosion occurring due to flow of water along surfaces. It is designed by Dafalla et al

(2013) to enable measurement of the influence of slopes and inclination on material loss. The flow of water is controlled using valves and flow meters attached to an open channel chamber which overflows on the test surface area. The apparatus is connected to a water supply and can provide a 5 mm head of flowing water. Water downstream of the test plate is intercepted by a fine mesh sieve to allow clear disposal of water through water drainage system.

The dimension of the plate accommodating the sample is 20cm by 30cm and lined at edges to a height of 10mm in the flow direction and 20mm in the other direction. A digital flow-meter measuring in a hundred thousandth fraction of a cubic meter is attached.

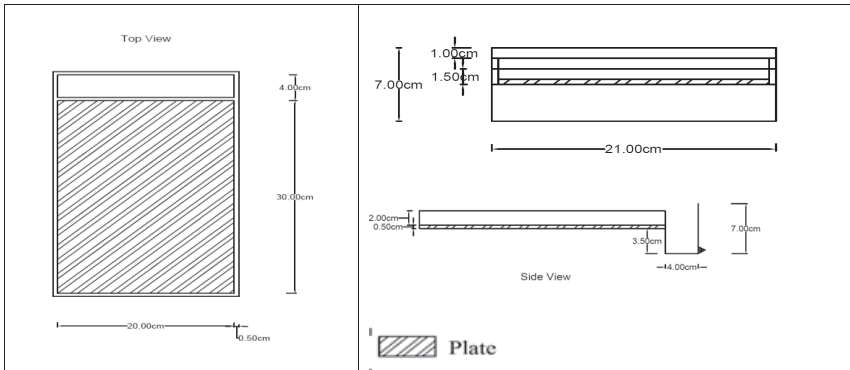


FIG. 1. Plan, front and side view of the erosion plate (Dafalla et al 2013).

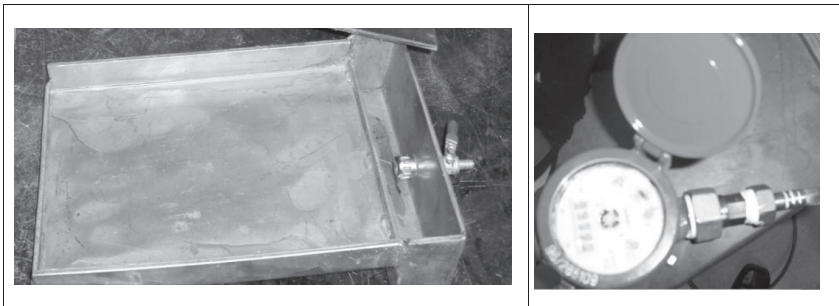


FIG.2. Top view of erosion plate and flow-meter used in testing. (Dafalla et al 2013).

Works of Long and Demars, (2004 and 2005) and studies of Musgrave (1947) were viewed for developing this testing approach.

EXPERIMENTAL PROGRAM

Material and Sample Preparation

The clay soil used for testing in this study was brought from Al-Qatif town in Eastern Province of Saudi Arabia. The sand material used is typical fine grained sand used in construction in the country. As the research project was targeting clay sand mixtures for use as hydraulic barriers, characterization tests were carried out for both clay and sand material. Routine classification tests included gradation, liquid limit, and plastic limit tests. The clay material was found to have high liquid limit and plastic limit and classified within CH group in accordance with the Unified Soil Classification System. Physical and chemical properties of Al Qatif clay are given in Table 1 and 2 respectively.

Table 1. The Physical Properties of Al-Qatif Clay.

| Property | Range |
|-----------------------------------|--|
| Material passing sieve number 200 | >90% |
| Liquid Limit | 130-150 |
| Plastic Limit | 60 -70 |
| Plasticity Index | 70- 80 |
| Maximum Dry density | 1.150 – 1.200 gm/cm ³ |
| Optimum Moisture Content | 32- 40%. |
| Swell Per cent (ASTM D4546) | 16-18% |
| Swelling pressure (ASTM D4546) | 5.0-8.0 gm/cm ³ ($\gamma = 1.2$ gm/cm ³) |

(after Dafalla et al 2013)

Table 2. Chemical composition of Al-Qatif clay.

| K ⁺ (%) | K ₂ O (%) | Al (%) | Al ₂ O ₃ (%) | Si (%) | SiO ₂ (%) | Ca ⁺² (%) | CaO (%) |
|--------------------|----------------------|--------|------------------------------------|--------|----------------------|----------------------|---------|
| 1.8 | 2.2 | 3.3 | 6.3 | 8.1 | 17.3 | 0.7 | 0.9 |

(after Dafalla et al 2013)

The fine grained sand mixed with 10% clay was investigated for compaction properties. Standard compaction tests were carried out in accordance with ASTM D 698 to establish the compaction characteristics of the sand-clay mixture used. The results of the tests are shown in Fig. 3. Trials made to investigate different ranges of clay content indicated that adding clay contributes in increasing the maximum dry density of the mixture and rendered the optimum moisture content increase and shift towards the right of the curve. This is only valid when the amount of clay added is not exceeding the volume of voids within the sand (Dafalla et al, 2013).

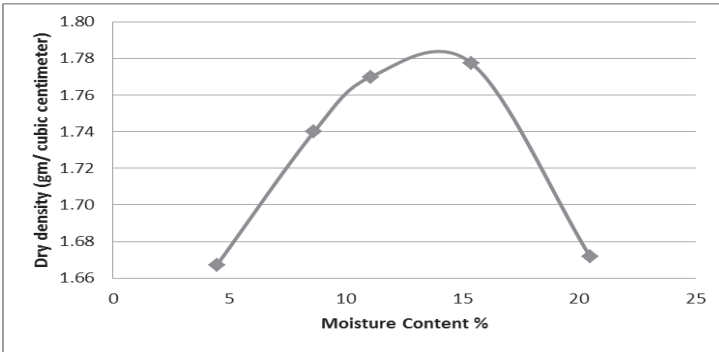


Fig.3. Dry density moisture content relationship of the sand -clay mixture

The polypropylene fiber material:

The polypropylene material used in this study takes two forms: The first one is 12mm in length produced by a United Kingdom manufacturer (Propex concrete systems). It can be described as a fine monofilament with a melting point of 162 °C (324 ° F) and ignition point of 593 °C (1100 ° F). The material is of low electrical and thermal conductivity. The specific gravity is on the order of 0.91.

The polypropylene geotextile material is supplied by a local Saudi manufacturer (Alyaf). Table 3 shows the main properties of the material used.

Table 3. The main properties of Geotextile XS 23(ALYAF)

| Property | Test Method | Unit | Result |
|------------------|---------------|--------------------------|--------|
| Tensile strength | EN ISO 10319 | kN/m | 11 |
| Elongation | EN ISO 10319 | % | 50/45 |
| Permeability | EN 11058 | m/sec x 10 ⁻³ | 100 |
| Opening size | EN ISO 12956 | microns | 100 |
| Thickness | EN ISO 9863-1 | mm | 1.15 |



Fig. 4. Views of treated and untreated clay-cement grout samples



Fig. 5. Sample Views of untreated clay-cement grout shrinkage molds

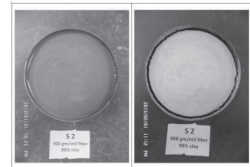


Fig. 6. Sample Views of polypropylene treated clay-cement grout shrinkage molds

Testing Procedure

The erosion plate was equipped with spacer rods at one side to create the required testing slope. The modelled slope for this experiment was 10%. This slope is selected as being relevant to hydraulic barriers over highly permeable ground. The samples were placed on the erosion plate by tamping the material uniformly using a rod after spraying a pre-calculated quantity of soil, mixed thoroughly at specific moisture content and left for 24 hours in a desiccator. Tamping continues until the required molding dry density is achieved. The dry weight and moisture of the soil were reported prior to flooding the soil. The erosion plate attached with an open channel was fed by a plastic hose connected to tap water. A flow meter and control valves were fitted along the plastic hose. The valves were used to adjust the flowing water to a level of approximately 5mm above the tested soil. Stop watch for time control was used and the quantity of water used was recorded. On completion of the test, the material remaining within the plate is collected and weighed in wet and oven dry state. The loss of dry soil material was quoted as the erosion loss. Erosion loss was measured for a sand-clay mixture of 10% clay at a 10% slope. In order to examine the effect of cement based grout material placed on sand clay mixture the same test was repeated and erosion loss was reported.

Adding a cement grout of 15% clay (by weight of cement) and a water grout ratio of 1:1 was considered. The test is also repeated for a clay-cement grout reinforced with 900 gm/m³ polypropylene fiber (This was chosen after trials of different fiber content).

In order to assess the use of polypropylene geotextile mesh in reducing erosion, the test is repeated for the same soil mixture covered by the polypropylene geotextile only.

TEST RESULTS AND DISCUSSION

Polymers in different forms are widely used in geotechnical, environmental and hydraulic applications (Bouazza et al., 2006). Polypropylene fiber products are introduced in construction industry to serve several applications. These include reinforcement, filtration and separation. Erosion control as dealt with in this study is served in two ways; reinforcement of a grout material covering the surface or using a woven or non-woven geotextile material to hold fines from passing away with flow. The shrinkage and expansion of clay are strongly related to erosion of near surface soils as cracks help in disintegration and wash away of fine soil material.

The test results indicated that grouts prepared at different clay-cement content behave differently with regard to shrinkage. It is reported that the more the clay the higher change in mold diameter. The role of polypropylene fiber was dependent on the fiber content. Optimum fiber content is believed to be ideal in reducing shrinkage. Low fiber content as 600 gm/m³ was found to cause shrinkage to increase for nearly all clay-cement mixtures. The same trend is reported for fiber rich mix of 1200 gm/m³. The 900 gm/m³ was found to be the optimum fiber content for reducing shrinkage and indicated reduction of shrinkage for all clay-cement content tested. The tested fiber length used in this study was 12mm and the length of fibers can also have a role in controlling the shrinkage, but this effect will be investigated in a later stage of this research. Since clay cement grouts are considered for erosion protection, shrinkage is the main source of cracking.

Adding fibers is looked at as a process to reduce or eliminate cracking but at the same time can add to erosion loss by creating loose lines of contact between fibers and soils. This will make room for extra water flow. The use of fiber reinforced grout was found to reduce erosion loss from 86% to 63%. This figure indicates less rating than the grout alone but this expected to be more durable and serve longer. The bond between clay and cement for untreated grout can be reduced and more scour and get worse by time while the fiber reinforced grout is likely to keep opening smaller as reflected from shrinkage control tests. The testing presented in this paper is aimed at providing a general guide and preliminary data and more testing is planned in this area. Table 4 presents the reduction in diameter as measured for a range of fiber content. Figure 7 presents a bar diagram to compare the data obtained.

The polypropylene geotextile placed on the erosion plate was found to give equivalent erosion reduction as for the cement-clay grout. The opening size of the geotextile is playing a significant role in erosion loss. Smaller opening size is expected to perform better but will cost more in material and will have more thickness. Table 5 presents the percentage of erosion loss for three different erosion protection arrangements as compared to soil without erosion protection. Fig 8 presents a bar diagram for three methods employed.

Table 4. Reduction in diameter due to grout shrinkage.

| Clay % | 0 gm/ m ³ fiber (mm) | 600 gm/ m ³ fiber (mm) | 900 gm/ m ³ fiber (mm) | 1200 gm/ m ³ fiber (mm) |
|--------|---------------------------------|-----------------------------------|-----------------------------------|------------------------------------|
| 15% | 1.41 | 1.75 | 1.2 | 1.78 |
| 30% | 2.02 | 2.71 | 1.75 | 2.7 |
| 45% | 3.09 | 3.17 | 2.42 | 3.48 |
| 60% | 3.87 | 4.19 | 3.27 | 4.54 |
| 75% | 4.47 | 4.2 | 4.24 | 4.37 |
| 90% | 5.5 | 5.15 | 5.07 | 6.05 |

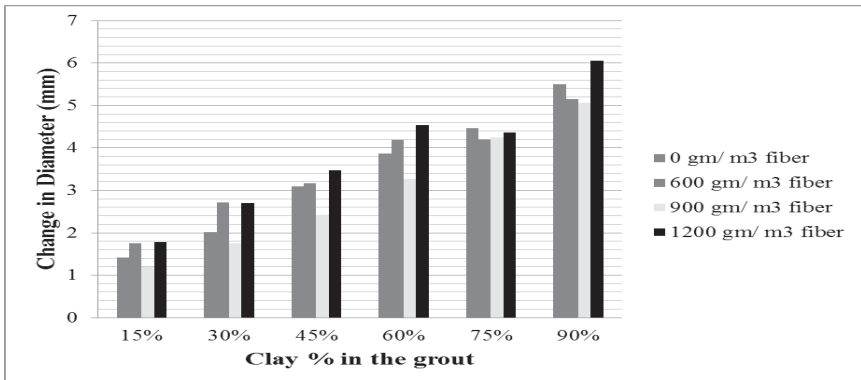


Fig. 7 Change in diameter due to shrinkage of grout with different polypropylene fiber content

Table 5. Percentage erosion loss of treated and untreated soils.

| Tested material | Slope | Initial dry weight (gm) | Water flow-meter (c.c) | Erosion loss (gm) | Percentage of loss |
|--|-------|-------------------------|------------------------|-------------------|--------------------|
| Sand +10% clay | 10% | 1097 | 0.160 | 943.19 | 86% |
| Grout-treated Sand+10% clay | 10% | 1109 | 0.218 | 591.61 | 53% |
| Grout and fiber treated Sand+10% clay | 10% | 1072 | 0.184 | 677.7 | 63% |
| Geotextile fiber treated Sand+10% clay | 10% | 1081 | 0.176 | 567.54 | 53% |

Notes : a- 1 hour of flow for all tests. b- Grout- treated means the sloping soil is covered by cement-clay grout.

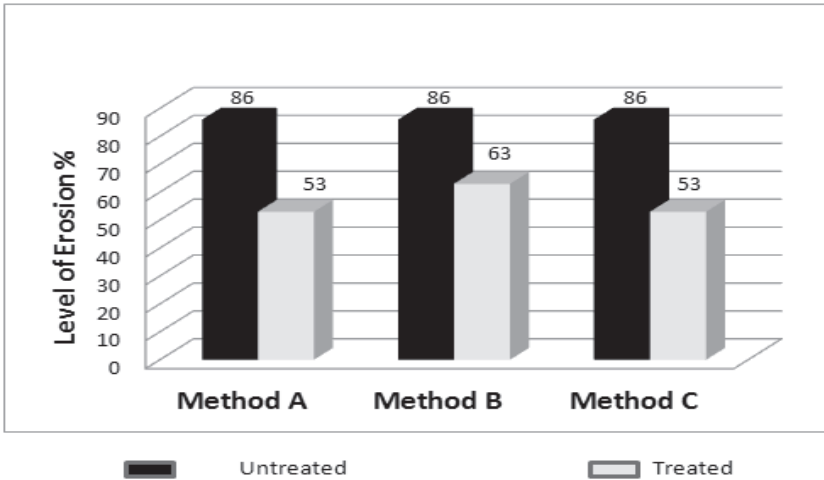


Fig. 8 Erosion results using Method A; clay-cement grout , Method B; clay cement grout with fibers and Method C; geotextile fibre

CONCLUSIONS

Adding a cement grout of 15% clay (by weight of cement) and a water grout ratio of 1:1 can reduce erosion in sand-Al-Qatif clay mixtures. Polypropylene can be used to arrest erosion. This can be achieved either by adding polypropylene fibers to a

cement-clay grout or by using a mesh of polypropylene geotextile material. Low fiber content as 600 gm/m^3 was found to cause shrinkage to increase for nearly all clay-cement mixtures. The same trend is reported for fiber rich mix of 1200 gm/m^3 . The 900 gm/m^3 was found to be the optimum and indicated reduction of shrinkage for all clay-cement content. The erosion reduction was found significant for a material with opening size of 100 micron for the material tested. Smaller opening size can better control erosion but is expected to add to the cost.

ACKNOWLEDGMENTS

This work is part of a research project supported through NPST program by King Saud University. The authors also thank the staff of Bugshan Research Chair in Expansive Soils for their help and support.

REFERENCES

- ASTM D4546-08 (2000). "Standard Test Methods for One-Dimensional Swell or Collapse of Cohesive Soils." *American Society for Testing and Materials*.
- ASTM D 698-02 (2000). "Standard Test Methods for Laboratory Compaction Characteristics of Soil Using Standard Effort (12 400 ft lbf/ft³ (600 kN m/m³))." *Annual book of ASTM Standards*, West Conshohocken, PA, Vol. 15.09.
- ASTM D 6459-99 (2000), "Standard Test Method for Determination of Erosion Control Blanket (EBC) Performance in Protecting Hill slopes from Rainfall-Induced Erosion," *American Society for Testing and Materials*, Philadelphia.
- ASTM D 6460-99 (2000). "Standard Test Method for Determination of Erosion Control Blanket (EBC) Performance in Protecting Earthen Channels from Stormwater Induced Erosion." *American Society for Testing and Materials*, Philadelphia.
- Dafalla, M.A., Al-Shamrani, M.A. and Obaid, A. (2013). Reducing Erosion Along the Surface of Sloping Clay-sand Liners. *Proceedings of Geocongress 2013*, San Diego, USA.
- Dafalla, M.A., Elkady, T.Y., Al-Shamrani, M.A. and Shaker, A. (2013). An Approach to Rank Local Clays for Use in Sand-Clay Liners. *Proceedings of ICGE 2013, International Conference of Geotechnical Engineering*. Tunisia.
- Bouazza, A., Freund, M., Nahlawi, H., 2006. Water retention of nonwoven polyester geotextiles. *Polymer Testing* 25, 1038e1043.
- Long, R. P. and K. R. Demars, (2004). "Feasibility Study of an Erosion Control Laboratory in New England." *New England Transportation Consortium Report NETCR 49*, December 2004, 61 p.
- Long, R. P. and K. R. Demars, 2005. "Design Considerations for a Prototype Erosion Control Testing Plot." *New England Transportation Consortium Report NETCR 56*, Project No. 03-3, December 2005.
- Musgrave, G. W. (1947). "A Quantitative Evaluation of Factors in Water Erosion. A First Approximation." *J. of Soil Water Conservation*, 2:133-138, 170.
- Mutaz E. (2011). "Chemical treatment of moderate to highly expansive clays." *MSC. Dissertation Civil Engineering, King Saud University, Saudi Arabia*.

Lateral Load on a Large Pile Group: A 3D Finite Element Model

Ning Wang¹, Jinchi Lu¹ and Ahmed Elgamal²

¹ Graduate Student Researcher, Dept. of Structural Engineering, Univ. of California, San Diego, La Jolla, CA 92093-0085. E-mail: n9wang@ucsd.edu

¹ Assistant Project Scientist, Dept. of Structural Engineering, Univ. of California, San Diego, La Jolla, CA 92093-0085. E-mail: jinlu@ucsd.edu

² Professor, Dept. of Structural Engineering, Univ. of California, San Diego, La Jolla, CA 92093-0085 (corresponding author). E-mail: elgamal@ucsd.edu

ABSTRACT: Practice shows that the analysis of laterally loaded pile foundations is critically important. For years, numerous experimental, theoretical and numerical investigations have been conducted to predict the behavior of such systems. In this paper, we are describing a computational study to investigate large pile-ground system response under lateral load based on 3 dimensional (3D) OpenSees finite element modeling. Primarily, pile group behavior in nonlinear soil with and without a tension-cutoff logic is discussed. Distribution of load within the pile group is analyzed and the group interaction effects are examined. A robust and versatile framework (OpenSeesPL, <http://cyclic.ucsd.edu/openseespl/>) for computational analysis of pile-ground systems is employed to facilitate the pre- and post-processing phases. Further validation and calibration of the analysis framework may be conducted with the aid of case histories and experimental data.

INTRODUCTION

Soil-structure interaction (SSI) plays a major role in the lateral response of structures to earthquakes. In order to satisfactorily reproduce such SSI effects computationally, it is often necessary to model a large domain of the soil surrounding the structure of interest. With the developments in material modeling techniques and high-speed efficient computers, linear and nonlinear three-dimensional (3D) finite-element (FE) methods are becoming a promising technique for understanding the involved SSI mechanisms (Chae et al. 2004; Dodds 2005; Elgamal et al. 2008, 2009b, 2010; Elgamal and Lu 2009; Lu et al. 2010; Maheshwari et al. 2004; Muqtadir and Desai 1986). In particular, special attention is given to the soil-pile response mechanisms and the pile group interaction effects. Pressley and Poulos (1986) employed an axially symmetric model to study group effects. Brown and Shie (1990) conducted a series of 3D FE studies on the behavior of single piles and closely spaced pile groups. Wakai et al. (1999) studied the behavior of free- and fixed-head 3×3 pile groups based on model

tests. Yang and Jeremic (2003) simulated the response of 3×3 and 4×3 pile groups in loose and medium dense sands and investigated the interaction effects for large pile groups.

This paper presents a systematic 3D FE study of a large pile group under lateral loading, embedded into a nonlinear soil domain (with an implemented tension cut-off logic). The piles are modeled by beam-column elements, and rigid beam-column elements are used to model the pile size (diameter). For comparison, a representative single-pile reference simulation is also studied. The open-source computational platform OpenSees (Mazzoni et al. 2006) is employed to conduct the 3D FE analysis. In order to facilitate the pre- and post-processing phases, a recently developed user interface OpenSeesPL (FIG. 1) is employed (Lu et al. 2006, Elgamal et al. 2009a). Along with the insights gained from these studies, the reported effort aims to highlight the analysis framework capabilities and range of potential applications.

COMPUTATIONAL FRAMEWORK

The Open System for Earthquake Engineering Simulation (OpenSees), an open-source platform developed for simulation of structural and geotechnical systems subjected to seismic load (<http://opensees.berkeley.edu>, Mazzoni et al. 2006) is employed throughout. The reported pre- and post-processing scenarios were generated by the user interface OpenSeesPL (FIG. 1) which allows for: i) convenient generation of the mesh (for surface load/footing, single pile, or pile group), associated boundary conditions, and soil/pile linear/nonlinear (e.g., Yang et al. 2003; Elgamal et al. 2008) material modeling parameters (i.e., the FE input file), ii) execution of the computations using the OpenSees platform, iii) single pile and pile group simulations under seismic excitation as well as push-over studies in prescribed displacement or prescribed force modes, iv) study of various ground modification scenarios by appropriate specification of the material within the pile zone (Elgamal et al. 2009b, Rayamajhi et al. 2012), and v) graphical display of the results for the footing/pile and the ground system (Elgamal et al. 2009a).

PILE GROUP CONFIGURATION AT DUMBARTON BRIDGE PIER 23

A model that is representative of salient characteristics of the Dumbarton Bridge (California) Pier 23 pile-group foundation geometry was studied (FIG. 2). The pile group is configured in an 8 x 4 arrangement with a longitudinal spacing of 2 pile diameters and a transversal spacing of 2.15 pile diameters on center. Each pile is 1.37 m in diameter and 30.8 m long. The group is rigidly connected by a pile cap 14.3 m above the mudline. A vertical load of 28,900 kN was estimated to represent the tributary own weight of the bridge deck.

Each concrete pile is encased by a prestressed concrete shell, with a wall thickness $h = 0.1778$ m. The effective bending stiffness for each pile was modeled as $EI = 2 \times 10^6$ kN-m² (Wang 2013), and pile response was assumed to remain linear.

As modeled in this study (Table 1), the upper 2 layers were 6.7 m each in thickness and the bottom layer had a thickness of 30.5 m. The pressure-independent (J_2) multi-yield surface plasticity model in OpenSees was employed in which a hyperbolic

relationship describes the soil shear stress-strain backbone response. A Poisson’s ratio of 0.4 was specified for all layers. In this soil model, the influence of an imposed no-tension strength cutoff (FIG. 3a and b) can be activated (where shear strength vanishes upon occurrence of tensile effective confinement).

In the employed 1/2 mesh of FIG. 3c (due to symmetry), the vertical dead load was imposed initially (after applying the soil domain own weight). A lateral pile cap longitudinal displacement was then applied (at the center of the pile cap) up to a maximum of 0.30 m in 30 steps, in order to clearly demonstrate the effects of nonlinear soil response. In the section below, results from the following three different computational simulations are contrasted: linear soil, nonlinear soil, and nonlinear soil with tension-cutoff.

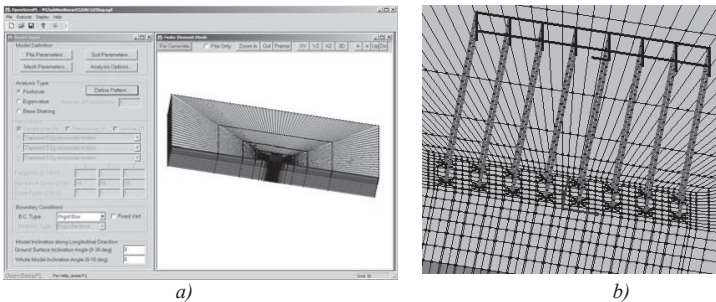


FIG. 1. OpenSeesPL user interface with a) finite element mesh; b) close-up of pile group; (Lu et al. 2006, <http://cyclic.ucsd.edu/openseespl/>).



FIG. 2. Dumbarton Bridge (<http://www.mtc.ca.gov>) and soil profile at Pier 23.

Table 1. Soil Material Properties

| Material Property | Top layer | Middle layer | Bottom layer |
|--|-----------|--------------|--------------|
| Thickness (m) | 6.7 | 6.7 | 30.5 |
| Mass density (kg/m ³) | 1300 | 1500 | 1800 |
| Shear wave velocity (m/s) | 120 | 250 | 300 |
| Shear strength (kPa) at a specified octahedral shear strain $\gamma_{max} = 3\%$ (based on triaxial compression) | 25 | 60 | 75 |

FINITE ELEMENT MODEL

In FIG. 3, length of the mesh in the longitudinal direction is 393 m, with 191 m transversally (in this half-mesh configuration, resulting in a 393 m x 382 m soil domain in plan view). Total layer thickness was 43.9 m (the base of the soil domain is 27.4 m below the pile tip). The soil domain was modeled by eight-node brick elements (23,040 in total) and the piles were modeled by beam-column elements (512 in total). Rigid beam-column elements (1,664 in total) were used around each pile to model the actual circumferential pile size (diameter). For comparison, a fixed head single pile was studied with the same geometrical and material properties and a vertical dead load of -903.5 kN (= -28900 kN / 32 piles).

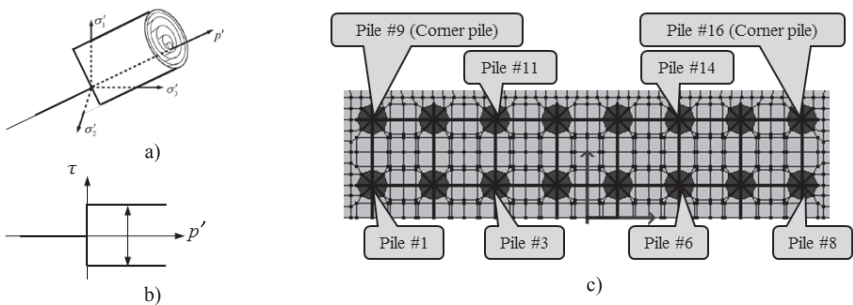


FIG. 3. a) Multi-surface plasticity J_2 model (Yang and Elgamal 2003); b) Illustration of tension-cutoff logic during tensile confinement; c) Plan view of pile group layout (back piles are 1 and 9 and front piles are 8 and 16).

SUMMARY OF MAIN RESULTS

FIG. 4 shows lateral load versus displacement for the entire pile group at the pile cap elevation. In this figure, average load is shown for the pile group (total pile-group load/32 piles). This average load corresponds to a total pile group load of 19,518 kN (i.e., approximately 70% of the bridge own weight is applied laterally) at the pile cap longitudinal displacement of 0.30 m (tension-cutoff scenario). At this level of displacement, pile-group lateral force in the tension cutoff case is about 92% of the nonlinear and 50% of the linear analysis case. Compared to the single pile scenario, it may be concluded (tension-cutoff scenario) that the pile group load efficiency η_e (lateral resistance of the pile group versus that of the single pile at equal levels of final deflection) for this case is $19518 / (909.9 \times 32) = 0.67$ which agrees well with efficiencies obtained from experimental studies under the maximum applied load (e.g. η_e in the range of 0.5 - 0.68 based on full-scale experiments of Brown et al. 1987 and Rollins et al. 1998). In the nonlinear simulations (FIG. 4), it might be noted that the tension-cutoff logic has a large impact on the single pile response, compared with that of the pile group.

The final deformed mesh is shown along with the stress-ratio contour fill (red color shows yielded soil elements) for the nonlinear soil (FIG. 5a) and the tension-cutoff (FIG. 5b) cases. As expected, more soil behind the pile group is clearly engaged in the case without the tension cutoff logic. Along with translation, the pile group is seen to

also undergo some overall rotation for both cases.

As for the pile displacements at the mudline at the 0.30 m pile cap longitudinal displacement, inner piles (2-5) experience the most lateral movement whereas the corner front pile 16 translates the least due to the resistance provided by the surrounding soil (FIG. 6). The tension-cutoff scenario allows the back piles to move a bit easier with the movement of piles 2-5 and 10-13.

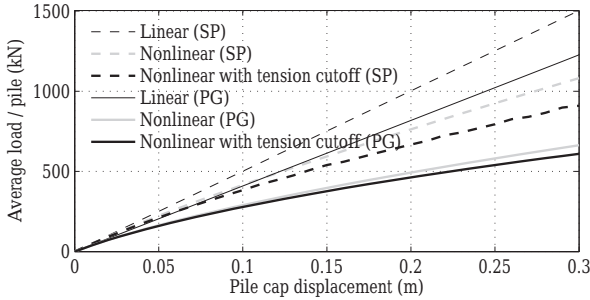


FIG. 4. Average longitudinal shear load at pile head versus displacement curve.

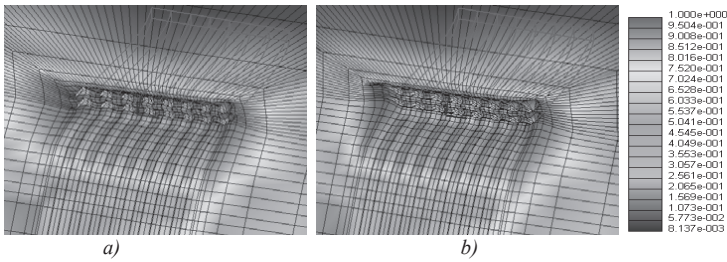


FIG. 5. Final deformed mesh (factor of 30): shear stress ratio contour (red color shows yielded soil elements), a) nonlinear soil; b) nonlinear with tension cutoff.

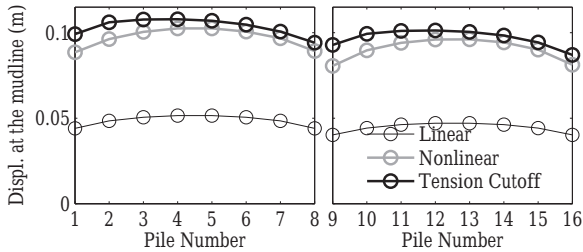


FIG. 6. Displacement at the mudline at 0.3 m pile cap deflection.

At the 0.30 m pile cap longitudinal displacement, the corresponding shear force and bending moment distribution between piles in the pile group are shown in FIG. 7. The outer (corner) front pile (pile 16) carries the highest portion of shear force and bending moment. The edge front pile 8, and back piles 1 and 9 also sustain relatively higher levels of load. Conversely, the inner piles (3-6) carry the least burden (about 80% of the share of pile 16 approximately).

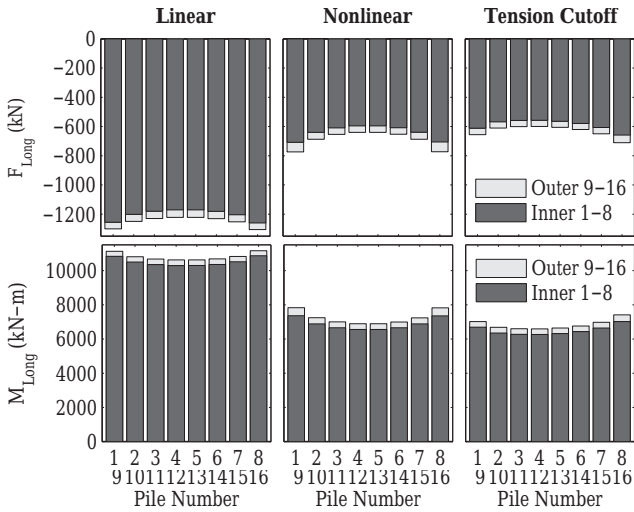


FIG. 7. Shear force and bending moment at the 0.3 m pile cap deflection.

Axial force distribution between piles in the pile group is shown in FIG. 8. Even in the initial axial load static state, the share of each pile varies in a wide range. Piles along the circumference carry most of the load and the corner piles shoulder the biggest burden. At the prescribed 0.30m pile cap displacement, the compressive axial forces increase dramatically in the front piles (6-8 and 14-16). Conversely, the back piles experience tensile forces in the range of 0.5-1.2 of the initial static compressive force.

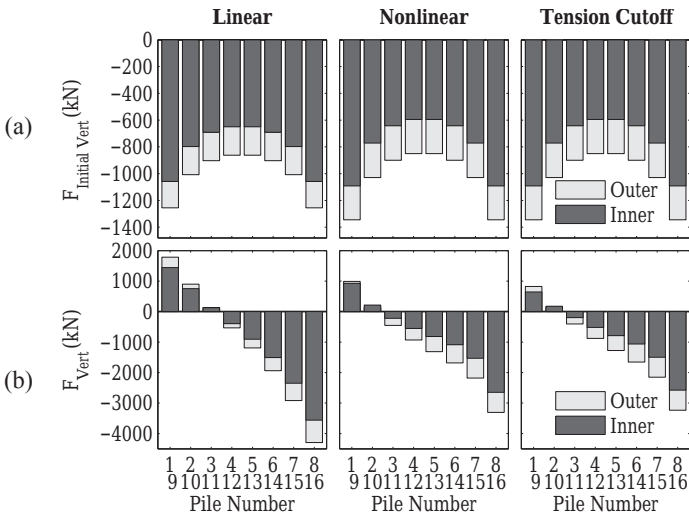


FIG. 8. Pile axial forces: (a) at the initial vertical dead load and (b) after application of the 0.30 m lateral pile cap deflection.

CONCLUSIONS

A pilot computational study of a large pile group system under lateral load was presented. An idealized linear-behavior pile group model was assumed, embedded within a 3-layer stratified soil stratum represented by linear as well as nonlinear J_2 elasto-plastic behavior. A tension cut-off shear strength logic was also exercised. A single pile scenario was studied for comparison. The open-source platform OpenSees was employed throughout. The reported pre- and post-processing scenarios were generated by a robust user interface OpenSeesPL for analysis of pile-group systems (<http://cyclic.ucsd.edu/openseespl>). Overall, the computed results indicate:

1. At an equal level of applied longitudinal displacement, a large soil domain surrounding the pile group was engaged with substantial potential yielding (compared to the single pile scenario).
2. With the tension-cutoff logic activated, a reduction in shear force and moment was noted in the back piles.
3. In the conducted study with close pile spacing (2 pile diameters), piles along the circumference of the 8 x 4 pile group carried much of the axial load (Scott 1981).
4. Due to application of lateral load, back piles may experience a significant reduction in compressive axial load, resulting eventually in possible tensile axial forces. This may in turn adversely affect the reinforced concrete pile bending stiffness and strength.

Generally, the conducted investigations bring insight into the behavior of a large pile group under axial/lateral load. Additional field data and numerical/experimental investigations will help to further refine and verify the presented analysis procedures.

ACKNOWLEDGMENTS

The authors are grateful for the funding provided by the Pacific Earthquake Engineering Research (PEER) Center, and the NSF grant No. CMMI-1201195.

REFERENCES

- Brown, D. A., and Shie, C.-F. (1990). "Numerical experiments into group effects on the response of piles to lateral loading." *Computers and Geotech.*, 10(3), 211-230.
- Chae, K. S., Ugai, K., and Wakai, A. (2004). "Lateral resistance of short single piles and pile groups located near slopes." *Int. J. of Geomechanics*, 4(2), 93-103.
- Brown, D. A., Reese, L. C., and O'Neill, M. W. (1987). "Cyclic lateral loading of a large-scale pile group." *J. of Geotechnical Engineering*, 113(11), 1326-1343.
- Dodds, A.M. (2005). "A numerical study of pile behavior in large pile groups under lateral loading." *PhD Dissertation*, Univ. of Southern California, Los Angeles.
- Elgamal, A., Yang, Z. H., Parra, E., and Ragheb, A. (2003). "Modeling of cyclic mobility in saturated cohesionless soils," *Int. J. Plasticity*, 19(6), 883-905.
- Elgamal, A., Yan, L., Yang, Z., and Conte, J. P. (2008). "3D seismic response of Humboldt Bay bridge-foundation-ground system." *J. Struct. Eng.*, 134(7), 1165.
- Elgamal, A., and Lu, J. (2009). "A framework for 3D finite element analysis of lateral pile system response." *Contemporary Topics in In Situ Testing, Analysis, and Reliability of Foundations*, ASCE GSP 186, 616-623.

- Elgamal, A., Lu, J., Yang, Z., and Shantz, T. (2009a). "Scenario-focused three-dimensional computational modeling in Geomechanics." *Alexandria, Egypt, 4 iYGE'09 - 4th Intl Young Geotech. Engineers' Conference, 2-6 October*, ISSMGE.
- Elgamal, A., Lu, J., and Forcellini, D. (2009b). "Mitigation of liquefaction-induced lateral deformation in a sloping stratum: 3D numerical simulation." *J. Geotech. Geoenviron. Eng.*, 135(11), 1672-1682.
- Elgamal, A., Yan, L., Lu, J., Yang, Z., Shantz, T., and Conte, J.P. (2010). "Computational modeling of soil-foundation structural systems." *Proc., the 9th US National and 10th Canadian Conf. on Earthq. Eng.*, Toronto, Canada, July 25-29.
- Rayamajhi, D., Nguyen, T.V., Ashford, S.A., Boulanger, R.W., Lu, J., Elgamal, A., and Shao, L. (2012). "Effect of discrete columns on shear stress distribution in liquefiable soil." *Proc., Geo-Congress 2012*, ASCE GSP 225, 1908-1917.
- Lu, J., Yang, Z., and Elgamal, A. (2006). "OpenSeesPL three-dimensional lateral pile-ground interaction version 1.00 user's manual", Report No. SSRP-06/03, Department of Structural Engineering, University of California, San Diego.
- Lu, J., Elgamal, A., Sikorsky, C., and Shantz, T. (2010). "Computational modeling of a large pile group under lateral load." *Proc., 5th International Conf. on Recent Advances in Geotech. Earthq. Eng and Soil Dyn*, San Diego, CA.
- Maheshwari, B. K., Truman, K. Z., El Naggari, M. H., and Gould, P. L. (2004). "Three-dimensional nonlinear analysis for seismic soil-pile-structure interaction." *Soil Dynamics and Earthquake Engineering*, 24(4), 343-356.
- Mazzoni, S., McKenna, F., and Fenves, G. L. (2006). "Open system for earthquake engineering simulation user manual", Pacific Earthquake Engineering Research Center, University of California, Berkeley (<http://opensees.berkeley.edu/>).
- Muqtadir, A., and Desai, C. S. (1986). "Three-dimensional analysis of a pile-group foundation." *Int. J. for Numer. and Anal. Meth. in Geomech.*, 10(1), 41-58.
- Pressley, J. S., and Poulos, H. G. (1986). "Finite element analysis of mechanisms of pile group behavior." *Int. J. for Numer. and Anal. Meth. in Geomech.*, 10, 213-221.
- Rollins, K. M., Peterson, K. T., and Weaver, T. J. (1998). "Lateral load behavior of full-scale pile group in clay." *J. of Geotech. and Geoenv. Eng.*, 124(6), 468-478.
- Scott, R.F. (1981). "Foundation analysis." Prentice Hall, Englewood Cliffs, NJ.
- Wakai, A., Gose, S., and Ugai, K. (1999). "3-D elasto-plastic finite element analyses of pile foundations subjected to lateral loading." *Soils&Foundations*, 39(1), 97-111.
- Wang, N. (2013). "Soil structure interaction for deep foundation systems," PhD Thesis, Dept of Structural Engineering, UC San Diego, in preparation (expected).
- Yang, Z., Elgamal, A., and Parra, E. (2003). "A computational model for cyclic mobility and associated shear deformation", *J. of Geotech. & Geoenv. Eng.*, 129(12), 1119-1127.
- Yang, Z., and Jeremic, B. (2003). "Numerical study of group effects for pile groups in sands." *Int. J. for Numer. and Analyt. Meth. in Geomech.*, 27(15), 1255-1276.

Evaluation of Effective Soil Density in Resonant Column Tests

Yanbo Huang¹ and Tong Qiu², P.E., M.ASCE

¹Graduate Research Assistant, Department of Civil and Environmental Engineering, The Pennsylvania State University, University Park, PA 16802, USA; Email: yvh5117@psu.edu

²Assistant Professor, Department of Civil and Environmental Engineering, The Pennsylvania State University, University Park, PA 16802, USA; Email: tqiu@engr.psu.edu (corresponding author)

ABSTRACT: This paper presents a theoretical study of effective soil density for small-strain shear wave propagation in saturated soil specimens in resonant column tests. Effective soil density is a term used to consider the fraction of pore water that moves with the solid skeleton during shear wave propagation. The ratio of effective soil density to saturated soil density is always ≤ 1 and is a function of porosity, specific gravity of solids, hydraulic conductivity, and shear wave frequency. In resonant column tests, the transition of effective density from the maximum value (i.e., saturated density) to the minimum value occurs primarily in coarse sands; in this region, the consideration of effective density is important in capturing the first resonance and interpreting resonant column test results. For soils less permeable than coarse sands (e.g., clays, silts, and fine sands), the consideration of effective density is not important and the saturated density can be used. For soils more permeable than coarse sands (e.g., gravels), the effective density is significantly less than the saturated density.

INTRODUCTION

Shear modulus G and shear wave velocity V are important soil dynamic properties and are often used as input parameters for various analyses in geotechnical earthquake engineering (e.g., ground motion analysis). In current research and practice, G is often calculated based on measured V in laboratory tests (e.g., resonant column tests) or field tests (e.g., seismic cone penetration tests) according to the following equation

$$G = \rho V^2 \quad (1)$$

where ρ is soil density. The use of Eq. (1) for multiphase soils requires an assumption regarding soil density. In current research and practice, the dry density ρ_d and saturated density ρ_{sat} are generally used for the cases of dry soil and

saturated soil, respectively. It is justifiable for the former case as the density of air is negligible; however, the validity of the latter case depends on the relative motion between the solid phase and fluid phase during the passage of a shear wave. If the relative motion is negligible, ρ_{sat} can be used without significant error; if the relative motion is not negligible, however, the use of ρ_{sat} in Eq. (1) may result in significant error in the calculated G (Qiu and Fox 2008a). To account for the effect of fluid-solid relative motion on soil density in Eq. (1), Qiu and Fox (2008a) introduced the concept of effective soil density ρ_{eff} , which is related to the fraction of pore water that moves with the solid skeleton during shear wave propagation and is defined as

$$G = \rho_{eff} V^2 \quad (2)$$

Based on Biot theory (Biot 1956), Qiu and Fox (2008a) provided an analytical solution for ρ_{eff} . Their solution suggests that the effective density ratio (i.e., ρ_{eff} / ρ_{sat}) is ≤ 1 and is a function of specific gravity of solids, porosity, hydraulic conductivity, and shear wave frequency. Their solution demonstrates that consideration of effective density is not important for clays and is unlikely to be important for silts unless the shear wave frequency is very high (e.g., > 10 kHz). For clean sands and gravels, consideration of effective density is important for all frequencies of geotechnical interest. When shear wave velocities from field tests such as the seismic cone penetration tests are available, Qiu and Fox's solution of effective soil density can be directly used to determine G using Eq. (2). As an extension to Qiu and Fox (2008a) and Qiu (2010), this paper presents a theoretical study to evaluate effective soil density in saturated soil specimens during resonant column tests. In the following sections, the solution for resonant frequency in a saturated soil specimen is first derived based on Biot theory, followed by the derivation of effective density based on the resonant frequency obtained.

RESONANT FREQUENCY

Following Biot theory (Biot 1956) and Qiu (2010), the governing equations for shear waves along x direction in saturated poroelastic soil can be presented as

$$\left[(1-n)\rho_s + \rho_a \right] \frac{\partial^2 \theta_s}{\partial t^2} - \rho_a \frac{\partial^2 \theta_f}{\partial t^2} = G \frac{\partial^2 \theta_s}{\partial x^2} - \frac{n^2 \rho_f g}{k} F \frac{\partial}{\partial t} (\theta_s - \theta_f) \quad (3a)$$

$$-\rho_a \frac{\partial^2 \theta_s}{\partial t^2} + (n\rho_f + \rho_a) \frac{\partial^2 \theta_f}{\partial t^2} = \frac{n^2 \rho_f g}{k} F \frac{\partial}{\partial t} (\theta_s - \theta_f) \quad (3b)$$

where n , ρ , θ , t , G , g and k denote porosity, density, angular displacement, time, shear modulus, acceleration of gravity and hydraulic conductivity, respectively. Eq. 3(a) and Eq. 3(b) describe the motion of the solid phase and fluid phase, respectively, and are obtained from the application of Newton's second law to the

two phases in a control volume (Qiu and Fox 2008b). Subscripts s and f denote solid phase and fluid phase, respectively. Coefficient ρ_a represents the mass coupling between the solid and fluid phases. Biot (1962) proposed the following relationship

$$\rho_a = n\rho_f(\delta_1 - 1) \quad (4)$$

where $\delta_1 =$ structural factor representing the “added mass” caused by the tortuosity of the pore space (Stoll and Bryan 1970) and $\delta_1 = n^{-0.5}$ based on an approximation provided by Sen et al. (1981). In Eq. (3) F is a complex function that accounts for the effect of non-Poiseuille flow at high frequencies and is given by Biot (1956). In this paper, the Darcy assumption is assumed to be valid and $F = 1$. In this study, the soil skeleton is treated as elastic assuming that shear strain and volumetric strain are decoupled. This assumption limits the application of this study to small strain levels. The treatment of soil skeleton as a continuum implies that the wave length is much larger than the particle sizes (Santamarina et al. 2001). This treatment is valid for most geotechnical applications.

The general solution for the steady-state response of the soil can be expressed as

$$\theta_s(x,t) = \phi_s(x)e^{i\omega t} \quad (5a)$$

$$\theta_f(x,t) = \phi_f(x)e^{i\omega t} \quad (5b)$$

where $\omega =$ circular frequency; $\phi_s(x)$ and $\phi_f(x) =$ amplitudes of the angular displacement of the solid and fluid phases, respectively; and $i = \sqrt{-1}$.

Eq. (3) is applied to a saturated soil specimen in resonant column test. In Hall’s (1962) fixed base model, a soil column with length L is fixed at its base ($x = 0$) and subject to a torsional excitation at its top ($x = L$). For harmonic excitation, the loading function can be expressed as

$$T = T_o e^{i\omega t} \quad (6)$$

where $T =$ applied torque and $T_o =$ torque amplitude. The boundary conditions of the soil specimen are (Hardin 1965)

$$\theta_s(0,t) = 0 \quad (7a)$$

$$T - GJ \frac{\partial \theta_s(L,t)}{\partial x} = I_t \frac{\partial^2 \theta_s(L,t)}{\partial t^2} \quad (7b)$$

where J = polar moment of inertia of the soil specimen and I_t = mass polar moment of inertia of the loading system connected to the specimen at the top. Based on the work of Qiu and Fox (2006) and Qiu (2010), the solution for $\phi_s(x)$ can be expressed in a normalized form by using normalized frequency Ω and hydraulic conductivity K as

$$\phi_s(x) = \frac{T_o L}{GJ} \frac{\sin\left(\frac{\Omega x}{\alpha L}\right)}{\frac{\Omega}{\alpha} \cos\left(\frac{\Omega}{\alpha}\right) - \frac{I_t}{I_{sat}} \Omega^2 \sin\left(\frac{\Omega}{\alpha}\right)} \quad (8)$$

where I_{sat} is the mass polar moment of inertia of the saturated specimen

$$I_{sat} = \rho_{sat} L J \quad (9)$$

$$\alpha = \sqrt{\frac{1 + i\delta_1 \omega k / ng}{1 + i(\delta_1 - n\beta) \omega k / ng}} \quad (10)$$

$$\beta = \frac{1}{n + (1 - n)G_s} \quad (11)$$

The normalized frequency Ω and hydraulic conductivity K are defined as

$$\Omega = \frac{\omega L}{\bar{V}_s} \quad (12)$$

$$K = \frac{k \bar{V}_s}{gL} \quad (13)$$

where $\bar{V}_s = \sqrt{G/\rho_{sat}}$ and it represents the shear wave velocity in the soil when $k = 0$ (i.e., no relative motion between solid and fluid).

Table 1. Typical values of soil parameters ($L = 0.2$ m)

| Soil Type | n | G_s | \bar{V}_s (m/s) | k (m/s) | K |
|-------------|-----|-------|----------------------|-----------------------|-----------------------|
| Gravel | 0.4 | 2.66 | 200 | 0.01 – 1 | 1 – 100 |
| Coarse Sand | 0.4 | 2.66 | 200 | 10^{-4} – 10^{-2} | 0.01 – 1 |
| Fine Sand | 0.4 | 2.66 | 200 | 10^{-5} – 10^{-4} | 10^{-3} – 10^{-2} |
| Silt | 0.4 | 2.66 | 200 | 10^{-7} – 10^{-5} | 10^{-5} – 10^{-3} |

Values of soil parameters used in this study are presented in Table 1. The range of k for different soil types is based on Das (2010). In order to emphasize the effect of hydraulic conductivity on the effective density in different soils, constant values of n , G_s , and \bar{V}_s are used. This treatment is justifiable because the variation of these parameters among different soils is significantly less than the variation of hydraulic conductivity. The height of the test specimen is assumed to be 0.2 m (i.e., $L = 0.2$ m) in the calculation of K . The dynamic amplification factor at the top of the specimen can be expressed as $|A(\Omega)|$ where the transfer function $A(\Omega)$ can be expressed as

$$A(\Omega) = \frac{\sin\left(\frac{\Omega}{\alpha}\right)}{\frac{\Omega}{\alpha} \cos\left(\frac{\Omega}{\alpha}\right) - \frac{I_t}{I} \Omega^2 \sin\left(\frac{\Omega}{\alpha}\right)} \quad (14)$$

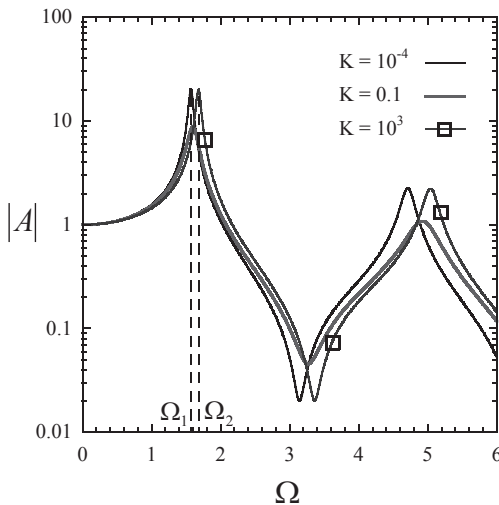


Fig. 1. Spectral response of $|A|$ for various K ($n = 0.4$, $I_t/I_{sat} = 0$).

Fig. 1 presents the spectral response of $|A|$ for a soil specimen with $n = 0.4$ and $I_t/I_{sat} = 0$. Values of $K = 10^{-4}$ and 0.1 correspond to fine sand and coarse sand, respectively. Value of $K = 10^3$ corresponds to a material with hydraulic conductivity and/or stiffness much higher than gravels as suggested by Table 1. Fig. 1 indicates that resonant frequencies and shear wave velocities are different for the cases of $K = 10^{-4}$ and 10^3 . This can be explained using two extreme cases: impermeable soil specimen (i.e., $K = 0$) and infinitely permeable soil specimen (i.e., $K = \infty$) as discussed in detail by Qiu and Fox (2008a) and Qiu (2010). For the impermeable

specimen, there is no relative motion between solid and fluid phases and the shear wave velocity is \bar{V}_s and $\rho_{eff}/\rho_{sat}=1$. This velocity will produce the first resonance at $\Omega_1 = \pi/2$. Conversely, there is no viscous coupling between the two phases for the infinitely permeable specimen and a shear wave propagates at velocity $\bar{V}_s \sqrt{\delta_1/(\delta_1 - n\beta)}$ and $\rho_{eff}/\rho_{sat} = (\delta_1 - n\beta)/\delta_1$, yielding the first resonance at $\Omega_2 = \Omega_1 \sqrt{\delta_1/(\delta_1 - n\beta)} = 1.68$. The dependence of the first resonant frequency on K is demonstrated in Fig. 2. It is clear that for $K \leq 10^{-2}$, corresponding to soils less permeable than coarse sand, the first resonance occurs essentially at Ω_1 , indicating that the response of these materials with regard to shear wave velocity and fundamental frequency resembles that of an impermeable soil with essentially undrained response. In this case, ρ_{eff} has the maximum value (i.e., ρ_{sat}) since all pore fluid moves with the solid skeleton. For $K \geq 10^3$, the first resonance occurs at Ω_2 , indicating that the response of these materials resembles that of an infinitely permeable soil with completely drained response. In this case, ρ_{eff} has the minimum value since only a small fraction of pore fluid moves with the solid skeleton due to the mass coupling (i.e., $\rho_{eff} = \rho_{sat}(\delta_1 - n\beta)/\delta_1$). Fig. 2 elucidates that in resonant column tests, the response of saturated fine sands is essentially undrained, the response of saturated gravel is mostly drained, and the transition from undrained response to drained response occurs mostly in saturated coarse sands.

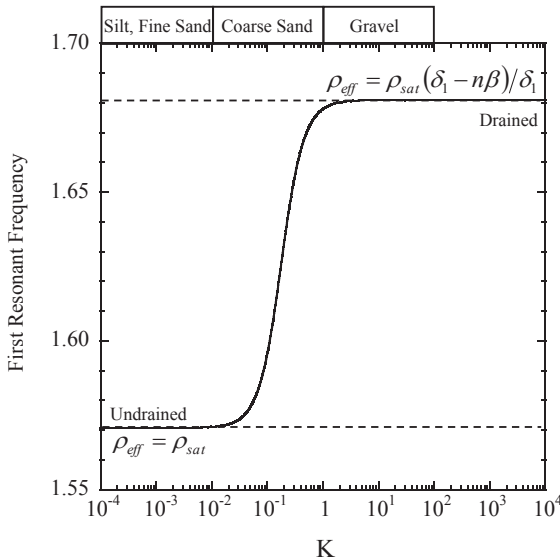


Fig. 2. Variation of first resonant frequency versus K ($n=0.4, I_t/I_{sat} = 0$).

EFFECTIVE DENSITY

Figs. 1 and 2 demonstrate that when Biot theory is applied to analyze resonant column tests of saturated specimens, the first resonance occurs at different frequencies (normalized) due to the relative motion between the solid and fluid phases. This observation suggests that a coupled two-phase analysis is needed to accurately analyze resonant column tests for soils with high permeability. In current soil dynamics research and practice, however, single-phase analyses are generally utilized to analyze resonant column tests regardless of the specimen's degree of saturation and permeability. To accommodate this practice, a single-phase analysis is conducted herein to analyze resonant column tests on saturated specimens to verify that the results shown in Figs. 1 and 2 can be reproduced by using the effective density, instead of the saturated density, to represent a saturated specimen.

If a saturated specimen is to be represented by a single-phase specimen having a density of ρ_{eff} , its resonant frequency satisfies the following equation

$$\frac{\omega L}{V} \tan\left(\frac{\omega L}{V}\right) = \frac{\rho_{eff} L J}{I_t} \quad (15)$$

Eq. (15) can be reorganized as

$$\frac{\omega L \bar{V}_s}{\bar{V}_s V} \tan\left(\frac{\omega L \bar{V}_s}{\bar{V}_s V}\right) = \frac{\rho_{sat} L J}{I_t} \frac{\rho_{eff}}{\rho_{sat}} \quad (16)$$

Substituting Eqs. (2), (9) and (12), as well as the definition of \bar{V}_s , into (16) yields

$$\Omega \sqrt{\frac{\rho_{eff}}{\rho_{sat}}} \tan\left(\Omega \sqrt{\frac{\rho_{eff}}{\rho_{sat}}}\right) = \frac{I_{sat}}{I_t} \frac{\rho_{eff}}{\rho_{sat}} \quad (17)$$

In Eq. (17), I_{sat}/I_t is typically known for a resonant column test. For a saturated specimen with a known K value, the first resonant frequency Ω can be obtained using the analytical approach presented in the previous section (e.g., Fig. 2 for the case of $I_t/I_{sat} = 0$). Thus, Eq. (17) involves one unknown parameter, ρ_{eff}/ρ_{sat} (i.e., effective density ratio), which can be solved using the Newton-Raphson method.

Fig. 3 presents the variation of effective density ratio versus K for various n and I_t/I_{sat} . This figure demonstrates that, in resonant column tests, the transition of ρ_{eff} from the maximum value (i.e., ρ_{sat}) to the minimum value (i.e., $\rho_{sat}(\delta_1 - n\beta)/\delta_1$) occurs primarily in coarse sands; in this region, the consideration of effective density is important in capturing the first resonance and interpreting resonant column test results. For soils less permeable than coarse sands (e.g., clays, silts, and fine sands),

the consideration of effective density is not important and ρ_{sat} can be used. For soils more permeable than coarse sands (e.g., gravels), the effective density is significantly less than the saturated density. Fig. 3 also indicates that the effective density ratio generally decreases as the porosity increases for a given K, which is consistent with the findings in Qiu and Fox (2008a). Fig. 3 demonstrates that boundary condition (i.e., I_t/I_{sat}) influences the effective density ratio in the transition between the maximum and minimum values but has no effect on these values.

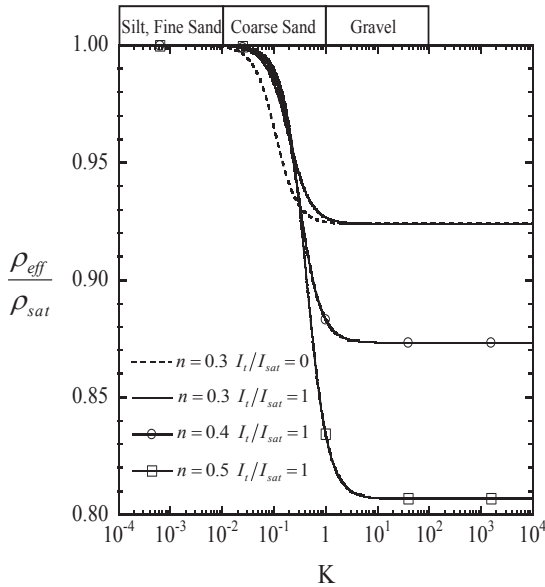


Fig 3. Variation of ρ_{eff} / ρ_{sat} versus K .

CONCLUSIONS

This paper presents a theoretical study to evaluate effective soil density in saturated soil specimens during resonant column tests. Effective density is the result of the relative motion between fluid and solid skeleton during shear wave propagation; it quantifies the fraction of pore fluid that effectively moves with the solid skeleton. Based on Biot theory and coupled two-phase analysis of the response of saturated soil specimens in resonant column tests, this paper demonstrates that, at the first resonance, the effective density ratio is a function of porosity, normalized hydraulic conductivity, and boundary conditions. In resonant column tests, the transition of effective density from the maximum value (i.e., saturated density) to the minimum value occurs primarily in coarse sands; in this region, the consideration of effective density is important in capturing the first resonance and interpreting resonant column test results. For soils less permeable than coarse sands (e.g., clays, silts, and fine sands), the consideration of effective density is not important and the

saturated density can be used. For soils more permeable than coarse sands (e.g., gravels), the effective density is significantly less than the saturated density.

ACKNOWLEDGEMENT

Support of this study is provided by the US National Science Foundation under Grant No. CMMI-0826097 and CMMI-1059588. This support is gratefully acknowledged.

REFERENCES

- Biot, M.A. (1956). "Theory of propagation of elastic waves in a fluid-saturated porous solid. I. Low-frequency range. II. Higher frequency range." *J. Acoust. Soc. Amer.*, 28(2), 168-191.
- Biot, M.A. (1962). "Mechanics of deformation and acoustic propagation in porous media." *J. Appl. Phys.*, 33(4), 1482-1498.
- Das, B.M. (2010). *Principles of Geotechnical Engineering*, 7th edition, Cengage Learning, 666 p.
- Hall, J.R. (1962). *Effect of Amplitude on Damping and Wave Propagation in Granular Materials*, Ph.D. dissertation, University of Florida, Gainesville.
- Qiu, T. and Fox, P.J. (2006). "Hydraulic damping of saturated poroelastic soils during steady-state vibration." *J. Eng. Mech.*, ASCE, 132(8), 859-870.
- Qiu, T. and Fox, P.J. (2008a). "Effective Soil Density for Propagation of Small Strain Shear Waves in Saturated Soil." *J. Geotech. & Geoenviron. Eng.*, ASCE, 134(12), 1815-1819.
- Qiu, T. and Fox, P.J. (2008b). "Numerical Analysis of 1-D Large Strain Compression Wave Propagation in Saturated Poroelastic Media." *Int. J. Numer. Anal. Meth. Geomech.* 32, 161-187.
- Qiu, T. (2010). "Analytical Solution for Biot Flow-Induced Damping in Saturated Soils during Shear Wave Excitations." *J. Geotech. & Geoenviron. Eng.*, ASCE, 136(11), 1501-1508.
- Santamarina, J.C., Klein, K.A., and Fam, M.A. (2001). *Soils and waves: Particulate materials behavior, characterization, and process monitoring*, Wiley, New York.
- Sen, P.N., Scala, C., and Cohen, J.H. (1981). "A self-similar model for sedimentary rocks with application to the dielectric constant of fused glass beads." *Geophys.*, 46(5), 781-795.
- Stoll, R.D. and Bryan, G.M. (1970). "Wave attenuation in saturated sediments." *J. Acoust. Soc. Amer.*, 47(5), 1440-1447.

Geotechnical Impact of 2008 Wenchuan Earthquake

Robert C. Lo, P.Eng., F.ASCE

Senior Geotechnical Engineer, Klohn Crippen Berger Ltd., 500 – 2955 Virtual Way, Vancouver, British Columbia, Canada V5M 4X6, rlo@klohn.com

ABSTRACT: This paper reviews the geotechnical impact of the 2008 Wenchuan Earthquake gleaned from references obtained through internet and other sources. It briefly describes the seismo-tectonic and geological setting of the seismic source region, and discusses various geotechnical aspects of the event. Strong ground motions and fault displacements in a setting of steep mountainous terrains trigger many failures of natural slopes and man-made structures. Coseismic hazards include landslides, debris flows and formation of landslide dams. These ground failures not only increase earthquake damage and hamper rescue and recovery effort, but also generate a secondary flood hazard due to potential breach of landslide dams. The epicentral region has also many high water-storage embankment dams, which seem to fare quite well. Finally, the event has set the stage for latent geological hazard caused by earthquake-weakened slopes and/or metastable landslide/debris-flow deposits. This hazard would materialize either in an aftershock or heavy storm/snow-melt event.

As the Wenchuan earthquake calamity recedes to memory, it behooves us to improve and apply our understanding of the event's multi-faceted impact in order to mitigate damage from similar future events.

1 GEOLOGICAL AND SEISMO-TECTONIC SETTING

Sichuan province is located in the southwest of China. On a continental scale, the regional seismicity is a result of northward convergence of the India plate against the Eurasia plate at a rate of about 50 mm/yr. The plate convergence is broadly accommodated by the uplift of the Qinhai-Tibet highlands as well as the extrusion of crustal material to the east away from the uplifted plateau (see Fig. 1). At the Longmen Shan, the eastern flank of the Tibetan Plateau rises 6 km above the Sichuan Basin within a short distance of 100 km.

The Wenchuan earthquake of May 12, 2008, occurred as the result of motion on the Yinxiu-Beichuan fault in the Longmenshan Fold and Thrust Belt, a northeast striking dextral-lateral, reverse (or thrust) fault system on the northwestern margin of the Sichuan Basin. The earthquake reflects tectonic stresses resulting from the

convergence of weak crustal material slowly moving from the west Qinhai-Tibet Plateau against Yantze Craton, a strong crust underlying the Sichuan Basin and southeastern China (see Fig. 2).

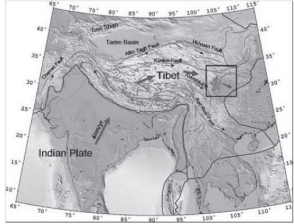


FIG. 1. Tectonic Setting of Qinhai-Tibet Plateau and Sichuan Basin (from Geoportalen.no 2008)

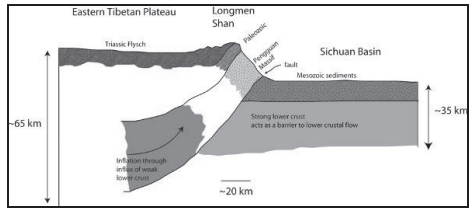


FIG. 2. Section through Qinhai-Tibet Plateau and Sichuan Basin (from MIT 2008)

The latent threat of the causative Longmenshan fault system was formally recognized by the geoscience research community about a year prior to the 2008 event (Densmore et al. 2007). Unfortunately, this finding did not influence the seismic code at the time. This major Mw 7.9 event impacted a large region in the southwest China, involving several provinces that were significantly under-designed for the event.

In the field of earthquake research, the inability to predict both Wenchuan and the 1976 M7.5 Tangshan Earthquakes has been regrettable. There are critical reviews of this perceived weakness, and considerable determination is expressed (Engineering Sciences 2009) to redouble the collective research efforts of this important topic. Among these reviews, Xu (2009, 2011) pointed out the problem might be related to the fact that most efforts have been focusing on observations of regional shallow crustal behaviour. He illustrated, admittedly after the fact, that by studying characteristics of dynamic forces in deep layer involving upper mantle at a continent-wide scale, the occurrence of Wenchuan earthquake could potentially be discerned from the distribution of recent seismic activities involving events of large magnitude (see Fig. 3a and 3b). Although earthquake prediction is beset by theoretical difficulty and practical-application problem, one cannot help but wishing its success sometime in the future.

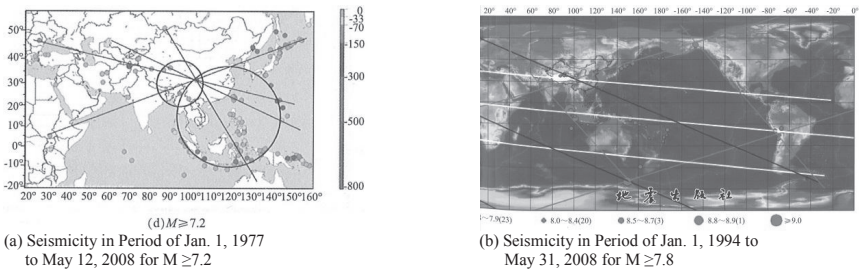


FIG. 3 Activities of Large Earthquakes in Recent Decades (after Xu, 2011)

2 MAIN GEOTECHNICAL IMPACTS

2.1 Strong Seismic Ground Motion

The peak ground acceleration values at four stations in the epicentral region: Wolong, Qingping, Bajiao and Zengjia shown in Fig. 4 are summarized in Table 1, together with their distances to the epicentre and reference fault (Li et al. 2008).

Table 1. Summary of Peak Ground Accelerations in Epicentral Region

| Station | Wolong | Qingping | Bajiao | Zengjia |
|------------------------------------|--------|----------|--------|---------|
| Epicentral Distance (km) | 19 | 88 | 67 | 314 |
| Distance from Reference Fault (km) | | | | |
| East-West (gal) | 957.7 | 824.1 | 556.2 | 424.5 |
| North-South (gal) | 652.9 | 802.7 | 581.6 | 410.5 |
| Vertical (gal) | 948.1 | 622.9 | 633.1 | 183.3 |

Notes: a) 1 gal = 1 cm/sec², and 1 g = 980 gal.

2.2 Fault Displacement

EEEV (2008) indicated that the main surface rupture propagated along the Yingxiu-Beichuan fault for more than 200 km with 2 m to 4 m general horizontal and vertical offset; it also splayed along the Jiangyu-Guanxian fault for more than 50 km with 0.5 m to 2 m offset (see Fig. 5). Maximum offset up to 11 m was reported for the main fault, and 3.5 m for the splayed fault.

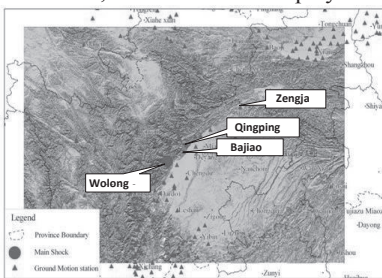


FIG. 4. Locations of Stations that Recorded Main Shock (after Li et al. 2008)

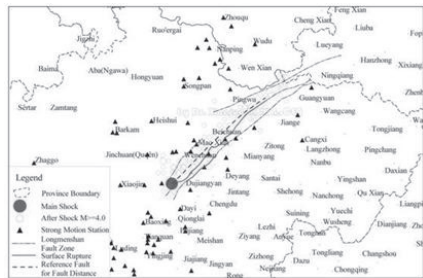


FIG. 5. Surface Rupture and Causative Fault (after Li et al. 2008)

2.3 Landslide

The main characteristics of landslides in the southwest region of China are steep topography, high seismic intensity and fragile geological environment. Figure 6 shows the empirical correlation of the area affected by landslides with earthquake magnitude. The upper bound curve and dot data points were taken from Keefer (1984). The triangle data points represent those seismic events with magnitude equal to or greater than 7 occurred in 814 to 2008 A.D. (Chen et al. 2012). The scatter of these data points reflects the important influence of local seismic intensity, slope steepness and geological condition.

Figure 7 shows the number and severity of landslides per km of National Highway Route #213 over the hanging wall versus foot wall. As expected in a thrust-fault earthquake, there is substantially more damage over the hanging wall as compared to that over the foot wall. Similarly there is more damage in the area along the earthquake propagation direction than in the opposite direction.

Large-scale landslides involve overburden covered bedrock. Thus, structural features such as bedding, faulting planes and joint systems play an important role on slope stability, and govern failure mechanisms of landslide development. Huang (2012) indicated that along a failure surface, the safety factor along failure surface (shear strength over mobilized shear stress) often varies from the head scarp to the slope toe. The segment of the failure surface that has the highest safety factor tends to take loads off from other segments until itself is finally overstressed resulting in a sudden failure of the slope. Also fast pore pressure change is facilitated by formation of cracks and/or the joint system of relatively higher permeability than that of the rock mass. Thus, only careful investigation and monitoring could lead to realistic understanding of the landslide failure mechanism and devising appropriate remedial measures. During Wenchuan earthquake, other factors affecting landslide include:

- high vertical acceleration in the epicentral region;
- toppling failure mechanism aided by the formation of tension cracks; and
- topographical amplification of ground motion.

Yin et al. (2011) indicated that geohazards, including slope failures, debris flows, rock slides and falls, caused over 20,000 deaths, nearly a quarter of the total earthquake fatality in Wenchuan earthquake. The largest volume of landslide reached 1.1 billion m^3 . Many of these landslides are characterized by their fast run-out velocity up to several tens of m/sec and long run-out distance up to several kms.

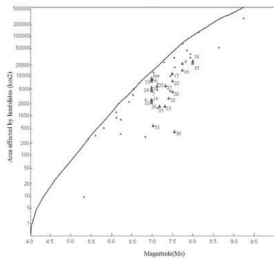


FIG. 6. Correlation of Area Affected by Earthquake-Induced Landslides with Magnitude (Chen et al. 2012)

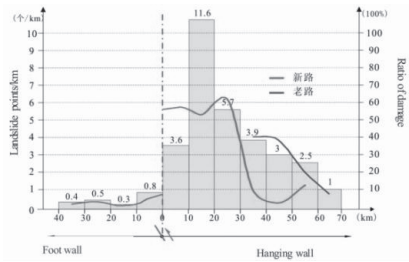


FIG. 7. Landslide Activities above Hanging Wall versus Foot Wall (from EEEV 2008)

2.4 Debris Flow

Debris flows occur coseismically or in the raining seasons after the earthquake. Those occurring during the earthquake are governed by the natural physical condition of the slope. Those occurring later, however, are governed by the loosened, distressed or disturbed state of the slope. Displaced debris from coseismic slope movement often perched precariously in a metastable state. The reduction of effective shear strength along a potential failure plane due to the increase of pore water pressure

resulting from infiltration of rain water is an important root cause of slope instability. The latent debris-flow hazard in raining season is further discussed in Section 3.1.

2.5 Landslide Dam

The formation of a landslide lake, caused by temporary blockage of river by unstable slide debris, poses a special flood hazard. Fan et al. (2012) analyzed a database of 828 landslide dams formed by the Wenchuan earthquake: 501 of those blocked river flow completely, while the remainder caused either partial blockage or river diversion. The distribution of landslide dams follows the same trend as that of the total landslides, most abundant in the steep watersheds of the hanging wall of the Yingxiu-Beichuan thrust fault and in the northeastern part of the strike-slip fault near Qingchuan. Figure 8 shows the initial rapid reduction of unbreached landslide dams since the May 12, 2008 event, while Fig. 9 shows the power law that governs the failure of landslide dams as the function of time applicable to the worldwide database, including the Wenchuan event. Thus, it is critically important to promptly remove the inundation threat of landslide-dam breach to public safety right after the seismic event.

Figure 10 shows example of a debris flow caused by a breached landslide lake located further upstream. Approximately 2 out of 8 million m³ of debris was moved to the area shown in the figure by the flood caused by a heavy rain four days after the earthquake. The debris raised the stream bed by 3 m and buried some houses located on the bank. Ten backhoes were mobilized to restore the stream channel.

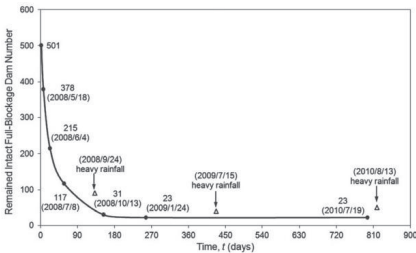


FIG. 8. Reduction of Remaining Landslide Dams with Time (Wenchuan database, Fan et al. 2012)

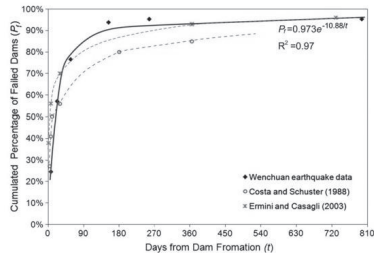


FIG. 9. Increase of Failed Landslide Dams with Time (Worldwide database, Fan et al. 2012)

The timely construction of a spillway to drain the lake behind the 124 m high Tangjiashan Landslide dam (see Fig. 11b, Liu and Yang 2009) was the successful emergency measure taken to ameliorate the downstream flood hazard to a population of 1.3 million (see Fig. 11). The spillway inlet was set at El. 740 m, about 12 m lower than the dam crest. The channel excavation started on May 26, and was completed on June 1. Additional measures were taken to increase the channel capacity, and on June 7 the channel flow began. It down cut the man-made channel, and reached a maximum rate of 6,500 m³/sec on June 10. By June 11, about a month after the quake, the lake level dropped from its maximum at El. 743.1 m to El. 714.13 m. The lake volume reduced from 247 to 86 million m³, and alleviated the dam-breach threat.



(a) Landslide Dam and Lake

(b) Emergency Spillway

FIG. 10. Debris Flow at Huosigou, Chongzhou.

(Engineering Resilient Cities - Mahin - Oct 2008)

(Liu and Yang 2009)

FIG. 11. Landslide Lake at Tangjiashan Landslide.

2.6 Damage and Failure of Man-made Structures

The destruction of school buildings and hospitals and loss of estimated over 10,000 school children hit the communities extremely hard, as most of them are the only child in the family. In the updated code, school, hospital and other structures that are required to maintain their function after earthquake are classified for higher design standard. Many heritage structures such as temples and pagodas were damaged or destroyed. Some of the tall structures such as chimneys and water towers were cracked or sheared off (EEEEV 2008).

The strong shaking along the ruptured fault accentuated by topographic amplification and ground failures such as fault displacements, landslides and debris flows caused substantial damages to lifelines facilities such as transportation, power, water supply and communication infrastructures in the mountainous region. This loss of lifelines has impeded the emergency response and rescue operations, and slowed the progress of recovery efforts.

2.7 Water Storage Dams

Zhang et al. (2010) provided an overview of the performance of high embankment dams in the Wenchuan earthquake. Five embankment dams higher than 100 m were in service during the earthquake. The two dams located in Intensity Zone 9 are 156 m high Zipingpu concrete-faced rockfill dam (completed in 2005) and 102 m high Bikou earth and rockfill dam with a loam core (completed in 1976), whose seismic displacements (Chen, S. 2008 and Zhang et al. 2010) are included in Fig. 12 as described later in this section. After the earthquake, dam seepage at Zipingpu increased from 10.38 L/s to a maximum value of 19.3 L/s. The murky seepage cleared up two days after the quake. The Zipingpu dam also suffered various damages including: small scale bank slope slides, cracks of road shoulder, damages to wave wall and concrete guard railings on dam crest, displacement and cracking of upstream concrete slabs and dislocation of slab vertical and horizontal construction joints, and movement of masonry stones on the downstream slope. Most of the essential repairs were complete by the end of October 2008. The two dams in Intensity Zone 7, Shuiniujia and Yaoji dams, experienced only nominal deformation, while Yelei Dam in Intensity Zone 6, showed no obvious deformation. Issues related to earthquake damages to water discharge appurtenance structures such as spillway gate, low-level outlet and intake structure were discussed by Wieland (2012).

Damages to other low embankment dams include: settlement, longitudinal cracks along the crest, transverse cracks, slope slump, cracked spillway tunnel and channel wall, a partial dam collapse and increased toe seepage (EEEEV 2008). Due to preparation for the approaching flood season, reservoir level was generally lowered at the time of earthquake. Further lowering of reservoir levels by emergency measures after the quake prevented dam breach incidents. Thus, due to prevalent low reservoir level condition during the earthquake, most of the dams have not experienced seismic loading under the “full-supply level” condition.

Chen (2009) highlighted the following strategic focuses on dam safety in China:

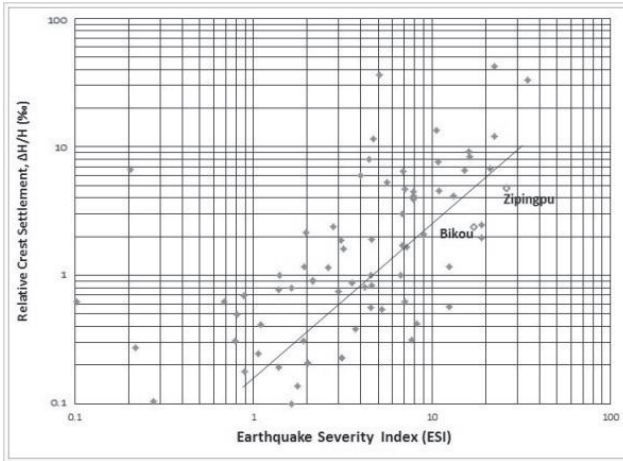
- Evaluate design ground motion time history corresponding to the maximum considered earthquake appropriate to the seismo-tectonic setting of a dam site;
- Conduct seismic response analysis of a dam-foundation-reservoir system for concrete dams to evaluate displacement-based dam performance using non-linear numerical model;
- Conduct three-dimensional, non-linear seismic response analysis for concrete-faced rockfill dams to study the interaction of the concrete face slab and underlying rockfill; and
- Conduct safety evaluation of existing dams to mitigate dam-breach risk, and strengthen water-discharge auxiliary structures to facilitate drawdown of reservoir level during emergency condition.

Figure 12 show updated plots of empirical relationships between relative crest settlement and horizontal displacement ($\Delta H/H$, and $\Delta D/H$ in per-mille) versus Earthquake Severity Index (ESI) (see Bureau et al. 1985, Lo and Klohn 1992 and Swaisgood 2003). Bureau et al. (1985) introduced ESI as a parameter related to AD^2 ; A and D represent peak horizontal ground acceleration and duration of the strong-shaking phase of an earthquake. By assuming $D = 7 (M-4.5)^{1.5}$, they arrived at the following expression of ESI.

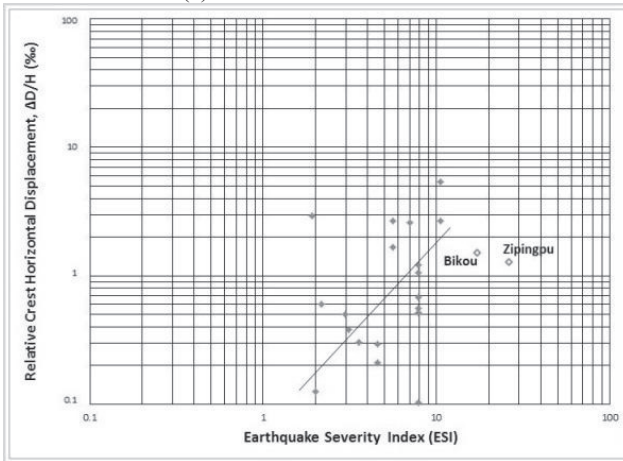
$$ESI = (PGA/g) * (M-4.5) ** 3$$

Where ΔH , ΔD = settlement and horizontal displacement of dam crest;
 H = dam height at maximum section;
 PGA = peak horizontal ground acceleration at dam site;
 g = gravitational acceleration; and
 M = magnitude of earthquake.

Figure 12 show that the relative settlement and horizontal displacement generally increase with the ESI. The scatter of settlement data points reflects the compressibility characteristics of the dam fill, which, in turn, is influenced by the fill material property as well as compaction equipment and effort used during fill placement. The scatter of horizontal displacement is further influenced by side slope angle, which is not reflected on the plot. The figure shows low values of relative settlement and horizontal displacement for Zipingpu dam, which has near highest value of the ESI on the plot. It illustrates the difference in seismic performance between the recent rockfill dam that has been heavily compacted systematically with modern equipment under stringent quality control procedures and those older rockfill dams that received little compaction.



(a) Relative Settlement



(b) Relative Horizontal Displacement

FIG. 12. Empirical Relationship Between Crest Deformation and Earthquake Severity Index (after Bureau et al. 1985, Lo and Klohn 1992 and Swaisgood 2003)

3 SEISMIC HAZARD AND RE-CONSTRUCTION

3.1 Post-earthquake Geological Hazard

Post-earthquake geological hazards include:

- Outburst of landslide lakes formed during earthquake;
- Debris flows triggered by heavy rain storms; and
- Slope failures, rock falls due to weakened ground.

The first and third types of hazard have been generally recognized, and remedial measures and precautions are taken to ward off dangers to people and structures.

However, the rain-storm triggered debris flow is a more insidious type of hazard (Tang et al. 2011). The relatively loose landslide debris tends to perch metastably on a steep terrain often remote from population centres. This latent hazard waits to reveal its destructive force, when the debris gets re-mobilized by heavy and/or sustained rainfall. In the aftermath of a severe earthquake, there are so many urgent tasks requiring attention by the authorities and public. Unless special attention is focused on careful investigation of this potential hazard and actions are taken to mitigate its threat to people and built environment, substantial loss of life and property could result from this geological hazard. Xu et al. (2012) described such a tragedy with about 100 casualties that occurred on August 13 and 14, 2010. Multiple debris flows occurred during rain storms in this period, including those at Wenjia and Zoumaling gullies, Hongchun gully and Longchi. Figure 13a shows the natural topography in Yinxiu vicinity prior to Wenchuan earthquake, while Fig. 13b and 13c show the same area after the 2008 earthquake and 2010 rain storms, respectively.

3.2 Site Assessment for Re-construction

Hwang et al. (2012) outlined the following principles adopted for site assessment for post-earthquake re-construction based on their engineering geological investigations carried out over a three-month period right after the earthquake:

- Avoid town sites along or adjacent to active faults with a fragile geology;
- Select sites with low risk of geologic hazard away from active faults, even heavy damages to structures occurred at these sites due to inadequate resistance to strong shaking; and
- Consider risk inducing factors and look out for hidden geological hazards.

Three town sites were presented as case histories to illustrate how the above principles were applied: Beichuan, Qingchuan and Muyu. Relocation of the town site was required for the first two, while the third was reconstructed at its original location, except with higher seismic resistant design standard adopted than before.

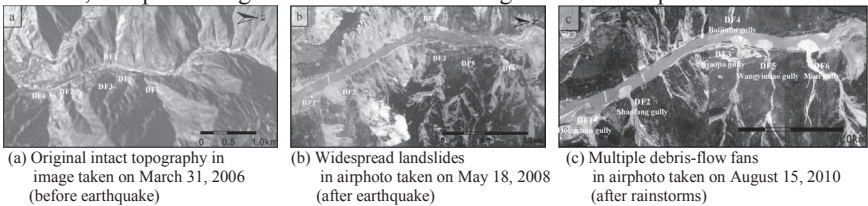


FIG. 13 Yinxiu Debris Flow Event after Rainstorm on August 14, 2010
http://www.itc.nl/pdf/newsevents/landslides/tang_chuan_presentation.pdf

4 SUMMARY

Besides strong shaking, ground failures played an important role in causing severe and wide spread damage to natural slopes and man-made structures during Wenchuan earthquake. We anticipate future geotechnical challenges in the development of the mountainous, highly seismic western China will be met by our Chinese colleagues, who have made such outstanding contributions reviewed here since the unfortunate event in 2008.

5 REFERENCES

Only limited references are listed below. Other references are identified in the text, but not included in the abridged list due to space limitation.

- Bureau, G., Volpe, R.L., Roth, W.H, and Udaka, T. 1985. Seismic Analysis of Concrete Face Rockfill Dams, Proc. of Symp. on Concrete Face Rockfill Dams – Design, Construction and Performance, ASCE, pp. 479-508.
- Chen, X.L., Zhou, Q., Ran, H. and Dong, R. 2012. Earthquake-triggered Landslides in Southwest China, Nat. Hazards Earth Syst. Sci. Vol. 12, pp. 351-363.
- Chen, H. 2009. Consideration on Seismic Safety of Dams in China after the Wenchuan Earthquake, (in Chinese), Engineering Sciences, 11 (6), pp. pp. 44 to 53.
- Densmore, A.L., Ellis, M.A., Li, Y., Zhou, R.J., Hancock, G.S. and Richardson, N. 2007. Active Tectonics of the Beichuan and Pengguan Faults at the Eastern Margin of the Tibetan Plateau, Tectonics, Vol. 6.
- EEEV 2008. General Introduction of Engineering Damage of Wenchuan Ms 8.0, Earthquake, Earthq. Eng. and Eng. Vib., Vol. 28 Supplement, October.
- Fan, X., van Westen, C.J., Xu, Q., Gorum, T. and Dai, F. 2012. Analysis of Landslide Dams Induced by the 2008 Wenchuan Earthquake, J. of Asian Earth Science, Vol. 57, pp. 25-37.
- Huang, R. Q., Li, Y.S. and Li, W.L. 2012. Engineering Geological Evaluation of Reconstruction Sites Following the Wenchuan Earthquake, Bull. Eng. Geol. Environ., Vol. 68, pp. 449-458.
- Huang, R. 2012. Mechanisms of Large-scale Landslides in China, Bull. Eng. Geol. Environ., Vol. 71, pp. 161-170.
- Li Xiaojun, et al. 2008. Strong Motion Observations and Recordings from the Great Wenchuan Earthquake, Earthq. Eng. and Eng. Vib., Vol. 7 No. 3, pp. 235-246, Sept.
- Liu, N. and Yang, Q. 2009. The Emergency Handling Technique and Practice of Tangjiashan Barrier Lake, (in Chinese), Engineering Sciences, 11 (6), pp. 74-81.
- Tang, C., Zhu, J., Qi, X. Ding, J. 2011. Landslides Induced by the Wenchuan Earthquake and the Subsequent Strong Rainfall, Engr. Geol. 2011.03.013.
- Wieland, M. 2012. Seismic Design and Safety Aspects of Bottom Outlets, Spillways, and Intake Structures of Large Storage Dams, 15th WCEE.
- Xu, Shaoxie 2011. Earthquake Should Be Predictable, Dizhenyingkeyuce, Earthquake Press, Beijing, pp. 26 to 32, Originally published in 2009, Engineering Sciences, 11 (6), pp. 16-18 (in Chinese).
- Xu, Q., Zhang, S., Li, W.L. and Th. W.J. van Asch, 2012, The 13 August 2010 Catastrophic Debris Flows after the 2008 Wenchuan Earthquake, China, Nat. Hazards Earth Syst. Sci. Vol. 12, pp. 201-216.
- Yin, Y. Zheng, W., Li, X., Sun, P. and Li, B. 2011. Catastrophic Landslides Associated with the M8.0 Wenchuan Earthquake, Bull. Eng. Geol. Environ. Vol. 70, pp. 15-32.
- Zhang, J.M., Yang, Z.Y, Gao, X.Z. and Tong, Z.X. 2010. Lessons from Damage to High embankment Dams in the May 12, 2008 Wenchuan Earthquake, GeoShanghai Int'l. Conf. on Soil Dynamics and Earthquake Engineering.

A Case History of Design and Construction of Corrosion Protection System for Steel Sheet Pile Wall

Ming Zhu¹, M. ASCE, Ph.D., P.E., Fan Zhu², A.M. ASCE, Chris Conkle³, M. ASCE, P.E., and John F. Beech⁴, M. ASCE, Ph.D., P.E.

¹Senior Geotechnical Engineer, Geosyntec Consultants, 1255 Roberts Boulevard NW, Suite 200, Kennesaw, GA 30144, USA, Email: mzhu@geosyntec.com

²Engineer, Jacobs China Limited, 15/F Cornwall House, 979 King's Road, Taikoo Place, Quarry Bay, Hong Kong, P.R. China, Email: gevfan@yahoo.com (formerly with Geosyntec Consultants)

³Project Geotechnical Engineer, Geosyntec Consultants, 2100 Main Street, Suite 150, Huntington Beach, CA 92648, USA, Email: cconkle@geosyntec.com

⁴Principal, Geosyntec Consultants, 1255 Roberts Boulevard NW, Suite 200, Kennesaw, GA 30144, USA, Email: jbeech@geosyntec.com

ABSTRACT: Steel sheet piles have been widely used in construction of earth retaining structures and seepage barrier walls. It is known that steel is susceptible to corrosion when in contact with the environment. Therefore, durability of permanent steel sheet pile structures against corrosion needs to be evaluated as part of the design of these structures. This paper presents a case history where a corrosion protection system was designed and constructed for a 1.5-kilometer long steel sheet pile barrier wall at a lake cleanup project site. The system includes a coal tar epoxy coating and a sacrificial anode cathodic protection. The paper discusses the methodology used to design the corrosion protection system and provides details of its construction. The case history is expected to be beneficial to geotechnical engineers working on similar projects.

INTRODUCTION

Steel sheet piles have been widely used to construct earth retaining walls to support excavations, underground facilities, river banks, ports, harbors, and similar projects. When properly sealed, the steel sheet piles can also provide a nearly water-tight barrier to control seepage of groundwater in applications such as underground tanks, cofferdams, and contaminated sites. Design of a steel sheet pile structure typically includes both geotechnical and structural considerations to select the appropriate wall type (i.e., cantilever or anchored), the steel grade, the sheet pile cross-section (or section), and the sheet pile length.

It is known that steel is susceptible to corrosion when in contact with its environment, such as air, water, and soil. The degree of corrosion depends on site-specific conditions. For example, a seawater environment is generally more

corrosive than a fresh water environment. Corrosion causes the oxidation of steel and thus may result in reduction in sheet pile thickness and, in extreme cases, formation of localized holes, which will adversely affect the integrity and permeability of the structure. Therefore, durability against corrosion needs to be evaluated in the design of a permanent steel sheet pile structure to determine whether corrosion protection is required.

This paper presents a case history where a corrosion protection system was designed and constructed for a 1.5-kilometer long steel sheet pile barrier wall at a lake cleanup project site. The remainder of this paper is organized to illustrate: (1) the mechanism of corrosion and typical corrosion control measures to protect steel sheet pile structures, (2) the project background, (3) the design methodology for the corrosion protection system, (4) construction details, and (5) a brief summary.

MECHANISM OF CORROSION

The mechanism of corrosion of a metal is well documented and can be found in the literature. Corrosion is caused by the electrochemical process that is conceptualized to take place in a system termed the *corrosion cell*, which consists of an anode, a cathode, an electrolyte, and a metallic connection between the anode and the cathode (see Figure 1). In the process, an electric current leaves the anode, where oxidation and metal loss occur, flows through the electrolyte, and enters the cathode where reduction occurs, while the electrons flow away from the anode toward the cathode through the metallic connection. The driving force behind the corrosion is the electrical potential difference between the anode and cathode, i.e., the anode's potential is lower (or more negative) than the cathode's potential.

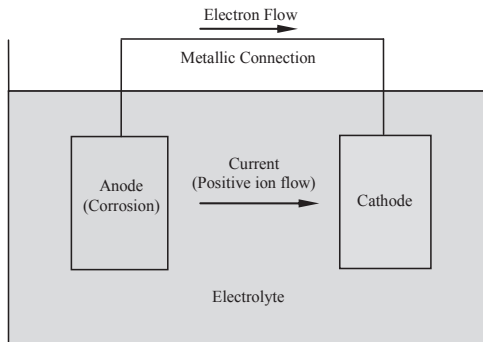


Figure 1. Mechanism of Corrosion Cell

In the case of a steel sheet pile buried underground, certain areas of the pile may have more negative potential than other areas because of slight differences in metal composition or the nature of the soil in contact with the sheet pile. These areas may become anode sites. The soil (and groundwater, if present) adjacent to and in contact with the sheet pile constitutes the electrolyte through which the electric current flows. The sheet pile itself acts as the metallic connection between the anode sites and the adjacent unaffected areas (i.e., the cathode sites). Having formed corrosion cells,

corrosion and deterioration of the steel may occur at these anode sites.

CONTROL MEASURES

There are several measures applied in engineering practice to mitigate or control corrosion of steel sheet pile structures. The most basic method is to compensate for the anticipated corrosion during the lifetime of the structure by selecting a heavier section of sheet pile. Alternatively, steel with a higher yield stress can be used, which provides more allowable bending stress and therefore, more acceptable loss in cross-section for a given load. This measure applies to a retaining structure where the serviceability of the structure is controlled by the sheet pile strength.

A prevalent method of protecting steel sheet pile against corrosion is through the use of a coating, such as coal tar epoxy, which acts as a barrier between the corrosive environment and the structure, although some of the coating could be damaged during the sheet pile installation. The effective life of the sheet pile is typically extended by approximately 10 to 25 years through the use of a coating.

Another effective measure used to control corrosion is the application of cathodic protection. There are two types of cathodic protection systems: a sacrificial anode system and an impressed current system. In the first system, a metal with a more negative potential than steel, such as magnesium or zinc, is installed adjacent to the steel sheet pile structure to be protected. The new metal is either attached to the structure or connected with a wire to provide a good electrical contact. The new metal will act as the anode and the steel sheet pile structure will act as the cathode. The new anode will corrode sacrificially to protect the structure. In the second system, an external power source is used to drive current from the external anode to the steel sheet pile structure. This is typically applied to large structures where the sacrificial anode cathodic protection system cannot deliver enough current for corrosion protection. Theoretically, cathodic protection systems can prevent any corrosion from occurring if the system is appropriately designed and regularly maintained.

One or more of the above corrosion control measures may be selected to protect a permanent steel sheet pile structure. The decision of which measures to employ depends on the required life expectancy of the structure and the associated construction costs.

PROJECT BACKGROUND

The case history presented in this paper is located in the northeastern United States where a lake cleanup plan is being implemented. One of the key components of the plan is to install an underground barrier wall along the lake shore. This barrier wall will function to intercept contaminated groundwater from the adjacent legacy industrial sites and prevent it from reaching the lake. The wall will also serve as an earth retaining structure facilitating dredging of contaminated lake sediments in front of the wall. The wall will be backfilled and covered after the dredging is complete.

The barrier wall is approximately 1.5 kilometers long. Based on geotechnical stability and structural analyses considering the dredging, a cantilever sheet pile wall was designed with hot-rolled AZ19-700 sections of ASTM A572 Grade 50 steel. The

sheet pile lengths vary between 12 to 24 meters. The toes of the sheet piles were installed into a subsurface clay layer to cut off the groundwater migration. The interlocks of the sheet piles were filled with hydrophilic sealants to minimize the seepage. A groundwater collection trench was also constructed behind the barrier wall to pump the groundwater to a nearby water treatment plant. The collected groundwater is released to the lake after treatment.

A corrosion protection system was designed and installed to address the long-term performance of the barrier wall. The goal was to increase the effective life of the wall to the extent reasonably practical. The system consists of a coal tar epoxy coating and sacrificial anode cathodic protection. The next sections discuss the design and construction of the corrosion protection system.

DESIGN METHODOLOGY

Effective Life Estimate

The effective life of the steel sheet pile barrier wall without any corrosion protection was first estimated based on the corrosion rates and the allowable loss of sheet pile thickness. Laboratory exposure tests were performed on coupons of the steel sheet piles to evaluate the corrosion rates of the steel in contact with the samples of groundwater and subsurface materials collected from the site. The steel coupons were submerged or buried in the collected site samples for a test period of four months. The thicknesses of the coupons before and after the tests were measured. The corrosion rates were calculated based on the difference in the measured thicknesses over the four months, which accounted for the loss on both sides of the steel coupons. Table 1 summarizes the corrosion rates obtained from the laboratory test results.

Table 1. Corrosion Rates for Steel

| Material in Contact with Steel | Corrosion Rate (mm/year) |
|--|--------------------------|
| Tap Water | 0.044 |
| Groundwater Impacted by Non-Aqueous Phase Liquid | 0.045 |
| Industrial Waste | 0.002 |
| Soil Impacted by Non-Aqueous Phase Liquid | 0.034 |

Note: The corrosion rate was calculated based on the laboratory exposure test results and accounts for the loss on both sides of the tested steel coupons.

The laboratory test results indicate that the measured corrosion rates are higher when in contact with the tap water or impacted water than the impacted soil or industrial waste. The wall serves as a retaining structure for a relatively short period of time (i.e., approximately four years) during the lake dredge and will eventually be backfilled and buried. Therefore, for the purpose of estimating the effective life of the wall, the measured corrosion rate for the impacted soil was considered. It was assumed that the allowable loss was the total thickness, i.e., the effective life of the wall was assumed to end when a hole is created by the corrosion. The thickness of an AZ19-700 sheet pile section is 9.5 millimeters as provided in the manufacturer's product specifications. Using the measured corrosion rate of 0.034 millimeters per year and the assumed allowable thickness loss of 9.5 millimeters, the effective life of the wall was estimated to be approximately 280 years.

The effective life of the barrier wall was also checked using the corrosion rate reported in Part 5: Piling of Eurocode 3: Design of Steel Structures (European Committee for Standardization, 1997). The code provides guidance on the loss of thickness of steel sheet piles due to corrosion under different conditions in soils, fresh water, and sea water. The corrosion rate corresponding to “*Aggressive natural soils (swamp, marsh, peat,...)*” was conservatively selected, which is 0.0325 millimeters/year for one side (or 0.065 millimeters/year for both sides). The effective life of the barrier wall was estimated to be approximately 150 years based on Eurocode 3.

Corrosion Protection System Design

The selected corrosion protection system was a combination of both coating and sacrificial anode cathodic protection.

A coal tar epoxy coating was selected to be applied to the top 4 meters of the sheet piles. The depth of coating was specified to cover both the land side and water side surfaces of the sheet pile wall from the top of pile to a minimum of 1.5 meters below the existing groundwater elevation. The uncoated area below the existing groundwater elevation was expected to be less severely impacted by corrosion due to reduced frequency of drying and wetting and resulting lower levels of oxygen at these deeper depths.

In addition, a sacrificial anode cathodic protection system was specified to reduce the corrosion rate and thus further increase the effective life of the barrier wall. Design guidance for the sacrificial anode cathodic protection can be found in published technical manuals (e.g., DOA, 1985, DOD, 1990, and USACE, 2004). It should be noted that the procedures and examples presented in most technical manuals assume that the design goal is to provide full protection (i.e., zero corrosion). In the case presented in this paper, the design goal was to increase the effective life of the barrier wall to the extent reasonably practical, rather than to design and construct a fully protected wall. A modified approach was developed based on the available design guidance to re-calculate the effective life after considering the protection from the sacrificial anodes. The procedure of designing the sacrificial anode cathodic protection system included the following steps:

Step 1: Calculate the area to be protected

The area to be protected was calculated using the following equation:

$$A = A_{uc} + A_c(1 - E_c) \quad (1)$$

where A is the total sheet pile wall area to be protected, A_{uc} is the uncoated area, A_c is the coated area, and E_c is the coating efficiency. The coating efficiency depends on the type of coating used and the quality of coating application. In the case presented in this paper, the coating efficiency was conservatively assumed to be zero.

Step 2: Calculate the current output from sacrificial anodes

The type and number of sacrificial anodes were selected during this step in order to calculate the total current output. Depending on the calculated effective life at the end of the procedure, the selected type and number of anodes may need to be changed

for another round of calculations.

The current output from a single sacrificial anode can be calculated according to Ohm's Law:

$$I_a = \Delta E / R_T \quad (2)$$

And the total current output from all the sacrificial anodes is:

$$I = NI_a \quad (3)$$

where I_a is the current output from a single sacrificial anode, ΔE is the net driving potential between the sacrificial anode and the protected structure, R_T is the total resistance of the circuit, I is the total current output from all sacrificial anodes, and N is the total number of sacrificial anodes. The potentials of iron and three commonly used sacrificial anodes are listed in Table 2.

Table 2. Typical Potentials of Metals (DOA, 1985 and DOD, 1990)

| Metal | Potential E (versus Copper-Copper Sulfate, volt) |
|-----------------|--|
| Magnesium Anode | -1.55 to -1.75 |
| Aluminum Anode | -1.10 to -1.15 |
| Zinc Anode | -1.1 |
| Iron | -0.55 to -0.85 |

The total resistance of the circuit is given by the equation below:

$$R_T = R_a + R_w + R_c \quad (4)$$

where R_a is the anode-to-electrolyte resistance, R_w is the metallic connection (e.g., wires) resistance, and R_c is the structure-to-electrolyte resistance. The metallic connection resistance R_w and the structure-to-electrolyte resistance R_c are relatively small compared to the anode-to-electrolyte resistance R_a and are usually not considered in the design. The anode-to-electrolyte resistance R_a can be calculated using Dwight's Equation:

$$R_a = 0.0052 \frac{p}{L} \left(\ln \frac{8L}{d} - 1 \right) \quad (5)$$

where L and d are the length and effective diameter of the sacrificial anode, respectively, which are provided by the manufacturer, and p is the soil resistivity. The soil resistivity can be measured at the site using the Wenner four-pin method or in a laboratory using the soil box resistivity test. Typical ranges of soil resistivity for different corrosive environments are listed in Table 3.

Table 3. Typical Ranges of Soil Resistivity (DOA, 1985)

| Corrosivity | Soil Resistivity Range (ohm-cm) |
|--------------------|---------------------------------|
| Severe | 0 to 2000 |
| Moderate to Severe | 2000 to 10,000 |
| Mild | 10,000 to 30,000 |
| Not Likely | above 30,000 |

Step 3: Calculate the corrosion rate after protection

The calculated total current output from the sacrificial anodes was then converted to equivalent mass of steel saved using Faraday's Law. Faraday's Law states that 96,486.7 Coulombs (equal to one Faraday) of charge transfer will oxidize or reduce one gram equivalent mass of the material involved in the electrochemical reaction. According to this law, the consumption rate of iron is approximately 9.1 kilograms/Ampere-year. The total mass of steel that is saved per year is calculated as:

$$m = 9.1I \quad (6)$$

The equivalent thickness of steel sheet piles that is saved per year is then calculated using the equation below:

$$t = \frac{m}{\rho A} \quad (7)$$

where ρ is the density of steel. The corrosion rate is reduced because of the additional current provided by the sacrificial anodes. The corrosion rate after protection is the estimated corrosion rate without protection subtracted by the calculated thickness saved each year.

Step 4: Calculate the effective life with protection

The effective life of the steel sheet pile wall was re-calculated using the reduced corrosion rate after protection, as calculated in Step 3. If the result does not meet the requirement, another type of sacrificial anode, which is either more massive or has larger net driving potential, can be evaluated. Alternatively, the number of sacrificial anodes can be increased.

Selected Corrosion Protection System

For the case presented in this paper, the Farwest PZ-150 zinc anodes were selected. Each anode weighs 68 kilograms. The length of each anode is 0.9 meters and the effective diameter is 0.1 meters. The spacing of the anodes was 4.5 meters and they were installed on both sides of the sheet pile wall in a staggered pattern. Based on the calculations, an equivalent thickness of 0.012 millimeters of steel can be saved by the corrosion protection system. As a result, the calculated effective life of the sheet pile barrier wall was increased from approximately 280 years (i.e., based on the measured site-specific corrosion rates) to approximately 430 years, which represents an increase of over 50%. Because the anodes corrode sacrificially to protect the steel sheet pile wall, they need to be inspected periodically and replaced with new anodes as necessary. The sacrificial anodes were estimated to last 5 to 6 years. The predicted lifetime of the barrier wall appeared to be reasonable and practical, and the selected corrosion protection plan was considered to be feasible and economical.

CONSTRUCTION

Coal Tar Epoxy Coating Application

A coal tar epoxy coating with a minimum thickness of 16 mils (400 microns) was applied in the sheet pile fabrication shop to the upper 4 meters of all sheet piles (see Figure 2). Prior to application of the coating, the portion of sheet surface to receive the coating was prepared to Joint Surface Preparation Standard (SSPC-SP NO. 10/NACE NO. 2) for near-white blast cleaning. This is a generally accepted standard for surface preparation prior to application of coal tar epoxy coatings which will be subject to “immersion” service. Incomplete removal of dirt, dust, oil and other contaminants could interfere with adhesion of the coating. Application of the coating was accomplished using spray equipment. The curing schedule of the coating was an important item which was considered by the coating applicator during development of their production schedule.

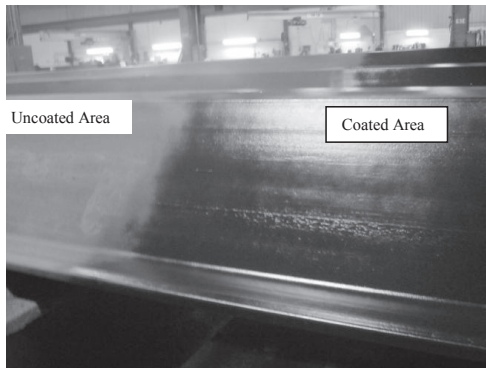


Figure 2. Shop Applied Coal Tar Epoxy Coating

After installation of the sheetpiles and attachment of the sacrificial anodes, field repairs were made to areas of the coating which had been damaged during installation and were readily accessible. Coating was also reapplied in areas subject to field welding. Field preparation of these repair areas required steel to be burnished and not polished prior to coating using a wire wheel and/or grinder. The use of a brush and roller was considered acceptable to apply coating repairs less than 0.1 square meters (or 1 square foot) in size.

Sacrificial Anode System Installation

After the installation of the sheet piles, sacrificial anodes were installed using a system of angle iron hangers welded to the upper portion of the sheet pile (see Figure 3). The bottom elevation of the anodes was selected to balance the desire to have the anodes in contact with less resistive soil containing groundwater as well as limit the effort required for installation. Typically, installation of the anodes required augering a small diameter hole in the subgrade soils adjacent to the sheet to allow for installation.

Galvanized steel hardware was used to connect the anode to the steel hanger. Protective steel plates were installed between adjacent legs of the sheet piles at the location of anodes to provide a steel “pocket” around the anode. The function of these plates was to facilitate future maintenance and, in the case of lakeside sheet piles, to protect the anodes from damage due to moving ice floes. During installation circuit continuity between the anode and the sheet piles was confirmed using a handheld digital multimeter.

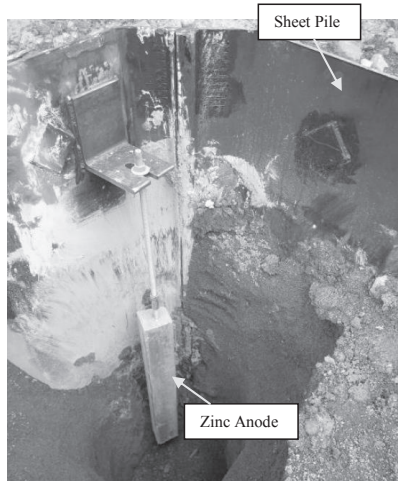


Figure 3. Typical Anode Installation

SUMMARY

This paper presented a case history of the design and construction of a corrosion protection system for a steel sheet pile wall. It illustrated the mechanism of corrosion, typical measures of corrosion control, the methodology and procedures to design the sacrificial anode cathodic protection system, and the construction details. The case history is expected to be beneficial to geotechnical engineers working on similar projects.

REFERENCES

- Department of the Army (DOA) (1985). “Technical manual – electrical design, cathodic protection.” *TM 5-811-7*, Washington D.C.
- Department of Defense (DOD) (1990). “Electrical engineering cathodic protection.” *MIL-HDBK-1004/10*.
- European Committee for Standardization (1997). “Eurocode 3: Design of steel structures.” *Part 5: Piling, European Prestandard ENV 1993-5*, pp. 150-154.
- U.S. Army Corps of Engineers (USACE) (2004). “Engineering and Design Cathodic Protection Systems for Civil Works Structures.” *EM 1110-2-2704*, Washington D.C.

Modeling of Debris Flow Using Distinct Element Method

Sung-Chi Hsu¹, Chich-Hong Jaing², and Ni-Chi Chen³

¹ Professor, Department of Construction Engineering, Chaoyang University of Technology, 168 Jifong East Road, Wufong District, Taichung 41349, Taiwan; Email: schsu@cyut.edu.tw

^{2,3} Post Graduate Student, Department of Construction Engineering, Chaoyang University of Technology, 168 Jifong East Road, Wufong District, Taichung 41349, Taiwan; Email: ce@cyut.edu.tw

ABSTRACT: The main purpose of this study was to use the discrete element method based program Particle Flow Code (PFC^{2D}) to study the mechanisms of particle movement, including contact forces, displacements, flow pattern, and the strength parameters between particles, of debris flow. The following simulated results based on the particles passing through the falling door tests and the inclined trough tests can be obtained: The particles start moving as the friction angle between particles equals to 28 to 30 degrees as the trough slope is 22 degrees. The angle of repose is about 56 to 60 degrees for particles with friction angle of 28 to 30 degrees. The angle of repose is about 34 to 38 degrees if subtract the trough slope. This angle of repose can be treated as the macro friction angle of the debris materials. The obtained results are similar to the friction angles, 34.7 to 36.2 degrees, tested by Su (1998) on valley deposits using direct shear test. It is found that slope angle is the major reason that controls the incident of debris flow, and then friction angle between particles, volume concentration of the mixture, and friction angle of a slope. The characteristics of the simulated debris flow from this study are very similar to the actual debris flow.

INTRODUCTION

Debris flow is a flow body produced after the action of gravity by materials, such as mud, sand, gravel, cobble and etc., and the mixture of water. Major disastrous damage caused by debris flow can be dated back to 1959 which is known as 8-7 flood occurred at south central part of Taiwan. However, debris flow was not paid great attention in Taiwan until the incident at Tonman Village in June of 1990 and serious damages caused by Typhoon Herb on July 31, 1996. Especially after 921 Chi-Chi Earthquake in 1999, a huge number of debris piled up at the foot of hills, hillsides, or mountain valley, the chance for occurrence of debris flow will be inevitable in the next 10 to 20 years. Many severe debris flows had been occurred in Taiwan almost every year during typhoon season and claimed lots of lives (Hung, 1996; Lin et al., 2006; Cheng, et al., 2000; Yu and Chen, 1990). Thus, researches had been investigated and performed to understand the risk and mechanisms of debris flow at different locations

and to mitigate the impacts of the disasters brought by debris flow.

Most of the slopes of the mountains in Taiwan are very steep due to the continuing pushing effects of two tectonic plates. The rock formations of these areas are young and contain lots of faults, folds, and fractures. Many villages, housings, roads, and slopes had to be constructed and situated on highly weathered rocks, colluviums, or high terrace deposits in these areas. Thus, disasters occurred very often due to landslides and debris flow during typhoon season and after heavy rainfall every year, especially the extreme weather conditions can also occur any time anywhere nowadays. The debris flows present a great threat to the people living in these areas. The objective of this study is to use distinct element method (DEM) based numerical software to model the water flume experiments of debris flow in the laboratory, and to understand the flow mechanism of debris flow between particles, including contact forces, friction angle, and movements.

DEBRIS FLOW AND GEOLOGY IN CENTRAL TAIWAN

Most of the debris flows in central Taiwan happened inside the watershed of the Chen-Yu-Lan River in Nantou County. There are thirty six tributaries that classified as potential debris flow torrents inside this watershed. The locations of the watershed and Nantou County were shown in Figure 1.

Chen-Yu-Lan River is at the central Taiwan and originates from the north peak of Yu Mountain with an elevation of 3910 m. The river length is 42.4 km with an average declination slope of 5% and its watershed area is about 45,000 hectares. There are three major faults, Dili, Chenyulan, and Shanshihchia Faults across this watershed which causes the rock formation contains many fractures and discontinuities. The Chenyulan fault, which almost parallels Chen-Yu-Lan River, separates the Miocene sedimentary rocks of the Western Foothills from the east side of the Oligocene metamorphic rocks of the Shuehshan Range (Figure 1). Differential uplifting along this fault has generated great topographic relief and abundant fractures that resulted in frequent landslides and debris flows even prior to the Chi-Chi earthquake (Lin et al., 2002). Slates and meta-sandstones are the dominant lithologies in the metamorphic terrane. Based on the relative amount of slate and meta-sandstone, the metamorphic strata are divided into four formations: in ascending order, the Shihpachuangchi, the Tachien Meta-Sandstone, the Paileng Meta-Sandstone, and the Shuichangliu. In the sedimentary terrane, sandstone and shale predominate and include the Nankang, Nanchuang, and Kueichulin Formations (Lin et al., 2002).

WATER FLUME EXPERIMENTS

The water flume equipment, shown in Figure 2, was built inside the laboratory and used to simulate the impacts of debris flow. The flume can be raised to 32 degrees. The width, height, and length of the flume are 40, 40, and 600 cm, respectively. Several studies had been performed using this equipment to understand the deposition pattern, depth, and grain separation effect of debris flow, and had been used to compare the effectiveness of several retaining structures that commonly used for reducing or stopping the impacts by debris flow in Taiwan. Therefore, this study tried

to use numerical software to simulate similar debris flow tests that performed using water flume experiments and to obtain the parameters that suitable for the materials for future numerical experiments of debris flow.

The materials used for the water flume tests were sampled inside the watershed of Chen-Yu-Lan River, shown in Figure 1. This location had suffered debris-flow hazards several times. The gravel content of the debris flow is 81.3% and the dry unit weight is 1.72 t/m^3 . The maximum size of the debris-flow material was large than 1m. In order to run water flume tests in the laboratory, the weight-replacement method was used to reduce the maximum size of the material to 38.1 (1.5 in) mm.

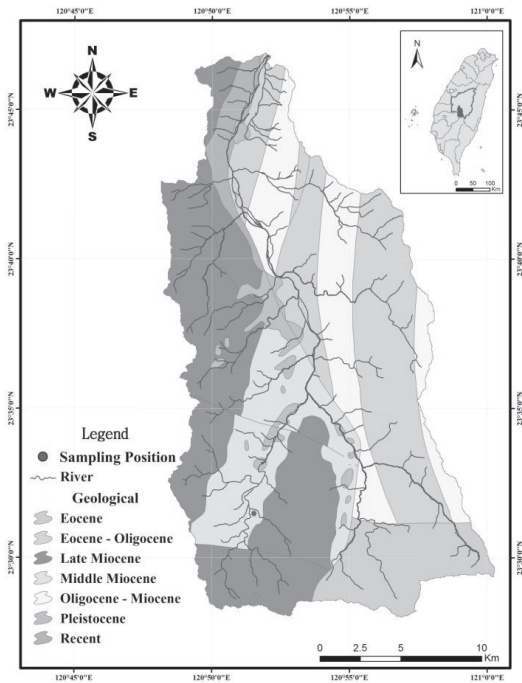


FIG. 1. Locations of Chen-Yu-Lan Watershed and sampling location.

METHOD OF NUMERICAL ANALYSES

In order to model the debris flow by water flume experiments in the laboratory, a discrete element method based numerical software was chosen to simulate the experiments. A discrete element method (DEM), also called a distinct element method, is a numerical method for computing the motion and interaction of granular particles. The method was developed by Cundall in 1971 (Cundall and Strack 1979) to apply on rock mechanics. The method can be used to analyze the stresses, movements, rotation, and separation between particles. It allows finite displacements and rotations of discrete bodies including complete detachment and also recognizes new contacts

automatically as the calculation progresses. The commercial program, two-dimensional Particle Flow Code, i.e. PFC^{2D}, developed by Itasca Consulting Group (2004) is used here in this study to model the debris flow simulated by water flume tests and to obtain the friction angles between particles and the flume.

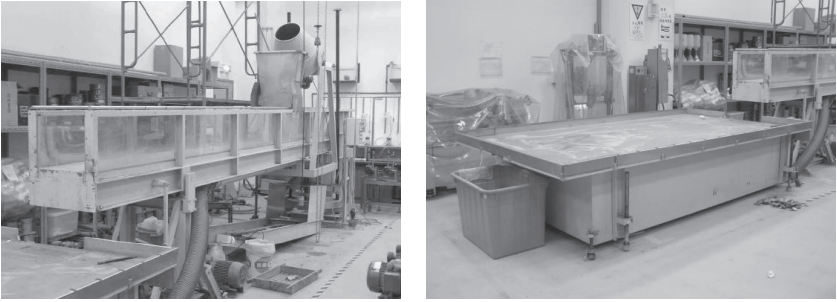


FIG. 2. The water flume equipment in the laboratory.

The reasonable ranges of mechanical properties of the particles used for the numerical analyses have to be chosen before modeling the water flume tests. The input properties for PFC include the amount of different sizes of particles, friction angle for each particle, and contact normal stiffness (K_n) and shear stiffness (K_s) of each particle (ball) and boundary (wall). The macroscopic friction angle of gravel-type debris flow was found to be around 30 to 40 degrees. Therefore, the simulated macroscopic friction angle (ψ) was chosen as 35 degrees in this study. Different microscopic (inter-particle) friction angles (φ) were assumed to model the test. The K_n and K_s were chosen based on previous studies by Lin (2006). The input parameters for the numerical analyses were tabulated in Table 1. The number and diameter of particles for modeling were calculated based on the sediment volume concentration (C_d) and grain-size distribution for the water flume experiments. The diameters of the particles between 0.3~1 cm, 1~2.05 cm, and 2.05~3.81 cm contained 20, 30, and 20% of the total volume used by the water flume tests after weight replacement method. The modeled volume concentrations (C_d) were 0.5, 0.55, and 0.6, and only the grain size greater than 0.3cm, i.e. D_{30} , was considered to generate in this study to minimize the time for numerical modeling. Therefore, the number of particles generated for the numerical simulation was estimated based on the volume concentration and percentage of grain-size distribution. The number of particles used for numerical experiments was around 8000 balls.

In order to model the water flume experiments, the boundaries (walls) for the flume and deposition pan and material particles (balls) on the dipped flume had to be generated first. A wall at the top of the flume was used to retain the generated particles. These particles were generated inside the space between the retaining wall and flume and subsided down by its self-weight, shown in Figure 3. The modeled gradients of the flume (α) were 16°, 19°, and 22°. The objective of the simulation is to understand the influence of friction angle between particles, flume gradient, and volume concentration on flowing distance of horizontal movement during deposition of debris

flow. The friction angle of the flume, i.e. the roughness of flowing gully, was assumed to be equal to 17.5 degrees according to the previous studies.

Table 1. Material parameters used in the numerical simulation.

| | | |
|------|------------------------------|---|
| Wall | Kn | 10^8 N/m |
| | Ks | 10^8 N/m |
| | Friction Angle | 17.5° |
| Ball | Density | 19.03 kN/m ³ |
| | Friction angle (φ) | $5^\circ \sim 45^\circ$ |
| | Kn | 1×10^6 N/m |
| | Ks | 3×10^5 N/m |
| | Spin | Coarser grain is fixed Finer grain is free to spin |

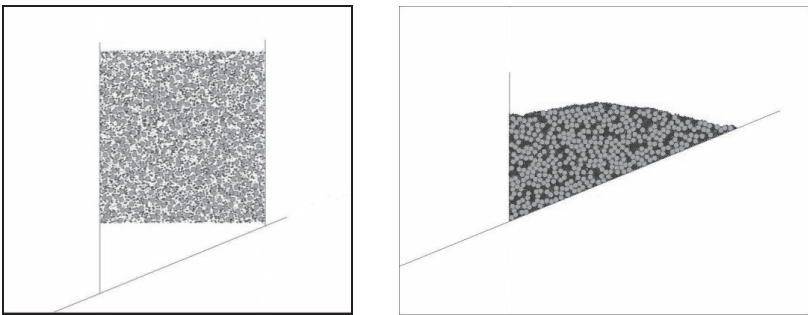


FIG. 3. Particles were generated between the walls and deposited above the flume.

RESULTS OF NUMERICAL EXPERIMENTS

Impacts of Flume Gradient and Friction Angle from Water Flume Test

The results of numerical experiments simulated by PFC showed that the friction angle of the particles that influenced the horizontal movement (counted from the stopping wall during deposition) of the materials that brought by the debris flow. Figure 4 showed that if the friction angle of the particles was greater than 30 degrees then most of the particles may stay on the flume except some particles fell off for the flume gradient (α) was 22 degrees. Lower volume concentration (C_d) yielded wider deposition range or horizontal flowing movement. The particles started moving as the friction angles were less than 30 degrees. The angles of repose for these particles on a flat ground were 60 degrees simulated by PFC. Thus, the friction angles between these particles and the flume with gradient of 22 degrees were around 38 degrees. The results are comparable to the measured friction angles, 34.7~36.2 degrees, using in-

situ direct shear tests on the deposited materials at the same valley by Su (1998).

For the flume gradient (α) was 19 degrees, the particles began to move or slide if the friction angle was smaller than 25 degrees. The obtained angle of repose was 50 degrees for the friction angle between particles is 25 degrees. The friction angles between these particles and the flume with gradient of 19 degrees were around 31 degrees. The flowing speed and the spreading range of the deposited particles would become smaller if the gradient of the flume was gentler.

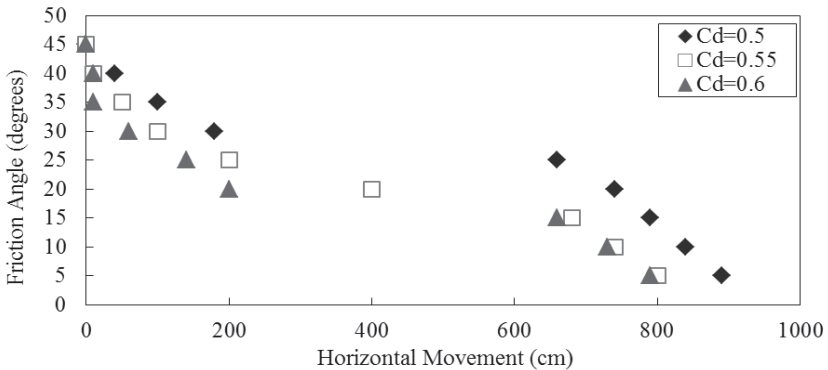


FIG. 4. Influence of friction angle of the particles and volume concentration (Cd) on horizontal movement of debris flow deposition. ($\alpha = 22^\circ$)

Modeling of In-situ Debris Flow

In order to know the impacts and interaction of different sizes of particles on debris flow, PFC was used to model the debris flow that may occur in situ. Through the experiments, the distinct element method based numerical program allows the particles to separate, rotate, collide and slide in order to simulate the processes of debris flow. The size and percentage of the particles used for simulation were based on the in-situ grain-size distribution (Yang, 2005). Only the grain sizes above D_{50} , 2.8cm~30cm, were considered in the modeling to save the simulation time.

The moving characteristic of debris flow was model first to compare with the in situ flowing pattern. Figure 5 showed the results of moving particles. There were bigger particles located on top and in front of the moving front. This was also observed from the in-situ debris flow. The shape and pattern of the moving particles were also similar to the pattern of in-situ debris flow, as shown in the left-upper corner plot of Figure 5.

The length and slope of the debris flow that occurred at Chushui Creek in Nantou County was used as an example to model (Yang, 2005). The slope of the creek that developed debris flow was around 29 degrees. The percentage and number of particles were generated according to the grain-size distribution. However, only the grain sizes greater than D_{50} , 2.8~30cm, were used in the analyses. Particles were generated above the designed slope and settled down on the slope as shown in Figure 6. The friction angle between particles was assumed as 17.5 degrees, then applied larger contact

normal and shear bounds between particles to maintain the particles on the slope. The particles started moving as the contact bounds smaller than 3×10^3 N as shown in Figure 7. The particles were allowed to move downward. The deposited pattern and range were shown in Figure 7. The highest deposited height was 11m and deposited length over the creek was 150m. The deposited height at this creek after the debris flow was measured as 7 to 10 m. The simulated result was comparable to the in-situ debris flow.

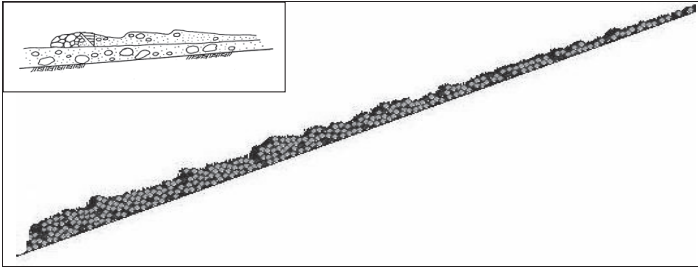


FIG. 5. The flowing shape and pattern of the debris flow simulated by PFC.

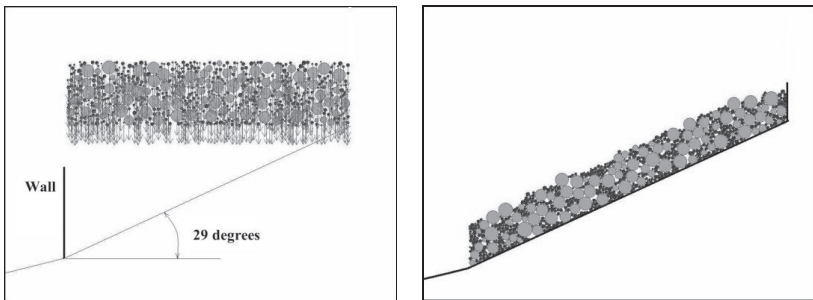


FIG. 6. Particles generated above the slope and settled on the slope.

CONCLUSIONS

This study use distinct element method based program PFC to model debris flow. Some conclusions can be drawn as below.

1. Lower volume concentration (Cd) yielded wider deposition range or horizontal flowing movement.
2. The flowing speed and the spreading range of the deposited particles would become smaller if the gradient of the flume was gentler.
3. The obtained shape and pattern of the moving particles were similar to the pattern of in-situ debris flow.
4. The particles started moving as the contact bounds smaller than 3×10^3 N. The simulated deposited height, 11m, was comparable to the in-situ debris flow.

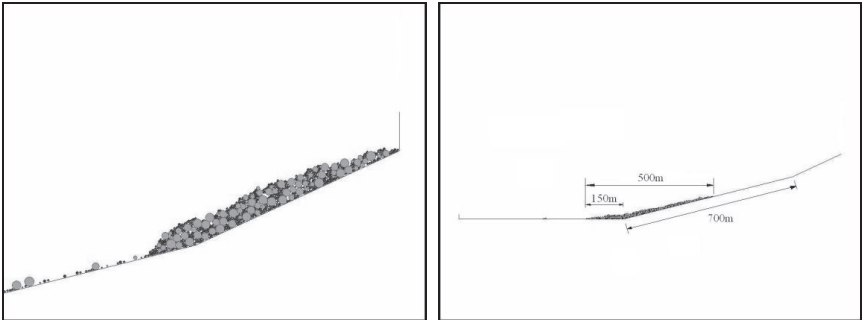


FIG. 7. Particles started moving downward and deposited ranges.

ACKNOWLEDGMENTS

The authors appreciate the support of the National Science Foundation of Taiwan.

REFERENCES

- Su, D.Y. (1998). "The Study of Engineering Geology Characteristic of Debris Flow along Hoshe River, Nantou." Master Thesis, Department of Geology, National Taiwan University (in Chinese).
- Hung, J.J. (1996). "Typhoon Herb, the New-Central-Cross-Island-Highway and slopland failures in central Taiwan. " *J. Sino-Geotech.* 57, 25–30 (in Chinese).
- Lin, P.S., Lin, J.Y., Hung, J.C., and Yang, M.D. (2002). "Assessing debris-flow hazard in a watershed in Taiwan. " *Engineering Geology* 66:295-313.
- Yu, F. C. and Chen, C. G. (1990). "Basic Study on the Debris Flow: Preliminary Study on the Flow Velocity of Debris Flow. " *Journal of Soil and Water Conservation*, No 21~22, pp115-142 (in Chinese).
- Lin, G.F., Chen, L.H., and Lai, J.N. (2006). "Assessment of Risk due to Debris Flow Events: A Case Study in Central Taiwan, Na. " *Natural Hazards* 39: 1–14.
- Cundall, P. A. and Strack, O. D. L. (1979). "A Discrete Numerical Model for Granular Assemblies." *Géotechnique*. 29: 47-65.
- Yang, T.F. (2005). "Study on characteristics of debris-flow retaining and deposition fro various dam types." Master Thesis, Department of Construction Engineering, Chaoyang University of Technology, Taiwan (in Chinese).
- Itasca Consulting Group Inc. (2004). *PFC^{2D}* (Particle Flow Code in 2 Dimensions), Version 3.1. Minneapolis: ICG.
- Lin, S.C. (2006). "Modeling of Shear Strength and Anchorage Behavior of Anchors in Gravel Formation Using Distinct Element Method." Master Thesis, Department of Construction Engineering, Chaoyang University of Technology, Taiwan (in Chinese).

Shear Stress-Strain Curves Based on the G/G_{\max} Logic: A Procedure for Strength Compatibility

James R. Gingery¹, PE, GE, M. ASCE and Ahmed Elgamal², PhD, M. ASCE

¹ Principal Engineer, Kleinfelder, San Diego, California and PhD Candidate, University of California, San Diego, Dept. of Structural Engineering, La Jolla, California; jgingery@kleinfelder.com.

² Professor, University of California, San Diego, Dept. of Structural Engineering, La Jolla, California; elgamal@ucsd.edu.

ABSTRACT: Hyperbolic models are frequently used in practice to represent nonlinear shear stress-shear strain behavior of soils in equivalent linear and nonlinear dynamic modeling problems. Several researchers have proposed shear modulus reduction (G/G_{\max} versus γ) curves that use the hyperbolic model as their basis, with parameters that fit the models to cyclic laboratory test results. However, cyclic laboratory tests often are not run to failure shear stress levels. Consequently, the model G/G_{\max} curves are well constrained by the data at small to moderate shear strains, but do not necessarily provide an accurate representation of soil strength at large shear strains. In some cases, the shear strength can be grossly inaccurate, which may result in significant errors for analyses involving shear stress levels at or near failure. In this paper, a new hybrid methodology is presented that permits simultaneous matching of: 1) the conventional shear modulus reduction curves that are well calibrated at small to moderate shear strains and; 2) the soil shear strength at large strain. This hybrid approach produces shear modulus reduction curves that result in corresponding hyperbolic-like smooth stress-strain backbone curves. These curves assure that the soil shear strength consideration is accurately represented for the purposes of both equivalent-linear and nonlinear analyses.

BACKGROUND

The hyperbolic model for shear stress (τ) versus shear strain (γ) backbone curves has found wide use in fitting laboratory test data (Konder & Zelasko 1963; Hardin & Drnevich 1972; Darendeli 2001; Menq 2003; Roblee & Chiou 2004) and in nonlinear site response analysis programs (i.e., Matasovic 1993; Hashash & Park 2001; Yang et al. 2003). The hyperbolic model proposed by Hardin & Drnevich (1972) for shear modulus reduction (G/G_{\max}) as a function of γ has the form:

$$\left(\frac{G}{G_{max}} \right)_{HD} = \frac{1}{1 + \frac{\gamma}{\gamma_{ref}}} \quad (1)$$

where the reference strain, $\gamma_{ref} = \tau_{ff}/G_{max}$, τ_{ff} is the shear stress at failure (peak or maximum shear stress) on the failure plane and G_{max} is the small strain maximum shear modulus. With $\tau = \gamma G$ it is apparent that Eqn. (1) results in τ approaching τ_{ff} asymptotically at large values of γ (at $\gamma = \infty$). This form of the hyperbolic model has the advantage that it can be easily calibrated to satisfactorily match shear strength, but it is often inconsistent with laboratory test data at small and moderate shear strains.

Darendeli (2001), Menq (2003) and Roblee & Chiou (2004) used an alternate form of the hyperbolic model which provides added flexibility that allows a better fit to laboratory test data at small to moderate strains:

$$\left(\frac{G}{G_{max}} \right)_{PRSH} = \frac{1}{1 + \left(\frac{\gamma}{\gamma_r} \right)^\alpha} \quad (2)$$

Where γ_r is a “pseudo-reference strain” and α is an additional fitting parameter. We refer to models of the form of Eqn. (2) as pseudo-reference strain hyperbolic (PRSH) models in this paper. The form of Eqn. (2) is such that a value of $(G/G_{max})_{PRSH} = 1/2$ occurs at $\gamma = \gamma_r$. Darendeli (2001) developed a family of $G/G_{max} - \gamma$ curves based on regression of data from numerous resonant column torsional shear (RCTS) tests conducted at the University of Texas, Austin. The parameter α was set at 0.919 and values of γ_r were reported as a function of soil plasticity index (PI), mean confining stress (σ_m) and overconsolidation ratio (OCR). Menq (2003) used the same form of Eqn. (2) to fit RCTS test data for sands and gravels with values of γ_r and α calculated as a function of uniformity coefficient (C_u) and mean effective stress. Roblee & Chiou (2004) provided values of α for three soil-type groups and six depth bins.

The laboratory test data used to curve-fit these PRSH model coefficients becomes sparse to non-existent at moderate to high shear strain levels. For instance, FIG. 1 from Darendeli (2001) shows that very little RCTS data was available above a shear strain of 0.3%. Therefore, it is evident that shear strains achieved in most of the RCTS tests were not sufficient to mobilize the full shear strength of the soil. Thus, PRSH models developed from such laboratory testing data sets require further information in the large shear strain regime in order to provide accurate representation of shear strength and the corresponding nonlinear soil response (beyond 0.3 % or so).

For the purpose of the study herein, shear strength is calculated from a shear modulus degradation curve as:

$$\tau_{ff} = G_{max} \cdot (G/G_{max})_{\gamma_f} \cdot \gamma_f \quad (3)$$

where $(G/G_{max})_{\gamma_f}$ is the shear modulus degradation value at a user-defined failure

strain γ_f . In conducting SHAKE-type (Schnabel et al. 1972) equivalent linear analyses: i) commonly available G/G_{max} curves are used, which include no special consideration of shear strength, and ii) G_{max} is calculated from small strain shear wave velocity information which might not strongly correlate with shear strength. Thus, any accuracy in τ_{ff} would only result from a fortuitous combination of G_{max} and the specified variation of G/G_{max} along the curve (beyond the range of the 0.3% or so data from experimentation).

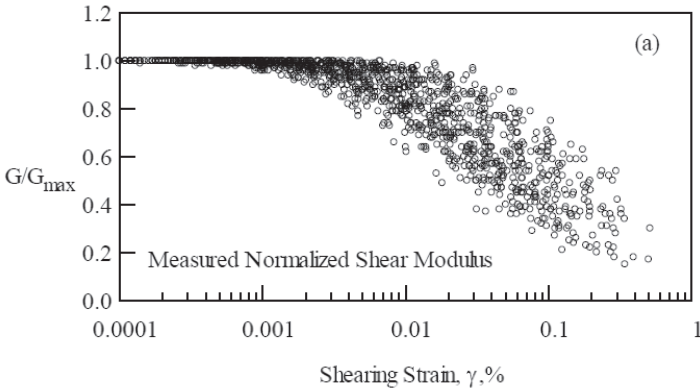


FIG. 1. RCTS data used in development of Darendeli (2001) G/G_{max} curves.

DEMONSTRATION OF ERROR POTENTIAL

The degree to which shear strength can be inaccurately predicted by a PRSH model is illustrated in Figure FIG. 2. The figure presents G_{max} and shear strength for a loose unsaturated sand profile and a fully saturated clay profile. The sand has a relative density of 40%, a friction angle (ϕ') of 30.6 degrees, and a density of 1.77 Mg/m³. The clay has a PI of 30, is normally consolidated and has a saturated density of 1.77 Mg/m³. Shear strength used in the sand profile is based on the Mohr-Coulomb definition for frictional materials, $\tau_{ff} = \sigma'_{v0} \tan(\phi')$ (Holtz & Kovacs 1981). Shear strength in the clay profile was calculated using the SHANSEP method, where $\tau_{ff} = S_u = S \times OCR^{0.8}$ (Ladd & Foot 1974), with $S = 0.22 \times 80\% = 0.18$ computed based on the recommendations of Idriss & Boulanger (2008) for cyclic direct simple shear in clay (i.e., $S_{u,DSS}$, the shear strength used in the profile) and $S = 0.31$ based on recommendations (Ladd & DeGroot 2003) for triaxial compression (i.e., $S_{u,TXC}$, the shear strength used to compute G_{max} described later).

The sand profile used $G_{max} = 1000 \cdot K \cdot (\sigma'_m)^{0.5}$ with $K=40$ according to Seed & Idriss (1971) while the clay profile used $G_{max}/S_{u,TXC} = 700$ for $PI=30$ clay based on Weiler (1988). In FIG. 2, the shear strength implied by the Darendeli (2001) PRSH model ($\tau_{ff,PRSH}$) is calculated using Eqns (2) and (3) with $\gamma = \gamma_f = 6\%$ (results are similar for other values of γ_f).

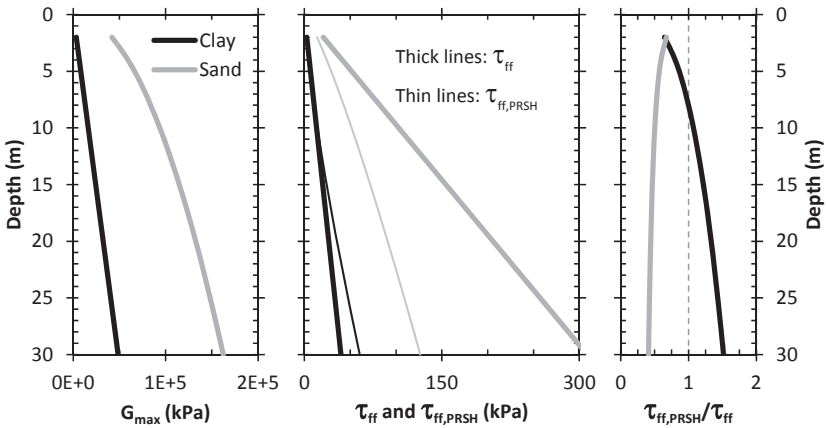


FIG. 2. Example sand and clay profiles illustrating differences between estimated shear strengths, and shear strengths implied by a PRSH model (as calibrated by low/moderate shear strain levels).

It is evident from Figure FIG. 2 that the shear strength implied by the Darendeli (2001) PRSH model is 41% to 67% of the actual shear strength for the sand profile. For the clay profile, the Darendeli (2001) shear strengths are 64% to 152% of the actual shear strengths. Such shear strength discrepancies could result in significant errors for equivalent linear or non-linear site response analyses where shear strains occur that are at or approaching the failure shear strain. Similar results can be obtained from any PRSH model (on account of the limitations of curve fitting as dictated by the underlying hyperbolic-model logic).

In order to address this important issue, Stewart et al. (2008) recommended a $G/G_{max} - \gamma$ curve adjustment procedure in which Eqn (2) is used below a shear strain of 0.1 to 0.3%, Eqn. (1) is used above the failure strain, and an interpolation scheme is used to transition from Eqn (2) and (1) at intermediate shear strains. However, in some instances, the Stewart et al. (2008) interpolation scheme unintentionally introduces a superfluous “kink” in the shear stress-strain backbone curve. If so, tedious manual smoothing of the kink is required, particularly for implementation within an automated computer code.

PROPOSED PRSH G/G_{max} CURVE MODIFICATION SCHEME

A new interpolation scheme is presented herein that produces $G/G_{max} - \gamma$ curves that simultaneously match: 1) the PRSH models where they are well constrained by data at small to moderate strains and; 2) the shear strength at large strains. The proposed model provides a smooth, “kinkless” hyperbolic-like curve to transition between moderate and failure-level shear strains. The Darendeli (2001) model is used for demonstration purposes in this paper, but the proposed modification scheme can be

applied to any PRSH model of the form shown in Eqn. (2) (such as Roblee & Chiou 2004 or Menq 2007). The proposed “GH model” scales Eqn (2) using a raised cosine function to force the curve to intercept a G/G_{max} value at γ_2 (i.e., the failure strain) that produces the correct shear strength given G_{max} , ϕ and σ'_{vo} . The GH model uses Eqn. (2) for $\gamma < \gamma_1$. Between γ_1 and γ_2 Eqn. (2) is multiplied by a raised cosine weighting function (W) and for $\gamma > \gamma_2$ values of G/G_{max} are provided that result in $\tau = \tau_{ff}$, viz.:

$$\left(\frac{G}{G_{max}}\right)_{GH} = W \cdot \left(\frac{G}{G_{max}}\right)_{PRSH} \tag{4}$$

where

$$W = \begin{cases} = 1 & \text{for } \gamma \leq \gamma_1 \\ = 1 + \left[\frac{(G/G_{max})_{\tau_{ff}, \gamma = \gamma_2}}{(G/G_{max})_{PRSH, \gamma = \gamma_2}} - 1 \right] \cdot \left\{ \frac{1}{2} - \frac{1}{2} \cos \left[\pi \frac{\ln(\gamma) - \ln(\gamma_1)}{\ln(\gamma_2) - \ln(\gamma_1)} \right] \right\}^n & \text{for } \gamma_1 < \gamma \leq \gamma_2 \\ = \frac{\tau_f}{\gamma G_{max} (G/G_{max})_{PRSH, \gamma}} & \text{for } \gamma > \gamma_2 \end{cases} \tag{5}$$

On this basis, the G/G_{max} value that provides the correct shear strength (τ_{ff}) at γ_2 is:

$$\left(\frac{G}{G_{max}}\right)_{\tau_{ff}, \gamma = \gamma_2} = \frac{\tau_{ff}}{\gamma_2 \cdot G_{max}} \tag{6}$$

and $(G/G_{max})_{PRSH, \gamma = \gamma_2}$ is the shear modulus reduction value predicted by the PRSH model at γ_2 . The exponent n can be used to manipulate the shape of the raised cosine weighting function, and in the current implementation n is taken as 1. The parameter γ_1 must be selected judiciously so that the adjustment does not produce $\tau/\tau_{ff} - \gamma$ curves with strain-softening behavior. A value of $\gamma_1=0.05\%$ has been found to avoid strain softening over a fairly wide range of conditions. The shape of the $\tau/\tau_{ff} - \gamma$ curves are less sensitive to the γ_2 parameter, which should be chosen at or near the shear strain where the shear strength is reached.

EXAMPLES OF MODIFIED G/G_{max} CURVES

The proposed modification scheme is illustrated by applying it at depths of 4, 8, 16 and 30 m within the sand and clay profiles from FIG. 2. The PRSH model G/G_{max} curves were computed using Darendeli (2001) and the soil parameters described earlier. Weighting values were calculated using Eq. (5) with $\gamma_1=0.05\%$ and $\gamma_2=6\%$, and G/G_{max} values adjusted according to the proposed model were calculated using Eq. (4). The results are presented for the sand profile in FIG. 3 and FIG. 4 and in FIG. 5 and

FIG. 6 for the clay profile.

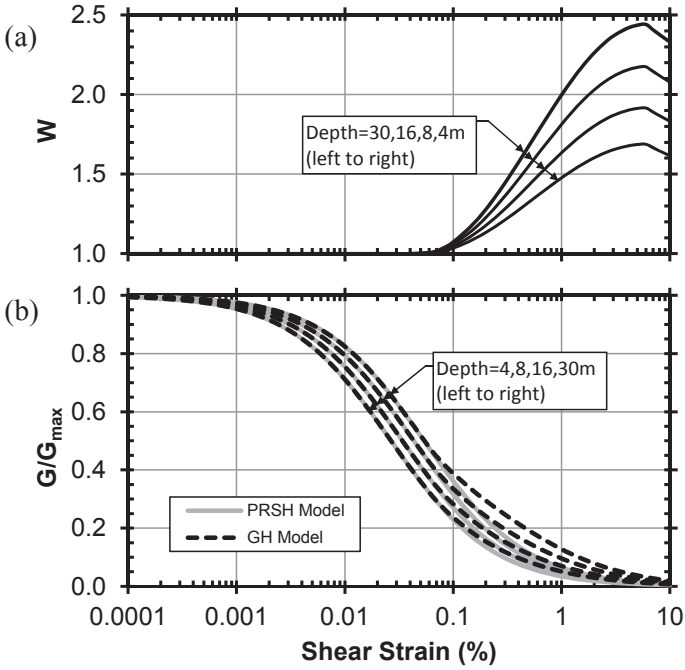


FIG. 3. (a) Weighting values (W), and (b) G/G_{max} curves computed using the PRSH and GH models at various depths in the sand profile.

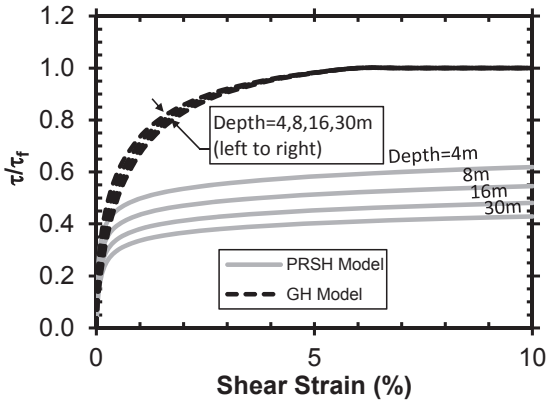


FIG. 4. Shear stress versus shear strain curves computed using the PRSH and GH models at various depths in the sand profile.

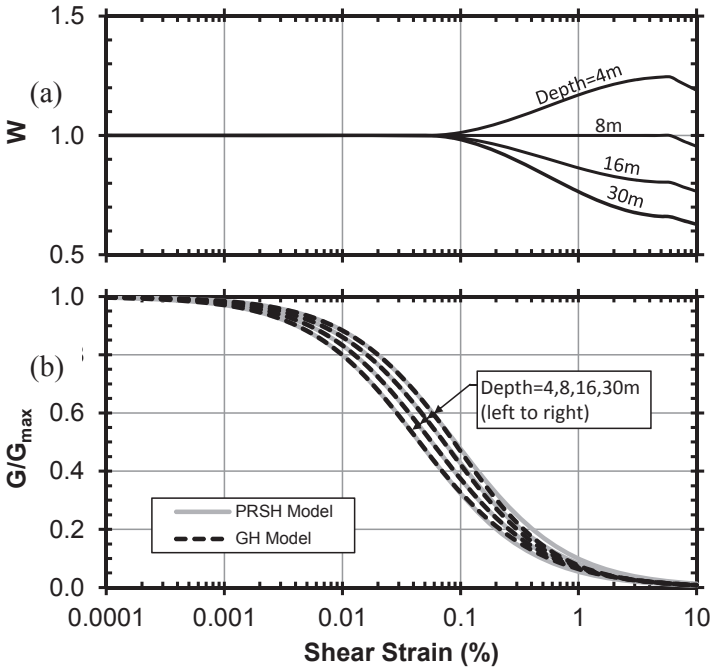


FIG. 5. (a) Weighting values (W), and (b) G/G_{max} curves computed using the PRSH and GH models at various depths in the clay profile.

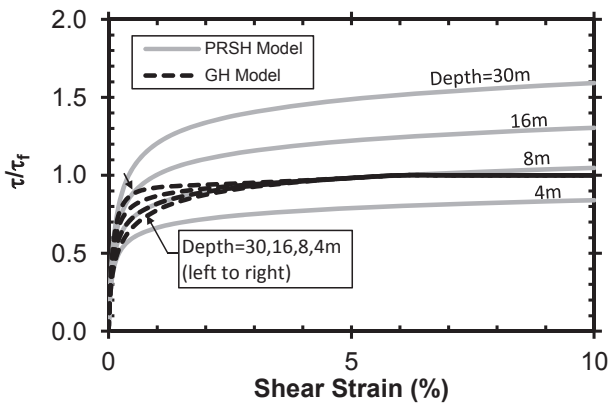


FIG. 6. Shear stress versus shear strain curves computed using the PRSH and GH models at various depths in the clay profile.

The adjusted $(G/G_{max})_{GH} - \gamma$ curves gradually diverge from the $(G/G_{max})_{PRSH} - \gamma$ curves above γ_1 and converge to $(G/G_{max})_{\tau/\tau_{ff}, \gamma=\gamma_2}$ at γ_2 . The $\tau/\tau_{ff} - \gamma$ curves maintain a smooth hyperbolic-like shape without strain softening and converge to the shear strength γ_2 .

CONCLUSIONS

Current PRSH models for $G/G_{max} - \gamma$ curves are calibrated based on test data at moderate to large (failure) shear strain levels, and therefore require further information and possible tweaking to produce an accurate representation of soil shear strength. An example has been provided that shows that use of a PRSH model results in under- and over-estimation of actual shear strengths by up to a factor of 2. A new method to adjust PRSH model $G/G_{max} - \gamma$ curves is presented herein which produces $\tau/\tau_{ff} - \gamma$ curves that match the material shear strength exactly at large strain levels while following the PRSH models at small to moderate shear strain levels where they are well constrained by laboratory data. Provided that parameters γ_1 and γ_2 are judiciously selected, the adjusted $\tau/\tau_{ff} - \gamma$ curves exhibit a smooth, hyperbolic-like shape without strain softening. The developed adjustment scheme can be easily implemented in a spreadsheet or similar tool for routine use in engineering application.

REFERENCES

- Darendeli, M. (2001). "A new family of normalized modulus reduction and material damping curves for equivalent linear analysis," PhD Dissertation, University of Texas, Austin.
- Hardin, B. O. & Drnevich, V. P. (1972). Shear modulus and damping in soils: design equation and curves. *J. Soil Mech. Found. Engng. Div., ASCE* **98**, No. 7, 667–691.
- Hashash, Y.M.A. and Park, D. (2001). "Non-linear one-dimensional seismic ground motion propagation in the Mississippi embayment," *Eng. Geol.*, 62(1-3), 185-206.
- Holtz, R.D. and Kovacs, W.D. (1981). *An Introduction to Geotechnical Engineering*, Prentice Hall, 733 pp.
- Idriss, I.M. & Boulanger, R.W. (2008). *Soil Liquefaction During Earthquakes*, EERI Monograph MNO-12.
- Konder, R.L. and Zelasko, J.S. (1963). "Hyperbolic stress-strain formulation of sands," *Proc. 2nd Pan American Conference on Soil Mechanics and Foundation Engineering*, Sao Paulo, Brazil.
- Ladd, C.C. and Foote, R. (1974). "A new design procedure for stability of soft clays," *J. of the Geotechnical Engr. Div., ASCE*, Vol. 100, No GT7, pp. 763-786.
- Ladd, C.C. and DeGroot, D.J. (2003). Invited Paper: "Recommended practice for soft ground site characterization." The Arthur Casagrande Lecture, *Proc. of the 12th Panamerican Conf. on Soil Mechanics and Geotechnical Engr.*, Boston, MA, 3-57.
- Matasovic, N. (1993). "Seismic response of composite horizontally-layered soil deposits," PhD Dissertation, University of California, Los Angeles.
- Menq, F-Y (2003). "Dynamic properties of sandy and gravelly soil," PhD Dissertation, University of Texas, Austin.
- Roble, C. and Chiou, B. (2004). "A proposed geoindeces model for design selection of

- non-linear properties for site response analyses,” *International Workshop on Uncertainties in Nonlinear Soil Properties and Their Impact on Modeling Dynamic Soil Response*, PEER Headquarters, UC Berkeley.
- Schnabel, P.B., Lysmer, J. and Seed, H.B. (1972). “SHAKE: A computer program for earthquake response analysis of horizontally layered sites,” Report No. UCB/EERC-72/12, University of California, Berkeley, December, 102p.
- Seed, H.B. and Idriss, I.M., (1971). “Simplified procedure for evaluating soil liquefaction potential,” *J. of the Geotech. Engr. Div.*, ASCE, 97(9), pp 1249-1273.
- Stewart, J.P., Kowk, A., Hashash, Y.M.A., Matasovic, N., Pyke, R., Wang, Z. and Yang, Z. (2008). “Benchmarking of nonlinear geotechnical ground response analysis procedures,” PEER Report 2008/04.
- Weiler, W.A. (1988). “Small strain shear modulus of clay,” *Proc. Of ASCE Conference on Earthquake Engr. and Soil Dyn. II: Recent Advances in Ground Motion Evaluation*, GSP 20, ASCE, New York, 331-345.
- Yang, Y., Elgamal, A. and Parra, E. (2003). “Computational model for cyclic mobility and associated shear deformation,” *J. Geotechnical & Geoenv. Engrg.*, Vol. 129 (12): 1119-1127

Micro-Structure behavior of soft clay under consolidation through radial flow using PVDs

Manish V. Shah¹ and Arvind V. Shroff²

¹Assistant Professor, Applied Mechanics Dep't, L.D. College of Engineering, Ahmedabad, India-380015; mvs2212@yahoo.co.in

²Professor Emeritus, Applied Mechanics Dep't, The M.S University of Baroda, Vadodara, India-390001; dravshroff@yahoo.co.in

ABSTRACT: Paper discusses some of the most critical issues related to behavior of clay particles during consolidation phenomena through radial flow using central vertical drains. The macro mechanics of consolidation of soil is evaluated using scanning electron microscopy of consolidated clay samples based on development and dissipation of excess pore water pressure using vertical drains viz. coir-jute fiber drain and sand drain of varying diameters. Micro compressibility of soft clay mass based on volumetric porosity is deduced with Quanti-image analyzer with system of micro structure characterization (MIC) software thereby introducing a relation between rate of consolidation, rate of suction and rate of repulsion of clay-pore water system. This methodology has given better clues to find eco-bio vertical geodrain for rapid consolidation of soft soils.

INTRODUCTION

This study an attempt is made to propose a theoretical philosophy of role of clay particle structure on pore water particle between soil and at drain interface. Kaolin clays are produced by chemical weathering of alumino-silicates and are generally grouped as colloidal particles. Clay particles are plate shaped or tubular because the layer-lattice structure results in strong bonding along two axes but weak bonding between layers. The variation in specific surface area is primarily due to different thicknesses of the tubular particles. Variation in other two dimensions of clay particles is related to degree of crystallinity of the clay minerals. Generally, water adsorption and formation of gels at low concentrations are properties of colloidal particles depending on specific surface area. The main force bonding water to the surface is due to hydrogen bond and as we are dealing with consolidation of saturated clays, role of such bonds on particle orientation and its possibility to diffuse at various stress levels should be properly determined.

Compressibility of soft clay mass depends both on 'microstructure' and 'macrostructure' which is function of many parameters viz. type of pore water, shape of pores, spacing of pores, pore forces (attraction and repulsion), rate of flowability of pore water and displacement of solid particle and lastly transformation of colloidal nano clay fabric into a more thicker clay fabric.

The objective of this paper is to discuss the above stated parameters and study the role of pore water and its various forms associated with clay particle under long duration loading, role of energy state of pore water in clay mass by creating energy

gradients, role of kinetic and potential energy to displace pore water and finally role of difference between external consolidation load and self weight of saturated clay mass in accelerating rate of consolidation through vertical drains. Objective is also to determine pore volume, angle of orientation of clay particle and tortuosity of consolidated clay mass using Quanti-image analyzer with system of micro structure characterization (MIC) software. It is also aimed to study consolidation characteristics of soft clay mass using vertical geodrain namely coir-jute fiber drain and sand drain of different diameters using theoretical solution given by authors based on isochrones. The above objective is divided into three phases (i) Theoretical aspects and Physicomechanics of consolidation (ii) Experimental investigations (iii) Microscopy of consolidated clay samples

THEORETICAL ASPECTS AND MECHANICS OF CONSOLIDATION-PHASE I

Theory of Consolidation

Shroff & Shah (2009, 2010) gave complete mathematical theory of one-dimensional consolidation through radial flow which incorporates non-homogeneity, time effects intrinsic to the soil skeleton along with physico-chemical changes, compressibility of pore fluid and solid, variation of compressibility and permeability during consolidation, type of the drain material, tortuosity effect, k_h/k_v ratio under load variation, effect of 'n' value (drain diameter) and drainage path. Generalized solution for computing average degree of consolidation (U_r) for different values of λ based on Laplace transform technique was also given by the authors as shown by equation 1. Based on various positive and negative values of lump parameter ' λ ' (as shown in equation 1) a series of isochrones are plotted from which average degree of consolidation is computed using Simpson's rule as explained in Taylor (1948) and Lambe-Whitman (1969).

$$R = \frac{r}{r_e}, \quad T = \frac{C_r t}{r_e^2}, \quad \lambda = r_e \frac{C_e}{C_r} \quad (1)$$

Taking,

$$U_r = \frac{e - e_o}{e_1 - e_o} = \exp\left\{\left(\frac{\lambda}{2}\right)\right\} * \left[\frac{\text{Sinh}\frac{\lambda}{2} R}{\text{Sinh}\frac{\lambda}{2}} + 2\pi \sum_{n=1}^{\infty} \frac{(-1)^n n \text{Sin}(n\pi R)}{\lambda^2/4 + n^2 \pi^2} \exp\left\{-\left(\lambda^2/4 + n^2 \pi^2\right) T\right\} \right] + \exp\left\{-\left(\lambda/2\right)\right\} * \left[\frac{\text{Sinh}\frac{\lambda}{2} (1-R)}{\text{Sinh}\left(\lambda/2\right)} - 2\pi \sum_{n=1}^{\infty} \frac{n \text{Sin}(n\pi R)}{\lambda^2/4 + n^2 \pi^2} \exp\left\{-\left(\lambda^2/4 + n^2 \pi^2\right) T\right\} \right] \quad (2)$$

Notations used: T= Time factor, C_e = Coefficient due to permeability and porosity, C_r = Coefficient of consolidation due to radial drainage, r_e = radius of influence, t = time in sec, r = any radial distance

The above theoretical solution is quite versatile as it covers effects of drain material, drain diameter, drain geometry and soil properties. After preparing series of charts for various values of ' λ ' a best economic drain suited to given field conditions can be selected and applied. These charts also predict probable consolidation time with particular drain along with settlement data which is very

necessary for any construction project schedule. These charts also define drain material properties, by which use of local available material can be well planned in advance for better economy.

Physicomechanics of Consolidation

Soil physics plays a very vital role in consolidation phenomena through radial flow using vertical drains. Roles of various agencies influencing consolidation process either individual or in group are mentioned below and its importance is discussed. First agency: role of clay particle in terms of body forces, shape of particle, arrangement/orientation of particle under stress, displacement of particle/velocity of particle, surface area of particle, viscosity of clay gel(paste at plastic state) and suction/vacuum capacity of clay particle. Similarly there is a very specific role of second agency: hydrostatic pore water pressure, its development and dissipation and finally role of pore diameter, pore shape, pore length, reaction of active and non-active pores, adhesion and repulsion of pores, layers of pores, diffusion of pores, rotation and displacement of pores. Third agency: role of pore-clay turbid water (colloidal or dispersive state) and viscosity of clay turbid water is influenced by drain material properties, permeability of drain material and either physical or chemical composition of drain material with the ease it can attract water radially. Fourth agency: role of ultramicroporosity ($d < 1\mu$), intermediate porosity divided as low intermediate porosity ($d < 20\mu$) and high intermediate porosity ($d > 20\mu$) and inter-particle/fabric porosity. Fifth agency: role of gravitational water, capillary water, water held by osmotic forces, loosely bound water, gases bound to the surface of particles and free gases which mix freely.

First agency

During the initial process of consolidation, the clay particles are randomly oriented in a saturated soil mass. The particles less than 2μ develop crystallographic contours and edges get diffused. They may be either flat-isometric or flat-elongated or prismatic or spherical or any other shape, while particles of size 0.002-0.05mm may be either of tablet shape or elongated or isometric or wedge shaped (platy type), while particles of size greater than 0.04mm may be crystalline or flat or plate type or elongated or mixed contour type or any irregular form.

The figure 1 to figure 4 shows the micrograph of consolidated clay sample with central coir-jute drain. Referring to this micrograph the shapes of oriented particles can be obtained at various stress levels at fix position from the centre of drain at same depth and at same radial distance. The orientation of particle is influenced by both displacement of particle and velocity of pore fluid. The reason is justified in following way: let us consider a layer of particles one above the other separated by thin and thick film of water along with pore water. When load is applied on the mass externally the stresses are transferred to solid part and pore water. Now as pore water is not able to escape and load is barred by clay fabric, the deformation of clay fabric starts along with its orientation to achieve equilibrium. Soon the drainage is allowed to dissipate pore water, sliding of particle starts, which is due to pore water and its velocity. Here pore water or clay is in colloidal state and will remain in suspension because of thin film of water. At this level there exists a potential gradient between particles of first layer to second layer till

last layer. This gradient changes with change in position of pore water itself in pore and in whole mass. Faster the dissipation the faster is orientation.

Potential gradient is maximum at intermediate period of test because initially particles which are in colloidal state moves along with pore water creating fluid friction on surface of clay fabric and gradient is minimum at final stage of consolidation. Potential gradient is created between two pores, as pore of higher diameter pushes pore of lower diameter under particular load at various locations along the sample. At this level it can be said that specific surface area of clay fabric (plate type) is more compare to other shape particles and so particles get rotate themselves nearer either in form of face-to-face or edge-to-face because of strong bonding attraction. Structural viscosity of fluid depends on the shape of pore water particulate, fluid velocity and clay particle/fabric shape. As shape of clay particle will become more plated type and orient towards horizontal plane, magnitude of viscosity decreases. Viscosity increases particle interaction and formation of floccs is found at low stresses. This floccs is responsible for edge-to-edge and edge-to-face arrangement.

The last component in first agency is suction capacity of clay fabric and vacuum capacity of pores. Due to good cation exchange capacity of Kaolinite intra-pores of clay particle starts suction of free movable water and the gap between two intra-pores create vacuum which is either occupied by air or gases. This cycle continues till bonds get broken and pore diffusion takes place. This diffusion is release of kinetic energy and thus pore water gets new path to escape freely.

Second agency

Development and dissipation of excess pore water pressure under given magnitude of loading depends on active and non-active pores. Active pores are those pores which are present in soil mass and soil fabric while non-active pores are those pores which are present in soil mass but do not involve themselves in dissipation of pore water process. As mentioned earlier that energy gradient is created either because of work done by clay particle to get deform (breaking of edges) or displacement and the amount of energy released in form of dissipation of pore water pressure and with time the energy gradient approaches to unity which is not always possible because bunch/cluster of clay particles now acts as thick plates which requires more energy and active pores and non-active pores remain under rest condition till new higher magnitude of load is not applied. At this level author proposes strong philosophy based on micro observations of dissipation of pore water, its rate and volume of pore water collected at end of each noted period, that formation of some new pores takes place between deformed soil particles and also the small amount of air which is not able to dissolve himself with free water, reduces movability of pore water both radially and vertically. Once again when new load is applied colloidal clay and turbid clay water are activated and so energy gradient is created and cycle gets repeat. These observations leads to a new clue in clay-water behavior and accepting the fact that pore water which can be in many forms as discussed above is to be measured or determined by other nano techniques.

Adhesion of pores (tension between pores) and repulsion of pores is one major governing factor as one big pore is occupied by many small pores which are attracted towards each other and some pores shows repulsion with each other.

Adhesion of pores attracts similar size and shape of pores and forms flocs of pores moving as vertex in clay water which gets diffused at any time or even gets break by displace soil fabric or it is held by edges of particle or even it can get bunched between two solid particles. As water film thickness increases this bunch of pores get separated and thus repulsion of pores takes place. Also structural viscosity of fluid is partly responsible for repulsion.

Third agency

There are many facts regarding the existence of pore-clay turbid water and it is observed that during consolidation under low magnitude of loads, clay-pore water of high turbidity is dissipated having very high structural viscosity. This clay-pore water consists nano-clay particles in colloidal form or in dispersive form. It is found that when clay fabrics is under particle rearrangement (plate) due to sliding over one another or due to inter-particle attraction then assuming a unit square centimeter area the particles will be oriented more towards the direction of flow and thus creating a gradient/slope near the clay-drain interface. The only change is that clay particles at lower height of soil sample get warped due to sample confinement and straining of vertical drain to accommodate lateral compressibility (strain) of soil sample. Author concludes that this complete phenomena depends on vertical drain properties, and so author further proposes a practical solution that chemical composition of drain material/fabric/synthetic (polymer chemistry) should be designed to prepare such drains which attract water radially and consolidation process can be faster accelerated. Also physical properties of drain are modified by modifying drain geometry (circular, triangular, rectangular) and changing fabric crystalline structure such that clogging potential can be reduced.

Author further suggests that physical and chemical composition of drain material should be made compatible with sub-soil profile such that at any stage of loading the efficiency of drain does not decrease. Particularly authors are presently working on drain material chemistry by inducing equivalent ions of more exchange capacity so that pore water attraction from clay fabric can be accelerated whose results will be produced later on.

SCANNING ELECTRON MICROSCOPY (SEM)- PHASE II

The following table illustrates the detail of SEM analysis carried out on consolidated clay samples of with central vertical drain viz. sand drain and coir-jute fiber drain at various locations. The further analysis of microscopy results was carried out using Quanti-image analyzer with system of micro structure characterization (MIC) software based on ASTM method.

Table. 1 Schedule of SEM

| Geodrain | 'n' value | location | Magnification factor |
|-----------------|-----------|-----------|----------------------|
| Sand drain (SD) | 11.04 | h_{tr2} | X2700 |
| Sand drain (SD) | 11.04 | h_{cr2} | X2700 |
| Sand drain (SD) | 11.04 | h_{br2} | X2700 |
| Sand drain (SD) | 11.04 | h_{br3} | X2700 |
| Sand drain (SD) | 11.04 | l_{trd} | X2700 |

| | | | |
|----------------------|-------|-----------|-------|
| Sand drain (SD) | 11.04 | l_{crd} | X2700 |
| Coir-Jute drain (CJ) | 11.04 | h_{tr2} | X2700 |
| Coir-Jute drain (CJ) | 11.04 | h_{cr2} | X5000 |
| Coir-Jute drain (CJ) | 11.04 | l_{crd} | X2700 |
| Coir-Jute drain (CJ) | 11.04 | h_{br2} | X2700 |
| Coir-Jute drain (CJ) | 11.04 | l_{tr1} | X2700 |
| Coir-Jute drain (CJ) | 11.04 | l_{brd} | X2700 |

Notes: Where, r_d = radius of drain

h_{tr2} = Top of final consolidated clay sample at mid radial point r_2

h_{cr2} = Centre of final consolidated clay sample at mid radial point r_2

h_{br2} = Bottom of final consolidated clay sample at mid radial point r_2

h = thickness of final consolidated clay sample

l_{trd} = Clay-Drain interface at top of final consolidated clay sample at location r_d

l_{crd} = Clay-Drain interface at centre of final consolidated clay sample at location r_d

Two photographs are presented for each SEM sample done at given location. First photograph represents microscopy of sample and other represents the Quanti image of same sample using MIC software to deduce pore volume fraction, orientation of particles, flow paths of pore water at edge-to-edge contact and edge-to-face contact.

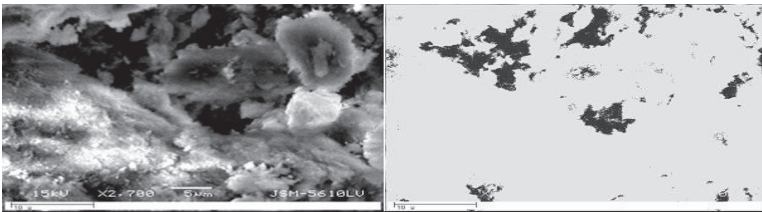


FIG.1. Microscopy of SD at location h_{tr2} at X2700 & Image of pore volume fraction of SD using MIC

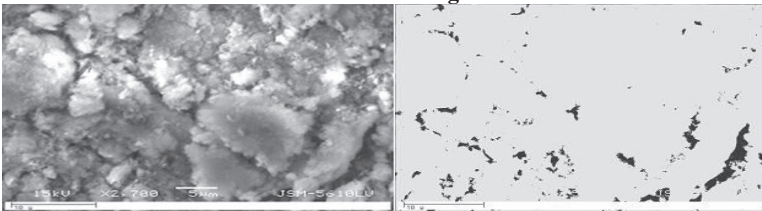


FIG.2. Microscopy of SD at location h_{br2} at X2700 & Image of pore volume fraction of SD using MIC

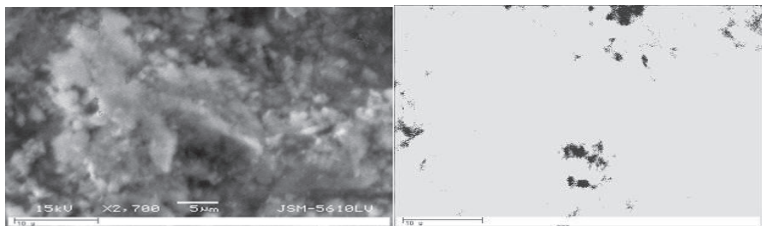


FIG.3. Microscopy of CJ at location h_{tr2} at X2700 & Image of pore volume fraction of CJ using MIC

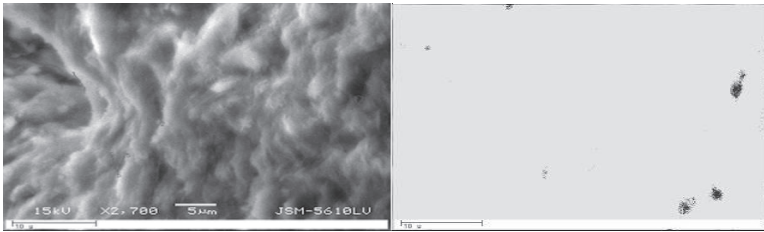


FIG.4. Microscopy of CJ at location I_{brd} at X2700 & Image of pore volume fraction of CJ using MIC

DISCUSSIONS

- From scanning electron microscopy (SEM) analysis of fig.1 it is observed that fabric structure orientation with respect to horizontal was obtained in range of 43° - 70° with respect to horizontal and percentage porosity(volume fraction) is measured as 8.48% as shown in fig.1.
- Comparing nano analysis of fig.2, it is noted micro channel formation is more in line at bottom height of sample compare to top, because of increasing stress and self weight of sample itself, and also advance creation of pore channels during pore pressure development of sample, same channels might be utilized during dissipation process with some bunch of floccs near the drain, while formation of micro channels at top of sample is difficult due to confinement of sample not allowing in-plane pore water to go towards drain, thus hindering compressibility of soft mass. This is the reason that particle orientation is range of 18° - 49° with respect to horizontal and percentage porosity (volume fraction) is measured as 4.17% as shown in fig.2.
- Comparing nano analysis of micrograph shown in fig.3 using CJ as central drain it is observed that due to fast dissipation of pore water pressure the percentage micro pores are decreasing from mid radial point r_2 to nearest radial point r_1 and similarly decrease in micro pores are also observed at different height of sample compare to SD for same location. Particle orientation is in range of 16° - 71° with respect to horizontal and percentage porosity (volume fraction) is measured as 2.24% as shown in fig.3.
- Comparing nano analysis for most interesting part, that is soil-drain interface for micrograph as shown in fig.4, it is observed that decrease in pore water volume is related to size of pore, diameter of pore, shape of pore, orientation of pore, displacement of pore, accommodation of small pore into bigger pore and finally author therefore suggests that above mentioned development of pore water is directly proportional to porosity of vertical geodrain and distribution of pore pattern at outside surface of drain, which actually accelerates dissipation process. This philosophy is further proved by doing clay-drain interface nano analysis at different height of sample. Referring to fig.4 and other micrographs taken at top and bottom of drain-soil interface, the percentage porosity (volume fraction) is measured as 0.48% and 1.82% respectively, also particle orientation for first one is in range of 20° - 56° and second has range of 29° - 100° .

CONCLUSIONS

- From nano analysis of other micrographs, it interprets that for same height level of sample the percentage micro pores are increasing from central drain radially to outer radial point. Between nearest radial point r_1 and clay-drain interface the percentage decrease of micro pore is more compared to mid plane radial point r_2 and outward radial point r_3 . Because of faster rate of dissipation the achieved void ratio or porosity which is worked out is less in case of coir-jute fiber drain compare to sand drain. This is true for same vertical drain material of other 'n' values also. Use of hydraulically pressurized Oedometer for consolidation through radial flow proves to be powerful tool to study nano mechanics of pore water dissipation at various time intervals.
- With reference to the philosophy of consolidation discussed as above and its measurement and interpretation done using MIC software and SEM it can be concluded that various physico-mechanical and chemical factors affect consolidation phenomena and in particular pore structure of clay sample and drain fabric plays a vital role. Its correct estimation helps to understand pore-tubular channel formation which drains pore water and how it's clogging at intermediate load levels decreases discharge can be measure in form of % porosity and tortosity. Micro pore distribution at interface (drain-soil) at any level (height) is less compare to nearest radial point (r_1), mid plane radial point (r_2) and farthest radial point (r_3), in general the distribution of the micro-porosity exhibit higher magnitude of consolidation with increase of depth at any radial point however, it has been confirmed this observation at mid plane radial point r_2 .
- Author's theory of consolidation based on pore water dissipation (isochrones) yields better comparative results more easily applicable to fields by design engineers. Also trajectory of curves for various degrees of consolidation acts as a readymade tool for selection of optimum drain w.r.t material, shape and size. The appropriate value of lumped parameter (λ) will directly give the clue to design engineer regarding the selection of prefabricated vertical geodrain with respect to field conditions.

To study micro behavior of clay-water system, role of clay particle surface and clay-drain interface on rate of consolidation along with soil structure effects can be best analysed by scanning electron microscopy (SEM) and use of micro-structure characterization (MIC) software.

ACKNOWLEDGEMENTS

The authors are highly thankful to the Prof.(Dr) Ambika Misra, Dean, Faculty of Technology & Engineering, Prof. (Dr) I.I. Pandya Head, AMD, Prof. (Dr) D.L.Shah, P.G.Incharge, AMD, The Maharaja Sayajirao University of Baroda, Vadodara and Prof. M.N.Patel, Dean, L.D.College of Engineering and Prof.(Dr) V.S.Purani, Head, AMD, LDCE, Ahmedabad, India for providing all necessary research facilities.

REFERENCES

- Shah, M.V. and Shroff, A.V. (2010), "Non-Linear Theory of Consolidation through Radial Drainage for Soft Soils using Vertical Drains", Proc. of 14th Danube-European Conf. on Geotechnical Engg, Bratislava, Slovakia, Vol-I, pg.113, ISBN 978-80-227-3279-6

Evaluation of Pile Foundations Subjected to Liquefaction Induced Lateral Spreading

Hua Liu¹, Ph.D., P.E. and Endi Zhai², M. ASCE, Ph.D., P.E., G.E.

¹Geotechnical Engineer, Kleinfelder West Inc., Irvine, CA 92618; hliu@kleinfelder.com

²Senior Principal Engineer and Vice President, Kleinfelder West Inc., Irvine, CA 92618; ezhai@kleinfelder.com

ABSTRACT: There have been many historical cases where pile foundations suffered severe damage from liquefaction during an earthquake. The pile foundation loading and deformation due to liquefaction induced lateral spreading are two major factors evaluating the behavior of pile foundations for bridges in seismically active areas. This paper presents a preliminary seismic evaluation of pile foundations for a bridge located in the coastal area in California subjected to a lateral spreading hazard. Pile groups consisting of 44 cast-in-steel-shell (CISS) piles with a diameter of 6 feet are proposed to support two bridge towers located on each side of a channel. Liquefaction potential is considered high at the site under the design earthquake event. Liquefiable layers of thicknesses of 28 feet and 26 feet are expected at the east and west side of the channel, respectively. The potential for lateral spreading under the design earthquake event towards the channel is considered to be high as the stratum of liquefaction appears consistently widespread at both sides of the channel. Pile group deformation and forces resulting from the potential lateral spreading were evaluated for both tower foundations by using an equivalent nonlinear static analysis procedure recommended by the California Department of Transportation (Caltrans). This approach imposes a lateral spreading soil displacement field on the foundation model in which p-y curves are used to consider nonlinear response of soils. Pile foundation deflection, moment and shear corresponding to the imposed lateral soil displacements were then calculated and compared with the performance criteria.

INTRODUCTION

Liquefaction-induced lateral spreading has historically resulted in severe damage to many bridges. A well-known example is the Showa Bridge in Japan which collapsed during the 1964 M_w 7.5 Niigata earthquake. The bridge pile foundations suffered from the loading induced by the left bank lateral spreading of about 3m towards the center of the river (Hamada and O'Rourke 1992). The bridge decks collapsed due to the excessive pile foundation deformation in the longitudinal direction of the bridge (Madabhushi et al. 2010).

This paper presents an evaluation of a proposed bridge pile group foundation subjected to liquefaction-induced lateral spreading. The main span of the proposed bridge crosses over a navigation channel supported by two towers located on each side of the channel. The longitudinal direction of the bridge runs approximately east-west and is perpendicular to the center line of the channel. Each bridge tower is supported by a pile group consisting of 44 six foot diameter CISS piles with a length of 150 feet and a shell thickness of 0.875 inches. Reinforced concrete is proposed to be placed inside the steel shell for the top portion of the pile to enhance lateral pile performance especially during a seismic event, and the reinforcement cut-off depth is at 30 feet below the bottom of the liquefiable layer. The pile cap has dimensions of 117 feet in length, 87 feet in width, and 16 feet in thickness. Finished grades are at an elevation of -8 feet and +10 feet at the west and east bank, respectively. The bottom of the cap is proposed to be at an elevation of -8 feet on both sides of the channel. A plan view of the proposed pile group configuration is presented in Fig. 1. The channel bed is approximately 65 feet below the top of the channel bank. Both channel banks have a slope of about 1.5H:1V (horizontal : vertical) towards the channel. The subsurface soils generally consist of medium stiff to stiff clays, silts and liquefiable sandy layers in the upper 30 feet and 46 feet on the west and east side of the channel, respectively.

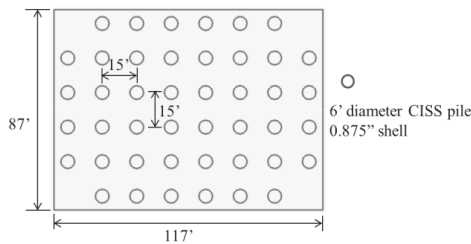


FIG. 1. Plan view of pile group foundation supporting east tower.

The analysis was performed following the guideline recently released by Caltrans (Caltrans 2011) which is based on recommendations suggested by Ashford et al. (2011). This guideline employs an equivalent nonlinear static analysis and uses the Beam on Nonlinear Winkler foundation (BNWF) approach. The effect of lateral spreading on the pile foundations is implemented by imposing the estimated free-field soil displacement to the soil-foundation model. The estimated results are compared with the foundation performance criteria. Different soil conditions on each side of the channel result in different pile foundation performances when lateral spreading occurs.

ANALYSIS

The proposed project site is located in a high seismicity area. The seismic parameters used in this analysis consisted of a design earthquake magnitude of 7.0 and a peak ground acceleration (PGA) of 0.62 g.

Liquefaction

Liquefaction analysis was conducted using the simplified empirical procedures

(Youd et al., 2001) based on available existing Standard Penetration Testing (SPT) blowcounts and Cone Penetration Testing (CPT) tip resistance. For silty and clayey soils, procedures from Boulanger and Idriss (2006) and Bray and Sancio (2006) criteria were used. The simplified empirical methods generally tend to be conservative but convenient for practice so it's used at this stage. At the west bank, two liquefiable soil layers with a total thickness of about 26 feet were identified from the ground surface to a depth of about 31 feet. These two liquefiable layers are separated by a five foot thick non-liquefiable layer located between elevation -25 feet and -30 feet at the west bank. Analysis results indicate that liquefaction is expected to occur in layers generally from 18 feet below the existing ground surface (elevation of -8 feet) to an elevation about -36 feet at east channel bank. There is a non-liquefiable layer above the liquefiable layer with a thickness of 18 feet which is considered to form a "crust" in the event of lateral spreading at the east bank.

The nonlinear soil response in the BNWF analysis is considered by using p-y curves. P-y curves for the liquefied soils were developed based on soft clay p-y curves (Matlock, 1974). The residual strength of the liquefied soil was taken as the undrained shear strength of the soft clay. The residual strength of the liquefied soil is usually estimated based on the empirical correlation with equivalent clean-sand SPT blowcounts (Seed and Harder, 1990), or SPT blowcounts corrected for energy efficiency and overburden stresses (Caltrans, 2011). The residual strength of the liquefied soil layer at the east channel bank was estimated to be about 650 pounds per square feet (psf). A residual strength of about 600 psf was estimated for the two liquefiable layers on the west side of the channel.

Lateral Spreading

The liquefiable layers identified in the analysis appear to be continuous, which leads to a potential for lateral spreading. The lateral soil displacement was estimated using the Newmark type sliding block analysis. We use the regression model developed by Bray and Ravasarou (2007) to calculate the soil displacement. Because shaking could happen in any direction, seismic slope stability analysis shows both channel banks have the potential for lateral spreading towards the center of the channel. Liquefaction-induced lateral spreading of about 10 inches and 18 inches towards the channel was estimated on the west and east bank side, respectively. The difference of the lateral spreading magnitude is considered to be attributed to the thickness and depth of the liquefiable layers, although both banks have similar soil properties at about the same elevation and slope ratio. The Newmark block analysis implies that the non-liquefiable layer located in between (west bank) or above (east bank) the liquefiable layers will slide towards the channel together with the liquefiable soils.

Soil Pressures

When lateral spreading occurs, the laterally-displaced soils will impose a kinematic load on the pile group foundation instead of providing lateral resistance. The magnitude of the kinematic load is obviously dependent on the spreading soil properties and the relative displacement between the spreading soils and the pile foundations. Passive earth pressure is considered to be the maximum pressure that could be generated by the laterally spreading soils. The strength of the liquefied soils

is usually reduced due to the presence of increased pore pressure. The kinematic load could be significant for cases where there is a non-liquefiable layer overlying the liquefiable layer. Loads on the foundation due to movement of the soil crust typically dominate other loads. A crust of about 18 feet in thickness extending from the ground surface to the bottom of pile cap was identified from the liquefaction analysis at the east channel bank. Obviously, the loads imposed on the pile foundation from the lateral spreading are much higher for the east tower foundation than that for the west tower foundation. The loading differences lie in the fact that the pile cap of the east tower foundation is embedded in the crust while the pile cap of the west tower foundation is exposed above the ground surface. The ultimate passive force caused by the crust on the east tower pile cap was estimated to be about 7,000 kips. Rather than applying the full ultimate passive force in the crust as proposed by Madabhushi et al. (2010), or 2/3 of the ultimate passive force previously recommended by Caltrans (2008), Caltrans recent guideline (2011) suggests a more realistic approach to estimate the kinematic loads that could be generated by laterally spreading soils. The ultimate passive force is not considered to be fully mobilized until a very large relative displacement is achieved. A required relative displacement of 48 inches is estimated to mobilize the full ultimate passive force following the recommendation by Brandenburg (2007). A tri-linear p-y curve is then developed to simulate the relationship between the relative displacement and mobilized passive force based on the calculated results. The actual loads acting on the foundation from the crust was calculated internally by the LPILE program using the specified p-y curve.

Pile Properties

The nonlinear behavior of piles was modeled in the analysis for more accurate results. Reinforced concrete is proposed to be placed into the pipe pile for the section from the top to a depth corresponding to 30 feet below the bottom of the deepest predicated liquefiable layer. The reinforcement cut-off depth is about 60 feet for both tower foundations. The nonlinear relationship between moment and curvature for the pipe pile section filled with reinforced concrete is presented in Fig. 2. A similar relationship was developed for the rest of the pipe piles. The nonlinear relationship between the pile moment and bending stiffness was used in the computer program LPILE for the lateral pile analysis.

LPILE was used due to its unique and critical capability of imposing lateral soil displacement. Since LPILE was developed for a single pile analysis, a so-called "superpile" is created to represent the pile group in LPILE program. In this study, a single superpile consisting of three sections was developed. The first section of the superpile with a length of 16 feet was used to model the pile group cap, and an arbitrary high bending stiffness (e.g. 100 times higher than that of the second section) was assigned to achieve rigidity. The second section with a length of 60 feet, with a moment and curvature relationship presented in Fig. 2, was used to model the pile filled with reinforced concrete. The third section with a length of 90 feet was used to model the rest of the pile. In summary, the superpile had a length of 166 feet with three different bending stiffness properties in three sections. It should be noted that the bending stiffness of the superpile in section two and three was scaled from that of a single 6-ft diameter pile.

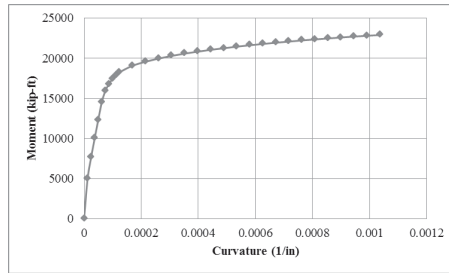


FIG. 2. Moment and curvature relationship of the 6-ft diameter pipe pile section filled with reinforced concrete.

The rotational stiffness was specified as one of the pile-head conditions in LPILE for this kind of analysis. The rotational stiffness of a pile group can be estimated based on the axial stiffness of a single pile and pile group layout. Caltrans (2011) recommends that the axial stiffness of a single pile can be calculated assuming 75% of the ultimate pile capacity is achieved at 0.25-inch axial displacement. Pile group rotational stiffness was then estimated as a summation of all single pile axial stiffnesses multiplied by the distance to the pile group centerline from each pile. The axial capacity of a single pile was estimated to be about 7,600 kips for the proposed pile group. Following the guideline, we calculated the rotational stiffness of the proposed pile group to be about 1.5×10^{11} kips·in/rad.

Analysis Procedure

The boundary conditions at the top of pile were specified by the axial, shear and rotational stiffness. It should be noted that only 50% of the inertial load is combined with 100% kinematic load, based on the argument that the peak of inertia load and kinematic load generally occur at different time phases. Thus, a shear force about 9,778 kips corresponding to 50% of the inertial load is applied. An axial service load of 86,080 kips was taken to be combined with the kinematic load. Lateral spreading soil displacement was implemented in such a way that it's constant within any non-liquefiable layer and linearly decreases within a liquefiable layer. For example, the applied soil displacement is a constant at 18 inches in the crust layer from the ground surface to the bottom of the pile cap, and then linearly decreases to 0 inches at the bottom of liquefied soil layer for the east tower foundation. The liquefiable layer thickness of 28 feet extends downwards from the bottom of the cap. The group effect was considered by averaging the group reduction factor of all the piles and multiplying with the total number of piles. The superpile model developed for the east tower foundation in LPILE is illustrated in Fig. 3.

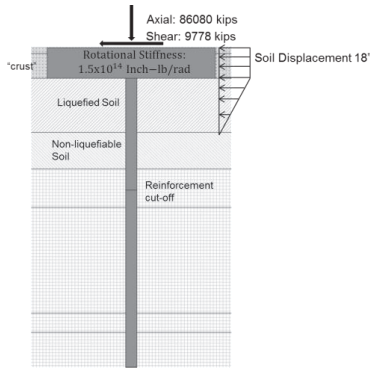


FIG. 3. Superpile model used for lateral spreading analysis.

A similar superpile model was also developed for the west tower foundation. It should be noted that the soil displacement imposed at the west tower foundation is quite different from that at the east tower foundation. The spreading soil displacement was 10 inches at the ground surface, and decreased linearly to seven inches at the top of non-liquefiable layer, remains constant within this layer, and linearly decreases to zero at the bottom of the lower liquefiable layer.

Fig.4. presents the diagrams of the calculated lateral displacement, bending moment and shear force diagrams of the superpile for the east tower foundation. A pile-top deflection of about seven inches was observed, resulting from the spreading soil displacement. The deflection was considered acceptable for the proposed bridge foundation. The maximum bending moment in the superpile was about 726,000 kip-ft, which is less than the allowable foundation capacities given in the Caltrans guideline. The results were provided to the structural engineers to evaluate the structural capacities.

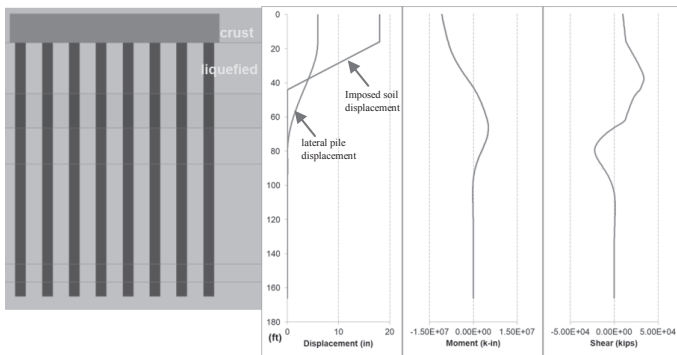


FIG. 4. Superpile lateral displacement, bending moment and shear force diagrams of the east tower foundation.

The analysis results for both east and west tower foundations are summarized in Table

1. The pile foundation lateral deflections caused by the lateral spreading are similar at the west tower and east tower, despite the fact that the imposed soil movement at the west tower was about half of the value at the east tower. The calculated maximum bending moment and shear force in the superpile for the east tower foundation were about 40% higher than that for the west tower foundation, due to the presence of the crust overlying the liquefied soil at the east channel slope. The calculated maximum bending moment occurs at a depth of 16 feet in the superpile for both the east and west towers, corresponding to the location at the bottom of the pile cap in the pile group foundation. The resulting maximum shear force occurred at a depth of about 40 feet from the top of the superpile in both towers, which was close to the bottom of the liquefiable layer.

CONCLUSIONS

The analysis of a pile foundation subjected to liquefaction induced lateral spreading is complicated. Advanced approaches such as nonlinear effective stress soil structure interaction analyses implemented by either the finite element or finite difference method has been verified in many studies to provide a rigorous analysis for seismic evaluation of waterfront structures. However, this kind of analysis requires high quality input data such as soil and structural properties and advanced skills from the implementer, and is often considered to be computationally expensive. For preliminary evaluation and design of piles, a simplified static or pseudo-static approach seems more attractive. This paper presented an example study of a preliminary evaluation on bridge pile group foundations subjected to liquefaction-induced lateral spreading following the guidelines recommended by Caltrans.

The procedures taken in this paper for the aforementioned evaluation are summarized as follows. Simplified liquefaction analysis is first performed to identify the thickness and depth of potentially liquefiable soil layers. Based on the liquefaction analysis results and the sloping condition, a Newmark-type rigid block analysis was used to estimate the yield acceleration of the slope. Liquefaction-induced lateral spreading was then calculated through empirical correlations with the yield acceleration of the slope and seismic design parameters such as design earthquake magnitude, PGA, etc. In case a crust overlies the liquefiable layer, the kinematic loads acting on the pile group foundation was estimated by implementing a specified p - y curve developed based on the ultimate passive force and the relative displacement to fully mobilize the ultimate force. A nonlinear moment and bending stiffness relationship of pile was adopted to better characterize the behavior of foundations under large soil displacements. The load and deformation of the pile group foundation was evaluated by applying the estimated soil displacement caused by lateral spreading, and kinematic loads combined with 50% of the inertia loads. The results are compared with the performance criteria listed in the Caltrans guidelines and checked by structural engineers for the structural capacities.

The simplified equivalent nonlinear static analysis procedure provide a practical approach to evaluate the pile foundation subjected to lateral spreading and require close collaboration between the geotechnical engineers and structural engineers. It can be seen from the study presented in this paper that this approach can be implemented

using the geotechnical analysis method and computer programs that are widely available to practicing engineers.

Table 1. Analysis Results Summary for East and West Tower Foundation

| Tower Foundation | Lateral Spreading Soil Movement (inches) | Superpile Analysis Results | | |
|------------------|--|-----------------------------|-------------------------|----------------------|
| | | Maximum Deflection (inches) | Maximum Moment (kip-ft) | Maximum Shear (kips) |
| West | 10 | 5 | 540,000 | 23,500 |
| East | 18 | 7 | 760,000 | 34,000 |

REFERENCES

- Ashford, S., Boulanger, R.W., and Brandenburg, S. (2011). "Recommended Design Practice for Pile Foundations in Laterally Spreading Ground.", Report PEER 2011/04, Pacific Earthquake Engineering Research Center (PEER), Berkeley, California.
- Brandenburg, S.J., Boulanger, R.W., Kutter, B.L., and Chang, D. (2007). "Liquefaction-induced softening of load transfer between pile groups and laterally spreading crusts.", *J. Geotech Geoenviron. Eng.*, ASCE, 133(1), 91-103
- Bray, J.D. and Sancio, R.B. (2006). "Assessment of the liquefaction susceptibility of fine-grained soils.", *J. Geotech Geoenviron. Eng.*, ASCE, 132(9), 1165-1176
- Bray, J.D., and Travasarou, T. (2007). "Simplified procedure for estimating earthquake-induced deviatoric slope displacements.", *J. Geotech Geoenviron. Eng.*, ASCE, 133(4), 381-392
- Boulanger, R.W. and Idriss, I.M. (2006). "Liquefaction susceptibility criteria for silts and clays.", *J. Geotech Geoenviron. Eng.*, ASCE, 132(11), 1413-1426
- California Department of Transportation (2011). "Guidelines on Foundation loading and Deformation Due to Liquefaction Induced Lateral Spreading.", Sacramento, California.
- California Department of Transportation (2008). "Memo To Designers, Section 20-15: Soil Liquefaction and Lateral Spreading Analysis Guidelines.", Sacramento, California.
- Hamada, M. and O'Rourke, T.D. (1992). "Case Studies of Liquefaction and Lifeline Performance during Past Earthquakes – Volume 1: Japanese Case Studies." *Technical Report NCEER-92-0001.*, National Centre for Earthquake Engineering Research, Buffalo, New York.
- Madabhushi, G., Knappett, J. and Haigh, S. (2010). "Design of Pile Foundations in Liquefiable Soils." Imperial College Press, London, UK.
- Matlock, H. (1970). "Correlations of design of laterally loaded piles in soft clay.", *Proceeding Offshore Technology Conference, Houston, TX, Vol. 1, No. 1204*, pp. 577-594
- Youd, et al. (2001). "Liquefaction resistance of soils: Summary Report from the 1996 NCEER and 1998 NCEER/NSF Workshops on Evaluation of Liquefaction Resistance of Soils.", *J. Geotech Geoenviron. Eng.*, ASCE, 127(10), 817-825

Nonlinear Analysis for the Cooling Effect of Road Subgrade with Varying Spacings of Thermosyphons in Cold Region

Yahu Tian¹ and Jiankun Liu²

¹ Lecturer, School of Civil Engineering and Architecture, Beijing Jiaotong University, Beijing, China 100044; yhtian@bjtu.edu.cn

² Professor, School of Civil Engineering and Architecture, Beijing Jiaotong University, Beijing, China 100044; jkliu@bjtu.edu.cn

ABSTRACT: Thermosyphons are usually used to maintain the stability of construction foundation in cold region. This paper presents a three-dimensional finite element thermal analysis conducted to simulate 30 years' running to study the cooling effect of the road subgrade with thermosyphons. The spacings of the thermosyphons used in the computation are 3m, 4m, 5m and 6m respectively, and the diameter of the thermosyphon is 89mm. Preliminary result indicates that the thermosyphon can lower the soil temperature substantially, and the cooling effect becomes less effective as spacing increase. For the geological conditions in Tibetan Plateau, the effective operating radius of the thermosyphon with the diameter of 89mm is about 1.6m and the reasonable spacing between thermosyphons is 4m.

INTRODUCTION

In order to avoid damage caused by foundation settlement as the result of freezing and thawing circles, thermosyphons are often utilized to maintain the stability of construction foundation in cold region. Thermosyphons have been used to maintain permafrost below structures for over forty years, and there are many successful experiences (Edward et al., 2002). A thermosyphon is the most widely used passive heat transfer device that operates by convection through vaporization and condensation. The heat transfer from the ground to the air is driven by a temperature difference between the evaporator portion and the radiator portion. On the Trans-Alaska pipeline system (TAPS) the massive use of thermosyphons clearly demonstrated the usefulness of natural convection devices (Heuer, 1979). Since TAPS, thermosyphons have become widely used with variations in design depending on the specific application, such as school building (Hayley, 1982), Bethel runway (Bradley et al., 1984), roadways (Zarling, 1993), frozen barrier to prevent migration of toxic material (Long et al., 1999), and so on. With the varying usage, the types and technologies of thermosyphons were developed continuously. Performance testing of thermosyphons with inclined evaporator has been conducted (Zarling et al., 1985;

Haynes et al., 1988). Recent developments allow thermosyphons to operate with evaporator section horizontal including undulations (Haynes et al., 1992; Zarlring, 1999, Yarmark et al., 2002).

The use of thermosyphons in Qinghai-Tibet railway and roadway show that thermosyphons can protect frozen soil, reduce the soil temperature considerably and assure the stability of the embankment in permafrost region. The beginning of the study on thermosyphons in China came late, and since 1970s few research results about the heat transfer mechanism and application of thermosyphon has been published (Ding, 1990; Wu et al., 2002; Pan et al., 2003). However, the long-term influence and spacing effects of thermosyphons in road subgrade were not discussed or studied. In this paper, based on design document of the Anduo testing embankment of Qinghai-Tibet railway, three-dimensional finite element analysis of the temperature fields of embankment at varying spacings of thermosyphons is conducted to simulate the cooling effect under the climate warming condition. The spacings of thermosyphons are: 3m, 4m, 5m and 6m, respectively. We aim to obtain the effective operating radius and reasonable spacing of the thermosyphon. It is hoped that the calculation results can provide a theoretical basis for the correlative design.

ANALYSIS FRAMEWORK

Governing equations

By assuming no water infiltration into the embankment and water in the active layer, the 3-D heat conduction with phase change in roadbed and base can be described as follows:

$$\rho c \frac{\partial T}{\partial t} = \frac{\partial}{\partial x} \left(\lambda \frac{\partial T}{\partial x} \right) + \frac{\partial}{\partial y} \left(\lambda \frac{\partial T}{\partial y} \right) + \frac{\partial}{\partial z} \left(\lambda \frac{\partial T}{\partial z} \right) \quad (1)$$

Where ρ —soil density, c —specific heat capacity of soil, t —time, λ —coefficient of heat conductivity, T —temperature.

Finite element formulation

For the problem of heat transfer with phase change in soil, the enthalpy transformation method has been proved to be an effective one. Enthalpy is the integral of specific heat of soil with respect to temperature.

$$H = \int_{T_0}^T \rho c(T) dT \quad (2)$$

Since enthalpy is a smooth function of temperature even in the phase change zone. Therefore, it is reasonable to interpolate the enthalpy rather than the heat capacity directly. By definition, it is:

$$\frac{\partial H}{\partial t} = \frac{\partial H}{\partial T} \frac{\partial T}{\partial t} = \rho c(T) \frac{\partial T}{\partial t} \quad (3)$$

Then the following equation was obtained:

$$\frac{\partial H}{\partial t} = \frac{\partial}{\partial x}(\lambda \frac{\partial T}{\partial x}) + \frac{\partial}{\partial y}(\lambda \frac{\partial T}{\partial y}) + \frac{\partial}{\partial z}(\lambda \frac{\partial T}{\partial z}) \tag{4}$$

The physical domain was divided into elements. By using the Galerkin residual weighted method for Eq.(4), the following finite element matrices were obtained:

$$C \frac{\partial H}{\partial t} = KT - P \tag{5}$$

Where $C = \sum_{\epsilon} \int_{\Omega^{\epsilon}} N_i d\Omega$, $P = \sum_{\epsilon} \int_{\Gamma_i^{\epsilon}} (\lambda \frac{\partial N_j}{\partial y} + \lambda \frac{\partial N_j}{\partial z}) N_i d\Gamma$

$$K = \sum_{\epsilon} \int_{\Omega^{\epsilon}} (\lambda \frac{\partial N_i}{\partial x} \frac{\partial N_j}{\partial x} + \lambda \frac{\partial N_i}{\partial y} \frac{\partial N_j}{\partial y} + \lambda \frac{\partial N_i}{\partial z} \frac{\partial N_j}{\partial z}) d\Omega$$

Where N_i, N_j —element shape functions.

Computational domain

The Anduo testing embankment is located on the Qinghai–Tibet railway in permafrost region. It is an arid climate region in the Qinghai–Tibet plateau, where the average mean annual air temperature is -3.2°C and the mean wind speed is 4.3m/s. The height of testing embankment is 1.1m. The subgrade width is 11.1m and the side slope is 1:1.5(vertical: horizontal). The outer diameter of the thermosyphon is 89mm and ammonia is used as working fluid. The locations of the thermosyphons are about 4m from the centerline of the embankment. The total length of the thermosyphon is 9m, the length of its evaporator section is 5.5m and the length of its vertical finned condenser section is 1.4m.

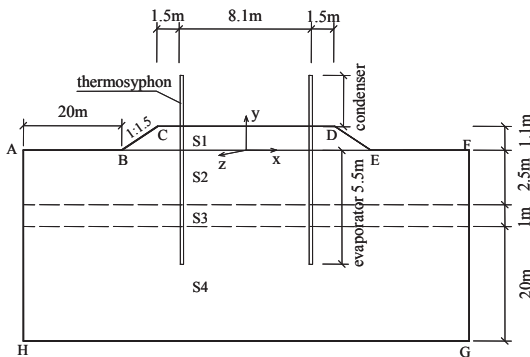


FIG.1. Illustration of computational model

Fig. 1 shows the computational model and its dimension, in which, part S1 is gravel with fine inclusion, part S2 is sub-clay, part S3 is ice-rich soil and part S4 is weathered mudstone. Their thermal parameters are given in Table 1. Due to the symmetry at left and right boundaries, the left of the embankment is selected as the computational domain.

Table 1. Soil Properties

| Soil type | | -20°C | -10°C | -5°C | -2°C | -1°C | -0.5°C | 0°C | 20°C |
|-----------|---|-------|-------|------|------|------|--------|------|------|
| S1 | ρ (kg m ⁻³) | 2100 | 2100 | 2100 | 2100 | 2100 | 2100 | 2100 | 2100 |
| | C (J m ⁻¹ h ⁻¹ °C ⁻¹) | 835 | 840 | 850 | 860 | 870 | 900 | 1070 | 1070 |
| | λ (J kg ⁻¹ °C ⁻¹) | 5400 | 5400 | 5400 | 5400 | 5400 | 5400 | 5050 | 5050 |
| S2 | ρ (kg m ⁻³) | 1950 | 1950 | 1950 | 1950 | 1950 | 1950 | 1950 | 1950 |
| | C (J m ⁻¹ h ⁻¹ °C ⁻¹) | 970 | 1050 | 1090 | 1115 | 1140 | 1210 | 1285 | 1285 |
| | λ (J kg ⁻¹ °C ⁻¹) | 6500 | 6500 | 6500 | 6500 | 6500 | 6500 | 5400 | 5400 |
| S3 | ρ (kg m ⁻³) | 1550 | 1550 | 1550 | 1550 | 1550 | 1550 | 1550 | 1550 |
| | C (J m ⁻¹ h ⁻¹ °C ⁻¹) | 1230 | 1280 | 1310 | 1350 | 1380 | 1420 | 1900 | 1900 |
| | λ (J kg ⁻¹ °C ⁻¹) | 7900 | 7900 | 7900 | 7900 | 7900 | 7900 | 3600 | 3600 |
| S4 | ρ (kg m ⁻³) | 2200 | 2200 | 2200 | 2200 | 2200 | 2200 | 2200 | 2200 |
| | C (J m ⁻¹ h ⁻¹ °C ⁻¹) | 950 | 1060 | 1110 | 1140 | 1190 | 1250 | 1350 | 1350 |
| | λ (J kg ⁻¹ °C ⁻¹) | 9000 | 9000 | 9000 | 9000 | 9000 | 9000 | 7250 | 7250 |

Boundary and initial conditions

The temperatures at the native surfaces AB and EF vary as per the following formula:

$$T = -0.7 + g(t) + 12 \sin(2\pi t / 8760 + \pi/2) \quad (6)$$

where $g(t) = At$ denotes the climate warming effect, $A = 0.02$ °C/a, t —time (year).

The temperatures at the side slopes BC and DE change as follows:

$$T = 0.7 + g(t) + 13 \sin(2\pi t / 8760 + \pi/2) \quad (7)$$

The temperatures at pavement surface CD changes as per the following formula:

$$T = 1.2 + g(t) + 15 \sin(2\pi t / 8760 + \pi/2) \quad (8)$$

The lateral boundaries (AH and FG) are assumed to be adiabatic. The temperature gradient at bottom boundary HG is 0.03 °C/m.

The initial temperature distribution was obtained through a long-term transient solution of Eq.(1) with no consideration of the climate warming effect by letting $g(t)$ equals to zero.

Heat transfer, q through a two-phase thermosyphon can be determined using the

following equations (David, 2004):

$$q = \frac{T_s - T_a}{R_s + R_f} \quad (9)$$

$$\text{where } R_f = 1/Aeh \text{ and } R_s = \frac{\ln(r_2/r_1)}{2\pi\lambda z} \quad (10)$$

where T_s is the soil temperature, T_a is the ambient air temperature surrounding the condenser, R_s is the soil thermal resistance, R_f is the thermal resistance through the radiator, A represents the total exposed surface of the condenser, 2.28m^2 , the term eh is the effective heat transfer coefficient, the average radius of heat transfer, r_2 , is assumed, r_1 is the outer radius of the thermosyphon, λ is the thermal conductivity of the soil surrounding the evaporator, and z is the length of evaporator section.

eh is usually determined empirically from fin surface test data as a function of wind velocity and exposure. Based on the research on Qinghai-Tibet plateau, eh is determined as follows (Ding, 1990):

$$eh = 2.75 + 1.51v^{0.5} \quad (11)$$

Where v is the mean wind velocity. During computation, the evaporator section is simulated by surface element and the heat flux q is applied on these surface elements. Heat flux is equal to zero when $T_s < T_a$.

RESULTS AND DISCUSSION

Temperature distributions in cross section

Fig. 2 shows the temperature distributions of the four kinds of embankment. Initially, the location of the permafrost table is 1.3m under the native surface. It can be seen that thermosyphons can cool the soil under the embankment and the position of the permafrost table of each embankment rises. After the thermosyphon operations, the permafrost tables at the position of embankment centerline are 0.5m~0.85m under native surface, however, at the same time the height of the permafrost table elevated decreases as the spacing of the thermosyphons increases. After 30 years, the position of permafrost table is always above the initial position, and it shows the long-term cooling effect of the thermosyphons is sustained. There is a low temperature core near the thermosyphon on October 1st because of the thermosyphon operation during the winter season. In Fig.2, the temperatures of the low temperature core are -1.5°C to -2°C , -1.5°C , -1.25°C to -1.5°C and -1.25°C , respectively. This illustrates that the cooling effect of the thermosyphons weakens as spacing increases. When the spacing exceeds 4m, the isotherms are similar to each other in Fig.2 (a) and Fig.2 (b) and gradient of temperatures changes insignificantly. These results indicate that the optimal spacing is in-between 4m and 5m.

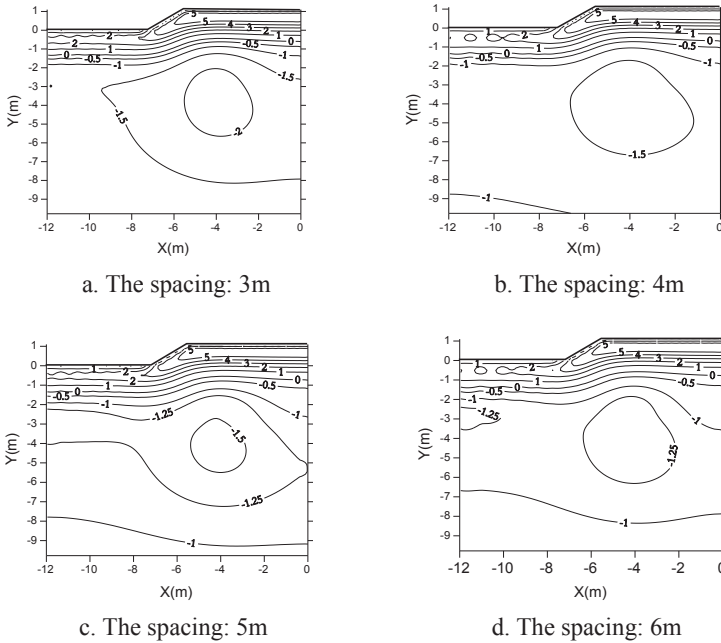


FIG. 2. Isotherm of the embankment with varying spacings of thermosyphons on October 1st after 30 years of the construction.

Temperature distributions in longitudinal section

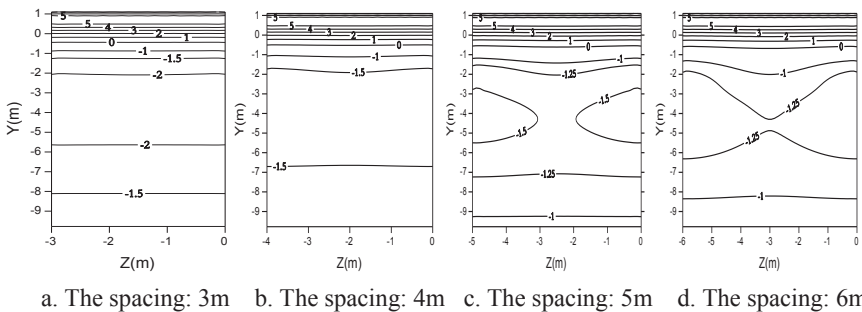


FIG. 3. Isotherm of the embankment with varying spacings of thermosyphons on October 1st after 30 years of construction.

Fig. 3 shows the temperature distributions in longitudinal sections, which is 4m from the centerline of the embankment. It is clearly observed that the position of the permafrost table of each embankment rises, however, a high temperature zone occurs

in the middle of the longitudinal section as the spacing of the thermosyphons exceeds 4m. When the spacing varies from 3m to 4m, the position of permafrost table is about 0.1m lower and the temperature of soil is 0.5 °C higher, but the temperature distribution is even. When the spacings are 5m and 6m, the temperatures of the soil are higher and there are high temperature zones in embankment. Those results indicate that the cooling effect of the whole embankment is better and the cost is more when the spacing is less than 4m, and when the spacing exceeds 4m the cooling effect is poorer and the cost is less.

Freezing radius analysis

According to Fig.2, the cooling effect of the thermosyphons is significant from 3m to 5m depth beneath native surface. Fig.4 shows the changes of the soil temperature with the horizontal distance in winter season when the depth is 3.5m. It can be seen that the temperature of the soil near the thermosyphon is the lowest on January, and the temperature increases with increasing air temperature. The temperature of the soil at centerline of roadbed is 0.4°C lower after 30 years of construction than after 1 year. The change of the soil temperature gradient is very profound when the distance is within 1.6m. The gradient is very little with the distance beyond 1.6m. That indicates the freezing radius is about 1.6m.

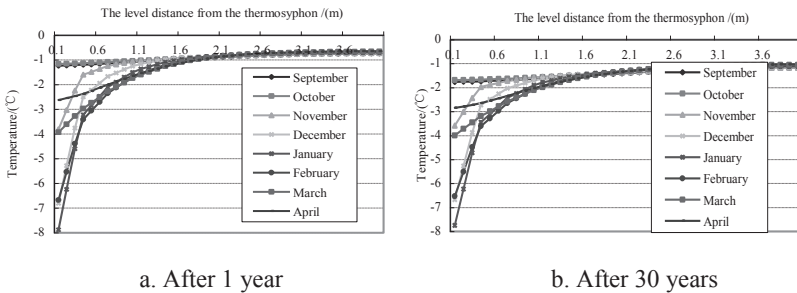


FIG. 4. 3.5m beneath native surface, the changes of soil temperature with the horizontal distance. The spacing of the thermosyphons: 4m.

CONCLUSIONS

Based on the above analysis, it can be concluded that thermosyphons can lower the temperature of embankment substantially, and over the 30 years of long-term operation, it can maintain the stability of the embankment. The cooling is less effective as the spacing increases. For the studied geological conditions and the same kind of thermosyphon, the effective radius is about 1.6m, and the whole cooling effect is better when the spacing is less than 4m. When the spacing exceeds 5m, the cooling effect will not be able to keep the stability of the embankment.

ACKNOWLEDGMENTS

The authors wish to acknowledge the support provided by the Fundamental Research Funds for the Central Universities (No. 2011JBZ009), National 973 Project of China (No. 2012CB026104), and National Science Foundation of China (NSFC) (No. 41271072).

REFERENCES

- Yarmak, E., and Long, E.. (2002). "Recent development in thermosyphon technology." *Cold Region Engineering. Proc. 11th international conference on Cold Regions Engineering*, ASCE, Alaska: 656-662.
- Heuer, C.E.. (1979). "The application of heat pipe on the Trans Alaska pipeline." *CRREL Report*.
- Hayley, D.W. (1982). "Application of heat pipes to design of shallow foundations on permafrost." *Proc. 4th Canadian Permafrost Conference*, Canada: 535-544.
- Bradley, G.P., and Yarmark, E..(1984). "Passive thermal stabilization of the Bethel runway." *Proc. 3th international cold regions engineering specialty conference*, CSCE, Canada: 221-228.
- Zarling, J.P. (1993). "Thermosyphon applications in cold regions." *Proc. 4th international symposium on thermal engineering and science for cold regions*, Hanover: 24-35.
- Long, E.L., and Phillips, E.. (1999). "The frozen soil barrier demonstration project." *Waste Management '99 conference*, Tucson: 121-129.
- Zarling, J.P., and Haynes, F.D.. (1985). "Laboratory tests and analysis of thermosyphons with inclined evaporator sections." *Proc. 4th International Offshore Mechanics and Arctic Engineering Symposium*, ASME, New York: 31-37.
- Haynes, F.D., Zarling, J.P., Gooch, G.E., et al.. (1992). "Laboratory tests with thermosyphon in soil." *Proc. 11th International Conf. on Offshore Mechanics and Arctic Engineering*, ASME, Canada: 139-144.
- Ding Jingkang. (1990). "Application of heat pipe on permafrost regions." *Report, Northwest Research Institute of China Railway Engineering Corporation, Lanzhou*.
- Wu Cunzheng, Sun Zhijian, and Pan Yang. (2002). "Theoretic study on the technology of applying heat pipe to solving frost heaving." *Chinese Journal of Geotechnical Engineering*, Vol. 24 (3): 347-351.
- Pan Weidong, Lian Fengyu, Deng, Hongyan. (2003). "Application principle and prospect of thermal-probe technique cold region engineering." *China Journal of Rock Mechanics and engineering*, Vol. 22 (2): 2673-2676.
- Xu Xuezu, Wang Jiacheng, Zhang Lixin. (2001). *Physics of permafrost science*. Beijing, Science Press.
- Wu Zhiwang, Cheng Guodong, Zhu Lanlin. (1988). *Roadbed engineering in permafrost regions*. Lanzhou, Lanzhou University Press.
- David C.E.. (2004). *Thermal analysis, construction and monitoring methods for frozen ground*. Reston, ASCE.

Prediction and Application of Equilibrium Water Content of Expansive Soil Subgrade

Jianlong Zheng¹, Rui Zhang²

¹PhD and Professor, School of Traffic and Transportation Engineering, Changsha University of Science and Technology, China; e-mail: zjl@csust.edu.cn

²PhD and Lecturer, Key Laboratory of Road Structure and Material of Ministry of Transport, Changsha University of Science and Technology, P R China; e-mail: zr_csust@yahoo.com.cn

ABSTRACT: In order to investigate water equilibrium of expansive soil subgrade, equilibrium water content of recompacted expansive soil under different stress conditions in wide suction range is measured, and the key parameter for numerical analysis is obtained; A two-dimensional subgrade-atmosphere interaction model is developed and used to numerically simulate variation of water content of a covered expansive soil subgrade in 10 years; Compaction control criterion for expansive soil subgrade is proposed considering the equilibrium water content. The results show that equilibrium water content is stress dependent in suction of 0-3MPa; Water content of subgrade increases slowly in 8 years and reaches equilibrium state finally; The optimum water content of wet compaction is close to equilibrium water content and natural water content of expansive soil in moist and hot climate. Compaction of expansive soil subgrade should be controlled in light of wet compaction criterion.

INTRODUCTION

Expansive soils undergo appreciable volume and strength changes following a change in moisture content. These changes can cause serious damage to highway expansive soil subgrade (Zheng 2009). It is important to keep water content of expansive soil subgrade in an equilibrium state under long-term atmospheric effect so that the stability of the subgrade can be insured (Zheng 2009). Therefore, it is necessary to correctly understand the rule of water equilibrium of expansive soil subgrade.

Change of water content of expansive soil subgrade and its influence factors have been studied by various researchers (HU 2004, Yang 2005, et al). Their field monitoring and model test results showed that the equilibrium conditions may be important to the road design in expansive soil area; water content of expansive soil in the core of subgrade will gradually increase from the initial water content state; close to the side of the embankment, the variation of water content is more obvious; water equilibrium of expansive soil subgrade is strongly effected by water retention ability of expansive soil and atmospheric condition. However, there are limitations on insight

of characteristics of water equilibrium of expansive soil and prediction for long-term water equilibrium of expansive soil subgrade.

In this paper, equilibrium water content of compacted expansive soil under different stress state and in wide suction range was experimentally studied. The key parameter for predicting equilibrium water content of expansive soil subgrade was obtained. Based on the ground-atmosphere interaction model (Wilson 1994), a two-dimensional finite element model was proposed to predict the equilibrium water content of expansive soil subgrade under long-term atmospheric effect. Based on the prediction and testing results of bearing capacity of expansive soil in different water content states, a compaction method for expansive soil subgrade was proposed and applied.

EQUILIBRIUM WATER CONTENT OF COMPACTED EXPANSIVE SOIL UNDER DIFFERENT STRESS AND SUCTION CONDITIONS

Soil-water characteristic curve (SWCC) defines the relationship between equilibrium water content and suction of soil, is a key parameter for predicting equilibrium water content of subgrade. In the previous experimental study, SWCC of expansive soil was measured under zero stress condition and in a small suction range (Zhang 2013). However, suction of expansive soil in subgrade may vary in wide range and the soil at different depth of subgrade is under different stress state.

On account of the limitations on measuring SWCC of expansive soil, three apparatus were jointly used for measuring SWCC of expansive soil under different stresses and in wide suction range. The first is the stress-controllable volumetric pressure plate extractor (FIG. 1(a)), which can control suction over 0-500kPa. The second and third apparatus are both shown in FIG. 1(b). One is a stress-controllable oedometer with osmotic technique (OMT) of controlling suction based on the principle of osmosis. Its controllable suction range is 1-10MPa according to the concentration of PEG solution. Another similar oedometer cell can control suction by vapor equilibrium technique (VET) according to different relative humidity produced by a saturated aqueous salt solution. Its controllable suction range is 10-1000MPa. For the three apparatus, vertical displacement and volume change of water in the specimen can be measured using a vertical dial gauge, burette or high accuracy balance respectively.

A soil sampled from Baise (BS) of Guangxi in China was used in the experimental study. The basic index properties of the soil are summarised in Table 1. According to

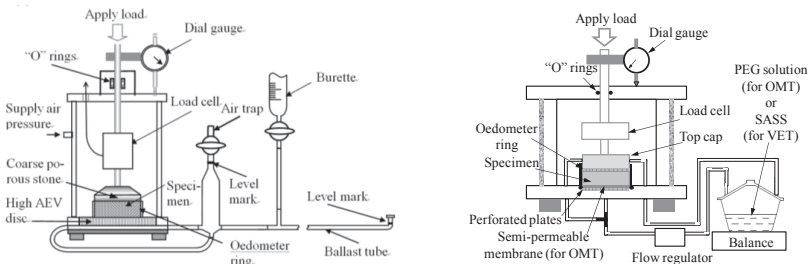


FIG. 1. (a) Stress-controllable volumetric pressure-plate extractor (Ng 2007), (b) Modified stress-controllable oedometer cells with OMT and VET (Leong 2011)

Chinese Specifications for Highway Design, the soil can be classified as expansive soil with medium swelling potential. For SWCC tests in this paper, the specimen was compacted in an oedometer mould which has 70mm diameter and 19mm height by static compaction method. The targeted dry density is 1.62 g/cm³, degree of compaction of 93% according to wet heavy compaction. The compacted specimen was saturated by submerging it in de-aired water in a desiccator. The saturated specimen was consolidated at 0kPa, 50kPa and 100kPa respectively corresponding to different depth in subgrade. Then a cyclic wetting and drying path are applied to the consolidated specimen in the suction range of 0-286.3MPa.

Table 1. Physical Properties of Guangxi Medium Expansive Soil

| Natural water content /% | Content of fine grain /% | | | Liquid Limit /% | Plastic Limit /% | Plastic Index /% | Content of montmorillonite /% | Free Swelling Ratio /% |
|--------------------------|--------------------------|------|------|-----------------|------------------|------------------|-------------------------------|------------------------|
| | Sand | Silt | Clay | | | | | |
| 20.4 | 2.5 | 52.3 | 45.2 | 56.3 | 21.4 | 34.9 | 16.6 | 82.0 |

FIG. 2 shows the variation equilibrium water content with suction under different vertical pressure. In the suction range of 1kPa-3MPa, for compacted specimens subjected to different stress states, the equilibrium water content under the same suction state is obviously different; the water retention ability is also different, the higher the applied load on the specimen, the lower the rate of desorption. This is likely caused by the presence of an average smaller pore-size distribution in the soil specimen under the higher applied load. As expected, there is marked hysteresis between the drying and wetting curves for the soil specimen under zero stress condition. The hysteresis loops seem to have reduced in size with an increase in the applied load. In the small suction range, the effect of stress on equilibrium of expansive soil is marked due to capillary effect and bottle neck effect. In the suction of 3MPa-286.3MPa, the differences in equilibrium water content of soil specimens under different stress states are not obvious. The hysteresis phenomena of equilibrium water content in the cycle of wetting and drying is not marked. It can be explain from the fact that in high suction range water retention ability is controlled by mineral absorption effect of expansive soil instead of capillary effect.

In order to obtain the computation parameter of predicting equilibrium water content of expansive soil subgrade, the median SWCCs in FIG. 2 are fitted by Equation 1 (Fredlund 1997). The fitting results are shown in Table 2.

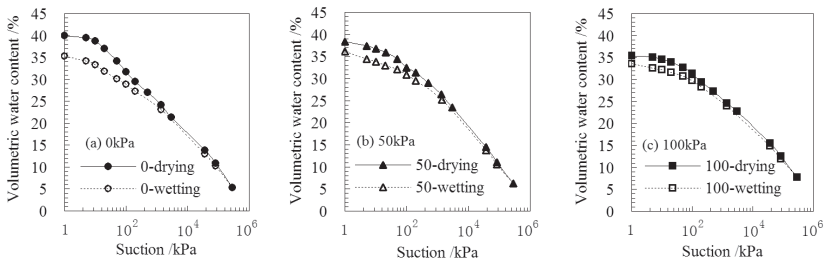


FIG. 2. Equilibrium water content of expansive soil under different stress and suction

$$\theta_w = \left(1 - \frac{\ln(1 + s/s_r)}{\ln(1 + 10^6/s_r)} \right) \frac{\theta_s}{\left\{ \ln \left[e + (s/a)^n \right] \right\}^m} \quad (1)$$

Where: θ_w is volumetric water content at any soil suction s ; θ_s is the saturated water content; and a , m , and n are fitting parameters. The variable e is the base of the natural logarithm, s_r is soil suction at residual conditions.

The fitting results in Table 2 shows that the stress state can affect the parameter a and m , corresponding to air entry value and water retention rate of SWCC respectively. Therefore, it is necessary for predicting equilibrium water content of subgrade to measure SWCC according the stress state of soil in the subgrade.

Table 2. Fitting Results of SWCC under different stress states

| σ_v /kPa | a | n | m | R^2 |
|-----------------|------|------|------|-------|
| 0 | 25.0 | 1.02 | 0.32 | 0.998 |
| 50 | 45.7 | 0.63 | 0.33 | 0.998 |
| 100 | 76.2 | 0.50 | 0.34 | 0.998 |

EQUILIBRIUM WATER CONTENT OF EXPANSIVE SOIL SUBGRADE SUBJECTED TO LONG-TERM ATMOSPHERIC EFFECT

Subgrade-atmosphere interaction model

A one-dimensional soil-atmosphere interface model was developed by Wilson (1994). The model defines the boundary condition at the soil surface in terms of temperature and water potential. Two balance equations are taken into account: the first concerns the water balance due to precipitation, runoff, evaporation and infiltration, and the second the energy balance at the soil surface. Based on the model, a subgrade-atmosphere interaction model is developed by considering two-dimensional calculation and the stress-dependent SWCC of soil in the subgrade. The model includes water (liquid and vapor) balance equation and thermal balance equation:

$$\frac{1}{\rho_w} \frac{\partial}{\partial x} \left(D_v \frac{\partial P_v}{\partial x} \right) + \frac{1}{\rho_w} \frac{\partial}{\partial y} \left(D_v \frac{\partial P_v}{\partial y} \right) + \frac{\partial}{\partial x} \left(k_x \frac{\partial \left(y + \frac{-s}{\rho_w g} \right)}{\partial x} \right) + \frac{\partial}{\partial y} \left(k_y \frac{\partial \left(y + \frac{-s}{\rho_w g} \right)}{\partial y} \right) + Q = \lambda_\sigma \frac{\partial s}{\partial t} \quad (2)$$

$$L_v \frac{\partial}{\partial x} \left(D_v \frac{\partial P_v}{\partial x} \right) + L_v \frac{\partial}{\partial y} \left(D_v \frac{\partial P_v}{\partial y} \right) + \frac{\partial}{\partial x} \left(\lambda_{tx} \frac{\partial T}{\partial x} \right) + \frac{\partial}{\partial y} \left(\lambda_{ty} \frac{\partial T}{\partial y} \right) + Q_T = \lambda_v \frac{\partial T}{\partial t} \quad (3)$$

Where: P_v is vapor pressure of soil moisture, D_v is vapor diffusion coefficient, y is the elevation head, s is soil suction, k_x and k_y is hydraulic conductivity in the x -direction and y -direction respectively, Q is the applied boundary flux, λ_σ is the slope of the volumetric water content and stress-dependent, t is time, L_v is the latent heat of vaporization, λ_{tx} and λ_{ty} is the thermal conductivity in the x -direction and y -direction respectively, Q_T is the applied thermal boundary flux, T is the soil temperature, λ_v is the volumetric specific heat value.

According to Kelvin's law, relationship between s and P_v can be expressed as:

$$s = -\frac{RT}{W_v} \ln \frac{P_v}{P_{vs}} \tag{4}$$

Where: R is the universal gas constant, W_v is the molecular weight of water, P_v saturated vapor pressure of soil moisture.

The applied boundary flux Q can be calculated by equation (5).

$$Q = P_r - E \tag{5}$$

Where: P_r is rainfall, E is Actual evaporation of soil and can be calculated based on modified Penman –Wilson formulation (Equation 6).

$$E = \frac{\Gamma N + 0.35\eta P_{vs} (1 + 0.15v_w) [RH_a^{-1} - RH_r (s)^{-1}]}{\Gamma + \eta/RH_r (s)} \tag{6}$$

Where: Γ is slope of the saturation vapor pressure versus temperature curve at the mean temperature of the air, N is net radiant energy available at the surface, η is humidity constant, v_w is wind speed, RH_a and RH_r is the relative humidity of air and soil surface respectively.

The surface temperature of subgrade may be estimated with the following:

$$T_s = T_a + \frac{1}{0.35\eta(1 + 0.15v_w)} (N - E) \tag{7}$$

Where: T_s is the temperature at the soil surface, T_a is the temperature of the air above the soil surface.

The above governing equations are solved using the Galerkin finite element method. Key input data include SWCC, the hydraulic conductivity suction function, thermal properties (soil thermal conductivity, mass specific heat capacity), and climate data (i.e., air temperature, wind speed, rainfall, relative humidity).

Modelling Water Equilibrium of Expansive Soil Subgrade

A trial covered expansive soil subgrade was built in Longlin-Baise Expressway in Guangxi. Considering the symmetry, a numerical model for the half subgrade is established and shown in FIG. 3. The subgrade is 5m in height. The core of subgrade was filled with the expansive soil which properties are shown in Table 1. The height of expansive soil core is 6m. The top and base is filled with gravel soil of 1.5m in height and both sides are covered with nonexpansive soil of 3.5m in width. The initial gravimetric water content is 19.0% corresponding to the volumetric water content of 30.2%, the optimum water content of wet compaction. Water table locates at 5m in depth under the ground. Asphalt concrete pavement is on the embankment. Six monitoring points are set on the central line and on the side of expansive soil respectively in the subgrade model.

The hydraulic and thermal parameters of subgrade materials and meteorological data used in the modelling are shown in Table 3 and FIG. 4. On account of upper pressure of expansive soil in the subgrade,

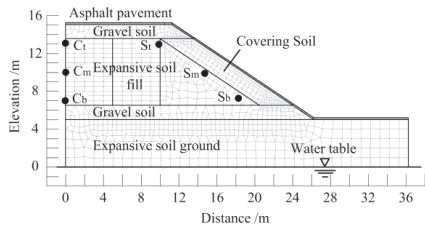


FIG. 3. Numerical Model for subgrade

the SWCC of expansive soil is 100kPa SWCC which characteristic value is shown in Table 1. In order to investigate the long-term variation of water content of the subgrade, a simulation of 10 years was conducted. The model was run with adaptive time stepping (with initial time step as 1 day) that is required for solving climate boundary conditions where the daily climate data are used.

Table 3. Hydraulically and Thermal Parameters for the Numerical Simulation

| Materials | Hydraulic Conductivity / m/s | SWCC | | | Thermal Conductivity / J/s·m·°C | Volumetric Heat Capacity / J/m ³ |
|------------------|------------------------------|-------|------|------|---------------------------------|---|
| | | a | n | m | | |
| Expansive soil | 2.5E-10 | 76.2 | 0.50 | 0.34 | 1.984 | 3.07E+6 |
| Cover soil | 3.1E-9 | 365.2 | 0.78 | 0.76 | 2.354 | 2.85E+6 |
| gravel soil | 5.2E-6 | 7.8 | 9.72 | 0.79 | 3.967 | 2.58 E+6 |
| Asphalt concrete | 1.0E-14 | / | | | 1.010 | 1.98 E+6 |

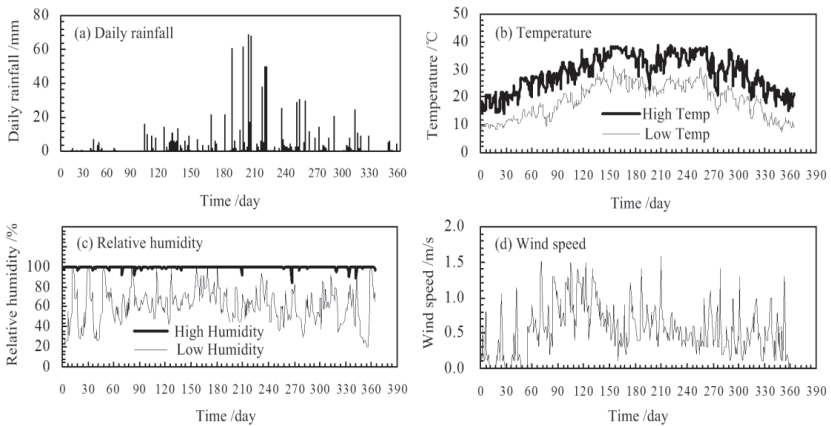


FIG. 4. Annual Meteorological Data of Guangxi Baise

FIG. 5 presents the variation of water content of expansive soil subgrade with elapsed time. It is observed that water content of the 6 monitoring points located in the expansive soil all increase slowly with elapsed time in the early, and trend to a equilibrium water content or fluctuate around certain water content. Water content of the point C_b and S_b close to the gravel soil base increases greatly in the first year, it might attribute to high relative humidity in the gravel soil base in the hot and humid weather condition. In the late 9 years it increases steadily to an equilibrium state and the increase range is less than 1%. In the middle of subgrade, at the point C_m and S_m , the water content increases gradually in 8 years and stays equilibrium finally. Close to the top of subgrade, at the point C_t and S_t , water content increases fluctuantly because it is influenced by atmospheric cyclic wetting and drying. The fluctuation is more obvious at point S_t which is close to the shoulder and much easier affected by the atmosphere. In the 7th year, the water content of S_t fluctuates around 31.8% and in a small range. In the water equilibrium state of the subgrade, the water content along

the depth is a little bit different due to different elevation, and the difference in water content is less than 1%. Approximately the equilibrium water content of the expansive soil subgrade is 31.8% corresponding to gravimetric water content of 19.9%.

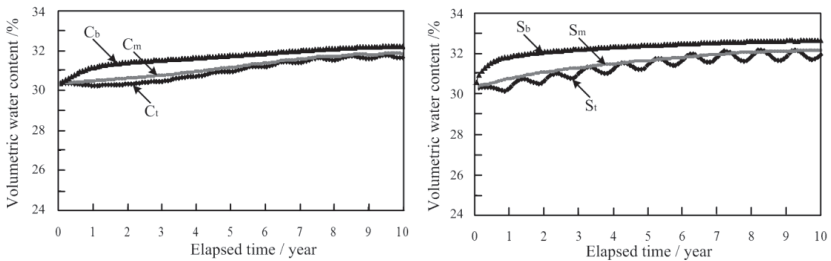


FIG. 5. Variation of water content of expansive soil subgrade with elapsed time

COMPACTION CONTROL CRITERION FOR EXPANSIVE SOIL SUBGRADE

The optimum water content w_{opt} and the maximum dry density ρ_{max} from compaction test on soil is used to control field compaction and can be obtained by two compaction methods, one is dry compaction in which soil specimen is prepared from air dry state to wet state by absorption, another is wet compaction in which soil specimen is prepared from natural state to a dry state by desorption. The w_{opt} and ρ_{max} obtained per the two methods are presented in Table 5. The California Bearing Ratio (CBR) is an index for evaluation of bearing capacity of subgrade fill. The testing results of CBR at w_{opt} and ρ_{max} are also presented in the Table.

The results show that w_{opt} of wet compaction is greater, but ρ_{max} is less than the one of dry compaction. CBR of dry compaction specimen is less than that of wet compaction specimen and 3% the threshold value for subgrade fill, and the swelling percent of dry compaction specimen is much greater. It can be deduced that in the moist and hot climate, if control subgrade compaction in light of dry compaction criterion, that is, compact subgrade in low water content state and high dry density, it will cause great increase in water content from the relative low initial water content to the equilibrium water content which is relative high and close to the nature water content. As a result, it will cause increase in swelling percent and decrease in bearing capacity of fill to an unacceptable state (CBR<3%). However for wet compaction, w_{opt} is close to equilibrium water content and natural water content, swelling percent is small, and CBR is greater than 3% which can meet the requirement of specifications for subgrade design. Therefore compaction of expansive soil subgrade should be controlled in light of wet compaction criterion in the moist and hot climate condition.

Table 4. Results of Compaction Tests and CBR Tests

| Compaction Method | Optimum Water Content /% | Maximum Dry Density / g/cm ³ | CBR /% | Swelling Percent /% |
|-------------------|--------------------------|---|--------|---------------------|
| Wet | 17.7 | 1.80 | 3.9 | 2.1 |
| Dry | 15.3 | 1.87 | 2.2 | 6.7 |

CONCLUSIONS

(1) Soil-water characteristic curve of expansive soil which defines the relationship between equilibrium water content and suction is stress dependent, especially in the suction range of 0-3MPa. The higher the applied load on the specimen, the lower the rate of desorption, and the smaller hysteresis loop. It is necessary for predicting equilibrium water content of expansive soil subgrade to use stress-dependent SWCC according the stress state of expansive soil fill in the subgrade.

(2) A two-dimensional subgrade-atmosphere interaction model is developed based on the one-dimensional soil-atmosphere interface model. Using the developed model, variation of water content of a covered expansive soil subgrade in 10 years was numerically simulated. Results show that water content of subgrade increases slowly in 8 years and reach equilibrium state.

(3) The optimum water content of wet compaction is close to equilibrium water content and natural water content of expansive soil in moist and hot climate condition. The water stability of wet compaction is better than that of dry compaction due to greater CBR and less swelling percent. Compaction of expansive soil subgrade should be controlled in light of wet compaction criterion.

ACKNOWLEDGMENTS

The authors appreciate the support of National Natural Science Foundation of China (51108049), the National Program on Key Basic Research Project (2011CB411910), Science Foundation of Ministry of Transport (2011318824730).

REFERENCES

- ZHENG J L, YANG H P. Highway Expansive Soil Engineering. Beijing: the People's Communications Publishing House, 2009.
- ZHENG J L, ZHANG R, YANG H P. Highway Subgrade Construction in Expansive Soil Areas. *Journal of Materials in Civil Engineering*, 2009, 21(4): 154-162.
- HU M J, LIU S G, KONG L W. Expansive Soil Character Later Test Verification on Freeway Embankment Treatment. *Rock and Soil Mechanics*, 9(25): 1418-1422.
- YANG G L, LIU Y H. Experimental Study on Moisture Content in Expansive Soil Roadbed under Different Weather Conditions. *Chinese Journal of Rock Mechanics and Engineering*, 2005, 24(24): 4524-955.
- WILSON G W, FREDLUND D G. Coupled soil-atmosphere modeling for soil evaporation. *Canadian Geotechnical Journal*, 1994, 31(1): 151-161.
- ZHANG R, ZHENG J L, NG C W W. Experimental Study on Stress-Dependent Soil Water Characteristic Curve of a Recomacted Expansive Soil. *Applied Mechanics and Materials*, 2013, 256-259: 283-286
- Ng C W W, Menzies B. *Advanced Unsaturated Soil Mechanics and Engineering*[M]. London: Taylor & Francis, 2007.
- LEONG A K. Field and laboratory studies of saprolitic hillslope subjected to seasonal variations. PhD Thesis, Hong Kong University of Science and Technology, 2011
- FREDLUND D G, XING A. Equations for the soil-water characteristic curve. *Canadian Geotechnical Journal*, 1994, 31: 521-532

Field Tests on Vibration Response of Ballastless Subgrade under Excitation of High Speed Train in China

Jianlin Ma¹, Yanxin Yang², Fuchun Xue³, Liping Yan⁴, Fei Jiang⁵, and Cong Shi⁶

¹Professor, Southwest Jiaotong University, Chengdu, Sichuan 610031, China; majianlin01@126.com

²Graduate Student, Southwest Jiaotong University, Chengdu, Sichuan 610031, China; actor99yyx@sina.com

³Postdoc, Tsinghua University, Beijing 100084, China; ocean2008xfc@163.com

⁴Civil Engineering Associate, Los Angeles Department of Water and Power, 111 N. Hope Street, Los Angeles, CA 90012, USA; lipingyan.ge@gmail.com

⁵Graduate Student, Southwest Jiaotong University, Chengdu, Sichuan 610031, China; swjtu@my.swjtu.edu.cn

⁶Graduate Student, Southwest Jiaotong University, Chengdu, Sichuan 610031, China; olivershicong@126.com

ABSTRACT: By conducting field dynamic tests on a ballastless track-subgrade system located in the Milestone JJK86+274 of Beijing-Tianjin Intercity Dedicated Passenger Line in China, vibration velocities and their distributions of the center and the edge of slab track, the concrete roadbed edge, and the subgrade surface were measured under excitation of a high-speed train at the highest speed of 344 km/h in the world. The relationship between the maximum vibration velocity of slab track and train speed was also obtained. The results of the dynamic tests expand findings of the behavior of the ballastless track system on high-speed railway in Germany. An S-shaped growth curve along with a fitting formula are derived and can be used to describe the correlation between the maximum vibration velocity V_d and train speed V . This paper provides a useful reference for evaluation, prediction and control on dynamic response of ballastless subgrade, high safety, high stability and high comfort for the running of high-speed trains in the future.

INTRODUCTION

Over the past decade, the construction of high-speed railway in China has developed rapidly. The “CRH” high speed train designed with a maximum speed of 350 km/h and operated at a speed of 300 km/h has run on multiple dedicated passenger lines. By the end of year 2012, China ranked the first place in the world with its high-speed railway mileage over 9,356 km.

To ensure the long-term safety, stability, high comfort and high smoothness of running of a high speed train, a ballastless track system on a roadbed consisting of a monolithic concrete support is usually used for high speed railway in China. Thus,

such system overcomes the disadvantage of a ballast track system, enhances the track geometry, strengthens the track stability, and maintains the physical integrity of the railway (Zhao, 2006).

Dynamic response of track and railway subgrade induced by running trains can in turn influence running safety of trains. Some researches have been performed on the topics such as field testing, propagation mechanism of energy, the law of propagation, vibrations prediction. Most of field testing was conducted on subgrade under excitation of train velocity lower than 200 km/h. Gao (2007) made field vibration measurements at various distances from the track center on Qinhuangdao-Shenyang Railway. Li (2004) obtained dynamic stress characteristics of a bridge-approach roadbed through dynamic testing system on Qin huangdao-Shenyang Railway. Zong (2007) measured subgrade dynamic response subjected to trains at the speed ranging from 17 km/h to 136 km/h on Shanghai-Nanjing Railway and did numerical simulations using the finite element method. Sun (2003) analyzed the factors that influence the dynamic stress distribution based on the field test results. Wang (2012) tested a full-scale subgrade model and obtained a loading time-history. Suiker (2005) conducted both static and cyclic tri-axial tests of ballast and sub-ballast materials. Hu (2004) proposed a procedure to evaluate the dynamic stability of subgrade composed of soils. Gotschol (2002) obtained the velocity response based on vibration monitoring of the German ballastless track system under the maximum train speed of 280 km/h. It can be seen that researches on dynamic field testing of subgrade subjected to high-speed train with running speed over 300 km/h have been very few.

Many factors influence dynamic response of a subgrade, such as train speed, train axel load, thickness of top subgrade layer and subgrade stiffness (Liang, 2006). Train speed is a major cause of dynamic response of the subgrade and directly impacts running safety of trains and the performance of track. When train runs at lower speed, the effect of train's dynamic loading is not obvious and the impacts on track and subgrade can be ignored. With the increase of train speed and the expansion of train lines on various soft foundations, the impacts can't be neglected since problems of soil dynamics occur. Long-term effects due to trains can lead to excessive deformation of the ballastless subgrade and track system, irregularity of the track, and even break-off of the train operation. therefore, it is necessary to conduct field tests of monitoring dynamic response of a subgrade under excitation of high-speed train for the evaluation, prediction and control on dynamic response of a ballastless subgrade, high safety, high stability and high comfort for the running of high-speed trains

This paper presents an experimental study of field tests on the Beijing-Tianjin Intercity Railway, the first dedicated passenger line in China. The dynamic response of the subgrade under excitation of a high-speed train with a maximum speed of 344 km/h was monitored.

FIELD TESTS

Site Location and Soil Conditions

The 114.3-km long Beijing-Tianjin Intercity Railway opened on August 1, 2008. The test cross-section is located at Milestone JJK86+274.

At this location, the track is straight and has a gradient of +0.6‰. The track uses the 60kg/m type rail, the Vossloh300-1 type fastening, and the CRTSII type ballastless track slab. Under the track slab there is a cement asphalt mortar layer, a 0.3-m thick concrete roadbed, and a 0.7-m thick frost resistant crushed rock layer on the top of the subgrade. The fill section of subgrade is an U-shaped embankment retained by cantilevered retaining walls on each side of the embankment. The top of the subgrade is 13.6-m wide and the base below the subgrade is filled with Groups A and B materials. The profile of the fill embankment is shown in Fig. 1.

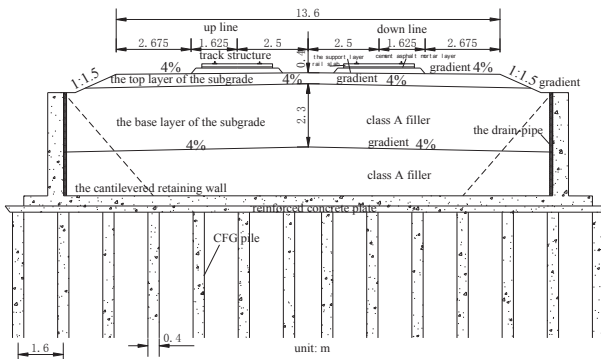


FIG. 1. The fill section of subgrade.

The foundation mainly consists of silty clay and mucky silty clay at deep layer, with characteristics of low bearing capacity, high compressibility, and a tendency of creeping and softening when encountering water. Therefore, the engineering geological conditions are very poor at the test site.

To prevent settlement during construction, post-construction settlement and uneven settlement from being beyond the allowable ones, a composite foundation using CFG (Cement Fly-ash Grave) piles were adopted to support the embankment. CFG piles are 25 to 30 m in length, 0.4 to 0.5 m in diameter, 1.5 to 1.7 m in spacing. A 0.2-m thick layer of crushed rock was placed as a balance layer between the bottom of U-shaped section and CFG piles, as shown in Fig. 2. The groundwater table was located at a depth of 1 to 2 m below the ground surface.

The CRH2C bullet train was used for the field tests. CRH2C, the Harmony China Railway High-speed series electric multiple units (EMUs), has 2 trailer cars and 6 motorized cars, with 8 marshalling cars and an axle load of 14 tons.

Sensor Arrangement

The test section is located on the down-line track (i.e., trains running from Beijing to Tianjin). Six measuring points were arranged along the surface of the subgrade, which are listed in Table 1 and shown in Fig. 2 and Fig. 3. Fig. 4 shows the sensors attached to the center and the edge of track slab. The sensors, data-transmission system, and software used in the field tests were developed by the Chinese Academy of Sciences. Fig. 5 shows the instrument.

Table 1. Layout of Sensors

| Point No. | Location | Distance from Center Line (m) | Type of Sensor |
|-----------|--|-------------------------------|---|
| 1 | the center of slab track | 0.00 | Vertical velocity |
| 2 | the edge of track slab | 0.85 | Vertical velocity and Horizontal velocity |
| 3 | the edge of concrete roadbed | 1.30 | Vertical velocity and Horizontal velocity |
| 4 | the surface of subgrade beneath concrete roadbed | 1.78 | Vertical velocity and Horizontal velocity |
| 5 | the bottom of the surface of subgrade | 3.55 | Vertical velocity and Horizontal velocity |
| 6 | the top of cantilevered retaining wall | 7.10 | Vertical velocity and Horizontal velocity |

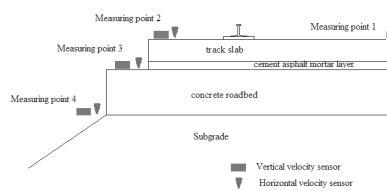


FIG. 2. The arrangement of sensors (half of the cross-section of subgrade).

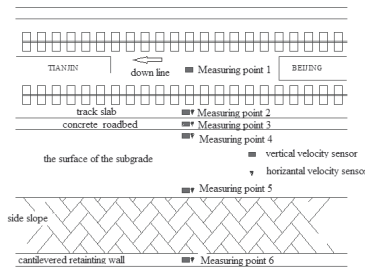


Fig.3. The plan view of sensors.

Testing

The field tests started on June 1, 2008 and ended on June 5, 2008. During the 41 round-trip operations of CRH2C trains running on the up-line track (trains running from Tianjin to Beijing) and the down-line track (trains running from Beijing to Tianjin), the train speed ranged from 113 km/h to 344 km/h. When the train ran on the track, the data acquisition system collected measurements of vibration velocities from the 10 velocity sensors installed on the six measuring points along the surface of

subgrade with a frequency of 2000 Hz.



FIG. 4. Sensors attached to the center and the edge of track slab.

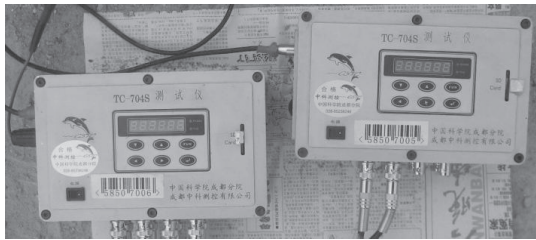


FIG. 5. The instrument for vibration measurements.

TEST RESULTS

Measurements of Time Histories

Based on the measurements collected from all the sensors, time histories of the vertical vibration velocity, the vertical vibration acceleration, and the vertical vibration displacement at all the measuring points have been obtained and processed.

Analysis of Test Data

Totally 410 sets of collected data were analyzed. Table 2 lists the maximum vibration velocities measured by the sensors when the train was running on the down-line track (i.e., trains running from Beijing to Tianjin).

Vibration Velocity versus Train Speed

Fig. 6 shows the maximum vertical vibration velocity of the edge of track slab under different train speed. For comparison, the results of field tests on the German high-speed railway conducted by Gotscho (2002) are also plotted in Fig. 6.

As indicated in Fig.6, our test results are in good agreement with the results from Gotschol (2002) when train speed is lower than 290 km/h. Our test results provide

additional data when train speed is more than 290 km/h. Table 3 summarizes the growth tendency of maximum vertical vibration velocity of track slab as the train speed increases.

Table 2. Measured Maximum Vibration Velocities

| Point No. | Measuring Point Location | Direction of Vibration Monitoring | Maximum of Vibration Velocity (mm/s) | Train speed (km/h) |
|-----------|--|-----------------------------------|--------------------------------------|--------------------|
| 1 | the center of slab track | Vertical | 3.537 | 344 |
| 2 | the edge of track slab | Vertical | 6.099 | 344 |
| | | Horizontal | 3.631 | 335 |
| 3 | the edge of concrete roadbed | Vertical | 3.834 | 335 |
| | | Horizontal | 2.291 | 315 |
| 4 | the surface of subgrade beneath concrete roadbed | Vertical | 2.675 | 344 |
| | | Horizontal | 2.053 | 335 |
| 5 | the bottom of the surface of subgrade | Vertical | 1.125 | 295 |
| | | Horizontal | 0.912 | 344 |

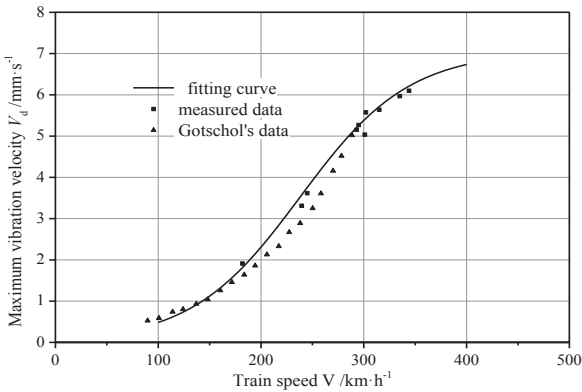


FIG. 6. Maximum vertical vibration velocity versus train speed.

Table 3. Growth Tendency of Maximum Vertical Vibration Velocity

| Train Speed | Maximum of Vertical Vibration Velocity (mm/s) | Growth Tendency of Vibration Velocity |
|---|---|--|
| $V < 150\text{km/h}$ | $V_d \leq 1\text{mm/s}$ | V_d has a generally slow growth tendency |
| $150\text{km/h} \leq V \leq 290\text{km/h}$ | $1\text{mm/s} < V_d \leq 5.4\text{mm/s}$ | V_d grows much faster, |
| $290\text{km/h} < V \leq 344\text{km/h}$ | $5.4\text{mm/s} < V_d \leq 6.2\text{mm/s}$ | V_d grows relatively slow |

The relationship between maximum vertical vibration velocity of track slab V_d and train speed V can be represented by the following formula:

$$V_d = \frac{a}{1 + b e^{-kV}} \tag{1}$$

where:

V_d = maximum vertical vibration velocity of track slab, mm/s;

V = running speed of high-speed train, km/h, ranging from 100 km/h to 350 km/h;

a, b, k = empirical parameters, $a = 7.05, b = 90, k = 0.0189$ for our test results.

Distributions of Vertical Vibration Velocity

Fig. 7 shows distributions of vertical vibration velocity along the surface of cross-section of subgrade for various values of the train speed. Following observations can be made from this figure:

The maximum vibration velocity occurs at the edge of track slab with a value of 6.099 mm/s. Also this point has the most obvious change of vibration velocity as train speed increases. When train speed increases from 182 km/h to 344km/h, vibration velocity rises from 1.92 mm/s to 6.099 mm/s, having a growth of 217.65%.

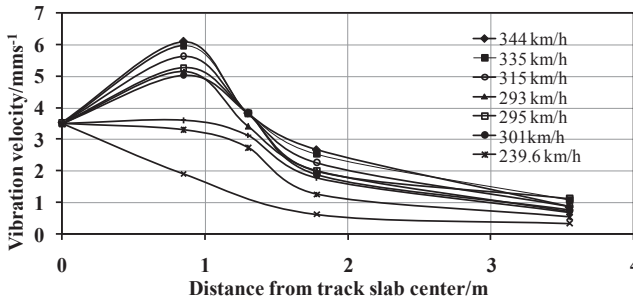


FIG. 7. Distribution of maximum vertical vibration velocity along the surface of cross-section of subgrade.

The vibration velocity of the edge of concrete roadbed rises when the train speed increases. When the train speed goes up from 182 km/h to 344km/h, the vibration velocity rises from 2.753 mm/s to 3.833 mm/s, having a growth of 39.23%.

The vibration velocity of the surface of subgrade beneath concrete roadbed rises when the train speed increases. When the train speed goes up from 182 km/h to 344 km/h, the vibration velocity rises from 0.625 mm/s to 2.675 mm/s, having a growth of 328%.

The vibration velocity of the bottom of the surface of subgrade rises when train speed increases. When the train speed goes up from 182 km/h to 344 km/h, the vibration velocity rises from 0.337 mm/s to 1.067 mm/s, having a growth of 216.6%.

CONCLUSION

Based on the tests of the field tests on vibration of the subgrade located at Milestone JJK86+274 of Beijing-Tianjin Intercity Dedicated Passenger Line in China under the train CRH2C with a highest speed of 344 km/h, conclusions can be drawn as follows:

1. An S-shaped growth curve can be used to describe the relationship between maximum vibration velocity V_d of the edge of track slab and train speed V .
2. The relationship between maximum vibration velocity V_d and train speed V of track slab can be represented by Equation (1).
3. The maximum vibration velocity appears at the edge of track slab with a value of 6.099 mm/s.

REFERENCE

- Zhao, Guotang (2006). High speed railway ballastless track structure. Beijing, *China Railway Press*. (in Chinese).
- Gao, Guangyun et al. (2007). "Experimental results and numerical predictions of ground vibration induced by high-speed train running on Qin-Shen Railway." *Rock and Soil Mechanics*, Vol. 28 (9): 1817-1822. (in Chinese).
- Li, Xianmin et al. (2004). "Study on the dynamic response of transition section roadbed subject to high speed." *Chinese Journal of Geotechnical Engineering*, Vol. 26 (1): 100-104. (in Chinese).
- Zong, Junliang Zong et al. (2007). "Dynamic response study on speed-increase subgrade of existing railway." *China Railway Science*, Vol. 28 (4): 7-11. (in Chinese).
- Sun, Changxin et al. (2003). "Test and analysis for the dynamic stress responses of the Qin-Shen Railway's subgrade." *Journal of Lanzhou Jiaotong University*, Vol. 22 (4): 110-112. (in Chinese).
- Wang, Qiyun et al. (2012). "Study on track-subgrade model of high-speed railway and dynamical loading." *Journal of the China Railway Society*, Vol. 34 (12): 90-96. (in Chinese).
- Hu, Y.F. et al. (2004). "ResCol-Versuche zur prüfung der dynamischen langzeitstabilität von TA/TM-B den untereisenbahnverkehr." *Bautechnik*, Vol. 4 (81): 295-306. (in German)
- Suiker, A.S.J. et al. (2005). "Static and cyclic triaxial testing of ballast and subballast." *J. Geotechnical & Geoenviron. Engrg.*, Vol. 131 (6): 771-778.
- Gotschol, A. (2002). *Veraenderlich elastisches und plastisches Verhalten nichtbindiger Boeden und Schotter unter zylich-dynamischer Beanspruchung*. University Kassel. (in German).
- Liang, Bo et al. (2006). "A study on the sudden changes or double peaks in the dynamic response of subgrade of high speed railway." *China Civil Engineering Journal*, Vol. 39 (9): 117-123. (in Chinese).

Field Test and Analysis of Piled-raft Structure of High-speed Railway Foundation

Duc-phong Pham¹, Su Qian², Bai Hao¹, Liu Bao¹
Sun Hong-lin³, Chen Shang-yong³

¹Graduate student, School of Civil Engineering, Southwest Jiaotong University, Chengdu 610031; email: ducphong357@gmail.com

²Professor, School of Civil Engineering, SWJTU, Chengdu 610031; email: suqian@126.com

³Senior engineer, China Railway Siyuan Survey and Design Group Co., Ltd, Wuhan 430063

ABSTRACT: Piled-raft structure is used in high-speed railway to deal with the deep quaternary strata compressibility foundation, which can effectively control total settlement and differential settlement, aiming at the efficient, economical and fast treatment subgrade deformation. In this paper, based on the field test of Beijing-Shanghai high-speed railway project, the dynamic response of high-speed railway piled-raft structure is investigated. The results agree fairly well with those obtained by theoretical approach and show that settlement of the subgrade is controlled effectively by the piled-raft structure.

INTRODUCTION

The piled-raft foundation is the complex combination of the pile and the raft (Ta et al., 1997). The advantages of the piled-raft structure are large stiffness, high bearing capacity and good overall stability, etc (Horikoshi 1998, Prakoso et al., 2002). After being connected to the piles, the raft will uniformly distribute the upper load to the subgrade, meanwhile the piles subjected most of the load before transferring it to the surrounding soil. Hence the issues of stress concentration and overall settlement can be solved effectively. This composition, as a result, is suitable for construction works with large loading and small bearing capacity subgrade. Simultaneously, the piled-raft structure has a highly overturning resistance. In construction projects, the piled-raft foundation has been applied, researched and a lot of achievements on it have been gained. It has been also tested via many practical projects, and has gradually become a complete scientific research, forming official process and procedure. Besides, the interaction between upper structure and pile-soil is considered in the calculating and designing method.

Piled-raft structure (Clancy 1993, Poulos 2001, Ziaie-Moayed 2010, Nguyen et al., 2013) was used in designing Suzhou station on the Beijing-Shanghai high-speed railway. In this paper, by researching the calculating theories and carrying out the field

test (Li Jun-cai 2009, Chen Shang-yong et al., 2010) of the high-speed railway foundation project to verify the suitability of piled-raft foundation calculating theory and the reliability of reinforcement effect; as well as to form a suitable method of designing, thereby piled-raft structure can be used widespread in the high-speed railway foundation reinforcement.

FIELD MEASURED

Project Summary and Field Test Description

The road embankment of Suzhou high-speed railway station which belongs to the Beijing-Shanghai high-speed railway system includes main line, arrival-departure line, maintenance position. Main line mileage varies from DK755+460.95 to DK757+377.44, maintenance position mileage varies from DK757+350 to DK757+700. East Suzhou central Station with the mileage of DK756+400 includes two sets divided into six lanes.

In order to test the capacity of the raft, piles, soil-pile interaction and settlement behavior of the foundation, five sections were designed to test including two natural sections and three reinforced sections. The natural sections located at DK757 + 570 (4 #) and DK757 + 600 (5 #). Three sections reinforced with pile-raft foundation located at main line DK755 + 654.96 (1 #), the station area DK756 +717.75 (2 #), the transition section DK757 +325 (3 #). The tested sections is shown in Fig.1 and Fig.2.

According to the calculation results:

- The foundation at the main line DK755+654.96 (1 #) was reinforced as the following: pile-raft with pile spacing of 2.4m, raft plate thickness of 0.5m, 0.2m thick gravel layer was under the backfill, reinforced depth of 19m, the slope rate of 1:1.5, preloading backfill height of 3.1m;

- At the DK756+717.75 (2#) pile with raft used for 4 rows in the middle (mainly load bearing area), pile spacing of 2.3m, raft plate thickness of 0.5m, 0.2m thick gravel layer was under the backfill; The sides were reinforced by composite pile foundation as the following: pile spacing of 2.4m, the top of piles were erected by square pile caps, with the side dimension of 1.6m, on the pile cap 0.7m thick gravel layer was intermixed by high-strength geocell, treated foundation depth of 19m, slope rate of 1:1.5, preloading backfill height of 4.1m ;

TEST RESULTS AND ANALYSIS

Test and Settlement Analysis of Piled-raft Structure

Sections which is reinforced by piled-raft foundation with preloading are chosen to be considered (the main line and station sections). To identify the settlement, measured-settlement plates are located above the raft foundation at the centre and both sides of the route as shown in Fig.3.

Ground Surface of Settlement Analysis

As can be seen by the data and distribution curves, the foundation settlement is gradually increased according to the preloading progress for the subgrade. However,

after the load remains stable, settlement curves tend to converge, which can be illustrated on the settlement curves that settlement measuring points are very close to each other, indicating that there are very small differential settlements among points at the same cross section of raft.

At the section of the main line (Fig.4a), the process of backfill loading is completed within about six months, the measured settlement of plate 3 (the maximum settlement) is 21.39 mm; after unloading the settlement is gradually decreased, instantaneously, the elastic phenomenon arises with the elasticity of 2.01 mm. After completing track-laying installation, the settlement is relatively stable. Hyperbola method applied to measure settlement with the total settlement of plates C1-1~3# are 23.3 mm, 22.3 mm, and 23.4 mm, respectively. The estimated settlement after executing are 3.2 mm, 1.6 mm, and 3.4 mm, respectively.

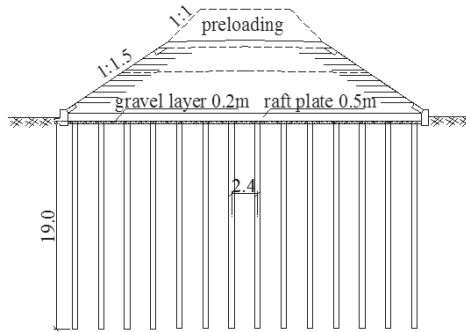


FIG. 1. 1# cross-sectional diagram (DK755+654.96)

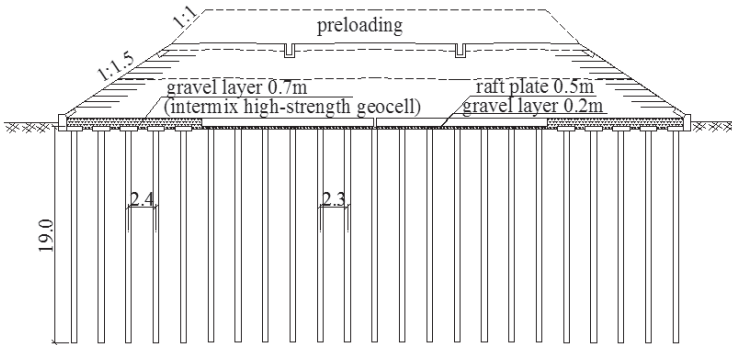
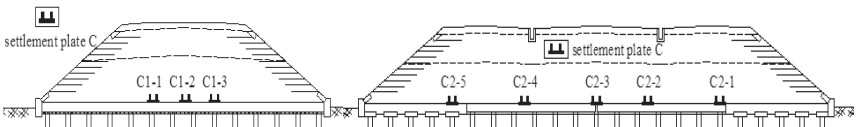


FIG. 2. 2# cross-sectional diagram (DK756+717.75)



(a) main line cross-section, C1-1 ~ 3# (b) station area cross-section, C2-1 ~ 5#

FIG. 3. The settlement plate embedded location map

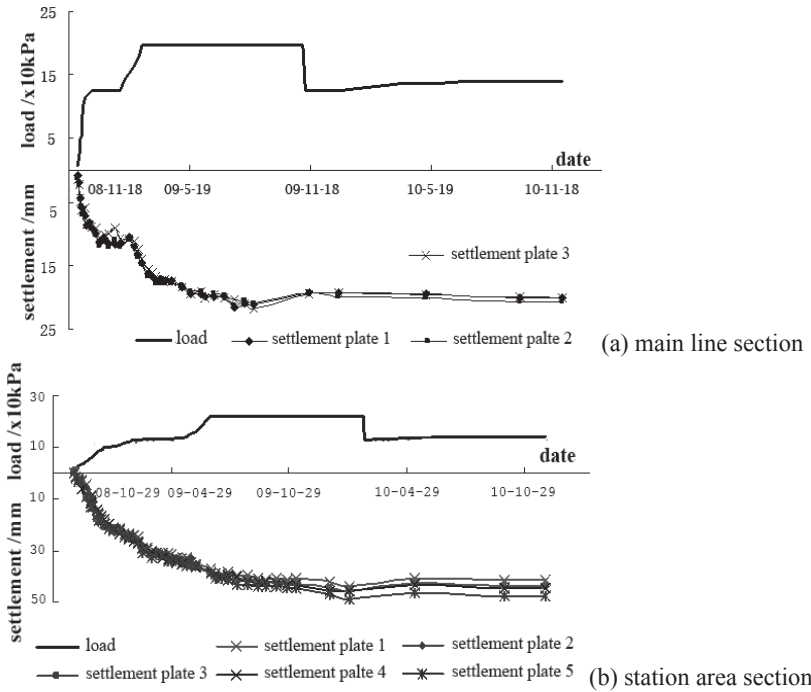


FIG. 4. Ground surface of settlement - time - load curve

At the measuring section of the station (Fig.4b), the process of backfill loading is completed within about 8 months, the measured settlement of plate 4 (the maximum settlement) is 45.90 mm; after unloading, the elastic phenomenon arises with the elasticity of 2.86 mm. After completing track-laying installation, the settlement is relatively stable. Hyperbola method applied to measure settlement, the final measured settlement of plates C2-1~5# are 45.0 mm, 47.0 mm, 46.7 mm, 51.4 mm, 49.6m, respectively. The estimated settlement after executing are 3.49 mm, 3.29mm, 3.01 mm, 7.01 mm, 2.12mm, respectively, that satisfies the required condition of settlement after executing of ballastless track railway project.

The total settlement of the measuring section at the station is greater than that of the main line. At the location of piled-raft structure, the settlement of the station section is greater than 1.34 ~ 2.13 times. This effect is due to the fact that the loading width in the station section is relatively large.

Test and Analysis of Layered Settlement

As can be seen in Fig.5, during preloading process, settlement will increase following with loading; after load is stable, settlement will tend to converge quickly. After unloading, there is no significant change in settlement value during time of

rack-laying installation until finishing the test, settlement is stable.

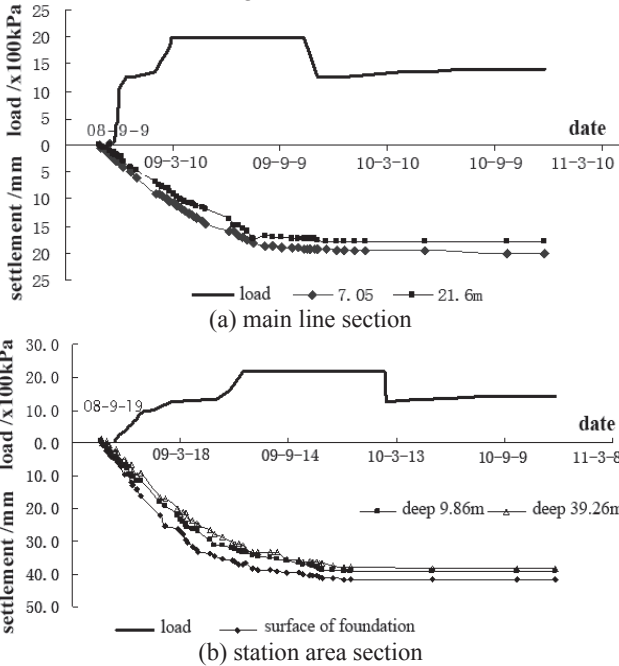


FIG. 5. Foundation layered settlement - time - load curve

As can be seen in table 1, in the reinforced foundation which is not at the same depth level, the settlement difference is not high. In comparison with the total settlement, the settlement in the reinforced foundation is relatively small, only about 11.4% and 8% of total settlement. The settlement of foundation mainly arises at the lower foundation.

Table 1. Layered settlement table

| Result | Unit | Main line section | | Station area section | |
|--|------|-------------------|-------|----------------------|-------|
| The pile embedded depth | (m) | 7.05 | 21.60 | 9.86 | 39.26 |
| The total settlement of subgrade | (mm) | 20.10 | 17.97 | 39.25 | 38.32 |
| Settlement difference for different depths | (mm) | 2.13 | | 0.93 | |
| The total settlement of the ground surface | (mm) | 20.29 | | 41.66 | |
| Settlement at pile area | (mm) | 2.32 | | 3.34 | |
| Settlement rate of the reinforced embankment | (%) | 11.4 | | 8.0 | |

Test and Analysis of Deformation Capacity of the Pile Plate Structure

Soil pressure cells, which are allocated at the top and bottom of the raft foundation, are used to measure the contact stress of the raft and the embankment, and of the raft and the soil foundation. The soil pressure cells allocation map is shown in Fig.6, where

soil pressure cells T1-T3 ~ 17# are embedded on the top of the raft, while T1-1 ~ 3#, T1-5 ~ 7#, T1-10 ~ 12# are embedded on the bottom of the raft.

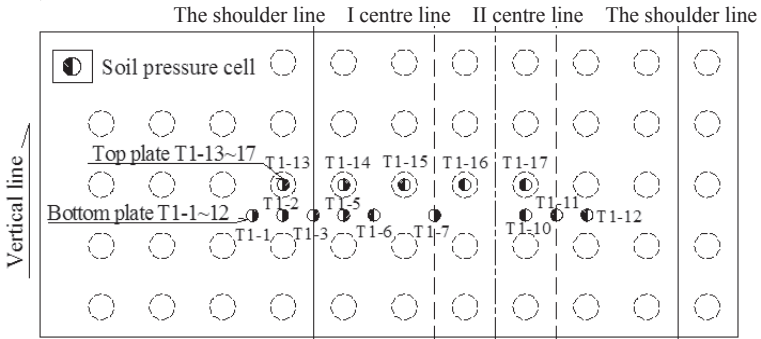


FIG. 6. Soil pressure cells embedded

Contact Stress Analysis of Raft and Foundation Soil

Results from soil pressure cells located on the lower side of the raft, at the centre position of the piles (soil pressure cell T1-7) and between two piles (T1-12), can be shown that: when start filling the embankment, the pressure of the soil under the raft increases as the load increases. After that the load subjected by the piles increases lead to the load subjected by the foundation slowly decreases, therefore the soil pressure also decreases. However, after the preloading progress, at the point of 07/2009 (Fig.7) the soil pressure starts increasing again. This is due to the fact that there is a certain settlement of the structure when the preloading progress lasts for a long time, and it also makes the soil foundation compacted, therefore the foundation begins to bear more load, that makes the soil pressure increases again. After unloading, as the loading pressure decreases, the soil pressure also decreases and tends to be stable.

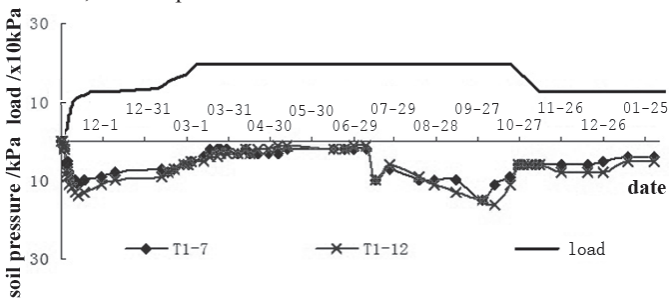


FIG. 7. The raft and foundation soil contact stress - time - load curve

As can be seen in Fig.7, at the same time of preloading, the soil pressure value at T1-12 is a little higher than at T1-7, indicating that the foundation between the two piles bearing more load than that in the center of the piles. This is due to the distance from the point in the middle of two piles is smaller than that from the center of pile to pile. On the other hand, due to the influence of “reinforcement and blind” (Shi

Ming-lei et al., 2003) effect of the pile on the foundation between two piles is larger than that in the center of piles. This shielding effect of the pile makes the shear module of the foundation in the middle of two piles increases more than the foundation in the center of piles.

During the preloading time, the maximum soil pressure value at T1-12 is 16kPa, after unloading, the maximum soil pressure value is 6kPa (Fig.7). These pressure are very small (not greater than 10% of the load on the raft) when comparing with the load of embankment filling 6.3m height + 3.6m load increasing (198kPa in total). It means that the foundation under the raft bears a relative small load. Hence it is reasonable to omit the support of the foundation to the piled-raft foundation when designing and calculating, and just consider it to be a safe value.

3.2.2 The raft's vertical and horizontal reinforcement stress translation bending moment analysis

The three-dimensional framework method is used to calculate the theoretical moment of the foundation after preloading process, taking the top point of the pile, the vertical latest stress value of the steel bar in the raft foundation to converse the moment section, simultaneously, converse the measured stress to moment. Then from rectangular section double girder, the tension stress in steel bar can be calculated as

$$\sigma_s = \frac{M}{A_s z} \leq [\sigma_s], \text{ thus obtained } M = A_s z \sigma_s, \text{ where } z \text{ is the internal force coupling arm,}$$

$z = h_0 - x + y$, where y is the distance from the force of compression zone C to the neutral axis.

After 186 days of completing preload filling, the measured stress values in steel bar were converted to moment and compared with the theoretical moment (Fig.8).

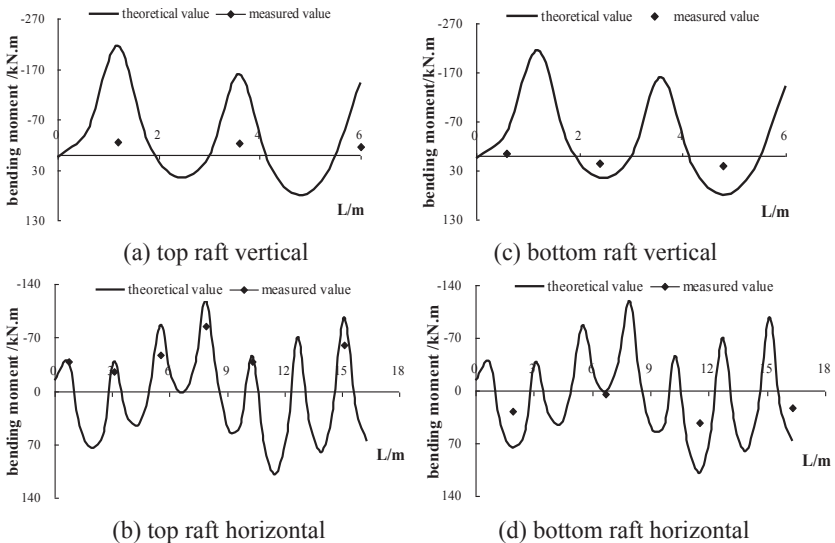


FIG. 8. Comparison between horizontal, vertical, top, bottom raft converted moment and theoretical calculating moment

As can be seen in Fig.8a, the measured values are relatively smaller than calculating values. This is mainly due to the fact that the calculation from the road embankment filling to preloading progress is performed directly on the raft without considering the extended effect of the load to the road embankment filling height. Therefore, the theoretical calculating value is much greater than the practical one. On the other hand, the moment conversion value in fact is the conversion value within the width of 2.4m, so the horizontal dimension of the plate is greater than the vertical one, the stress within the horizontal width of 2.4m is distributed very unevenly. It can be seen that, it is not accurate enough for the stress of the whole pillar zone to be converted to the stress on the width of 2.4m, so that the moment that is converted from the measured stress cannot present correctly the one on the width of 2.4m, so there is a big difference between measured value and calculating value.

The moment converted from the horizontal steel bar stress is relative close to the theoretical calculating moment (Fig.8b), the average measured value is 31.9% smaller than the calculating value. Comparing to the vertical, the horizontal converted measured values is close to calculating values. This is due to the fact that the horizontal dimension is larger than the vertical dimension, thus the horizontal moment value difference is smaller than the vertical one when converting to the width of 2.4m.

At the bottom of the raft in vertical direction, the measured stress values are converted to moments and calculating values are shown in Fig.8c. The average measured value is 87.6% smaller than the calculating value, this difference in comparison to that of vertical upper of the raft due to the same reason.

Similarly, At the bottom of the raft in horizontal direction, the measured stress values are converted to moments and calculating values are shown in Fig.8d, the average measured value is 57.4% smaller than the calculating value. In comparison to the vertical, the relative converted measured value is close to the calculating value on the horizontal, showing that the steel bar layout in horizontal direction is more reasonable than the vertical one.

CONCLUSION

For the section of the main line, with the subgrade surface width of 14.2m, backfill height of 6.8m, and preloading height of 3.1m, the final maximum settlement measure is 23.4mm, the effect of controlling the settlement of piled-raft structure is very good; in the reinforcement area, the settlement of the foundation soil is 3.4mm, which is correlated to 14.5% of total settlement. The settlement of the foundation arises mostly at the lower layer. On the section at the station, due to the loading area is relative large, the additional stress slowly decreases, the height of backfill is not large, but the total settlement of the foundation increases rapidly. The final maximum settlement is estimated of 51.40mm after completing track laying. The settlement has similar features to the main line, the foundation settlement mainly occurs on the underlying layer, in the reinforcement area settlement is 7.01mm, equivalent to 13.6% of the total settlement. It is indicated that although the foundation soil subjected partly additional pressure but it is very small, most of the load subjected by the piled-raft structure.

By field test and long-term test study, distribution of principal stress, contact stress components in piled-raft structure and the deformation characteristics of subgrade

foundation are obtained. At the same time, the field test results and the theoretical calculation results were analyzed and compared. The both of results are basically consistent and can be used to verify the reasonableness and reliability of the theoretical calculation method. Field measured data illustrated that soil foundation under the raft also carried a certain pressure but the pressure value is relatively small. Hence it is reasonable to neglect the bearing capacity of the soil beneath the raft when designing and calculating, and just consider it to be a safe value.

ACKNOWLEDGEMENT

This work was financially supported by the Fundamental Research Funds for the Central Universities (A0920502051206-3), Program for New Century Excellent Talents in University (NCET-12-0941).

REFERENCES

- Ta, L.D. & Small, J.C. (1997). "An Approximation for Analysis of Raft and Piled Raft Foundations." *J. Computers and Geotechnics*, Vol 20(2): 105-123.
- Horikoshi, K. & Randolph, M.F. (1998) "A Contribution to Optimal Design of Piled Rafts." *J. Geotechnique*, Vol 48(3): 301-317.
- Prakoso, W.A. & Kulhawy, F.H. (2002). "Retaining Structure Effect on Piled Raft Foundation Performance." *P. Deep Foundation 2002 - An International Perspective on Theory, Design, Construction and Performance*, 236-244.
- Ziaie-Moayed, R., Kamalzare, M. & Safavian, M. (2010). "Evaluation of Piled Raft Foundations Behavior with Different Dimensions of Piles." *J. Journal of Applied Scientific*, Vol 10(13): 1320-1325.
- Poulos, H.G. (2001). "Piled Raft Foundations: Design and Applications." *J. Geotechnique*, Vol 51(2): 95-113.
- Clancy, P. & Randolph, M.F. (1993). "An Approximate Analysis Procedure for Piled Raft Foundations." *J. International Journal for Numerical and Analytical Methods in Geomechanics*, Vol 17: 849-869.
- Nguyen, D.D.C., Seong-Bae Jo, Dong-Soo Kim. (2013). "Design Method of Piled-raft Foundations under Vertical Load Considering Interaction Effects." *J. Computers and Geotechnics*, Vol 47: 16-27.
- Li Jun-cai, Ji Guang-qiang, Song Gui-hua, Zhang Qiong, Wang Zhi-liang, Yan Xiao-min. (2009). "In-situ Measurement and Analysis of Sparse Pile-raft Foundation of High-rise Building." *J. Rock and Soil Mechanics*, Vol 30(4): 1018-1022.
- Chen Shang-yong. (2010). "Treatment of Thick Soil Foundation with Pile Pipe Raft Base for High-speed Railway." *J. High speed railway technology*, Vol 1(3): 35-38.
- Shi Ming-lei, Deng Xue-jun, Liu Song-yu. (2003). "Study of Restrain Effect Among Piles." *J. Journal of Southeast University (Nature Science Edition)*, Vol 33(3): 343-346.

Experimental Study on Strength Characteristics of Unsaturated Remolded Loess

Sun Hui¹, Hu Bo²

¹ Senior Engineer, Yangtze River Scientific Research Institute, Jiangda Road, Wuhan, Hubei, China, +86-27-82827538; sunhui_hust@126.com

² Senior Engineer, Yangtze River Scientific Research Institute, Jiangda Road, Wuhan, Hubei, China, +86-27-82827141; woshihubo135@sina.com

ABSTRACT: In order to study the unsaturated remolded strength characteristics of loess, loess in a region of Gansu is selected for remolded samples, by using direct shear apparatus for unsaturated soils made by GDS of the UK, 12 unsaturated direct shear testing are made. The test results show that: the stress-strain curve of the rebuilding unsaturated loess is strain hardening or weak strain softening, in addition, comparison of different matric suction under the conditions of the stress strain curve shows that, along with the increase of matrix suction, unsaturated loess shear stress increases; in the same matric suction, shear stress increases gradually with increase of vertical load; and in the analysis of the curve of cohesion C and matrix suction of unsaturated loess, the cohesion and matric suction of C was in low suction range linear growth relationship, so that the double variable strength formula is suitable for the loess in that region, and the friction angle related to the matric suction is $\varphi_b = 2.23^\circ$.

INTRODUCTION

In the unsaturated soil, the gas phase shrink effect causes the pore air pressure and the negative pore water pressure at the same time, the difference of pore air and water pressure ($u_a - u_w$), is called the "matric suction". Because of the influence of suction, the unsaturated soil and saturated soil characters have huge difference. The effective stress of soil is not equal to the intergranular pressure, and the strength formula of saturated soil can not be simply extended to unsaturated soils. Therefore, the shear strength of unsaturated loess are wildly discussed. Li Jia-gui (2010) studies the structural impact on unsaturated undisturbed loess Q3 deformation and strength characteristics. Through 12 of unsaturated undisturbed loess Q3 CT-three axis lateral unloading test, microscopic structure parameters are established, and by using it as parameters, it can reflect the characteristics of deformation and strength of unsaturated intact Q3 loess. Dang Jing-qian (2001) analyzes the source of form and structural

strength of unsaturated Loess. And determining methods of the structural strength is given. The variation of structure strength is researched. Xie Ding-yi (1999) analyzes the structure of soil, then gets a soil structural quantitative parameters which can comprehensively reflect the characteristics of soil particle arrangement (geometry) and the coupling characteristics of soil particles (mechanical properties). The relationship between the deformation and strength of soil is analyzed and discussed. Chen Zheng-han(1999) uses the stress paths of three triaxial test to systematically discusses the deformation characteristics, unsaturated soil strength characteristics, yield and water content change characteristics.

As a typical unsaturated soil, it is necessary to study the shear strength characteristics of Loess. So far, Fredlund (1993) establishes the shear strength theory of unsaturated soil based on the two stress state which is more mature and widely used. Its expression is:

$$\tau = c' + (\sigma - u_a)\tan\phi' + (u_a - u_w)\tan\phi^b \quad (1)$$

Where

c' is effective cohesion (kPa); ϕ' is the effective internal friction angle; σ is the total normal stress (kPa); u_a is the pore air pressure (kPa); u_w is the pore water pressure (kPa); ϕ_b is the friction angle which is associated with the matric suction. Among them, ϕ_b is used to reflect the suction contribution to strength parameters. the strength caused by Net normal stress is related with the effective internal friction angle; Matric suction caused by the strength is associated with another angle. Many researchers' test results show that: ϕ_b is a linear increase in low matric suction range (LEE S Barbour. 1998). Based on above theory ,by controlling matric suction condition, the strength characteristics of unsaturated remolded loess is researched by the direct shear test in some area of Gansu province.

TEST SAMPLES AND METHOD

The loess test samples are from Gansu. The sample is the Yellow silty soil. Use striking method to complete loess remodeling sample preparation. Preparation sample's moisture content is 20.25%, dry density is 1.28g/m³. Ring knife in this experiment is 75mm long, 75mm wide, 30mm high. three layer compaction. It is divided into three layers of compacted specimen molding.

The direct shear apparatus produced by British GDS Company is used for unsaturated soils. The device is set under the control of the advanced unsaturated direct shear computer test system(AUDS). The range and accuracy of the main instruments in the system are shown in table 1.

The direct shear tests include constant suction, constant suction consolidation and constant suction shear three stages.Suction equilibrium stage: after the sample installation, change the sample suction state by controlling the pore air pressure and water pressure, and the suction distributes is uniformly in the whole sample, this is the force equilibrium stage. The Force balance criterion is that sample drainage or water amount less than the volume of sample 0.02% in 24h.Constant suction consolidation stage: when the suction reaches to balance, keep the constant suction. The sample is

under constant suction condition consolidation. The consolidation of direct shear test's criterion is that measured drainage or absorption water amount is less than the sample volume's 0.02% in 24h, and vertical deformation readings per hour does not exceed 0.005mm. Constant suction shear stage: operate shear test under the constant suction; the shear rate is 0.002mm/min, and the maximum shear displacement is 8mm.

Table 1 Range and Accuracy of the Instrument

| Name | range | accuracy |
|---|------------|------------------------|
| GDS back pressure / volume controller | 200cc/3MPa | 1mm ³ /1kPa |
| The horizontal load / displacement controller | 5kN/25mm | 5N/0.001mm |
| The single channel pressure controller | 1000kPa | 1kPa |
| Vertical displacement sensor (LVDT) | 15mm | 0.001mm |
| Pore air (water) pressure sensor | 2MPa | 1kPa |

RESULTS ANALYSIS OF UNSATURATED DIRECT SHEAR TEST

Relation Curves between Shear Displacement and Shear Stress

Under different vertical loads in the matric suction of 50kPa, 100kPa, 150kPa and 200kPa, the stress-strain curve of remolded loess samples ($\rho_d=1.28\text{g/cm}^3$) is shown in figure 1. As can be seen from the graph, in addition to the two unsaturated loess remodeling sample having a peak intensity has obvious strain softening behavior, then the peak intensity of other specimens are not obvious which indicates that the stress-strain relationship curve is hardening strain. It is caused by the remodeling resulting in structural destruction of the soil. Gansu unsaturated loess stress-strain relationship shows more strain hardening. Different suction conditions under the stress-strain curve can be seen the unsaturated loess shear stress increases with the increase of the suction; in the same matric suction, shear stress as the vertical load increases gradually increases.

Unsaturated Remolded Loess's Shear Strength

Figure 2 shows the different vertical loads of the same suction of unsaturated expansive soil shear strength curve. As can be seen from the graph, when the suction is 50kPa, the c is 19.03kPa and ϕ' is 12.52°; when the suction is 100kPa, the c is 25.88kPa and ϕ' is 13.06°; when the suction is 150kPa, the c is 27.61kPa and ϕ' is 11.42°; when the suction is 200kPa, the c is 28.38kPa and ϕ' is 11.48°. The c contains suction on shear strength contribution of the cohesion. Figure 3 shows the different matric suction stick cohesion ($c'+\tau_s$) and matric suction curve, which τ_s is $(\mu_a - \mu_w)\tan\phi_b$. The slope of the curve is the friction angle with suction. Unsaturated direct shear test results show that the unsaturated loess cohesion c in low suction with the suction is linear growth relationship. It can be considered accordingly the bivariate strength formula for remolded loess, and the friction angle with suction ϕ_b is 2.23°.

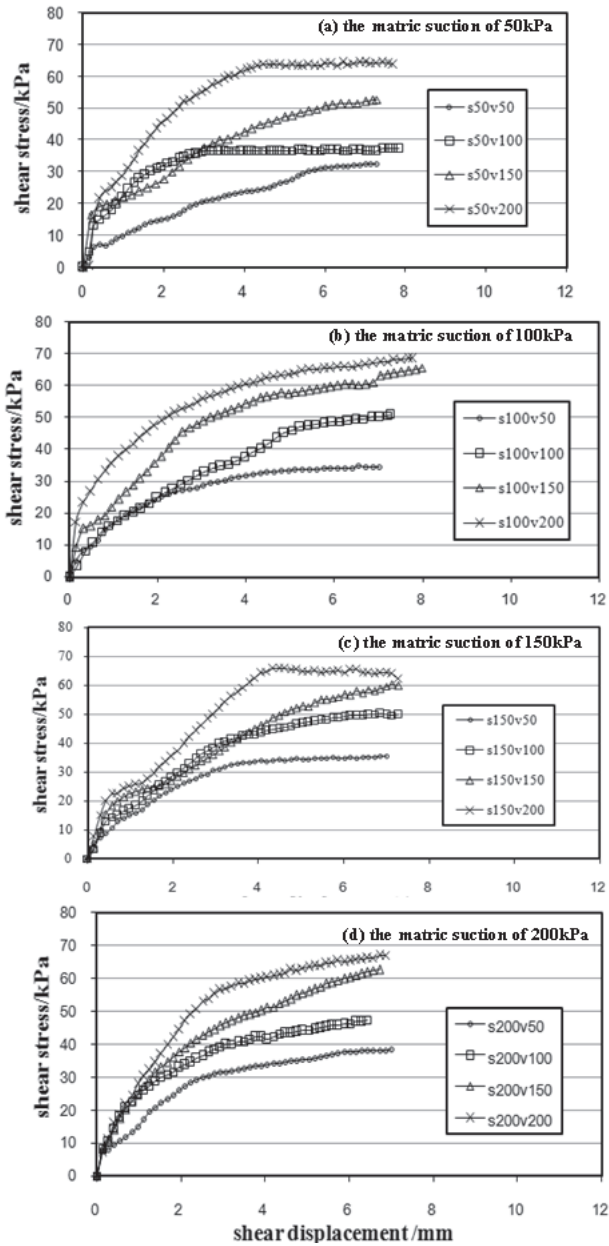


FIG. 1 the stress-strain curve of loess ($\rho_d=1.28g/cm^3$) under different vertical loads remodeling loess unsaturated shear strength curve

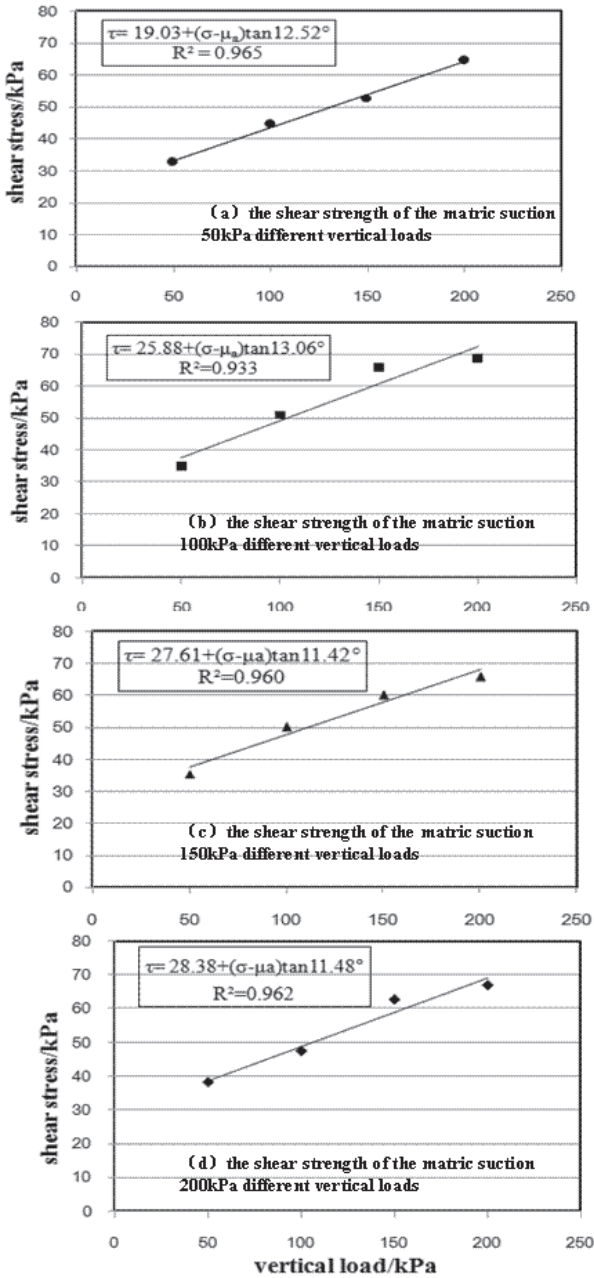


FIG. 2 the shear strength of loess under different matric suction and vertical loads conditions

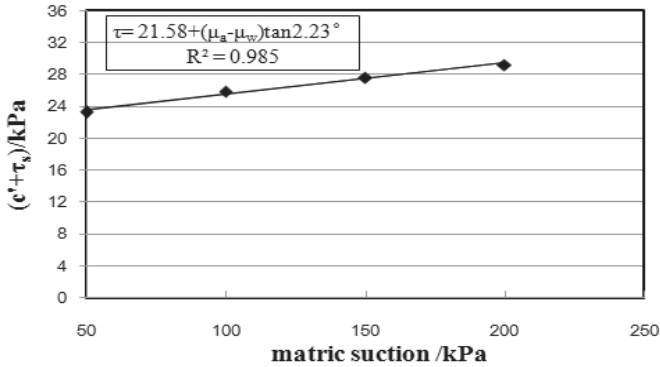


FIG. 3 Loess stick cohesion($c'+\tau_s$)and matric suction relationship curve

CONCLUSIONS

The following conclusions can be received through this research:

(1) Due to structural damage, the stress-strain relationship of the remolded loess samples exhibits the strain hardening characteristics under different matric suctions and vertical loads. Comparing the stress-strain relationship curves under different suctions, the shear strength increases with the increase of suction; the shear strength increases with the increase of vertical load when subjected to the same matric suction.

(2) Suction to the shear strength of soil is improved, the increment for the $\tan \varphi_b$. The unsaturated direct shear test results show that within low suctions, the shear strength for the reconstituted unsaturated loess generally varies linearly with the suctions. The unsaturated shear strength parameters φ_b is 2.23° .

ACKNOWLEDGMENTS

This research is financially supported by the National Natural Science Foundation of China (51108042, 51008035)

REFERENCES

- LI Jia-gui, CHEN Zheng-han, HUANG Xue-feng. "Stress-strain Relationship and Strength Formula of Unsaturated Original Q3 Loess with Meso-structural Parameter". *Journal of Logistical Engineering University*, 2010, 26(2):5—10
- Dang Jin-qian, LI Jing. "The structural strength and shear strength of unsaturated loess". *Journal of Hydraulic Engineering*, 2001, (7): 79—83
- XIE Ding-yi, QI Ji-lin, ZHU Yuan-lin. "Structure parameter and its relations to deformation and strength". *Journal of Hydraulic Engineering*, 1999, (10):1—6
- Chen Zheng-han. "Deformation, strength, yield and moisture of a remolded unsaturated loess". *Journal of Hydraulic Engineering*, 1999, 21(1): 82—90
- Fredlund, D.G. and Rahardjo, H., "Soil Mechanics for Unsaturated Soil". 1993: Wiley.
- LEE S Barbour. "Nineteenth Canadian Geotechnical Colloquium: the soil-water characteristic curve: a historical perspective". *Can J Geotech J*, 1998, 35: 873—894

Computer Simulations on the Effects of Desaturation on Soil Liquefaction Resistance

Quan Gao¹, Zhen Liu², and Xiong (Bill) Yu^{3*}

¹Graduate Assistant, Department of Civil Engineering, Case Western Reserve University, Cleveland, OH, USA, qxg29@case.edu

²Postdoctoral Associate, Department of Civil Engineering, Case Western Reserve University, Cleveland, OH, USA, zxl73@case.edu

^{3*}Associate Professor, Department of Civil Engineering, Case Western Reserve University, Cleveland, OH, USA, xyy1@case.edu, corresponding author

ABSTRACT: Ground liquefaction remains as one of the major causes of infrastructure damages during earthquakes. The concept of artificially creating “desaturation or partial saturation” in liquefiable soils has been introduced to improve soil liquefaction resistance. This paper describes the theory and computational implementation to simulate the effects of desaturation on soil liquefaction resistance. The theoretical basis of the computational model is developed based on Biot’s consolidation theory. Computational simulations were conducted to simulate the behaviors of soils under cyclic loading. From these, the trends of pore water pressure evolution and liquefaction resistance of soils under different initial degree of saturation were predicted. Simulation results show that as degree of saturation decreases from 100% to 86%, the number of loading cycles to initialize liquefaction increases from 86 cycles to 237 cycles or increases by 175%. This indicates that desaturation or artificial induction of partial saturation in soils is an effective approach for soil liquefaction mitigation. This can be accomplished by, for example, introducing air bubbles into the pore spaces of soils. While promising, the procedures to introduce air bubbles into soils need to be further developed in light of practice requirements.

INTRODUCTION

Soil liquefaction, which refers to the transition of soil into fluidic status during pore pressure development under ground shaking, can cause catastrophic damages to the structures overlying the liquefiable deposits. Liquefaction has been widely observed in major earthquakes such as the 1964 Niigata earthquake, the 1964 Alaska earthquake, the 1989 Loma-Prieta earthquake, and the 2008 Wenchuan earthquake,

etc. Different technologies have been developed to increase soil liquefaction resistance, e.g., densification, chemical grouting, soil mixings, etc. An emerging concept for improving the liquefaction resistance is “desaturation” of soils, i.e., to make the original saturated soil to be partially saturated. This can be accomplished, for example, by introducing gas bubbles into saturated soils either dissolving or suspending in the pore water. Gas bubbles can also be introduced into soil system via different physical, chemical and microbiology methods (He et al. ; He et al. 2013; Okamura et al. 2006; Okamura et al. 2011; Yegian et al. 2007; Yegian et al. 2006). Most of these previous studies focused on measuring the magnitude and trends of pore water pressure development in ‘desaturated’ soils subjected to cyclic loading. Laboratory tests were the primary method in the previous investigations. The conclusions were therefore of empiristic nature from the experimental phenomena. In our view, knowledge on the effects of desaturation on soil liquefaction resistance needs to be advanced by understanding the fundamental mechanisms.

In this paper, we developed a computational simulation model to describe the liquefaction performance of sand of different degrees of saturations under cyclic loading. The model was implemented in a FEM simulation platform. The model is based on extension of the Biot consolidation theory to soils with different degrees of saturation. It considers the compressibility of air/water mixture commonly used in unsaturated soil mechanics and the effects of saturation on liquefaction resistance, as illustrated in Fig. 1. Put in a simple statement: with the degree of saturation decreases via introduction of air bubble, the compressibility of pore fluid increases, consequently the rate of excessive pore pressure development will be reduced. These ultimately lead to the increases in the liquefaction resistance.



FIG. 1. Relationship among saturation, compressibility and liquefaction resistance

THEORETICAL BACKGROUND

Compressibility of Pore Water

Fredlund (1976) and subsequent studies proposed that the water, free air and air dissolved in water can be described as a fluid of air/water mixture in unsaturated soils (Fredlund 1976; Fredlund and Rahardjo 1993). The properties of the equivalent pore fluid, such as its compressibility, are dependent on the compressibility of the three components and their proportions, which is mathematically described as Equation (1) (Fredlund 1976; Fredlund and Rahardjo 1993).

$$C_{aw} = SC_w B_w + (1 - S + hS) C_a B_a \quad (1)$$

where C_{aw} is the compressibility of air-water mixture; S is the degree of saturation; C_w is the compressibility of water, $C_w = 4.58 \times 10^{-7}$ (1/kPa); C_a is the isothermal compressibility of air $C_a = 4.94 \times 10^{-3}$ (1/kPa); h is the coefficient of air dissolved by water, which is the percentage of dissolved air with respect to the volume of water;

B_w, B_a are the pore-water and pore-air pressure coefficient for isotropic loading, both of which are usually assumed to 1.0;

As the degree of saturation, S , varies, the compressibility of pore fluid varies. Figure 2 shows the variation of compressibility of pore fluid when the air pressure is set as 202.6 kPa (i.e. 2 atm). In general, the compressibility of the pore fluid increases significantly with decreasing of the degree of saturation. It is noted that there is a rapid change in the compressibility of pore fluid in the range of degree of saturation between points A and B. At point A, the soil is completely saturated with no dissolved air, the compressibility of pore fluid is equal to that of pure water (i.e. $C_{aw}=C_w=4.58e-7(1/kPa)$). Whereas at point B, the inclusion of small amount of dissolved air (even less than 1%) causes a significant increase in the pore fluid compressibility to the tune of almost three orders of magnitude.

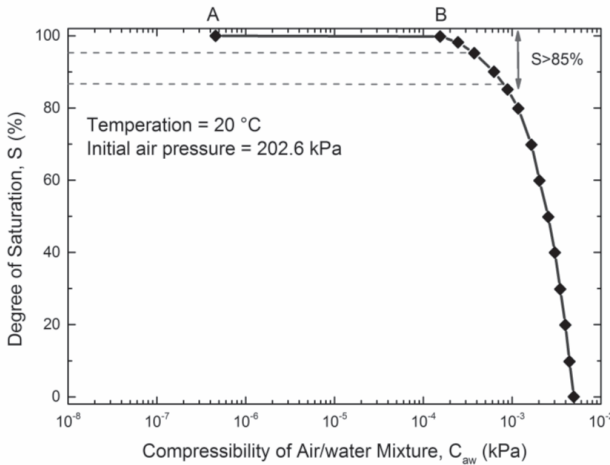


FIG. 2. Compressibility of air/water mixture

Under the laboratory conditions, however, it is extremely difficult if not impossible to prepare fully saturated soil specimens due to unavoidable dissolution of air into water. So researchers have treated quasi-saturated soil ($85\% \leq S \leq 95\%$) as fully saturated soil (Faybishenko 1995; Sakaguchi et al. 2005). Based on equation (1), the compressibility of pore water in the quasi-saturated soil is approximately in the range of $3.5e-4$ to $8.7e-4$ (1/kPa). Table 1 lists the compressibility of pore fluid in the range of saturation between $85\% \leq S \leq 100\%$. The study of this paper focuses on soils in this range, or quasi-saturated soils achievable in the laboratory conditions.

Table 1. Compressibility of porous fluid in quasi-saturated soil

| Saturation, S (%) | Compressibility of air/water mixture, C_{aw} ($\times 10^{-4}$ /kPa) | Saturation, S (%) | Compressibility of air/water mixture, C_{aw} ($\times 10^{-4}$ /kPa) |
|-------------------|---|-------------------|---|
| 0.85 | 8.75 | 0.93 | 5.16 |
| 0.86 | 8.49 | 0.94 | 4.68 |
| 0.87 | 8.01 | 0.95 | 4.20 |
| 0.88 | 7.54 | 0.96 | 3.73 |
| 0.89 | 7.06 | 0.97 | 3.25 |
| 0.90 | 6.58 | 0.98 | 2.78 |
| 0.91 | 6.11 | 0.99 | 2.30 |
| 0.92 | 5.63 | 1.00 (B) | 1.83 |
| | | 1 (A) | 0.00458 |

THEORETICAL BASIS OF THE COMPUTATIONAL MODEL

Biot Consolidation Theory

Soil liquefaction is associated with the interactions between the solid materials and fluids in the pore space. Biot developed a general dynamic theory for saturated porous materials (Biot 1941; Biot 1957; Biot 1962). The simplified formulations of the Biot's theory is adopted in the numerical simulations in this study (Parral-Colmenares 1996; Yang and Elgamal 2000), in which displacement of solid phase, u , and pore fluid pressure, p , are the primary parameters. The primary governing equations of u-p simplification of Biot theory are described as following:

Equation of motion for fluid-solid mixture

$$\sigma_{,j} - \rho_f \left(\ddot{u}_i - b_i \right) = 0 \quad (2)$$

The strain-displacement equation, are respectively:

$$\varepsilon_{ij} = \frac{1}{2} (u_{i,j} + u_{j,i}) \quad (3)$$

The constitutive equation:

$$\sigma_{ij} = D_{ijkl} \varepsilon_{kl} \quad (4)$$

The effective stress principles:

$$\sigma'_{ij} = \sigma_{ij} - \alpha \delta_{ij} p \quad (5)$$

Mass conservation of the fluid-solid mixture

$$\frac{\dot{p}}{Q} + \varepsilon_{ii} - \left(k_{ji} \left(p_{,i} + \rho_f \dot{u}_i - \rho_f b_i \right) \right) = 0 \quad (6)$$

where u_i - displacement of the solid phase; w_i - displacement of the fluid relative to the

solid phase; p - pore fluid pressure; ρ_f - mass density of fluid; b_i - body force per unit volume; Q - bulk modulus of the solid and fluid mixture; σ_{ij} - Cauchy stress tensor (σ , σ' represent total and effective stress, respectively); ε_{ij} - infinitesimal strain tensor; D_{ijkl} - fourth-order tensor of the material stiffness; k_{ij} - permeability tensor; δ_{ij} - Kronecker's constant; α - Biot coefficient, which is usually set as 1.0.

Shear Modulus Reduction

Numerous models have been developed to describe the shear modulus reduction of soils subjected to cyclic loading (Alarcon-Guzman et al. 1988; Elgamal et al. 2005; Hardin and Drnevich 1972; Hardin and Drnevich 1972; Seed and Lee 1966; Tokimatsu and Seed 1987; Vucetic and Dobry 1991; Zhang et al. 2005; Zhou and Chen 2005). Most of them correlate the normalized shear modulus (G/G_m) to the shear strain in small strain range ($10^{-6} \sim 10^{-1}$) (Hardin and Drnevich 1972; Ishibashi and Zhang 1993). It has been observed that liquefaction occurs at much larger strain levels (Vucetic 1994). Therefore, to capture the relationship between normalized shear modulus and number of loading cycles in a wider range of shear strain, we compiled experimental data of around 20 dynamic triaxial tests on Nevada sand (Shen et al. 1994) to develop the relationship of modulus reduction with loading circles. The data and curve fitting are shown in Figure 3. The relationship between normalized shear modulus and number of cycles is shown in Eq.7. From the Figure 3, the shear modulus reduction behavior is clearly observed, which is similar to that in previous publications (Hardin and Drnevich 1972; Ishibashi and Zhang 1993; Zhang et al. 2005).

$$G = G_m (1 + N)^{-1.60845} \tag{7}$$

where G and G_m are the secant shear modulus and maximum shear modulus of soil subjected dynamic loading. N is the number of loading cycles.

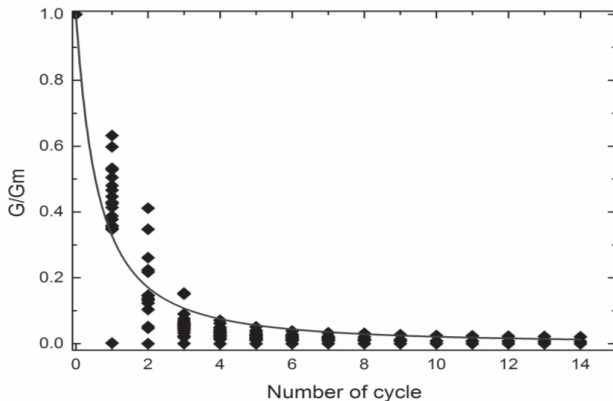


FIG. 3. Relation between normalized shear modulus and number of cycle

Initial Shear Modulus, G_m

In the process of simulation, the value of maximum shear modulus in Eq.7 is computed with the Eq.8 (Hardin and Black 1969; Hardin and Black 1968; Hardin and

Drnevich 1972), in which e represents void ratio; σ_0' denotes the initial mean effective stress; and both σ_0' and G_m are in pounds per square inch.

$$G_m = 1230 \frac{(2.973 - e)^2}{1 + e} \sigma_0'^{0.5} \quad (8)$$

COMPUTATIONAL MODEL IMPLEMENTATION

The governing equations of the computational model discussed in the previous sections are highly nonlinear. Therefore, the equations have to be solved numerically. A general finite element platform was employed to implement the computational simulations. Simulation was designed to simulate the behaviors of Nevada sand under dynamic triaxial tests. An axial symmetric specimen was constructed for this purpose (Fig. 4). An isotropic confining pressure is applied to the boundary of the specimens. A sinusoidal loading, $F = 25 / (0.25 * \pi * D^2) * \sin(0.2 * \pi * t)$, is also applied in the axial direction of specimens. Details of the specimen and primary model parameters are listed in Table 2. The dynamic responses of the soil specimen are analyzed from the experimental outputs.

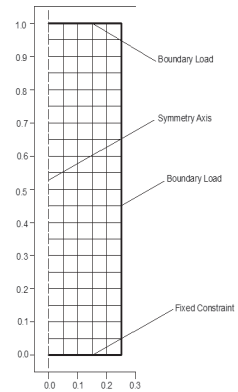


FIG. 4. FEM meshing sketch for computation domain

Table 2. Model input parameters used in simulation

| Constant | Value | Units | Description |
|----------|-------|--------------------|--|
| D | 0.05 | m | Diameter of specimen |
| H | 0.1 | m | Height of specimen |
| k_s | 3e-04 | m/s | Hydraulic conductivity of porous media |
| ρ_w | 1000 | kg/cm ³ | Density of water |
| ρ_s | 2670 | kg/cm ³ | Density of solid skeleton |
| Pc | 25 | kPa | Confining pressure |
| n | 0.4 | N/A | Porosity |
| α | 1 | N/A | Biot coefficient |
| μ | 1e-03 | Pa.s | Dynamic viscosity of water |
| nu | 0.5 | N/A | Possion's ratio of solid skeleton |

SIMULATION RESULTS AND ANALYSIS

Effects of Degree of Saturation on Liquefaction Initialization

(Castro & Seed et. al) categorized liquefaction as partial liquefaction (initial liquefaction) and completely liquefaction. "Initial liquefaction" describes the first point after which the value of pore water pressure at zero deviator stress is

momentarily equal to the confining pressure (Castro 1975; Seed and Lee 1966). In this paper, we only consider the soil responses up to the status of initial liquefaction. We did not consider in this paper soil behavior after initial liquefaction and the subsequent variation of pore water pressure, in which pore water pressure dissipation model is mandatory. The time or number of loading cycles to the initial liquefaction for soils with different degree of saturation is considered in the simulation results. Figure 5 shows a typical simulation result of pore water pressure built-up for a saturated soil specimen subjected cyclic loading. It can be easily observed that the pore water pressure gradually increases with loading cycles. Point A in figure 5, where the ratio of P_f/P_c is equal to 1, describes the initial liquefaction state.

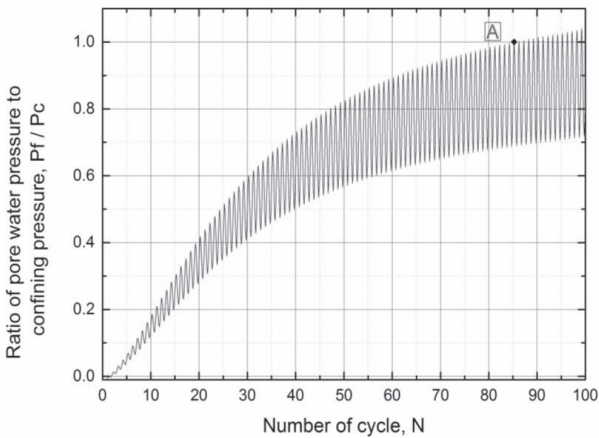


FIG. 5. A typical pore water pressure built-up during cyclic loading

Computational simulations were conducted on the dynamic responses of soils under different degrees of saturation. 17 different cases as shown in Table 1 were studied. For each degree of saturation, pore water pressure development curves were obtained. Examples are plotted in figure 6 (a). Comparison of the pore water pressure development trend for three distinct degrees of saturation shows that the lower the degree of saturation, the longer it takes for the samples to liquefy. For low degree of saturation, such as 88%, the specimen did not liquefy even after 200 cycles of loading. Figure 6 (b) plots the degree of saturation and the corresponding number of loading cycles for initial liquefaction. Two different phases can be identified. In phase II (between B and C), where the degree of saturation decreases from 100% to 86%, the number of cycles needed for liquefaction increases from 86 to 237, or 175% increases. A linear relationship appears between the degree of saturation and number of loading cycles. In Phase I (between A and B), the liquefaction resistance decreased slightly with decreasing degree of saturation. This may be explained by the fact that at degree of saturation of 85%, the soil can't be treated as saturated specimens. The soil behaviors might deviate from Darcy's law or Biot theory described in the previous section. Further study the dynamic behaviors of soil in such degree of saturations requires to study the matric suction between soil particles and how this will influence

soil behaviors, which is described in the unsaturated soil mechanics (Fredlund and Rahardjo 1993).

Effects of Air Dissolution on Soil Liquefaction Resistance

The influence of the degree of saturation on liquefaction initialization or pore water pressure development under cyclic loading is partially contributed to the compressibility of porous fluid described in the previous section. Skempton (1954) proposed the famous pore water pressure coefficient as shown in Eq.9.

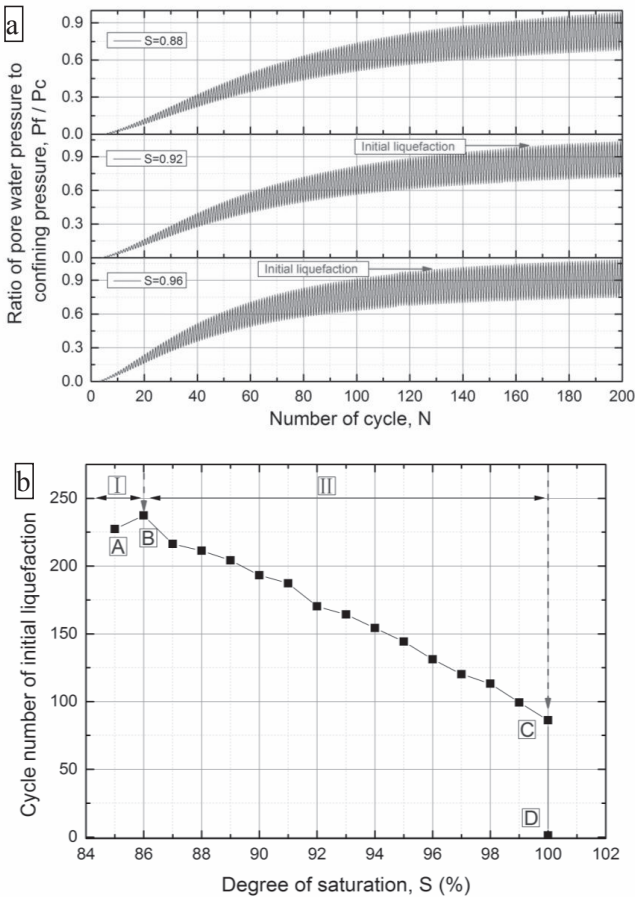


FIG. 6. Influence of saturation on liquefaction

$$B = \frac{\Delta u}{\Delta \sigma_3} = \frac{1}{1 + n \frac{C_{aw}}{C_s}} \quad (9)$$

where B - pore water pressure coefficient, also called Skempton's coefficient; Δu -

variation of pore water pressure; $\Delta\sigma_3$ - variation of confining pressure; n - porosity; C_s - compressibility of solid particles; C_{aw} - compressibility of porous fluid, which is also the compressibility of air/water mixture described in Eq.1.

Equations (1) and (9) together help to illustrate the relationship among the degree of saturation, compressibility of pore fluid, pore water pressure increment and number of cycles for initial liquefaction. Eq.1 indicates that an increment of degree of saturation, S , will result in the reduction of the compressibility of pore fluid, C_{aw} , which, as described in Eq.9, could subsequently give rise to the increases of the coefficient B or build-up of pore water pressure. It means that initial liquefaction is faster when the soil is close to completely saturated condition, which is consistent with what is shown in Figure 6 (a) (b). Practically, this means that methods to reduce the degree of saturation, such as by introduction of air bubbles into pore fluid, will help to improve the soil liquefaction resistance.

CONCLUSIONS

A computational model was developed and implemented in this paper to study the influence of the degree of desaturation on the soil liquefaction resistance. The model is based on the extension of Biot's consolidation theory to desaturated pore fluid conditions. Computational simulations were conducted to predict the dynamic behaviors of sand with different degrees of saturations under dynamic triaxial tests, including the pore water pressure development and liquefaction initialization. It was found that the liquefaction resistance increases with decreasing degree of saturation. Compressibility of air/water mixture was introduced to explain the relationship between the degree of saturation and liquefaction resistance of soils. The practical implication is liquefaction resistance of saturated soils can be significantly improved by dissolving air into pore water. Therefore desaturation of soils, i.e., by introducing gas bubble into soil, is a feasible approach to prevent liquefaction. Effective methods to de-saturate soils need to be further developed considering practice constraints.

ACKNOWLEDGMENTS

We acknowledge the support of the Saada Family fellowship. This study is also partially supported by the U.S. National Science Foundation.

REFERENCES

- Alarcon-Guzman, A., Leonards, G., and Chameau, J. (1988). "Undrained monotonic and cyclic strength of sands." *Journal of geotechnical engineering*, 114(10), 1089-1109.
- Biot, M. A. (1941). "General theory of three - dimensional consolidation." *J Appl Phys*, 12(2), 155-164.
- Biot, M. A. (1957). "The Elastic Coefficients of the Theory of Consolidation." *J Appl Phys*, 594-601.
- Biot, M. A. (1962). "Mechanics of deformation and acoustic propagation in porous media." *J Appl Phys*, 33(4), 1482-1498.
- Castro, G. (1975). "Liquefaction and cyclic mobility of saturated sands." *Journal of the geotechnical engineering division*, 101(6), 551-569.
- Elgamal, A., Yang, Z., Lai, T., Kutter, B. L., and Wilson, D. W. (2005). "Dynamic response of saturated dense sand in laminated centrifuge container." *J Geotech Geoenviron*, 131(5), 598-609.
- Faybishenko, B. A. (1995). "Hydraulic Behavior of Quasi - Saturated Soils in the Presence of Entrapped Air: Laboratory Experiments." *Water Resour Res*, 31(10), 2421-2435.

- Fredlund, D. (1976). "Density and compressibility characteristics of air-water mixtures." *Can Geotech J*, 13(4), 386-396.
- Fredlund, D. G., and Rahardjo, H. (1993). *Soil mechanics for unsaturated soils*, Wiley-interscience.
- Hardin, B., and Black, W. (1969). "Closure on vibration modulus of normally consolidated clay." *Journal of Soil Mechanics & Foundations Div.*
- Hardin, B. O., and Black, W. (1968). "Vibration modulus of normally consolidated clay." *Journal of Soil Mechanics & Foundations Div.*
- Hardin, B. O., and Drnevich, V. P. (1972). "Shear modulus and damping in soils design equations and curves." *Journal of the Soil Mechanics and Foundations Division*, 98(7), 667-692.
- Hardin, B. O., and Drnevich, V. P. (1972). "Shear Modulus and Damping in Soils: Measurement and Parameter Effects (Terzaghi Lecture)." *Journal of the Soil Mechanics and Foundations Division*, 98(6), 603-624.
- He, J., Chu, J., and Ivanov, V. "Remediation of Liquefaction Potential of Sand Using the Biogas Method."
- He, J., Chu, J., and Ivanov, V. (2013). "Mitigation of liquefaction of saturated sand using biogas." *Geotechnique*, 63(4), 267-275.
- Ishibashi, I., and Zhang, X. (1993). "Unified dynamic shear moduli and damping ratios of sand and clay." *Soils Found*, 33(1), 182-191.
- Okamura, M., Ishihara, M., and Tamura, K. (2006). "Degree of saturation and liquefaction resistances of sand improved with sand compaction pile." *J Geotech Geoenviron*, 132(2), 258-264.
- Okamura, M., Takebayashi, M., Nishida, K., Fujii, N., Jinguji, M., Imasato, T., Yasuhara, H., and Nakagawa, E. (2011). "In-situ desaturation test by air injection and its evaluation through field monitoring and multiphase flow simulation." *J Geotech Geoenviron*, 137, 643.
- Parra-Colmenares, E. J. (1996). "Numerical modeling of liquefaction and lateral ground deformation including cyclic mobility and dilation response in soil systems."
- Sakaguchi, A., Nishimura, T., and Kato, M. (2005). "The effect of entrapped air on the quasi-saturated soil hydraulic conductivity and comparison with the unsaturated hydraulic conductivity." *Vadose Zone Journal*, 4(1), 139-144.
- Seed, B., and Lee, K. L. (1966). "Liquefaction of saturated sands during cyclic loading." *Journal of Soil Mechanics & Foundations Div*, 92(ASCE# 4972 Proceeding).
- Shen, C., Kutter, B. L., and Chen, Y.-R. (1994). "Triaxial and Torsional Shear Test Results for Sand." CALIFORNIA UNIV DAVIS DEPT OF CIVIL ENGINEERING.
- Tokimatsu, K., and Seed, H. B. (1987). "Evaluation of settlements in sands due to earthquake shaking." *Journal of geotechnical engineering*, 113(8), 861-878.
- Vucetic, M. (1994). "Cyclic threshold shear strains in soils." *Journal of geotechnical engineering*, 120(12), 2208-2228.
- Vucetic, M., and Dobry, R. (1991). "Effect of soil plasticity on cyclic response." *Journal of geotechnical engineering*, 117(1), 89-107.
- Yang, Z., and Elgamal, A.-W. M. (2000). *Numerical modeling of earthquake site response including dilation and liquefaction*, University of California at San Diego, Dept. of Structural Engineering.
- Yegian, M., Eseller-Bayat, E., Alshawabkeh, A., and Ali, S. (2007). "Induced-partial saturation for liquefaction mitigation: experimental investigation." *J Geotech Geoenviron*, 133(4), 372-380.
- Yegian, M., Eseller, E., and Alshawabkeh, A. (2006). "Preparation and cyclic testing of partially saturated sands." *GEOTECHNICAL SPECIAL PUBLICATION*, 147(1), 508.
- Zhang, J., Andrus, R. D., and Juang, C. H. (2005). "Normalized shear modulus and material damping ratio relationships." *J Geotech Geoenviron*, 131(4), 453-464.
- Zhou, Y.-g., and Chen, Y.-m. (2005). "Influence of seismic cyclic loading history on small strain shear modulus of saturated sands." *Soil Dyn Earthq Eng*, 25(5), 341-353.

Reliability-Based Dam Erodibility Assessment

Chin Man Mok¹, Robert Wright², James Cooley³, Eng Sew Aw⁴, and Robert White⁵

¹Principal Engineer, AMEC Environment and Infrastructure, CA, USA; bill.mok@amec.com

²Associate Engineering Geologist, AMEC E&I, CA, USA; bob.wright@amec.com

³Survey Project Manager, AMEC E&I, TN, USA; james.cooley@amec.com

⁴Project Engineer, AMEC E&I, CA, USA; engsew.aw@amec.com

⁵Senior Civil Engineer, Pacific Gas & Electric Company, San Francisco, CA, USA

ABSTRACT: When dam overtopping occurs, the hydraulic power of the impinging water jet might cause rock foundation erosion/scouring, which potentially could lead to significant consequences. As future flood events are expected to be more severe due to climate change, dam erodibility is becoming a significant risk concern. This paper (1) provides an overview of erodibility analysis, including project examples to illustrate the use Annandale's Erodibility Index method, Bolleart's Comprehensive Scour Model, and Goodman and Shi's rock block theory; (2) describes a reliability-based approach to address the issues of uncertainties, such as first-order reliability method and importance sampling; (3) and discusses the measurement of rock properties for developing probabilistic models, including a field example of using land-based LiDAR to obtain rock joint statistics.

INTRODUCTION

In recently years, a number of dams worldwide have experienced significantly larger flood events than they were designed for, resulting in dam overtopping. Many existing dams were constructed over 50 years ago. Although some dams have been upgraded after they were constructed, the design criteria might still be inadequate as future flood events are expected to be more severe due to global climate change. The hydraulic power of the overtopping jet might cause foundation and downstream erosion, which potentially could lead to significant consequences. This paper focuses on addressing the prominent risk concern associated with erodibility of foundation rock supporting tall concrete dams, particular for sites with unrecognized adverse rock conditions.

Dam erodibility assessment consists of four components: (1) selection of extreme precipitation event to be considered, such as the probable maximum precipitation (PMP), (2) hydrologic rainfall-runoff analysis to estimate the extreme flood event, such as probable maximum flood (PMF), that a dam will experience under the extreme precipitation event, (3) hydraulic analysis to compute the impinging water jet load on

rock foundation under the extreme flood event, and (4) geomechanical analysis to assess the stability/erodibility of the rock foundation subject to the hydraulic load. Hydrologic and geologic systems are dynamic and heterogeneous. However, our knowledge of geologic and hydrologic parameters is often limited, raising the concern of uncertainties in dam erodibility analysis. This paper focuses on geomechanical analysis approach, including the Annandale's Erodibility Index (EI) (Annandale, 1995) and Bolleart's Comprehensive Scour Model (CSM) methods (Bollaert and Annandale, 2004), as well as the Goodman and Shi's rock block theory (Goodman and Shi, 1985). This paper also addresses the uncertainty issues, including the reliability-based analysis approach. In addition, this paper discusses the field methods for obtaining rock joint statistics, including the use of land-based LiDAR.

ERODIBILITY ASSESSMENT USING EI AND CSM METHODS

Erodibility Index Method

The EI method (Annadale, 2006) developed by Annandale (1995) is an empirical method for assessing the potential for scour and erosion of dam foundation, abutment, plunge pool, and unlined spillway materials. Based on approximately 150 field observations and published experimental data, Annandale (1995) established an erosion threshold criterion expressed in terms of the erosive power of the impinging water jet, represented by its Stream Power, P , and the erosion resistance of the rock, represented by an Erodibility Index, K , at the point of impact (Figure 1).

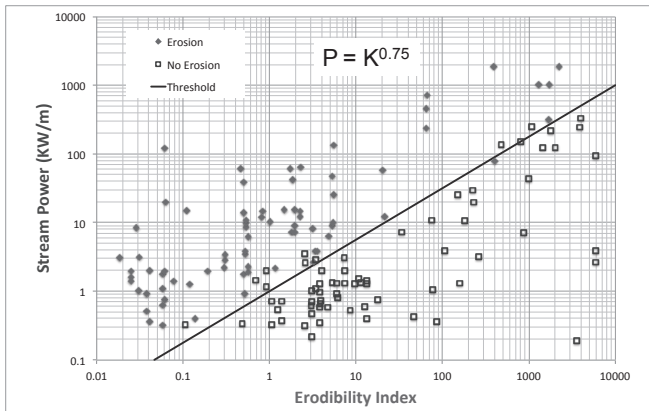


Figure 1. Annandale's Erosion Threshold

The index, K , is expressed as the product of four parameters as:

$$K = M_s K_b K_d J_s \quad (1)$$

K = Erodibility Index (dimensionless)

M_s = Intact Rock Strength Parameter (dimensionless)

K_b = Block Size Parameter (dimensionless)

K_d = Inter-Particle Shear Strength Parameter (dimensionless)

J_s = Relative Orientation Parameter (dimensionless).

The values of these parameters are calculated from field measurements and observations of rock properties (Annandale, 1995). The intact rock strength parameter is equated to its unconfined compressive strength in MPa for strengths greater than 10 MPa. The block size parameter is a function of rock quality (RQD) or a joint set number in the case of rock. The shear strength parameter is a function of a joint roughness number and a joint alteration number in the case of rock. Relative orientation is a function of the relative shape of the rock block, its dip angle, and dip direction relative to the direction of flow (apparent dip).

The erosive stream power of the impinging jet is calculated as (Annandale, 2006):

$$P = \alpha \cdot \frac{\gamma \cdot Q \cdot H}{A} \quad (2)$$

where γ is the unit weight of water (N/m^3), Q is the volumetric discharge rate over dam crest (m^3/s), H is the falling jet head drop (m), A is the jet impact area of (m^2), and α is an adjustment factor accounting for the effects of air entrainment, amplification for closed rock joints, and varying degrees of jet breakup.

Comprehensive Scour Model

Bolleart (2010) developed a CSM for predicting rock scour depth of fissured and jointed rock under a plunge pool based on the geometry, height and erosive power of the falling jet, the depth of the plunge pool, and the joint features of the rock mass. The CSM calculates the ejection of rock blocks due to sudden net uplift impulsions by incorporating the comprehensive fracture mechanics (CFM) that use crack propagation techniques and the dynamic impulsion (DI) method. The fissured rock can fail either by brittle fracture or time-dependent failure. Brittle fracture occurs when the stress intensity in the rock joints (induced by water pressures at the tip of the joint) exceeds the fracture toughness of the rock and is often instantaneous. Time dependant failure is caused by fatigue growth of cracks in the rocks, dependent upon the amplitude of pressure fluctuations, frequency of the loading, and the rock's ability to resist fatigue cracking. Joint application of the EI method and CSM provides improved understanding of rock scour potential and extent.

Example – Tiger Creek Regulator Dam

Tiger Creek Regulator Dam in California is 35m high, 150m long, and has a 40m base width. The dam consists of a concrete slab supported by twenty-three buttresses. It has not undergone any major modifications since its completion in 1931. The dam is underlain by meta-quartz siltstone and phyllite. Meta-quartz siltstone crops out near the left abutment, along the cut slope for the outlet channel, below the left side of the dam at the intersection of the dam and outlet channel, and along the cut for the access road below the outlet channel. The meta-quartz siltstone is generally siliceous, variably fractured, and less foliated (more blocky) than the host phyllite. Phyllite crops out in both abutments, in the bays, and along much of the toe of the dam. The phyllite is generally argillaceous, very closely fractured, flaky and weak to siliceous, moderately fractured and strong. The phyllite has a strongly developed, sub-vertical to vertical dipping, north-northwest trending foliation sub-parallel to the dam axis. Three

sub-orthogonal primary joint sets are present oriented approximately N60°W, sub-vertical, N25°W, sub-vertical, and NS, sub-horizontal. The joints and foliation typically bound rectangular to tabular blocks measured predominately between 0.03m by 0.03m by 0.06m and 3m by 3m by 6m. Data from four exploratory borings and associated laboratory testing, together with field observations, were used to characterize the bedrock properties and compute the index K at eight representative Points of Impact (POI). The data included rock descriptions, structural data, rock quality RQD, unconfined compressive strength. The recovered core indicated that both the meta-quartz siltstone and phyllite was generally slightly to moderately weathered, closely to moderately fractured, and of low to moderate strength. Foliation and joints were generally coated with limonite and/or an orange-brown staining.

The probable maximum flood (PMF) event at the dam results in overtopping the dam by 0.5 m with an overtopping discharge of 90 cubic meters per second. Maximum backwater depth during the PMF is approximately one meter. Since the P at each POI is smaller than the threshold corresponding to the K value at the POI (Figure 1).

ERODIBILITY ASSESSMENT USING ROCK BLOCK THEORY

Goodman and Shi's Block Theory

Goodman and Shi (1985) developed the key block theory for analyzing the stability of rock blocks. Block theory assumes that rock blocks are rigid and formed by fully extended planar joints. Based on the strikes and dips of the rock joint sets, block theory defines the criteria for evaluating whether a rock block is removable. The rock blocks that are readily removable are referred to as key blocks. Goodman and Shi (1985) and Mauldon and Goodman (1996) presented criteria to identify the plausible kinematic translational and rotational models for the removable blocks. Analysis can be performed to evaluate the stability of the rock blocks with respect to the removable modes. George and Sitar (2012) has applied block theory to assess the scouring of unlined rock spillways. Unlike the EI method, the block theory provides a rigorous mechanics and kinematic based framework for dam erodibility analysis.

Example – Relief Dam

Relief Dam is located in the Sierra Nevada of California and is underlain by granitic bedrock. The spillway is located on the left side of the dam and consists of an unlined rock channel with vertical walls approximately 15 meters high. The right wall of the channel is covered with shotcrete. The left wall consists of slightly weathered to fresh, hard, and closely to widely fractured granitic rock. Four main joints sets are present in the wall: two sub-vertical (80 to 90 degree dips) striking north-northwest and northeast; one steeply northwest dipping (45 to 85 degrees) striking north-northeast, and one low-angle exfoliation joint dipping toward the spillway. These joints and the free face of the wall intersect to form unfavorably oriented rock blocks and wedges. The spillway is designed to pass the PMF event with 25 cm of freeboard.

Figure 2 (left) shows block theory analysis using the stereographic projection of the four major joint sets. The results indicated that Blocks A and C (Figure 2 right) is

removable. Based on kinematic analysis, block or wedge failure of Block A is unlikely to occur if the friction angle of Joint Set 1 is greater than 35 degrees (assuming no cohesion). The small block C failed in 2009.

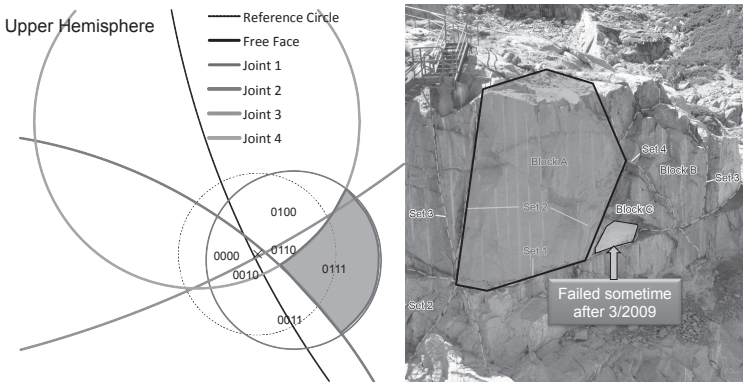


Figure 2. Relief Dam Joint Sets and Removable Block

RELIABILITY ANALYSIS

There are considerable uncertainties associated with rock parameters and hydrologic predictions in dam erodibility analysis. Reliability analysis provides an objective approach to account for uncertainties in the analysis. Reliability, R,

$$R = 1 - p_f \tag{3}$$

where p_f is the probability of failure given by an n-fold integral,

$$p_f = \int_{\Omega} f(\mathbf{x}) d\mathbf{x} \tag{4}$$

where $f(\mathbf{x})$ is the joint probability density function representing the uncertainties and Ω is the part of sample space that dam erosion occurs.

The general-purpose reliability analysis code, such as CALREL (Der Kiureghian, 2008), can be applied to dam erodibility analysis. The user defines the failure criteria in the context of dam erodibility. CALREL is equipped with a large collection of reliability methods. Monte Carlo simulations (MCS) is the most general but computationally intense. The probability of failure is computed by randomly sampling the random variables according to their statistical distributions and counting the percentage of simulations that result in dam erosion:

$$P_f = \frac{1}{n} \sum_{i=1}^n I_G(\underline{x}_i) \tag{5}$$

where n is the number of realizations, I_G is an indicator function ($I_G = 1$ means failure). On the contrary, first-order mean-value second-moment reliability method is commonly used in practice because of its computational efficiency. However, it is

inaccurate if the failure criterion is nonlinear or the statistical information is non-Gaussian.

The first-order reliability method (FORM) treats non-Gaussian model by transforming the random variables into uncorrelated standard normal multivariates. The probability integral (Equation 4) is approximated by linearizing the failure region boundary in the standard normal space at an optimal point (\mathbf{u}^*) (referred to as design point) closest to the origin. The first-order approximation of the failure probability is completely defined by the distance β from the origin. Second-order reliability method (SORM) approximates the failure boundary by a parabolic surface. The accuracy of FORM and SORM depends the shape of the failure boundary.

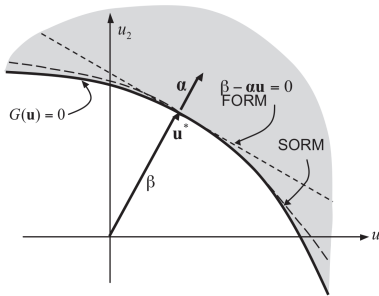


Figure 3: FORM and SORM Approximations

Importance sampling simulation (ISS) method can be used to improve the accuracy of the FORM results. A statistical distribution centered at the design point from FORM is used to generate realizations of random variables.

$$\frac{1}{n} \sum_{i=1}^n I_G(\underline{u}_i) \cdot \frac{\varphi(\underline{u})}{\phi(\underline{u})} \quad (6)$$

where φ is the probability density function (PDF) of the random variables and ϕ is the PDF of the importance sampling distribution. High accuracy can be achieved with a less number of realizations in comparison with the MCS. Importance sampling can be easily adopted to address the uncertainty in Annandale's erosion threshold criterion.

APPLICATION OF LAND-BASED LIDAR TO COLLECT ROCK DATA

Terrestrial LiDAR

Terrestrial LiDAR (Light Detection and Ranging) and digital image processing is increasingly being used for rock mass characterization. LiDAR technology is based on laser rangefinder systems and electronic distance meters. The LiDAR scanner rapidly generates and transmits laser beam pulses along a constantly changing and precisely measured trajectory, as well as timing the round trip of each laser pulse reflected back from objects to the device. The locations of the points where the pulses are reflected can be registered to a referenced coordinate system, and results in a 3-D point cloud containing millions of data points. The scanner can also generate a high-resolution

digital image. The point cloud data can be analyzed to accurately measure several of the rock parameters used in the EI methodology, including block size, inter-particle shear strength (joint separation and roughness), and relative orientation (orientation and spacing of joints). Sections at any orientation and scale can be generated. Detailed, accurate topographic maps, which are often not available for dams, can be generated. LiDAR can reduce the uncertainty inherent in traditional field measurements that results from the natural variability of the parameters, manual measurement methods, and the experience and judgment of the field geologist making the measurements, and can significantly increase the volume of the data which is constrained by the traditional measurement methods and time available in the field. The volume and accuracy of rock data available for an EI evaluation increases the reliability of the results, and allows for cost-effective probabilistic analysis. Terrestrial 3D photogrammetry has also been used to obtain cost-effective statistical information on rock joint properties.

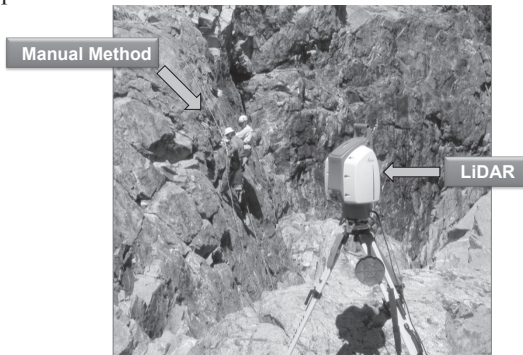


Figure 4. Land-based LiDAR

Example – Spaulding Dam Spillway No. 2

Spaulding Dam No. 2 is located in California. Since construction in 1916, there has been significant scour and erosion of the unlined rock spillway channel, resulting in an eroded slot up to approximately 60 meters deep, and the deposition of a debris fan at the mouth of the slot estimated at approximately 180,000 cubic meter. High Definition targets were placed on known control points to register the individual scans performed to California State Plane coordinates (NAD83/NAVD88, US survey feet). All field work was completed in three days providing a data set that averaged one X,Y,Z point every 1cm on crucial joint faces. Five scanner setups were utilized to obtain the necessary data required for this study. From this model strikes, dips, block sizes, joint spacing, and many other rock parameters can be measured.

ADAPTAIVE RELIABILITY-BASED RISK MANAGEMENT

We are developing a holistic reliability-based decision support framework that utilizes monitoring data to predict future risk and incorporate decision support tools to minimize the predicted risk (Figure 5). Monitoring data not only provide statistical information for conditional prediction of future conditions, but also serve as the basis

for bias correction and for prediction error reduction. Bayesian method provides a logical framework to integrate rain gauge and radar rainfall data for developing stochastic rainfall model that simulates the spatial and temporal characteristics. The monitored rainfall and stream flow data are also used to update the hydrologic model using stochastic updating techniques. It removes model bias and reduces uncertainties associated with model predictions.

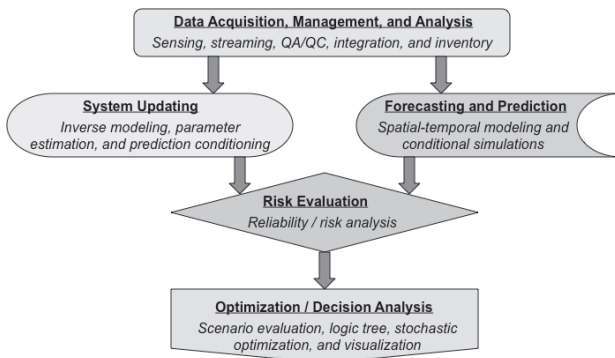


Figure 5: Reliability-Based Decision Support Framework

CONCLUSIONS

Dam Erodibility assessment can be performed using the empirical Erodibility Index method or the Goodman and Shi's block theory. Reliability analysis allows uncertainties to be considered in dam erodibility assessment. Land-based LiDAR is a cost-effective method to obtain rock joint statistics.

REFERENCES

- Annandale, G.W. (1995). Erodibility. *Journal of Hydraulic Research*, Vol. 33, No. 4.
- Annandale, G.W., 2006, *Scour Technology*, 1st Edition, New York: McGraw-Hill, p430
- Bollaert, E.F.R., and Annandale G. W., (2004), Parametric Comparison of Erodibility Index Method and Comprehensive Scour Model, *Int. Conference on Hydraulics of Dams and River Structures*, Tehran, Iran
- George, M.F. and N. Sitar (2012). *Block Theory Application to Scour Assessment of Unlined rock spillways*, UC Berkeley Report No. UCB GT 12-02
- Goodman, R. E., and Shi, G. 1985. *Block Theory and Its Application to Rock Engineering*. Prentice Hall. Englewood Cliffs, N.J.
- Mauldon, M. and Goodman, R. 1996. Vector analysis of keyblock rotations. *J. of Geotech. Eng.*, 122:12, 976-987.
- Der Kiureghian, A. (2008). – First- and second-order reliability methods, in Nikolaidis, E., D.M. Ghiocel, and S. Singhai, eds, *Engineering Design Reliability Handbook*, Chapter 14, CRC Press, Boca Raton, FL.